NASA Conference Publication 3186

Flight Mechanics/Estimation Theory Symposium 1992

Proceedings of a symposium held at Goddard Space Flight Center May 5–7, 1992

NASA

NASA Conference Publication 3186

Flight Mechanics/Estimation Theory Symposium 1992

Thomas H. Stengle, *Editor*
Goddard Space Flight Center
Greenbelt, Maryland

Proceedings of a symposium sponsored by
NASA Goddard Space Flight Center and held at
Goddard Space Flight Center
Greenbelt, Maryland
May 5–7, 1992

NASA
National Aeronautics and
Space Administration
Office of Management
Scientific and Technical
Information Program
1993

FOREWORD

The papers presented here have been derived primarily from speakers' summaries of talks presented at the Flight Mechanics/Estimation theory Symposium held May 5-7, 1992 at Goddard Space flight Center. For completeness, abstracts are included of those talks for which summaries were unavailable at press time. Papers included in this document are presented as received from the authors with little or no editing.

CONTENTS

SESSION 3

SESSION 4

SESSION 5

SESSION 6

FLIGHT MECHANICS/ESTIMATION THEORY SYMPOSIUM

MAY 5-7, 1992

SESSION 1

157721

MOMENTUM ACCUMULATION DUE TO SOLAR RADIATION TORQUE, AND REACTION WHEEL SIZING, WITH CONFIGURATION OPTIMIZATION

N93-24695

Hari B. Hablani†
Rockwell International, Space Systems Division, Seal Beach, CA 90740

Abstract

This paper has a two-fold objective: determination of yearly momentum accumulation due to solar radiation pressure, and optimum reaction wheel sizing. The first objective is confronted while determining propellant consumption by the attitude control system over a spacecraft's lifetime. This, however, cannot be obtained from the daily momentum accumulation and treating that constant throughout the year, because the orientation of the solar arrays relative to the spacecraft changes over a wide range in a year, particularly if the spacecraft has two arrays, one normal and the other off-normal to different extent at different times to the sun rays . The paper therefore first develops commands for the arrays for tracking the sun, the arrays articulated to earth-pointing spacecraft with two rotational degrees of freedom and spacecraft in an arbitrary circular orbit. After developing expressions for solar radiation torque due to one or both arrays, arranged symmetrically or asymmetrically relative to the spacecraft bus, momentum accumulation over an orbit and then over a year are determined. The remainder of the paper is concerned with designing reaction wheel configurations. Four-, six-, and three-wheel configurations are considered, and for given torque and momentum requirements, their cant angles with the roll/yaw plane are optimized for minimum power consumption. Finally, their momentum and torque capacities are determined for one-wheel failure scenario, and six configurations are compared and contrasted.

1. Introduction

This paper is concerned with: a) determination of momentum accumulation due to solar radiation torque acting on an earth-observing spacecraft with sun-pointing solar arrays, and b) reaction wheel sizing and its pyramid configuration optimization for maximum momentum storage and minimum power consumption. These topics are classical; yet it seems there is no single reference in the published literature that treats this subject with sufficient comprehensiveness so that a control engineer, confronting this task, could accurately size the reaction wheels, select a wheel configuration, and estimate yearly propellant consumption for momentum dumping, all without extensive or expensive computer simulation. This paper, hopefully, fulfills that need. The contents of the paper and related previous contributions known to this author are summarized below.

Solar arrays' influence on spacecraft configuration, attitude control system, and mission operation is so far-reaching that a brief elaboration of this topic appears in order. For an earth-pointing three-axis stabilized spacecraft rotating once per orbit about the orbit normal, an attached solar array must at least have one relative rotational degree of freedom about the orbit normal so that the array can be held inertially fixed and sun-pointing. Although economical, this arrangement becomes inadequate if the spacecraft's life span is more than several (say, six) months, because in this duration the earth moves around the sun in the ecliptic plane so much that the sun-rays deviate significantly away from the array normal and therefore a considerable power loss begins to occur. Consequently, for spacecraft with one year or longer life span, the solar array is accorded a second degree of freedom in the form of spacecraft yaw rotation. If the spacecraft at hand has only one solar array, this yaw rotation is of 180 degrees and may take place once in six months when the off-normality between the sun-rays and the array on one side of the orbit plane exceeds limits. The 180-degree rotation takes the solar array to the other side of the orbit plane where the off-normality in the following six months will be smaller. Although to minimize cost and to gain simplicity, there are many spacecraft with one solar array (TOPEX for example), this configuration is asymmetric and might generate significant disturbance torques on the spacecraft arising from solar radiation pressure, gravity gradient, atmospheric drag, and thermal shocks at each sun-rise and sun-set; savings are therefore somewhat offset by stronger control torque requirements. To eliminate this asymmetry and/or to generate enough power for on-orbit needs, two solar arrays, one on each side of the orbit normal, are sometimes employed. Then, instead of once in six months, a yaw rotation from zero to 2π or from $-\pi/2$ to $+\pi/2$ takes place as continuously as one about the orbit normal. The corresponding sun-tracking commands were derived by McElvain (1961)[1] and Kalweit (1983)[2]. GPS satellites have opted for this approach. Although TOPEX satellite has one solar array, it also employs continuous yaw rotation instead of 180° yaw rotation. Some missions are not interfered with by these persistent yaw rotations, but others are. For these latter situations, Kalweit[2] has determined best-fit minimum-power-loss, average yaw angles, constant over each half orbit. Nonetheless, persistent yaw rotation of a spacecraft is cumbersome because the torque and momentum capacity of the reaction wheels, usually employed for attitude control, must now accommodate the yaw rotation. A superior alternative appears to be, at least on the basis of technical merits if not cost, to bestow each array with two rotational degrees of freedom relative to the spacecraft, one about the orbit normal and the other about an axis in the orbit plane. Such is the spacecraft configuration considered in this paper; that is, a spacecraft with two solar arrays, arranged symmetrically on each side of the orbit normal and each array having two articulation degrees of freedom. Section 2 of the paper furnishes sun-tracking commands about the two just-mentioned axes. Explicit relationship is furnished between the so-called beta angle (also called flap angle) of the array and parameters such as earth's position in the ecliptic plane, the angle between the ecliptic and the equator planes, inclination of the spacecraft orbit, and its ascending node angle.

†*Senior Member AIAA, Senior Engineering Specialist; Guidance, Control, and Navigation Group*

Turning our attention to solar radiation torque on a space vehicle, this arises from arrays as well as the vehicle bus. Moreover, of the two arrays, one may be normal to the sun while the other may be off-normal (thermal requirements may dictate so), and the bus and the arrays may cast shadow on each other at different times, changing the lit area, center of pressure, and moment arm from the vehicle mass center to the pressure center; see an example of shadowing in Evans (1964)[3]. These complex effects are formulated and illustrated in Section 3. For typical spacecraft however, the torque contribution of the bus and the shadow effects are secondary; so by ignoring them, simple radiation torque expressions for arrays normal as well as off-normal to the sun are obtained which are used in Section 4 to determine secular and cyclic momentum accumulation in the roll-yaw plane and about the pitch axis. Because of significant variation in the array's flap angle over a year, the corresponding momentum accumulation over each orbit changes considerably, particularly if the array is positioned off-normal to the sun. A simple expression of annual, secular momentum accumulation is therefore developed and illustrated in Section 4, and its dependence on the orbit inclination is investigated. From this result, yearly propellant consumption for momentum dumping is determined easily. DeBra and Cannon (1961)[4] have also performed preliminary analysis along these lines.

Section 5 of the paper is concerned with sizing reaction wheels and optimizing their pyramid configuration, keeping cost and redundancy in mind. Four-, six-, and three-wheel configurations with and without one wheel failure are considered. Optimum cant angles for these pyramid configurations for minimum power consumption and for given ratios between the roll, pitch, and yaw torque requirements are determined. Simple relationships are developed relating momentum or torque requirements about spacecraft axes to those about the wheel axes for all configurations with and without one wheel failure. These relationships then provide the required momentum and torque capacities of the wheels. The paper is finally concluded in Section 6.

2. Commands for Sun-Tracking

Coordinate Transformations

In order to express sun-ray direction from the sun to the Earth in terms of solar arrays' frames, and to develop pointing commands for the arrays for tracking the sun,the following angles, all anticlockwise positive unless stated otherwise, are introduced. The angle ν, measured from the the first day of *autumn* (September 23), denotes the earth's rotation around the sun in the ecliptic plane. The *clockwise* positive angle λ (= 23.44 degrees) about the Vernal Equinox is the angle between the ecliptic and the equatorial plane. The angle Ω_N and i are, respectively, the usual ascending node angle of the spacecraft orbit in the equatorial plane and the orbit inclination angle from the equatorial plane. In this paper we will be concerned exclusively with circular spacecraft orbit. The local-vertical-local-horizontal (LVLH) frame $\mathcal{F}^c$: $X_c\ Y_c\ Z_c$ at any point in the orbit locates the spacecraft mass center with X_c along the velocity vector of the spacecraft, Z_c along the local vertical from spacecraft to the earth, and Y_c opposite to the orbit normal. To maintain the earth-pointing attitude, the spacecraft rotates clockwise about Y_c-axis at the rate $-\omega_0$ (ω_0 thus is a positive quantity and it equals the orbit rate of the spacecraft). The frame $\mathcal{F}^c$ is the standard roll, pitch, yaw frame of a spacecraft with these three attitude angles zero. When the angles are nonzero, the spacecraft frame is denoted $\mathcal{F}^0$: $X_0\ Y_0\ Z_0$, as shown in Fig. 1. In this paper however, we assume that the spacecraft is controlled perfectly, and it always maintains its ideal LVLH orientation.

We now define the orientation of the solar arrays relative to the frame $\mathcal{F}^c$ or, equivalently, $\mathcal{F}^0$. As stated in the Introduction and portrayed in Fig. 1, the two arrays turn relative to the spacecraft at the two-degree-of-freedom hinges O_1 and O_2. Considering +y-array first, its relative rotation is measured from the frame $X_{10}\ Y_{10}\ Z_{10}$ which is parallel to the spacecraft frame $\mathcal{F}^0$. In order to track the sun, the first rotation of the array is θ_{1y} about the longitudinal axis y_{10}; this rotation annuls the clockwise rotation $\omega_0 t$ of the earth-pointing spacecraft measured from the ascending node line. The second rotation (often called beta angle), denoted here θ_{1z}, takes place about the once-displaced Z_{10}-axis. We thus arrive at the array-fixed frame $\mathcal{F}^1$: $X_1\ Y_1\ Z_1$, with the array in the Y_1Z_1 plane and its outward normal along X_1. Note that when the array is normal to the sun, the sun vector $\underline{S}$ from the sun to the earth is opposite to the array normal X_1. The transformation between the frame $\mathcal{F}^0$ and the array frame $\mathcal{F}^1$ for the sequence θ_{1y}, θ_{1z} is

$$\begin{bmatrix} X_0 \\ Y_0 \\ Z_0 \end{bmatrix} = \begin{bmatrix} c\theta_{1y}\, c\theta_{1z} & -c\theta_{1y}\, s\theta_{1z} & s\theta_{1y} \\ s\theta_{1z} & c\theta_{1z} & 0 \\ -s\theta_{1y}\, c\theta_{1z} & s\theta_{1y}\, s\theta_{1z} & c\theta_{1y} \end{bmatrix} \begin{bmatrix} X_1 \\ Y_1 \\ Z_1 \end{bmatrix} \tag{1}$$

where $c(\bullet) = \cos(\bullet)$ and $s(\bullet) = \sin(\bullet)$. The initial orientation of the $-$y-array is the same as that of the +y-array, and the rotations of the $-$y array are conveniently measured relative to the frame $X_{20}Y_{20}Z_{20}$ with Y_{20} opposite to Y_0 and Z_{20} opposite to Z_0. The frame $X_{20}Y_{20}Z_{20}$ is selected such that the solar cell face of both arrays are on the same side. The first rotation θ_{2y} about the Y_{20}-axis (Fig. 1) nullifies the orbit rotation, and the rotation θ_{2z} about the edge Z_2 brings the array to the desired normal orientation relative to the sun. The transformation matrix from the spacecraft frame $\mathcal{F}^0$ to the array-fixed frame $\mathcal{F}^2$: $X_2Y_2Z_2$ is

$$\begin{bmatrix} X_0 \\ Y_0 \\ Z_0 \end{bmatrix} = \begin{bmatrix} c\theta_{2z}\, c\theta_{2y} & -s\theta_{2z}\, c\theta_{2y} & s\theta_{2y} \\ -s\theta_{2z} & -c\theta_{2z} & 0 \\ c\theta_{2z}\, s\theta_{2y} & -s\theta_{2z}\, s\theta_{2y} & -c\theta_{2y} \end{bmatrix} \begin{bmatrix} X_2 \\ Y_2 \\ Z_2 \end{bmatrix} \tag{2}$$

Commands For Sun-Tracking

Because the solar arrays are hinged to the spacecraft, it is helpful to express the unit vector $\underline{S}$ from the Sun to the Earth in the spacecraft frame $\mathcal{F}^0$, or equivalently, in the orbit frame $\mathcal{F}^c$. Let S_{c1}, S_{c2}, and S_{c3} be the components of $\underline{S}$ in $\mathcal{F}^c$. Then, using coordinate transformations involving the angles ν, λ, Ω_N, i, and $\omega_0 t$, defined above, these components are found to be

$$\begin{aligned} S_{c1} &= c\omega_0 t\ \{ci(-s\Omega_N c\nu + c\Omega_N c\lambda s\nu) + sis\lambda s\nu\} \\ &\quad -s\omega_0 t(c\Omega_N c\nu + s\Omega_N\, c\lambda s\nu) \\ S_{c2} &= si(-s\Omega_N c\nu + c\Omega_N c\lambda s\nu) - cis\lambda s\nu \\ S_{c3} &= -s\omega_0 t\ \{ci(-s\Omega_N c\nu + c\Omega_N c\lambda s\nu) + sis\lambda s\nu\} \\ &\quad -c\omega_0 t(c\Omega_N c\nu + s\Omega_N\, c\lambda s\nu) \end{aligned} \tag{3}$$

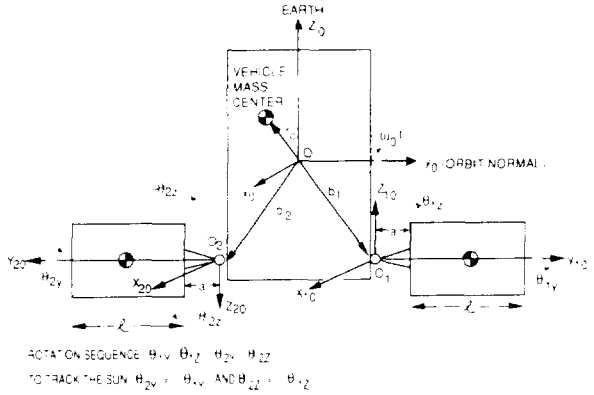

Fig. 1. A Spacecraft with +Y and -Y Arrays, their Frames, and Articulation Degrees of Freedom

+Y-Array Commands

Because the first rotation θ_{1y} about the longitudinal axis y_{10} annuls the once-per-orbit rotation of the earth-pointing spacecraft, it may be clear that, ideally,

$$\theta_{1y}(t) = \omega_0 t + \theta_{10} \tag{4}$$

where θ_{10} is $\theta_{1y}(t=0)$. Note that $\theta_{1y}(t)$ is anticlockwise positive, whereas the negative sign of $\omega_0 t$ has already been accounted for in (3), so $\omega_0 t$ in Eq. (4) is positive: $\omega_0 t \geq 0$. To determine θ_{10} and the second rotation θ_{1z}, we observe that when the array is normal to the sun, the incoming sun vector $\underline{S}$ is opposite to the outgoing array normal X_1:

$$\underline{S}^{\mathcal{F}1} = [\, X_1 \;\; Y_1 \;\; Z_1 \,]^T = [\, -1 \;\; 0 \;\; 0 \,]^T \tag{5}$$

where the superscript T means the transpose of the column vector. Substituting Eq. (5) in Eq. (1) the sun-ray vector $\underline{S}$ in the LVLH frame is found to be

$$\begin{bmatrix} S_{c1} \\ S_{c2} \\ S_{c3} \end{bmatrix}^{\mathcal{F}0} = \begin{bmatrix} -c\theta_{1y}\, c\theta_{1z} \\ -s\theta_{1z} \\ s\theta_{1y}\, c\theta_{1z} \end{bmatrix} \tag{6}$$

The unknown initial angle θ_{10} is determined by substituting Eq. (4) in Eq. (6), yielding:

$$\theta_{10} = \tan^{-1} \frac{-[\, c\Omega_N\, cv + s\Omega_N\, c\lambda\, sv \,]}{-[\, ci\,(-s\Omega_N\, cv + c\Omega_N\, c\lambda\, sv) + si\, s\lambda\, sv \,]} \tag{7}$$

where the negative signs in the numerator and denominator are retained so as to arrive at a unique value of θ_{10} within the range $-\pi \leq \theta_{10} \leq \pi$; this will ensure that the solar cell face of the array looks at the sun. The array's inclination angle θ_{1Z} is obtained from the second components of Eqs. (3) and (6):

$$\theta_{1Z} = \sin^{-1} [\, si\,(s\Omega_N\, cv - c\Omega_N\, c\lambda\, sv) + ci\, s\lambda\, sv \,] \tag{8}$$

Eq. (8) indicates that, as the earth rotates around the sun ($0 \leq v \leq 2\pi$), the angle θ_{1z} varies sinusoidally with a certain amplitude; this is illustrated below in three examples.

Example 1: $\Omega_N = 0$, $v = \pi/2$

The correctness of Eq. (7) and Eq. (8) can be illustrated by considering $v = \pi/2$ and $\Omega_N = 0°$ for which

$$\theta_{10} = \tan^{-1} \; 0 / [\, -c\,(\lambda - i) \,] \;\; = \pi \tag{9a}$$

$$\theta_{1z} = \lambda - i \tag{9b}$$

If we further assume that the satellite orbit lies in the ecliptic plane, which means the orbit inclination i equals λ, we will have $\theta_{1Z} = 0$. In Eq. (9a), the choice $\theta_{10} = \pi$ and not zero is selected to ensure that the solar cell face of the array, not its back side, is towards the sun. Moreover, Eq. (9a) and $\theta_{1Z} = 0$ together imply that in order to be normal to the sun rays at $t = 0$, the array must be in the plane $Y_c\, Z_c$. Physically, the conclusion $\theta_{10} = \pm\pi$ and $\theta_{1z} = 0$ is seen to be valid in Fig. 2 for the parameters $v = \pi/2$, $\Omega_N = 0$, and $i = \lambda$ at $t = 0$.

Example 2: $\Omega_N = 0$, and arbitrary v

For $\Omega_N = 0$, Eq. (7) and Eq. (8) yield

$$\theta_{10} = \tan^{-1} \frac{-cv}{-c\,(\lambda - i)\, sv}, \quad \theta_{1z} = \sin^{-1} [\, \sin v \, \sin(\lambda - i) \,] \tag{10a,b}$$

Eq. (10b) states that, inasmuch as $(\lambda - i)$ is fixed, the angle θ_{1z} will change periodically as the earth moves around the sun in one year, $0 \leq v \leq 2\pi$; the extremes of θ_{1z} will be $(\lambda - i)$ when $v = \pi/2$, and $(i - \lambda)$ when $v = 3\pi/2$. This is illustrated in Fig. 3 for $i = 28.5°$ and $43.5°$. Now considering the satellite orbit in the ecliptic plane ($\lambda = i$), Eqs. (10) simplify and, consistent with Example 1, furnish

$$\theta_{10} = -\pi/2 - v \tag{11a}$$

$$\theta_{1y}(t) = \omega_0 t - (\pi/2 + v) \tag{11b}$$

For $v = 0$, +y array's rotation $\theta_{10} = -\pi/2$ about the axis Y_c, measured from its datum orientation in the $Y_c Z_c$ plane, is illustrated in Fig. 2. Also, for $\Omega_N = 0$ and $i = 28.5°$ the linear relationship (11a) is seen to be true in Fig. 3.

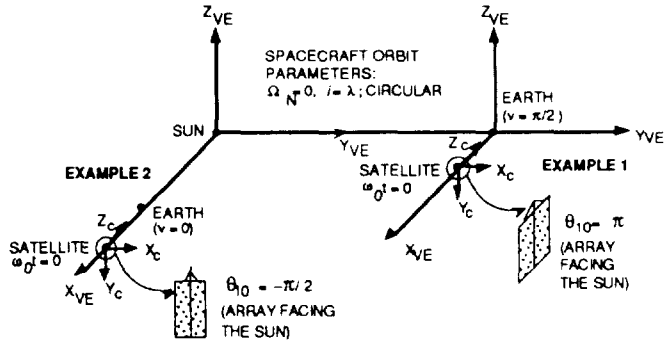

Fig. 2. +y Solar Array Orientations at t=0 for Examples 1 and 2 (VE = Vernal Equinox)

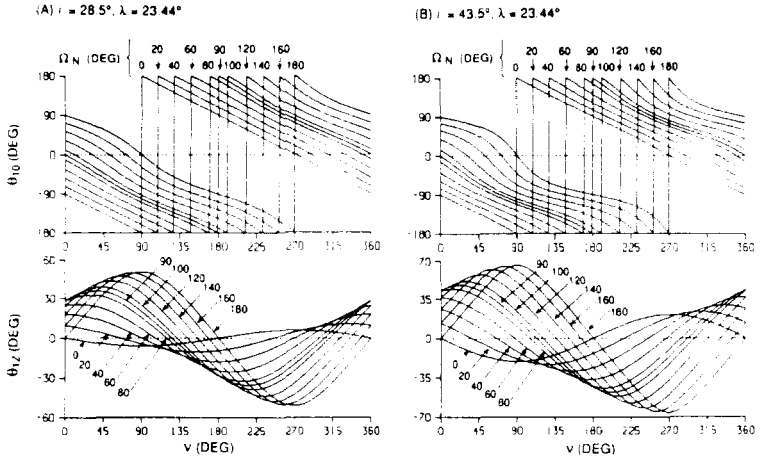

Fig. 3. Initial Angle θ_{10} about the pitch axis y_0 and inclination angle θ_{1Z} about the short edge Z_1-axis of +y array versus angle ν

Table 1. Extrema of the tilt angle θ_{1Z}

Earth's Position in the Ecliptic Plane (ν,deg)	Ascending Node Angle of the Spacecraft's Orbit (Ω_N, deg)	Extreme Value of θ_{1Z}
90°	0 °	λ–i
90°	180 °	λ+i
-90° (or 270°)	0 °	i–λ
-90° (or 270°)	180 °	–λ–i

Example 3: Arbitrary Ω_N and ν

Fig. 3 illustrates the variation of θ_{10} and θ_{1Z} as a function of the earth's position in the ecliptic plane ($0 \le \nu \le 2\pi$) for i = 28.5° and 43.5° and eleven values of the ascending node angle Ω_N. The apparent discontinuities in θ_{10} curves at $\pm\pi$ are inconsequential because the angle θ_{10} has a range of 2π and $+\pi = -\pi$. Furthermore, from Eq. (8), we infer that

$$\text{for } \Omega_N = \pi: \quad \theta_{1Z} = \sin^{-1}[\, s\,(\lambda+i)\, s\nu \,] \tag{12}$$

which is a counterpart of Eq. (10b) in Example 2. Clearly, the extremes of θ_{1Z} are

$$\theta_{1Z} = \begin{cases} \lambda+i \;@\; \nu = \pi/2 \\ -(\lambda+i) \;@\; \nu = 3\pi/2 \end{cases} \tag{13}$$

These, as well as the sinusoidal variation of the angle θ_{1Z} versus ν, are illustrated in Fig. 3. Also, see Table 1.

-Y Array Commands

Regarding the -y-array, because the angles θ_{2y} and θ_{2Z} are defined about the axes Y_{20} and Z_{20} which are respectively opposite to the +y-array axes Y_{10} and Z_{10}, it is clear that for keeping the array normal to the sun-rays

$$\theta_{2y} = -\theta_{1y} \tag{14a}$$
$$\theta_{2z} = -\theta_{1z} \tag{14b}$$

Recalling Eq. (4), the desired $\theta_{2y}(t)$ will therefore be

$$\theta_{2y}(t) = -\omega_0 t - \theta_{10} \tag{15}$$

It is instructive to compare the commands developed above with those developed by McElvain[1] and Kalweit[2].

3. Solar Radiation Torque

Radiation Torque on a Solar Array

For momentum accumulation study, the radiation torque $\underline{g}$ at the spacecraft mass center is required. Referring to Fig. 1, let $\underline{b}_j$ (j = 1,2) be the vector from the reference origin O to the solar array hinge O_j (j = 1,2), and $\underline{\rho}_{pj}$ (j = 1,2) the vector from the hinge O_j to the pressure (or geometric) center of the array. Additionally, let $\underline{r}_c$ be the vector from the reference origin to the vehicle mass center. Denote the moment arm vector of the solar radiation force on the j-array as $\underline{c}_{pj}$. Then,

$$\underline{c}_{pj} \triangleq -\underline{r}_c + \underline{b}_j + \underline{C}_{0j}\, \underline{\rho}_{pj} \qquad (j = 1,2) \tag{16}$$

where $\underline{C}_{0j}$ is the transformation matrix defined by Eq. (1) and Eq. (2) for j=1.2. Following Reference 5, Section 8.3, the radiation torque experienced by a spacecraft about its mass center owing to the sun rays off-normal to the jth-array, is

$$\underline{g}_j = pA_j c\alpha_j \underline{c}_{pj}^{\times} [\, (\sigma_a + \sigma_{rd})\, \underline{S} + 2\,(\sigma_{rd}/3 + \sigma_{rs}\, c\alpha_j)\, \underline{n}_{Aj} \,] \quad (j=1,2) \tag{17}$$

where p denotes the radiation pressure on a totally absorbing normal surface, A_j is the array's area, $c\alpha_j = \cos\alpha_j$ and α_j is the angle between the inward normal unit vector $\underline{n}_{A_j}$ and the sun vector $\underline{S}$, σ_a is the absorptivity coefficient of the surface under consideration, σ_{rd} is the diffused reflectivity coefficient, and σ_{rs} the specular reflectivity coefficient. The notation × in Eq. (17) transforms a column vector to a 3x3 skew-symmetric matrix, as defined by Eq. (13), Section B.2, Reference 5.

Array Normal to the Sun

When the sun rays are normal to the j^{th} array, $c\alpha_j = 0$, and $\underline{n}_{Aj} = \underline{S}$ and Eq. (17) simplifies to

$$\underline{g}_j = p A_j \sigma_A \underline{\rho}_{pj}^{\times} \underline{S} \tag{18}$$

where

$$\sigma_A = 1 + \sigma_{rs} + 2\sigma_{rd}/3 \tag{19}$$

The three components of the radiation torque, Eq. (18), on the spacecraft in an arbitrary orbit, with the array normal to the sun, will now be shown explicitly. For concreteness, we assume that the spacecraft mission is such that the power and thermal requirements allow the +y-array to be normal to the sun. To express the vector $\underline{\rho}_{p1}$ component-wise, note that the length of the A-frame along the pitch axis is 'a' (Fig. 1), and the rotation θ_{1z} takes place about the Z_1-axis of the array without involving the A-frame. Because in the $X_1Y_1Z_1$ frame, the pressure center of the array is at a distance $\ell/2$ along the y_1-axis from the transverse edge of the array (Fig. 1), the vector $\underline{C}_{01}\,\underline{\rho}_{p1}$ in Eq. (16) can be calculated easily using Eq. (1). Furthermore, we assume that when the arrays are in the y_0z_0 plane ($\theta_{1z} = 0 = \theta_{2z}$), the vectors $\underline{r}_c$ and $\underline{b}_1$ are in that plane (Fig. 1). Therefore, in the LVLH frame $\mathcal{F}^c$:

$$-\underline{r}_c + \underline{b}_1 = [\,0 \qquad -r_{cy}+b_{1y} \qquad -r_{cz}+b_{1z}\,]^T \tag{20}$$

The vector $\underline{\rho}_{p1}$, Eq. (16), will therefore be

$$\underline{\rho}_{p1} = \begin{bmatrix} -b\, s\theta_{1z}\, c\theta_{1y} \\ -r_{cy} + b_{1y} + a + b\, c\theta_{1z} \\ -r_{cz} + b_{1z} \qquad +b\, s\theta_{1z} s\theta_{1y} \end{bmatrix}, \quad b \triangleq \ell/2 \tag{21}$$

For analytical convenience, define

$$b_{1y}^{\oplus} = -r_{cy} + b_{1y} + a \qquad b_{1z}^{\oplus} = -r_{cz} + b_{1z} \tag{22}$$

Using (21), (22)in Eq. (18) the following components of the torque $\underline{g}_1$ in the LVLH frame are obtained:

$$\underline{g}_1 = p A_1 \sigma_A \begin{bmatrix} b_{1z}^{\oplus}\, s\theta_{1z} + (b + b_{1y}^{\oplus} c\theta_{1z})\, s\theta_{1y} \\ -b_{1z}^{\oplus} c\theta_{1z}\, c\theta_{1y} \\ (b + b_{1y}^{\oplus} c\theta_{1z})\, c\theta_{1y} \end{bmatrix}^{\mathcal{F}_c} \tag{23}$$

While the angle $\theta_{1y}(t)$ varies linearly at the rate ω_o, changing by 2π over one orbital period, the angle θ_{1z} is virtually constant in that period. Eq. (23) therefore indicates that, in the LVLH frame, the roll (x-) torque comprises a constant and a cyclic torque, the pitch and yaw torques are cyclic, and the cyclic yaw torque is in quadrature with the cyclic component of the roll torque. (Also, see Ref. 4.)

–Y-Array Off-Normal To The Sun

When the spacecraft at hand has two arrays, power and thermal requirements might dictate one array to be normal to the sun rays and the other array off-normal. Fig. 4 depicts one such posture for the spacecraft in Fig. 1, with +Y-array normal and –Y-array off-normal.

To keep the mass center of the –y-array on the rotational axis y_0, the A-frame is turned about the z_2-axis by an angle $\theta_{2z,a}$ (a negative $\theta_{2z,a}$ is shown in Fig. 4); also, the array's normal-to-the-sun orientation angle is denoted θ_{2z}, whereas the off-normal orientation angle is denoted θ_{2z}'. Under these circumstances, the transformation matrix $\underline{C}_{02}$, defined by Eq. (2), is altered to $\underline{C}_{02,A}$ for the A-frame replacing θ_{2z} with $\theta_{2z,a}$, and to $\underline{C}_{02}'$ for the –y-array substituting θ_{2z}' for θ_{2z}.

Thus the pressure center vector $\underline{C}_{02}\,\underline{\rho}_{p2}$ in Eq. (16) is revised to

$$\underline{C}_{02}\,\underline{\rho}_{p2} = = a \begin{bmatrix} -s\theta_{2z,a}\, c\theta_{2y} \\ -c\theta_{2z,a} \\ -s\theta_{2z,a}\, s\theta_{2y} \end{bmatrix} + b \begin{bmatrix} -s\theta_{2z}'\, c\theta_{2y} \\ -c\theta_{2z}' \\ -s\theta_{2z}'\, s\theta_{2y} \end{bmatrix} \tag{24}$$

To evaluate the torque $\underline{g}_j$ (j=2), we note that the vector $-\underline{r}_c + \underline{b}_2$ for the –y-array in the frame $\mathcal{F}^c$ is, following Eq. (20)

$$-\underline{r}_c + \underline{b}_2 = [\,0 \qquad -r_{cy} + b_{2y} \qquad -r_{cz} + b_{2z}\,]^T \tag{25}$$

where, to symmetrize the mass distribution

$$b_{2y} = -b_{1y} \qquad b_{2z} = b_{1z} \tag{26}$$

Using the equation $\theta_{2y} = -\theta_{1y}$ and Eqs. (24), (25), and (26), the vector $\underline{\rho}_{pj}$ (j = 2), Eq. (16), is found to be

$$\underline{\rho}_{p2} = \begin{bmatrix} -b_s\, c\theta_{1y} \\ -r_{cy} - b_{1y} - b_c \\ -r_{cz} + b_{1z} + b_s\, s\theta_{1y} \end{bmatrix}^{\mathcal{F}^c} = \begin{bmatrix} c_{p2x} \\ c_{p2y} \\ c_{p2z} \end{bmatrix}^{\mathcal{F}^c} \tag{27}$$

where the lengths b_c and b_s are defined as

$$\begin{aligned} b_c &= a\, c\theta_{2z,a} + b\, c\theta_{2z}' \\ b_s &= a\, s\theta_{2z,a} + b\, s\theta_{2z}' \end{aligned} \tag{28}$$

The vector $\underline{S}$ and the inward normal $\underline{n}_A$ for the –y-array in the off-normal frame $\mathcal{F}^{2A}$: $X_{2A}\, Y_{2A}\, Z_{2A}$ (Fig. 4) are

$$\underline{S}^{\mathcal{F}^{2A}} = [-c\delta_{2z} \quad -s\delta_{2z} \quad 0\,]^T, \quad \underline{n}_A^{\mathcal{F}^{2A}} = [\,-1 \quad 0 \quad 0\,]^T \tag{29}$$

where δ_{2z} is the off-normal angle, defined by

$$\delta_{2z} = \theta_{2z} - \theta_{2z}' \tag{30}$$

and equal to the angle α_2 between the vectors $\underline{S}$ and $\underline{n}_A$ for the array. Therefore the vector [•] in (17) the spacecraft frame is found to be

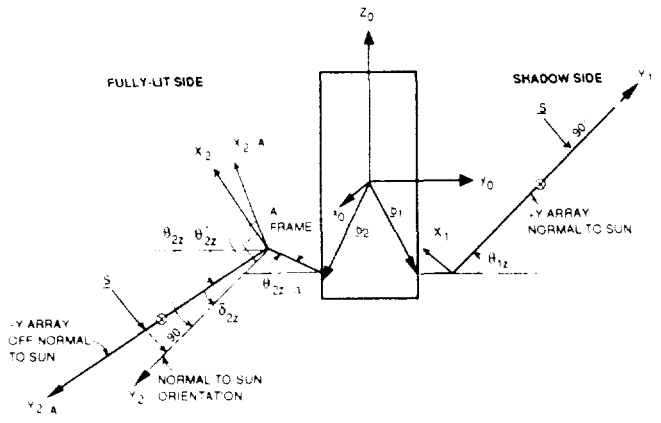

Fig. 4. A Spacecraft With +Y Array Normal to the Sun and -Y Array Off-Normal

$$[\,(\sigma_a + \sigma_{rd})\,\underline{S} + 2\,(\sigma_{rd}/3 + \sigma_{rs}\,c\alpha_2)\,\underline{n}_A\,]^{\mathcal{F}^0} = [\,-\sigma_{cx}\,c\theta_{2y} \quad \sigma_{cy} \quad -\sigma_{cx}\,s\theta_{2y}\,]^T \tag{31}$$

where

$$\begin{aligned}\sigma_{cx} &= \sigma_{x2}\,c\theta_{2z}' - \sigma_{y2}\,s\theta_{2z}'\\ \sigma_{cy} &= \sigma_{x2}\,s\theta_{2z}' + \sigma_{y2}\,c\theta_{2z}'\\ \sigma_{x2} &= (1+\sigma_{rs})\,c\delta_{2z} + 2\sigma_{rd}/3\\ \sigma_{y2} &= (1-\sigma_{rs})\,s\delta_{2z}\end{aligned} \tag{32}$$

Using the vector $\underline{c}_{p2}$ in Eq. (27) and the vector Eq. (31) the torque $\underline{g}_2$ is found to be

$$\underline{g}_2{}^{\mathcal{F}^c} = pA_2\,c\delta_{2z}$$

$$\begin{bmatrix} -(-r_{cz}+b_{1z})\,\sigma_{cy} - \{b_s\,\sigma_{cy} + (r_{cy}+b_{1y}+b_c)\,\sigma_{cx}\}\,s\theta_{1y} \\ -(-r_{cz}+b_{1z}) \quad \sigma_{cx}\}\,c\theta_{1y} \\ -\{b_s\,\sigma_{cy} + (r_{cy}+b_{1y}+b_c)\,\sigma_{cx}\}\,c\theta_{1y} \end{bmatrix} \tag{33}$$

which exhibits the same attributes as those exhibited by $\underline{g}_1$ in Eq. (23).

Example 1: Off-Normal Angle $\delta_{2z} = 0$ and A-Frame Angle $\theta_{2z,a} = 0$

In this circumstance, the +y- and -y-array become parallel because now $\theta_{2z}' = -\theta_{1z}$, and the torque $\underline{g}_2{}^{Fc}$, Eq. (33), simplifies to

$$\underline{g}_2{}^{\mathcal{F}^c} = pA_2\,\sigma_A \begin{bmatrix} b_{2z}^{\oplus}\,s\theta_{1z} + (-b + b_{2y}^{\oplus}\,c\theta_{1z})\,s\theta_{1y} \\ -b_{2z}^{\oplus}\,c\theta_{1z}\,c\theta_{1y} \\ (-b + b_{2y}^{\oplus}\,c\theta_{1z})\,c\theta_{1y} \end{bmatrix} \tag{34}$$

where

$$b_{2y}{}^{\oplus} = -r_{cy} - b_{1y} - a \qquad b_{2z}{}^{\oplus} = b_{1z}{}^{\oplus} \tag{35}$$

Example 2: Both Arrays Normal to the Sun: Resultant Torque

Adding Eq. (34) to Eq. (23), and assuming that the arrays are identical in geometry as well as in optical surface properties so that $A_s = A_1 = A_2$, the resultant torque $\underline{g}$ equal to $\underline{g}_1 + \underline{g}_2$) is found to be

$$\underline{g}^{\mathcal{F}^c} = 2pA_s\,\sigma_A \begin{bmatrix} (-r_{cz}+b_{1z})\,s\theta_{1z} - r_{cy}\,c\theta_{1z}\,s\theta_{1y} \\ (r_{cz}-b_{1z})\,c\theta_{1z}\,c\theta_{1y} \\ -r_{cy}\,c\theta_{1z}\,c\theta_{1y} \end{bmatrix} \tag{36}$$

Mass asymmetries in the spacecraft generate the components r_{cy} and r_{cz}; how each component contributes to the radiation torque on the spacecraft is seen clearly in Eq. (36). We also observe that, because the two arrays are parallel and geometrically identical, the A-frame length a and the array's half-length b do not contribute to the total torque, only the hinge location referenced from the vehicle mass center matters.

Example 3: +y-Array Normal and -y-Array Off-Normal: Resultant Torque

The resultant torque $\underline{g}^{\mathcal{F}^c}$ is now obtained by adding Eq. (23) with Eq. (33). To build a simple expression for $\underline{g}^{\mathcal{F}^c}$, we observe that, in the $\mathcal{F}^c$ frame, ignoring the variation in the angle θ_{1z} over one orbit period, the constant part g_c of the x-torque (roll torque) is found to be

$$g_c \triangleq pA_s\,b_{1z}{}^{\oplus}\,[\sigma_A\,s\theta_{1z} - \sigma_{cy}\,c\delta_{2z}) \tag{37a}$$

and the amplitude g_a of the sinusoidally varying part $g_a\,s\theta_{1y}$ of the x-torque is

$$g_a \triangleq pA_s\,[\sigma_A\,(b + b_{1y}{}^{\oplus}\,c\theta_{1z}) - c\delta_{2z}\,\{b_s\,\sigma_{cy} + (r_{cy} + b_{1y} + b_c)\,\sigma_{cx}\}\,] \tag{37b}$$

The z-component (yaw torque) has no constant part, and its sinusoidal variation is in quadrature with the roll component. Lastly, the y-component (pitch torque) also varies sinusoidally, with its amplitude g_b equal to

$$g_b = -pA_s\,b_{1z}{}^{\oplus}\,[\sigma_A\,c\theta_{1z} + \sigma_{cx}\,c\delta_{2z}] \tag{37c}$$

Thus, the total radiation torque $\underline{g}^{\mathcal{F}^c}$ acting on the spacecraft at its mass center, in the spacecraft frame, is

$$\underline{g}^{\mathcal{F}^c} = \begin{bmatrix} g_c + g_a\,s\theta_{1y} \\ g_b\,c\theta_{1y} \\ g_a\,c\theta_{1y} \end{bmatrix} \tag{37d}$$

The constant roll torque g_c in the rotating frame $\mathcal{F}^c$ becomes a periodic torque in the orbit plane in a non-rotating frame; conversely, the periodic roll-yaw torque in $\mathcal{F}^c$ becomes a constant torque in the orbit plane in an inertial frame.

Meanwhile, the periodic pitch torque remains periodic even in a non-rotating frame because the rotation $\omega_0 t$ takes place about the pitch axis.

Radiation Torque on Spacecraft Bus

Usually the surface area of spacecraft bus is much smaller than that of the deployed solar arrays, and therefore the radiation torque caused by the bus is an order of magnitude smaller than that caused by the arrays. For this reason and to conserve space the analytical details of derivation of the radiation torque on a bus will not be given here.

Torque On An Array Shadowed By the Spacecraft Bus

Fig. 5 portrays a spacecraft with a cylindrical bus and a solar array, the bus casting a shadow on the array. The lit semi-cylindrical surface is ABC. The shadow boundary on the array may utmost consist of three segments: an arc cast by the lit end-face of the cylinder and two straight lines, enclosing the arc, cast by the boundary rulings at A and C. The shadow in Fig. 5, though, has two segments only because the shadow of the ruling at A falls off the array. The shadow boundary is determined as follows

It may be clear that at any time only one array at the most will be shadowed. Knowing the angle β between the sun-ray unit vector $\underline{S}$ and nadir unit vector $\underline{c}_3$, we first determine which end-face is lit:

> if $\beta < \pi/2$, the earth-pointing end-face is dark, and the opposite end-face is lit;
>
> if $\beta > \pi/2$,the earth-pointing end-face is lit, and the opposite end-face is dark

and the lit semi-cylindrical surface is then identified. Next, let $\underline{r}$ be the vector from the reference origin O to any point P on the edge of the fully-lit face of the bus or along the two boundary rulings of the lit semi-cylinder. The vector from the hinge O_j of j^{th} array (j = 1,2) to the point P is then $-\underline{b}_j + \underline{r}$. The two components of this vector in the array plane $y_j z_j$, which is not necessarily normal to the sun, are

$$(-\underline{b}_j + \underline{r}) \cdot \underline{j}_j \qquad \text{and} \qquad (-\underline{b}_j + \underline{r}) \cdot \underline{k}_j \qquad (38)$$

where $\underline{j}_j$ and $\underline{k}_j$ are the unit vectors along y_j- and z_j-axis of the array, respectively. If these components fall on the array, that is,

$$a \le (-\underline{b}_j + \underline{r}) \cdot \underline{j}_j \qquad (39a)$$

$$-w/2 \le (-\underline{b}_j + \underline{r}) \cdot \underline{k}_j \le w/2 \qquad (j = 1,2) \qquad (39b)$$

where w is the width of the array along the z_j axis, then the array j is clearly shadowed. In that event, as the vector $\underline{r}$ moves along the edge of the lit end-face and the boundary rulings, the above two components will delineate the shadow boundary.

The radiation torque due to the array is still given by Eq. (17). The area A_j represents the lit area of the array, and the vector $\underline{\rho}_{pj}$ in the moment arm $\underline{c}_{pj}$, Eq. (16), is the vector from O_j to the instantaneous center of pressure of the shadowed array. The instantaneous lit area and the vector $\underline{\rho}_{pj}$ are calculated numerically.

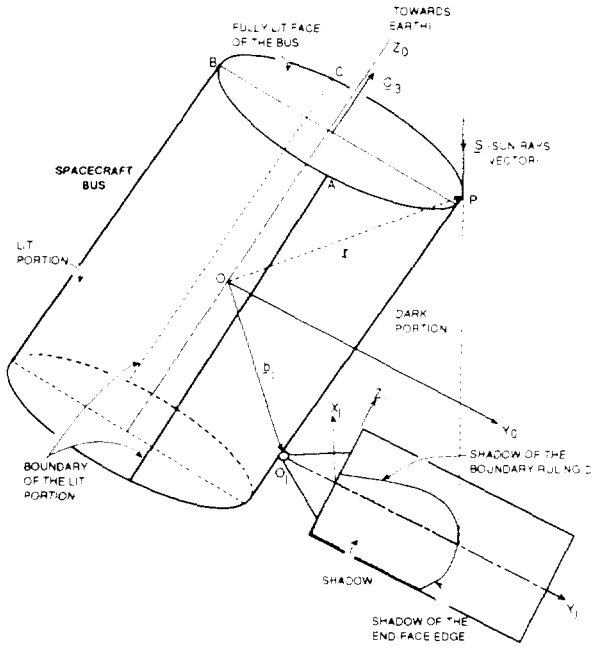

Fig. 5 Cylindrical Spacecraft Bus Casting Shadow on the Solar Array

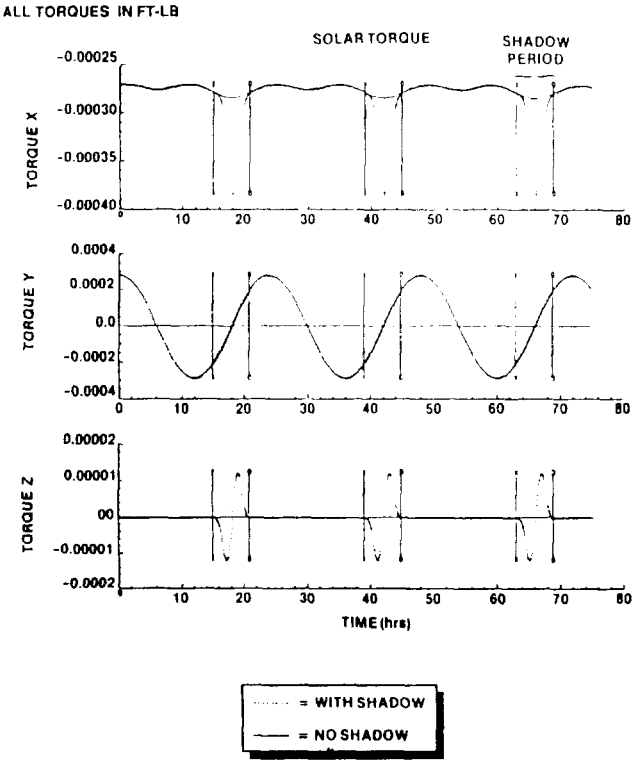

Fig. 6. Comparison of the total radiation torque on the spacecraft with and without considering the shadow; Orbital parameters: $\nu = 90°$, $\Omega_N = 180°$, $i = 20°$, corresponding solar arrays' inclinations: $\theta_{1z} = -\theta_{2z} = 43.5°$ (arrays parallel and both normal to the sun)

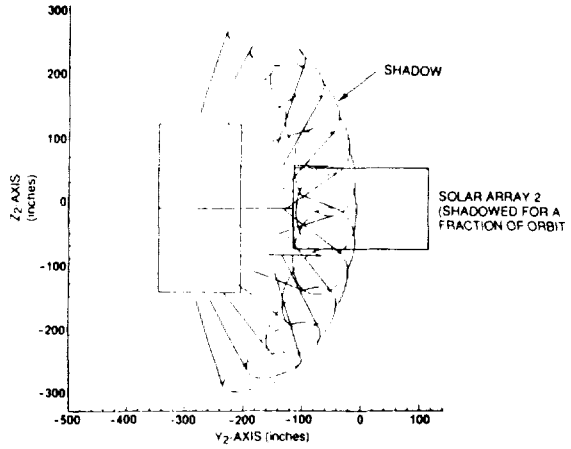

Fig. 7. Shadowing of –y array: Orbital Parameters and solar arrays' inclinations same as those in Fig. 6

Illustration

For parameters not recorded here because of space limitations, Fig. 6 furnishes total radiation torque (two arrays plus cylinder) with and without considering the shadow of the bus on the array, for r_c=0 and both arrays normal to the sun rays. When the shadow is ignored, we observe that, in conformance with Eq. (36), the yaw torque is zero and the roll torque a constant over a few orbits. Slight oscillations in the roll torque are present because of the cylindrical bus. The variation of the pitch torque in Fig. 6 conforms with the y-component of the solar radiation torque in Eq. (36). Regarding the effect of shadow on the array, we observe that while the shadow does not alter y-torque, the trough of the x-torque plummets from –0.29E-3 ft.lb to –0.38E-3 ft.lb during the shadow period. A small (0.1E-4 ft.lb amplitude) cyclic z-torque also arises during the shadow period. For the parameters under consideration, it turns out that the –y-array is shadowed, +y-array is not. Traversal of the cylinder's shadow on the –y-array is shown in Fig. 7. The growth of the shadow area on the –y-array is shown in Fig. 8 for three parametric sets, including the set for Fig. 6. Fig. 8a shows that, for example, when θ_{2z} = –43.5°, the maximum shadow area equals 88 sq.ft [(shadow area) / (array area) = 88/202.85 = 0.43] and the array remains partially shadowed for nearly 6 hours (one-fourth of the orbital period). We nonetheless also observe that the shadow occupies 43% area of one array only briefly (several minutes), occupying progressively smaller area before and after the maximum shadow epoch. As the shadow traverses, the pressure center of the lit portion travels also; the loci of the instantaneous pressure center, from the moment the shadow enters the array till the moment it leaves, are shown in Fig. 8b for three sets of parameters. As expected, these loci are closed curves, and the bigger the angle $|\theta_{2z}|$, the wider the loci. The shadows occur around different orbit angles $\omega_0 t$ for different sets of orbital parameters ν and Ω_N (even if the orbit inclination i is the same for these orbits). For plotting convenience, however, the maximum shadow epoch is shown to be the same (t = 18 hrs) in Fig. 8a for all three sets of parameters. In the preceding results, the center of mass vector r_c is zero. However, as the arrays orientations change relative to the spacecraft bus while

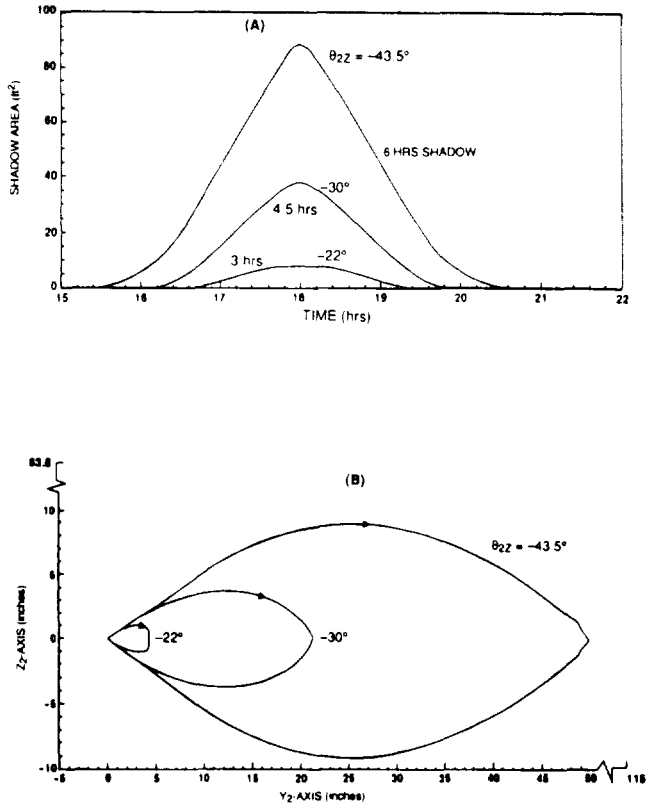

Fig. 8. (A) Shadow area on the –y-array versus time; (B) Locus of the pressure center of the –y-array as shadow travels on the array; orbital parameters for θ_{2z} = –43.5° the same as those in Fig.7; for θ_{2z} = –30°, the parameters are ν = 30° and Ω_N = 140°; for θ_{2z} = –22°, ν = 80°, Ω_N = 80°, and i = 20°

tracking the sun, r_c may vary depending on the arrays' arrangement. In the case at hand, this variation is found to be small, and it was *not* ignored in the computations.

The preceding results show that the spacecraft bus shadow on the array does not change radiation torque significantly. Also, based on the results not shown here due to space limitations and as stated before, the radiation torque on the bus is found to be an order of magnitude less than, and so negligible compared to, that on the arrays

4. Momentum Accumulation Due to Solar Radiation Torque

In the following analysis we will determine the momentum accumulation due to the arrays' torque only. It is instructive to compare the following development with that by McElvain[1].

Short Term Accumulation

Let $\underline{H}_b$ be the inertial angular momentum vector of the earth-pointing spacecraft under consideration. If H_x, H_y, H_z are the components of $\underline{H}_b$ in the body-fixed frame, then, in the presence of the radiation torque, (37d), they will be governed by the following three equations, expressed in the $\mathcal{F}^o$:

$$\dot{H}_x - \omega_0 H_z = g_c + g_a s\theta_{1y} \quad (40a)$$

$$\dot{H}_y = g_b c\theta_{1y} \quad (40b)$$

$$\dot{H}_z + \omega_0 H_x = g_a c\theta_{1y} \quad (40c)$$

As is well known, the roll (H_x) and yaw (H_z) momentums are gyrically coupled, whereas the pitch momentum (H_y) is independent of roll and yaw. Examining the definitions of g_a, g_b, g_c in Eqs. (37 a, b, c), we observe that they are functions of, among other things, the inclination angle θ_{1z} and the off-normal angle δ_{2z}. Because these angles depend on the earth's motion around the sun (the angle ν), they are held constant in flight over a few days, and therefore, within this period, the quantities g_a, g_b, g_c can be regarded as constant. Moreover, assuming that time t can be measured such that θ_{1y} (t=0) = 0, instead of θ_{10} according to Eq. (7), θ_{1y} (t) in Eq. (40) can be replaced with $\omega_0 t$. With these two assumptions, Eq. (40a) and (40c) can be integrated together, yielding ($i^2 = -1$)

$$H_x + iH_z = -i\,(g_c/\omega_0)\,(1-e^{-i\omega_0 t}) + i\,t\,g_a\,e^{-i\omega_0 t} \quad (41)$$

The integration of Eq. (40b), on the other hand, yields the pitch momentum H_y as

$$H_y\,(t) = (g_b/\omega_0)\,\sin\omega_0 t + H_{y0} \quad (42)$$

Because a constant torque g_c in the orbiting frame is a cyclic torque in the inertial frame, whereas a cyclic torque g_a in the orbit frame is a constant torque in the inertial frame, it is natural to find in Eq. (41) a cyclic variation in ($H_x + iH_z$) owing to g_c and a secular growth owing to g_a. At any arbitrary instant, the magnitude of the secular term in H_x+iH_z is tg_a, showing a linear growth in the spacecraft momentum in the roll-yaw plane. The pitch momentum H_y (t), Eq. (42), varies cyclically, with the amplitude equal to g_b/ω_0. The constant H_{y0} in Eq. (42) equals $H_y(0)$ and it embodies the spacecraft's y-momentum arising from its once-per-orbit equilibrium rotation.

Yearly Accumulation

It was just shown that the secular momentum in the roll-yaw plane at the end of one orbit ($\omega_0 t = 2\pi$) is ($H_x + iH_z$) = $i\,2\pi\,g_a/\omega_0$, where the coefficient g_a, Eq. (37b), is a function of the solar array's inclination angle θ_{1z} for an array normal to the sun, and of the inclination angles θ'_{2z} and off-normal angle δ_{2z} for an off-normal array. Fig. 3 shows that the angle θ_{1z} (or θ_{2z} which is equal to $-\theta_{1z}$) varies as a function of the angle ν (the earth's motion around the sun); therefore in order to calculate the yearly momentum accumulation, this variation must be considered. To separate the linearly varying angle $\nu(t)$, $0 \le \nu \le 2\pi$, from other constant orbital elements λ, Ω_N, and i in the definition of θ_{1z}, Eq. (8d) is rewritten thus:

$$\theta_{1z} = \sin^{-1}\,[\,(si\,s\Omega_N)\,c\nu + (-si\,c\Omega_N\,c\lambda + ci\,s\lambda)\,s\nu] \triangleq \sin^{-1}\,[A_0\,\sin\,(\nu_0 + \dot{\nu}t)] \quad (43)$$

with the amplitude A_0 and the phase angle ν_0 defined by:

$$A_0 = (A_s^2 + A_c^2)^{1/2} \le 1; \qquad \nu_0 = \tan^{-1}\,[A_s/A_c] \quad (44)$$

$$A_s = si\,s\Omega_N \qquad A_c = -si\,c\Omega_N\,c\lambda + ci\,s\lambda \quad (45)$$

Strictly speaking, because of orbit regression the ascending node angle Ω_N is not constant, but this variation is ignored here.

Spacecraft With +Y-Array Only; Array Normal to the Sun

When the +y-array is normal to the sun, the coefficient g_a given by Eq. (37b) simplifies to

$$g_a = pA_s\,\sigma_A\,(b + b_{1y}^{\oplus}\,c\theta_{1z}) \quad (46)$$

ignoring the second term in [•] in Eq. (37b) because it pertains to the –y-array. The magnitude of the secular momentum accumulated at any instant t then becomes

$$|H_x + iH_z| = pA_s\,\sigma_A\,(b + b_{1y}^{\oplus}\,c\theta_{1z})\,t \quad (47)$$

The yearly momentum is obtained by integrating (47) over the annual variation of the angle θ_{1z}. Let n_y be the current orbit under consideration:

$$n_y = t/\tau_0\,, \qquad \tau_0 \triangleq 2\pi/\omega_0 \quad (48)$$

where τ_0 is spacecraft orbit period, and let N_y be the total number of spacecraft orbits in one year. Then the yearly accumulation will be

$$H_{yT} = (pA_s\,\sigma_A\,\tau_0)\int_0^{N_y}(b + b_{1y}^{\oplus}\,c\theta_{1z})\,dn_y \quad (49)$$

Because $-\pi/2 < \theta_{1z} < \pi/2$, $c\theta_{1z}$ will always be positive. With the aid of Eq. (43) and recalling that b is constant (= $\ell/2$), and treating $b_{1y}^{\oplus}$, Eq. (22a), as constant, Eq. (49) transforms to

$$H_{yT} = (pA_s\,\sigma_A\,\tau_0)\,[bN_y + b_{1y}^{\oplus}\int_0^{N_y}\{1-A_0^2\,\sin^2 (\nu_0 + \dot{\nu}\tau_0\,n_y)\}^{1/2}\,dn_y] \quad (50)$$

(The assumption $b_{1y}^{\oplus}$ a constant may not be always valid, because the quantity r_{cy} involved in the definition of $b_{1y}^{\oplus}$ may change due to θ_{1z}, but this change can be minimized by keeping the array's mass center on the axis of rotation.) Now, while n_y changes from 0 to N_y, the argument of $\sin^2$ in Eq. (50) varies from ν_0 to $\nu_0+2\pi$; therefore, the integral in (50) is an elliptic integral of the second kind. Measuring the time t such that the phase angle $\nu_0 = 0$ and capitalizing on the symmetry properties of the elliptic integral at hand, H_{yT} after integration is found to be

$$H_{yT} = (pA_s\,\sigma_A\,\tau_0)\,[bN_y + 4\,(b_{1y}^{\oplus}/\dot{\nu}\tau_0)\,E\,(\pi/2\,,\,A_0)] \quad (51)$$

where $E(\pi/2, A_0)$ is a complete elliptic integral given by the series:

$$\left[E(\pi/2, A_0) = (\pi/2)\left\{1 - \frac{1}{2^2}A_0^2 - \frac{1^2 \cdot 3}{2^2 \cdot 4^2}A_0^4 - \ldots - \left[\frac{(2n-1)!!}{2^n\, n!}\right]^2 \frac{A_0^{2n}}{2n-1} - \ldots\right\}\right] \tag{52}$$

Becasue the number of the spacecraft orbits in one year is

$$N_y = 2\pi/(\dot{\nu}\tau_0) \tag{53}$$

the yearly momentum accumulation H_{yr} simplifies to

$$H_{yr} = N_y\, \tau_0\, pA_s\, \sigma_A\, [b + b_{1y}{}^{\oplus}\, (1 - A_0{}^2/2^2 - \ldots)\,] \tag{54}$$

In the series (52) or (54), as many terms are retained as are necessary to evaluate the sum up to a desired accuracy.

Spacecraft With +Y and –Y Arrays:

a) Both Arrays Normal to the Sun

The coefficient g_a, Eq. (37b), now simplifies to

$$g_a = -2pA_s\, \sigma_A\, r_{cy}\, c\theta_{1z} \tag{55}$$

This is corroborated by the coefficient of $s\theta_{1y}$ in the first element of the vector equation (36). Comparing (55) with (46), the yearly momentum accumulation in the present case can be written down following Eq. (54):

$$H_{yr} = N_y\, \tau_0\, pA_s\, \sigma_A\, [\,-2r_{cy}\, (1 - A_0{}^2/2^2 - \ldots)] \tag{56}$$

b) +Y-Array Normal, –Y-Array Off-Normal to the Sun

In this case, the coefficient g_a is given by the full-length equation (37b). The definition of the coefficients b_c, b_s [Eq. (28)], and σ_{cx}, σ_{cy} [Eq. (32] reveal the presence of the products of the trigonometric functions of the angles θ'_{2z} and $\theta_{2z,a}$. The analysis therefore seems intractable, and developing a closed-form expression for H_{yr} infeasible; consequently, numerical integration of the equation $|H_x + iH_z| = t\, g_a$ over one year seems inevitable.

Yearly Propellant Consumption

Annual propellant consumption, W_p, should not be based on the momentum accumulation over one orbit and treating that constant for entire year, for the daily momentum varies significantly over one year (illustrated later in Fig. 10). Instead, knowing H_{yr} from Eq. (54), Eq. (56), or otherwise, and knowing the specific impulse I_{sp} of the propellant under consideration and moment arm ℓ_J of the thrusters from the vehicle mass center, W_p is obtained from

$$W_p = H_{yr} / (I_{sp}\, \ell_J) \tag{57}$$

Illustrations

Example 1. Spacecraft With Two Arrays: Momentum Accumulation Over Three Orbits

Fig. 9 illustrates momentum accumulation in the roll-yaw plane, Eq. (41), with the orbit angle $\omega_0 t$ as parameter. In particular, it applies to the spacecraft configuration shown in Fig. 4, with +y-array normal to the sun and –y-array off-normal at an angle δ_{2z}. Fig. 9 shows the linear, radial growth of $(H_x + iH_z)$—the term $itg_a e^{-i\omega_0 t}$ in Eq. (41)—superimposed upon a cyclic variation with an amplitude of g_c/ω_0.

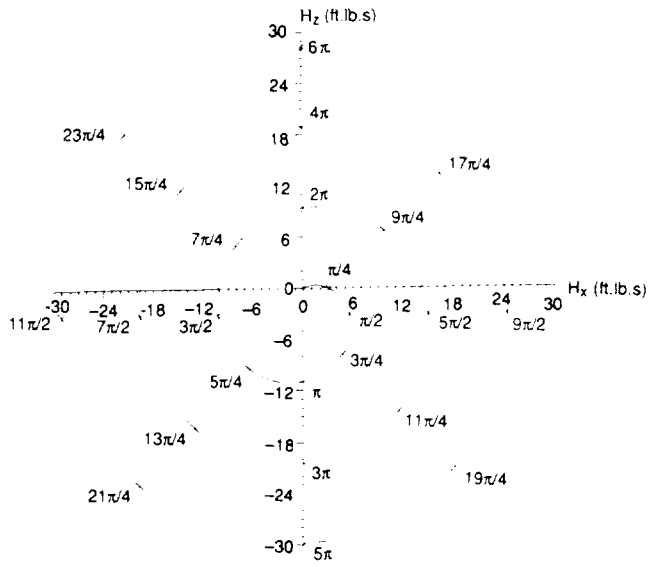

Fig. 9. Momentum accumulation in roll-yaw plane, due to the two arrays only: +Y array normal to the sun, $\theta_{1z} = -45°$; –Y array off-normal, $\theta_{2z}' = 25°$, $\delta_{2z} = 20°$, –Y array A-frame angle $\theta_{2z,a} = -37°$

Example 2. Momentum Accumulation As a Function of Earth's Position in the Ecliptic Plane

In order to obtain complete dependence of the daily momentum accumulation over a one year period, we next illustrate in Fig. 10 the roll-yaw momentum at $\omega_0 t = 2\pi$ and the pitch momentum amplitude g_b/ω_0 as a function of the angle ν: $0 \le \nu \le 2\pi$, with the off-normal angle δ_{2z} as a parameter. Figs. 10a and 10b show that, for off-normal angle $\delta_{2z} = 0$, the roll-yaw and pitch momentum amplitude varies periodically with ν, with half-year period; the corresponding ratio $H_y / |H_x + iH_z|$ remains constant for entire year. When the off-normal angle δ_{2z} of the –y-array is introduced, the half-yearly periodic variation of the roll-yaw momentum disappears and, instead, it begins to vary asymmetrically with ν. Also, the peaks and valleys of the roll-yaw momentum grow further apart as δ_{2z} increases. The half-year periodic variation of the pitch momentum amplitude alters little with the angle δ_{2z}. Fig. 10c illustrates the ratio $H_y / |H_x + iH_z|$; the variations in this ratio with ν become more pronounced as δ_{2z} increases. This ratio is of interest because it helps decide the cant angle of the reaction wheel configurations considered in the next section.

Example 3. Yearly Momentum Accumulation

When the off-normal angle δ_{2z} equals zero (that is, when both arrays are normal to the sun) the yearly momentum can be obtained analytically using Eq. (56), and when $\delta_{2z} \neq 0$, the yearly momentum is obtained by numerical integration of the

area under the curves $|H_x + iH_z|$ in Fig. 10a for the entire range $0 \le \nu \le 2\pi$. Fig. 11 depicts the yearly momentum against δ_{2z} for the range $0 \le \delta_{2z} \le 20°$ for different orbit inclination angles, keeping Ω_N at 170°. For $\delta_{2z} = 0$, the analytic prediction was compared and found identical with the numerical results. The number of terms that must be retained in the infinite series in Eq. (56) increases with the orbit inclination i, and yearly momentum diminishes a little. The yearly momentum, however, increases significantly with the off-normal angle δ_{2z}, as seen in Fig. 11.

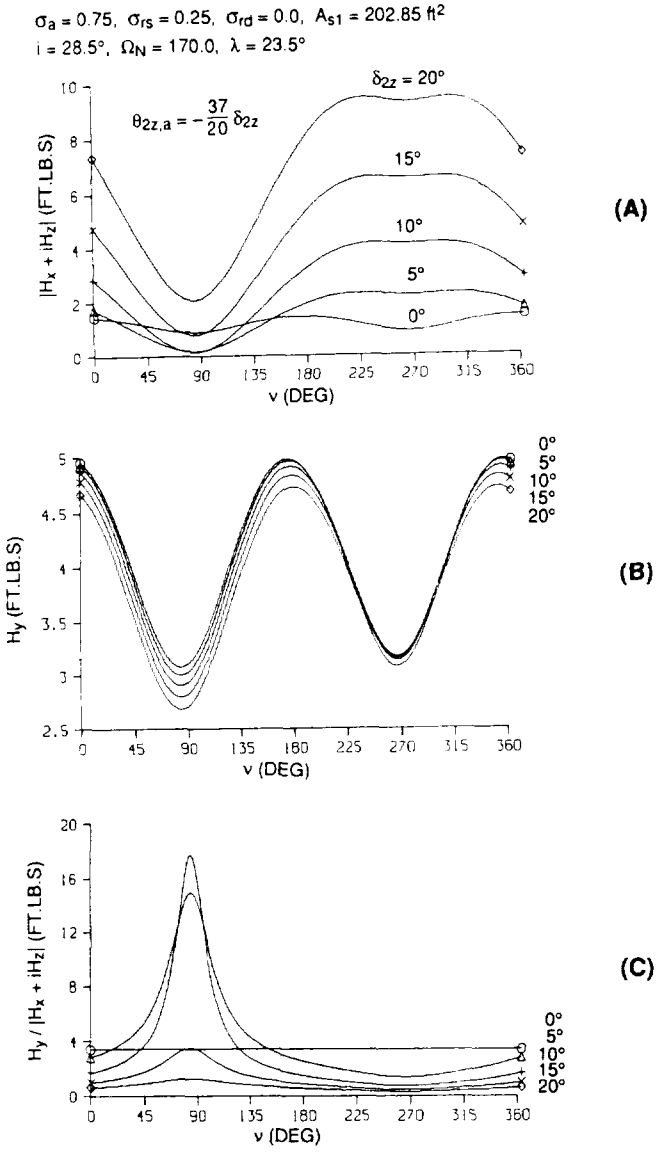

Fig. 10. Variation of roll-yaw and pitch momentum with the earth's position (the angle ν) in the ecliptic plane; y-array normal to the sun, –y-array off-normal at an angle δ_{2z} and its A-frame at an angle $\theta_{2z,a}$; λ = 23.44°, orbit ascending node angle Ω_N = 170°, and inclination angle i = 28.5°

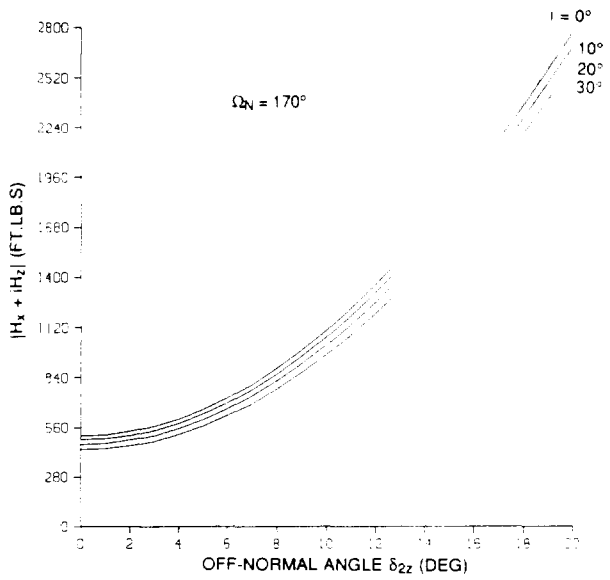

Fig. 11. Annual roll-yaw momentum versus off-normal angle of –y-array; +y-array always normal to the sun; Ω_N = 170°

5. Reaction Wheel Sizing and Configuration Optimization

In Section 4, we observed that the momentum along the roll and yaw axes are coupled. Depending on the initial conditions, the secular momentum build-up tg_a can exceed the capacity of the wheels either about the roll-axis, yaw-axis, or any other direction in the roll-yaw plane. Therefore, for the design purposes, the desired momentum capacity in the roll-yaw plane is the same in all directions. In contrast, the pitch momentum caused by the radiation torque is cyclic, with the amplitude equal to (g_b/ω_0). Hence, the pitch and roll-yaw momentum requirements leads to the well-known right circular cylinder momentum requirement for designing a wheel configuration, with cylinder axis along the pitch axis. On the other hand, the reaction wheels are also required to produce certain peak control torque about each of the three spacecraft axes. The torque requirements therefore form a rectangular parallelepiped. Both the momentum and the torque requirements can be met, in principle, using three wheels (not necessarily an orthogonal set); but for the sake of redundancy, four or more are often employed. In the following subsections, four-, six-, and three-wheel configurations are analyzed, two arrangements of the wheels and one-wheel failure are considered for each configuration.

To visualize the wheel configuration most easily, first place the spin axes of all the wheels in the roll-yaw plane, perhaps radially symmetrically along the roll and yaw axes or otherwise, and then cant all spin axes, equally or unequally depending on the design, towards the pitch axis or its opposite. When the wheels are not along the spacecraft axes, a transformation matrix $\underline{C}_{bw}$ is required to transform the wheel momentum vector $\underline{H}_{ww}$ along the wheel axes to the total wheel momentum $\underline{H}_{bw}$ along the spacecraft axes:

$$\underline{H}_{bw} = \underline{C}_{bw}\,\underline{H}_{ww} \tag{58}$$

When the number of wheels, n_w, is more than 3, the matrix $\underline{C}_{bw}$ is rectangular, $3xn_w$, and its pseudo-inverse $\underline{C}_{bw}^{\dagger}$

$$\underline{C}_{bw}^{\dagger} = \underline{C}_{bw}^{T} (\underline{C}_{bw} \underline{C}_{bw}^{T})^{-1} \tag{59}$$

is required for the inverse transformation of (58):

$$\underline{H}_{ww} = \underline{C}_{bw}^{\dagger} \underline{H}_{bw} \tag{60}$$

The above two transformation matrices are useful also for transforming the desired control torque $\underline{T}_c$ (3x1) about the spacecraft axes to the desired rate of change of the wheel angular momentum vector $\dot{\underline{H}}_{ww}$ (n_w x 1):

$$\dot{\underline{H}}_{ww} = - \underline{C}_{bw}^{\dagger} \underline{T}_c \tag{61}$$

To determine the optimum cant angle(s) with the roll-yaw plane, it is logical to impose the requirement that, for a desired momentum vector capacity $\underline{H}_{bw}$ in spacecraft axes, the norm of the wheel momentum vector $\underline{H}_{ww}$ be the least so as to minimize the cost and weight of the wheels. One suitable norm of the vector $\underline{H}_{ww}$ is its Euclidean norm $\| \underline{H}_{ww} \|$ defined by

$$\| \underline{H}_{ww} \| = \left[\sum_{i=1}^{n_w} H_{wi}^2 \right]^{1/2} \tag{62}$$

where H_{wi} ($i = 1, ..., n_w$) are the elements of the vector $\underline{H}_{ww}$. The minimization of $\| \underline{H}_{ww} \|$ also results in minimum power consumption by the wheels for controlling the spacecraft, as shown below.

Let $\omega_{wi}(0)$ be the initial speed of the wheel i, and $\omega_{wi}(t)$ the instantaneous speed while the wheel is acted upon by an electric motor, changing the wheel's momentum H_{wi} at the rate $\dot{H}_{wi}(t)$. Then

$$\omega_{wi}(t) = \omega_{wi}(0) + I_w^{-1} \int \dot{H}_{wi}(t)\, dt \tag{63}$$

where I_w equals wheel's moment of inertia about the spin-axis. For a constant $\dot{H}_{wi}$, the instantaneous power P_{wi} consumed by the wheel i is given by,

$$P_{wi} = | \dot{H}_{wi} | \, | \omega_{wi}(0) + I_w^{-1} \dot{H}_{wi} \, t | \tag{64}$$

where absolute values are taken to ensure that the power P_{wi} is positive for both signs of $\dot{H}_{wi}(t)$ and $\omega_{wi}(t)$. To determine the worst power consumption by the wheel assembly, we assume that $\omega_{wi}(0)$ has the same sign as that of $\dot{H}_{wi}$. Furthermore, assuming that $\omega_{wi}(0)$ is the same for all wheels, the total power P_w consumed by the n_w wheels will be

$$P_w = | \omega_w(0) | \sum_{i=1}^{nw} | \dot{H}_{wi} | + t\, I_w^{-1} \| \dot{\underline{H}}_{ww} \|^2 \tag{65}$$

Thus, we see that, ignoring the linear term, minimization of power consumption leads to the minimization of the norm $\| \dot{\underline{H}}_{ww} \|$.

The vectors $\underline{H}_{ww}$ and $\dot{\underline{H}}_{ww}$ are related, respectively, to the required momentum capacity $\underline{H}_{bw}$ and the control torque capacity $\underline{T}_c$ through the same pseudo-inverse matrix $\underline{C}_{bw}^{\dagger}$. Therefore, the minimization of both $\underline{H}_{ww}$ and $\dot{\underline{H}}_{ww}$ yields the same optimum cant angle if the components of $\underline{H}_{bw}$ and $\underline{T}_c$ are proportional. This condition, however, is not always obeyed; for instance, in the presence of radiation torque, the desired roll and yaw momentum requirements are the same, but the desired roll and yaw torque requirements may be different because the roll and yaw errors might be controlled with controllers of different bandwidths, and the corresponding moments of inertia might be quite different. As a different example, the roll and yaw torques limits could be the same to facilitate momentum dumping with thrusters. The need for deliberation is thus evident.

Four-Wheel Pyramid Configurations

One possible arrangement of four wheels is shown in Fig. 12. The angle between two adjacent wheels is 90°, and they all are equally canted toward the -y axis by an angle η measured from the roll-yaw plane. When the cant angle η and the angle γ in the roll-yaw plane are both zero, the momentum h_1 of the wheel 1 is along the z-axis, h_2 along the x-axis, h_3 opposite to h_1, and h_4 opposite to h_2. The angle γ is introduced so that the wheel torque can contribute, if desired, to all three axes and not just to roll and pitch or yaw and pitch. The corresponding rectangular matrix $\underline{C}_{bw}$ is

$$\underline{C}_{bw} = \begin{bmatrix} c\eta s\gamma & c\eta c\gamma & -c\eta s\gamma & -c\eta c\gamma \\ -s\eta & -s\eta & -s\eta & -s\eta \\ c\eta c\gamma & -c\eta s\gamma & -c\eta c\gamma & c\eta s\gamma \end{bmatrix} \tag{66}$$

whose pseudo-inverse, Eq. (59), is found to be

$$\underline{C}_{bw}^{\dagger} = \begin{bmatrix} s\gamma/2c\eta & -1/4s\eta & c\gamma/2c\eta \\ c\gamma/2c\eta & -1/4s\eta & -s\gamma/2c\eta \\ -s\gamma/2c\eta & -1/4s\eta & -c\gamma/2c\eta \\ -c\gamma/2c\eta & -1/4s\eta & s\gamma/2c\eta \end{bmatrix} \tag{67}$$

Let H_x, H_y, H_z be the desired momentum capacity of the reaction wheels about the roll-, pitch-, and yaw-axis of the spacecraft. These three components disperse along the four wheel axes as follows, using Eqs. (60) and (67):

$$\underline{H}_{ww} = \begin{bmatrix} (H_x s\gamma + H_z c\gamma)/2c\eta & - H_y/4s\eta \\ (H_x c\gamma - H_z s\gamma)/2c\eta & - H_y/4s\eta \\ (-H_x s\gamma - H_z c\gamma)/2c\eta & - H_y/4s\eta \\ (-H_x c\gamma + H_z s\gamma)/2c\eta & - H_y/4s\eta \end{bmatrix} \tag{68}$$

Let, T_x, T_y, T_z be the desired maximum control torques about the x-, y-, and z-axis of the spacecraft. The maximum rate of change of the wheel angular momentum about wheel axes is then, according to Eqs. (61) and (67)

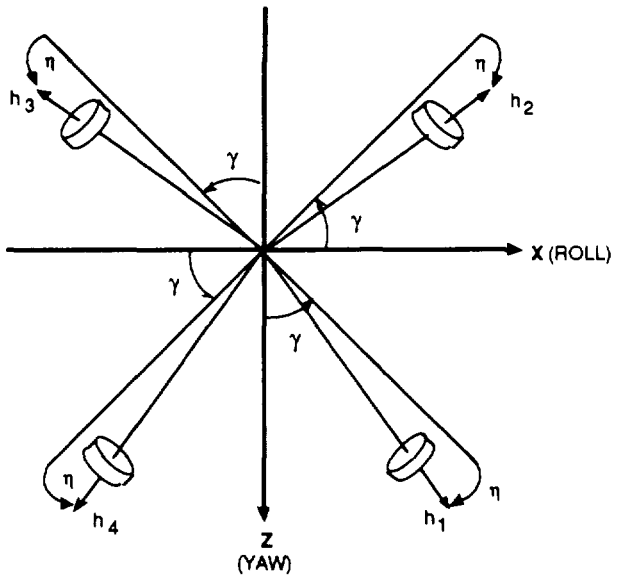

Fig. 12. Four-Wheel Configuration

$$\dot{\underline{H}}_{ww} = \begin{bmatrix} (-T_x s\gamma - T_z c\gamma)/2c\eta & + T_y/4s\eta \\ (-T_x c\gamma + T_z s\gamma)/2c\eta & + T_y/4s\eta \\ (\ T_x s\gamma + T_z c\gamma)/2c\eta & + T_y/4s\eta \\ (\ T_x c\gamma - T_z s\gamma)/2c\eta & + T_y/4s\eta \end{bmatrix} \qquad (69)$$

If H_x, H_y, H_z are the desired momentum capacity of the reaction wheels about the roll, pitch, and yaw axis of the spacecraft, the 4x1 vector $\underline{H}_{ww}$ is calculated analogously. Based on the definition (62), the norms $\| \underline{H}_{ww} \|$ and $\| \dot{\underline{H}}_{ww} \|$ are then found to be:

$$\| \underline{H}_{ww} \|^2 = (H_x^2 + H_z^2) / (2c^2\eta) + H_y^2 / (4s^2\eta) \qquad (70)$$

$$\| \dot{\underline{H}}_{ww} \|^2 = (T_x^2 + T_z^2) / (2c^2\eta) + T_y^2 / (4s^2\eta) \qquad (71)$$

which are independent of the angle γ because the angle between two adjacent wheels is 90°. Comparing the two norms, it is clear that if (H_x, H_y, H_z) and (T_x, T_y, T_z) are proportional,the minimization of one is the minimization of the other. The optimum cant angle η^* is found to be

$$\tan^4 \eta^* = H_y^2/2(H_x^2 + H_z^2) = T_y^2/2(T_x^2 + T_z^2) \qquad (72)$$

which may be rewritten in a more revealing form:

$$T_x^2/\ T_y^2 + T_z^2/\ T_y^2 = 1/(2\tan^4 \eta^*) \qquad (73)$$

which is the equation of a circle in the plane $(T_x/\ T_y,\ T_z/\ T_y)$ and the radius of the circle equals $1/(\sqrt{2}\ \tan^2 \eta^*)$. Eq. (73) states that as the torque requirements about x- and z-axis diminish, the radius of the circle shrinks and the optimum cant angle η^* increases. This is exemplified in Fig.13 where Eq. (73) is plotted for $\eta^* = 25°, 30°, ..., 60°$.

The norm $\| \dot{\underline{H}}_{ww} \|$ can be made dimension-free by dividing Eq. (71) with T_y^2. This dimension-free right side of Eq. (71) is plotted in Fig. 14 as a function of η for a given $(T_x^2 + T_z^2)/T_y^2$. The minimum value of the norm occurs at the optimum cant angle η^*, and that minimum norm is found to be

$$\| \dot{\underline{H}}_{ww} \|^2_{\ min} / T_y^2 = [\ \sqrt{2}\ (\sigma_{xy}^2 + \sigma_{zy}^2)^{1/2} + 1\ ]^2/4 \qquad (74)$$

where the torque ratios σ_{xy} and σ_{zy} are defined as

$$\sigma_{xy} = T_x / T_y \qquad \sigma_{zy} = T_z / T_y \qquad (75)$$

Table 2 furnishes optimum cant angle η^* for several desired torque ratios; it also demonstrates that, for example, $\eta^* = 35.26$ as long as $\sigma_{xy}^2 + \sigma_{zy}^2 = 2$, regardless of the individual values of σ_{xy} and σ_{zy}.

To determine the torque (or momentum) capacity of the wheels to produce the desired maximum torques (or momentums) along the spacecraft axes, we again consider $\dot{\underline{H}}_{ww}$, Eq. (69). Because T_x, T_y, T_z are only *three* independent torque requirements, the *four* elements of $\dot{\underline{H}}_{ww}$ are not all independent. Indeed, they are constrained by a relationship that is divulged from

$$\dot{\underline{H}}_{ww} = \underline{C}_{bw}^{\dagger}\ \underline{C}_{bw}\ \dot{\underline{H}}_{ww}, \qquad (76)$$

$$(T_x / T_y)^2 + (T_z / T_y)^2 = 1/(2\text{TAN}^4\eta)$$

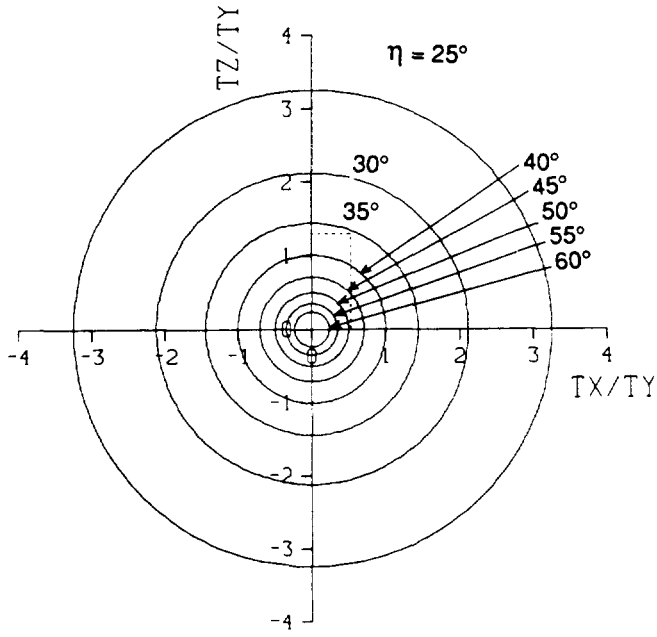

Fig. 13. Dependence of minimum-power cant angle on desired torque ratios

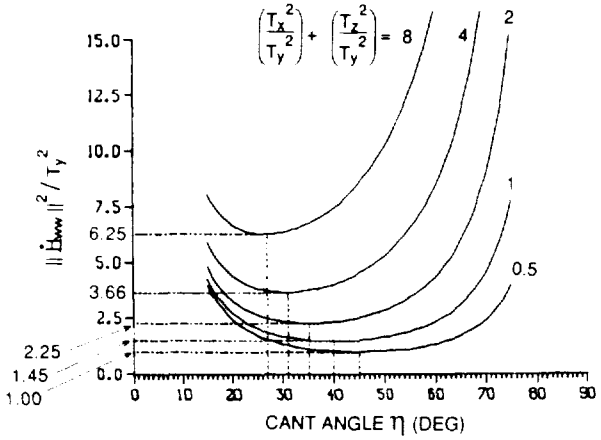

Fig. 14. $\|\dot{H}_{ww}\|^2 / T_y^2$ versus cant angle η for a four-wheel configuration

Table 2. Examples of dependence of optimum cant angle on the desired torque ratios (σ_{xy} and σ_{zy})

$(T_x/T_y)^2 + (T_z/T_y)^2$	Optimum Cant Angle	Example Ratios	
		T_x/T_y	T_z/T_y
0.5	45°	0.5	0.5
1	40.06°	$1/\sqrt{2}$	$1/\sqrt{2}$
2	35.26°	1 0 $\sqrt{2}$	1 $\sqrt{2}$ 0
4	30.73°	$\sqrt{2}$	$\sqrt{2}$
8	26.56°	2	2

Recalling (66) and (67), Eq. (76) yields four identical equations stating

$$\dot{H}_{w1} + \dot{H}_{w3} = \dot{H}_{w2} + \dot{H}_{w4} \tag{77}$$

The wheel momentums observe a similar relationship.

Because of (77) and because of the nature of decomposition of the three desired torques T_x, T_y, T_z along the four wheel axes, Eq. (69), it may be intuitively clear that the magnitude of each element in (69) will not simultaneously reach $\dot{H}_{w,max}$—the maximum achievable rate of change of wheel's angular momentum. Therefore, recalling the definition (62)

$$\| \dot{\underline{H}}_{ww} \|^2 < 4\dot{H}_{w,mx}^2 \tag{78}$$

When the cant angle is optimum, the norm $\| \dot{\underline{H}}_{ww} \|$ is related to the specified torques T_x, T_y, T_z according to Eq. (74). Therefore, in view of (78)

$$[\sqrt{2}\,(T_x^2 + T_z^2)^{1/2} + T_y\,]/4 < \dot{H}_{w,mx} \tag{79}$$

By way of illustration, if the torque requirements about the three axes are all equal ($T_x = T_y = T_z$), the inequality (79) yields

$$\dot{H}_{w,mx} > 3T_x/4 \tag{80}$$

Considering that there are four wheels, each of capacity $\dot{H}_{w,mx}$, for controlling three axes of the spacecraft each requiring the torque T_x, the inequality (80) is perhaps a natural result, but it does not reveal just how much $\dot{H}_{w,mx}$ must at last be, to size the wheel. For that, the Euclidean norm is not helpful and we must focus on Eq. (69) itself, as illustrated in the following two illustrations.

Wheels Contributing to Roll and Pitch or Yaw and Pitch Only

In Fig. 12, when $\gamma = 0$ or 90°, each wheel contributes to either roll and pitch or yaw and pitch axes only. Regardless of γ, the optimum cant angle for equal torque and momentum requirements satisfies, according to Eq. (72):

$$\eta^* = 35.26°, \quad \tan\eta^* = 1/\sqrt{2}, \quad \sin\eta^* = 1/\sqrt{3}, \quad \cos\eta^* = \sqrt{2/3} \tag{81}$$

Substituting $T_x = T_y = T_z$ and $s\eta^*$ and $c\eta^*$ from (81) in (69), we obtain, for $\gamma = 90°$

$$\dot{\underline{H}}_{ww} = T_x\,[\,-0.179 \quad 1.045 \quad 1.045 \quad -0.179\,]^T \tag{82a}$$

which yields the desired maximum wheel torque capacity when not one wheel has failed

$$\dot{H}_{w,mx} \geq 1.045\,T_x \tag{82b}$$

It is illuminating to compare the inequality (80) with (82b).

Regarding the required momentum capacity of the wheels, we first obtain $\underline{H}_{ww}$, from Eq. (60), for $\gamma = 90°$. Next, recall that from Eq. (41), the secular roll or yaw momentum at the end of one orbit is $g_a\tau_0$ (τ_0 = orbital period) and, from Eq. (42), the pitch momentum amplitude is g_b/ω_0. The least momentum capacity of a wheel for momentum dumping per orbit and for optimum cant angle (81) is then

$$H_{w,mx} \geq \sqrt{3}\,|g_a|\tau_0 / 2\sqrt{2} + \sqrt{3}\,|g_b| / 4\omega_0 \tag{83}$$

Finally, in order to calculate the power consumption P_w versus time t, Eq. (65), we require the quantities $\sum_{i=1}^{nw} |\dot{H}_{wi}|$ and $\| \dot{\underline{H}}_{ww} \|^2$. From Eq. (82a),

$$\sum_{i=1}^{nw} |\dot{H}_{wi}| = 2.449\,T_x \tag{84a}$$

which determines the intercept of the P_w versus t curve at t = 0. The slope of this curve is proportional to the norm $\| \dot{\underline{H}}_{ww} \|^2$

which, for equal torque requirement, is obtained from Eq. (74) by inserting $\sigma_{xy} = 1 = \sigma_{yz}$:

$$\| \dot{\underline{H}}_{ww} \|^2 = 2.25\, T_x^2 \tag{84b}$$

The indexes (84a) and (84b) should be kept as small as consistent with performance specifications.

Wheels Contributing to All Three Axes

In Fig. 12, when $\gamma = 45°$, each of the four wheels contributes equally to the roll and yaw axes, as evident from Eq. (69). Reference 6 has examined this configuration to some depth. For $\gamma = 45°$, for equal torque requirements ($T_x = T_y = T_z$) and optimum cant angle (81), Eq. (69) yields

$$\dot{\underline{H}}_{ww} = T_x \left[-\sqrt{3}/4 \quad \sqrt{3}/4 \quad 3\sqrt{3}/4 \quad \sqrt{3}/4 \right]^T \tag{85a}$$

The element with maximum absolute value yields the desired torque capacity of the wheel:

$$\dot{H}_{w,mx} \geq 3\sqrt{3}\, T_{mx}/4 = 1.3\, T_x \tag{85b}$$

Comparing (85b) with (82), we conclude that, to produce a torque of magnitude T_x about each of the three axes, the reaction wheels corresponding to $\gamma = 45°$ configuration must have 24.4% higher torque capacity than the wheels corresponding to $\gamma = 0°$ configuration. This is not surprising because for $\gamma = 45°$, the wheel's torque capacity is dispersed along all three axes, whereas in the case $\gamma = 0°$, it is distributed along roll and pitch or yaw and pitch only.

Following the derivation of the wheel momentum capacity, Eq. (83), the desired capacity for the configuration at hand is

$$H_{w,mx} \geq \sqrt{3}\, (|g_a|\, \tau_0 + |g_b| / \omega_0)/4 \tag{86}$$

where the optimum cant angle (81) has been used. Comparing (86) with (83), we find that $H_{w,mx}$ now ($\gamma = 45°$) is smaller than before ($\gamma = 0°$), in contrast with the torque capacity conclusion drawn above. The reason of course is that the secular momentum $\tau_0 g_a$ is either about the roll-axis or yaw-axis, not both, whereas the torque capacity T_x is desired about both roll and yaw axes.

The two indexes of the power consumption are calculated with the aid of (85a) and (74):

$$\sum_{i=1}^{4} | \dot{H}_{wi} | = 2.598\, T_x \tag{87a}$$

$$\| \dot{\underline{H}}_{ww} \|^2 = 2.25\, T_x^2 \tag{87b}$$

Comparing (87a) with (84a) and (87b) with (84b), we conclude that, for producing equal torque about the three spacecraft axes, and for the same initial wheel speed, the $\gamma = 45°$ wheel-configuration begins with a slightly higher power consumption and increases at the same rate as the $\gamma = 90°$ or 0° configuration.

One-Wheel Failure

For the four-wheel configuration shown in Fig. 12, we are usually interested in either $\gamma = 45°$ or 90° ($\gamma = 0°$ or 90° are effectively the same). And for these values, because all wheels are arranged symmetrically, failure of any wheel has the same consequences as the failure of any other. Therefore, to facilitate analysis, we arbitrarily assume the failure of wheel-3, and in that case the 3x4 transformation matrix $\underline{C}_{bw}$, Eq. (66), condenses to a 3x3 matrix $\underline{C}_{bw,3}$, formed by deleting the third column of $\underline{C}_{bw}$. The inverse $\underline{C}_{bw,3}^{-1}$ of $\underline{C}_{bw,3}$ is found and then used to determine the torque vector $\dot{\underline{H}}_{ww}$, following (61):

$$\dot{\underline{H}}_{ww} = \begin{bmatrix} -T_x s\gamma/c\eta & & -T_z c\gamma/c\eta \\ T_x(s\gamma - c\gamma)/2c\eta + T_y/2s\eta + T_z(s\gamma + c\gamma)/2c\eta & & \\ 0 \text{ (wheel-3 failed)} & & \\ T_x(s\gamma + c\gamma)/2c\eta + T_y/2s\eta - T_z(s\gamma - c\gamma)/2c\eta & & \end{bmatrix} \tag{88}$$

The wheel momentum vector $\underline{H}_{ww}$ is determined likewise. For one-wheel failure case, the cant angle is not re-optimized because the cant angle of the wheels, once installed, is not changeable in the flight.

Maximum Torque and Momentum Capacity When $\gamma = 90°$

For $\gamma = 90°$, and for the optimum cant angle (81), Eq. (88) yields

$$\dot{\underline{H}}_{ww} = T_x \left[-1.225 \quad 2.091 \quad 0 \quad 0.866 \right]^T \tag{89a}$$

which in turn yields the required torque capacity of the wheel as

$$\dot{\underline{H}}_{w,mx} \geq 2.091\, T_x \tag{89b}$$

This is twice the required torque capacity in the no-failure case, Eq. (82b).

Following the derivation of the momentum capacity Eq. (83) for the no-failure case, the momentum capacity for one-wheel failure case is:

$$\underline{H}_{ww} = \begin{bmatrix} \sqrt{3}\, |g_a|\, \tau_0 / \sqrt{2} \\ \sqrt{3}\, |g_a|\, \tau_0 / 2\sqrt{2} + \sqrt{3}\, |g_b| / 2\omega_0 \\ 0 \text{ (wheel-3 failed)} \\ \sqrt{3}\, |g_a|\, \tau_0 / 2\sqrt{2} + \sqrt{3}\, |g_b| / 2\omega_0 \end{bmatrix} \tag{90}$$

Depending upon the relative magnitudes of g_a and g_b, either wheel-1 or wheel-2 will yield the required momentum capacity (wheel-4 will yield the same capacity as the wheel-2).

Regarding the two indexes of power consumption, Eq. (89a) furnishes

$$\sum_{i=1}^{4} | \dot{H}_{wi} | = 4.182\, T_x \qquad (91a)$$

$$\| \dot{\underline{H}}_{ww} \|^2 = 6.62\, T_x^2 \qquad (91b)$$

which may be compared with the no-failure results, Eqs. (87).

Maximum Torque and Momentum Capacity When $\gamma = 45°$

For equal torque requirements about the roll, pitch, and yaw axes ($T_x = T_y = T_z$), and for the optimum cant angle $\eta^* = 35.26$, the desired torque capacity of each wheel is

$$\dot{H}_{w,mx} \geq 1.732\, T_x \qquad (92)$$

juxtaposed to the no-failure size (85b). By comparing the size (92) with the size (89b), the advantage of $\gamma = 45°$ configuration over $\gamma = 0°$ or 90° configuration emerges: when one wheel fails, the $\gamma = 45°$ configuration can control the spacecraft with the wheels of smaller torque capacity than the $\gamma = 0°$ or 90° configuration can.The two indexes of power consumption are:

$$\sum_{i=1}^{4} | \dot{H}_{wi} | = 3\sqrt{3}\, T_x = 5.196\, T_x$$

$$\| \dot{\underline{H}}_{ww} \|^2 = 9\, T_x^2 \qquad (93b)$$

Comparing (93) with (91), a disadvantage of the $\gamma = 45°$ configuration is also unveiled: its power consumption is significantly greater than that of the $\gamma = 90°$ configuration. Finally, the desired momentum capacity is

$$H_{w,mx} = \sqrt{3}\, (|g_a|\, \tau_0 + |g_b|\, / \omega_0) /2 \qquad (94)$$

Compared with its no-failure counterpart, Eq. (86), the desired momentum capacity is now twice.

Reference 6 may be reviewed for a different aspect regarding the selection of cant angle for the configuration at hand.

Six-Wheel Pyramid Configurations

Two-Cant-Angle Configuration

One such configuration is shown in Fig. 15 where the wheels are arranged symmetrically ($\gamma = 60°$), wheels 2 and 5 controlling roll and pitch axes, and wheels 1, 3, 4, and 6 controlling all three axes. Because of this fundamental difference between the two subsets of wheels, the cant angle η_2 of the former subset is allowed to be, in general, different from the cant angle η_1 of the latter subset. This freedom permits a greater economy in power consumption, if desired, and allows the reaction wheels to be of smaller torque and momentum capacity than the one-cant-angle configuration does.

To determine the optimum cant angles η_1^* and η_2^*, define

$$c_i = \cos \eta_i \qquad s_i = \sin \eta_i \qquad (i = 1,2) \qquad (95)$$

The transformation matrix $\underline{C}_{bw}$ (3x6) is

$$\underline{C}_{bw} = \begin{bmatrix} c_1/2 & c_2 & c_1/2 & -c_1/2 & -c_2 & -c_1/2 \\ -s_1 & -s_2 & -s_1 & -s_1 & -s_2 & -s_1 \\ \sqrt{3}c_1/2 & 0 & -\sqrt{3}c_1/2 & -\sqrt{3}c_1/2 & 0 & \sqrt{3}c_1/2 \end{bmatrix} \qquad (96)$$

where, from the second and fifth column, it is apparent that the wheels 2 and 5 do not control the yaw axis, while the remaining four wheels control all axes. The pseudo-inverse matrix $\underline{C}_{bw}^{\dagger}$ is determined using the definition (59):

$$\underline{C}_{bw}^{\dagger} = \begin{bmatrix} \begin{Bmatrix} c_1/2 \\ c_2 \\ c_1/2 \\ -c_1/2 \\ -c_2 \\ -c_1/2 \end{Bmatrix} /(c_1^2 + 2c_2^2) & \begin{Bmatrix} -s_1 \\ -s_2 \\ -s_1 \\ -s_1 \\ -s_2 \\ -s_1 \end{Bmatrix} /(4s_1^2 + 2s_2^2) & \begin{Bmatrix} 1 \\ 0 \\ -1 \\ -1 \\ 0 \\ 1 \end{Bmatrix} /2\sqrt{3}c_1 \end{bmatrix} \qquad (97)$$

and the Euclidean norm of the vector $\dot{\underline{H}}_{ww}$ is

$$\| \dot{\underline{H}}_{ww} \|^2 = T_x^2/(c_1^2 + 2c_2^2) + T_y^2/2(2s_1^2 + s_2^2) + T_z^2/3c_1^2 \qquad (98)$$

which is minimized by the optimum angles η_1^* and η_2^* defined by

$$s^2\eta_1^* = (T_x + T_y - T_z) / (T_x + T_y + T_z),$$
$$c^2\eta_1^* = 2T_z / (T_x + T_y + T_z) \qquad (99a)$$

$$s^2\eta_2^* = \{2(T_z - T_x) + T_y\} / (T_x + T_y + T_z),$$
$$c^2\eta_2^* = (3T_x - T_z) / (T_x + T_y + T_z) \qquad (99b)$$

Fig. 16 portrays the optimum angles η_1^* and η_2^* for specified torque ratios σ_{xz} and σ_{yz}. Substituting the optimum trigonometric functions in Eq.(98), the minimum value of the norm $\| \dot{\underline{H}}_{ww} \|^2$ is found to be

$$\| \dot{\underline{H}}_{ww} \|^2 = (T_x + T_y + Tz)^2 /6 \qquad (100)$$

The three torque components T_x, T_y, T_z are independent, and once specified, they are produced by the six $\dot{H}wi$ (i=1, ..., 6), given by Eq. (61). Clearly, these six quantities are constrained by three relations which are obtained from the expanded version of Eq. (76). Due to these constraints,

$$\| \dot{\underline{H}}_{ww} \|^2 < 6\, \dot{H}_{w,mx}^2 \qquad (101)$$

analogous to the inequality (78) for the 4-wheel configurations. Combining (101) with (100), we obtain

$$(T_x + T_y + T_z) / 6 < \dot{H}_{w,mx} \qquad (102)$$

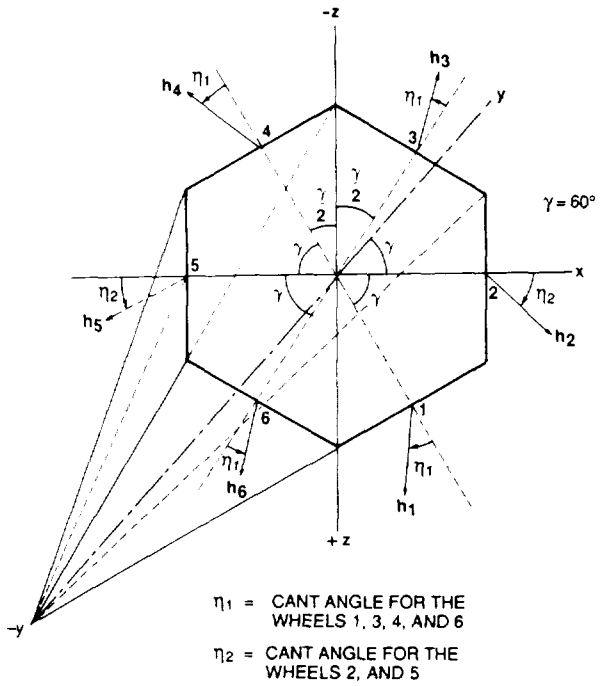

Fig. 15. Six-wheel hexagonal configuration

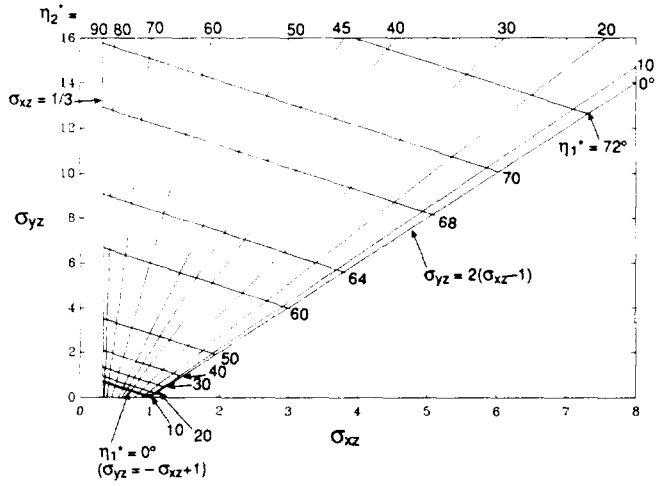

Fig. 16. Dependence of optimum cant angles η_1^* and η_2^* on the torque ratios σ_{xz} and σ_{yz}

which states that the sum of the maximum torques that can be produced about the three spacecraft axes must be less than the total torque capacity of the wheels—the cant angles being the underlying reason. For equal torque requirements ($T_x = T_y = T_z$), the inequality (102) reduces to

$$\dot{H}_{w,mx} > T_x/2 \tag{103}$$

which may be compared with (80). It is intuitively clear that, instead of arranging six wheels as shown in Fig. 15, if they were arranged two wheels per axis, then for equal torque requirement about the three axes each wheel's torque capacity must satisfy

$$\dot{H}_{w,mx} \geq T_x/2 \tag{104}$$

instead of (103).

When the maximum required torque components T_x, T_y, T_z are all equal, Eqs. (99) yield Eq. (81)

$$s\eta_1^* = 1/\sqrt{3} = s\eta_2^*;\quad c\eta_1^* = \sqrt{2}/\sqrt{3} = c\eta_2^*;$$
$$\eta_1^* = 35.26° = \eta_2^* \tag{105}$$

The two cant angles, therefore, coalesce and indeed they become the same as that for the 4-wheel configurations. The desired maximum torque capacity of the wheel is then found to be

$$\dot{H}_{w,mx} \geq 0.846\, T_x \tag{106}$$

which is smaller than the torque capacity (82b) or (85b) for 4-wheel configurations for the same torque requirements about the spacecraft axes.

Regarding the power consumption, the Euclidean norm (100) yields

$$\| \dot{\underline{H}}_{ww} \|^2 = 1.5\, T_x^2 \tag{107}$$

Comparing (107) with (84b) and (87b), we observe that for the same T_x about all three axes, the power consumption of the 6-wheel configuration increases at a smaller rate than that of the 4-wheel configuration. Finally,

$$\sum_{i=1}^{6} | \dot{H}_{wi} | = 2.509\, T_x \tag{108}$$

which is within the two values (84a) and (87a) for the two 4-wheel configurations.

One-Cant-Angle Configuration

A hexagonal wheel assembly with two different cant angles might be difficult to install in a spacecraft bus; so we now optimize a hexagonal configuration with one cant angle. The pseudo-inverse matrix, Eq. (97), simplifies and Eq. (61) yields the Euclidean norm

$$\| \dot{\underline{H}}_{ww} \|^2 = (T_x^2 + T_z^2) / 3c^2\eta + T_y^2/6s^2\eta \tag{109}$$

where the subscript 1 of η_1 is dropped because now there is only one cant angle. Minimization of this norm leads to, surprisingly, the condition (72) for the 4-wheel configurations. The minimum value of the norm (109) is

$$\| \dot{\underline{H}}_{ww} \|^2 = \left[T_y + \sqrt{2\,(T_x^2 + T_z^2)} \right]^2 / 6 \tag{110}$$

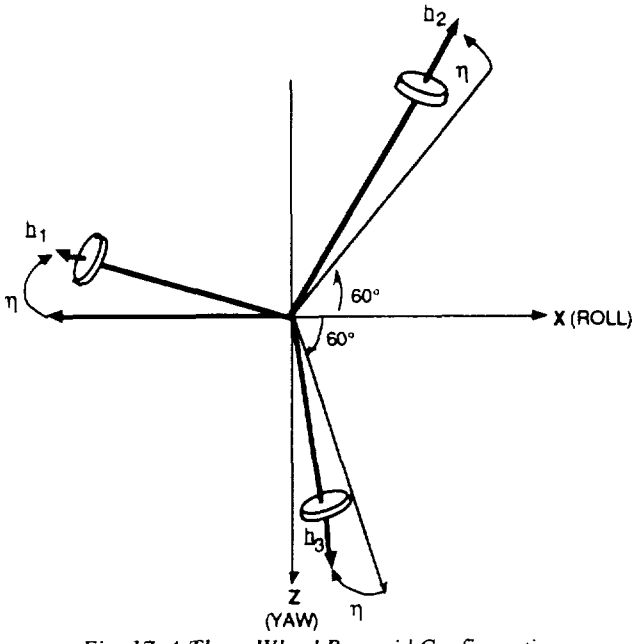

Fig. 17. A Three-Wheel Pyramid Configuration

which is two-thirds of the value in (74) for the 4-wheel configuration. Also, because of the inequality (101), we arrive at

$$\dot{H}_{w,mx} > \left[\sqrt{(T_x^2 + T_z^2)/18} + T_y/6\right] \qquad (111)$$

which is different form (102) but, for equal torque requirement, reduces to (103).

The one-wheel failure analysis, considered above for the four-wheel configurations, becomes unwieldy because of the 5x3 size of the reduced matrix $\underline{C}_{bw}$. Therefore, pertinent results such as wheel torque capacity and power consumption are obtained with the aid of a computer and summarized later in Table 3.

Three-Wheel Pyramid Configuration

When wheel redundancy is not warranted, when for reasons of cost and weight the number of wheels must be bare minimum, and when the torque requirements about the three axes are not necessarily equal, the three-wheel pyramid configuration shown in Fig. 17 might be an ideal choice. For this arrangement, the three wheel angular momentums can be expressed in spacecraft axes as follows:

$$\begin{bmatrix} H_x \\ H_y \\ H_z \end{bmatrix} = \begin{bmatrix} -c\eta & 1/2\ c\eta & 1/2\ c\eta \\ -s\eta & -s\eta & -s\eta \\ 0 & -\sqrt{3}/2\ c\eta & \sqrt{3}/2\ c\eta \end{bmatrix} \begin{bmatrix} H_{w1} \\ H_{w2} \\ H_{w3} \end{bmatrix} \qquad (112)$$

wherein the 3x3 transformation matrix is $\underline{C}_{bw}$. Because now there is no redundancy, the pseudo-inverse matrix $\underline{C}_{bw}^{\dagger}$ becomes the regular inverse matrix $\underline{C}_{bw}^{-1}$. After determining $\underline{C}_{bw}^{-1}$ and substituting that in Eq. (61), the vector $\dot{\underline{H}}_{ww}$ in terms of the required torque components T_x, T_y, T_z turns out to be

$$\dot{\underline{H}}_{ww} = \begin{bmatrix} 2T_x/3c\eta + T_y/3s\eta \\ -T_x/3c\eta + T_y/3s\eta + T_z/3c\eta \\ -T_x/3c\eta + T_y/3s\eta - T_z/3c\eta \end{bmatrix} \qquad (113)$$

For minimization of power consumption, we arrive at the followin Euclidean norm.

$$\| \dot{\underline{H}}_{ww} \|^2 = 2\,(T_x^2 + T_z^2) / 3c^2\eta + T_y^2/3s^2\eta \qquad (114)$$

which is four-thirds of the norm (71) for 4-wheel configurations and six-thirds (twice) of the norm (109) for 6-wheel configuration, implying that if they all begin from zero wheel speed, the 3-wheel configuration will consume greater power in the stated ratio. For example, for equal torque requirements ($T_x = T_y = T_z$), while the minimum value of the 4-wheel norm is 2.25, that of the 3-wheel norm is 3.0, which is, incidentally, the same as that for the three orthogonal wheels one per axis. Moreover, if the cant angle is not set to be the optimum ($\eta \neq \eta^*$), the three-wheel pyramid configuration will use more power than the one-per-axis configuration.Next, the norm (114) yields the same optimum angle as one for the 4- and 6-wheel configurations, Eq. (72). For this optimum angle, the following minimum value of the norm emerges:

$$\| \dot{\underline{H}}_{ww} \|^2_{\ min} = [\ T_y + \sqrt{2(T_x^2 + T_z^2)}\ ]^2/3 \qquad (115)$$

which is twice the value (110) for the 6-wheel configuration and four-thirds of the value (71) for the 4-wheel configuration.

The required torque capacity of the wheels for equal torque requirements about roll, pitch, and yaw axes is found to be

$$\dot{H}_{w,mx} \geq 1.39\ T_x \qquad (116)$$

As a check, note that the norm of $\dot{\underline{H}}_{ww}$ for three-wheel configuration is indeed

$$\| \dot{\underline{H}}_{ww} \|^2 = 3T_x^2 \qquad (117)$$

equal to that for a one-wheel-per-axis configuration; but the power consumption of each wheel would be quite different from that for the one-wheel-per-axis configuration.

Overall Comparison of Six Configurations

When the torque requirements about the roll, pitch, and yaw axes are not the same, the wheels of different torque capacities along different axes might be selected; but from the standpoint of reliability and cost, that is usually not preferred. Perhaps a more attractive choice is a six-wheel configuration with identical wheels, the cant angle selected according to the desired torque ratios. For equal torque requirements, the optimum cant angle is $\eta^* = 35.26°$, and the associated wheel torque capacity for the required torque T_{mx} must be at least $0.846\ T_{mx}$ [Eq. (106)]—greater than $0.5\ T_{mx}$ for the two-wheel-per-axis arrangement. The two power consumption indexes in the case of

no wheel failure shown in the second row of Table 3 restate Eqs. (107) and (108). When the wheel in the roll-pitch plane fails, the torque capacity of the remaining five wheels must be boosted to at least 1.311 T_{mx} to produce the required torque T_{mx} about the spacecraft axes. This result is obtained by failing the wheels 1,2,...,6, one at a time, and then determining the absolute maximum value of the wheel torque in each case for generating T_{mx} torque about each of the three spacecraft axes. The maximum Euclidean norm and the associated absolute sum $\sum_{i=1}^{6} |\dot{H}_{wi}|$ are also shown in Table 3. Comparing the 2-wheel-per-axis and 6-wheel hexagon configurations, we find that for *equal torque requirements*, the latter (hexagon) configuration requires wheels of larger torque capacity and it consumes more power—and therefore not as favored as—the former configuration. However, when the roll, pitch, and yaw torque requirements are not the same, the conclusion will possibly swing in favor of the hexagon configuration.

Although six-wheel configurations provide substantial reliability and three-wheel redundancy, they could be expensive, so four-wheel configurations may be desirable instead, which provide a one-wheel redundancy. Two such configurations—one with pyramid base parallel to roll-yaw axes and the other with the base at 45°—are discussed above. For the purpose of comparison , call these configurations *parallel-* and *45°-*configuration, respectively. Under no-failure case, the 45°-configuration requires wheels of larger torque capacity than the parallel-configuration, but in the event of a one wheel failure, the situation reverses. On the other hand, from the power consumption viewpoint, under no-failure case, the 45°-configuration uses only slightly more power than the parallel-configuration, but the failure of a wheel aggravates this difference. Because the final design is usually based on one-wheel failure performance, we infer that if power is relatively abundant and the wheel torque capacity is at a premium, the 45°-configuration should be selected. On the other hand, if power is expensive and the cost of the wheels depends only weakly on its torque capacity, the parallel configuration will then be a more prudent choice.

When wheel redundancy is not warranted, only three wheels—necessary and sufficient for spacecraft control—can be employed. If the torque and momentum requirements about the three axes are identical, the control engineer may opt for one-wheel-per-axis configuration. But in the case of dissimilar requirements, 3-wheel pyramid, with the cant angle suitable to the desired torque and momentum ratios, might be preferred. Table 3 compares these two 3-wheel configurations for equal torque requirements, and shows that the pyramid configuration requires wheels of 39% bigger torque capacity, although its power consumption may be slightly less than or equal to that of the one-wheel-per-axis configuration.

Fig. 18 sums up the comparison between the power consumption of the six configurations considered in Table 3 for equal torque requirements. In particular, the Euclidean norm of the vector $\underline{\dot{H}}_{ww}$ versus the cant angle for each configuration for the no-wheel-failure case are shown in the figure. As noted before, the cant angle η^* ($\eta^* = 35.26°$) for minimum power consumption is the same for 3-, 4-, or 6-wheel pyramid configurations.

Concluding Remarks

Among a variety of disturbance torque that act on a space-craft, only solar radiation is considered in the preceding. For clarity, the torque expressions are further specialized by assuming that the vehicle mass center always remains in the pitch-yaw plane. Although this was true for the spacecraft that led to this study, the roll component of the vector from instantaneous vehicle mass center to the geometric center of the array or bus may not be zero for other spacecraft. Also, while solar torque varies at orbit frequency, aerodynamic torque, for

Table 3. Comparison of Six Configurations for Equal Torque Requirements about Roll, Pitch, and Yaw Axes, Based on Minimum Power Consumption

REQUIRED CONTROL TORQUE: $T_{cx} = T_{cy} = T_{cz} = T_{mx}$

CONFIGURATION	OPTIMUM ANGLE η^* (Deg)	NO-FAILURE			WORST 1-WHEEL FAILURE					
					TORQUE			POWER		
		Required Torque Capacity $\dot{H}_{w\cdot mx}/T_{mx}$	Total Power Consumption Rate $\sum_{i=1}^{n_w} \dot{h}_i^2/T_{mx}^2$	Total Power Intercept Due to Nonzero Initial Wheel Speed $\sum_{i=1}^{n_w-1} \lvert\dot{h}_i\rvert/T_{mx}$	Failed Wheel #	Wheel Producing Max. Torque	Required Torque Capacity $\dot{H}_{w\cdot mx}/T_{mx}$	Failed Wheel #	Total Power Consumption Rate $\sum_{i=1}^{n_w} \dot{h}_i^2/T_{mx}^2$	Total Power Intercept Due to Nonzero Initial Wheel Speed $\sum_{i=1}^{n_w-1} \lvert\dot{h}_i\rvert/T_{mx}$
2 Wheel/Axis (n_w=6)		0.5	1.5	3.0	Any One		1.0	Any One	2.0	3
6-Wheel Hexagon (n_w=6)	35.26	0.846	1.5	2.509	#5	#4	1.311	#4	2.933	3.073
4-Wheel Pyramid, Base Edges ll to Axes (n_w=4)	35.26	1.045	2.25	2.449	#1 #2	#2 #1	2.091	#1,2	6.62	4.182
4-Wheel Pyramid, Base Edges at 45° to X,Z Axes (n_w=4)	35.26	1.3	2.25	2.598	#3	#1, 2, 4	1.732	#3	9.0	5.196
3-Wheel Pyramid (n_w=3)	35.26	1.39	3.0	2.8	FAILURE DISALLOWED					
3-Orthogonal Wheels (n_w=3)		1	3.0	3.0						

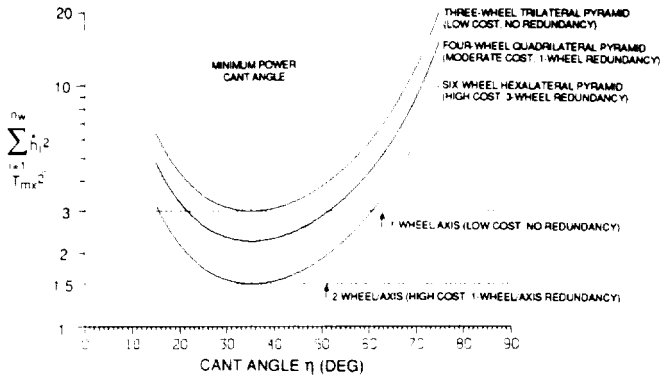

Fig. 18. Reaction wheel configurations trade-offs for equal roll, pitch, and yaw torque requirements

instance, may vary at twice the orbit frequency and a yaw bias torque might arise. For these different circumstances, the torque and momentum expressions have to be derived afresh to size the wheels. Regarding the wheel configurations, besides the two four-wheel configurations considered in the paper, there are two more: 1) NASA's standard four-wheel arrangement of one wheel along each body-axis and the fourth wheel inclined equally to all three axes; and 2) all four wheels canted equally to the pitch axis and each controlling roll and yaw as well, but more inclined to roll-axis than to yaw-axis or the converse depending on the roll and yaw unequal torque requirements. In the first arrangement, the cant angle of the fourth wheel is already determined, only the wheels' torque and momentum capacity need to be sized for one-wheel failure scenario. In contrast, in the second arrangement, two angles must be optimized to minimize power consumption for given torque and momentum requirements: the cant angle η with the roll-yaw plane and the angle γ with the roll axis for all four wheels. For these optimum angles, the torque and momentum capacity of the wheels will be sized according to one-wheel failure condition, as shown in the paper.

References

1. McElvain, R.J , "Effects of Solar Radiation Pressure on Satellite Attitude Control," *ARS Guidance, Control, and Navigation Conference*, Stanford, Ca., August, 1961, also *Guidance and Control—II, Progress in Astronautics and Aeronautics*, Vol. 13, Ed. Langford, R.C. and Mondo, C.J., pp. 543-564
2. Kalweit, C.C., "Optimum Yaw Motion for Satellites with a Nadir-Pointing Payload," *Journal of Guidance, Control, and Dynamics*, Vol. 6, No. 1, January-February, 1983, pp. 47-52
3. Evans, W.J., "Aerodynamic and Radiation Disturbance Torques on Satellites Having Complex Geometry," Chap. 5 in *Torques and Attitude Sensing in Earth Satellites*, Ed. by S.F. Singer, Academic Press, 1964
4. DeBra, D.B., and Cannon, R.H., "Momentum Vector Considerations in Wheel-Jet Satellite Control System Design," *Guidance and Control, Progress in Astronautics and Rocketry*, Vol. 8, Ed. R.E. Roberson and J.S. Farrior, pp. 565-598
5. Hughes, P.C., *Spacecraft Attitude Dynamics*, John Wiley and Sons, 1986
6. Fleming, A.W., and Ramos, A., "Precision Three-Axis Attitude Control Via Skewed Reaction Wheel Momentum Management," AIAA Paper No. 79-1719, Guidance, Naviation, and Control Conference, pp. 177-190

Spacecraft Detumbling Through Energy Dissipation

Norman Fitz-Coy† and Anindya Chatterjee*
Department of Aerospace Engineering, Mechanics, and Engineering Science
University of Florida

Abstract

The attitude motion of a tumbling, rigid, axisymmetric spacecraft is considered. A methodology for detumbling the spacecraft through energy dissipation is presented. The differential equations governing this motion are stiff, and therefore an approximate solution, based on the variation of constants method, is developed and utilized in the analysis of the detumbling strategy. Stability of the detumbling process is also addressed.

Introduction

As human expectations and scientific frontiers expand, the capabilities of satellites and space platforms must expand to meet these challenges. This results in more expensive satellites and space platforms being designed and launched. These elaborate systems will require on-orbit servicing/repairs and recovery missions to correct system malfunctions. In the past, on-orbit servicing and recovery missions have been uncommon operations since the cost of a replacement satellite was far less than the cost of these missions. However, today's high cost of manufacturing and launching of space systems make servicing and recovery missions an economical alternative to spacecraft replacement.[1-4] For example, the INTELSAT 6 communication satellite with an initial cost of $265M will be repaired on orbit at a total cost of $150M.[5]

In addition to monetary costs, there is the "cost" of human lives when manned space flights are involved. For these missions, recovery is not an alternative, it is the only choice. Finally, the growing concern over space debris mandates that at the end of a spacecraft's useful life, it must be retrieved and properly disposed of.

Malfunctioning of a spacecraft could result in a wildly gyrating, uncontrolled system. In the case of a manned spacecraft, it may not be feasible to wait for a period of several days while the spacecraft settles into a state of pure spin[6] before a rescue mission is attempted. It is also reasonable to assume that the manned spacecraft may be a module from a larger system, and as such, does not possess the degree of flexibility necessary to dissipate energy at a sufficiently high rate in order to quickly detumble itself. Consequently, it can be expected that during some recovery missions, the uncontrolled spacecraft will have non-zero precession and nutation rates which must be reduced to zero as quickly as possible.

The dynamic interactions involved in detumbling one spacecraft (uncontrolled vehicle) by another spacecraft (rescue vehicle), of perhaps comparable mass, are non-trivial. The task of grasping the uncontrolled (tumbling) spacecraft poses quite a challenge to the recovery

† Assistant Professor
* Graduate Student

vehicle since the grappling point on the disabled spacecraft may traverse a cone in space. In addition to the grasping task, the disabled spacecraft must be stabilized in a manner which maintains the motion of both vehicles within some safe bounds. This requires detailed knowledge of the dynamic characteristics of the spacecraft and places greater demands on the rescue vehicle's attitude control system, as well as fuel reserves. More importantly, this situation involves great safety hazards, particularly if either the disabled spacecraft or the rescue vehicle is manned. Yet the philosophy behind current approaches to the spacecraft retrieval problem is to "grapple and wrestle" the spacecraft,[2–4] since the time required for the spacecraft to settle into a state of pure spin may well exceed the time available during a retrieval mission.

An alternative to the current "grapple and wrestle" retrieval approach is a retrieval strategy which first reduces the motion of the spacecraft to that of pure spin and then despins the spacecraft. In this paper, a process by which this may be achieved, within the time frame of a retrieval mission, is presented. In the following section, a strategy for detumbling the spacecraft is presented. The equations governing the detumbling motion are developed and presented. An approximate solution to the governing equations is presented and used to investigate the proposed detumbling strategy. The paper concludes with suggestions for future work.

Detumbling Strategy

It is well known that the general rotational motion of a torque–free rigid body involves spin, nutation and precession.[7–9] Also, when dissipative effects are present (e.g., a flexible body), the rotational motion of the body eventually reduces to a state of pure spin about the axis of maximum moment of inertia. This state of pure spin rotational motion is a result of energy dissipation, and therefore represents the steady state rotational motion of all real spacecraft (i.e., non–rigid bodies). It is worth noting that for an axisymmetric body (one where the two smaller principal moments of inertia are equal) the nutation rate as measured with respect to the (constant) angular momentum vector is zero.

In practice, the time required for this state of rotational motion to occur is typically on the order of several days.[6] It is proposed that in order to decrease the required time, the energy dissipation rate of the spacecraft should be increased. This would be accomplished by attaching a dissipative device to the spacecraft; that is, retroactively fitting the spacecraft with external precession and nutation dampers.

The dissipative device consists of a flexible rod with an end mass as shown in Fig. 1. Damping effects in the rod would be tailored to dissipate energy at a rate which decreases the nutation angle within the time frame of the mission. The length and stiffness of the rod, and the size of the end mass are design criteria which are governed by stability requirements. As depicted in Fig. 1, usage of this device requires only a slight modification of the Tumbling Satellite Retrieval (TSR) Kit developed by Grumman.[4] It is proposed that the arm of the device be constructed from "smart" materials such that, during instances when the device is attached to the rescue vehicle, it will be sufficiently stiff to allow rapid maneuvers. However,

once grappling has been accomplished, the device will be detached from the rescue vehicle, eliminating its source of power, thereby rendering the device passive.

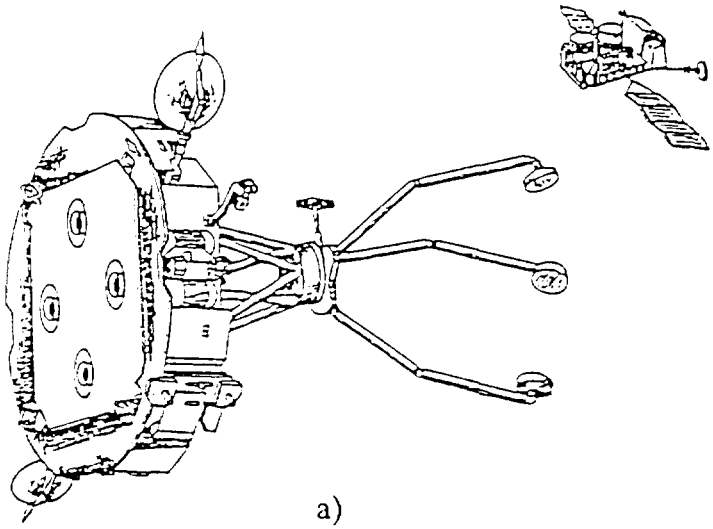

a)

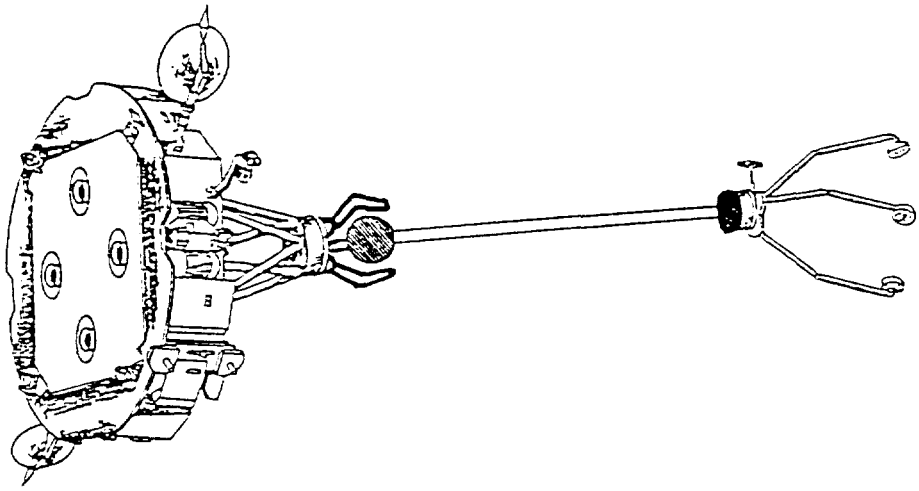

b)

Fig. 1. Retrieval vehicle: a) current concept (Grumman), b) proposed concept

In this paper, the issues associated with attaching the device to a tumbling spacecraft (i.e., locating/tracking/spin-rate matching and gripping), or the actual design of the dissipative device are not addressed. In what follows, it is assumed that the device has been successfully attached to the spacecraft. The following sections present an analysis of the dynamic performance of the device.

Equations of Motion

The spacecraft model adopted for the present study is shown schematically in Fig. 2. It consists of an axisymmetric rigid spacecraft, S, an end–mass, E, and a flexible link, L. The end–mass is attached to the spacecraft via the flexible link in such a manner that when the link is in its undeformed state, both the link and the end–mass are along the axis of symmetry of the spacecraft.

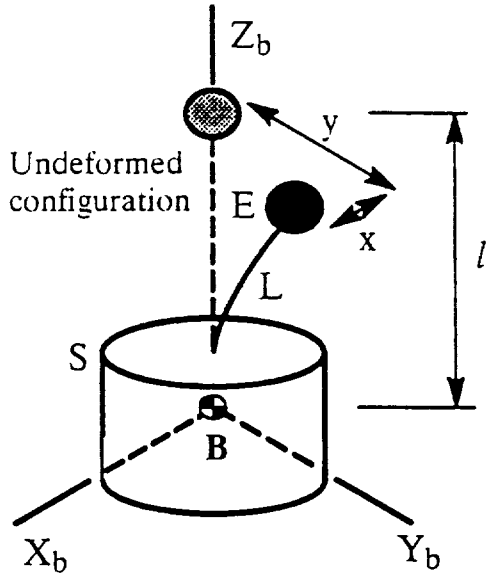

Fig. 2. Spacecraft Model

The dextral orthogonal coordinate system $BX_bY_bZ_b$ is fixed in the spacecraft. The axes are centroidal principal axes for the spacecraft. The Z_b axis lies along the axis of maximum inertia which is also the axis of symmetry. The displacements of the end–mass in the Z_b–direction are assumed small and therefore are neglected. That is, the end–mass is assumed to move parallel to the X_bY_b–plane; in this plane, the displacements of the end–mass relative to the spacecraft are denoted by x and y as shown in Fig. 1.

The centroidal moments of inertia of the spacecraft are I_{xx}, I_{yy}, and I_{zz}, where $I_{xx} = I_{yy} < I_{zz}$. The contribution of the end–mass to the overall system mass is neglected since its mass, m, is significantly smaller than the mass , M, of the spacecraft. The flexible link connecting the end–mass to the spacecraft is assumed "massless." Under these assumptions, the center of mass location, B, is unchanged by the the addition of the dissipation device.

Denoting the stiffness and the damping of the flexible rod by K and C, respectively, then the equations governing the motion of the system can be expressed as

$$\ddot{x} + c\dot{x} + (k - \omega_z^2 - \omega_y^2)x - 2\omega_z\dot{y} + (\omega_x\omega_y - \dot{\omega}_z)y = -(\omega_x\omega_z + \dot{\omega}_y)l \tag{1}$$

$$\ddot{y} + c\dot{y} + (k - \omega_z^2 - \omega_x^2)y + 2\omega_z\dot{x} + (\omega_x\omega_y + \dot{\omega}_z)x = -(\omega_y\omega_z - \dot{\omega}_x)l \tag{2}$$

$$I\dot{\omega}_x = -\omega_y\omega_z(\mu - 1)I - l(ky + c\dot{y}) - F_z y \tag{3}$$

$$I\dot{\omega}_y = \omega_x\omega_z(\mu - 1)I + l(kx + c\dot{x}) + F_z x \tag{4}$$

$$\mu I\dot{\omega}_z = c(\dot{y}x - \dot{x}y)\,, \tag{5}$$

where l is the distance of the end-mass from B, c, k, and I, are mass "normalized" quantities, μ is a nondimensional inertia ratio ($\mu > 1$), and F_z is the z-direction inertia force associated with the end-mass. Note that the mass normalized stiffness, k, is actually the square of the fundamental frequency for the dissipative device.

$$c = \frac{C}{m};\ k = \frac{K}{m} = \omega_n^2 \tag{6.a}$$

$$I = \frac{I_{xx}}{m} = \frac{I_{yy}}{m};\ \mu = \frac{I_{zz}}{I_{xx}} \tag{6.b}$$

$$F_z = \dot{\omega}_x y - \dot{\omega}_y x + 2(\omega_x\dot{y} - \omega_y\dot{x}) + \omega_z(\omega_x x + \omega_y y) - l(\omega_x^2 + \omega_y^2) \tag{6.c}$$

Equations (1) through (5) represent a set of stiff differential equations since there are two disparate time scales. An approximate analytical solution for these equations is developed in the next section.

Approximate Solution

Assuming a small attached end-mass E ($m \ll M$) and relatively small dissipation rates, the rotational motion of the system (spacecraft and device) can be approximated for a few cycles of oscillation by Euler's equations for an axisymmetric, torque free, rigid body. These equations are

$$\dot{\omega}_x = -\omega_y\omega_z(\mu - 1), \tag{7.a}$$

$$\dot{\omega}_y = \omega_x\omega_z(\mu - 1), \tag{7.b}$$

$$\dot{\omega}_z = 0, \tag{7.c}$$

where μ is as defined in Eq. (6.b). Euler's equation (Eq. (7)) has a solution

$$\omega_x = A\cos\Omega(t + t_0), \tag{8.a}$$

$$\omega_y = A\sin\Omega(t + t_0), \tag{8.b}$$

$$\omega_z = \text{constant} \tag{8.c}$$

where A represents the tangential angular velocity (i.e., the resultant of ω_x and ω_y; see Fig. 4), and $\Omega = (\mu - 1)\omega_z$. Equations (1) and (2) can now be rewritten as

$$\ddot{x} + c\dot{x} + (k - \omega_z^2 - A^2S_\Omega^2)x - 2\omega_z\dot{y} + A^2S_\Omega C_\Omega y = -\mu\omega_z l AC_\Omega \tag{9}$$

$$\ddot{y} + c\dot{y} + (k - \omega_z^2 - A^2C_\Omega^2)y + 2\omega_z\dot{x} + A^2S_\Omega C_\Omega x = -\mu\omega_z l AS_\Omega \tag{10}$$

where

$$S_\Omega = \sin\Omega(t + t_0);\ C_\Omega = \cos\Omega(t + t_0). \tag{11}$$

Equations (9) and (10) have time varying coefficients; thus, a study of stability via the Routh–Hurwitz criterion is inapplicable. To circumvent this problem, a coordinate system, $B\xi\eta\zeta$, which rotates relative to the spacecraft–fixed Z_b–axis with angular rate Ω is defined (see Fig. 3). The counterparts of Eqs. (9) and (10) in this coordinate system are constant

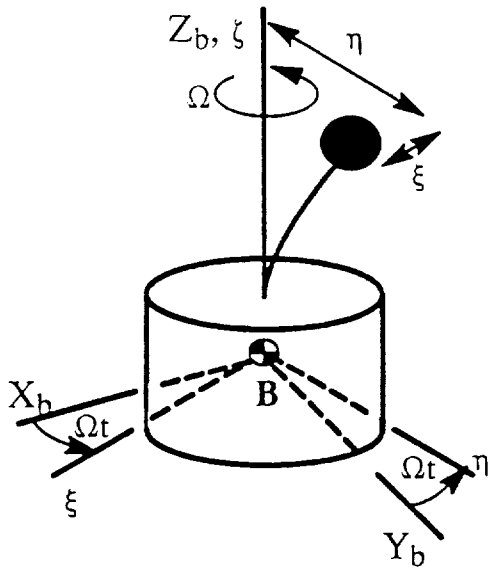

Fig. 3. $B\xi\eta\zeta$ coordinate system

coefficient differential equations for ξ and η. Routh–Hurwitz criterion can now be applied to show that the complementary solutions of ξ and η decay provided that the normalized stiffness satisfies

$$k - \mu^2\omega_z^2 - \frac{A^2}{2} > 0, \tag{12}$$

and the normalized damping is positive (i.e., $c > 0$). Note that if H is the magnitude of the angular momentum of the tumbling spacecraft, then

$$H^2 = m^2I^2(\mu^2\omega_z^2 + A^2). \tag{13}$$

which implies $\mu^2\omega_z^2 + \frac{A^2}{2} < \frac{H^2}{m^2I^2}$ is bounded at all times for any given set of initial conditions. Therefore, proper selection of k will always satisfy Eq. (12).

It can also be shown that in the $B\xi\eta\zeta$ coordinate system, the particular solutions for the counterparts of Eqs. (9) and (10) are constants ξ_1 and η_1. Since the complementary solutions decay to zero and the particular solutions are constant, then steady state solutions for Eqs. (9) and (10) can be expressed as

$$x = \zeta_1 C_\Omega - \eta_1 S_\Omega \tag{14.a}$$

$$y = \zeta_1 S_\Omega + \eta_1 C_\Omega \tag{14.b}$$

The energy dissipation rate D then becomes

$$D = mc(\dot{x}^2 + \dot{y}^2) = mc\Omega^2(\zeta_1^2 + \eta_1^2) \tag{15}$$

where the entire energy dissipation is considered as energy lost by the tumbling spacecraft. That is,

$$\frac{dT}{dt} = - D \tag{16}$$

where T is the spacecraft's (rotational) kinetic energy.

$$T = \frac{mI}{2}(\mu\omega_z^2 + A^2) \tag{17}$$

Now, the quantity A is a measure of how far the spacecraft is from a state of pure spin. When A is zero, the nutation angle is zero, therefore, the spacecraft is in a state of pure spin. The angle that the axis of symmetry makes with the direction of the constant angular momentum vector is given by (see Fig. 4)

$$\tan\theta = \frac{A}{\mu\omega_z} \tag{18}$$

where θ is the nutation half angle.

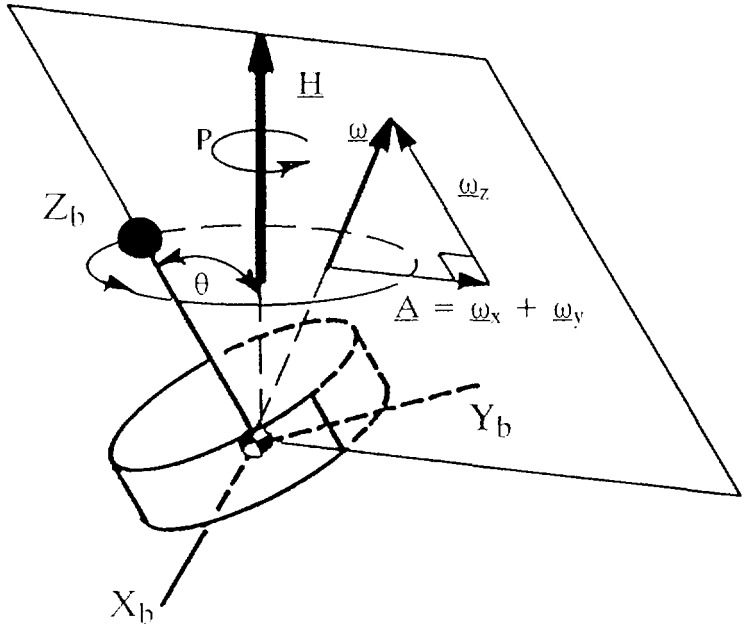

Fig. 4. Precessing spacecraft

Via Eqs. (13) through (17), a constant coefficient, ordinary differential equation for the A^2 can be developed. Omitting the algebra, this equation is

$$\frac{d}{dt}(A^2) = -\frac{2c\varrho l^2 A^2 (P^2 - A^2)^2 (Q^2 - c^2\varrho^2 A^2)}{I(Q^2 + (k - P^2 - c^2\varrho^2)A^2)^2} \tag{19}$$

where ρ, P^2, and Q^2 are defined respectively as

$$\varrho = \frac{\mu - 1}{\mu},$$

$$P^2 = \frac{H^2}{m^2 I^2} = \mu^2\omega_z^2 + A^2,$$

$$Q^2 = (k - P^2)^2 + c^2\varrho^2 P^2.$$

Note that the P is the precession rate of the spacecraft (see Fig. 4).

Equation (19) is of the form

$$\frac{dx}{dt} = -\frac{\alpha x(\beta - x)^2(\gamma - x)}{(\delta + x)^2},$$

which may be rewritten as

$$dt = -\frac{1}{\alpha}\frac{(\delta + x)^2}{x(\beta - x)^2(\gamma - x)}dx$$

Using a partial fraction expansion, an analytical solution can be obtained, resulting in a solution of Eq. (19) of the form $t = f(A^2)$. For studies of settling time versus A^2, this form of the anti-derivative of Eq. (19) is quite convenient. However, when A^2 as a function of time is required, it is more convenient to numerically integrate Eq. (19).

Results

In order to validate the approximate solution, Eqs. (1) through (5) and Eq. (19) were numerically integrated using the MATLAB[10] function "ODE45." Initial conditions for the approximate solution were $A = 6$, $\omega_z = 3$ whereas initial conditions for the complete solution were $\omega_x = 6$, $\omega_y = 0$, $\omega_z = 3$, $\dot{x} = \dot{y} = 0$, and $x = y = 0$. (Note, any combination of ω_x and ω_y resulting in $A = 6$ is applicable since the transients decay rapidly.) In both cases, $\mu = 1.5$ resulting in $P^2 = 56.25$. The results of these numerical integrations for two different scenarios are shown in Figures 5 and 6. While the accuracy of the approximate solution is quite acceptable, its computational requirement is typically three to four orders of magnitude less than that required for the "complete" solution. Figures 5 and 6 show that the relative error for the approximate solution decreases as the detumbling time becomes longer (i.e., the energy dissipation rate decreases). This is expected since the approximation becomes more accurate as the dissipation rate decreases.

Figures 7 through 11 demonstrate the dependence of energy dissipation rate, hence settling time, on system the parameters c, k, l, μ, and H, respectively. For an effective

comparison, an initial value of $A=6$ is used in each investigation. In Figs. 7 through 10, the parameter P^2 remains unchanged at $P^2=56.25$ (i.e., $\mu=1.5$, $\omega_z=3$), whereas, in Fig. 11, P^2 changes as ω_z is varied from 2 to 5. That is, in Fig. 11 the angular momentum is varied while keeping the inertia properties constant. In contrast, in Fig. 10 the angular momentum is held constant while the inertia properties are varied ($0.5< \mu <2$ and ω_z adjusted such that P^2 is maintained at 56.25). In Figs. 7 through 10, the label by each curve represents the value of the parameter which was varied; in Fig. 11, the label by each curve represents the value of ω_z.

Damping obviously has a strong effect on the dissipation rate and generally an increase in damping leads to a decrease in settling time (Fig. 7). However, a relatively high damping value ($c=500$) causes the settling time to increase indicating that for a given configuration, there is an optimal value of c. Increasing c beyond this optimal value will result in increasing settling times. As expected, decreasing the length of the rod (Fig. 8) or increasing its stiffness (Fig. 9) increases the settling time since both of the processes decrease the energy dissipation rate. Values of $1< \mu <2$ are required for stability about the Z_b-axis (Fig. 10). For cases in which $\mu < 1$, the system is unstable about the Z_b-axis, therefore A increases instead of decreasing. Note that $\mu < 1$ does not violate the assumptions used in formulating the problem, but represents an inappropriate configuration. Figure 11 demonstrates that the settling time increases as the initial spin rate of the spacecraft decreases.

Figure 12 shows contours of constant settling time for various combinations of normalized damping and stiffness. Settling time was defined as the time required for A^2 to decrease to 1% of its original value. The contours of Fig. 12 were developed using values of $I=400$, $\mu=1.5$, $l=1$, and $\omega_z=3$; the parameter P^2 was 56.25 (i.e., $A=6$ initially). Each contour is labelled with the settling time in hours. These contours again demonstrate that for a given stiffness, there is an optimal value of c, beyond which the settling time increases. For large values of k, the optimal points on each contour lie approximately on a straight line. It can be shown that for cases where $(A^2 \ll k)$, the "optimal" value of c is proportional to $(k-P^2)$; the constant of proportionality depends on the choice of the initial and final values of A^2 used in the definition of settling time. Superimposed on the contours of Fig. 12 is the theoretically derived straight line. Excellent agreement is observed for cases involving large stiffness values. It should be noted that the "optimal" values of c are unrealistically large; therefore we may assume as a general rule of thumb that the damping should be made as large as possible.

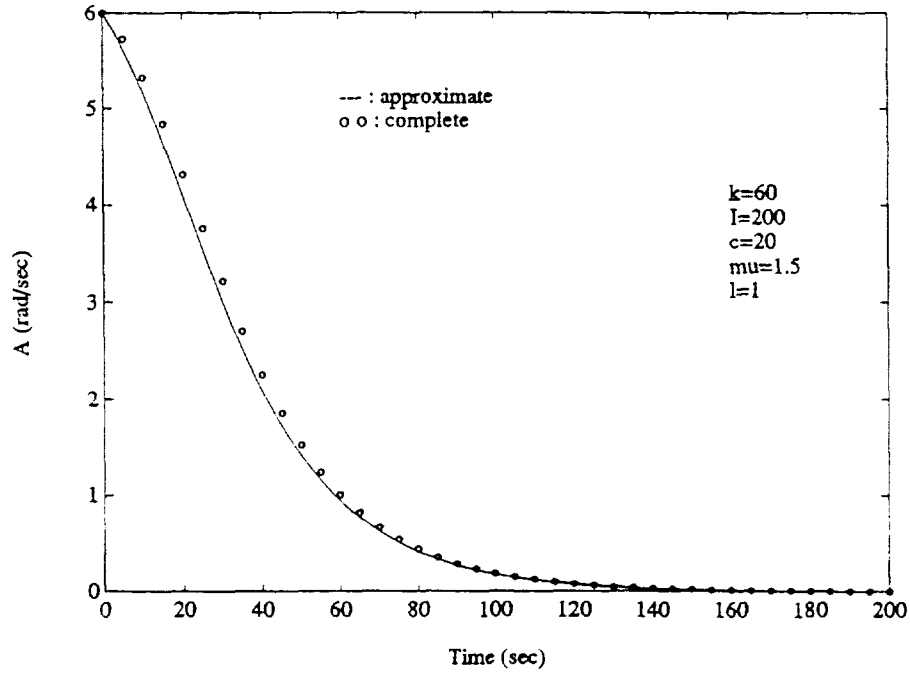

Fig. 5. Spacecraft's state of spin: Complete vs. Approximate (Case 1)

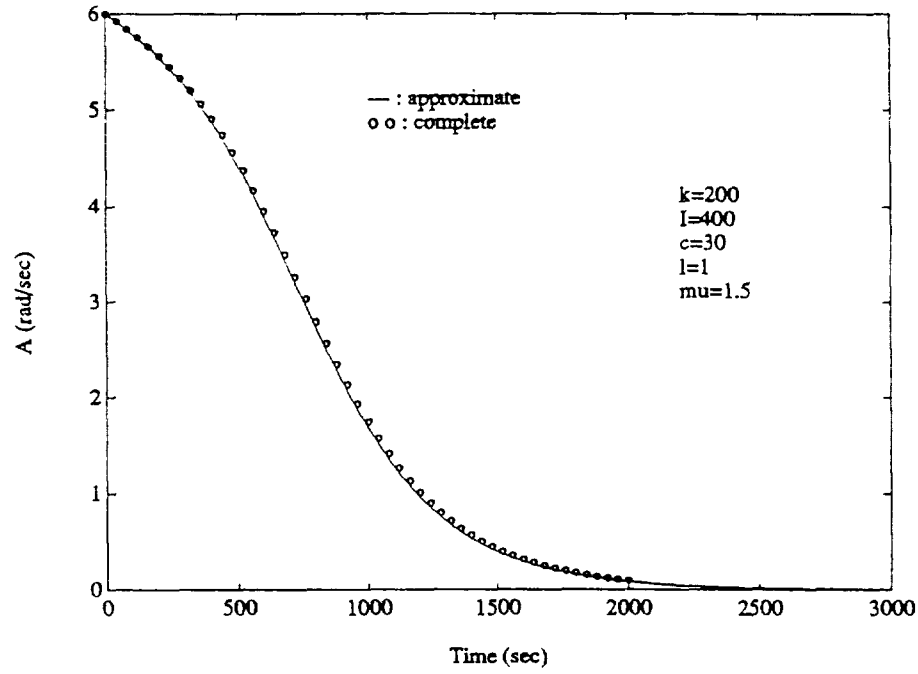

Fig. 6. Spacecraft's state of spin: Complete vs. Approximate (Case 2)

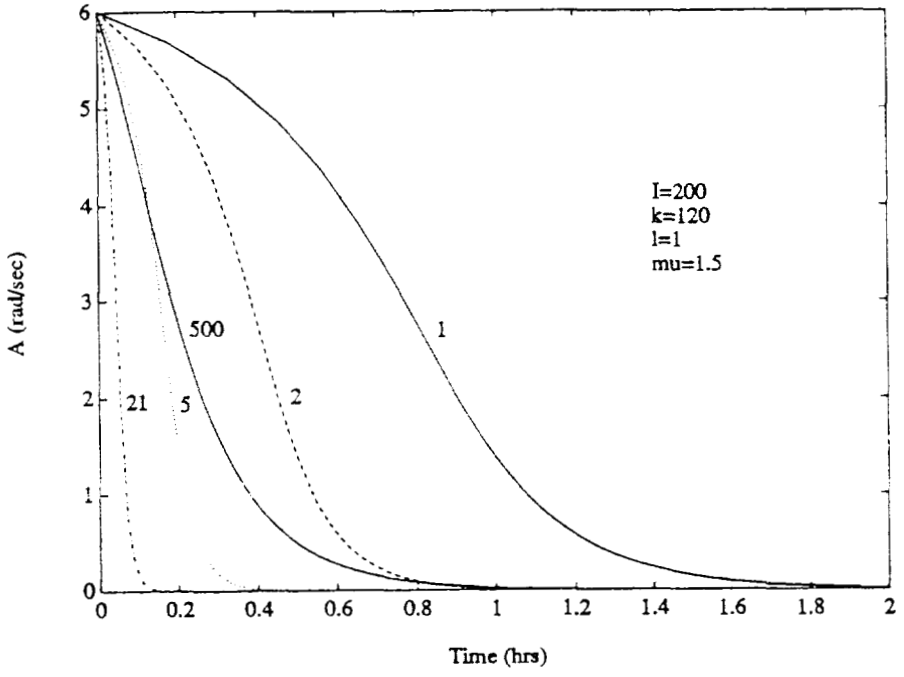

Fig. 7. Effects of damping on dissipation rate

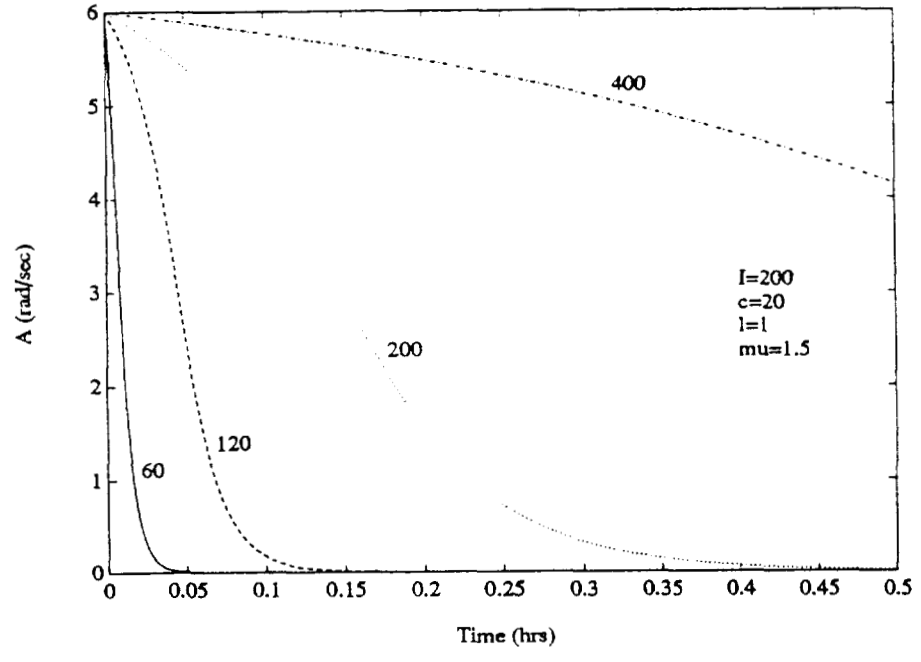

Fig. 8. Effects of stiffness on dissipation rate

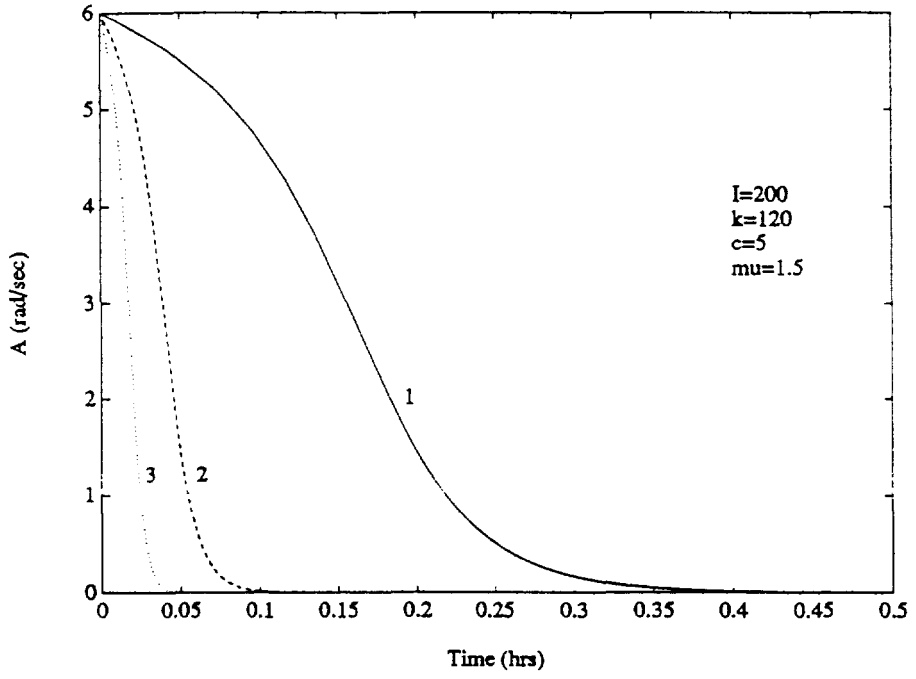

Fig. 9. Effects of length on dissipation rate

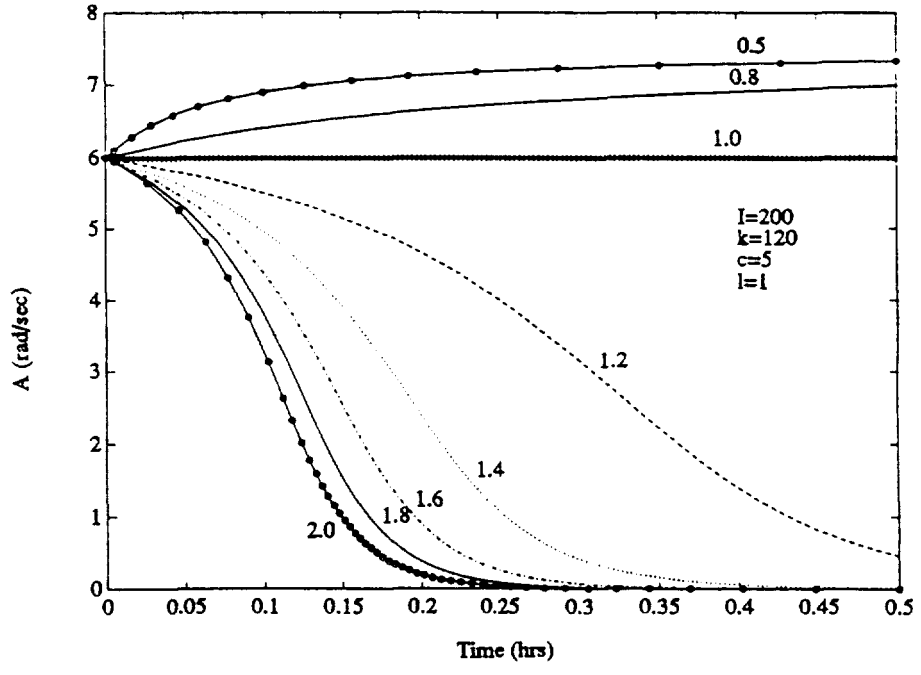

Fig. 10. Effects of spacecraft inertia properties on dissipation rate

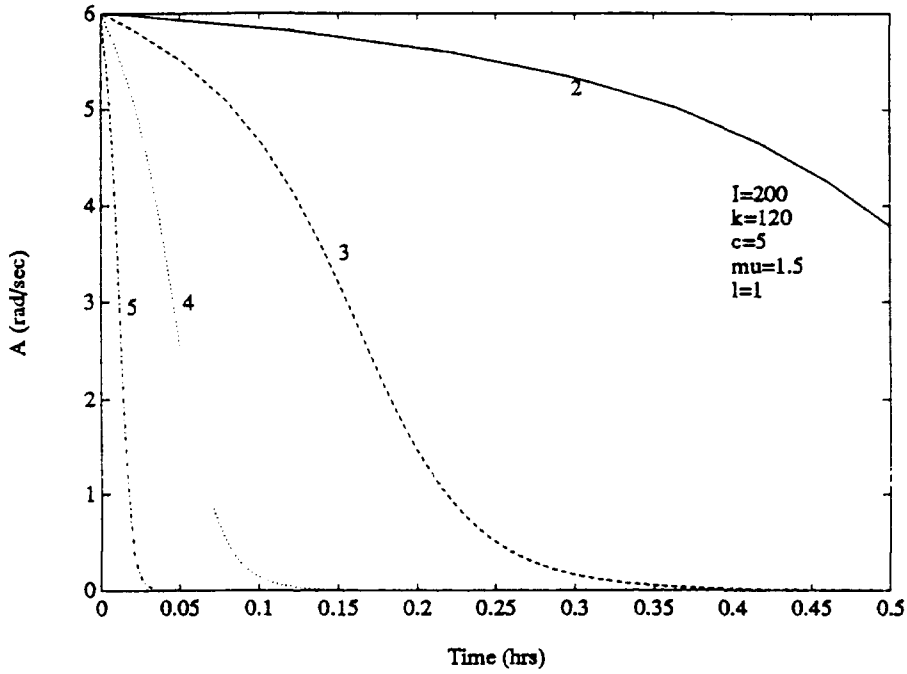

Fig. 11. Effects of angular momentum on dissipation rate

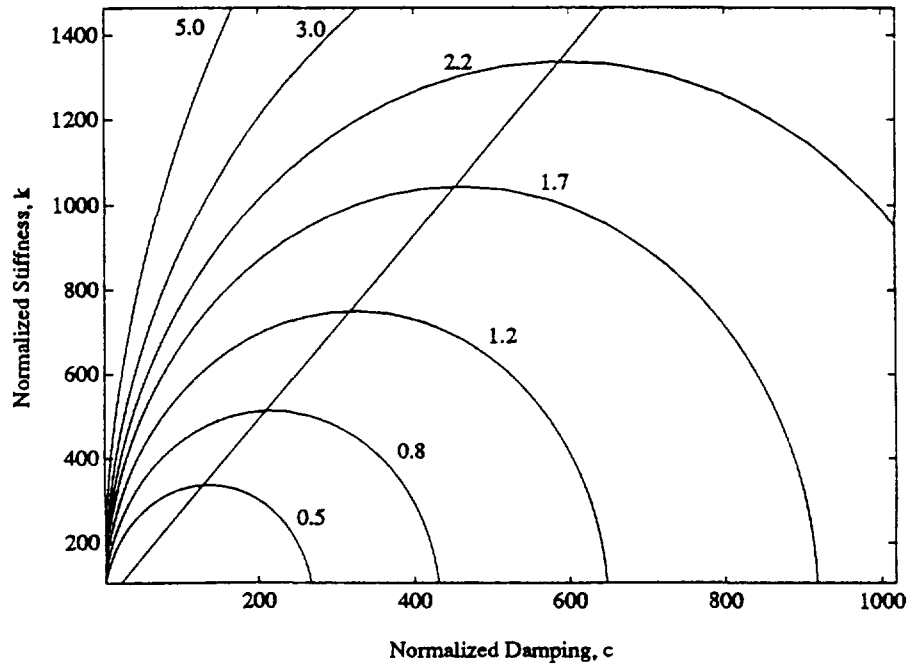

Fig. 12. Constant settling time contours

Summary

The approximate solution developed closely parallels the energy-sink approach.[11] The device presented in this paper is an extension of the one-degree-of-freedom (dof) ball-in-tube precession dampers studied by previous authors;[11,12] this device represents a two dof damper.

The problem addressed in this paper is an important part of the bigger problem of devising safe and efficient spacecraft detumblimg and retrieval strategies. Although the results presented in this paper are based on somewhat higher than normal initial rotational rates and normalized damping characteristics, the usefulness of the proposed device is well demonstrated. Currently, the "optimal" normalized damping coefficients are not realizable; however, with developments in the area of material sciences, these "optimal" damping coefficients may eventually be achievable. Future work of direct practical utility will include (1) a detailed study of desired settling time as a function of system parameters, (2) stability analyses associated with misalignment of the device, and (3) despin strategies.

References

1. Cochran, J. E., Jr., and Lahr, B. S., "Satellite Attitude Motion Models for Capture and Retrieval Investigations," Final Technical Report prepared for NASA (Marshall Space Flight Center), Auburn University, AL, 1986.

2. Cable, D. A., DeRocher, Jr., W. L., Cathcart, J. A., Keeley, M. G., Madayev, L., Nguyen, T. K., and Preese, J. R., "Concept Definition Study for Recovery of Tumbling Satellites," Final Technical Report prepared for NASA (Marshall Space Flight Center), Martin Marietta Denver Aerospace, CO, 1986.

3. _____, "Concept Evaluation/Test for the Tumbling Satellite Retrieval (TSR) Kit: Parts 1 & 2," Final Report prepared for NASA (Marshall Space Flight Center), Grumman Aerospace, NY, April, 1990.

4. _____, "Tumbling Satellite Retrieval Kit: Final Design Document," Technical Report prepared for NASA (Marshall Space Flight Center), Grumman Aerospace, NY, Nov., 1988.

5. Kolcum, E. H., "Separation Failure Places Intelsat 6 in Useless Orbit," Aviation Week and Space Technology, March 19, 1990, pp. 212.

6. Lenorovitz, J.M., "Emergency Recovery Effort Bringing Olympus 1 Satellite under Control," Aviation Week and Space Technology, July 29, 1991, pp. 60.

7. Goldstein, Herbert, Classical Mechanics, 2nd Edition, Addison Wesley Publishing Co., Inc., Reading, MA, 1980.

8. Ginsberg, Jerry H, Advanced Engineering Dynamics, Harper & Row, Publishers, New York, 1988.

9. Hughes, Peter C., Spacecraft Attitude Dynamics, John Wiley and Sons, Inc., New York, NY, 1986.

10. _____, Pro-MATLAB User's Guide, The Math Works, Inc., South Natick, MA, 1990.

11. Cochran, J. E., Jr., and Thompson, J. A., "Nutation Dampers vs Precession Dampers for Asymmetric Spacecraft," Journal of Guidance and Control, Vol. 3, No. 1, Jan-Feb, 1980, pp. 22-28.

12. Chobotov, V. A., Spacecraft Attitude Dynamics and Control, Krieger Publishing Co., Malabar, FL, 1991.

The Results of the In-Flight Attitude Sensor Calibration for the Arthur Holly Compton Gamma Ray Observatory*

W. S. Davis, A. H. Eudell, L. S. Kulp, and L. A. Lindrose
COMPUTER SCIENCES CORPORATION (CSC)

R. R. Harman
GODDARD SPACE FLIGHT CENTER (GSFC)

ABSTRACT

The Arthur Holly Compton Gamma Ray Observatory (GRO) was launched by the shuttle Atlantis in April 1991. This paper presents the results of the attitude sensor calibration that was performed during the early mission.

The GSFC Flight Dynamics Facility (FDF) performed an alignment calibration of the two fixed-head star trackers (FHSTs) and two fine Sun sensors (FSSs) on board Compton GRO. The results show a 27-arcsec shift between the boresights of the FHSTs with respect to prelaunch measurements. The alignments of the two FSSs shifted by 0.20 and 0.05 degree. During the same time period, the Compton GRO science teams performed an alignment calibration of the science instruments with respect to the attitude reported by the onboard computer (OBC). In order to preserve these science alignments, FDF adjusted the overall alignments of the FHSTs and FSSs, obtained by the FDF calibration, such that when uplinked to the OBC, the shift in the OBC-determined attitude is minimized.

FDF also calibrated the inertial reference unit (IRU), which consists of three dual-axis gyroscopes. The observed gyro bias matched the bias that was solved for by the OBC. This bias drifted during the first 6 days after release. The results of the FDF calibration of scale factor and alignment shifts showed changes that were of the same order as their uncertainties.

* This work was supported by the National Aeronautics and Space Administration (NASA)/Goddard Space Flight Center (GSFC), Greenbelt, Maryland, Contract NAS 5-31500.

1. INTRODUCTION AND BACKGROUND

The Arthur Holly Compton Gamma Ray Observatory (GRO) was launched by the shuttle Atlantis in April 1991. This paper presents the results of the attitude sensor calibration that was performed during the early mission by the Goddard Space Flight Center (GSFC) Flight Dynamics Facility (FDF).

1.1 Summary

Section 1 of this paper provides an introduction and background information, consisting of a summary of the paper and its results, a brief history of the GRO mission, a description of the attitude sensors, and the attitude requirements. Section 2 discusses the purpose of in-flight calibration of the attitude sensors, describing the impact of calibration errors and how such errors are parameterized. Section 3 provides an overview of the methods used for the in-flight calibration of the attitude sensors and briefly summarizes the algorithms and FDF software system. Section 4 provides the results of the calibration. These results include a description of the data, the numerical results, and how the results were used. Section 5 gives a brief discussion of these results.

FDF performed an alignment calibration of the two fixed-head star trackers (FHSTs) and two fine Sun sensors (FSSs) on board Compton GRO. The results show a 27-arcsec shift between the boresights of the FHSTs with respect to prelaunch measurements. The alignments of the two FSSs shifted by 0.20 and 0.05 degree. During the same time period, the Compton GRO science teams performed an alignment calibration of the science instruments with respect to the attitude reported by the onboard computer (OBC). In order to preserve these science alignments, FDF adjusted the overall alignments of the FHSTs and FSSs, obtained by the FDF calibration, such that when uplinked to the OBC, the shift in the OBC-determined attitude is minimized.

FDF also calibrated the inertial reference unit (IRU), which consists of three dual-axis gyroscopes. The observed gyro bias matched the bias that was solved for by the OBC. This bias drifted during the first 6 days after release. The results of the FDF calibration of scale factor and alignment shifts showed changes that were of the same order as their uncertainties.

1.2 Mission and Brief History of Compton GRO

The Compton Gamma Ray Observatory was the second great observatory launched by the National Aeronautics and Space Administration (NASA). Its purpose is to observe astronomical sources in the the gamma ray spectrum. The 18,000-kg spacecraft has four gamma ray instruments, which cover a wide range of capabilities. These capabilities include fields of view (FOV) ranging from all-sky down to 4 degrees, a total energy range of 0.1 to 30,000 MeV, a time resolution of as small as 0.1 ms, and a position resolution of as small as 5 arcmin (1σ).

The shuttle Atlantis was launched from the Kennedy Space Center on April 5, 1991 at 14:22:44 UTC. The observatory was deployed on April 7, 1991. During the deployment, the high-gain antenna became stuck, and the astronauts performed an unscheduled extravehicular activity (EVA) to free it. Compton GRO was released from the shuttle at 22:37 UTC into a near-circular orbit with a semimajor axis of 6833 km and an inclination of 28.48 degrees. Attitude calibration maneuvers were performed from April 9 through April 14, 1991. That was followed by a series of observations designed to calibrate the scientific instruments. Calibrated attitude sensor alignments were uplinked on May 14, 1991. On May 16, the spacecraft maneuvered to its first science target, which initiated the start of normal operations. Normal operations consist of 2-week observation periods, during which Compton GRO is maintained in an inertial attitude.

1.3 Attitude Sensors of Compton GRO

Compton GRO is a multimission modular spacecraft (MMS) with two FHSTs, two FSSs, an IRU, two three-axis magnetometers (TAMs), and coarse Sun sensors (CSSs). Attitude control during normal

operations is performed with reaction wheels and magnetic torquer bars. This discussion is limited to the in-flight calibration of the FHSTs, FSSs, and IRU. FDF did perform a bias determination for the primary TAM (bias = [0,0,-4] mG). However, based on comparisons of FHST attitude solutions to FSS/TAM attitude solutions, the error in the FSS/TAM solutions meets the requirement of less than 2 degrees (3σ) without the bias solution; thus no changes to the TAM bias were made.

The FHSTs are the NASA standard star tracker built by Ball Aerospace Systems Division (serial numbers 7 and 8). This model uses digital electronics, which replace much of the analog electronics of previous models. These devices are capable of locking onto and tracking the position and magnitude of one star at a time. The valid magnitude range is 2.0 to 5.7. The FOV is an 8-degree square and the digital resolution is 7.78 arcsec per count. The position measurements have a random error of 8 to 24 arcsec (1σ), depending on the magnitude and position in the FOV, and systematic calibration errors of less than 10 arcsec (1σ). For Compton GRO, the FHSTs are mounted with their boresights separated by 90 degrees.

The IRU is the DRIRU II manufactured by Teledyne. It consists of three dual-axis gyroscopes, giving a total of six channels of information. The precision output of this device is in the form of pulses that provide increments of rotation. Each gyroscope operates at two rate ranges, the low rate being 0.05 arcsec per pulse and the high rate being 0.8 arcsec per pulse. For Compton GRO, inertial attitudes are maintained in the low-rate range and maneuvers are done in the high-rate range. The angular rate bias is specified to vary by no more than 0.0012 arcsec/sec over 6 hours and 0.0008 arcsec/sec over one year.

The FSS, manufactured by Adcole, has a 64-by-64-degree FOV. It consists of two orthogonal sensor heads, each of which provides the angle between the Sun and a plane defined by a slit and a set of reticules. The digital resolution is about 0.004 degrees per count. The noise of each measurement is specified to be half the digital resolution. The calibrated accuracy is specified to be less than 0.02 degree. The two FSSs on Compton GRO are mounted so that their FOVs overlap by about 2 degrees.

1.4 Attitude Requirements for Compton GRO

The Compton GRO mission requires coarse attitude determination to an uncertainty of 2 degrees (3σ) per axis, using FSS, TAM, and IRU data. Fine attitudes determined using FHST and IRU data are required with an uncertainty of 0.024 degrees (3σ) per axis. After each maneuver, the attitude must be within 0.5 degree of the target attitude so that the OBC can correctly identify stars.

2. PURPOSE OF IN-FLIGHT CALIBRATION

Before launch, the manufacturers of spacecraft and attitude sensors measure the alignments and other calibration quantities. These measurements, made before and after various vibration, thermal, and vacuum tests, show slight shifts in calibration parameters. The shock and vibration of launch and the weightlessness, temperature, and vacuum of the space environment also result in slight shifts in calibration parameters. Such shifts introduce error into the attitude determination process. To reduce this error, the attitude sensor models are constructed to incorporate small changes in calibration parameters; in-flight sensor measurements are then used to solve for small shifts in calibration parameters from the best prelaunch values. This section presents models for small adjustments to calibration and discusses the impact of calibration errors.

2.1 FHST and FSS Alignment Calibration Error

The mission requires alignment calibration of the FHSTs and FSSs. Let M_{AS} be the prelaunch value of the 3-by-3 transformation matrix from the sensor coordinates to the coordinates of the attitude control system (ACS), which coincides with the body coordinates of the spacecraft. Each sensor has its own value for this

matrix, which gives the alignment of the sensor with respect to the ACS. Let $M_{AS'}$ be the postlaunch value of the alignment matrix and let $M_{SS'}$ be the difference between the prelaunch and postlaunch alignment matrices, sometimes called the misalignment matrix, such that

$$M_{AS'} = M_{AS}\, M_{SS'} \tag{1}$$

To perform an alignment calibration, an algorithm must determine $M_{SS'}$ for each sensor. For the Compton GRO and many other missions, it is assumed that all the matrices in equation 1 are orthonormal; thus there are only three degrees of freedom to each matrix. Let $M_{SS'}$ be parameterized by the 3-vector $\vec{\theta}$ as follows:

$$M_{SS'} = M_{AS}^{T}\, \mathrm{Rot}(\vec{\theta})\, M_{AS} \tag{2}$$

$\vec{\theta}$ is the Euler rotation vector which is converted to the corresponding rotation matrix with the function $\mathrm{Rot}(\vec{\theta})$,

$$\mathrm{Rot}(\vec{\theta}) = \cos(\theta)\ \mathrm{I} + \frac{1 - \cos(\theta)}{\theta^2}\, \vec{\theta}\, \vec{\theta}^{T} - \frac{\sin(\theta)}{\theta} \begin{bmatrix} 0 & -\theta_3 & \theta_2 \\ \theta_3 & 0 & -\theta_1 \\ -\theta_2 & \theta_1 & 0 \end{bmatrix} \tag{3}$$

where $\theta = |\vec{\theta}|$ and I is the 3-by-3 identity matrix. The postlaunch alignment becomes

$$M_{AS'} = \mathrm{Rot}(\vec{\theta})\, M_{AS} \tag{4}$$

The algorithm discussed in Section 3 solves for a value of $\vec{\theta}$ for each of the two FHSTs and each of the two FSSs on board Compton GRO. Unfortunately, not all 12 components of these four vectors are independently observable. An overall rotation of all the attitude sensors with respect to the scientific instruments or the body coordinate system is not observable by any calibration process that is limited to using attitude sensor data: thus only 9 of the 12 degrees of freedom in these alignments are observable. The criteria for the selection of the unobservable degrees of freedom are discussed in Section 3.

FHST and FSS alignment errors have two main effects on the attitude of the spacecraft. First, an overall alignment error introduces a systematic error in the pointing of the scientific instruments. This overall error is related to the three unobservable degrees of freedom already mentioned. Second, the relative alignment errors between these sensors results in higher measurement residuals and inconsistencies between attitude solutions obtained with one FHST and both FHSTs.

2.2 IRU Calibration Errors

The OBC and FDF ground software use the following model of the digital IRU output to obtain the measured angular velocity of the spacecraft, $\vec{\omega}$,

$$\vec{\omega} = G \begin{bmatrix} k_x & \Delta N_x \\ k_y & \Delta N_y \\ k_z & \Delta N_z \end{bmatrix} \frac{1}{\Delta t} - \vec{b} \tag{5}$$

where G is a 3-by-3 matrix that transforms the IRU outputs to the ACS, $\vec{b}$ is a bias vector, k_i is the scale factor for the i^{th} IRU axis, and ΔN_i is the change in the accumulated angle counts during the time interval Δt. By allowing the G-matrix to be nonorthogonal, the nonorthogonality of the IRU measurement axes can be taken into account. The adjustable parameters of this model are G, the ks, and $\vec{b}$. Small variations of these parameters are applied to obtain an improved rate, $\vec{\omega}'$,

$$\vec{\omega}' = (I + \delta A)\, G \begin{bmatrix} (1 + S_x)\, k_x\, \Delta N_x \\ (1 + S_y)\, k_y\, \Delta N_y \\ (1 + S_z)\, k_z\, \Delta N_z \end{bmatrix} \frac{1}{\Delta t} - (\vec{b} + \delta\vec{b}) \qquad (6)$$

where δA is a 3-by-3 matrix of small adjustments to the prelaunch value of alignment, S_i is a small adjustment to the scale factor of the i^{th} axis, and δb is an adjustment to the prelaunch value of the bias. Since δA contains independent adjustments to three axes, this matrix has six degrees of freedom. However, by allowing all nine components to vary, the scale factor adjustments can also be incorporated. Let δM be the 3-by-3 matrix that includes both alignment and scale factor adjustments as follows:

$$\vec{\omega}' = (I + \delta M)\, G \begin{bmatrix} k_x\, \Delta N_x \\ k_y\, \Delta N_y \\ k_z\, \Delta N_z \end{bmatrix} \frac{1}{\Delta t} - (\vec{b} + \delta\vec{b}) \qquad (7)$$

If $\vec{\omega}'$ is the true angular rate vector and the bias is assumed small, then the rate error is given to first order in the calibration error by

$$\delta\vec{\omega} = \vec{\omega}' - \vec{\omega} \approx \delta M\, G\, \vec{\omega}' - \delta\vec{b} \qquad (8)$$

For an inertially pointing attitude, $\vec{\omega}'$ is very small, so the errors in the IRU alignment and scale factors do not contribute any first-order errors to the attitude solution. The IRU bias error does contribute significantly to the rate error at all times, which is why it is continuously solved for by the OBC. During a maneuver, IRU alignment and scale factor errors can accumulate to produce a noticeable effect on the attitude. This is especially true for Compton GRO, because the OBC uses only IRU data during maneuvers to compute the attitude. Section 3 discusses the algorithm that uses maneuver data to solve for adjustments to the IRU calibration parameters.

2.3 Calibration Parameters Uplinked

FDF has the capability to provide calibrated parameters for the attitude sensors in the form of uplink tables to the OBC. The information in these tables includes postlaunch alignments $M_{AS'}$ for each of the two FHSTs and each of the two FSSs and a postlaunch IRU alignment matrix $G' = [I + \delta M]\, G$. The OBC uses a Kalman filter to continuously solve for the spacecraft attitude and the IRU bias; thus ground-determined biases need not be uplinked. However, the ground-determined bias is compared with the OBC-determined bias.

3. METHOD OF IN-FLIGHT CALIBRATION

This section describes two algorithms used for the in-flight calibration of the Compton GRO attitude sensors. The alignments of the FHSTs and FSSs were determined by FDF with an algorithm derived by Shuster

(1982). FDF solved for the IRU alignments, scale factors, and biases with an algorithm originated by Davenport (Keat 1977). This section also presents an overview of the FDF attitude ground support system (AGSS) for attitude calibration of Compton GRO.

3.1 Calibration of FHST and FSS Alignments

Malcolm Shuster has derived two algorithms for determining the in-flight alignments of attitude sensors such as FHSTs and FSSs (Shuster 1982 and 1990, Bierman 1988). Both algorithms work by comparing the dot products of unit vectors in spacecraft coordinates from different sensors measured at the same time with the dot products of the corresponding unit vectors in inertial coordinates. The vectors in inertial coordinates come from a star catalog or Sun ephemeris. Errors in the alignments used to compute the measured spacecraft coordinate vectors produce differences in these dot products. The algorithms parameterize the alignment adjustment to each sensor with the Euler rotation vector $\vec{\theta}$ defined in Section 2.

These vectors are varied in a batch least-squares process to minimize the differences between dot products. These algorithms have the advantage of not requiring IRU propagation or attitudes except to identify stars. An overall rotation applied to all the sensors does not affect the relative measurements or the dot products. The Shuster algorithms resolve these three unobservable degrees of freedom by incorporating the prelaunch alignments into the least-squares sum. In effect, the three unobservable degrees of freedom retain their prelaunch value. The two algorithms differ in the way they weight the data in the least-squares sum. The older algorithm (Shuster 1982) does not optimally weight the data: this weighting ignores correlations between dot products which share a measurement vector. However, it is not necessary for a least-squares algorithm to be optimally weighted to give good results. Given sufficient data, the solved-for alignments of the older algorithm are still valid. However, the older algorithm assumes that the weighting is optimal in the derivation of the covariance of the solution. Thus, the solution is correct, but the covariance of the solution is not correct. Shuster remedied this problem in a newer version of the alignment algorithm (Bierman 1988 and Shuster 1990) in which correlations between dot products at the same time are optimally weighted. However, the newer algorithm still ignores correlations between dot products at different times; the capability to optionally weight such correlations would be very difficult to implement. The FDF Compton GRO attitude ground support system uses the older algorithm, because the newer algorithm was not available soon enough.

During the early mission of Compton GRO, the scientific instruments were calibrated before the attitude sensor calibrations were uplinked. The science calibrations included an alignment adjustment with respect to the attitude provided by the OBC. FDF personnel noticed that the alignments provided by the Shuster algorithm would shift the attitude computed by the OBC and thus degrade the alignment calibration of the scientific instruments. To prevent this, FDF personnel adjusted the overall alignment of the FHSTs and FSSs with a single rotation, which minimized the shift to the OBC-determined attitude. The algorithm for doing this adjustment is presented in the appendix. The adjusted alignments are indicated with double-prime subscripts, $M_{AS''}$ and $M_{SS''}$.

3.2 Calibration of the IRU

The IRU of Compton GRO was calibrated in flight by FDF with a batch least-squares algorithm of P. Davenport (Keat 1977). This algorithm uses data from maneuvers. The attitude difference is computed from inertial attitude solutions with FHST and IRU data before and after the maneuver. The attitude difference is also computed by integrating the IRU data over the time interval of the maneuver. The difference between these two attitude differences is directly related to errors in the IRU calibration parameters. Each such maneuver interval can provide 3 of the 12 degrees of freedom of the calibration. Thus, a minimum of four independent maneuver intervals is required for a full calibration. Typically, three of the intervals are chosen to be maneuvers around each of the spacecraft axes. The fourth interval must not duplicate any of the first three intervals: it could be a time span spent at an inertial attitude or a maneuver that is in the opposite direction

from one of the first three maneuvers. The algorithm assumes the difference between the attitude solutions at each end of the interval to be independent of IRU calibration errors. The IRU alignment and scale factor errors do not contribute significantly to an inertial attitude solution. However, care must be taken to minimize the impact of bias errors on the inertial attitude solution by solving for the attitude at the center of a batch of uniformly distributed data. The same algorithm can also be used to do a partial IRU calibration. A single interval at an inertial attitude is sufficient to solve for the IRU bias.

3.3 FDF Attitude Ground Support System

Figure 1 shows a simplified diagram of the FDF attitude ground support system for calibration. The telemetry processor (TP) reads the raw telemetry data from the flight dynamics data link (FDDL) and unpacks and converts the data to engineering units. The data adjuster (DA) applies the calibration parameters to the engineering data from TP and generates vectors in the spacecraft coordinate system. The DA obtains the calibration parameters from files that initially contain the prelaunch parameters. The fine attitude determination system (FADS) obtains measured FHST and FSS vectors from DA, identifies stars, and solves for the attitude. The FHST/FSS calibration system (FFCAL) obtains star and Sun vectors from DA and identified star information from FADS. It then uses the old Shuster alignment algorithm to solve for improved FHST and FSS alignment matrices. These matrices are adjusted to minimize the shift of the OBC-determined attitude and then written to the calibration file accessed by DA. The IRU calibration system (IRUCAL) obtains fine attitude solutions from FADS and IRU rate vectors from DA. IRUCAL then uses the Davenport algorithm to solve for the IRU calibration parameters and writes the results to a file accessed by DA.

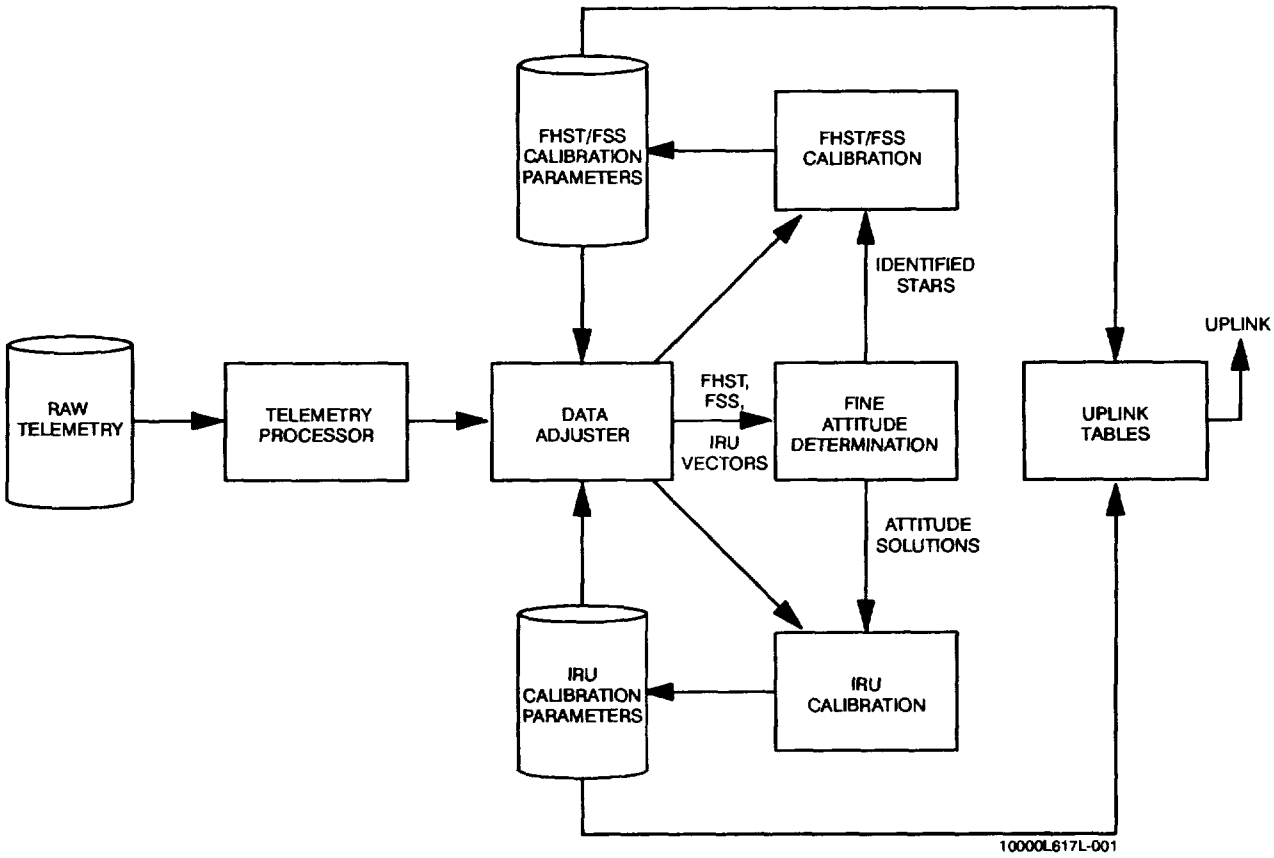

Figure 1. FDF Calibration System for Compton GRO

4. RESULTS OF CALIBRATION

4.1 Results of FHST/FSS Alignment Calibration

The data used for the FHST/FSS alignment calibration were obtained from observations at six different inertial attitudes (Davis 1991a). These observations include the Sun at four different positions in the FOV of FSS1 and three different positions in the FOV of FSS2. The FFCAL results were then adjusted to be consistent with the science instrument calibration that occurred at the same time. Misalignments of 0.20 degree and 0.05 degree were observed for FSSs 1 and 2, respectively. The significant part of the FHST calibration consisted of a 27-arcsec misalignment between the FHST boresights. These results were validated by comparing the residuals of the fine attitude solutions computed from the calibrated alignments with the residuals computed from the prelaunch alignments. The residuals from the calibrated alignments were significantly smaller than those from the prelaunch alignments. Figure 2 shows an example of the effect of the calibrated alignments on the residuals. The calibrated alignments were then uplinked to the spacecraft.

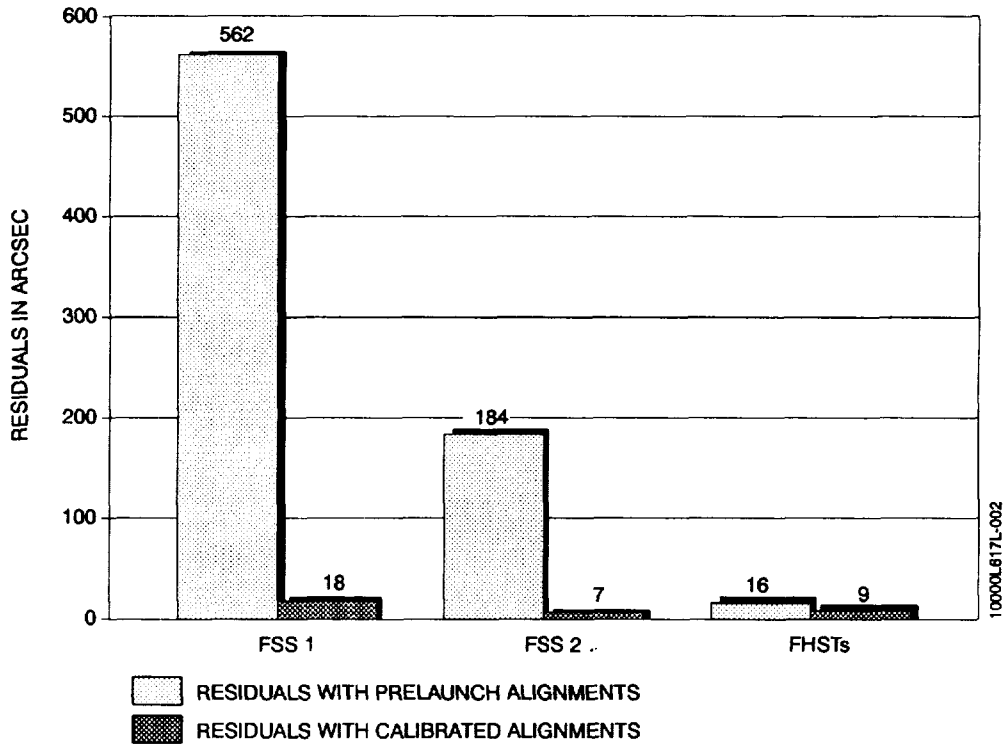

Figure 2. Fine Attitude Measurement Residuals with Pre-launch and Calibrated Alignments

Table 1 gives the prelaunch alignment matrices, M_{AS}, obtained from the final OBC database before launch. Table 2 gives the misalignment matrices, $M_{SS''}$, obtained by adjusting the FFCAL results to preserve the average attitude solution with two trackers. Table 3 gives the calibrated and adjusted alignments, consisting of the product of the prelaunch alignment matrices with the misalignment matrices. These matrices were uplinked to the OBC on May 14, 1991. The rotation vectors that rotate the prelaunch alignments to the adjusted calibrated alignment matrices are:

ROTATION VECTORS IN ACS COORDINATES				
	FHST1 (ARCSEC)	FHST2 (ARCSEC)	FSS1 (ARCSEC)	FSS2 (ARCSEC)
X-axis	41.7	56.4	236	-153
Y-axis	-41.7	56.3	-407	2
Z-axis	-13.8	13.7	-562	110
Magnitude	60.5	80.3	733	189

The angle between the FHST boresights of the calibrated alignments is 27.5 arcsec smaller than the angle between the prelaunch boresights.

4.2 Results of IRU Bias Calculation

The FDF operations team used IRUCAL to compute the in-flight IRU biases as a function of time over a 6-month period from April 9 to October 27, 1991 (Kulp 1991). Biases were determined for the three channels of the primary configuration and the three channels of the backup configuration, both in the low-rate IRU mode. For each bias solution, 90 minutes of data were processed. The attitude solutions were computed near each end of a 90-minute data span, and each solution was centered in a 10-minute batch of uniformly distributed FHST data. Figures 3 and 4 show the IRUCAL-determined bias vectors as a function of time for the primary and backup channels. Figure 3 also shows the bias solutions of the OBC. Note that the IRUCAL and OBC bias solutions follow one another and that both show some drift in the x- and z-axes of the primary channels early in the mission.

4.3 Results of IRU Alignment/Scale Factor Calibration

The Compton GRO calibration team used IRU data and fine attitude solutions with the IRUCAL utility to solve for IRU alignment, scale factor, and bias during the early mission (Davis 1991b). Maneuvers were done with all channels in the high-rate mode. The calibration team used data from four calibration maneuvers on April 9 through April 13, 1991. The full IRU calibration was done with data intervals from the following maneuvers:

MANEUVER AXIS AND ANGLE (DEGREES)	SENSORS FOR INITIAL ATTITUDE	SENSORS FOR FINAL ATTITUDE	INTERVAL DURATION (MINUTES)
X 60	FHST1 FHST2	FSS2 FHST2	19
Z -28	FHST1 FHST2	FHST1 FHST2	15
Y 31	FSS1 FHST2	FHST1 FHST2	15
Y -60	FSS1 FHST2	FHST1 FHST2	20

Table 1. Prelaunch FHST and FSS Alignments for Compton GRO; M_{AS}

ROTATION MATRIX FROM PRELAUNCH FHST1 FRAME TO ACS FRAME

$$\begin{bmatrix} -0.707293868 & 0.000641730 & -0.706919372 \\ -0.706919611 & -0.000965840 & 0.707293212 \\ -0.000228880 & 0.999999344 & 0.001136780 \end{bmatrix}$$

ROTATION MATRIX FROM PRELAUNCH FHST2 FRAME TO ACS FRAME

$$\begin{bmatrix} -0.706911922 & -0.000668710 & -0.707301319 \\ 0.707300782 & 0.000884930 & -0.706912220 \\ 0.001098630 & -0.999999404 & -0.000152590 \end{bmatrix}$$

ROTATION MATRIX FROM PRELAUNCH FSS1 FRAME TO ACS FRAME

$$\begin{bmatrix} 0.003753100 & -0.865531862 & 0.500839829 \\ 0.999986291 & 0.001422380 & -0.005035412 \\ 0.003645920 & 0.500851870 & 0.865525305 \end{bmatrix}$$

ROTATION MATRIX FROM PRELAUNCH FSS2 FRAME TO ACS FRAME

$$\begin{bmatrix} 0.000871080 & 0.034161031 & 0.999415934 \\ 0.999991417 & -0.004071418 & -0.000732420 \\ 0.004044019 & 0.999408066 & -0.034164291 \end{bmatrix}$$

Table 2. Postcalibration and Adjustment Alignment Change Matrices; $M_{SS''}$

ROTATION MATRIX FROM ADJUSTED FHST1 FRAME TO PRELAUNCH FHST1 FRAME

$$\begin{bmatrix} 0.99999991 & -0.00028956 & 0.00006638 \\ 0.00028955 & 0.99999990 & 0.00000000 \\ -0.00006631 & 0.00000001 & 0.99999988 \end{bmatrix}$$

ROTATION MATRIX FROM ADJUSTED FHST2 FRAME TO PRELAUNCH FHST2 FRAME

$$\begin{bmatrix} 0.99999989 & -0.00039545 & 0.00006634 \\ 0.00039545 & 0.99999987 & 0.00000000 \\ -0.00006634 & 0.00000003 & 0.99999996 \end{bmatrix}$$

ROTATION MATRIX FROM ADJUSTED FSS1 FRAME TO PRELAUNCH FSS1 FRAME

$$\begin{bmatrix} 0.99999373 & -0.00220720 & 0.00272080 \\ 0.00220561 & 0.99999742 & 0.00058720 \\ -0.00272209 & -0.00058124 & 0.99999596 \end{bmatrix}$$

ROTATION MATRIX FROM ADJUSTED FSS2 FRAME TO PRELAUNCH FSS2 FRAME

$$\begin{bmatrix} 0.99999959 & 0.00051921 & 0.00053489 \\ -0.00051950 & 0.99999973 & 0.00053081 \\ -0.00053462 & -0.00053110 & 0.99999961 \end{bmatrix}$$

Table 3. Postcalibration and Adjustment Alignment Matrices; $M_{AS''}$

ROTATION MATRIX FROM CALIBRATED & ADJUSTED FHST1 FRAME TO ACS FRAME

$$\begin{bmatrix} -0.70724671 & 0.00084653 & -0.70696623 \\ -0.70696675 & -0.00076114 & 0.70724624 \\ 0.00006060 & 0.99999928 & 0.00113677 \end{bmatrix}$$

ROTATION MATRIX FROM CALIBRATED & ADJUSTED FHST2 FRAME TO ACS FRAME

$$\begin{bmatrix} -0.70686513 & -0.00038918 & -0.70734814 \\ 0.70734791 & 0.00060520 & -0.70686522 \\ 0.00070319 & -0.99999967 & -0.00015251 \end{bmatrix}$$

ROTATION MATRIX FROM CALIBRATED & ADJUSTED FSS1 FRAME TO ACS FRAME

$$\begin{bmatrix} 0.00048072 & -0.86582899 & 0.50033978 \\ 0.99999690 & -0.00078186 & -0.00231379 \\ 0.00239455 & 0.50033946 & 0.86582589 \end{bmatrix}$$

ROTATION MATRIX FROM CALIBRATED & ADJUSTED FSS2 FRAME TO ACS FRAME

$$\begin{bmatrix} 0.00031903 & 0.03363069 & 0.99943420 \\ 0.99999357 & -0.00355182 & -0.00019969 \\ 0.00354310 & 0.99942801 & -0.03363162 \end{bmatrix}$$

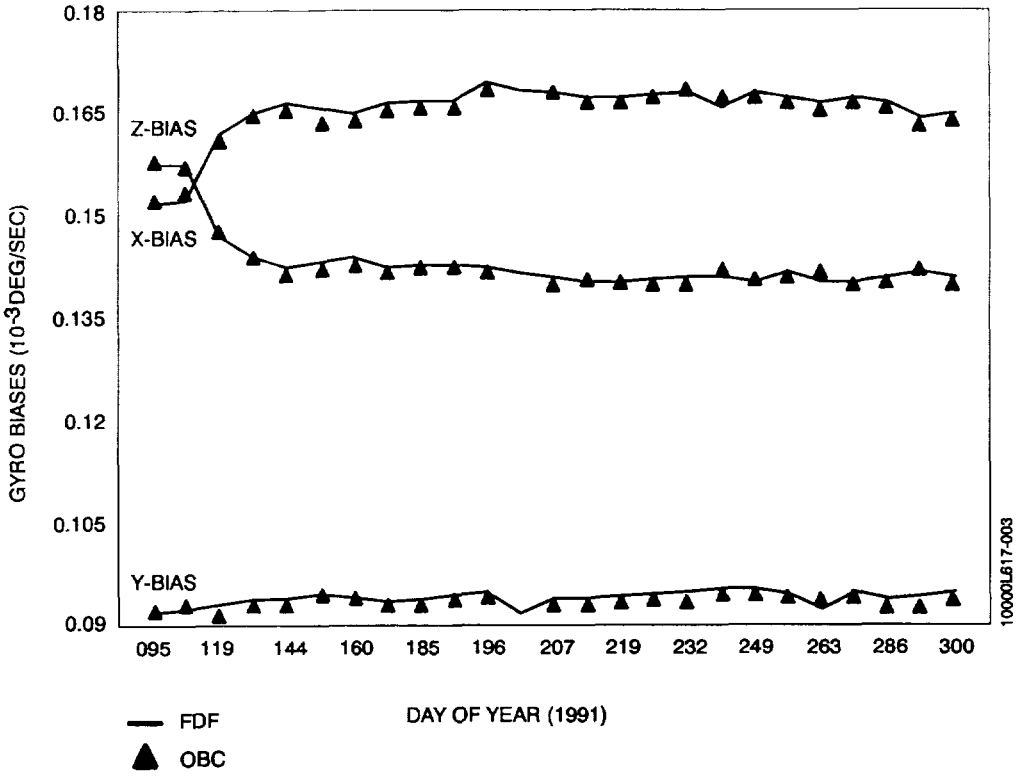

Figure 3. GRO OBC and Ground Gyro Biases Primary Configuration

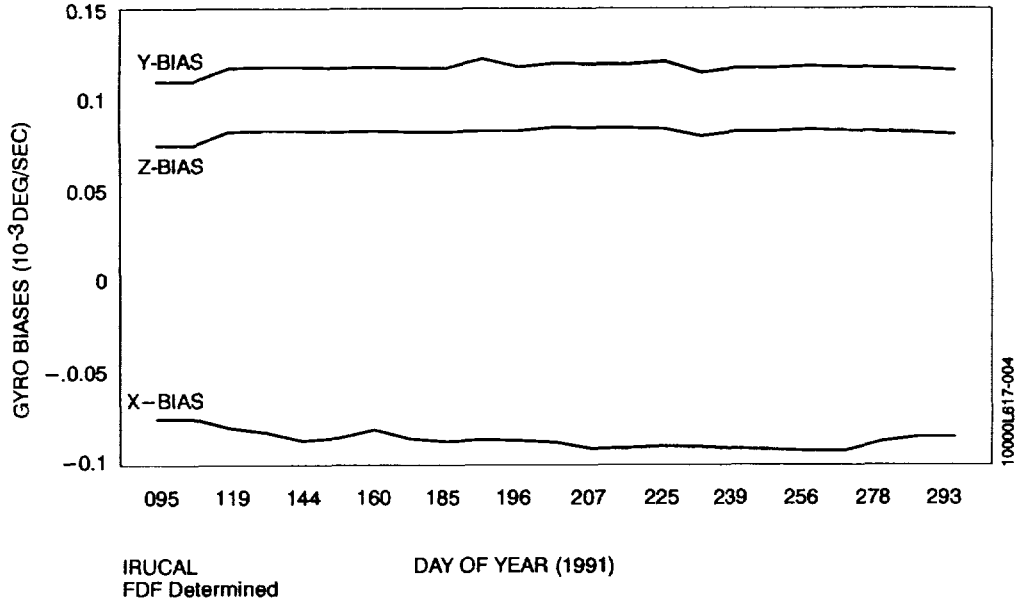

Figure 4. GRO Gyro Biases Backup Configuration

Even though two of the maneuvers are around the y-axis, they contribute different information about the calibration parameters because they are in different directions.

The solved-for corrections to the primary configuration scale factor/alignment calibration and its uncertainty are:

Solved-for δM-Matrix Uncertainty

$$\delta M = \begin{bmatrix} 0.000167 & 0.000374 & 0.000167 \\ -0.000511 & -0.000265 & -0.000048 \\ -0.000547 & 0.000365 & 0.000037 \end{bmatrix} \pm \begin{bmatrix} 0.000507 & 0.000229 & 0.000610 \\ 0.000524 & 0.000223 & 0.000602 \\ 0.000527 & 0.000229 & 0.000608 \end{bmatrix}$$

The observed corrections are of the same order as the estimated uncertainties. To improve these results, it would be necessary to process larger amounts of data or process different data with lower errors. A major source of error in processing the above data for IRU calibration comes from the FSS. The lack of coverage by both FHSTs forced the use of FSS data for three of the eight attitude solutions. The FSS has an inherent error (not removed by alignment calibration) of about 0.022 degrees (0.00038 radians). The IRU calibration uncertainties could be reduced by using only FHST data to compute the epoch attitudes: such data may be available in more recent maneuvers. On the other hand, the observed uncertainties in the calibration and the observed error after maneuvers are easily within the requirements of a successful mission; these results were thus not uplinked to the OBC. The OBC and the ground software are still using the prelaunch measurements of the scale factor and alignment. That alignment/scale factor matrix is

$$\begin{bmatrix} 1.00000 & 0.00108 & 0.00079 \\ -0.00100 & 1.00000 & -0.00156 \\ -0.00056 & 0.00128 & 1.00000 \end{bmatrix}$$

The solved-for high-rate gyro biases are

primary configuration		
channel X2	bx = 1.66E-4 deg/sec	+/- 0.10E-4 deg/sec
channel Y1	by = 0.99E-4 deg/sec	+/- 0.09E-4 deg/sec
channel Z1	bz = 1.41E-4 deg/sec	+/- 0.10E-4 deg/sec
backup configuration		
channel X1	bx = -0.84E-4 deg/sec	+/- 0.10E-4 deg/sec
channel Y2	by = 1.22E-4 deg/sec	+/- 0.09E-4 deg/sec
channel Z2	bz = 0.81E-4 deg/sec	+/- 0.10E-4 deg/sec

These solutions reflect the gyro bias during maneuvers when the IRU is in the high-rate mode. The high-rate bias agrees with that obtained from low-rate data to within the estimated uncertainty.

There was no observable change in scale factor and alignment to within the estimated uncertainty of the solution. The solved-for gyro bias is consistent with results obtained from data at inertial attitudes.

5. CONCLUSIONS AND RECOMMENDATIONS

The in-flight attitude sensor calibration provides results that meet the requirements of the mission. The time history of the IRU bias is especially relevant to this and other missions with the same type of sensor. It would be useful to repeat the FHST/FSS alignment calibration to observe any time dependence on these parameters. It would also be worthwhile to redo the IRU alignment calibration with only FHST/IRU data for the attitude solutions to obtain a result with lower uncertainty.

REFERENCES

1. Bierman, G. J. and Shuster, M. D., "Spacecraft Alignment Estimation," 27th Conference on Decision and Control, Austin, Texas, December 7-9, 1988.

2. Davis, W. S., "Summary of GRO FHST/FSS Alignment Calibration," Computer Sciences Corporation, SEAS Quick Note GRO-414-91014, June 1991a.

3. Davis, W. S., "Summary of Full Calibration of GRO IRU," Computer Sciences Corporation, SEAS Quick Note GRO-414-91018, June 1991b.

4. Keat, J. E., "Gyro Calibration Analysis for the High Energy Astronomy Observatory Observatory-A (HEAO-A)," Computer Sciences Corporation, CSC/TM-77/6082, June 1977.

5. Kulp, L. S., "GRO Gyro Bias History," Computer Sciences Corporation, SEAS Quick Note GRO-325-92002, November 1991.

6. Shuster, M. D., Chitre, D. M., and Niebur, D. P., "In-Flight Estimation of Spacecraft Attitude Sensor Accuracies and Alignments," *Journal of Guidance and Control*, Vol. 5, No. 4, pp. 339-343, 1982.

7. Shuster, M. D., "In-flight Estimation of Spacecraft Sensor Alignment," *Advances in the Astronautical Sciences*, Vol. 72, No. 1, pp. 253-274, 1990.

APPENDIX — ADJUSTMENT ALIGNMENT SOLUTIONS TO PRESERVE OBC ATTITUDE

This appendix describes the method used to adjust the alignment results from the Shuster algorithm so that the OBC computes the same average attitude with the adjusted alignments as with the prelaunch alignments. This adjustment is done to preserve the alignment calibration of the scientific instruments, which is done with respect to the OBC-determined attitude using the prelaunch FHST alignments. Let the following matrices represent alignments that transform from the sensor to the ACS coordinates for the prelaunch alignments, solved-for alignments, and adjusted solved-for alignments.

	prelaunch	solution	adjusted solution
FHST1 TO ACS	M_{AT1}	$M_{AT1'}$	$M_{AT1''}$
FHST2 TO ACS	M_{AT2}	$M_{AT2'}$	$M_{AT2''}$
FSS1 TO ACS	M_{AF1}	$M_{AF1'}$	$M_{AF1''}$
FSS2 TO ACS	M_{AF2}	$M_{AF2'}$	$M_{AF2''}$

where the subscripts A, T1, T2, F1, and F2 mean the ACS, FHST1, FHST2, FSS1, and FSS2 coordinate frames, respectively. The unprimed, single-primed, and double-primed subscripts stand for prelaunch, solved-for, and adjusted solved-for alignments, respectively. The columns of each of these matrices provide the x-, y-, and z-axes of each sensor in the ACS coordinate system. Let $\hat{X}_A^{T1}$, $\hat{Y}_A^{T1}$, and $\hat{Z}_A^{T1}$ be the axes of the FHST1 prelaunch alignment. Then

$$M_{AT1} = \left[\hat{X}_A^{T1} \quad \hat{Y}_A^{T1} \quad \hat{Z}_A^{T1} \right]$$

A similar relationship applies to the other sensor coordinate frames. The sensor boresight is defined by its z-axis.

To preserve, on the average, the attitude computed by the OBC with the two FHSTs, consider the following intermediate coordinate frame (subscript N) obtained from the boresights of the two trackers, $\hat{Z}_A^{T1}$, and $\hat{Z}_A^{T2}$,

$$M_{AN} = \left[-\frac{\hat{Z}_A^{T1} + \hat{Z}_A^{T2}}{\left| \hat{Z}_A^{T1} + \hat{Z}_A^{T2} \right|} \quad \frac{\left(\hat{Z}_A^{T1} + \hat{Z}_A^{T2} \right) \times \left(\hat{Z}_A^{T1} \times \hat{Z}_A^{T2} \right)}{\left| \left(\hat{Z}_A^{T1} + \hat{Z}_A^{T2} \right) \times \left(\hat{Z}_A^{T1} \times \hat{Z}_A^{T2} \right) \right|} \quad \frac{\hat{Z}_A^{T1} \times \hat{Z}_A^{T2}}{\left| \hat{Z}_A^{T1} \times \hat{Z}_A^{T2} \right|} \right]$$

The z-axis of this coordinate frame is along the direction formed by the cross-product of the boresights of the prelaunch alignments. The x-axis is opposite the direction formed by the sum of the boresights. The x- and z-axes are perpendicular. The y-axis completes the orthonormal frame. This intermediate coordinate frame is defined to be close to the ACS coordinate frame, although that definition is not necessary for the adjustment method. The prelaunch alignments can then be expressed as follows:

$$M_{AT1} = M_{AN}\, M_{NT1} \qquad M_{AT2} = M_{AN}\, M_{NT2}$$

Together, the two matrices M_{NT1} and M_{NT2} contain only three degrees of freedom, the angle between the boresights and a rotation angle of each tracker around its boresight. It is claimed here without proof that all pairs of tracker alignment matrices, related by a small rotation, with the same intermediate frame will produce, on the average, the same attitude solution.

The matrix $M_{AN'}$, computed from the FHST boresights of the Shuster algorithm, is in general different from the matrix M_{AN}, computed from the prelaunch matrices. Adjust the solved-for alignments as follows:

$$M_{AT1''} = M_{AN}\, M_{N'A}\, M_{AT1'}$$
$$M_{AT2''} = M_{AN}\, M_{N'A}\, M_{AT2'}$$
$$M_{AF1''} = M_{AN}\, M_{N'A}\, M_{AF1'}$$
$$M_{AF2''} = M_{AN}\, M_{N'A}\, M_{AF2'}$$

where $M_{N'A} = M_{AN'}{}^{T}$. The intermediate coordinate frame $M_{AN''}$, computed from the FHST boresights of the adjusted solved-for alignments, equals M_{AN}. Thus, attitude solutions computed with the adjusted solved-for alignments will, on the average, be the same as attitudes computed with the prelaunch alignments.

Testing of the On-board Attitude Determination and Control Algorithms for SAMPEX

Jon D. McCullough[1], Thomas W. Flatley [1], Debra A. Henretty[2],
F. Landis Markley [3], and Josephine K. San [1]

Algorithms for on-board attitude determination and control of the Solar, Anomalous, and Magnetospheric Particle Explorer (SAMPEX) have been expanded to include a constant gain Kalman filter for the spacecraft angular momentum, pulse width modulation for the reaction wheel command, an algorithm to avoid pointing the Heavy Ion Large Telescope (HILT) instrument boresight along the spacecraft velocity vector, and the addition of digital sun sensor (DSS) failure detection logic. These improved algorithms were tested in a closed-loop environment for three orbit geometries, one with the sun perpendicular to the orbit plane, and two with the sun near the orbit plane - at Autumnal Equinox and at Winter Solstice. The closed-loop simulator was enhanced and used as a truth model for the control systems' performance evaluation and sensor/actuator contingency analysis. The simulations were performed on a VAX 8830 using a prototype version of the on-board software.

Introduction

SAMPEX, the first in the Small Explorer (SMEX) series, will be launched by a Scout launch vehicle from the Western Test Range in June 1992. The mission is designed to obtain scientific data on several different natural phenomena. A statistically large sample of anomalous cosmic ray oxygen nuclei will be obtained to estimate their ionization state. The intensity, latitude, and local time dependence of the precipitating magnetospheric particle fluxes, particularly relativistic electrons, will be continuously recorded. In addition, the SAMPEX mission hopes to detect solar flare events from a low altitude, near-polar orbit during the declining phase of solar activity. The scientific instruments on board are the Low Energy Ion Composition Analyzer (LEICA), the Heavy Ion Large Telescope (HILT), the Mass Spectrometer Telescope (MAST), and the Proton/Electron Telescope (PET).

The spacecraft mechanical configuration is shown in Fig. 1. The SAMPEX spacecraft has a body-fixed pair of solar arrays pointed in the "+y" direction and an experiment complement looking along the "+z" axis. The yaw axis is oriented along the instrument boresights, the pitch axis perpendicular to the solar panels, and the roll axis completes the orthonormal triad. The locations of some of the Attitude Control System (ACS) hardware and science instruments are shown in Fig. 2. The ACS hardware consists of one momentum wheel, three torquer bars, one two-axis fine sun sensor, five coarse sun sensors, and one three-axis magnetometer. The nominal attitude control system function is to point the solar arrays continuously within 5 degrees of the sun and to rotate the spacecraft around the sun line at a rate of 1 revolution per orbit, keeping the experiment axis pointed generally away from the earth. For a complete discussion of the ACS control laws, see Forden, et. al. (Ref. 1). The ACS control laws can be briefly summarized as follows:

---

[1] *Aerospace Engineer, Guidance and Control Branch, NASA/GSFC.*
[2] *Aerospace Engineer, Guidance and Control Branch, NASA/GSFC; Member AIAA.*
[3] *Assistant Branch Head, Guidance and Control Branch, NASA/GSFC; Associate Fellow AIAA, Senior Member AAS.*

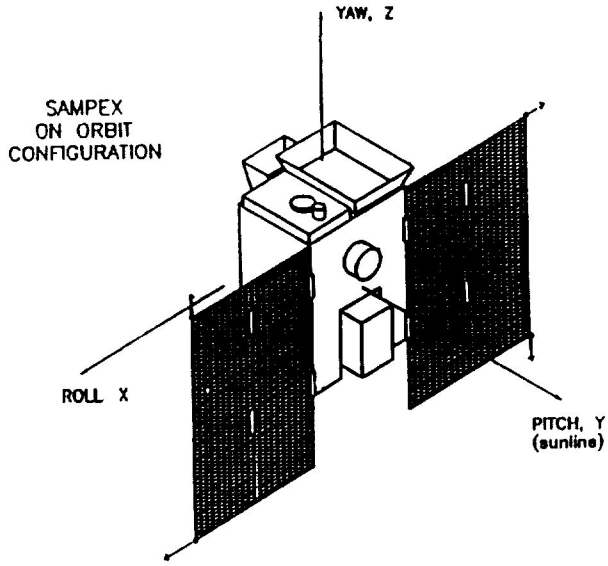

Fig. 1

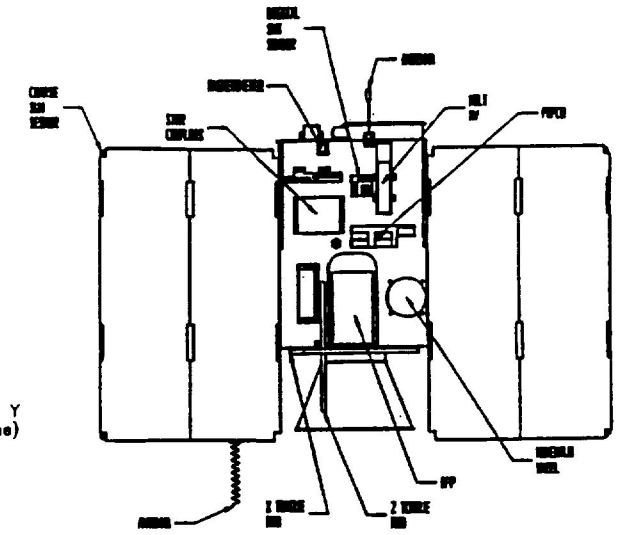

Fig. 2

Initial Acquisition

The spacecraft is inserted into orbit by a spin-stabilized solid rocket motor. Following separation from the launch vehicle and a yo-yo despin, sun pointing must be achieved from an essentially unknown attitude and rate initial state. A small momentum wheel along the intended sun-pointing axis (+y) is spun up to a constant speed, and a conventional three-axis "B-dot" analog controller is used to damp residual body rates. This controller uses a three-axis magnetometer as a sensor and three magnetic torquer bars as actuators.

The despun spacecraft then has a momentum bias along the y-axis (due to the momentum wheel) and the sun sensors are used to determine a sun-pointing error. There are coarse sun sensors which essentially measure the direction cosines of the sun vector in body coordinates for all attitudes and a single two-axis digital sun sensor whose boresight is aligned with the +y axis. The digital sun sensor output is used for control whenever it indicates "sun presence".

Using sun sensor and magnetometer data, precession control logic drives the y-axis torquer bar in a bang-bang fashion to generate torques which precess the momentum vector toward the sun. During this maneuver, the "B-dot" controller acts as a nutation damper.

Normal Control

No additional equipment is employed for so-called "normal" control. Because of the modest pointing accuracy required, the spacecraft is controlled using on-board attitude determination based on the "Algebraic Method" (Ref. 2), probably for the first time ever. This method is based on the fact that if two vectors are known in both body coordinates and in inertial space, the attitude (as represented by an inertial-to-body transformation matrix A) can be unambiguously determined by simple matrix manipulations.

When the spacecraft is in sunlight, the two vectors here are the sun vector and the magnetic field vector. The sensors mentioned determine the components of these vectors in body

coordinates, but their inertial counterparts must be computed on-board based on uplinked ephemeris information and a spherical harmonic magnetic field model. When the spacecraft is in the shadow of the earth, the system angular momentum vector, which is assumed to be inertially fixed due to the pitch axis momentum bias, is used along with the magnetic field vector for attitude determination.

Once A is determined, its derivative is approximated and classical matrix manipulations produce estimated three-axis body rates. Those rates, and the momentum wheel speed are then used to calculate an angular momentum vector. We would like this momentum vector ($\mathbf{H}$) to have some amplitude, say H_0 , and be aligned with the sun, i.e. $\mathbf{H} = H_0\mathbf{S}$. For no nutation we would also like to have it aligned with the +y axis, $\mathbf{H} = H_0\mathbf{j}$. We define a momentum error $\Delta\mathbf{H}$ by

$$\Delta\mathbf{H} = (\mathbf{H} - H_0\mathbf{S}) + (\mathbf{H} - H_0\mathbf{j}) = 2\mathbf{H} - H_0(\mathbf{S} + \mathbf{j})$$

and use the familiar $\mathbf{H} \times \mathbf{B}$ magnetic unloading law to drive the torquer bars for control, i.e. the commanded dipole moment $\mathbf{M}$ is given by

$$\mathbf{M} = k\Delta\mathbf{H} \times \mathbf{B},$$

where k is a gain factor.

The momentum wheel, in addition to providing a momentum bias, is used in a "pitch control loop" to achieve the desired 1 rpo spin rate and "away from the earth" experiment pointing. The yaw axis (the boresights of the instruments) points as close to north as possible at the northernmost point of the orbit, as close to south as possible at the southernmost point of the orbit, and close to the equator at the equatorial crossings. The north pole vector $\mathbf{NP}$ and orbit normal vector $\mathbf{N}$ in GCI coordinates are given as:

$$\mathbf{NP} = [0\ 0\ 1]^T \qquad \text{and} \quad \mathbf{N} = \mathbf{R} \times \mathbf{V} / |\mathbf{R} \times \mathbf{V}|,$$

where $\mathbf{R}$, $\mathbf{V}$ are the inertial position vector and inertial velocity vector of the spacecraft, respectively, estimated from the uplinked ephemeris data. The orbit angle as measured from the northernmost point in the orbit is computed from the two vectors:

$$\mathbf{AN} = \mathbf{NP} \times \mathbf{N} / |\mathbf{NP} \times \mathbf{N}|,$$

the unit vector in the direction of the ascending node, and

$$\mathbf{NMP} = \mathbf{N} \times \mathbf{AN},$$

the unit vector in the direction of the northernmost point of the orbit. The sine and cosine of the orbit angle can now be computed,

$$\sin\alpha = -\mathbf{R}\bullet\mathbf{AN} / |\mathbf{R}|, \qquad \cos\alpha = \mathbf{R}\bullet\mathbf{NMP} / |\mathbf{R}|.$$

The target vector $\mathbf{U}$ must lie in the plane perpendicular to the sun. The following two vectors provide an orthonormal basis for the target vector $\mathbf{U}$:

$$\mathbf{W} = \mathbf{NMP} \times \mathbf{S} / |\mathbf{NMP} \times \mathbf{S}|, \qquad \mathbf{S} \times \mathbf{W}.$$

$\mathbf{W}$ is a unit vector perpendicular to the sun that lies close to the equatorial plane. Thus when the spacecraft is near the equator, we would like $\mathbf{U}$ to point along $\mathbf{W}$. This corresponds to orbit angles of $\alpha = \pi / 2$ and $\alpha = 3\pi / 2$. The unit vector $\mathbf{S} \times \mathbf{W}$ is also perpendicular to the sun and points as close to the northernmost point as possible, given the sun constraint. Thus when the spacecraft is near the poles, we would like $\mathbf{U}$ to point along $\mathbf{S} \times \mathbf{W}$. This corresponds to orbit angles of $\alpha = 0\ , \pi$. Since it is desired to rotate the yaw axis about the positive sun line, the orientation of the orbit normal relative to the sun line must be taken into consideration. A candidate for the target vector $\mathbf{U}$ is

$$\mathbf{U}_{orr} = \cos\alpha(\mathbf{S} \times \mathbf{W}) + \text{TargetSign}\ \sin\alpha\mathbf{W},$$

where TargetSign is set equal to the negative of SIGN(**S**·**N**) whenever the spacecraft comes within 0.5 degrees of the northernmost or southernmost point of the orbit. This avoids a 180 degree pitch flip if the sun passes through the orbit plane when the spacecraft is near the equator.

For the case where the sun is perpendicular to the orbit plane, the orbit rate rotation mode reduces to a zenith pointing mode. Fig. 3 shows that

$$\mathbf{S} = \mathbf{N}, \qquad \mathbf{W} = \mathbf{NMP} \times \mathbf{S}, \qquad \mathbf{NMP} = \mathbf{S} \times \mathbf{W},$$

and the orientation of the yaw axis along the orbital path is zenith pointing.

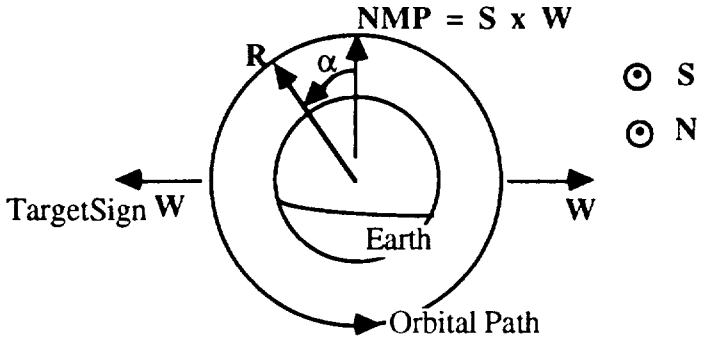

Fig. 3a ORR Mode Geometry When Sun Is Perpendicular To Orbit Plane

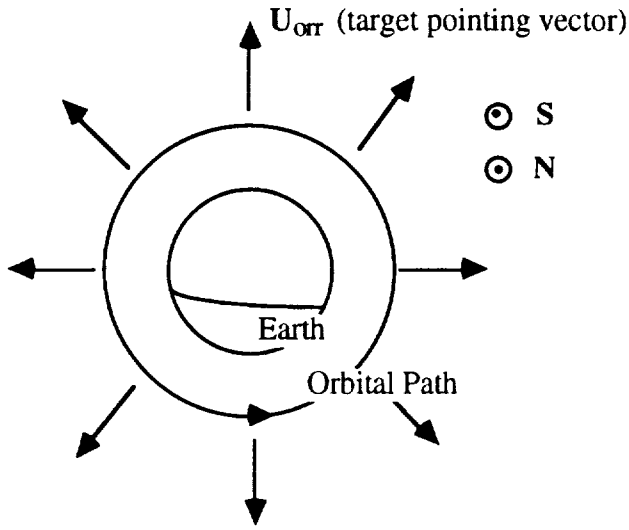

Fig. 3b ORR Mode Target Pointing Vector Along The Orbital Path With Sun Perpendicular To Orbit Plane

For the case where the sun is parallel to the orbit plane, the orbit rate rotation mode becomes a zenith pointing mode over the poles and points in the $\mathbf{R} \times \mathbf{NMP}$ direction at the equator. Fig. 4a shows that $\mathbf{W} = \mathbf{NMP} \times \mathbf{S}$, and so the orientation of the yaw axis can be determined throughout the orbital path and is shown in Fig. 4b.

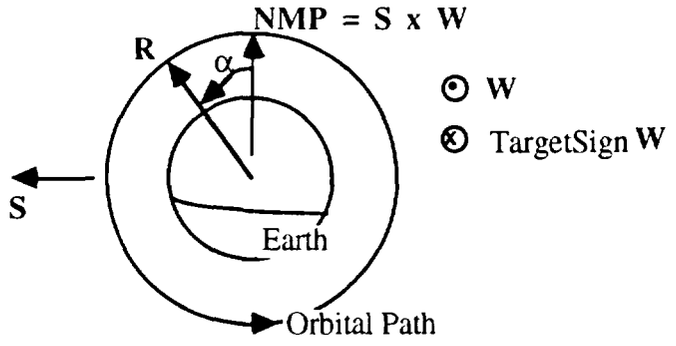

Fig. 4a ORR Mode Geometry When Sun Is In Orbit Plane

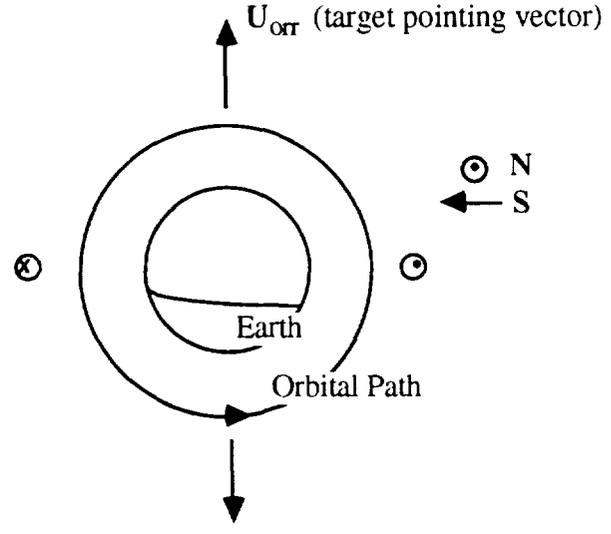

Fig. 4b ORR Mode Target Pointing Vector Along The Orbital Path With Sun Parallel To Orbit Plane

System Angular Momentum Filter

The attitude matrix $A(t)$ is computed at $\Delta t = 0.5$ second intervals, and the least significant bit of the DSS output is 0.5 degrees. Therefore, if the angular velocity is computed by simply back-differencing the attitude matrix, as described above, the roll and yaw rates in sunlit portions of the orbit (the components depending on the DSS data) will be computed as either zero or one degree per second. These exceedingly noisy inputs to the control algorithm produced poor pointing performance in simulations, so it was decided to filter the rate estimates. Let the "derived" system angular momentum in the spacecraft body frame be given by

$$\mathbf{H}_{\text{derived}} = I\omega + H_{\text{wheel}}\mathbf{j},$$

where I is the spacecraft moment-of-inertia tensor, ω is the (noisy) angular velocity vector derived from the attitude matrix, H_{wheel} is the wheel angular momentum (computed from its moment of inertia and tachometer data), and $\mathbf{j}$ is the wheel axis (pitch) unit vector. We

can also predict the system angular momentum at time t based on its dynamics by

$$\mathbf{H}_{\text{predicted}}(t) = A(t)A^{\mathrm{T}}(t - \Delta t)\mathbf{H}(t - \Delta t) + (\mathbf{M} \times \mathbf{B})\Delta t,$$

where $\mathbf{M} \times \mathbf{B}$ is the magnetic control torque in body coordinates. Other external torques are ignored, a reasonable approximation. The reaction wheel torque does not affect the total system angular momentum, of course; it merely shifts the momentum between the spacecraft body and the wheel. The filtered angular momentum is computed as the linear combination

$$\mathbf{H} = (1 - K)\mathbf{H}_{\text{predicted}} + K\mathbf{H}_{\text{derived}},$$

where K is a gain constant. This is referred to as a "constant-gain Kalman filter," although it is too simple to justify this name. The default value of K is 0.01, which corresponds to a time constant of 100 control cycles, or 50 seconds. Simulations show that this gives much smoother performance without introducing excessive lag into the control.

Velocity Avoidance Algorithm

Within 2000 kilometers of the earth's surface, there are 3,000,000 kilograms of orbital debris (Ref. 3), consisting of fragments from explosions, solid rocket effluent, paint flecks, waste, refuse, etc. There are 6,645 orbiting objects currently being tracked which comprise 99.9% of the total mass of all orbiting objects. However, untrackable orbiting pieces (diameter less than 10 cm) number in the millions and are potentially catastrophic or at the least mission degrading (Ref 4). These pieces are almost all in high inclination circular orbits with velocities on the order of 10 km/sec. The EnviroNET (Ref. 5) orbital debris model was used to calculate fluxes for the SAMPEX mission. The assumptions and equations used in computing the fluxes can be found in Kessler, et. al. (Ref. 3).

The HILT proportional counter has a triple entrance foil system with 80μm combined thickness. However, it has the effectiveness of a 380μm single foil for a particle velocity and density of 15 km/sec and 1 gm/cm^3, respectively. Using these results and triple foil penetration limit equations, the smallest particle of concern for the HILT sensor has been determined by Klecker (Ref. 6) to be 0.01 cm.

Meteoroids are part of the interplanetary environment and have average velocities of 20 km/sec with respect to the earth's orbital space. There are 200 kg of meteoroid mass within 2000 km of the earth's surface and most of the mass is concentrated in particles of diameter 0.01 cm (Ref. 3). This coincides with the smallest particle of concern for the HILT sensor. The EnviroNET meteoroid model was used to calculate fluxes for the SAMPEX mission, using assumptions and equations found in Grun, et. al. (Ref. 7); and it was found that orbital debris is significantly more hazardous than micrometeoroids for the SAMPEX mission (Ref. 8). The maximum flux was found to be in the direction of the velocity vector and to be reduced by a factor of 3 for an 80 degree ram angle.

The velocity avoidance algorithm to protect the HILT sensor from hazardous debris is discussed in Reference 8. The velocity avoidance feature, if desired, can be turned on and off by a ground command. Let

$\mathbf{V}$	- unit velocity vector (body coordinates)
$\mathbf{U}$	- target vector
$\varphi_{\min}$	- minimum ram angle (currently 90 degrees)

If $\mathbf{V}\cdot\mathbf{U} \le \cos\varphi_{\min}$, then the velocity avoidance algorithm is unnecessary. The spacecraft target vector is determine by the orbit rate rotation mode. However, if $\mathbf{V}\cdot\mathbf{U} > \cos\varphi_{\min}$, then the algorithm is implemented.

The algorithm is defined in the Flatley coordinate system. Let the sun unit vector **S** be the 1 axis, the normal science mode target vector **U** be the 3 axis (which by construction is already perpendicular to the sun vector), and $\mathbf{U} \times \mathbf{S}$ be the 2 axis, as defined in Fig. 5.

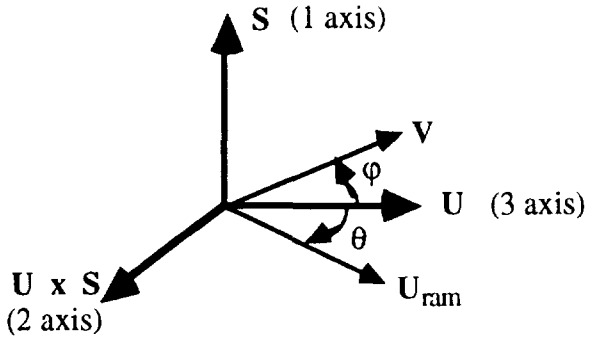

Fig. 5 Flatley Coordinate System

The unit velocity vector **V** and the target vector with velocity avoidance $\mathbf{U}_{ram}$ can be expressed in the Flatley coordinate system as

$$\mathbf{V}_F = [\ V_{F1} \quad V_{F2} \quad V_{F3}\ ]^T, \qquad \mathbf{U}_{ram} = [\ 0 \quad \sin\theta \quad \cos\theta\ ]^T.$$

The desired constraint, $\mathbf{U}_{ram} \cdot \mathbf{V}_F = \cos\varphi_{min}$, is used to determine $\mathbf{U}_{ram}$. This implies

$$V_{F3}\cos\theta = \cos\phi_{min} - V_{F2}\sin\theta.$$

Squaring both sides and using a trigonometric identity results in a quadratic equation for $\sin\theta$ with the solution

$$\sin\theta = \frac{V_{F2}\cos\varphi_{min} \pm |V_{F3}|\sqrt{V_{F2}^2+V_{F3}^2-\cos^2\varphi_{min}}}{(V_{F2}^2 + V_{F3}^2)}.$$

If $V_{F2} \geq 0$, then $\sin\theta < 0$ and the negative sign is chosen for the radical. If $V_{F2} < 0$, then $\sin\theta > 0$ and the positive sign is chosen for the radical. Thus $\mathbf{U}_{ram}$ is given by

$$\mathbf{U}_{ram} = \sin\theta(\mathbf{U} \times \mathbf{S}) + \cos\theta\ \mathbf{U}.$$

The testing of the velocity avoidance algorithm is descibed in detail in Reference 8, and can be summarized as follows. For the best case orbit geometry (sun in the orbit plane), there is a small sun pointing error (< 0.3°) for all minimum ram angles. Only for the 100° minimum ram angle does the zenith offset, the angle between zenith and the spacecraft yaw axis, become significant, reaching approximately 10 degrees. The velocity avoidance scheme keeps the yaw axis pointed at least the desired minimum ram angle away from the velocity vector, and science pointing performance is not affected by including the velocity avoidance algorithm.The worst case orbit geometry (sun in the orbit plane) dramatically illustrates the effect of increasing the minimum ram angle. The sun pointing error increases from 1° to 2°. The zenith offset and the ram angle show that the spacecraft flips when the minimum ram angle reaches 100°. Also, science pointing performance begins to decrease

significantly for increasing minimum ram angles. Intermediate cases were also considered in Reference 8.

Table 1 shows the percent of the orbit that the spacecraft is pointing within 15 degrees of zenith. These numbers were calculated for the periods of the orbit where the spacecraft was within 60 degrees of either pole. This table demonstrates how well the science pointing requirement is satisfied while maintaining the five degree sun pointing requirement.

Table 1 - SCIENCE POINTING PERFORMANCE (percent of orbit)

	best case	intermediate case	worst case
No Avoidance	100.0	68.9	0.0
80 deg ram	100.0	68.9	4.9
90 deg ram	100.0	59.3	4.7
100 deg ram	100.0	27.0	11.2

The probability of survival for the HILT sensor was computed for the orbit rate rotation mode with and without the velocity avoidance scheme (Ref. 8), with the results shown in Table 2.

Table 2 - HILT SURVIVAL ESTIMATES

Mode	Mean Flux (coll/m^2 yr)	τ (yrs/coll)	P_S (%)
ORR	3.11485	21.690	87.1
ORR w/ 80° ram	2.92332	23.111	87.8
ORR w/ 90° ram	2.68487	25.164	88.8
ORR w/100° ram	1.90232	35.515	91.9

Sun Sensor Failure Detection Logic

The Small Explorer spacecraft, including SAMPEX, are designed as single-string systems with very little ACS sensor and actuator redundancy. The only sensor redundancy on SAMPEX is that the sun vector can be obtained from either the digital sun sensor (DSS) or the coarse sun sensor (CSS) eyes. Since the sun-pointing constraint is critical for powering the spacecraft, it is desirable to substitute CSS data for DSS data in the unlikely event of failure of the latter sensor.

The logic to decide which sun sensor to trust makes use of the fact that the dot product of two vectors is frame-independent, specifically the dot product of the sensed sun vector and magnetic field **B** in the body and the dot product of the modeled sun vector and magnetic field in inertial space. Thus the ACS performs three tests on each control cycle when the spacecraft is in sunlight:

DSS and CSS disagree if $\cos^{-1}(\mathbf{S}_{CSS} \bullet \mathbf{S}_{DSS}) >$ CSS tolerance,

CSS and models disagree if $\left|\cos^{-1}(\mathbf{S}_{CSS} \bullet \mathbf{B}) - \cos^{-1}(\mathbf{S}_{model} \bullet \mathbf{B}_{model})\right| >$ CSS tolerance,

DSS and models disagree if $\left|\cos^{-1}(\mathbf{S}_{DSS} \bullet \mathbf{B}) - \cos^{-1}(\mathbf{S}_{model} \bullet \mathbf{B}_{model})\right| >$ DSS tolerance.

The DSS tolerance is conservatively set to 5°, to allow for a combination of sensor and modeling errors. The CSS tolerance is much larger, 30°, to allow for earth albedo corruption of the CSS sun vector.

If the DSS agrees with either the models or the CSS, the ACS uses the sun vector computed from DSS data. If the DSS disagrees with both the CSS and the models, but the CSS and models agree, the ACS sets a flag indicating that the DSS data are bad and uses the sun vector computed from CSS data. In all other cases of disagreement, it is not possible to determine whether the DSS, the CSS, the magnetometer, or the models (including the onboard ephemeris) are in error, so the data source for computing the sun vector is left unchanged.

If SAMPEX enters safehold, the analog safehold control will use DSS data if available. Thus it is desirable to turn off the DSS by ground command if telemetry shows that the DSS data are consistently bad.

Contingency Analyses

Through the use of the closed-loop simulator, tests were run to ascertain the performance and stability of spacecraft control in the presence of sensor or actuator failures. The simulations were run for a 9 p.m. orbit in which the aerodynamic torques on the spacecraft are greatest. Some of the tests are summarized below.

DSS Failures

The two-axis DSS that will be used on SAMPEX consists of two measurement components mounted at right angles that yield a 128 x 128 degree Field of View (FOV). The two measurement components generate two eight bit Gray-coded outputs which are digital representations of the angle between the sunline and the normal to the sensor when the sun is in the FOV of the command component (Ref. 9). The purpose of the command component is to indicate when there is sun presence. These outputs are then converted to two eight bit binary outputs which are translations of the Gray-coded outputs and have values (counts) ranging from 0 to 255. Simulations were run to evaluate spacecraft controllability for failures in both the Most Significant Bit (MSB) and the second bit of the Gray-coded output.

The MSB, or sign bit, determines which side of the sensor the sun is on, and can fail to either 0 or 1. Since both of these failures result in similar behavior, a true reading on one side of the boresight and a false reading (error signal with the opposite sign) on the other side of the boresight, only one of these failures was modeled. This is illustrated in Fig. 6.

The plot of the Sun Pointing Error (Fig. 7) shows an average error of approximately 15 degrees in ORR mode for a failure in the sign bit. The failure was initiated 3,000 seconds into the run so that it could be modeled in steady-state. The plot of the Bad FSS Flag (Fig. 8) shows continual shifting between the CSS and DSS. As long as the truth models agree with the DSS and the CSS to within 30 degrees, the Bad FSS Flag is not toggled and the spacecraft may be controlled entirely by the failed DSS. This is a result of the way the DSS/CSS switching logic is implemented and can result in the spikes shown in the Sun Pointing Error.

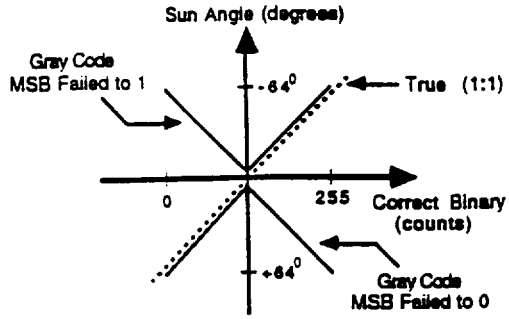

Fig. 6 Sun Angle with a Failure in the MSB

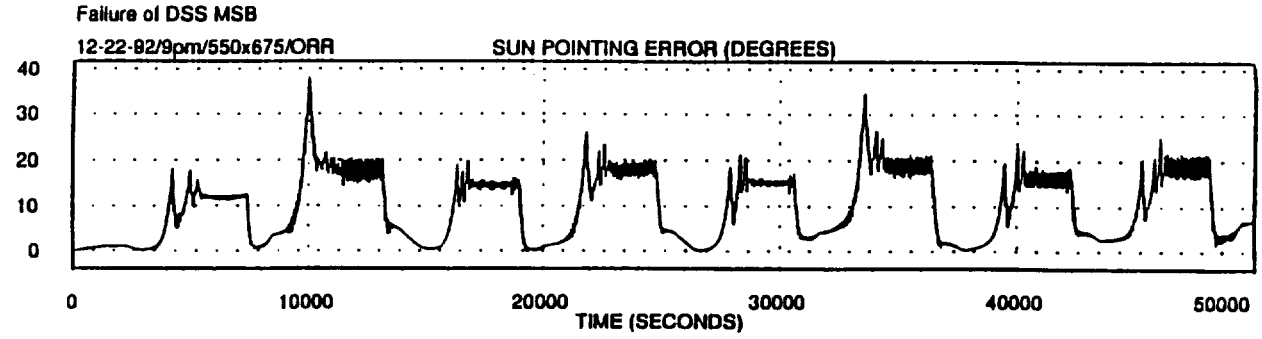

Fig. 7 Sun Pointing Error (Failure of DSS MSB)

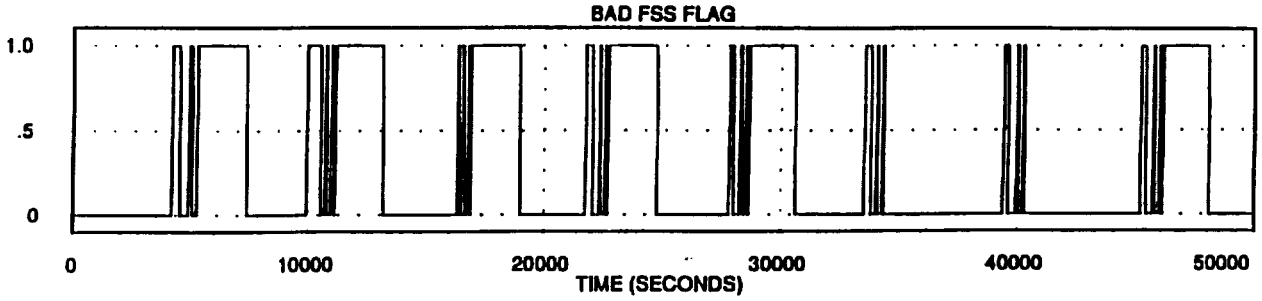

Fig. 8 Bad FSS Flag (Failure of DSS MSB)

The failure of the second bit to either a 0 or 1 results in very different behaviors, as illustrated in Fig. 9. Both of these failures were modeled and are discussed below.

A failure of the 2nd bit to 0 results in a "bang-bang" control since the effective Least Significant Bit (LSB) of the DSS becomes 64 degrees near null rather than 0.5 degrees, causing the pitch axis to move away from the sun. The simulation shows that this failure of the DSS is easily detected and the spacecraft is controlled entirely by the CSS. The plot of the Sun Pointing Error (Fig. 10) for a 2nd bit failure to 0 shows that the average error is

approximately 6 degrees in ORR mode, which reflects the +/- 6 degree blind spot of the CSS on the positive pitch axis.

A failure of the 2nd bit to 1 results in a very benign failure as long as the spacecraft remains within 32 degrees of the sun, since the second bit of the Gray code should be 1 in this case. However, if the spacecraft is pointing between 32 degrees and 64 degrees of the sun there will be an error in the DSS. This computed pointing error will be smaller than the true sun error but will be of the correct sign. The plot of the Sun Pointing Error (Fig. 11) shows that the spacecraft pitch axis remains within 32 degrees of the sun in ORR, and a failure in the 2nd bit is never detected. Thus, the DSS continues to control the spacecraft maintaining a sun pointing error of less than 5 degrees.

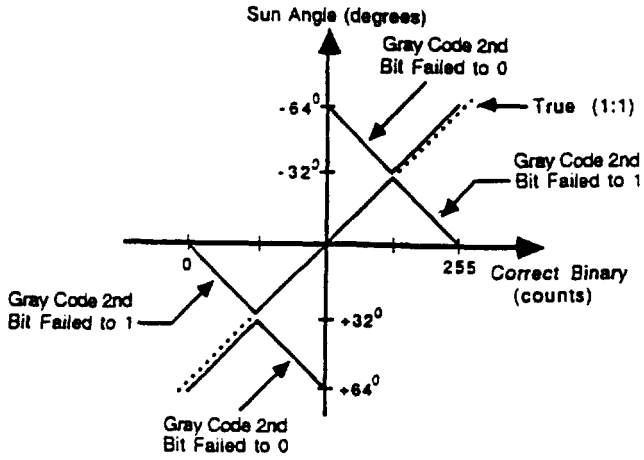

Fig. 9 Sun Angle (DSS Failure of 2nd Bit)

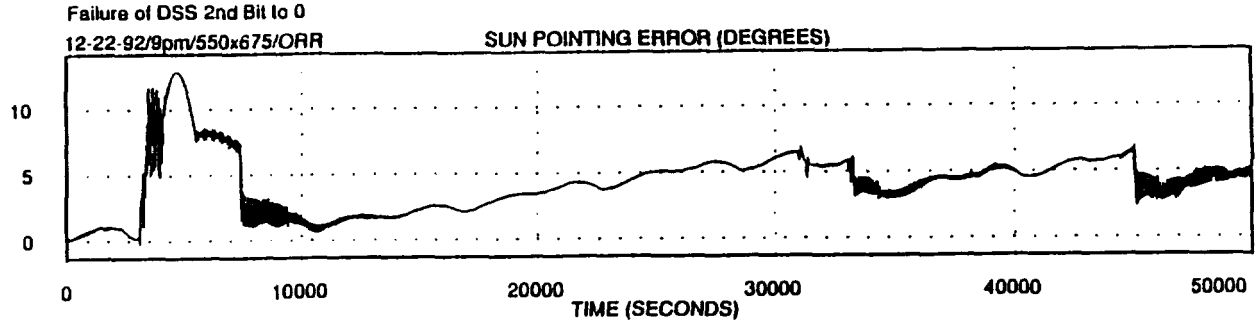

Fig. 10 Sun Pointing Error (Failure of 2nd Bit to 0)

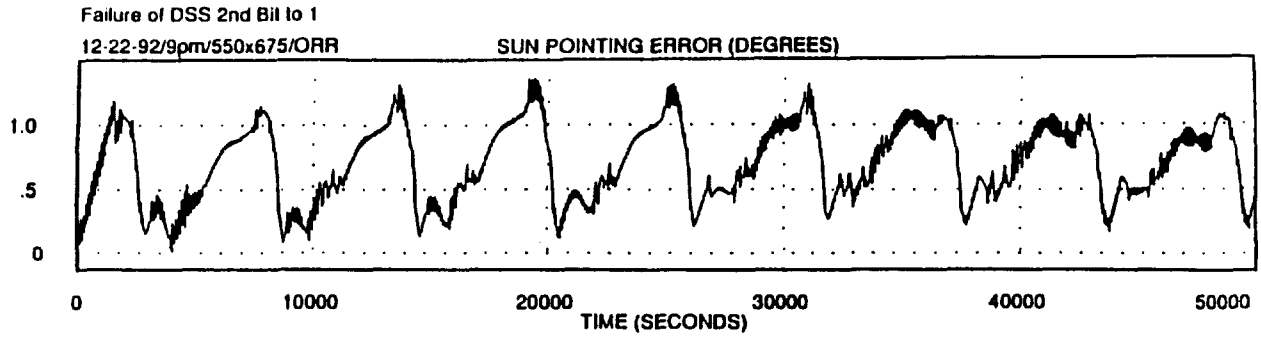

Fig. 11 Sun Pointing Error (Failure of 2nd Bit to 1)

Wheel Failures

Simulations were also run to evaluate the controllability of the spacecraft for a failure in the momentum wheel. The failure was simulated by setting the commanded wheel torque to zero and allowing friction to slow the wheel speed to zero.

The average sun pointing error for a failure in the momentum wheel is approximately 4 degrees in ORR mode. As the wheel speed decreases the momentum of the wheel is distributed to the spacecraft which generates a spin about the pitch axis. Thus, the system momentum vector along the pitch axis is conserved and the magnetic torquers continue to precess this momentum vector towards the sun line. As long as the sun pointing error does not exceed 20 degrees the spacecraft will not enter Safehold.

After initial acquisition, the x and z B-dot controls will be turned off. In this way, if Safehold is entered due to a momentum wheel failure, the spin of the spacecraft will not be damped out, thus conserving the momentum vector needed for sun pointing. It should be noted that the y B-dot control must always be active while in Safehold. The precession control is inherently unstable if it is used by itself. If the sun line is inside the nutation cone, the torques produced by the magnetic torquers will increase any nutation that is present. Therefore, the y B-dot is needed to dampen this nutation.

Magnetometer Failures

The SAMPEX three-axis magnetometer contains an x-axis redundant coil which is available to ORR mode but not to Safehold. If the spacecraft were to enter Safehold with a failure in the primary x-axis coil and sun pointing were not satisfactory, then autonomous switching between the x-axis coils in ORR would be required. Simulations showed an average sun pointing error of 6 degrees in Safehold and the spacecraft remains power safe. Thus, autonomous switching is unnecessary.

Conclusions

The SAMPEX attiude control system has been shown by simulations to meet the SAMPEX mission requirements for sun-pointing and instrument pointing. The velocity avoidance algorithm with a minimum ram angle of 90 degrees added to the orbit rate rotation mode provides the HILT sensor with an 89 percent chance of survival over a three year period without seriously degrading science pointing performance. Larger ram angles cause the spacecraft to flip and seriously decrease science pointing performance. During safehold

mode or when the HILT is switched off for an extended period of time, a retractable cover will be closed to protect the HILT sensor.

Several contingeny cases were analyzed by simulation, to verify that the attitude control algorithms are robust in the presence of sensor or actuator failures. Autonomous logic was added to switch from digital to coarse sun sensor data in the presence of digital sun sensor failures. Simulations of failure of the most significant bit and second significant bit of the digital sun sensor output showed that the failures were either benign or were successfully detected. Adequate sun-pointing performance was maintained for all sun sensor failures studied. Simulations of a momentum wheel failure indicate that the default x and z B-dot switches in Safehold mode be set to open after the initial acquisition phase of the mission Then, if the spacecraft enters Safehold due to a failure in the momentum wheel, the spin of the spacecraft about the pitch axis will not be damped out, and the angular momentum bias produced by the spinning spacecraft will enable SAMPEX to remain sun-pointing. The x and z B-dot switches should be closed during initial acquisition to accomplish acquisition as quickly as possible. Simulations of a failure in the primary x-axis magnetometer show that the sun pointing error remains less than approximately 6 degrees. Thus the spacecraft is in a power safe attitude, and autonomous swithing to the redundant x-axis magnetometer is not required.

The SAMPEX attitude control system algorithms provide robust spacecraft control, and are expected to contribute to a succesful mission.

Acknowledgements

The authors would like to thank Phillip Anz-Meador of Lockheed and Donald Kessler of NASA/JSC. Both were very helpful in providing background information on the orbital debris and micrometeoroid models that they developed. Professor Robert Culp of the University of Colorado also gave useful information on orbital debris. Michael Lauriente and John Ruby, both of NASA/GSFC, provided information on EnviroNET capabilities. Professor Glenn Mason of the University of Maryland, principal investigator of the SMEX/SAMPEX mission, advised the Guidance and Control Branch on the susceptibility of the HILT sensor to hazardous debris. Their contributions were extremely valuable in completing this study.

References

1. Forden, J. K., T. W. Flatley, D. A. Henretty, E. G. Lightsey, and F. L. Markley *On-board Attitude Determination and Control Algorithms for SAMPEX*, NASA/GSFC Flight Mechanics/Estimation Theory Symposium, Greenbelt, MD, May 22-24, 1990.

2. Lerner, Gerald M., *Three-Axis Attitude Determination*, in Spacecraft Attitude Determination and Control, James R. Wertz, editor, D. Reidel, Dordrecht, Holland, 1978.

3. Kessler, D. J., R. C Reynolds, and P. D. Anz-Meador, *Orbital Debris Environment for Spacecraft Designed to Operate in Low Earth Orbit*, NASA Technical Memorandum 100 471, April 1989.

4. Culp, R. D., *Orbital Debris*, 14th Annual AAS Guidance and Control Conference, February 2-6, 1991, Keystone, Colorado.

5. Lauriente, M., NASA/GSFC EnviroNET User Guide, Third Edition, April 2, 1990.

6. Klecker, B., *Study of the Micrometeoroid Hazard for the Experiment HILT/SAMPEX*, Max-Plank-Institut fur Extraterrestrische Physik, December 1990.

7. Grun, E., H. A. Zook, H. Fechtig, and R. H. Giese, *Collisional Balance of the Meteoritic Complex*, Icarus 62 (1985), pp. 244-272.

8. Frakes, J. P., T. W. Flatley, J. K. San, D. A. Henretty, F. L. Markley, and E. G. Lightsey, *SAMPEX Science Pointing with Velocity Avoidance*, AAS Papaer 92-182, AAS/AIAA Spaceflight Mechanics Meeting, Colorado Springs, CO, February 24-26, 1992

9. Lerner, Gerald M., *Sun Sensors*, in Spacecraft Attitude Determination and Control, James R. Wertz, editor, D. Reidel, Dordrecht, Holland, 1978, (Figure 6-15).

STAR TRACKER OPERATION IN A HIGH DENSITY PROTON FIELD

Kenneth J. Miklus, Frank Kissh, and David J.Flynn
Hughes Danbury Optical Systems, Inc.

ABSTRACT

Algorithms that reject transient signals due to proton effects on charge coupled device (CCD) sensors have been implemented in the HDOS ASTRA-1 Star Trackers to be flown on the TOPEX mission scheduled for launch in July 1992. A unique technique for simulating a proton-rich environment to test trackers is described, as well as the test results obtained.

Solar flares or an orbit that passes through the South Atlantic Anomaly can subject the vehicle to very high proton flux levels. There are three ways in which spurious proton generated signals can impact tracker performance: the many false signals can prevent or extend the time to acquire a star; a proton-generated signal can compromise the accuracy of the star's reported magnitude and position; and the tracked star can be lost, requiring reacquisition. Tests simulating a proton-rich environment were performed on two ASTRA-1 Star Trackers utilizing these new algorithms. There were no false acquisitions, no lost stars, and a significant reduction in reported position errors due to these improvements.

STAR TRACKER OPERATION IN A HIGH DENSITY PROTON FIELD

Star sensors have been utilized in high-accuracy attitude determination systems since the early 1960's, providing precise measurement of the position and magnitude of stars in the sensor's field of view (FOV). As applications continue to demand higher performance, the effects of a natural or enhanced radiation environment need to be accommodated by the star sensor's design. HDOS recently delivered two star trackers for the TOPEX/Poseidon mission which is scheduled for launch in July 1992. These enhanced trackers contain an efficient mix of hardware and firmware that permits effective acquisition and tracking throughout their orbit, which includes extensive exposure to the transient rich environment of the South Atlantic Anomaly. This paper discusses the algorithms employed, the environment simulated, and the results of the tests performed, demonstrating successful operation in a proton-rich environment.

BACKGROUND

State-of-the-art star sensors (see Figure 1) have recently benefited from two major technological developments, the CCD detector and the microprocessor. The heart of the current HDOS ASTRA star sensors is the RCA 504 CCD, a 256 × 403 pixel array which operates in the frame transfer mode. The thinned, backside illuminated device provides high quantum efficiency in the visible range. A thermoelectric cooler is used in the ASTRA-1 sensors to provide low noise operation in harsh environments. Fitted with a wide FOV (7×9 degree) color corrected lens, the ASTRA star sensors can provide position accuracy to 10 arc-seconds or better, and sensitivity down to a visual magnitude of 6. The HDOS ASTRA star sensors also utilize a versatile 16-bit microprocessor. Acquisition and tracking, centroid determination and correction, debris and transient event discrimination, and self-test functions are performed autonomously by the microprocessor. This design provides a flexible interface and reduces the computation burden on the host computer.

Star sensors utilizing mosaic CCD arrays can be separated into two classes: star trackers and star mappers. Star trackers have two distinct functional modes: acquisition and track. During acquisition, the sensor field of view is searched for valid targets. High-pass spatial filtering and pixel amplitude thresholding are often used to limit the amount of data saved each frame. Data from multiple frames can be used during acquisition to discriminate valid stars from debris and transient events. Once a star has been acquired, the sensor enters the track mode. During the track mode, data from previous frames is used to estimate the current position of

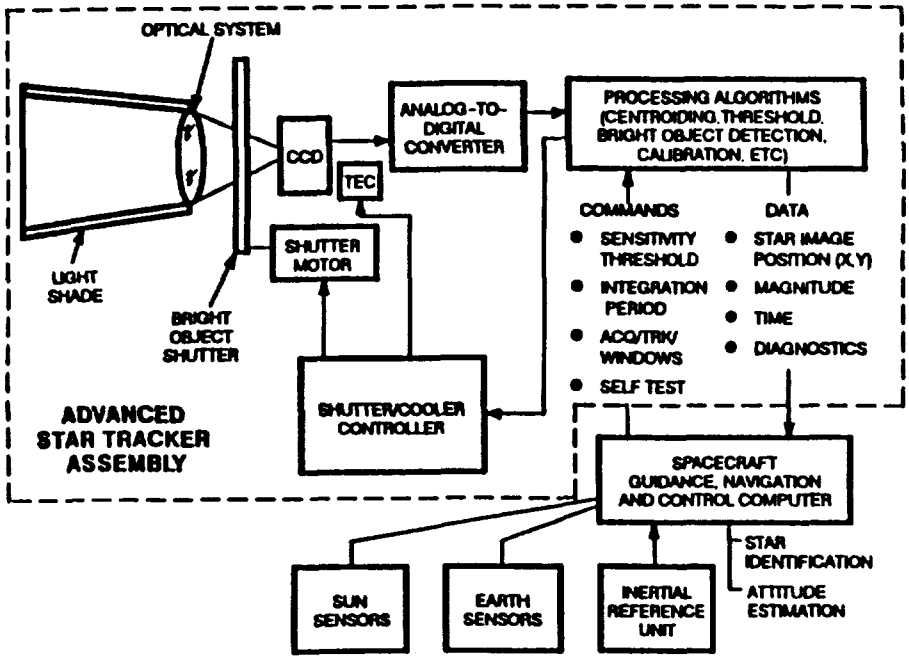

Figure 1. Functional Diagram of the Advanced Star Tracker (ASTRA).

the star. A reduced field surrounding the star is then read, processed, and the magnitude and position of the star are output to the host. The HDOS ASTRA-1 built for the TOPEX/Poseidon mission is an example of a star tracker. The ASTRA Star Tracker currently being built for Space Station Freedom will operate as four virtual star trackers allowing simultaneous acquisition and tracking of up to four stars.

Star mappers acquire stars throughout the total sensor field of view and report their magnitude and position each frame. High pass filtering and pixel amplitude thresholding are used to limit the amount of data that must be processed each frame. Normally, information is not saved from frame to frame. The HDOS ASTRA-2 built for the JH/APL START experiment[1] is an example of a star mapper. It outputs the position and magnitude of up to five stars at a 10 Hz update rate.

Trackers have a number of functional advantages over star mappers when operating in a transient event-rich environment. Once a star tracker has acquired a star, only a small fixed number of pixels must be read, stored, and processed each frame. A star mapper must process the entire CCD array each frame and the number of transient events will impact the amount of data that must be processed. By using data from multiple frames, star trackers can discriminate between stars (with predictable magnitudes and positions) and transient events during acquisition. Using magnitude and position data from previous frames during track mode also allows a star tracker to determine if a transient event has corrupted the reported magnitude and position data. Star mappers do not store information from previous frames and cannot discriminate between transient events and valid targets; this task must be performed by the host. Star mappers can also report a different set of stars each frame which requires identification of stars each frame. In a star tracker system, once a valid star has been identified, there is no need for the host to re-identify a star so long as it remains in track.

THE ENVIRONMENT

For a star sensor to operate in a natural or enhanced radiation environment, the effects of radiation damage and radiation induced noise events on the CCD must be addressed. Space radiation that will interact with the CCD can be divided into two major groups, trapped particles and solar protons.[2,3] Trapped particles are protons and electrons trapped in the magnetic fields surrounding the earth. The energy and fluence profiles will

vary with the altitude and inclination of the orbit. In low earth orbits, anomalies at the poles and off the coast of Brazil (the South Atlantic Anomaly) can result in high fluxes of energetic protons. Solar protons are emitted during solar flares which occur randomly. Intense solar flares occur about every 11 years. At high altitudes, i.e. geostationary orbit, solar protons can dominate, with fluxes sometimes orders of magnitude greater than the trapped particle radiation. HDOS has developed the capability to evaluate the radiation environment in space and its impact on sensor systems for given orbits. These models are based on the RADBELT AP-8, AE-8 radiation environment data supplied by NASA-GSFC.

The effects of radiation damage in CCDs have been the focus of much recent work.[4] HDOS has developed the tools required to model the end-of-life performance of CCD detectors, and has also performed experiments to measure these effects on irradiated devices. The primary concern of this paper is the effect of transient noise events that occur when high energy particles impact the CCD. Charged particles interact directly with the CCD pixels, causing a random series of ionization events. These events can be localized to within a few pixels or can result in streaks, depending on the angle of incidence of the particle, the geometry of the device, and the energy of the particle.[5,6] A large number of events in the sensor field of view can interfere with the operation of the sensor. If the system must operate in a high density proton environment, a method to reduce the impact of these events on the sensor operation is required. The most obvious solution is to increase the shielding around the CCD to reduce the number of events. However, this will increase system size and weight. A more elegant solution is to apply real-time processing to reject these transient events.

Transient events can degrade a star tracker's performance in a number of ways. During acquisition, transient events can be acquired falsely or can impede acquisition of a valid target. During track, transient events can corrupt position and magnitude data or can result in the sensor dropping a valid star track. For the TOPEX mission, Fairchild Space Co.[7] determined that the star tracker must operate with up to 150 transient events in the sensor FOV per frame, 100 milliseconds. All of these events were assumed to be indistinguishable from real stars to the CCD. Since these transient events were independent of one another their position and magnitude were random and uniformly distributed over the CCD array.

The system had to meet the following requirements:

- Acquire and track stars with up to 150 transient events per frame
- Acquire and track stars moving up to 0.3 degree/second
- Probability of acquiring a valid star within 22 seconds is 95%
- Alert host if data has been corrupted
- Maintain track of valid stars during proton event disturbances.

ALGORITHM IMPLEMENTATION

Any solution is dependent on determining what information is available to discriminate between transient events and valid stars. Star image size is a function of the point spread of the optics and the motion and jitter of the spacecraft. Therefore, bounds can be placed on the size of valid targets and single pixel upsets and events that result in long streaks can be rejected. Proton events only last for one frame. Since they are independent of one another, the position and magnitudes of the proton events randomly change from frame to frame. Positions of the star images on the array are determined by the dynamics of the spacecraft and therefore change systematically from frame to frame. By applying spatial and magnitude filtering, we can reject transient events. The probability of transient events passing this filter will be a function of the number of transient events per frame and the size of the discrimination windows. The line-of-sight (LOS) motion requirement (up to 0.3 degree/second) thus determines the minimum spatial window to be used. The size of the magnitude window is determined by the tracker's predicted error in determining star magnitude. Once a star is acquired, magnitude can be checked to determine if a transient event is contiguous with the star image, causing an error in the centroid of the image and in its reported magnitude.

Our selected approach was to limit the data processing load during each tracker frame when in the acquisition mode to be consistent with existing hardware capabilities. The tracker FOV was divided into 19 acquisition bands (19 pixel rows by 403 pixel columns). The bands were stacked in the row direction with a small overlap and the search for a star confined to one band at a time. If the acquisition sequence fails to find a star in the current band, the tracker sequences to the next band and searches for a valid star. This sequence continues until the tracker acquires a star in one of the bands and transitions to track mode. If the entire FOV is searched unsuccessfully, the sequence is repeated.

The acquisition sequence consists of two acquisition states (A1 and A2) and five validation states (H1 through H5). Each state takes one tracker frame to implement.

The acquisition sequence searches an acquisition band to determine if any group of pixels with signal exceeding a threshold exists that could quality as a star. If no such group exists the tracker transfers to the next acquisition band and the sequence is repeated. If candidate stars are found in the A1 state, the tracker enters the A2 state. If any of the candidate stars identified in A1 is also found in A2, the tracker goes into the validation phase of the acquisition sequence. During validation states, the tracker continues to evaluate the candidate star's characteristics for temporal and spatial consistency. Upon transition to the track state, sufficient history has been established so that it is highly probable that the group represents a valid star and is not caused by transient events. If the star is not confirmed in any of the validation states the tracker increments to the next acquisition band and the acquisition sequence is continued.

Upon transition to track, a small track window is defined which is centered about the last validated star position. The window position is updated each frame to track the updated star position. The window is made small enough to limit the data processing load and exclude the majority of transient proton signals; but it is large enough to account for vehicle LOS rates.

The track window is scanned in a raster fashion each frame, and the magnitude and position characteristics of the candidate star are evaluated. If the star is evaluated as a "valid" star, the centroid data and star magnitude data are sent to the host and a bit is set in the data word that indicates the data is valid. If no valid star is found in the track window after multiple attempts to recover from proton hits, the star is considered lost and the tracker reverts to the acquisition mode.

TEST METHOD

The CCD's inability to distinquish between proton or photon generated-signals was utilized to test the tracker with the proton flux improvements. A Scene Simulator (SS) concept was implemented. Scenes consisting of point sources of light were generated on a computer monitor. The point sources were collimated and then imaged by the tracker on its CCD detector. The signals generated in this fashion at the CCD could be considered as having been generated by either protons or stars. This technique achieved complete control of the interactions between a simulated star and simulated proton events.

The SS equipment shown in Figure 2 consisted of a VGA monochrome monitor and a personal computer (PC) with a 386 processor running at 25 MHz. The monitor was positioned at the focal plane of an achromatic collimating lens with a focal length (FL) of 1185 mm. The scene was generated by commanding 150 monitor pixels on, to serve as "proton" sources, and one pixel to serve as a "star". The intensity of each monitor pixel was controlled by the SS software. The collimated light from each monitor pixel was imaged by the tracker optics on its CCD detector. The tracker optics had an FL of 41 mm which imaged the monitor pixels at the CCD detector, resulting in a demagnification factor of 29. All images at the tracker, simulated protons as well as simulated stars, were equivalent in size to predictions for a valid star in orbit, i.e. between two and 25 CCD pixels. The angular FOV that the monitor accommodated exceeded the 9×7 degree FOV of the tracker.

To ensure a worst-case test scenario, all proton events were sized (in pixels) within the range considered by the tracker to be acceptable stars. Figure 3 (frames 299 and 300) shows the excellent image size achieved with the Scene Simulator.

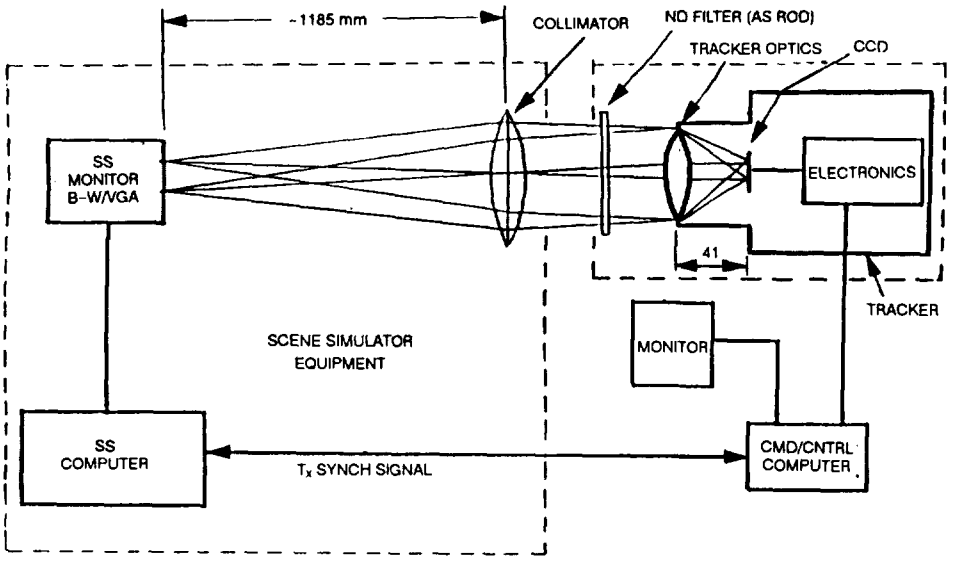

Figure 2. Configuration for Simulation of Stars and Proton Events in a Laboratory Environment.

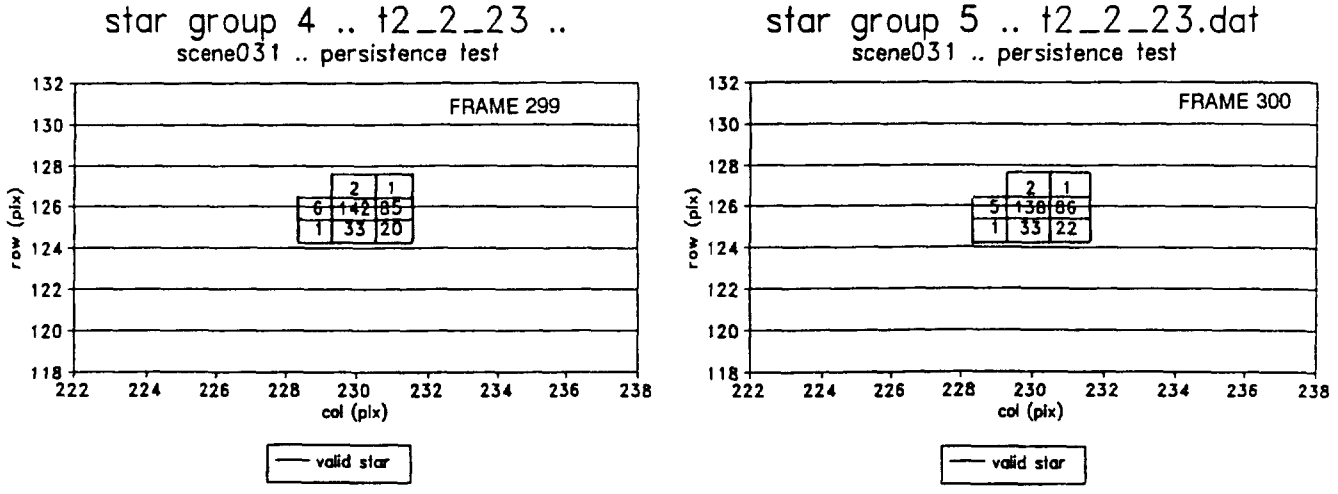

Figure 3. Excellent Image Properties Were Achieved with the Scene Simulator (Mi~3.7).

To limit simulated proton signals to one tracker frame, the generated scene display was synchronized with the 10 Hz frame rate of the tracker. This synchronization was mandatory because a star will be imaged at a spatially consistent location during successive tracker frames, whereas a proton signal will be transitory both spatially and temporally.

TESTS RESULTS

The tests described were designed to verify three basic aspects of the tracker software performance in a proton-rich field, specifically:

- A star being tracked will not be lost as a result of the proton events
- Acquisition of a valid star will occur within 22 seconds of the start of the search and star position
- Magnitude data corrupted by proton events will be identified for the host.

The scene simulator technique was especially useful since the intensities and positions of the simulated protons could be varied by the software to have any desired relationship to the simulated star. In all, 14 unique scenarios were used to test the response of the tracker to various combinations of "proton" influences on tracker performance. Generally the scenes simulated conditions of near or direct proton hits on the star position. In addition a "no stars" scene was used to verify that the tracker software was not fooled by the "proton" signals and did not erroneously report star acquisitions. Both moving and stationary stars were simulated.

Each test scene scenario always consisted of 150 simulated protons and one simulated star. The simulated proton positions were generated in a random fashion in the tracker's FOV. Consistent with Fairchild's radiation analysis/specifications, 35 of the simulated proton signals were at an equivalent star Instrument Magnitude (Mi) of 3.2; 115 ranged between the equivalent Mi of 3.7 and 5. The simulated star was set at Mi = 3.7. Generally the "star" in the scenes was not subjected to random "proton" influences. Each scene was carefully designed to introduce specific and periodic occurrences of "proton/star" interactions so that tracker software processes could be evaluated. Completely random occurrences of "proton/star" interactions were used to gather statistical information regarding frequency of "star" disturbances, to ensure that the three primary performance requirements were met and that interacting events did not cause unanticipated results.

The results of a test designed to demonstrate ASTRA's capability to reject "protons" during the star acquisition sequence are shown in Figure 4. The particular scenario contains 150 "protons" but no valid star in the FOV. As required, at no time did the tracker indicate a star acquisition. If no signals were found during the search of the tracker's FOV, the highest acquisition state achieved by the tracker is the A1 state, and the minimum time to search the entire FOV is 3.8 seconds. The figure shows that the "protons" caused the search of each band to extend routinely to the A2 state, periodically to the H1 state and occasionally to the H2 state. Each state beyond the A1 state, caused by proton signals, typically adds 100 msec to the overall search time.

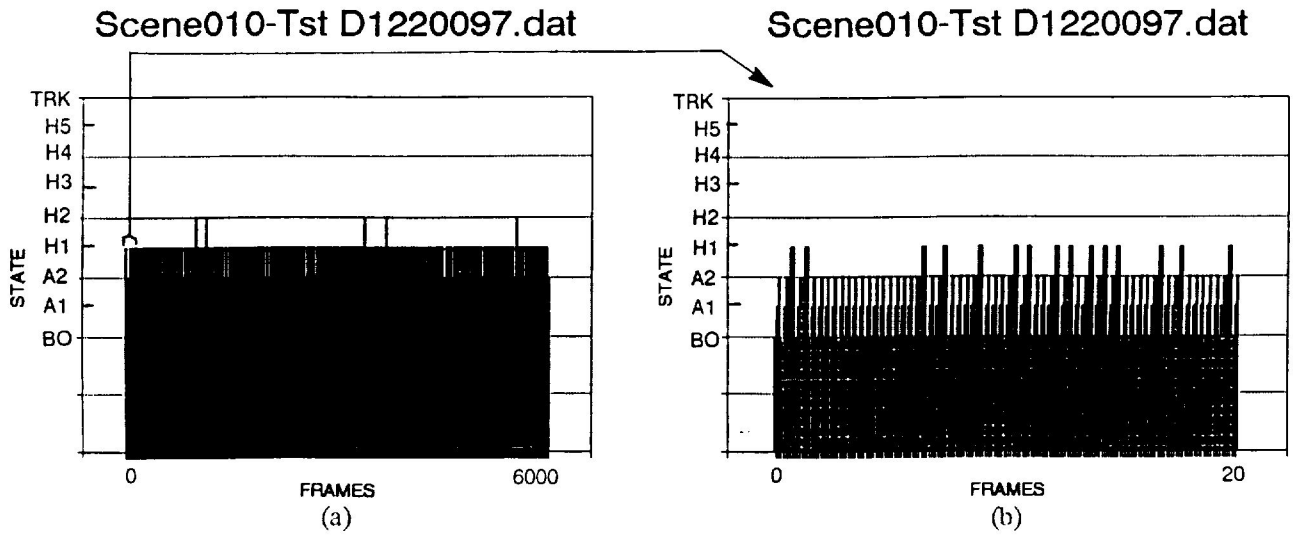

Figure 4. The ASTRA Design Never Reports a Proton as a Star.

Figure 5 shows the results of a test in which a "star" moves horizontally across the FOV at an apparent velocity of 0.35 degree/second and periodically experiences a direct and "near proton" hit. The figure is similar to many of the following figures. Row, Column, and Intensity are displayed as a function of tracker frame number. Row and Column are plotted in CCD pixel space, Intensity is in output counts. Any time a star signal is invalid or lost, the values of all three parameters drop to zero. A momentary dropout is characterized by a zero signal for no more than 10 frames. If the signals go to zero for more than 10 frames, the tracker has reentered the acquisition mode, and the time that the signal remains at zero is indicative of the time required to reacquire the star.

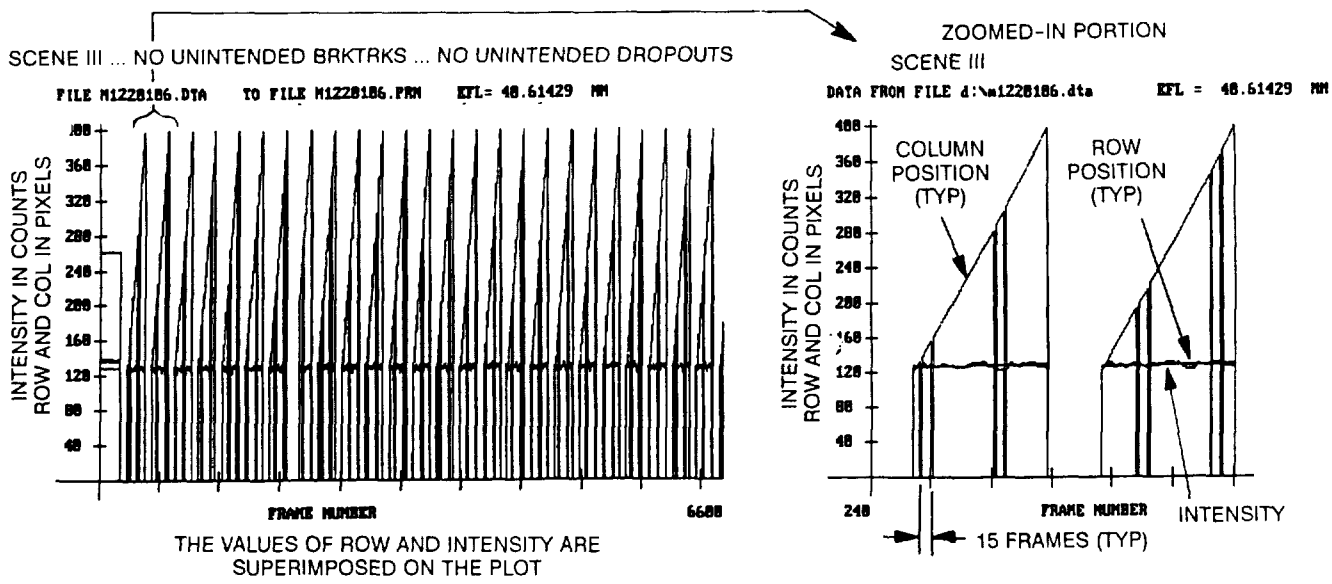

Figure 5. ASTRA Does Not Report Star Data Corrupted by Direct or Very Near Proton Hits.

Every 100 tracker frames, the SS causes a "proton" hit directly at the star position and 15 frames later a "proton" hit occurs 0.035 degree from the star. It can be seen from the data in Figure 5 that each event causes a dropout (i.e., the star position data is not used by the host). The increased intensity of the direct "proton" hit causes the "star" to be evaluated as invalid since its increased intensity is outside the average intensity limits being continuously determined and updated by the tracker for the valid star. The near hit, 15 frames later, drops out for the same reason since the near "proton" signal merges with the "star" signal and increases the signal intensity. If the position determination had been reported for the "near hit" condition, the position would have been in error by the bias that the "proton" signal would have introduced. For the "direct hit" condition an incorrect star magnitude would have been reported potentially impeding star identification by the host.

It was also of interest to determine how close a "proton" could come to a "star" without perturbating the star (see Figure 6). This scene has a diagonally moving star which is approached within 0.16 degree by a "proton" every 100 frames. As a benchmark, a simulated direct hit on the star by a proton was introduced causing a dropout for one frame, 15 frames prior to the near "proton" event. The data 15 frames after the dropout was reviewed and no effect of the close approach of the "proton" to the "star" was evident. View (a) of Figure 6 shows the entire test results in which the regular "star" dropouts due to the direct "proton" hit are evident. View (b) of the figure shows a single transit of the star over the tracker's FOV; view (c) shows a greatly magnified view of an area of interest. This plot is typical of all of the proton event occurrences during more than two hours of testing.

Figure 7 demonstrates the ability of ASTRA to maintain track even when a significant number of sequential frames were impacted by interfering "protons". The SS scenario was a stationary "star" interrupted by four blank scenes every 100 frames. Despite the long periodic interruptions, the tracker did not revert to the acquisition mode.

Table 1 provides statistical data on acquisition of a star in a "proton"-rich field. All the tests had either moving stars that left the FOV at one edge and then were re-introduced at the other edge or stationary stars that were deliberately caused to break-track periodically. In all but the diagonal scan cases the SS scenario was

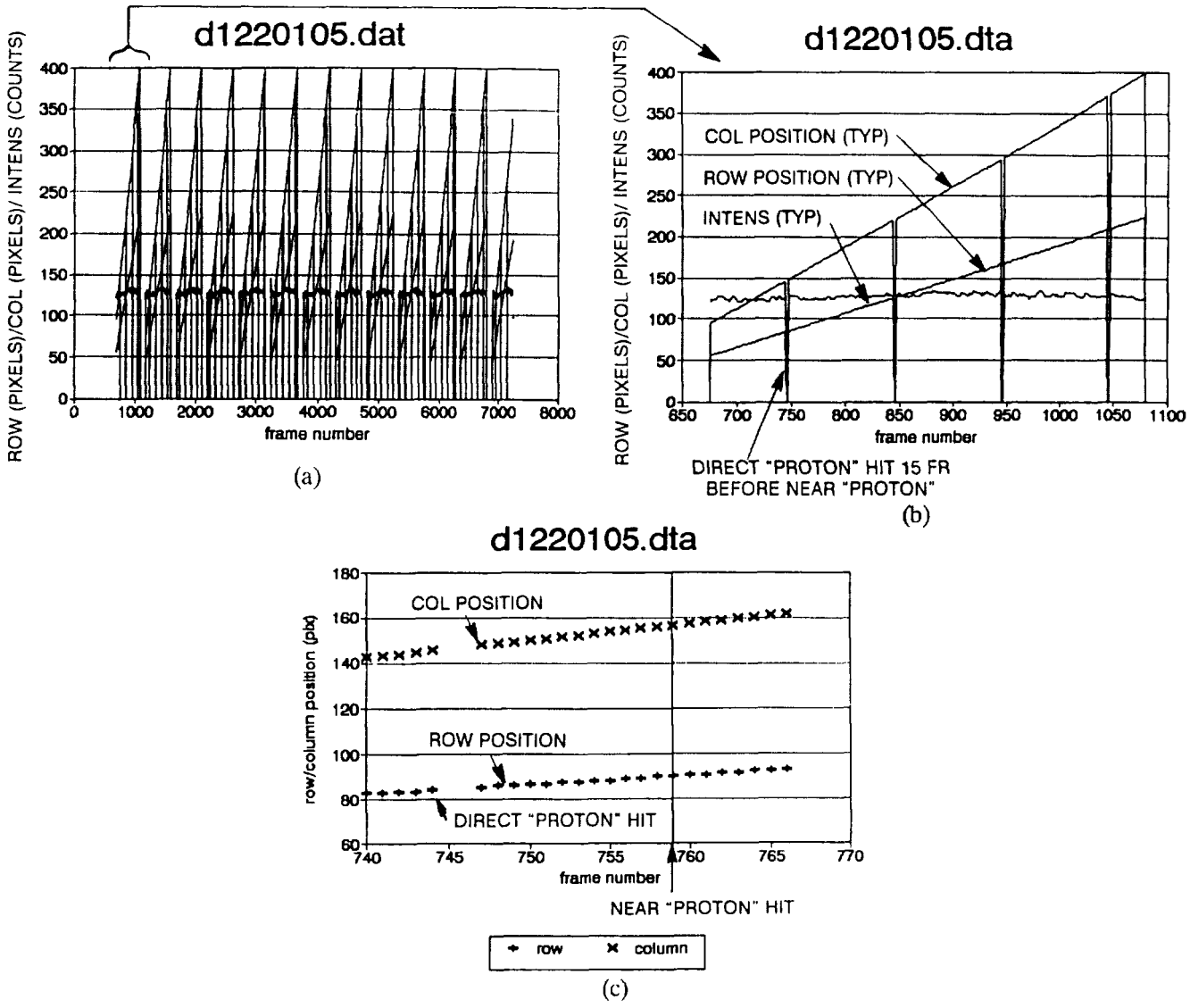

Figure 6. ASTRA Accommodates Near (Non-Interfering) Proton Hits.

designed so that the tracker had to search the entire FOV before it was in a position to find the star. The minimum time required to reacquire a lost star without proton interferences would be 4.4 seconds. Since the average time to acquire a star (see the table) is 7.1 seconds, the acquisition delay due to proton effects is 2.7 seconds.

TRACKER PERFORMANCE COMPARISONS IN A PROTON FIELD

Results of tests in which the SS generates a stationary "star" positioned approximately in the center of the FOV and 150 "protons" are generated in a completely random fashion in the FOV without regard to "star" position are shown in Figures 8 through 10. Random interferences with the "star" do occur. A comparison of the data from the three tests quantitatively demonstrates the increased error in the reported "star" position due to "proton" interference with the intensity discrimination disabled (Figure 9) and with both the intensity and position discrimination disabled (Figure 10). The latter case is indicative of the performance expected from the tracker if no consideration were made in the design to accommodate proton events.

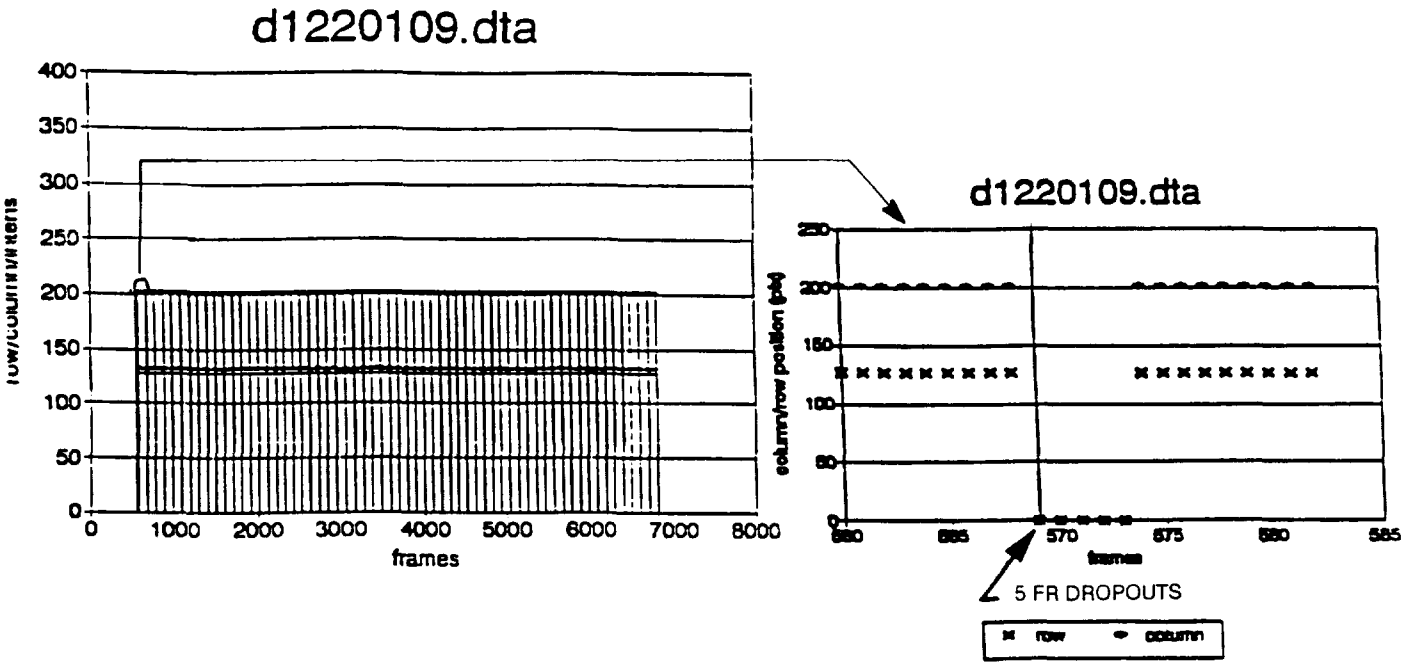

Figure 7. Tracking of a Valid Star is Maintained for Multiple Sequential Proton Events.

View (a) of Figure 8 illustrates the "star" position variation over an 11.6 minute test as reported by the tracker. An evaluation of the data shows that the uncorrupted data sent to the host represented 90 percent of the total number of frames. This statistic was valid for two separate trackers within 0.5 percent. This particular test displayed a standard deviation of the reported row and column positions of 5.1 arc-seconds and 3.2 arc-seconds, respectively. Figure 7(b) shows the row, column and intensity of the star plotted against time. Although there are numerous dropouts of data due to "proton" induced variations in star position or magnitude beyond preset limits, the tracker never lost the "star" long enough for the tracker to re-enter the acquisition mode.

Figure 9 presents the results from the same SS test scene but with the intensity compare discriminator disabled during the track mode. The standard deviation of the position data reported to the Host increased to 14.1 and 12.5 arc-seconds in row and column positions, respectively. Since the position comparator remains enabled the increase in the the position error is due solely to direct interference of the "protons" with the star, since the "proton" signals merge with the star signal to form an erroneous star position centroid. Despite the relatively large position errors and the numerous dropouts of "star" data, the tracker never lost the "star" to the extent that it re-entered the acquisition mode, see View (b) of Figure 9.

Figure 10 presents the results from the same SS test scene but with both the intensity compare and position compare discrimination of the tracker disabled during the track mode. The standard deviation of the reported "star" position increased to 145.3 and 173.7 arc-seconds in row and column positions, respectively. These large errors are due not only to interference with the "star" by the "protons" but, in addition, "proton" generated centroid positions are mistakenly reported as the "star" position. This case of mistaken identity

Table 1. Average Acquisition Times in "Proton" Rich Environment

TEST IDENT	SEARCH PERIODS	TIME OF RUN(SEC)	AVG ACQ TIME(SEC)	STD DEV(SEC)	MAX TIME(SEC)	MIN TIME(SEC)	MOTION DIRECTION
T4_6_18	110	5691	9.2	2.6	20.3	7.3	DIAGONAL
T2_6_13	139	7191	7.5	2.5	15.1	1.2	DIAGONAL
D1220098	20	630	6.7	1.3	12.1	6.1	STATIONARY
D1220101	20	639	6.1	0.16	6.3	5.8	STATIONARY
D1220104	13	678	7.7	1.2	8.5	3.7	DIAGONAL
D1220105	13	680	8.2	0.75	10.5	7.6	DIAGONAL
D1220106	26	688	6.7	1.2	12.7	6.1	HORIZONTAL
D1220121	25	646	6.8	1.3	12.7	6.1	HORIZONTAL
D1210048	21	743	6.5	0.29	7.0	6.0	STATIONARY
D1210051	20	672	6.1	0.18	6.5	5.8	STATIONARY
D1210056	23	590	6.9	1.6	14.2	6.1	HORIZONTAL
D1210057	26	714	6.9	1.4	13.5	6.1	HORIZONTAL

THE TOTAL NUMBER OF SEARCHES WAS_____ 456
THE TOTAL TEST TIME (HOURS) WAS_____ 5.4

THE AVERAGE ACQUISITION TIME (SECONDS) WAS___ 7.11
WITH A STANDARD DEVIATION (SECONDS) OF___ 2.00

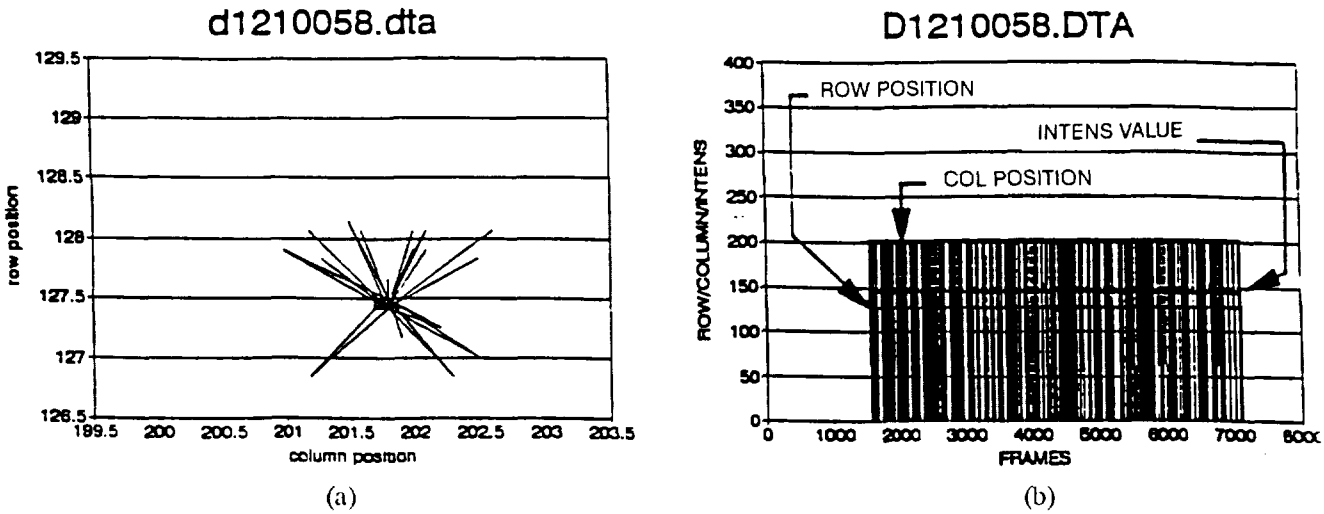

Figure 8. Tracker Performance With Proton Flux Design Features. (a) "Star" Position Variations During a 10 Minute Test; and (b) Row/Col/Intensity Values Plotted Over the Test Time.

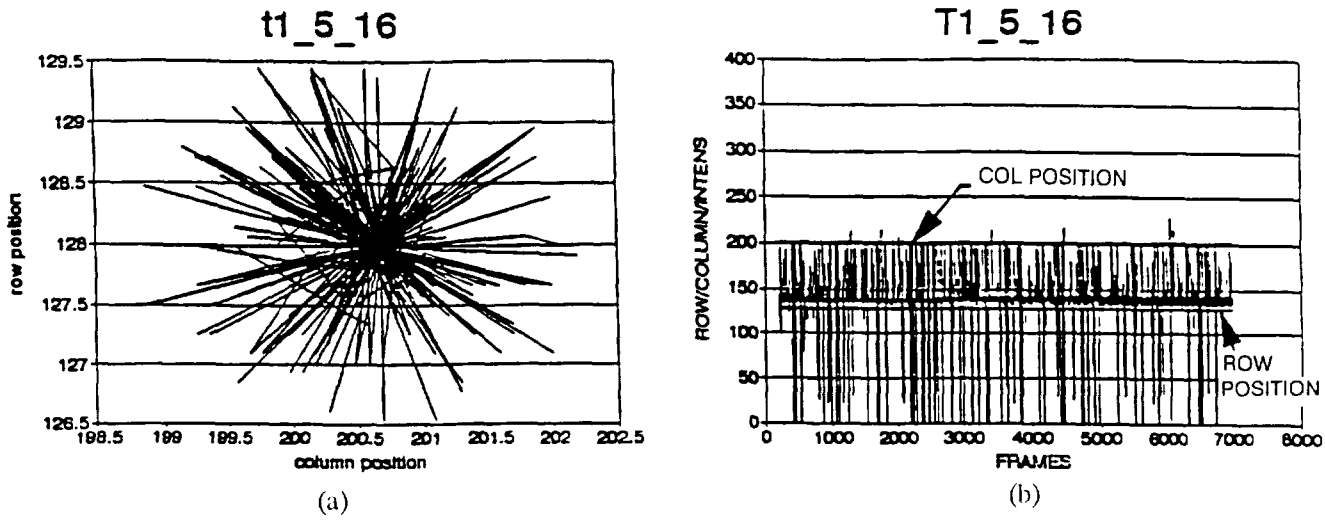

Figure 9. Effect of "Proton" Events on Tracker Performance With Magnitude Compare Disabled. (a) "Star" Position Variation Over 11.6 Minutes Caused By "Proton" Events; and (b) Row/Col/Intensity Values Plotted Over the Test Time.

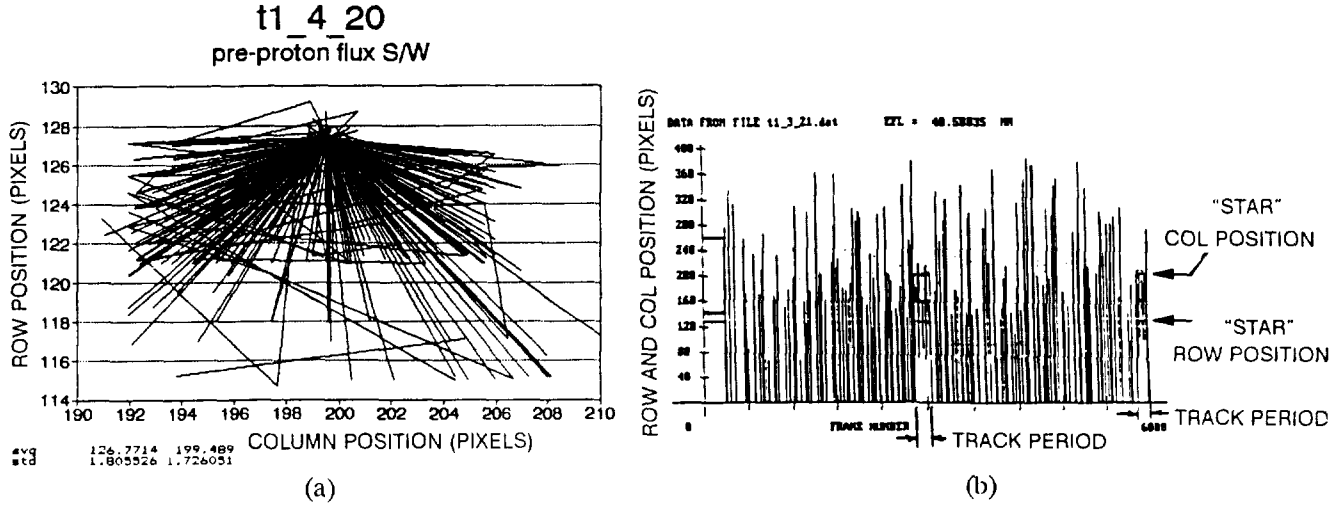

Figure 10. Effect of "Proton" Events on Tracker Performance Without Proton-Flux Design Features. (a) "Star" Position Variation Over 30 Minutes Caused By "Proton" Events; and (b) Part of 30 Minute Test.

occurs if the proton signal occurs within the Track Window and precedes the star position during the raster scan of the window. The dissymmetry of the "star" position variations shown in view (a) of Figure 10 is explained by this phenomena. View (b) shows a case in which the errors have become so large that the "star" is lost and the tracker must re-enter the acquisition mode to re-acquire the "star".

Figure 11 evaluates the same data from an acquisition perspective. The software of the tracker with the position and magnitude comparators disabled was also modified so that during acquisition the first signal with the characteristics of a valid star (i.e., proper size and magnitude) would cause a transition to track. (The multiple frames and tests implemented in the design for use in high-proton flux environments were disabled.) In the proton-rich environment, as simulated here, a large number of false star acquisitions were caused by proton signals. The actual "star" was acquired only nine times in 30 minutes of tracker operation, and was tracker for only six percent of the time.

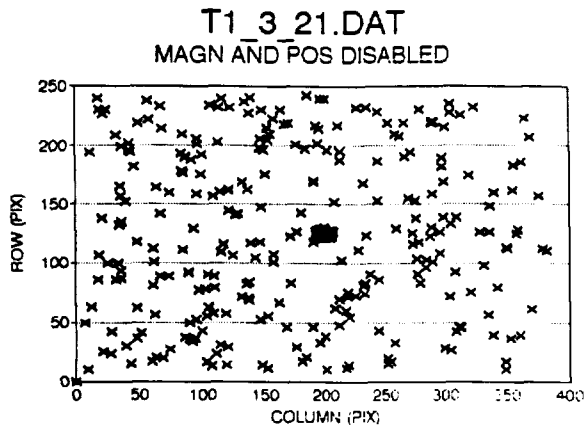

Figure 11. Without the Proton Flux Design Features, the Tracker Will Usually Acquire and Attempt to Track Proton Events.

SUMMARY

Radiation-induced proton events can result in anomalous operation of solid-state star trackers, specifically:

- Erroneous acquisition of proton events and/or failure to acquire valid stars
- Loss of track of valid stars
- Incorrect position and intensity data.

Through incorporation of hardware-efficient processing algorithms, HDOS has completed delivery of two flight trackers for the TOPEX/Poseidon mission which can operate effectively in a proton-rich environment. Using a scene simulator to produce effects similar to those caused by protons, tests validating the performance gains achieved have been completed on both units. For an environment that produces 150 false multi-pixel events at the detector, the following results were obtained:

- No acquisition of false stars (proton events)
- Reliable acquisition of valid stars
- No loss of tracking a valid star
- Identification of corrupted data for the host, caused by proton impact upon valid star pixel groups.

The algorithms incorporated into the tracker firmware can be tailored to unique user mission requirements. The scene simulation techniques developed provide a powerful tool for validating performance for rather unique and complex test conditions.

REFERENCES

1. H. L. Fisher, T. E. Strickwerda, C. C. Kilgus, L. J. Frank, "Autonomous, All-Stellar Attitude Determination Experiment: Ground Test Results" "Autonomous Star Sensing and Attitude Determination", AAS 91-025, 1991.

2. R. Rau, "Space Radiation, Protons, and CCDs" HDOS TechNews vol. 2 iss 6, December 1991.

3. E. G. Stassinopoulos, J. P. Raymond, "The Space Radiation Environment for Electronics" Proc. IEEE, vol. 76, no. 11, Nov. 1988.

4. J. Janesick, T. Elliott, F. Pool, "Radiation Damage in Scientific CCDs" IEEE 1988 Nuclear Science Symposium, Orlando FL.

5. T. Lomheim, R. Shima, J. Angione, W. Woodard, D. Asman, R. Keller, L. Schumann, "Imaging CCD Transient Response to 17 and 50 MeV Proton and Heavy-Ion Irradiation" (preprint submitted to IEEE Trans. on Nuclear Science).

6. F. Kubick, "Statistical Aspects of CCD Radiation Noise", (HDOS internal memo).

7. B. Bloom, "TOPEX Star Tracker 'False' Star Contour Maps", presented to Fairchild TOPEX Attitude Control Group, July 12, 1990.

Resolution of the COBE Earth Sensor Anomaly

J. Sedler
COMPUTER SCIENCES CORPORATION (CSC)

ABSTRACT

Since its launch on November 18, 1989, the Earth sensors on the Cosmic Background Explorer (COBE) have shown much greater noise than expected. The problem was traced to an error in Earth horizon acquisition-of-signal (AOS) times. Due to this error, the AOS timing correction was ignored, causing Earth sensor split-to-index (SI) angles to be incorrectly time-tagged to minor frame synchronization times. Resulting Earth sensor residuals, based on gyro-propagated fine attitude solutions, were as large as ±0.45 deg [much greater than ±0.10 deg from scanner specifications (Reference 1).] Also, discontinuities in single-frame coarse attitude pitch and roll angles (as large as 0.80 and 0.30 deg, respectively) were noted several times during each orbit.

However, over the course of the mission, each Earth sensor was observed to independently and unexpectedly reset and then reactivate into a new configuration. Although the telemetered AOS timing corrections are still in error, a procedure has been developed to approximate and apply these corrections. This paper describes the approach, analysis, and results of approximating and applying AOS timing adjustments to correct Earth scanner data.

Furthermore, due to the continuing degradation of COBE's gyroscopes, gyro-propagated fine attitude solutions may soon become unavailable, requiring an alternative method for attitude determination. By correcting Earth scanner AOS telemetry, as described in this paper, more accurate single-frame attitude solutions are obtained. All aforementioned pitch and roll discontinuities are removed. When proper AOS corrections are applied, the standard deviation of pitch residuals between coarse attitude and gyro-propagated fine attitude solutions decrease by a factor of 3. Also, the overall standard deviation of SI residuals from fine attitude solutions decrease by a factor of 4 (meeting sensor specifications) when AOS corrections are applied.

1. INTRODUCTION

Since its launch on November 18, 1989, the Cosmic Background Explorer's (COBE's) Earth sensors have shown greater noise than expected. It was determined that the acquisition-of-signal (AOS) timing correction was in error. Since no useful information could be extracted from this telemetry, the total AOS timing correction was ignored altogether, causing the split-to-index (SI) angles to be time-tagged incorrectly.

However, over the course of the mission, each Earth scanner was observed to independently and unexpectedly reset and then reactivate into a new configuration. Although the telemetered AOS corrections are still in error, a procedure has been developed to approximate the AOS corrections by assuming certain scanner attributes. This paper describes the approach, analysis, and results of approximating and applying these AOS timing corrections.

Section 2 describes predicted Earth scanner performance. Section 3 presents observed Earth scanner performance, both before and after reconfiguration. Section 4 explains the procedure to determine the AOS timing corrections. Section 5 compares the results both from applying and from ignoring the AOS timing corrections. Section 6 lists major assumptions and possible sources of error in the procedure.

2. PREDICTED EARTH SCANNER PERFORMANCE

COBE is equipped with three independent Earth horizon scanners (manufactured by Barnes Engineering, Inc.) to provide pitch control signals to orient the spacecraft with respect to the nadir (Earth-pointing) vector.

Each scanner consists of a small infrared telescope whose 2.5-deg diameter field-of-view (FOV) rotates at 240 $\pm$ 24 rpm by means of a spinning mirror. The rotating FOV defines a scan plane whose normal is a control axis (Reference 2).

During each revolution of the scanner FOV, the detector line of sight will nominally intersect the Earth. As it does, each sensor produces five signal pulses:

1. One pulse at the space-Earth transition (referred to as the AOS);
2. Three pulses as the scanner line of sight is aligned with respect to the spacecraft +X-axis at rotation angles of -90, 0, and +90 degrees (referred to as index pulses);
3. One pulse at the Earth-space transition (referred to as the loss-of-signal (LOS)).

It is assumed that an Earth pulse occurs midway between the AOS and LOS pulses. This Earth pulse, referred to as the "split," is the projection of the nadir vector onto the scan plane. During the primary spacecraft control mode (mission mode), the index pulse produced at 0 deg is used. These pulses start and stop clock counters that give a count proportional to the SI angle that is finally telemetered (Reference 1).

Each scanner also produces the time of occurrence (referred to as the telemetered AOS timing correction) of the AOS crossing pulse with respect to the minor frame synchronization (MFS) pulse by counting the number of changes in state of the spacecraft clock. The nominal minor frame period is 0.25 sec.

In the event that the scanner FOV is not spinning at 240 rpm, it is possible for the SI data to be referenced to a previous minor frame. Each scanner, therefore, telemeters a minor frame offset (MFO) as follows:

MFO equals zero for the current minor frame, one for one minor frame previous, two for two minor frames previous, or three for three minor frames previous.

(Under nominal scanner conditions and FOV rates, the MFO should oscillate between 0 and 1.)

Due to the 0.83 rpm spin rate of the spacecraft, total AOS timing corrections (consisting of the telemetered AOS timing correction and the MFO output) must be applied to SI measurements. At polar crossings during summer solstice, the measured SI angles (under nominal conditions) will oscillate approximately between ± 36 degrees over the 72 sec spin cycle. The rate of change of the SI angle will be (36 deg) * (2π)/(72 sec) = 3.2 deg/sec. If the total AOS correction is ignored and the SI calculation corresponds to one minor frame previous (MFO 21), the error in the SI measurement will approach 3.2 deg/sec * (1) * 0.25 sec = 0.8 deg (outside of 0.1 deg from scanner specifications).

A hypothetical plot of scanner output signal versus time is illustrated in Figure 1a (shown for a scanner FOV rate less than 240 rpm). Four pieces of information are of interest: the time of the minor frame synchronization pulse, the time of AOS crossing pulse, the time of the SI calculation from the scanner electronics, and time of the serial input/output (I/O) request for Earth scanner data. (The amount of time between the LOS crossing pulse and the SI calculation time is assumed to be small and is neglected in this analysis.) These four pieces are labeled in Figure 1a as M, A, C, and R, respectively.

An explanation of Figure 1a follows:

1. At COBE's altitude of 900 km, the full angular width of the Earth is approximately 120 deg. Thus, the time between the AOS and LOS pulses should be approximately 1/3 of a scanner FOV period, or (0.25 sec)*(1/3) = 0.0833 sec (assuming a near-nominal FOV rate).
2. The nominal transmission bit rate of 4.096 kbps requires the time between MFS pulses to be 0.25 sec.
3. The serial I/O request for Earth scanner telemetry occurs approximately midway between MFS pulses.
4. In this example, the scanner FOV rate is 216 rpm.

Figure 1b depicts the corresponding AOS and MFO output for this example.

In order for the MFO to equal 0, the AOS pulse and the updated SI angle must occur *between* the MFS pulse and its respective serial I/O request time (e.g., minor frames 1 and 2 in Figure 1a).

If the scanner FOV is spinning slower than 240 rpm, the serial I/O request time for Earth scanner telemetry will be out of phase with the SI calculation time. The request time will eventually occur before the new SI angle is calculated. When this happens, the SI angle and AOS timing correction of the previous minor frame should be telemetered and the MFO set equal to 1 (e.g., minor frame 3 in Figure 1b).

Earth scanner data corresponding to one minor frame previous will continue to be telemetered until the AOS and SI calculation times occur within the current MFS and data request times, at which time, the MFO returns to 0 (e.g., minor frame 11 in Figure 1b).

Assuming the scanner FOV rate remains relatively constant and less than 240 rpm, this output will repeat itself with a period proportional to the scanner rate. It can be shown that the scanner FOV rate can be approximated by the following equation:

$$\Omega_{FOV} = [240 - (60/T)], \qquad (1)$$

where Ω_{FOV} is the scanner FOV rate in rpm and
T is the number of seconds between successive 0-to-1 MFO transitions.

(NOTE: If the telemetered AOS timing corrections decrease, the scanner FOV rate is greater than 240 rpm. In this case, Equation 1 becomes $\Omega_{FOV} = [240 + (60/T)]$.

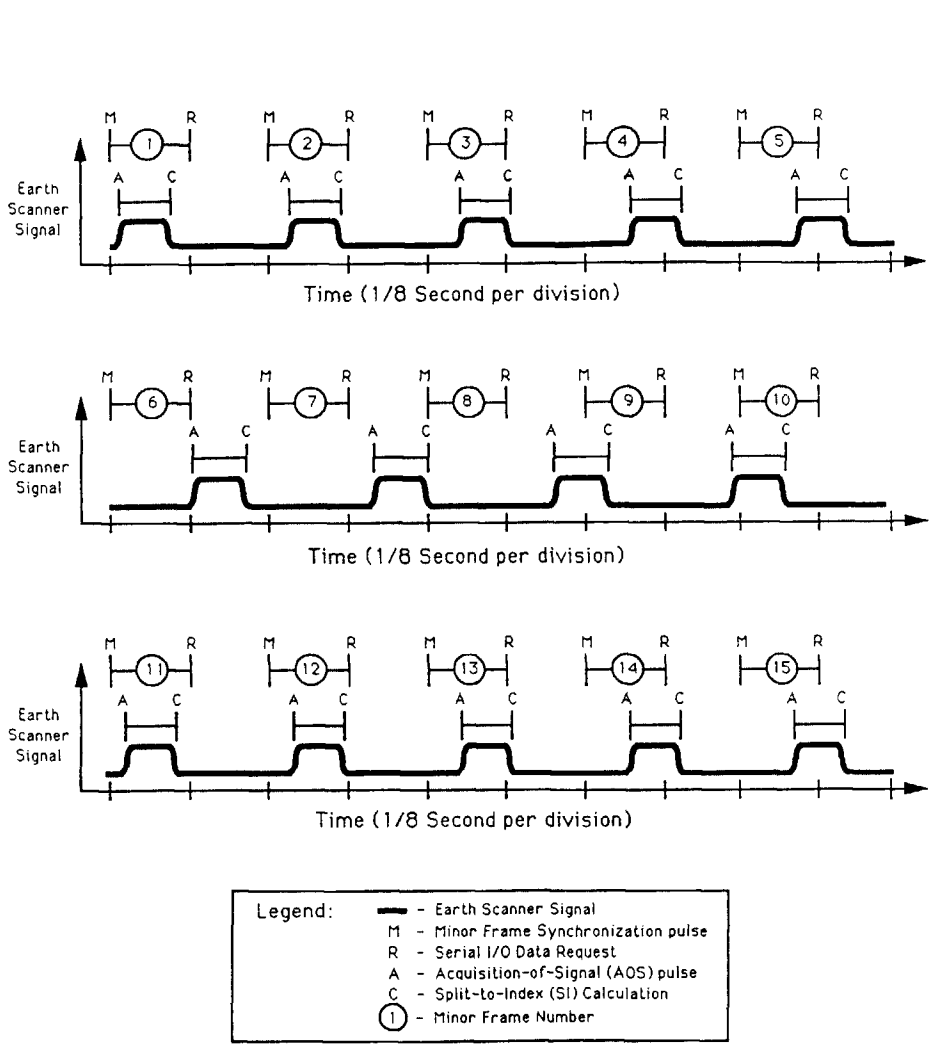

Figure 1a. Typical Phasing of Earth Scanner Output Signal for FOV Rate Less Than 240 rpm

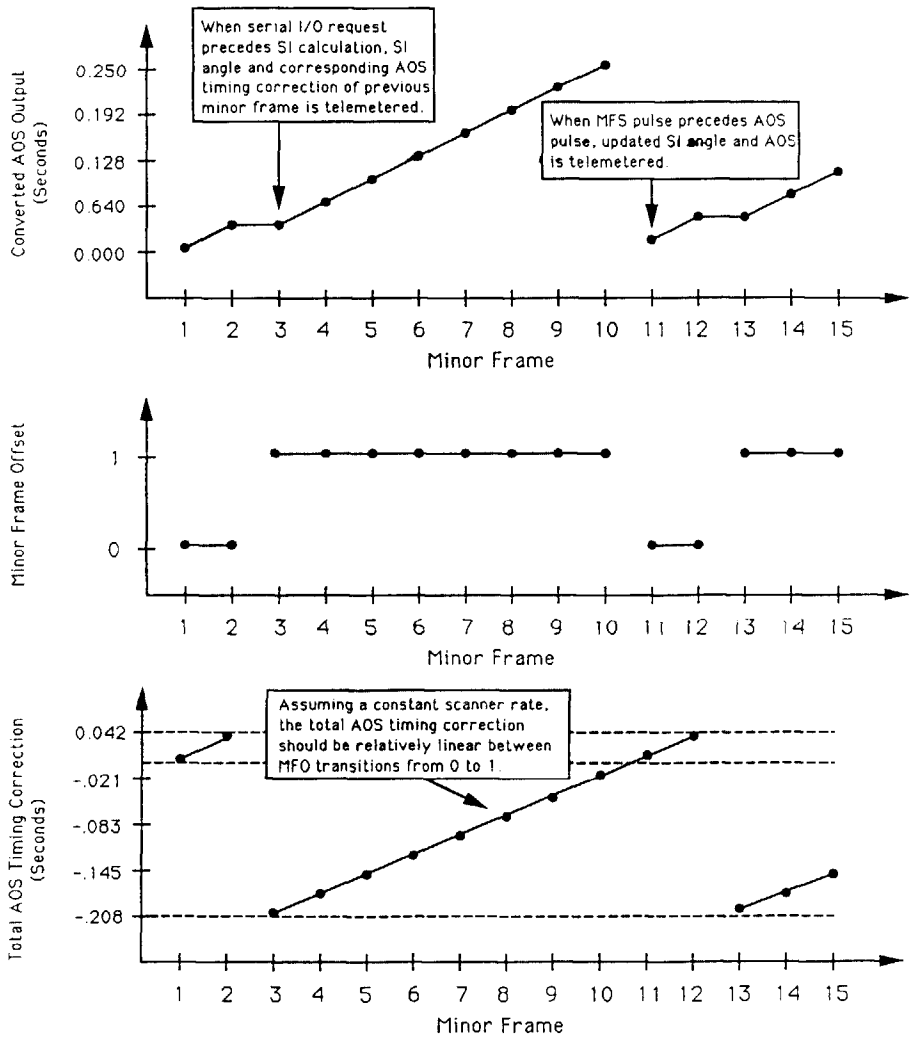

Figure 1b. Corresponding AOS and MFO Output for FOV Rate Less Than 240 rpm

Ground Processing

Once the telemetry is received, the COBE Attitude Determination System (ADS) converts the SI to angles and AOS timing corrections to seconds. The SI angle is then time-tagged to the time of the AOS pulse by the equation:

$$t_{SI} = [t_{S/C} - 64 * 8/BR] + [\delta t_{AOS} - N * (128 * 8/BR)] \quad (2)$$

where t_{SI} is the adjusted time tag of the SI angle ;

$t_{S/C}$ is the spacecraft clock time (64 * 8 is the bit offset of the spacecraft clock from the MFS pulse);

δt_{AOS} is the telemetered AOS timing correction (sec);

N is the MFO corresponding to the SI angle and AOS timing correction (128 × 8 bits = 1 minor frame); and

BR is the transmission bit rate, 4.096 kbps.

The number in the first set of brackets is equivalent to the time of the current MFS pulse. In this report, the number in the second set is referred to as the "total AOS timing correction."

3. OBSERVED EARTH SCANNER PERFORMANCE

Before Earth Scanner Reconfigurations

Figure 2 shows MFO output and the corresponding total AOS timing corrections for Earth scanner A at the beginning of the mission. (Scanners B and C show similar output.) While scanner SI angles were correct, both the AOS timing correction and the minor frame offset telemetry were inexplicable. A characteristic 11-second rollover in the AOS timing correction (Figure 2) was observed for each scanner. This decreasing AOS correction is consistent with a FOV rate of approximately 245 rpm (greater than 240 rpm).

Given this scanner rate, the corresponding MFO should oscillate between 0 and 1 with the same 11-sec period. No such oscillation is observed. Also, at AOS rollover points, slight discontinuities in the SI angles should exist as the SI angle is updated within a given minor frame. No discontinuities in SI angles with an 11-sec period were observed.

It was therefore determined that both the AOS timing correction and minor frame offset output were incorrect. Practice became to set the total AOS timing correction to zero, thus time-tagging the SI angles to the MFS pulse (see Equation 2).

Discontinuities in SI angles were, however, observed for each scanner approximately every 5 to 10 minutes, corresponding to scanner FOV rates of approximately 239.8 to 239.9 rpm. It was postulated that total AOS timing corrections could be simulated by first locating these discontinuities in SI telemetry. Then, if various scanner attributes were assumed (see Section 2), AOS corrections could be linearly interpolated between SI discontinuities. Unfortunately, noise in SI telemetry at nodal crossings along with Sun and Moon interference made locating the SI discontinuities difficult and unreliable.

After Earth Scanner Reconfigurations

Over the course of the mission, each Earth scanner was observed to independently and unexpectedly "reset" itself. Upon its initial reactivation, each scanner would change into and remain in a new configuration. The MFO output was no longer constant at 0 but was observed to oscillate between 0 and 3 with the 11-sec AOS rollover period. The telemetered AOS timing correction, δt_{AOS}, remained unchanged in the new configuration. Figure 3 shows the new MFO output pattern and the corresponding total AOS timing correction. Even in this new configuration, the total AOS timing correction is still incorrect.

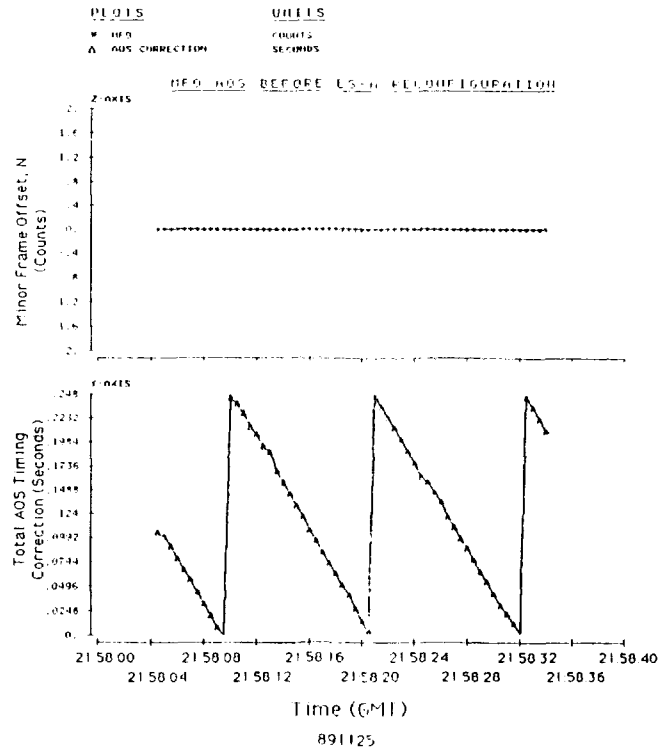

Figure 2. MFO/AOS Output Before Earth Scanner Reconfiguration (Shown for Scanner A)

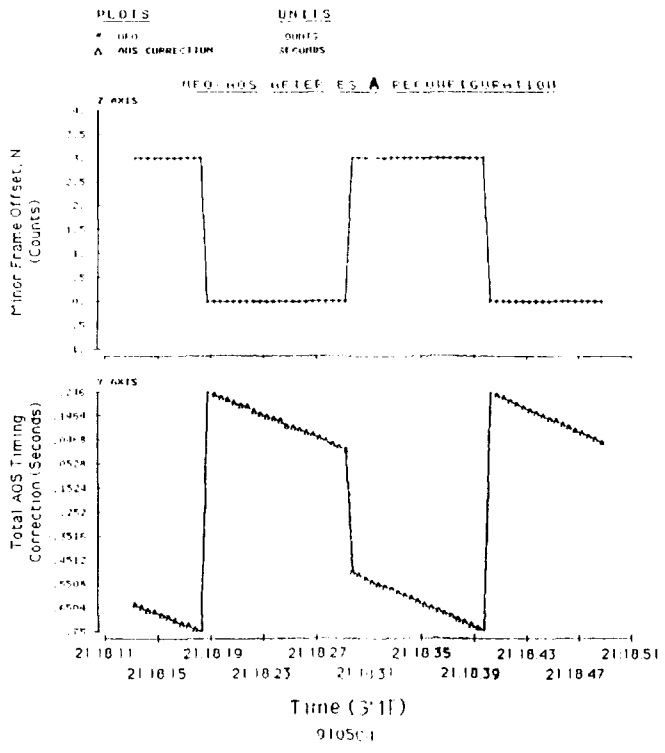

Figure 3. MFO/AOS Output After Earth Scanner Reconfiguration (Shown for Scanner A)

Fortunately, changes in this characteristic MFO output were simultaneous with discontinuities in SI angle (see Figure 4). It was therefore assumed that a "true" MFO transition occurred when the MFO pattern was broken. Since the MFO output was independent of SI noise and Sun/Moon interference, these characteristic breaks were used to reliably signal SI discontinuities due to MFO transitions. Total AOS timing corrections for each Earth scanner could then be interpolated and subsequently applied to SI angle time-tags. The reconfiguration times for each Earth scanner are recorded in Table 1.

4. PROCEDURE FOR ADJUSTING AOS TIMING CORRECTIONS

For a selected time span, minor frame offsets were compared with the AOS rollover periods for each individual Earth scanner. Each break in the MFO characteristic pattern previously described was assumed to be a "true" MFO transition from 0 to 1 or from 1 to 0.

To determine which transition had actually occurred, the number of seconds between successive "true" MFO transitions was calculated. Table 2 contains an example of MFO transition times for Earth Scanner A.

Two classifications of transitions were discovered:

1. "Type I" transitions: separated by 300 sec or more and
2. "Type II" transitions: separated by 100 sec or less.

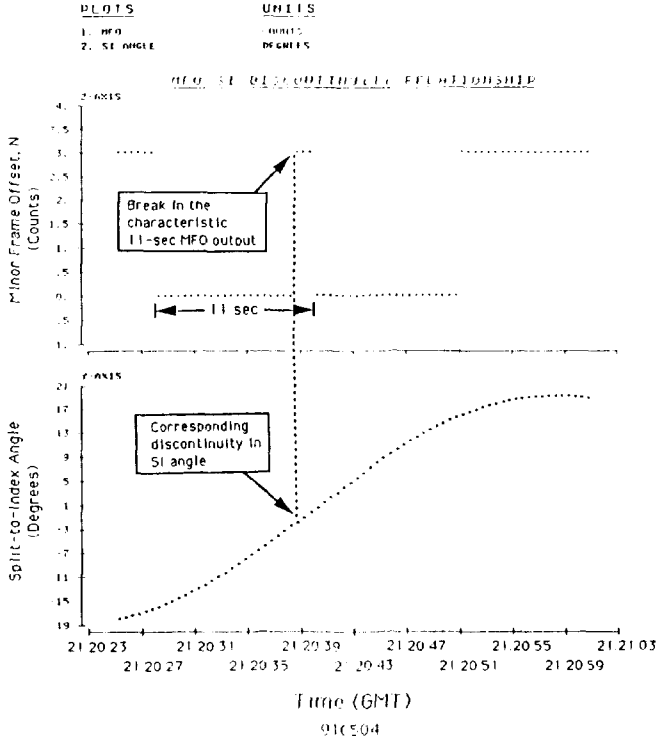

Figure 4. MFO/SI Discontinuity Relationship After Earth Scanner Reconfiguration (Shown for Scanner A)

Table 1. Reconfiguration Times of COBE Earth Scanners

Earth Scanner	Reconfiguration Time (GMT)
A	900814.130047
B	910926.173059
C	910101.181415

Table 2. MFO Transition Times for Earth Scanner A

Minor Frame Time (GMT)	Difference (sec)	Transition Type	Total AOS Correction (sec)
910504.203406267	—	—	—
910504.204050767	404.5	I	−0.208
910504.204051767	1.0	II (1)	−0.208
910504.204052267	0.5	II (2)	+0.042
910504.204055767	3.5	II (3)	−0.208
910504.204131267	35.5	II (4)	+0.042
910504.204936267	485.0	I	−0.208
910504.205007767	31.5	II (1)	−0.208
910504.205008267	0.5	II (2)	+0.042
910504.205008767	0.5	II (3)	−0.208
910504.205009267	0.5	II (4)	+0.042
910504.205010267	1.0	II (5)	−0.208
910504.205010767	0.5	II (6)	+0.042
910504.205737267	446.5	I	−0.208
910504.210458267	441.0	I	−0.208
910504.211324767	506.5	I	−0.208

The Type I transitions could be explained by the following hypothesis:

If the scanner FOV rate was slightly less than the nominal 240 rpm, then the serial I/O request would be out of phase with the SI angle calculation (see Section 2). The request time would eventually occur before the new SI angle was calculated, causing the previous minor frame SI angle to be telemetered. The "true" MFO transition would, therefore, be from 0 to 1. Furthermore, if scanner FOV rate is assumed relatively constant, this process would repeat itself periodically. Using Equation 1, for $T \geq 300$ sec, the approximate scanner FOV rates range between 239.8 and 240 rpm.

At the initial Type I MFO transition, the request time is assumed to occur just before the new SI is calculated. The AOS timing correction is then approximately equal to the time difference between the MFS pulse to data request and the AOS pulse to calculation (see Figure 5), or +0.042 sec. Since the MFO is assumed to equal 1, the total AOS timing correction, measured from the current MFS pulse (see Equation 2), is +0.042 - (1)*0.250 = -0.208 sec at the initial transition.

Prior to the next Type I transition, the data request time is assumed to occur just after the new SI is calculated (i.e., N equals 0 in Equation 2). The total AOS timing correction is then equal to +0.042 - (0)*0.250 = +0.042 sec. Assuming a constant scanner rate, the total AOS timing corrections for the intervening SI angles are then linearly interpolated between these two corrections according to the equation:

$$AOS_T = \left\{[(t_{MF} - t_1)/(t_2 - t_1)] * 0.250\right\} + (-0.208), \quad (3)$$

where t_{MF} is the minor frame time; $t_1 \leq t_{MF} < t_2$;
t_1 is the time of the first Type I MFO transition;
t_2 is the time of the second Type I MFO transition; and
AOS_T is the total AOS timing correction (sec).

Type II transitions could be explained in a similar manner. The serial I/O request occurs at a fixed period of 0.250 sec. However, the period at which the SI calculation is determined is not fixed. It is dependent upon both the AOS and LOS pulses which, in turn, vary according to spacecraft attitude, orbit location, time of year, etc. It is plausible, therefore, to assume that these transitions, which are separated by less than 100 sec, result from the movement of the calculation time with respect to the serial I/O request.

When the calculation time occurs after the request time, the "true" MFO transition would be from 0 to 1 (see Figure 6), corresponding to a total AOS timing correction of

$$AOS_T = -0.208 \text{ sec}$$

When the calculation time occurs just before the request time, the MFO transition would be from 1 to 0, corresponding to a total AOS timing correction of

$$AOS_T = +0.042 \text{ sec}$$

All intervening AOS corrections are assumed constant between these Type II MFO transitions.

Assuming the scanner FOV rate is less than 240 rpm, there should always exist either zero or an even number of Type II MFO transitions between Type I transitions (see Table 2). Even though the data request and calculation times may toggle back and forth several times, the data request time eventually will remain before the calculation time. Examination of SI angle discontinuities supports both explanations of Type I and Type II MFO transitions.

In summary, the total AOS timing corrections are determined in the following manner:

1. If the SI angle occurs at or within a set of Type I MFO transitions, the total AOS timing correction is linearly interpolated according to Equation 3;

2a. If the SI angle occurs at or within an odd-numbered set of Type II MFO transitions, the total AOS timing correction is -0.208 sec;

2b. If the SI angle occurs at or within an even-numbered set of Type II MFO transitions, the total AOS timing correction is +0.042 sec.

5. RESULTS

Figures 7a and 7b show coarse attitude determination subsystem (CADS) solutions over a typical 30-minute span, using the AOS timing corrections directly from telemetry. Discontinuities (as large as 2.5 deg in pitch and 1 deg in roll) are observed with an 11-sec periodicity (at all AOS rollover locations).

(NOTE: For all the attitude solutions contained in this report:

1. Corrections for Earth oblateness and spacecraft spin have been applied to the SI angles.
2. For the selected timespan, Earth scanner B had not yet been reactivated into the new configuration by which AOS corrections could be made. Therefore, only data from Earth scanners A and C are used.
3. In the fine attitude solutions, the X-gyro scale factor has been corrected for a known temperature dependence.)

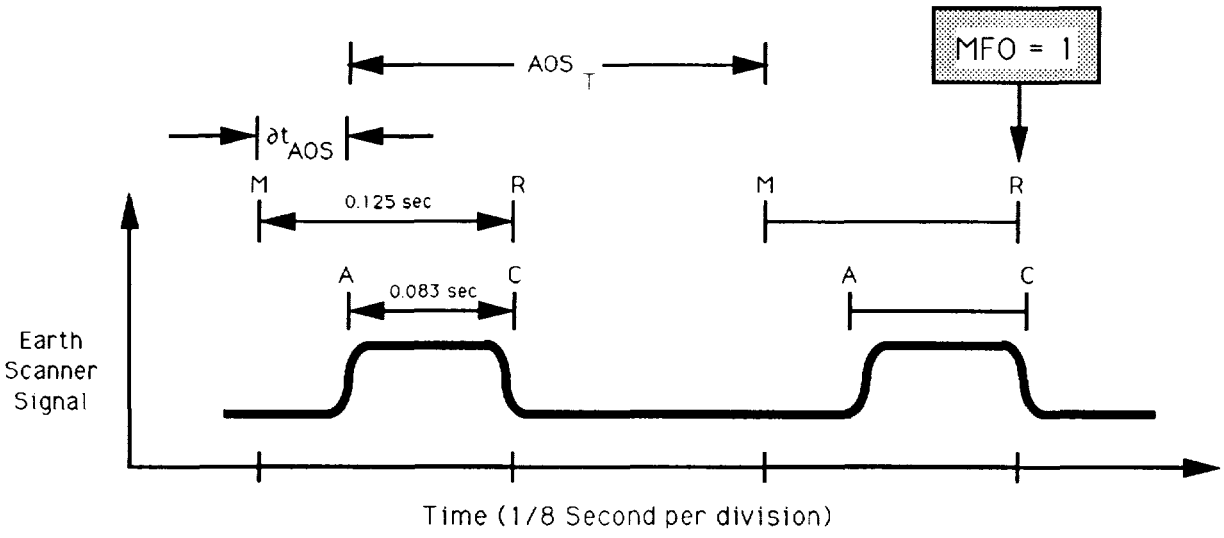

When the serial I/O data request precedes the SI calculation, the SI angle from the previous minor frame is telemetered. The corresponding total AOS timing correction, measured from the current MFS pulse, is:

$$AOS_T = \partial t_{AOS} - (1)*0.25 \text{ sec} = +0.042 \text{ sec} - 0.250 \text{ sec} = -0.208 \text{ sec}$$

Figure 5. Explanation of Type I MFO Transitions

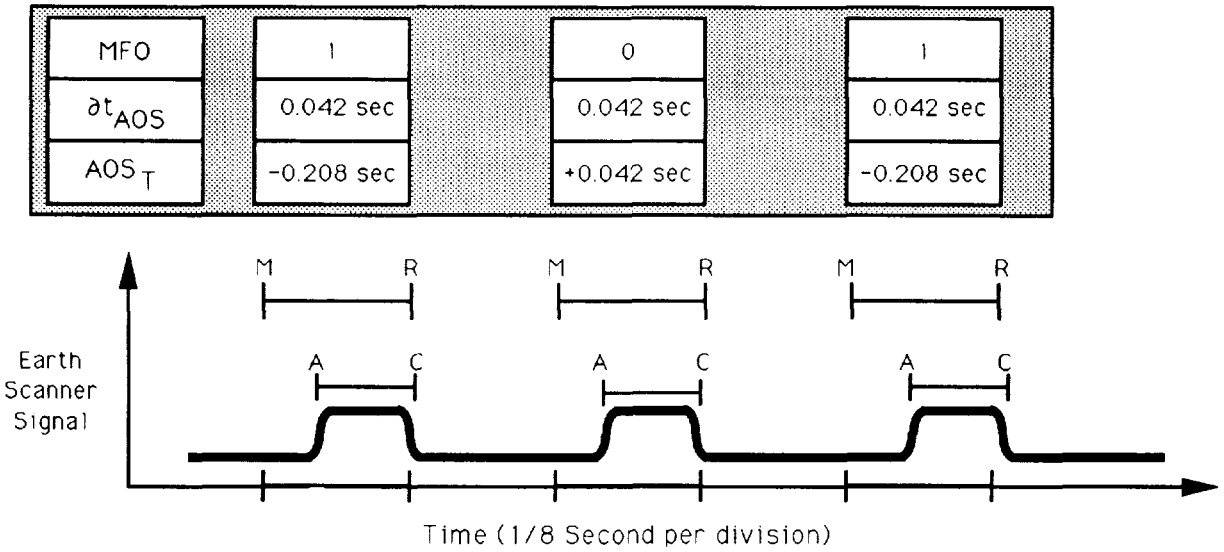

Since the AOS and LOS signals are dependent upon several factors (i.e., spacecraft attitude, orbit location, etc.), the exact SI calculation time will vary. It is possible for the calculation time to toggle before and after the serial I/O request time, causing multiple Type II MFO transitions to occur. If the scanner FOV is less than 240 rpm, there will always exist an even number of such transitions.

Figure 6. Explanation of Type II MFO Transitions

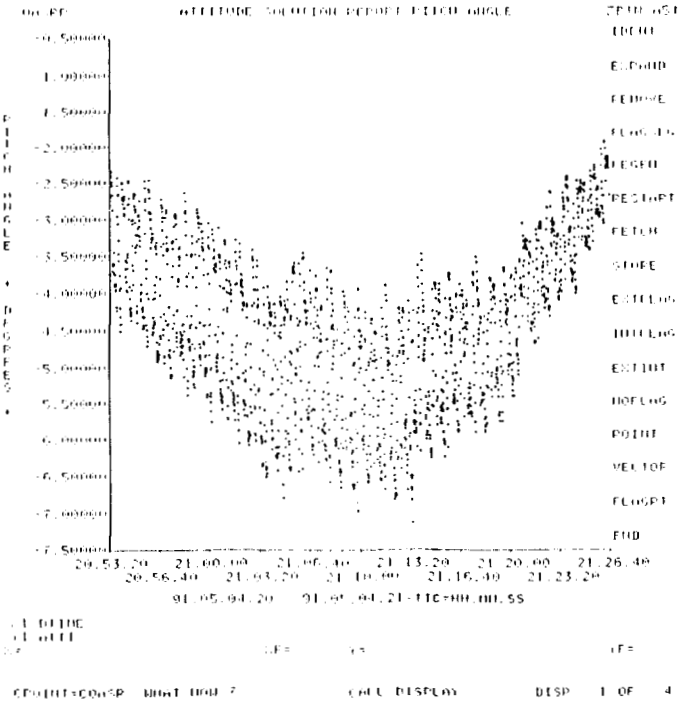

Figure 7a. Coarse Attitude Using Unadjusted AOS Timing Corrections (Pitch Angle)

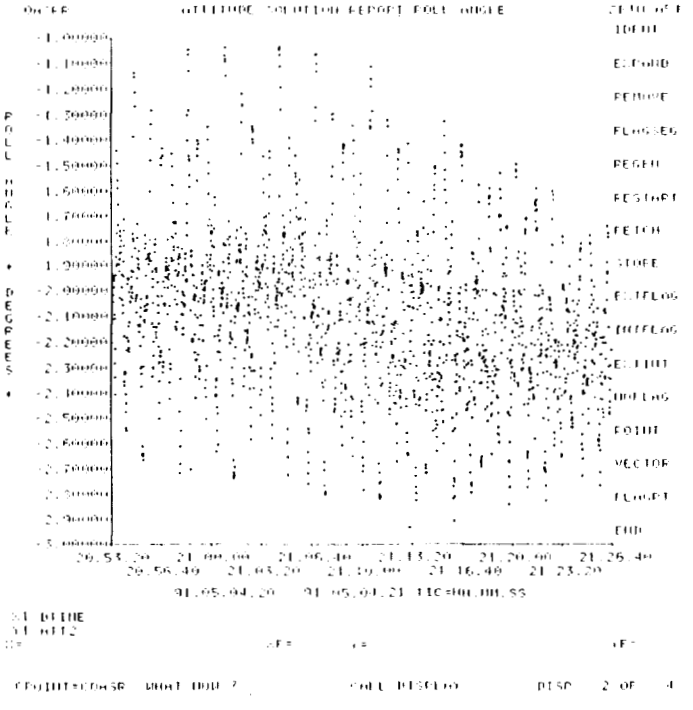

Figure 7b. Coarse Attitude Using Unadjusted AOS Timing Corrections (Roll Angle)

Figures 8a and 8b depict corresponding CADS solutions when the AOS corrections are ignored altogether (time-tagging SI angle to the MFS pulse). Discontinuities (0.80 deg in pitch, 0.30 deg in roll) are observed with a 5- to 10-minute periodicity resulting from "true" MFO transitions.

Figures 9a and 9b show CADS solutions using the AOS timing correction method presented in this paper. All attitude discontinuities are removed.

To measure the solution accuracies, two gyro-propagated fine attitude determination system (FADS) solutions were determined. One solution was computed ignoring the total AOS corrections (time-tagging SI observations to the MFS pulse), and the other applied the AOS correction procedure described above.

Graphs of SI residuals, equal to the observed SI angles minus the predicted SI angles from the gyro-propagated solution, were created for Earth scanner A without AOS corrections (Figure 10) and with AOS corrections (Figure 11). Similar results were found for Earth scanner C. By applying the corrections, the maximum SI residual was observed to decrease from ± 0.45 deg to ± 0.10 deg for each scanner (meeting sensor specifications). Also, the overall standard deviation of SI residuals decreased by a factor of 4, from 0.126 deg (without AOS corrections) to 0.032 deg (with AOS corrections).

The gyro-propagated fine attitude solutions were then compared with their respective coarse attitude solutions for each case. Corresponding pitch residuals (equal to the fine pitch angle minus the coarse pitch angle) are found in Figure 12 (when AOS corrections are ignored) and Figure 13 (using AOS corrections). By applying the AOS corrections, the maximum pitch residual was observed to decrease from ± 0.50 deg to ± 0.15 deg. Similarly, the overall standard deviation of the pitch residuals decreased by a factor of 3, from 0.159 deg (without AOS corrections) to 0.062 deg (with AOS corrections). In addition, the root mean square of the deviation angle decreased from 0.262 deg to 0.199 deg when the AOS corrections were applied.

These results indicate an increase in both fine attitude and coarse attitude accuracy when the AOS correction method is applied.

6. SOURCE OF ERRORS

The following is a list of assumptions and possible sources of error:

1. Earth scanner FOV rates are assumed to be less than 240 rpm. All examinations of SI data for each reconfigured scanner were consistent with this assumption.
2. Earth scanner FOV rates are assumed constant between both types of MFO transitions. Examination of the envelope of SI residuals using the AOS correction method (Figure 11) is not constant throughout the time span and may indicate a varying FOV rate. Application of a different interpolation method, such as a natural cubic spline, may minimize this source of error.
3. The time between AOS to LOS pulses (i.e., Earth width) is assumed constant. This measured width changes most rapidly at polar crossings, sinusoidally oscillating with spacecraft yaw angle. The width is also dependent upon the commanded spacecraft attitude and Sun declination. Unfortunately, the time span analyzed in this report is centered about the spacecraft's northern-most passage. The oscillatory behavior of the SI residuals in Figure 11 may be caused by the assumption of a constant Earth width. Further analysis is needed.
4. No correction for Earth horizon radiance is made. With the increase in accuracy of the attitude solutions, its detection and determination may now be possible.
5. A drawback to this method is its susceptibility to data dropout. If a "true" MFO transition is omitted due to data dropout, AOS timing corrections may be interpolated between improper times. It is possible, however, to predict the MFO output (using its characteristic 11-sec periodicity). By comparing the predicted and actual MFO, it can be determined if a "true" MFO transition occurred during the dropout period.

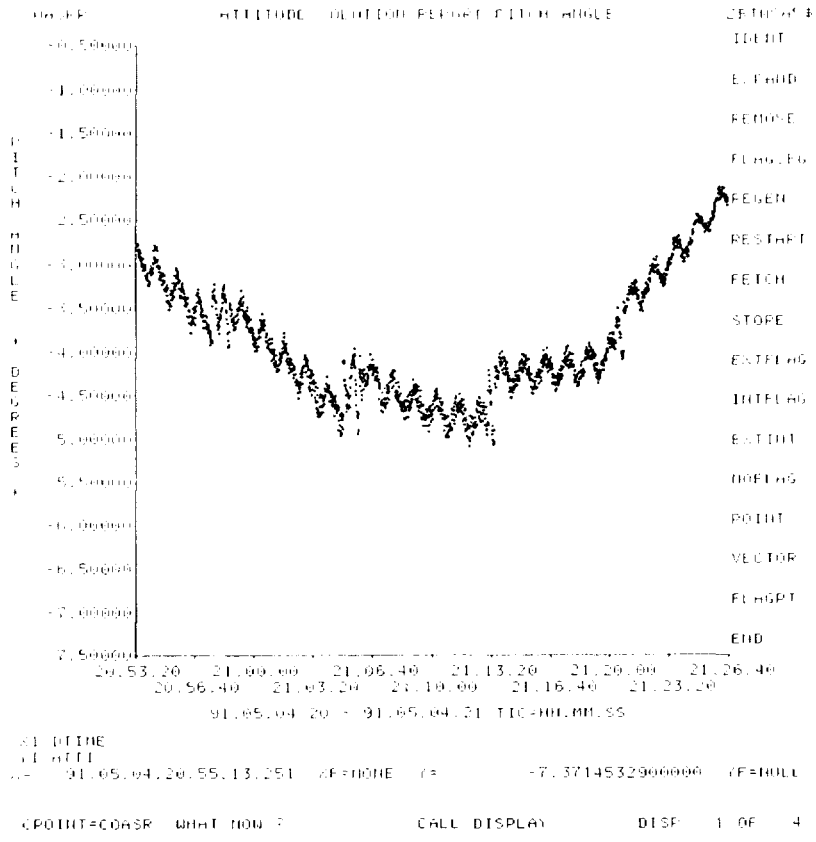

Figure 8a. Coarse Attitude Ignoring AOS Timing Corrections (Pitch Angle)

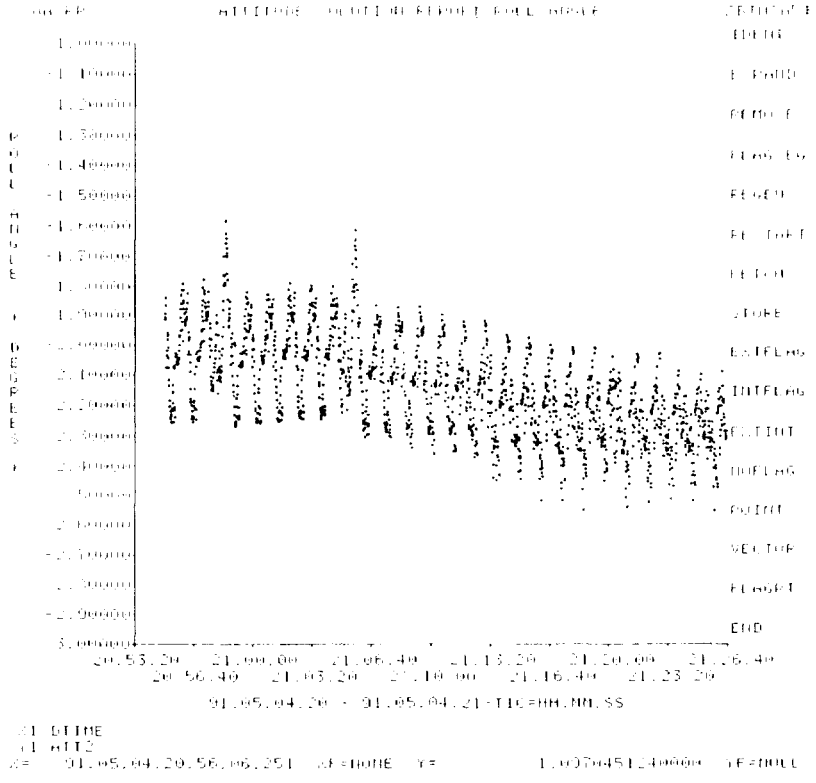

Figure 8b. Coarse Attitude Ignoring AOS Timing Corrections (Roll Angle)

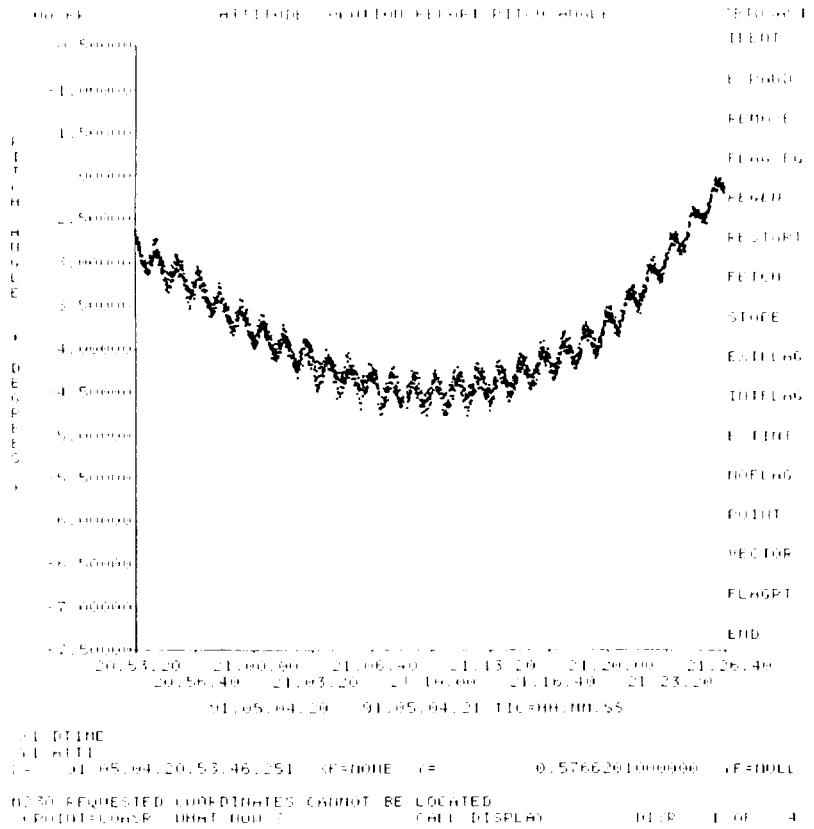

Figure 9a. Coarse Attitude Using Adjusted AOS Timing Corrections (Pitch Angle)

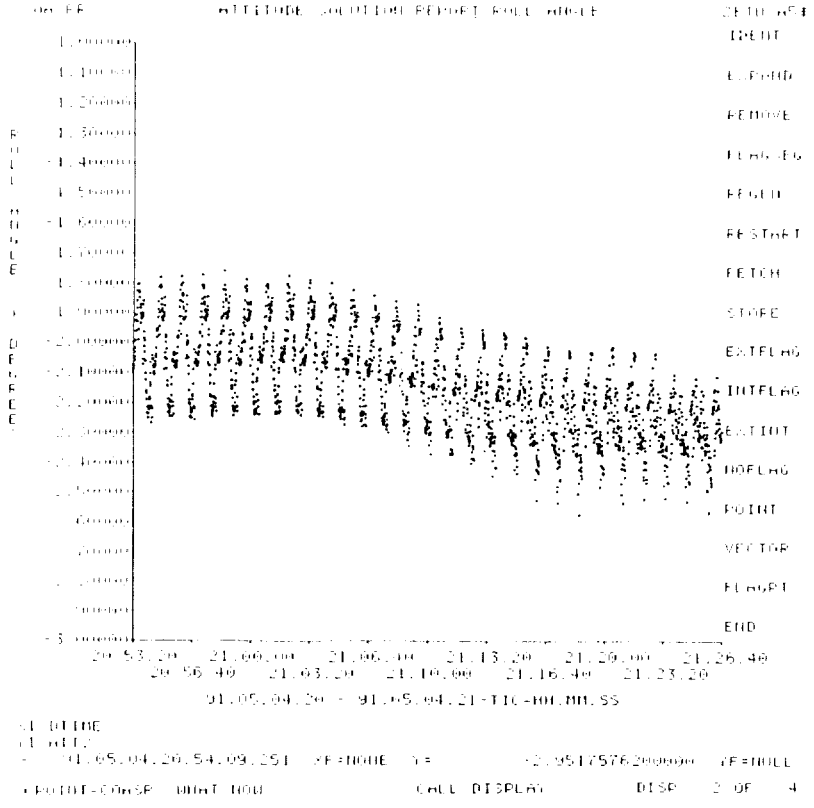

Figure 9b. Coarse Attitude Using Adjusted AOS Timing Corrections (Roll Angle)

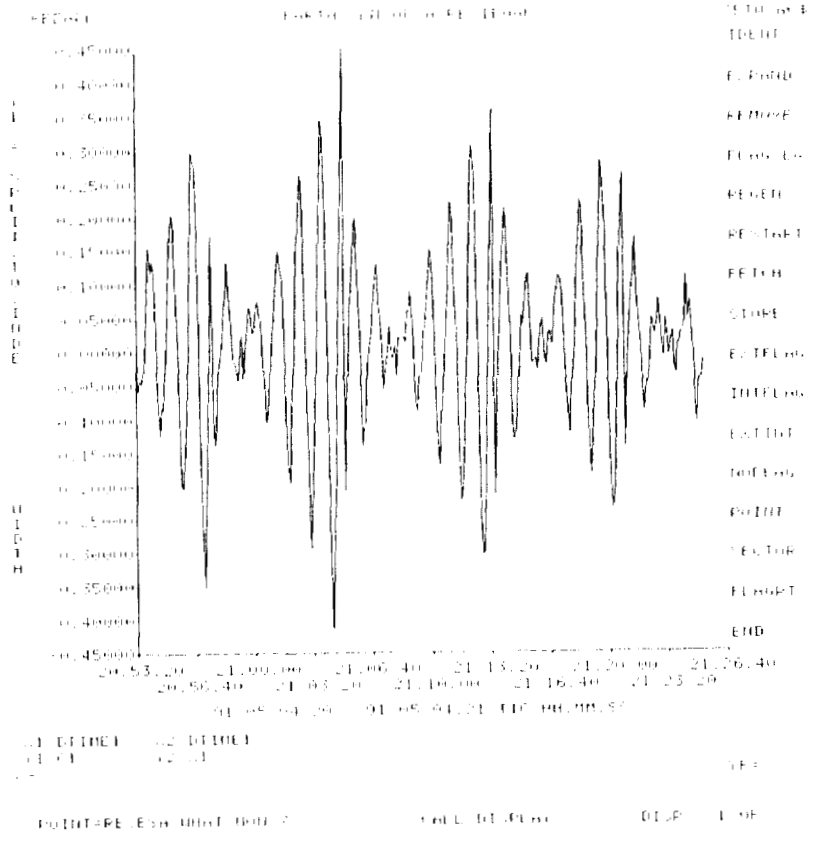

Figure 10. Earth Scanner A SI Residuals (Ignoring AOS Timing Corrections)

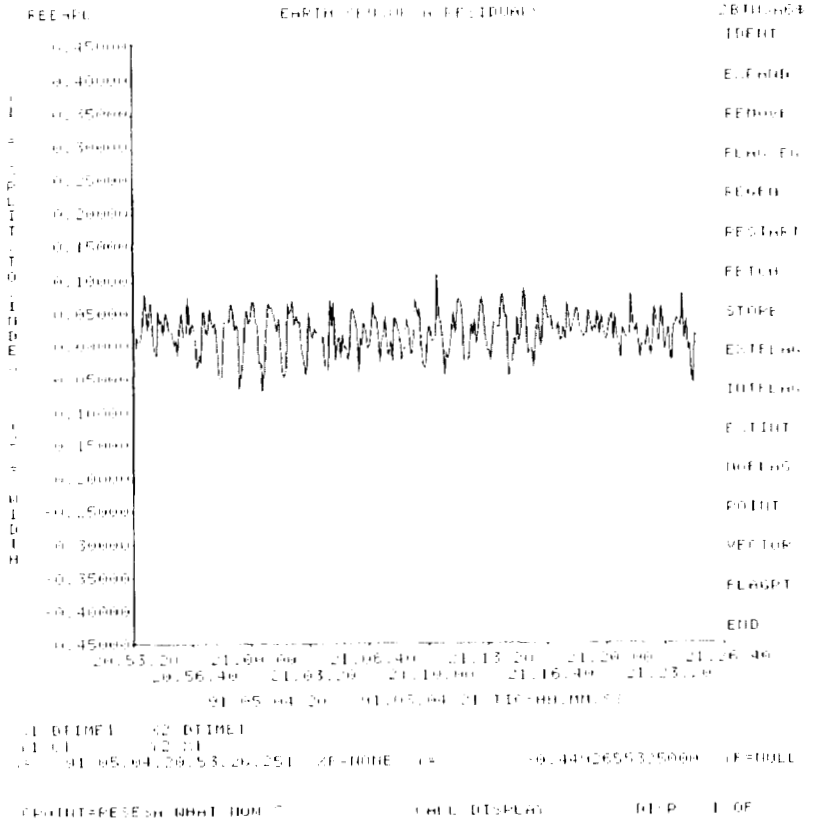

Figure 11. Earth Scanner A SI Residuals (Applying AOS Timing Corrections)

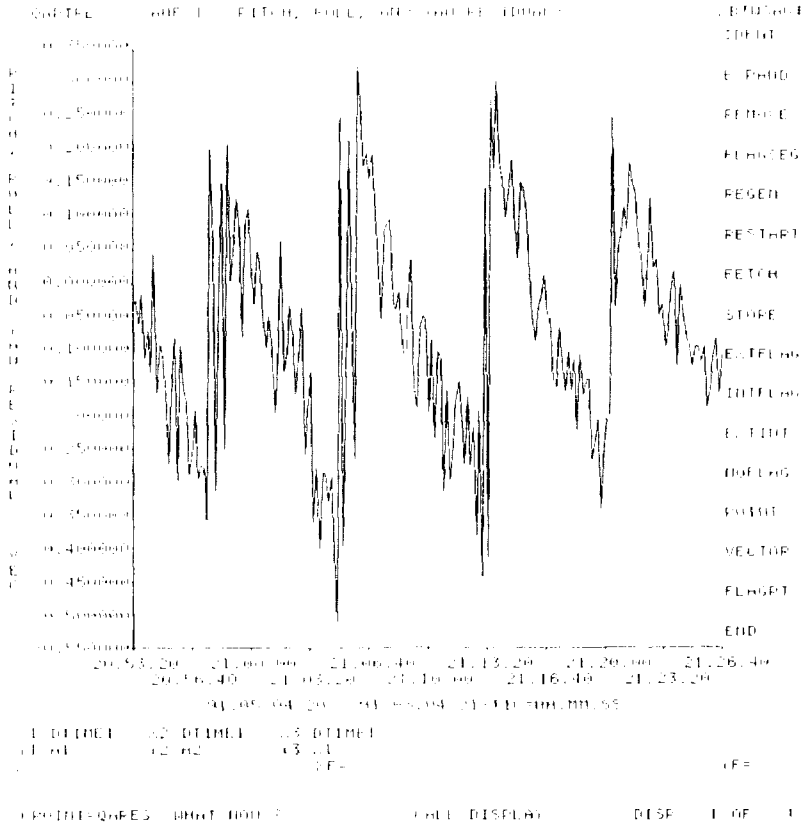

Figure 12. Gyro-Propagated Fine Pitch Angle Minus Coarse Attitude Pitch Angle (Ignoring AOS Timing Corrections)

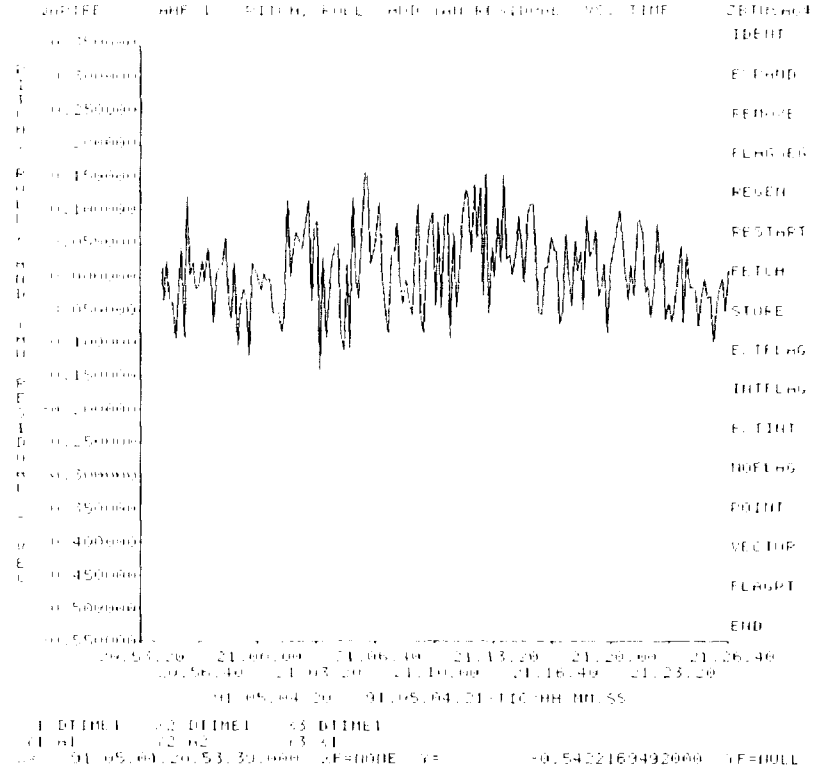

Figure 13. Gyro-Propagated Fine Pitch Angle Minus Coarse Attitude Pitch Angle (Applying AOS Timing Corrections)

7. CONCLUSION

Using the new scanner configuration, "true" MFO transitions can be located and total AOS timing corrections can be interpolated accurately and reliably. When the AOS timing corrections are applied, Earth scanner accuracy is observed to be within ± 0.10 deg (meeting sensor specifications), yielding more accurate coarse attitude and fine attitude solutions.

Furthermore, with the continued degradation of COBE's gyroscopes, gyro-propagated fine attitude solutions may soon become unavailable, requiring an alternative method for attitude determination. By correcting Earth scanner AOS telemetry, as described in this paper, more accurate single-frame attitude solutions are obtained and all pitch and roll discontinuities are removed. When proper AOS corrections are applied, the standard deviation of pitch residuals between coarse attitude and gyro-propagated fine attitude solutions decreases by a factor of 3. Also, the overall standard deviation of SI residuals from fine attitude solutions decreases by a factor of 4 (meeting sensor specifications) when AOS corrections are applied.

This method of adjusting the AOS timing correction was formulated solely from observations in telemetry and assuming scanner attributes. It is hoped that an inspection of the actual electronics diagram may assist in the development of a more sophisticated and accurate AOS adjustment procedure for each Earth scanner, especially before the scanner reconfiguration times listed in Table 1.

REFERENCES

1. National Aeronautics and Space Administration (NASA)/Goddard Space Flight Center (GSFC), COBE-SP-712-1102-04, *Component Specification for the COBE Earth Scanner*, P. A. Newman, May 1984

2. Computer Sciences Corporation, CSC/TM-89/6007, *Cosmic Background Explorer (COBE) Compendium of Flight Dynamics Analysis Reports*, Mission Report 89008, "COBE Attitude Control System (ACS)," J. Sedlak, October 1989

FLIGHT MECHANICS/ESTIMATION THEORY SYMPOSIUM

MAY 5-7, 1992

SESSION 2

TDRSS Orbit Determination Using Short Baseline Differenced Carrier Phase

S.Nandi, C.D.Edwards, and S.C.Wu
Jet Propulsion Laboratory, California Institute of Technology
Pasadena, California 91109

Abstract

This paper discusses a covariance study on the feasibility of using station-differenced carrier phase on short baselines to track the TDRSS satellites. Orbit accuracies for the TDRSS using station-differenced carrier phase data and range data collected from White Sands, NM are given for various configuarations of ground stations and range data precision. A one-sigma position position accuracy of 25 meters can be acheived using two orthogonal baselines of 100 km for the station-differenced phase data and range data with 1 m accuracy. Relevant configuration parameters for the tracking system and important sources of error are examined. The ability of these data to redetemine the position after a station keeping maneuver is addressed. The BRTS system, which is currently used for TDRSS orbit determination, is briefly described and its errors are given for comparison.

I. Introduction

The Tracking and Data Relay Satellite System (TDRSS) is a network of geosynchronous satellites used to communicate with low earth orbiters. Each satellite has two single access (SA) high gain antennae which operate at 2 GHz (S-band) and 14 GHz (Ku-band) and one multiple access (MA) array at 2 GHz that receive signals from users. Telemetry received from a user satellite is sent from a Tracking and Data Relay satellite (TDRS) to White Sands, NM on a dedicated link at 14 GHz. A user satellite may obtain 2-way range and doppler data from a TDRS in order to determine the user's position. The two TDRSS satellites currently in use are 67° of longitude west and east of White Sands. The TDRSS positions are required to be known to 50 m at one-sigma and their position must be redetermined to this accuracy within 2 hours of a station-keeping maneuver.[1] Currently, position determination for the TDRSS is done using range and doppler data at 2 GHz collected using the Bi-lateral ranging transponder system (BRTS) described below. In addition, rough position determination is done using angle and range radio metric data from three ground antennae at the White Sands complex also described below. The tracking technique presented in this paper is part of a study of alternative tracking strategies for supporting orbit determination of the Advanced Tracking and Data Relay Satellites (ATDRS). Other approaches, involving GPS tracking techniques, are also being explored.[2]

In this paper, the possibility of using station-differenced carrier phase data on short baselines to perform TDRSS orbit solutions is explored. Biased carrier phase data could be obtained passively by each of a few antennae near White Sands by tracking the 14 GHz carrier on which telemetry is sent from a TDRSS satellite to White Sands. The differenced phase between a pair of stations measures the plane-of-sky position of a transmitter in the direction of the baseline formed by the stations. The precision of the measurment is given by $\Delta\theta = \Delta\phi/B\sin\theta$, where B is the baseline length, $\Delta\phi$ is the precision of the differenced phase measurement and θ is the angle between the baseline and the transmitter. The differenced phase observable has a remaining bias due to the difference in instrumental signal path through the two stations; as a result, only the change in plane-of-sky position over a data arc is effectively measured. This technique differs from Connected Element Interferometry (CEI)[3] in which the phase bias between the stations and the integer cycle ambiguity is resolved. While station-differenced biased phase provides weaker position information than CEI, it is operationally simpler and does not require a capability to record quasar signals for calibration as required for CEI.

Table 1

Error budget for TDRSS orbit determination with BRTS

Error Source	Error model	Position Error (m)
Computed error:		
Range data noise†	10 m white noise, 10 m bias	
Doppler data noise†	0.003 Hz white noise	
Total computed error		69
Considered errors:		
Solar pressure	2% error in reflectivity	4
Troposphere	5 cm zenith error	2
Ionosphere	10 TEC error	18
BRTS station locations	5 m error per axis	13
RSS position error:		73

† The data have a 10 second integration time, and are scheduled for 4 minutes every four hours for a 34 hour arc.

In this paper, baselines small enough to fit within the few hundred kilometer footprint of the TDRSS space-to-ground link signal are considered. Because of the high precision with which phase delay can be measured, the station-differenced phase data type can provide good plane-of-sky velocity measurements with baselines of this modest size. For stations within about 100 km, it is possible to distribute a common frequency reference signal to the stations over a fiber optic link, reducing errors associated with drifts in separate station clocks.[4] Baselines of 1 km, 10 km and 100 km with stations sharing a frequency reference and baselines of 100 km and 500 km in which the stations have separate frequency references are discussed.

II. Current TDRSS Orbit Determination

a) BRTS system

The BRTS consists of several ground-based transponders at four near equatorial locations around the globe. Each TDRS can view two or three BRTS stations. A range code particular to the transponder is sent from White Sands through a TDRSS satellite to each BRTS transponder and back once every four hours. TDRSS orbit solutions are calculated for 34 hour passes of BRTS four-way range and doppler data. The BRTS geometry results in a robust orbit solution for the TDRSS; however, data-taking with BRTS occupies the SA or MA user antenna of each satellite for about four minutes every four hours.

Because it is the operational data type used for TDRSS orbit determination, many studies have been done to determine the accuracy of the BRTS solutions.[1] BRTS regularly achieves 50 - 100 m one-sigma position errors. For completeness, an error budget for BRTS is included here (Table 1). A data accuracy of 10 m for the BRTS range data and 0.003 Hz for the BRTS doppler data is used for 10 second integration times.[5] Four minute arcs of data are scheduled every four hours, and an epoch state solution is found for a 34 hour data arc. A systematic error in the range measurements was included by estimating a bias parameter with an *a priori* error of 10 m. Errors from propagation media, solar pressure mismodelling and station location mismodelling are considered at the levels shown in Table 1. The computed error dominates the TDRSS position error; however, ionosphere mismodelling and station location uncertainty contribute significant consider error.

b) White Sands Ground Tracking System

The White Sands site has angle and range radio metric data available for rough TDRSS position determination. The angle data, consisting of azimuth and elevation measurements from antenna pointing,

Table 2
Differenced Troposphere Models for Several Baseline Lengths

Station separation (km) (baseline length)	Differenced troposphere sigma (cm) at 10° elevation	Differenced troposphere time constant (s)
1†	0.63	370
	0.11	2380
10	2.53	1333
100	5.86	7050
500	9.40	17,460
1000	11.2	30,000

† In the case of a 1 km baseline, the model used was the sum of two Gauss-Markov processes (see text).

have a precision of 0.1° and are biased. The current ranging system at White Sands is used to maintain an uncertainty in TDRSS range better than 10 km when the TDRSS position solution is propagated forward a few days.[6] The ranging signal has a 4 MHz bandwidth and the code is 244 μs long. The precision of the range measurements is about 20 m one-sigma for a 1 minute integration time with systematic error of about 30 m one-sigma. The system is not intended to be used for precision orbit determination and it may not be possible to calibrate the existing ground any antennae better. For the purposes of this study, it is assumed that a better ranging system could be put in place, although the current ranging system enhanced with station-differenced phase data is also studied.

III. Data Modelling and Filter Assumptions

a) Configuration

Figure 1 shows the configuration of antennae used in the covariance study. Three antennae, all near White Sands, form a north-south and an east-west baseline. For simplicity, north-south and east-west baselines of the same length are used. Baselines from 1 to 500 km are considered. In addition to the station-differenced phase data, range and doppler data collected at one of the stations are also included. The position solutions are found for 24 hour data arcs including station-differenced phase measurements on each of the two baselines and range data points every 10 minutes using the OASIS filter.[7] Position solutions calculated for TDRS-east and TDRS-west are very similar due to their symmetrical location with respect to White Sands. Hence, only the solutions for TDRS-east are shown.

Stochastic troposphere and station clock models are used to simulate the station-differenced phase data noise as discussed below. The station-differenced phase data are weighted at one-tenth of the line-of-sight troposphere sigma for each baseline, in order that it have negligible effect on the computed position error in the filter program. This results in data weights from about 0.025 cycle to about 0.5 cycle for the 14 GHz (Ku-band) phase data, depending on the baseline length. While carrier phase precision is much better than 1/40th of a cycle the data weight must be kept large enough to prevent unrealistic sensitivity to modelling errors. A constant phase bias is estimated at each of the three stations. The phase biases, which would result from integer cycle ambiguity and uncalibrated signal path delays at each station, are taken to be constant and initially unknown.

b) Noise modelling for station-differenced phase data

While carrier phase can be measured with high precision at each antenna, there would be noise in the station-differenced phase due to fluctuations in the difference between the propagation media along the two lines of sight and the difference between the station frequency references. If the stations have a common frequency reference, the noise in the station-differenced phase data should result mainly from fluctuations in the signal propagation media. For 14 GHz signals, the dominant media fluctuations are

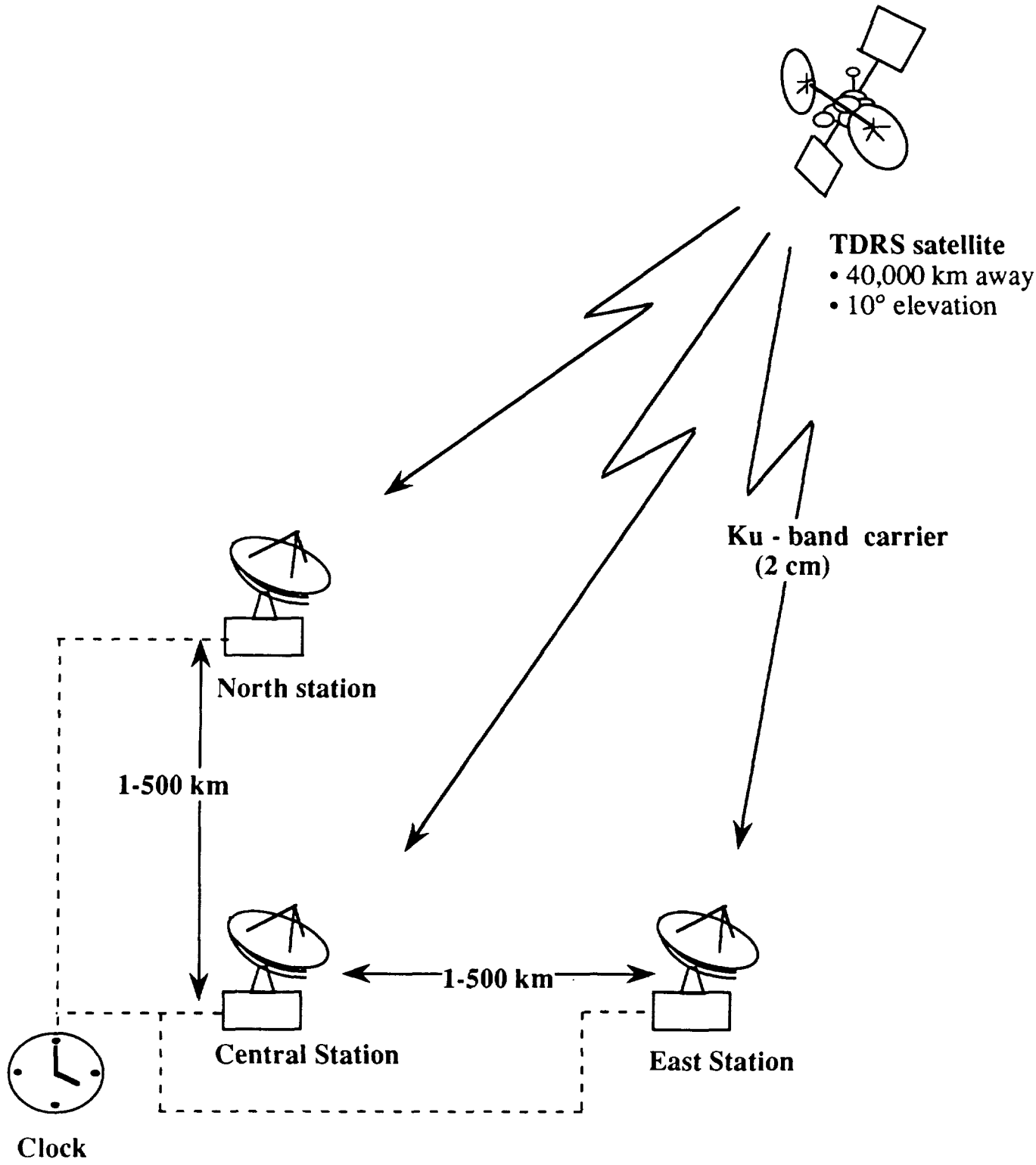

Figure 1. Configuration of antennae for carrier phase measurements used in covariance study.

Table 3
Station Clock Models Used

Clock type	Phase Random Walk growth (km/√s)	Frequency Random Walk growth ((km/s)/√s)	Phase growth in 24 hours (cm)
Rubidium	1.5×10^{-6}	4.7×10^{-10}	1200
Cesium	1.5×10^{-6}	1.5×10^{-11}	40
Hydrogen Maser	1.5×10^{-8}	4.7×10^{-12}	10

from troposphere, so charged particle media are ignored in this analysis. The data noise for differenced phase data from two stations sharing a frequency reference is simulated by estimating a stochastic troposphere model at each station. To simulate the noise in the differenced phase data from stations with separate references, a stochastic clock model at each station is also estimated.

i) Troposphere modelling

The sigma-squared and time constant of the Gauss-Markov stochastic troposphere model used for each baseline are determined by fitting the autocorrelation of the station-differenced troposphere to an exponential (table 2). In the case of a 1 km separation between stations, two exponentials, one accounting for the short term fluctuations and one for the longer term fluctuations, are required to fit the autocorrelation function well. For the longer baselines, a single exponential fits well. The autocorrelation function is calculated in a flat-earth frozen troposphere model using a wind velocity of 10 m/sec and a tropospheric height of 1 km.[8,9] The autocorrelation is calculated for north-south and east-west baselines of several sizes accounting for the 10° elevation of the TDRSS satellites from White Sands and the projection factor between the wind direction and baseline (fig 2). Since there is little dependence on baseline orientation, the autocorrelation with the largest value at t=0 for a given baseline length is used to model all the baselines of that length. For symmetry, a troposphere model is applied at each station, with a sigma-squared half the value of the differenced troposphere autocorrelation sigma. The differenced troposphere fluctuations grow with baseline; but they grow slower than the enhanced precision in angle measurement due to the longer baseline.

ii) Station Clock Modelling

Slightly longer baselines can be considered if frequency reference sharing between stations is not required. Baselines of 100 and 500 km in which the stations each have their own frequency reference are considered in this paper. If the stations forming a baseline have separate frequency references, drifts between the clocks at the stations increases the noise in the measurement of station-differenced phase.

Typical frequency standard stabilities have a short term behavior of a white frequency noise and long term behavior of a random walk in frequency. In the OASIS program, the phase of a station clock is modelled as a polynomial in time, $\phi = \phi_0 + \omega_0 \tau + \alpha \tau^2$, where τ is time past some epoch, ϕ_0 is a bias parameter, ω_0 is a drift parameter and α is a drift rate parameter. In this analysis, the white frequency noise behavior of the station clocks is modelled by applying a random walk noise model to ϕ_0, the clock bias, and the random walk of frequency behavior is modelled by applying a random walk model to ω_0, the station clock drift. Clock models representing the performance of rubidium, cesium and hydrogen maser standards, shown in table 3, are used in this study.[10] The rubidium and cesium standards have comparable short term stability, but the cesium has better stability on a 24 hour or greater time scale. A hydrogen maser is stable enough over a 24 hour data arc that would result in position solutions comparable to the case in which the stations share a common clock.

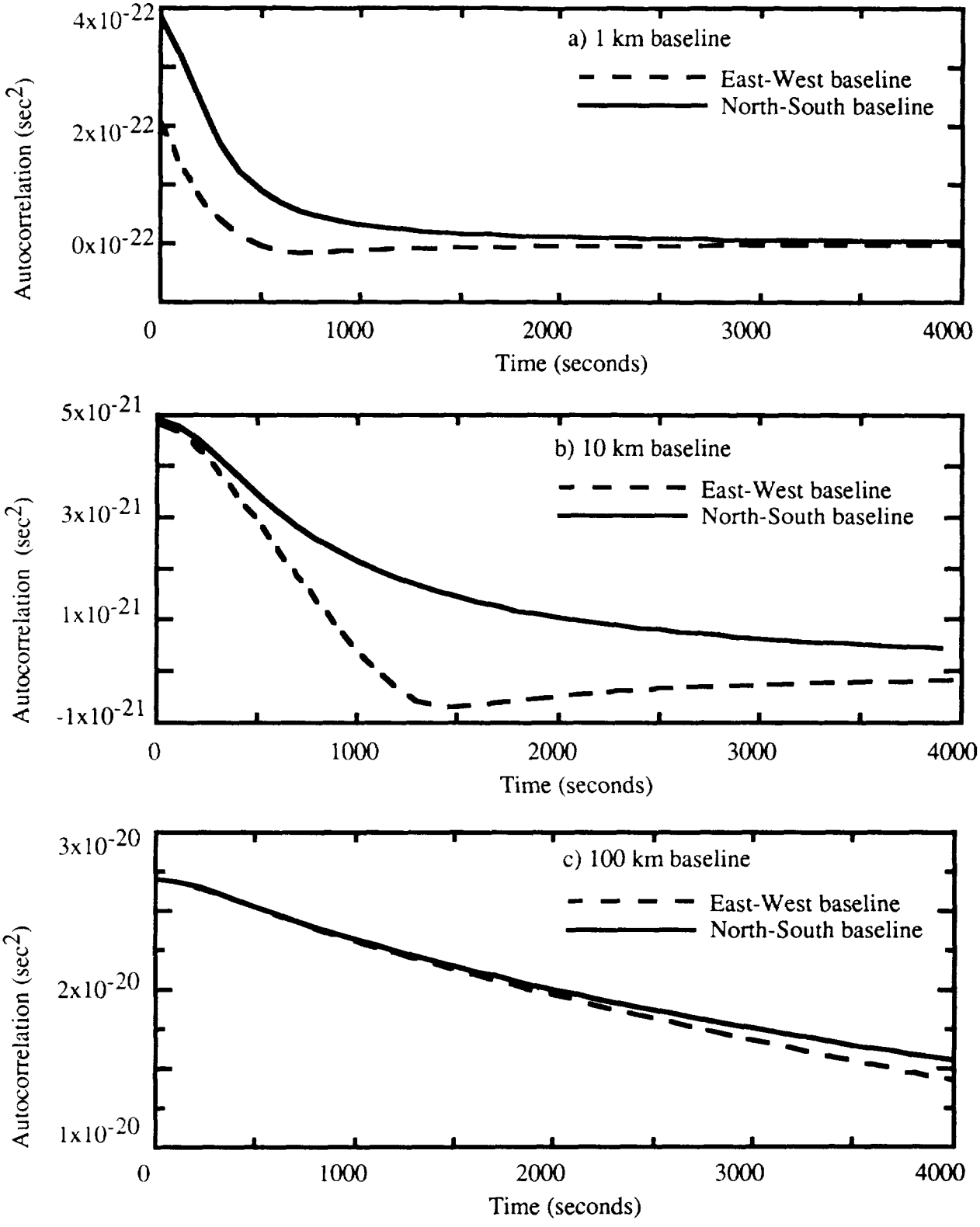

Figure 2. Autocorrelation function of the troposphere differenced between two lines of sight with elevation of 10° from stations forming an east-west or a north-south baseline of size: a) 1 km, b) 10 km or c) 100 km. These are based on the model developed in ref 9.

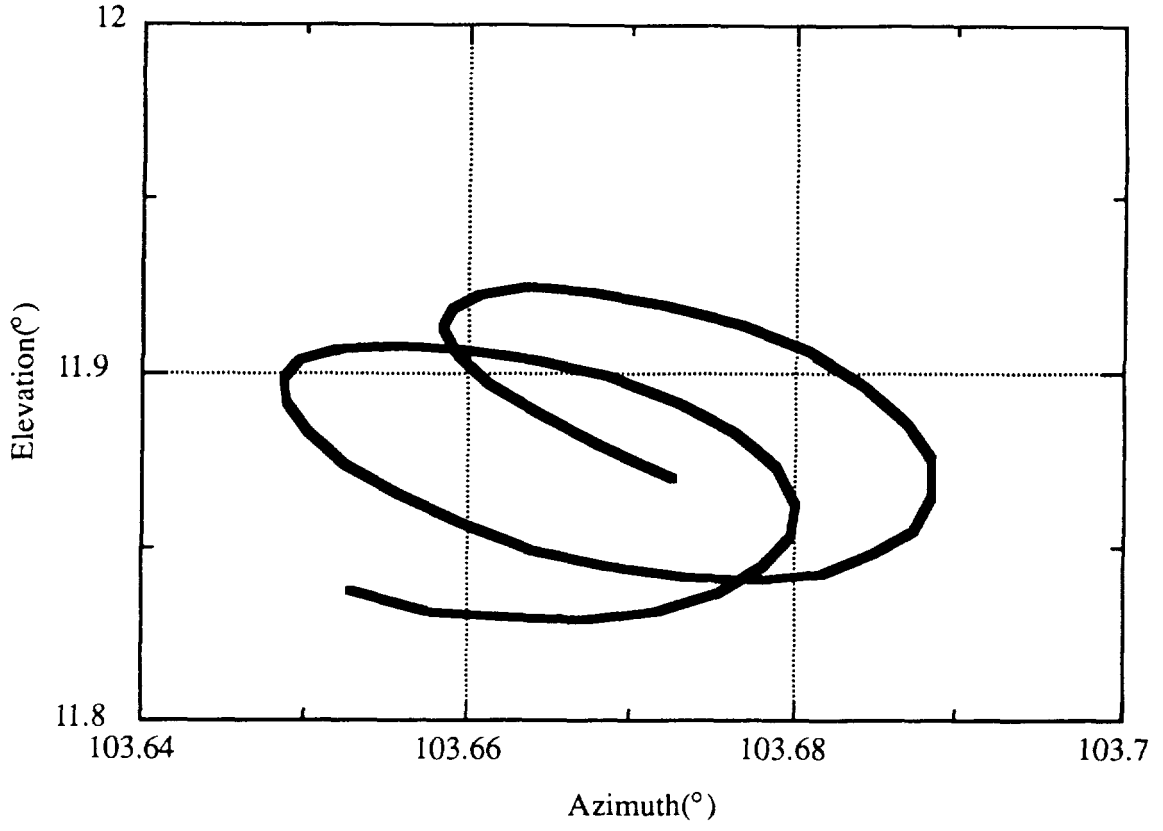

Figure 3. Signature on the plane of the sky of the TDRS-east as seen from White Sands, NM.

c) Range data

Station-differenced phase data are able to trace the small signature in the plane-of-sky made by a geosynchronous satellite over a day (fig 3). In the geometry at hand, this determines 5 elements of the TDRSS orbits well, but leaves the longitude-of-node poorly determined. In addition, an orbit solution with this data type alone is very sensitive to mismodelling of forces such as solar pressure. A small mismodelling results in a several hundred meter error in the satellite position with most of the error in the satellite longitude. For these reasons, it is impractical to perform TDRSS orbit determination with station-differenced phase data alone.

In the analysis, range and doppler data from one station are included in the simulated data set. The range data are modeled with a white noise measurement error along with systematic bias parameter which is estimated, with an *a priori* constraint corresponding to the ranging system calibration accuracy. Doppler data are modeled simply with white measurement errors. We will consider weights and biases for the range measurements between 1 and 30 meters.

Range data can help determine the along-track position, which helps constrain the satellite longitude. Low precision range data (20-100m) is good enough to control the error due to solar pressure mismodelling. Better range data are required to reduce the computed along-track error to an acceptable level. The range partial with respect to the longitude of the TDRSS satellite orbit, $\delta\rho/\delta\phi$, for the geometry discussed here is 1/7, so a range measurement of better than 7m is required to get the longitude component of the TDRSS position error below 50m. The range data precision does not have to be quite this good, since it averages down over several measurments. However, the systematic error in the range measurment must be less than 1/7 of the required position error.

Table 4

TDRS-east satellite position errors using station-differenced phase data from connected-clock stations and range from White Sands.

	case 1	case 2	case 3	case 4	case 5
inputs					
Data weights:					
Station-differenced phase baseline (km)†	100	100	100	10	1
Dopper Noise (mm/s)‡	1.0	1.0	1.0	1.0	1.0
Range Noise (m)‡	10	10	1	1	1
Range Bias (m)	30	10	1	1	1
Consider Inputs:					
Range station location(m)	2	2	2	2	2
Station-differenced phase station locations(m)	.35	.35	.35	.35	.35
Solar pressure(% of reflectivity)	2%	2%	2%	2%	2%
results (epoch)					
Computed error (m)	247	84	14	25	63
Consider errors (m)					
Solar pressure	12.1	10.4	12.4	12.4	12.6
Range station location	14	14	14	14	14
Station-differenced phase station location	0.12	0.12	0.10	0.12	11.9
RSS position error (m)	**248**	**86**	**23**	**31**	**67**

† Two orthogonal baselines of this size are used.

‡ Data noise for 10 minute points.

IV. Covariance Results

a) Computed Errors

Table 4 shows the computed errors that result in several scenarios with station-differenced phase on two orthogonal baselines combined with range and doppler data all taken from White Sands for a 24 hour data arc. The first case corresponds to using the current WSGT ranging system data enhanced with station-differenced phase data. The others are examples of performance with various combinations of baseline length and improved range data.

i) Dependence on Range Bias

As is apparent from Table 4, the position accuracy is limited by the ranging system accuracy in several cases. Figure 4 shows the dependence of TDRS position error on range bias *a priori* uncertainty when the range data are combined with station-differenced phase data from various sized baselines. In all cases the range data noise was 1 m. In order that the position error be limited only by the station-differenced phase data, the range data bias must be better than approximately 1 m in the 100 km baseline connected frequency reference case. For smaller baselines, the station-differenced phase data are weaker and the TDRS position error becomes dominated by the station-differenced phase data at larger values of range bias error. In all cases, the range data largely determine the component of the TDRS position in the longitude direction, while the station-differenced phase data determine the other orbital elements. In order to obtain a range bias of 1 m it may be necessary to upgrade the current 2-way ranging from White Sands to TDRSS. Typically, a ranging system can be calibrated to about 90% of the inverse bandwidth of the system; thus a ranging system calibrated to 1 m would require a 30 MHz bandwidth.

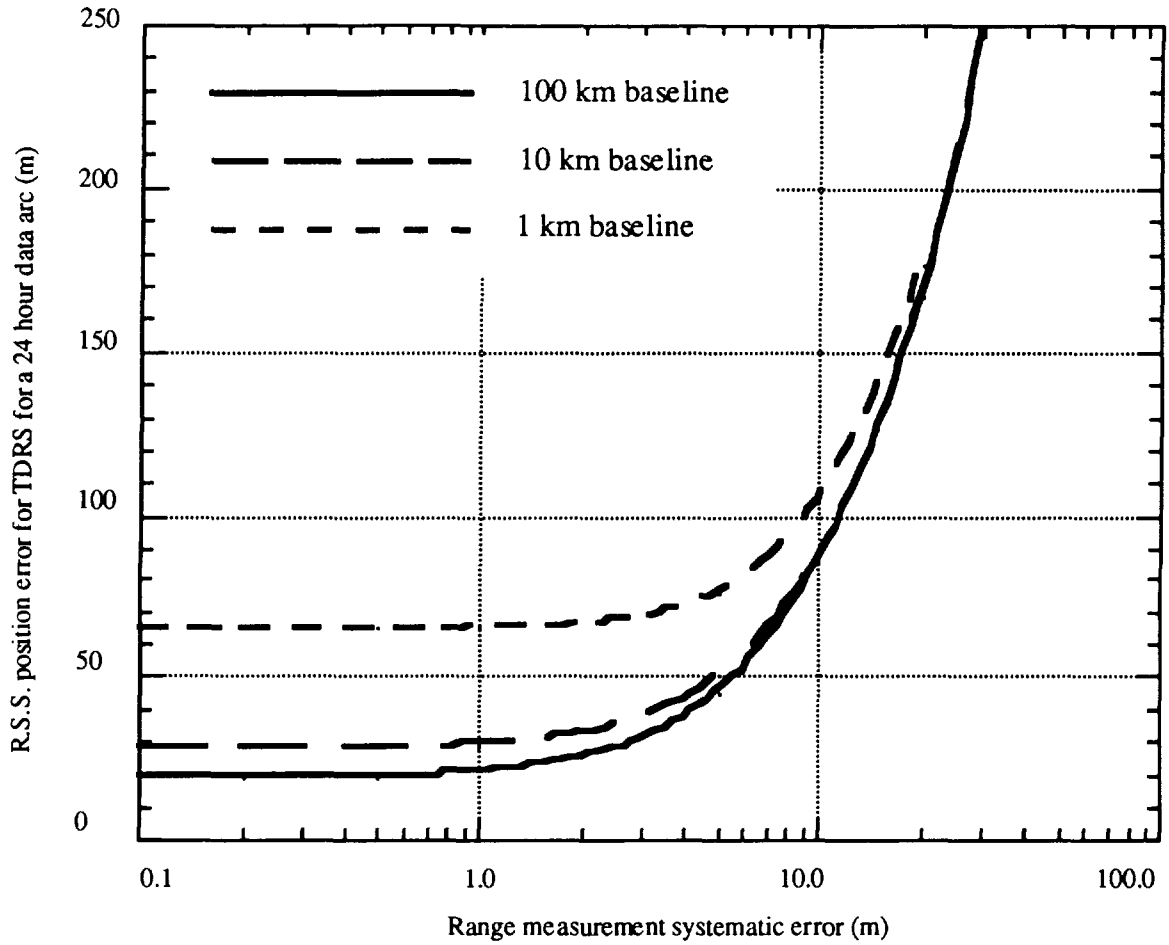

Figure 4. R.S.S. position error for a TDRSS satellite using a one day arc of station-differenced phase and range data from White Sands as a function of systematic error in the range measurement. The range noise is held fixed at 1 m for a 10 minute point.

ii) Dependence on Troposphere model

Since the troposphere model is the important source of data noise for the station-differenced phase data in the case where the stations share a common clock, it is useful to know how the troposphere model parameters affect the TDRS position error. The two parameters that describe the station-differenced troposphere, as modelled in this paper, are the steady-state sigma and the correlation time constant. Figure 5 shows how TDRS position accuracy varies with these model parameters. In Fig. 5a, The magnitude of the troposphere sigma is varied by a factor of two from the nominal values shown in Table 2, while the time constant is held fixed at its nominal value. In Fig. 5b, the time constant for the stochastic station-differenced troposphere is varied, while the steady-state sigma is held fixed. In both cases the position error changes slowly with the variation in troposphere parameters.

iii) Effect of Separate Station Clocks

Because a configuration in which the stations have independent freqeuncy references may be simpler to build, we consider it as well, despite the cost in position accuracy. Position determination with station-differenced phase depends on tracing the signature in the plane-of-sky from the station made by the satellite. In the case of a geosynchronous satellite like TDRS, there is a 24-hour period to the signature (Fig 3), so that is the time scale during which the difference in the station clocks must be stable. The expected plane-of-sky error from clock phase error growth is approximately $\rho\Delta\phi_C/B$, where ρ is the

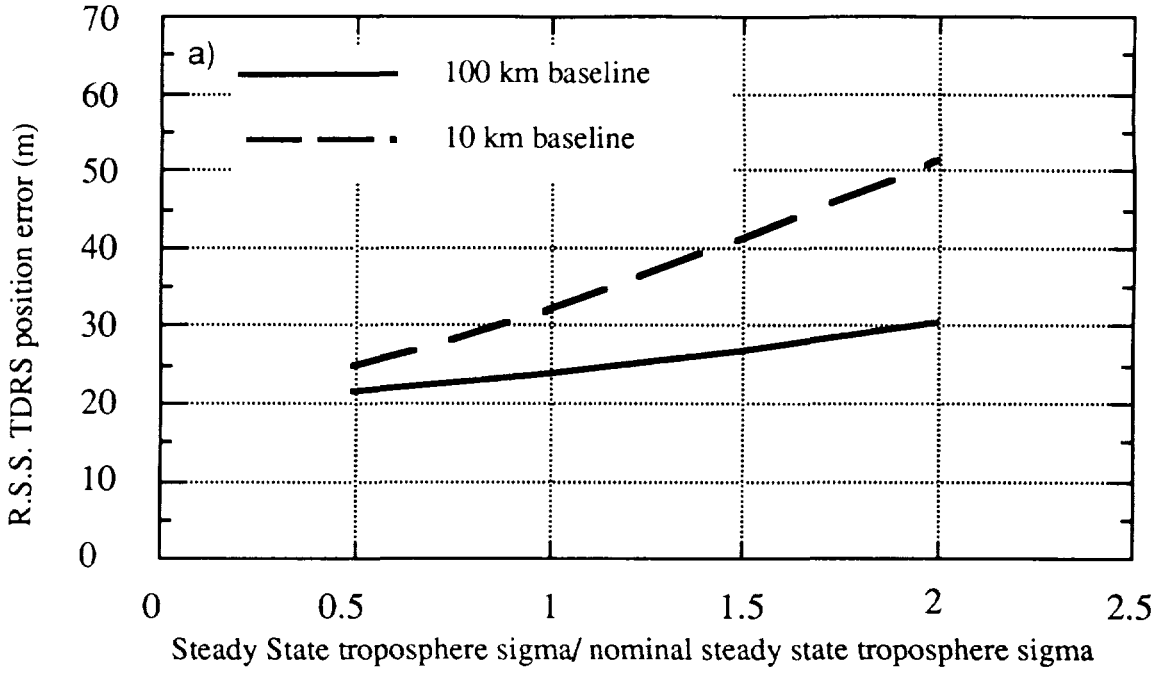

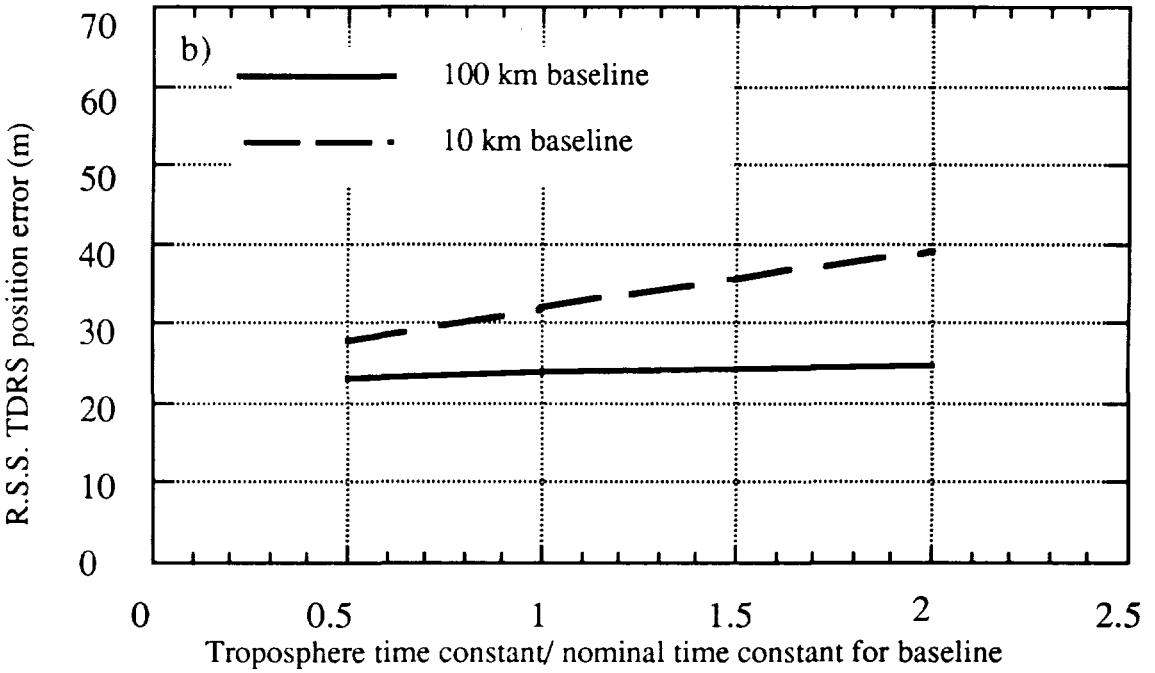

Figure 5 a.) R.S.S. position error for a TDRSS satellite using a one-day arc of differenced carrier-phase and range data from White Sands as a function of sigma of station-differenced zenith troposphere. b.) R.S.S.position error for a TDRSS satellite using a one day arc of differenced carrier-phase and range data from White Sands as a function of station-differenced zenith troposphere autocorrelation time constant. A range data noise of 1 m and range bias of 1 m were used in both figures.

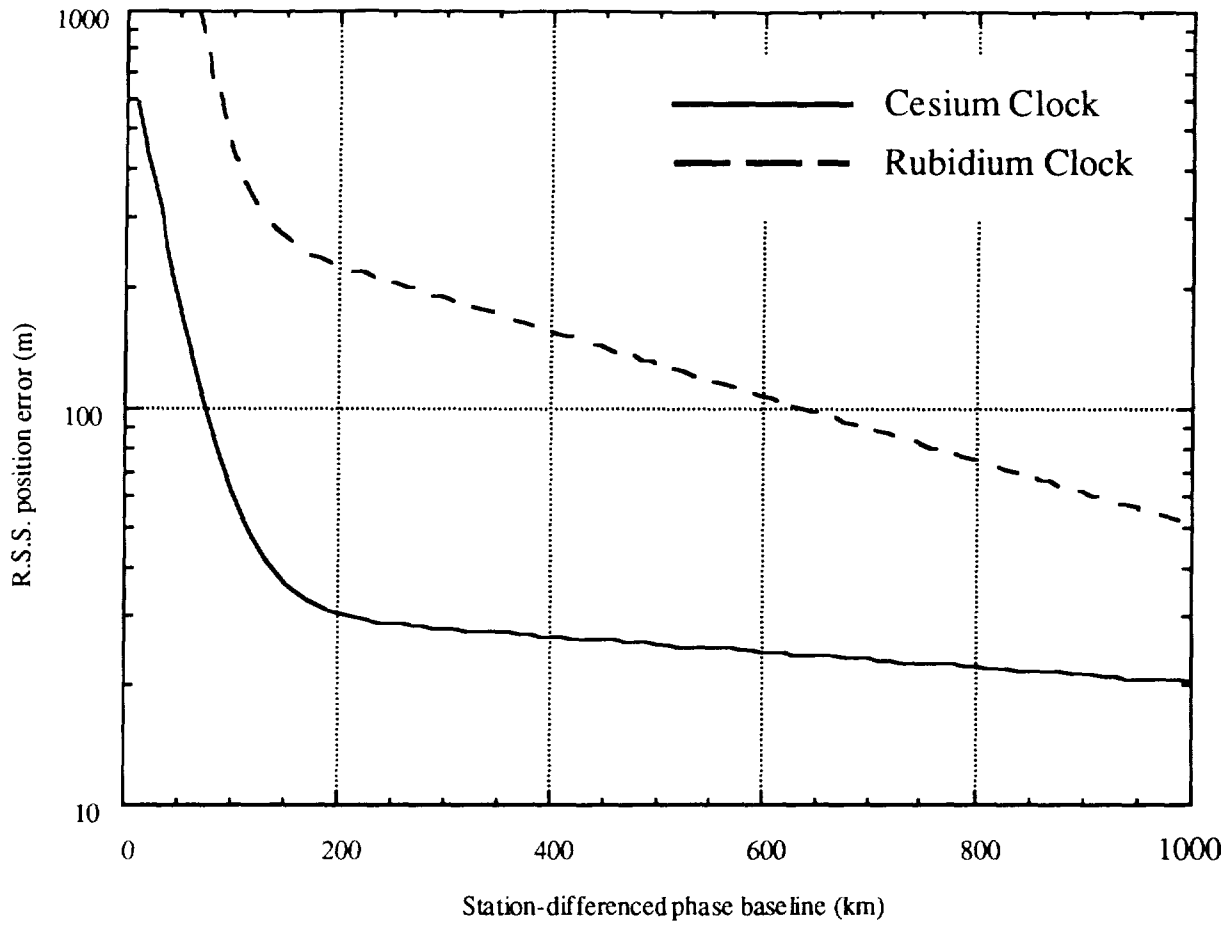

Figure 6 The position error for TDRS-east using station-differenced phase data from two orthogonal baselines plus range data (1 m error) as a function of the baseline size, if the stations have separate frequency references of the type indicated.

distance between the satellite and the tracking antennae, B is the projected baseline length, and $\Delta\phi_C$ is the path delay due to the phase error from the two clocks drifting. Clearly, somewhat larger baselines are required to offset the loss.

Figure 6 shows the expected position error as a function of baseline length if each of the three stations measuring phase (see Fig 1) have their own frequency reference. Only cesium and rubiduim standards are shown, since consider and troposphere errors dominate the position error if each station has a hydrogen maser standard. In these examples, the range data have a 1 m data noise and 1 m bias error and are unaffected by the clock model.

b) Consider Errors

A consider analysis was performed to assess the sensitivity of the solution to mismodelling due to solar pressure and station location uncertainty. Errors due to polar motion uncertainty and mismodelling of gravity harmonics are found to be small, and not included in Table 4. The same consider errors are applied to all the cases described in this paper.

In this covariance analyis, solar pressure is modelled as a force due to specular reflection from the satellite surface: $F = CA\,(1 + \eta)/r^2$, where C is the solar flux, r is the distance between the sun and the satellite, A is the reflecting area, and η is its reflectivity. The reflecting area is assumed to be constant with a value of 40 m^2. Solar pressure mismodelling is simulated as a 2% of the solar reflectivity

Table 5

Position error (m) achieved after a station-keeping maneuver

	case 1	case 2	case 3	case 4	case 5
inputs					
carrier phase baselines (km)	100	100	100	10	1
range weight (m)	10	10	1	1	1
range bias (m)	30	10	1	1	1
doppler weight (mm/s)	1	1	1	1	1
results					
error after 30 mins†	379	301	287	124	319
error after 60 mins†	249	94	49	97	242
error after 90 mins†	248	91	43	85	206
error after 120 mins†	247	88	40	76	182

† The solution includes 22 hours of data from before the maneuver and data after the maneuver up to the times listed in column one of table (see text). The errors include consider errors at the same levels as table 2.

parameter, $(1+\eta)$, with a nominal value of 1.42. It has been shown that solar pressure effects on the TDRSS satellites can be modelled to 2%.[11] Operationally, the solar reflectivity might be estimated, enlarging the computed error somewhat, and a much smaller mismodelling error could be considered.

The error due to uncertainty in the antenna locations is also determined with consider analysis. A 2 m uncertainty in each component of the ranging station location is used. A 35 cm uncertainty in each component of the stations measuring carrier phase is used. This corresponds to allowing about 0.5 m uncertainty in the baselines formed by pairs of stations. The sensitivity to the baseline length error is small except in the case of the smallest baselines studied.

c) Recovering Position After a Maneuver

The TDRSS satellites occasionally make corrective maneuvers in order to stay in their desired orbits to the required tolerance. The requirement for TDRSS is 50 m position error one-sigma within two hours after the maneuver. Because good position determination with station-differenced phase data requires about a 1-day arc, it is impossible to redetermine all the state parameters to this accuracy within two hours. Instead of redetermining the whole state, we may take advantage of the good instantaneous plane-of-sky velocity information in this data type by estimating the velocity change in the satellite state associated with the maneuver. Line-of-sight doppler data collected along with the range data at one station, provides the third component of the satellite velocity.

It is assumed that there is nearly a day long arc of station-differenced phase, range and doppler data prior to the maneuver. The corrective maneuver is modelled as a velocity impulse with well known time of burn. No *a priori* knowledge of the error in the impulses is assumed. Table 5 shows position error achievable after such a maneuver, if the state and the maneuver are both estimated using a day long arc of data ending two hours after the maneuver. In each case, the position error is about twice as large as after a full day data arc uninterupted by a maneuver.

V. Conclusions

We have examined the possibility of using station-differenced carrier phase with stations forming small baselines for orbit determination for the TDRS satellites. We find that two orthogonal baselines between 10 and 100 km, located near White Sands, are sufficient to obtain position accuracies of 25 to 50 meters. However, for the geometry considered, station-differenced phase data alone poorly determine the longitude of the spacecraft, and thus range data with systematic error of about 1 m must be included to

obtain these accuracies. The accuracy of the station-differenced carrier phase data from such moderate baselines results from the use of a common frequency reference at the stations. As can be seen in figure 6, acceptable position accuracies can also be acheived with separate station clocks; however, much larger baselines are required.

The station-differenced phase data along with two-way doppler can be used to estimate the velocity change associated with a station-keeping maneuver well enough to determine TDRSS position to 50-100 meters within two hours of a maneuver. Nearly a full day is required to recover the best possible position accuracy with this method. No *a priori* knowledge of the size of the impulse is required; though the time of the impulse is assumed to be known.

Range data with accuracy of about 1 m is crucial for this technique to be viable independent of the baseline size used and whether or not the stations share a frequency reference. With a 1 m systematic error in the ranging system, the position accuracy is only slowly dependent on the exact value of the bias.

Acknowledgment

The work described in this paper was carried out by the Jet Propulsion Laboratory, California Institute of Technology, under contract with the National Aeronautics and Space Administration.

References

1)A.Weinberg, *etal,* "Assement of Candidate ATDRS Tracking Techniques", Stanford Telecommunications, Inc., TR91002, May 20, 1991.

2) Other ATDRS tracking methods explored in our study can be found in B.Haines, *etal,* "Application of GPS Tracking to Orbit Determination for TDRSS", in this proceedings.

3) C.D.Edwards, "Angular Navigation on Short Baselines Using Phase Delay Interferometry", *IEEE Transactions on Instrumentation and Measurement,* vol. 38, pp.665-667, 1989.

4) C.D.Edwards, "Development of Realtime Connected Element Interferometry at the Goldstone Deep Space Communications Complex", *AAS/AIAA Astrodynamics Conf.,* August 20-22, 1990.

5) Osvaldo Cuevas, private communication, September 1991. These are similar to the data weights used for current BRTS orbit determination.

6) V.Guedeney, "WSGT Ground Antennas Calibration", Contel Intra-Company Communication no. IOC-87-915-005, March 19, 1987.

7) S.C.Wu, *etal,* "OASIS Mathematical Description V. 1.0", JPL Internal Document D-3139, April 1, 1986.

8) R.N.Treuhaft and G.E.Lanyi,"The Effects of the Dynamic Wet Troposphere on Radio Interferometric Measurements", *Radio Science, vol 22,* pp.251-265, 1987.

9) C.D.Edwards, "The Effect of Spatial and Temporal Wet-Troposphere Fluctuations on Connected Element Interferometry", *TDA Prog. Rept. 42-97,* May 15, 1989, pp 47-57.

10) Samuel R. Stein and John R. Vig, "Freqency Standards for Communications", U.S. Army R and D Tech. Rept. no. SLCET-TR-91-2, January 1991.

11) M.Bobrowsky, P.Y.Kay, A.K.Drew, S.L.Hoge, and O.O.Cuevas, "Short- and Long-Term Determination of the TDRS Solar Reflectivity Parameter using the Goddard Trajectory Determination System", *AAS/AIAA Conf. Proceedings,* August 10-13, 1987.

Application of GPS Tracking Techniques to Orbit Determination for TDRS

B. J. Haines, S. M. Lichten, R. P. Malla, and S. C. Wu

Jet Propulsion Laboratory, California Institute of Technology
Pasadena, California 91109

In this paper, we evaluate two fundamentally different approaches to TDRS orbit determination utilizing Global Positioning System (GPS) technology and GPS-related techniques. In the first, a GPS flight receiver is deployed on the TDRSS spacecraft. The TDRS ephemerides are determined using direct ranging to the GPS spacecraft, and no ground network is required. In the second approach, the TDRSS spacecraft broadcast a suitable beacon signal, permitting the simultaneous tracking of GPS and TDRSS satellites from a small ground network. Both strategies can be designed to meet future operational requirements for TDRS-II orbit determination.

1. INTRODUCTION

The Tracking and Data Relay Satellite System (TDRSS) is used by NASA to support positioning and data relay activities for a wide variety of Earth orbiting spacecraft [1]. The present operational system is composed of two geosynchronous satellites (TDRS-E and TDRS-W at 41° and 171° W longitude respectively), a central ground station located at White Sands, New Mexico, and remote tracking sites at Ascension Island, American Samoa, and Alice Springs, Australia. Accurate real-time positioning of the TDRSS spacecraft is fundamental to the proper operation of the system, and is achieved via the relay of coherent signals broadcast by unmanned transponders at the remote tracking sites. These remote beacons are collectively referred to as the Bilateration Ranging Transponder System (BRTS). Range and Doppler observations from BRTS are routinely scheduled by the central ground processing facility at White Sands, where they are used in conjunction with models of the forces perturbing the spacecraft motion to determine the TDRS positions. Evaluation of the TDRS ephemerides suggests that orbit consistency is maintained to better than 70 m using the operational BRTS method [2]. This level of precision is adequate for current applications; however, the technique requires valuable TDRS antenna time that could otherwise be used for servicing user spacecraft.

In recognition of the need for improved tracking for the next generation TDRS System (TDRSS-II), a number of alternative methods have been explored [3–6]. The demand for improved accuracies provides an important motivation for these efforts. This requirement, however, is balanced by the appeal of a simple, reliable and autonomous system that requires no disruption of TDRSS user services and delivers the ephemerides in near real-time. One technique which promises the potential to meet these sometimes conflicting demands relies on technology from the U. S. Department of Defense Global Positioning System (GPS). Previous efforts addressing this option have produced encouraging results. *Wu* [7] proposed two GPS related-techniques for determining the orbits of high-altitude Earth satellites. He envisioned a wide variety of possible applications; hence the breadth of the study prevented a thorough treatment of TDRSS. Recent efforts have focused directly on TDRSS, but software limitations precluded a complete evaluation [3]. In this paper, we build on these earlier studies by revisiting their assumptions, and revising them to insure they reflect current state-of-the-art. The new assumptions form the basis of a covariance study that exploits software and methodology that have evolved over the past decade as part of a program at the Jet Propulsion Laboratory (JPL) to support GPS-based tracking of Earth orbiters.

Results for two distinct solutions strategies, as prescribed by *Wu* [7], are reported. In the first, a GPS receiver is deployed on the TDRSS spacecraft and the ephemerides are determined using direct measurements from the GPS to TDRSS spacecraft. In the second, the TDRSS spacecraft broadcast wide-beam beacon signals which permit the simultaneous tracking of GPS and TDRSS satellites from a small ground network.

2. GPS-BASED TECHNIQUES FOR ORBIT DETERMINATION

For both military and civilian customers, the principal application of GPS is the precise positioning of ground sites and of moving vehicles near the Earth's surface [8]. The space segment of this system, which is due for completion in mid-1993, will consist of 21 satellites and 3 active spares orbiting in 6 uniformly spaced orbit planes inclined at 55° with respect to the equator. The satellites, which are at an altitude of about 20,200 km, transmit unique navigational signals centered on two L-band carrier frequencies (L1 at 1575.42 MHz and L2 at 1227.60 MHz). Each carrier is modulated with pseudo-random square-wave codes: a coarse acquisition (C/A) code on L1, and a precise (P) code on both L1 and L2. An additional Y-code may be used to encrypt the P-code (anti-spoofing or AS).

A GPS receiver generates a replica of these codes and correlates them with the received signals, from which a

pseudorange to each visible spacecraft can be inferred. (Pseudorange is simply a range biased by the unknown offset between the spacecraft and receiver clocks.) The receiver uses these pseudorange measurements together with ephemeris and clock information broadcast by the respective GPS spacecraft to determine its location. A minimum of 4 satellites must be in view of the receiver in order for the user to solve for the three components of position and the clock offset. The accuracy with which the user can determine his position is dependent on a number of factors; principal among them is the geometric configuration of the satellites in view. The quality of the broadcast ephemeris and clock information, which can be intentionally degraded as part of Selective Availability (SA), is also an important factor.

The same principles can be applied to the positioning of low-Earth orbiters equipped with GPS receivers. Because the applications in this area are primarily in the field of precise geodesy, a more robust approach is generally required. In particular, multidirectional pseudorange and carrier phase measurements collected simultaneously at ground stations and the user spacecraft can be combined over suitable intervals of time—typically a few hours to several days—in order to determine the ephemerides of the orbiter [9–11]. The simultaneous measurements from the ground stations can be combined to nearly eliminate effects of clock errors SA degradation, while also mitigating the effects of errors in the GPS ephemerides.

What makes this approach especially attractive is that the robust observation geometry permits orbit solutions without dynamic model constraints on the spacecraft motion [12]. (Errors in dynamic models are the principal limitations in traditional approaches to satellite orbit determination.) Where advantageous, however, dynamic models can still be exploited to improve the accuracy [13]. Although a state-of-the-art GPS receiver capable of providing proof-of-concept has not flown at this writing, covariance analyses suggest that positioning at the sub-decimeter level should be achievable. Plans for a number of U. S. and international missions include flight-hardened, high performance GPS receivers. Two such missions, the joint U. S.–French Topex/Poseidon satellite [14] and NASA's Extreme Ultraviolet Explorer, are to be launched in 1992.

While the application of GPS for the positioning of low-Earth orbiters has received considerable attention, this is not the case for high-Earth orbiters such as the geosynchronous TDRSS spacecraft. The GPS constellation illuminates the Earth from an altitude of 20,200 km and as such, is better suited for low-Earth users. Since the TDRSS spacecraft are located above the GPS constellation, they must look down to receive GPS signals spilled over the limb of the Earth from satellites on the other side of the planet. The configuration, hereinafter referred to as "down-looking GPS" in keeping with *Wu* [7], is shown in Figure 1.

Although an observer traveling with TDRS would be able to establish a direct line of sight to many GPS satellites, the number of useful GPS spacecraft is limited to those that fall within an annular region delineated on the inside by the Earth blockage and on the outside by the beamwidth of the GPS signals. The half-width of the mainbeams are 22° and 27° respectively at L1 and L2 frequencies, while the angle subtended by the Earth at GPS altitude is 27°. Together these constraints imply that, on average, the signals from only 1 GPS satellite can be seen from geosynchronous altitude at any given time [7]. Of course this entirely precludes the possibility of kinematic positioning, and the orbits must be determined dynamically. For a spacecraft at geosynchronous altitude, however, the perturbative accelerations due to the non-spherical Earth are highly attenuated and the effects of atmospheric drag are negligible. As a result, the proper modeling of the forces acting on a spacecraft is much less problematic than it is for a low-Earth orbiter.

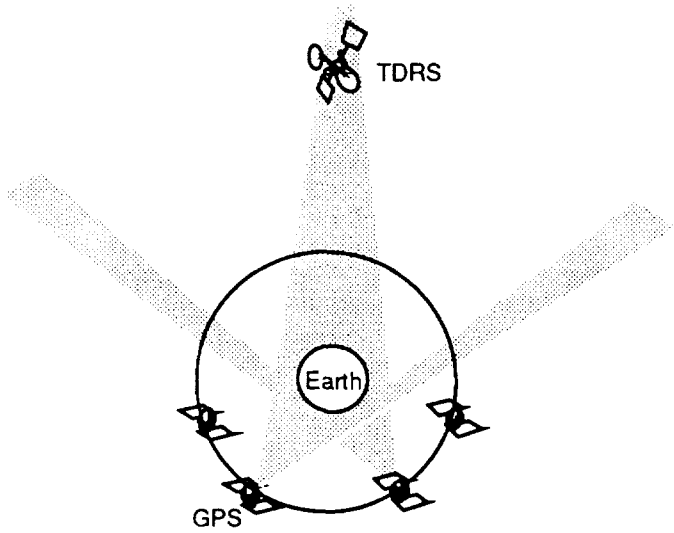

Figure 1. 2-d view of down-looking GPS tracking configuration: Geosynchronous TDRSS satellite with GPS receiver sees GPS signals spilled over limb of Earth.

Aside from these special limitations, the overall strategy for down-looking GPS is not unlike that for the up-looking variation used by low-Earth orbiters. In particular, the determination of the orbit can be made using simultaneous observations formed with data collected at ground stations, or directly, without the aid of a ground network. The benefit gained from the use of simultaneous observations, however, is somewhat limited owing to visibility constraints. Simultaneous observations of the same 2 GPS spacecraft from geosynchronous orbit and the ground are possible less than half the time even with the most optimistic scenarios [3,7]. Implicit in both approaches therefore is a greater vulnerability to clock errors, and to the effects of SA if the

flight receiver is not equipped with a decryption module. Despite these problems, the down-looking GPS approach is quite attractive for TDRS orbit determination because of the high level of autonomy and the greater potential for achieving real-time results.

An alternative strategy requires that the high-Earth orbiter transmit a suitable signal which can be monitored at the same ground stations observing GPS [7, 15]. This method is referred to as "inverted GPS" because the major factor affecting the orbit accuracy is the number of ground stations, rather than GPS satellites, in common view of the user spacecraft (Figure 2). Inverted GPS promises the highest accuracies for geosynchronous tracking because any number of ground sites may be visible from the TDRSS spacecraft [7]. Coincident observations of the GPS satellites from the ground are desired in order to enable estimation of clock biases. As is the case for down-looking GPS, dynamic models of the forces governing the orbital motion are used to supplement the geometric content of the measurements.

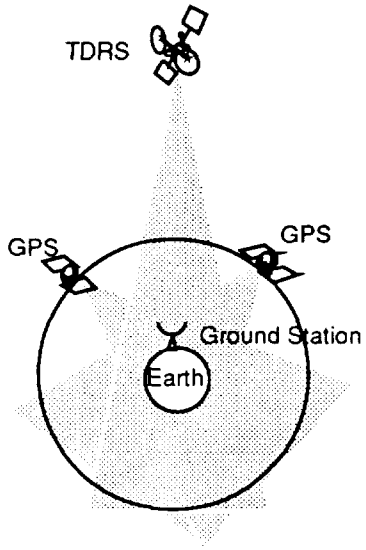

Figure 2. Inverted GPS tracking configuration: TDRSS and GPS beacon signals tracked simultaneously from ground.

3. COMMON STRATEGY

The assumptions forming the foundation of this study are governed by guidelines that have been advanced by NASA for future TDRS-II orbit determination [*e.g.* 3,4]. These guidelines reflect a balance between the demands for increased accuracy and system autonomy. For this effort, the figure of merit for the accuracy is 50 m in total position (1-σ). We assumed that this level of accuracy should be met in nominal operations with 24-hours of tracking, although we also examined the feasibility of achieving 50 m after only 2 hours of tracking (for the cases where the trajectory is to be recovered rapidly after a station-keeping maneuver). For system autonomy, the primary drivers include: minimized impact on TDRSS user services, minimized human intervention during normal operations, and for the inverted technique, a simple ground network. We began with the premise that the inverted-technique would provide the best accuracy, and focused on identifying compromises that would ensure greater autonomy. Conversely, for the down-looking approach, we devoted our efforts to determining ways to improve the accuracy.

The Orbit Analysis and SImulation Software (OASIS) package developed at JPL served as the primary evaluation tool. The OASIS system is designed to provide a flexible,versatile and efficient covariance analysis tool for Earth satellite navigation and GPS-based geodetic studies [16]. It has been used extensively for spacecraft orbit error analysis, and its factorized Kalman filter strategies [17] also form the basis for the GPS Inferred Positioning SYstem (GIPSY) software used in the reduction of actual GPS data for recovering geodetic baselines and improving satellite orbits.

For both strategies, a full 24-satellite GPS constellation was assumed. The TDRSS-II satellites were assumed to be at the same locations as the present TDRS-W and TDRS-E. The actual TDRSS-II constellation will contain additional satellites, but they should be clustered in the same vicinities as the current spacecraft. The results therefore should not be significantly different for these additional satellites. The next sections detail specific error models applied in the two solution strategies, along with the results. Covariance analysis results portray the actual expected errors only to the extent that the a priori models are authentic. In order to address the possibility of unanticipated errors, we therefore adopted a set of a priori assumptions that were somewhat conservative.

4. INVERTED GPS

Assumptions

As a starting point, we propose some small ground networks suitable for the simultaneous tracking of GPS and TDRSS spacecraft. An initial stated goal for TDRSS-II orbit determination was to confine all stations to the continental U.S [3]. This constraint was subsequently relaxed [4]; it nonetheless remains essential to identify a minimum network that will deliver the desired orbit accuracy. For this effort, we selected various station configurations from the 6-site global GPS network that has been established to support the Topex/Poseidon mission. Three of the 6 sites are collocated with NASA Deep Space Network (DSN) stations at Goldstone, California; Madrid, Spain; and Canberra, Australia. The remaining three are at Santiago, Chile; Usuda, Japan; and Hartebeesthoek, South Africa. An additional receiver at the TDRSS ground control station at White Sands was assumed for some of the variations. The visibilities of these sites from the TDRS-E and TDRS-W respectively are shown in Figure 3.

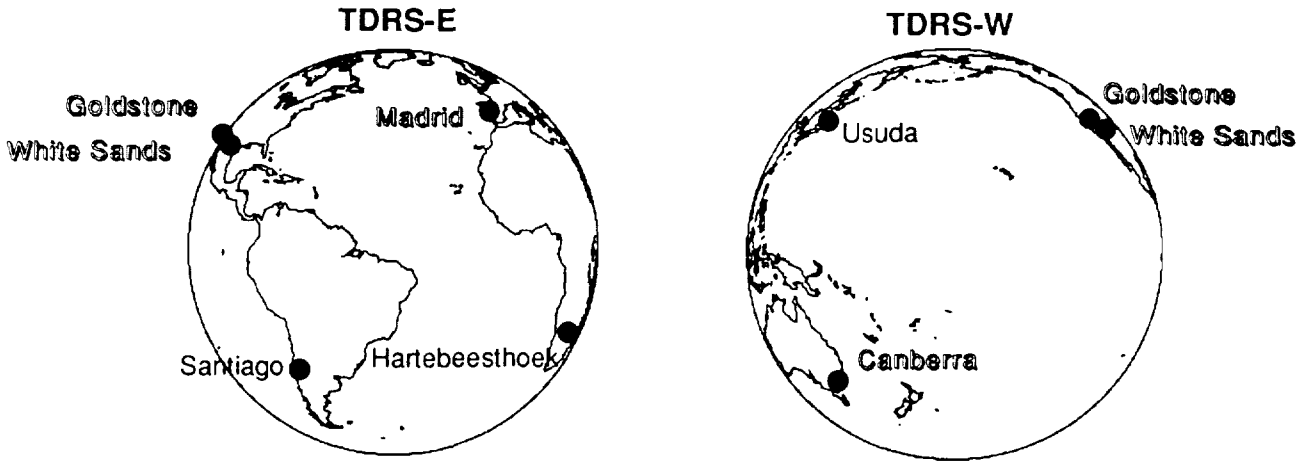

Figure 3. Visibility of proposed GPS ground network for TDRS tracking. The views show the perspectives of the Earth from the TDRS-E and TDRS-W geosynchronous orbit positions respectively. The minimum network considered, consisting of stations at the DSN sites and the White Sands TDRSS ground control center is shown in shadowed text.

It is instructive to note that these sites are presently used to support well-established NASA programs. Each is equipped with a JPL Rogue digital receiver capable of tracking pseudorange and carrier phase from 8 GPS spacecraft simultaneously [18]. Although the receivers are designed to operate unattended, staff are always on call at these sites should any problems develop. For this study, we assumed that the Rogue receivers at each of the tracking sites were retrofitted so that a TDRSS beacon signal could be tracked continuously on 1 of the 8 channels (Figure 4). We note that GPS receivers have already been used in demonstrations to track Pioneer Venus and Magellan at X and S bands [19].

A critical design parameter for the inverted GPS technique is the measurement characteristic of the TDRS beacon signal. Several options for the design of an advanced beacon signal have been considered [3, 4]. For the present study, ranging tones broadcast by the TDRSS spacecraft at Ku band served as the nominal configuration for the transmission. A major advantage of exploiting the high-frequency Ku band is the relatively small signal delay due to ionospheric refraction. Equivalent range delays at Ku band vary from less than 1 cm to 20 cm depending on the level of solar activity. Ionospheric calibration based on the GPS dual frequency L-band data collected at the various tracking sites can then be applied in modeling the delay to better than 1 cm in range. A similar activity is already underway at the DSN sites, where the GPS data is used to calibrate ionospheric delays for deep-space tracking [20].

The proposed Ku-band signal could, in theory, provide pseudorange measurements with a random noise component of 1 cm averaged over 30 minutes, assuming a 100 MHz bandwidth (L. Young, private communication, 1992). In practice, the implementation of new Rogue hardware to down-convert the Ku-band signal to GPS frequencies (L band) would introduce an additional error because separate signal paths would be used for the TDRS and GPS signals. This instrumental error would manifest itself as a slowly varying delay offset in the TDRS pseudorange residuals. Preliminary analysis indicates the effect would be bounded by about 1 nsec (amounting to 30 cm in range delay) and would modulate with a period of about one-half day. Because of the long period, the error appears as a constant bias over a typical measurement interval, permitting us to model it as a stochastic process in OASIS. Several variations from these nominal characteristics were explored in order to assess how deviations from these assumptions would impact the TDRS orbit accuracies. Results and additional details are presented in the next section.

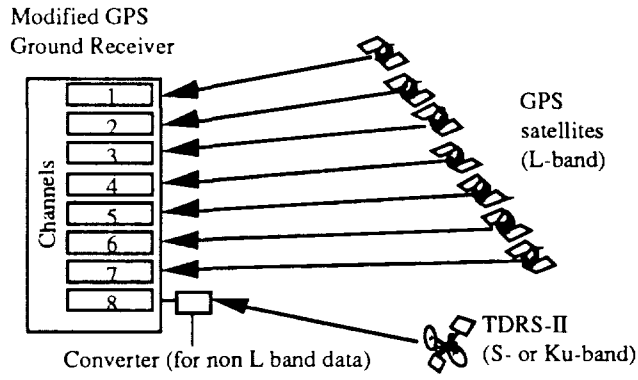

Figure 4. Schematic showing 8-channel GPS receiver modified for TDRS tracking on one channel.

The noise of the ionosphere-corrected GPS P-code pseudorange and carrier phases measurements was set at 25 and 1 cm respectively for 30 minute measurement intervals.

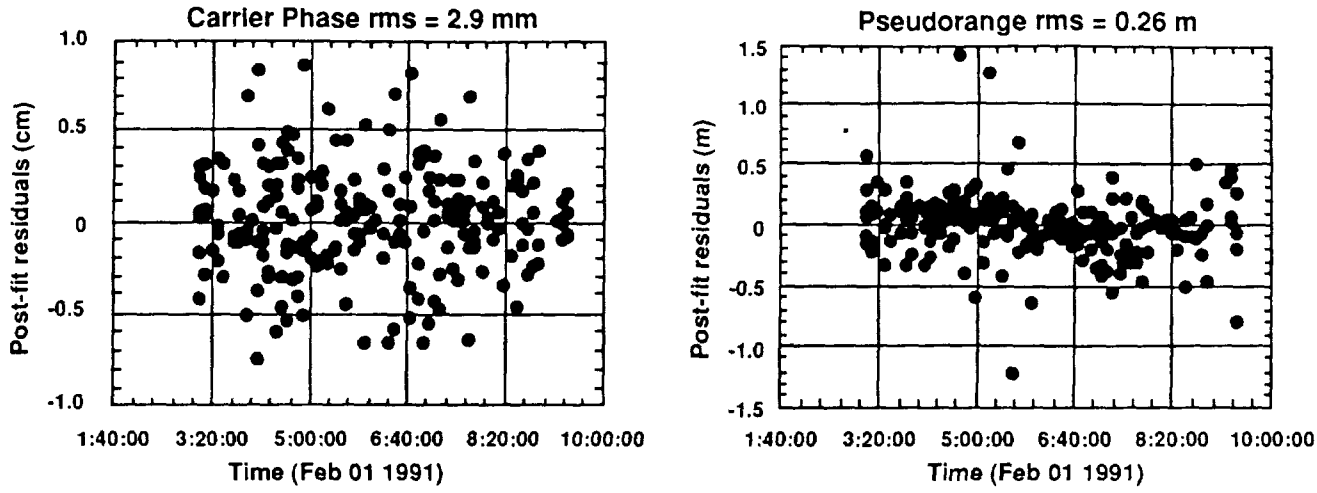

Figure 5. Actual post-fit GPS data residuals from Rogue receiver at Goldstone for carrier phase (left) and pseudorange (right). The GPS measurements are at a 6-minute rate.

As Rogue receivers are presently providing this level of precision for 6 minute measurement intervals (cf. Figure 5), these estimates are quite conservative. The higher levels of data noise, however, are intended to accommodate periods when the receivers must track using codeless techniques because AS is turned on. Additional assumptions applied in OASIS for evaluating the inverted GPS technique are listed in Table 1. We assumed the a priori knowledge of the GPS ephemerides was very poor, and solved for the 24 GPS and 2 TDRSS epoch states together. Additional estimated parameters included a single solar radiation pressure coefficient for each TDRS, and GPS solar radiation pressure coefficients and carrier phase biases. Clock errors were estimated as stochastic white noise processes with a reference frequency standard at Goldstone, an approach which is analogous to (but more general than) using doubly differenced measurements. A random-walk process noise parameter was used to model the zenith troposphere delay at each of the stations [21].

The sensitivities of the TDRS orbit to errors in several important unestimated parameters were also computed. These unestimated or "consider" parameters, can be included in covariance studies in order to yield more realistic error estimates. The additional error contributions from the consider parameters are added to formal errors from the filter, which contain only the effects of data noise. The consider parameters and their associated errors (1-σ) are also shown in Table 1. Note that these errors for consider parameters represent fixed systematic errors [17]. Most important among them are the tracking station coordinates and Earth orientation parameters. For individual components of the DSN station positions, errors of 3 cm were assumed. Recent analyses suggest that cm-level accuracies are already being achieved for the locations of GPS antennae at the 2 DSN sites in the Northern Hemisphere [22]. Coordinates for non-DSN sites were assigned conservative errors of 10 cm. Uncertainties in the X and Y pole positions were set at 25 cm, while the error in the variation of Earth rotation as manifest in UT1 – UTC was set at 6.0×10^{-4} s. In a unified GPS/TDRSS solution strategy at JPL, these Earth orientation parameters could be adjusted to reduce these errors by at least an order of magnitude. By using higher errors, we allow for a real-time system where accuracy may be degraded.

The lumped effects of errors in the Earth's gravity model were represented by 25 % of the difference between the Goddard Earth Models (GEM) –10 and –L2 [23,24]. Our own analysis suggest that for many applications this representation is comparable to the errors in the GEM-T3 gravity field [25], a state-of-the-art model developed in support of the Topex/Poseidon mission. Owing to the extremely high altitude of a geosynchronous orbiter, the gravity model errors have only a minor effect on the TDRS orbit determination in comparison with other sources.

Table 1: Error models for inverted-GPS

A PRIORI FOR ESTIMATED PARAMETERS				
TDRS Position, Vel. (X, Y, Z)	5	km,	50	m/s
TDRS Solar Radiation Pressure	5	%		
GPS Position, Vel. (X, Y, Z)	100	m,	1	m/s
GPS Solar Radiation Pressure	25	%		
GPS Y Bias	10^{-12}	m/s^2		
GPS Carrier Phase Biases	1000	km		
GPS/TDRS/Station Clocks	1000	μsec	white noise	
Zenith Troposphere	40	cm	+12 cm/day	
CONSIDERED PARAMETERS				
DSN Station Coordinates	3	cm		
Non-DSN Station Coordinates	10	cm		
GM Earth	2	ppb		
Lumped Earth Gravity Field	25	%	GEM-10 – L2	
X, Y Pole Motion	25	cm		
UT1 – UTC	6×10^{-4}	s		

Results for Routine Orbit Determination

We consider first a nominal case which is characterized by the TDRS Ku-band beacon design outlined in the previous section and a minimal ground network consisting of the 3 DSN sites and White Sands. Figure 6 depicts the mapped orbit error (1-σ) for TDRS-W as a function of time past the epoch of the arc. The formal (computed) error reflecting the effects of data noise is shown along with the systematic error from unestimated (consider) parameters. We adopt the maximum RSS total error as the basis for comparing various strategies in relation to the TDRSS requirement. For the 24-hour period in question, the total position error for TDRS-W never exceeds 15 m, well under the 50 m requirement.

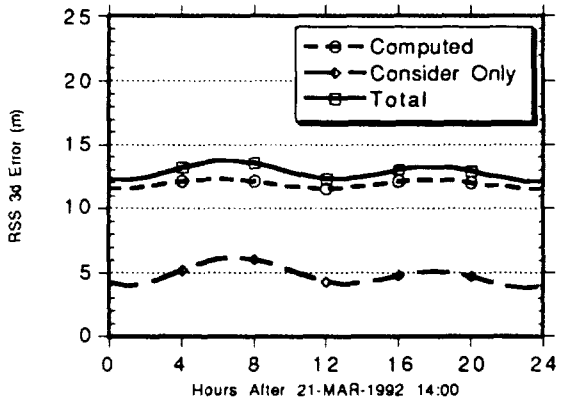

Figure 6. TDRS-W position error for 24-hour arc. Orbit determined using inverted technique with tracking from 2 DSN sites and White Sands. TDRS-W carries nominal Ku-band beacon.

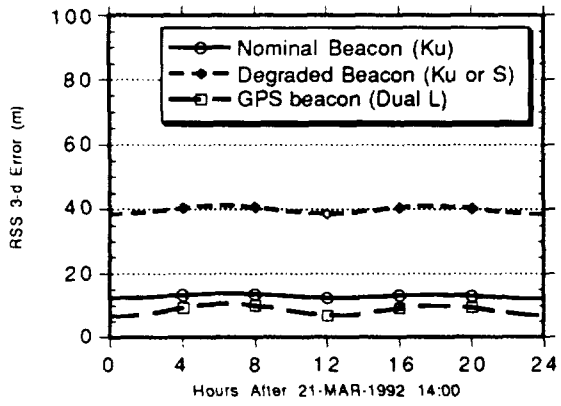

Figure 7. TDRS-W position error over 24-hour arc for hypothetical beacon signals. Orbit determined using inverted technique with tracking from 2 DSN sites and White Sands.

In interpreting Figure 6, it is instructive to note that the total error is dominated by the formal (computed) error contribution, indicating the results may be highly sensitive to our assumptions for the TDRS beacon signal. To address this concern, we examined two limiting cases. In the first, the TDRS signal was degraded by increasing the magnitude of the systematic contribution from 30 cm to 100 cm. Introducing this increase allows the partial accommodation of unmodeled ionospheric refraction errors, in addition to aggravated instrumental effects. For instance, if the TDRS beacon broadcast at S band instead of Ku band, the calibration of the ionospheric delay would yield accuracies of only a few decimeters. For the case of this degraded beacon, the maximum total error grew to 41 m (Figure 7), a value which is still lower than the 50-m requirement.

In the second case, the systematic contribution was removed entirely, but the noise was increased by a factor of 25 (from 1 cm to 25 cm for 30 minute averaging). Inasmuch as the GPS pseudorange signals were also assigned a data noise of 25 cm, this approach is analogous to the situation in which the TDRSS spacecraft are equipped with actual GPS beacons. The maximum total RSS error was 10 m, an improvement over the nominal case, showing that the 25-fold increase in the noise contribution was more than balanced by the elimination of the slowly varying bias (cf. Figure 7). Taken together, these results indicate that the greatest concern for the TDRS beacon signal lies in the minimization of the systematic, slowly varying bias introduced by the different path lengths for the GPS and TDRS signals.

It is also instructive to investigate how the period of these systematic errors in the TDRS beacon signal affect the orbit determination. To answer this question, we assigned different values to the time constant for the 30 cm bias and computed the formal position error for TDRS-W at epoch. (Recall that the nominal 1/e folding time constant, τ, was one-half day.) The results, depicted in Figure 8, indicate that the worst accuracies are experienced when the period of the systematic error is about 5 hours. As the time constant of the systematic error decreases below 5 hours, the orbit error also decreases until the limiting case of white noise is reached. This phenomenon is evidently a consequence of increased decoupling with other parameter errors, even though smaller τ represents higher process noise. Likewise, as the period approaches 1-day, the orbit error decreases as the systematic error appears more like a single constant bias over the entire 24 hour arc.

We examine now the effects of various different tracking network configurations. While it is adequate for observing TDRS-W at 171° W, the minimum network consisting of stations at the 3 DSN sites and White Sands is not well-suited for tracking TDRS-E at 41° W. The situation is best illustrated in Figure 3. TDRS-W is viewed by 2 DSN sites (Goldstone and Canberra) plus White Sands. Although the distance between the two American stations is rather short, the overall baseline orientation is adequate enough to provide the necessary geometric diversity in the observations. In contrast, TDRS-E is viewed by only Madrid and White Sands. (The elevation of TDRS-E above the horizon at

Goldstone is about 2°, rendering any observations collected there unreliable.) The network consists of a single, long baseline which can provide TDRS-E orbit accuracies no better than 300 m. Even in a best-case scenario, in which we assume that useful observations can be made from Goldstone, the maximum orbit error for TDRS-E cannot be brought below the 50 m level without tuning of Earth orientation parameters. For tracking TDRS-E, it is therefore necessary to consider an augmented tracking network.

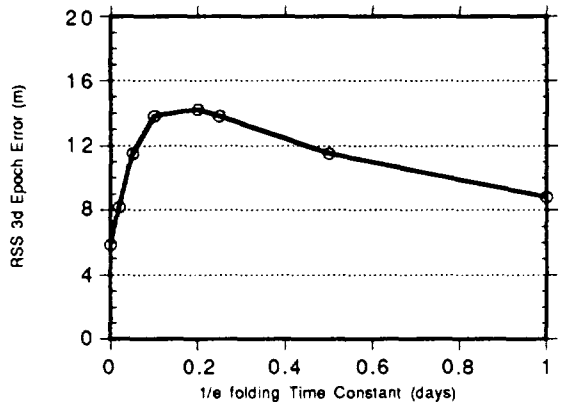

Figure 8. TDRS-W epoch position error for various systematic signal errors in TDRS beacon. The time constant refers to the period of the systematic error. The error is bound by 1 nsec (about 30 cm in range).

The simplest augmented network is a 5-station configuration consisting of the 3 DSN sites, White Sands, and the Topex site in Santiago, Chile. While the tracking geometry for TDRS-W remains identical to the nominal case, the situation for TDRS-E is dramatically improved. The introduction of the Santiago site implies that TDRS-E is observed by 3 well-distributed stations. Indeed, Table 2 reveals that with this 5-station network the TDRS-E orbit can be determined to the sub-5 m level, a factor of three better than the TDRS-W orbit.

Table 2: TDRSS orbit error for various tracking strategies

TRACKING NETWORK	TDRS-W max error	TDRS-E max error
3 DSN + White Sands	14	>300
3 DSN + White Sands + Santiago	14	4
3 DSN + 3 Topex	4	4

As a final case, we considered the 6-station Topex network. This configuration supplies the most robust and consistent geometry for observing both spacecraft – TDRS-E is observed by Madrid, Hartebeesthoek, and Santiago, while TDRS-W is viewed by Canberra, Goldstone, and Usuda. It is noteworthy that no tracking from White Sands is involved, a scenario which is attractive because: 1) Among all the sites discussed, White Sands is the only location not presently part of the operational NASA GPS network. 2) In many of the strategies, tracking of both TDRS-W and TDRS-E is required from White Sands, implying that the single TDRS channel in the reconfigured GPS receiver would have to be shared. Figure 9 shows the orbit accuracies for TDRS-W and -E throughout a 24-hour simulated arc with tracking from the full Topex network. The accuracies achieved are better than 5-m for both spacecraft, an order of magnitude better than the the 50-m requirement.

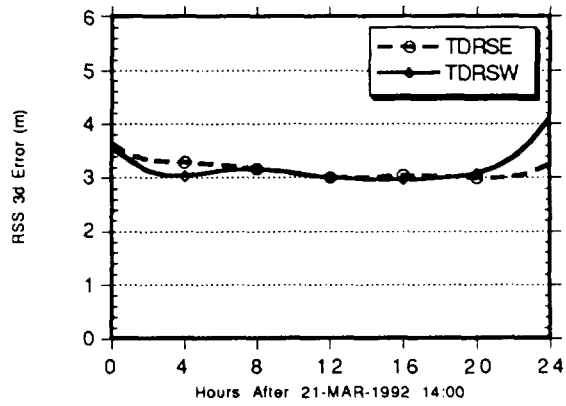

Figure 9. TDRS-E and -W position error for 24-hour arc. Orbit determined using inverted technique with tracking from 6 Topex sites. Both satellites carry nominal Ku-band beacon.

Results for Trajectory Recovery and Prediction

The TDRSS spacecraft are actively maneuvered as part of routine station-keeping activities. In order that minimum disruption to user services occurs, it is desirable to recover the trajectory as quickly as possible after the thrust maneuvers. In this section, we explore the capability of the inverted technique for determining the TDRS positions to better than 50 m within 2 hours of a thrust event. Two different approaches are adopted: In the first, a complete recovery of the TDRS epoch state immediately after the maneuver is performed. No a priori information on the TDRS trajectory is assumed. In contrast to the nominal approach outlined in the previous section, however, the GPS orbits are well determined from routine tracking for 12 hours prior to the maneuver. In the second approach, a 3-component velocity increment at the maneuver time is used to augment the TDRS state vector; thus the thrust maneuver is determined as part of the orbit determination process.

Figure 10 depicts the TDRS-W orbit accuracy as a function of time after the thrust event for these two

approaches. Two different tracking configurations are also considered. For complete orbit state recovery with the nominal tracking network, the 50-m requirement is nearly met after 2 hours. Using the full Topex network, sub 40-m accuracy can be achieved after only 2 hours of tracking. Assuming that the 3-component velocity increments can adequately model the thrust event, and moreover that the time of the maneuver is known, the 50-m requirement can be easily met with minimal tracking.

Finally, we consider how long the quality of the TDRS trajectories can be maintained after cessation of tracking. To examine this, we predicted the TDRS-W orbit state forward for 3 days following the end of the 24-hour definitive orbit determination interval. The results, shown in Figure 11, suggest that the 50-m requirement would continue to be satisfied, even with a total loss of tracking for three days.

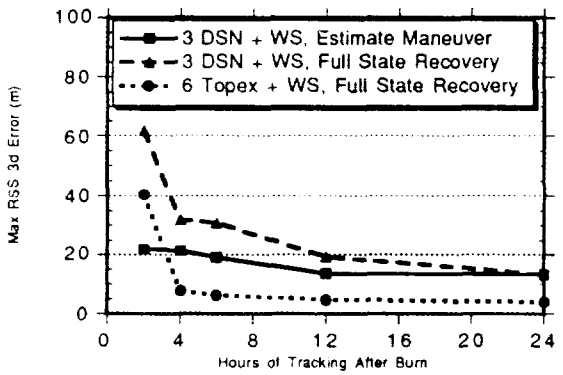

Figure 10. TDRS-W position error after station-keeping maneuver for inverted technique. Orbit after maneuver is determined either using full TDRS-W state recovery or via the solution of 3-component velocity increments.

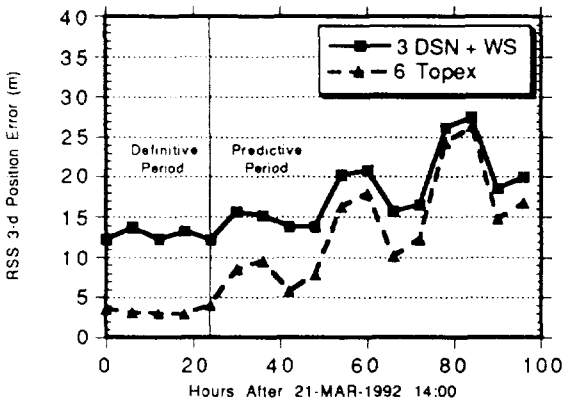

Figure 11. TDRS-W position error as a function of time for definitive and predictive orbit determination. Actual observations are reduced only for the first day.

5. DOWN-LOOKING GPS

Assumptions

For the down-looking GPS tracking option, we elected not to introduce any NASA tracking from the ground. The enhancement in accuracy that might be achieved with only a very limited number of differential observations is outweighed by the benefit of the increased autonomy associated with no ground sites. The estimation strategy for nondifferential down-looking GPS is quite different from that for the inverted option, owing in large part to the weak observability. Many of the parameters, such as the solar radiation pressure coefficient and the GPS orbit states, cannot be recovered reliably with the limited set of observations. Moreover, tracking in nondifferential mode implies that the GPS measurements are sensitive to the effects of the intentional dithering of the GPS clocks and ephemerides (SA). For our nominal case, then, we assumed that the on-board flight receiver would be a military-class instrument with a decryption module. We note that the introduction of this type of flight instrument on TDRSS-II spacecraft should not pose a problem since considerable military data are already processed through TDRSS. We assumed additionally that the receiver would represent an advanced design capable of 35 cm pseudorange measurements with averaging over 15 minutes.

Table 3: Error models for down-looking GPS

A PRIORI FOR ESTIMATED PARAMETERS		
TDRS Position (X, Y, Z)	10	km
TDRS Velocity (X, Y, Z)	1	m/s
TDRS Clock Bias	33	μsec
TDRS Clock Drift	3	nsec/s

CONSIDERED PARAMETERS	w/ decrypt.	w/o decrypt.
TDRS Solar Radiation Pressure	5 %	5 %
GPS Position (RSS 3-d)	7 m	30 m
GPS Clock Error	6 nsec	60 nsec
Earth GM	2 ppb	2 ppb

Table 3 lists the nominal set of a priori assumptions for the down-looking approach. The TDRSS spacecraft epoch positions and clock errors (bias and linear drift) served as the only estimated parameters. Solar radiation pressure was considered at 5 %, a value which is conservative in comparison with the 2 % value that is representative of current modeling efforts [26]. GPS satellite epoch states and clock errors were also considered. For the nominal case, in which it was assumed that the flight receiver was equipped with a decryption module, the GPS ephemeris and clock

errors were set at the few-m level. For the degraded case, these values were increased by a factor of 4 or more to account for the effects of SA [27].

Results for Routine Orbit Determination

Figure 12 shows the position error for TDRS-W as a function of time for nominal 24-hour tracking. Because the down-looking technique considered herein does not rely on ground tracking, the overall results are invariant to the position of the satellite and should not be much different for TDRS-E. The results suggest that with the decryption module on the TDRS satellites, the down-looking technique yields orbit accuracies at the sub-10 m level. In contrast, without the module, the position error reaches 80 m, and the 50-m requirement is not met. Longer data spans are not expected to provide appreciably higher accuracies – after 24 hours the TDRS position errors approach the limiting values governed by the GPS ephemeris and clock errors.

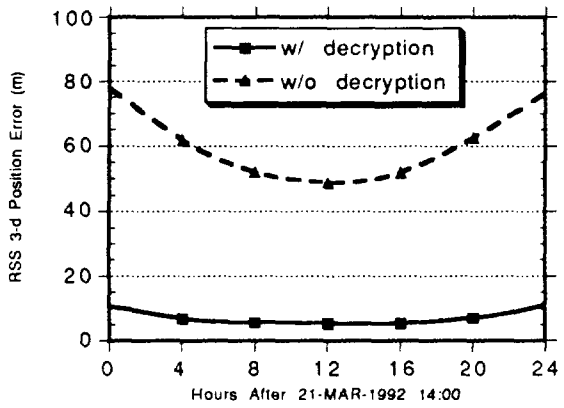

Figure 12: TDRS-W Position Error for 24-hour arc. Orbit determined using down-looking technique.

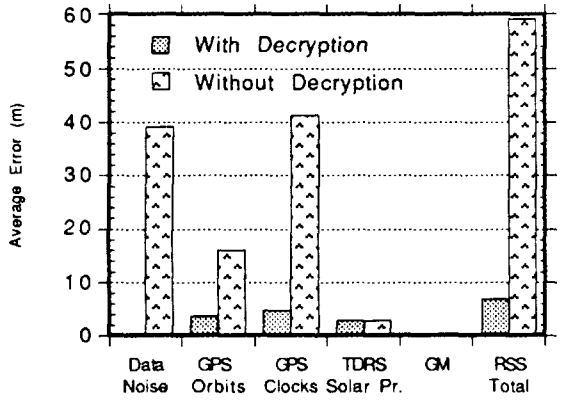

Figure 13: TDRS-W orbit error for 24-hr arc. Orbit determined using down-looking technique.

Because the TDRS orbit errors for the down-looking approach are dominated by errors in unadjusted parameters, it is instructive to examine a simple error budget. Figure 13 shows the breakdown of the TDRS-W orbit error for the 24-hour arc. For the nominal case (with decryption), the limiting error sources are the GPS clocks and ephemerides. The data noise contribution from the filter estimation is negligible, owing to the high quality of the pseudorange measurements. For the case in which the receiver is not equipped to handle SA degradation, the GPS errors increase several-fold. In addition, the data noise contribution from the filter estimation becomes quite significant. This increase reflects the dithering of the GPS clocks, which can introduce apparent range errors as high as 60 m into the pseudorange observables [27].

Results for Trajectory Recovery and Prediction

The figure of merit for evaluating the trajectory recovery capability of down-looking GPS is simply the shortest interval of tracking that can provide sub-50 m position error for TDRS. In this context, rapid recovery of the trajectory after station keeping can be achieved only if the flight receiver is equipped with a decryption module. Without the module, the TDRS position error after 2 hours of tracking is in excess of 4 km; approaching the 50-m requirement requires at least 24 hours of tracking. With the module, the 50-m requirement can be met with tracking as short as 4 hours (Figure 14).

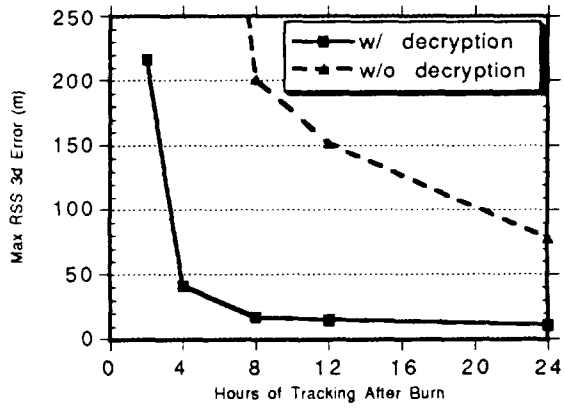

Figure 14. TDRS-W maximum position error after station-keeping maneuver for down-looking technique. Orbit after maneuver is determined using full TDRS-W orbit state recovery.

The nature of the predicted orbit error for TDRS-W was not explicitly examined for the down-looking case. We note that predicted orbit error is a function of: 1) the error in the satellite state at the beginning of the predictive interval (also called the initial condition error); and 2) the errors in the

dynamic models used to integrate the satellite position. To the extent that the initial condition errors for the down-looking and inverted approaches are roughly equivalent in magnitude, the predictive errors should also be similar. In this context, we conclude that the 50-m requirement cannot be met during the predictive interval unless the flight receiver is equipped with a decryption module. Without the module, the errors in the initial conditions estimated with 24-hours of tracking prior to the predictive interval would exceed the 50-m threshold. With the module, sub-15 m initial condition error is achieved after 24-hours of tracking, and the pattern of the predicted error would likely be similar to that shown in Figure 11.

6. CONCLUSIONS

We have explored two GPS-based strategies for tracking the geosynchronous TDRSS spacecraft. Direct tracking of the TDRSS spacecraft from the GPS constellation promises the greatest autonomy since no ground network is required. For this strategy, the primary impairment is the poor geometry—the TDRSS spacecraft must look down to find signals broadcast from GPS satellites on the other side of the Earth. The situation is exacerbated by sensitivity of the TDRS orbit accuracy to Selective Availability (SA), because measurements from the ground cannot be exploited to form differential observations which are free from these effects. In order to circumvent this difficulty, the TDRS-II satellites can carry military qualified GPS flight receivers which are designed to decrypt the degraded signals. Our results suggest that, equipped in this manner, a GPS receiver should be able to provide the TDRS positions autonomously to better than 15 m for routine 24-hour tracking. Implicit in this result is the assumption that nominal Department of Defense operations are maintained. Moreover, if this technique is adopted, the effects of the long GPS to TDRS transmission paths and near-Earth grazing need to be further examined.

An alternative approach relies on simultaneous tracking of TDRSS and GPS beacon signals from the ground. If accuracy is the prime concern, then this inverted technique is the best suited for tracking geosynchronous orbiters. However, the introduction of a ground network makes it less autonomous than its down-looking counterpart. For this study, we relied on a small number of current NASA GPS tracking sites and assumed that the receivers operating at those sites would be retrofitted to track TDRSS-II on 1 of the 8 channels that are normally reserved for GPS. Moreover, we assumed that the TDRSS-II spacecraft would be configured to broadcast continuously a suitable wide-beam beacon signal, preferably at Ku band to mitigate the effects of ionospheric refraction. Our results suggest that data collected at the ground sites introduces a robust differential observation geometry that promises to deliver few-m accuracies for TDRS with as few as 6 global stations. Smaller networks could still meet the 50-m TDRSS accuracy requirement, but each satellite must be observed by a minimum of 3 stations that are moderately well distributed. The TDRSS-II orbit determination activities could be incorporated into routine GPS data processing that is currently done at JPL to support ongoing NASA programs. The mechanisms for near real-time operations are already in place, as the GPS data from these remote sites are transmitted to JPL on a daily basis for automated processing.

ACKNOWLEDGEMENTS

The research described in the paper was performed at the Jet Propulsion Laboratory, California Institute of Technology, under contract with the National Aeronautics and Space Administration. The authors would like to thank Larry Young for providing the fundamental design and signal characteristics of the proposed GPS/TDRSS Rogue satellite receiver.

REFERENCES

[1] Holmes, W. J, Jr., NASA's Tracking and Data Relay Satellite System, *IEEE Communications Magazine*, September, 1978.

[2] Teles, J., Y. Nakai, and M. V. Samii, TDRS tracking and orbit determination, presented at CNES Intl. Conference on Space Dynamics for Geostationary Satellites, Toulouse, France, October, 1985.

[3] A. Long, R. Potash, A. Jacobsen, J. McCarthy *et al.*, Advanced tracking systems design and analysis, *Computer Sciences Corporation Contractor Report, CSC/TM-88/6060*, September, 1989.

[4] Weinberg, A., D. D. Elrod, D. F. Eggerts, and A. Jacobsen, Assessment of candidate ATDRS tracking techniques, *Stanford Telecom Contractor Report, TR91002*, May, 1991.

[5] Ray, J., C. Knight, N. Zelensky, P. Liebrecht, and A Jones, VLBI Tracking of the TDRS, *J. Astronaut. Sci., 36(4)*, 347–364, 1988.

[6] Nandi, S., C. Edwards, and S. C. Wu, TDRSS orbit determination using short-baseline differenced carrier phase, paper presented at NASA Goddard Flight Mechanics Estimation Theory Symposium, May, 1992.

[7] Wu, S. C., Differential GPS approaches to orbit determination of high-altitude satellites, *AAS paper 85-430*, Astrodynamics Specialists Conference, Vail, Colo., August, 1985.

[8] Janiczek, P. M., ed., Global Positioning System papers published in *Navigation* , Institute of Navigation, Washington, D. C., 1980.

[9] Yunck, T. P., W. G. Melbourne, and C. L. Thornton, GPS-based satellite tracking system for precise positioning, *IEEE Trans. Geoscience Remote Sensing*, GFE-23, 450–457, 1985.

[10] Yunck, T. P., S. C. Wu, S. M. Lichten, W. I. Bertiger, U. J. Linqwister and G. Blewitt, Toward centimeter orbit

determination and millimeter geodesy with GPS, Proc. 5th Int. Geodetic Symposium on Satellite Positioning., 1, 272–281, 1989.

[11] Yunck, T. P., S. C. Wu, J. T. Wu and C. L Thornton, Precise tracking of remote sensing satellites with the Global Positioning System, *IEEE Trans. Geoscience Remote Sensing*, 28(1), 108–116, 1990.

[12] Yunck, T. P., and S. C. Wu, Non-dynamic decimeter tracking of Earth satellites using the Global Positioning System, *AIAA Paper 86-0404*, presented at 24th Aerospace Sciences Meeting, Reno, Nev., Ja., 1986.

[13] Wu, S. C., T. P. Yunck, and C. L. Thornton, Reduced dynamic technique for precise orbit determination of low-Earth satellites, *J. Guidance Contr. and Dyn., 12(1)*, 24–30, 1991.

[14] Fu, L, E. J. Christensen, and M. Lefebvre, Topex/Poseidon: The ocean topography experiment, *EOS Trans., 72(35)*, 369,372–373, 1991.

[15] Yunck, T. P., and S. C. Wu, Ultra-precise orbit determination by GPS, *AAS Paper 83–315*, presented at Astrodynamics Specialists Conference, Lake Placid, N.Y., August, 1983.

[16] Wu, S. C., and C. L. Thornton, OASIS–A new GPS covariance and simulation analysis software system, paper presented at 1st Int. Symposium on Precise Positioning with GPS, IUGG, Rockville, Md., 1985.

[17] Bierman, G. J., *Factorization Methods for Discrete Sequential Estimation*, Academic Press, Orlando, 1977.

[18] Thomas, J. B., Functional description of signal processing in the Rogue GPS receiver, *JPL pub. 88-15*, 1988.

[19] K. Zukor, Comparison of NCB and TurboRogue Phase Measurements, Jet Propulsion Lab., IOM 335.1–91–016, May 15, 1991.

[20] Srinivasan, J. M., T. K. Meehan and L. E. Young, Code and codeless ionospheric measurements with NASA's Rogue GPS receiver, proceedings of the Inst. of Nav. GPS–89 Conference,

[21] Lichten, S. M., and J. S. Border, Strategies for high-precision Global Positioning System orbit determination, *J. Geophys. Res.*, 92, 12751–12762, 1987.

[22] Blewitt, G., M. B. Heflin, F. H. Webb, U. L. Linqwister, and R. P. Malla, Global coordinates with centimeter accuracy in the International Terrestrial Reference Frame using the Global Positioning System, submitted to *Geophys. Res. Let.*, February, 1992.

[23] Lerch, F. J., S. M. Klosko, R. E. Laubscher, and C. A. Wagner, Gravity model improvement using GEOS-3 (GEM-9 and 10), *J. Geophys. Res., 84*, 3897–3915, 1979.

[24] Lerch, F. J., S. M. Klosko, and B. G. Patel, A refined gravity model from Lageos (GEM-L2), *Geophys. Res. Letters, 9(11)*, 1263–1266, 1982.

[25] Lerch, F. J., *et al.*, Geopotential Models of the Earth from Satellite Tracking, Altimeter, and Surface Gravity Observations: GEM-T3 and GEM-T3S, *NASA Tech. Memo.104555*, January, 1992.

[26] Bobrowsky, M., P.Y. Kay, A. K. Drew, S. L. Hoge, and O. O. Cuevas, Short- and long-term determination of the TDRS solar reflectivity parameter using the Goddard Trajectory Determination System, *AAS Paper 87–531*, presented at Astrodynamics Specialists Conference, Kalispell, Mt., 1987.

[27] Davis, E. S., W. G. Melbourne, and T. P. Yunck, GPS applications to space-based remote sensing missions: coping with denial of accuracy, proceedings of the 2nd Intl. Symposium of Positioning with GPS, Ottawa, 1990.

TDRSS-User Orbit Determination Using Batch Least-Squares and Sequential Methods*

D. H. Oza, T. L. Jones, M. Hakimi, and M.V. Samii
COMPUTER SCIENCES CORPORATION (CSC)

C. E. Doll, G. D. Mistretta, and R. C. Hart
GODDARD SPACE FLIGHT CENTER (GSFC)

ABSTRACT

The Goddard Space Flight Center (GSFC) Flight Dynamics Division (FDD) commissioned Applied Technology Associates, Incorporated, to develop the Real-Time Orbit Determination/Enhanced (RTOD/E) system on a Disk Operating System (DOS)-based personal computer (PC) as a prototype system for sequential orbit determination of spacecraft . This paper presents the results of a study to compare the orbit determination accuracy for a Tracking and Data Relay Satellite System (TDRSS) user spacecraft, Landsat-4, obtained using RTOD/E, operating on a PC, with the accuracy of an established batch least-squares system, the Goddard Trajectory Determination System (GTDS), operating on a mainframe computer. The results of Landsat-4 orbit determination will provide useful experience for the Earth Observing System (EOS) series of satellites.

The Landsat-4 ephemerides were estimated for the January 17–23, 1991, timeframe, during which intensive TDRSS tracking data for Landsat-4 were available. Independent assessments were made of the consistencies (overlap comparisons for the batch case and covariances and the first measurement residuals for the sequential case) of solutions produced by the batch and sequential methods.

The forward-filtered RTOD/E orbit solutions were compared with the definitive GTDS orbit solutions for Landsat-4; the solution differences were less than 40 meters after the filter had reached steady state.

* This work was supported by the National Aeronautics and Space Administration (NASA)/Goddard Space Flight Center (GSFC), Greenbelt, Maryland, under Contract NAS 5-31500.

1. INTRODUCTION

This paper compares the orbit determination accuracy of a prototype sequential orbit determination system with the accuracy achieved using an established batch least-squares system for a Tracking and Data Relay Satellite (TDRS) System (TDRSS) user spacecraft.

The National Aeronautics and Space Administration (NASA) has completed a transition from tracking and communications support of low Earth-orbiting satellites with a ground-based station network, the Ground Spaceflight Tracking and Data Network (GSTDN), to the geosynchronous relay satellite network, the TDRSS. TDRSS currently consists of three operational geosynchronous spacecraft (TDRS-East, TDRS-West, and TDRS-Spare) and the White Sands Ground Terminal (WSGT) at White Sands, New Mexico. TDRS-East, TDRS-West, and TDRS-Spare are located at 41, 171, and 174 degrees west longitude, respectively. The target TDRSS relay constellation will consist of four operational TDRSs, one each at 174, 171, 62, and 41 degrees west longitude. The ground network can provide only about 15-percent visibility coverage, while TDRSS has the operational capability to provide 85-percent to 100-percent coverage, depending on the spacecraft altitude.

The Bilateration Ranging Transponder System (BRTS) provides range and Doppler measurements for maintaining each TDRS orbit. The ground-based BRTS transponders are tracked as if they were TDRSS user spacecraft. Since the positions of the BRTS transponders are known, their ranging data can be used to precisely determine the trajectory of the TDRSs.

The focus of this paper is an assessment of the relative orbit determination accuracy of the batch least-squares method, used for current operational orbit determination support, with that of a sequential method implemented in a prototype system, used for analysis in the GSFC Flight Dynamics Facility (FDF). The batch weighted least-squares algorithm implemented in the Goddard Trajectory Determination System (GTDS) estimates the sets of orbital elements, force modeling parameters, and measurement-related parameters that minimize the squared difference between observed and calculated values of selected tracking data over a solution arc (Reference 1). GTDS resides and operates on the mainframe computer system at the FDF.

The sequential estimation algorithm implemented in a prototype system, the Real-Time Orbit Determination/ Enhanced (RTOD/E), simultaneously estimates the TDRSS user and relay spacecraft orbital elements and other parameters in the force and observation models at each measurement time (Reference 2). RTOD/E performs forward filtering of tracking measurements using the extended Kalman filter with a process noise model to account for serially correlated, geopotential-induced errors, as well as Gauss-Markov processes for drag, solar radiation pressure, and measurement biases. The main features of RTOD/E are summarized in Reference 3.

An orbit determination analysis of Landsat-4 using TDRSS is reported here. Motivation for an orbit determination evaluation of Landsat-4 derives from the fact that the orbital characteristics of Landsat-4 are similar to those of the Earth Observing Satellite (EOS) series of missions, planned for launch starting in 1998. The results of a study for Landsat-4 will provide useful experience and verification of EOS flight dynamics support requirements. Early assessment of conclusions regarding meeting EOS support requirements will provide adequate opportunity to develop comprehensive support scenarios.

The estimated Landsat-4 ephemerides were obtained for the January 17–23, 1991, timeframe. This particular timeframe was chosen because dense TDRSS tracking data for Landsat-4 were available. Independent assessments were made to examine the consistencies (overlap comparisons for the batch case and state error covariances and the first measurement residuals for the sequential case) of results obtained by the batch and sequential methods.

Section 2 of this paper describes the orbit determination and evaluation procedures used in this study, and Section 3 gives the results obtained by the batch least-squares and sequential estimation methods and provides the resulting consistency and cross comparisons. Section 4 presents the conclusions of this study.

2. ORBIT DETERMINATION AND EVALUATION PROCEDURE

This section describes the analysis procedures used in this study. The TDRSS and BRTS tracking data characteristics are presented in Section 2.1, and the orbit determination evaluation methodology and options used are described in Section 2.2.

2.1 Tracking Measurements

Landsat-4 was deployed by Delta-3920 in July 1982. It has a nearly circular orbit, an altitude of approximately 715 kilometers, an inclination of 98 degrees, and a period of approximately 99 minutes. The time period chosen for this study was from 0 hours Greenwich mean time (GMT) on January 17, 1991, through 10 hours GMT on January 24, 1991.

During this interval, unusually dense TDRSS tracking of the Landsat-4 satellite was made available. The tracking consisted of an average of 15 passes of two-way TDRSS range and Doppler observations each day, each pass ranging from 3 minutes to 45 minutes in duration. The normal TDRSS tracking of Landsat-4 (less dense) typically consists of about six 5-minute passes each day. A timeline plot of the TDRSS tracking data distribution is given in Figure 1.

The typical scenario for BRTS tracking of the TDRSs during the period of study included approximately 4 or 9 minutes of range and two-way Doppler measurements from two ground transponders for each relay every 2 to 3 hours, consisting of an average of 12 BRTS passes per TDRS each day. BRTS stations for TDRS-East are located at White Sands and Ascension Island. BRTS stations for TDRS-West are located at White Sands, American Samoa, and Alice Springs, Australia.

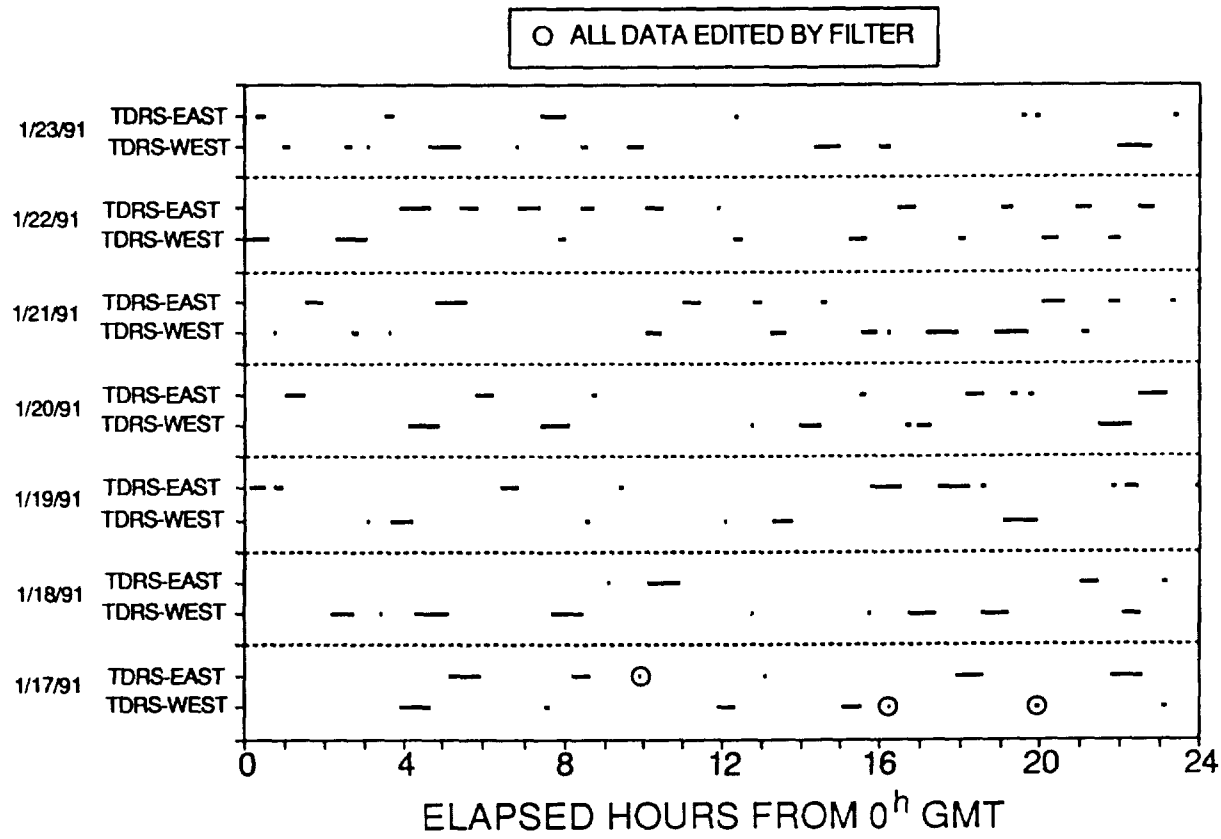

Figure 1. Tracking Data for Landsat-4

2.2 Evaluation Methodology

The evaluation methodologies for the batch least-squares and sequential estimation methods are described below. Since there are some known differences between the GTDS and RTOD/E force models (geopotential, atmospheric density, solar and planetary ephemerides presentation, solid Earth tides, and process noise modeling), and since the RTOD/E TDRSS and BRTS measurement models were implemented independently from GTDS, the two systems are not expected to provide identical results. Therefore, this study assumes that each system is used in its optimal configuration. Table 1 gives the parameters and options for the simultaneous solutions of the user and relay spacecraft. Table 2 gives the force and measurement model specifications.

Table 1. Parameters and Options for the Simultaneous Solutions of User and Relay Spacecraft

ORBIT DETERMINATION PARAMETER OR OPTION	GTDS VALUES		RTOD/E VALUES	
	USER (LANDSAT-4)	RELAY (TDRS-EAST & TDRS-WEST)	USER (LANDSAT-4)	RELAY (TDRS-EAST & TDRS-WEST)
ESTIMATED PARAMETERS	STATE, DRAG SCALING PARAMETER (ρ_1), RANGE AND DOPPLER MEASUREMENT BIASES FOR TRACKING VIA EACH GROUND STATION	STATE, TRANSPONDER DELAYS FOR EACH BRTS TRANSPONDER	STATE, COEFFICIENT OF DRAG, RANGE AND DOPPLER MEASUREMENT BIASES FOR TRACKING VIA EACH TDRS	STATE, SOLAR REFLECTIVITY COEFFICIENT (C_R), RANGE AND DOPPLER MEASUREMENT BIASES FOR TRACKING VIA EACH TRANSPONDER
INTEGRATION TYPE	FIXED-STEP COWELL	FIXED-STEP COWELL	VARIATION OF PARAMETERS	VARIATION OF PARAMETERS
COORDINATE SYSTEM OF INTEGRATION	MEAN OF 1950.0	MEAN OF 1950.0	MEAN OF 1950.0	MEAN OF 1950.0
INTEGRATION STEP SIZE (SECONDS)	30.0	600.0	60.0	600.0
TRACKING DATA	TDRSS	BRTS	TDRSS	BRTS
DATA RATE	1 PER 20 SECONDS	1 PER 10 SECONDS	1 PER 20 SECONDS	1 PER 20 SECONDS
DC CONVERGENCE PARAMETER	0.005	0.005	N/A	N/A
EDITING CRITERION	3σ	3σ	3σ	3σ
MEASUREMENT σ's:				
RANGE	30.0 METERS	10.0 METERS	0.4 METER	0.4 METER
DOPPLER	0.25 HERTZ	0.003 HERTZ	0.004 HERTZ	0.003 HERTZ
GAUSS-MARKOV PARAMETERS:	N/A	N/A		
DRAG HALF-LIFE			1440 MINUTES	N/A
DRAG SIGMA			0.207	N/A
C_R HALF-LIFE			N/A	11520 MINUTES
C_R SIGMA			N/A	0.2
RANGE BIAS HALF-LIFE			60 MINUTES	60 MINUTES
RANGE BIAS SIGMA			6 METERS	4.5 METERS
DOPPLER BIAS HALF-LIFE			8 MINUTES	60 MINUTES
DOPPLER BIAS SIGMA			0.034 HERTZ	0.02 HERTZ
SATELLITE AREA	12.26 METERS^2	40 METERS^2	12.26 METERS^2	40.0 METERS^2
SATELLITE MASS	1900 KILOGRAMS	1991 KILOGRAMS (TDRS-EAST) 1735 KILOGRAMS (TDRS-WEST)	1900 KILOGRAMS	1991 KILOGRAMS (TDRS-EAST) 1735 KILOGRAMS (TDRS-WEST)

6130L-5

N/A = NOT APPLICABLE

Table 2. Force and Measurement Model Specifications

ORBIT DETERMINATION PARAMETER OR OPTION	GTDS VALUES		RTOD/E VALUES	
	USER (LANDSAT-4)	RELAY (TDRS-EAST & TDRS-WEST)	USER (LANDSAT-4)	RELAY (TDRS-EAST & TDRS-WEST)
GEOPOTENTIAL MODEL	GEM-T3 (50 x 50)	GEM-T3 (8 x 8)	GEM-10B (30 x 30)	GEM-10B (6 x 6)
ATMOSPHERIC DENSITY MODEL	JACCHIA-ROBERTS DAILY SOLAR FLUX VALUES (209, 203, 199, 204, 202, 224, 223)	N/A	CIRA 1972 DAILY SOLAR FLUX VALUES (209, 203, 199, 204, 202, 224, 223)	N/A
SOLAR AND LUNAR EPHEMERIDES	JPL DE-118	JPL DE-118	ANALYTICAL	ANALYTICAL
SOLAR REFLECTIVITY COEFFICIENT (C_R)	1.5	APPLIED (SEE TEXT)	1.5	ESTIMATED
COEFFICIENT OF DRAG (C_D)	ESTIMATED	N/A	ESTIMATED	N/A
IONOSPHERIC REFRACTION CORRECTION	BENT MODEL	BENT MODEL	NO	NO
GROUND-TO-SPACECRAFT	N/A	YES		
SPACECRAFT-TO-SPACECRAFT	YES	N/A		
TROPOSPHERIC REFRACTION CORRECTION	YES	YES	YES	YES
POLAR MOTION CORRECTION	YES	YES	YES	YES
EARTH TIDES	YES	NO	NO	NO

GEM = GODDARD EARTH MODEL
JPL = JET PROPULSION LABORATORY
N/A = NOT APPLICABLE

6130L-5

Batch Least-Squares Method

Except for the variations noted, the computational procedures and mathematical methods used in this study are those used for routine operational orbit determination in the GSFC FDF. The choice to expand the state space of the least-squares solutions to include measurement biases was motivated by the fact that the RTOD/E orbit determination algorithm estimates an equivalent set of bias parameters. The batch weighted least-squares algorithm implemented in GTDS (Reference 1) solves for the set of orbital elements and other parameters that minimizes the squared difference between observed and calculated values of selected tracking data over a solution arc. Parameters solved for, other than the spacecraft state at epoch, include free parameters of the force model and/or the observation model.

A detailed study of the Earth Radiation Budget Satellite (ERBS) with the batch least-squares estimation method was reported in Reference 4, and it was further refined in Reference 5. The models and options found optimal in the previous study of ERBS are used here for Landsat-4. The options used for the study described in this paper are summarized in columns 2 and 3 of Tables 1 and 2.

The solar reflectivity coefficients (C_R) for TDRS-East and TDRS-West were not estimated in the simultaneous solutions of Landsat-4, TDRS-East, and TDRS-West but were applied. The values of C_R applied in the present calculations were obtained from a set of separate companion solutions of TDRS-East and TDRS-West using only BRTS tracking data.

To evaluate the orbit determination consistency achievable with a particular choice of options using least-squares estimation, a series of seven 34-hour definitive solutions was performed with 10-hour overlaps between neighboring arcs. The GTDS Ephemeris Comparison Program was used to determine the root-mean-square (RMS) position differences between the definitive ephemerides for neighboring solutions in the 10-hour overlap time period. These "overlap" comparisons measure the adjacent solution consistency, not the absolute accuracy.

Sequential Estimation Method

RTOD/E was recently developed by Applied Technology Associates, Incorporated (ATA) for the GSFC Flight Dynamics Division (FDD) to respond to the need for a realtime estimation capability, to address future increased TDRSS-navigation accuracy requirements, and to provide automation of some routine orbit determination operations. The goal for future orbit determination accuracy is 10 meters total position error (1σ) for the user and 25 meters total position error (1σ) for the TDRSs. RTOD/E provides a proof of concept for the use of sequential estimation techniques for orbit determination with TDRSS tracking data and offers the potential for enhanced accuracy navigation with realtime responsiveness. RTOD/E is a research tool for assessing sequential estimation for FDF navigation applications in realistic operational situations.

RTOD/E uses the extended Kalman filter form for sequential orbit estimation. With the sequential estimation method, each tracking measurement can be processed immediately upon receipt to produce an update of a spacecraft's state vector and auxiliary state parameters. This fact makes it well suited for realtime or near-realtime operation. Sequential estimation is particularly well suited to the development of systems to perform orbit determination autonomously on the spacecraft's onboard computer (Reference 6). Spacecraft orbit determination during and just after a maneuver is a critical support function for which orbit determination is needed in near-realtime. Therefore, sequential estimation is also well suited for such an application. In addition, the forward filter can be augmented with a backward smoothing filter to further improve the overall accuracy, especially during periods without tracking data.

RTOD/E employs a sequential estimation algorithm with a process noise model to stochastically account for gravity model errors (Reference 7). In addition to the spacecraft orbital elements, the filter estimates free parameters of the force model and the measurement model, treating these parameters as random variables whose behavior is governed by a Gauss-Markov stochastic process.

RTOD/E uses a forward-processing extended Kalman filter for sequential orbit estimation. The mathematical algorithms and computational procedures are described in References 2 and 7. The specific options used in RTOD/E for this study are listed in the last two columns of Tables 1 and 2.

A good indicator of the consistency of the sequential estimation results is provided by the state error covariance function generated during the estimation process (Reference 8). In addition, the relationship of the first predicted measurement residual of each tracking pass to the associated predicted residual variance provides an indication of the physical integrity of the state error covariance of the filtered orbits. These parameters were monitored during the sequential estimation process.

3. RESULTS AND DISCUSSION

The results of this study for the Landsat-4 and TDRSS relay spacecraft are presented in this section, along with an analysis of the results. Greater emphasis is placed on the Landsat-4 results, since the primary objective is to study TDRSS user orbit determination. The orbit determination results using batch least-squares calculations and sequential estimation are given in Sections 3.1 and 3.2, respectively; the comparisons are presented in Section 3.3.

3.1 Batch Least-Squares Results

The RMS values of six Landsat-4 overlap comparisons are summarized in Figure 2. The overlap values vary from about 3 to 5 meters. The mean and sample standard deviation of this distribution, in the form of mean $\pm$ standard deviation, is 3.8 $\pm$ 1.0 meters. The maximum total position differences over the same distribution vary between 5 and 9 meters, with a mean and standard deviation of 6.1 $\pm$ 1.8 meters. The maximum position difference values for Landsat-4 are typically a factor of 1.6 larger than the RMS values.

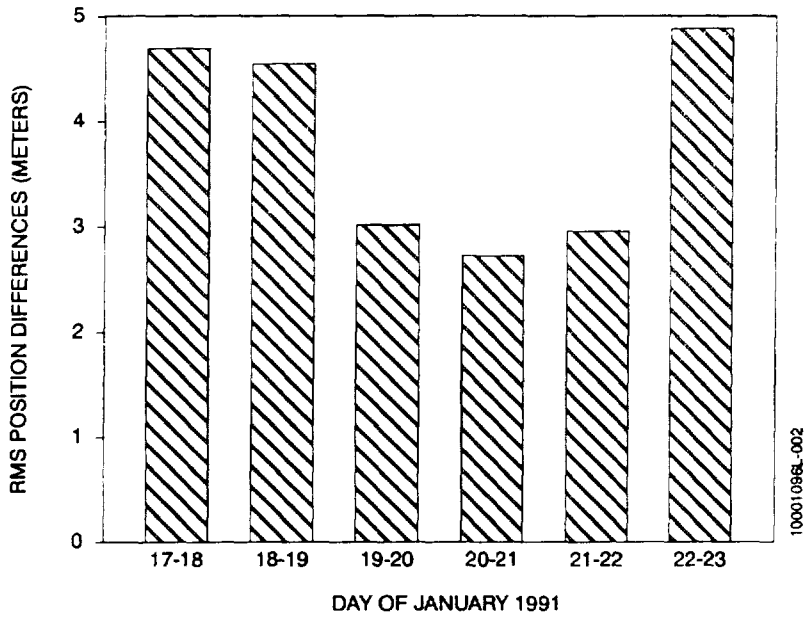

Figure 2. Landsat Overlap Comparisons

It should be noted that all data arcs for Landsat-4 solutions consisted of 34 hours, beginning at 0 hours GMT of each day from January 17 to January 23, 1991, with one exception. The exception was made for the arc beginning at 0 hours GMT on January 20, 1991. There is a long data gap of about 5 hours (see Figure 1) at the end of the nominal 34-hour period, resulting in a predicted solution for the last 5 hours instead of a definitive solution. Therefore, for this particular solution, the arc length was extended by 2 hours to 36 hours so that the next tracking pass was included in the solution.

The RMS values of six TDRS-East and TDRS-West overlap comparisons are summarized in Figure 3. The overlap values for TDRS-East vary from about 7 to 30 meters. The mean and sample standard deviation of this distribution is 14.2 ± 7.8 meters. The maximum total position differences over the same distribution vary between 9 and 35 meters, with a mean and standard deviation of 19.1 ± 9.1 meters. The overlap values for TDRS-West vary from about 10 to 55 meters. The mean and the sample standard deviation of this distribution is 21.6 ± 16.9 meters. The maximum total position differences over the same distribution vary between 12 and 74 meters, with a mean and standard deviation of 26.2 ± 23.8 meters. The maximum position difference values for the TDRSs are typically a factor of 1.2 larger than the RMS values.

The possible advantage of estimating a set of bias parameters versus not estimating the set was evaluated. The mean values of the TDRSS range and Doppler measurement residuals (i.e., the observed-minus-computed values for each solution) calculated without estimating biases indicated the existence of a small systematic error. The mean range measurement residuals varied between –0.8 ± 3.0 meters and +1.1 ± 3.5 meters for the seven solution arcs. The mean Doppler measurement residuals varied between –15.8 ± 80.3 millihertz and –3.8 ± 85.3 millihertz. The estimation of a set of bias parameters in the calculations in this study effectively removed the systematic error, thereby significantly reducing the mean range (0.4×10^{-6} to 0.2×10^{-4} meters) and mean Doppler measurement (0.2×10^{-7} to 0.3×10^{-3} millihertz) residual values, as expected. The standard deviations of the residuals were also somewhat reduced. However, although the removal of a bias may improve accuracy, it was not expected to improve consistency. As a matter of fact, the mean RMS overlap value without estimating for a set of bias parameters was larger for Landsat-4 (4.7 ± 1.1 meters) and for TDRS-East (38.5 ± 13.2 meters) and somewhat smaller for TDRS-West (15.1 ± 10.4 meters).

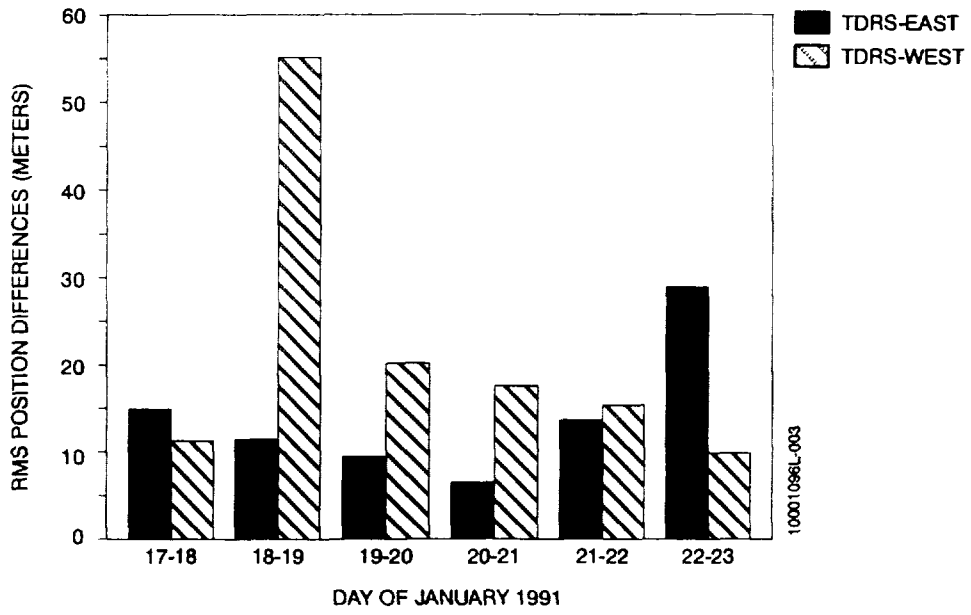

Figure 3. TDRS-East and TDRS-West Overlap Comparisons

3.2 Sequential Estimation Results

During sequential processing of the TDRSS and BRTS measurements using RTOD/E, the position component standard deviations from the state error covariance function (3σ) were closely monitored. The filter was started with high initial diagonal values in the covariance matrix. In the initial phases of filtering, the 3σ values were as high as 6000 meters for Landsat-4 and were 1200 meters for the TDRSs. This is not unusual before the filter has reached steady-state performance, especially considering that there is no TDRSS data for Landsat-4 in the first 4 hours (see Figure 1). After an initial filter settling period (about 24 hours), the 3σ values varied from about 10 to 40 meters in the RMS position for Landsat-4 and 40 to 60 meters for the TDRSs. The 3σ values for Landsat-4 dropped to their lowest levels during a tracking pass and then gradually rose to the maximum values during the time update phase (propagation phase). (The duration of the time update phases can be seen in Figure 1.) Unlike Landsat-4, the 3σ values for the TDRSs continued to decline gradually for about 4 days. Subsequently, the 3σ values for TDRS-West and TDRS-East remained relatively steady at about 25 meters and 35 meters, respectively.

The first predicted range residuals of Landsat-4 tracking passes after the filter processed the tracking data for 6 days are shown in Figure 4a. The tracking passes via TDRS-East and TDRS-West are plotted separately. The value of the residual varied from nearly −12 meters to about 12 meters. The largest value occurred after about 1 hour of the prediction period following the previous tracking pass. The ratio of the predicted range residual to the predicted residual standard deviation corresponding to Figure 4a is plotted in Figure 4b. The first residual of each pass was within the 3σ bound in the residual space. The postmeasurement-update range residuals were negligibly small, typically of the order of 0.3 meter or less.

The estimated force model parameters varied as a function of time and were updated after each measurement was processed. The time variation of the atmospheric drag coefficient for Landsat-4 is shown in Figure 5. It varied from a low value of 1.6 to a high value of 3.0. The 3σ uncertainty boundary (C_D minus the 3σ uncertainty) in the drag parameter on the lower side is also plotted in NO TAG. The boundary on the upper side (C_D plus the 3σ uncertainty) is not plotted so as not to clutter the figure. The variations in the drag parameter are smaller than the 3σ uncertainty. The 3σ uncertainty converges to an approximate value of 1.2 at

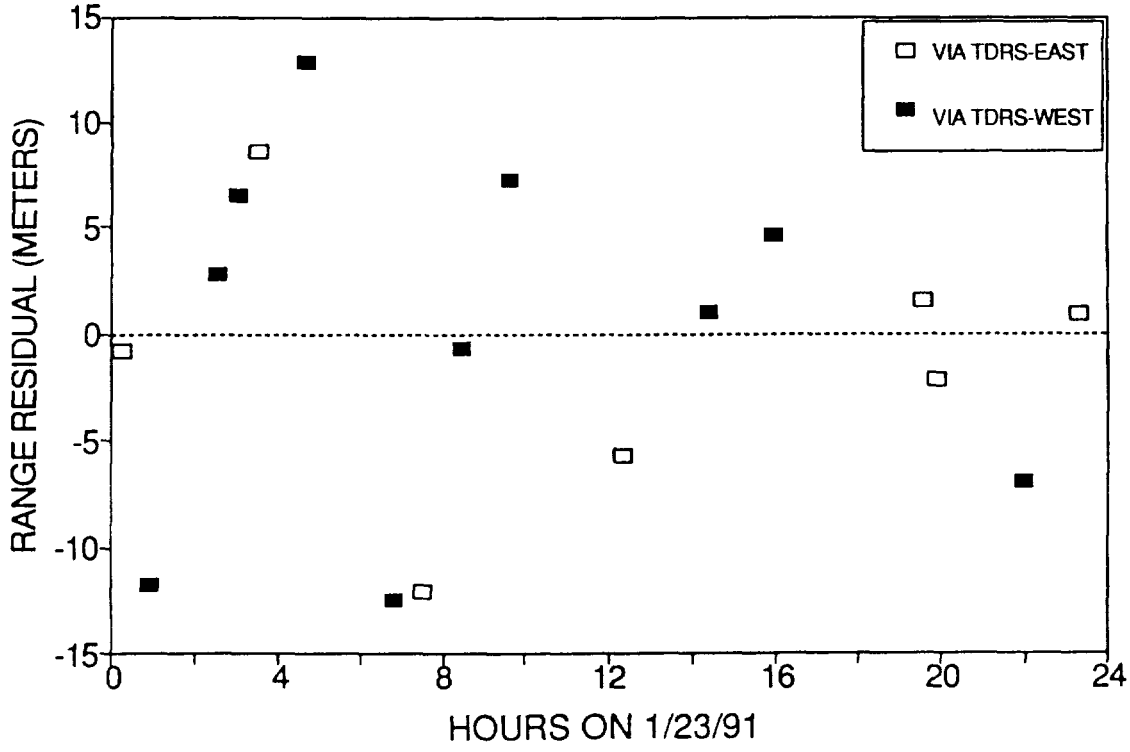

Figure 4a. First Predicted Range Residual of TDRSS Tracking Passes for Landsat-4

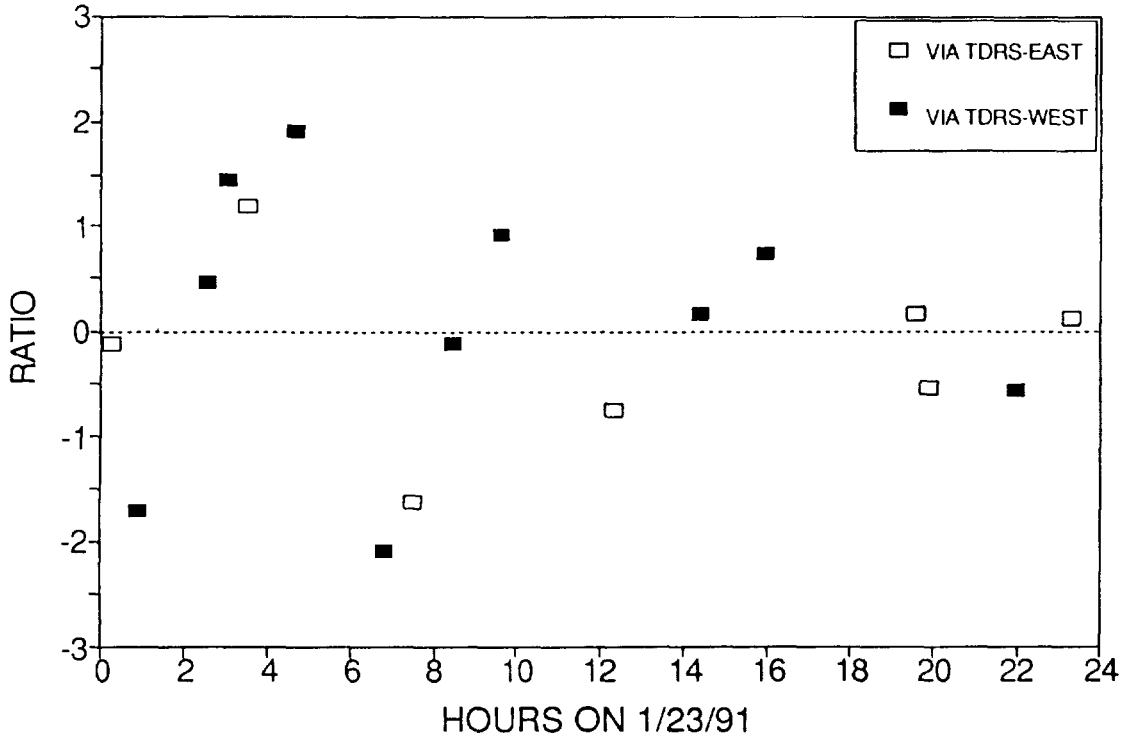

Figure 4b. Ratio of the Predicted Range Residual to the Predicted Standard Deviation

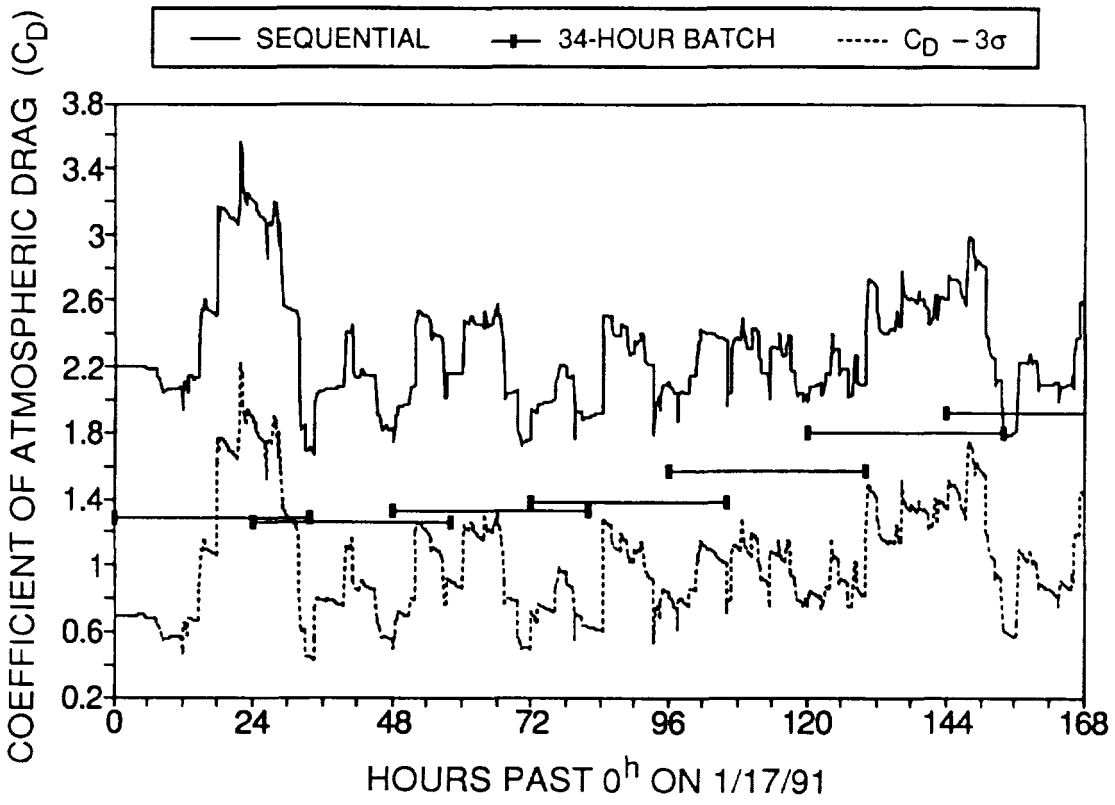

Figure 5. Coefficient of Atmospheric Drag (C_D) for Landsat-4

steady state. The time variations of the solar radiation pressure coefficient for TDRS-East and TDRS-West are given in Figures 6 and 7, respectively, along with the 3σ uncertainty boundaries ($C_R \pm 3\sigma$ uncertainty). After the filter reached steady state, the coefficient varied between 1.3 and 1.5. The variations in the estimated solar radiation pressure coefficients are smaller than the 3σ uncertainty, which varies between 0.15 and 0.2 at steady state. The estimated values obtained from the batch least-squares solutions are also shown in Figures 5 through 7 for comparison.

The solar flux values are input to RTOD/E on a daily basis. The time variation of the flux value over the 24-hour period is not input. Therefore, the atmospheric drag coefficient must be adjusted to compensate for the variation (NO TAG). RTOD/E models the area of the TDRS to be a constant throughout the day, whereas in actuality the TDRS surface area exposed to the solar flux varies with a 24-hour period. The C_R estimated values for TDRS-East, shown in Figure 6, display an approximately repeated variation over 24 hours for the last 5 days during steady-state performance. Such a clear signature of variation is not evident in the C_R values for TDRS-West shown in Figure 7.

The time variation of the estimated range bias values for Landsat-4 via TDRS-East and TDRS-West are shown in Figures 8 and 9, respectively, along with the 3σ uncertainties. The bias values varied from approximately –15 meters to approximately 10 meters, with an average value of approximately –1 meter. The 3σ uncertainty is 18 meters during data gaps. During tracking passes, it reduces to about 7 meters; following each tracking pass, it returns to 18 meters, with a half-life of 60 minutes (a priori input; see Table 1). There are some known physical phenomena and considerations that are absorbed in the estimation of the range bias: the time-varying tropospheric refraction delay and ionospheric refraction delay, which are not modeled in the measurement model; static position biases; and TDRS transponder delays.

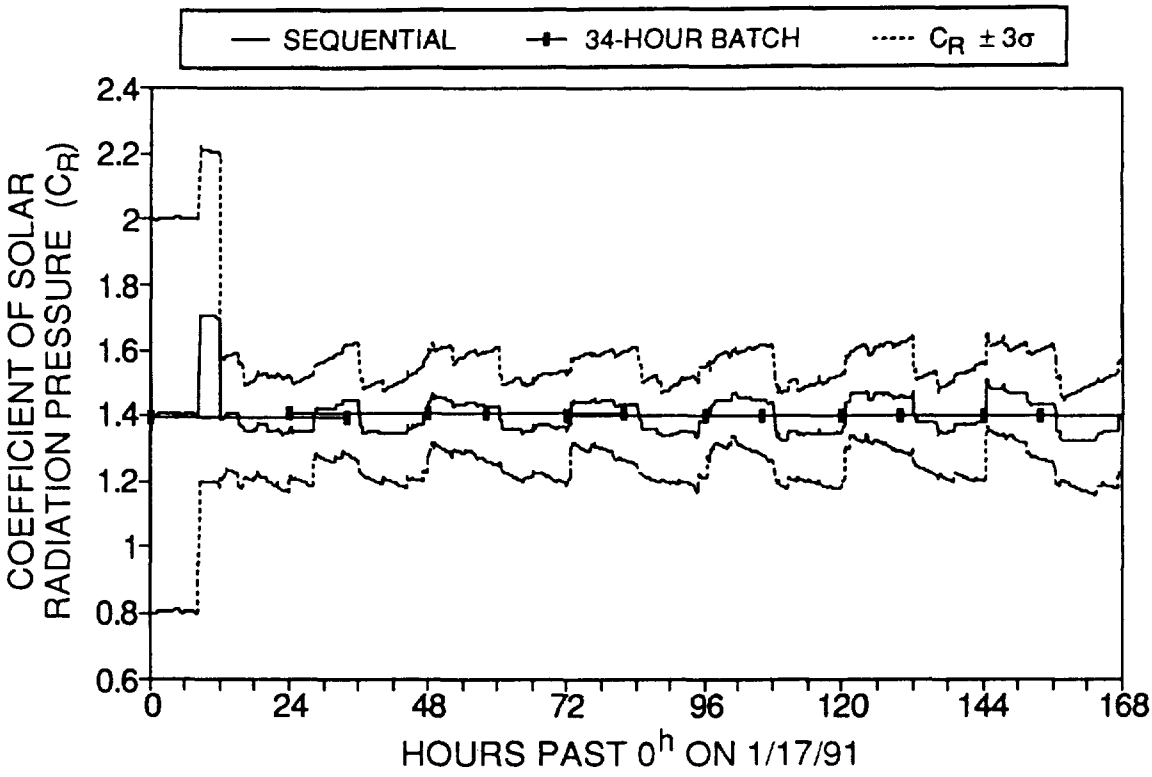

Figure 6. Coefficient of Solar Radiation Pressure (C_R) for TDRS-East

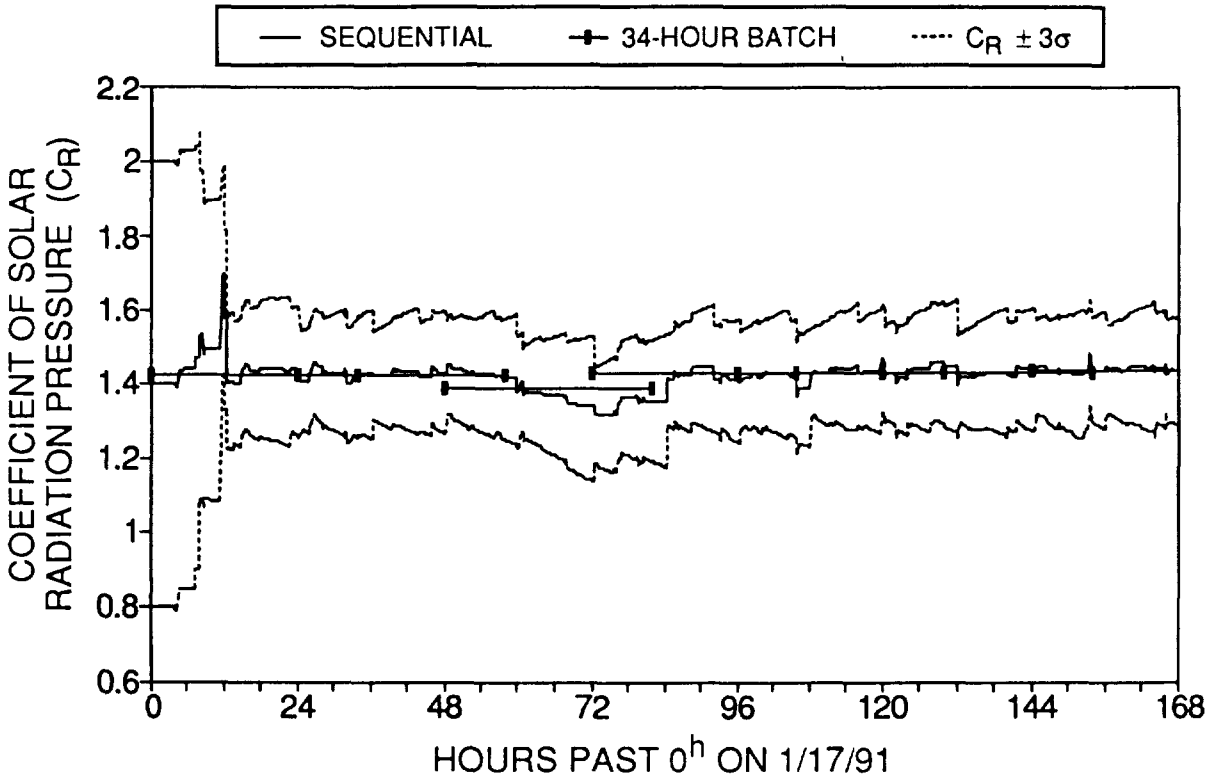

Figure 7. Coefficient of Solar Radiation Pressure (C_R) for TDRS-West

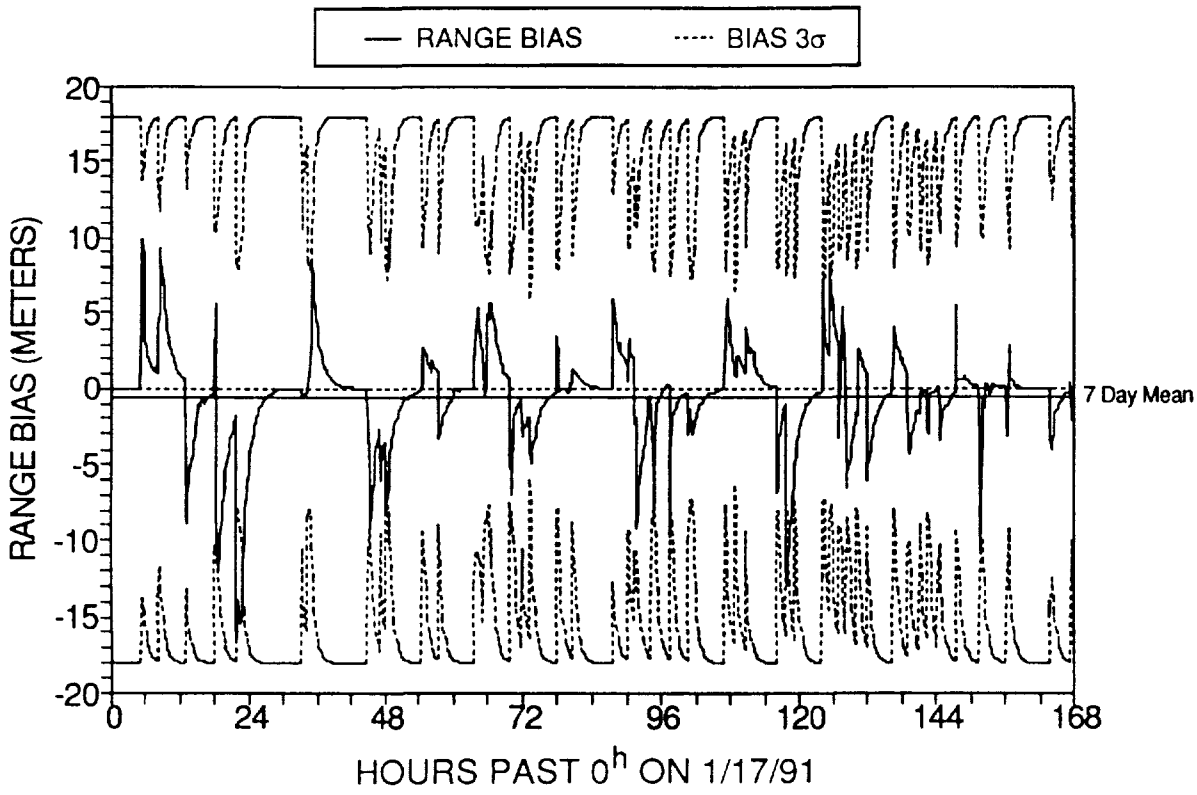

Figure 8. Range Bias Estimates for Landsat-4 via TDRS-East

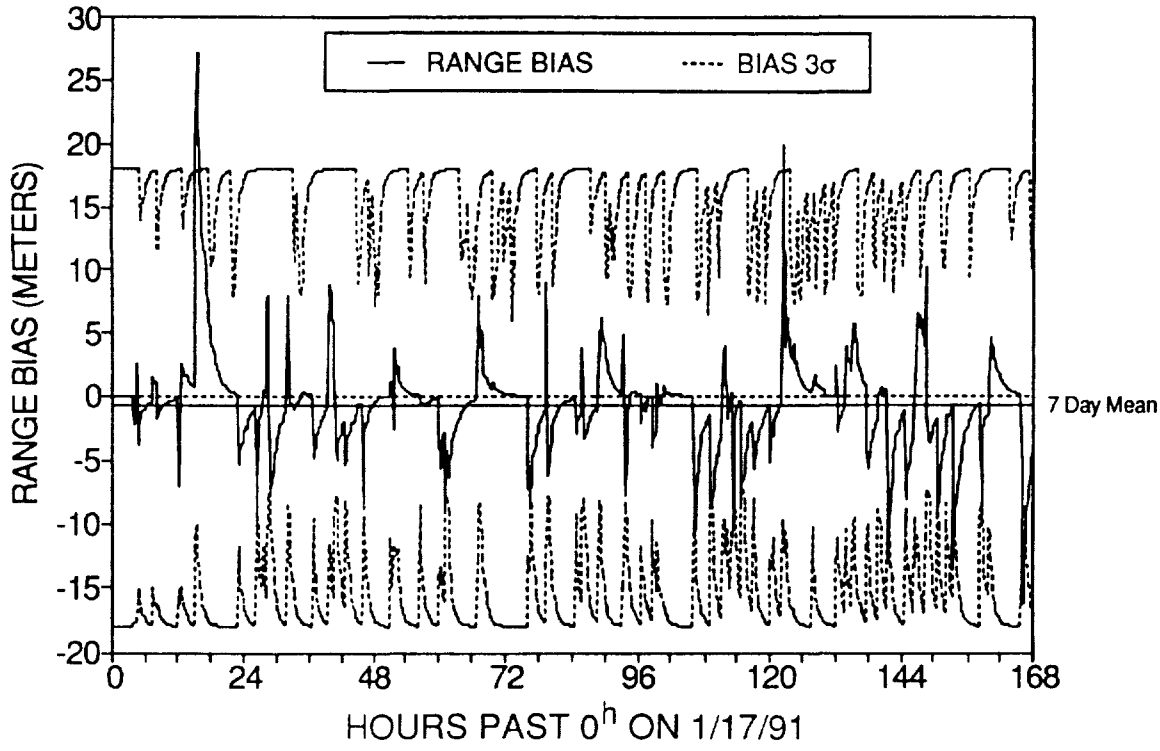

Figure 9. Range Bias Estimates for Landsat-4 via TDRS-West

3.3 Comparison of Batch and Sequential Estimation Results

Comparisons of the estimated Landsat-4 orbits between GTDS solutions and RTOD/E forward-filtered solutions are presented in Figures 10 and 11. Figure 10 shows the differences during the first day of the filtered solution. Since the filter had not reached steady state during the early phases of this period, the position difference was as large as about 300 meters. However, this difference is not larger than the corresponding state error covariance values of the filter, an indicator of the internal consistency of the filtered solution. After the filter had reached steady state, the differences between the GTDS and RTOD/E solutions were much smaller than on the first day. Therefore, these results are plotted in Figure 11 with a different vertical scale, along with the filter 3σ uncertainty; the position differences (root-sum-square (RSS) of the radial, along-track, and cross-track components) shown in this figure are mostly less than 40 meters. The maximum difference did not increase or decrease toward the end of the 7-day comparison period. Figure 12 shows the position differences on the seventh day, along with the tracking timeline for Landsat-4 and the estimated uncertainty in consistency (3σ covariance function) obtained from RTOD/E.

A few important features shown in Figure 12 are of note. Every time a tracking pass is processed by the sequential filter, the filter's confidence level in the solution increases; conversely, the error covariance function decreases. During the tracking passes, the 3σ position uncertainty estimated by the filter is between 10 and 25 meters. If continuous tracking were available, theoretically it would have been possible to sustain a near-uniform steady-state 3σ uncertainty. Conversely, with a relatively normal gap of about 3 hours in tracking, the 3σ position uncertainty rises to as high as 45 meters. This study was performed during the period of dense Landsat-4 tracking (Figure 1). During normal operation, the tracking is performed with interpass gaps of 4 hours or longer.

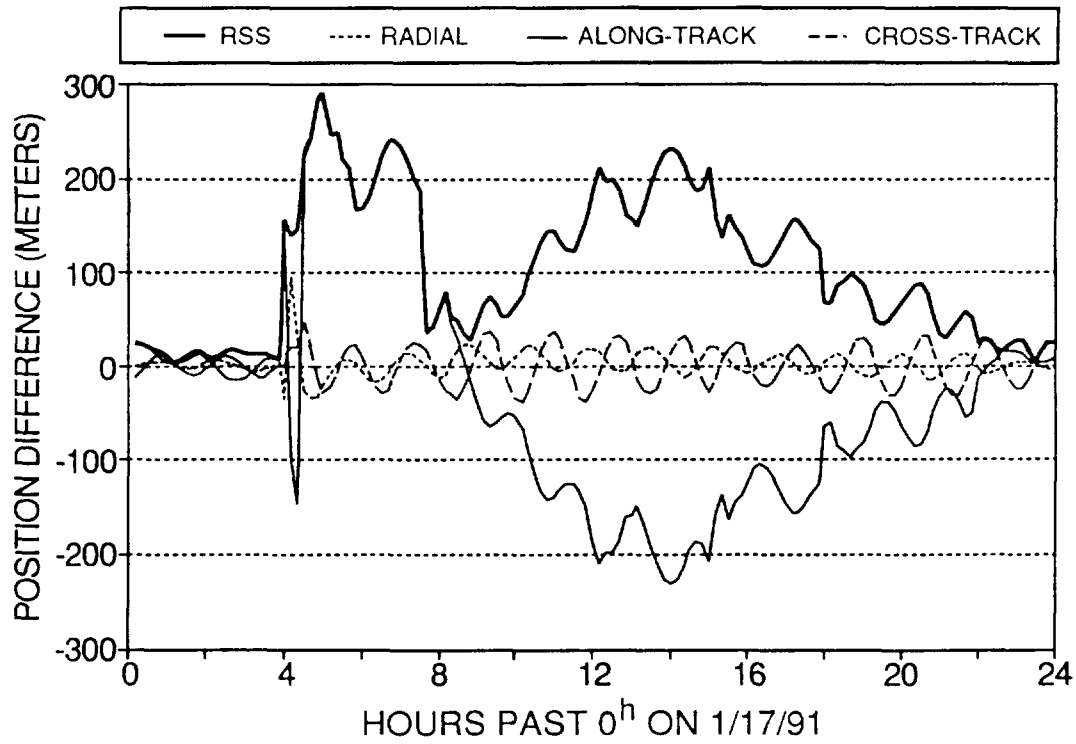

Figure 10. GTDS and RTOD/E Ephemeris Estimate Differences for Landsat-4 (Day 1)

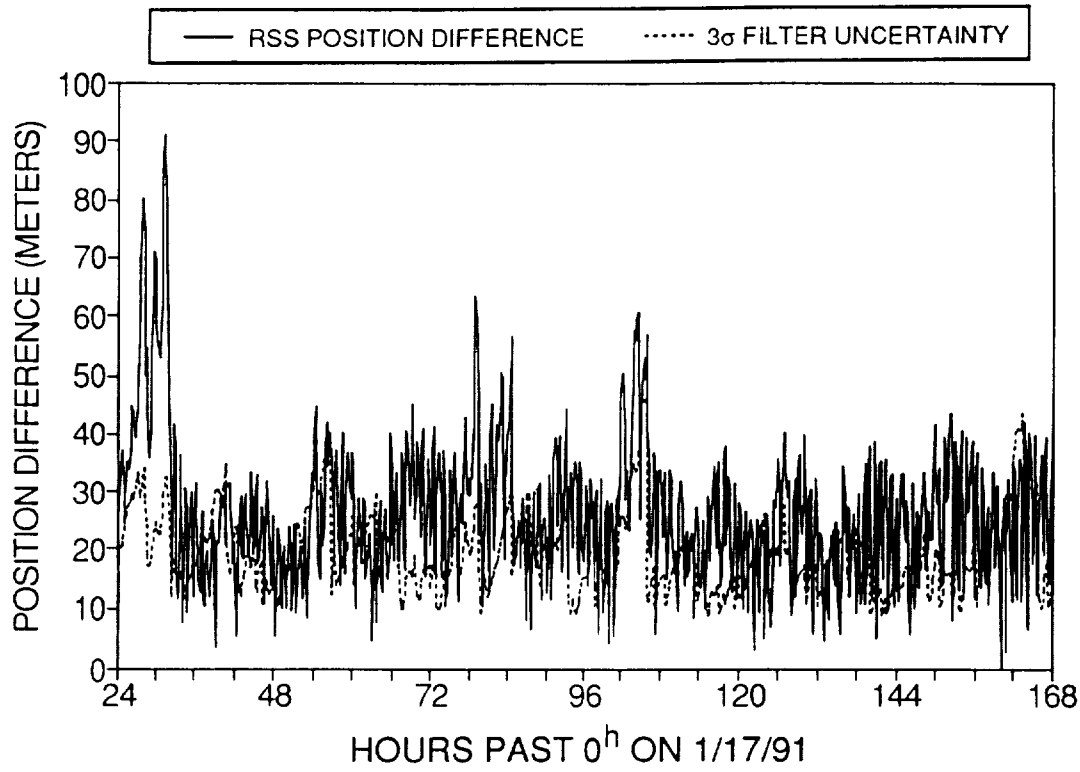

Figure 11. GTDS and RTOD/E Ephemeris Estimate Differences for Landsat-4 and 3σ Filter Uncertainty (Days 2 Through 7)

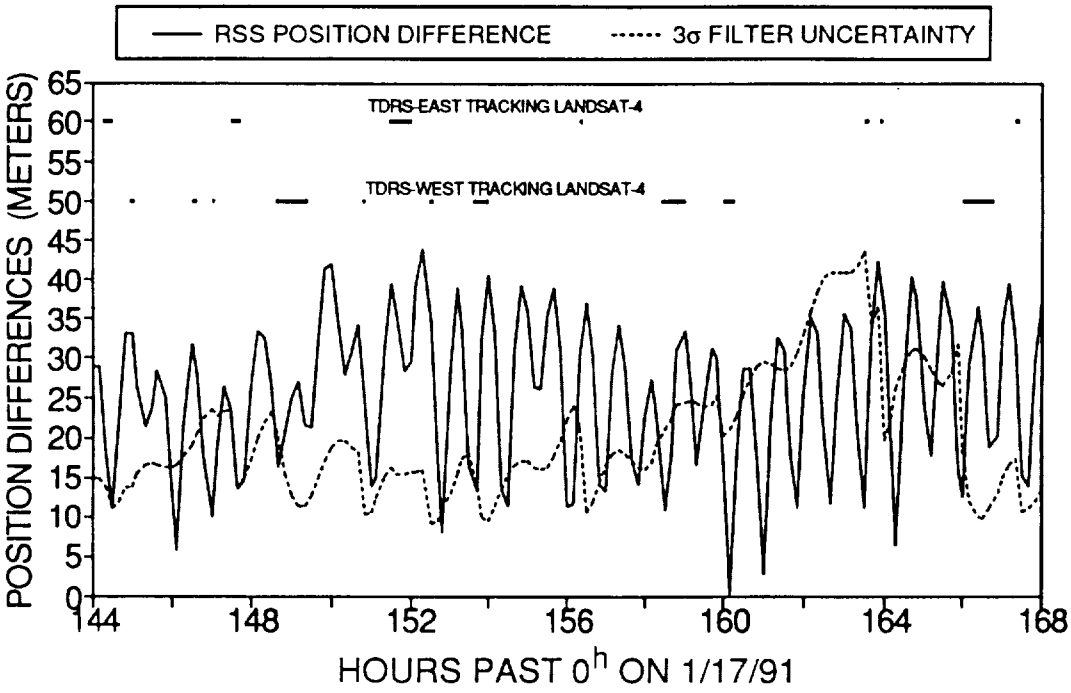

Figure 12. GTDS and RTOD/E Ephemeris Estimate Differences for Landsat-4 and 3σ Filter Uncertainty and Tracking Schedule (Day 7)

The position differences between the GTDS and RTOD/E solutions in Figure 12 exceed the estimated uncertainty of the RTOD/E solution more than half the time. The maximum difference of about 40 meters is not consistent within the cumulative consistencies of the batch and sequential solutions. An analysis to identify the source of this discrepancy and resolve it is in progress.

A significant part of the difference between the batch and sequential orbit determination results in Figure 12 can be attributed to the differences in the force and measurement models used for GTDS and RTOD/E. Quantitative estimates for some of these model difference effects are available from previous studies using GTDS. It was reported in Reference 4 that the maximum position difference for 34-hour definitive ERBS solutions using the Goddard Earth Model-T2 (GEM-T2) (50 x 50) and GEM-10B (36 x 36) geopotential models can be as high as 30.1 $\pm$ 5.2 meters. RTOD/E uses the GEM-10B geopotential model with order and degree 30. Due to the inclusion of a process noise model for geopotential errors in RTOD/E and its absence in GTDS, the impact of differences in the geopotential models used would be different in the two systems. The maximum position differences observed in the definitive ERBS orbits due to the presence and absence of ionospheric refraction correction in the measurement model for the spacecraft-to-spacecraft leg can be 2.6 $\pm$ 0.9 meters (Reference 4). The maximum position difference due to solid Earth tide effects on ERBS were measured at 7.0 $\pm$ 3.2 meters. A detailed analysis of the influence of polar motion and solid Earth tides on ERBS orbits is given in Reference 9. ERBS is at an altitude of about 600 kilometers, whereas Landsat-4 is at an altitude of about 715 kilometers. Therefore, all the stated effects above for ERBS should be somewhat diminished in magnitude for Landsat-4. However, Landsat-4 has a polar orbit, which has a significant adverse effect on the tracking geometry.

Another source of the difference between the GTDS and RTOD/E estimated ephemerides is due to the fundamental difference in the way the estimated parameters are obtained in the batch least-squares and sequential estimation techniques. In the batch least-squares method, a single set of parameter values is estimated over an entire arc. In the sequential estimation process, the set of estimated parameter values is updated at each measurement time. The time variations in selected estimated parameters are shown in Figures 5 through 9.

Based on the magnitude of these differences and the differences in the estimation techniques, the maximum position difference of about 40 meters between the GTDS and RTOD/E results is not unusual.

3.4 Remarks

The results presented in this paper were obtained using dense-tracking TDRSS measurements for Landsat-4. A previous study of ERBS with single-relay (TDRS-East only) TDRSS tracking has shown that to achieve the highest precision orbit determination using the batch least-square method, the tracking coverage should not fall below 10 minutes every two orbits (Reference 10). The tracking coverage used in the present study, as shown in Figure 1, was well above this criterion. The impact of tracking coverage on accuracy using sequential estimation techniques will be pursued in future studies. In theory, the filter is expected to be more sensitive to large gaps in tracking data than the batch least-squares method; conversely, it would benefit more from more continuous tracking than would the batch least-squares method.

A covariance analysis to further understand the orbit determination results and to identify the major contributing factors to the errors in the estimated orbits is in progress.

4. CONCLUSIONS

This study presented an analysis of TDRSS user orbit determination using a batch least-squares method and a sequential estimation method. Independent assessments were performed of the orbit determination consistency within each method, and the estimated orbits obtained by the two methods were also compared. This assessment is applicable to the dense-tracking measurement scenario for tracking Landsat-4.

In the batch least-squares method analysis, the orbit determination consistency for Landsat-4, which was heavily tracked by TDRSS during January 1991, was found to be about 4 meters in the RMS overlap comparisons and about 6 meters in the maximum position differences in overlap comparisons. In the sequential method analysis, the consistency was found to be about 10 to 30 meters in the 3σ state error covariance function; and, as a measure of consistency, the first residual of each pass was within the 3σ bound in the residual space.

After the filter had reached steady state, the differences between the definitive batch least-squares ephemerides and the forward-filtered sequentially estimated ephemerides were no larger than 40 meters. Further studies are in progress to investigate the relative qualities of the two methods within this difference.

REFERENCES

1. Goddard Space Flight Center, Flight Dynamics Division, FDD/552-89/001, *Goddard Trajectory Determination System (GTDS) Mathematical Theory, Revision 1*, A. C. Long and J. O. Cappellari, Jr. (CSC) and C. E. Velez and A. J. Fuchs (GSFC) (editors), prepared by Computer Sciences Corporation, July 1989

2. Goddard Space Flight Center, Flight Dynamics Division, FDD/554-91/064, *Enhanced RTOD Demonstration System*, W. Chuba (ATA), prepared by Applied Technology Associates, Inc., March 1991

3. D. H. Oza, T. L. Jones, S. M. Fabien, G. D. Mistretta, R. C. Hart, and C. E. Doll, "Comparison of ERBS Orbit Determination Using Batch Least-Squares and Sequential Methods," NASA Conference Publication 3123, *Proceedings of the Flight Mechanics/Estimation Theory Symposium*, p. 79, Paper No. 5, presented at Goddard Space Flight Center, Greenbelt, Maryland, May 21–23, 1991

4. D. H. Oza, M. Hodjatzadeh, M. S. Radomski, C. E. Doll, and C. J. Gramling, "Evaluation of Orbit Determination Using Dual-TDRS Tracking," Paper No. AIAA-90-2925-CP, *A Collection of Technical Papers Part 1*, p. 410, published by the AIAA; presented at the AIAA/AAS Astrodynamics Conference, Portland, Oregon, August 20–22, 1990

5. D. H. Oza, T. L. Jones, M. Hodjatzadeh, M. V. Samii, C. E. Doll, G. D. Mistretta, and R. C. Hart, "Evaluation of TDRSS-User Orbit Determination Accuracy Using Batch Least-Squares and Sequential Method," paper presented at the Third International Symposium on Spacecraft Flight Dynamics, Darmstadt, Germany, September 30 – October 4, 1991

6. Goddard Space Flight Center, Flight Dynamics Division, 554-FDD-91/105R3UD0, *Tracking and Data Relay Satellite System (TDRSS) Onboard Navigation System (TONS) Flight Software Mathematical Specifications, Revision 3*, A. C. Long, D. H. Oza, et al. (CSC), prepared by Computer Sciences Corporation, March 1992

7. J. R. Wright, "Sequential Orbit Determination with Auto-Correlated Gravity Modeling Errors," *Journal of Guidance and Control*, vol. 4, 1981, p. 304

8. A. Gelb (editor), *Applied Optimal Estimation*. Cambridge, Massachusetts: M.I.T. Press, 1974

9. Goddard Space Flight Center, Flight Dynamics Division, FDD/554-90/103, "Effects of Polar Motion and Earth Tides on High-Accuracy Orbit Determination of the Earth Radiation Budget Satellite (ERBS)," *Operational Orbit Techniques, 1990 Flight Dynamics Analysis Report 1*, D. H. Oza and T. Mo (CSC), prepared by Computer Sciences Corporation, May 1990

10. C. E. Doll, C. J. Gramling, D. H. Oza, and M. S. Radomski, "Sensitivity of High-Accuracy Tracking and Data Relay Satellite System (TDRSS) User Spacecraft Orbit Determination to Tracking Schedules," Paper No. CNES 89/143, presented at the CNES International Symposium on Space Dynamics, Toulouse, France, November 6–10, 1989

Orbit Determination Support of the Ocean Topography Experiment (TOPEX)/Poseidon Operational Orbit*

A. F. Schanzle, J. E. Rovnak, D. T. Bolvin
COMPUTER SCIENCES CORPORATION (CSC)

C. E. Doll
GODDARD SPACE FLIGHT CENTER (GSFC)

ABSTRACT

The Ocean Topography Experiment (TOPEX/Poseidon) mission is designed to determine the topography of the Earth's sea surface over a 3-year period, beginning shortly after launch in July 1992. TOPEX/Poseidon is a joint venture between the United States National Aeronautics and Space Administration (NASA) and the French Centre Nationale d'Etudes Spatiales. The Jet Propulsion Laboratory is NASA's TOPEX/Poseidon project center. The Tracking and Data Relay Satellite System (TDRSS) will nominally be used to support the day-to-day orbit determination aspects of the mission. Due to its extensive experience with TDRSS tracking data, the NASA Goddard Space Flight Center (GSFC) Flight Dynamics Facility (FDF) will receive and process TDRSS observational data.

To fulfill the scientific goals of the mission, it is necessary to achieve and maintain a very precise orbit. The most stringent accuracy requirements are associated with planning and evaluating orbit maneuvers, which will place the spacecraft in its mission orbit and maintain the required groundtrack.

To determine if the FDF can meet the TOPEX/Poseidon maneuver accuracy requirements, covariance analysis was undertaken with the Orbit Determination Error Analysis System (ODEAS). The covariance analysis addressed many aspects of TOPEX/Poseidon orbit determination, including arc length, force models, and other processing options. The most recent analysis has focused on determining the size of the geopotential field necessary to meet the maneuver support requirements. Analysis was undertaken with the full 50x50 Goddard Earth Model (GEM) T3 field as well as smaller representations of this model.

* This work was supported by the National Aeronautics and Space Administration (NASA)/Goddard Space Flight Center (GSFC), Greenbelt, Maryland, Contract NAS 5-31500.

1. INTRODUCTION

1.1 Background

Error analysis has been used in a long succession of investigations to evaluate the orbit determination capabilities of the TOPEX/Poseidon mission. Reference 1 gives a mission overview and summarizes the day-to-day operational orbit determination requirements and nominal capabilities. The requirements were provided by the Jet Propulsion Laboratory (JPL), and the capabilities were obtained from previous error analyses presented in References 2 and 3.

The TOPEX mission has been divided into two general phases: the assessment phase, where maneuvers will be used to navigate the spacecraft from the injection orbit to the operational orbit, and the observational phase, where the majority of scientific data will be obtained. Maneuvers will also be required during the observational phase to maintain the stringent groundtrack requirements necessary for the scientific goals.

The TOPEX mission scientific goals require orbit determination accuracies that have spurred the development of new mathematical models for representing the motion of near-Earth satellites. One such improvement is a special 50x50 geopotential field called GEM T3. Approximately 6 months after launch of the satellite, TOPEX tracking data will be added to the observations used to develop GEM T3 to create a gravity field tailored specifically for TOPEX.

1.2 Goal of Study

The use of a full 50x50 geopotential field in conjunction with other improved models for representing near-Earth satellite motion is expected to produce orbit ephemerides that will support the scientific goals of the TOPEX mission. However, for operational day-to-day orbit solutions, use of a full 50x50 geopotential field places a significant burden on computer resources. Consequently, the specific goal of this study is to determine if day-to-day operational orbit determination requirements can be achieved with smaller representations of the GEM T3 field.

This investigation uses the Orbit Determination Error Analysis System (ODEAS) to estimate the effect of reducing the size of GEM T3 on day-to-day operational solutions. The most stringent requirements are for support of maneuver evaluations in the observational phase. Consequently, this is the specific area addressed in this study.

1.3 Maneuver Support Requirements

The orbit determination requirements specified by JPL for support of maneuver evaluation during the observational phase are given in Table 1. The requirement that is the most difficult to achieve is the 0.2 millimeter/second (mm/sec) change in the alongtrack component of velocity.

Table 1. TOPEX Orbit Determination Requirements for Evaluation of Changes in Osculating Parameters Due to a Maneuver

PARAMETER	MAXIMUM 3-σ ERROR
CHANGE IN RADIAL COMPONENT OF VELOCITY	10.0 MM/SEC
CHANGE IN CROSSTRACK COMPONENT OF VELOCITY	10.0 MM/SEC
CHANCE IN ALONGTRACK COMPONENT OF VELOCITY	0.2 MM/SEC
CHANGE IN OSCULATING VALUE OF SEMIMAJOR AXIS	0.2 M*
CHANGE IN OSCULATING VALUE OF INCLINATION	5.0×10^{-4} DEG*

*M - METER(S)
DEG - DEGREE(S)

2. ANALYSIS

2.1 Geopotential Error Models

This investigation is concerned with the effect of different-size representations of the GEM T3 gravity field on maneuver evaluation capabilities. The GEM T3 field is a full 50x50 set of coefficients developed by S. Klosko (Reference 4).

Covariance analysis estimates the effect of uncertainties in measurement and force model parameters on the solved-for quantities. An error model for the GEM T3 geopotential field has been developed in Reference 5 by creating a 1-sigma standard deviation "clone" geopotential model by a purely mathematical method. The difference between the original GEM T3 and GEM $T3_{clone}$ represents a 1-sigma error model for GEM T3. A 3-sigma error model is constructed by simply applying a multiplicative factor of 3 to the 1-sigma error model.

Two additional geopotential models have been generated from the same observations used in the development of the 50x50 GEM T3 model. The additional models solve only for geopotential coefficients up to 20x20 and 30x30. These latter fields are called "folded-over" models. Clone representations for these two additional reduced-size models have not been undertaken because the process requires extensive computer resources on very large systems. Consequently, error models are not currently available for these two folded-over representations, and without error models, these reduced-size fields cannot be used in conjunction with covariance analysis.

Two possibilities exist for developing an error model for the folded-over fields without the use of clone representations. The first is based on analysis presented in Reference 6 and reproduced in Table 2, which summarizes the quality of orbit determination fits to the Starlette, Ajisai, and Lageos satellites with five different geopotential fields based on GEM T3 (the full 50x50 field, folded-over 20x20 and 30x30 fields, and GEM T3 truncated at 20x20 and 30x30). The TOPEX altitude will lie between that of Starlette and Ajisai. Table 2 suggests that the root mean square (RMS) of fit to the observations for a spacecraft between these two altitudes will be best for the full 50x50 field, with a poorer fit for the folded-over fields and the worst fit using the truncated fields.

Error analysis is usually concerned with presenting "worst-case" scenarios. Table 2 suggests that truncated models produce the worst results, so that if error models could be developed for the truncated 20x20 and 30x30 fields, those error models would likely produce error estimates that are larger than those obtained from the folded-over fields. While this procedure may produce excessively pessimistic results, the results would at least indicate a worst-case scenario. Error models for truncated fields *can* be constructed without using clone representations by differencing the original and clone models up to, say, 20x20, and adding to this set of error coefficients 100 percent of the original GEM T3 model from 21x21 up to 50x50.

Table 2. Fit to Residuals of Different Satellites as a Function of Gravity Field

SATELLITE	SATELLITE SEMIMAJOR AXIS (KM*)	RMS OF FIT (CM*)				
		FULL 50 × 50 GEM T3	FOLDED-OVER 30 × 30 GEM T3	FOLDED-OVER 20 × 20 GEM T3	FULL GEM T3 TRUNCATED AT 30 × 30	FULL GEM T3 TRUNCATED AT 20 × 20
STARLETTE	7371	11.4	90.9	166.9	141.1	573.3
AJISAI	7820	8.7	10.7	22.4	10.3	38.3
LAGEOS	12273	7.5	7.5	7.5	7.5	7.5

*CM = CENTIMETER(S)
KM = KILOMETER(S)

The second alternative for producing an error model for the folded-over fields without the benefit of clone representations is to assume that the full 50x50 GEM T3 field is absolute truth, and simply difference the 50x50 and 20x20 fields. Two problems arise with this representation. First, the error in GEM T3 itself is ignored. Second, the error model would include 100 percent of the 50x50 coefficients above degree and order 20x20, and yet, to the extent possible, the dynamics of these high-order terms might already be included in the folded-over field. Some of this apparent "excessive error" might be removed when differencing the 50x50 GEM T3 and folded-over 20x20 fields due to inherent correlations, but without evidence to this effect, it appears that the best alternative is to use error models based upon truncated fields and accept a worst-case scenario. Table 3 presents the different geopotential fields and associated error models used in this investigation.

Table 3. Geopotential Fields and Associated Error Models

GEOPOTENTIAL MODEL	3-σ ERROR MODEL
50 x 50 GEM T3	3 x (GEM T3 – GEM $T3_{CLONE}$)
GEM T3 TRUNCATED AT 30 x 30	3 x (GEM T3 – GEM $T3_{CLONE}$) UP TO 30 x 30 PLUS 100% OF (GEM T3) 31 x 31 UP TO 50 x 50
GEM T3 TRUNCATED AT 20 x 20	3 x (GEM T3 – GEM $T3_{CLONE}$) UP TO 20 x 20 PLUS 100% OF (GEM T3) 21 x 21 UP TO 50 x 50

2.2 Input Parameters

Epoch conditions for TOPEX and TDRS-East (E) and -West (W) are given in Table 4. Table 5 presents the station locations and Table 6 defines the error sources and associated 3-sigma uncertainties.

Because this investigation is primarily concerned with the effect of geopotential size on maneuver evaluation capabilities, there is no need to propagate errors into the future. Consequently, Table 6 indicates an uncertainty of 2.5 percent for solar flux errors throughout the definitive period, with no errors for prediction periods.

The tracking schedule for determining the orbits of TDRS-E and -W consists of 5 minutes of range and Doppler observations every other hour with a sampling frequency of 60 seconds. The nominal tracking scenario for the observational phase of TOPEX by the two TDRS spacecraft was specified by JPL. It consists of a 7-day arc with 40 minutes per revolution of one-way noncoherent Doppler and a single 20-minute pass per day of two-way coherent range and Doppler. The two-way pass replaces the one-way pass for that particular revolution. For three revolutions before and after a maneuver, the 40-minute one-way Doppler pass is replaced by a 40-minute pass of two-way range and Doppler. TDRS tracking of TOPEX incorporates a 10-second sampling frequency.

2.3 Evaluation of Capabilities for Computing the Changes in Osculating Parameters as a Function of Geopotential Field Size

An outline of the procedure used to estimate the error in the change of a parameter due to an instantaneous maneuver is given in Reference 3. In general, the process involves computing and saving the error budget at the time of the maneuver based on the premaneuver solution. A corresponding error budget is obtained at the maneuver time from the postmaneuver solution. If all the error parameters are assumed to be perfectly correlated, the error in the change of a parameter due to an instantaneous maneuver is obtained by differencing the two error budgets, parameter by parameter and component by component. Uncertainties in station position and C_D can certainly be assumed to be correlated for the premaneuver and postmaneuver solutions.

Table 4. Epoch Conditions

PARAMETER	TDRS-E	TDRS-W	TOPEX
EPOCH	92/06/08 22^h 00^m 00^s	92/06/08 22^h 00^m 00^s	92/06/08 22^h 00^m 00^s
SEMIMAJOR AXIS (KM)	42168.29724487	42163.80284769	7706.82281771
ECCENTRICITY	0.00019745860	0.00024304387	0.0010889678
INCLINATION (DEG)	4.50609744	3.72087923	66.04679405
ASCENDING NODE (DEG)	70.15012793	162.83194621	142.72939563
ARGUMENT OF PERIGEE (DEG)	337.82089362	91.11231707	6.09376125
MEAN ANOMALY (DEG)	138.32697568	162.69648054	358.38472966
E. LONG. (DEG)	318.85566801	189.08900083	
AREA/MASS (M^2/KG*)	0.02	0.02	0.0064865
C_R	1.5	1.5	1.3
C_D	N/A	N/A	2.3
SOLAR FLUX (WATTS/M^2/HZ*)			225.0

*KG = KILOGRAM(S)
HZ = HERTZ

Table 5. Station Locations

STATION	ACRONYM	E. LONGITUDE (DEG, MIN,* SEC)	LATITUDE (DEG, MIN, SEC)	HEIGHT (M)
WHITE SANDS	WHSK	253 23 29.21	32 30 03.56	1430
WHITE SANDS BRTS	WHSJ	253 23 16.92	32 30 22.53	1413
ASCENSION BRTS	ASCJ	345 36 33.24	–07 55 04.47	42
ALICE SPRINGS BRTS	ALSJ	133 52 57.36	–23 45 31.65	547

*MIN = MINUTES

Table 6. Error Sources and Associated 3-Sigma Uncertainties

PARAMETER	ACRONYM IN LISTING	3-σ UNCERTAINTY		
GRAVITY FIELD	GEOERROR	SEE TABLE 3		
C_D	USERDRAG	30% IF NOT SOLVED FOR		
SOLAR FLUX	SOLFLUX	MEAN SOLAR FLUX = 225 × 10^{-22} WATTS/M^2/HZ. DAILY ERROR = 2.5%.		
C_R				
TOPEX	SOLRAD 1	30%		
TDRS-E	SOLRAD 2	2%		
TDRS-W	SOLRAD 3	2%		
STATION POSITIONS				
ASCENSION TRANSPONDER	NAME = ACNJ			
ALICE SPRINGS TRANSPONDER	NAME = ALSJ			
WHITE SANDS TRANSPONDER	NAME = WHSJ			
WHITE SANDS GROUND	NAME = WHSK			
LOCAL X	XLT–NAME	3 M		
LOCAL Y	YLT–NAME	3 M		
LOCAL Z	ZLT–NAME	3 M		
TROPOSPHERE	TRP–NAME	45%		
IONOSPHERE				
FROM STATIONS	ION–NAME	100%		
FROM TDRS-E	IONSAT 2	100%		
FROM TDRS-W	IONSAT 2	100%		
MEASUREMENTS		NOISE	WEIGHTσ	BIAS
BRTS RANGE (M)	MEASBI 3,4,5,6	1.5	3.0 × 10^{-4}	7.0
TDRSS RANGE (M)	MEASBI 1,2	1.5	90.0	7.0
TDRSS TWO-WAY R/R* (MM/SEC)		2.82	100.0	0.0
TDRSS ONE-WAY R/R (MM/SEC)		6.29	6.29	SOLVE FOR CLOCK DRIFT AND CLOCK ACCELERATION

*RANGE/RATE

Other parameters, such as the uncertainties in the ionospheric and tropospheric refraction, are not necessarily correlated; as a result, errors in the change of the solved-for parameters due to these latter uncertainties are not differenced, but the RSS is computed. The total error in the change of a specific component is obtained by forming the RSS of the individual error sources of the differenced/RSS'ed error budget.

The premaneuver arc was selected to be 7 days, because this will be the typical definitive period for the observational phase. JPL requested deliveries of the changes in parameters at 8 and 24 hours after the maneuver. GSFC personnel indicated that it would take approximately 1 hour to process the data and send the results to JPL. Consequently, postmaneuver data spans of 7 and 23 hours were selected as nominal postmaneuver data arcs. However, the requirements apply only to the 23-hour postmaneuver solution.

Simulations were constructed using the epoch conditions, tracking scenarios, and error models noted in Section 2.2 and Table 3. The maneuver time was selected as exactly 7 days past the epoch time noted in Table 4.

If a maneuver is assumed to be instantaneous, the maneuver will change only the velocity (not the position at this instant of time). It is possible to simulate this scenario by applying the appropriate weight sigmas to the position components of the postmaneuver a priori covariance matrix. This process ensures the same position for the pre- and postmaneuver solutions at the time of the maneuver, but the operational version of ODEAS

does not produce the necessary output to allow the same *error* in the pre- and postmaneuver solution. Consequently, it is not currently possible to properly simulate the process of constrained solutions. The following analysis assumes unconstrained postmaneuver solutions, but the subject of constrained solutions will be addressed in Section 2.4.

Tables 7, 8, and 9 indicate the maneuver evaluation capabilities as a function of postmaneuver data span and gravity model size for semimajor axis, inclination, and crosstrack velocity. The capabilities for evaluating radial and alongtrack velocity components will be discussed later.

Consider first Table 7, which contains the maneuver evaluation capabilities for the semimajor axis. Separate columns are included for the premaneuver and postmaneuver solutions as well as the error in the change of the parameter. The results indicate that for all postmaneuver solutions, the error in the semimajor axis due to the uncertainty in the gravity model is relatively small when compared to the RSS of all other error sources. This is not the case for the premaneuver solutions, where the uncertainties in the gravity field dominate the RSS of all errors. As would be expected, 23-hour postmaneuver data spans produce smaller errors in the change of the semimajor axis than 7-hour data spans. The larger gravity field representations also produce smaller errors in the change of the semimajor axis, but there is relatively little difference between them. The dominant contributor to the error in the change of the semimajor axis is a result of the uncertainty in the geopotential field for the 20x20 gravity model simulations. For the 30x30 and 50x50 gravity fields, the dominant errors are due to the uncertainties in the tropospheric refraction and measurement biases.

Table 7. TOPEX Observational Phase Maneuver Evaluation Capabilities for the Semimajor Axis With No Constraints on the Postmaneuver Position

PREMANEUVER DATA SPAN = 7 DAYS REQUIREMENT ON CHANGE OF SEMIMAJOR AXIS = 0.2 METERS						
POST-MANEUVER DATA SPAN (HR*)	GRAVITY MODEL	ERROR IN SEMIMAJOR AXIS (M)				
		POSTMANEUVER		PREMANEUVER		ERROR IN CHANGE OF SEMIMAJOR AXIS DUE TO ALL ERRORS
		RSS OF ALL ERRORS	ERROR FROM GRAVITY	RSS OF ALL ERRORS	ERROR FROM GRAVITY	
23	50 x 50	0.1969	0.042	0.0855	0.084	0.1968
7	50 x 50	0.2716	0.084	0.0855	0.084	0.2592
23	30 x 30	0.1961	0.038	0.1112	0.110	0.2055
7	30 x 30	0.2722	0.086	0.1112	0.110	0.2603
23	20 x 20	0.2087	0.081	0.2962	0.296	0.2885
7	20 x 20	0.2723	0.086	0.2962	0.296	0.3332

*HR = HOURS

In summary, no unusual or unexpected results appear in Table 7, and it appears that a 30x30-size gravity field will meet the requirement of 0.2 meters for the 23-hour solutions. However, it must be remembered that errors in the premaneuver and postmaneuver solutions change as a function of time, and the results noted in Table 7 are valid for only a single maneuver epoch. Different maneuver evaluation capabilities may be obtained for different epochs. This concern will be addressed later in Section 2.5. In addition, the geopotential error model used to produce the results in Table 7 represents a truncated geopotential field, whereas operational solutions will probably be based on folded-over fields, which should be superior to the truncated results (see Table 2).

Table 8 presents the corresponding results for the inclination. No unusual results appear, with little or no sensitivity to the gravity model size. The requirement of $1x10^{-4}$ degrees can be met with a 20x20 geopotential representation. The dominant error source in the change of the inclination is the ionospheric refraction from the ground stations.

Table 8. TOPEX Observational Phase Maneuver Evaluation Capabilities for the Inclination With No Constraints on the Postmaneuver Position

PREMANEUVER DATA SPAN = 7 DAYS REQUIREMENT ON CHANGE IN INCLINATION = 1 × 10^{-4} DEGREES						
POST-MANEUVER DATA SPAN (HR)	GRAVITY MODEL	ERROR IN INCLINATION (DEGREES × 10^{-4})				
		POSTMANEUVER		PREMANEUVER		ERROR IN CHANGE OF INCLINATION DUE TO ALL ERRORS
		RSS OF ALL ERRORS	ERROR FROM GRAVITY	RSS OF ALL ERRORS	ERROR FROM GRAVITY	
23	50 × 50	0.205	−.0064	0.272	.0439	0.34
7	50 × 50	0.562	.0097	0.272	.0439	0.63
23	30 × 30	0.202	−.0031	0.271	.0372	0.34
7	30 × 30	0.146	.0117	0.271	.0372	0.63
23	20 × 20	0.211	−.0602	0.275	−.0587	0.34
7	20 × 20	0.560	.0019	0.275	−.0587	0.63

Table 9 gives the maneuver evaluation capabilities for the crosstrack component of velocity. Once again, the results are not sensitive to the size of the geopotential, and the requirement of 10 mm/sec can be obtained with a 20x20 gravity field. The dominant error source in the change of the crosstrack component of velocity is again the uncertainty in the ionospheric refraction at the ground stations.

The final set of requirements deals with the errors in the change of the in-plane velocity components. To help explain these results, it is beneficial to first examine the errors in the change of the radial *position* (not the radial *velocity*), which are given in Table 10.

The important feature of this table is that the errors in the change of the radial position are about 15 times larger than those for the semimajor axis noted in Table 7. The semimajor axis reflects the orbital period, while errors in the radial position involve not only errors in the semimajor axis, but also the eccentricity and the eccentric (or true) anomaly. The fact that the radial position error is substantially larger than that of the semimajor axis is due to the errors in these two additional parameters, which produce a tendency to point the velocity vector in the wrong direction. This in turn produces errors in the in-plane velocity components.

Table 10 also indicates that the 20x20 gravity model produces smaller errors than the larger gravity fields, which is opposite to intuition. This feature may be a result of certain correlations in the truncated field, and it might not occur if the maneuver epoch were changed. Since the radial errors are smaller for the 20x20 gravity field, the corresponding in-plane velocity errors are likely to be smaller for the 20x20 geopotential representation, as well.

Table 9. TOPEX Observational Phase Maneuver Evaluation Capabilities for the Crosstrack Velocity With No Constraints on the Postmaneuver Position

PREMANEUVER DATA SPAN=7 DAYS REQUIREMENT ON CHANGE IN CROSSTRACK VELOCITY=10 MM/SEC						
POST-MANEUVER DATA SPAN (HR)	GRAVITY MODEL	ERROR IN CROSSTRACK VELOCITY (MM/SEC)				
		POSTMANEUVER		PREMANEUVER		ERROR IN CHANGE OF CROSSTRACK VELOCITY DUE TO ALL ERRORS
		RSS OF ALL ERRORS	ERROR FROM GRAVITY	RSS OF ALL ERRORS	ERROR FROM GRAVITY	
23	50×50	2.5	0.0	3.6	−0.6	4.3
7	50×50	7.2	−0.1	3.6	−0.6	8.1
23	30×30	2.5	0.0	3.5	−0.5	4.3
7	30×30	7.2	−0.1	3.5	−0.5	8.1
23	20×20	2.6	0.7	3.6	0.7	4.3
7	20×20	7.2	−0.0	3.6	0.7	8.2

Table 10. TOPEX Observational Phase Maneuver Evaluation Capabilities for the Radial Position With No Constraints on the Postmaneuver Position

PREMANEUVER DATA SPAN = 7 DAYS NO REQUIREMENTS ON RADIAL POSITION						
POST-MANEUVER DATA SPAN (HR)	GRAVITY MODEL	ERROR IN RADIAL POSITION (M)				
		POSTMANEUVER		PREMANEUVER		ERROR IN CHANGE OF RADIAL POSITION DUE TO ALL ERRORS
		RSS OF ALL ERRORS	ERROR FROM GRAVITY	RSS OF ALL ERRORS	ERROR FROM GRAVITY	
23	50×50	0.93	0.39	2.92	−2.80	3.3
7	50×50	1.67	−0.04	2.92	−2.80	3.4
23	30×30	0.89	0.30	3.01	−2.89	3.3
7	30×30	1.67	−0.05	3.01	−2.89	3.4
23	20×20	1.10	0.70	1.17	−0.81	1.8
7	20×20	1.67	−0.01	1.17	−0.81	2.1

Table 11 presents the results for the radial component of velocity. The most notable feature of these results is that they do not meet the requirements. However, as conjectured, superior results are estimated when the gravity model is smaller. The dominant error in the change of the radial component of velocity is due to the uncertainty in the geopotential. Smaller errors in the change of the radical component might be obtained with the use of a shorter premaneuver data span.

Table 11. TOPEX Observational Phase Maneuver Evaluation Capabilities for the Radial Velocity With No Constraints on the Postmaneuver Position

PREMANEUVER DATA SPAN = 7 DAYS REQUIREMENT ON CHANGE IN RADIAL VELOCITY = 10 MM/SEC						
POST-MANEUVER DATA SPAN (HR)	GRAVITY MODEL	ERROR IN RADIAL VELOCITY (MM/SEC)				
		POSTMANEUVER		PREMANEUVER		ERROR IN CHANGE OF RADIAL VELOCITY DUE TO ALL ERRORS
		RSS OF ALL ERRORS	ERROR FROM GRAVITY	RSS OF ALL ERRORS	ERROR FROM GRAVITY	
23	50 × 50	11.9	1.0	11.2	−10.5	17.3
7	50 × 50	9.3	−0.1	11.2	−10.5	14.2
23	30 × 30	11.9	1.2	11.0	−10.4	17.4
7	30 × 30	9.3	−0.1	11.0	−10.4	14.1
23	20 × 20	11.9	0.6	7.7	−6.7	14.9
7	20 × 20	9.3	−0.1	7.7	−6.7	11.6

The last parameter to be addressed is the alongtrack component of velocity. The requirement for this parameter is, by far, the most stringent (0.2 mm/sec).

JPL requested that the error in the alongtrack component of velocity be estimated with the use of the Vis Viva energy equation. The development of the relationship is straightforward. The energy integral,

$$V^2 = GM * (2/r - 1/a)$$

renders

$$2 * V * (\Delta V) = \frac{\partial V^2}{\partial a} (\Delta a) + \frac{\partial V^2}{\partial r} (\Delta r)$$

Taking the appropriate partial derivatives, this becomes

$$\Delta V = \frac{GM}{2 * V * a^2} (\Delta a) - \frac{GM}{V * r^2} (\Delta r)$$

Substituting typical values for the TOPEX orbit (r = 7698.8 km, a = 7706.8 km, and V = 7.2 km/sec) gives

$$\Delta V = 4.66 \times 10^{-4} * (\Delta a) - 9.341 \times 10^{-4} * (\Delta r) \quad \text{km/sec} \qquad (1)$$

The terms (Δa) and (Δr) are the errors in the change in a and r respectively. When this equation is used in conjunction with unconstrained postmaneuver solutions, both (Δa) and (Δr) must be included in the

computation. If, on the other hand, we could properly simulate a constrained postmaneuver solution where there would be no discontinuity in the position (and consequently, no error in the change of position), then only the (Δa) term would be included in the equation. Table 12 presents the errors in the alongtrack component of velocity. Note that a factor of 10^6 has been applied to Equation (1) to convert the units from km/sec to mm/sec.

Table 12 indicates three particular features: first, the requirements are not met; second, there is good agreement between the two methods of computing the error in the change of the alongtrack component of velocity; third, the conjecture that the 20x20 gravity field would produce smaller errors also holds true for the alongtrack component of velocity. The uncertainty in the gravity field is the dominant error source.

Table 12. TOPEX Observational Phase Maneuver Evaluation Capabilities for the Alongtrack Velocity With No Constraints on the Postmaneuver Position

PREMANEUVER DATA SPAN = 7 DAYS REQUIREMENT ON CHANGE IN ALONGTRACK VELOCITY = 0.2 MM/SEC			
POSTMANEUVER DATA SPAN (HR)	GRAVITY MODEL	ERROR IN CHANGE OF ALONGTRACK VELOCITY FROM ODEAS (MM/SEC)	ERROR IN CHANGE OF VELOCITY FROM VIS VIVA EQUATION (MM/SEC)
23	50×50	3.1	3.0
7	50×50	3.1	3.0
23	30×30	3.1	3.0
7	30×30	3.2	3.1
23	20×20	1.8	1.5
7	20×20	1.9	1.8

2.4 Constrained TOPEX Maneuver Evaluation Capabilities Implied by Analysis of ERBS Data

The preceding results assume an unconstrained postmaneuver solution, while a constrained postmaneuver position is the proper simulation technique for instantaneous maneuvers. Due to limitations in the output capabilities of the ODEAS program, the proper technique cannot be simulated, but previous analysis presented in Reference 7 indicates what can be expected from constrained solutions.

Reference 7 has used the Goddard Trajectory Determination System (GTDS) in conjunction with actual tracking data of the Earth Radiation Budget Satellite (ERBS) to estimate the accuracy of changes in the velocity components. The technique used was to find an interval of time where a maneuver did *not* occur and to break this tracking interval into premaneuver and postmaneuver solutions. Ideally, there should be no discontinuities in the velocity components for the two solutions at the time chosen for the maneuver. The differences in the velocity components of the pre- and postmaneuver solutions at the maneuver time are a measure of GTDS's ability to resolve the change in the velocity. Reference 7 refers to this as the "Null" maneuver evaluation. GTDS solutions were made that constrained and did not constrain the postmaneuver position. A truncated 30x30 GEM T2 (not T3) gravity field was used in the analysis.

In addition to the GTDS solutions, unconstrained ODEAS simulations were constructed using the same tracking data schedule as incorporated in GTDS. Table 13 indicates the error in the change of the alongtrack velocity. Two important results are apparent. First, constrained GTDS solutions produce errors that are

approximately an order of magnitude smaller than unconstrained solutions. Second, the corresponding ODEAS 3-sigma errors are slightly larger than those obtained with GTDS but follow similar trends, giving a certain measure of credibility to the ODEAS results.

The errors in the changes of the alongtrack component of velocity provided by ODEAS in Table 12 (for TOPEX) and Table 13 (for ERBS) are of the same order of magnitude. This implies that constrained postmaneuver solutions for TOPEX should be of the same order of magnitude as obtained for ERBS, as noted in Table 13, and perhaps even smaller, since the ERBS results were obtained with GEM T2. This in turn suggests the TOPEX requirements for the error in the change of the alongtrack component of velocity should be achievable most of the time with a truncated GEM T3 30x30 geopotential field, with additional improvements for a folded-over representation. Extrapolation to a GEM T3 20x20 geopotential field is difficult due to the unusual results noted in Table 12 for the smaller-size gravity field.

Table 13. Comparison of GTDS Null Velocity Changes and ODEAS 3-Sigma Error Estimates for Changes in the Alongtrack Velocity for ERBS

MANEUVER NUMBER	CHANGES IN ALONGTRACK COMPONENT OF VELOCITY (MM/S)		
	FROM GTDS		FROM ODEAS WITH NO POST-MANEUVER CONSTRAINTS
	NOT CONSTRAINED	CONSTRAINED	
1	2.50	0.13	3.38
2	1.27	0.54	2.10
3	2.65	0.21	5.84

2.5 The Effect of Maneuver Epoch

The preceding results are based on a single maneuver epoch. Reference 3 (Table 2-29) indicates that the error in the change of the semimajor axis is sensitive to time. For three selected epochs, the error in the change of the semimajor axis varied from .12 to .60 meters.

The operational scenario for TOPEX allows for maneuvers to be postponed for one revolution if deemed necessary by the project office. Consequently, error analysis was undertaken for a second epoch, which was chosen as one revolution before the one used in the previous set of results.

Table 14 presents the results for both maneuver epochs. In general, the results indicate relatively small variations in the error of the change of parameters. This is not surprising, given the difference in the epochs of exactly one revolution. Larger variations might be seen if the second maneuver epoch were selected at a different point in the orbit.

3. CONCLUSIONS

This study has applied covariance analysis to investigate maneuver evaluation capabilities of the TOPEX satellite in the observational phase as a function of gravity model size. Three representations of the GEM T3 geopotential field have been considered: a full 50x50 model and 30x30 and 20x20 truncated models. Truncated fields were incorporated rather than folded-over representations, because error models for folded-over fields are not available. Orbit solutions using actual tracking data have indicated that folded-over fields should produce results superior to those based on truncated fields.

Table 14. Maneuver Evaluation Capabilities as a Function of Gravity Model Size and Time of Maneuver Using Unconstrained Postmaneuver Solutions

PREMANEUVER DATA SPAN = 7 DAYS POSTMANEUVER DATA SPAN = 23 HOURS				
PARAMETER	GRAVITY MODEL	REQUIREMENT	CAPABILITY	
			EPOCH 1	EPOCH 2
SEMIMAJOR AXIS (M)	FULL 50 × 50 TRUNCATED 30 × 30 TRUNCATED 20 × 20	0.2	0.20 0.21 0.29	0.20 0.21 0.31
INCLINATION (DEG × 10^4)	FULL 50 × 50 TRUNCATED 30 × 30 TRUNCATED 20 × 20	1.0	0.34 0.34 0.34	0.35 0.35 0.35
CROSSTRACK VELOCITY (MM/SEC)	FULL 50 × 50 TRUNCATED 30 × 30 TRUNCATED 20 × 20	10.0	4.3 4.3 4.3	4.3 4.3 4.3
RADIAL VELOCITY (MM/SEC)	FULL 50 × 50 TRUNCATED 30 × 30 TRUNCATED 20 × 20	10.0	17.3 17.4 14.9	15.1 15.0 12.3
ALONGTRACK VELOCITY (MM/SEC)	FULL 50 × 50 TRUNCATED 30 × 30 TRUNCATED 20 × 20	0.2	3.0 3.0 1.5	3.2 3.2 1.9

The proper methodology for analyzing instantaneous maneuvers is to incorporate constraints on the postmaneuver position components. The current version of the covariance analysis software cannot properly simulate constrained postmaneuver solutions. The covariance analysis results presented here are therefore limited to unconstrained postmaneuver simulations.

GTDS solutions using tracking data of the ERBS satellite have indicated two important features. First, errors in the change of parameters are substantially smaller for constrained postmaneuver solutions than unconstrained simulations, and, second, covariance analysis corresponding to the unconstrained ERBS solutions gives generally good agreement with the unconstrained GTDS simulations. These two features give credence to the error analysis results and suggest that if the requirements can be met with unconstrained simulations, they should also be met with constrained solutions.

Requirements on errors in the change of parameters have been placed on the semimajor axis, inclination, and three spacecraft-centered components of velocity (radial, crosstrack, and alongtrack). In general, the requirements on the inclination and crosstrack component of velocity can be met with any of the three gravity models using unconstrained postmaneuver solutions. The semimajor axis requirement is slightly exceeded for the 20x20 field, but these results assume the use of an unconstrained postmaneuver solution and a truncated field. The use of constrained postmaneuver solutions and folded-over fields should produce smaller errors.

The in-plane velocity component requirements are not met. The error in the change of the radial component of velocity is exceeded by a factor of approximately 2, while the error in the change of the alongtrack component of velocity is exceeded by a factor of 30. The analysis of tracking data using the GTDS program indicates an order-of-magnitude reduction in the error in the change of the alongtrack component of velocity for constrained solutions compared with unconstrained solutions. If this condition prevails for TOPEX, the requirement for the error in the change of the alongtrack component of velocity should be met or only slightly exceeded.

ACKNOWLEDGMENTS

The authors wish to acknowledge the contributions of Dr. Taesul Lee and Dr. Mina Samii in the preparation of this paper.

REFERENCES

1. NASA Conference Publication 3123, Flight Mechanics/Estimation Theory Symposium, *Flight Dynamics Facility Operational Orbit Determination Support for the Ocean Topography Experiment*, D. Bolvin, A. Schanzle, M. Samii (CSC), C. Doll (GSFC), May 1991

2. Goddard Space Flight Center, Flight Dynamics Division, FDD/554-90/131, *Ocean Topography Experiment (TOPEX) Satellite 1990 Flight Dynamics Analysis Report 1: Prelaunch Orbital Error Analysis*, A. Schanzle and J. Rovnak, prepared by Computer Sciences Corporation, August 1990

3. ——, 554-FDD-91/018, *Ocean Topography Experiment (TOPEX) Satellite 1990 Flight Dynamics Analysis Report 4: Orbital Error Analysis for Maneuver Planning and Maneuver Evaluation in the Observational Phase*, A. Schanzle and J. Rovnak, prepared by Computer Sciences Corporation, February 1991

4. NASA Technical Memorandum 104555, *Geopotential Models of the Earth from Satellite Tracking, Altimeter and Surface Gravity Observations: GEM-T3 and GEM-T3S*, F. J. Lerch et al., January 1992

5. *Geocenter Definition in the Determination of Dynamic Height Using GEOSAT Satellite Altimetry*, Koblinsky et al., in preparation

6. Schanzle, A., private communication with S. Klosko, STX Corporation, December 1991

7. Goddard Space Flight Center, Flight Dynamics Division, 554-FDD-91/156R0UD0, *Ocean Topography Experiment (TOPEX) Satellite 1991 Flight Dynamics Analysis Report 1: TOPEX In-Plane Maneuver Evaluation*, M. Nemesure and J. Rovnak, prepared by Computer Sciences Corporation, January 1992

ORBIT DETERMINATION AND ORBIT CONTROL FOR THE EARTH OBSERVING SYSTEM (EOS) AM SPACECRAFT

Joseph R. Herberg
General Electric Astro-Space Division

David C. Folta
Flight Dynamics Analysis Branch
Goddard Space Flight Center

ABSTRACT

Future NASA Earth Observing System (EOS) Spacecraft will make measurements of the earth's clouds, oceans, atmosphere, land and radiation balance. These EOS Spacecraft will be part of the NASA Mission to Planet Earth. This paper specifically addresses the EOS AM Spacecraft, referred to as "AM" because it has a sun-synchronous orbit with a 10:30 AM descending node. This paper describes the EOS AM Spacecraft mission orbit requirements, orbit determination, orbit control, and navigation system impact on earth based pointing. The EOS AM Spacecraft will be the first spacecraft to use the TDRSS Onboard Navigation System (TONS) as the primary means of navigation. TONS flight software will process one-way forward Doppler measurements taken during scheduled TDRSS contacts. An extended Kalman filter will estimate spacecraft position, velocity, drag coefficient correction, and ultrastable master oscillator frequency bias and drift. The TONS baseline algorithms, software, and hardware implementation are described in this paper. TONS integration into the EOS AM Spacecraft Guidance, Navigation and Control (GN&C) System, TONS assisted onboard time maintenance, and the TONS Ground Support System (TGSS) are also addressed.

This work was performed for the National Aeronautics and Space Administration (NASA) Goddard Space Flight Center (GSFC), Greenbelt, MD, under contract NAS5-32500.

1.0 INTRODUCTION AND BACKGROUND

Future NASA Earth Observing System (EOS) Spacecraft will make measurements of the earth's clouds, oceans, atmosphere, land and radiation balance. These EOS Spacecraft will be part of the NASA Mission to Planet Earth. This paper specifically addresses the EOS AM Spacecraft, referred to as "AM" because it has a sun-synchronous orbit with a 10:30 AM descending node. The EOS AM Spacecraft is shown in Figure 1. The first EOS AM Spacecraft is scheduled for launch in 1998. A second and third EOS AM Spacecraft will subsequently be launched in five year intervals. The five year mission life for each EOS AM Spacecraft will yield 15 years of continuous scientific observations. Normal command, telemetry, and primary science data return will be through the Tracking and Data Relay Satellite System (TDRSS). Additionally, a direct downlink capability will be provided to send science data directly to user ground stations.

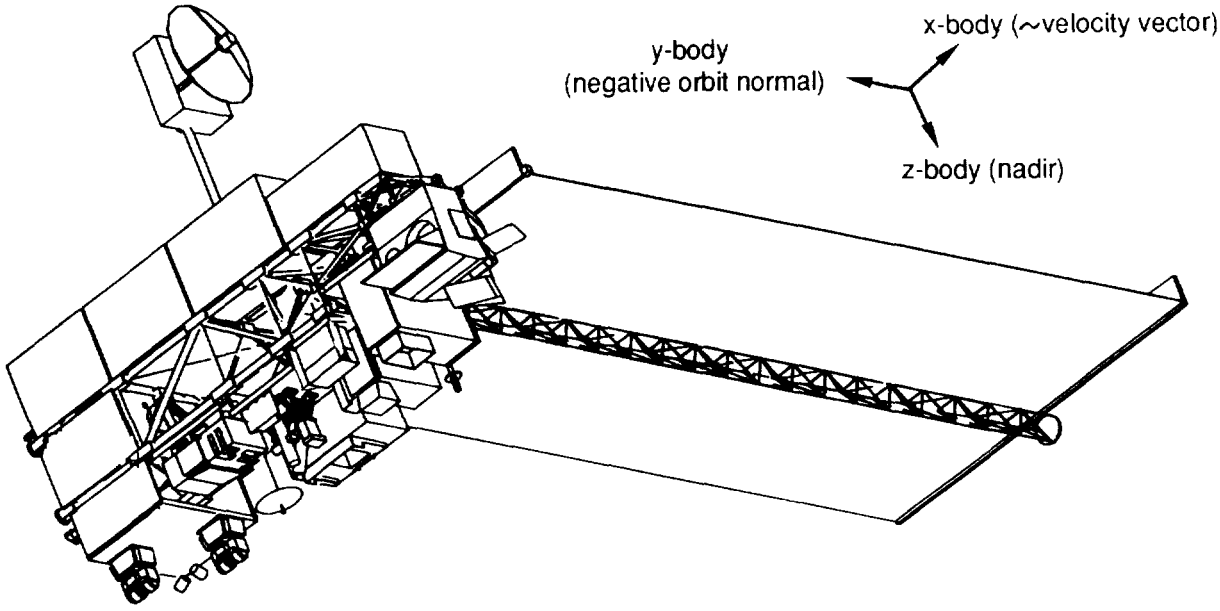

Figure 1 : EOS AM Spacecraft

Table 1 lists the EOS AM Spacecraft mission requirements that are related to orbit determination and orbit control. These requirements were derived from and are driven by instrument science requirements (Reference 1). Requirements include earth pointing knowledge and control, earth pointing jitter and stability, and navigation. Additional effort is in process to refine jitter and stability requirements, and to refine estimates of spacecraft performance with respect to jitter and stability. Jitter as used here refers to peak-to-peak spacecraft attitude motion over time periods required to image one pixel. Stability as used here refers to peak-to-peak spacecraft attitude motion over time periods required to image one scene composed of many pixels. The location of a pixel or scene on the surface of the earth is referred to as the geolocation. Navigation as used here refers to real-time onboard orbit determination. The EOS AM Spacecraft is currently baselined with a geocentric attitude, meaning the spacecraft z-body axis will point toward the center of the earth.

Table 1 : EOS AM Spacecraft Mission Related Requirements (3-sigma)

Parameter	Requirement
Repeating Ground Track	16 day repeat cycle, 233 orbits per cycle, +/- 20 kilometers at all latitudes
Sun-Synchronous Orbit	10:30 AM descending node, +/- 15 minutes, local mean solar time
Radial Orbit Position Repeatability	+/- 5 kilometers at a given latitude
Earth Pointing Knowledge	+/- 90 arc-seconds, per axis
Earth Pointing Control	+/- 150 arc-seconds, per axis
Earth Pointing Jitter and Stability (Requirements Definition in Progress)	Peak-to-peak, per axis, over time periods from less than 1 second up to 1000 seconds
Navigation Radial Position	+/- 150 meters
Navigation Intrack Position	+/- 150 meters
Navigation Crosstrack Position	+/- 150 meters
Navigation Crosstrack Velocity	+/- 0.160 meters/second
Time Knowledge	+/- 100 microseconds

Table 2 lists the mean orbit elements that satisfy the mission requirements in Table 1. This orbit is very similar to the Landsat-4/5 orbits and may use the same World Reference System (WRS) ground track. The repeating ground track period of 16 days and the sun-synchronous orbit require a mean semimajor axis of 7078 kilometers and a mean inclination of 98.2 degrees. The mean nodal period is 5933 seconds and the mean equatorial altitude is 705 kilometers. The sun-synchronous descending node time is specified with respect to a fictitious mean sun. The local true solar time will actually vary by as much as 16 minutes from the local mean solar time. Radial orbit position repeatability of +/- 5 kilometers requires a frozen orbit with a mean eccentricity of 0.0012 and a mean argument of perigee of 90 degrees.

Table 2 : EOS AM Spacecraft Mean Orbit Elements

Parameter	Value
Semimajor Axis	7078 kilometers
Inclination	98.2 degrees
Eccentricity	0.0012
Argument of Perigee	90 degrees
Descending Node	10:30 AM Sun-Synchronous

The EOS AM Spacecraft will use the TDRSS Onboard Navigation System (TONS) as its primary means of navigation. The Global Positioning System (GPS) had previously been considered as the source of measurements for the navigation system. GPS is a satellite based navigation system owned and operated by the Department of Defense (DoD). A TONS / GPS trade study addressed accuracy, power, weight, security, risk, and cost. A TONS implementation would require the addition of TONS software, and would use the S-band transponder and ultrastable oscillator already provided for communications and for ground based TDRSS tracking. A GPS implementation would require additional and redundant flight hardware including antennas, preamps, cabling, and receiver / processors. Performance analyses showed that both TONS and GPS could meet a +/-150 meter navigation requirement under nominal conditions. However, the cost and security concerns of the military version of GPS, and the inability to guarantee the performance of the civilian version of GPS during times of crises, were major factors in the decision to select TONS rather than GPS.

Section 2.0 of this paper describes how navigation errors affect attitude control and geolocation. Section 3.0 provides an overview of TONS and describes the TONS implementation baseline for the EOS AM Spacecraft. Section 4.0 discusses TONS interfaces with the real-time navigation and attitude control system. Example jitter and stability results are also presented in section 4.0. Section 5.0 describes the TONS ground support system and other ground system interfaces. Section 6.0 briefly describes orbit control. Section 7.0 provides a summary and conclusions.

2.0 NAVIGATION IMPACT ON ATTITUDE CONTROL AND GEOLOCATION

The EOS AM Spacecraft navigation system will generate real-time estimates of spacecraft position and velocity. Near real-time position and velocity estimates will be obtained by processing TDRSS Doppler measurement data in an onboard extended Kalman filter. These estimates will then be propagated up to real-time and used to compute the commanded spacecraft body axis inertial attitude as illustrated in Figure 2 and detailed in the Appendix. Examples 1 and 2 in the Appendix show how navigation errors impact the commanded attitude on a per axis basis. TONS and the short term high rate propagator are described later in sections 3.0 and 4.0, respectively.

The EOS AM Spacecraft primary mode attitude determination system will generate real-time estimates of the actual spacecraft body axes inertial attitude. These estimates will be obtained by processing star tracker and rate gyro measurement data in an onboard extended Kalman filter. The attitude control system will compute an attitude error by taking the difference between the commanded attitude and the estimated attitude. The attitude control system will then drive this error toward zero by commanding reaction wheel or thruster torques. Errors in the navigation system will therefore result in errors in the actual spacecraft attitude.

A navigation error will also result in an error in the projection of the spacecraft position on to the surface of the earth, referred to as the subsatellite location knowledge error. The navigation induced subsatellite location knowledge error and the navigation induced attitude error are both illustrated in Figure 3 using the example of a 150 meter intrack position knowledge error. This 150 meter error will result in a 135 meter subsatellite location knowledge error. This 150 meter

error will also result in a 4.4 arc-second attitude error. The 4.4 arc-second attitude error contributes an additional 15 meters to the geolocation knowledge error as shown by example 3 in the Appendix. The total geolocation knowledge error from a 150 meter intrack position knowledge error is therefore 150 meters (135 meters + 15 meters).

A navigation correction will result in spacecraft attitude motion with respect to the desired spacecraft attitude. This attitude motion must be considered when evaluating jitter and stability. The 150 meter intrack position knowledge error is used here again as the example. Assume that the navigation error had grown to 150 meters, then a measurement was processed and the navigation error reduced to 0 meters. Although this situation represents a desirable correction to the navigation estimate, it results in a 4.4 arc-second change in the commanded spacecraft attitude with respect to the desired spacecraft attitude. The actual spacecraft attitude will then change by 4.4 arc-seconds with respect to the desired spacecraft attitude, as the attitude control system tracks this command. The 150 meter correction to the navigation estimate will therefore result in a 150 meter correction to geolocation knowledge, and a 15 meter correction to geolocation pointing.

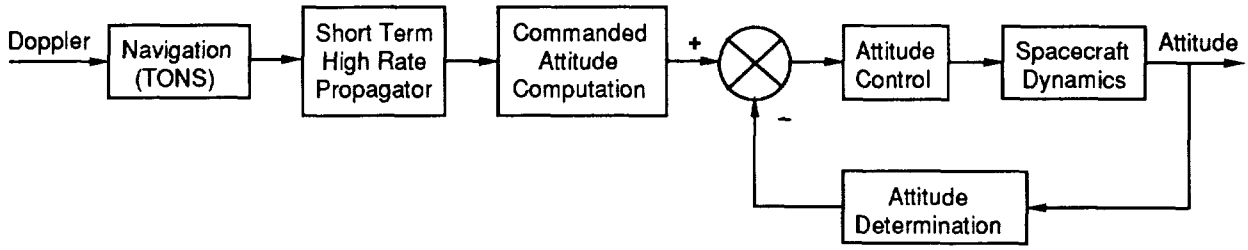

Figure 2 : TONS / Attitude Control System Interface Block Diagram

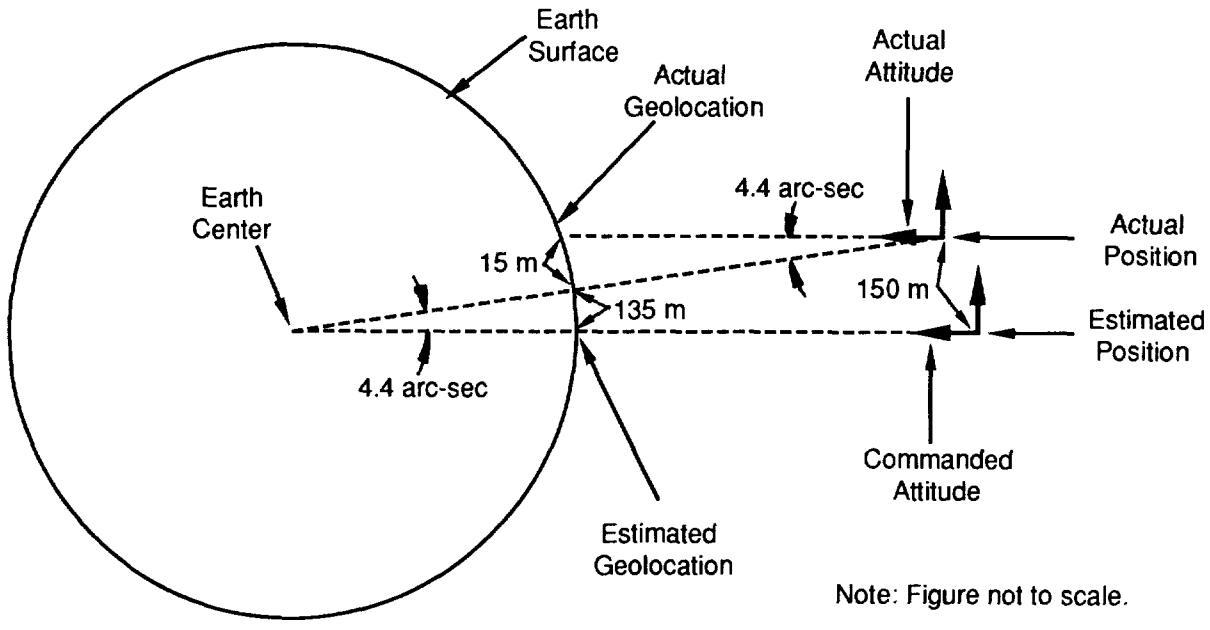

Figure 3 : Geocentric Earth Based Pointing

3.0 TDRSS ONBOARD NAVIGATION SYSTEM (TONS)

TONS Overview

There are two user implementations of TONS, referred to as TONS-I and TONS-II. TDRSS infrastructure currently supports a TONS-I user capability. During scheduled TDRSS communication contacts the TONS-I user extracts, time tags and processes one way forward S-Band (approximately 2106.4 MHz) Doppler measurements. White Sands Ground Terminal Doppler compensation is inhibited so that the user can extract valid Doppler measurements. A TONS-II user would also have access to the planned TDRS-II navigation beacon and would not require scheduled TDRSS services. The TONS-II navigation beacon will include a pseudorange measurement and a navigation message similar to GPS. TONS-II offers the following advantages over TONS-I: reduced TDRSS scheduled resources, near continuous Doppler tracking, more current and accurate TDRS ephemerides, and onboard time determination. The EOS AM Spacecraft is baselined with TONS-I and is expected to have provisions for TONS-II.

A TONS experiment will be performed in conjunction with the Explorer Platform (EP) / Extreme Ultraviolet Explorer (EUVE) mission to flight qualify TONS-I (References 2 and 3). Onboard Doppler extraction, onboard Doppler compensation, and TONS algorithms and software will be proven by this experiment. A GPS receiver / processor will also be flown on EP / EUVE for comparison purposes with TONS. EP / EUVE is currently scheduled for launch in May 1992. TONS data collection and analysis will continue for one year after launch. Lessons learned from the EP / EUVE experiment will be factored into the EOS AM Spacecraft implementation of TONS. Algorithms and software will be optimized for the EOS AM Spacecraft with respect to speed, accuracy and robustness. EOS AM Spacecraft unique features will also be added.

TONS uses an extended Kalman filter to measurement update the state vector estimate and the associated state error covariance matrix. The state vector includes user spacecraft position, velocity, drag coefficient correction, spacecraft ultrastable oscillator frequency bias and drift, and a spacecraft clock time bias. The state error covariance matrix represents the uncertainty in the state vector estimate. The filter computes measurement residuals by taking the difference between actual measurements and estimated measurements. The actual measurement is considered valid if it passes a 3-sigma or 4-sigma measurement residual edit test. The fraction of the measurement residual to be incorporated in the measurement update is a function of the uncertainty in the measurement, and the uncertainty in the current state vector estimate. Spacecraft position and velocity are propagated between measurement updates with a [30 x 30] earth gravity model, drag, solar gravity and lunar gravity. A physically connected state noise model (References 4 and 5) is used to account for uncertainties in the [30 x 30] earth gravity model.

The actual observation from the S-Band transponder is an accumulated Doppler cycle count. A Doppler cycle count difference is computed by taking the difference between two successive accumulated Doppler cycle counts, approximately 10 seconds apart. An average Doppler measurement is computed by dividing the Doppler cycle count difference by the 10 second integration time. The Doppler measurement is modeled in the TONS Kalman filter as a change in range over the 10 second integration time. The measurement model also includes the ultrastable

oscillator frequency bias and drift. TONS requires knowledge of TDRS positions when estimating Doppler measurements. TDRS state vectors will be uplinked daily and propagated in TONS-I with an [8 x 8] earth gravity model, lunar gravity, solar gravity and solar pressure. TDRS positions will be accurate to +/-150 meters (3-sigma) after a one day onboard propagation.

Current and near term TONS algorithm development studies are addressing covariance factorization for numerical stability (Reference 6), addition of a state vector element to model the time correlated measurement noise characteristics of TDRS ephemeris errors, refinements to the earth gravity state noise model, additional measurement residual edit tests, and thrust acceleration modeling during orbit maneuvers. Current and near term error analyses are addressing TDRSS scheduling sensitivities, the effects of a flight processor 48 bit word length, processing requirements for different sections of the EP / EUVE TONS software, ionospheric refraction during periods of high solar activity, and Doppler measurement time tag errors.

EOS AM Spacecraft Implementation of TONS

The EOS AM Spacecraft will use TONS as the primary means of navigation. TONS performance will vary somewhat as a function of the number, duration, and location of TDRSS scheduled contacts, and the selection of TDRS East or TDRS West. Nominal EOS AM Spacecraft performance analyses have assumed one 20 minute contact every 99 minute orbit. On average, TONS must therefore propagate its state vector estimate and state error covariance matrix for 79 minutes between measurement updates. EOS AM Spacecraft performance assessments for TONS are based on TONS-I (Reference 7). Performance estimates ranged from a best case of 16 meters (1-sigma), to a worst case of 35 meters (1-sigma) for the case of high drag and degraded TDRSS scheduling. The nominal performance estimate is 25 meters (1-sigma).

Communication and navigation requirements will both be factored into the EOS AM Spacecraft TDRSS scheduling process. Multiple shorter duration contacts, e.g., two 10 minute contacts instead of one 20 minute contact, are preferable for navigation because (1) they are easier to optimally schedule than one long contact, (2) they provide the opportunity to observe different parts of the orbit, and (3) they reduce the propagation time between measurement updates. Navigation requirements will be specified by geometric criteria that maximize Doppler observability and minimize ionospheric refraction. Doppler observability is maximized for the radial and intrack directions when the scheduled TDRS is in the EOS AM Spacecraft orbit plane. Ionospheric refraction is minimized by avoiding long, low altitude, signal paths through the earth's atmosphere. In general, geometric requirements for TONS are similar to those for standard ground based orbit determination with TDRSS.

The EOS AM Spacecraft has one 4.5 foot diameter Ku/S-Band high gain antenna, one zenith facing S-Band omni antenna, and one nadir facing S-Band omni antenna. The TONS-I Doppler measurement can be obtained via the high gain antenna with S-Band Multiple Access (SMA) service or S-Band Single Access (SSA) service, or via the zenith S-Band omni antenna with SSA service. Link margin analysis has shown that the TDRS-II navigation beacon could be obtained via the EOS AM Spacecraft high gain antenna.

TONS software will be located in the EOS AM Spacecraft Control Computer (SCC) as shown in the TONS functional interface block diagram in Figure 4. Attitude determination, attitude control, delta-v control, high gain antenna control, solar array drive control, and navigation are all elements of the EOS AM Spacecraft Guidance, Navigation and Control (GN&C) System. The SCC will be a MIL STD 1750A instruction set architecture computer. SCC processing and memory requirements include allocations for TONS Ada flight software, based on EP / EUVE TONS software (Reference 2) with modest growth provisions for EOS AM Spacecraft unique features.

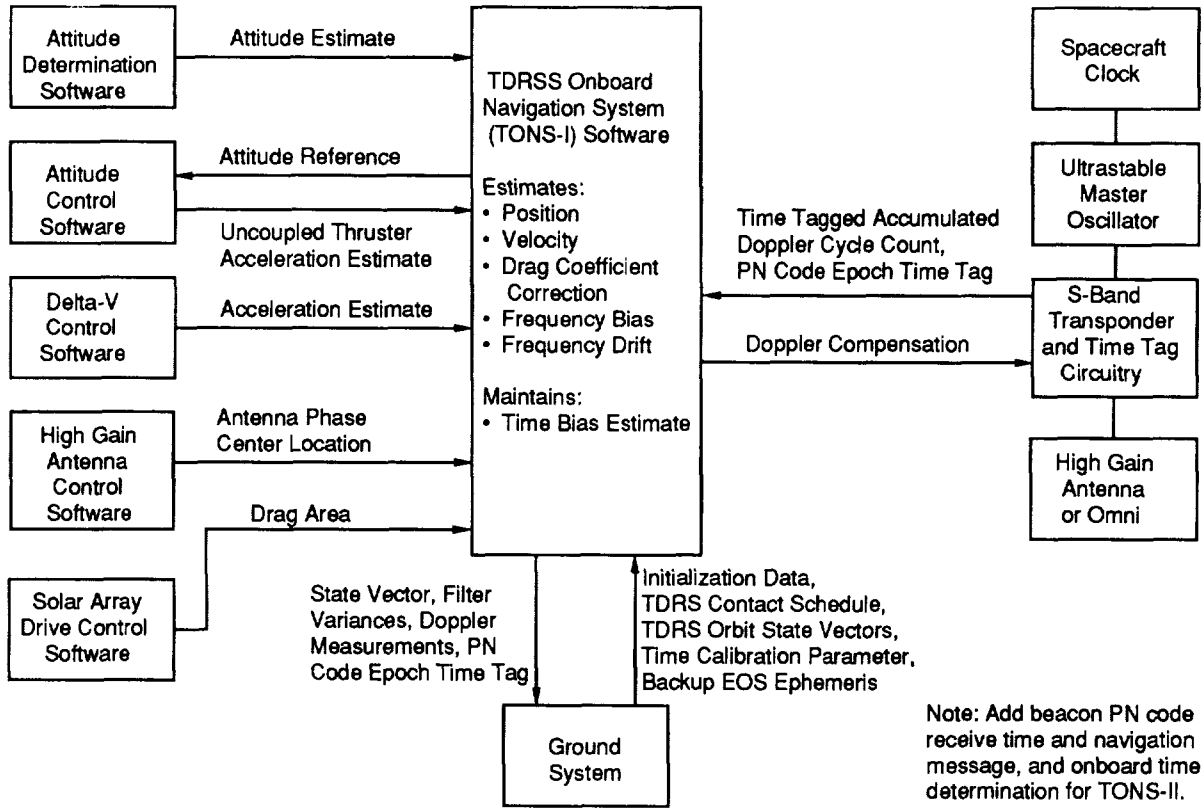

Figure 4 : TONS / EOS AM Spacecraft Functional Interface Block Diagram

The EOS AM Spacecraft baseline has a 20 MHz ultrastable master oscillator that provides commonality in reference frequencies for the Command and Data Handling subsystem and the Communication subsystem. The drift in the ultrastable master oscillator will be less than 1.0E-10 parts per day. Short term stability will be approximately 1.0E-12 parts over 10 seconds. The Command and Data Handling subsystem will use the 20 MHz frequency to derive the 1 MHz spacecraft clock. The 20 MHz master oscillator will also be used to derive a 5 MHz frequency for the S-band transponder. The S-Band transponder will be a third generation transponder with a built-in Doppler extraction function. The S-Band transponder will control the Doppler integration interval within an accuracy of +/- 25 nanoseconds. The S-Band transponder will have access to the spacecraft time and frequency bus and will generate time tags for the Doppler measurement.

The EOS AM Spacecraft requires accurate onboard time for (1) time tagging Doppler measurement data for TONS, (2) incorporating uplinked TDRS state vectors and initial EOS state vectors in TONS, (3) time tagging spacecraft position, velocity, attitude, and other data in the spacecraft ancillary telemetry stream, and (4) time tagging instrument science data. The spacecraft time knowledge requirement is +/- 100 microseconds. Actual time knowledge accuracy may vary from +/-5 to +/-30 microseconds, depending upon the accuracy and frequency of ground based spacecraft clock calibrations. TONS-I Doppler only measurements can not estimate the spacecraft clock time bias, but TONS-I frequency bias and drift estimates can be integrated to maintain an onboard software estimate of the spacecraft clock time bias. Preliminary analyses have shown that TONS-I can maintain the time bias estimate within a few microseconds of its uplinked value for days to weeks. Ground based spacecraft clock calibration is described briefly in section 5.0.

In the event of TDRSS contact outages, TONS will continue to propagate an accurate EOS AM Spacecraft state vector and accurate TDRS state vectors. Additionally, a backup onboard ephemeris will be provided for the EOS AM Spacecraft. This ephemeris will be sufficient for S-Band high gain antenna pointing and will also be used periodically in the flight software Fault Detection, Isolation, and Recovery (FDIR) logic for TONS. The TONS position estimate and the backup onboard ephemeris will be differenced, and a flag set if this difference exceeds the accuracy of the backup onboard ephemeris. If this flag is set, the ground system will be notified so that appropriate action can be taken. Various backup ephemeris representations are presently being considered. TONS estimates of the ultrastable master oscillator frequency bias and drift, drag coefficient correction, and time bias could also be compared onboard with uplinked backups.

TONS is not required to meet EOS AM Spacecraft mission requirements during propulsive orbit and attitude maneuvers. Additional TDRSS contacts will be requested during and after these maneuvers for monitoring and tracking. As shown in Figure 4, TONS will have knowledge of thrust accelerations acting on the spacecraft center of mass. TONS will maintain a valid state vector estimate and state error covariance matrix during drag makeup maneuvers. Future analyses will determine if the +/-150 meter navigation requirement can be maintained during drag makeup maneuvers, and if not, the time required to reconverge.

4.0 TONS REAL-TIME INTERFACE

As discussed in section 2.0 and shown in the Appendix, real-time position and velocity estimates will be used to generate the commanded spacecraft attitude. This section discusses the interface between TONS and the EOS AM Spacecraft real-time navigation and attitude control system. Simulation programs and simulation results are presented as necessary to understand the associated jitter and stability issues. TONS accuracy estimates were presented in section 3.0.

A TONS truth model simulation, a TONS filter model simulation, and an example TONS real-time interface simulation were used to generate the jitter and stability results in this section. These simulations are currently being used for real-time navigation sensitivity studies and for TONS real-time interface algorithm development. The TONS filter model algorithms and simulation results are similar to those in Reference 7.

The TONS truth model simulation used the Artificial Satellite Analysis Program (ASAP), (Reference 8) to generate simulated truth trajectories for the EOS AM Spacecraft, TDRS East, and TDRS West. The EOS AM Spacecraft trajectory was generated with a [36 x 36] GEM-T1 earth gravity model, solar gravity, lunar gravity, solar pressure and drag. Atmospheric density was based on the Jacchia J70 model with a Solar Flux (F10.7) of 230 and a Geomagnetic Activity Index (Ap) of 400. TDRS truth trajectories and TDRS filter trajectories were generated with 150 meter errors similar to those in Reference 7. The TONS "average Doppler" measurement was modeled in the TONS truth model as a "range difference + integrated frequency error range difference equivalent". Units are therefore expressed in meters rather than Hz. The simulated observation was corrupted with timewise uncorrelated Gaussian noise with a 1-sigma value of 0.0141 meters at each sample time. Because the average Doppler measurement (range difference) involves two independent samples, the measurement noise is statistically greater by the square root of two and would be 0.020 meters. Assuming no cycle slips, the measurement noise is actually correlated in a desirable fashion from one measurement to the next. Simulated measurements include the effects of the ultrastable master oscillator frequency bias and drift. The simulated frequency drift was 1.0E-10 parts per day.

The TONS filter model simulation used a ten element state vector (XYZ position, XYZ velocity, drag coefficient correction, oscillator frequency bias, oscillator frequency drift, and a time bias). A fourth order Runge-Kutta integrator was used with a 10 second time step. The TONS state vector estimate and the state error covariance matrix were always propagated to the measurement start time, then to the measurement stop time, but never ahead of the start time in order to prevent backward integration when estimating the measurement. The acceleration model used a [22 x 22] GEM-10B earth gravity model and an exponential atmospheric density model. Position and velocity state noise were modeled in the radial, intrack, and crosstrack directions. In comparison to the simulated truth measurement noise of 0.020 meters, the filter measurement noise value was set high at 0.142 meters to compensate for the unmodeled TDRS ephemeris biases. The oscillator frequency drift and the drag coefficient correction were modeled in the filter as first order Gauss-Markov variables with time constants of 100,000 seconds. The oscillator frequency bias was modeled as the integral of the oscillator frequency drift. The time bias was modeled as the integral of the normalized frequency bias and drift. No effort was made to optimally tune the filter.

The TONS real-time interface simulation used the example timeline and algorithms in Figure 5. Simulated measurements were processed every 10 seconds. A short term high rate propagator took the latest near real-time TONS estimate, measurement updated or not, propagated it forward in time and blended it in with the real-time navigation estimate. The commanded spacecraft attitude was then computed. A third order Taylor series integrator and a J2 earth gravity model were used to propagate the TONS estimate up to real-time. The Taylor series integrator, acceleration and its derivatives were taken from Reference 9. The propagated estimate was blended into the real-time system over a 10 second period in 0.5 second increments. The Taylor series integrator only required one evaluation of acceleration and its derivatives at the start of the 10 second blending interval for all twenty 0.5 second increments. The example interface algorithm in Figure 5 introduced an error less than 0.1 meters in position and less than 0.005 meters/second in velocity. A [4x4] earth gravity model could be used in the acceleration computation to improve accuracy.

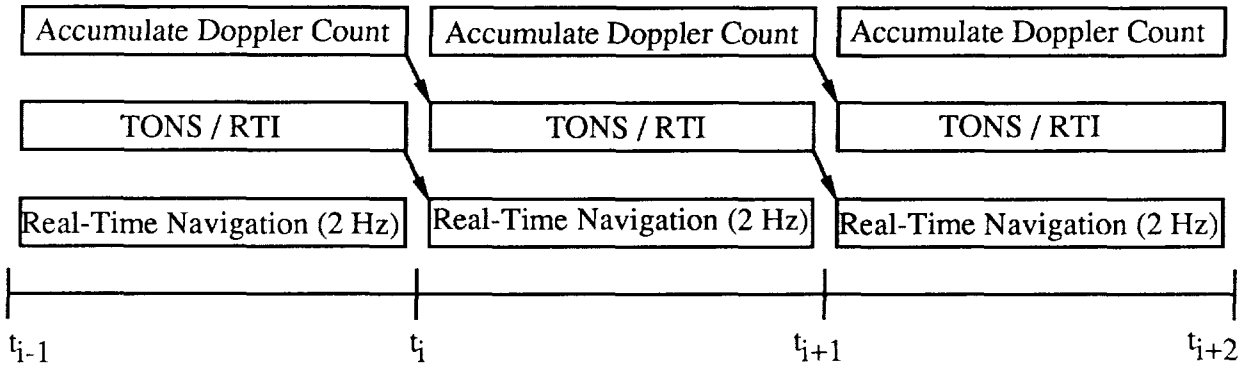

TONS / RTI Software Processing Every 10 Second Cycle ($t_{i+1} - t_i = 10$ seconds)

TONS Receive time tagged accumulated Doppler cycle count N_i.

TONS Compute Doppler cycle count difference: $\Delta N_i = N_i - N_{i-1}$. Count N_{i-1} and time t_{i-1} known from previous cycle.

TONS Propagate TONS state estimate and covariance: $\hat{x}_{i-1} \rightarrow \hat{x}_i^-$; $P_{i-1} \rightarrow P_i^-$. TONS state estimate $\hat{x}_{i-1}$ and covariance P_{i-1} known from previous cycle.

TONS Estimate measurement using TONS state estimates $\hat{x}_{i-1}$ and $\hat{x}_i^-$, then perform edit test.

TONS Measurement update TONS state estimate and covariance: $\hat{x}_i^- \rightarrow \hat{x}_i^+$; $P_i^- \rightarrow P_i^+$.

RTI Propagate TONS state estimate using Taylor series integrator*: $\hat{x}_i^+ \rightarrow \tilde{x}'_{i+1}$.

RTI Compute available correction to real-time state estimate: $\Delta\tilde{x}_{i+1} = [\tilde{x}'_{i+1} - \tilde{x}_{i+1}]$. Real-time estimate $\tilde{x}_{i+1}$ is known from previous cycle.

RTI Compute real-time state estimates $\tilde{x}_{i+1+1/20}$, ..., $\tilde{x}_{i+2}$ using Taylor series integrator* with one evaluation of acceleration and its derivatives for time t_{i+1}:

$$[\tilde{x}_{i+1} + \Delta\tilde{x}_{i+1} \cdot j/20] \rightarrow \tilde{x}_{i+1+j/20} \qquad j = 1, 2, ..., 20.$$

---

*Third order Taylor series integrator propagates position ($\bar{R}$) and velocity ($\dot{\bar{R}}$) from any time step (k) to (k+1). Acceleration ($\ddot{\bar{R}}$) and its derivatives include the J_2 earth zonal harmonic.

$$\bar{R}(k+1) = \bar{R}(k) + \dot{\bar{R}}(k)\,\Delta T + \ddot{\bar{R}}(k)\,\Delta T^2/2 + \dddot{\bar{R}}(k)\,\Delta T^3/6.$$

$$\dot{\bar{R}}(k+1) = \dot{\bar{R}}(k) + \ddot{\bar{R}}(k)\,\Delta T + \dddot{\bar{R}}(k)\,\Delta T^2/2 + \ddddot{\bar{R}}(k)\,\Delta T^3/6.$$

Figure 5 : Example Real-Time Interface (RTI) for TONS

Simulation results were generated using a two day TDRSS contact schedule that had 20 minutes of geometrically favorable contact with a TDRS every orbit (Reference 7). Simulated errors were computed by comparing simulated filter estimates with simulated truth data. The intrack position error was larger than the radial and crosstrack position errors. A representative one day simulated intrack position error profile is shown in Figure 6. The 1-sigma values from the filter state error covariance matrix were consistent with the simulated errors for all state vector elements.

Peak navigation transients occur during TONS measurement updates as can be seen in Figures 6 and 7 at time [45 hours : 11 minutes = 2711 minutes]. The intrack position error and the associated filter state error covariance matrix had both grown for 79 minutes since the last TONS measurement update at time [43 hours : 52 minutes = 2632 minutes]. At time [45 hours : 11 minutes = 2711 minutes] a measurement was obtained and a 40 meter correction made to the intrack position estimate. Although this 40 meter change is a correction to the TONS intrack position estimate, its effects must be considered in jitter and stability analyses. If incorporated immediately, the 40 meter correction would result in a 1.2 arc-second step change in the commanded pitch attitude. If blended in smoothly over the next 10 seconds as shown in Figure 8, this would result in a 0.12 arc-second per second ramp change in the commanded pitch attitude. Note that the TONS measurement update valid at time [2711 minutes : 00 seconds] was not incorporated into the real-time system until time [2711 minutes : 10.5 seconds].

Figure 8 also shows the approximate attitude control system / spacecraft rigid body response to a navigation transient. This dynamic response is very approximate and is shown here for illustration only. The dynamic response was modeled as a second order system with an undamped natural frequency of 0.14 radians / second and a damping ratio of 0.6. Jitter and stability can be evaluated from the simulated attitude control system response in Figure 8. As an example, the peak-to-peak attitude error change was 0.7 arc-seconds over 10 seconds. A longer blending time will result in a smaller rate of change. Blending the 1.2 arc-second command in over 60 seconds resulted in a peak-to-peak attitude error change of 0.2 arc-seconds over 10 seconds. Navigation transients will be incorporated into the EOS AM Spacecraft attitude control system simulation in the future.

Analysis to date has demonstrated the feasibility of interfacing TONS with the EOS AM Spacecraft real-time navigation / attitude control system. Future studies will address longer blending times and other interface algorithms. For example, the TONS integrator and force model could be used to propagate a state vector ahead of real-time, then real-time data obtained by interpolation. Final algorithm selection will depend upon spacecraft jitter and stability requirements, TONS Doppler measurement processing rate and propagation step size (e.g. every 10 seconds vs. every 60 seconds), and associated accuracy vs. processing trades.

5.0 TONS GROUND SYSTEM INTERFACE

The TONS Ground Support System (TGSS) will be used to perform quality assurance checking of downlinked TONS state vectors, support initial on-orbit filter tuning, evaluate performance, provide diagnostic assistance, and verify flight software updates. The TGSS is currently independent of standard GSFC Flight Dynamics Facility (FDF) operations such as orbit

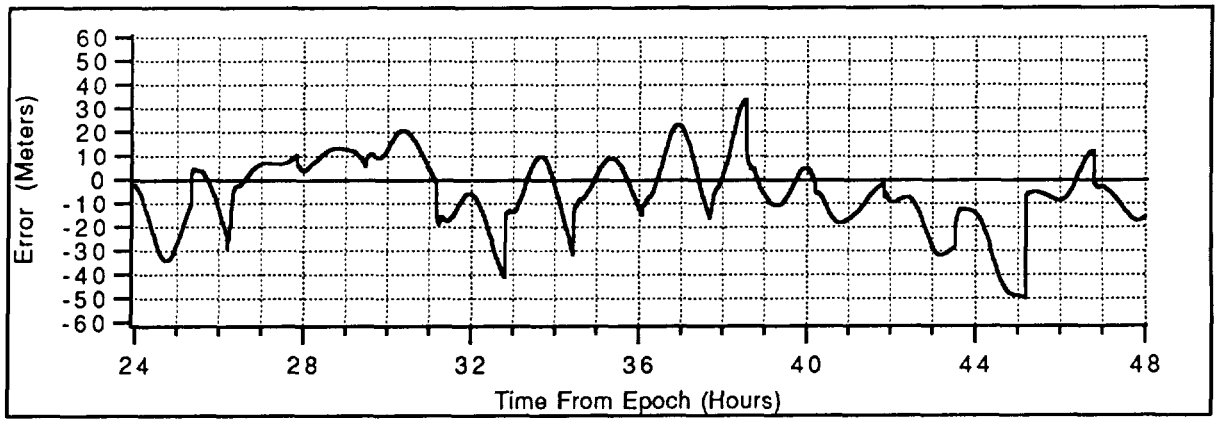

Figure 6 : TONS Intrack Position Error

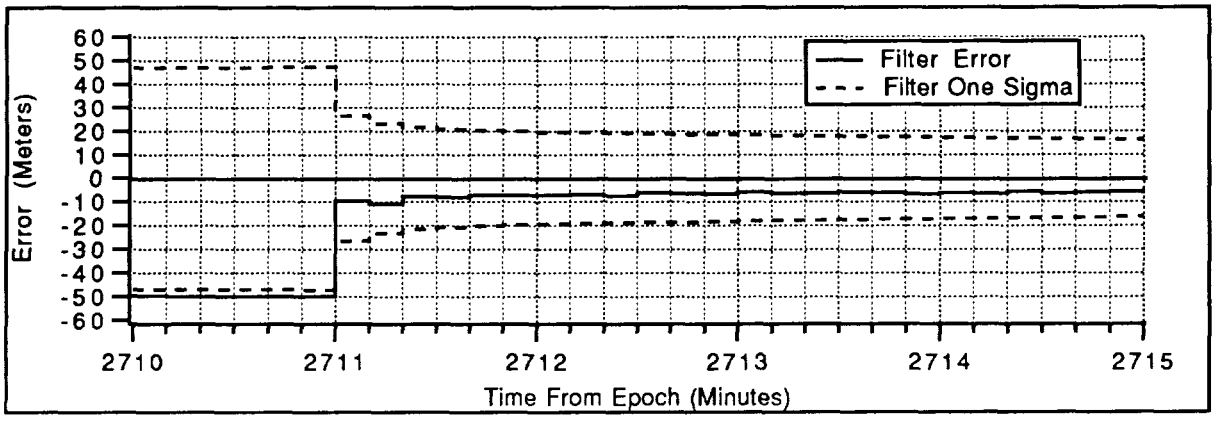

Figure 7 : TONS Intrack Position Error Transient

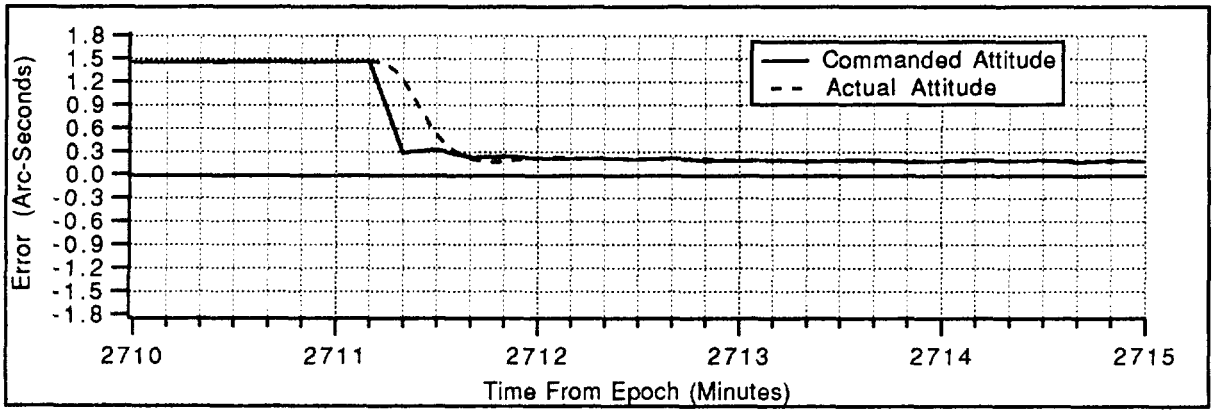

Figure 8 : Approximate Pitch Axis Response

determination and ephemeris generation. The TGSS will be independent of the EOS AM Spacecraft Operations Center which will factor navigation requirements into the TDRSS scheduling process, perform spacecraft clock calibration, and handle normal command and telemetry.

Backup orbit determination and any ephemeris generation functions will be performed by the GSFC FDF. Two way coherent range and Doppler measurements, or one way return noncoherent Doppler measurements will be obtained via TDRSS tracking. Coherent and noncoherent measurements can be obtained simultaneously with TONS onboard Doppler extraction. Ground based measurements will be processed in a batch least squares process to generate an estimate of the spacecraft orbit state vector at a given epoch. This orbit state vector, a table of predicted state vectors, or a Fourier power series fit to a predicted ephemeris will then be uplinked to the EOS AM Spacecraft. This backup ephemeris data will be generated and uplinked as often as necessary depending upon the level of solar activity and drag. Ground based orbit determination results will be used in the TGSS for quality assurance checking of downlinked TONS state vectors.

The EOS AM Spacecraft will use the User Spacecraft Clock Calibration System (USCCS) developed for the Gamma Ray Observatory (GRO). The USCCS is a method designed for calibrating a spacecraft clock using TDRSS pseudo-random noise (PN) ranging epochs. The USCCS is expected to provide time calibration accuracy of approximately +/- 5 microseconds with respect to Universal Time Coordinated (UTC). The USCCS is described in Reference 10. EOS AM Spacecraft clock calibration will be performed by the EOS AM Spacecraft Operations Center in conjunction with the White Sands Ground Terminal. A brief description of the USCCS is given here: (1) The spacecraft S-band transponder extracts and time tags a PN code epoch from the TDRSS forward S-band signal. This time tag is based on the PN code epoch receive time as observed by the spacecraft clock; (2) This time tag is then sent to the ground system in spacecraft telemetry; (3) The ground system estimates the time at which the spacecraft should have received the PN code epoch, then computes the difference between the telemetered time tag and the ground predicted time tag. This difference is the clock calibration parameter; (4) This clock calibration parameter is then uplinked to the spacecraft.

Normal one per orbit navigation telemetry will include time tagged state vector estimates and filter variances, time tagged Doppler measurements, the number of edited Doppler measurements, a flag to indicate if the filter position or velocity variances exceeded pre-specified limits, a flag to indicate if the TONS state estimate exceeded a pre-specified tolerance when compared with the backup onboard ephemeris, and a flag to indicate if other TONS state vector elements exceeded a pre-specified tolerance when compared with onboard backup values. When requested for initial filter tuning, performance evaluation, or diagnostics, telemetry will also include measurement data quality, time tagged filter measurement residuals, and time tagged state error covariance matrices.

Normal one per day navigation commands and data will include TDRS state vectors, a backup EOS ephemeris, a backup for other TONS state vector elements, and a time calibration parameter. As necessary, commands and data will also include an initial state vector estimate and initial state error covariance matrix for TONS, filter tuning parameters for TONS, TDRS contact schedules, flags indicating TDRS orbit adjusts, flags indicating EOS AM Spacecraft orbit and attitude maneuvers, a solar activity parameter, major changes to spacecraft mass, and flight software updates.

Ground based post-processing could be a solution for instruments that might desire non-real-time accuracies significantly better than +/-150 meters. Ground based post-processing has the following advantages in comparison to onboard real-time navigation: (1) Real-time estimates are based on measurement data up to the current time. Post-processed estimates can include additional "future" measurement data when the epoch of interest is centered within the fit interval. In other words, today's estimate of the orbit state vector at yesterday's epoch can be better than yesterday's estimate of the orbit state vector at yesterday's epoch; (2) Ground based computers have more processing and data storage capability than flight computers. This allows for the use of more sophisticated models and algorithms; (3) Ground based post-processing can incorporate additional measurement data types not available to the onboard navigation system, such as two way range data; (4) Ground based post-processing can incorporate today's knowledge of yesterday's solar activity; (5) Ground based post-processing allows for manual inspecting and editing of potentially bad measurements.

6.0 ORBIT CONTROL

The GSFC FDF will perform orbit maneuver prediction and orbit maneuver planning. Orbit maneuvers include initial mission orbit acquisition, drag makeup, frozen orbit maintenance, inclination correction, and end-of-life safe re-entry if required. Maneuver command tables will be generated at the GSFC FDF and uplinked via the EOS AM Spacecraft Operations Center. The maneuver planning algorithm considers uncertainties in orbit determination, maneuver execution, and orbit propagation. The maneuver plan will include burn start time, total required ΔV, and estimated burn duration. The onboard system will compute the delivered ΔV open loop and stop the burn when the commanded ΔV has been achieved. The closed loop attitude control system will fire thrusters as necessary to maintain attitude control. TONS state vectors will be used by the GSFC FDF for orbit maintenance maneuvers.

The EOS AM Spacecraft will be launched with an expendable launch vehicle from the Vandenberg Air Force Base in California. The launch vehicle will inject the EOS AM Spacecraft into an orbit with a 300 kilometer perigee altitude and a 705 kilometer apogee altitude. The target apogee altitude may be biased low to account for launch vehicle dispersions, and apogee altitude increases during the mission orbit acquisition sequence. The EOS AM Spacecraft will use its hydrazine based propulsion system to boost up to the mission orbit. The target inclination may also be biased to maximize the time to the first inclination correction maneuver (Reference 11).

Atmospheric drag will cause a decay in semimajor axis. This will result in a decrease in the nodal period and a drift in the ground track. Drag makeup maneuvers will be required to reset the semimajor axis and thus maintain the ground track within the +/- 20 kilometer tolerance. The time between drag makeup maneuvers will vary with the level of solar activity. The time between maneuvers is expected to vary from approximately 7 days to approximately 3 months.

A frozen orbit minimizes altitude variations at any given latitude. The orbit is frozen when secular perturbations due to even zonal harmonics are balanced by long period perturbations due to odd zonal harmonics in the earth's gravity field. This condition exists for the EOS AM Spacecraft orbit

when the mean eccentricity is approximately 0.0012 and the mean argument of perigee is approximately 90 degrees. Once initially acquired, the frozen orbit can be maintained by optimally locating drag makeup burns so as to provide maximum correction to the eccentricity vector. The nominal orbit will have altitudes that range from approximately 705 kilometers at the equator to approximately 732 kilometers near the south pole. Altitude variations due to drag and a non-ideal frozen orbit will result in few kilometers of altitude variation, within the +/-5 kilometer tolerance.

Solar gravity causes a secular decrease in mean inclination for a 10:30 AM descending node orbit. This results in a drift in the descending node time. The time to the first inclination correction maneuver will depend upon the initial inclination and the initial ascending node. If the ideal combination is achieved during launch or during mission orbit acquisition, inclination corrections can be postponed for 5 years (Reference 11). Inclination corrections could typically be expected every few years. Inclination must also be controlled to maintain the ground track at high latitude. Note that inclination corrections require a 90 degree yaw maneuver.

NASA requires that space debris and effects of re-entering space hardware be minimized (Reference 12). EOS is addressing these requirements through detailed break-up / passive re-entry analyses (and design modifications as necessary). This approach meets NASA requirements and requires less propellant and operational complexity than other options (i.e., powered disposal or safe orbit).

7.0 SUMMARY AND CONCLUSIONS

1. This paper has summarized the orbit determination and orbit control baseline for the EOS AM Spacecraft. This paper has shown how the TDRSS Onboard Navigation System (TONS) can be integrated into the EOS AM Spacecraft Guidance, Navigation, and Control System. Current and future analyses and design studies have been addressed.

2. Onboard navigation will improve real-time geolocation knowledge and control when compared to previous ephemeris upload methods. Accurate navigation data will be available in the spacecraft telemetry stream and in the direct downlink to user ground stations.

3. Onboard navigation will also reduce the magnitude of geolocation jitter and stability when compared to the magnitude of ephemeris upload transients that typically occur once per day. Blending can be used to further reduce the magnitude of navigation induced transients.

Acknowledgements

The authors wish to acknowledge the following individuals for their contributions to this paper: Jerry Teles and Cheryl Gramling of the NASA Goddard Space Flight Center; Terry Ford and Paul Miller of the General Electric Astro-Space Division. The authors also wish to acknowledge the following individuals for their contributions and discussions on TONS: Anne Long of Computer Sciences Corporation; and Bryant Elrod of Stanford Telecom.

References

1. Linder, D., *EOS Observatory Pointing and Orbit Requirements*, Prepared for the NASA Goddard Space Flight Center EOS AM Spacecraft Project by the GE Astro-Space Division, EOS-DN-SE&I-020, November 11, 1991.

2. Gramling, Cheryl J., Hart, Roger C., *Onboard Configuration and Operation of the TDRSS Onboard Navigation System (TONS)*, AAS paper 92-010, Presented at 15th Annual AAS Guidance and Control Conference at Keystone Colorado, February 8-12, 1992.

3. Gramling, C. J., et al., *Preliminary Navigation Accuracy Analysis for the TDRSS Onboard Navigation System (TONS) Experiment on EP / EUVE*, NASA GSFC Flight Mechanics / Estimation Theory Symposium, May 21-23, 1991.

4. Wright, J. R., *Sequential Orbit Determination with Auto-Correlated Gravity Modeling Errors*, Journal of Guidance and Control, Vol. 4, No. 3, page 304, 1981, AIAA 80-0239R.

5. Long, A. C., et. al., *TONS Experiment Flight Software Mathematical Specification, Revision 2*, 554-FDD-91/105, Prepared for the NASA Goddard Space Flight Center by Computer Sciences Corporation, June 1991.

6. Bierman, G. J., *Factorization Methods for Discrete Sequential Estimation*, Academic Press, Inc., 1977.

7. Elrod, B., et al., *Earth Observing System (EOS), Analysis of Navigation Performance Using the TDRSS Onboard Navigation System (TONS)*, 544-FDD-91/155, Prepared for the NASA Goddard Space Flight Center by Stanford Telecom, November 1991.

8. Kwok, J. H., *The Artificial Satellite Analysis Program (ASAP)*, Version 2.0, Jet Propulsion Laboratory, April 20, 1987.

9. Lear, William M., *Kalman Filtering Techniques*, JSC-20688, Prepared for the NASA Johnson Space Flight Center, September 1985.

10. *User Spacecraft Clock Calibration System (USCCS) User's Guide*, 531-TR-001, Prepared for the NASA Goddard Space Flight Center by Fredrick Herold and Associates, Inc., October 9, 1991.

11. Folta, D., Kraft, L., NASA Goddard Space Flight Center, *Methodology for the Passive Control of Orbital Inclination and Mean Local Time to Meet Sun-Synchronous Orbit Requirements*, AAS / AIAA Space Flight Mechanics Meeting, Paper # AAS-92-143, Colorado Springs, Colorado, February 24-26, 1992.

12. National Aeronautics and Space Administration (NASA), Office of Safety and Mission Quality, Code Q, *NASA Management Instruction (NMI) : Safety Policy for Space Debris*, Draft, November 11, 1991.

Appendix : Commanded Body Axes Attitude and Examples

The commanded spacecraft body axes unit vectors ($\bar{x}_b$, $\bar{y}_b$, $\bar{z}_b$) are computed using the spacecraft position vector ($\bar{R}$) and velocity vector ($\dot{\bar{R}}$) as shown below. A commanded attitude matrix [A], a direction cosine matrix, can be formed from ($\bar{x}_b$, $\bar{y}_b$, $\bar{z}_b$). All vectors are defined in an earth centered inertial coordinate system.

$$\bar{z}_b = -\bar{R}/|\bar{R}| \; ; \; \bar{y}_b = -\bar{R} \times \dot{\bar{R}}/|\bar{R} \times \dot{\bar{R}}| \; ; \; \bar{x}_b = \bar{y}_b \times \bar{z}_b.$$

($\bar{x}_b$, $\bar{y}_b$, $\bar{z}_b$) origin is at the spacecraft center of mass.

$\bar{z}_b$ axis is (+) in the nadir direction. A small rotation about $\bar{z}_b$ is referred to as yaw.

$\bar{y}_b$ axis is (+) in the direction opposite to the orbital angular momentum vector. A small rotation about $\bar{y}_b$ is referred to as pitch.

$\bar{x}_b$ axis completes the right handed orthogonal coordinate system, and is not necessarily aligned with the velocity vector direction. A small rotation about $\bar{x}_b$ is referred to as roll.

Example 1

A 150 meter intrack position knowledge error results in a commanded pitch attitude error of approximately 4.4 arc-seconds as shown below, using the 7,083,000 meter orbit radius. The same results apply for a crosstrack position error and the resulting commanded roll attitude error.

$$\frac{150 \text{ meters}}{7{,}083{,}000 \text{ meters}} \times \frac{(180)(3600) \text{ arc-seconds}}{\pi \text{ radians}} = 4.4 \text{ arc-seconds.}$$

Example 2

A 0.160 meter / second crosstrack velocity knowledge error results in a commanded yaw attitude error of approximately 4.4 arc-seconds as shown below, using the 7502 meter / second orbit velocity. The crosstrack velocity knowledge error is an error in the knowledge of the velocity vector direction, not an error in the knowledge of the velocity vector magnitude.

$$\frac{0.160 \text{ meters / second}}{7502 \text{ meters / second}} \times \frac{(180)(3600) \text{ arc-seconds}}{\pi \text{ radians}} = 4.4 \text{ arc-seconds.}$$

Example 3

A 4.4 arc-second pitch or roll attitude error results in a geolocation pointing error of approximately 15 meters as shown below, using the 705,000 meter orbit altitude. A yaw error will rotate an instrument scene, but it will not result in a geolocation pointing error by itself.

$$4.4 \text{ arc-seconds} \times \frac{\pi \text{ radians}}{(180)(3600) \text{ arc-seconds}} \times 705{,}000 \text{ meters} = 15 \text{ meters.}$$

Analysis of the Effects of Mean Local Node-Crossing Time on the Evolution of Sun-Synchronous Orbits*

P. Jordan, V. Blaes, and L. Roszman
COMPUTER SCIENCES CORPORATION (CSC)

J. Cooley
GODDARD SPACE FLIGHT CENTER (GSFC)

ABSTRACT

This study, an investigation of the effect of mean local node-crossing time on the evolution of Sun-synchronous orbits, was undertaken during Phase-A orbit analysis for the National Oceanic and Atmospheric Administration (NOAA) O,P,Q environmental spacecraft. That analysis added to the growing body of evidence that individual Sun-synchronous missions, at differing node-crossing times, experience nodal drift rates that can differ in both magnitude and direction. A Sun-synchronous orbit is obtained by means of a nodal drift rate approximating the 0.9856-degree-per-day apparent precession of the position of the mean Sun. This drift rate is achieved through the interaction of the orbital semimajor axis and inclination in Earth's geopotential field. Influencing perturbations include atmospheric drag and, most important, the effects of solar gravitation on inclination. The present analysis examines a series of Sun-synchronous orbits with mean local node-crossing times at 1-hour intervals from 6 a.m. to 6 p.m. It considers the fixed geometry of each orbital plane with respect to both the Sun and the diurnal atmospheric bulge, then analyzes the influence of these features upon the evolution of the semimajor axis and inclination and thus upon the rate of the nodal drift in the course of 1 year.

* This work was supported by the National Aeronautics and Space Administration (NASA)/Goddard Space Flight Center (GSFC), Greenbelt, Maryland, Contract NAS 5-31500.

1. INTRODUCTION

Because of the nonspherical mass distribution of the Earth, satellite orbits between roughly 200 kilometers (km) and 6000 km in altitude experience gravitational perturbations that cause the orbital plane to rotate about the Earth's polar axis. As shown in Figure 1 (from Reference 1), the resulting nodal rotation is negative for direct orbits [inclination (i) < 90 degrees (deg)]. For retrograde orbits (i > 90 deg) the nodal rotation is positive. The rate of the nodal drift can be approximated by:

$$\dot{\Omega} = -2.06474 \times 10^{14} a^{-7/2} \left(1 - e^2\right)^{-2} (\cos i) \qquad (1)$$

where $\dot{\Omega}$ = nodal drift rate (deg/day)

a = semimajor axis (km)

i = inclination (deg)

e = eccentricity

[derived from Equation (3-41), Reference 1]. In a near-circular retrograde orbit, the altitude and inclination may be chosen to produce a nodal drift rate equal to the 0.9856 deg/day precession of the position of the mean Sun. With such a drift rate and without other perturbations, the orbital plane would maintain a fixed geometry with respect to the Sun's position throughout the course of the year. In practice, the altitude and/or inclination are selected to maintain Sun-synchronicity for a specified period within specified bounds. The orientation of a specific Sun-synchronous orbit with respect to the Sun is identified by its mean local time (MLT) of node-crossing: i.e., the local Sun time (LST) of the nodal crossing nearest the Sun.

Figure 2 plots the results of Equation 1, showing mean altitude versus mean inclination for Sun-synchronous orbits from 200 km to 5974 km in altitude. The resulting curve approximates the full range of altitude/inclination (a/i) combinations which, without other perturbations, would produce nodal drift rates equaling the Sun's precession. A/i combinations above and to the left of this Sun-synchronous curve produce nodal drift rates of less than 0.9856 deg/day. The MLT of such an orbit gradually decreases as the node moves westward toward 06:00 LST (6 a.m.). Similarly, an a/i combination below and to the right of the curve produces a drift rate greater than 0.9856 deg/day, with an MLT that gradually increases as the node moves eastward toward 18:00 LST (6 p.m.).

It has been widely observed both in orbit determination and in theoretical studies (Table 1, References 2 and 3) that nodal drift rates can differ significantly from mission to mission, in direction as well as in magnitude. Where the a/i's are similar, the rate differences can occur with differing MLTs. One example comes from early mission planning for the NOAA O,P,Q series of Sun-synchronous environmental spacecraft, scheduled for launch after 2001. These spacecraft are designed to operate in one of two orbits with similar a/i's but differing MLTs (orbit parameters are given in Table 2). Figure 3 [from orbit propagations using the Goddard Mission Analysis System (GMAS)] shows that, when each orbit is targeted to an a/i point lying on the Sun-synchronous curve, the MLT drift of the 08:00 LST morning ("AM") orbit is opposite to that of the 13:45 LST afternoon ("PM") orbit. The mean attitude and inclination for both orbits in Figure 3 are plotted against time in Figures 4 and 5, respectively. The differences in the altitude decay rates of the two orbits is attributed to atmospheric drag effects, which are discussed below. The directional difference in the a/i drift is explained in Figure 5, where the inclination is shown to be increasing in the PM orbit and decreasing in the AM. As demonstrated by K. I. Duck in 1973 (References 2 and 3) and supported by analysis in GMAS (shown in Figures 6a and 6b), the source of this inclination drift is solar gravitation.

2. PERTURBATIONS IN SUN-SYNCHRONOUS ORBITS

Because of the fixed geometry with respect to the Sun, Sun-synchronous orbits are subject to the cumulative effects of solar gravitation. This force, which is greater on the Sunward side of the orbit, produces a small resultant (orbit-averaged) torque that acts on the angular momentum vector, thereby changing the inclination as shown diagrammatically in Figure 7 (adapted from Reference 4) and analytically (from GMAS outputs) in Figures 6a and 6b. As can be readily deduced from Figure 7, the torque is opposite in direction for MLTs on opposite sides of local noon, whether ascending or descending nodal crossings are involved. According to Duck's analysis, maximum inclination drift rates should occur at 09:00 and 15:00 LST, with minimum drifts at 06:00, 12:00, and 18:00 LST. Since there is no fixed geometry with respect to the Moon, lunar gravitation produces no cumulative torque on the orbit but does cause the oscillation in the rate of the inclination drift seen in Figures 5 and 6a.

As in all near-Earth orbits, the altitude is subject to decay due to atmospheric drag. Due to the fixed geometry, however, Sun-synchronous orbits decay at differing rates depending on the orientation of the orbit plane to the diurnal bulge in Earth's atmosphere. Daily heating of the atmosphere results in a bulge of warmed air which lies about 2 hours east of the Sun line. Thus, Sun-synchronous spacecraft with MLTs near 14:00 LST pass through increased densities at each node crossing on the Sunward side. This causes the difference in decay rates in Figure 4.

3. EFFECT OF NODE-CROSSING TIME ON NODAL DRIFT

To examine systematically the effect of node-crossing time, a series of 1-year orbit propagations was generated in GMAS using the Goddard Space Flight Center (GSFC) Flight Dynamics Division (FDD) mainframe computing system. The GMAS force model [calibrated on observed Television Infrared Observation Satellite (TIROS) data] included the following: the Goddard Earth Model (GEM9) geopotential field model with a 21 × 21 matrix, atmospheric drag modeling based on modified Harris-Priester atmospheric density tables with July 1, 1991, Schatten $+2\sigma$ solar flux prediction data, and solar and lunar gravitational perturbations. The Averaged Variation of Parameters (AVGVOP) propagator was used with a 1-day step size. Identical initial Brouwer mean element sets (Table 3) were used in each run, with the exception of the right ascensions of the ascending node (RAANs, Table 4), which were chosen as necessary for MLTs at 1-hour intervals from 06:00 to 18:00 LST. The 800-km altitude and 98.603-deg inclination were taken from Figure 2, with other elements from a NOAA O,P,Q, AM orbit and an epoch of January 1, 1999. Rates of change of the mean altitude and inclination over the year were calculated from the GMAS output and plotted for analysis using the Quattro Pro commercial spreadsheet package running on an IBM PC.

The resulting 1-year drift rates in inclination and altitude are plotted against MLT in Figures 8a and 8b, respectively. As K. I. Duck predicted (References 2 and 3), the direction of inclination drift is negative at morning MLTs and positive at afternoon MLTs, with maximum rates at 09:00 and 15:00 LST and near-zero drift at 06:00, 12:00, and 18:00 LST. The rates at intermediate MLTs show an orderly progression between the predicted means and extremes, suggesting that, with appropriate altitudes, the long-term result of the Sun's gravitational torque would be to align Sun-synchronous orbits perpendicular to the Sun vector. This variation of the drift rates across the day also accords well with the 08:00 and 13:45 LST NOAA O,P,Q inclination changes seen in Figure 5. The drift rates at 08:00 and 14:00 LST are indeed opposite in direction, with the same near-maximum magnitudes. As expected, the maximum altitude decay rate was at 14:00 LST, with the minimum rate 6 hours earlier at 08:00 LST, when the spacecraft would encounter the lowest atmospheric densities. Again, this agrees with the altitude decay rates seen in the PM and AM NOAA O,P,Q orbits (Figure 4).

Figure 8c shows the combined changes in a/i for each MLT. As expected, the lines for the 06:00 (6 a.m.), 12:00 (noon), and 18:00 (6 p.m.) LST MLTs lie near the center of the plot, indicating little inclination change. The

curves for the morning (6 to 11 a.m) MLTs curve to the left, showing decreasing inclinations, and the curves for afternoon (1 to 6 p.m.) MLTs curve right, showing increasing inclinations. The lengths of the curves, indicating the change in altitude, decrease from 06:00 to 08:00 LST, then increase to a maximum at 14:00 (2 p.m.) LST, after which they begin decreasing again. Figure 8d shows the inclination drifts in a 1200-km Sun-synchronous orbit where altitude decay is no longer a factor.

It is evident from Equation (1) that the initial nodal drift rate at each MLT is dependent upon both altitude and inclination. Subsequent nodal drift rates at each MLT are controlled chiefly by the altitude and inclination drift rates in effect at that MLT, as described above. A third factor in the determination of the long-term MLT drift at a given MLT is the solar flux level, determined by the phase of the 11-year solar cycle, which affects the rate of altitude decay at lower altitudes. To test this effect, an additional series of GMAS runs was performed using the original elements (Table 3) with the MLT-specific RAANs (Table 4), but changing the epoch to 2006 and the solar flux data to -2σ, effectively changing the solar flux level from near maximum to near minimum. As shown in Figure 9a, this change has little effect on inclination drift. However, the effect on altitude decay (Figure 9b) is more significant. Figure 10 shows the effect on MLT drift for the NOAA O,P,Q PM orbit due to flux differences between the maximum and minimum phases of the solar cycle.

4. COMBINED EFFECTS OF INCLINATION, ALTITUDE, AND NODE-CROSSING TIME ON NODAL DRIFT

How, then, do altitude decay and inclination drift rates vary across the day for Sun-synchronous orbits at varying a/i combinations? Further GMAS propagation runs, modeled as described above, were executed for selected a/i combinations from Table 1 and/or Figure 2. Again, the MLT-specific RAANs were taken from Table 4 and the remaining elements from Table 3. The epoch in all cases was January 1, 1999, with $+2\sigma$ solar flux data. The resulting altitude and inclination drift rates are shown in Figures 11a and 11b, respectively. The disparity in the inclination drift rates at 500 km is due to rapid altitude decay at that altitude. Figure 11c shows the resulting MLT drift rates at 14:30 LST for 500-, 800-, and 1200-km Sun-synchronous orbits.

Note the inclination drift rate (from Table 1) indicated in Figure 11a by the numeral 1, a value of 0.053 deg/year as calculated in GMAS. This value agrees very well with K. I. Duck's 1973 prediction of 0.0552 deg/year inclination drift for a 3:00 p.m. (15:00 LST) orbit at this altitude (References 2 and 3). [The inclination for the GMAS runs at this altitude was estimated using Equation (1).] Other key data points from Table 1 are also indicated by item number on Figure 11a.

5. MISSION PLANNING ISSUES

Though the drift rates in Figure 8c, 11a, and 11b will vary with the solar cycle, as has been shown, they can be used together with the methods described in References 5 and 8 to guide the initial design of Sun-synchronous orbits. For one example, altitude-sensitive missions would do well to avoid the 13:00 to 15:00 LST MLT range. For another, the low inclination drift rates at MLTs near 06:00, 12:00, and 18:00 LST (Figure 11a) suggest that long-duration missions might operate more efficiently at near-noon or near-terminator node crossings. Figure 12b confirms this for orbits in the 800 km altitude range, showing how closely the 12:00 LST (noon) A/I drift tracks the Sun-synchronous line. However, with the low altitude decay rates in 1200 km orbits (Figure 12a), even a small inclination drift moves the A/I curve away from the Sun line very quickly. With the high altitude decay rates in 500 km orbits (Figure 12c) no MLT will hold the A/I drift near the Sun line, but a comparison of Figures 12b and 12c suggests that, for altitudes in the 600 to 750 km range, a morning MLT might be found which would hold the A/I drift curve very near the Sun-line. This would allow a very stable node-crossing MLT for an extended period. Where the science or operational requirements of a mission make these choices impossible, an understanding of the direction and rate of a/i drift at a given MLT, altitude, and/or inclination can lead very quickly to a Sun-synchronous or biased-Sun-synchronous targeting

scenario to meet the general MLT constraints. With such a scenario in hand, relatively few GMAS propagation runs are needed to optimize the a/i targets for a detailed plan to meet mission constraints over a given phase of the solar flux cycle. As an example of such a plan, the biased Sun-synchronous orbit plan for NOAA O,P,Q (complete with a mid-life maneuver for the PM orbit) is given in Figures 13a through 13c. Figure 13a shows the 5-year a/i drift; the resulting MLT drifts in the PM and AM orbits are shown in Figures 13b and 13c, respectively.

6. SUMMARY

The evolution of the MLT of node-crossing of Sun-synchronous orbits depends upon drifts in the orbital inclination and altitude, which arise from perturbations due to solar gravitation and atmospheric drag. As shown in Figures 8c, 11a, and 11b, the rates of these drifts vary with the node-crossing time as well as with the initial altitude and inclination. Though the drift rates will vary to some extent with the solar cycle, these figures can be used according to methods described in References 5 and 8 to simplify early mission planning for any Sun-synchronous orbit.

REFERENCES

1. J. R. Wertz, "Summary of Orbit Properties and Terminology," *Spacecraft Attitude and Control*, New York: D. Reidel Publishing Company, 1978

2. K. I. Duck, GSFC Memorandum 733:5, "Analysis of Solar Gravitational Effect on Sun Synchronous Orbit Inclination," January 1973

3. K. I. Duck, GSFC Memorandum 733:73, "Inclination Biases for Sun Synchronous Spacecraft," April 1973

4. D. Folta to W. Barnes, "Analysis of Earth Observing System Zenith Angles, Sun Angles, Mean Local Time, and Ground Track," private communication, December 12, 1990

5. D. Folta and L. Kraft, AAS 92-143, "Methodology for the Passive Control of Orbital Inclination and Mean Local Time to Meet Sun-Synchronous Orbit Requirements," February 1992

6. Private communication with L. Kraft, NASA/GSFC, Code 554, March 12, 1992

7. Private conversations with M. Schmidt, C. Cox, and S. Goode, CSC, March 9–11, 1992

8. Goddard Space Flight Center, Flight Dynamics Division, *Phase-A Orbit Feasibility Analysis for the National Oceanic and Atmospheric Administration (NOAA) Polar Orbiting Environmental Satellite Series O,P,Q*, P. Jordan (CSC), in preparation

BIBLIOGRAPHY

1. National Aeronautics and Space Administration, *NOAA O,P,Q Phase-A Analysis Report, Volumes I and II*, T. Karras, ed., January 29, 1992

2. M. D. Griffin and J. R. French, *Space Vehicle Design*, Washington, DC: AIAA Inc., 1991

3. B. Kampos, NASA CR-1008, "General Perturbation Theory," April 1968

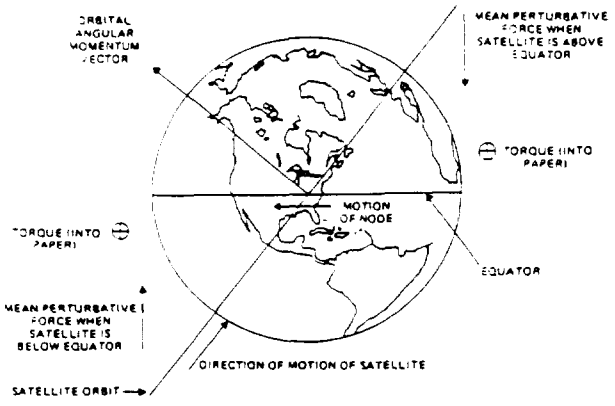

Figure 1. Regression of Nodes Due to the Earth's Oblateness

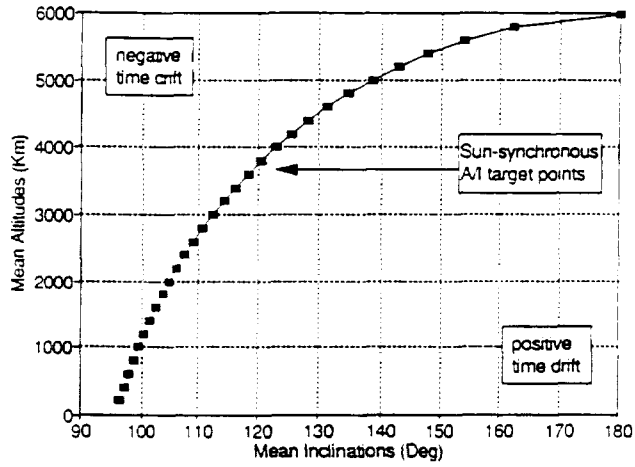

Figure 2. Altitude and Inclination Required for Sun-Synchronous Orbits, 200 to 5974 km

Table 1. Observed and Theoretical Data on the Evolution of MLT Drift Rates as a Function of MLT

ITEM	SPACECRAFT/COMMENT	REF	TYPE OF DATA	ALTITUDE (KM)	INCLINATION (DEG)	MLT (LST)	INCLINATION DRIFT (DEG/YEAR)
1	DUCK ANALYSIS	2	THEORETICAL	1684.0	102.9850*	15:00	0.0552
	ESSA-8	2	OBSERVED			09:00	–0.0540
	TIROS-M	2	OBSERVED			15:00	0.0560
2	EOS-PM	5, 6	THEORETICAL	708.3	98.1355	13:30	0.0310
3	LANDSAT-4**	7	OBSERVED	699.6	98.2320	09:31	–0.0430
4	LANDSAT-5**	7	OBSERVED	699.7	98.2890	09:32	–0.0480
5	COBE (POSTVENTING)**	7	OBSERVED	881.0	99.0210	06:11	–0.0080

*ESTIMATED USING EQUATION 1
**NO LONGER FULLY SUN-SYNCHRONOUS

Table 2. NOAA O,P, Q Mission Parameters

PARAMETER	AFTERNOON ORBIT	MORNING ORBIT
NODE-CROSSING TIME	13:45 LST	8:00 LST
MLT CONSTRAINT	±10 MIN	±10 MIN
TARGET ELEMENTS:		
MEAN ALTITUDE	824 KM	844 KM
MEAN INCLINATION:		
SUN-SYNCHRONOUS	98.616°*	98.833°**
BIASED SUN-SYNC	98.581°*	98.868°**

*For January 1, 1999
**For January 1, 2006

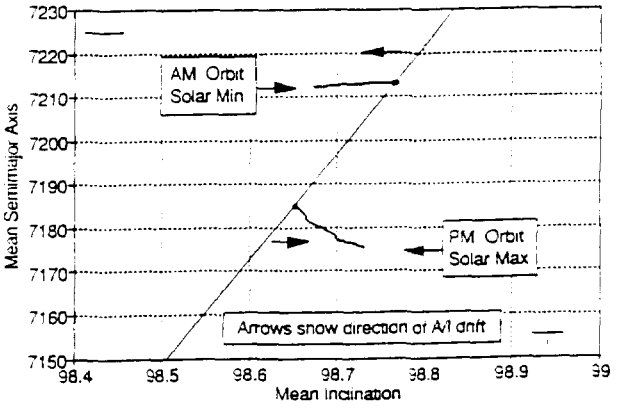

Figure 3. Evolution of SMA and Inclination for NOAA O,P,Q Afternoon and Morning Orbits

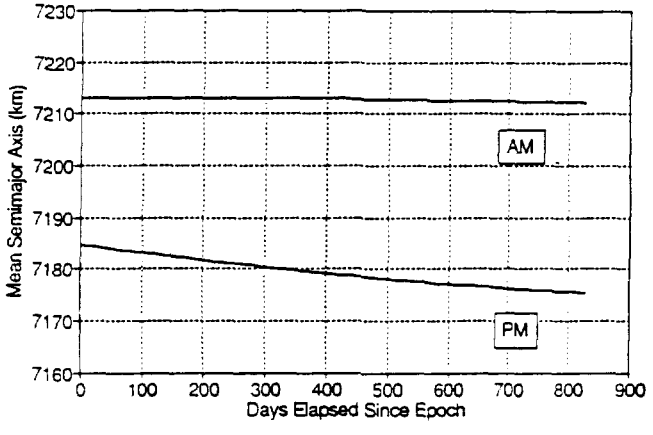

Figure 4. Semimajor Axis Decay for NOAA O,P,Q Afternoon and Morning Orbits

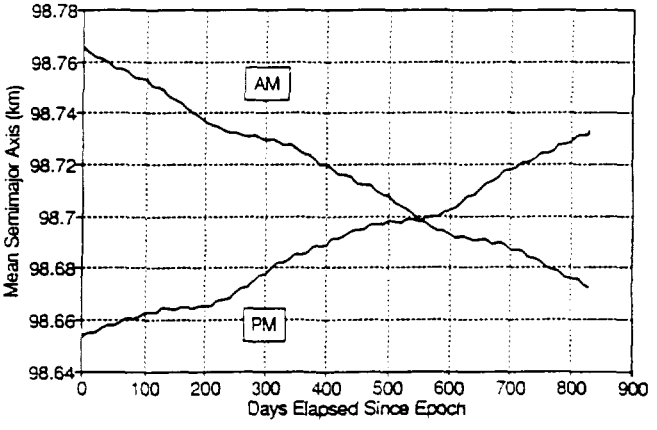

Figure 5. Inclination Drift for NOAA O,P,Q Afternoon and Morning Orbits

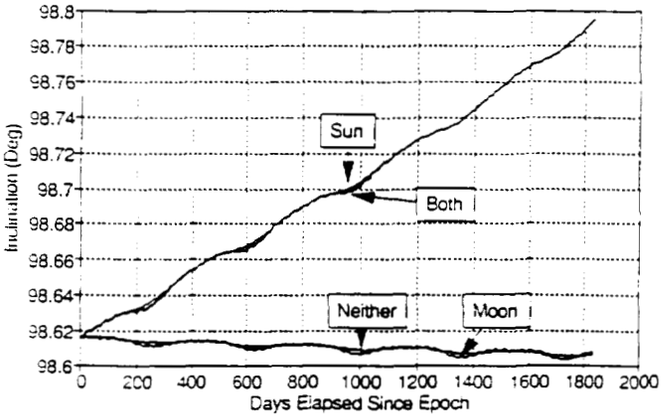

Figure 6a. Effect of Solar and Lunar Gravitation Perturbations on the Inclination of the NOAA O,P,Q Afternoon Orbit

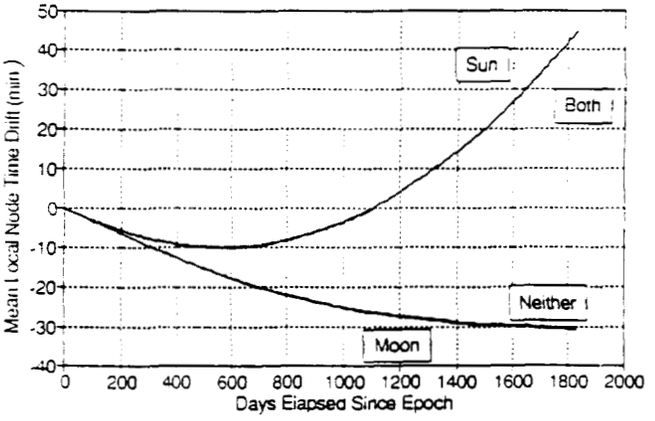

Figure 6b. Effect of Solar and Lunar Gravitation Perturbations on MLT Drift in the NOAA O,P,Q Afternoon Orbit

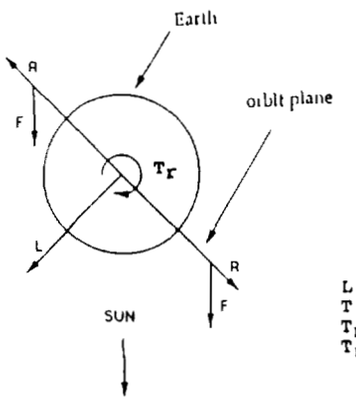

$L = R \times mV$
$T = R \times F$
$T_r = \Sigma R_i \times F_i$
$T_r = w \times L$

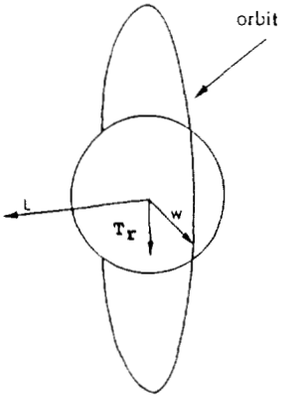

Where:
L = Angular momentum vector
R = Spacecraft position vector
V = Spacecraft velocity vector
F = Force due to solar gravitiation

T = Instantaneous torque due to solar gravitation
T_r = Resultant (orbit averaged) solar gravitation torque
w = Resultant torque precession vector

Figure 7. Torques Due to Solar Gravitation

Table 3. Mean Elements Used in GMAS Runs

SEMIMAJOR AXIS	7178.14
ECCENTRICITY	0.00114
INCLINATION	98.603°
RIGHT ASCENSION OF ASCENDING NODE	SEE TABLE 4
ARGUMENT OF PERIGEE	90.0
MEAN ANOMALY	270.0

Table 4. RAANS Used in GMAS Runs

MLT	RAAN
06:00	190.196
07:00	205.196
08:00	220.196
09:00	235.196
10:00	250.196
11:00	265.196
12:00	280.196
13:00	295.195
14:00	310.196
15:00	325.196
16:00	340.196
17:00	355.196
18:00	10.196

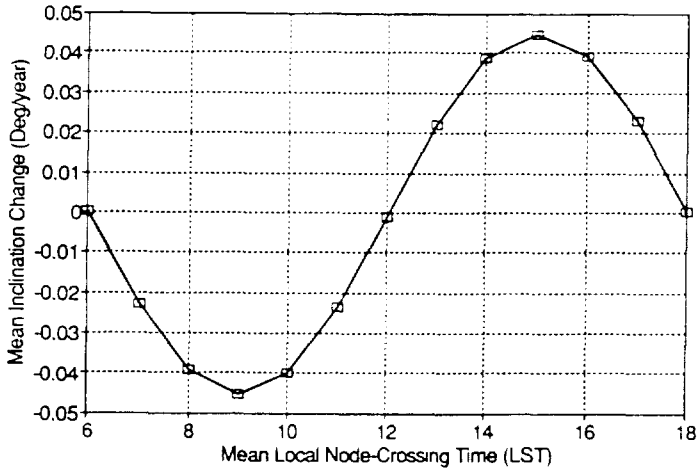

Figure 8a. Effect of Initial MLT on Inclination Drift: Mean Altitude = 800 km, Mean Inclination = 98.603 deg

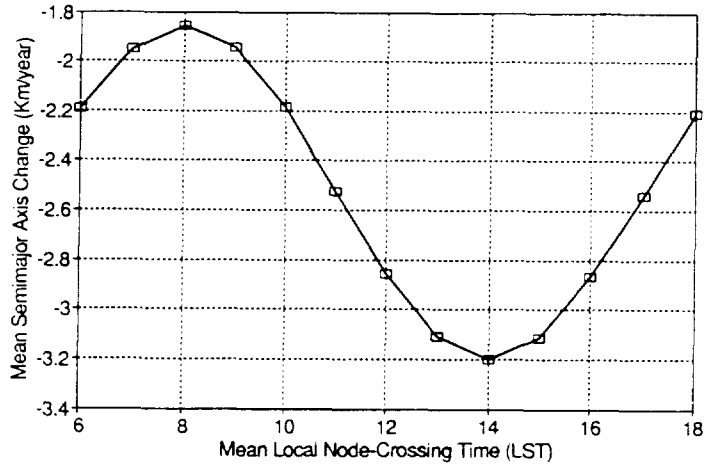

Figure 8b. Effect of Initial MLT on Altitude Decay Rate: Mean Altitude = 800 km, Mean Inclination = 98.603 deg

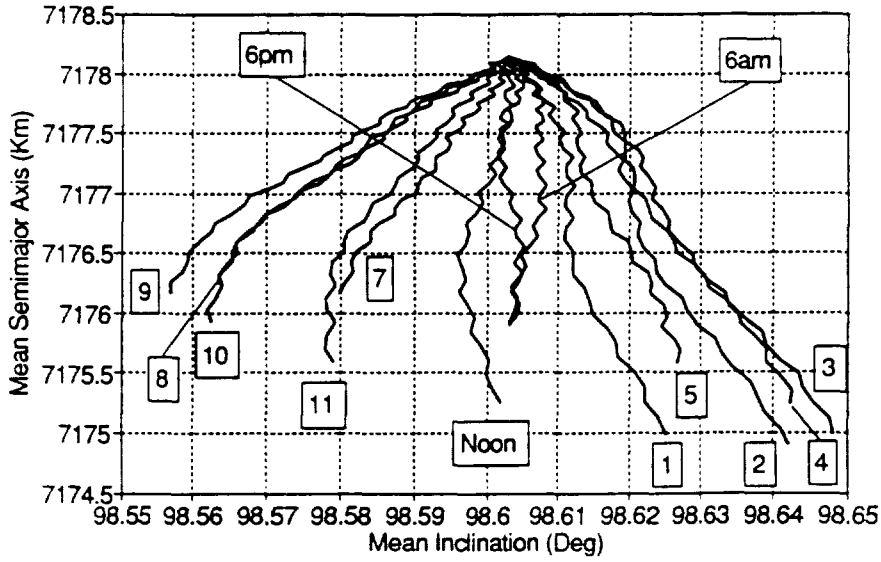

Figure 8c. Effect of Initial MLT on Altitude Decay and Inclination Drift: Mean Altitude = 800 km, Mean Inclination = 98.603 deg

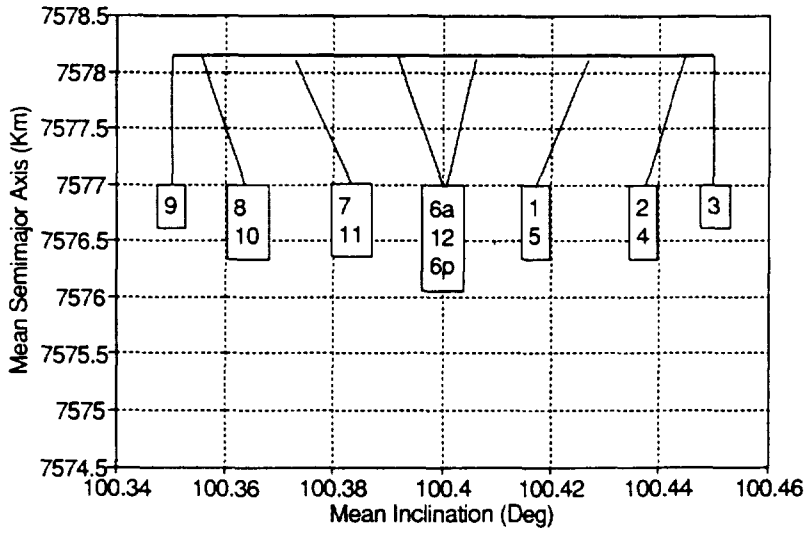

Figure 8d. Effect of Initial MLT on Altitude Decay and Inclination Drift: Mean Altitude = 1200 km, Mean Inclination = 100.4 deg

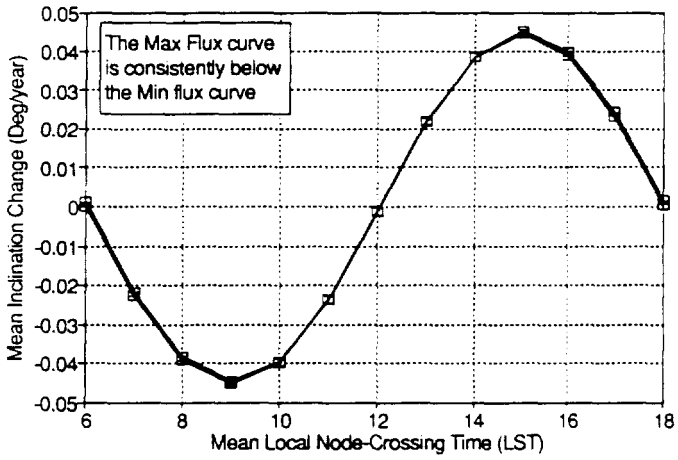

Figure 9a. Effect of Solar Maximum v. Solar Minimum Flux Predictions and MLT on Inclination Drift

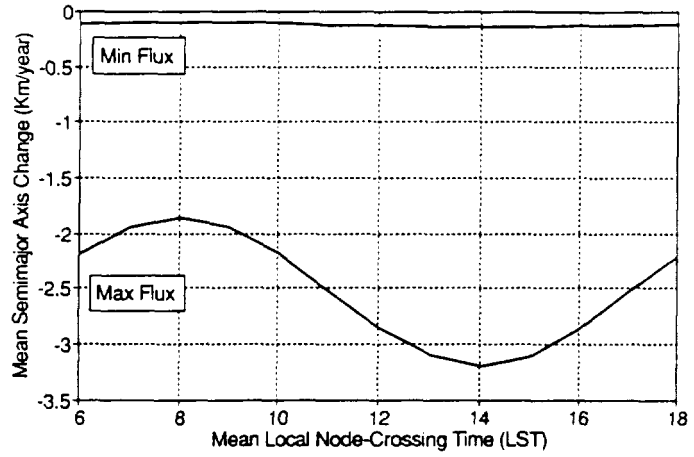

Figure 9b. Effect of Solar Maximum v. Solar Minimum Flux Predictions and MLT on Altitude Decay Rate

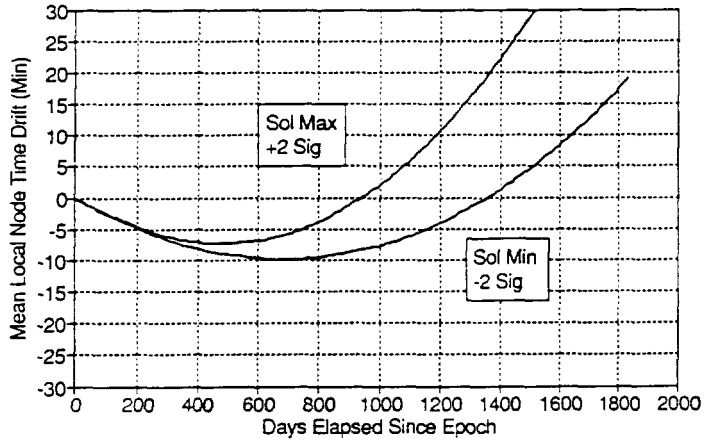

Figure 10. 5-Year MLT Drift in the NOAA O,P,Q P.M. Orbit Solar Maximum v. Solar Minimum Flux Predictions

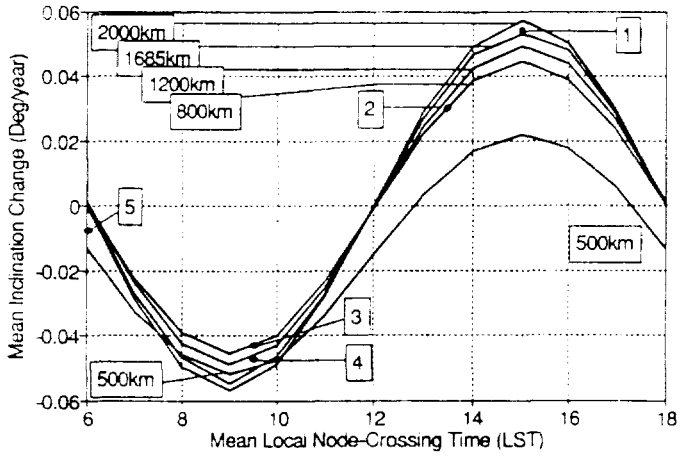

Figure 11a. Effect of Initial MLT on Inclination Drift at Varying Altitudes

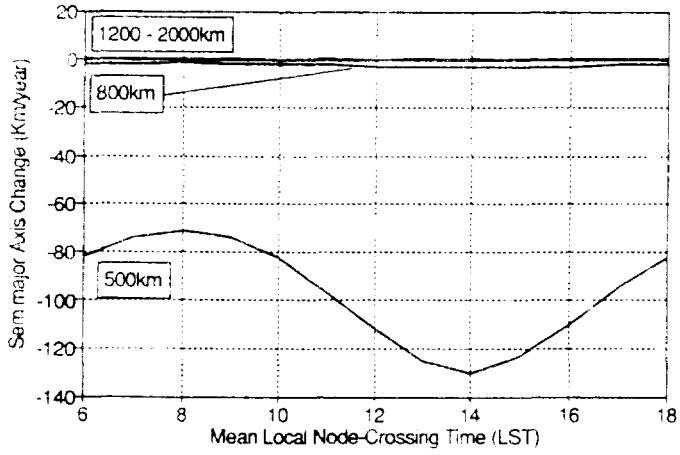

Figure 11b. Effect of Initial MLT on Altitude Decay Rate at Varying Altitudes

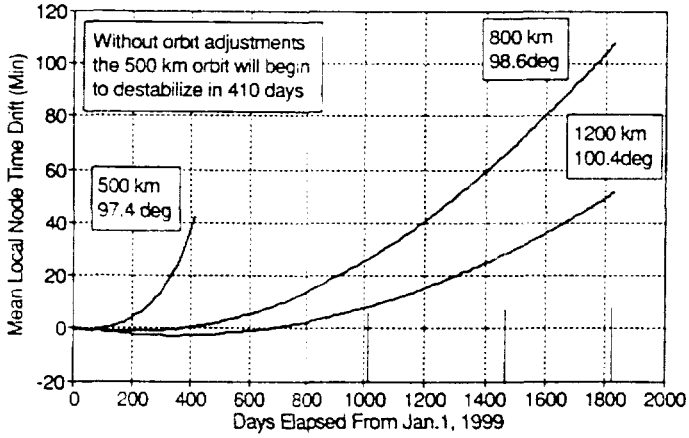

Figure 11c. Effect of Initial Altitude and Inclination on MLT Drift Rates for 1430 LST Sun-Synchronous Orbits

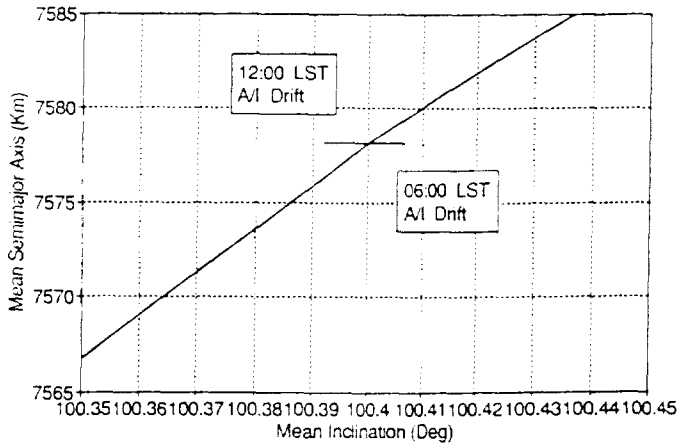

Figure 12a. A/I Drift From the Sun Line at Specified MLTs: 1200-km Sun-Synchronous Orbit at 06:00 and 12:00 LST

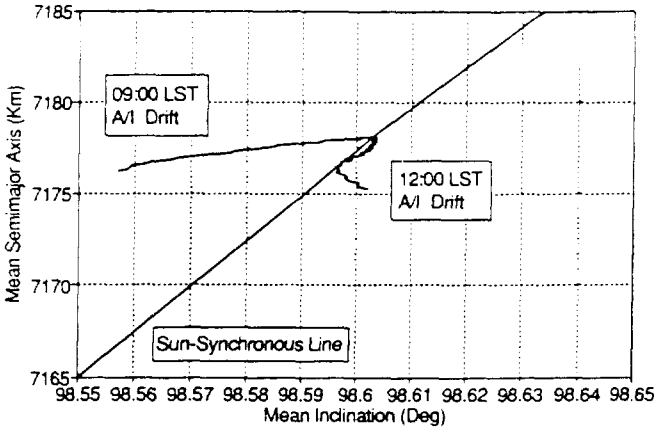

Figure 12b. A/I Drift From the Sun Line at Specified MLTs: 800-km Sun-Synchronous Orbit at 09:00 and 12:00 LST

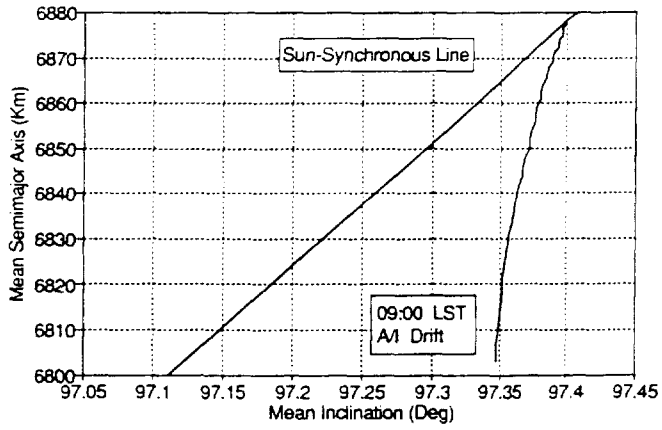

Figure 12c. A/I Drift From the Sun Line at Specified MLTs: 500-km Sun-Synchronous Orbit at 09:00 LST

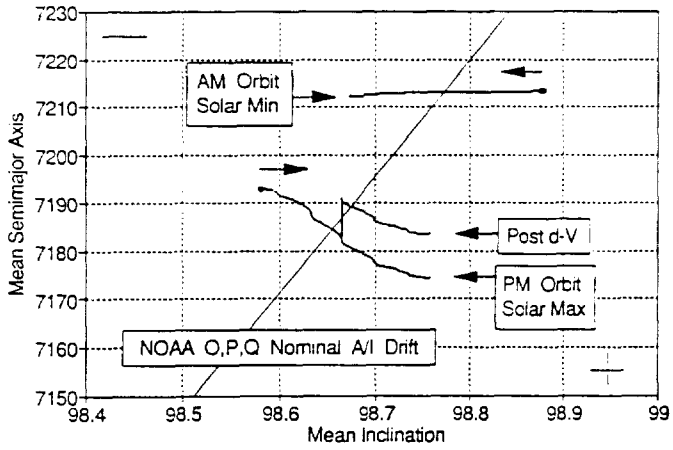

Figure 13a. Five-Year Altitude and Inclination Drift in NOAA O,P,Q Afternoon and Morning Biased Sun-Synchronous Orbits

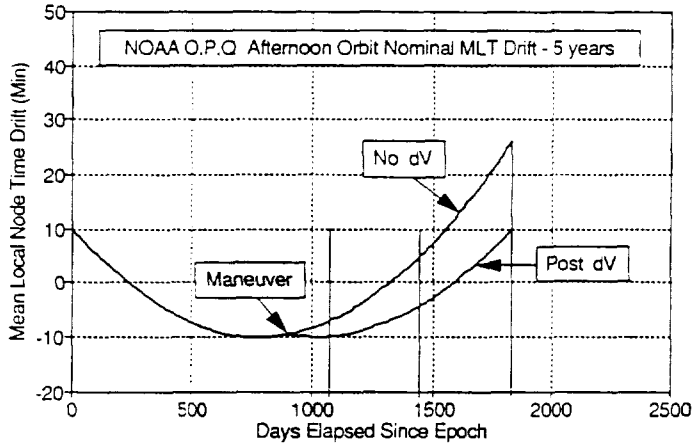

Figure 13b. Five-Year Mean Local Node Time Drift in the NOAA O,P,Q Afternoon Biased Sun-Synchronous Orbits

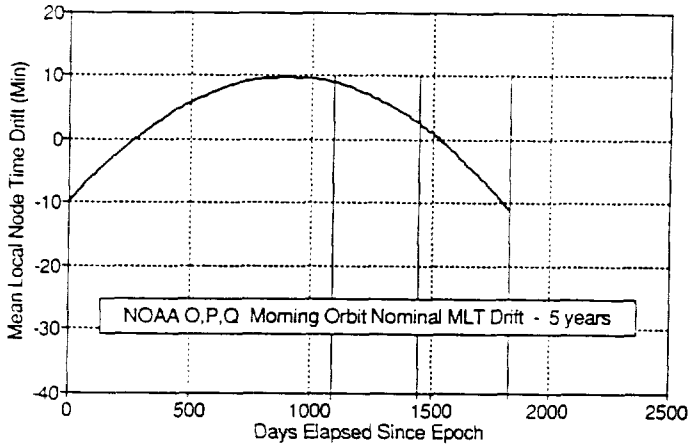

Figure 13c. Five-Year Mean Local Node Time Drift in the NOAA O,P,Q Morning Biased Sun-Synchronous Orbits

A Ground Track Control Algorithm for the Topographic Mapping Laser Altimeter (TMLA)*

V. Blaes, R. McIntosh, and L. Roszman
Computer Sciences Corporation (CSC)

J. Cooley
Goddard Space Flight Center (GSFC)

Abstract

The Topographic Mapping Laser Altimeter (TMLA) will measure the surface elevation of the Earth's landmass and ice sheets to 10-cm precision. With the spacecraft flying in a polar Sun-synchronous orbit in the altitude range of 350 to 400 km, the laser altimeter will illuminate three 100-m diameter circular spots on the ground and scan rapidly in the cross track direction, producing a swath width of 6 km. The objective is to cover the entire Earth gradually, overlapping slightly between adjacent swaths. Providing complete Earth coverage requires precise ground track control, necessitating frequent maneuvers to counteract the effects of atmospheric drag. Therefore, the spacecraft will carry a propulsion system with small thrusters for this purpose.

This paper presents the results of an analysis of an algorithm that will provide autonomous onboard orbit control using orbits determined with Global Positioning System (GPS) data. The algorithm uses the GPS data to (1) compute the ground track error relative to a fixed longitude grid and (2) determine the altitude adjustment required to correct the longitude error. A program was written on a personal computer (PC) to test the concept for numerous altitudes and values of solar flux using a simplified orbit model including only the J_2 zonal harmonic and simple orbit decay computations. The algorithm was then implemented in a precision orbit propagation program having a full range of perturbations. The analysis showed that, even with all perturbations (including actual time histories of solar flux variation), the algorithm could effectively control the spacecraft ground track and yield more than 99 percent Earth coverage in the time required to complete one coverage cycle on the fixed longitude grid (220 to 230 days depending on altitude and overlap allowance).

1. INTRODUCTION

The objective of the Topographic Mapping Laser Altimeter (TMLA) mission will be to measure the surface elevation of the Earth's landmass and landmass ice sheets to submeter (10 cm) precision. The TMLA spacecraft will be launched into orbit by an enhanced Scout or Pegasus booster on or about 1 June 1999. The anticipated mission lifetime will be 3 years with a 30 percent duty cycle.

The spacecraft will fly in a low, Sun-synchronous Earth orbit, with 6 a.m. ascending node nodal crossings. A laser altimeter illuminates three 100-m diameter circular spots on the ground, which are rapidly scanned in the across-track direction. The combined swath width scanned by the lasers is 6 km. Figure 1 illustrates the laser ground scanning geometry. A sweep rate of 70 scans per second produces a 100-m along-track interval between successive scans. The satellite incorporates a hydrazine/electric-arc-jet thruster with a thrust of 0.01 lbs. The specific impulse of the thruster is

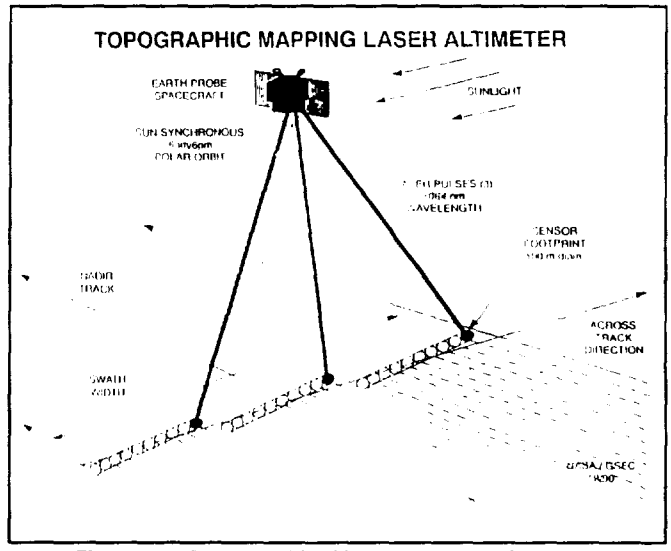

Figure 1. Topographic Mapping Laser Altimeter

* This work was supported by the National Aeronautics and Space Administration (NASA)/Goddard Space Flight Center (GSFC), Greenbelt, Maryland, Contract NAS 5-31500.

in the range of 600 to 800 sec when electric power is supplied to the thruster or 250 to 300 sec without electric power. Ground track positions for the science measurements will be determined from Global Positioning System (GPS) data.

This paper introduces a concept for autonomous ground track control using GPS data as the primary data type. The onboard computer (OBC) determines longitude position errors at the ascending nodes and commands altitude-raising maneuvers to correct those errors. The following steps were carried out in the development of the ground track control algorithm:

- For a range of orbit skip cycles, the altitudes required for efficient ground coverage (i.e., sensor ground swaths with specified, small overlaps) were determined for a range of altitudes between 300 and 400 km using a 6-km ground swath width.
- An algorithm for autonomous orbit control was developed on a personal computer (PC) using a simplified analytical two-body model.
- Performance of the orbit control algorithm was determined with a realistic Earth gravity field, third body perturbations, and solar flux variations, using the Goddard Mission Analysis System (GMAS).

It was concluded that the ground track control algorithm developed could meet the coverage objectives in a 3-year mission.

2. ALTITUDES FOR REPEATING GROUND TRACKS

Complete Earth coverage requires choosing an altitude that results in sufficient overlap of adjacent swaths to cover the dispersions in ground track position attributable to orbit control inaccuracies and all other orbit perturbations. Frequent altitude-raising maneuvers are required to maintain the desired ground track overlap and avoid gaps in coverage. The number of orbits between adjacent ground tracks (the repeat cycle) and the minimum number of orbits necessary for complete Earth coverage are functions of the nominal orbit altitude, the swath width, and swath overlap, assuming no orbit perturbations.

The geometry associated with ground track spacing and swath coverage is illustrated in Figure 2. The longitude interval, DL, between successive ascending nodes for repeat cycle, R, and ground track spacing, S, for an eastward-advancing ground track is

$$Mod\ (R \times |\ DL\ |)_{360} = 360 - \frac{S}{R_e} \times \frac{\pi}{180},\ deg \qquad (1)$$

and for a westward-advancing ground track by

$$Mod\ (R \times |DL|)_{360} = \frac{S}{R_e} \times \frac{\pi}{180},\ deg \qquad (1a)$$

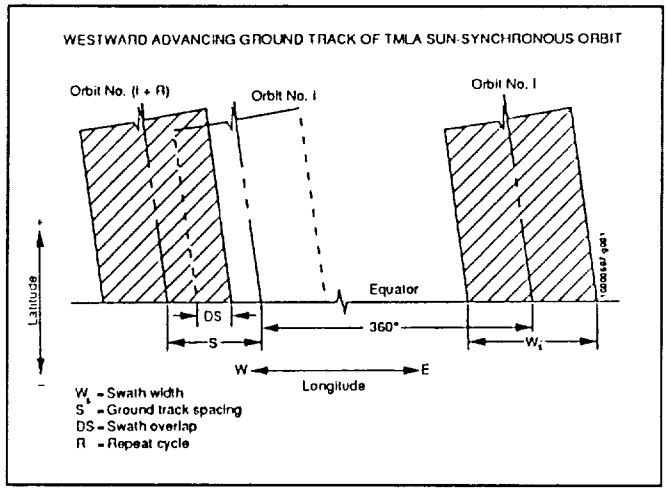

Figure 2. Westward-Advancing Ground Track of TMLA Sun-Synchronous Orbit

For a Sun-synchronous orbit,

$$DL = \left[\omega_e + \frac{360}{T_y}\right] \times 2\pi \left[\frac{a^3}{\mu}\right]^{\frac{1}{2}},\ deg, \qquad (2)$$

where ω_e = rotational rate of the Earth (deg/sec)
T_y = length of a sidereal year in seconds
a = semimajor axis
μ (km^3/sec^2) = Earth's gravitational attraction

The semimajor axis is the sum of the spherical Earth radius, R_e, and height, H, above the ground:

$$a = R_e + H = 6378.14 + H,\ km \qquad (3)$$

Because the equator is traversed twice in every orbit, the minimum number of orbits needed for complete Earth coverage is

$$N_{min} = \frac{\pi R_e}{(W_s - DS)},\ orbits \qquad (4)$$

where W_s is the swath width, and DS is the swath overlap distance. The nominal spacing, S, between ground tracks at the equator is $S = W_s - DS$. Complete Earth coverage for a given repeat cycle and nominal altitude is seldom obtained in exactly N_{min} orbits.

The repeat cycle is efficient if the number of orbits needed for complete Earth coverage is not significantly greater than N_{min}. Equations 1 and 2 were solved for values of S equal to 5.6 and 5.8 km (overlap of 0.4 km and 0.2 km) in a range of R between 50 and 600 and a range of altitudes between 300 and 400 km. Altitudes with a potential for producing a high percentage total coverage in N_{min} orbits were selected to evaluate the ground track control algorithm.

3. GROUND TRACK CONTROL ALGORITHM

At every ascending node, the OBC determines whether an orbit maneuver is needed to correct a ground track error. The longitude at the ascending node is determined from GPS data. The longitude error is the difference between the observed longitude and a nominal longitude. The sign of the error determines whether the spacecraft is too high or too low. If the longitude error is positive, the altitude must be raised, and a Hohmann orbit-raising maneuver is used; otherwise, no maneuver is performed. The first burn of the Hohmann orbit maneuver is performed at the ascending node; the second burn is performed half an orbit later. The OBC determines when an ascending node is reached, then computes a longitude error, determines the necessary thruster burn times if a maneuver is required, and issues commands to start and stop the burns. The orbit control algorithm has two control modes.

Control Mode 1

Control Mode 1 uses a relative longitude error, defined as the difference between two longitude differences; one is the difference between estimated longitudes at two successive ascending nodes, the other is an uplinked reference delta longitude (the difference between longitudes of successive ascending nodes of a reference orbit). In this control mode, the spacecraft altitude is caused to move toward the nominal altitude. This mode is used only after orbit injection, or after a command to change the nominal altitude is uplinked from the ground.

Control Mode 2

Control Mode 2 is based on an absolute longitude error. The absolute error is the difference between the estimated longitude and a longitude obtained from a fixed-longitude grid. The first longitude of the fixed-longitude grid is created by setting it equal to the estimated longitude the first time the sign of the relative longitude error in Mode 1 changes, which occurs when the nominal altitude is reached. Thereafter, a new reference longitude is computed at every node by adding the uplinked reference delta longitude to the longitude at the previous nodal crossing. The reference delta longitude is changed only if it becomes necessary to change the reference altitude. Ground support for satellite navigation consists entirely of uplinking a reference delta longitude, when needed, and uplinking the measured solar flux at regular intervals.

The Control Equation

The altitude correction required to cancel a ground track error consists of two parts. One part results from a longitude error at the ascending node, the other part results from the rate of change of the longitude error. Each part is the product of a gain constant and a corresponding error, divided by the sensitivity of the delta longitude between successive ascending nodes to a change in the semimajor axis. The resulting semimajor axis correction is as follows:

$$\Delta a = \frac{k_d \, \Delta\lambda_i + k_r \, \frac{d}{dt} (\Delta\lambda_i)}{\frac{d\lambda_i}{da}} \tag{5}$$

where k_d is the dimensionless displacement gain constant, and k_r is the dimensionless rate gain constant.

$$\frac{d\lambda_i}{da} = \frac{180}{\pi} (\omega_e - \dot{\Omega}) \, P, \; deg/km \tag{6}$$

where P is the orbital period, ω_e is the Earth's rotation rate, and $\dot{\Omega}$ is the node rate.

The rate error term damps longitude error oscillations. The nodal regression rate, $\dot{\Omega}$, is a function of the semimajor axis, a, eccentricity, e, and orbit inclination, i. The following relation for $\dot{\Omega}$ from Reference 1 is accurate to first order in J_2.

$$\dot{\Omega} \approx -\frac{3}{2} J_2 \sqrt{\mu} \, R_e^2 \, a^{-\frac{7}{2}} (1 - e^2)^{-2} \cos(i)$$

$$= \frac{-2.06474 \times 10^{14} \times \cos(i)}{a^{\frac{7}{2}} \times (1 - e^2)^2 \times 86164.09} \tag{7}$$

The semimajor axis, a, in Equation 7 is assumed to be constant, and eccentricity is assumed to be zero.

In the simulation, the estimated longitude at the node is assumed to have a standard deviation of 30 m, with a Gaussian distribution and zero mean.

4. PC SIMULATION OF AUTONOMOUS ORBIT CONTROL

The orbit control algorithm was tested in a PC program to investigate the feasibility of the concept. Several simplifying assumptions were made:

- Two-body analytic circular orbits, with J_2 only.
- The semimajor axis reduction per orbit due to atmospheric drag is approximated from energy considerations; hence, integration of the equations of motion is not necessary.
- Instantaneous altitude corrections are made at the ascending node.
- An exponential density is fitted to the Harris-Priester (H-P) atmospheric density model between 300 and 400 km altitude. Density is modeled empirically as a function of solar flux and adjusted for the effects of the atmospheric bulge.

Altitude Loss Per Orbit

A calculation is made at every ascending node to determine the altitude loss in the preceding orbit. The altitude loss is obtained by equating the energy loss in one orbit to the work done by the drag force on the spacecraft. The work done by the drag force, D, is

$$W = 2\pi aD = \pi a\rho\, C_d\, AV^2,\ N \cdot m \qquad (8)$$

where A = reference area (m^2)
a = semimajor axis (m)
ρ = atmospheric density
C_d = drag coefficient
V = velocity

The total energy loss per orbit (potential plus kinetic) is

$$E = -\frac{1}{2}\mu m \left[\frac{1}{a_i} - \frac{1}{a_f}\right],\ N \cdot m \qquad (9)$$

where a_i and a_f are initial and final values of semimajor axis, and m is the spacecraft mass. Because

$$a_{avg}^2 \approx a_i a_f \qquad (10)$$

the change in the semimajor axis, $\Delta a = (a_i - a_f)$, from Equations 8 and 9 becomes equal to

$$\Delta a = -2\pi\, \rho\, \frac{C_d A}{m}\, a_{avg}^2 \qquad (11)$$

The Atmospheric Density Approximation

The H-P density between altitudes of 300 and 400 km was approximated at solar flux levels of 80 and 240 by exponential functions fitted to an orbital density intermediate between the minimum and maximum density values in the H-P density model. The intermediate value was equal to the H-P minimum, plus 0.2 times the difference between the H-P maximum and minimum densities. It approximates the effects of an atmospheric bulge on the density for a Sun-synchronous (0600 hrs ascending node) TMLA orbit. The atmospheric density equations for the 300 to 400 km altitude range are as follows:

For solar flux level of 80,

$$\rho = 5.761091 \times Exp(-0.0216952\ H),\ kg/km^3 \qquad (12)$$

For solar flux level of 240,

$$\rho = 4.142531 \times Exp(-0.01566959\ H),\ kg/km^3 \qquad (13)$$

The exponential density functions are compared with H-P data at 20 km intervals between 300 and 400 km altitude in Figure 3. The solar flux is measured at the 10.7 cm wave length ($F_{10.7}$) and is in units of 10^{-22} Watts/m^2/Hertz.

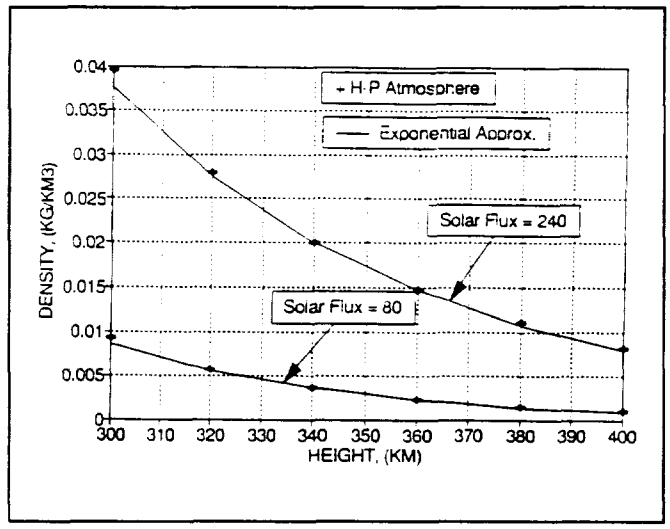

Figure 3. Atmospheric Density Functions Compared With H-P Data

Optimized Control Gain Constants

Values of k_d and k_r that minimize the dispersion of longitude error were determined experimentally from runs made with constant flux values of 80 and 240 (Equations 12 and 13). The control gains, formulated as functions of altitude and solar flux, are given in the following equations, which are the default optimum control gains in the PC simulation.

$$k_d = 0.08 + F_{10.7} \times (0.0083 - 0.325\times10^{-4}\ H + 3.0\times10^{-8}\ H^2) \quad (14)$$

$$k_r = 0.0035 \quad (15)$$

In Figure 4, k_d is presented as a function of altitude and solar flux.

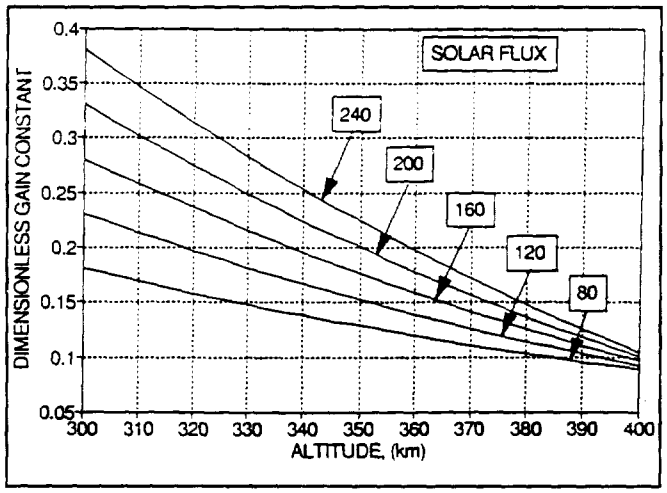

Figure 4. Displacement Gain as a Function of Altitude and Solar Flux

PC Simulation Numerical Results

A sequence of runs with optimum control gains was made to determine the effects of ground track spacing, altitude, solar flux, and position measurement accuracy on the standard deviation of the controlled position error and the total delta-V for N_{min} orbits. The solar flux was either held constant at 80 or 240, or else actual past daily values of $F_{10.7}$ from a flux file were used (covering a period of time in which the flux levels approximated the levels predicted by Schatten (Reference 2) after the TMLA epoch).

Constant Solar Flux

Numerical results are presented in Table 1 for a nominal ground track spacing of 5.8 km; altitudes of 300, 350, and 400 km; constant solar flux values of 80 and 240; and measurement noise standard deviations of 0 and 30 m. The standard deviation of the longitude distance error for perfect position measurements is between 3 and 7 meters, due largely to a transient at the start of the runs. For a 30 m measurement noise, the standard deviation of the distance error is 37 to 39 m for both low and high flux values (i.e., up to 30 percent larger than the measurement noise). An

Table 1. Orbit Control Performance From PC Simulation Based on Constant Solar Flux

NOMINAL GROUND TRACE SPACING = 5.8 KM
3455 ORBITS; I_{sp} = 275 LBM-SEC/LBM

Nom Alt	Flux	Std. Dev. Meas. Noise	Distance Error (m) Min	Max	Std Dev	Altitude (km) Min	Max	W_{prop} lbs	NB*	Delta V m/s	Burn Per Maneuv. sec
300	240	0	-3	146	5	299.686	300.090	47.30	3455	264.11	188.3
300	80	0	-81	193	6	299.827	300.018	18.94	3455	102.70	75.4
300	240	30	-131	147	37	299.748	300.075	36.57	3455	201.87	145.5
300	80	30	-130	148	37	299.862	300.153	11.38	3455	61.19	45.2
350	240	0	-9	313	6	349.866	350.040	22.82	3455	124.18	90.8
350	80	0	-21	60	3	349.877	349.978	11.90	3455	64.03	47.3
350	240	30	-132	168	38	349.808	350.123	17.94	3455	97.10	71.3
350	80	30	-127	176	39	349.849	350.175	7.37	3455	39.49	29.2
400	240	0	-2	96	6	399.877	399.989	14.41	3455	77.76	57.4
400	80	0	-4	88	7	339.927	400.037	9.96	3455	53.48	39.6
400	240	30	-131	146	37	399.834	400.145	10.45	3455	56.13	41.6
400	80	30	-115	160	38	399.856	400.160	6.06	3455	32.44	24.1

orbit maneuver is required at every ascending node. Total mission delta-V, based on propellant specific impulse (I_{sp}) of 275 seconds, ranges from a low of 32.44 m/s for an altitude of 400 km with a low flux, to a high of 262.11 m/s for an altitude of 300 km with a high flux. Burn times (half of a Hohmann maneuver) for the 0.01 lb thruster ranged between 24.1 and 188.3 sec for the two altitude and flux conditions investigated.

Similar data for a 5.6 km nominal ground track spacing are presented in Table 2. The control error statistics are unaffected by the ground track spacing. However, because

Table 2. Orbit Control Performance From PC Simulation Based on Constant Solar Flux

NOMINAL GROUND TRACE SPACING = 5.6 KM
3579 ORBITS; I_{sp} = 275 SEC

Nom Alt (km)	Flux	Std. Dev. Meas. Noise m	Distance Error (m) Min	Max	Std Dev	Altitude (km) Min	Max	W_{prop} lbs	NB*	Delta V m/s	Burn Per Maneuv. sec
300	240	0	-3	146	5	299.686	300.090	48.92	3578	273.59	187.9
300	80	0	-81	193	6	299.827	300.018	19.61	3579	106.36	75.3
300	240	30	-131	147	37	299.797	300.075	37.83	3579	209.10	145.3
300	80	30	-130	148	37	299.824	300.153	11.75	3579	63.23	45.1
350	240	0	-9	313	6	349.866	350.040	23.62	3579	128.63	90.7
350	80	0	-21	60	3	349.877	349.978	12.32	3579	66.32	47.3
350	240	30	-132	168	38	349.806	350.123	18.55	3579	100.53	71.3
350	80	30	-127	176	39	349.847	350.175	7.61	3579	40.75	29.2
400	240	0	-2	96	6	399.877	399.989	14.92	3579	80.55	57.3
400	80	0	-4	88	7	339.927	400.037	10.31	3579	55.40	39.6
400	240	30	-131	146	37	399.834	400.145	10.84	3579	58.29	41.7
400	80	30	-115	160	38	399.856	400.160	6.30	3579	33.71	24.2

* NB is the number of orbits with orbit-raising maneuvers

more orbits (N_{min}) are necessary to obtain total coverage, the total delta-V is increased by the ratio of 5.8/5.6 = 1.0357.

The standard deviation of position errors shown in Tables 1 and 2 is a useful measure of the control accuracy obtainable from the algorithm. The standard deviations do not translate directly into a percent coverage; however, when the nominal altitude is properly chosen, smaller position error dispersions correlate with a higher percent coverage for a given swath overlap.

Daily Varying Solar Flux

A daily solar flux variation from observations made during the last solar cycle that approximates the predicted solar flux variation after the TMLA epoch is presented in Figure 5. This flux variation was used to determine the altitude loss per orbit. The same data, delayed one day, were used as the flux input to the control law. This simulated an operational scenario in which the 1-day-old measured solar fluxes would be uplinked daily.

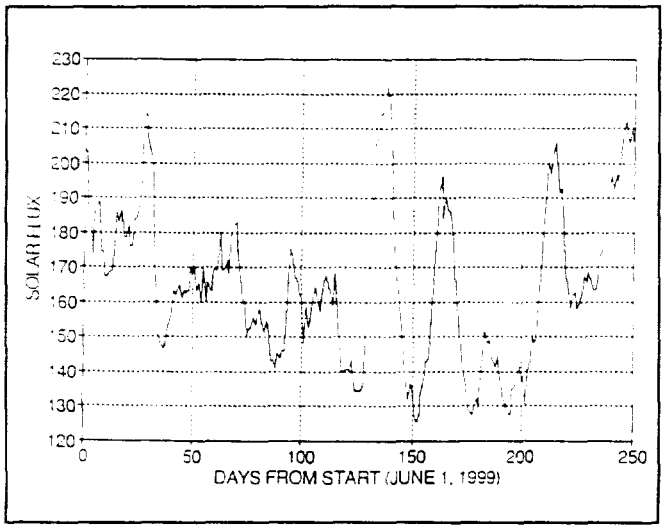

Figure 5. Daily Solar Flux for TMLA Simulation

The performance of the control law with the daily solar flux data is presented in Table 3 for a ground track spacing of 5.8 km and in Table 4 for a ground track spacing of 5.6 km. With no error in orbit determination, the standard deviation of distance error is 1.6 to 4.2 times greater than when solar flux is constant, the error decreasing with an increase of altitude. With a 30 m orbit determination accuracy, the standard deviation of position error is 24 percent greater at an altitude of 300 km than if solar flux were constant, but only 1 percent greater at an altitude of 400 km. For a daily flux variation and a 30 m orbit determination error, the ratios of the standard deviation of longitude error to the nominal overlap (6 km swath minus

Table 3. Orbit Control Performance From PC Simulation Gain Constants Based on 1-Day-Old Solar Flux

NOMINAL GROUND TRACE SPACING = 5.8 KM
3455 ORBITS; I_{sp} = 275 SEC

Nom Alt (km)	Std. Dev. Meas. Noise m	Distance Error (m) Min	Max	Std Dev	Altitude (km) Min	Max	W_{prop} lbs	NB*	Delta V m/s	Burn Per Maneuv. sec
300	0	-107	312	21	299.649	300.056	33.46	3455	184.08	133.1
300	30	-174	198	48	299.646	300.151	34.68	3455	191.06	138.0
350	0	- 95	236	14	349.741	350.027	18.26	3455	98.90	72.7
350	30	-157	156	42	349.744	350.163	20.31	3455	110.24	80.8
400	0	- 33	251	11	399.852	399.969	14.11	3455	76.11	56.2
400	30	-134	151	39	399.780	400.150	15.97	3455	86.31	63.6

Table 4. Orbit Control Performance From PC Simulation Gain Constants Based on 1-Day-Old Solar Flux

NOMINAL GROUND TRACE SPACING = 5.6 KM
3579 ORBITS; I_{sp} = 275 SEC

Nom Alt (km)	Std. Dev. Meas Noise	Distance Error (m) Min	Max	Std Dev	Altitude (km) Min	Max	W_{prop} lbs	NB	Delta V m/s	Burn Per Maneuv. sec
300	0	-107	312	21	299.649	300.056	34.63	3579	190.79	137.8
300	30	-174	198	47	299.646	300.151	35.88	3579	197.93	137.9
350	0	- 95	236	13	349.741	350.027	18.94	3579	102.63	72.7
350	30	-157	156	42	349.744	350.163	21.04	3579	114.3	80.8
400	0	- 33	251	11	399.852	399.969	14.63	3579	78.97	56.2
400	30	-134	151	39	399.780	400.150	16.55	3579	89.46	63.6

* NB is the number of orbits with orbit-raising maneuvers

the ground track spacing) and the maximum longitude error to the overlap are summarized below:

Altitude	Std Dev/Overlap	Max Error/Overlap
300	0.12	0.50
350	0.11	0.39
400	0.10	0.38

With careful selection of the nominal altitude, the percent coverage for ground track spacing of 5.6 and 5.8 km at low or high altitude in the 300 to 400 km range is between 98.35 and 99.98 percent in N_{min} orbits. On the basis of these results, it was concluded that the performance of the TMLA ground track control algorithm merited further analysis, including the effects of orbit perturbations from higher order gravitational potential model terms and third-body effects of the Sun and Moon. Additional analyses were, therefore, performed using the Goddard Mission

Analysis System (GMAS) program. Those analyses are described in the sections that follow.

5. GMAS SIMULATION OF AUTONOMOUS ORBIT CONTROL

The orbit control algorithm detailed in the previous sections was implemented in a special module for use with the GMAS Cowell orbit propagator. This propagator can include perturbations resulting from drag, the geopotential field, and solar and lunar gravitational effects, as desired. The program stops at each ascending node and checks the longitude error from the reference (the error includes simulated measurement noise).

If the error is positive (the altitude is below nominal), the required Hohmann transfer delta-V is computed. Half the delta-V is applied as an impulse at the current nodal crossing, and the remainder is applied at the next descending node. The longitudes at all ascending and descending nodes are recorded for later sorting and generating statistics. Ground track error at each ascending node is also output.

The procedure followed is first to choose a case from the PC simulation that gives good coverage, input the nominal longitude separation between successive nodal crossings *(DLONG)*, and iterate on the initial osculating semimajor axis until the longitude separation matches *DLONG*. The GMAS implementation uses only Control Mode 2 (see Section 3), so the simulator must start at the correct altitude. A long run is then made and gains are adjusted in an attempt to improve the resulting coverage.

Computation of statistics involves sorting the crossings in ascending order of longitude, computing the spacing between adjacent longitudes, and summing all the gaps and overlaps. The number of crossings (ascending and descending) used to generate statistics is the theoretical minimum needed to give total coverage. This number is 6910 for a grid with 5.8 km spacing and 7157 for a spacing of 5.6 km. The swath width used in this analysis is 6 km.

Simulations were performed with J_2 only, an 8 by 8 geopotential, constant solar flux, a smoothly varying flux, and daily flux variations for both 5.8 and 5.6 km spacings. Initial runs were made with constant gains in the control law. After the algorithm was verified, the computations for gain as a function of flux described in Section 4 were implemented and runs were made using daily flux variations with a 1-day delay. The results of each are discussed in the following sections.

Initial GMAS Tests

The initial runs were made with J_2 only to simplify the modeling and ensure the algorithm was working properly. The spacecraft was assumed to have a mass of 230 kg, area of 1 m^2, and coefficient of drag equal to 2.2. The epoch for all runs is June 1, 1999. Densities were computed with the H-P atmosphere model.

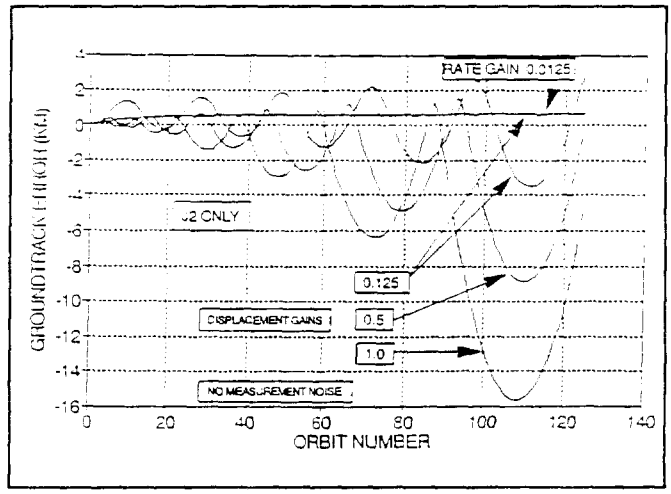

Figure 6. Effect of Various Gain Settings on Ground Track Error

Figure 6 shows the evolution of ground track error for 125 orbits using different gain values. The three curves that show a large buildup in fluctuations did not have a rate gain applied; while the nearly horizontal line from the fourth case used a rate gain of 0.0125. This plot clearly shows the need for using both rate and displacement gains and for choosing good values.

Figure 7 shows the effects of added measurement noise. The noise used in all GMAS simulations assumes a Gaussian distribution with a standard deviation of 30 m, as in the PC simulations. The plot shows ground track error for two sets of displacement gain (DG) and rate gain (RG). The smooth

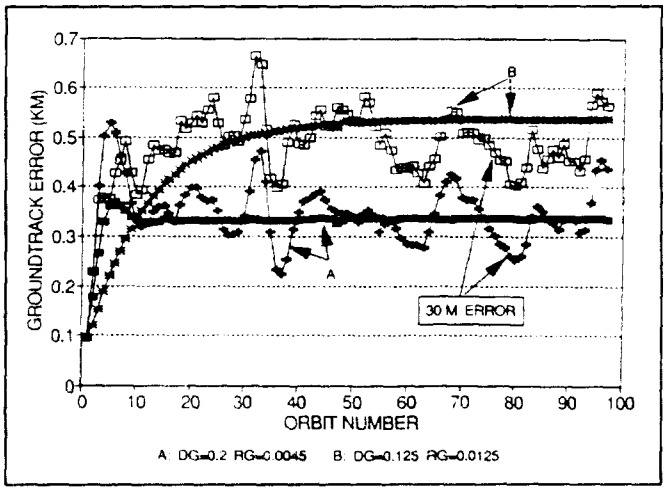

Figure 7. TMLA Ground Track Error J_2 (With and Without 30 M Orbit Error)

curves represent J_2 only with no noise; while the fluctuating ground track error shows the effect of the added noise.

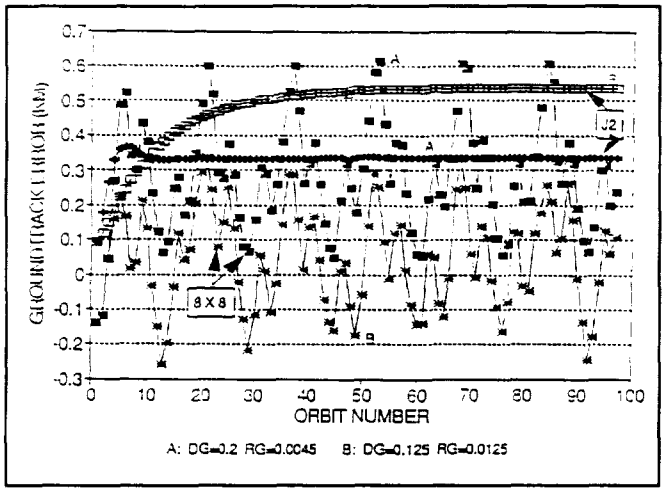

Figure 8. TMLA Ground Track Error J_2, 8x8, Different Gains

Figure 8 compares the difference between using J_2 only or a more realistic 8 by 8 geopotential model (noise not included). The 8 by 8 model causes the ground track to vary over a range of between 0.5 and 0.6 km.

Figure 9 shows the response of the algorithm to values of solar flux and gains. These runs were made with J_2 only and no noise. The top curve, A, shows the ground track error history for 4000 orbits (8000 nodal crossings) with a slowly increasing flux that follows the Schatten +2 sigma prediction. The predicted flux values for 1 year are as follows:

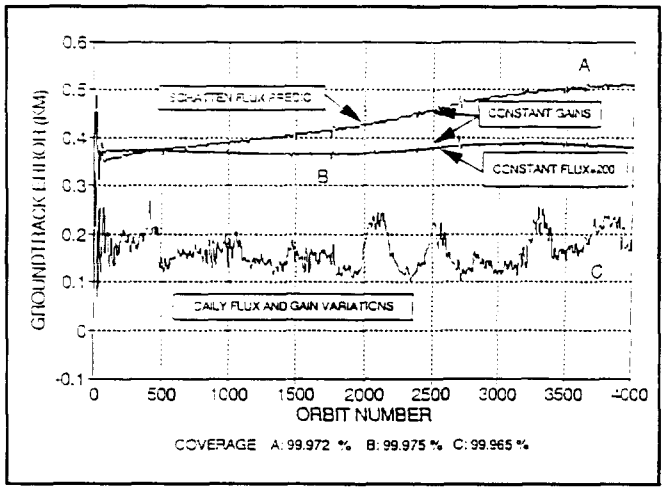

Figure 9. TMLA Ground Track Error J_2 Only, No Noise

Date	Flux
Jun 1, 1999	195
Jul 1, 1999	201
Aug 1, 1999	207
Sep 1, 1999	213
Oct 1, 1999	218
Nov 1, 1999	223
Dec 1, 1999	228
Jan 1, 1999	232
Feb 1, 2000	236
Mar 1, 2000	239
Apr 1, 2000	242
May 1, 2000	244
Jun 1, 2000	246

Curve B results from a constant flux of 200. Both A and B use constant gains. The bottom curve, C, shows the error resulting from a flux that varies daily (see Figure 5) and gains that are computed daily from the observed flux. There is a 1-day delay between the observed flux value and the use of that value in the control computations. Coverage statistics were generated for these three cases and are as follows:

Case	Percent Coverage at Equator
A	99.972
B	99.975
C	99.965

Using J_2 only, no orbit error, and a constant flux yields the best total coverage that the algorithm can produce. Adding orbit error, the geopotential, and flux variations for more realistic modeling will always yield less coverage. However, the total coverage can still be above 99 percent, as will be shown later. A coverage of 99.975 percent means that a total of only 10 km (out of 40,075) remains uncovered at the equator.

GMAS Simulations With All Perturbations

Simulations were run for several different altitudes with grid spacings of both 5.8 and 5.6 km. The spacing is controlled by using the correct semimajor axis in combination with the appropriate value of DLONG for each case. DLONG is the separation in deg between successive equator crossings (one orbit apart) and is a precise number that is determined by the PC program. Using an incorrect value for DLONG results in greatly reduced total coverage. Runs were made first with constant gains and the Schatten flux predictions and then with daily varying flux and gains. The results of each are discussed below.

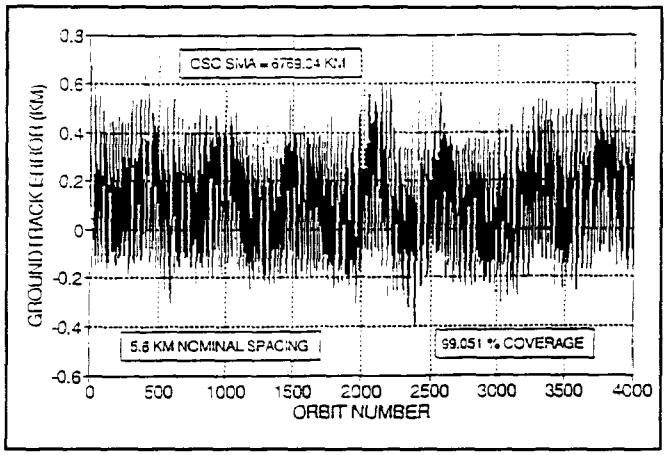

Figure 10. TMLA Ground Track Error Daily Flux Variations (1-Day Delay)

Sample Results With Daily Flux Variations. Figure 10 shows ground track error versus time for a case when the initial osculating semimajor axis is 6769.34 km (391 km altitude at the initial ascending node), and DLONG is set to give a desired ground track spacing of 5.6 km. For this case, the daily flux variations shown previously in Figure 5 were used. The value of *RG* was set to 0.001, and *DG* was computed from the daily flux, assuming a 1-day delay. The ground track repeat cycle for this run was 78 orbits; that is, the time between two adjacent ground track swaths is 78 orbit periods. With all perturbations included, the ground track error varies over a range of about 0.8 km and is fairly well behaved.

Figure 11 shows the number of node crossings as a function of ground track spacing for this run. The longitudes at each crossing are sorted in ascending order, the difference between two adjacent equator crossings is computed, and the result is assigned to the appropriate 0.1-km-wide bin. This process is repeated until spacing has been computed for all 7157 longitudes (the minimum number for 5.6 km spacing). The number of points in each bin are then plotted.

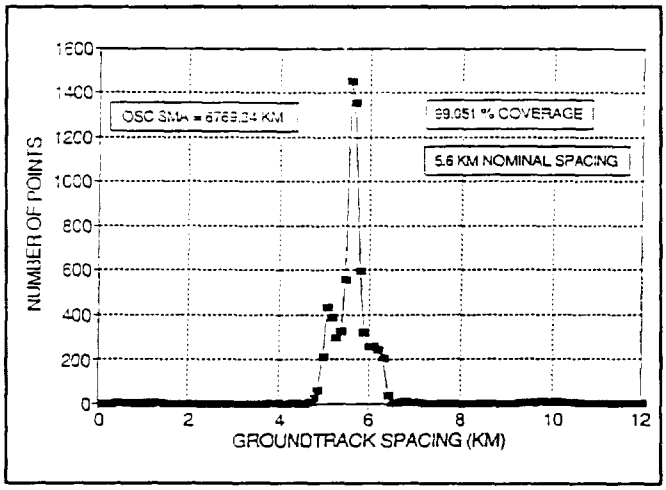

Figure 11. TMLA Ground Track Spacing Daily Flux Variations (1-Day Delay)

Ideally, all points would fall in one bin (between 5.5 and 5.6 km or 5.6 and 5.7) to obtain 100 percent coverage and the plot would show one central spike. Perturbations cause errors in the spacing, thus leaving gaps and lowering the overall coverage. The resulting coverage for this run was 99.051 percent, meaning that 380 km total remain uncovered along the equator after one coverage cycle.

Comparison of Results from Different Runs. The results of a series of runs were presented in Table 5. These results include runs at several altitudes, 5.8 and 5.6 km spacing, different flux levels, and constant or varying gains. The table gives a reference run number, spacing, *DLONG*, altitude, gains, orbital elements, solar flux, total delta-V, and resultant coverage. The runs showing "COMP" for the gain (computed by the program) and "DAILY1" for the flux (daily flux with one day delay) represent the most realistic simulations. Other runs with predicted flux and constant gains are included for comparison. Run 8 is the one that was discussed in the previous section.

Also included is a column indicating whether a frozen orbit was used for the run. Several runs were made to determine whether a frozen orbit would yield improved coverage over an arbitrary initial orbit. For a frozen orbit, the heights above the equator at each nodal crossing should show only slight variations over time, which may lead to better control of coverage at the equator. Comparing the runs in Table 5 indicates a small improvement in coverage with the frozen orbit. More details on the frozen orbit will be given in the next section.

Table 5 also demonstrates the importance of choosing the correct value for *DLONG*. For example, Runs 8 and 11 were run with identical initial orbital elements but with values for *DLONG* that differ after the third decimal place (0.001 deg). The one case gives 99.051 percent coverage, while the other only 52.173 percent.

Figure 12 shows the resulting distribution of ground track spacing for Run 11 and shows the peak occurring near 2.9 km. This results in a large overlap between adjacent swaths of about 3.2 km on the average (0.2 to 0.4 km is desirable) leading to large gaps in coverage after 7157 nodal crossings. There were 155 coverage gaps averaging 123.6 km each for a total of 19,158 km uncovered along the equator.

Table 5 also includes the total delta-V for each run. This total represents the total delta-V expended during one coverage cycle (3455 orbits for 5.8 km separation or 3578 orbits for 5.6 km) and depends on the altitude and flux level. The flux levels for the Schatten prediction (PL0391) are

Table 5. Comparative Results of GMAS Runs

Run	Space (km)	DLONG (deg)	Alt (km)	Gain	RGain	Elements	Frozen	Flux	Delta-V (m/sec)	Cover (%)
1	5.8	22.8165345	339.9	0.050	0.023	6718.1400 0.00001 96.8134	N	PL0391	83.57	98.229
2	5.8	22.8165345	336.6	0.050	0.023	6718.1495 0.001419 96.8134	Y	PL0391	83.28	99.283
3	5.8	23.0762551	391.0	0.025	0.001	6769.2400 0.000001 97.0116	N	PL0391	39.42	99.032
4	5.8	23.0762551	387.7	0.025	0.001	6769.2493 0.001398 97.0116	Y	PL0391	37.55	99.653
5	5.8	23.0762551	391.0	COMP	0.001	6769.2400 0.00001 97.0116	N	DAILY1	21.73	98.776
6	5.6	23.0775680	391.1	0.025	0.001	6769.3400 0.00001 97.0116	N	PL0391	40.76	99.115
7	5.6	23.0775680	387.8	0.025	0.001	6769.3400 0.001398 97.0116	Y	PL0391	40.59	99.590
8	5.6	23.0775680	391.1	COMP	0.001	6769.3400 0.00001 97.0116	N	DAILY1	23.78	99.051
9	5.6	23.0775680	387.8	COMP	0.001	6769.3400 0.001398 97.0116	Y	DAILY1	23.65	99.610
10	5.6	23.0766006	391.1	0.025	0.001	6769.3400 0.00001 97.0116	N	PL0391	40.75	52.234
11	5.6	23.0766006	391.1	COMP	0.001	6979.3400 0.00001 97.0116	N	PL0391	40.72	52.173
12	5.6	23.0772455	391.1	COMP	0.001	6769.3400 0.00001 97.0116	N	PL0391	40.71	50.987

Notes:

Space = Ground track spacing (km)
DLONG = Longitude difference between successive crossings (deg)
Alt = Initial altitude at ascending node (km)
Gain = Displacement gain (COMP = computed by program)
RGain = Rate gain
Elements = Osculating orbital elements (semimajor axis, eccentricity, inclination)
Frozen = Frozen orbit (Yes/No)
Flux = Solar flux used: PL0391 = Schatten +2 sigma prediction from March 1991
DAILY1 = Daily varying flux with 1-day delay
Delta-V = Total delta-V (m/sec) expended during one coverage cycle
Cover = Percent coverage at equator

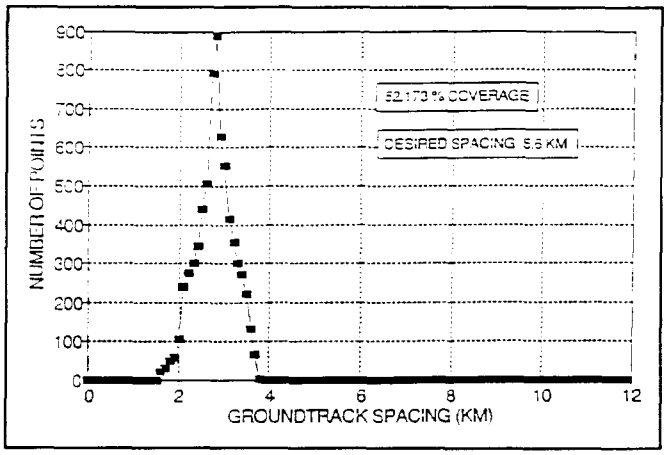

Figure 12. TMLA Ground Track Spacing Initial OSC (SMA = 6769.34)

generally higher than those used for the daily flux runs (DAILY1) and, therefore, show higher delta-Vs. The delta-V will change if the spacecraft mass and area are altered from the values used in this study.

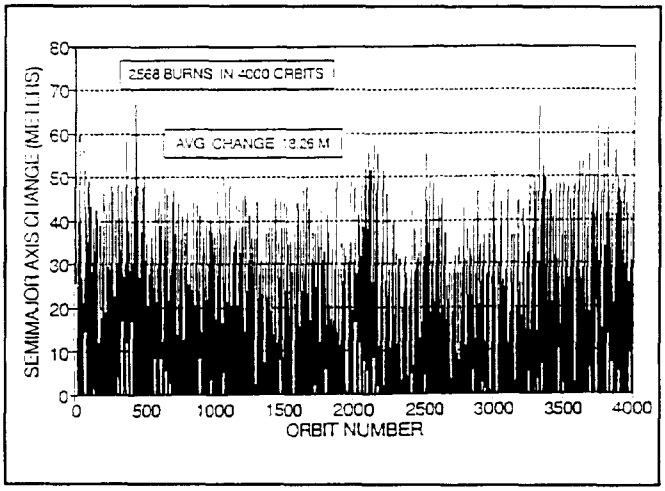

Figure 13. TMLA Delta SMA Per Maneuver Initial OSC (SMA = 6769.34 km)

The expected fuel use during one cycle can be computed from the rocket equation and is given in Table 6 for each run assuming specific impulses of 250 and 600 sec. Also given is the percentage of orbits on which maneuvers occurred (100 percent means a maneuver is performed on every orbit). Figure 13 presents a sample maneuver profile using data from Run 8, showing the semimajor axis change at each maneuver. This case required 2568 maneuvers (two-burn Hohmann transfers) in 4000 orbits; that is, maneuvers were performed at 64.2 percent of the nodal crossings. The changes in semimajor axis ranged from 1 to 79 m with an average change of 18.26 m.

Table 6. Summary of Delta-V and Fuel Requirements

Run	Delta-V (m/sec)	Fuel Required (kg)		Percent of Orbits With Maneuvers
		250 I_{sp}	600 I_{sp}	
1	83.57	7.71	3.24	68.3
2	83.28	7.68	3.23	67.5
3	39.42	3.67	1.54	77.7
4	37.55	3.50	1.46	75.6
5	21.73	2.03	0.85	61.6
6	40.76	3.79	1.59	78.0
7	40.59	3.78	1.58	78.0
8	23.78	2.22	0.93	64.2
9	23.65	2.21	0.92	63.8
10	40.75	3.79	1.59	77.8
11	40.72	3.79	1.59	74.6
12	40.71	3.79	1.58	76.5

Frozen Orbit

As mentioned previously, the use of a frozen orbit was examined to determine whether any benefits existed for TMLA. The concept of a frozen orbit is detailed in Reference 3. In a frozen orbit, the argument of perigee remains in the vicinity of 90 deg (the north point of the orbit), and the altitude above a given latitude remains nearly constant,

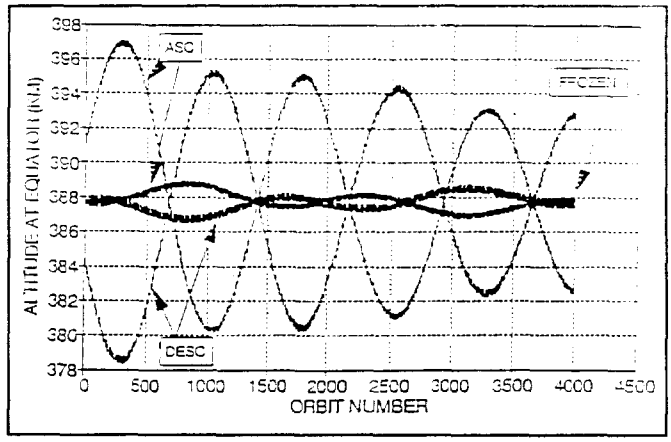

Figure 14. TMLA Height at Nodes (Mean SMA = 6759.62 km) Frozen and Nonfrozen Orbits

assuming maneuvers are performed to counteract the effects of atmospheric drag. This has advantages for an Earth-

observing spacecraft with a repeating ground track, in that each time the spacecraft passes over a given landmark, it will be at nearly the same altitude. This point is illustrated in Figure 14, which shows altitudes above the ascending and descending nodes for frozen and nonfrozen orbits with the same mean semimajor axis. The data were generated by Runs 3 and 4 (see Table 5).

The initial altitudes at the ascending and descending nodes are 391.03 and 384.46 km, respectively, for the nonfrozen orbit. As the orbit evolves in time, the differences between ascending and descending nodal heights increase until the heights differ by almost 19 km. The height differences then decrease to zero and the cycle repeats. The amplitudes of successive cycles, however, decrease with time, which is due to the maneuvers done at the nodal crossings to maintain the orbit. The orbit is slowly evolving to the frozen condition as a result of the maneuvers but may take several ground track cycles to reach that point. The frozen orbit starts with both ascending and descending node altitudes at 387.7 km. As this orbit evolves, the differences in height at the nodes never exceeds about 2.5 km.

The results of the analysis of a small number of cases indicate that the frozen orbit improves the total ground track coverage slightly and greatly improves altitude control over a given part of the orbit. Controlling the altitude in this manner may have advantages for operating the laser or processing laser data.

6. CONCLUSIONS

This paper described an algorithm for a simple autonomous ground track controller for the TMLA mission, using orbit determined from GPS data and a fixed-reference ground track spacing at the equator. Analysis of computer simulations using the control algorithm, with all orbit perturbations including daily solar flux variations, resulted in the following conclusions:

- More than 99 percent coverage at the Equator is obtainable in one cycle of Earth coverage (220 to 230 days) with a 6-km sensor swath width and 5.6 or 5.8 km ground track spacings, in a range of orbit altitudes between 340 and 390 km. A high probability exists that 100 percent coverage will be obtained in a 3-year TMLA mission.
- The percent coverage is critically dependent on the combination of nominal altitude and delta longitude between ascending nodes selected for the mission. A difference of 0.001 degrees in delta longitude, with the same nominal altitude, can make a 47 percent difference in the coverage.
- An orbit that is initially frozen offers a slight improvement in total coverage, compared with an arbitrary near-circular initial orbit. The maintenance maneuvers generated by the algorithm preserve a frozen orbit. A near-circular orbit becomes a frozen orbit after the passage of time.

REFERENCES

1. Wertz, et al., *Spacecraft Attitude Determination and Control*, D. Reidel Publishing Company, 1978
2. K. Schatten, *Predicted Solar Data as of March 1991*, Goddard Space Flight Center, Code 914, March 1991
3. K. Nickerson et al., "Application of Altitude Control Techniques for Low Altitude Earth Satellites," paper presented at AAS/AIAA Astrodynamics Conference, Jackson Lake, Wyoming, September 1977

FLIGHT MECHANICS/ESTIMATION THEORY SYMPOSIUM

MAY 5-7, 1992

SESSION 3

Real-Time Attitude Determination and Gyro Calibration*

M. Challa, O. Filla, J. Sedlak, and D. Chu
COMPUTER SCIENCES CORPORATION (CSC)

ABSTRACT

We present results for two real-time filters prototyped for the Compton Gamma Ray Observatory (GRO), the Extreme Ultraviolet Explorer (EUVE), the Cosmic Background Explorer (COBE), and the next generation of Geostationary Operational Environmental Satellites (GOES). Both real and simulated data were used to solve for attitude and gyro biases. These filters promise advantages over single-frame and batch methods for missions like GOES, where startup and transfer-orbit operations require quick knowledge of attitude and gyro biases.

* This work was supported by the National Aeronautics and Space Administration (NASA)/Goddard Space Flight Center (GSFC), Greenbelt, Maryland, Contract NAS 5-31500.

1. INTRODUCTION

Mishaps of the distant past have prevented sequential filters from becoming part of the operational ground support systems in the Flight Dynamics Facility (FDF). Experience gained over the past few years with prototype filters for several spacecraft, however, bolsters the conviction that sequential filters have a place in real-time attitude and gyro bias estimation in the FDF.

Two very different filters, filter QUEST and the Real-Time Sequential Filter (RTSF), both show themselves to be reliable alternatives to the original single-frame QUEST for real-time systems. As long as attitude is continuously observable, divergence does not appear to be a problem, and the filters work over a wide range of tuning parameter values.

This article provides an account of recent attitude and gyro bias filtering experience using data from COBE, GOES, GRO, and EUVE. The filters perform well and provide attitude and gyro bias solutions in less time than would be necessary to obtain a batch estimate.

2. FILTER QUEST

Filter QUEST is a sequential version of the q-algorithm as implemented in the widely used QUEST software (Reference 1). The q-algorithm only estimates attitude, but for the sake of accuracy, it is almost essential that gyro biases be estimated as well. In order to make filter QUEST satisfy the demand for gyro biases, a bias filter was added to run in parallel with the attitude filter.

The bias filter takes the attitude predicted using gyro measurements $\bar{q}(-)$ and compares it to the attitude updated using sensor measurements $\bar{q}(+)$. First, the difference between the two attitude quaternions is computed:

$$\Delta\bar{q} = \begin{bmatrix} \Delta q_1 \\ \Delta q_2 \\ \Delta q_3 \\ \Delta q_4 \end{bmatrix} = \begin{bmatrix} q(-)_4 & q(-)_3 & -q(-)_2 & q(-)_1 \\ -q(-)_3 & q(-)_4 & q(-)_1 & q(-)_2 \\ q(-)_2 & -q(-)_1 & q(-)_4 & q(-)_3 \\ -q(-)_1 & -q(-)_2 & -q(-)_3 & q(-)_4 \end{bmatrix} \begin{bmatrix} -q(+)_1 \\ -q(+)_2 \\ -q(+)_3 \\ q(+)_4 \end{bmatrix} \tag{1}$$

Then, this difference is transformed into a rotation vector $\Delta\vec{a}$ and divided by the time step Δt to provide an observation of the gyro bias $\Delta\vec{b}$:

$$\Delta\vec{a} = \frac{2\,\mathrm{atan2}\left(\sqrt{\Delta q_1^2 + \Delta q_2^2 + \Delta q_3^2}, \Delta q_4\right)}{\sqrt{\Delta q_1^2 + \Delta q_2^2 + \Delta q_3^2}} \begin{bmatrix} \Delta q_1 \\ \Delta q_2 \\ \Delta q_3 \end{bmatrix} \tag{2}$$

These observations are averaged using the same fading memory parameter, α, as is used for the attitude (Reference 2). The fading memory parameter is a scalar between 0 and 1.

$$\vec{b}_n = \vec{b}_{n-1} + (1 - \alpha)\frac{\Delta\vec{a}_n}{\Delta t} \tag{3}$$

The enhanced filter QUEST was originally applied to COBE where the spin (X-axis) gyro bias is of primary concern. The COBE Fine Attitude Determination System (FADS) found the X-axis gyro bias to be 14.4 degrees per hour (deg/hr) for these data. Figure 1 through Figure 3 show the filter QUEST bias solutions for different values of α. An initial bias value of 0 deg/hr was used. Figure 1 shows that α equal to 0.9 is too low to filter out sensor noise. In Figure 2, the bias converges to within 1 deg/hr of the FADS bias in only 6 minutes. Setting α to 0.999 as in Figure 3 further reduces the noise but slows convergence.

Figure 4 differs from the preceding figures in that the initial bias is close to the correct value. Filter QUEST with α equal to 0.999 shows variation in the estimated bias. The COBE X-axis gyro is known to be temperature sensitive, and the enhanced filter QUEST may be useful in studying this sensitivity.

The COBE solutions were obtained by replacing the standard QUEST subroutines in the Coarse Attitude Determination Subsystem (CADS) with the new filter QUEST subroutines. All the data were synchronized in the Data Adjuster Subsystem (DA), and every data point was processed. The filter is updated every half-second.

Filter QUEST has also been tested with simulated data for GOES. In this case, the standard QUEST routines were replaced with their filter counterparts in the Real-Time Attitude Determination System (RTADS). There, at most one data point can be processed for every 8 seconds (sec) of data, and the different data types may come from any time in that interval. These attributes of RTADS are clearly undesirable, but there has not yet been time to change them.

Nonetheless, Figure 5 shows the filter QUEST roll and pitch bias solutions converging over the course of 15 minutes (yaw is similar). The data were simulated to reproduce that expected during the GOES transfer orbit but without systematic errors other than gyro biases. The filter was started from initial estimates of 0 deg/hr and was given an α value of 0.9999, which should slow the convergence. There are initial transients and oscillations in the bias solutions, but even with the less than ideal RTADS preprocessing and a fairly short data span, biases approach the batch estimated values. The filter solutions are within 10% for yaw, 30% for pitch, and 40% for roll.

3. RTSF

The RTSF is a scaled-down version of the extended Kalman filter originally prototyped for the Earth Radiation Budget Satellite (ERBS) (References 3 and 4). Whereas the 37-component state vector of the ERBS filter included various sensor misalignments and scale factors, the RTSF estimates a 7-component state vector consisting of the attitude quaternion and the three components of the gyro bias (Reference 5). The objective of the present study is to evaluate the RTSF in a real-time situation with its attendant data processing problems. To this end, we integrated the RTSF into current real-time attitude determination software and evaluated it using real telemetry data from GRO and simulated data from EUVE.

The theory of the filter has been presented elsewhere (References 3 and 4) and will not be repeated here, except to note that the GRO RTSF updates the attitude quaternion using a multiplicative method. Thus, if (ϕ, Ω, μ) are three small Euler angles representing corrections to the attitude estimate, the corresponding correction to the quaternion is specified by

$$\delta\vec{q} = \begin{bmatrix} \phi/2 \\ \Omega/2 \\ \mu/2 \\ 1 \end{bmatrix} \tag{4}$$

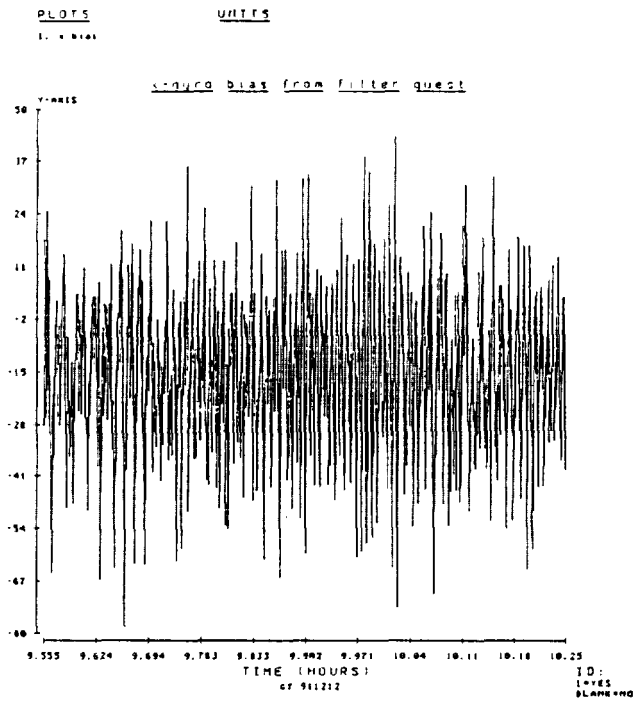

Figure 1. Filter QUEST Gyro Bias Fading Memory Equal to 0.9

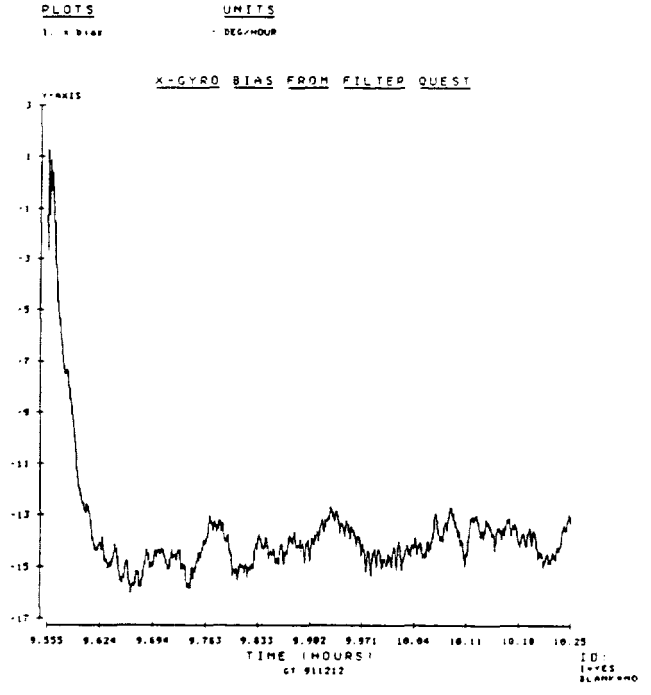

Figure 2. Filter QUEST Gyro Bias Fading Memory Equal to 0.99

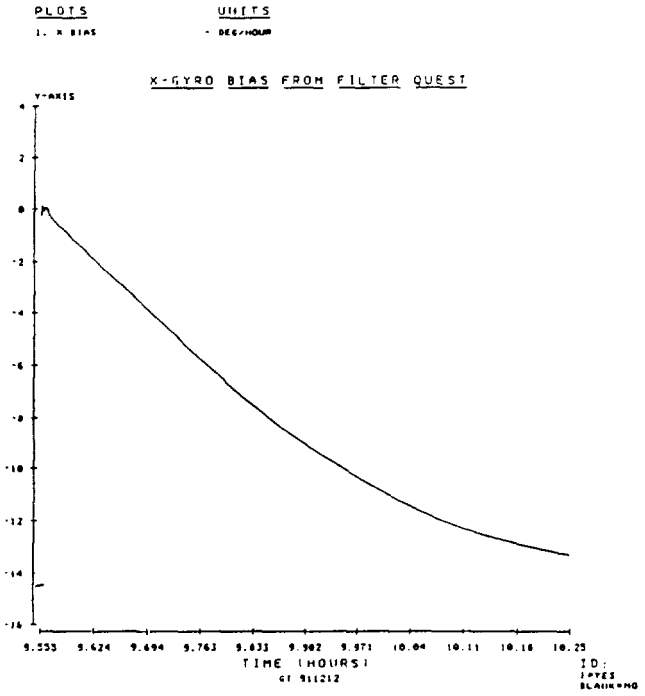

Figure 3. Filter QUEST Gyro Bias Fading Memory Equal to 0.999

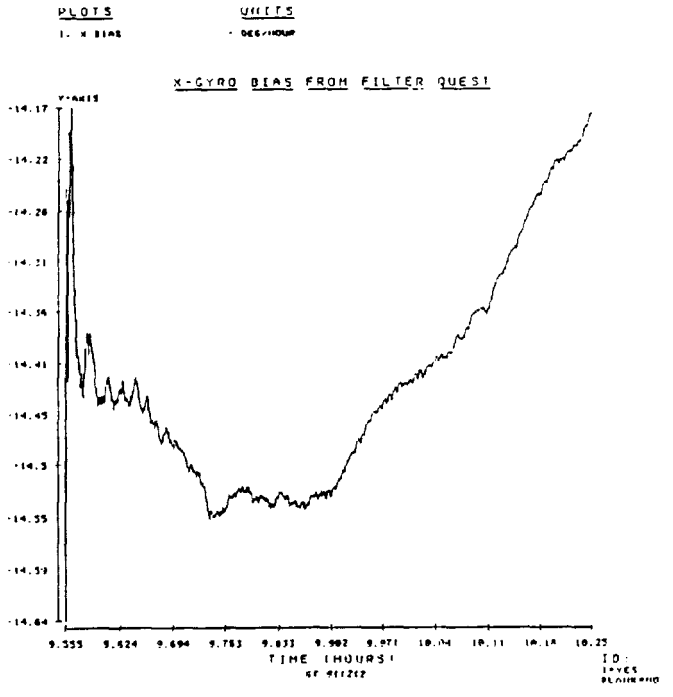

Figure 4. Filter QUEST Gyro Bias Good a Priori Bias—Memory 0.999

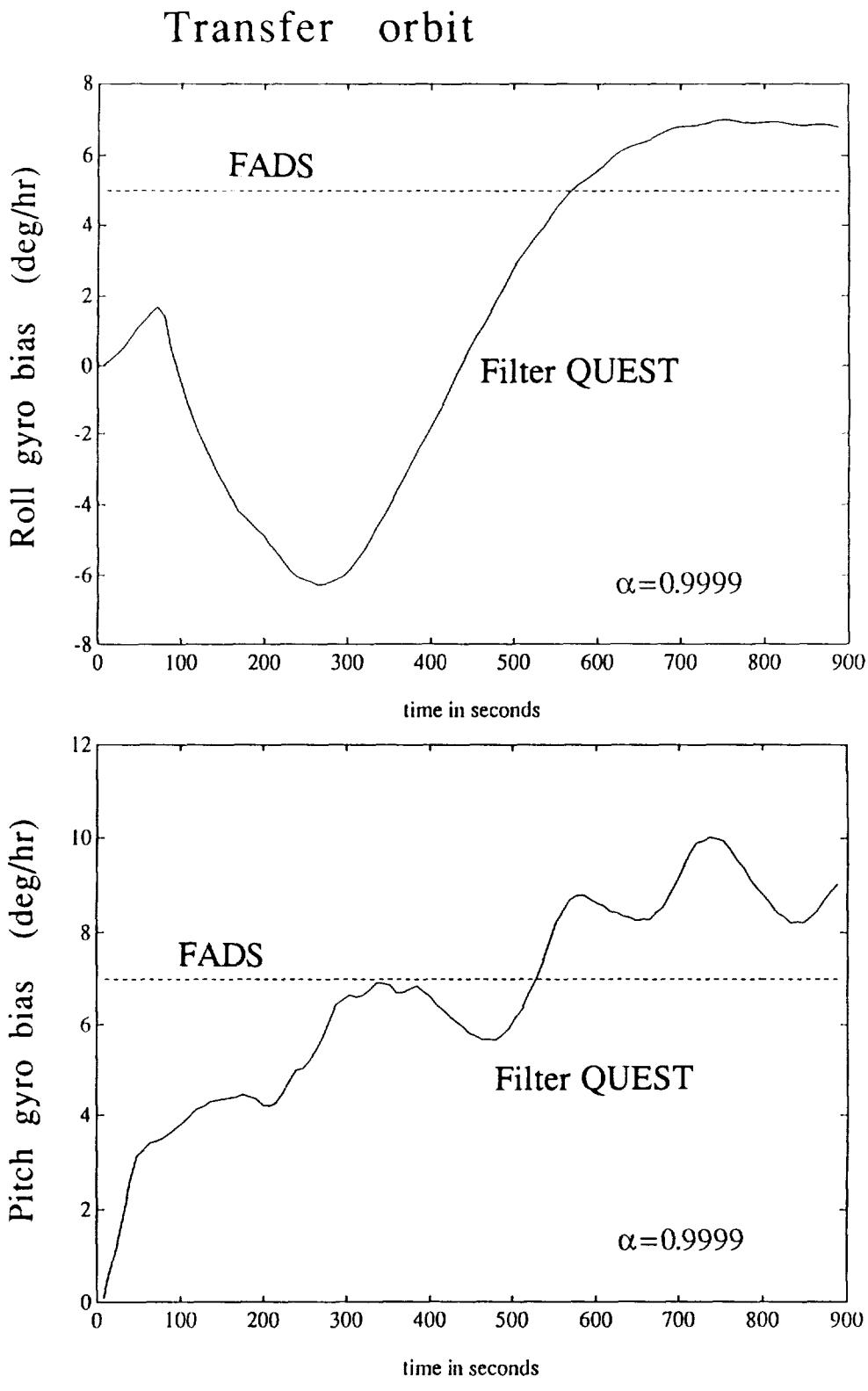

Figure 5. GOES Filter QUEST Gyro Bias

and the quaternion is updated through:

$$\vec{q}_{k+1}(+) = \vec{q}_{k+1}(-)\delta\vec{q}^{-1} \tag{5}$$

GRO is an inertially fixed spacecraft. The attitude hardware consists of: two fine Sun sensors (FSS); two three-axis magnetometers (TAM); two fixed-head star trackers (FHST); and an inertial reference unit containing three two-axis gyroscopes. Although the onboard computer (OBC) uses the full sensor complement, the GRO RTSF does not process the more accurate FHST data; thus, we take here the OBC's attitude estimate as the truth model. A different scheme was used to evaluate the RTSF gyro bias estimation, since (1) the OBC's estimates of the biases were not readily available in telemetry, and (2) batch estimates showed that the real biases were comparable to the noise in the RTSF estimates (0.5 to 1.0 deg/hr). Biases were introduced into the gyro rates before they were input to the filter, and these were taken as the truth model. (Several different combinations of simulated biases were used, ranging in magnitude from 1 to 60 deg/hr). The attitude matrix for inertial-to-body transformation is described here by a 1-2-3 Euler angle sequence about the body X, Y, and Z axes, respectively, and the respective Euler angles are denoted roll, pitch, and yaw.

We present here the RTSF results using real telemetry data from GRO spanning a roll maneuver on April 9, 1991. The maneuver lasted about 2200 sec, during which only the roll gyro rate is nonzero and is maintained at about 0.06 deg/sec. The initial and final OBC estimates of the attitude Euler angles are, respectively, (146.27, 17.54, -11.00) and (-96.85, -17.96, -10.26) deg.

Figure 6 shows the roll angle estimated by the RTSF. We see that, starting from an a priori roll estimate of 120 deg, the RTSF converges to the OBC estimate in about 1500 sec (75 filter updates). It then varies about the OBC estimate with an error of about 2 deg. For this set of data, the FSS boresight was very close to the roll axis, so that the roll estimate is obtained essentially from TAM data alone. Thus, we attribute the relatively large error in the RTSF estimates as being due to the coarseness of the TAM data.

The orientation of the FSS does not pose a problem for estimating yaw and, as shown in Figure 7, we see that the RTSF errors are now less than 0.5 deg. Note also the spikes in the estimate at about 7000 and 7500 sec; inspection of the data shows that abnormally large gyro data were received at those points. However, the filter recovers very quickly after the anomalies. Another interesting feature is the effect of the covariance matrix on the convergence rate of the RTSF. Whereas the a priori covariance matrix used to generate Figure 6 was large, the a priori matrix used to obtain the data of Figure 7 was the converged matrix obtained at the end of the run of Figure 6. Starting from an a priori value of –20 deg, the RTSF's yaw estimate now converges within 500 sec (about 25 updates).

An example of the GRO RTSF's gyro bias estimation is presented in Figure 8. We see that, until the start of the maneuver, the RTSF recovers the true yaw bias of +2.4 deg/hr with an error of about 0.5 deg/hour. There is substantial noise during the maneuver—about 3.6 deg/hr or 0.001 deg/sec. We attribute this to a combination of an effective yaw component of the rate due to errors in the attitude estimate and greater noise in the high-rate gyro data during the maneuver.

The EUVE sensor complement consists of two FHSTs, an FSS, two coarse Sun sensors, and two triaxial magnetometers. The EUVE RTSF performs real-time star identification by a direct match method enhanced by an attitude-independent dot-product check between the star and Sun vectors.

Shortly after orbit insertion, EUVE will be spun up to 1.3 revolutions per orbit to allow its FHSTs to scan for acquisition stars. As stars move through the FHST fields of view, the filter solution shows discontinuities (Figures 9 and 10) due to small misalignments and biases in the simulated sensors. (The Kalman filter only

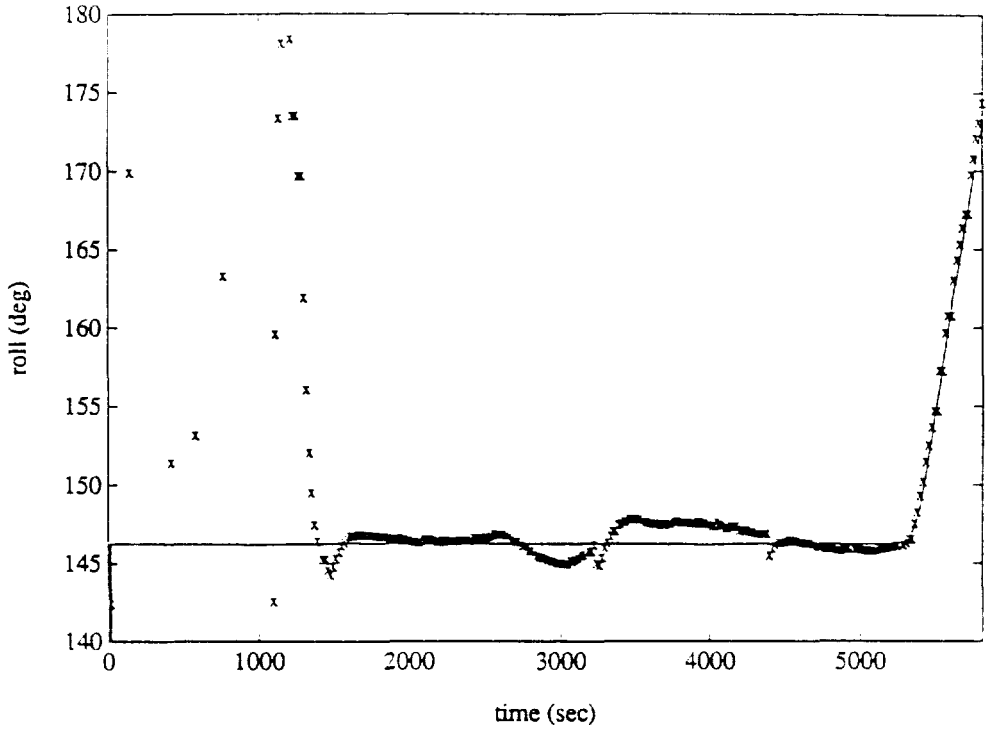

Figure 6. Estimates of the roll (Euler) angle. Solid line represents the OBC estimate, and 'x' represents the RTSF estimates. The a priori roll estimate was +120 deg.

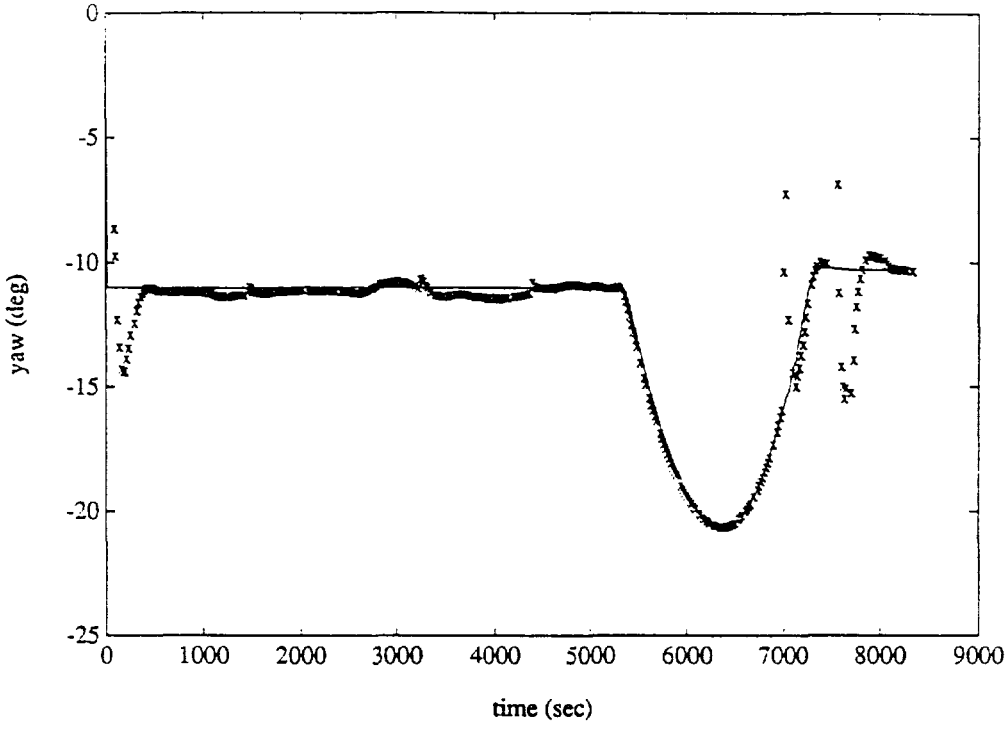

Figure 7. Estimates of the yaw (Euler) angle. Notation is that of Figure 6. The a priori yaw estimate was –20 deg.

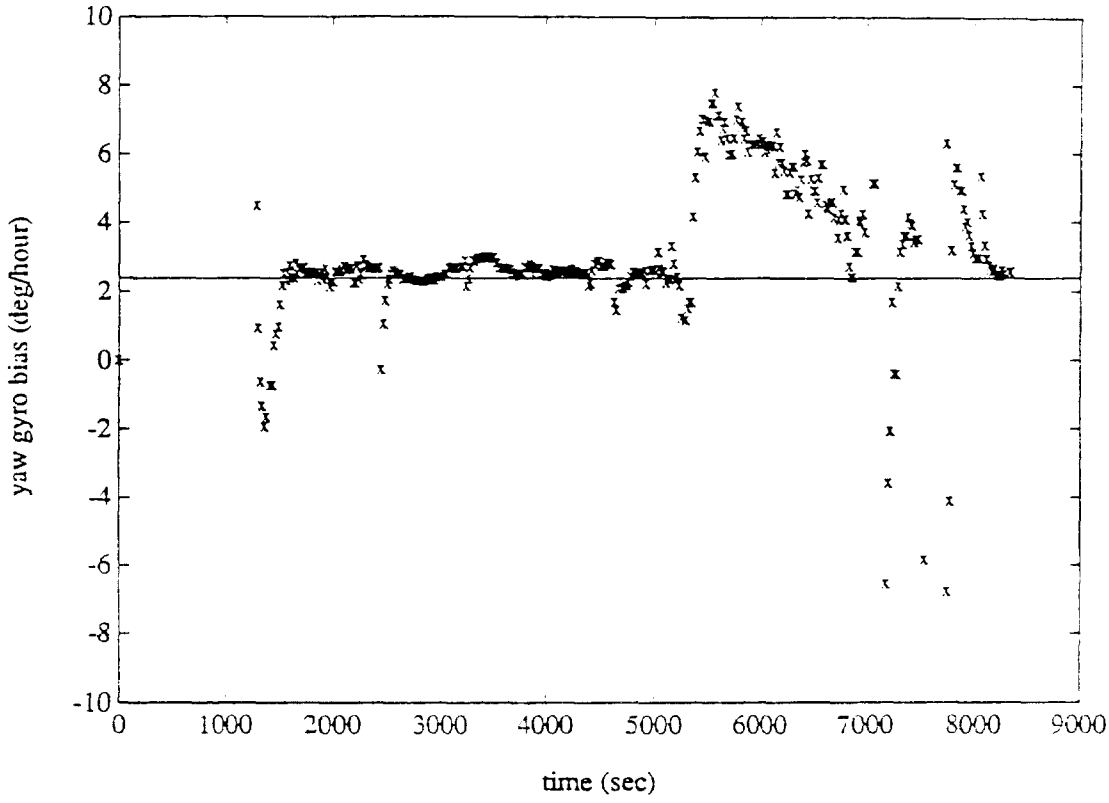

Figure 8. **RTSF estimates ('x') of the gyro bias along the yaw axis. The horizontal line represents the bias of +2.4 deg/hr included in the gyro data input to the RTSF. The a priori bias estimate was 0.0 deg/hr.**

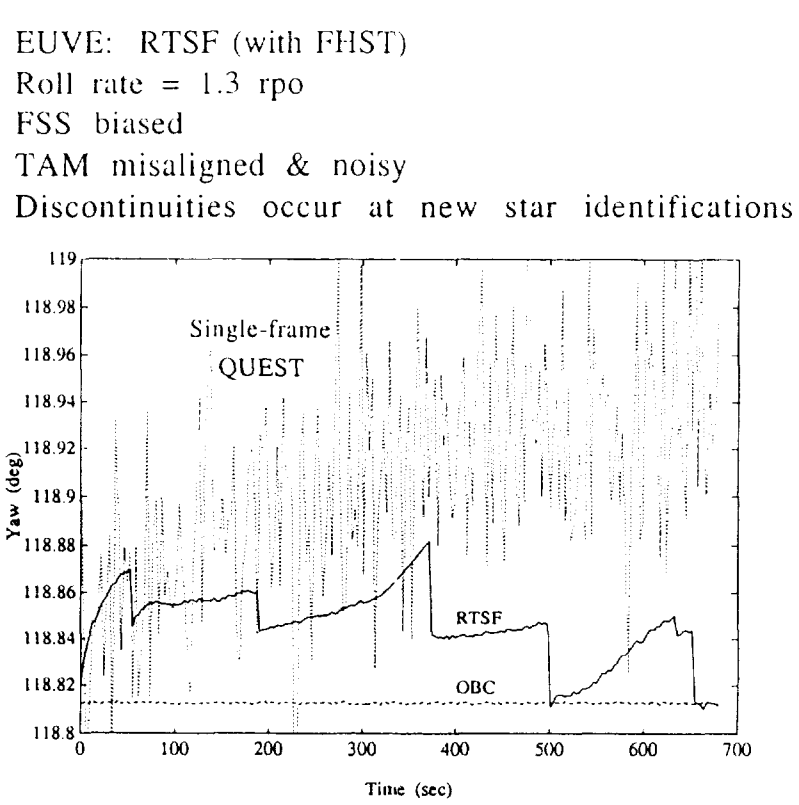

Figure 9. EUVE yaw angle determined by RTSF and single-frame QUEST. The dashed line marked "OBC" is the true yaw angle.

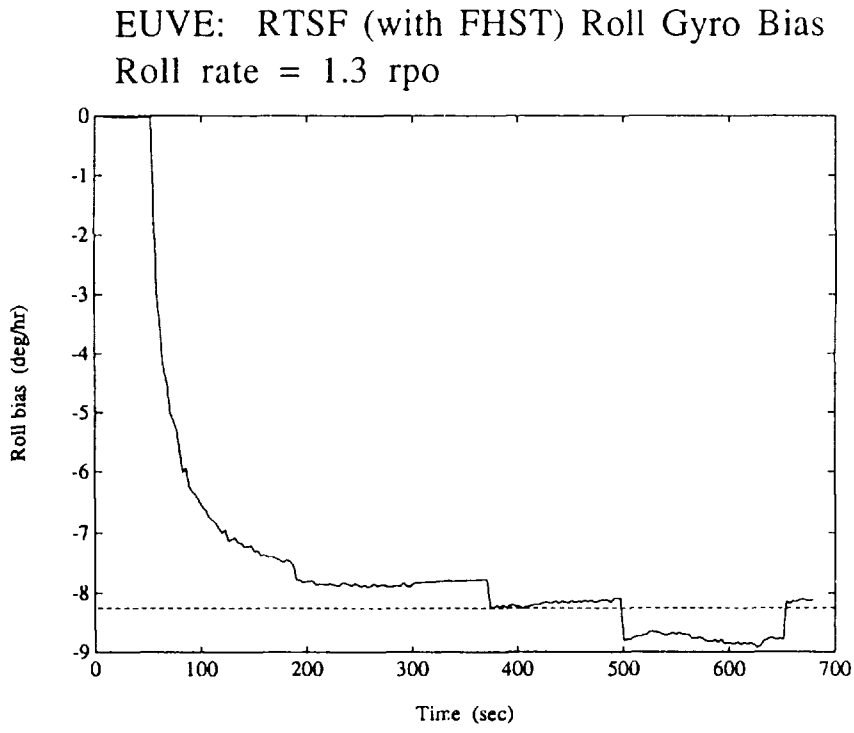

Figure 10. EUVE RTSF solution for roll gyro bias. The dashed line indicates the true bias.

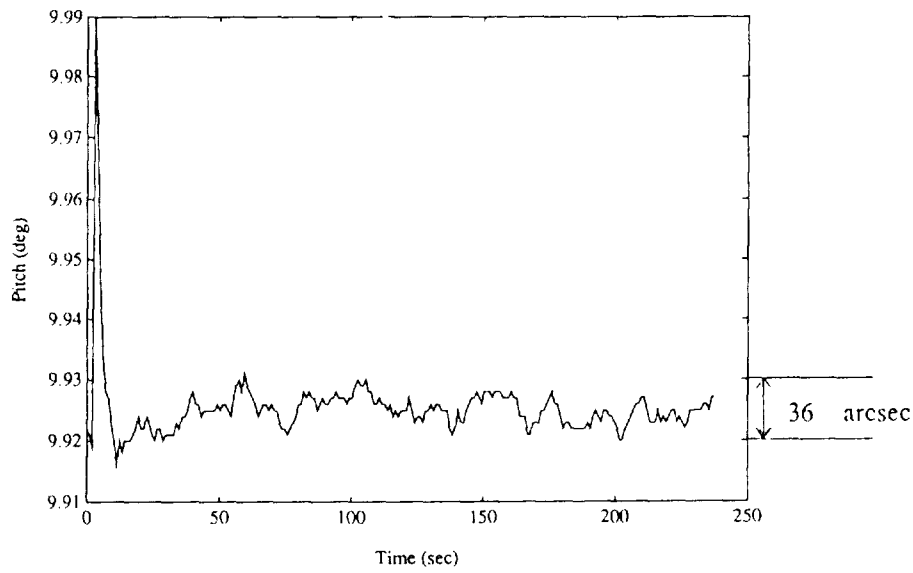

Figure 11. EUVE RTSF solution for pitch angle. True pitch is constant at 9.82 deg. FSS misalignment causes the 0.1-deg offset.

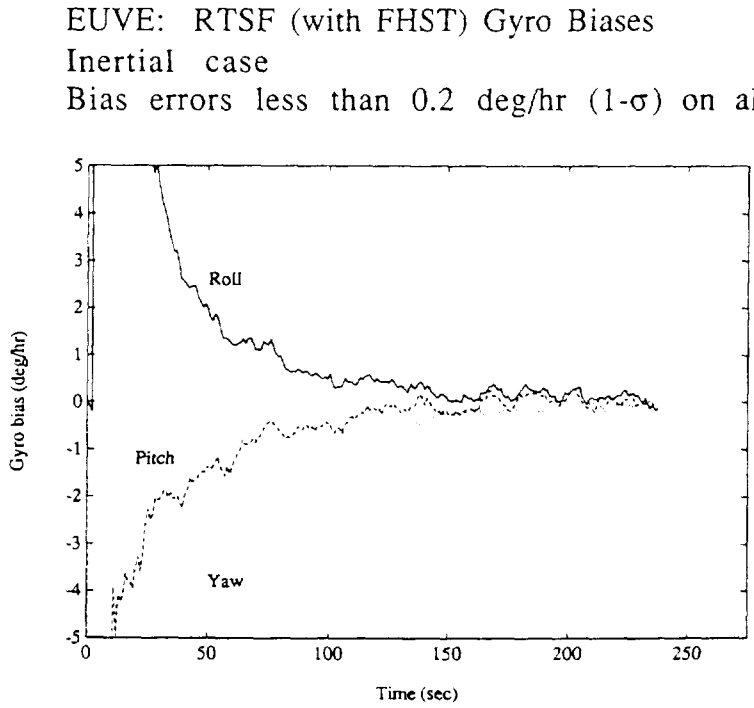

Figure 12. EUVE RTSF solution for the gyro biases. The true biases are all zero in this example.

filters out random noise, not systematic errors). The discontinuities in attitude are under 0.04 deg. They can be greatly reduced by tuning the filter for a longer memory and increasing the sensor noise parameters to put less reliance on current incoming data. However, this leads to noisier solutions and longer bias convergence times.

Figure 11 and 12 show a case where EUVE is inertially pointing with the Sun in view of the FSS and an identified star in FHST-1. The attitude solution converges within 1 minute (the filter is updating once per second), with residual noise under 15 arcsec (1-σ). After 4 minutes, the gyro bias errors are under 0.2 deg/hr (1-σ) and still decreasing.

4. CONCLUSIONS

Adding a simple gyro bias estimator to filter QUEST gave COBE and GOES biases within 1 to 2 deg/hr of the batch estimator values. This filter proved stable under a wide range of memory length parameter values. Increasing the memory parameter slowed response and smoothed the time history but did not affect the final result. The COBE data used were all clean and synchronized. The GOES data were simulated and clean but not synchronized. Attitude was continuously observable for both spacecraft.

For the GRO RTSF, using real data provided a useful test of the filter's performance in a real-time situation. The attitude errors using FSS and TAM data depended upon Sun observability by the FSS and ranged from 0.5 to 2 deg; the gyro bias errors varied correspondingly between 0.5 and 20 deg/hr.

The GRO RTSF proved to be robust in the presence of gyro data anomalies. However, its solutions for roll angle and roll gyro bias are relatively noisy and slow to converge due to the limitation to only FSS and magnetometer measurements (the Sun being close to the roll axis). The inclusion of FHST data in the EUVE RTSF greatly improves the solutions. The EUVE RTSF solutions were subject to offsets and small discontinuities due to misalignments and biases. This problem is expected to affect the early stages of any mission until the full ground support system estimates these systematic errors.

REFERENCES

1. M. D. Shuster, "A Simple Kalman Filter and Smoother for Spacecraft Attitude," *Journal of the Astronautical Sciences*, 37.1, January–February 1989

2. O. Filla, J. Keat, and D. Chu, "COBE Experience with Filter QUEST," Flight Mechanics/Estimation Theory Symposium, National Aeronautics and Space Administration Conference Publication 3123, May 21–23, 1991

3. J. Deutschmann and I. Y. Bar-Itzhack, "Extended Kalman Filter for Attitude Estimation of the Earth Radiation Budget Satellite," Flight Mechanics/Estimation Theory Symposium, National Aeronautics and Space Administration Conference Publication 3050, May 23–24, 1989

4. J. Deutschmann, I. Y. Bar-Itzhack, and M. Rokni, "Comparison and Testing of Extended Kalman Filters for Attitude Estimation of the Earth Radiation Budget Satellite," Flight Mechanics/Estimation Theory Symposium, National Aeronautics and Space Administration Conference Publication 3102, May 22–24, 1990

5. Goddard Space Flight Center, Flight Dynamics Division, FDD/544-90/060, *Attitude Determination: A Prototype Real-Time Sequential Filter (RTSF) Evaluation Report,* M. Rokni and J. Deutschmann, prepared by Computer Sciences Corporation, February 1990

Computationally Efficient Algorithms for Real-time Attitude Estimation

Steven R. Pringle

McDonnell Douglas Space Systems Company

ABSTRACT

For many practical spacecraft applications, algorithms for determining spacecraft attitude must combine inputs from diverse sensors and provide redundancy in the event of sensor failure. A Kalman filter is suitable for this task, however, it may impose a computational burden which may be avoided by sub optimal methods. A sub optimal estimater is presented which was implemented successfully on the Delta Star spacecraft which performed a 9 month SDI flight experiment in 1989. This design sought to minimize algorithm complexity to accommodate the limitations of an 8K guidance computer. The algorithm used is interpreted in the framework of Kalman filtering and a derivation is given for the computation.

INTRODUCTION

Historically, satellite attitude determination has relied on simple deterministic calculations for batch processing of telemetry data because real-time recursive algorithms such as Kalman filters imposed an impractical computational burden. This burden has become less daunting with advances in flight-qualified microprocessors, however, simple algorithms remain important for maintaining the reliability and controlling the development cost of real-time software.

This paper examines the algorithm used to estimate attitude for Delta Star. This algorithm applies deterministic gains to measurement data. Nonetheless, it is desirable to perform an statistical error analysis. The attitude estimation problem is cast as a Kalman filtering problem such that the performance of the sub optimal deterministic gains can be quantified. As a convenient byproduct, the Kalman gains implicit in this setup provide an alternative estimation procedure with only a modest increase in computations.

DELTA STAR BACKGROUND

The SDIO sponsored Delta Star spacecraft operated on-orbit for nine months during 1989. Its objectives included multi-spectral observation of low earth orbital phenomena against various earth and space backgrounds. Numerous pointing and tracking guidance modes required modest but reliable, knowledge of spacecraft attitude.

The spacecraft consisted of two sections: a guidance and propulsion section and a sensor section. Each was controlled by separate processors designated guidance computer (GC)

and flight processor (FP) respectively. All primary GN&C functions resided in the GC. Because the guidance and propulsion section was based on the Delta launch vehicle second stage, the GC was a Delco Magic 352 guidance computer, featuring 8K of random access memory to accommodate data, program instructions and a resident operating system. In addition to GN&C functions, the GC flight program sequenced discretes to control avionics subsystems, processed telemetry and uplinks from the ground, and provided a protocol for communication with the FP. The limited memory budgeted for attitude determination made a simple design imperative.

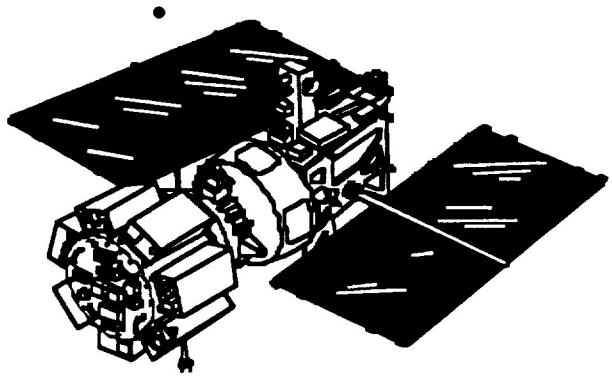

Figure 1. Delta Star Spacecraft

QUATERNION CONVENTIONS

In this section notation and conventions are developed for the quaternion q. The two primary coordinate frames of interest in this report are an inertial reference frame I, and a spacecraft body-fixed frame **B**. A coordinate frame is given by a triad of orthonormal basis vectors which obey the right-hand rule. A change of basis is specified by a rotation or direction cosine matrix T_I^B defined by

$$y_B = T_I^B y_I \qquad (1.)$$

where $y_B \in \Re^3$, $y_I \in \Re^3$

are the same vector expressed in **I** and **B** coordinates.

The rotation matrix T_I^B can be represented by a quaternion q. the quaternion is a globally nonsingular mapping of the rotation matrix. The set of attitude quaternions is defined as

$$Q = \left\{ (q_s, q_v) \in \Re \times \Re^3 : q_s^2 + \|q_v\|^2 = 1; q_s \geq 0 \right\} \qquad)$$

where the first condition is the unit quaternion normality constraint and the second is a convention to eliminate the ambiguity of sign which arises because (q_s, q_v) and $(-q_s, -q_v)$ represent the same attitude. With these conventions, T_I^B can be computed from the quaternion q by the formula

$$T_I^B = I + 2\Omega_{q_v}^2 - 2q_s\Omega_{q_v} \qquad (3.)$$

where for $a \in \Re^3$, Ω_a is defined as

$$\begin{aligned} &\Omega_a : \Re^3 \times \Re \\ &c = \Omega_a b \\ &c = a \times b \end{aligned} \qquad (4.)$$

for $a, b \in \Re^3$. Quaternion multiplication is defined as follows:

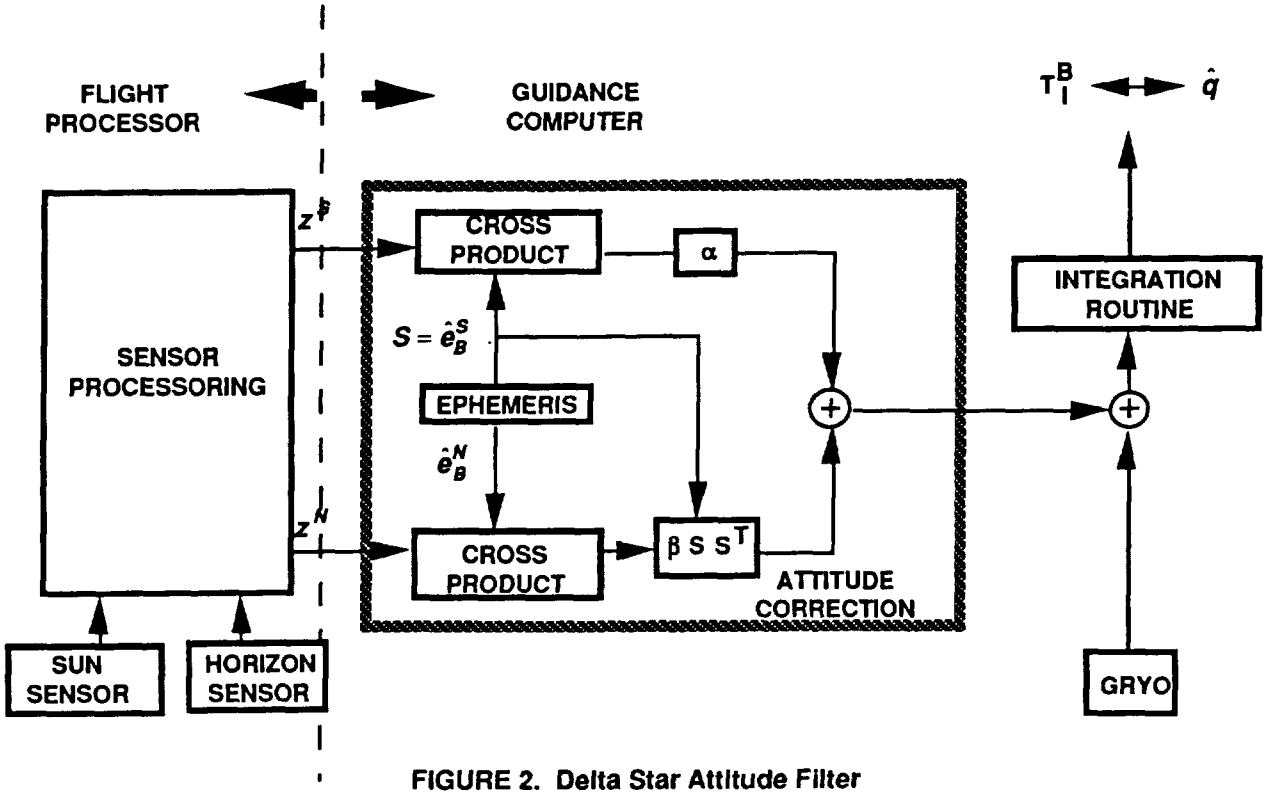

FIGURE 2. Delta Star Attitude Filter

$$
\begin{aligned}
&c = ab; \quad a,b \in Q \\
&c_s = a_s b_s - [a_v, b_v] \\
&c_v = a_s b_v + b_s a_v + a_v \times b_v \\
&c = (c_s, c_v) \in Q
\end{aligned}
\tag{5.}
$$

Quaternion multiplication is important because it corresponds to compositions of quaternion rotations. That is, for coordinate frames **A**,**B**,**C**, if q_1 rotates **A** into **B** and q_2 rotates **B** into **C**, then $q_3 = q_1 q_2$ rotates **A** into **C**.

The quaternion q. representing T_I^B, evolves in time according to the equation

$$\dot{q} = \frac{1}{2} q(0,\omega) \tag{6.}$$

where ω is the instantaneous angular velocity of the B-frame with respect to the I-frame specified in B coordinates.

The inverse of q is denoted q^* which is also called the conjugate of q [3] and is defined by

$$q^* = (q_s, -q), \text{ and } qq^* = q^*q = (1,0)$$

)

Finally, a vector $v_I \in \Re^3$ in I coordinates is transformed into $v_B \in \Re^3$ in B coordinates by

$$(0, v_B) = q^*(0, v_I)q = (0, T_I^B v_I) \tag{8.}$$

DELTA STAR ATTITUDE DETERMINATION

The attitude sensors on Delta Star spacecraft consisted of five sun sensors and a dual conical scan horizon sensor. The five sun sensors were configured to provide omni-directional sun coverage. The horizon sensor had a 26°x26° field of view. These sensors provided attitude measurements for comparison against on-line

ephemeris. The FP edited sensor data for wild points and compensated horizon sensor data for earth oblateness before passing unit vectors for sun and nadir across a communication interface. Modern earth sensors are equipped to provide such compensation using embedded microprocessors. The Delta Star Attitude Filter (DSAF)design is shown in *Figure 2.*

Traditional deterministic methods which compute a direction cosine matrix from a pair of independent measured vectors, such as the TRIAD algorithm [2], offer extreme simplicity but suffer from several deficiencies,

1. Only the current vector pair factor into the attitude estimate (i.e. noisy measurements are not averaged).
2. Nearly collinear measured vectors produce dubious solutions
3. The two vectors of a pair must be synchronous for a solution and cause complications if they arrive asynchronously.
4. Measurements from different sensors cannot be weighted to reflect relative noise levels.

A Kalman filter will eliminate these deficiencies. However, the computations required by such a filter were considered prohibitive for the Delta Star application. The design shown in *Figure 2.* also eliminates these deficiencies, but without the matrix computations required by the Kalman filter to propagate a covariance matrix and compute a gain as a function of the covariance.

The constants α and β are design parameters used to control noise rejection and to weight measurements from sun and horizon sensors with respect to each other.A method for preforming a statistical error analysis of this design is presented below. Sub optimal gains are derived in terms of α and β. A statistical interpretation of these gains is given which provides considerations for selecting α and β.

In *Figure 2.*, a running estimate of attitude is maintained by integrating angular rates from gyros according to (6.). This running estimate denoted by $\hat{q}$ differs from q as a result of gyro drift and initial condition errors.

A sun sensor produces two measurements from which the sun vector in B-coordinates can be derived. An earth nadir vector is similarly derived from the outputs of an horizon sensor. Specification of this processing will not be given here. These computations were performed by the FP for Delta Star are not formally considered a part of the DSAF design.

We will distinguish between observation vectors and measurements of these vectors. An observation vector will be denoted by $e^A_{Ck} \in \Re^3$ for time t_k where **A** is a tag denoting the type of observation {**S**:sun,**N**:nadir}.and **C** denotes the coordinate frame in which the vector is expressed.

A measurement $z^A{}_k \in \Re^3$ of e^A_{Bk} is derived from sun and horizon sensors. For our

purposes, the former is a "noisy" version of the latter.

The vectors $e_{I\,k}^{N}$ and $e_{I\,k}^{S}$ are available from an on board ephemeris calculator. From these reference vectors estimates of e_{Bk}^{A} denoted by $\hat{e}_{Bk}^{A}$ are computed by

$$(0,\hat{e}_{Bk}^{A}) = \hat{q}^{*}(0,e_{I\,k}^{A})\hat{q} \qquad (9.)$$

The discrepancy between q and $\hat{q}$ is then estimated from the discrepancy between $\hat{e}_{Bk}^{A}$ and z_k^A. In *Figure 2.*, we note that the discrepancy between $\hat{e}_{Bk}^{A}$ and z_k^A. is captured in the form of the cross product of these two vectors which is used to compute a corrective rate by which to improve the estimate $\hat{q}$.

The discrepancy between q and $\hat{q}$ will be defined by

$$q = \delta q\,\hat{q} \qquad (10.)$$

Because δq_s can be computed from δq_v using the normality constraint in (2.), δq_v will be used to define the attitude error. In the statistical error analysis below, we investigate the behavior of $P = Cov(\delta q_v)$ for the DSAF given specified statistical assumptions.

In the following, we derive a measurement sequence $\{v_k^A\}_{k=1}^{\infty}$ and matrix sequences $\{\Phi_k, H_k, K_k\}_{k=1}^{\infty}$ such that under specified conditions the following error propagation and update equations apply for the DSAF:

$$\begin{aligned}
&\delta q_{v\,k+1}^{-} = \Phi_k \delta q_{v\,k}^{+} \\
&v_k^A = H_k^A \delta q_{v\,k}^{-} + \eta_k^A ; Cov(\eta_k^A) = R_k^A \qquad (11.)\\
&\delta\hat{q}_{v\,k}^{+} = \delta\hat{q}_{v\,k}^{-} + K_k^A (v_k^A - H_k^A \delta q_{v\,k})
\end{aligned}$$

To begin, v_k^A is defined by

$$v_k^A = \hat{e}_{Bk}^{A} \times z_k^A \qquad (12.)$$

where η_k^A is considered gaussian white noise with covariance matrix R_k^A Given $\hat{q}$, we can define $h_k^A : \Re^3 \to \Re^3$ from (11.) by

$$v_k^A = h_c^A(\delta q_{vk}) + \eta_k \qquad (13.)$$

The Jacobian matrix of $h_k^A : \Re^3 \to \Re^3$ is given by

$$H_k^A = Dh_k(\delta q_{v\,k}) = -2\hat{T}_I^B \Omega_e^2 \qquad (14.)$$

where D is the derivative operator, $\hat{T}_B^I$ is computed from (2.) and $e = \hat{e}_B^A$

Then

$$v_k^A - h_k(0) = H_k^A \delta q_{v\,k} + \eta_k^A + o(\|\delta q_{v\,k}\|)$$

so that to first order

$$v_k^A = H_k^A \delta q_{v\,k} + \eta_k^A \qquad (16.)$$

This is the linearized observation equation.

By (5.) and (9.) if $\varepsilon = 0$ over the interval $[t_k, t_{k+1})$

$$\begin{aligned}
\delta q_{v\,k+1} &= \delta q_{v\,k} \\
&= \Phi_k \delta q_{v\,k} ; \Phi_k = I
\end{aligned} \qquad (17.)$$

This is the linearized state provides Φ_k and gives the linearized state equation Finally,

$$\dot{\hat{q}} = \frac{1}{2}\hat{q}(0, \omega + \varepsilon);\ \hat{q}(t_k) = \hat{q}_k;\ \hat{q}_{k+1} = \hat{q}(t_k) \tag{18.}$$

To first order this is equivalent to the Extended Kalman Filter (EKF) update scheme defined by the procedure

$$\bar{q}_k^- = \hat{q}_k$$
$$\bar{q}_k^+ = (*, \frac{\tau}{2}\hat{T}_B^I \varepsilon)\bar{q}_k^-$$
$$\dot{\bar{q}} = \frac{1}{2}\bar{q}(0, \omega + \varepsilon);\ \bar{q}(t_k) = \bar{q}_k^+;\ \bar{q}_{k+1}^- = \bar{q}(t_k) \tag{}$$

where

$$\bar{q}_{k+1}^- = \hat{q}_{k+1} + o(\tau);\quad \tau = t_{k+1} - t_k \tag{20.}$$

Then to summarize , (16.),(17.) and (19.) provide an a set of propagation and update equations in the same form as (11.) with

$$K_k^S = \alpha\tau\hat{T}_{Bk}^I$$
$$K_k^N = \beta\tau\hat{T}_{Bk}^I SS^T;\ S = \hat{e}_{Bk}^S \tag{22.}$$

This signal generation model enables us to analyze the behavior of the covariance

$$P_k = Cov(\delta q_{vk}) \cdot \tag{23.}$$

The covariance for this setup propagates according to

$$P_{k+1} = F_k^A P_k (F_k^A)^T + G_k^A \tag{}$$

where

$$F_k^A = \left(I - K_k^A H_k^A\right);\ G_k^A = K_k^A R_k^A \left(K_k^A\right)^T \cdot$$

By (17.) we need not distinguish between pre-update and post-update covarances (i.e.. $P_{k+1}^- = P_k^+$). If R_k^A is constant, which we shall assume, then it is easy to see than G_k^A is also constant.

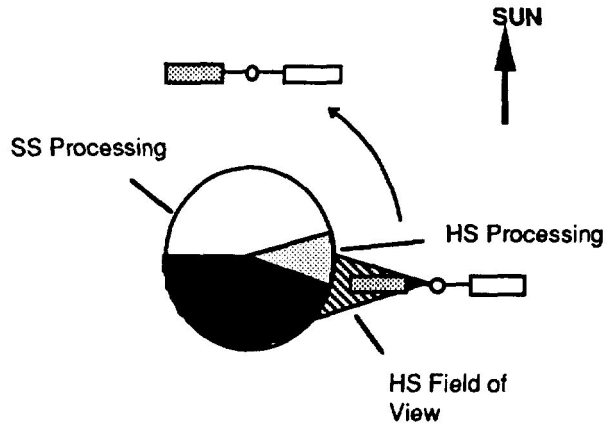

FIGURE 3. Solar Inertial Geometry

To understand the significance of α, and β in (22.), consider the simple geometry shown in *Figure 3.*. The sun vector lies in the orbit plane and intervals of sun sensor and horizon sensor usage are as shown. Define the set of basis vectors S, B_1, B_2 where S is the sun vector and B_1, B_2 are chosen to form a right handed orthonormal triad or coordinate frame. We will call this coordinate from the I'-frame.

The vectors S, B_1, B_2 are all eigenvectors of F_k^S, with eigenvalues $\lambda_S, \lambda_{B_1}, \lambda_{B_2}$ such that

$$\lambda_S = 1$$
$$\lambda_{B_1} = \lambda_{B_2} = 1 - \alpha\tau \tag{25.}$$

The matrix F_k^S modifies the covariance according to (24.) when sun sensor data is processed. If δq_v is expressed in I' coordinates, then by (24.)

$$\sigma_{S\,k+1}^2 = \lambda_S^2 \sigma_{S\,k+1}^2 + \gamma_S$$
$$\sigma_{B_1 k+1}^2 = \lambda_{B_1}^2 \sigma_{B_1 k+1}^2 + \gamma_{B_1} \tag{26.}$$
$$\sigma_{B_2 k+1}^2 = \lambda_{B_2}^2 \sigma_{B_2 k+1}^2 + \gamma_{B_2}$$

where

$$\sigma^2_{S_k} = P_{1,1_k}; \quad \gamma_S = G_{1,1_k}$$
$$\sigma^2_{B_{1k}} = P_{2,2_k}; \quad \gamma_{B_1} = G_{2,2_k}$$
$$\sigma^2_{B_{2k}} = P_{3,3_k}; \quad \gamma_{B_2} = G_{3,3_k}$$

and it is assumed that G_k^A is constant. The behavior of the variances defined in (26.) is simple to understand in terms of the difference equations. The error around the sun vector increases at a constant rate (in terms of variance) at a rate determined by the sensor noise and the gain α. The orthogonal components decay to a steady-state value as the corresponding eigenvalues are less than unity. The steady-state residual can be computed using the Final Value Theorem for Z-transforms. The decay rate is exponential and easily determined from $\lambda_{B_1}, \lambda_{B_2}$. A design value for α is achieved by establishing acceptable values for error growth around the sun vector, and steady-state residual and decay rate for error about the orthogonal vectors. and trading off one for the other for an "optimal" compromise The horizon sensor gain β, can be selected similarly.

ERROR ANALYSIS

The covariance propagation above is limited because only the effects of sensor noise are considered. To investigate the effects of other errors such as a constant gyro drift, the method described in [1] is used. The basic idea is shown in *Figure 4.*

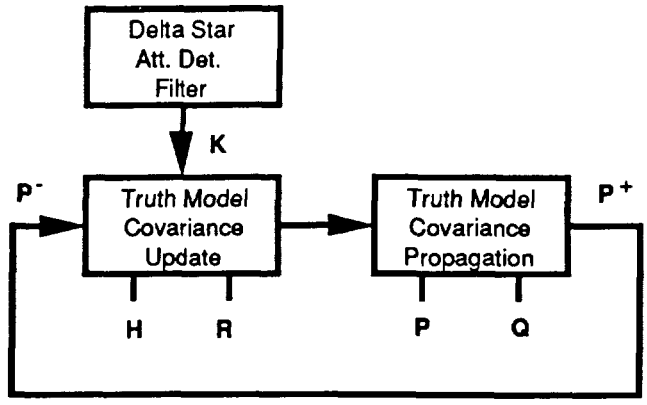

FIGURE 4. Error Analysis Method

For the geometry shown in *Figure 3* this method was used to generate a covariance history assuming that,

$$R_k^S = Diag[3.05\times10^{-6}, 3.05\times10^{-6}, 3.05\times10^{-6}]$$
$$R_k^N = Diag[8.46\times10^{-8}, 8.46\times10^{-8}, 8.46\times10^{-8}]$$
$$P_k^S = Diag[7.61\times10^{-7}, 7.61\times10^{-7}, 7.61\times10^{-7}]$$
$$Q_k = Diag[6.53\times10^{-13}, 6.53\times10^{-13}, 6.53\times10^{-13}]$$
$$\alpha = 0.01$$
$$\beta = 0.06$$

where Q_k is the covariance of the constant gyro bias error in radians per second, quaternion error is dimensionless but, approximately half of angular error in radians and sensor error is similarly approximately half of the angle error produced by sensor noise given in radians The factor of two comes from the definition of quaternion in terms of rotation angle and rotation vector[3]. The result is shown in *Figure 5.*

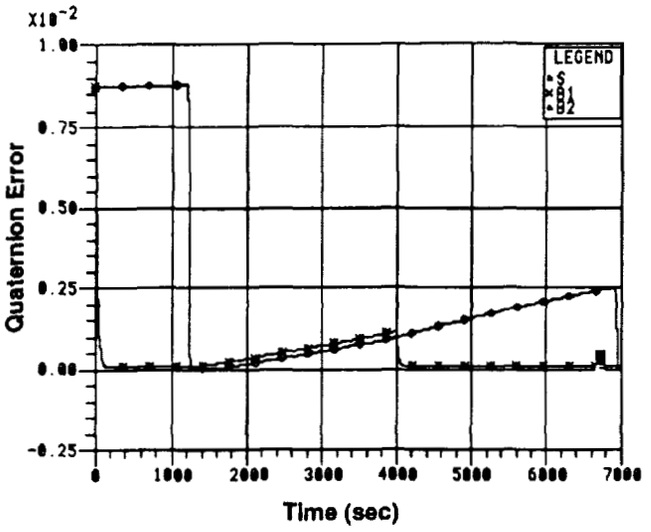

FIGURE 5. DSAF Covariance Analysis

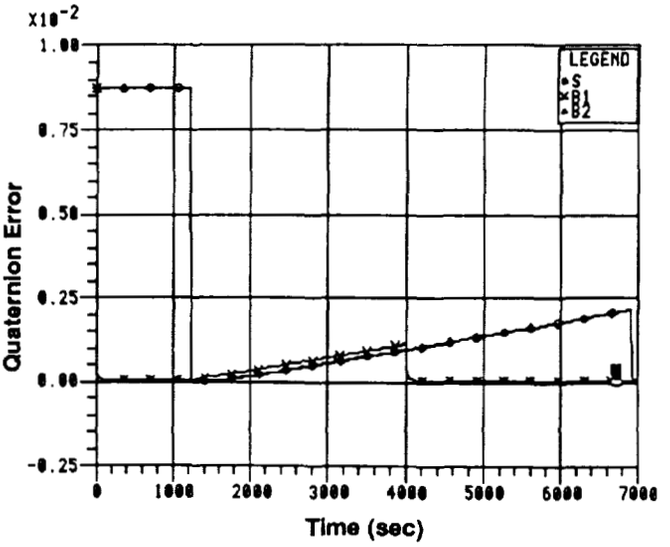

FIGURE 6. Kalman Filter Covariance Analysis

For comparison, the gains in (22.) are replaced by Kalman gains computed using

$$K_k^A = P_k H_k^{A^T} \left(H_k^A P_k H_k^{A^T} + R_k^A \right)^{-1} \tag{27.}$$

The result is shown in *Figure 6*

In each of these cases, the spacecraft begins by processing sun sensor data. The error around the sun line slowly increases, and the orthogonal components are reduced. At approximately 1100 seconds, an horizon sensor update occurs. On the time interval (1200-4000), no sensor data is processed and pure gyro drift is observed. At 4000 seconds sun sensor data is processed again and a new cycle begins. We observe that the convergence rates are faster for the Kalman filter, that the Kalman filter variances converge to smaller values and that the Kalman filter performs better with respect to orthogonal components of error during horizon sensor updating. Note that no attempt is made to estimate gyro drift from the sensor data.

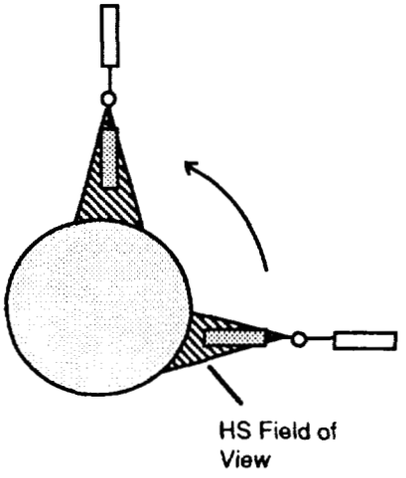

FIGURE 7. Nadir Pointing Geometry

We see that for the scenario described by *Figure 4*. the DSAF compares favorably with the Kalman filter without having to propagate a covariance or compute a Kalman gain. The Kalman filter does, however, afford an advantage which is not evident in the above analysis. The DSAF will not work if only horizon

sensor data is available. Clearly, such a capability is desirable for attitude determination reliability in the event of a sensor failure. The Kalman filter does have this capability. For the same statistical assumptions as above, but using only horizon sensor data for the geometry shown in *Figure 7.* we obtain the covariance history shown in *Figure 8.*

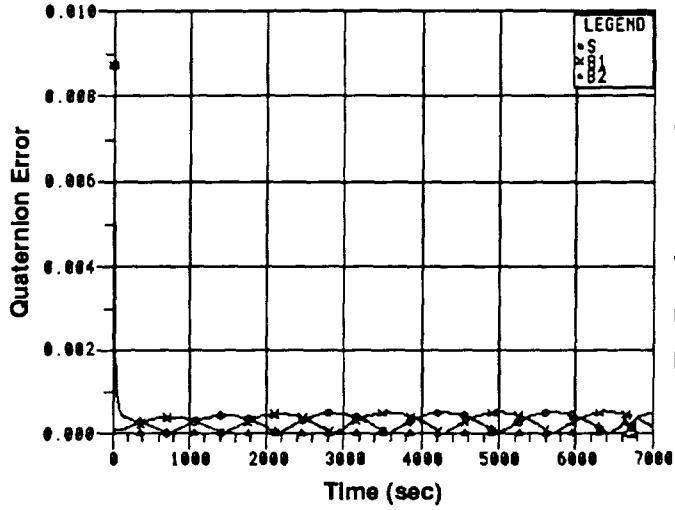

FIGURE 8. DSAF Covariance Analysis Horizon Sensor Only

CONCLUSION

This paper has presented a simple filtering algorithm DSAF for determining spacecraft attitude from vector observations. This algorithm was used successfully on-orbit for the Delta Star SDIO flight experiment in 1989. It offers several advantages over simple deterministic methods such as TRIAD, but does not require as much computation as a Kalman filter mechanization. If a Kalman filter is required or desired for an application, the DSAF is easily extendible to a Kalman filter by means of a more elaborate gain computation. The design parameters of the DSAF are motivated, an error analysis is presented, and performance is compared against a Kalman filter.

REFERENCES

Gelb, A., Ed., *Applied Optimal Estimation,* MIT Press, Cambridge Mass. 1974.

Shuster, M.D. and Oh, S.D. "Three Axis Attitude Determination from Vector Observations", Journal of Guidance and Control, Vol., Jan.-Feb. 1981, pp. 70-77.

Wertz, J.R., Ed., Spacecraft Attitude Determination and Control, Kluwer Academic Publishers, The Netherlands, 1978.

Improvements in ERBS Attitude Determination Without Gyros

D. Chu, J. Glickman, and E. Harvie
COMPUTER SCIENCES CORPORATION (CSC)

ABSTRACT

Previous papers have described the modification of the Earth Radiation Budget Satellite (ERBS) Attitude Determination System (ADS) to overcome the impact of onboard gyro degradation and failure on attitude ground support of the mission. Two approaches were taken: implementing a Kalman filter in place of the batch-least-squares attitude estimator to account for the propagation error produced by high-noise gyro data, and modeling the ERBS attitude dynamics to restore rate information in the case of gyro failure. Both of these methods had shortcomings. In practice, the filter attitude diverged without complete sensor observability; and accurate dynamics modeling required knowledge of disturbance torque parameters that had to be determined manually. These difficulties have been overcome by improved tuning of the filter and by incorporating dynamics parameter estimation into the ERBS ADS.

* This work was supported by the National Aeronautics and Space Administration (NASA)/Goddard Space Flight Center (GSFC), Greenbelt, Maryland, Contract NAS 5-31500.

1. INTRODUCTION

During the past 2-1/2 years, considerable effort has been devoted to overcoming the impact of gyro degradation and failure in Flight Dynamics Facility ground support of the ERBS mission. The ERBS Fine Attitude Determination System (FADS) is a batch-least-squares algorithm designed to use gyro measurements of spacecraft motion for propagating one-orbit attitude histories, which are critical for ground support activities such as sensor bias determination. Fine Sun sensor data for computing accurate single-frame attitudes are typically available for only 20 percent of one orbit. Propagation is especially important for yaw, which is directly observable only with the Sun sensor. At present, four of six gyro channels have failed completely. Prior to each failure, there was an extended period (up to 16 months) when the accuracy of the gyro-propagated batch attitudes was degraded by high gyro noise. Reference 1 summarizes the ERBS gyro performance over the mission and the impact of gyro degradation on attitude determination accuracy.

Two approaches have been taken by the ERBS attitude support team to cope with the loss of accurate gyro data. Reference 2 describes the implementation of a Kalman filter recursive attitude estimation algorithm in the ERBS ADS to account for high gyro noise that caused up to 0.7-degree errors in standard batch attitudes. The filter was found to improve pitch and roll in the case of the high gyro noise, but yaw diverged due to incomplete sensor observability. To restore rate information when the gyros failed completely, attitude rates were modeled in the ADS and used for propagation in the standard batch FADS (References 3 and 4). Results of the dynamics modeling were good, but several torque parameters had to be determined manually—a time-consuming process that made operational use of the model impractical.

Continued efforts have improved the performance of both alternative attitude determination methods. This paper describes the improvements and evaluates the accuracy of each method.

2. ERBS BACKGROUND

The ERBS is a three-axis stabilized, Earth-oriented spacecraft, launched in 1984 into a near-circular orbit with an altitude of 600 km and an inclination of 57 degrees. Attitude is referenced to a geodetic coordinate system with pitch defined about negative orbit normal (y-axis), yaw about the local nadir vector (z-axis), and roll approximately along the velocity vector (x-axis). Attitude is controlled to plus or minus 1.0 degree on each axis. The control system used for normal flight consists of a pitch axis momentum wheel that maintains a strong angular momentum bias and controls pitch, two differentially driven horizon scanners mounted with their axes in the y-z plane to control yaw, and electromagnetic dipoles to control roll and manage pitch axis angular momentum. Requirements for ground attitude determination accuracy are 0.25 degree on each axis. This accuracy was to be achieved using gyros, horizon scanner measurements, and digital fine Sun sensor data, which are usually available for only 20 percent of one 97-minute orbit. At present, the pitch and roll channels of both redundant gyro packages have failed.

3. THE ERBS KALMAN FILTER

The software modifications to convert the batch FADS to a recursive Kalman filter are minimal, as many computations in the two algorithms are identical (Reference 2). In practice, the relative merits of each estimator must be considered when using them under different conditions. Batch algorithms offer robustness with respect to sensor error, but are strongly dependent on the accuracy of the propagation model. A recursive estimator is less dependent on the accuracy of the propagation model, but is sensitive to sensor error and difficult to tune. Gyro-based propagation in a batch estimator gives good results as long as the gyro data are accurate. However, there is a point at which propagation error degrades the accuracy of batch attitudes enough that, even with its limitations, the Kalman filter performs better.

One-orbit batch and filter attitudes are compared in Figures 1 through 6, where the time span is from a period in the mission when the gyro data were accurate and had low noise (0.003 deg/sec root-mean-square [RMS] standard deviation on each axis). The reference attitude is a single frame QUaternion ESTimator (QUEST) solution computed using fine Sun sensor data. Single-frame QUEST attitudes computed with fine Sun sensor data are accurate to within 0.05 degree for roll and yaw and are considered an absolute reference for those axes. Due to the close alignment of the pitch axis and Sun line for the full Sun sensor coverage geometry, the QUEST pitch solution is based mostly on horizon scanner data and is accurate only to within about 0.2 degree. To simulate typical sensor observability conditions in the batch and filter runs, 80 percent of the Sun sensor data have been manually flagged and are not used in the estimation process. The timespan is chosen so that Sun sensor coverage occurs at the beginning and end of the orbit. The filter pitch and roll (Figures 1 and 2) follow the sensor observations closely and remain within 0.3 degree of the reference QUEST pitch and roll. The filter yaw generally diverges when Sun sensor data are lost through the middle of the orbit. However, trial-and-error tuning can postpone divergence until Sun sensor data are reacquired (Figure 3). The batch attitude (Figures 4 through 6) diverges from the QUEST solution by up to 0.3 degree. Departures of the batch solution from the reference are attributed to a nonoptimal value of the epoch state, owing to the dependence on the less accurate horizon scanner data, and to a random walk in the gyro propagation that exists even for low-noise gyros.

Figures 7 through 12 show batch and filter comparisons from a period in the mission when the pitch and roll gyro noise was very high (0.012 deg/sec RMS). The batch pitch and roll (Figures 7 and 8) diverge by up to 0.7 degree. Pitch and roll propagation shows little correlation with real attitude motion. Even the batch yaw (Figure 9), with lower gyro noise (0.005 deg/sec RMS), is degraded through coupling of the large roll error into yaw. The Kalman filter (Figures 10 through 12) clearly performs better than the standard batch FADS in

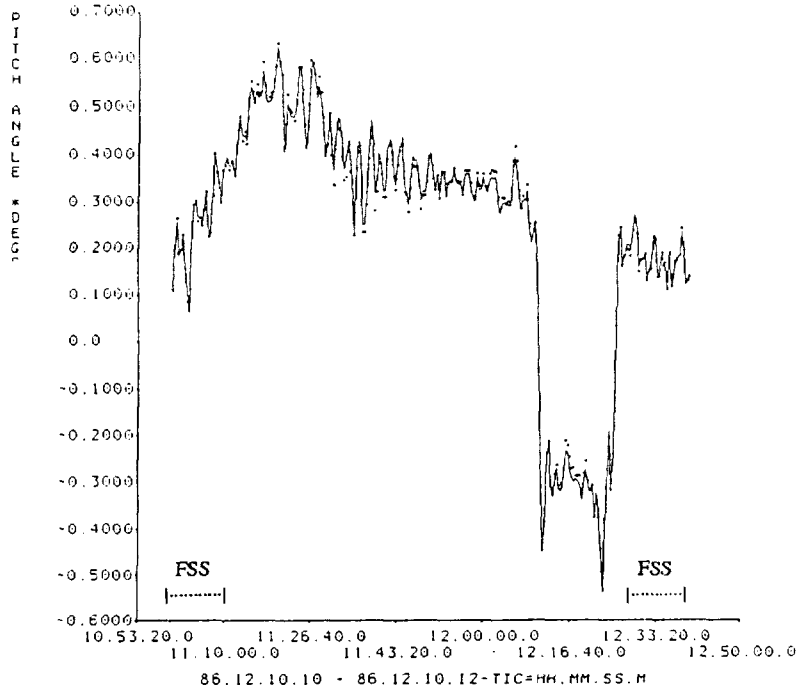

Figure 1. One-orbit pitch comparisons for the filter solution using accurate gyro data for propagation (solid line) and the single frame QUEST reference solution (points)
(Periods of fine Sun sensor data availability for this timespan are denoted by the dashed line.)

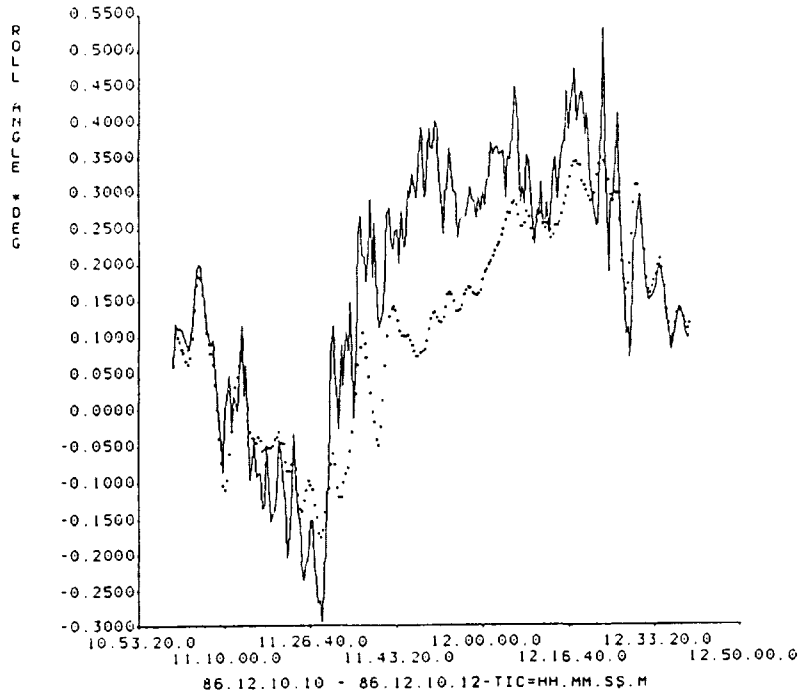

Figure 2. **One-orbit roll comparisons for the filter solution using accurate gyro data for propagation (solid line) and the single frame QUEST reference solution (points)**

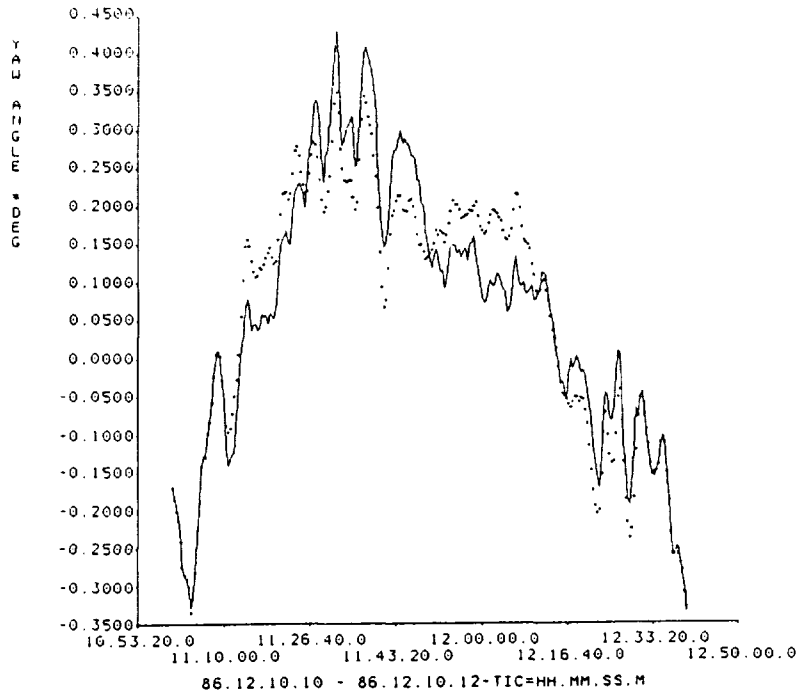

Figure 3. **One-orbit yaw comparisons for the filter solution using accurate gyro data for propagation (solid line) and the single frame QUEST reference solution (points)**

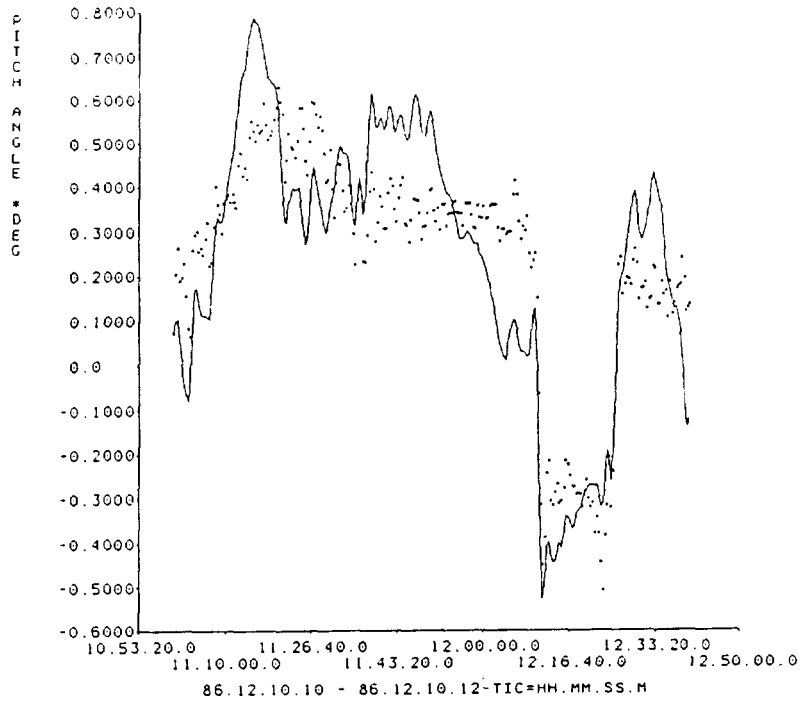

Figure 4. **One-orbit pitch comparisons for the batch solution using accurate gyro data for propagation (solid line) and the single frame QUEST reference solution (points)**

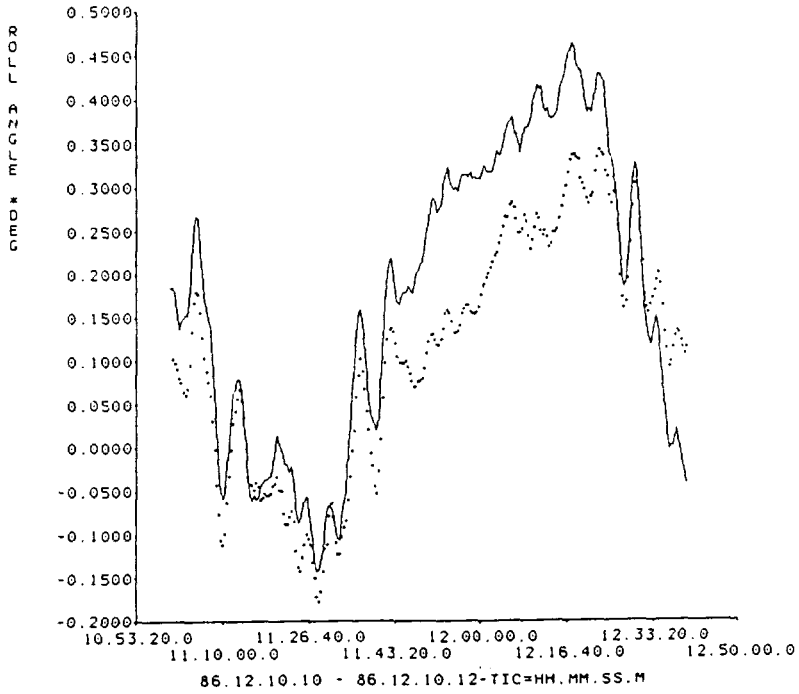

Figure 5. **One-orbit roll comparisons for the batch solution using accurate gyro data for propagation (solid line) and the single frame QUEST reference solution (points)**

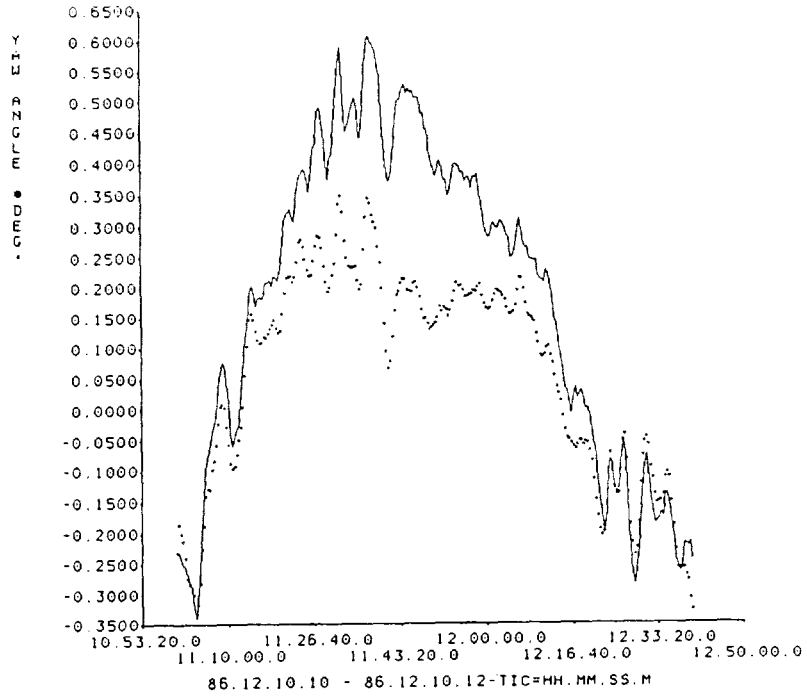

Figure 6. **One-orbit yaw comparisons for the batch solution using accurate gyro data for propagation (solid line) and the single frame QUEST reference solution (points)**

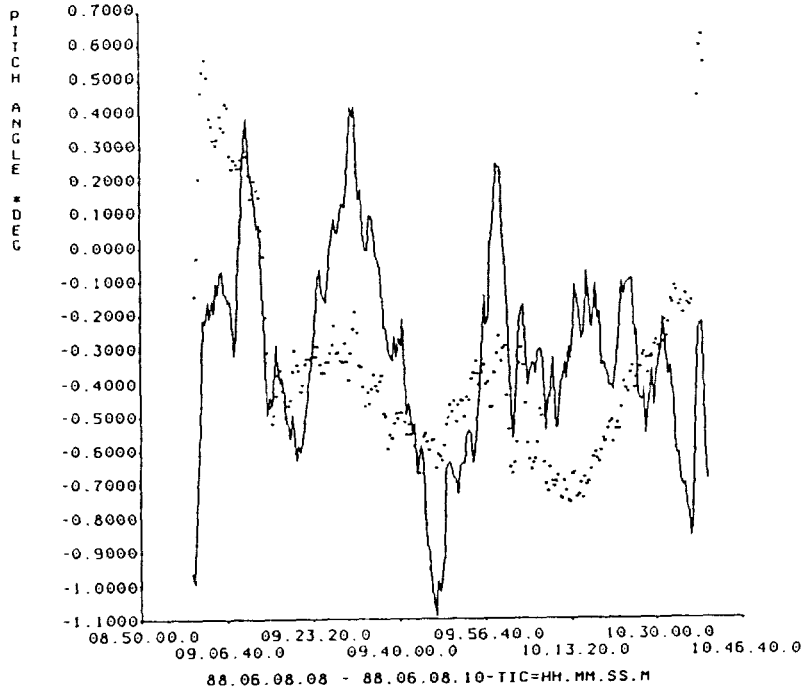

Figure 7. **One-orbit pitch comparisons for the batch solution using high noise gyro data for propagation (solid line) and the single frame QUEST reference solution (points)**
(Periods of fine Sun sensor data availability for this time span are denoted by the dashed line.)

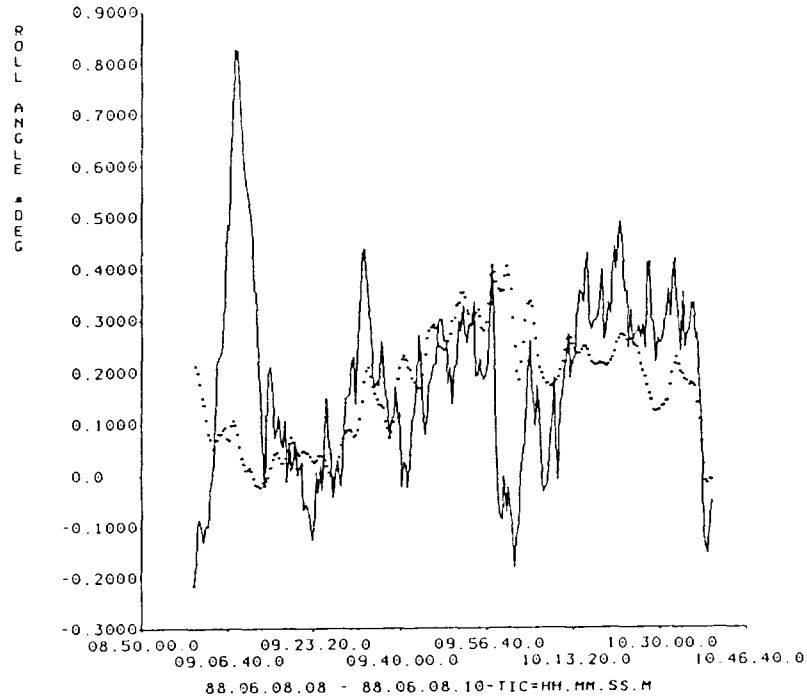

Figure 8. **One-orbit roll comparisons for the batch solution using high noise gyro data for propagation (solid line) and the single frame QUEST reference solution (points)**

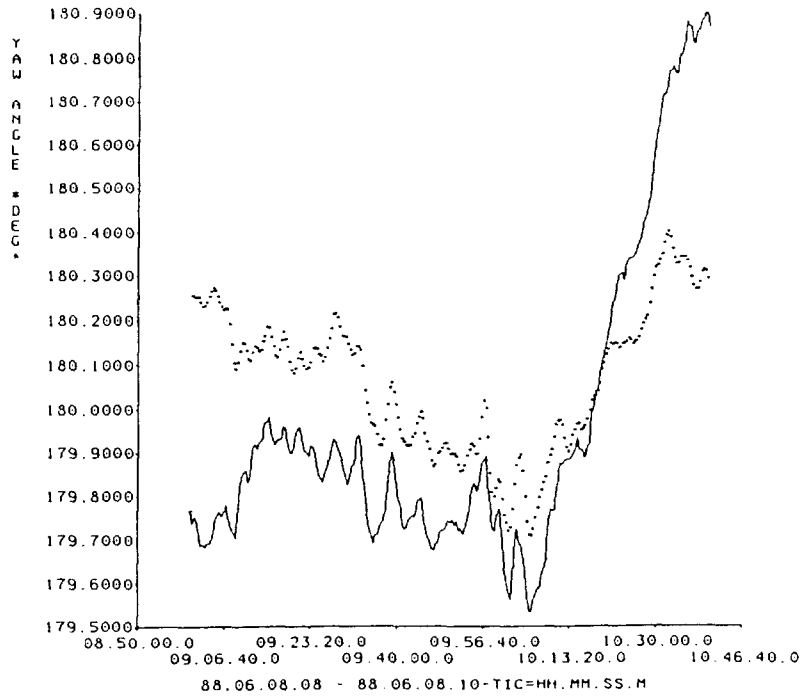

Figure 9. **One-orbit yaw comparisons for the batch solution using high noise gyro data for propagation (solid line) and the single frame QUEST reference solution (points)**

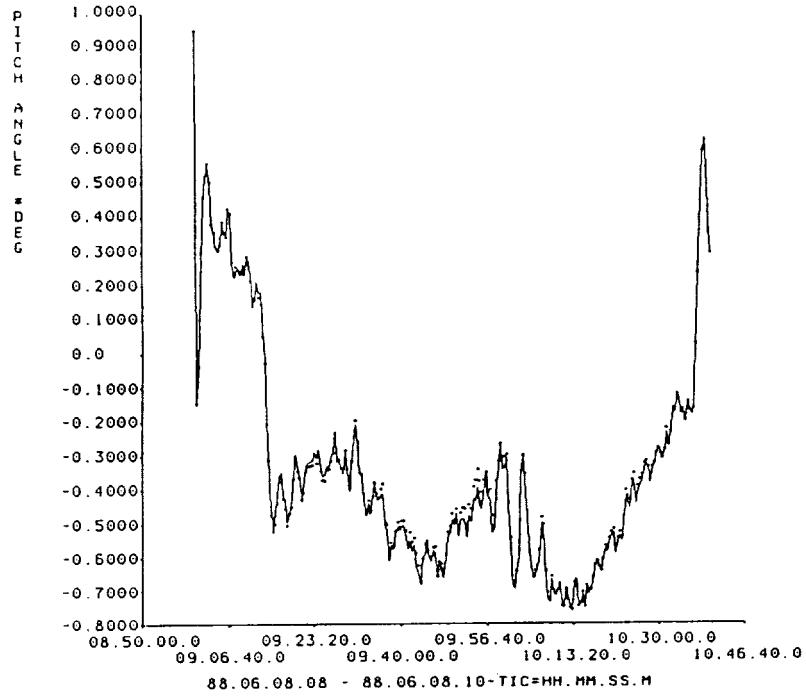

Figure 10. One-orbit pitch comparisons for the filter solution using high noise gyro data for propagation (solid line) and the single frame QUEST reference solution (points)

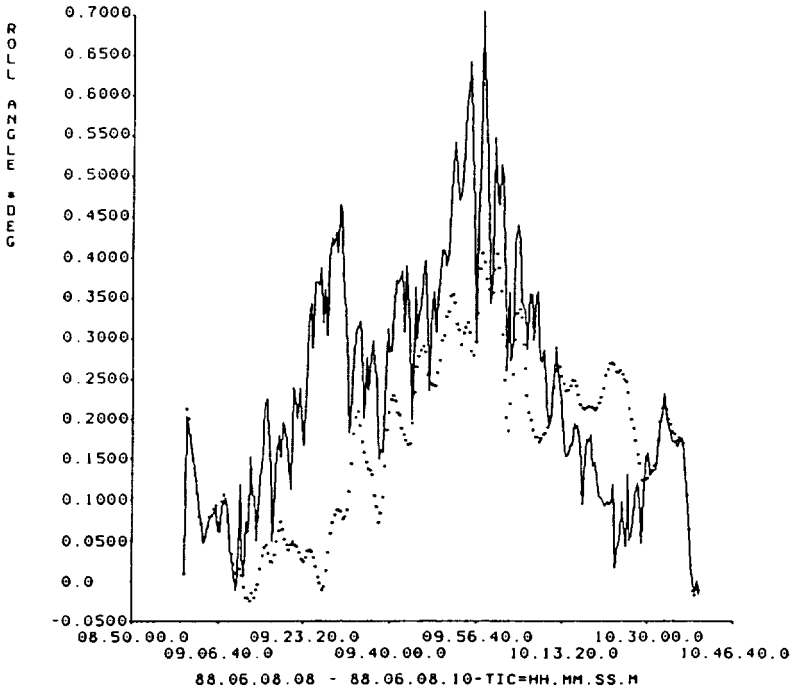

Figure 11. One-orbit roll comparisons for the filter solution using high noise gyro data for propagation (solid line) and the single frame QUEST reference solution (points)

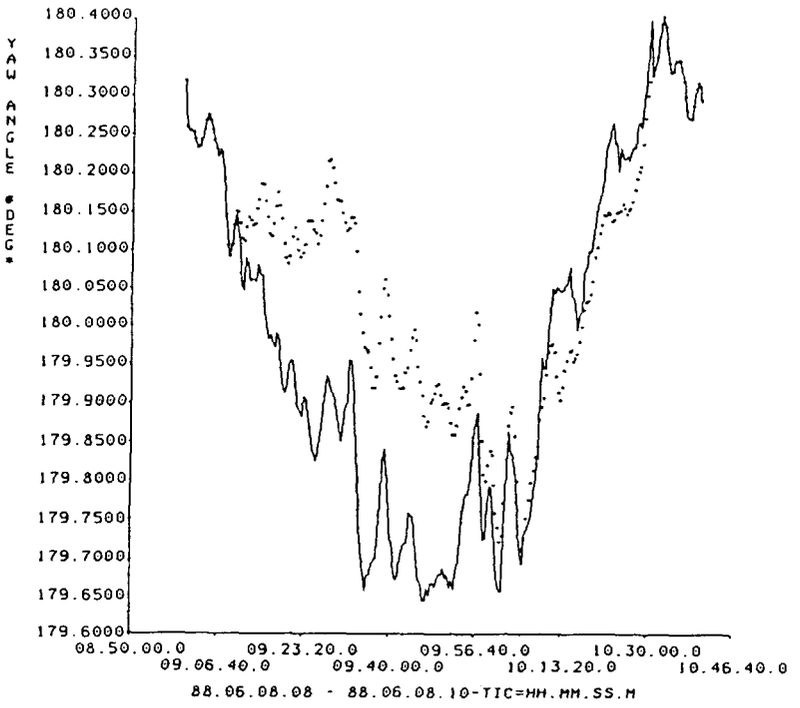

Figure 12. One-orbit yaw comparisons for the filter solution using high noise gyro data for propagation (solid line) and the single frame QUEST reference solution (points)

this example. However, the value of the process noise covariance matrix (the principal tuning parameter of the filter) that removes the divergence in yaw is inconsistent for different time spans. This difficulty may be overcome by determining different process noise terms for various levels of gyro noise, but it limits the usefulness of the filter for routine attitude determination.

4. DYNAMICS ESTIMATION – BACKGROUND

An alternative to gyro propagation altogether has been implemented in ERBS attitude support (References 3 and 4). Euler's equation for rigid-body motion was solved for the angular velocity using spacecraft control system telemetry data for computing the control torques and mathematical models for computing the disturbance torques. Using these modeled rates for propagation in the standard batch FADS, matches to within 0.2 deg of accurate gyro–propagated solutions were obtained. However, modeled attitudes of this accuracy require the use of several uncertain parameters to compute the pitch axis disturbance torque. These parameters were identified as the spacecraft x-z product of inertia, I_{xz}, important in the pitch component of the gravity gradient torque; and the x and z residual dipole moments, m_x and m_z, important in the pitch axis magnetic disturbance torque. Values for these parameters were found to be inconsistent for different data spans and had to be determined manually for each run by trial and error.

To make routine use of the dynamics model practical, an automatic method of determining the uncertain torque parameters is necessary. The original batch FADS offers a convenient framework for estimating these parameters. The original FADS solves for a nine-dimension state vector consisting of the epoch attitude, gyro drift rate biases, and gyro scale factors. In the dynamics estimator, the three gyro scale factor state vector elements are replaced with the dynamics parameters I_{xz}, m_x, and m_z. (Adding more state vector elements to the nine-dimension state would require extensive software modifications, and the gyro scale factor is not strictly applicable to the modeled rates anyway.) In the modified FADS, the epoch attitude estimation method

is unchanged; however, the epoch rate biases now correspond to the initial angular velocity in the integration of Euler's equation and are estimated slightly differently (a priori values for the three rates are taken as zero for roll and yaw, and the one-revolution-per-orbit rate for pitch). The only changes in the estimation are the partial derivatives of the attitude with respect to the new state parameters. To obtain a correct nonlinear solution of the dynamics parameters, the Euler solution is performed inside the FADS differential correction iteration loop (the new estimates of the torque parameters change the modeled rates for each iteration).

The following is a discussion of the modifications to the FADS estimation process. The partial derivatives of the current attitude error, $\Delta\vec{a}$, with respect to the state parameters (epoch attitude, $\Delta\vec{a}_0$, epoch angular velocity, $\Delta\vec{\omega}_0$, and $\Delta\vec{p}$ comprising the dynamics parameters) are

$$\Delta\vec{a} = \begin{bmatrix} \frac{\partial\Delta\vec{a}}{\partial\Delta\vec{a}_0} & \frac{\partial\Delta\vec{a}}{\partial\Delta\vec{\omega}_0} & \frac{\partial\Delta\vec{a}}{\partial\Delta\vec{p}} \end{bmatrix} \begin{bmatrix} \Delta\vec{a}_0 \\ \Delta\vec{\omega}_0 \\ \Delta\vec{p} \end{bmatrix} \equiv F \begin{bmatrix} \Delta\vec{a}_0 \\ \Delta\vec{\omega}_0 \\ \Delta\vec{p} \end{bmatrix} \tag{1}$$

There are two linearized differential equations governing the propagation of attitude and angular velocity error.

$$\frac{d\Delta\vec{a}}{dt} = -\tilde{\omega}\Delta\vec{a} + \Delta\vec{\omega} \tag{2}$$

$$\frac{d\Delta\vec{\omega}}{dt} = I^{-1}\left(\tilde{H}' - \tilde{\omega}I\right)\Delta\vec{\omega} + I^{-1}\frac{\partial\Delta\vec{N}}{\partial\Delta\vec{p}}\Delta\vec{p} \tag{3}$$

The primed angular momentum $\vec{H}'$ is the total angular momentum, including both that of the body ($I(\vec{\omega} + \Delta\vec{\omega})$) and the wheel $\vec{h}$. (The tilde denotes the antisymmetric matrix construction of a vector.)

$$\vec{H}' = I(\vec{\omega} + \Delta\vec{\omega}) + \vec{h} \tag{4}$$

The vector $\Delta\vec{N}$ is the error in the torque used to propagate the attitude. The columns of the torque derivative matrix are

$$\frac{\partial\Delta\vec{N}}{\partial\Delta I_{xz}} = \frac{3\mu}{r^3}(0 \;\; 1 \;\; -\text{roll})^T \equiv (0 \;\; \alpha \;\; -\beta)^T \tag{5}$$

$$\frac{\partial\Delta\vec{N}}{\partial\Delta m_x} = (0 \;\; -B_3 \;\; B_2)^T \tag{6}$$

$$\frac{\partial\Delta\vec{N}}{\partial\Delta m_z} = (-B_2 \;\; B_1 \;\; 0)^T \tag{7}$$

where μ is the gravitational constant, r is the distance to the center of the Earth, and $\vec{B}$ is the measured geomagnetic field in body coordinates.

The solutions to the attitude and angular velocity error equations have the following form

$$\Delta\vec{a}(t) = \phi(t)\Delta\vec{a}_0 + \psi(t)\Delta\vec{\omega}_0 \tag{8}$$

$$\Delta\vec{\omega}(t) = \xi(t)\Delta\vec{\omega}_0 + \gamma(t)\Delta\vec{p} \tag{9}$$

If the coefficient matrices can be considered constant over a short time, the state transition matrix (ϕ) is the matrix exponential of the coefficient matrix.

$$\phi = e^{-\tilde{\omega}t} = \cos\omega t[1] + (1 - \cos\omega t)\frac{\omega\omega^T}{\| \omega \|^2} - \sin\omega t\frac{\tilde{\omega}}{\| \omega \|} \tag{10}$$

The variational matrix (Ψ) is the integral of the state transition matrix.

$$\psi\ (t) = \int_0^t \phi(\tau)d\tau = \frac{\sin\omega t}{\| \omega \|}[1] + (\cos\omega t - 1)\frac{\tilde{\omega}}{\| \omega \|} - (\sin\omega t - \omega t)\frac{\omega\omega^T}{\| \omega \|^2} \tag{11}$$

Such closed-form expressions are not now available for the angular velocity error (equation 3). These will be approximated by the first few terms of the power series expansion for the matrix exponential

$$e^{At} = [1] + At + \frac{1}{2}A^2t^2 + \frac{1}{3!}A^3t^3 + \ldots \tag{12}$$

where

$$A = I^{-1}(\tilde{H}' - \tilde{\omega}I) \tag{13}$$

Over long time spans, when the coefficient matrices may not be constant, these equations can be solved recursively. The closed-form expressions and truncated series approximations above can be used over the short individual time steps to update the previous solution values.

$$\Delta\vec{a}_i = \phi_i\Delta\vec{a}_{i-1} + \psi_i\Delta\vec{\omega}_i \tag{14}$$

$$\Delta\vec{\omega}_i = \xi(\tau)_i\Delta\vec{\omega}_{i-1} + \gamma_i\Delta\vec{p} \tag{15}$$

where

$$\xi_i = e^{A_i t} \tag{16}$$

and

$$\gamma_i = \int_{t_i}^{t_i+\Delta t} \xi(\tau)I^{-1}\frac{\partial\Delta\vec{N}_i}{\partial\Delta\vec{p}}d\tau \tag{17}$$

If the partial derivative of the torque with respect to the dynamics parameters is almost constant over the short time step, it can be brought outside of the integral. This last expression then can be approximated as follows:

$$\gamma_i \approx A_i^{-1}\ (e^{A_i\Delta t} - [1])\ I^{-1}\begin{bmatrix} 0 & 0 & -B_2 \\ \alpha & -B_3 & B_1 \\ -\beta & B_2 & 0 \end{bmatrix} \tag{18}$$

The accumulated matrix for the attitude error is

$$\frac{\partial \Delta\vec{a}_i}{\partial \Delta\vec{a}_0} = \phi_i\phi_{i-1}\phi_{i-2}\cdots\phi_2\phi_1 \equiv \Phi_i \tag{19}$$

The accumulated matrix for the angular velocity error is

$$\frac{\partial \Delta\vec{a}_i}{\partial \Delta\vec{\omega}_o} = \phi_i\frac{\partial \Delta\vec{a}_{i-1}}{\partial \Delta\vec{\omega}_o} + \frac{\partial \Delta\vec{a}_i}{\partial \Delta\vec{\omega}_i}\frac{\partial \Delta\vec{\omega}_i}{\partial \Delta\vec{\omega}_o} = \phi_i\frac{\partial \Delta\vec{a}_{i-1}}{\partial \Delta\vec{\omega}_o} + \psi_i\Xi_i \tag{20}$$

where

$$\frac{\partial \Delta\vec{a}_o}{\partial \Delta\vec{\omega}_o} = [0] \tag{21}$$

$$\Xi_i = \xi_i\xi_{i-1}\xi_{i-2}\cdots\xi_2\xi_1 \tag{22}$$

The accumulated matrix for the product of inertia and residual dipole moments is

$$\frac{\partial \Delta\vec{a}_i}{\partial \Delta\vec{p}} = \phi_i\frac{\partial \Delta\vec{a}_{i-1}}{\partial \Delta\vec{p}} + \frac{\partial \Delta\vec{a}_i}{\partial \Delta\vec{\omega}_i}\frac{\partial \Delta\vec{\omega}_i}{\partial \Delta\vec{p}} = \phi_i\frac{\partial \Delta\vec{a}_{i-1}}{\partial \Delta\vec{p}} + \psi_i\Gamma_i \tag{23}$$

Γ_i is computed recursively as follows:

$$\Gamma_i = \xi_i\Gamma_{i-1} + \gamma_i \tag{24}$$

where

$$\Gamma_o = [0] \tag{25}$$

Combining these results, the partial derivative matrix of current attitude error with respect to the epoch attitude and angular velocity errors and dynamics parameters can be computed

$$F_i = \phi_i F_{i-1} + \psi_i \left[\, 0 \,\middle|\, \Xi_i \,\middle|\, \Gamma_i \,\right] \tag{26}$$

where

$$F_o = \left\{ [1] \,\middle|\, [0] \,\middle|\, [0] \right\} \tag{27}$$

5. DYNAMICS ESTIMATION – RESULTS

To evaluate the performance of the ERBS dynamics estimation algorithm, pitch attitudes computed using the manual trial and error method and the dynamics estimator are compared with the gyro-propagated reference pitch. Figure 13 shows the modeled-to-reference pitch attitude history with the manually determined values of I_{xz}, m_x, and m_z. With the manual variation of parameters method, approximately 12 runs of the Euler solution and FADS subsystem by an experienced analyst and about 2 hours of wall clock time were required to achieve a match of about 0.2 degree to the reference pitch. The modeled-to-reference pitch for the dynamics estimation is shown in Figure 14. Automatic estimation of the dynamics parameters was accomplished in five differential correction iterations and in a wall clock time of only 5 minutes. Table 1 gives the values of the parameters for each run, together with the RMS standard deviation of the fit to reference pitch and the weighted observation residuals. Not only does the automatic estimation greatly increase the efficiency of the dynamics determination process, but it also results in a better fit to the sensor measurements than was accomplished manually. Roll and yaw from the dynamics estimator solution, shown in Figures 15 and 16, match the gyro reference to within 0.1 degree RMS.

It is possible that the improvement in modeled pitch is due to the increased degrees of freedom in estimating the pitch axis disturbance torque and that the actual perturbations may be other than those modeled as gravity gradient and magnetic. However, these two disturbance torques are expected to be dominant for pitch.

Knowledge of the dynamics parameters may also be used to improve the onboard control system performance. For example, a momentum wheel bias voltage could be uplinked to offset the constant gravity gradient pitch torque from the non-zero I_{xz} inertia product, or a dipole bias could be uplinked to offset torques produced by the residual magnetic dipole moment if consistent values were observed. Trend analysis of the dynamics parameters is also possible. Table 2 shows estimated values of I_{xz}, m_x, and m_z from recent mission data.

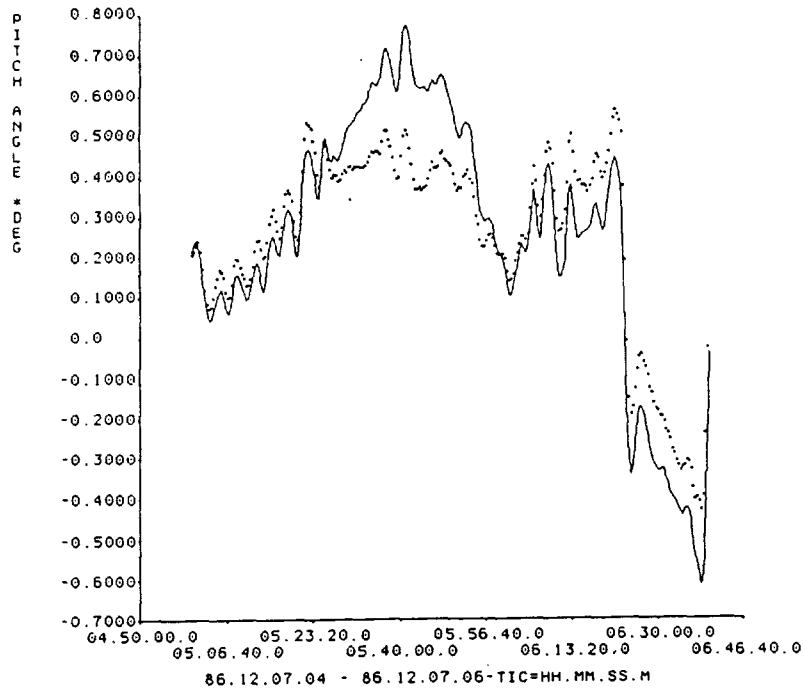

Figure 13. One-orbit pitch solution using modeled rates for propagation and manually determined disturbance torque parameters (solid line) and gyro-propagated reference (points)

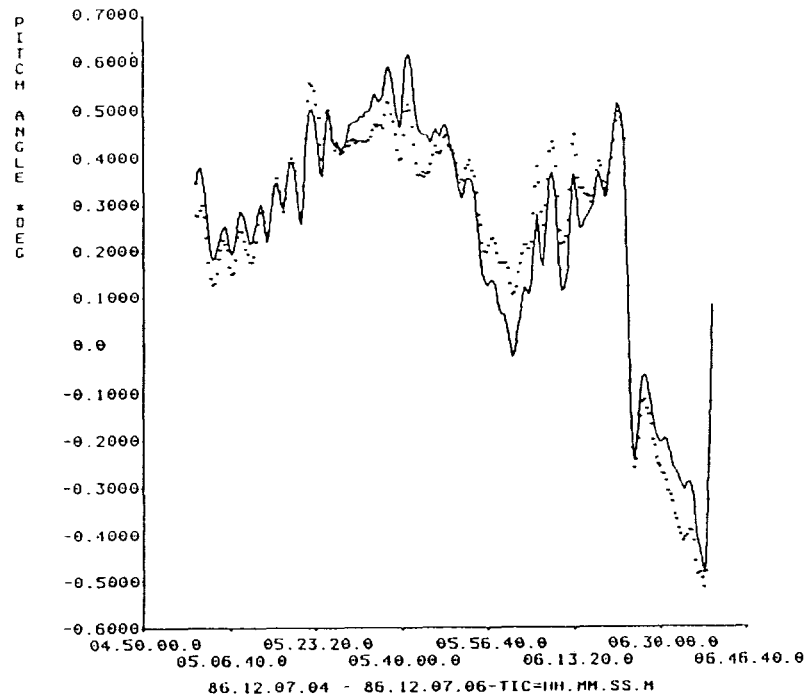

Figure 14. One-orbit pitch solution using modeled rates and automatically determined disturbance torque parameters (solid line) and gyro-propagated reference (points)

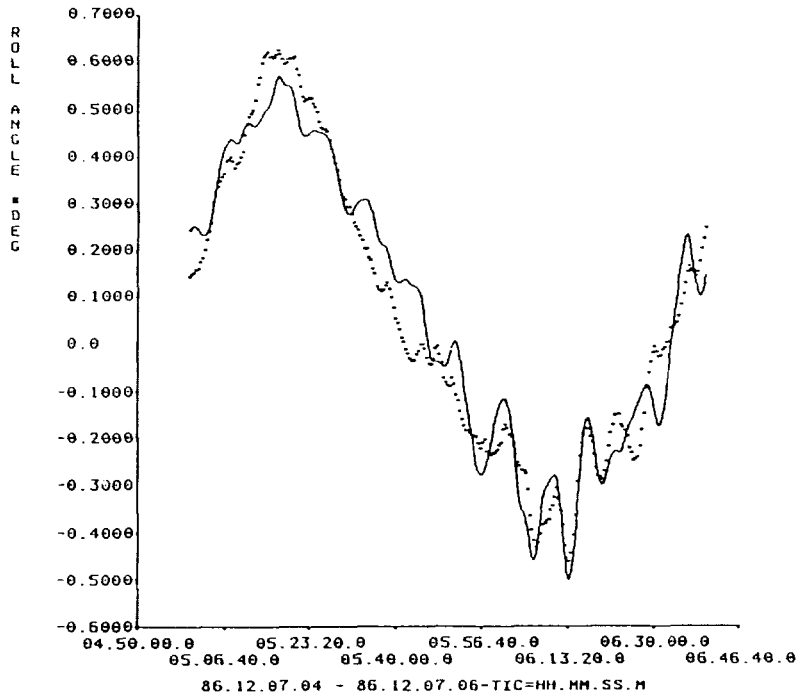

Figure 15. One-orbit roll solution using modeled rates and automatically determined disturbance torque parameters (solid line) and gyro-propagated reference (points)

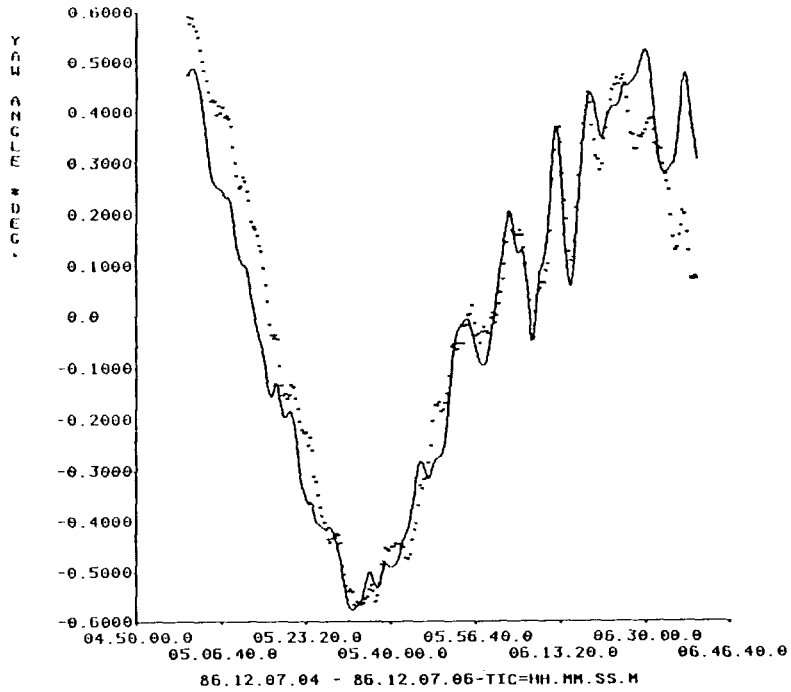

Figure 16. One-orbit yaw solution using modeled rates and automatically determined disturbance torque parameters (solid line) and gyro-propagated reference (points)

Table 1. Dynamics Estimation Comparisons for 861207

METHOD	I_{xz} (kg–m2)	m_x (ATm2)	m_z (ATm2)	FIT TO REFERENCE PITCH (RMS)	WEIGHTED OBSERVATION RESIDUALS (RMS)
MANUAL	–20.00	3.50	0.50	0.12	0.901
DYNAMICS ESTIMATOR	–20.47	3.02	0.26	0.06	0.816
GYRO REFERENCE	–	–	–	–	0.776

Table 2. Dynamics Parameter Trends

DATE	I_{xz} (kg–m2)	m_x (ATm2)	m_z (ATm2)	RESIDUALS (RMS)
920311	–42.6	1.71	–2.26	0.91
920320	–48.5	–0.51	1.03	1.21
920325	–52.1	0.42	2.05	1.35
920401	–42.8	0.93	2.64	1.13

6. CONCLUSIONS

Two strategies to overcome the loss of accurate gyro data in ground attitude determination support of the ERBS mission have been implemented. Both methods involve a modification of the existing ADS, taking advantage of existing software to minimize development effort.

Although the Kalman filter performs better than the batch estimator for very high gyro noise, the filter yaw solution is very sensitive to the process noise. Divergence in the filter yaw may be reduced by appropriate tuning of the process noise terms, but the tuning was found to be inconsistent even for time spans with the same gyro noise levels. This inconsistency in yaw behavior makes routine use of the filter impractical. An adaptive Kalman filter that determines the process noise automatically would be more suitable for the application to ERBS attitude determination, where the propagation noise has varied widely over the course of the mission.

The dynamics estimator is a viable solution to the problem of gyro failure for ERBS attitude ground support. Modeled rates can be used to propagate one-orbit attitudes to an accuracy within the 0.25-degree requirement with no a priori knowledge of disturbance torque parameters. Values of the dynamics parameters determined in the estimation process are also useful for analysis of control system performance. The dynamics estimator is currently being evaluated for operational use to restore full Flight Dynamics Facility attitude ground support of the ERBS mission.

REFERENCES

1. Computer Sciences Corporation, 553-FDD-91/025R0UD0 (CSC/TM-91/6080R0UD0), *Earth Radiation Budget Satellite (ERBS) Inertial Reference Unit (IRU) Performance Analysis*, E. Harvie, J. Glickman, and K. Tran, February 1992

2. D. Chu and E. Harvie, *Accuracy of the ERBS Definitive Attitude Determination System in the Presence of Propagation Noise*, Flight Mechanics/Estimation Theory Symposium, NASA—Goddard Space Flight Center, May 1990

3. E. Harvie, D. Chu, and M. Woodard, *The Accuracy of Dynamic Attitude Propagation*, Flight Mechanics/Estimation Theory Symposium, NASA—Goddard Space Flight Center, May 1990

4. E. Harvie and D. Chu, *Dynamics Modeling for ERBS Attitude Propagation*, Third International Symposium on Spacecraft Flight Dynamics, Darmstadt, Germany, October 1991

POLAR DECOMPOSITION FOR ATTITUDE DETERMINATION FROM VECTOR OBSERVATIONS

by

Itzhack Y. Bar-Itzhack*
Faculty of Aerospace Engineering
Technion - Israel Institute of Technology
Haifa 32000, Israel

Abstract

This work treats the problem of weighted least squares fitting of a 3D Euclidean-coordinate transformation matrix to a set of unit vectors measured in the reference and transformed coordinates. A closed-form analytic solution to the problem is re-derived. The fact that the solution is the closest orthogonal matrix to some matrix defined on the measured vectors and their weights is clearly demonstrated. Several known algorithms for computing the analytic closed form solution are considered. An algorithm is discussed which is based on the polar decomposition of matrices into the closest unitary matrix to the decomposed matrix and a Hermitian matrix. A somewhat longer improved algorithm is suggested too. A comparison of several algorithms is carried out using simulated data as well as real data from the Upper Atmosphere Research Satellite. The comparison is based on accuracy and time consumption. It is concluded that the algorithms based on polar decomposition yield a simple although somewhat less accurate solution. The precision of the latter algorithms increase with the number of the measured vectors and with the accuracy of their measurement.

---

*Professor, member Technion Space Research Institute.
This work was done at the Flight Dynamics Analysis Branch of NASA Goddard Space Flight Center while the author held a National Research Council - NASA Research Associateship.

1. INTRODUCTION

The problem of attitude determination from vector observations is as follows. A sequence, $\mathbf{b}_i$, i=0,1,2,...K of unit vectors is given. These unit vectors are the result of measurements performed in vehicle body axes of the directions to known objects. The sequence, $\mathbf{r}_i$, i=0,1,2,...K of unit vectors, is the sequence of the corresponding representation of these directions with respect to some reference coordinate system. We wish to find the attitude matrix, A, such that the cost functional p(A) defined as follows

$$p(A) = \frac{1}{2} \sum_{i=1}^{K} a_i \| \mathbf{b}_i - A\mathbf{r}_i \|^2 \tag{1}$$

is minimized. This problem, which is basically a least-squares fit problem for the attitude matrix, A, was posed in [1] and is generally known as Wahba's problem. This problem has been treated extensively [see, e.g. 2-11].

In the next section we derive an analytic solution to Wahba's problem, then in Section III we show, in a rather simple way, that this solution is actually the closest orthogonal matrix to a matrix defined on the reference and measured unit vectors $\mathbf{r}_i$ and $\mathbf{b}_i$ respectively, and on their relative weight. Several algorithms for computing the attitude matrix are considered in that section. The connection between polar decomposition of matrices and the solution to Wahba's problem is then discussed in Section IV. Two algorithms for computing the solution, which are based on the polar decomposition, are considered. A numerical comparison between these algorithms and other suggested ones, using simulated as well as real satellite data, is presented in Section V. The conclusions of this work are finally presented in Section VI.

II. DIRECT SOLUTION OF WAHBA'S PROBLEM

Since only the relative value of the weights, a_i, matter, we may, with no loss of generality, normalize the weights to give

$$\sum_{i=1}^{K} a_i = 1$$

It can be shown [2] that

$$p(A) = 1 - \mathrm{tr}(AB^T) \tag{2}$$

where tr denotes the trace of a matrix and

$$B = \sum_{i=1}^{K} a_i \mathbf{b}_i \mathbf{r}_i^T \tag{3}$$

We seek the orthogonal matrix, A, which minimizes p(A). Obviously, that matrix maximizes $\mathrm{tr}(AB^T)$. Using the method of Lagrange multipliers, we can incorporate the orthogonality constraint on A into the maximization problem of $\mathrm{tr}(AB^T)$ by defining the new functional p*(A)

$$p^*(A) = \mathrm{tr}(BA^T) + \mathrm{tr}[\tfrac{1}{2}L(AA^T - I)] \tag{4}$$

where I is the 3x3 identity matrix. The matrix L is a matrix of Lagrange multipliers scaled to enable the inclusion of the one half factor which is added for simplicity of the ensuing derivation. Also note that with no loss of generality, we may choose L to be symmetric. The new cost function, p*(A), can be written as follows

$$p^*(A) = \mathrm{tr}[(BA^T) + \frac{1}{2} L(AA^T - I)] \tag{5}$$

Use now the directional derivative to maximize p*(A). To accomplish this, express A as follows

$$A = A_o + eH \tag{6}$$

where A_o is the A matrix which maximizes p*(A), e is a scalar variable, and H is any 3x3 real matrix. Note that A in (6) is expressed as a sum of the maximizing matrix, A_o, and a "step", e, in the "direction" of H. Also note that any real 3x3 matrix can be expressed in this way. Substitution of (6) into (5) gives

$$p'(e) = \mathrm{tr}\{B(A_o + eH)^T + \frac{1}{2} L[(A_o + eH)(A_o + eH)^T - I]\} \tag{7}$$

Next differentiate p'(e) with respect to e to obtain

$$\frac{dp'(e)}{de} = \mathrm{tr}[BH^T + \frac{1}{2} LH(A_o^T + eH^T) + \frac{1}{2} L(A_o + eH)H^T] \tag{8}$$

A necessary condition for p'(e) to have a maximum at A_o is

$$\left.\frac{dp'(e)}{de}\right|_{e=0} = 0 \qquad \text{for all H} \tag{9}$$

Applying (9) to (8) yields

$$\mathrm{tr}[(B + LA_o)H^T] = 0 \qquad \text{for all H} \tag{10}$$

The latter can exist only if

$$B + LA_o = 0$$

or, assuming L is non-singular,

$$A_o = L^{-1}B \tag{11}$$

Using (11) in the orthogonality constraint on A_o and making use of the fact that L is symmetric we obtain

$$A_oA_o^T = L^{-1}BB^TL^{-1} = I$$

which yields

$$BB^T = L^2$$

The matrix BB^T is a positive definite matrix thus it can be decomposed as follows

$$BB^T = V \, \mathrm{diag}\{\beta_1^2,\beta_2^2,\beta_3^2\} \, V^T$$

where $\mathrm{diag}\{\beta_1^2,\beta_2^2,\beta_3^2\}$ is a diagonal matrix whose elements are β_1^2,β_2^2 and β_3^2. Consequently

$$L = \pm(BB^T)^{1/2} = V \, \mathrm{diag}\{\pm\beta_1, \pm\beta_2, \pm\beta_3\} \, V^T \tag{12}$$

Substitution of (12) into (11) yields

$$A_o = \mp(BB^T)^{-1/2}B = V \, \mathrm{diag}\{\pm\beta_1, \pm\beta_2, \pm\beta_3\} \, V^T \, B \tag{13}$$

It can be verified that to obtain maximum of p*(A) we need to choose the plus signs in (13). We designate it by choosing the plus sign in front of $(BB^1)^{1/2}$; that is

$$\boxed{A_o = (BB^T)^{-1/2}B} \tag{14}$$

which is the sought solution of Wahba's problem.

The expression given in (14) is also the solution of another problem as discussed next.

III. THE CLOSEST ORTHOGONAL MATRIX

Consider the following problem. Given a real matrix, B, what is the closest (in the Euclidean-norm sense) orthogonal matrix to it? To solve this problem denote the square of the Euclidean norm of the difference between B and any same order real matrix, A, by s(A); that is

$$s(A) = ||B - A||^2$$

(where $||.||$ denotes the Euclidean-norm) and find the 3x3 orthogonal matrix, A, which minimizes s(A). It can be easily shown that

$$s(A) = \mathrm{tr}[(B - A)(B - A)^T]$$

thus

$$s(A) = \mathrm{tr}(BB^T - BA^T - AB^T + AA^T)$$

Using the fact that A has to be orthogonal and the properties of the trace operation it can be easily shown that

$$s(A) = \mathrm{tr}(BB^T) + 3 - 2\mathrm{tr}(AB^T) \tag{15}$$

Obviously, that A which minimizes s(A) is the A which maximizes the term $\mathrm{tr}(AB^T)$. An

inspection of (2) reveals that this particular A is also the solution to Wahba's problem. This result can be stated as follows. *The closest orthogonal matrix to B, where B is as defined in (3), is the solution to Wahba's problem.* Indeed if we proceed with finding that orthogonal A which minimizes (15), we will obtain the result given in (14); namely,

$$A_o = (BB^T)^{-1/2}B \tag{16}$$

Consequently, any solution to the closest orthogonal matrix problem is also a solution to Wahba's problem. This conclusion will be exploited in the ensuing.

The solution expressed in (16) to the closest orthogonal matrix problem was obtained and investigated quite extensively in the past [12 - 19]. The solution of A_o using (16) is cumbersome. Various iterative solutions have been investigated [15 - 19].

Another solution to the closest orthogonal matrix problem, and hence to Wahba's problem, makes use of the singular value decomposition (SVD) of A_o. This solution is presented next. It is well known [20] that any matrix, and therefore also B, can be decomposed as follows

$$B = USV^T$$

where U and V are 3x3 orthogonal matrices and S is a diagonal matrix whose elements are the nonnegative square roots of the eigenvalues of B^TB. It can be shown that

$$A_o = UV^T$$

The latter was used in [21] to solve Wahba's problem.

IV. POLAR DECOMPOSITION

It is well known [22] that B can be decomposed as follows

$$B = PH \tag{17}$$

where P is orthogonal and H is symmetric. This decomposition is known as polar decomposition (PD). It was shown [23] that P is precisely the orthogonal matrix closest to B; that is, P of the polar decomposition is the solution to Wahba's problem when B is as defined in (3). We can write therefore

$$B = A_oH$$

(where A_o is, of course, the closest orthogonal matrix to B). This yields

$$A_o = BH^{-1} \tag{18}$$

We wish now to utilize the PD concept for solving Wahba's problem. We consider two cases as follows.

IV. 1: The Error Free Case

Assume now that both sequences of vectors $\mathbf{b}_i$ and $\mathbf{r}_i$ i=1,2,3,...K are error free. We can then write $\mathbf{b}_i=A\mathbf{r}_i$. Substitution of this equation into (3) yields

$$B = \sum_{i=1}^{K} a_i \mathbf{b}_i \mathbf{r}_i^T = \sum_{i=1}^{K} a_i A \mathbf{r}_i \mathbf{r}_i^T = A \sum_{i=1}^{K} a_i \mathbf{r}_i \mathbf{r}_i^T \tag{19}$$

Define now the matrix R as follows

$$R = \sum_{i=1}^{K} a_i \mathbf{r}_i \mathbf{r}_i^T \tag{20}$$

then from (19) we obtain

$$B = AR \tag{21}$$

where R is a symmetric matrix. Comparing (21) with (17) it is easy to see that in this case (21) is the PD of B where A=P and R=H. It is clear then that A_o=A. In this case A_o can be found as follows

$$A_o = BR^{-1} \tag{22}$$

provided that in constructing R, according to (20), we use at least 3 non-collinear vectors. (This assures that R is invertible.)

IV. 2: The Actual Case

In practice the vectors $\mathbf{b}_i$ are contaminated by measurement noise. However, since the position of the body and the time of measurement are known within a high degree of precision, the error in the determination of the $\mathbf{r}_i$ vectors is negligible. Denote the error in $\mathbf{b}_i$ by $\mathbf{n}_i$ then we can write that

$$\mathbf{b}_i = \mathbf{n}_i + A\mathbf{r}_i$$

Using the last equation in (3) we obtain

$$B = \sum_{i=1}^{K} a_i (\mathbf{n}_i + A\mathbf{r}_i) \mathbf{r}_i^T$$

This can be written as

$$B = \sum_{i=1}^{K} a_i \mathbf{n}_i \mathbf{r}_i^T + \sum_{i=1}^{K} a_i A \mathbf{r}_i \mathbf{r}_i^T$$

which yields

$$B - \sum_{i=1}^{K} a_i \mathbf{n}_i \mathbf{r}_i^T = A \sum_{i=1}^{K} a_i \mathbf{r}_i \mathbf{r}_i^T$$

Using (20) we obtain from the last equation

$$A = \left[B - \sum_{i=1}^{K} a_i \mathbf{n}_i \mathbf{r}_i^T \right] R^{-1} \tag{23}$$

We can now use the last equation to obtain the "best" estimate of A. We note that B contains all measured information, therefore we compute $\hat{A}$, the "best" estimate of A, as the conditional expectation of A given B [24]. Performing the conditional expectation on both sides of (23) yields

$$E\{A/B\} = \left[B - \sum_{i=1}^{K} a_i E\{\mathbf{n}_i/B\} \mathbf{r}_i^T \right] R^{-1} \tag{24}$$

It is assumed that the measurement errors are unbiased, therefore

$$E\{\mathbf{n}_i/B\} = 0 \tag{25}$$

(The latter assumption is based on the premise that the measurement biases have been removed or else are very small. If this is not the case, there is no way to obtain the correct attitude from the biased measured vector no matter what algorithm is used.) Substitution of (25) into (24) yields

$$E\{A/B\} = BR^{-1}$$

thus

$$\boxed{\hat{A} = BR^{-1}} \tag{26}$$

where B and R are computed according to (3) and (20) respectively.

Note that this result was first obtained by Brock [13, eq. (5)] in a way unrelated to the notion of polar decomposition and with no consideration of the randomness of $\mathbf{n}$.

If $\mathbf{n}_i$ are very small or the number of measurements is large such that the particular realization of $\mathbf{n}_i$ has a negligible mean, which complies with the assumption in (25), then the computation of $\hat{A}$ according to (26) yields an accurate estimate of A. When this is not the case, the estimate can be quite erroneous. It is interesting to note that when K<4, $\hat{A}$ zeros the cost function of Wahba's problem which is given in (1) as follows

$$p(A) = \frac{1}{2} \sum_{i=1}^{K} a_i ||\mathbf{b}_i - A\mathbf{r}_i||^2$$

even if A is not equal to $\hat{A}$. This is a result of the approximation $\mathbf{b}_i = A\mathbf{r}_i$ which was made in the derivation of $\hat{A}$. However, while $\hat{A}$ drives p(A) to its minimal value, $\hat{A}$ is not necessarily orthogonal. (Recall that we seek the *orthogonal* matrix which minimizes p(A)). We can correct the non-orthogonality of $\hat{A}$ by the application of one orthogonalization iteration as follows [17, 18]

$$\hat{A}' = 0.5(\hat{A}^{-T} + \hat{A}) \tag{27}$$

This operation yields a close to orthogonal matrix, $\hat{A}'$, which is usually also closer

to A. (The superscript -T denotes the inverse of the transpose.) We can, of course, bypass the computation of $\hat{A}$ by using (26) in (27) to obtain

$$\boxed{\hat{A}' = 0.5(B^{-T}R + BR^{-1})} \tag{28}$$

V. NUMERICAL COMPARISON

Five possible solutions to Wahba's problem are considered as follows.

(1) QUEST

Use the algorithm QUEST [6] to obtain, **q**, the quaternion which corresponds to the solution matrix of Wahba's problem, and then use **q** to compute the solution matrix itself which we denote by A_{qst}.

(2) ITERATIVE ALGORITHM (IA)

Apply the iterative orthogonalization algorithm [17, 18] starting with the computation of B according to (3) and then continue with

$$\hat{A}_o = B \tag{29.a}$$

$$\hat{A}_{j+1} = 0.5(\hat{A}_j^{-T} + \hat{A}_j) \tag{29.b}$$

which converges to the solution of Wahba's problem given in (13). We denote the final matrix by A_{itr}.

(3) SINGULAR VALUE DECOMPOSITION (SVD)

Apply the SVD algorithm to decompose B into

$$B = USV^T \tag{30.a}$$

and compute

$$A_{svd} = UV^T \tag{30.b}$$

As explained in Section III, A_{svd} too is the solution of Wahba's problem.

(4) FAST OPTIMAL MATRIX ALGORITHM (FOAM)

Use the FOAM algorithm [25] to obtain the solution matrix to Wahba's problem. We denote the computed solution by A_{fom}.

(5) POLAR DECOMPOSITION (PD)

Compute the matrices B and R, the latter according to (20), and then calculate the *estimate* of the solution to Wahba's problem according to (26)

$$\hat{A} = BR^{-1} \tag{26}$$

(6) IMPROVED POLAR DECOMPOSITION (IPD)

Compute an *improved estimate* of the solution to Wahba's problem by performing one orthogonalization iteration on the preceding estimate. The overall algorithm is as in (28)

$$\hat{A}' = 0.5(B^{-T}R + BR^{-1}) \tag{28}$$

V.1 Results with Simulated Data

The five algorithms were tested with simulated data. The importance of tests with simulated data stems from the fact that using real data we do not know the correct attitude. This constitutes a major difficulty since the difference between algorithms may be smaller than the difference between the correct attitude and the computed ones. Only when we use simulated data can we observe the difference between the computed attitude and the correct one. The simulated measurements of vectors in body axes were obtained by transforming the reference, $\mathbf{r}_i$, vectors to body axes using A, the correct attitude matrix, addition of a noise component to each component of the transformed vector and normalization of the resultant vectors. The added noise components had a zero mean and a standard deviation value of 0.144. Typical simulation results are shown next for four and three measured vectors. Three cost values were computed in order to evaluate the accuracy of the results. The cost p is Wahba's cost function computed according to (3) for the particular solution matrix. The cost f is the Euclidean norm of the difference between the particular solution matrix and the correct attitude matrix. Finally, the cost J is a measure of the non-orthogonality of the solution matrix. It is the Euclidean norm of the matrix XX^T-I where X is the particular solution matrix.

V.1.1 Four reference vectors

$$\mathbf{r}_1 = \begin{bmatrix} .267261 \\ .534522 \\ .801784 \end{bmatrix} \quad \mathbf{r}_2 = \begin{bmatrix} -.666667 \\ -.666667 \\ -.333333 \end{bmatrix} \quad \mathbf{r}_3 = \begin{bmatrix} .267261 \\ -.801784 \\ .534522 \end{bmatrix} \quad \mathbf{r}_4 = \begin{bmatrix} -.447214 \\ .894427 \\ .000000 \end{bmatrix}$$

Four "measured" body vectors

$$\mathbf{b}_1 = \begin{bmatrix} .815399 \\ .577901 \\ -.033975 \end{bmatrix} \quad \mathbf{b}_2 = \begin{bmatrix} -.872214 \\ -.075280 \\ .483296 \end{bmatrix} \quad \mathbf{b}_3 = \begin{bmatrix} .290203 \\ -.206009 \\ .934528 \end{bmatrix} \quad \mathbf{b}_4 = \begin{bmatrix} -.118959 \\ .679197 \\ -.706940 \end{bmatrix}$$

Four weights

$a_1 = .100000 \qquad a_2 = .300000 \qquad a_3 = .400000 \qquad a_4 = .200000$

The correct attitude matrix

$$A = \begin{bmatrix} .764744 & .293558 & .573576 \\ -.636031 & .486370 & .599090 \\ -.103103 & -.822963 & .558660 \end{bmatrix}$$

Solutions

$$A_{qst} = \begin{bmatrix} .770135 & .274589 & .575754 \\ -.629265 & .474889 & .615228 \\ -.104485 & -.836111 & .538518 \end{bmatrix} \qquad \begin{aligned} p_{qst} &= .44078E\text{-}03 \\ f_{qst} &= .37578E\text{-}01 \\ J_{qst} &= .20588E\text{-}06 \end{aligned}$$

$$A_{itr} = \begin{bmatrix} .761290 & .266299 & .591204 \\ -.639697 & .457436 & .617689 \\ -.105948 & -.848432 & .518593 \end{bmatrix} \qquad \begin{aligned} p_{itr} &= .22933E\text{-}03 \\ f_{itr} &= .67264E\text{-}01 \\ J_{itr} &= .19037E\text{-}06 \end{aligned}$$

$$A_{svd} = \begin{bmatrix} .761290 & .266299 & .591204 \\ -.639697 & .457436 & .617689 \\ -.105948 & -.848432 & .518593 \end{bmatrix} \qquad \begin{aligned} p_{svd} &= .22933E\text{-}03 \\ f_{svd} &= .67264E\text{-}01 \\ J_{svd} &= .18014E\text{-}15 \end{aligned}$$

$$A_{fom} = \begin{bmatrix} .770135 & .274589 & .575754 \\ -.629265 & .474889 & .615228 \\ -.104485 & -.836111 & .538518 \end{bmatrix} \qquad \begin{aligned} p_{fom} &= .44078E\text{-}03 \\ f_{fom} &= .37578E\text{-}01 \\ J_{fom} &= .86667E\text{-}16 \end{aligned}$$

$$\hat{A} = \begin{bmatrix} .770556 & .263174 & .561689 \\ -.654729 & .455528 & .628148 \\ -.143061 & -.851596 & .551271 \end{bmatrix} \qquad \begin{aligned} p &= .67846E\text{-}04 \\ f &= .75595E\text{-}01 \\ J &= .11190E{+}00 \end{aligned}$$

$$\hat{A}' = \begin{bmatrix} .768038 & .263582 & .584080 \\ -.630931 & .473739 & .615274 \\ -.115625 & -.840565 & .530461 \end{bmatrix} \qquad \begin{aligned} p' &= .33350E\text{-}03 \\ f' &= .52240E\text{-}01 \\ J' &= .25319E\text{-}02 \end{aligned}$$

V.1.2 Three reference vectors

$$\mathbf{r}_1 = \begin{bmatrix} .267261 \\ .534522 \\ .801784 \end{bmatrix} \qquad \mathbf{r}_2 = \begin{bmatrix} -.666667 \\ -.666667 \\ -.333333 \end{bmatrix} \qquad \mathbf{r}_3 = \begin{bmatrix} .267261 \\ -.801784 \\ .534522 \end{bmatrix}$$

Three "measured" body vectors

$$\mathbf{b}_1 = \begin{bmatrix} .815399 \\ .577901 \\ -.033975 \end{bmatrix} \qquad \mathbf{b}_2 = \begin{bmatrix} -.872214 \\ -.075280 \\ .483296 \end{bmatrix} \qquad \mathbf{b}_3 = \begin{bmatrix} .290203 \\ -.206009 \\ .934528 \end{bmatrix}$$

Three weights

$$a_1 = .125000 \qquad a_2 = .375000 \qquad a_3 = .500000$$

The correct attitude matrix

$$A = \begin{bmatrix} .764744 & .293558 & .573576 \\ -.636031 & .486370 & .599090 \\ -.103103 & -.822963 & .558660 \end{bmatrix}$$

Solutions

$$A_{qst} = \begin{bmatrix} .767731 & .276451 & .578069 \\ -.631488 & .479442 & .609392 \\ -.108683 & -.832893 & .542658 \end{bmatrix} \qquad \begin{aligned} p_{qst} &= .55884E\text{-}03 \\ f_{qst} &= .29705E\text{-}01 \\ J_{qst} &= .67617E\text{-}07 \end{aligned}$$

$$A_{itr} = \begin{bmatrix} .758264 & .271018 & .592946 \\ -.643834 & .454336 & .615676 \\ -.102537 & -.848604 & .518997 \end{bmatrix} \qquad \begin{aligned} p_{itr} &= .23600E\text{-}03 \\ f_{itr} &= .67219E\text{-}01 \\ J_{itr} &= .32845E\text{-}06 \end{aligned}$$

$$A_{svd} = \begin{bmatrix} .758264 & .271018 & .592946 \\ -.643834 & .454336 & .615676 \\ -.102537 & -.848604 & .518997 \end{bmatrix} \qquad \begin{aligned} p_{svd} &= .23600E\text{-}03 \\ f_{svd} &= .67219E\text{-}01 \\ J_{svd} &= .11102E\text{-}15 \end{aligned}$$

$$A_{fom} = \begin{bmatrix} .767731 & .276451 & .578069 \\ -.631488 & .479442 & .609392 \\ -.108683 & -.832893 & .542658 \end{bmatrix} \qquad \begin{aligned} p_{fom} &= .55884E\text{-}03 \\ f_{fom} &= .29705E\text{-}01 \\ J_{fom} &= .30626E\text{-}15 \end{aligned}$$

$$\hat{A} = \begin{bmatrix} .739265 & .275664 & .586784 \\ -.664499 & .459428 & .635984 \\ -.172692 & -.839769 & .575035 \end{bmatrix} \qquad \begin{aligned} p &= .11783E\text{-}14 \\ f &= .97131E\text{-}01 \\ J &= .16640E\text{+}00 \end{aligned}$$

$$\hat{A}' = \begin{bmatrix} .753716 & .268839 & .600058 \\ -.645610 & .483007 & .593789 \\ -.131702 & -.833708 & .539069 \end{bmatrix} \qquad \begin{aligned} p' &= .60457E\text{-}03 \\ f' &= .53687E\text{-}01 \\ J' &= .53638E\text{-}02 \end{aligned}$$

We observe that, as expected, A_{itr} and A_{svd} are practically identical. We also observe that as expected, for three measured vectors (K=3) Wahba's cost, p, for $\hat{A}$ is practically zero. The single normalization cycle which generates $\hat{A}'$ improves the orthogonality (reduces J) considerably. This comes at the expense of an increase in p. For four measured vectors (K=4), p for $\hat{A}$ is similar in value to that of the other algorithms, and again, the single normalization cycle improves orthogonality considerably at the expense of Wahba's cost.

V.2 Results with UARS Data

The following are results of the application of the five algorithms to data measured on-board the Upper Atmosphere Research Satellite (UARS). UARS was deployed on September 15, 1991 at 04:23 GMT by the shuttle spacecraft Discovery which was launched on September 12, 1991, at 23:12 GMT. The data were measured on September 30, 1991 at 18:32:31.206749916 GMT. The first vector corresponds to the Sun Sensor, the second to the triad of Magnetometers, and the third to the Infra-Red Horizon Sensor.

The reference vectors

$$\mathbf{r}_1 = \begin{bmatrix} -.992324 \\ -.113458 \\ -.049192 \end{bmatrix} \qquad \mathbf{r}_2 = \begin{bmatrix} -.814177 \\ .550862 \\ -.183487 \end{bmatrix} \qquad \mathbf{r}_3 = \begin{bmatrix} .543295 \\ -.542620 \\ .640619 \end{bmatrix}$$

The measured body vectors

$$\mathbf{b}_1 = \begin{bmatrix} -.810765 \\ -.294952 \\ -.411403 \end{bmatrix} \qquad \mathbf{b}_2 = \begin{bmatrix} -.455867 \\ .186491 \\ -.870291 \end{bmatrix} \qquad \mathbf{b}_3 = \begin{bmatrix} .002528 \\ .003031 \\ .999992 \end{bmatrix}$$

Three weights

$$a_1 = .243291 \qquad a_2 = .002506 \qquad a_3 = .754203$$

Solutions

$$A_{qst} = \begin{bmatrix} .826549 & .178850 & -.533694 \\ .178119 & .816336 & .549426 \\ .533939 & -.549189 & .642885 \end{bmatrix} \qquad p_{qst} = .96423E\text{-}03 \qquad J_{qst} = .20183E\text{-}06$$

$$A_{itr} = \begin{bmatrix} .832537 & .172669 & -.526372 \\ .180280 & .814010 & .552166 \\ .523814 & -.554593 & .646564 \end{bmatrix} \qquad p_{itr} = .89246E\text{-}03 \qquad J_{itr} = .15599E\text{-}07$$

$$A_{svd} = \begin{bmatrix} .832537 & .172669 & -.526372 \\ .180280 & .814010 & .552166 \\ .523814 & -.554593 & .646564 \end{bmatrix} \qquad p_{svd} = .89246E\text{-}03 \qquad J_{svd} = .19700E\text{-}15$$

$$A_{fom} = \begin{bmatrix} .826549 & .178850 & -.533694 \\ .178119 & .816336 & .549426 \\ .533939 & -.549189 & .642885 \end{bmatrix} \qquad p_{fom} = .96423E\text{-}03 \qquad J_{fom} = .46516E\text{-}15$$

$$\hat{A} = \begin{bmatrix} .818163 & .211577 & -.510709 \\ .182985 & .778550 & .508996 \\ .466235 & -.700019 & .572641 \end{bmatrix} \qquad p = .13611E-12$$

$$J = .28575E+00$$

$$\hat{A}' = \begin{bmatrix} .837978 & .176650 & .517931 \\ .217866 & .767101 & .613477 \\ .503300 & -.622646 & .606208 \end{bmatrix} \qquad p' = .39206E-02$$

$$J' = .16305E-01$$

Here too we observe the identity between A_{itr} and A_{svd}. As before, we also observe the reduction in J at the expense of an increase in p when a single orthogonalization cycle is applied to $\hat{A}$ to generate $\hat{A}'$.

V.3 Time Consumption Analysis

A computation-time measurement was performed on all five algorithms using the simulated three and four measured vectors. The runs were made on a VAX 9210 computer employing the VMS Version 5.4-2 operating system. The time measurement routine used the internal machine clock at a resolution of 10 msec. In order to increase the resolution, the runs were performed over 50000 successive solutions and the total time was then divided by 50000. The results are presented in Table I.

Table I: Algorithm Computation Time (msec).

	A_{qst}	A_{itr}	A_{svd}	A_{fom}	$\hat{A}$	$\hat{A}'$
Three measured vectors	0.0890	0.790	0.548	0.060	0.058	0.084
Four measured vectors	0.1060	0.694	0.526	0.070	0.068	0.094

Note the decrease in computation time of A_{itr} when the number of measured vectors increased from 3 to 4. This is due to the fact that in the four vector case the convergence criterion was met after only 7 iterations whereas in the 3 vector case 8 iterations were performed until the same convergence criterion was met. In all our tests it was found that when a fourth measured vector was added, less iterations were required. This stemmed from the fact that when a fourth measured vector is added the orthogonality of B increases provided the fourth vector is not a linear combination of the other three. The decrease of the computation time of A_{svd} with the increase of the number of measured vectors is not consistent. It depends on the number of iterations needed for the completion of the SVD calculations.

VI. CONCLUSIONS

It was shown that the solution to Wahba's problem is the closest orthogonal matrix to B where B is defined on the measured vectors and on weights associated with their measurements. The weights signify the confidence assigned to the measurements. The matrix B includes all the information contained in the measurement.

Once it was established that the sought solution is the orthogonal matrix closest to B, algorithms for computing that orthogonal matrix were considered, and an algorithm was discussed which is based on the polar decomposition of matrices into the closest unitary (in our case: orthogonal) matrix and a Hermitian (in our case symmetric) matrix. The accuracy of the algorithm increases with the accuracy of the measurements and with their unbiasedness. If the measurements are error free the algorithm yields the exact solution.

When only three measured vectors are used the new algorithm yields a solution which zeros Wahba's cost; however, the solution is not necessarily orthogonal. An application of one orthogonalization iteration to the solution matrix constitutes a modified algorithm which yields a better solution. Although the latter algorithm generates a matrix which increases Wahba's cost. The new matrix is closer to orthogonality. We note that the same iteration cycle if applied repeatedly to B itself, yields eventually the optimal solution as shown in the examples; however, since B is usually quite far from orthogonality, it takes several iterations to obtain the solution.

The advantage of the algorithm is in its simplicity which enables its use for obtaining first cut solutions using "back-of the envelop" like programs such as MathCAD. Another advantage of the first new algorithm is its ability to indicate the precision of the measurements. This stems from the fact that generally the closeness of the solution matrix to orthogonality is indicative of the precision of the measurements. It is interesting to note that the fact that the two PD algorithms yield the exact solution in the noise-free case is analogous to the fact that the largest eigenvalue of the 4x4 K matrix used in the QUEST algorithm is precisely 1 in the noise-free case.

The two PD algorithms were tested vis-a-vis other popular algorithms using simulated and real UARS data.

Acknowledgment

The author wishes to thank Jerry Teles, the Head of NASA-Goddard Space Flight Center Flight Dynamics Analysis Branch and Tom Stengle, the Head of the Attitude Analysis Section of that branch, for authorizing the use of UARS data, and to Scott Greatorex for extracting and supplying the data. The author is grateful to Malcolm D. Shuster for providing him with the coding of QUEST, to F. Landis Markley for providing him with the coding of FOAM and to both of them for their constructive remarks. Thanks are also due to Miriam Shaked for performing most of the computer runs.

References

1. G. Wahba, "A Least Squares Estimate of Spacecraft Attitude", *SIAM Review*, Vol. 7, No. 3, July 1965, p. 409.
2. J.L. Farrell and J.C. Stuelpnagel, "A Least Squares Estimate of Spacecraft Attitude", *SIAM Review*, Vol. 8, No. 3, July 1966, pp. 384-386.
3. R.H. Wessner, ibid.4. J.R. Welman, ibid.
5. J.E. Brock, ibid.
6. M.D. Shuster and S.D. Oh, "Three-Axis Attitude Determination from Vector Observations", *J. of Guidance and Control*, Vol. 4, Jan.-Feb. 1981, pp. 70-77.

7. M.D. Shuster, "Approximate Algorithms for Fast Optimal Attitude Computation", *Proceedings, AIAA Guidance Navigation and Control Conference*, Palo Alto, CA, Aug. 7-9, 1978.
8. F.L. Markley, "Attitude Determination and Parameter Estimation using Vector Observations: Theory", *J. of the Astronautical Sciences*, Vol. 37, Jan.-Feb. 1989, pp. 41-58.
9. M.D. Shuster, "Maximum Likelihood Estimation of Spacecraft Attitude", *J. of the Astronautical Sciences*, Vol. 37, Jan.-March 1989, pp. 79-88.
10. M.D. Shuster, "A Simple Filter and Smoother for Spacecraft Attitude", *J. of the Astronautical Sciences*, Vol. 37, Jan.-Feb. 1989, pp. 89-106.
11. F.L. Markley, "Attitude Determination and Parameter Estimation using Vector Observations: Application", *J. of the Astronautical Sciences*, Vol. 39, July-Sept. 1991, pp. 367-381.
12. H.T. Gains, "Attitude Matrix Orthonormality Correction", Honeywell, Interoffice Correspondence, October 1965.
13. J.E. Brock, "Optimal Matrices Describing Linear Systems", *AIAA J.*, Vol. 6, July 1968, pp. 1292-1296.
14. I.Y. Bar-Itzhack and K.A. Fegley, "Orthogonalization Techniques of a Direction Cosine Matrix", *IEEE Transactions on Aerospace and Electronic Systems*, Vol. 12, March 1976, pp. 146-151.
15. A. Björck and C. Bowie, "An Iterative Algorithm for Computing the Best Estimate of an Orthogonal Matrix", *SIAM J. on Numerical Analysis*, Vol. 8, 1971, pp. 358-364.
16. I.Y. Bar-Itzhack, "Iterative Optimal Orthogonalization of the Strapdown Matrix", *IEEE Transactions on Aerospace and Electronic Systems*, Vol. AES-11, Jan. 1975, pp. 30-37.
17. I.Y. Bar-Itzhack, J. Meyer and P.A. Fuhrmann, "Strapdown Matrix Orthogonalization: the Dual Iterative Algorithm", *IEEE Transactions on Aerospace and Electronic Systems*, Vol. 12, Jan. 1976, pp. 32-37.
18. I.Y. Bar-Itzhack and J. Meyer, "On the Convergence of Iterative Orthogonalization Processes", *IEEE Transactions on Aerospace and Electronic Systems*, Vol. 12, March 1976, pp. 146-151.
19. J. Meyer and I.Y. Bar-Itzhack, "Practical Comparison of Iterative Matrix Orthogonalization Algorithms", *IEEE Transactions on Aerospace and Electronic Systems*, Vol. 13, May 1977, pp. 230-235.
20. G.E. Forsythe and C.B. Moler, "*Computer Solution of Linear Algebraic Systems*, Prentice-Hall, Englewood Cliffs, N.J., 1967.
21. F.L. Markley, "Attitude Determination using Vector Observations and the Singular Value Decomposition", *J. of the Astronautical Sciences*, Vol. 36, July-Sept. 1988, pp. 245-258.
22. F.R. Gantmacher, *The Theory of Matrices*, Vol. 1, Chelsea Publishing Co., New York, 1960, pp. 276, 277.
23. K. Fan and A. Hoffman, "Some Metric Inequalities in the Space of Matrices", *Proc. of the American Mathematical Society*, Vol. 6, 1955, pp. 111-116.
24. A.E. Bryson, Jr. and Y.C. Ho, *Applied Optimal Control*, Blaisdell Publishing Co., Waltham, MA, 1989, p. 379.
25. F.L. Markley, "Attitude Determination Using Vector Observations: A Fast Optimal Matrix Algorithm", *Proceedings of the 1992 Flight Mechanics/ Estimation Theory Symposium*, NASA-Goddard Space Flight Center, Greenbelt MD, May 5-7, 1992.

ATTITUDE ANALYSIS IN FLATLAND: THE PLANE TRUTH

Malcolm D. Shuster

The Johns Hopkins University Applied Physics Laboratory
Laurel, Maryland 20723-6099

ABSTRACT

Many results in attitude analysis are still meaningful when the attitude is restricted to rotations about a single axis. Such a picture corresponds to attitude analysis in the Euclidean plane. The present report formalizes the representation of attitude in the plane and applies it to some well-known problems. In particular we study the connection of the "additive" and "multiplicative" formulations of the differential corrector for the quaternion in its two-dimensional setting.

Introduction

I call our world Flatland, not because we call it so, but to make its nature clearer to you, . . . who are privileged to live in Space.
— A. Square in Flatland

The treatment of attitude, because of the non-linearity and non-commutivity of the composition rule, is much more difficult to treat than position, for which components may be combined by simple addition. The complexity of the attitude composition rule leads to virtually all attitude problems being intrinsically three-dimensional or, in the case of the quaternion, four-dimensional. There is, however, a class of attitude problems which are much simpler, namely, single-axis problems, and the study of these will in many cases illuminate the more complex problems. The present report attempts to formalize such a treatment.

Attitude in Flatland

Having amused myself til a late hour with my favourite recreation of Geometry, I had retired to rest with an unsolved problem in my mind.

Let us imagine that the world, Flatland, has only two dimensions and a constant isotropic Euclidean metric. Such a world was imagined by Edwin Abbott Abbott [1], with the intent of satirizing the social and political foibles of his day as much as of clarifying the concepts related to the dimensionality of space. Our interest here is more limited than Abbott's. We develop the mathematical structure of Flatland somewhat further in order to better understand those aspects of attitude which do not depend on the dimensionality of space. The quotations which appear in this report are from [1]. Following Abbott we will refer to our three-dimensional world as *Space*.

In Flatland, vectors are, of course, two-dimensional

$$\mathbf{v} = \begin{bmatrix} v_1 \\ v_2 \end{bmatrix} . \tag{1}$$

The "dot" product takes the usual form

$$\mathbf{u} \cdot \mathbf{v} = u_1 v_1 + u_2 v_2 , \tag{2}$$

while the "cross product" is now a scalar

$$\mathbf{u} \times \mathbf{v} = u_1 v_2 - u_2 v_1 . \tag{3}$$

There is, therefore, no *vector* product, and as alternate names to scalar and vector products we might prefer symmetric and asymmetric products. The lack of a meaningful vector product in two dimensions was ultimately the cause of many years of grief for Hamilton [2–4].

The *attitude matrix* in two dimensions is a 2 × 2 proper orthogonal matrix, A, which transforms column vectors in the usual way

$$\mathbf{W} = A\,\mathbf{V} , \tag{4}$$

with

$$A^T A = A A^T = \mathbf{I} , \tag{5}$$

$$\det A = +1 , \tag{6}$$

where $\mathbf{I}$ denotes the 2 × 2 identity matrix,

$$\mathbf{I} \equiv \begin{bmatrix} 1 & 0 \\ 0 & 1 \end{bmatrix} . \tag{7}$$

It is a simple matter to show that in two dimensions the attitude matrix may be represented as

$$A = \begin{bmatrix} \cos\theta & \sin\theta \\ -\sin\theta & \cos\theta \end{bmatrix} , \tag{8}$$

and θ is the *angle of rotation*. If we define the matrix $\mathbf{J}$ according to

$$\mathbf{J} = \begin{bmatrix} 0 & 1 \\ -1 & 0 \end{bmatrix}, \tag{9}$$

which satisfies

$$\mathbf{J}^2 = -\mathbf{I}, \tag{10}$$

then *Euler's formula* becomes simply

$$A = \cos\theta\,\mathbf{I} + \sin\theta\,\mathbf{J}, \tag{11}$$

which is much simpler than the three-dimensional form [5–10]. Note that $\mathbf{J}$ acting on a vector always generates a vector perpendicular to it. The matrices $\mathbf{I}$ and $\mathbf{J}$ in Flatland have an importance similar to that of the 3×3 identity matrix and the Levi-Civita symbol in Space. They are, in fact, the representations of these objects in two dimensions.

If we define now

$$[[\,a\,]] \equiv a\,\mathbf{J}, \tag{12}$$

then trivially

$$[[\,a\,]]\,[[\,b\,]] = -ab\,\mathbf{I}, \tag{13}$$

which again is much simpler than the three-dimensional variant, and Euler's formula becomes

$$A = \exp[[\,\theta\,]], \tag{14}$$

as in Space.

Corresponding to the quaternion in Space, in Flatland we must be content with the *biernion* (pronounced "by-Ernie-on" and named in honor of Ernest P. Worrell, the character portrayed by Jim Varney). The biernion is defined as

$$\bar{q} \equiv \begin{bmatrix} \sin(\theta/2) \\ \cos(\theta/2) \end{bmatrix}, \tag{15}$$

for which

$$\bar{q}^T \bar{q} = 1\,. \tag{16}$$

We continue to use the notation $\bar{q}$ (rather than $\bar{b}$) in order to retain a greater resemblance to the equations in Space.

In terms of the biernion Euler's formula becomes

$$A(\bar{q}) = (q_2^2 - q_1^2)\,\mathbf{I} + 2\,q_2\,q_1\,\mathbf{J} \tag{17a}$$

$$= (q_2^2 - q_1^2)\,\mathbf{I} + 2\,q_2\,[[\,q_1\,]] \tag{17b}$$

$$= (q_1\,\mathbf{I} + q_2\,\mathbf{J})^2\,. \tag{17c}$$

The biernion may be extracted from the attitude matrix in a manner similar to the method for extracting the quaternion from the attitude matrix in Space,

$$q_2 = \frac{1}{2}\sqrt{2 + \mathrm{tr}A}\,, \tag{18a}$$

$$q_1 = \frac{1}{4q_2}(A_{12} - A_{21})\,, \tag{18b}$$

where

$$\mathrm{tr}A \equiv A_{11} + A_{22}\,. \tag{19}$$

Biernion composition follows directly from the trigonometric formula and reads

$$\bar{q}'' = \bar{q}' \otimes \bar{q} \tag{20a}$$

$$= \{\,\bar{q}'\,\}\,\bar{q} = \{\,\bar{q}\,\}\,\bar{q}'\,, \tag{20b}$$

where

$$\{\,\bar{q}\,\} \equiv \begin{bmatrix} q_2 & q_1 \\ -q_1 & q_2 \end{bmatrix} = q_2\,\mathbf{I} + q_1\,\mathbf{J}\,. \tag{21}$$

Note that biernion composition is commutative, as is the multiplication of attitude matrices in two dimensions.

The *Gibbs scalar* or *Rodrigues scalar* is given by

$$g = q_1/q_2 = \tan(\theta/2)\,. \tag{22}$$

Thus,

$$\bar{q} = \frac{1}{\sqrt{1+g^2}} \begin{bmatrix} g \\ 1 \end{bmatrix}\,, \tag{23}$$

and Cayley's formula takes the familiar form

$$A = \frac{\mathbf{I} + [[\,g\,]]}{\mathbf{I} - [[\,g\,]]}\,. \tag{24}$$

The composition of Gibbs scalars is given by

$$g'' = \frac{g' + g}{1 - g'g}\,, \tag{25}$$

in complete analogy to the formula for the Gibbs vector in Space.

The *Cayley-Klein parameters* are

$$\alpha \equiv q_2 + i\,q_1 = e^{i\theta/2}\,, \quad \text{and} \quad \beta \equiv q_2 - i\,q_1 = e^{-i\theta/2} = \alpha^c\,, \tag{26}$$

and the superscript c denotes complex conjugation. These obviously satisfy

$$\alpha\beta = 1\,. \tag{27}$$

It follows that

$$A = \frac{1}{2}(\alpha^2 + \beta^2)\,\mathbf{I} + \frac{1}{2i}(\alpha^2 - \beta^2)\,\mathbf{J}\,. \tag{28}$$

Attitude Kinematics in Flatland

> *Restraining my impatience—for I was now under a strong temptation to rush blindly at my visitor and precipitate him into Space ...*

The kinematic equation for the attitude matrix is given as usual by

$$\frac{d}{dt}\,A(t) = [[\,\omega(t)\,]]\,A(t)\,, \tag{29}$$

which, in fact, defines $\omega(t)$. If we define the biernion analogue,

$$\bar{\omega} \equiv \begin{bmatrix} \omega \\ 0 \end{bmatrix}, \tag{30}$$

then the kinematic equation for the biernion is simply

$$\frac{d}{dt}\,\bar{q}(t) = \frac{1}{2}\,\bar{\omega}(t) \otimes \bar{q}(t) = \frac{1}{2}\,\Omega(\omega(t))\,\bar{q}(t), \tag{31}$$

where

$$\Omega(\omega) \equiv \omega\,\mathbf{J}. \tag{32}$$

Likewise, we can partition $\{\,\bar{q}\,\}$ defined by equation (21) in terms of column matrices as

$$\{\,\bar{q}\,\} \equiv [\,\Xi(\bar{q})\;\;\bar{q}\,], \tag{33}$$

which leads to

$$\frac{d}{dt}\,\bar{q}(t) = \frac{1}{2}\,\Xi(\bar{q}(t))\,\omega, \tag{34a}$$

and

$$\Xi(\bar{q}) = \begin{bmatrix} q_2 \\ -q_1 \end{bmatrix} = \mathbf{J}\,\bar{q}. \tag{34b}$$

The kinematic equation for the Gibbs scalar becomes finally

$$\frac{d}{dt}\,g(t) = \frac{1}{2}\,[1 + g^2(t)]\,\omega(t), \tag{35}$$

while that for the angle of rotation is just

$$\frac{d\theta}{dt} = \omega. \tag{36}$$

Euler's equation for rigid-body dynamics is simply

$$I\,\frac{d\omega}{dt} = N, \tag{37}$$

where N, the *torque*, is a scalar and I, the *moment of inertia*, another scalar, is given by

$$I = \int r^2\,dm. \tag{38}$$

Attitude Errors in Flatland

> *If Fog were non-existent, all lines would appear equally and indistinguishably clear.*

The representation of attitude errors in Flatland follows that in Space, with obvious simplifications. The error in the attitude matrix, since it has only a single degree of freedom, can be written as

$$A^{*} = (\delta A)\,A^{\text{true}}, \tag{39}$$

with A^* a random variable, usually an attitude estimate, and δA is the (multiplicative) attitude error,

$$\delta A = \exp\{[[\,\Delta\xi\,]]\} \approx \mathbf{I} + [[\,\Delta\xi\,]]\,, \tag{40}$$

with $\Delta\xi$, the attitude error angle, generally an infinitesimal quantity assumed to have zero mean. The attitude variance is defined to be

$$P_{\xi\xi} = E\{\,(\Delta\xi)^2\,\}\,, \tag{41}$$

where $E\{\,\cdot\,\}$ denotes the expectation.

The modeling of vector measurement errors follow a similar pattern. We write

$$\hat{\mathbf{W}} = e^{[[\,\epsilon\,]]}\,A\hat{\mathbf{V}}\,, \tag{42}$$

where ϵ is a zero-mean random variable with variance σ_W^2. In linear approximation this may be written as

$$\hat{\mathbf{W}} = A\,\hat{\mathbf{V}} + \Delta\hat{\mathbf{W}}\,, \tag{43}$$

with

$$\Delta\hat{\mathbf{W}} = \epsilon\,\mathbf{J}\,A\hat{\mathbf{V}} = [[\,A\hat{\mathbf{V}}\,]]\,\epsilon\,, \tag{44}$$

and we have defined $[[\,\mathbf{v}\,]]$ with *vector* argument to be

$$[[\,\mathbf{v}\,]] \equiv \mathbf{J}\,\mathbf{v} = \begin{bmatrix} v_2 \\ -v_1 \end{bmatrix}\,. \tag{45}$$

Thus,

$$[[\,\mathbf{u}\,]]^T\,\mathbf{v} = -\mathbf{u}\times\mathbf{v} = -\mathbf{u}^T\,[[\,\mathbf{v}\,]]\,, \tag{46a}$$

$$[[\,\mathbf{v}\,]]^T\,\mathbf{v} = \mathbf{0}\,, \tag{46b}$$

$$[[\,\mathbf{u}\,]]^T[[\,\mathbf{v}\,]] = \mathbf{u}\cdot\mathbf{v}\,, \tag{46c}$$

$$[[\,\mathbf{u}\,]]\,[[\,\mathbf{v}\,]]^T = (\mathbf{u}\cdot\mathbf{v})\,\mathbf{I} - \mathbf{v}\mathbf{u}^T\,, \tag{46d}$$

$$[[\,a\,]]\,\mathbf{v} = [[\,\mathbf{v}\,]]\,a\,. \tag{46e}$$

Batch Attitude Determination in Flatland

> *I answer that though we cannot see angles, we can infer them, and this with great precision.*

We can now examine some well-known algorithms in their Flatland setting. These are the DYAD algorithm, the two-dimensional analogue of the TRIAD algorithm [11–12], and the BEST algorithm, the two-dimensional analogue of the QUEST algorithm [12]. The development of these algorithms in two dimensions is very similar to that of their forbears in Space. As can be expected, the results are much simpler in the smaller dimension.

The DYAD Algorithm

For the DYAD algorithm we seek an attitude matrix which satisfies

$$\mathbf{W} = A\,\mathbf{V}\,, \tag{47}$$

where V and W are arbitrary vectors. In a space of n dimensions, $n-1$ linearly independent vector measurements are required to uniquely determine the attitude matrix [13]. In two dimensions, therefore, a single measurement suffices. (In one dimension, zero measurements are sufficient.)

To construct the attitude matrix we first construct orthonormal dyads of reference and observation vectors as

$$\hat{\mathbf{r}}_1 = \frac{\hat{\mathbf{V}}}{|\hat{\mathbf{V}}|} \quad \text{and} \quad \hat{\mathbf{r}}_2 = \mathbf{J}\,\hat{\mathbf{r}}_1\,, \tag{48a}$$

and

$$\hat{\mathbf{s}}_1 = \frac{\hat{\mathbf{W}}}{|\hat{\mathbf{W}}|} \quad \text{and} \quad \hat{\mathbf{s}}_2 = \mathbf{J}\,\hat{\mathbf{s}}_1\,. \tag{48b}$$

From

$$\mathbf{J}^3 = -\mathbf{J}\,, \tag{49}$$

it follows that

$$\mathbf{J}\,A\,\mathbf{J}^T = A\,. \tag{50}$$

Hence,

$$\hat{\mathbf{s}}_i = A\,\hat{\mathbf{r}}_i\,, \quad i = 1, 2\,, \tag{51}$$

Defining now orthogonal matrices (labeled by their columns)

$$M_R = [\,\hat{\mathbf{r}}_1 \quad \hat{\mathbf{r}}_2\,]\,, \quad \text{and} \quad M_S = [\,\hat{\mathbf{s}}_1 \quad \hat{\mathbf{s}}_2\,]\,, \tag{52}$$

it follows that

$$M_S = A\,M_R\,, \tag{53}$$

whence

$$A = M_S M_R^T\,. \tag{54}$$

The development of the DYAD attitude variance follows almost identical steps as in the calculation of the TRIAD attitude covariance in Space [12] with the result

$$P_{\mathrm{DYAD}} = \sigma_W^2\,. \tag{55}$$

The BEST Algorithm

The BEST (Biernion ESTimator) algorithm in Flatland is only slightly less complicated than the QUEST algorithm in Space. As usual, we seek an attitude matrix which minimizes [12, 14]

$$J(A) = \frac{1}{2}\sum_{i=1}^{n} a_i\,|\hat{\mathbf{W}}_i - A\,\hat{\mathbf{V}}_i|^2\,, \tag{56}$$

where the a_i, $i = 1, \ldots, n > 2$, are a set of positive weights, whose sum, we will assume, is unity. As in the Space we define a gain function, $g(A)$, such that

$$g(A) = 1 - J(A) = \mathrm{tr}(B^T A)\,, \tag{57}$$

which is a maximum when $J(A)$ is a minimum, and, as before the attitude profile matrix is given by

$$B = \sum_{i=1}^{n} a_i \hat{\mathbf{W}}_i \hat{\mathbf{V}}_i^T\,. \tag{58}$$

Substituting equation (17a) in equation (57) leads straightforwardly to

$$g(\bar{q}) = (q_2^2 - q_1^2)\, s + 2\, q_1\, q_2\, z\,, \tag{59}$$

where

$$s \boxminus \mathrm{tr}(B^T) = \mathrm{tr}B = B_{11} + B_{22}\,, \tag{60a}$$

$$z \equiv \mathrm{tr}(\mathbf{J}B^T) = -\mathrm{tr}(\mathbf{J}\,B) = B_{12} - B_{21}\,. \tag{60b}$$

Thus,

$$g(\bar{q}) = \bar{q}^T K \bar{q}\,, \tag{61}$$

with

$$K = \begin{bmatrix} -s & z \\ z & s \end{bmatrix}\,. \tag{62}$$

The maximization of $g(\bar{q})$ leads to the familiar eigenvalue problem

$$K\bar{q}^* = \lambda_{\max}\,\bar{q}^*\,, \tag{63}$$

but in Flatland $\lambda_{\max}$ can be calculated in closed form as

$$\lambda_{\max} = \sqrt{s^2 + z^2}\,, \tag{64}$$

and

$$\bar{q}^* = \frac{1}{\sqrt{z^2 + (\lambda_{\max} + s)^2}} \begin{bmatrix} z \\ \lambda_{\max} + s \end{bmatrix}\,. \tag{65}$$

The attitude variance of the BEST algorithm is calculated most easily from the Fisher information matrix using the fact that the BEST algorithm is a maximum-likelihood estimator [15]. Assuming the errors to have a Gaussian distribution, the calculation is straightforward and leads to

$$P_{\mathrm{BEST}}^{-2} = \sum_{i=1}^{n} \sigma_{W_i}^{-2}\,. \tag{66}$$

The optimal angle of rotation can also be computed directly by noting that the gain function can be written in the form

$$g(\theta) = s\,\cos\theta + z\,\sin\theta\,, \tag{67}$$

which is obviously a maximum when $\theta = \theta^*$, with

$$\cos\theta^* = \frac{s}{\sqrt{s^2 + z^2}} \quad \text{and} \quad \sin\theta^* = \frac{z}{\sqrt{s^2 + z^2}}. \tag{68}$$

We write the solution of equation (68) more conveniently as

$$\theta^* = \arctan_2(z, s), \tag{69}$$

where $\arctan_2$ is the same function as ATAN2 in FORTRAN. Equation (68) leads directly to a solution for the optimal attitude matrix, namely,

$$A^* = \frac{1}{\sqrt{s^2 + z^2}} \begin{bmatrix} s & z \\ -z & s \end{bmatrix}. \tag{70}$$

Substitution of equation (65) into equation (17) leads somewhat less directly to the same result, which should be compared with the construction of the optimal attitude matrix in Space developed by Markley [16]. Markley's FOAM algorithm [17] carries over with little change into Flatland and yields necessarily the same result as equation (70).

General Comments on Attitude Estimation in Flatland (*and Space*)

I am about to appear very inconsistent.

There seems to be some confusion concerning the use of representations in attitude estimation, which we will now attempt to muddy further. Typically in attitude determination, one is given a set of measurements, $\{\mathbf{z}_1, \ldots, \mathbf{z}_N\}$, from which one wishes to infer the attitude, which we will denote without reference to a representation by $\mathcal{A}$. The space of $\mathcal{A}$ we know from long experience is an m-dimensional manifold, where $m = 1$ in Flatland, $m = 3$ in Space, and $m = 6$ in worlds so unfortunate as to be four-dimensional. An important milestone in every probabilistic estimate of the attitude is the construction of the probability density function (pdf) of the measurements as a function of the attitude, $p_{\mathbf{z}_1,\ldots,\mathbf{z}_N}(\mathbf{z}'_1, \ldots, \mathbf{z}'_N; \mathcal{A})$, where the primed variables denote the values taken by the (unprimed) random variables, and the attitude manifold is assumed to be simply a parameter space rather than a space of random variables. If $\mathcal{A}$ is also a random variable then the pdf of interest is $p_{\mathbf{z}_1,\ldots,\mathbf{z}_N,\mathcal{A}}(\mathbf{z}'_1, \ldots, \mathbf{z}'_N, \mathcal{A}')$. When one constructs a square loss function, one is, in fact, constructing part of the appropriate pdf assuming Gaussian random noise.

The maximum-likelihood estimate is simply the value of $\mathcal{A}$ (or $\mathcal{A}'$) which maximizes the appropriate pdf [18]. In mathematical notation we can write*

$$\mathcal{A}^*_{ML} \equiv \arg\max_{\mathcal{A}} p_{\mathbf{z}_1,\ldots,\mathbf{z}_N}(\mathbf{z}'_1, \ldots, \mathbf{z}'_N, \mathcal{A}), \tag{71a}$$

or

$$\mathcal{A}'^*_{ML} \equiv \arg\max_{\mathcal{A}'} p_{\mathbf{z}_1,\ldots,\mathbf{z}_N,\mathcal{A}}(\mathbf{z}'_1, \ldots, \mathbf{z}'_N, \mathcal{A}'), \tag{71b}$$

*In the particular case where $\mathcal{A}$ is a random variable one usually speaks of a maximum *a posteriori* estimate.

according to whether or not $\mathcal{A}$ is a random variable, and the maximum is taken over the manifold of $\mathcal{A}$ (or $\mathcal{A}'$). Likewise, in the special case that $\mathcal{A}$ is a random variable, we can define a minimum variance estimate of the attitude as

$$\mathcal{A}'^{*}_{MV} \equiv E\{\mathcal{A} \mid \mathbf{z}'_1, \ldots, \mathbf{z}'_N\}, \tag{72}$$

that is, as the conditional expectation of $\mathcal{A}$. This form of the minimum variance as given by equation (72) is not meaningful, generally, unless the representation of $\mathcal{A}$ has minimum dimension. Otherwise, the conditional expectation will usually lead to a value which is not on the manifold, and, therefore, unacceptable as a solution. It is difficult, in general, to calculate the minimum variance estimate except in the case where the probability distribution of the measurement noise is Gaussian, in which case the minimum-variance estimate is identical to the maximum-likelihood estimate.

The general method of solution by maximum-likelihood estimation to an attitude estimation problem given a set of measurements and a probabilistic measurement model is to write the negative-log-likelihood function

$$J(\mathcal{A}') \equiv -\log p_{\mathbf{z}_1, \ldots, \mathbf{z}_N, \mathcal{A}}(\mathbf{z}'_1, \ldots, \mathbf{z}'_N, \mathcal{A}'), \tag{73}$$

where for definiteness we consider the case that $\mathcal{A}$ is a random variable. The negative-log-likelihood function is a minimum at the maximum-likelihood estimate. The procedure is thus to minimize the expression in equation (73) by an iterative method, such as the Newton-Raphson method. Thus, if $\mathcal{A}'_i$ is the i-th iteration we write

$$\mathcal{A}' = \mathcal{A}(\beta) \otimes \mathcal{A}'_i, \tag{74}$$

where $\mathcal{A}(\beta)$ denotes the general attitude as a function of β, which is one of the many minimum-dimensional representations of the attitude which is Euclidean at the origin and for which $\mathcal{A}(\mathbf{0})$ is the identity rotation. Expanding $\mathcal{A}$ as a function of β leads to

$$\begin{aligned} J(\mathcal{A}') = J(\mathcal{A}'_i) &+ \left[\frac{\partial}{\partial \beta} J(\mathcal{A}(\beta) \otimes \mathcal{A}'_i)\right]_{\beta=0} \beta \\ &+ \frac{1}{2} \beta^T \left[\frac{\partial^2}{\partial \beta \partial \beta^T} J(\mathcal{A}(\beta) \otimes \mathcal{A}'_i)\right]_{\beta=0} \beta + O(|\beta|^3), \end{aligned} \tag{75}$$

and minimizing this expression keeping terms only up to second order in β leads to the next iteration

$$\beta_{i+1} = -\left[\frac{\partial^2}{\partial \beta \partial \beta^T} J(\mathcal{A}(\beta) \otimes \mathcal{A}'_i)\right]^{-1}_{\beta=0} \left[\frac{\partial}{\partial \beta} J(\mathcal{A}(\beta) \otimes \mathcal{A}'_i)\right]_{\beta=0}, \tag{76}$$

$$\mathcal{A}'_{i+1} = \mathcal{A}(\beta_{i+1}) \otimes \mathcal{A}'_i. \tag{77}$$

This procedure will generally converge to a minimum of the negative-log-likelihood function. In well-defined attitude problems this minimum is usually unique and hence,

$$\mathcal{A}'^{*}_{ML} = \lim_{i \to \infty} \mathcal{A}'_i. \tag{78}$$

In the limit that the amount of data is infinite the attitude covariance matrix can be written as

$$P_{\beta\beta}^{-1} = E\left\{\left[\frac{\partial^2}{\partial\beta\partial\beta^T} J(\mathcal{A}(\beta)\otimes\mathcal{A}')\right]\right\}_{\beta=0,\mathcal{A}'=\mathcal{A}'_{ML}} . \tag{79}$$

If the measurement errors are Gaussian, then within the linearization approximation, equation (79) will be true even for small samples.

Treatment of the Biernion/Quaternion in Attitude Estimation

It is high time that I should pass from these brief and discursive notes about things in Flatland to the central event ...

Several schemes have been proposed [19] for mechanizing the Kalman filter update for the quaternion. The effect of these and other schemes has been studied via numerical examples by Bar-Itzhack, Deutschman and Markley [20, 21]. These latter authors make a distinction between the update step of the Kalman filter using what they call the additive as opposed to the multiplicative update. This distinction is artificial and misleading, as we shall now show.

Let us write the relation between the updated and predicted quaternions/biernions as

$$\bar{q}_k(+) = \bar{q}_k(-) + \Delta\bar{q}_k(+) , \tag{80}$$

which Bar-Itzhack *et al.* call the additive approach. The components are all resolved with respect to inertial axes. Let us examine the same equation expressed with respect to the predicted spacecraft body frame, i.e., we express all rotations as rotations from the predicted spacecraft body frame. Denoting the quaternions/biernions of rotation with respect to this frame by $\bar{q}'$ where

$$\bar{q}'_k = \bar{q}_k \otimes \bar{q}_k^{-1}(-) , \tag{81}$$

it follows that

$$\bar{q}'_k(+) = \bar{1} + \Delta\bar{q}'_k(+) , \tag{82}$$

where $\bar{1} = [\,0 \quad 0 \quad 0 \quad 1\,]^T$ for quaternions, and $\bar{1} = [\,0 \quad 1\,]^T$ for biernions. If we write now

$$\delta\bar{q}_k(+) \equiv \bar{q}'_k(+) , \tag{83}$$

then it follows that

$$\bar{q}_k(+) = \delta\bar{q}_k(+) \otimes q_k(-) , \tag{84}$$

which is the so-called multiplicative correction. Thus, the distinction between the additive and the multiplicative formulations of the Kalman filter is not one of the fundamental mechanization of the filter but simply the frame in which it is desired to compute the update. These two formulations are present in Reference [19], where they are given the names "truncated covariance representation" and "body-fixed covariance representation." Admittedly, the presentation by those authors gave the appearance of there being one more distinct formulation of the Kalman filter than was actually the case. This has even led one careful study to test both formulations, as if they were distinct [22].

Where the important distinctions do lie is in how $\Delta\bar{q}_k$ or $\Delta\bar{q}'_k$ is calculated, and consequently, whether $\delta\bar{q}(+)$ has unit norm. From the earlier discussion it is clear that a correct

approach is obtained by expressing this quantity in terms of some representation of the attitude of minimal degree. In this case it is clearly advantageous to work from the spacecraft body frame so that this minimal-dimensional representation will be far from a singularity, and it will be most revealing to compare the results of References [19] and [20, 21] in that frame. The results of [20, 21], however, are not directly comparable to [19] because the former rests on the attitude Kalman filter of Bar-Itzhack and Oshman [23]. However, many points of commonality will be apparent.

Consider now the estimation of a constant biernion from scalar measurements of the form

$$z_k = \hat{\mathbf{u}}_k^T \mathbf{W}_k , \quad k = 1, \ldots , N , \tag{85}$$

where $\hat{\mathbf{u}}_k$ is a known direction in the spacecraft body and $\mathbf{W}_k$ is some vector measured in the body frame. We assume that $\mathbf{W}_k$ is related to a representation of the same vector in the inertial frame according to

$$\mathbf{W}_k = A \, \mathbf{V}_k + \mathbf{v}_k , \tag{86}$$

where A is the attitude matrix and $\mathbf{v}_k$ is white Gaussian noise. We wish to compute the batch attitude estimate from these measurements, using an good approximate estimate of the attitude as a point of departure.

If we write now

$$A = (\delta A) \, A_o , \tag{87}$$

where A_o is the approximate value of the optimal attitude estimate, then the measurement equation becomes

$$z_k = \hat{\mathbf{u}}_k^T (\delta A) \, \mathbf{W}_{o,k} + \hat{\mathbf{u}}_k^T \mathbf{v}_k , \tag{88}$$

where $\hat{\mathbf{W}}_{o,k} = A_o \mathbf{V}_k$, the expected value of the measurement in the body frame. δA is now an infinitesimal rotation, which we shall parameterize in terms of the additive biernion error as in equation (82). Recalling equation (17c) it is a simple manner to expand z_k to lowest order in $\Delta \bar{q}$ with the result

$$\nu_k \equiv z_k - z_{o,k} = H_k \, \Delta \bar{q} + v_k , \tag{89}$$

where $z_{o,k}$ is the value of the measurement with $\Delta \bar{q} = \bar{0}$, v_k is the scalar white Gaussian noise term appearing in equation (88) and the 1×2 sensitivity matrix H_k is given by

$$H_k = [\, H_{1,k} \quad H_{2,k} \,] = [\, (\hat{\mathbf{u}}_k \times \mathbf{W}_{o,k}) , \quad (\hat{\mathbf{u}}_k \cdot \mathbf{W}_{o,k}) \,] . \tag{90}$$

The maximum likelihood estimate of Δq (for the additive biernion correction, which is not constrained to preserve the norm) is given by

$$\Delta \bar{q}^*_{\text{add}} = P_{qq} \, \mathbf{p} , \tag{91}$$

where the covariance matrix, P_{qq}, and the information vector, $\mathbf{p}$, are given by

$$P_{qq} = \left[\sum_{k=1}^{N} H_k^T R_k^{-1} H_k \right]^{-1} , \quad \mathbf{p} = \sum_{k=1}^{N} H_k^T R_k^{-1} \nu_k . \tag{92}$$

For the multiplicative correction (which is norm-preserving) the estimate for the same data is

$$\Delta \bar{q}^*_{1,\text{mult}} = P_{\text{mult}} \, p_1 ,$$

with

$$P_{\text{mult}} = \left[\sum_{k=1}^{N} H_{1,k}^T R_k^{-1} H_{1,k}\right]^{-1} = \left(P_{qq}^{-1}\right)_{11}^{-1} , \tag{93a}$$

$$p_1 = \sum_{k=1}^{N} H_{1,k}^T R_k^{-1} \nu_k , \tag{93b}$$

so that p_1 is just the first component of p. Note that we have written unnecessary (but not incorrect) transpose signs and not commuted symbols, even between scalars, to preserve the resemblance with the equations of Space. We can find a relation between the additive and the multiplicative corrections to the biernion by solving for p in terms of $\Delta\bar{q}^*_{\text{add}}$ and using the value of p_1 in equation (93).

This leads to

$$\Delta\bar{q}^*_{1,\text{mult}} = \Delta\bar{q}^*_{1,\text{add}} + \left(P_{qq}^{-1}\right)_{11}^{-1} \left(P_{qq}^{-1}\right)_{12} \Delta\bar{q}^*_{2,\text{add}} . \tag{94}$$

We will return to this equation soon.

The additive correction, $\Delta\bar{q}^*_{\text{add}}$, allows us to construct an optimal biernion, $\bar{q}^*_{\text{add}}$,

$$\bar{q}^*_{\text{add}} = \bar{1} + \Delta\bar{q}^*_{\text{add}} . \tag{95}$$

Because it does not necessarily have unit norm, $\bar{q}^*_{\text{add}}$ does not without further effort have an unambiguous connection to the attitude. However, we note that although $\bar{q}^*_{\text{add}}$ is not a "biernion of rotation," it is a sufficient statistic [18] for the attitude, certainly within the linear approximation of equation (89). It is, in fact, an estimate of the biernion of rotation, and we know also that were the measurement noise covariance to vanish (perfect measurements), $\bar{q}^*_{\text{add}}$ would have unit norm and be the desired biernion. Thus, denoting the desired biernion of rotation by $\bar{\eta}$, we have that

$$\bar{q}^*_{\text{add}} = \bar{\eta} + \Delta\bar{\eta}_{\text{add}} , \tag{95}$$

and

$$\Delta\bar{\eta}_{\text{add}} \sim \mathcal{N}(0, P_{qq}) . \tag{96}$$

Hence, the negative log-likelihood function of $\bar{q}^*_{\text{add}}$ given $\bar{\eta}$ is

$$J(\bar{q}^*_{\text{add}} \mid \bar{\eta}) = \frac{1}{2}\left[(\bar{q}^*_{\text{add}} - \bar{\eta})^T P_{qq} (\bar{q}^*_{\text{add}} - \bar{\eta}) + \log\det P_{qq} + 4\log 2\pi\right] . \tag{97}$$

and the maximum-likelihood estimate of $\bar{\eta}$ is simply

$$\bar{\eta}^* = \arg \max_{\bar{\eta}\,:\,\bar{\eta}^T\bar{\eta}=1} J(\bar{q}^*_{\text{add}} \mid \bar{\eta}) , \tag{98}$$

where, since we know that the true biernion must lie on the manifold of unit four-vectors, we must maximize the negative log-likelihood subject to the norm constraint.

We handle the constraint in the usual way, using Lagrange's method of multipliers, and optimize

$$J(\bar{q}^*_{\text{add}} \mid \bar{\eta}) + \frac{1}{2}\lambda\bar{\eta}^T\bar{\eta}$$

without constraint and then choosing the value of the Lagrange multiplier, λ, for which the constraint is satisfied. Differentiating the above expression with respect to $\bar{\eta}$ and setting the derivative equal to zero leads to

$$\bar{\eta}^* = \left(I + \lambda P_{qq}\right)^{-1} \bar{q}^*_{\rm add} \,, \tag{99}$$

and λ is a solution of

$$f(\lambda) \equiv \bar{\eta}^{*T}(\lambda)\,\bar{\eta}(\lambda) = \bar{q}^{*T}_{\rm add}\left(I + \lambda P_{qq}\right)^{-2} \bar{q}^*_{\rm add} = 1 \,. \tag{100}$$

We expect λP_{qq} to be small. Therefore, it will usually be sufficient to calculate λ using one iteration of the Newton Raphson method with vanishing initial value. Thus,

$$\lambda \approx \frac{1 - f(0)}{f'(0)} = \frac{1}{2}\left(\bar{q}^{*T}_{\rm add}\, P_{qq}\, \bar{q}^*_{\rm add}\right)^{-1} \left(\bar{q}^{*T}_{\rm add}\, \bar{q}^*_{\rm add} - 1\right) \,. \tag{101}$$

To first order

$$\bar{q}^{*T}_{\rm add}\, \bar{q}^*_{\rm add} = 2\,\Delta q_2 \,. \tag{102}$$

Hence,

$$\lambda = \left(P_{qq}\right)^{-1}_{22} \Delta q_2 \,. \tag{103}$$

Substituting this in equation (99) leads to lowest order in $\Delta \bar{q}^*_{\rm add}$

$$\bar{\eta}^* = \left(I + \lambda P_{qq}\right)^{-1} \bar{q}^*_{\rm add} \tag{104a}$$

$$\approx \left(I - \lambda P_{qq}\right) \bar{q}^*_{\rm add} \tag{104b}$$

$$= \bar{q}^*_{\rm add} - \Delta q^*_{2,\rm add} \left(P_{qq}\right)^{-1}_{22} P_{qq}\, \bar{q}^*_{\rm add} \,. \tag{104c}$$

The first component of the desired optimal biernion is simply (to this same order)

$$\eta^*_1 = \Delta q^*_{1,\rm add} - \left(P_{qq}\right)^{-1}_{22} \left(P_{qq}\right)_{12} \Delta q^*_{2,\rm add} \,. \tag{105}$$

But

$$-\left(P_{qq}\right)_{12} \left(P_{qq}\right)^{-1}_{22} = \left(P^{-1}_{qq}\right)^{-1}_{11} \left(P^{-1}_{qq}\right)_{12} \,, \tag{106}$$

so that, in fact, comparing equation (106) with equation (94) we have

$$\eta^*_1 = \Delta q^*_{1,\rm mult} \,. \tag{107}$$

Since the other component must also agree to linear order in $\Delta q^*_{\rm mult}$, it follows that

$$\bar{\eta}^* = \delta \bar{q}_{\rm mult} \,. \tag{108}$$

Thus, the additive correction to the biernion, followed by the normalization correction *dictated unambiguously by the maximum likelihood criterion*, is identical (at least up to linear terms in $\Delta \bar{q}^*$) to the so-called multiplicative correction. It is hard to imagine that any other answer could be possible. It is obviously less burdensome to calculate the multiplicative correction

directly. Identical arguments hold for sequential correction of the biernion as in the Kalman filter.

Discussion

... my Lord has shewn me the intestines of all my countrymen in the Land of Two Dimensions ...

The representation of attitude in two dimensions has been described in detail. Two-dimensional analogues have been presented for the well known TRIAD and QUEST algorithms. General properties of attitude estimation in two and three dimensions have been discussed. The question of whether the multiplicative or additive correction to the quaternion is to preferred has been has a clear answer in Flatland.

The additive correction, if done correctly, is identical to the multiplicative correction but is much more burdensome. The first commandment of biernion correction (and, one can show, also for quaternion correction in Space), therefore, is to multiply. We emphasize that this result is not the product of some heuristic argument or arbitrary procedure to be justified by experiment but the unavoidable conclusion to which one is led unambiguously and rigorously by the maximum likelihood criterion.

Acknowledgements

"You see ... how little your words have done."

The author is grateful to F. Landis Markley and Itzhack Bar-Itzhack for many passionate discussions on this topic over the years.

References

[1] ABBOTT, E. A., "Flatland, a Romance of Many Dimensions," New York, Dover Publications, 1884.

[2] ALTMANN, S. L., *Rotations, Quaternions, and Double Groups*, Oxford, Oxford University Press, 1986.

[3] ALTMANN, S. L.., "Hamilton, Rodrigues, and the Quaternion Scandal," *Mathematics Magazine*, Vol. 62, pp. 291–307, 1989.

[4] VAN DER WAERDEN, B. L., *A History of Algebra*, New York and Heidelberg, Springer-Verlag, 1985.

[5] GOLDSTEIN, H., *Classical Mechanics*, Reading, Mass., Addison-Wesley, 1980.

[6] HUGHES, P. C., *Spacecraft Attitude Dynamics*, New York, John Wiley & Sons, 1986.

[7] JUNKINS, J. L., and TURNER, J. D., *Optimal Spacecraft Rotational Maneuvers*, Amsterdam, Elsevier, 1986.

[8] MARKLEY, F. L., " Parameterization of the Attitude," in WERTZ, J. R. (ed.) [9], *op. cit.*, pp. 410–420, 1978.

[9] WERTZ, J. R. (ed.), *Spacecraft Attitude Determination and Control*, Dordrecht, the Netherlands, Kluwer Academic Publishers, 1978.

[10] SHUSTER, M. D., "A Survey of Attitude Representations," *Journal of the Astronautical Sciences*, (to appear).

[11] BLACK, H. D., "A Passive System for Determining the Attitude of a Satellite," *AIAA Journal*, Vol. 2, pp. 1350–1351, 1964.

[12] SHUSTER, M. D., and OH, S. D., "Three-Axis Attitude Determination from Vector Observations," *Journal of Guidance, Control and Dynamics*, Vol. 4, No. 1, pp. 70–77, 1981.

[13] SHUSTER, M. D., "Attitude Determination in Higher Dimensions," *Journal of Guidance, Control and Dynamics*, (to appear).

[14] J. KEAT, "Analysis of Least Squares Attitude Determination Routine, DOAOP," Computer Sciences Corporation, CSC/TM-77/6034, February 1977.

[15] SHUSTER, M. D., "Maximum Likelihood Estimation of Spacecraft Attitude," *Journal of the Astronautical Sciences*, Vol. 37, 1989, pp. 79–88.

[16] MARKLEY, F. L., "Attitude Determination Using Vector Observations and the Singular Value Decomposition," *Journal of the Astronautical Sciences*, Vol. 36, pp. 245–258, 1988.

[17] MARKLEY, F. L., "Attitude Determination Using Vector Observations: A Fast Optimal Matrix Algorithm," Flight Mechanics/Estimation Theory Symposium, NASA Goddard Space Flight Center, Greenbelt, Maryland, May 5–7, 1992.

[18] SORENSON, H. W., *Parameter Estimation*, New York, Marcel Dekker, 1980.

[19] LEFFERTS, E. J., MARKLEY, F. L., and SHUSTER, M. D., "Kalman Filtering for Spacecraft Attitude Estimation," *Journal of Guidance, Control and Dynamics*, Vol. 5, No. 5, pp. 417–429, 1982.

[20] BAR-ITZHACK, I. Y., MARKLEY, F. L., and DEUTSCHMAN, J., "Quaternion Normalization in Additive EKF for Spacecraft Attitude Determination," *Flight Mechanics/Estimation Theory Symposium*, NASA Goddard Space Flight Center, May 1991.

[21] DEUTSCHMAN, J., MARKLEY, F. L., and BAR-ITZHACK, I. Y., "Quaternion Normalization in Spacecraft Attitude Determination," *Flight Mechanics/Estimation Theory Symposium*, NASA Goddard Space Flight Center, May 1992, and works cited therein.

[22] FERRARESI, V. A., *Utilização conjunta de sensores inerciais e não-inerciais em determinação de atitude de satélites via filtro de Kalman*, Instituto Nacional das Pesquisas Espaciais, Publicação No. INPE-4313-TDL/280, August 1987.

[23] BAR-ITZHACK, I. Y., and OSHMAN, Y., "Recursive Attitude Determination from Vector Observations: Quaternion Estimation," *IEEE Transactions on Aerospace and Electronics Systems*, Vol. 21, 1985, pp. 128–135.

RATE DETERMINATION FROM VECTOR OBSERVATIONS

By

Jerold L. Weiss

Ball Space Systems Division, Boulder CO

ABSTRACT

Vector observations are a common class of attitude data provided by a wide variety of attitude sensors. Attitude determination from vector observations is a well-understood process and numerous algorithms such as the TRIAD algorithm [Shuster] exist. These algorithms require measurement of the line of site (LOS) vector to reference objects and knowledge of the LOS directions in some predetermined reference frame. Once attitude is determined, it is a simple matter to synthesize vehicle rate using some form of lead-lag filter, and then use it for vehicle stabilization. Many situations arise, however, in which rate knowledge is required but knowledge of the nominal LOS directions are not available. This paper presents two methods for determining spacecraft angular rates from vector observations without apriori knowledge of the vector directions. The first approach uses an extended Kalman filter with a spacecraft dynamic model and a kinematic model representing the motion of the observed LOS vectors. The second approach uses a "differential" TRIAD algorithm to compute the incremental direction cosine matrix, from which vehicle rate is then derived.

1.0 INTRODUCTION

The development of small, light-weight, low-cost spacecraft that are reasonably complex requires an attitude determination and control system (ADCS) design in which the ADCS hardware supports more than a single operating mode or function. For example, a three axis magnetometer can be used in aiding reaction wheel desaturation and in support of coarse attitude determination; reaction control jets can be configured to provide both delta-V and control torques; and a horizon scanner that can be locked in place can support both spinning and 3-axis stabilized modes of operation.

The primary motivation for the work reported in this paper came from applying this principle to the following problem : Given a zero-net momentum ADCS that includes a 4π Sr sun sensor (used in a sun-seek safe mode), a 3 axis magnetometer (used in reaction wheel desaturation), and reaction control system (RCS) jets (used during orbit raising); provide a capability to detumble the spacecraft following large launch vehicle separation transients. Normally, this problem would be solved by adding a gyro package to the suite of ADCS hardware. The gyro data would be used to measure body rates that would be fed back to the RCS jets to detumble the spacecraft. However, to keep costs and weight down the gyro package is undesirable. The alternate solution that was developed was to use the existing hardware to measure the motion of the sun vector and the Earth's magnetic field vector and use this motion to (approximately) determine the vehicle's inertial rate. One way of accomplishing this would be to use an algorithm such as the TRIAD algorithm [Shuster] to compute the vehicle attitude and then determine rate with a lead-lag filter. However, this would require both a current vehicle ephemeris and an orbit propagator since the direction of the sun and magnetic field vector in a non-rotating earth-centered frame is required. The methods presented in this paper provide alternatives which do not require either an ephemeris or orbit propagator.

A secondary motivation for this work comes from recent gyro-failure problems on the Hubble Space Telescope. Currently, the redundant gyros on HST are working and will probably be used to stabilize the spacecraft for shuttle-capture during the upcoming repair mission. If the redundant gyros were to fail, however, a method of stabilizing the spacecraft using only star tracker data may be needed. The work presented in this paper could be used to stabilize a spacecraft using star tracker data without performing the complex star identification process.

The remainder of this paper is organized as follows. Section 2 develops a standard extended Kalman Filter (EKF) approach to the problem of estimating spacecraft rate using LOS vector observations without apriori knowledge of the LOS reference directions. Section 3 presents an alternative approach which is less accurate but computationally more efficient. This approach is based on the TRIAD algorithm and is called DTRIAD for "differential" TRIAD. Section 4 presents several simulation results using both methods and compares the rate determination accuracy and vehicle stabilization capability for the two methods. Finally, section 5 presents conclusions and suggestions for further work.

2.0 EXTENDED KALMAN FILTER (EKF)

The EKF approach applies the standard EKF equations [Gelb] to a system whose state is defined as the body-referenced angular rate vector, ω, augmented with the body-referenced vectors pointing to the n reference objects that are potentially observable, e_i, $i = 1 \ldots n$. The next two sections develop the state and covariance propagation and update equations . For clarity of presentation in the following, assume that $n = 2$.

2.1 State and Covariance Propagation

The nonlinear state dynamics are derived from Euler's equations and the well known expressions for the motion of vectors in a rotating frame. They are :

$$\dot{\omega} = I^{-1}\left\{N_{ext} - \omega \times (I\omega + h_{whl})\right\} \tag{1}$$

$$\dot{e}_i = -\omega \times e_i \quad i = 1 \ldots n \tag{2}$$

where N_{ext} is the vector of external torques applied to the vehicle, I is the vehicle's inertia matrix and h_{whl} is the stored momentum in reaction wheels (I includes the the inertias of the wheels; see [Wertz]). The implicit assumption in Eq. 2 is that the e_i are fixed in a non-rotating inertial reference frame.

At time t_k the EKF propagation step requires that these equations be integrated from time t_k to t_{k+1} using the updated estimate at time t_k as a starting point. Numerous integration methods are available (Runge-Kutta, Forward/Backward Euler, Trapezoidal) each with its own merits (e.g., see [Hildebrand]). When the sample rate is fast and the magnitude of of ω is small, the simplest method is Forward Euler or rectangular integration. This method will be used in Section 4.0 to demonstrate results.

In addition to propagation of the state vector, the EKF must propagate the state covariance matrix. The typical approach is to assume small deviations of the state from the estimate between t_k to t_{k+1}. This implies that the linearized

equations of motion adequately represent the error dynamics and can therefore be used to form the Lyapunov equation that represents the dynamics of the covariance matrix. For this problem, the linearized dynamics are :

$$\delta\dot{x} = \begin{bmatrix} \Phi(\omega) & 0 & 0 \\ \Omega(e_1) & \Omega(\omega) & 0 \\ \Omega(e_2) & 0 & \Omega(\omega) \end{bmatrix} \delta x + \begin{bmatrix} I^{-1} \\ 0 \\ 0 \end{bmatrix} w \tag{3}$$

or

$$d\delta x/dt = A\delta x + Bw$$

where,

$$\delta x = \begin{bmatrix} \omega - \hat{\omega} \\ e_1 - \hat{e}_1 \\ e_2 - \hat{e}_2 \end{bmatrix} \qquad \Phi(\omega) = -\begin{bmatrix} 0 & \frac{I_z - I_y}{I_x}\omega_z - h_z & \frac{I_z - I_y}{I_x}\omega_y + h_y \\ \frac{I_z - I_x}{I_y}\omega_z - h_z & 0 & \frac{I_z - I_x}{I_y}\omega_x + h_x \\ \frac{I_y - I_x}{I_z}\omega_y + h_y & \frac{I_y - I_x}{I_z}\omega_x - h_x & 0 \end{bmatrix} \qquad \Omega(\zeta) = \begin{bmatrix} 0 & \zeta_z & -\zeta_y \\ -\zeta_z & 0 & \zeta_x \\ \zeta_y & -\zeta_x & 0 \end{bmatrix}$$

and where we have assumed a diagonal inertia matrix, I. The extension to nondiagonal inertia matrices and to $n > 2$ is straightforward. The 3x1 process noise vector, w, is assumed to be a zero mean white Gaussian noise process with covariance matrix Q. It is intended to represent the uncertainty in N_{ext} but is also used to represent expected errors in the integration process for state propagation.

Given the linearized perturbation equation (3), the covariance propagation equation is the standard Lyapunov equation :

$$dP/dt = AP + PA^T + BQB^T \tag{4}$$

where P is the covariance matrix of perturbation state δx and A and B are evaluated at $\hat{x}(k)$. This can be solved by any number of methods. A common simple approach [Jazwinski] that works well in practice is to discretize (3) and use the discrete Lyapunov formulation, viz.

$$P^-(k+1) = F\,P^+(k)\,F^T + GQG^T \tag{5}$$

where $F = I + A\Delta$, $G = B\Delta$, $P^-(k+1)$ is the covariance matrix at time t_{k+1} before updating with measurements at time t_{k+1}, $P^+(k)$ is the covariance matrix at t_k after updating with measurements at time t_k and $\Delta = t_{k+1} - t_k$. Another simple approach is to integrate Eq. (4) using forward Euler integration.

2.2 State Update

The second step in the EKF approach updates the state estimate based on measurements and requires an observation equation that relates the measurements to the states. The actual observation equation depends on the type of sensor being used. For example, a vector magnetometer directly measures the earth's magnetic field vector resulting in the simplest measurement equation

$$y = e_i + v \tag{6}$$

where v is the measurement error.* A two-axis sun sensor or a star tracker, however, produces two measurements that are, in general, a nonlinear function of e_i (e.g., two components of the orthogonal projection of e_i onto an image plane). In these cases, it is a straightforward matter to derive the general nonlinear observation equation

$$y = h(e_i) + v \tag{7}$$

and to determine the Jacobian matrix $H = \delta y/\delta e_i$. The standard EKF update equations are then

$$P^+(k) = \left\{P^-(k)^{-1} + H^T R^{-1} H\right\}^{-1} \tag{8}$$

$$K = P^+(k)\, H^T R^{-1} \tag{9}$$

$$\hat{x}(k) = \bar{x}(k) + K\left[y - h(\bar{e}_i(k))\right] \tag{10}$$

where $\bar{x}(k)$ is the result of integrating Eq. 's (1) and (2) forward from t_{k-1} to t_k starting at $\hat{x}(k-1)$, the $\bar{e}_i(k)$ are the reference vector components of $\bar{x}(k)$, and R is the covariance matrix of v. The inverse formulation for the covariance matrix is used here to avoid numerical problems in the subsequent simulations. It is not the fastest implementation (e.g., see [Bierman]). Further work is needed to establish the best scaling and covariance update method for this problem. Note that the option of transforming the nonlinear measurements into a vector observation and then employing (6) as the measurement equation was not considered since the correct corresponding value of R is singular. When R is singular, P^+ can become singular, [Gelb] and K can not be calculated. If the transformation method is used, an approximate nonsingular R matrix should be used (e.g., R_{ii} = arcsine(angle error)).

* Strictly speaking, the earth's magnetic field violates the assumption that the vector e_i be fixed in a nonrotating inertial frame since the direction varies as the spacecraft orbits the earth. The resulting rate errors are insignificant in several applications.

2.3 Implementation Notes

(1) The EKF as described above must be initialized with a state and covariance estimate. The method described in the next section is an excellent and simple way to obtain an initial state estimate. Further work is needed to derive the corresponding initial covariance estimate corresponding to this state-initialization method.

(2) Choice of sample rate, Δ, depends on accuracy requirements and is influenced by the magnitude of the vehicle angular rate, ω, and applied torques, N_{ext} and by processing resources.

(3) While Q is normally used to represent uncertainty in N_{ext} it should also account for the errors made in integrating the state equations (1) and (2). As with most EKFs, it is likely that some degree of tuning of the parameter Q will be needed.

(4) The covariance update equation (8) as written requires inversion of a $3n+3 \times 3n+3$ matrix. As mentioned, this is not the most efficient propagation equation. The experience gained so far with simulation of this approach suggests that the covariance matrix P and hence the Kalman gain K converge to steady state values that are a function of the problem geometry (angle between the vectors e_1 and e_2). The rate of convergence appears to be dependent on vehicle rate. These results suggest that for constant problem geometry a constant gain EKF (which does not require on-line covariance propagation or update) might provide satisfactory performance.

(5) While it is clear that the angular rate vector is not completely observable when $n = 1$, the EKF equations can still be executed in this case. If a good estimate of ω is initially available, then the result should be that the component of the rate estimate that is aligned with $e_1$has a random walk error behavior. This is a convenient feature in cases where sensor dropouts occasionally occur.

(6) Measurement biases and sensor misalignments will not affect rate determination accuracy (for this method or the one presented in the next section) since neither affects the change in LOS measurements from one time to the next.

3.0 DIFFERENTIAL TRIAD APPROACH

While the EKF approach described in Section 2 provides near-optimal solutions and can operate, with reduced accuracy, when n=1, the computational complexity of the algorithm can be relatively large for the current generation of spacecraft flight computers. The approach discussed in this section provides a simpler alternative.

The idea for this approach comes from the basic strapdown equations of motion for the direction cosine matrix, A, [Wertz],

(11) $$\dot{A} = \Omega(\omega) A$$

Assuming that ω is constant over the interval t_k to t_{k+1},

(12) $$A(t_{k+1}) = e^{\Omega(\omega)\Delta} A(t_k)$$

(13) $$A' = A(t_{k+1}) A(t_k)^T = e^{\Omega(\omega)\Delta}$$

which implies that knowledge of the direction cosine matrix representing the transformation from the vehicle attitude at time t_k to time t_{k+1} (A') is sufficient for determining ω.

The TRIAD algorithm [Shuster, Wertz] is a well known method for determining the direction cosine matrix from vector observations assuming that the direction of the vector observations in some arbitrary reference frame is known. If this reference frame is the vehicle's attitude at time t_k then it is clear that the TRIAD algorithm produces the matrix A' from which the vehicle body rate can be derived. Let $e_i^m(k)$, $i=1,2$ be the measured vectors to two reference objects at time k. The "Differential TRIAD" (DTRIAD) approach to rate determination is as follows :

(Step 1) Form the "reference" matrix A_r from

$$A_r = \left[e_1^m(k) \;\vdots\; e_1^m(k) \times e_2^m(k) \;\vdots\; e_1^m(k) \times \left(e_1^m(k) \times e_2^m(k) \right) \right] \tag{14}$$

(Step 2) Form the "observation" matrix

$$A_m = \left[e_1^m(k+1) \;\vdots\; e_1^m(k+1) \times e_2^m(k+1) \;\vdots\; e_1^m(k+1) \times \left(e_1^m(k+1) \times e_2^m(k+1) \right) \right] \tag{15}$$

(Step 3) Compute $A' = A_m A_r^T$.

(Step 4) Solve (13) for ω. If the magnitude of $\Delta\omega$ is sufficiently small, then the identity

$$A' = I + \Omega(\omega)\Delta \tag{16}$$

makes this step straightforward. As the magnitude of $\Delta\omega$ increases, one can expand (13) in the standard power series and solve the polynomial equations that result; or one can reduce Δ until acceptable accuracy is achieved with (16). These steps are repeated at every t_k . Recognizing that $A_r(k) = A_m(k-1)$, we see that at each time t_k, only steps 2 - 4 need to be repeated.

The performance of the DTRIAD algorithm, like the performance of TRIAD, depends on problem geometry. The accuracy of the rate estimate in the direction which bisects the two reference vectors is the least accurate and can be estimated using standard methods. Like the EKF, performance will degrade with large values of $\Delta\omega$. Unlike the EKF, however, degradation of the estimate will also occur when large external torques are applied. Also, like the EKF, measurement biases and sensor misalignments will not affect the rate determination accuracy.

4.0 SIMULATION RESULTS

This section presents two simulation cases to demonstrate performance of the two algorithms. The first case assumes that the vehicle is tumbling at a relatively high rate (say ~10 deg/sec resulting from an open loop despin operation

following an SRM firing) and that continuous measurement of the Earth's magnetic field and the solar vector are available. For this case, we show both the accuracy of the two rate determination methods and the resulting tumble recovery capability assuming a feedback control law using reaction control jets. The second case assumes that the vehicle is slowly tumbling (say ~1deg/sec as the result momentum accumulation due to external disturbances and wheel run-down following the failure of primary attitude control gyros) and that continuous tracking of stellar objects from a star tracker are available. In this case, we show the rate stabilization capability using both methods and reaction wheels for control. In all cases the EKF is initialized by adding a small error to the true state. In practice, the EKF is initialized using the DTRIAD algorithm. All the simulations presented herein are full nonlinear 3 degree of freedom simulations that use 6'th-order Runge-Kutta integration to solve Eq. 1 along with the standard quaternion kinematic equations.

4.1 High-rate Tumble Recovery using Sun Sensor and Magnetometer Data

For the purposes of this simulation, we assume that both the sun sensor and the magnetometer provide measurements of reference vectors (i.e., Eq. (6) applies). It is assumed that the sun vector measurement is corrupted by a constant bias corresponding to a 1 degree rotation of the true sun vector and a white noise whose magnitude corresponds to 0.25 degrees error (i.e., $R = (.25*\pi/180)^2*E$, where E is the identity matrix). The magnetic field vector measurement is also corrupted by a 1 deg rotation bias and a white noise with a standard deviation of 9 nano Tesla (about 1 part in 25 for low earth orbits). The sensor errors correspond to commonplace sensor capabilities. The 1 degree bias error in the magnetometer vector includes errors due to electronic bias and misalignments of the sensor. The sun sensor bias error includes electronic bias, misalignments and Earth albedo effects (albedo effects are significant only for non-imaging cosine-law sun detectors).

Figure 1 shows the body rate profile and EKF-estimated rates for a vehicle with diagonal inertia matrix I = diag([156 85 186]) kg-m^2 and a 10Hz update rate (Δ=0.1). **Figure 2** shows the corresponding EKF and DTRIAD rate errors. The EKF produces superior results due to the inclusion of a dynamic model which allows filtering to take place.*

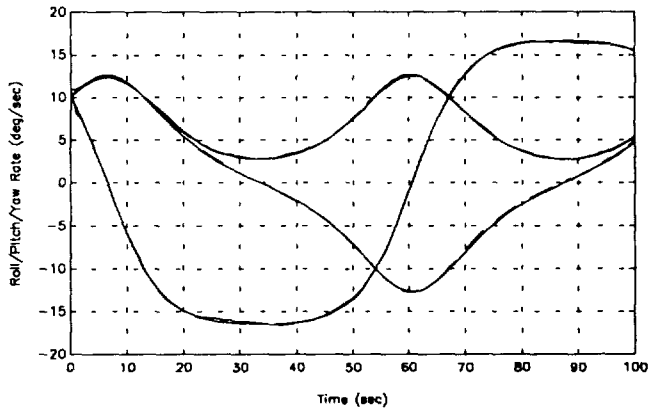

Fig. 1 - Actual and EKF-Estimated Body Rates; N_{ext} = 0, Δ=0.1

* This result is somewhat artificial since a dynamic model can be used to form a simple filter (Kalman or otherwise) with the DTRIAD rate estimates used as "measurements".

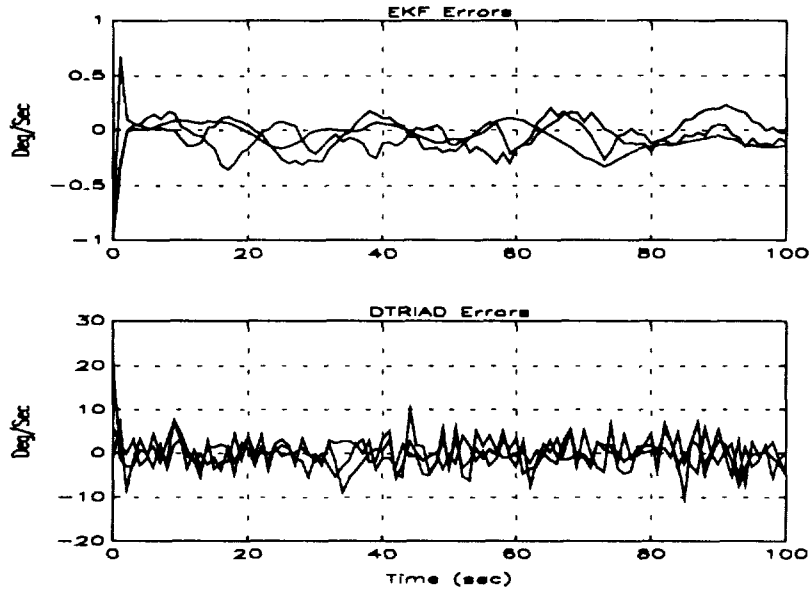

Fig. 2 - EKF and DTRIAD Estimation Errors For Fig. 1 Rates.

Figure 3 shows the result when the EKF-determined rates are fed back to a reaction control system to stabilize the vehicle. In this simulation, it is assumed that the control system operations at a sample rate of 2Hz and that the reaction control jets are pulse-width-modulated using the standard impulse-matching algorithms. The thruster torques available in each axis are 1.1Nm in roll 0.86Nm in pitch and 0.23 Nm in yaw. The jet pulse times are quantized in 20msec increments. **Figure 4** shows the feedback response using the DTRIAD algorithm with all other parameters the same as for Fig. 3. The EKF is substanitally better than DTRIAD in this case because it includes a dynamics model that allows it to predict spacecraft motion based on applied RCS jet torques.

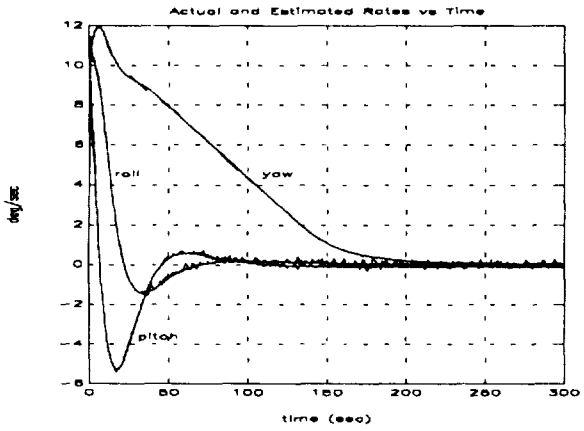

Fig. 3 - Actual and Estimated Rates during Tumble Recover EKF Feedback. Δ=0.5, $N_{ext} = g\omega$.

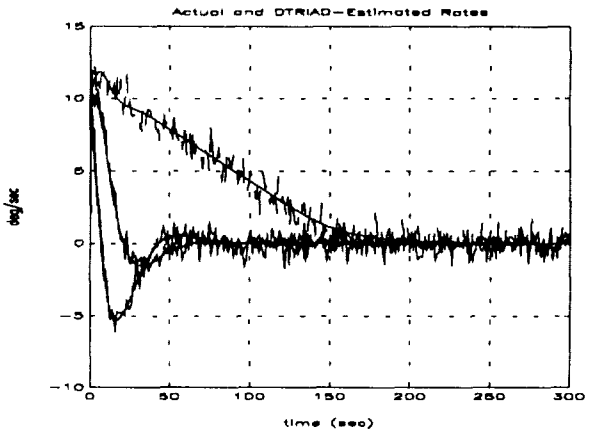

Fig. 4 - Actual and Estimated Rates during Tumble Recovery with DTRIAD Feedback. Δ=0.5, $N_{ext} = g\omega$.

4.2 Low Rate Stabilization using Star-Tracker Data

In this simulation we assume that the star trackers provide reference vector measurements (Eq. 6 applies again). Two "guide star" measurements are used. They are separated by 5 deg and corrupted by a 6 arcsec noise-equivalent angle (typical values). For these simulations, the spacecraft inertia properties correspond to a large platform (I = diag([1000;1000;2000]) kg-m^2) and control is provided by large reaction wheels (0.8Nm torque capability). In all simulations a 2 Hz sample rate is used and the initial total angular rate is 0.5 deg/sec.

Figure 5 shows the magnitude of the vehicle rate and the rate errors using the DTRIAD algorithm. The 0.5 deg/sec rate error is damped in about 50 seconds and the RMS residual rate is between 0.0001 and 0.002 deg/sec per axis. **Figure 6** shows the rate magnitude and rate errors using the EKF. The damping time constant is the same as DTRIAD (the control gains are the same) and the RMS residual rate is between 0.00003 and .0002 deg/sec, much smaller than DTRIAD. The smaller residual rate is due to the better rate prediction accuracy which is due to the incorporation of applied torques in the EKF rate prediction algorithm.

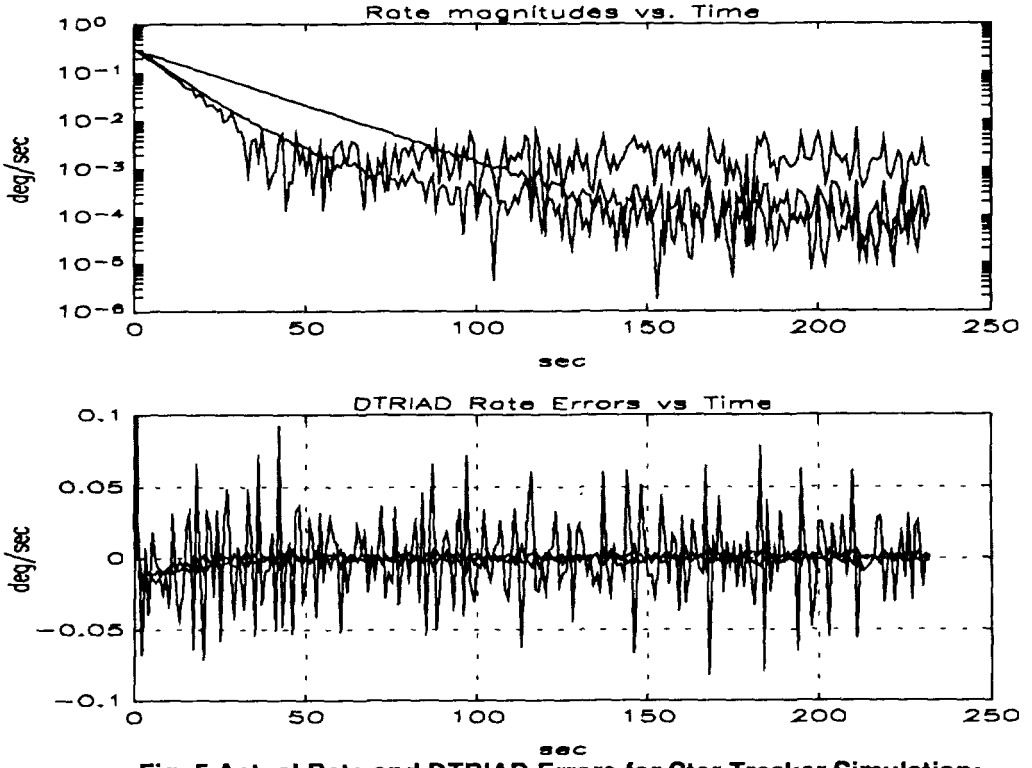

Fig. 5 Actual Rate and DTRIAD Errors for Star Tracker Simulation; $\Delta = 0.5$ and $N_{ext} = g\omega$.

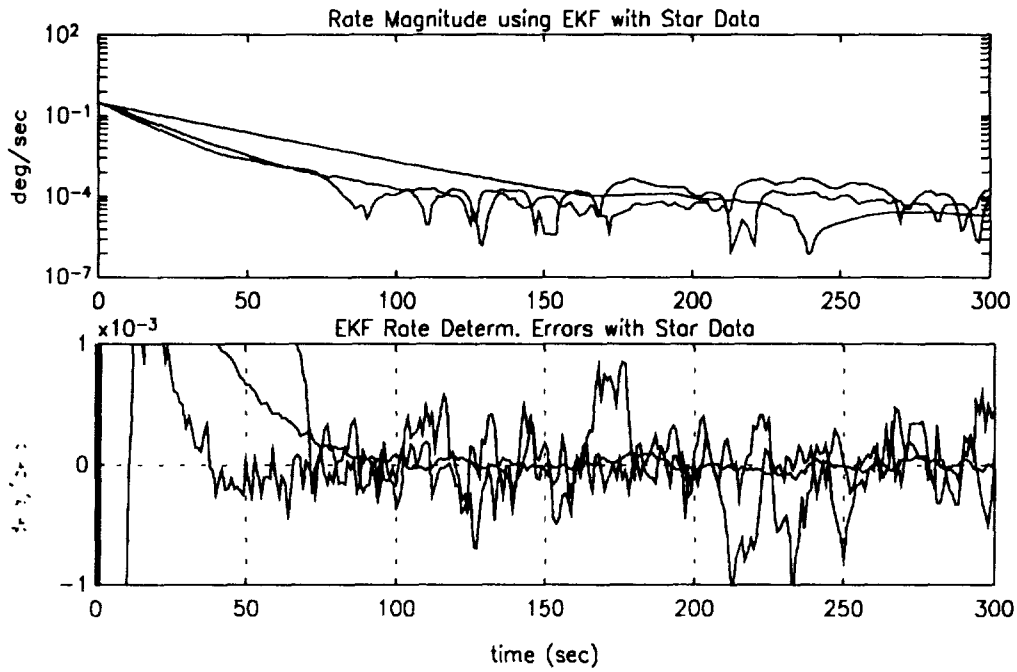

Fig. 6 - Actual Rate and EKF Errors Errors For Star Tracker Simulation; Δ = 0.5 and $N_{ext} = g\omega$.

5.0 CONCLUSIONS

Two methods of computing the body-referenced angular rate vector from vector observations without knowledge of the LOS vector directions in inertial space have been presented. The EKF approach is based on spacecraft dynamics models and the rotational kinematics of the observed reference vectors. The DTRIAD approach uses the TRIAD algorithm to compute incremental direction cosine matrices from which approximate rate is derived. The EKF is computationally more complex but produces superior estimates, especially in the presence of large control torques. Further work is needed to provide analytic bounds on accuracy for both methods, to determine the best covariance update implementation, and to determine the feasibility of using a constant gain EKF.

REFERENCES

Bierman, G.J., Factorization Methods for Discrete Sequential Estimation, Academic Press, N.Y., 1977.

Gelb, A., ed., Applied Optimal Estimation Theory, MIT Press, 1974.

Hildebrand, F. B., Introduction to Numerical Analysis, Second Edition, McGraw Hill, N.Y., 1982.

Jazwinski, A. H., Stochastic Processes and Filtering Theory, Academic Press, N.Y., 1970.

Shuster, M. and S.D. Oh, "Three Axis Attitude Determination from Vector Observations", J. Guidance and Control, Vol. 4, No. 1, 1981.

Wertz, J. ed., Spacecraft Attitude Determination and Control, Kluwer Academic Publishers, Boston, 1978.

A Multimission Three-Axis Stabilized Spacecraft Flight Dynamics Ground Support System*

J. Langston, K. Krack, and W. Reupke
COMPUTER SCIENCES CORPORATION (CSC)

ABSTRACT

The Multimission Three-Axis Stabilized Spacecraft (MTASS) Flight Dynamics Support System (FDSS) has been developed in an effort to minimize the costs of ground support systems. Unlike single-purpose ground support systems, which attempt to reduce costs by reusing software specifically developed for previous missions, the multimission support system is an intermediate step in the progression to a fully generalized mission support system in which numerous missions may be served by one general system. The benefits of multimission attitude ground support systems extend not only to the software design and coding process, but to the entire system environment, from specification through testing, simulation, operations, and maintenance.

This paper reports the application of an MTASS FDSS to multiple scientific satellite missions. The satellites are the Upper Atmosphere Research Satellite (UARS), the Extreme Ultraviolet Explorer (EUVE), and the Solar Anomalous Magnetospheric Particle Explorer (SAMPEX). Both UARS and EUVE use the multimission modular spacecraft (MMS) concept. SAMPEX is part of the Small Explorer (SMEX) series and uses a much simpler set of attitude sensors. This paper centers on algorithm and design concepts for a multimission system and discusses flight experience from UARS.

* This work was supported by the National Aeronautics and Space Administration (NASA)/Goddard Space Flight Center (GSFC), Greenbelt, Maryland, Contract NAS 5-31500.

1. INTRODUCTION

In 1987 the Upper Atmosphere Research Satellite (UARS) Attitude Ground Support System (AGSS) was being specified for Goddard Space Flight Center (GSFC). At this time the specifications support started for another mission, the Extreme Ultraviolet Explorer (EUVE). During the initial requirements analysis for EUVE, it was realized that UARS and EUVE were very similar in both hardware configuration and support requirements. The decision was made to generalize the UARS software specifications to include the EUVE support requirements.

Flight Dynamics Division (FDD) attitude support falls into three categories: attitude determination, attitude sensor calibration, and prediction of flight dynamics-related parameters that are used for mission and science planning. A typical AGSS is composed of many functions, but can be broken down into six areas: telemetry processing, data adjustment, attitude determination, sensor calibration, sensor monitoring, and planning aids prediction.

Data come into the system as spacecraft telemetry. The telemetry processing function unpacks and time tags the data and passes them to the next function, data adjustment. The data adjustment function corrects the data for known misalignments and biases and applies validation tests to reject bad data. The adjusted data are then ready for the attitude determination and sensor calibration functions.

There is usually more than one attitude determination function to support different levels of accuracy and response time. Also, there is a sensor calibration function for each calibration parameter being computed. The attitude determination and sensor calibration results are usually delivered to the spacecraft control center for uplink to the spacecraft in support of onboard attitude determination. The sensor monitoring function is an analysis aid that supports sensor performance evaluations.

The planning aids prediction function is a collection of functions for the production of mission and science planning aids. Some of these planning aids are mission-unique, but many are meant to meet similar requirements for a variety of missions. The common planning aids include guide star interference predictions, antenna contact times, spacecraft range predictions, and solar array position predictions.

The multimission concept is an intermediate step in the progression to a generalized mission support system in which numerous missions may be served by one general system. Multimission systems are useful when generalized systems are not available or cannot be fully achieved. The benefits of multimission systems extend not only to the software design and coding process but to the entire system environment, from specification through testing, training, operations, and maintenance.

The Multimission Three-Axis Stabilized Spacecraft (MTASS) Flight Dynamics Support System (FDSS), referred to as MTASS in the remainder of this paper, is an institutional system that provides key functions required for spacecraft attitude ground support (see Reference 1). The AGSS for a specific mission is composed of mission-specific functions in combination with MTASS.

2. SYSTEM DEVELOPMENT

This section deals with the specification and design aspects of the MTASS systems development process.

2.1 Specifications

In the requirements analysis and functional specifications phase, the inherent commonality of the UARS and EUVE modular attitude determination and control systems influenced our approach. Since the EUVE AGSS was regarded, to first order, as a subset of the UARS AGSS, the UARS requirements and functional specifications were generalized to include the EUVE requirements.

During the generalization of the UARS specifications, it became clear that, with minimal extra effort, the specifications could be generalized much further than simply necessary to support two missions. During every step of the specifications support, ways were investigated to generalize the system as far as possible. As an example, spacecraft attitude is usually represented as a set of roll, pitch, and yaw angles with respect to some reference coordinate system. The most straightforward approach to producing a two-spacecraft system would be to specify an "If UARS...if EUVE..." type of construction to define the coordinate system. This method is obviously a dead-end that does not allow for other mission definitions. Instead, the specifications allow the user to specify the transformation Euler sequence and the reference coordinate system. This approach makes the system configurable and usable for any mission. Through this approach to generalization, MTASS was born.

To go beyond the reuse seen in previous ground systems, it was recognized that reuse on the subsystem level was required. Each of the functions described above have traditionally been implemented as separate subsystems; however, each subsystem was coded to be mission-specific with, at best, reuse of low-level software units. The MTASS concept was to organize the generic and mission-specific functions into separate subsystems, thereby allowing reuse of higher-level functions and entire subsystems. MTASS specified only generic algorithms for a given subsystem and thereby built up generic subsystems. Those algorithms that were unavoidably mission-unique were segregated into separate subsystems.

2.2 Design Considerations

This section reviews MTASS design considerations and shows that the design is sensor-oriented, MTASS is table-driven, the files are sensor-oriented, and the design is extensible.

2.2.1 MTASS Design Is Sensor-Oriented

The traditional functional approach to the design of MTASS was supplemented successfully with sensor/actuator-oriented thinking and software partitioning. Although object-oriented design techniques were not employed, the design partitioning was conceived with sensors as the design objects within each major functional partition (i.e., subsystem). The sensor-oriented partitioning lies along the intermediate level in that each subsystem contains software packages for each type of sensor and actuator appropriate to the subsystem function.

For example, the data adjustment subsystem (DA) is a major functional partition that prepares the engineering data for attitude determination and other functions by applying calibration parameters (biases and misalignments), smoothing, and performing a few cross-sensor validation checks. The major portion of the DA is the application of calibration parameters. This function is partitioned by sensor type, resulting in a separate software package for the fine Sun sensor (FSS), the three-axis magnetometer (TAM)/magnetic torquer assembly (MTA), the inertial reference unit (IRU), etc.

Table 1 contains an entry for each of the MTASS subsystems. Each entry includes the subsystem function, operating mode, and selectable subfunctions.

2.2.2 MTASS Is Table-Driven

Each MTASS subsystem has user-supplied configuration parameters that specify which sensors are present on a particular spacecraft, in a particular telemetry format, or needed for a particular operational scenario. Using these parameters, subsystems can be configured to support any three-axis stabilized spacecraft that contains a subset of the currently supported hardware and for which the engineering data are supplied in the MTASS formats. The one restriction is that IRU data are required for attitude determination using the MTASS coarse and fine attitude determination subsystem (CFADS), which employs a differential correction least-squares fit and uses body rates from the IRU data to propagate. This restriction will be alleviated when a new single-frame attitude determination subsystem, which employs the QUEST algorithm, is completed.

Table 1. MTASS Subsystems and Selectable Subfunctions (1 of 2)

SUBSYSTEMS	FUNCTION
ATTITUDE DETERMINATION SYSTEM (ADS) EXECUTIVE (ADSEXEC)	• ALLOW SELECTION OF INTERACTIVE ADS SUBSYSTEMS: MISSION SPECIFIC TELEMETRY PROCESSOR (TP), DA, STARID, DS, CFADS, DADS (ALSO OPERATES IN BATCH MODE)
DATA ADJUSTMENT (DA)	• APPLY MISALIGNMENTS AND/OR BIASES TO: (A) COARSE SUN SENSORS (UP TO 2 CSSs) (B) EARTH SENSOR ASSEMBLIES (UP TO 2 ESAs) (C) FIXED HEAD STAR TRACKERS (UP TO 2 FHSTs) (D) FINE SUN SENSOR (UP TO 1 FSS) (E) INERTIAL REFERENCE UNIT (UP TO 1 IRU) (F) THREE-AXIS MAGNETOMETER (UP TO 2 TAMs, OPTIONALLY INCLUDING EFFECTS FROM MAGNETIC TORQUER ASSEMBLIES (MTAs)) • OPTIONALLY SMOOTH BODY RATES FROM IRU • OPTIONALLY VALIDATE DATA USING DOT PRODUCT CHECKS
STAR IDENTIFICATION (STARID)	• USE TRIPLET, DOUBLET, SINGLE MATCH (STARID) HIERARCHY TO IDENTIFY STAR OBSERVATIONS FROM FHST AGAINST STAR CATALOG
COARSE/FINE ATTITUDE DETERMINATION (CFADS)	• DETERMINE SPACECRAFT ATTITUDE USING BATCH LEAST-SQUARES DIFFERENTIAL CORRECTION TECHNIQUE (NOTE: REQUIRES IRU) • PRECISION OF ATTITUDE SOLUTION IS DETERMINED BY SELECTION OF SENSOR DATA ADJUSTED BY THE DA • OPTIONALLY CALCULATE TAM BIASES • OPTIONALLY WRITE ATTITUDES AT AN EPOCH TIME AND/OR A SPECIFIED DELTA TIME, AND/OR WRITE ATTITUDE RATES AT THE SPECIFIED DELTA TIME
DATA SEGMENTER (DS)	• DETERMINE OPTIMUM/SUITABLE TIMESPANS TO ENSURE IRU DATA ARE AVAILABLE AND LOCATE FHST OBSERVATIONS NEAR BATCH BOUNDARIES FOR BEST PRECISION IN CFADS
DEFINITIVE ATTITUDE DETERMINATION (DADS)	• USE ATTITUDE PROPAGATION AND CORRECTION TO FORCE MULTIPLE SEQUENTIAL BATCHES OF CONTINUOUS ATTITUDES TO MATCH AT BATCH BOUNDARIES FOR CONTINUOUS ATTITUDES
GRAPHICS USER INTERFACE (GUI)	• ALLOW SELECTION OF INTERACTIVE CALIBRATION AND ATTITUDE VALIDATION SUBSYSTEMS • MAINTAIN AND REPORT CALIBRATION PARAMETERS FROM SENSOR CALIBRATION FILES • MANUALLY LOG AND REPORT MESSAGES IN ACTIVITIES LOG FILE(S)
ATTITUDE VALIDATION (ATTVAL)	• COMPARE PAIRWISE THE OBC-COMPUTED ATTITUDE, THE PREDICTED ATTITUDE, AND THE GROUND-DETERMINED ATTITUDE • EXAMINE ATTITUDES FROM INDIVIDUAL SOURCES
INERTIAL REFERENCE UNIT CALIBRATION (IRUCAL)	• CALIBRATE IRUs BY CONFIGURATION
FINE SUN SENSOR, EARTH SENSOR, FIXED–HEAD STAR TRACKER CALIBRATION (FEFCAL)	• CALIBRATE FSSs, ESAs, FHSTs

Table 1. MTASS Subsystems and Selectable Subfunctions (2 of 2)

SUBSYSTEMS	FUNCTION
FINE SUN SENSOR FIELD OF VIEW CALIBRATION (FSSFOV)	• CALIBRATE FSS FIELD OF VIEW
THREE-AXIS MAGNETOMETER CALIBRATION (TAMCAL)	• CALIBRATE TAMS
BATCH MODE SUBSYSTEMS	• FOLLOWING SUBSYSTEMS ARE OPERATED IN BATCH MODE ONLY AND ARE INDIVIDUALLY SUBMITTED FOR EXECUTION
(UARS) STS ATTACHED MONITOR (UMON)	• GENERATE DISPLAY FOR CCTV DISTRIBUTION OF SPACECRAFT PARAMETERS INCLUDING ONBOARD ATTITUDE AND STS PARAMETERS DURING DEPLOYMENT FROM STS
ATTITUDE PREDICTION (ATTPRED)	• PREDICT ATTITUDES
HIGH-GAIN ANTENNA, TDRSS CONTACT PREDICTION (HGA)	• PREDICT POTENTIAL CONTACT TIMES BETWEEN HGA AND TDRSS
GUIDE STAR OCCULTATION PREDICTION (GSOC)	• PREDICT WHEN GUIDE STARS ARE OCCULTED BY THE EARTH, MOON, AND PLANETS
ORBIT VALIDATION (UTEP)	• CONVERT OBC-DETERMINED SPACECRAFT POSITION TO STANDARD CODE 500 EPHEMERIS FILE FORMAT FOR SUBSEQUENT COMPARISON WITH GROUND-DETERMINED AND PREDICTED ORBIT VECTORS USING INSTITUTIONAL SOFTWARE
CALIBRATION DELIVERY FORMATTING (CALFORM)	• SELECT AND CONVERT CALIBRATIONS FOR FORMATTING (ULTIMATE USE AS UPLOAD TO OBC)
PRODUCT DELIVERY FORMATTING (DELFORM)	• PACK DELIVERY RECORDS INTO STANDARD CODE 550 PRODUCT DELIVERY FORMAT

2.2.3 MTASS Files Are Sensor-Oriented

Another crucial aspect of the MTASS design is the organization of the primary data interfaces. They are the engineering data sets data base (EDS), processed engineering data sets data base (PEDS), attitude history files (AHFs), and sensor calibration files (SCFs). Table 2 contains a functional description of each of the major file types unique to MTASS. MTASS also uses the institutional spacecraft ephemeris, solar/lunar/planetary (SLP) ephemeris, activities log, report data base, MMS star catalog, and tracking station geodetics file types.

The primary spacecraft data input to MTASS is through the EDS. The EDS is an MTASS-specific data base of spacecraft engineering data produced by a mission-specific telemetry processing (TP) subsystem. The EDS is a collection of engineering data sets tied together by an EDS directory data set.

Each individual engineering data set contains batches of engineering data corresponding to one sensor or actuator. Each batch is user definable, but nominally corresponds to the data processed in one session from one telemetry transmission. The user can delete and overwrite the oldest batches, add new batches, or concatenate data to the most recent batch. The directory data set contains summary information for each batch, including which sensors are in the batch.

The specific subset of engineering data sets included in a given EDS is definable by the user when that EDS is initialized. Further, the specific sub-subset of engineering data sets included in a given batch is definable at run time. Using these options, an EDS can be initialized that can contain data from only those sensors and actuators that are desired for a specific operational scenario using a specific spacecraft telemetry mode. Alternatively, an EDS can be initialized that can contain data from all of the sensors and actuators on a given spacecraft, and a given batch can contain data only for those sensors involved in a specific operational scenario.

Table 2. MTASS Data Sets

SUBSYSTEM	FUNCTION
ATTITUDE HISTORY FILE	• QUATERNIONS, EULER ANGLE RATES
ENGINEERING DATA SET (EDS) DIRECTORY FILE	• GENERAL DATA FOR EACH BATCH (HEADERS)
EDS FSS	• FSS ALPHA, BETA ANGLE COUNTS
EDS ESA	• ESA PITCH, ROLL ANGLES
EDS FHST	• FHST H AND V COUNTS AND INTENSITY
EDS TAM	• MAGNETIC FIELD VECTOR
EDS IRU	• IRU ACCUMULATED ANGLES
EDS ANALOG IRU	• ANALOG IRU RATE VECTOR
EDS CSS	• CSS PITCH, YAW ANGLES AND SOLAR PANEL ANGLES
EDS HGA	• HIGH-GAIN ANTENNA GIMBAL ANGLES
EDS MTA	• MAGNETIC TORQUER DIPOLE MOMENT VECTOR
EDS RWA	• ANGULAR MOMENTUM OF REACTION WHEELS
EDS THRUSTER FIRING	• THRUSTER FIRING COUNTS AND PULSE WIDTH
EDS THRUSTER TANKS	• THRUSTER TANK TEMPERATURES AND PRESSURE
EDS OBC EPHEMERIS	• OBC-DERIVED SPACECRAFT POSITION AND VELOCITY
PROCESSED ENGINEERING DATA SET (PEDS) DIRECTORY FILE	• GENERAL DATA FOR EACH BATCH (HEADERS)
PEDS FSS	• OBSERVED SUN UNIT VECTOR
PEDS ESA	• OBSERVED EARTH UNIT VECTOR
PEDS FHST	• OBSERVED STAR UNIT VECTOR, REFERENCE STAR UNIT VECTOR, AND STAR MAGNITUDE
PEDS TAM	• OBSERVED MAGNETIC FIELD VECTOR
PEDS IRU	• OBSERVED BODY ROTATION RATES
PEDS CSS	• SUN UNIT VECTOR AND SOLAR PANEL ANGLES
ESA SENSOR CALIBRATION FILE (SCF)	• ESA ALIGNMENT AND BIAS
FHST SCF	• FHST ALIGNMENT
FSS SCF	• FSS ALIGNMENT AND FOV CALIBRATION
IRU SCF	• IRU ALIGNMENT, SCALE FACTOR, AND BIAS
TAM SCF	• TAM ALIGNMENT, SCALE FACTOR, AND BIAS
HGA GIMBAL MASK FILE	• FILE DEFINING HGA MASK

Most of the attitude determination-related engineering data contained in an EDS are processed by the DA, which produces the PEDS. The PEDS are organized like and contain the same selectivity as the EDS. One significant feature specific to the PEDS is the commonality of data representation. For each appropriate sensor type in the PEDS, the processed engineering data are represented as a vector. The PEDS are the most central data storage point for the MTASS. PEDS batches are created by the DA. Numerous subsystems obtain data from the PEDS, although a few use EDS data directly.

Each batch of PEDS data contains the complete set of calibration parameters applied to that data. The DA obtains these calibrations from the SCFs. One SCF exists for each type of sensor. Each SCF can contain the

calibration parameters for up to 10 of that sensor type. For each sensor represented in an SCF, a complete history of calibrations can be maintained. Additionally, the current default set of calibration parameters for each sensor is marked for easy retrieval by the DA, and every past default set of parameters is identified as such.

When the DA retrieves a set of calibration parameters, the current default can be selected, or the user can select the desired set from a list of all sets for the specific sensor in question. A separate maintenance function also exists that allows the user to delete obsolete sets of calibration parameters and change the default set.

At several points in MTASS the spacecraft attitude is written to an AHF. The onboard computed (OBC) attitude can be written from the mission-specific TP, the coarse or fine attitude is written from the CFADS, and a definitive attitude series is written from the definitive attitude determination subsystem (DADS). Additionally, the CFADS can optionally write attitude rates with or without the accompanying attitudes.

The MTASS AHF was defined as a new standard file for storing attitude information. The attitude is stored as a quaternion in the geocentric inertial (GCI) frame. The attitude rates are stored as angular rates about each spacecraft body axis. The data on an AHF are stored in batches. Each batch has a set of header records, optionally followed by a series of attitude data records. The header records contain an optional epoch attitude quaternion and an optional epoch spacecraft orbit vector. The attitude data records in a given batch can contain attitude quaternions, attitude rates, or both.

The concept of generalized data structures was also applied to the definition of delivery file formats for planning aids. If the delivered product is the same for each mission, there is no need for a different software system. The FDD negotiated with other NASA/GSFC ground support elements for the acceptance of generalized file formats as standard FDD products. This standardization has been most successful for planning aids.

MTASS uses the well defined GSFC Code 500 standard ephemeris (EPHEM) file format for spacecraft position vectors, and the SLP ephemeris file for positions of the Sun, Moon, and planets.

As is traditional in GSFC Code 550 flight dynamics software, the FORTRAN NAMELIST technique is used for all user-definable configuration and control parameters. The NAMELIST files allow the user to override the hard-coded default values. These NAMELIST files are created or modified prior to the time of execution of MTASS. NAMELIST files can be set up for each operational scenario for each spacecraft to define each needed configuration. Most configuration and control parameter values can also be modified at execution time for those subsystems containing an interactive user interface.

2.2.4 MTASS Design Is Extensible

The list of sensors supported by MTASS can be extended through enhancement development efforts. The spacecraft hardware currently supported by MTASS was defined by the needs of UARS. The sensor-oriented design in MTASS, however, allows for the addition of other sensor and actuator types. Each appropriate subsystem would be modified to add a new software package to process data from the new hardware type, and corresponding configuration and control parameters would be added.

An alternative approach was employed for the Solar, Anomalous, and Magnetospheric Particle Explorer (SAMPEX) spacecraft. The SAMPEX hardware was similar, but different from that supported by MTASS. Consequently, the SAMPEX telemetry processor (TP) contained special processing to convert the SAMPEX digital Sun sensor (DSS) data to comply with the MTASS FSS EDS format. The SAMPEX coarse Sun sensor (CSS) arrays were processed to produce MTASS CSS EDS data. Finally, SAMPEX does not contain an IRU, so the SAMPEX TP calculates body rates to store in the MTASS IRU engineering data sets (which are needed by the CFADS to propagate attitudes). Finally, the SAMPEX attitude needs to be reported in a special

Sun-based reference frame, so the SAMPEX AGSS contains an attitude postprocessor that converts the MTASS attitudes from the AHF into the desired form. This SAMPEX AGSS is a good example of building a relatively small amount of extra processing in the front and back of the system in order to reuse entire MTASS subsystems.

3. FLIGHT EXPERIENCE WITH MTASS

At present, flight experience with MTASS consists primarily of experience with UARS, although some prelaunch spacecraft telemetry processing experience is now available from EUVE. Our discussions of MTASS flight experience are thus primarily directed to the UARS mission (see Reference 3).

UARS flight experience with MTASS can be divided roughly into nominal behavior and non-nominal behavior. Although the bulk of mission events to date fall into the class of nominal behavior, and although MTASS has performed in most respects like any other attitude support system created for the Mission Operations and Data Systems Directorate (MO&DSD), such non-nominal behavior as has been observed to date is reviewed here with the objective of identifying any features of this behavior that could be traced to the multisatellite character of MTASS. Our finding is that the non-nominal behavior was not attributable to the multisatellite character of MTASS.

Areas of nominal behavior with MTASS identified to date in the UARS mission experience include the following:

Phase	Behavior
Prelaunch	Generating and transmitting FDF products
	Prelaunch readiness testing
Launch to Release	Monitoring UARS attitude
	Monitoring solar array release
	Monitoring HGA deployment
	Fine attitude determination
Early Mission	Monitoring UARS release
	TAM bias determination
	Observing solar array thermal snap
	IRU bias determination
	Monitoring ascent maneuvers
	Monitoring yaw maneuver
	Monitoring roll maneuver
	Monitoring orbit adjust
	Preliminary OBC validation

An example of MTASS nominal behavior is found in the results of OBC validation. Ground solutions for roll, pitch, and yaw angles, including corrections for all known calibration errors, were determined from 911028.0150 to 911028.0328, with an estimated uncertainty of less than 10 arc-seconds in each of the angles. The root-mean-square differences of the OBC and the ground angles over this interval were found to be 8 arc-seconds in roll, 21 arc-seconds in pitch, and 5 arc-seconds in yaw. At all times the OBC knowledge was within the required 60 arc-seconds. The root-mean-square differences between ground solutions and the desired or target attitudes over this interval were 35 arc-seconds in roll, 41 arc-seconds in pitch, and 34 arc-seconds in yaw. The differences, which are a measure of the accuracy of OBC control, were at all times within the required 108 arc-seconds for pitch and yaw. The roll angle accuracy exceeded the requirement

approximately 1 percent of the time and is related to the solar snap phenomenon. The good agreement of ground-determined attitudes, OBC-determined attitudes, and control attitudes provides an excellent example of the nominal performance of the combined MTASS and flight systems.

Areas of non-nominal behavior with MTASS identified to date in the UARS mission experience include the following:

Phase	Behavior
Launch to Release	TP timing problem
Early Mission	FHST attitude propagation problem

The telemetry processing problem consisted of errors in unpacking data when a UARS minute boundary was being crossed. The problem was traced to a requirement to handle data gaps of any length of time. A workaround was developed to remove the original calculation of the UARS minute counter and replace it with calculations dependent on the engineering minor frame counter.

The fixed-head star tracker (FHST) attitude propagation problem was manifested by several symptoms: the star clumps were spread out, the residuals were high, and the attitude solution did not match the OBC solution. The problem was traced to an erroneous counts-to-angles field-of-view (FOV) scale factor in the FHST.

Neither of the problems discussed above arose from the innovative multisatellite features of MTASS; they could have arisen in any system. On the whole, MTASS performance with UARS was as good as or better than experienced with previous ground systems.

4. BENEFITS

Multimission flight dynamics ground support systems like MTASS are being developed to achieve significant cost reduction. Unlike single-purpose ground systems, which achieve a much lower level of reuse and thus a lower level of cost saving, the multimission attitude support system is an intermediate step to a generalized system in which numerous missions are served by one general system. The benefits of multimission attitude ground support systems extend not only to the software design and coding process but to the entire system environment, from specification through testing, simulation, operations, and maintenance.

4.1 Benefits for Specifications

As described in Section 2.1, there were significant advantages to raising the level at which reuse occurred from low-level reuse to subsystem reuse. Thus, entire areas of functionality were generalized. The benefit is that specifications do not need to be reworked at such a fine level of detail for each new satellite. Additional benefits were realized by segregating mission-specific algorithms into separate subsystems.

4.2 Benefits for Software Design and Coding

The cost of software development from the software design phase through the acceptance testing phase is strongly related to the size of the system, where the cost for verbatim reused software is approximately 20 percent of the cost of newly developed software. The cost to develop AGSSs for EUVE and SAMPEX has been greatly reduced by reusing MTASS. Based on this success, the development of the Total Ozone Mapping

Spectrometer (TOMS) AGSS has begun and similarly plans to satisfy significant major functions with MTASS. Additionally, plans are being made to base the AGSSs for the International Solar-Terrestrial Physics (ISTP) Solar and Heliospheric Observatory (SOHO) and X-ray Timing Explorer (XTE) missions on MTASS. Using the relationship between software development cost and system size, the relative cost savings for EUVE and SAMPEX can be inferred from Table 3. This table shows total source lines of code (SLOC), new SLOC, and reused SLOC for UARS, EUVE, and SAMPEX. The reused SLOC for EUVE and SAMPEX is primarily reused from MTASS. The reuse for UARS is primarily existing utility packages.

Table 3. System Size for AGSSs Using MTASS

MISSION	TOTAL SLOC (K)	NEW SLOC (K)	REUSED SLOC (K)
UARS	335.4	294.8	40.6
EUVE	273.5	48.8	224.5
SAMPEX	176.1	24.1	152.0

Note: Size is measured in 1000 SLOC.

4.3 Benefits for Testing, Simulation, Operations, and Maintenance

UARS and EUVE combined *acceptance testing* provided a good example of test systems that could not only benefit from a high degree of commonality but could be operated in a single test environment. That is, from the beginning UARS and EUVE testing was conceived and implemented by a single acceptance testing process group. Personnel already familiar with the pattern of UARS tests readily adapted to requirements for EUVE-specific tests and readily applied the techniques and methods that had proved successful for UARS tests also to EUVE tests. Thus, methods of test evaluation and scoring, test tracking, and scheduling used for UARS could be adapted almost without change to EUVE.

In a manner similar to testing, the high requirements and software commonality for UARS and EUVE exhibited by MTASS supported the *simulation* phase. Thus, personnel already familiar with the setup and conduct of UARS mission simulations quickly adapted their methods and skills to the generation of EUVE simulations. On the other hand, the MTASS system, as adapted to UARS, or, alternatively, EUVE, with mission-specific job control language (JCL) and input data, tended to diverge with time, thus diluting some of the benefits observed during the earlier stages of the cycle.

Similarly, the entry of the mission-tailored systems into the *operations* phase tended to further dilute some of the benefits because of differences in the details of mission operations support; for example, differences in the single, Earth-pointing control mode of UARS and the multiple, survey and inertial-pointing modes of EUVE were reflected in the number and frequency of predictions required for the two missions. Moreover, the intensified effort and staffing peak required by the actual launch and deployment of UARS tended to compete with an ongoing demand for EUVE support and resulted ultimately in separate management arrangements for UARS and EUVE flight dynamics support.

The benefits accruing to *maintenance* from multisatellite systems like MTASS follow from the fact that corrections and enhancements originating from experience with one satellite, say UARS, usually apply to the other satellite, say EUVE. In this way, maintenance effort is streamlined.

5. ISSUES

Our experience with developing and implementing a three-axis stabilized multisatellite flight dynamics support system raises several issues. These issues concern performance, testing, maintenance, and configuration management.

5.1 Performance Issues

The increased generality in some MTASS algorithms results in some increased execution time and memory requirements for some program steps. The necessary provision of some mission-specific modules for several satellites in MTASS could also increase code storage requirements. In practice, the actual savings are determined by competition among conflicting trends. For MTASS, the execution time of some program steps has not been as small as desired; for example, under certain conditions attitude determination has not occurred in near-real time. Moreover, the MTASS code storage requirement, measured in numbers of SLOC, has been larger than for previous systems, but is offset by the need to store only one copy of the MTASS code.

5.2 Testing Issues

Another issue concerning MTASS is whether, and to what extent, the benefits of a multisatellite capability that were realized in the specification and development phase extend also to the testing phase. It is well known that testing can address only a small subset of the total number of possible paths through the software system; consequently the question arises whether test cases generated for one satellite in the multisatellite system are representative of the program paths that will be used for all satellites, or whether test cases specific to every satellite must be used.

About 80 percent of MTASS consists of requirements and software common to UARS and EUVE. Thus, the pathway through the programs exercised by a UARS-specific acceptance test often exercises the pathway that would have been exercised in a comparable EUVE test, and thus separate UARS- and EUVE-specific tests were unnecessary and redundant. In this way, significant economies were realized in the combined acceptance testing of the multisatellite system.

In the 20 percent of the system where no overlap existed, separate UARS- and EUVE-specific test cases were executed. For example, in the case of antenna contact predictions, the EUVE case involved test cases in two control modes (survey mode and inertial pointing mode), whereas in the UARS case only one control mode (Earth pointing) was tested.

The common pathway approach was also utilized in the acceptance testing of the UARS and EUVE telemetry simulators, which served as test drivers for the telemetry processing programs used with MTASS. Although the telemetry processing programs are not considered part of MTASS proper, it is nonetheless instructive to consider the approach used. Although a single, multisatellite telemetry simulator might have been desirable, in fact a separate EUVE telemetry simulator was developed through a high degree of reuse of the UARS simulator. In testing the EUVE simulator, it was found possible in some cases simply to operate the simulator with UARS input and identify the expected results with the corresponding output from a previously accepted UARS simulation.

Apart from the benefits to testing that accrued from a large UARS/EUVE requirements and software commonality, a common management structure fully exploited the potential benefit of a multisatellite development environment. The acceptance testers, test coordinators, and task leaders for the testing of both satellites belonged to a single administrative unit under a single manager. This arrangement followed through on the promise and potential of the multisatellite approach and achieved significant economies and efficiency.

5.3 Maintenance Issues

Issues connected with the maintenance of multisatellite ground support systems are potentially more severe than issues connected with acceptance testing. The reason is that the maintenance phase of the software development life cycle is closer in time to the actual satellite launch, when the multisatellite system is more fully adapted to the idiosyncrasies of each satellite. For example, product delivery requirements and data set

size requirements dictated different tailoring of associated software, such as JCL and command lists (CLISTs), for EUVE than for UARS. Thus, as the fully adapted systems approach satellite launch, the systems tend to diverge in detail and the maintenance efforts tend to lose the benefit of overlap. Moreover, because of the high concentration of effort with the approach of launch and the existence of separate project teams for the different satellites, there is pressure for separate, dedicated launch support organizations to form, and with this development some of the benefits of a common management structure may be lost. In the case of UARS and EUVE, however, we were fortunate to have the same nucleus of software maintenance personnel for both satellites in the critical prelaunch maintenance phases, thus simplifying our efforts.

5.4 Configuration Management Issues

MTASS is maintained under a single configuration management structure and changes originating from one satellite or another are managed as a general case. Moreover, changes are instituted simultaneously without regard for the fact that in practice one satellite will go to the launch phase before another satellite.

Configuration management issues arise from several sources. For example, the need for change may arise first in, say, a UARS launch simulation and pressures of time and budget may tempt implementation of the change in a way that is not at first sufficiently general to cover EUVE and SAMPEX. Or, a EUVE simulation may uncover the need for a change that can impact the already-launched UARS, but the routine operations organization for UARS may prefer to defer the change. For reasons such as these, the configuration management of MTASS raises issues that do not arise in conventional single-satellite systems.

6. TRENDS

As mentioned above, plans are in place to use MTASS to satisfy significant major functions for the flight dynamics support of TOMS, ISTP SOHO, and XTE. Other potential missions to reuse MTASS will be examined. The one major limitation of MTASS is that the spacecraft be three-axis stabilized. Since there is lately a resurgence of spin-axis stabilized spacecraft with the ISTP/Global Geospace Science (GGS) Project Interplanetary Physics Laboratory (designated WIND) and Polar Plasma Laboratory (designated POLAR) missions and the SMEX-2 Fast Auroral Snapshot Telescope (FAST) mission, the usefulness of a multimission FDSS for spinning spacecraft was recognized. Consequently, the multimission spin-axis stabilized spacecraft (MSASS) FDSS was born (see Reference 2). It is currently completing development to support both WIND and POLAR, and plans are in place to satisfy significant major functions for the SMEX-2 FAST mission.

The trend to use MTASS and MSASS for upcoming missions will continue until a more generalized, mission configurable system replaces them.

REFERENCES

1. Goddard Space Flight Center, Flight Dynamics Division, FDD/552-90/085, *Upper Atmosphere Research Satellite (UARS)/Extreme Ultraviolet Explorer (EUVE) Flight Dynamics Support System (FDSS) Overview*, R. Coon (CSC), et al., prepared by Computer Sciences Corporation, October 1990

2. --, 552/FDD-91/027, *Multimission Spin-Axis Stabilized Spacecraft (MSASS) Flight Dynamics Support System (FDSS) System Description (Draft)*, C. Crognale (CSC), et al., prepared by Computer Sciences Corporation, August 1991

3. --, 554/FDD-92/029, *Upper Atmosphere Research Satellite (UARS) Post Launch Report*, J. Bez (CSC), et al., prepared by Computer Sciences Corporation, March 1992

FLIGHT MECHANICS/ESTIMATION THEORY SYMPOSIUM

MAY 5-7, 1992

SESSION 4

What Is The Relationship Between Altitude And Weight In A Model Rocket?

Abstract:

This experiment was designed to find a function of payload weight for altitude. The same rocket was launched a repeated number of times with the same engine and varying amounts of weight. After performing experimentation, it was calculated that the altitude in meters could be predicted with the equation $A=2.8W^2-70.6W+310.3$, with weight expressed in the unit ounces.

EDITOR'S NOTE: The author of this paper is Mr. Jonathan Betz, a freshman at Thomas Jefferson High School in Falls Church, Virginia.

Introduction:

Aerodynamics, the science with which this project deals, is the study of the forces acting upon an object as it moves through a fluid, such as air. Most often, aerodynamics is applied to studying heavier-than-air craft, such as airplanes.

The four main forces acting upon such an object are lift, gravity, thrust and drag. Lift is the force acting on an object perpendicular to its velocity vector. Gravity is the force which pulls an object towards the center of the earth. For a rocket, thrust is the force which propels an object along its velocity vector. Thrust is opposed by drag, the force which slows an object moving through a fluid.

Governing most of the work done in aerodynamics are the laws of motion developed in the seventeenth century by Sir Isaac Newton. Also, his concept of a fluid's resistance to motion, known as viscosity, has an effect on work concerning aerodynamics.

In 1738, Daniel Bernoulli applied Newton's laws of motion to fluids. In his work he formulated what is known as Bernoulli's Law, which states that the sum of the dynamic pressure and the static pressure must always equal a given constant value, without regard to frictional losses. A bit more simply stated, this means that if the outward, or static, pressure of a fluid decreases, the dynamic pressure, or pressure against an object blocking the flow of the fluid, must increase enough that their sum remains the same. This brings us to the main point of Bernoulli's Law, that if a fluid speeds up, some of the static pressure must be traded off to allow for the increase in dynamic pressure.

An airfoil, the cross-sectional shape of an airplane wing, utilizes this in order to achieve flight. An airfoil is shaped like this:

This shape is used in order to increase the speed of the airflow over the top of the airfoil. When this happens, the air pressure on the underside of the airfoil exceeds the air pressure on the upper side of the airfoil. This creates an imbalance in pressure which is what causes lift.

Purpose:

The purpose of this experiment was to find a mathematical equation for predicting the altitude that a model rocket will attain with any given weight. More importantly, this experiment outlined a procedure for finding such a relationship for any model rocket.

Hypothesis:

While conducting background research, no reference to any relationship between altitude and weight in a heavier-than-air craft that accounted for all factors could be found. However, information from Estes Model Rocket Co. contained formulas for predicting altitude which did not account for aerodynamic drag or air resistance, and these formulas showed that qualitatively, a relation between altitude and weight would be parabolic in nature. However, a quantitative hypothesis as to the relationship between altitude and weight could not be made.

Procedure:

To find a relationship between altitude and payload weight, an Estes Nova Payloader model rocket was launched 6 times with each of 7 different payload weight values. Then, using the average values, an equation was derived to represent the average rocket behavior. The engines used in the rocket have a thrust range between 0.56 and 1.12 Pound-Seconds. For further information on the materials and methods, refer to Appendix 3.

Results:

For the data collected in the experiment, refer to Appendix 1. These data are displayed in various ways in Appendix 2.

Figure 1 in Appendix 2 shows the average altitude for each of the weights for the first day, the second day, and a combined average. The fourth bar shows an average using only values that fall within 1 standard deviation value. Interestingly, this graph shows that on the first day there was an altitude increase between 3 and 3.5 ounces. Most likely, this is due simply to chance. Figure 2 is very similar, but shows only the values for combined and combined adjusted averages. The discrepancy mentioned about day 1 flights is no longer evident when the values are averaged with values from day 2 flights. Figure 3 is just a simple line graph showing the values for the combined adjusted average. This graph is what first suggested that a relation between altitude and weight would be parabolic in nature. Figure 4 shows both the combined adjusted average and the parabolic curve fit to the combined adjusted average values. Figure 5 shows the combined adjusted average of the flight altitudes and calculated flight altitude using calculations from Estes Model Rocket Co.

Conclusions:

As I hypothesized, there seemed to be a parabolic relationship between altitude and weight as suggested by Figure 3. Using the data from maximum, medium, and median weights, I was able to find that when launching a Nova Payloader model rocket with a B4-4 engine, the altitude of the rocket can be predicted by the equation $A=2.8W^2-70.6W+310.3$, where A is the rocket's altitude in meters and W is the weight of the rocket in ounces. This equation yields about an 11% margin of error. This margin of error can possibly be attributed to experimental error and uncontrollable variables such as weather conditions and engine thrust consistency.

Appendix 1
Data

MODEL ROCKET TEST DATA
FLIGHT TRIAL ALTITUDE VS. GROSS WEIGHT

Set #1, Total Rocket Weight = 2.0 Oz.

Launch	Day 1	Day 2	Combined
1	143.5	189.0	
2	156.0	179.5	
3	209.5	198.5	
Range	66.0	19.0	**66.0**
Average	169.3	189.0	**179.3**
STD DEV	35.0	9.5	**25.3**
+/- 1 SDU			**204.6 : 154.0**
ADJ AVE			**180.7**

Set #2, Total Rocket Weight = 2.5 Oz.

Launch	Day 1	Day 2	Combined
1	198.5	156.0	
2	101.0	143.5	
3	137.5	137.5	
Range	97.5	18.5	**97.5**
Average	145.5	145.7	**145.6**
STD DEV	49.3	9.4	**31.7**
+/- 1 SDU			**177.3 : 113.9**
ADJ AVE			**143.6**

Set #3, Total Rocket Weight = 3.0 Oz.

Launch	Day 1	Day 2	Combined
1	109.0	127.0	
2	81.5	113.0	
3	101.0	113.0	
Range	27.5	14.0	**27.5**
Average	97.2	117.7	**107.4**
STD DEV	14.1	8.1	**15.2**
+/- 1 SDU			**122.6 : 92.2**
ADJ AVE			**109.0**

Set #4, Total Rocket Weight = 3.5 Oz.

Launch	Day 1	Day 2	Combined
1	109.0	90.5	
2	113.0	101.0	
3	90.5	84.5	
Range	22.5	16.5	28.5
Average	104.2	92.0	98.1
STD DEV	12.0	8.4	11.4
+/- 1 SDU			109.5 : 87.1
ADJ AVE			97.8

Set #5, Total Rocket Weight = 4.0 Oz.

Launch	Day 1	Day 2	Combined
1	66.5	57.5	
2	42.5	44.5	
3	42.0	42.5	
Range	24.5	15.0	24.0
Average	50.7	48.2	49.3
STD DEV	14.0	8.1	10.3
+/- 1 SDU			59.6 : 39.0
ADJ AVE			45.8

Set #6, Total Rocket Weight = 4.5 Oz.

Launch	Day 1	Day 2	Combined
1	32.5	40.5	
2	37.0	40.5	
3	37.0	39.0	
Range	4.5	1.0	8.0
Average	35.5	40.0	37.8
STD DEV	2.6	0.9	3.0
+/- 1 SDU			40.8 : 34.8
ADJ AVE			38.8

Set #7, Total Rocket Weight = 5.0 Oz.

Launch	Day 1	Day 2	Combined
1	22.5	37.0	
2	23.5	31.5	
3	10.5	32.5	
Range	13.0	6.0	27.0
Average	18.8	33.6	26.2
STD DEV	7.2	2.9	9.5
+/- 1 SDU			35.7 : 16.7
ADJ AVE			27.5

MODEL ROCKET TEST DATA
AVERAGE ALTITUDE VS. GROSS WEIGHT

Weight	Combined Average	Standard Deviation	Adjusted Average
2.0 Oz	179.3	25.3	180.7
2.5 Oz	145.6	31.7	143.6
3.0 Oz	107.4	15.2	109.0
3.5 Oz	98.1	11.4	97.8
4.0 Oz	49.3	10.3	45.8
4.5 Oz	37.8	3.0	38.8
5.0 Oz	26.2	9.5	27.5

Appendix 2
Graphs

Average Model Rocket Altitude With Different Weights

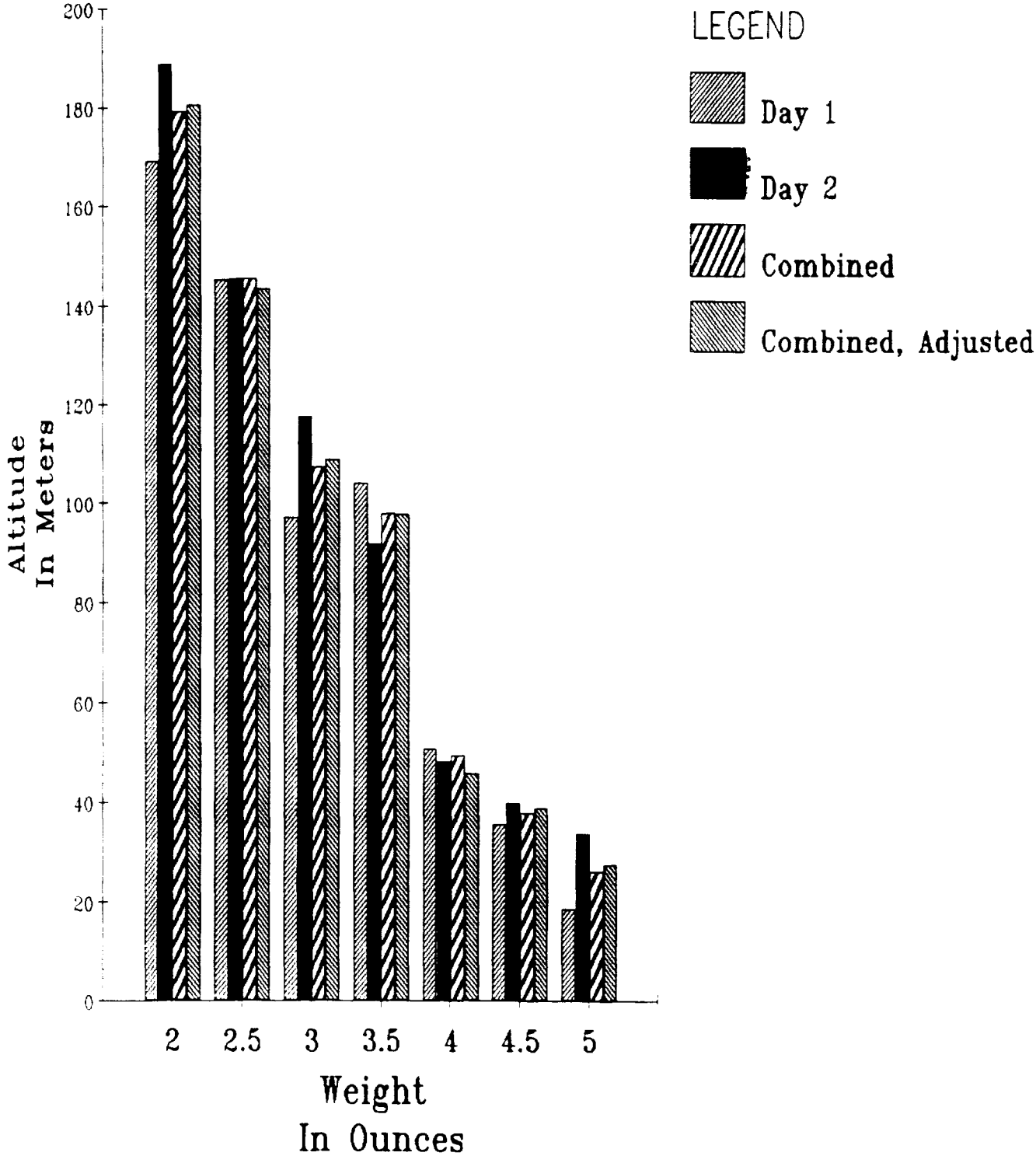

Figure 1

Average Model Rocket Altitude With Different Weights

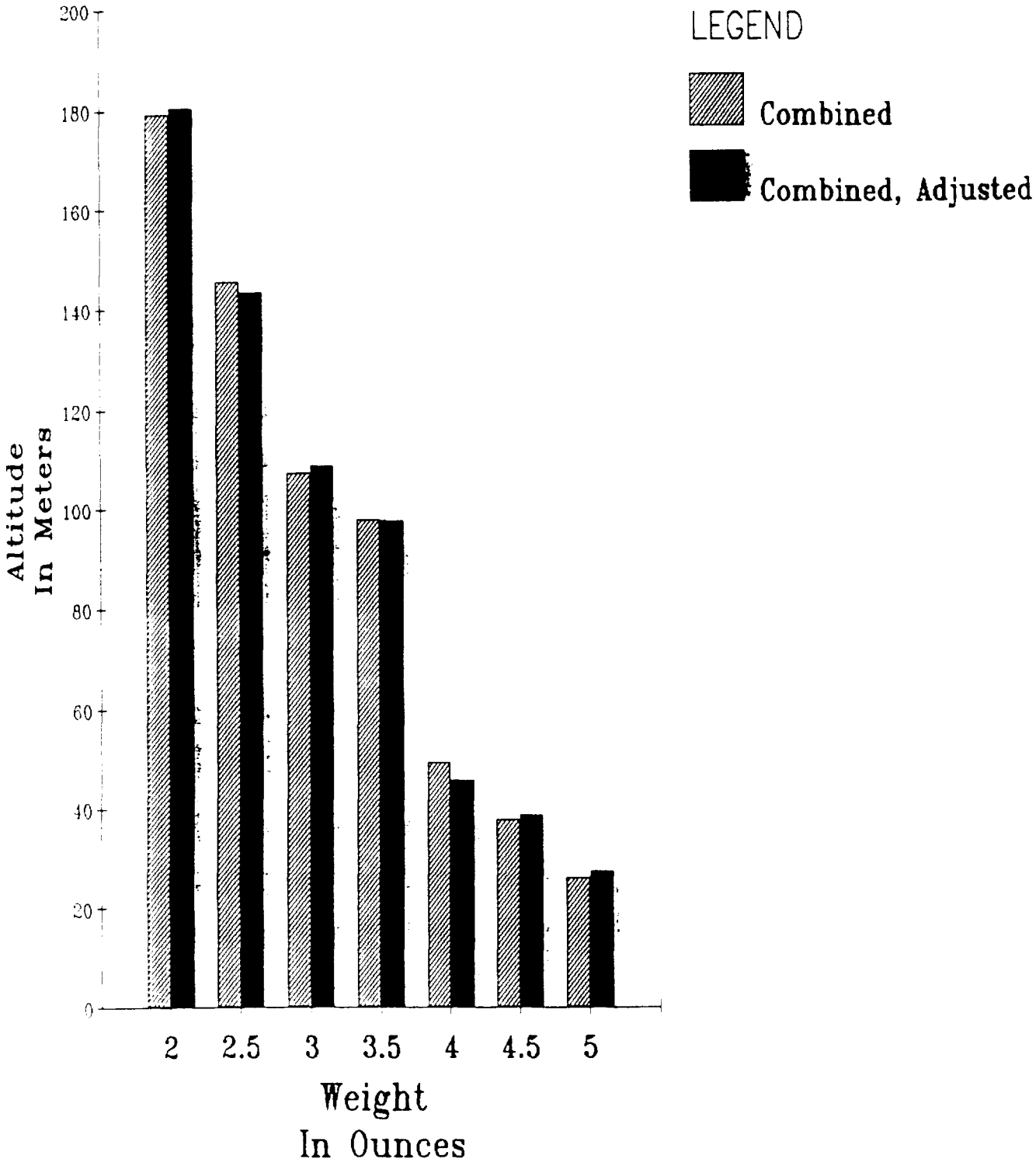

Figure 2

Average Model Rocket Altitude With Different Weights

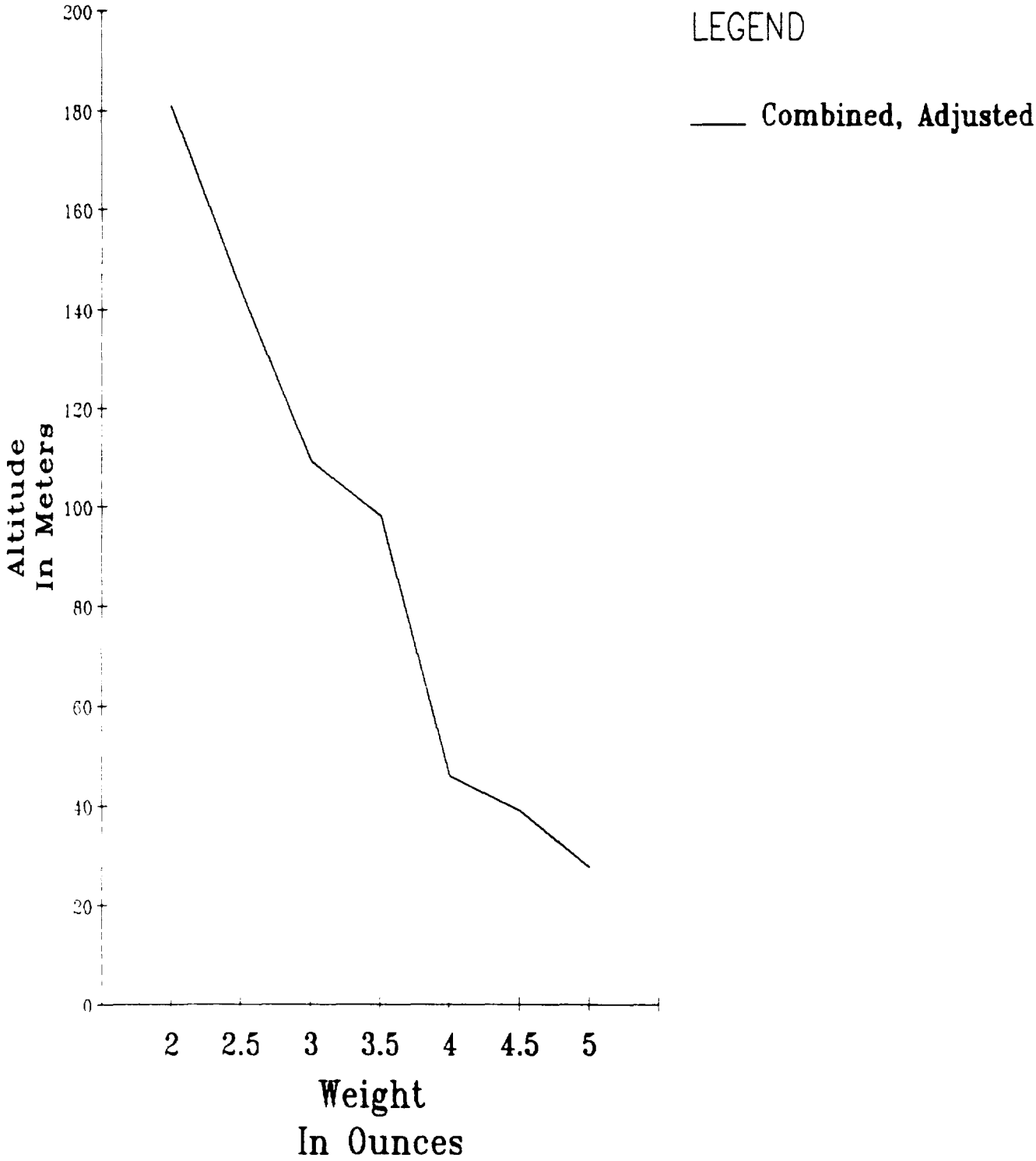

Figure 3

Comparison of Calculated Altitude and Actual Altitude

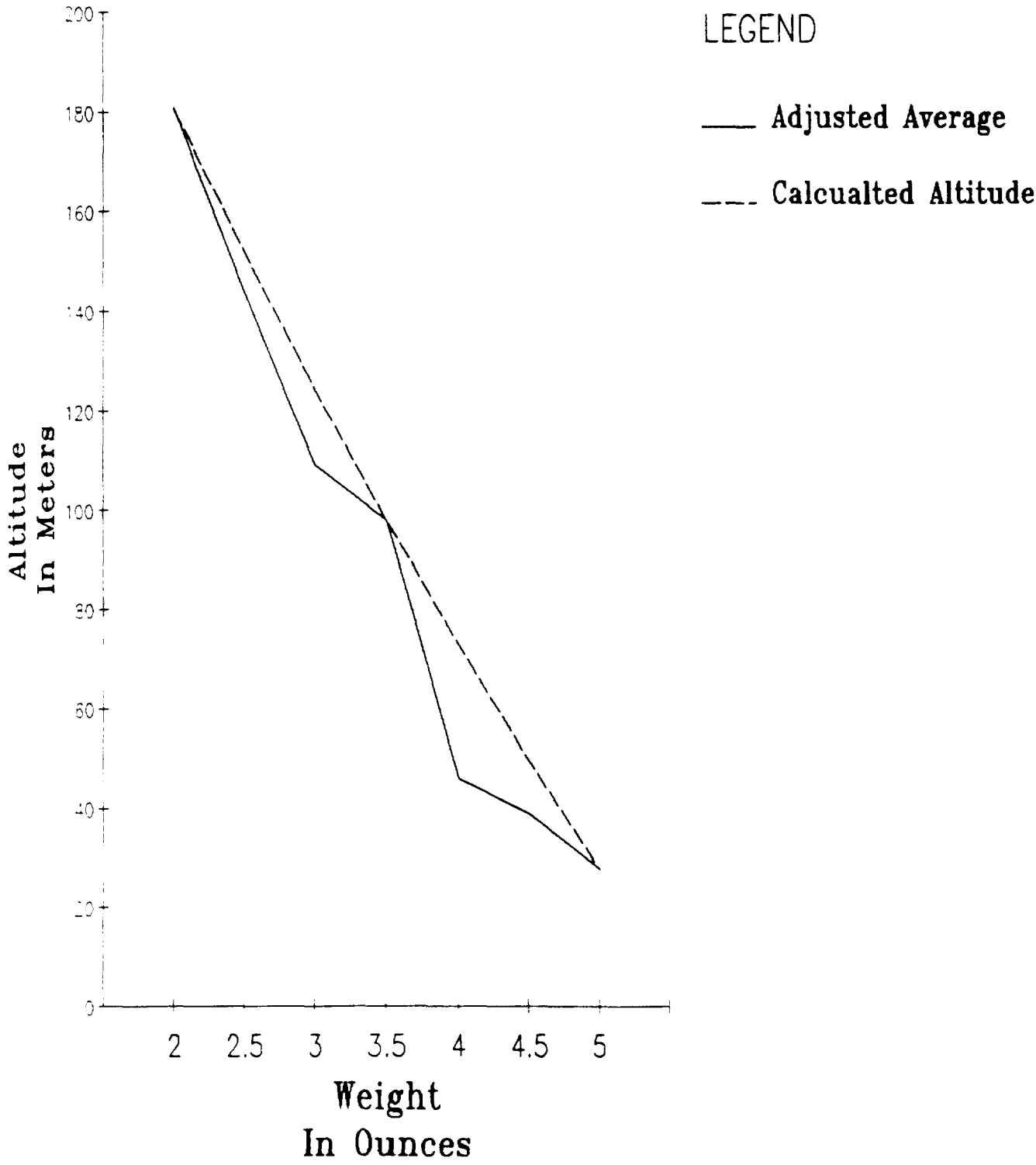

Figure 4

Comparison of Calculated Altitude and Actual Altitude

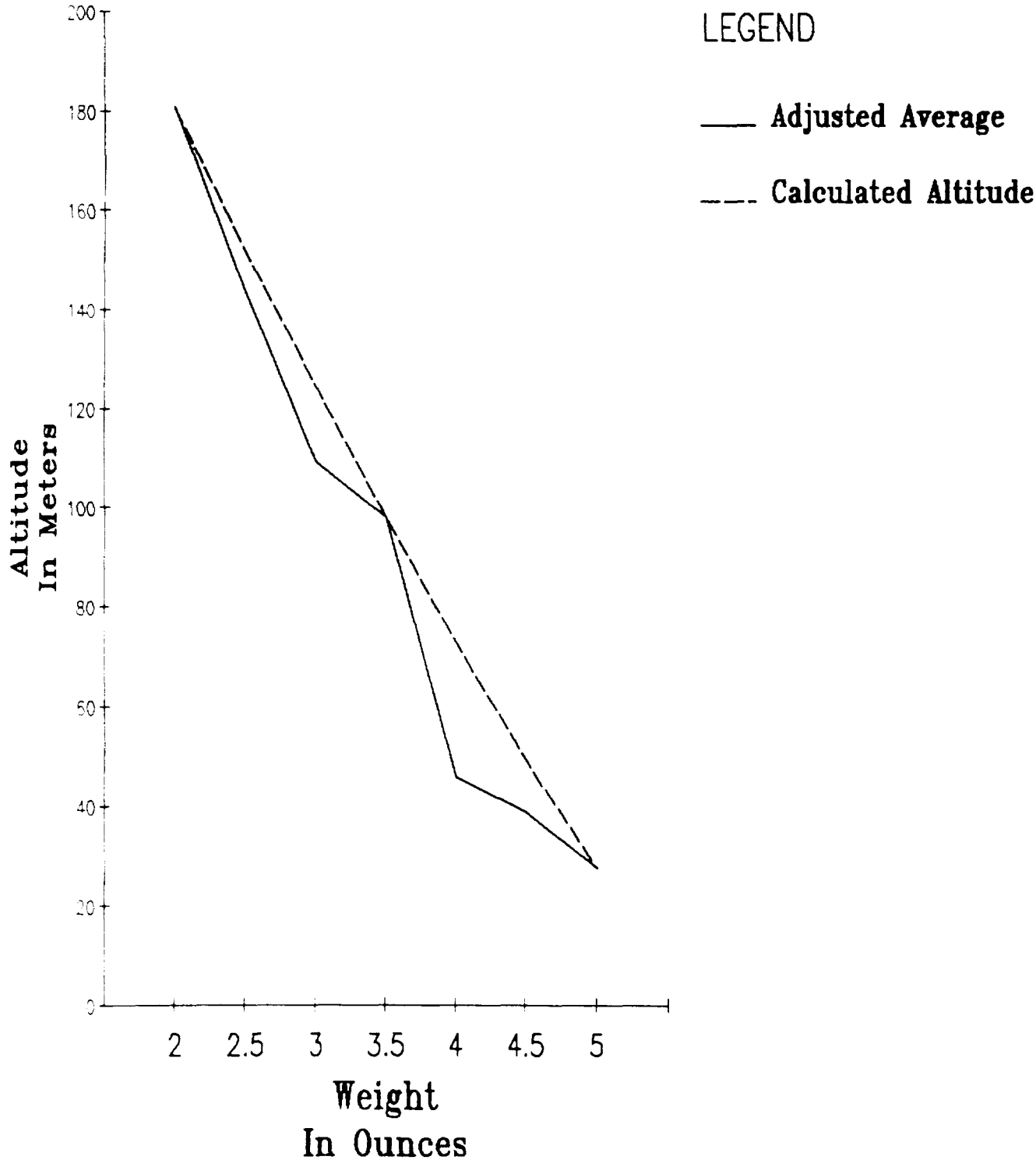

Figure 5

Appendix 3
Materials and Methods

1 Estes Nova Payloader model rocket
1 Estes Altitrak altitude finder
44 Estes B4-4 model rocket engines
2 Estes A8-3 model rocket engines
2 Estes B6-4 model rocket engines
3 packages of Estes model rocket recovery wadding
6 packages of Estes model rocket igniters
1 roll of masking tape
1 scale
1 Estes launch pad
1 Estes model rocket launcher and safety key
75 meters of twine
2 tent pegs
1 level
8 packages of lead fishing sinkers

1. Assemble Nova Payloader model rocket
2. Assemble Altitrak altitude finder
3. Weigh out 6 sets of weights, beginning with 1/2 ounce and continuing to 3 ounces, in 1/2 ounce increments
4. Measure 75 meters of twine, attaching a tent peg to each end
5. Proceed to launch site, Manassas battlefield picnic area
6. Set up launch site:
    a) set launch pad down and check launch rod to be vertical
    b) hammer one tent peg into the ground by the launch pad
    c) stretch twine out until taught and hammer second peg into the ground
    d) station one observer at the far end of the twine with altitraker
    e) prepare launch controller for launching
7. Prepare the rocket for launch
    a) insert 3 crumpled squares of recovery wadding into the rocket
    b) insert and tape an igniter into a rocket engine
    c) insert engine into rocket
    d) roll parachute and insert into body of rocket with shock cord
    e) insert nose cone and payload section into body tube of rocket
8. Determine the best rocket engine for use in experimentation
    a) launch rocket twice with each of the B6-4, B4-4, and A8-3 engines, once with no payload, once with maximum payload
    b) record altitude of each launch
    c) using this information, decide on the best engine to use
9. Conduct experimentation
    a) for each flight, prepare the rocket as in step 7
    b) launch the rocket 3 times with no payload
    c) launch the rocket 3 times with each premeasured payload

d) record the altitude and launch time of each flight
e) record weather conditions every hour while launching rockets

10. Repeat steps 4-7 and 9 at a later date
11. Calculate relationship between altitude and weight

Appendix 4 Other Information

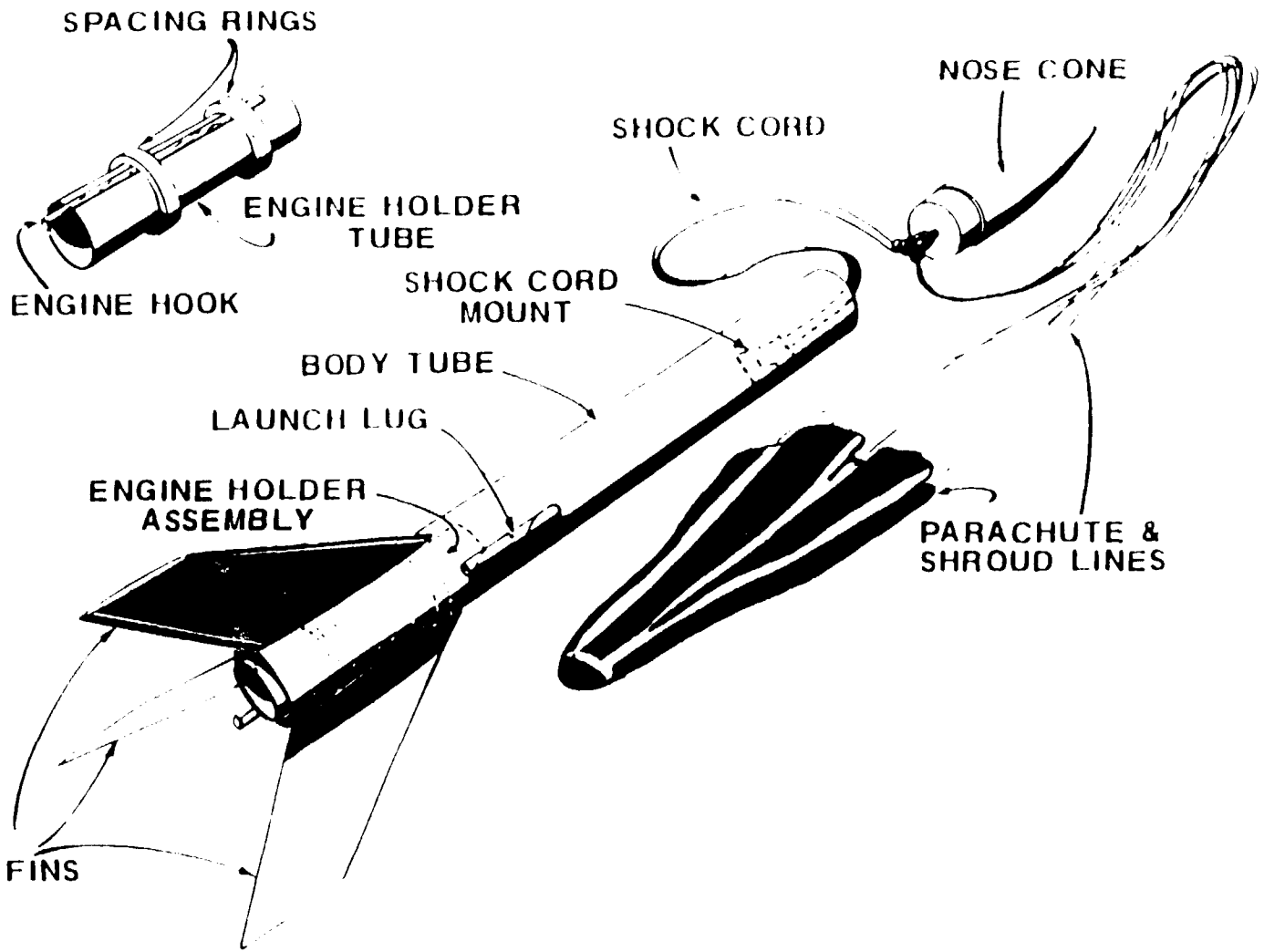

PARTS OF A MODEL ROCKET

ALTITUDE TRACKING GEOMETRY

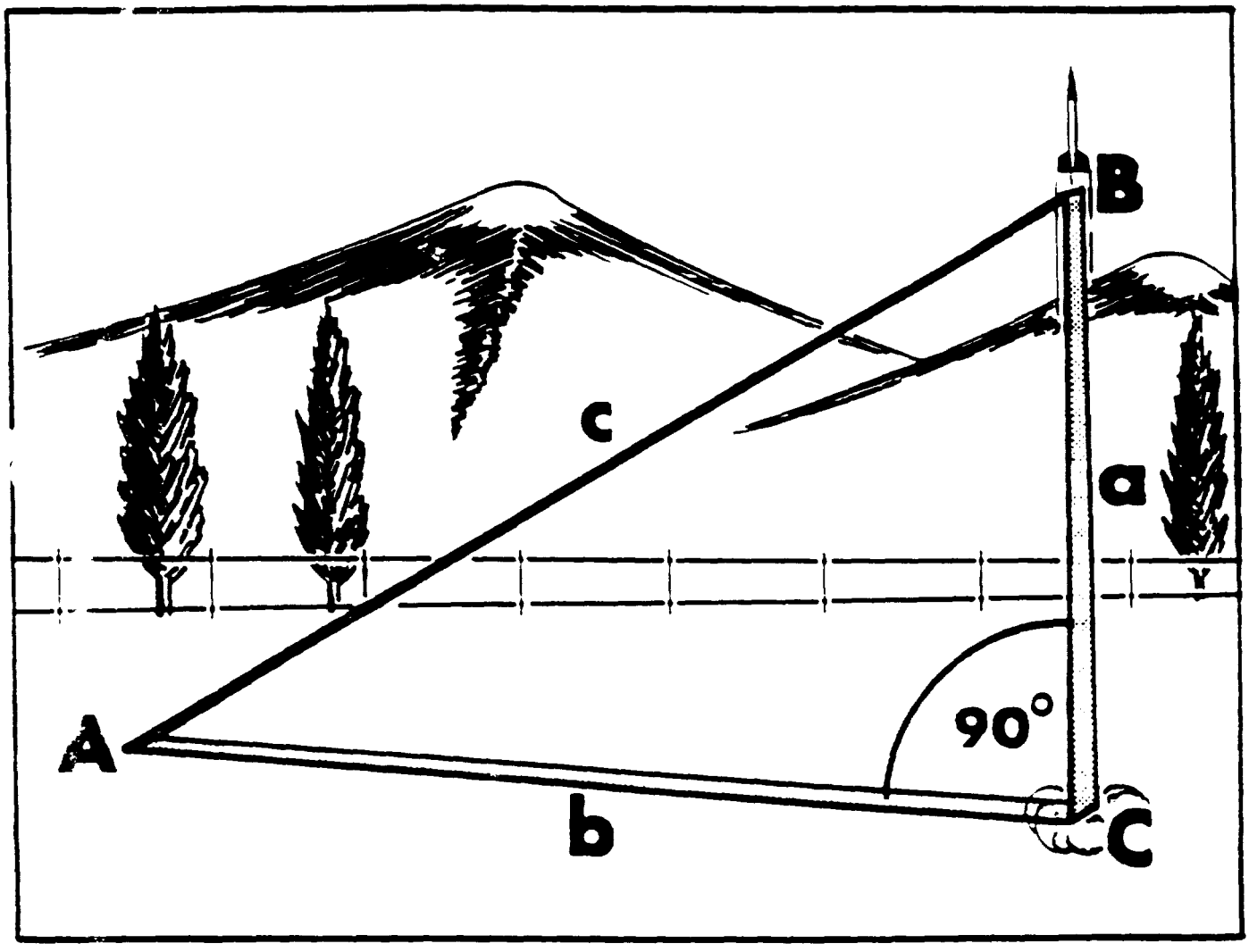

Nonlinear Techniques for Forecasting Solar Activity Directly From Its Time Series*

S. Ashrafi and L. Roszman
COMPUTER SCIENCES CORPORATION (CSC)

J. Cooley
GODDARD SPACE FLIGHT CENTER (GSFC)

ABSTRACT

This paper presents numerical techniques for constructing nonlinear predictive models to forecast solar flux directly from its time series. This approach makes it possible to extract dynamical invariants of our system without reference to any underlying solar physics. We consider the dynamical evolution of solar activity in a reconstructed phase space that captures the attractor (strange), give a procedure for constructing a predictor of future solar activity, and discuss extraction of dynamical invariants such as Lyapunov exponents and attractor dimension.

1. INTRODUCTION

1.1 Review of Solar Activity

Need for Solar Flux Prediction. Solar flux $F_{10.7}$ [radio flux emitted at a wavelength of $\lambda = 10.7$ centimeters (cm)] is the best indicator of the strength of ionizing radiations, such as solar ultraviolet and X-ray emissions, that directly affect the atmospheric density and thereby change the orbit lifetime of satellites. Thus, accurate forecasting of solar flux $F_{10.7}$ is crucial for orbit determination of spacecrafts.

Sunspots and Solar Flux. The strong correlation between sunspots and the solar flux $F_{10.7}$ is probably due to the enhanced radiation from limited areas of the Sun where sunspots are active. Sunspot activity depends on the wavelength of radiated solar flux. For waves shorter than 3 cm, the intensity is steady. From 3 to 60 cm, often called the decimeter range, the intensity occasionally increases for a few minutes. Rising from the vicinity of active sunspot regions, decimeter intensity also tends to exhibit a 27-day period associated with solar rotation (Reference 1).

The dynamics of sunspots and their formation are still a mystery. They are often more than 1000 degrees Kelvin cooler than the surrounding photosphere. Although many explanations for sunspot cooling have been proposed (the Biermann field inhibition mechanism and the superadiabatic downflow mechanism), the huge difference in temperature between sunspots and their surroundings suggests a similarity with solitons of multilevel turbulence. One may think of sunspots as solitons in a fluid turbulent Sun (Reference 2). Orbit lifetime is a function of atmospheric drag, which is a function of atmospheric density, which in turn is a function of solar flux. For this reason, spacecraft orbit determination requires accurate forecasting of solar flux.

* This work was supported by the National Aeronautics and Space Administration (NASA)/Goddard Space Flight Center (GSFC), Greenbelt, Maryland, Contract NAS 5-31500.

Nonlinear Structure in Solar Flux. Until recently, we had little reason to doubt that weather is in principle predictable, given enough data. Recently, a striking discovery changed our perspective: simple deterministic systems with only a few degrees of freedom can generate random behavior. When a system exhibits apparent random behavior that is fundamental to its dynamics, such that no amount of information gathering will make the system predictable, the system is considered to be chaotic. Much evidence supports our assertion that solar flux signal falls in this category (References 3 through 11). Perhaps paradoxically, chaos is generated by fixed rules that do not themselves involve any element of chance. Theoretically, the future of a dynamic system is completely determined by present and past conditions. In practice, however, amplification of small initial uncertainties makes a system with short-term predictability unpredictable in the long term.

Many people speak of random processes as though they were a fundamental source of randomness. This idea is misleading. The theory of random processes is an empirical method to deal with incomplete information; it does not attempt to explain randomness. As far as we know, the only truly fundamental source of randomness is the uncertainty principle of quantum mechanics; everything else is deterministic, at least in principle. Nonetheless, we call many phenomena, such as solar dynamics, random, even though we may not ordinarily think of them in terms of quantum mechanics. Historically, scientists have assumed that randomness derives solely from complication. In this paper, we will take the practical position that randomness occurs to the extent that a system's behavior is unpredictable. We believe that randomness is subjective and a matter of degree; that is, some systems are more predictable than others (e.g., solar activity is more predictable than geomagnetic activity).

Solar Activity Prediction. Interest in solar activity has grown in the past two decades for many reasons. Some reports claim a correlation between solar activity and weather on Earth (Reference 12), although a correlation has not yet been convincingly established (Reference 13). We have some evidence for the coincident occurrences of the Maunder minimum (a period of little or no solar activity occurring from 1645 to 1715) and the "Little Ice Age" (a period of abnormally cold weather) (Reference 14). Perhaps most importantly for flight dynamics, solar activity changes the atmospheric density, which has important implications for spacecraft trajectory and lifetime prediction (Reference 15). The seemingly random nature of solar flux has misled us for many decades, causing us to assume that the underlying physics must necessarily be complex as well. Therefore, researchers have generally used statistical models to predict solar activity (Reference 16). However, new developments in chaos and nonlinear dynamics allow us to model the behavior of a system in terms of some invariants directly extractable from system dynamics, without reference to any underlying physics. Using chaos theory, we can predict short-term activity more accurately than with statistical methods; however, chaos theory imposes a fundamental limit on long-term predictions.

1.2 Brief Review of Chaotic Dynamics

Self-Organization and Attractors. Imagine a very simple system: a pendulum. The pendulum exhibits two fundamental degrees of freedom: position and momentum. However, in its stable periodic state (limit cycle), the pendulum can be described by only one degree of freedom, the phase angle. Here, the dynamic is attracted to a lower-dimensional phase space, and the dimension of this reduced phase space is equal to the number of active degrees of freedom in the self-organized system.

Attractors are not limited to zero dimension (fixed point) or one dimension (limit cycle), but for nonlinear systems they could be high dimensional and in some cases even fractional or fractal (strange attractors).

Nonlinear Dynamical Systems. Anything that moves or evolves in time is a dynamical system. (If it does not move, it is a dynamical system at a fixed point.) Mathematically speaking, a dynamical system can be represented by a state space (phase space) R^M and an evolution operator ψ that defines how the state of the system evolves in time. M is the number of degrees of freedom in the dynamics; ψ can be visualized as the physics of the system.

The attractor A of a dynamical system is the subset of phase space toward which the system evolves:

$$\lim_{t \to \infty} \psi_t(S) = A.$$

An initial condition $\vec{X}_0$ that is sufficiently near the attractor will evolve in time so that $\psi_t(\vec{X}_0)$ gets very close to the set A as $t \to \infty$.

Phase-Space Construction Directly From a Time Series. When confronted with a complicated physical system, an experimenter normally measures at regular and discrete intervals of time the value of some state variable (e.g., flux $F_{10.7}$) and records the time series $f(t_0), f(t_1), f(t_2),...$, with $f(t_i) \in R$ and $t_i=t_0+i\Delta t$. From the observed time series, the experimenter attempts to infer something about the dynamics (i.e., the physics) of the system. The measure f(t) represents a projection π from R^M to R:

$$\pi: R^M \to R.$$

Because the time series is one-dimensional, it is an incomplete description of a system during a time evolution. Nonetheless, many features of the dynamics can still be inferred from the time series alone. From time-delayed values of the scalar time series, Takens (Reference 17) and Packard et al. (Reference 18) have shown that one can embed the time series into a higher dimensional space. Vectors are created with components as

$$\vec{f}(t) = [f(t), f(t-\tau), ... f(t-(m-1)\tau)]^T,$$

where τ (time delay) and m (the embedding dimension) are parameters of the embedding procedure. Here $\vec{f}(t)$ represents a more complete description of dynamics than f(t) and can be thought of as a mapping:

$$\pi^m: R^M \to R^m.$$

An embedding dimension of $m > 2D+1$, where D is the fractal dimension of the attractor, almost always ensures the construction of the topology of the attractor (Takens' theorem, Reference 17).

If unlimited infinitely precise data are available, almost any delay time τ and embedding dimension $m > D$ will work, at least in principle. However, choosing the optimal parameters for real data is a nontrivial process.

For example, if τ is too large then the components f(t) and $f(t+(m-1)\tau)$ of the reconstructed vector $\vec{f}$ will be effectively uncorrelated, which will inflate the estimated dimension. On the other hand, if $(m-1)\tau$ is too small, then the components $f(t), ...,f(t+(m-1)\tau)$ will all be very nearly equal, and the reconstructed attractor will look like one long diagonal line. Generally, τ must not be less than some characteristic decorrelation time, and $(m-1)\tau$ must not be much greater than this decorrelation time. One such characteristic time is the local minima of the autocorrelation function $R(\tau) = \langle (f(t)-\langle f \rangle)(f(t+\tau)-\langle f \rangle) \rangle$, where $\langle\ \rangle$ represents average over time.

1.3 Some Invariants of Dynamical Systems

Lyapunov Exponent. In a chaotic system, the adjacent points of the time series become separated under the action of a map; in our case, f_n is the value of solar flux measured daily.

$$f_{n+1} = M(f_n),$$

which leads to satic motion. The Lyapunov exponent $\lambda(\vec{f}_0)$ measures this exponential separation, as shown in Figure 1.

Therefore,

$$\varepsilon_0 e^{N\lambda(f_0)} = |M^N(f_0 + \varepsilon_0) - M^N(f_0)|.$$

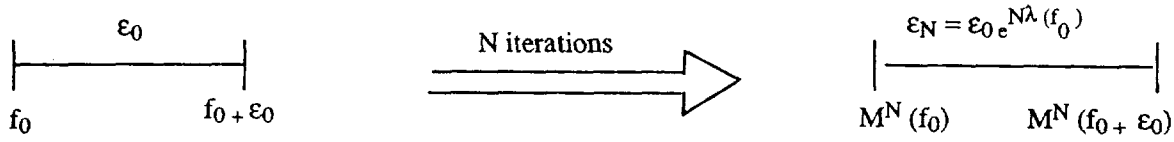

Figure 1. Exponential Separation Measurement

In the limit $\varepsilon_0 \to 0$ and $N \to \infty$, we get the formal expression for Lyapunov exponent $\lambda(f_0)$:

$$\lambda(f_0) = \lim_{N\to\infty} \lim_{\varepsilon_0\to\infty} \frac{1}{N} \ln \left| \frac{M^N(f_0 + \varepsilon_0) - M^N(f_0)}{\varepsilon_0} \right|$$

$$= \lim_{N\to\infty} \frac{1}{N} \ln \left| \frac{dM^N(f_o)}{df_0} \right|.$$

The Lyapunov exponent also measures the average loss of information.

Invariant Measure. The invariant measure $\varrho(f)$ determines the density of the iterates of a map over the unit interval and is defined to be

$$\varrho(f) = \lim_{N\to\infty} \frac{1}{N} \sum_{i=0}^{N} \delta \left[f - M^i(f_0) \right].$$

Kolmogorov Entropy. Kolmogorov entropy K describes the dynamical behavior at the strange attractor. K is the analog of thermodynamic entropy that measures the disorder in a dynamical system. For a one-dimensional map, it is just the Lyapunov exponent. The rate K (at which information about the system is lost) is equal to the average sum of positive Lyapunov exponents:

$$K = \int d^d f \, \varrho(f) \sum_i \lambda_i^+(f),$$

where the superscript d is the dimensionality of our phase space.

In most cases, the λs are independent of f, so

$$K = \sum \lambda_i^+(f).$$

K is, indeed, a useful measure of chaos. K becomes zero for regular motion. It is infinite for totally stochastic or random systems but is a constant larger than zero for chaotic systems (Figure 2). In higher dimensional systems, we lose information about the system (as shown in Figure 3). Here, a sphere of radius ε_0 changes its geometry in phase to an ellipsoid as the system evolves in time.

Hausdorff Dimension. One of the invariants of an attractor that can be extracted directly from the time series is called *Hausdorff Dimension D*, an infinite set of dimensions $D=D_0, D_1, D_2, \ldots$ that describes the inhomogeneity of the attractor. It can be shown that D_2 (which yields a lower bound on the Hausdorff dimension) and many other invariants of the system can be directly obtained from a time series:

- D_2, that is, a lower bound on the Hausdorff dimension ($D_2 < D_1$)
- d, that is, the embedding dimension of the attractor
- The amplitude of the white noise on the signal; that is, separating the deterministic chaotic motion of the system from disturbing white noise

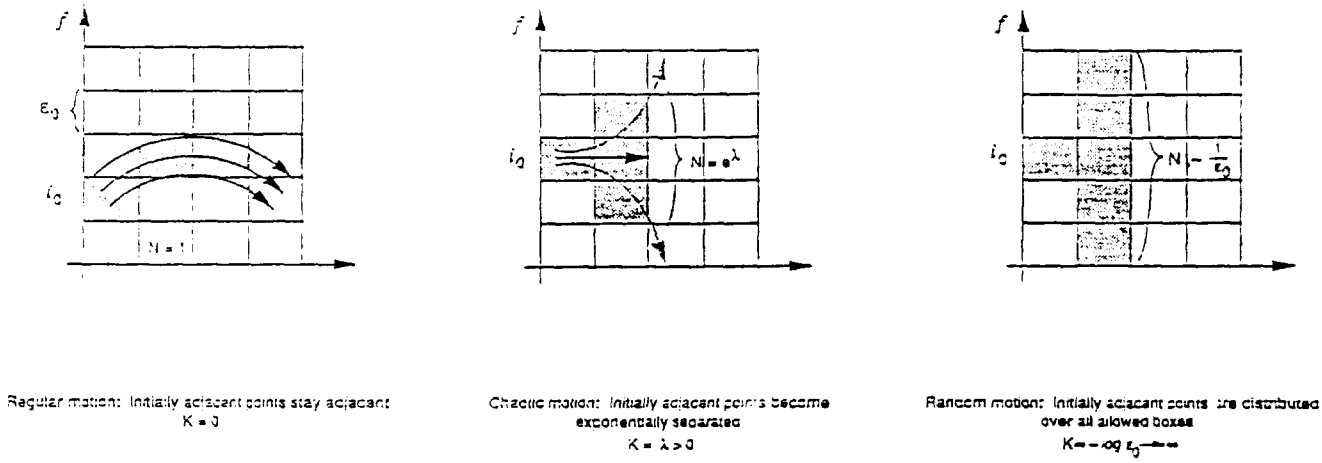

Regular motion: Initially adjacent points stay adjacent
K = 0

Chaotic motion: Initially adjacent points become exponentially separated
$K = \lambda > 0$

Random motion: Initially adjacent points are distributed over all allowed boxes
$K = -\log \varepsilon_0 \to \infty$

6360G(25)-2

Figure 2. Kolmogorov Entropies for Regular, Chaotic, and Random Motions

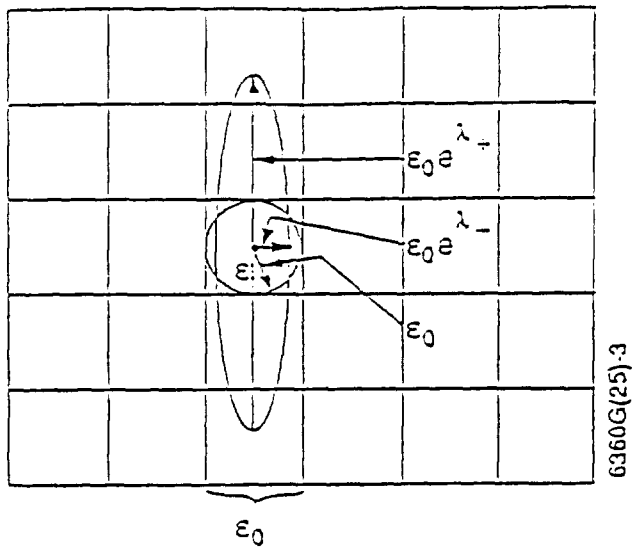

6360G(25)-3

Figure 3. A Two-Dimensional Map of Small Circle Into an Ellipse

- A lower bound on the Kolmogorov entropy; that is, determining "how chaotic" the signal is
- The Kaplan-Yorke dimension: connects the static structure of the attractor (as measured by $D=D_0, D_1, D_2, \ldots$) and the dynamical behavior at the attractor (as measured by the Lyapunov exponents)

Dimensions of a Strange Attractor. To characterize the inhomogeneous static structure of the attractor, we introduce an infinite set of dimensions D_n related to the nth powers of P_i via

$$D_n = \lim_{\varepsilon_0 \to 0} \frac{1}{n-1} \frac{\log \left[\sum_{i=0}^{Q(\varepsilon_0)} P_i^n \right]}{\log \varepsilon_0}$$

$$n = 0, 1, 2, \ldots,$$

where P_i is the probability of finding a point of attractor in the cell number i [i=1, 2, ... $Q(\varepsilon_0)$]. For n=0, we get the Hausdorff dimension of the attractor $D=D_0$; for n=1, we get dimension $D=D_1$ (called the *information dimension*). It should be noted that for $n \to \infty$, the dimension is still a finite number (D_∞=finite), which in general is not an integer.

Largest Lyapunov Exponent of Solar Flux Time Series. The sum of the Lyapunov exponents is the time-averaged divergence of the phase space trajectory; hence, any dissipative dynamical system will have at least one negative exponent. Any dynamical system without a fixed point will have at least one zero Lyapunov exponent.

A small positive Lyapunov exponent is an indication of chaos, and a very large positive Lyapunov exponent is an indication of a totally stochastic or random system. Therefore, the sign of the exponent provides a qualitative picture of a system's dynamics—a positive exponent represents chaos, a zero exponent represents marginally stable systems, and a negative exponent represents periodic systems. Figures 4 and 5 show the actual solar flux data and the largest Lyapunov exponent, respectively, for more than 4000 points. Here, we have used the well known technique of phase space reconstruction with delay coordinates (Reference 18). After embedding the solar flux time series in a state space using the Takens-Packard delay coordinate technique, one can "learn" the induced nonlinear mapping using a local approximation. This will allow us to make short-term forecasting of the future behavior of our time series using information based only on past values. The error estimate of such a technique has already been developed by Farmer and Sidorowich (Reference 19).

$$E \approx Ce^{(m+1)KT} N^{-(m+1)/D},$$

where
- E = normalized error of prediction ($0 \leq E \leq 1$, where zero is perfect prediction and one is a prediction no better than average)
- m = order of local approximation
- K = Kolmogorov entropy
- T = forecasting window
- N = number of data points
- D = dimension of the attractor
- C = normalization constant

Using the Farmer-Sidorowich relation, we can find the prediction horizon T for the zeroth order of local approximation. Any prediction above T_{max} is no better than average constant prediction.

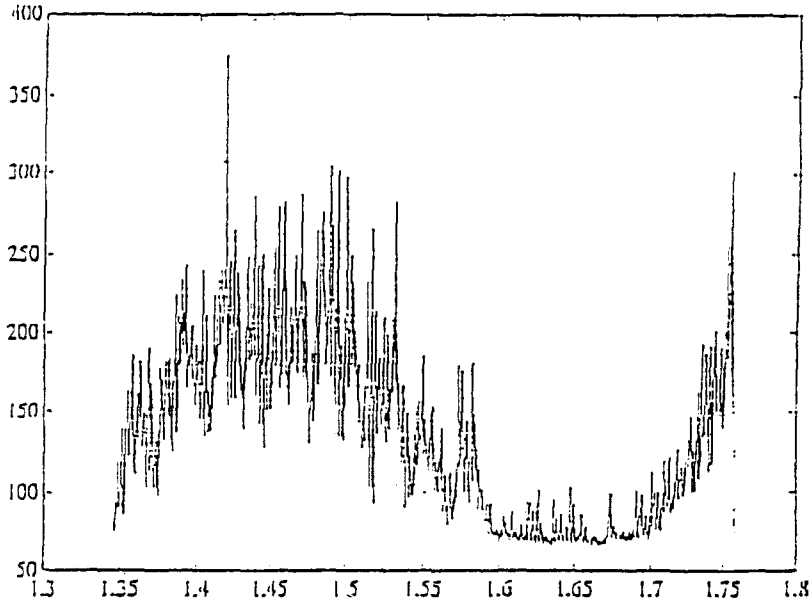

Figure 4. Actual Solar Flux Time Series

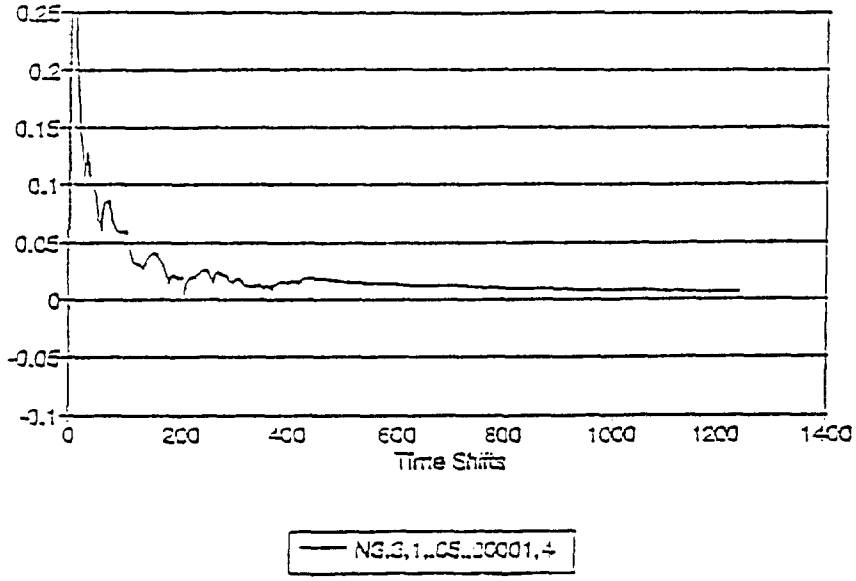

Figure 5. Largest Lyapunov Exponent of Solar Flux Time Series of Figure 4

$$E(T_{max}) = 1$$

Thus, for m = 0, K is the largest Lyapunov exponent λ. Therefore,

$$e^{KT_{max}} N^{-1/D} \sim 1 \qquad \text{or} \qquad T_{max} \sim \frac{\ln (N)}{KD}$$

$$T_{max} \sim \frac{\ln (N)}{\lambda D}$$

Any prediction beyond the indicated horizons is no better than average value. The connection between the local and the global Lyapunov exponents has recently been found (March 1991) by Abarbanel et al. (Reference 20) in a form of power law as

$$\lambda(l) = \lambda_G + \frac{c}{l^v}$$

$$N = \omega l,$$

where $\lambda(l)$ = local Lyapunov exponent
l = length of observed data (observation window)
v = a constant dependent to the dynamical system ($0.5 \leq v \leq 1.0$)
c = a constant dependent to initial conditions of the system
λ_G = well known global Lyapunov exponent
ω = frequency of data points

Because any data are finite length data, using the Abarbanel-Kennel power law and Farmer-Sidorowich relation, we can find T_{max} as

$$T_{max} \sim \frac{\ln(l\omega)}{\left(\lambda_G + \frac{c}{l^v}\right) D}.$$

This means that as l increases linearly, T_{max} increases logarithmically to a certain asymptotic T because of the denominator c/l^v (Figure 6).

Therefore, our relation shows that at the asymptote $T_{max} = T_0$ (Reference 11) and $dT_{max}/dl = 0$. Thus, we can find what observation window is required for forecasting up to T_{max} within some confidence level.

$$\frac{dT_{max}}{dN} \rightarrow 0, \text{ thus } N_0 \sim e^{\frac{x_0(\delta)}{v}}, \; x_0(\delta) > 2,$$

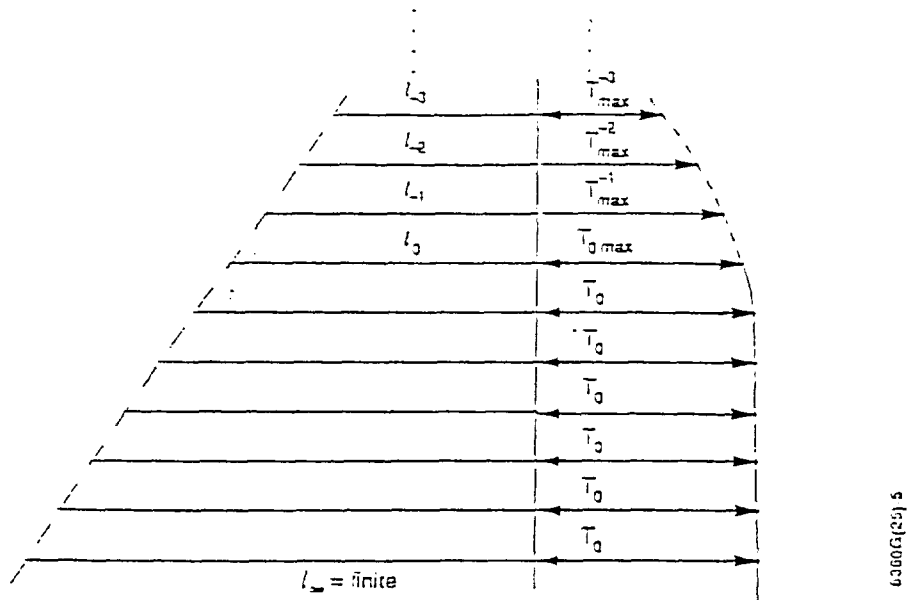

Figure 6. Relationship of l to T_{max}

where $x_0(\delta)$ is the solution to $e^{-x}(x - 1) = \delta$, and where

$$\delta = \frac{\lambda_G}{c\omega^v}$$

is the scaled global Lyapunov exponent.

This result shows that any observation window greater than $l_0 = N_0/\omega$ will not improve our prediction horizon T_0; so more data beyond this limit are not needed to understand a dynamical system. This conclusion is indeed consistent with weather prediction and also with empirical results concluded from neural networks training.

2. STRUCTURE OF THE COMPUTER PROGRAM

Once we know the state space representation, the next goal is to fit a model to the data. There are several methods. The simplest method is to assume that the dynamics can be written as a map in the form

$$f_{n+1} = M(f_n),$$

where the current state is f_n, and f_{n+1} is a future state. Methods such as the polynomial method, rational approximation, radial basis functions, neural networks, and local approximations have been proved to be successful. Here we only introduce local approximation technique, which is the method used to structure the computer program.

Local Approximation. The basic idea is to break up the domain of M into local neighborhoods and fit different parameters into each neighborhood. This fit is generally better than global approximation, especially for large data sets. Most global representations reach a point of diminishing returns, at which adding more parameters or data gives only an incremental improvement in accuracy. After a certain point, adding more local neighborhoods is usually more efficient than adding more parameters and going to higher order. With local approximation, it is possible to use a given functional representation efficiently. The key is to choose the local neighborhood size correctly, so that each neighborhood has just enough points to make the local parameter fits stable. The basic idea is shown in Figure 7 .

Moving to representations of higher degree involves a tradeoff—higher degree representations promise more accuracy, but also require larger neighborhoods. A larger neighborhood implies that the complexity of M increases. Finding the best compromise between these two effects is a central issue in local approximation.

An example of local approximation is *first order*, or *nearest neighbor*, approximation. Look through the data set for nearest neighbor, and predict the current state based on what the neighbor did at time T later. We approximate $f(t + T)$ by $f(t, T) = f(t' + T)$, where $f(t')$, is the nearest neighbor of $f(t)$. That is, to predict tomorrow's solar flux, we would search the historical record and find the solar flux pattern most similar to that of today, and predict that tomorrow's solar flux pattern will be the same as the neighboring pattern 1 day later.

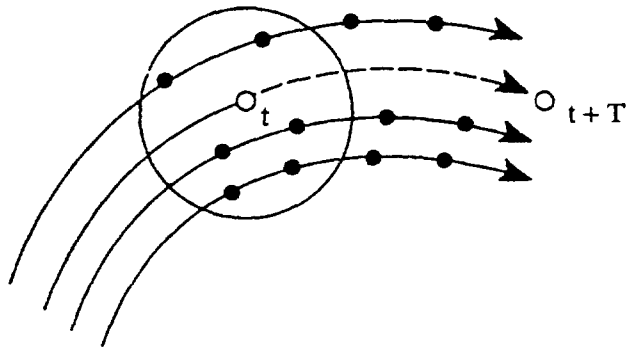

Figure 7. Phase Space Trajectories

First order approximation can sometimes be improved by finding more neighbors and merging their predictions, for example, by weighting according to distance from the current state. If the data are noise, it is better to use a larger number of neighbors. This procedure can be improved by weighting the contributions of neighbors according to their distance from the current state. The beauty of linear approximation is that the neighborhood size grows slowly with the embedding dimension. The order of approximation may depend on factors such as the choice of neighborhoods, the dimension, or peculiarities of the data set. For low dimensional problems, a third order approximation is good.

Nonstationary Behavior. If the trajectory is on an attractor, the data must be stationary, as long as the parameters are constant. However, parameter variations can result in nonstationary behavior. To deal with this problem, we include time as one of the state space coordinates. Time can be included in the metric, so that the search for nearest neighbors favors recent data. This approach takes into account the trends, other time-dependent effects, and seasonality.

Implementation of Local Approximation. Finding neighbors in a multidimensional data set is time consuming when considering many points. A straightforward method is to compute the distance to each point, which takes approximately N steps for N points. This can be reduced to roughly log N steps by organizing the data with a decision tree, such as a k–d tree (Reference 21).

In this method, the data set is partitioned one coordinate at a time. We can take the coordinate with largest range and partition it at its median value. These values are stored in the tree as *keys*. It is now possible to eliminate many points form consideration when looking for the nearest neighbors. This way, we minimize processing time considerably.

2.1 CHOICE OF THE EMBEDDING DIMENSION d

Here we would like to determine the correct value of the embedding dimension d from the scalar time series x(n), n=1,2,...,N_D. We assume that there are enough data that we need not be concerned with statistical issues about numerical accuracy. We also assume that extrinsic noise is absent from the x(n) when we receive them. We further assume that by following Takens' phase-space reconstruction technique we have successfully captured the dynamics and embedded our time series. This requires a correct choice of τ, which will be discussed in the next section.

For now, let's further assume we have a correct τ to construct the attractor in the phase space. To establish dimension d, we need some characteristic of the attractor that becomes unchanging as d becomes large enough, thus indicating that the attractor can be embedded in R^d. This invariant characteristic of the attractor is the attractor dimension d_A. One increases d until d_A remains constant and identifies the minimum d where d_A "saturates" as the embedding dimension. But computation of d_A is difficult, so we use the correlation function D(r) proposed by Takens (Reference 17).

$$D(r,N,d) = \frac{2}{N(N-1)} \sum_{i=1}^{N} \sum_{j=i}^{N} U(r - \| \vec{f}(j) - \vec{f}(i) \|) \; i \neq j,$$

where U(z) is just the unit step function $U(z) = \begin{cases} 1 & z>0 \\ 0 & z<0 \end{cases}$.

For N large enough, the behavior of D(r,N,d) for r becomes independent of N and D(r,N,d) takes the form

$$D(r,N,d) = \Phi(r,d) r^{\nu(d)}.$$

If we plot D(r,N,d) versus r we can single out the correct value of dimension d as in Figure 8. From Figure 8 it is concluded that the minimum value of d=3 is the right choice beyond which attractor dimension d_A does not change or the slope of our graph becomes constant.

In the next section we study the correct choice of τ to reconstruct the phase-space attractor.

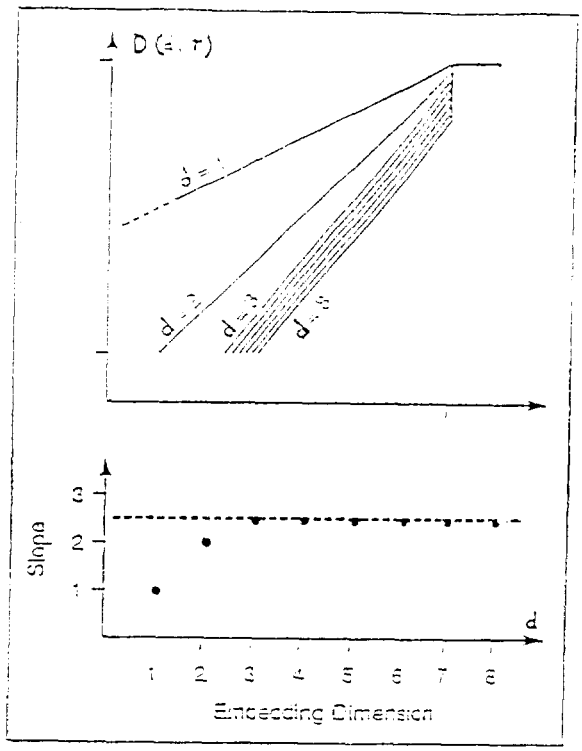

Figure 8. Correlation and Attractor Dimensions

2.2 Choice of the Time Shift τ

The choice of time shifts τ is not well agreed upon. If the underlying system is described by a differential equation and scalar variable x(t) were measured at discrete times $x(n) = x(t_o + n\,\Delta t)$, then we would be, by the choice of lagged variables, trying to find a discrete replacement for the usual phase-space coordinates:

$$x(t), \dot{x}(t), \ddot{x}(t), \ldots \frac{d^{d-1}x(t)}{dt^{d-1}}.$$

The best choice for time shift τ is a fraction of the time associated with the first local minimum of the autocorrelation function

$$\frac{1}{T}\int x(t+\tau)x(t)dt\,.$$

We find that this choice, although somewhat arbitrary, works well in practice and gives a simple systematic way of determining τ.

3. RESULTS

Figure 9 shows the daily observed values of solar flux $F_{10.7}$ for about four solar cycles from February 1947 to November 1991. A close examination of this graph shows low daily variability at solar cycle minima and large daily variability at solar cycle maxima. Therefore, the challenge for solar physicists is to forecast solar flux in the region of solar cycle maxima.

Here forecasts are made in the region of solar cycle maxima, where the variations are as large as 150 units of solar flux, and in regions between a maximum and a minimum, where the variations are as large as 100 units of solar flux. Comparisons are made versus 27-day NOAA predictions, Schatten's monthly predictions, and

observed values of flux $F_{10.7}$. Figure 10 shows 27-day predictions using chaos theory with undecoupled (raw) data. Predictions were made in the region of solar cycle maxima. Comparisons show clearly that chaos predictions are at worst 20 units off from observed values, whereas the best NOAA 27-day predictions are about 40 units off from observed values, with a wrong phase on the 27-day local maximum.

Here it is clear that chaotic long-term prediction is very close to the 81-day average of actual $F_{10.7}$, which is useful for calculating exospheric temperature using the Jacchia-Roberts atmospheric density model.

Figure 11 shows the same conclusion for predictions made for a 60-day span. Here it is very clear that NOAA predictions (best updated values to the end of 60 days) do not carry any of the significant dynamical features of the observed values, whereas the chaos prediction does carry the inherent dynamical features. Figure 12 shows a comparison of MSFC and Schatten's predictions. Figure 13 also shows comparisons of 81-day average $F_{10.7}$, Schatten's predictions, and chaos predictions.

Figure 14, which was made for a region between solar cycle maxima and minima, shows a 30-day prediction indicating that chaos prediction is at worst 20 units off from the observed values, but it should be noted that the signal-to-noise ratio characteristic of solar activity indicators are ~ 35 for $F_{10.7}$, ~ 20 for sunspot numbers, and ~ 10 for sunspot areas.

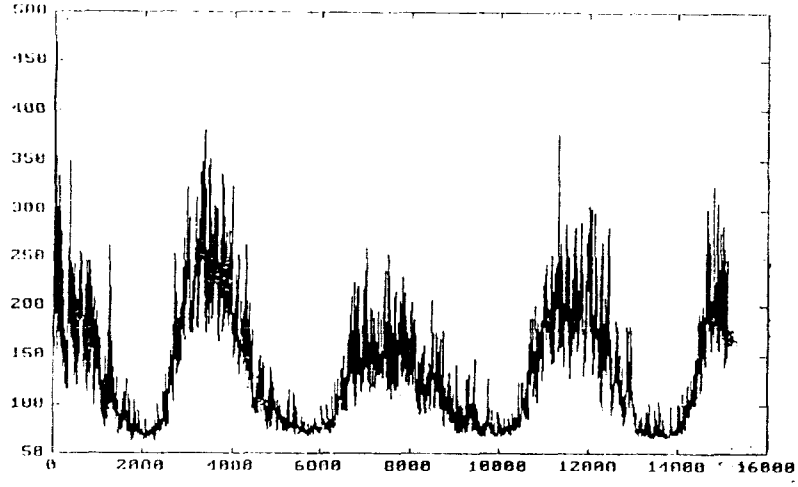

Figure 9. Daily Observed Values of Solar Flux $F_{10.7}$ (Watt per m^2 per Hz x 10^{-22}) Versus Modified Julian Date

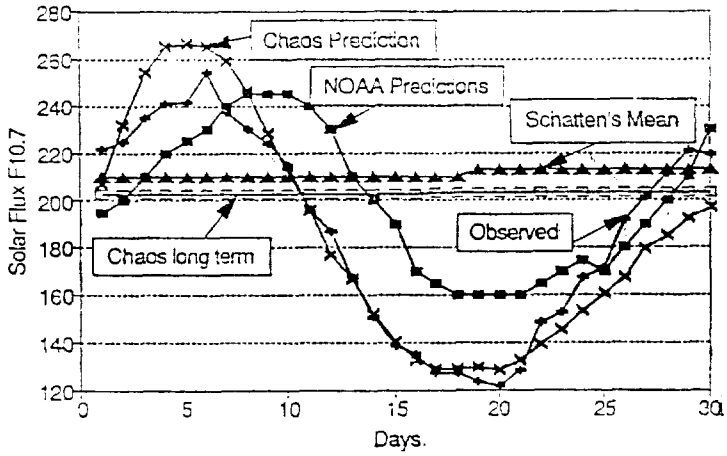

Figure 10. 27-Day Chaos and NOAA Predictions Compared With Observed Solar Flux $F_{10.7}$ From April 13, 1990

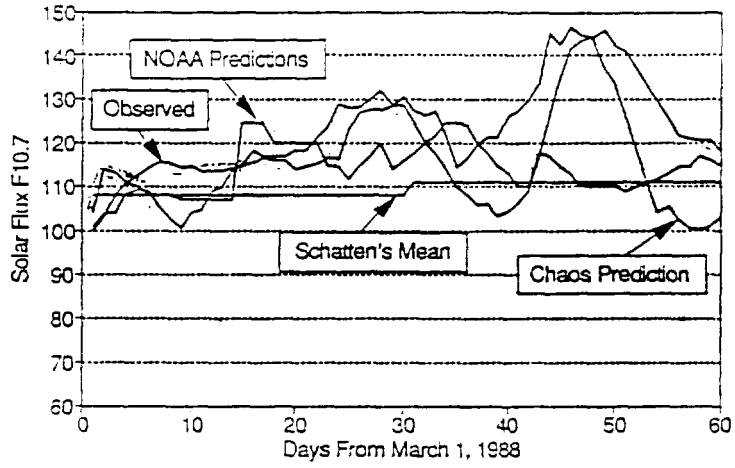

Figure 11. 60-Day Chaos and NOAA Predictions (Best Weekly Updates) Compared With Observed Solar Flux $F_{10.7}$

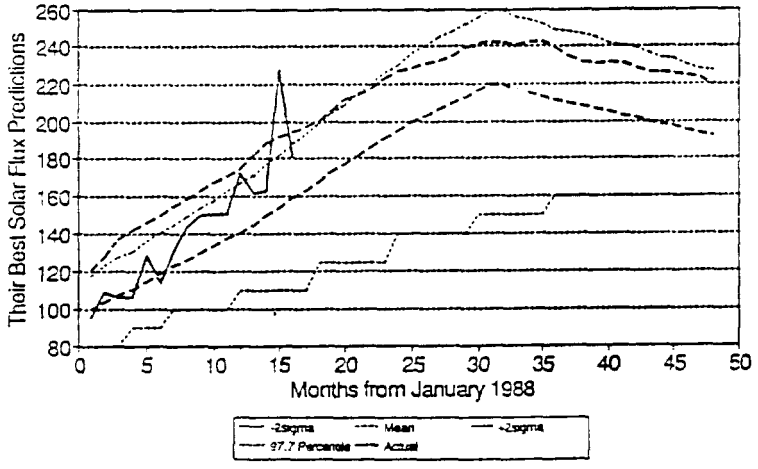

Figure 12. Comparison of MSFC and Schatten Solar Flux $F_{10.7}$ Predictions With Observed $F_{10.7}$

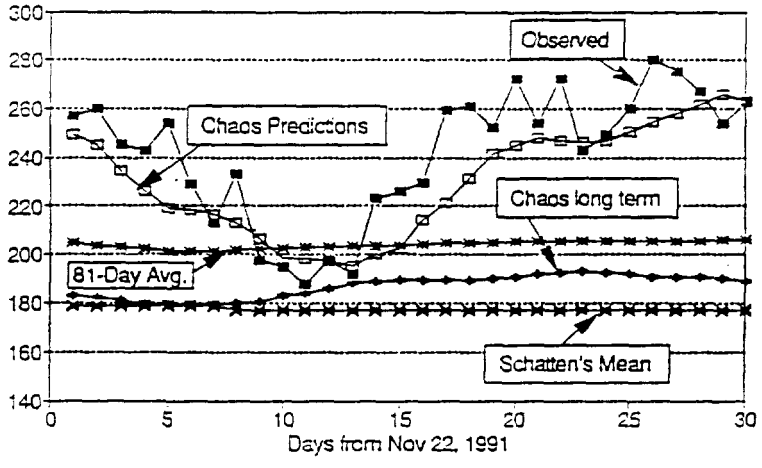

Figure 13. 30-Day Comparison of 81-Day Average of Observed $F_{10.7}$, Schatten's Prediction and Chaos Prediction With Observed Daily $F_{10.7}$

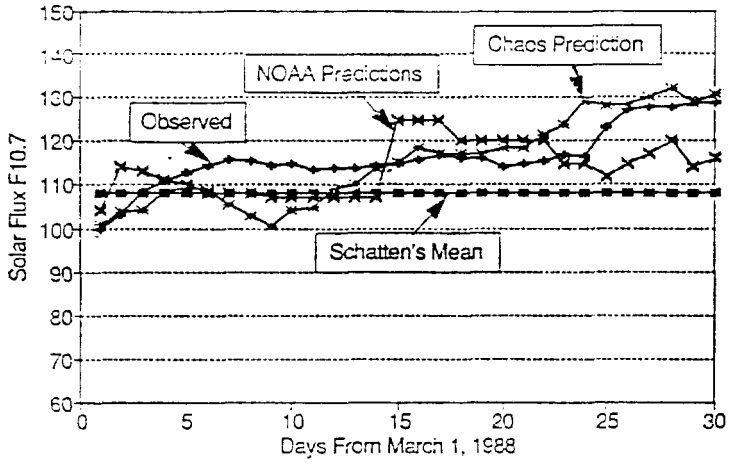

Figure 14. 30-Day Comparison of Schatten's Prediction and Chaos Prediction With Observed Daily $F_{10.7}$

Figure 15 shows chaos predictions for embedding dimensions 3 and 4, the Schatten mean, and $+2\sigma$ predictions. Figure 15 clearly shows that, for long-term forecasting, the chaotic method carries all the inherent structures of Schatten's method. Figure 16 shows that chaos prediction captures the cyclical behavior of solar cycles (the minimum of the cycle is very clear). Figure 17 shows the observed $F_{10.7}$ and its 81-day average, and Figure 18 shows chaos prediction for about 50 months after November 1991 (the time of our analyis). Comparsions of chaotic predictions (Figure 16) with Schatten's predictions show the chaos model to be predicting $F_{10.7}$ even higher than Schatten's $+2\sigma$. Recently, the observed $F_{10.7}$ have in fact been higher than Schatten's $+2\sigma$. As seen in Figure 17, after October the average flux is about 200, as is clear from the first couple of points in Figure 18. It is certainly possible to fine tune the model by adjusting the embedding dimension and the time shift τ. Figure 19 shows predictions for various time shifts τ, with D=3. Figure 20 shows predictions for various time shifts τ, with embedding dimension D=4.

4. CONCLUSIONS

In this paper we presented numerical techniques for constructing nonlinear predictive models to forecast solar flux $F_{10.7}$ directly from its time series. Using this approach, we extracted dynamical invariants of our system

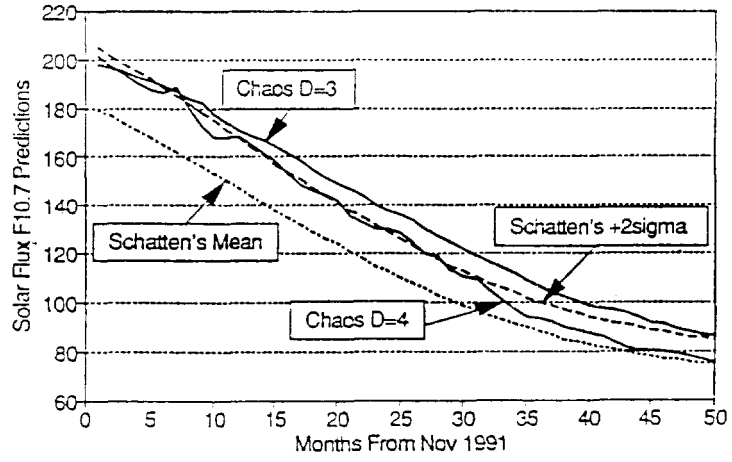

Figure 15. Chaos Long-Term Prediction With Embedding Dimension D=3 and D=4 Compared With Schatten's Mean and Schatten's $+2\sigma$

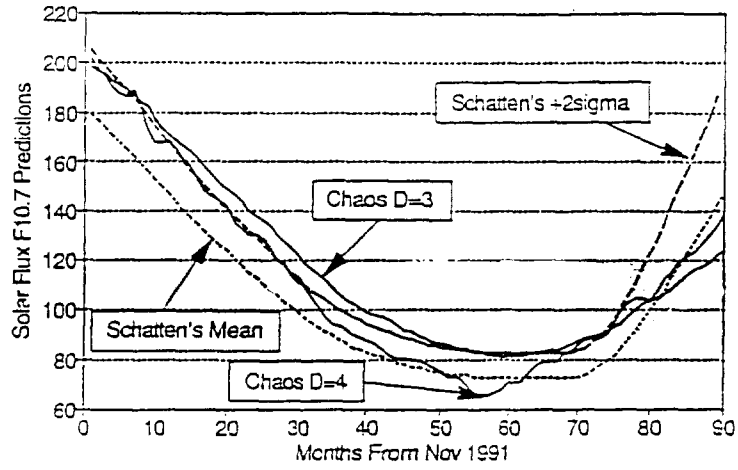

Figure 16. Predictions of Schatten and Chaos Theory for Solar Cycle Minima

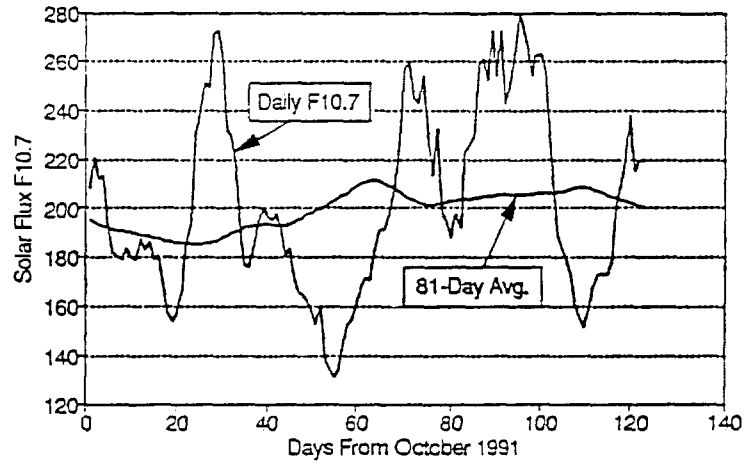

Figure 17. Observed Solar Flux $F_{10.7}$ and Its 81-Day Average, Starting From October 1991

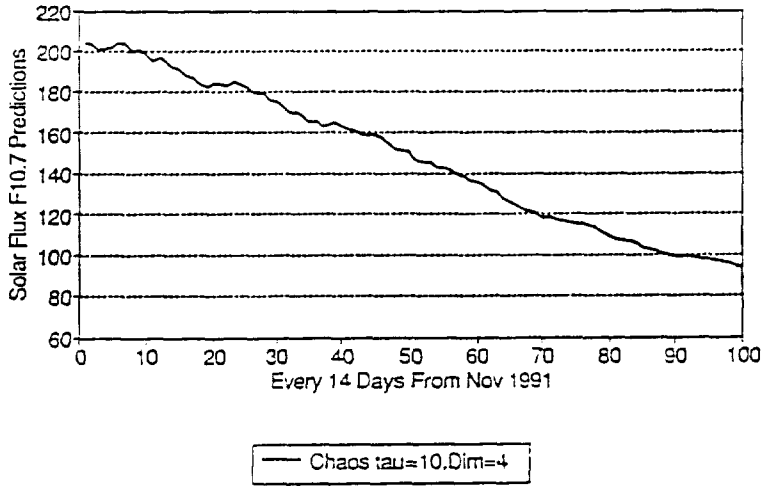

Figure 18. 50-Month Chaos Prediction With Embedding Dimension D=4 and Time Shift τ =10 Days

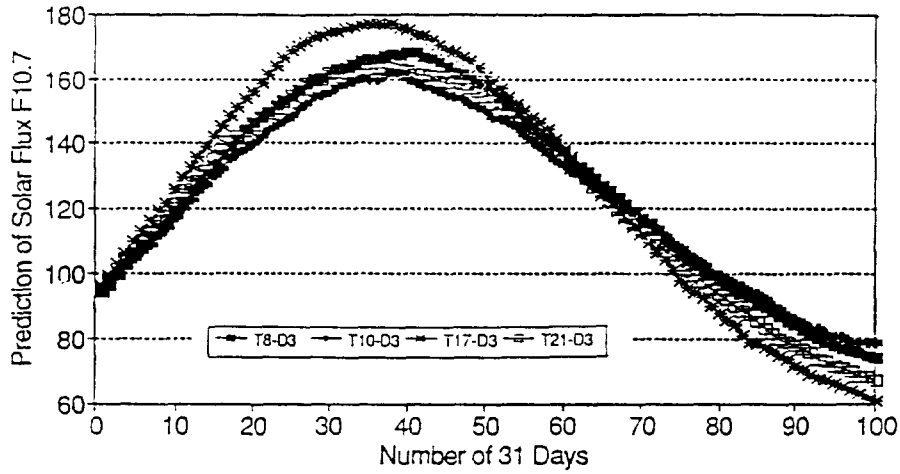

Figure 19. Variability of Predictions as a Function of Change in Time Shift τ. Here Embedding Dimension Is Kept Constant (D=3), and τ Is Varied by 8, 10, 17, and 21 Days

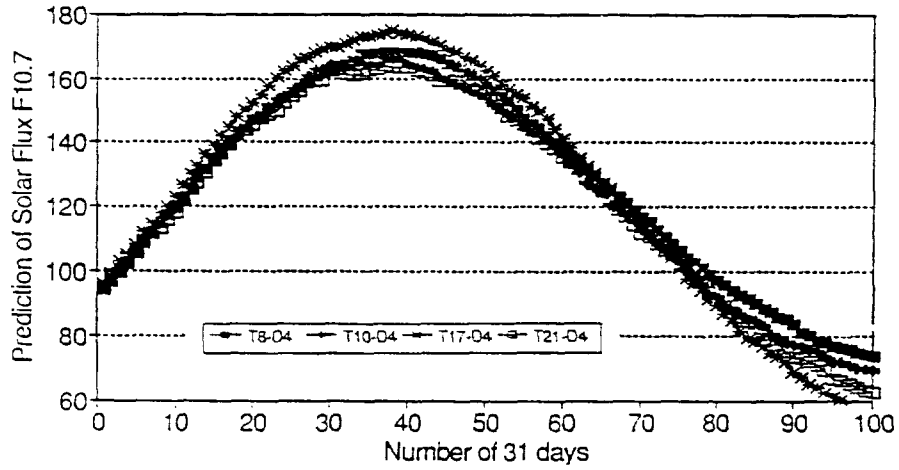

Figure 20. Variability of Predictions as a Function of Change in Time Shift τ. Here Embedding Dimension Is Kept Constant (D=4), and τ Is Varied by 8, 10, 17, and 21 Days

without reference to any underlying solar physics, thereby circumventing the complicated physics and modeling the system directly from data.

Comparison of our prediction of solar flux activity using chaotic dynamics with conventional methods used by Schatten, MSFC, and NOAA demonstrated the validity of our approach to modeling solar activity using nonlinear dynamics. This approach could also be used to model other complicated systems, such as geomagnetic activity and atmospheric density, to name just two.

ACKNOWLEDGMENTS

Thanks to D. Ashrafi, C. Schiff, and J. Kissel for valuable discussions, suggestions, and support. It is also a pleasure to thank K. Schatten for his many suggestions, such as a combined chaos-Schatten model, and C. Grebogi and E. Ott for teaching me the fundamental concepts of chaos (S. A.).

REFERENCES

1. Brandt, C. J., *Introduction to the Solar Wind,* W. H. Freeman and Company, San Francisco, 1990
2. Goddard Space Flight Center, Flight Dynamics Division, *Future Missions Studies: Generalized Model of Sunspots as E-Solitons of Multilevel Turbulence,* S. Ashrafi, in preparation (Computer Sciences Corporation)
3. Goddard Space Flight Center, Flight Dynamics Division, FDD-554-91-004, *Future Missions Studies: Preliminary Comparisons of Solar Flux Models,* S. Ashrafi, prepared by Computer Sciences Corporation, January 1991
4. Goddard Space Flight Center, Flight Dynamics Division, FDD-554-91-006, *Future Missions Studies: Solar Flux Analysis Using Chaos,* S. Ashrafi, prepared by Computer Sciences Corporation, January 1991
5. Evidence of Chaotic Pattern in Solar Flux Through a Reproducible Sequence of Period-Doubling-Type Bifurcations, *Proceedings of Flight Mechanics/Estimation Theory Symposium,* S. Ashrafi and L. Roszman, prepared by Computer Sciences Corporation, May 1991
6. Goddard Space Flight Center, Flight Dynamics Division, 554-FDD-91/112, *Future Missions Studies: Chaotic Solar Flux (Structural Stability, Attractor Dimension, Application of Catastrophe),* S. Ashrafi, prepared by Computer Sciences Corporation, June 1991
7. Computer Sciences Corporation (under contract to Goddard Space Flight Center, Flight Dynamics Division) *Limits on the Predictability of Solar Flux Time Series,* S. Ashrafi and L. Roszman, June 1991 (submitted for publication in *J. Geophys. Res.*)
8. Goddard Space Flight Center, Flight Dynamics Division, 554-FDD-91/113, *Future Missions Studies: Forecasting Solar Flux Directly From Its Time Series,* S. Ashrafi, prepared by Computer Sciences Corporation, July 1991
9. Goddard Space Flight Center, Flight Dynamics Division, *Future Missions Studies: Existence of a Unique Canonical Transformation to Transform Dynamo Equations to Lorenz Equations,* S. Ashrafi, prepared by Computer Sciences Corporation, unpublished manuscript
10. Goddard Space Flight Center, Flight Dynamics Division, *Future Missions Studies: Intermittency of Dynamo Can Explain Maunder Minimum,* S. Ashrafi, prepared by Computer Sciences Corporation, unpublished manuscript
11. Goddard Space Flight Center, Flight Dynamics Division, 554-FDD-91/125, *Future Missions Studies: Combining Schatten's Solar Activity Prediction Model With a Chaotic Prediction Model,* S. Ashrafi, prepared by Computer Sciences Corporation, November 1991
12. Van Loon, H., and K. Labitzke, Association between the 11-year solar cycle, the QBO, and the atmosphere, Part II, *J. Climate,* 1, 1988
13. Kerr, R. A., Sunspot-weather link is down but not out, *Science,* 248, 1990
14. Bray, J. R., Solar-climate relationships in the post-Pleistocene, *Science,* 171, 1971
15. Walterscheid, R. L., Solar cycle effects on the upper atmosphere: Implications for satellite drag, *J. Spacecraft,* 26, 1989
16. Withbroe, G. L., Solar activity cycle: History and predictions, *J. Spacecraft,* 26, 1989
17. Takens, F., Detecting strange attractors in turbulence, in *Lecture Notes in Mathematics, Vol. 898: Dynamical Systems and Turbulence,* Springer, New York, 1981
18. Packard, N., et al., Geometry From a Time Series, *Phys. Rev. Lett.,* 45, 1980
19. Farmer, J., and J. Sidorowich, Predicting chaotic time series, *Phys. Rev. Letts.,* 59, 1987
20. Abarbanel, H., et al., Lyapunov exponents in chaotic systems, *Rev. Modern Phys. Letts.* [B], (in press)
21. Bentley, J. H., Multidimensional binary search trees in data base applications, *IEEE Transactions on Software Engineering,* 5 (4), 1979

Analysis of Reentry Into the White Sands Missile Range (WSMR) for the LifeSat Mission*

M. Hametz and L. Roszman
COMPUTER SCIENCES CORPORATION (CSC)

F. Snow and J. Cooley
GODDARD SPACE FLIGHT CENTER (GSFC)

ABSTRACT

This study investigates the reentry of the LifeSat vehicles into the WSMR. The LifeSat mission consists of two reusable reentry satellites, each carrying a removable payload module, which scientists will use to study long-term effects of microgravity, Van Allen belt radiation, and galactic cosmic rays on living organisms. A series of missions is planned for both low-Earth circular orbits and highly elliptic orbits. To recover the payload module with the specimens intact, a soft parachute landing and recovery at the WSMR is planned. This analysis examines operational issues surrounding the reentry scenario to assess the feasibility of the reentry.

* This work was supported by the National Aeronautics and Space Administration (NASA)/Goddard Space Flight Center (GSFC), Greenbelt, Maryland, Contract NAS 5-31500.

1. INTRODUCTION

The LifeSat program is envisioned to employ two reusable reentry satellites (RRS), each carrying a removable payload module (PM), to be used by scientists to study long-term effects on living organisms of microgravity, Van Allen belt radiation, and galactic cosmic rays (GCR). The effects of GCR are separable from those due to Van Allen belt radiation by orbit selection. Both highly elliptical polar and circular near-equatorial orbits will be used to provide the range of environments necessary to perform a comprehensive study. Mission lengths of approximately 60 days will provide full life-cycle observation for some of the organisms. The spacecraft is returned to Earth at the White Sands Missile Range (WSMR) in New Mexico, U.S. for a soft landing to recover the PM containing the specimens intact, and allow the RRS to be refurbished for future missions.

Four missions are currently planned: two highly elliptical orbit missions [200 x 20,600 kilometer (km)], each to place a single RRS in a polar orbit from the Western Test Range (WTR); and two circular orbit missions that will each fly two RRSs at differing altitudes. The circular missions will launch from the Eastern Test Range (ETR) and will have altitudes of 350, 700, and 900 km, with an inclination of 34 degrees. This paper focuses on the reentry phase for all four mission orbits. Operational issues such as burn sequencing, burn errors, range safety, and contingency operations are discussed.

2. REENTRY

WSMR will recover the LifeSat vehicles at the end of each 60-day mission. Execution of a controlled, soft landing and recovery will be done by performing a primary deorbit burn followed by a trim burn to correct for dispersions in the primary burn. Deployment of a parachute system at an altitude of approximately 50,000 feet will then slow the velocity of the spacecraft to allow an impact of less than 10 g's. The spacecraft position will be closely monitored, and with the aid of a homing beacon, ground recovery crews will retrieve the PM within two hours after impact.

The analysis performed for this paper concentrates on both the deorbit and trim burn. The analysis of the primary deorbit burn begins by calculating the nominal delta-v for ballistic reentry of the four mission orbits. The effects of thrust and attitude errors on the deorbit burn are quantified to provide a landing footprint. The off-nominal cases for the deorbit burn are then remodeled with a trim burn to find the delta-v's required to readjust the orbit path to land at WSMR. The trim burn accuracy is then varied to generate a revised landing footprint which includes both off-nominal deorbit and trim burns.

2.1 Nominal Deorbit Burn

The nominal deorbit burn location is defined as the point in the mission orbit that is one half an orbit before passing over WSMR. This was chosen because it requires the minimum delta-v to reenter the spacecraft. Figures 2-1 and 2-2 show the burn points and the nominal reentry paths for the 900 km circular mission and the highly elliptic mission, respectively.

The modeling of the burns and the orbit propogations are performed using the Goddard Mission Analysis System (GMAS). The burns are modeled assuming four 100-pound force hydrazine thrusters with a specific impulse (I_{sp}) of 215 seconds. All burns are assumed to be performed in-plane (yaw angle = 0 degrees, pitch angle = 180 degrees) and are targeted to a landing site at WSMR located at latitude 33.1 degrees north and longitude 253.63 degrees east. Finite burn approximations and fuel consumptions were calculated in GMAS using the rocket equation. The burn data for each of the four mission orbits are listed in Table 2-1.

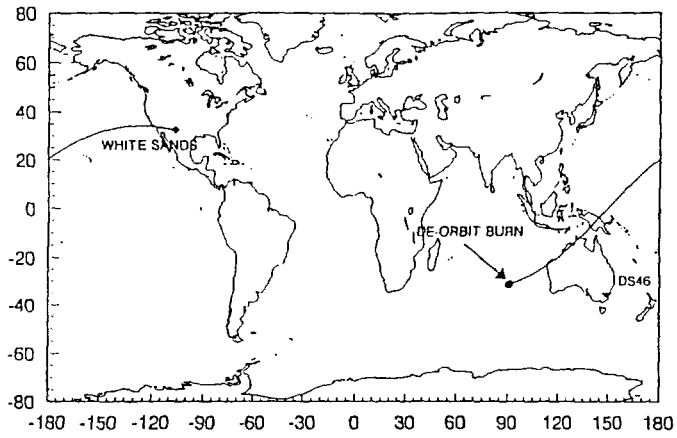

Figure 2-1. LifeSat Reentry Groundtrack 900 km Orbit North-to-South Trajectory to WSMR (Inclination equals 34 degrees)

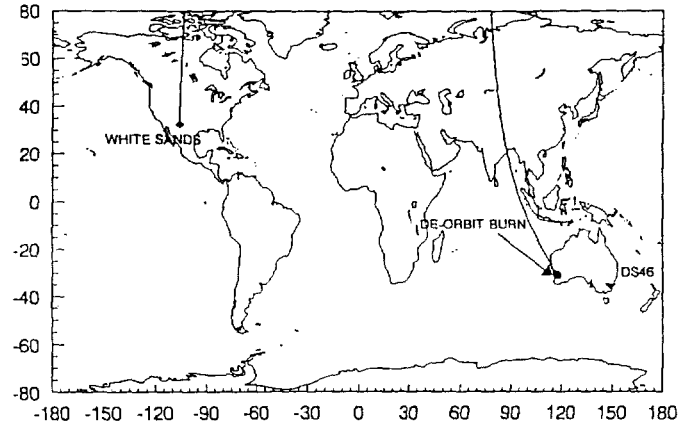

Figure 2-2. LifeSat Reentry Groundtrack 200 x 20,600 km Orbit North-to-South Trajectory to WSMR (Inclination equals 90 degrees)

Table 2-1. Nominal Deorbit Finite Burn Data

MISSION ORBIT DESCRIPTION	DEORBIT DELTA-V (M/SEC)	BURN LENGTH (SEC)	FUEL USED (LBS)
350 km circular	79.8	63.9	118.9
700 km circular	174.6	136.7	254.3
900 km circular	230.0	177.8	330.7
200 x 20,600 km	24.2	19.6	36.5

The deorbit burn which requires the lowest delta-v is the highly elliptic mission. Because the total change in semimajor axis is small, a delta-v of only 24.2 meters per second (m/sec) is needed for spacecraft reentry. For the circular orbits, as the altitude of the orbit increases, the change in semimajor axis from the mission orbit to the reentry orbit increases, resulting in a much longer burn. The largest delta-v, 230.0 m/sec, occurs for the 900 km orbit.

2.1.1 Range Safety

To land at WSMR, the RRS must meet various range safety criteria. The ground tracks of the reentry path and the associated altitudes were studied for the nominal cases. The footprints of various off-nominal cases were also analyzed and are presented in Section 2.2.

The ground tracks of the reentry path are plotted to depict when the spacecraft travels over populated areas. Graphs depicting altitude versus downrange distance from WSMR are generated to be used in conjunction with the ground track plots. These graphs aid in determining safe avoidance of the regions surrounding WSMR as well as in determining the need for the Federal Aviation Administration (FAA) to restrict airspace.

The circular orbit with the lowest reentry altitude is the 350 km case. A north-to-south trajectory was initially chosen for the reentry to avoid overflying Mexico (see Figure 2-1). A more detailed view of this reentry path is shown in Figure 2-3. The reentry path enters the U.S. over the northernmost part of Los Angeles. However, Figure 2-4 shows that at that point in the orbit, the altitude of LifeSat is 230 thousand feet (kft). Once over New Mexico, U.S., the spacecraft passes close to Truth or Consequences. However, although the city is near WSMR, the altitude of the spacecraft is approximately 120 kft.

For the elliptic polar mission, Figure 2-5 shows that LifeSat will reenter from the north. This reentry path does not pass directly over any cities but does pass between Albuquerque and Santa Fe, a region of frequent air traffic. Figure 2-6 shows that the altitude of LifeSat is over 150 kft when passing between the cities. Since airplanes travel at an altitude, of at most, 40 kft, an airspace conflict does not exist. For all cases, LifeSat will not begin to descend below 50 kft until directly over WSMR.

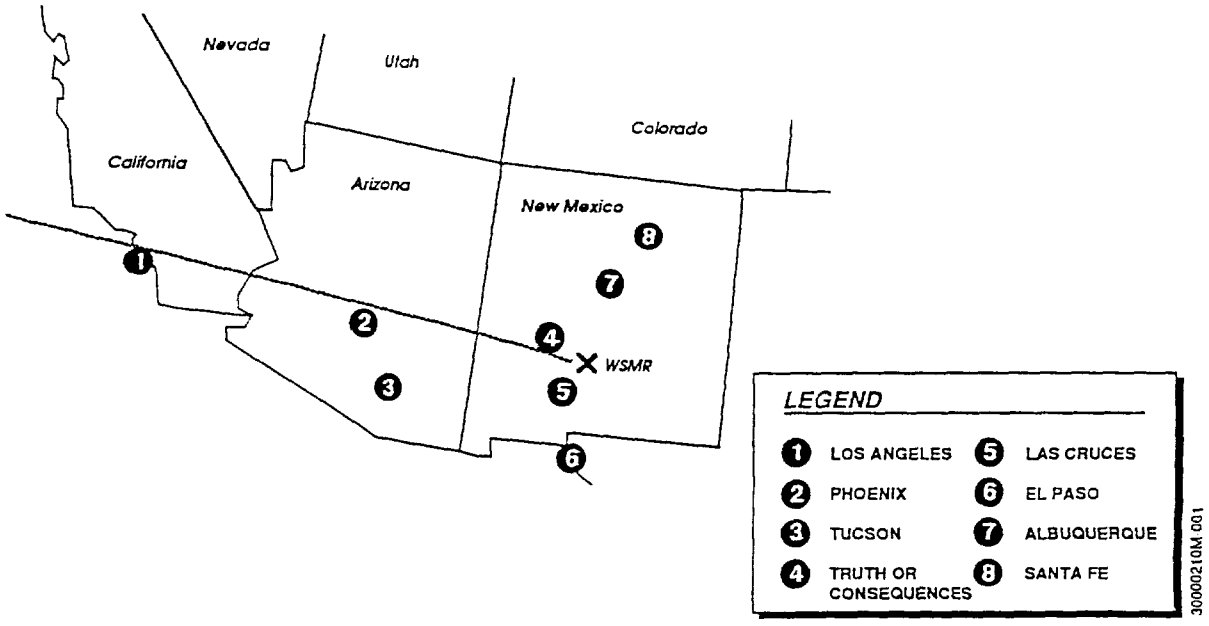

Figure 2-3. Detail Reentry Groundtrack; 350 km Orbit North-to-South Trajectory

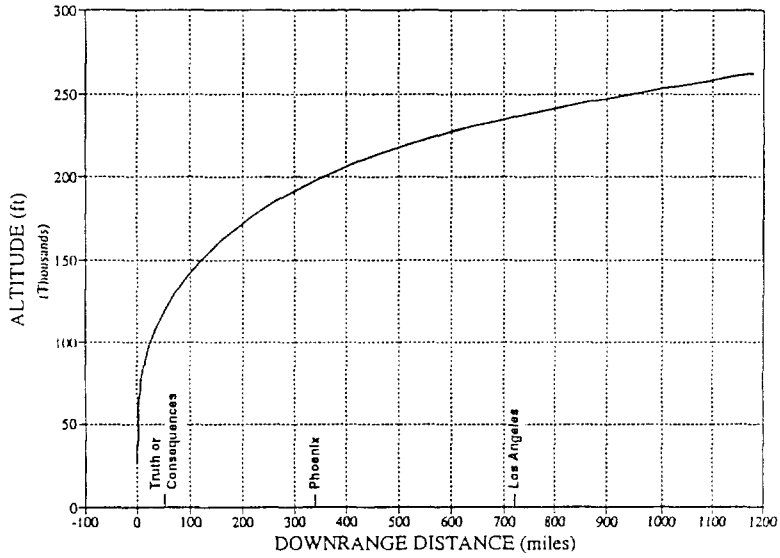

Figure 2-4. LifeSat Reentry Altitude vs. Distance; 350 km Orbit North-to-South Trajectory

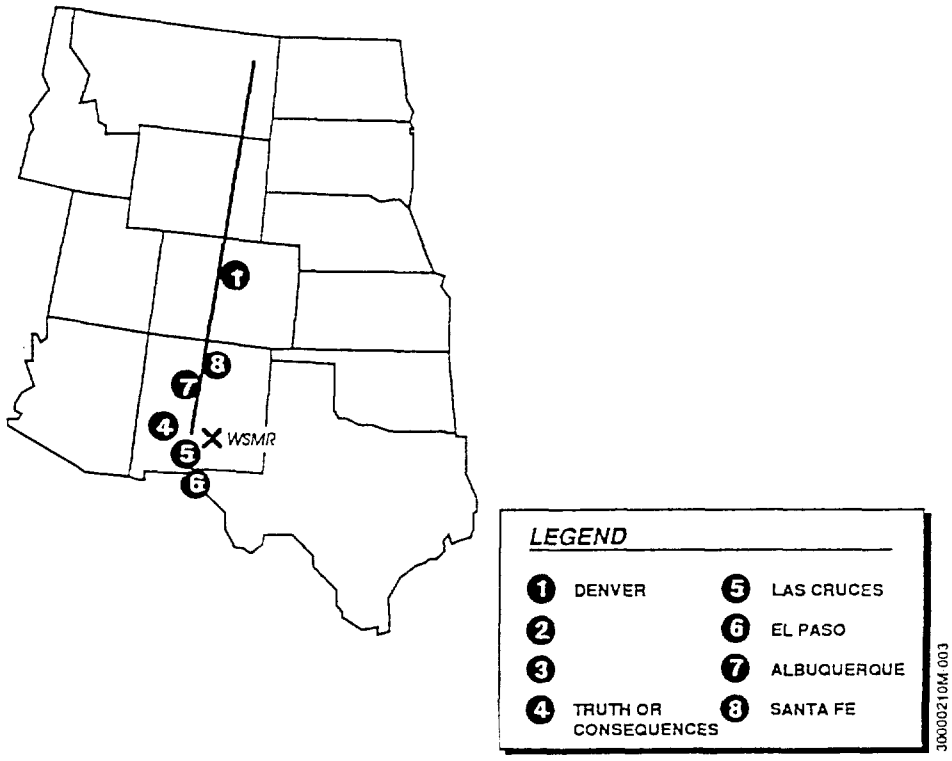

Figure 2-5. Detail Reentry Groundtrack; 200 km x 20,600 km Orbit North-to-South Trajectory

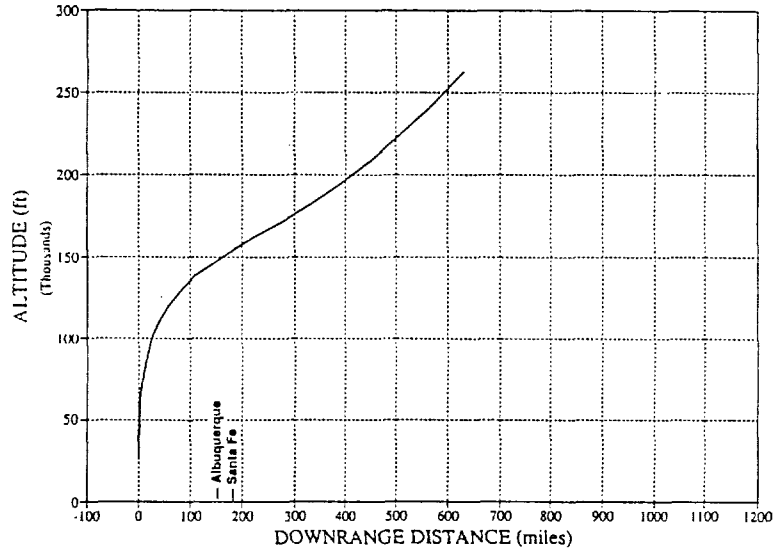

Figure 2-6. LifeSat Reentry Altitude vs. Distance; 200 x 20,600 km Orbit

2.2 Off-Nominal Deorbit Burn: Delta-V Errors

One other major reentry issue is the size of the possible footprint and the accuracies that are necessary to land the spacecraft at WSMR. For LifeSat, the reentry will be performed by two burns: a primary deorbit burn and a secondary trim burn. This section presents the results of an off-nominal deorbit burn and the resulting footprint. Section 2.4 presents the trim burn calculations, which use the results of this section to model the burns necessary to recover from off-nominal deorbit burns.

2.2.1 Circular Orbits

For the 350 km mission orbit, a delta-v of 79.8 m/sec is required to reenter at WSMR. A 3-sigma range of ± 20 percent of the nominal delta-v was tested for the burn; however, only a range of +20 percent to –7 percent reentered (Figure 2-7). If the burn is leaner than 7 percent, the spacecraft skips out and reenters on the following orbit.

The footprint extends from approximately 150 miles west of Los Angeles, California (+20 percent) to just northwest of Puerto Rico (–7 percent). The state of New Mexico is included on the graph to show that an error of only 1 percent will cause the spacecraft to reenter in the neighboring state. In fact, accuracies of approximately 0.75 percent are required to contain the spacecraft reentry to New Mexico.

Currently, no calibration burns are planned for the deorbit thrusters. Therefore, although a 20 percent error would be the maximum error expected, a 5 percent error is likely. If the thrusters are calibrated, a 1 percent error would still be expected, which would still result in a large footprint.

Reentry from the 700- and 900-km orbits are even more sensitive to delta-v errors due to the increase in the nominal delta-v. For the 900-km orbit, the footprint extends about 30 miles farther west than the 350 case, but only reaches Miami, Florida for a cold burn. The east boundary is shortened because a burn error greater than 3 percent cold will not reenter. Furthermore, a burn accuracy of ± 0.5 percent is required to land in the state of New Mexico.

2.2.2 Elliptical Orbit

A nominal deorbit delta-v from the elliptical orbit is 24.2 m/sec. If the burn is 20 percent hot, the spacecraft will land due west of Denver, Colorado, as shown in Figure 2-8. A 10 percent hot burn will result in reentry in

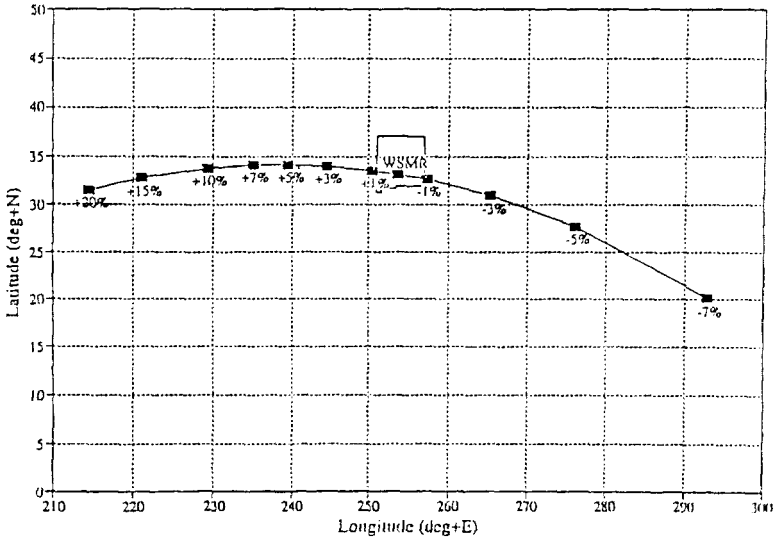

Figure 2-7. Reentry Footprint Delta-v Errors; 350 km North-to-South Trajectory

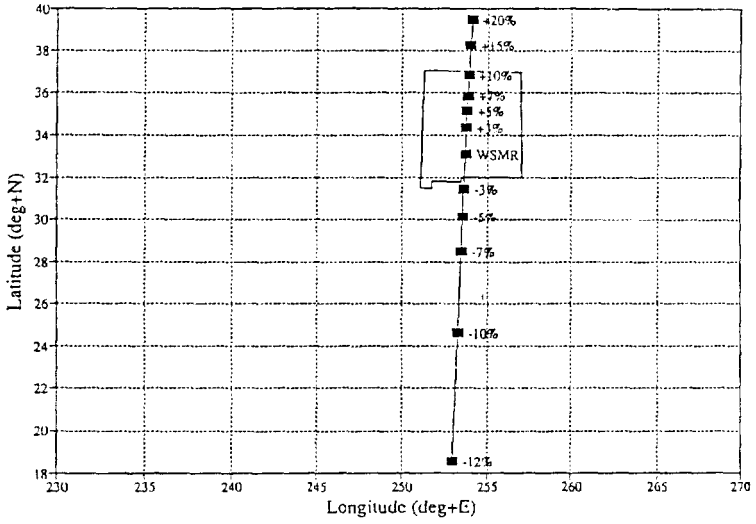

Figure 2-8. Reentry Footprint Delta-v Errors; 200 x 20,600 km; 90 Degrees

New Mexico. If the burn is cold, a –12 percent error is the limit at which the spacecraft will reenter. This extends the footprint into Mexico to a point just south of Guadalajara.

For both the circular and elliptic cases, the size of the footprint may be reduced by reentering at a steeper flight path angle. This is accomplished by lowering the perigee in the reentry orbit. Therefore, to still reenter at WSMR, the deorbit burn must occur later than the current nominal position. In similar studies, such as the Earth Observing System (EOS) reentry analyses, reducing the perigee by 100 km decreased the size of the footprint by 43 percent.

There are disadvantages to lowering perigee. The deorbit delta-v will increase due to the larger change in the semimajor axis. Firing late also decreases the time between the deorbit and trim burns. This is crucial because of the time required to assess the deorbit burn and plan the trim burn. Finally, the g forces experienced by the

spacecraft will increase because the flight path angle at the atmospheric interface will increase. Further analysis is needed on the alternative trajectories to be able to measure the various trade-offs.

2.3 Off-Nominal Deorbit Burn: Attitude Errors

In addition to thrust errors, misalignments in the yaw and pitch angles were also analyzed. Figures 2-9 and 2-10 show the results of yaw and pitch errors of ± 3 degrees on the thrust vector for the 350 km and 900 km mission orbits. (The case of the polar orbit is not shown because yaw and pitch errors of ± 3 degrees do not perturb the spacecraft out of the missile range.)

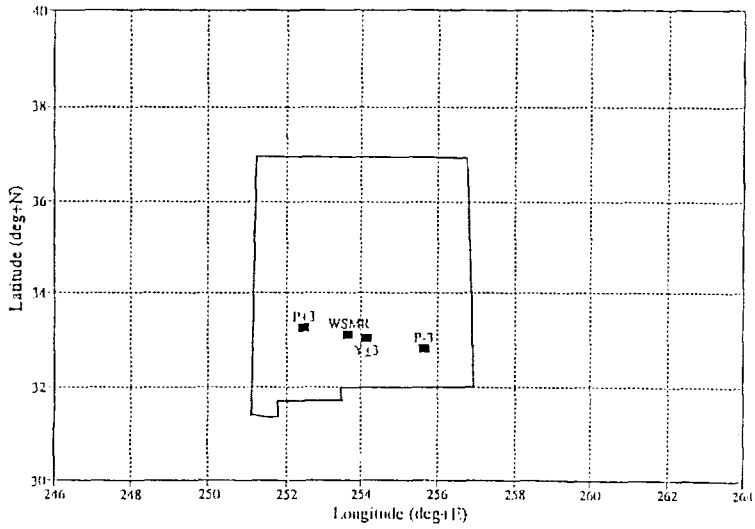

Figure 2-9. Reentry Footprint Yaw and Pitch Errors (Degrees); 350 km North-to-South Trajectory

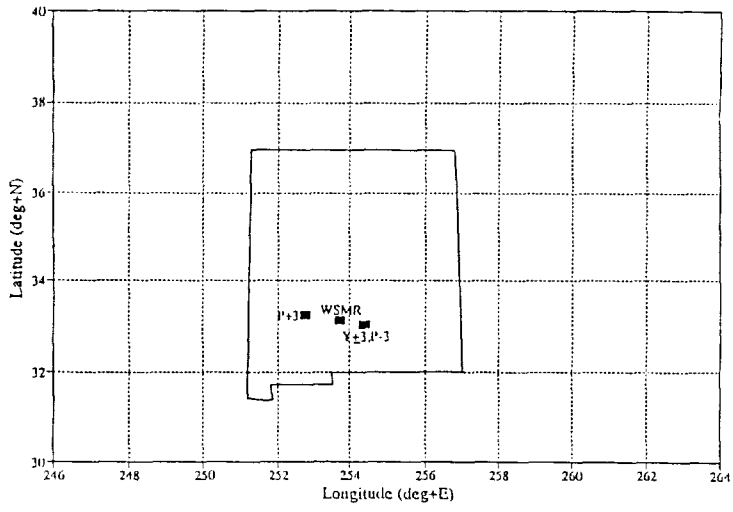

Figure 2-10. Reentry Footprint Yaw and Pitch Errors (Degrees); 900 km North-to-South Trajectory

In both cases, yaw angle errors (out of plane errors) of both ± 3 degrees cause the spacecraft to impact in the identical position. This occurs because the out-of-plane component of velocity is not large enough to perturb the plane of the orbit and is therefore negligible. Consequently, the only effect on the spacecraft is a small reduction of the magnitude of the in-plane vector; thus, the impacts are the same for both ± 3 degrees. Furthermore, this result is comparable to a thrust error, because the only effect is to reduce the in-plane velocity vector. The effects are greater for the 900 km orbit because the nominal delta-v is larger.

An error in the pitch angle rotates the line of apsides, causing an along-track error. This error is more predominant for the 350 km orbit than for the 900 km orbit. Although the delta-v is less for the 350 km orbit, the eccentricity of the reentry orbit is less. Consequently, the orbit is more sensitive to a change in the line of apsides.

Both yaw and pitch errors affect the impact point only in the along track direction. The magnitude of the errors are also small in proportion to the delta-v errors previously discussed. For future analysis, a delta-v error will be applied to the nominal burn that is intended to encompass all three types of errors.

The burn errors studied show two major results. First, the accuracy of the deorbit burn is crucial in executing a landing at WSMR. Each of the footprints is large, and shows that the spacecraft is especially sensitive to cold burns. Therefore, a method must be developed to control the burn. One possible method is through the use of accelerometers. These instruments may be used to measure the burn to a high degree of accuracy and can be used to command the thrusters to shut off once the nominal value of thrust is reached.

The second result of the analysis is the need for a trim burn. An accurate landing requires a near perfect burn. Despite all precautions, some alternative measurements of the success of the burn [such as a Global Positioning System (GPS) generated ephemeris solution] should be employed to model and assess the deorbit burn and to calculate the trim burn if necessary.

2.4 Trim Burn

Once the deorbit burn is completed, a new orbit solution must be computed to determine the success of the burn. If the burn was not acceptable, a trim burn will be executed using the attitude thrusters to correct the burn error.

2.4.1 Burn Data

In this analysis, the attitude thrusters are modeled using 30 lbs of thrust with an Isp of 220 seconds. For the circular mission orbits, the trim burn is modeled 15 minutes after the deorbit burn. For the elliptic orbit, a trim burn is modeled 30 minutes after the deorbit burn.

Tables 2-2 and 2-3 summarize the results for the trim burns that are needed to recover from various off-nominal deorbit burns. For all cases, a recovery is possible with one in-plane burn (yaw angle of 0 degrees) that is along the velocity vector (pitch angle of 0 or 180 degrees).

Table 2-2. Trim Burn Recovery Data for the 200 x 20,600 km Mission Orbit

DEORBIT BURN ERROR (DELTA-V, ATTITUDE)	YAW ANGLE (DEGREES)	PITCH ANGLE (DEGREES)	DELTA-V (M/SEC)	BURN LENGTH (SEC)
DV-5 Percent	0	180	1.3	13.6
DV+5 Percent	0	0	1.2	13.3
DV-10 Percent	0	180	2.5	27.2
DV+10 Percent	0	0	2.5	27.2
DV-20 Percent	0	180	5.0	54.1
DV+20 Percent	0	0	5.0	54.1

Table 2-3. Trim Burn Recovery Data for the 900 km Mission Orbit

DEORBIT BURN ERROR (DELTA-V, ATTITUDE)	YAW ANGLE (DEGREES)	PITCH ANGLE (DEGREES)	DELTA-V (M/SEC)	BURN LENGTH (SEC)
DV-5 Percent	0	180	17.2	186.3
DV+5 Percent	0	0	17.0	184.2
DV-10 Percent	0	180	32.5	350.9
DV+10 Percent	0	0	34.5	372.3
DV-20 Percent	0	180	67.5	722.8
DV+20 Percent	0	0	70.3	752.3
Yaw-3 Degrees	0	180	0.6	6.5
Yaw+3 Degrees	0	180	0.6	6.5
Pitch-3 Degrees	0	180	1.4	15.2
Pitch+3 Degrees	0	0	0.6	5.4

As noted in the footprint analysis in the previous section, thrust and attitude errors cause impact to occur either before or after crossing WSMR along the orbit path. For cases where the impact occurs before reaching WSMR, the deorbit burn is greater than the nominal value. Therefore, the trim burn should occur opposite to the deorbit burn, or pitch angle equal to 0 degrees. If the impact occurs past WSMR, the deorbit burn is not strong enough, and more delta-v should be added with a pitch of 180 degrees.

If a thrust error occurs during deorbit from the elliptical orbit, a trim burn could be executed to correct all expected dispersions. Table 2-2 shows that for the worst case scenario of a ± 20 percent burn error, a trim burn would require 5 m/sec delta-v (54 seconds duration), which is an acceptable load on the attitude thrusters. For the circular missions, however, the size of the trim burn is much larger. For the 900 km orbit (see Table 2-3), ± 5 percent burn error would require a trim burn of 3 minutes while a ± 20 percent error recovery would last 12.5 minutes.

The size of the trim burn increases proportionally to the size of the nominal deorbit burn. Therefore, the circular orbit cases could require larger trim burns than the elliptic orbit case. If the large errors occur in the circular missions, the trim burns may be too large for the attitude thrusters. This again shows the need for a tightly controlled deorbit burn.

2.4.2 Trim Burn Footprint

The attitude thrusters used in the analysis are assumed to have been calibrated during the mission. Therefore, burn errors of ± 5 percent were used to model worst-case estimates of both thrust and attitude errors. The results of the revised footprints are shown in Figures 2-11 and 2-12 for the elliptic mission and the 900 km circular mission, respectively.

The elliptic mission required a deorbit delta-v of only 24.2 m/sec. For a 20 percent error during the deorbit burn, the trim burn delta-v required is 5 m/sec. If a 5 percent error occurs during the trim burn, the delta-v lost is 0.25 m/sec. Consequently, the footprint is expected to be small. In addition, LifeSat will reenter directly from the north. Since WSMR is aligned north-to-south, LifeSat has a large area in which to land. As a result, Figure 2-11 shows that the worst case scenarios of ± 20 percent and ± 5 percent errors in the deorbit (primary) burn and trim burn, respectively, will keep the landing of LifeSat at WSMR.

Reentry from the circular orbits require larger delta-v's in the deorbit burn, and potentially in the trim burn. Therefore, a larger footprint is expected for the circular orbit missions with the largest occurring for the 900 km reentry. Figure 2-12 shows that for the 900 km orbit, the footprint extends outside of New Mexico for large primary burn errors coupled with a 5 percent trim burn error.

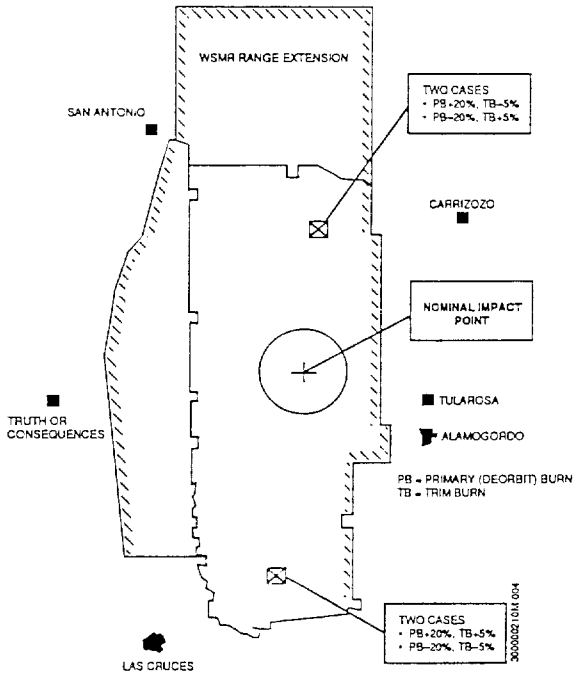

Figure 2-11. Reentry Footprint with Trim Burn Error, Elliptical Mission

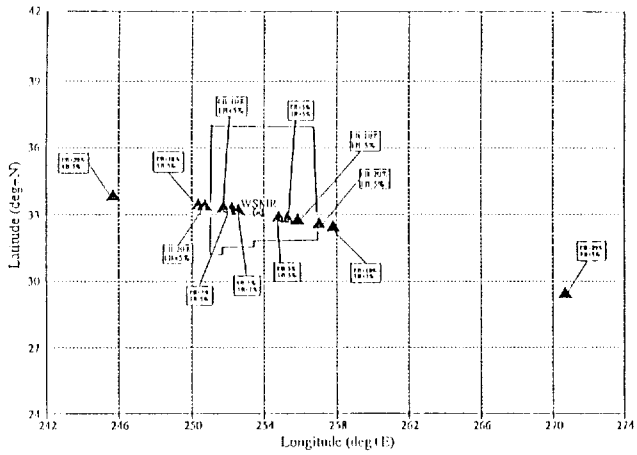

Figure 2-12. Reentry Footprint with Trim Burn Error, 900 km North-to-South Trajectory

In addition to the large footprints shown, the reentry path approaches WSMR from the west; this requires impact in the narrow region of WSMR. These factors combined indicate that the accuracy requirements for the trim burn are quite rigid. Sample accuracies were found for both the 350 km and 900 km circular orbits following ± 5 percent deorbit burn errors.

To recover from ± 5 percent primary burn errors and land in WSMR (not including extensions), the trim burn must be within a 2 percent accuracy for the 350 km mission and 1 percent accuracy for the 900 km mission. As the deorbit burn error increases, the accuracy requirement of the trim burn will tighten. However, an error of at least 1 percent is still quite likely even if the attitude thrusters are fairly well calibrated. Therefore, these

preliminary results indicate that the deorbit burn accuracy must be well within 5 percent. This again shows the need for a tightly controlled burn.

3. LANDING CONTINGENCIES

The dependency on favorable weather is a concern for the parachute landing and ground recovery team. Certain variables in reentry planning, i.e., time of day and time of year, have been chosen to reduce the likelihood of unfavorable weather; however, some degree of uncertainty will always exist. Therefore, it is imperative to design a contingency plan for employment in the event of a landing waveoff.

Two elements were considered in the design of the contingency plan. First, since the waveoff cannot be preplanned, the duration of the delay from decision to execution will be variable. Therefore, the contingency plan needs to be flexible to allow a time for the next opportunity. Second, the spacecraft operates under rigid power constraints that require the next attempt to occur within a few days. Consequently, the contingency plan must allow for a second reentry attempt within 1 to 5 days. With these restrictions, a contingency maneuver plan was developed.

In addition to creating a contingency plan for waveoffs, one additional requirement levied by the project is the ability to command spacecraft reentry prior to 60 days. To accomplish this, an approach similar to the waveoff plan may be used. For both contingency applications, reentry is not immediate. Once the contingency maneuver is planned and executed, a new orbit solution must be obtained. From this solution, a new reentry plan may be developed. This process may require two or more days.

3.1 Elliptic Mission

3.1.1 Waveoffs

The orbit of the highly elliptic mission is designed to place perigee over WSMR at the end of the 60 day mission. If a waveoff occurs, LifeSat will travel near WSMR the following day, however, the groundtrack will have shifted slightly. If the waveoff condition exists for several days, this shift will accumulate to a groundtrack error of over 4 degrees in 5 days. An out-of-plane burn would then be needed to correct the accumulated error; this is not feasible under the current fuel budget.

One approach to the problem is to maintain the groundtrack once it has reached the WSMR location. This is done by adjusting the semimajor axis to change the orbit period to create a repeating groundtrack. Operationally, after waveoff has occurred, a maneuver executed at the perigee pass over WSMR will lower apogee by approximately 30 km. This will fix the groundtrack over WSMR once per day.

Although this method will align the groundtrack to the proper location, it does not fix the perigee location. Due to the Earth's geopotential field, the perigee of the orbit will rotate northward. However, perigee will rotate 2 degrees in 5 days which should not impair reentry.

3.1.2 Early Return

A similar approach may be used in the event of an early return. The semimajor axis must be altered to align the groundtrack for a reentry attempt. The nominal mission orbit is designed such that the groundtrack will advance to WSMR after 60 days. If a return is necessary prior to 60 days, elimination of the difference between the current longitude of the groundtrack and the longitude of WSMR must occur by lowering apogee to increase the groundtrack advancement. The rate of advancement will increase as the altitude of apogee decreases. Therefore, the magnitude of the contingency maneuver depends on the mission elapsed time and the urgency of the return.

In addition to the groundtrack advancement, the line of apsides must also advance to WSMR. As with the groundtrack, the natural rotation is planned for a 60 day mission. Therefore, the contingency maneuver must also rotate the line of apsides. Since the contingency maneuver will need to accomplish two goals on a limited fuel budget, an early return may not be possible for the early stages of the mission. Further analysis must be performed to determine how early a reentry is feasible.

3.2 Circular Missions

3.2.1 Waveoffs

In the event of waveoffs for the three circular missions, the semimajor axis could be adjusted to create a repeating groundtrack. However, the circular missions are inclined at 34 degrees. This causes a much greater shift in the groundtrack due to the precession of the nodes from perturbations by the second zonal harmonic, J_2. As a result, the semimajor axis may need a larger change. Consequently, a slightly different approach is taken in the contingency plan.

For the elliptic polar mission, a daily repeat ground track is the simplest method to employ. However, for the circular missions, a wider range of alternative solutions is needed. Repeat cycles of 1 to 5 days were determined for each mission for an eccentric orbit with apogee fixed at the mission altitude. In this way, a perigee lowering maneuver would occur in place of the deorbit burn followed by a small adjustment maneuver to place perigee over WSMR.

The advantage of perigee lowering is that no additional delta-v is required. Recall that the function of the reentry burn is to lower perigee close to the earth so that the atmosphere can pull the spacecraft to the ground. If the deorbit burn from the mission altitude is done in two perigee lowering burns, the total delta-v for the two burns is equivalent to a single deorbit burn.

Table 3-1 shows perigee altitudes needed to achieve a repeat cycle for each of the three mission altitudes. Lowering perigee to 312.1 km is apparently the best candidate for the 350 km mission orbit. This solution will allow for a reentry attempt every 2 days. A return to WSMR after 1 day is not feasible.

Table 3-1. Elliptical Repeat Groundtrack Cycles

MISSION ALTITUDE	NUMBER OF DAYS IN REPEAT CYCLE	PERIGEE ALTITUDE REQUIRED (KM)
350 KM	1	17.5
350 KM	2	312.1
350 KM	3	212.3
350 KM	4	162.9
350 KM	5	252.0
700 KM	1	271.6
700 KM	2	598.6
700 KM	3	487.6
700 KM	4	432.9
700 KM	5	666.1
900 KM	1	743.8
900 KM	2	398.2
900 KM	3	511.3
900 KM	4	923.9
900 KM	5	887.5

Both the 700 and 900 km orbits can maneuver least to a 5 day repeat cycle. However, power requirements may not last the full 5 days, thus a larger contingency maneuver may be required. For the 700 km orbit, the next best solution is for a 2 day repeat cycle; the next best solution for the 900 km orbit is a 1 day repeat cycle. For all contingency solutions, the rotation of perigee is not a concern. Perigee will rotate, on average, approximately 1 degree in 5 days.

3.2.2 Early Return

An early return during the majority of the mission should be feasible because the groundtrack frequently passes near WSMR. A groundtrack correction maneuver is still necessary to adjust the groundtrack precisely over WSMR. In addition to the north-to-south crossings, reentry possibilities may be gained through the use of a south-to-north trajectory over the Baja region of Mexico. Future analyses should address the frequency of the early landing opportunities based on the fuel budget of the 900 km mission orbit.

4. CONCLUSIONS

The reentry analysis concentrates on the deorbit burn for both nominal and off-nominal conditions. One of the LifeSat project Phase B reports suggests the use of a solid fuel deorbit motor. The present analysis shows that very small variations in the delta-v from the deorbit burn can cause extremely large variations in the landing footprint. Since it is not possible to control the burn of a solid fuel rocket motor, this suggests that: (1) a liquid fuel deorbit motor controlled by an accelerometer is needed, and (2) a trim burn using the attitude thrusters is also required. Since a trim burn is necessary, the tolerable variation in the trim burns that would allow LifeSat to safely reenter over WSMR was analyzed.

The landing at WSMR must occur in weather conditions that meet certain criteria; therefore, a waveoff situation is quite possible and must be accommodated. Since the experiments and the spacecraft life support system operate within a fairly tight set of defined time constraints, this would require that the next reentry attempt occur within a few days. Consequently, contingency plans were examined that would allow another reentry within 1 to 5 days. A technique of adjusting the apogee to cause the groundtrack to repeat is proposed for the elliptical orbit. A perigee lowering maneuver is recommended to create a repeating groundtrack for the circular missions. Several scenarios are presented.

If an emergency occurs requiring an early reentry, the orbit must be adjusted to allow for a reentry attempt. Similar maneuver strategies would be employed to align the groundtrack over WSMR. In addition, for the elliptic case, perigee would need to be positioned over WSMR.

REFERENCE

Computer Sciences Corporation, CSC/TM-91/6159, *LifeSat Mission Analysis Report*, D. W. Denzler, M. E. Hametz, and L. J. Roszman, November 1991

TSIEN'S METHOD FOR GENERATING NON-KEPLERIAN TRAJECTORIES
Part II- The Question of Thrust to Orbit a Sphere and the Restricted Three-Body Problem

P. A. Murad*
Defense Intelligence Agency, Washington, D.C.

ABSTRACT

Tsien's method is extended to treat the orbital motion of a body undergoing accelerations and decelerations. A generalized solution is discussed for the generalized case where a body undergoes azimuthal and radial thrust and the problem is further simplified for azimuthal thrust alone. Judicious selection of thrust could generate either an elliptic or hyperbolic trajectory. This is unexpected especially when the body has only enough energy for a lower state trajectory. The methodology is extended treating the problem of vehicle thrust for orbiting a sphere and vehicle thrust within the classical restricted three-body problem. Results for the latter situation can produce hyperbolic trajectories through eigenvalue decomposition. Since eigenvalues for no-thrust can be imaginary, thrust can generate real eigenvalues to describe hyperbolic trajectories. Keplerian dynamics appears to represent but a small subset of a much larger non-Keplerian domain especially when thrust effects are considered. The need for high thrust long-duration space-based propulsion systems for changing a trajectory's canonical form is clearly demonstrated.

Nomenclature

a	Semi-major axis
A	Areal velocity
e	Eccentricity
E	Energy state
F	Thrust acceleration
g	Gravity
h	Integration constant
p	Semilatus rectum
ϕ	Spherical coordinate angle
V	Gravity potential
r	Radial distance between mass centers
R	Earth radius
t	Time
θ	azimuthal coordinate angle
x,y,z	Cartesian coordinate variables
μ	Earth's gravitational constant

* "The views expressed in this paper are solely those of the author and do not reflect the official policy or position of the Defense Intelligence Agency, the Department of Defense, or the U.S. Government."

Subscripts

o	Initial or reference value
az	Azimuthal
rd	Radial
e	Earth reference value

I. INTRODUCTION

This paper is a continuation of efforts previously presented in Murad[1]. Some aspects from this reference are included for continuity and the analysis is considerably expanded to treat more problems of general interest to the astrodynamicist. The original problem will be briefly addressed followed by a discussion that treats these other situations.

There was a problem of interest concerning a missile event captured on photographic data. The data consisted of two streaks against a star background. Simple evaluations based upon the local sidereal time and the expected distance to the earth day-night terminator indicated that at least one and possibly both streaks were produced in total darkness, possibly by a missile. The problem was to place a trajectory through the streaks to define apogee and velocity which would be used to identify a specific missile system.

Gauss' method[2-4] was used unsuccessfully to place a trajectory through both streaks. The method is adequate for either an elliptic or hyperbolic trajectory, however, it was expected that the missile energy was too low to reach hyperbolic velocities although the software implied that hyperbolic trajectories ought to match the spatial data alleviating any constraint on time. When an elliptic trajectory was considered, adequate spatial matches were obtained, however, the calculated time period was larger than required to support the data.

Clearly a contradiction exists. Assuming that the software was correct, under what conditions could a missile trajectory be defined by a hyperbola when the energy is insufficient to reach hyperbolic velocities? This paper partially examines this concern by evaluating the equations of motion for a vehicle in orbit having azimuthal thrust. As a consequence of treating this problem, significant insights were obtained that have more general applicability to other problems of interest.

A. Background

To correctly use Gauss' method, several assumptions are implied in the derivation of these orbits. Specifically, the body under investigation is not accelerating or decelerating from forces other than through the attraction of a central force field; bodies undergoing thrust or reentry clearly violate this assumption.

Some words regarding the original data are noteworthy. Several hypotheses were tested concerning what caused the streaks. These hypothesis were used to explain reasons that would have allowed the data to be photographically captured. In the course of trying to match the data, it appeared that the streaks involved thrust creating lateral and axial accelerations or decelerations.

Thus, if these streaks were thrust related, Gauss' method is not applicable.

This problem provided the initial motivation to develop the methodology. This effort's main theme is to present a rationale suggesting that the trajectory canonical form can be altered by thrust.

B. Current Considerations

There is additional motivation regarding the present paper. During a recent conversation with V. R. Bond[5], it was suggested that the time required for long space voyages can be reduced significantly by altering thrust to generate specific trajectories based upon suggestions from the author's original paper. This idea generated a different modus operandi. If Tsien's method simplified the problem of altering a spacecraft orbit using thrust, what other problems could be resolved?

The original paper judiciously selected an analytical thrust term to reduce angular momentum simplifying the governing equations of motion. Admittedly biased, the thrust term allows the spacecraft to fly either an elliptical, parabolic or hyperbolic trajectory without any real stipulation on initial velocity. Could this approach treat more complex trajectory problems?

This paper will show that an answer is mathematically tractable, however, several issues should be briefly mentioned. Use of control thrust to alter interplanetary trajectories or for station-keeping was limited by technology developed during the sixties and the early seventies. Thrust from reaction control motors or launch boosters used either a single constant setting or several distinct settings; the latter demanded feedback to regulate flowrate of oxidizer or propellant. Inert structural weight of cooling systems, fuel lines, turbines and engines, as well as large amounts of propellants created limitations that stressed launch booster capabilities. Weight and reliability kept propulsion systems to the bare essentials. Thus, altering thrust as a function of orbital parameters or time, was not technically feasible. Furthermore, instrumentation and interpretation of on-board inertial data to identify these parameters also stressed available technology.

The advent of the Shuttle-C[6] and other large boosters such as the Soviet Energiya concepts and its many adaptations[7] (i.e.: Buran-T Space Launch Vehicle, etc.), provides future designers with more flexibility in the design of spacecraft and subsequent payloads. However, chemical propellent mass fraction greatly limits the scope of any extraterrestrial exploration in the near future.

The original paper implies and will be further demonstrated here, large thrust to weight ratios and variable time-dependent long-duration thrust profiles to meet future contingencies are clearly needed. Technology limitations have displaced such ideas only as subliminal thoughts due to the need for finding practical and timely solutions to contemporary problems. Chemical systems have their limitations, although several exciting high risk technology approaches offer promise[8-11]. These potential concepts include: nuclear propulsion, nuclear propulsion with electrical

hybrids, MHD, tachyon beam ejection, and space warp concepts. Gravity gradient or gravity potential drives with their analogues (i.e.: magnetic potential or magnetic gradient concepts) should be included to extend this list.

Admittedly, these are far-reaching propulsion concepts yet to demonstrate technical maturity. Feasibility must parallel long-term serious funding efforts. Without political emphasis, present concepts will keep man bound to both this planet and solar system for a longer period limiting man's imagination and possibilities for growth.

Realizing the thrust-to-weight problem may be unsolvable, there are solutions that are technically feasible that should be examined. Time-dependent thrust appears to offer advantages. Amongst these is the intuitive feeling that expended propellent can be used more efficiently than with constant thrust systems. Time-dependent thrust can be incorporated in liquid rocket chemical systems and hybrid propulsion systems. Hybrid rockets offer the advantage of half the plumbing of a liquid rocket propulsion system with the reliability of a solid propellent rocket motor albeit with a performance degradation. Furthermore, if thrust variation is gradual, a solid core nuclear rocket engine, such as NERVA, could be designed with this built-in feature.

C. Preliminaries

The equations of motion were examined and cast to account for thrust effects. In the classical derivation, a body in polar coordinates is moving about a much larger body located at the coordinate system origin. The angular momentum equation is simplified, applying Kepler's law, reducing the mathematical complexities. Subsequent substitutions provide an expression for the radius as a function of anomaly. If eccentricity is less than one, the trajectory reduces to an ellipse and if the eccentricity is greater than one, the solution describes a hyperbola. In both cases, foci of the conic represents the location of the larger body central force field.

A brief review of the two-body problem followed by Tsien's approach will be presented as a frame of reference. This is followed by looking at the equations with both axial and azimuthal thrust with the specific example of examining azimuthal thrust and its effects. This problem is extended to a spacecraft with thrust orbiting a large body in two-dimensions to one in three-dimensions. Finally, the problem of a single thrusting spacecraft orbiting two large bodies will be examined by generating different canonical types of trajectories based upon extending further some earlier work by the author.

C-1. The Classical Two-Body Problem

The equations of motion in the radial and transverse directions under the influence of a radial inverse gravitational potential are:

$$\ddot{r} - r\dot{\theta}^2 = -g_o\left(\frac{R}{r}\right)^2 = -\frac{\mu}{r^2} \qquad (1a)$$

$$r\ddot{\theta} + 2\dot{r}\dot{\theta} = \frac{1}{r}\left[\frac{d}{dt}(r^2\dot{\theta})\right] = 0 \qquad (1b)$$

the dot signifies time differentiation, r is the radial distance to the body measured from the center of the force field and θ is the true anomaly.

The integrals for the above ordinary differential equations are:

$$\frac{1}{2}[(\dot{r})^2 + (r\dot{\theta})^2] - \frac{\mu}{r} = E \qquad (2a)$$

$$r^2\dot{\theta} = A \qquad (2b)$$

where A, a constant value, is the areal velocity and the trajectory is Keplerian. By Keplerian, it is implied that the area swept by the radius vector from the central force field to the spacecraft is equal for similar time intervals along the spacecraft's orbit. The quantity E represents the sum of the spacecraft's kinetic and potential energy which remains constant throughout the trajectory.

Substituting the second expression into the first, and changing the independent variable from time to anomaly results in:

$$\frac{d}{d\theta}\left[\frac{1}{r}\right]\left[\frac{d^2}{d\theta^2}\left[\frac{1}{r}\right] + \frac{1}{r} - \frac{\mu}{A^2}\right] = 0 \qquad (3)$$

The solution for this initial value problem has the form:

$$r = \frac{p}{1 + e\cos(\theta - \theta_o)} \qquad (4)$$

where p is the semilatus rectum and e is the eccentricity necessary to satisfy initial conditions. This equation represents an ellipse or a hyperbola depending upon the eccentricity which is based upon parameters such as the kinetic energy, E, to satisfy this initial value problem.

C-2. Tsien's Approach

Battin[4] gives an excellent perspective concerning Tsien's contribution to the field of orbital mechanics with regard to non-Keplerian* two-body motion. Tsien in several classic papers[12-14] examined two basic problems for predicting orbital change due to constant thrust directed either radially or tangentially along the flight path. Tsien's insights made these difficult problems mathematically tractable and from these initial results, sensitivities resolving problems of practical interest can easily be formulated.

Following Battin's development, Tsien included a constant term in the radial momentum equation signifying radial thrust acceleration. After an integration of the azimuthal momentum equation and substitutions into the radial momentum equation, an integration

* The definition of non-Keplerian used in this evaluation is that the areal velocity is no longer a constant.

provided a closed form solution for the velocity as a function of radius and acceleration for an initially circular orbit to reach escape velocity.

$$\frac{d^2r}{dt^2} - r\left(\frac{d\theta}{dt}\right)^2 + \frac{\mu}{r^2} = a_{rd} \tag{5a}$$

$$\frac{d}{dt}\left(r^2\,\frac{d\theta}{dt}\right) = 0 \tag{5b}$$

or

$$\frac{r^2\,d\theta}{dt} = \sqrt{\mu r_o} \tag{5c}$$

Various solutions are obtainable. Depending upon definition, the radial thrust problem is Keplerian because of the treatment of the azimuthal equation; the areal velocity is still constant.

For tangential thrust, the case is entirely different. Here, the integration of the azimuthal equation results in an expression for the areal velocity which, even for constant thrust, is now a function of time. In this case, the trajectory should be considered non-Keplerian.

$$\frac{d^2r}{dt^2} - r\left(\frac{d\theta}{dt}\right)^2 + \frac{\mu}{r^2} = 0 \tag{6a}$$

$$\frac{d}{dt}\left(r^2\,\frac{d\theta}{dt}\right) = r a_{az} \tag{6b}$$

which yields various solutions.

Although these examples treat constant thrust acceleration, there are many solutions involving variable thrust which will not be discussed here. Can other more general families of solutions be derived that have practical value to simplify the vehicle trajectory undergoing tangential thrust?

II. ANALYSIS

A. The Two-Body Problem

Examining the momentum equations for a vehicle simultaneously having radial and azimuthal thrust yields:

$$\ddot{r} - r\dot{\theta}^2 = -\frac{\mu}{r^2} + a_{rd} \tag{7a}$$

$$2\dot{r}\,\dot{\theta} + r\,\ddot{\theta} = a_{az} \tag{7b}$$

The integral for these equations has the generic form:

$$\frac{1}{2}\left[\dot{r}^2 + (r\dot{\theta})^2\right] - \frac{\mu}{r} = \tilde{E}_o + \int_{t_o}^{t} \left\{a_{rd}\,\dot{r} + a_{az}\,r\dot{\theta}\right\} dt \tag{8}$$

In this equation, the vehicle's energy is no longer equal to the integration constant E_o which includes the kinetic and potential energy at the initial state. The expression for spacecraft energy includes an additional quantity that depends upon the time-

dependent integration of the separate thrust components. As expected, thrust effects alter the vehicle's energy as a function of time or position within the trajectory.

It is feasible to reduce these equations into other simpler forms. For a general class of solutions, let the azimuthal thrust term have the following generic form:

$$a_{az} = \frac{B\dot{r}}{r(r^2\dot{\theta})^n} \tag{9}$$

which, when substituted into the azimuthal momentum equation produces:

$$\frac{1}{(n+1)}\left\{(r^2\dot{\theta})^{n+1} - (r_o^2\dot{\theta}_o)^{n+1}\right\} = B(r - r_o) \tag{10}$$

The B parameter is selected to eliminate terms defined at the initial state integration.

There are many interesting classes of solutions as well as mathematical problems arising from these expressions. If the exponent n is equal to zero, the term within the integral, using the expression for the rate of change of anomaly, becomes:

$$\int_{t_o}^{t} a_{az}\, r\dot{\theta}\, dt = B^2 \ln\left\{\frac{r}{r_o}\right\} \tag{11}$$

which represents an embedded logarithmic singularity within the energy integral. Similarly, when n is equal to 1, this term has the same form in the energy expression as the term generated from an inverse-square gravitational force field. If n is larger, the exponent will accordingly increase in the energy forcing function which alters the form of the resulting equation of motion. These higher-order problems require elliptical integral solutions or other more unorthodox approaches.

Let us return to the more restrictive case for treating azimuthal thrust alone. The equations of motion are as follows:

$$\ddot{r} - r\dot{\theta}^2 = -\frac{\mu}{r^2} \tag{12a}$$

$$2\dot{r}\dot{\theta} + r\ddot{\theta} = a_{az} \tag{12b}$$

Let us examine the situation for azimuthal thrust and assume a form that allows closure to reduce the azimuthal equation of motion to a quadrature:

$$a_{az} = \frac{B\dot{r}}{r(r^2\dot{\theta})} \tag{13a}$$

$$\frac{d}{dt}\left\{\frac{1}{2}(r^2\dot{\theta})^2\right\} = B\dot{r} \tag{13b}$$

Clearly orbits described by this expression are non-Keplerian. The thrust term is non-conservative and alters the nature of the solution. Here, the expression is simplified by judiciously selecting

the following integration factors:

$$B = \frac{1}{2} r_o^3 \dot{\theta}_o^2 \tag{14}$$

resulting in:

$$\dot{\theta} = \frac{1}{r^2} [2Br]^{\frac{1}{2}} \tag{15}$$

There is a need to explain the selection of the acceleration profile and how it satisfies the overall problem regarding the initial streak data. For the case when a missile accelerates toward the apogee (i.e.: boost) and decelerates moving away from apogee (i.e.: reentry/retro thrust), B is positive. The terms involving radius and the rate of change in anomaly are positive valued; they only change in overall magnitude but not in sign. The inclusion of the rate of change of radius with time, however, does change sign when the vehicle passes through apogee. The positive sense of this term represents positive thrust where a negative sign implies retro or reentry decelerations. It is assumed the accelerating/decelerating forces on the body act tangential to the flight path represented by the azimuthal term.

By non-Keplerian, the implication is that areal velocity is not constant and the body governing the central force field may not be collocated with the geometric foci for either an ellipse or hyperbola. This is important in the analysis for the latter situation; the apogee must be the closest point to the foci while for an ellipse the apogee is the furthest from the foci at the center of the Earth for a surface-to-surface missile trajectory.

When used with the radial equation of motion and integrated, the constant E_o term representing initial energy is not directly removed from the formalism as in the classic sense but remains throughout the derivation. This becomes:

$$\frac{d^2}{d\theta^2}\left\{\frac{1}{r}\right\} + \lambda^2\left\{\frac{1}{r}\right\} = \gamma \tag{16}$$

with a solution that takes either of the following forms depending upon whether lambda is real or imaginary:

$$r = \begin{cases} \dfrac{\alpha}{1 + \beta \cosh \lambda [\theta - \theta_o]} & \text{for } \lambda^2 < 0 \\ [\frac{E}{B}\theta^2 + \delta_1 \theta + \delta_2]^{-1} & \text{for } \lambda^2 = 0 \\ \dfrac{\alpha}{1 + \beta \cos \lambda [\theta - \theta_o]} & \text{for } \lambda^2 > 0 \end{cases} \tag{17}$$

where:

$$\gamma = \frac{1}{2B}\left[\tilde{E}_o + \frac{B}{r_o}\right]$$

$$\lambda^2 = \left[2 - \frac{\mu}{B}\right] \qquad (18)$$

$$\alpha = \lambda^2/\gamma \text{ and } \beta = \gamma/\lambda^2$$

Baxter[15] derives a similar expression for the case of force field perturbations in the radial direction. Baxter suggests that the fundamental problem of Keplerian representations of real orbits is the failure to correctly account for the energy of the orbiting body. This could lead to in-track errors in Keplerian mean motion. Baxter compensates by using perturbation terms in the gravitational potential to remove in-track drift. Furthermore, the method can produce Keplerian trajectories in a non-Keplerian environment by inclusion of these radial terms where orbital elements are changed to include perturbative quantities. For example, energy is directly included in these expressions and is not treated as a secondary term through the definition of eccentricity.

The change in the form of the trajectory relies principally upon the nature of whether lambda is real or imaginary. Values for B depend upon location along the trajectory where thrust is applied and as the value of B increases, the sense of lambda becomes more negative. When the magnitude of this term is equal to 2.0, the equation is parabolic. When larger than 2.0, the equation is hyperbolic. This is independent of energy considerations which enters the problem only through eccentricity.

If the coefficients are altered to reflect when this expression is identical to the classically derived equation, an interesting analogy develops. For specific initial conditions defining B and the azimuthal thrust profile, a thrusting trajectory could be derived having the same spatial-time dependency as a Keplerian trajectory. Thus it is entirely feasible, with caveats, that an inefficient trajectory, using thrust, could be replaced by a trajectory without thrust.

B. The Problem of a Spacecraft Orbiting a Spherical Body

The equations of motion for a spacecraft orbiting a spherical body are:

$$\ddot{r} - r\dot{\theta}^2 - r\dot{\phi}^2 \sin^2\theta = -\frac{\partial V}{\partial r} \qquad (19a)$$

$$r\ddot{\theta} + 2\dot{r}\dot{\theta} - r\dot{\phi}^2 \sin\theta\cos\theta = -\frac{1}{r}\frac{\partial V}{\partial \theta} \qquad (19b)$$

$$r\sin\phi\,\ddot{\phi} + 2\dot{r}\sin\theta\,\dot{\phi} + 2r\cos\theta\,\dot{\theta}\,\dot{\phi} = -\frac{1}{r\sin\theta}\frac{\partial V}{\partial \phi} \qquad (19c)$$

where: ϕ is the out-of-plane angle required for a spherical coordinate system. The gravity gradient can have the simple form:

$$V(r,\theta,\phi) = -\frac{\mu}{r} \tag{20}$$

These expanded equations include terms in both the radial and azimuthal momentum equations as well as a third equation describing momentum in a second angular plane. These three-dimensional spherical coordinate equations more accurately predict trajectories for non-thrust situations due to gravity potential variations acting outside of the original plane of motion.

If the out-of-plane angle phi is constant regardless of orbit inclination, or if the time rate of change of this angle is zero, terms in the first two equations are zero and the third equation vanishes. Here, the problem reduces to two dimensions. Similarly, if the angular rate of change of phi is constant, these additional terms may still appear although the third equation is greatly simplified. If it is assumed that the gravity potential consists only of terms involving radial and azimuthal variations, the constant term creates a rate of change in either radial or azimuthal variables or both.

Here, the last equation reduces to:

$$\frac{d}{dt}(r \sin\theta) = 0 \tag{21}$$

This is consistent with the two-dimensional case and may provide another 'integral' to reduce the equations of motion. Again, this is still without looking at thrust effects.

The emphasis will require examining out-of-plane thrust and subsequent effects on the spacecraft's trajectory. One can assume thrust components can be defined as a gradient acting in similar directions as the gravity potential gradient for example:

$$\nabla V' = \nabla V + \nabla F \tag{22}$$

The following insights can be gained from these equations with thrust. Out-of-plane thrust impacts both radial and azimuthal momentum adding to the non-linear mathematical coupling of these expressions. Clearly, the spacecraft's radius and its rate of angular rotation are dependent upon this thrust component as it alters the time rate of change of phi. Thrust in either radial and azimuthal directions have either little influence on the out-of-plane momentum or no influence if there is no time variation in phi.

Obviously, these equations are difficult to solve in closed-form. There are two alternatives. Can these equations be reduced to those in two dimensions or can the thrust term be selected such that either the coupling or non-linearities are reduced or removed?

B-1. Reduction of the Spherical Orbit Problem to Two-Dimensions

The solution is straight forward. In both of the radial and azimuthal momentum equations, select the thrust term to exactly cancel the additional terms induced by the second angular coordinate variable:

$$\frac{\partial F}{\partial r} = r\dot{\phi}^2 \sin\theta \tag{23a}$$

$$\frac{1}{r}\frac{\partial F}{\partial \theta} = r\dot{\phi}^2 \sin\theta \cos\theta \qquad (23b)$$

This reduces the first two equations to identical expressions of a spacecraft moving about a body with no thrust. By standard definitions, the orbits are Keplerian within the plane of motion. However, due to the third equation of motion and the rate of change of all variables, the rate of change of phi may not vanish. If this is so, then azimuthal thrust should be selected such that angular acceleration disappears and the remaining terms are compensated by the third thrust vector component.

$$\frac{\partial F}{\partial \phi} = -\dot{\phi}\frac{d}{dt}(r\sin\theta)^2 \qquad (24)$$

Note that all of these thrust components depend upon $\dot{\phi}$; they also contain the expression identified in equation (21).

B-2. Removal of Coupling Terms

In a similar fashion using superposition, thrust components are selected to cancel the coupling terms. Angular momentum effects from out-of-plane motion are prevented from influencing the momentum in the remaining coordinate variables. Here, the equations of motion, based upon the two momentum integrals, are rewritten to define the force components:

$$r - \frac{k^2}{r^3} - \frac{f^2}{r}\dot{\phi}^2 = -\frac{\partial V}{\partial r} \qquad (25a)$$

$$r\frac{dk}{dt} - \dot{\phi}^2 \cos\theta f = -\frac{1}{r}\frac{\partial V}{\partial \theta} \qquad (25b)$$

$$r\sin\phi\,\ddot{\phi} + 2\dot{\phi}\frac{df}{dt} = -\frac{1}{f}\frac{\partial V}{\partial \phi} \qquad (25c)$$

where $k = r^2\dot{\theta}$ and $f = r\sin\theta$.

C. The Restricted Three-Body Problem

In an earlier effort[17], the thesis was presented that a potential of motion could be defined which reduced the coupling and complexity of the two-dimensional equations of motion governing a spacecraft in motion about two larger bodies. The potential was not a Hamiltonian in the purest sense and required several mathematical restrictions in its definition.

First, the potential has to be analytical in a complex variable context. Second, the potential would satisfy rules of partial differentiation, and third, the potential possesses an integration property that did not violate energy considerations. If this potential is admissable, pseudo-analytical terms can be defined that allow for the principle of superposition This accounts for effects from gravity potential perturbations or the influence of additional larger bodies at considerably far distances. The problem is extended to consider thrust.

By psuedo-analytical, the functions solve a similar relation-

ship as the Cauchy-Reiman conditions for analytical functions. They do, however, represent solutions to the inhomogeneous Laplace equation. Briefly, psuedo-analytical functions consist of analytical functions which are solutions to Laplace's equation and may be multiplied by a complex function based upon the inhomogeneous source term, cross-product term(s), or first-order derivatives; they represent solutions to elliptical partial differential equations.

The equations of motion in three-dimensional rotating cartesian coordinates for a spacecraft having thrust moving about two larger bodies are:

$$\ddot{x} - 2\dot{y} - x = -V_x + F_x \tag{26a}$$

$$\ddot{y} + 2\dot{x} - y = -V_y + F_y \tag{26b}$$

$$\ddot{z} = -V_z + F_z \tag{26c}$$

where acceleration components are: F_x, F_y and F_z. The gravity potential for the two large primaries, located on the x axis, is defined as:

$$V(x, y, z) = -\frac{(1-\mu)}{r_1} - \frac{\mu}{r_2} \; ; \quad r_1^2 = (x-x_1)^2 + y^2 + z^2 \quad r_2^2 = (x-x_2)^2 + y^2 + z^2 \tag{27}$$

and the energy integral for no thrust accelerations is defined as:

$$E = \frac{1}{2}(\dot{x}^2 + \dot{y}^2 + \dot{z}^2) - \frac{1}{2}(x^2+y^2) + V(x, y, z) \tag{28}$$

C-1. The Two-Dimensional Case Without Thrust

Accordingly, a potential may be defined such that:

$$\dot{x} = \frac{dx}{dt} = \Psi_x, \text{ and } \dot{y} = \frac{dy}{dt} = -\Psi_y \tag{29}$$

where the potential is a perfect differential which means the cross-derivatives are equal. The derivative is defined as:

$$d\Psi = \Psi_t dt + \Psi_x dx + \Psi_y dy \tag{30}$$

then the cross-derivatives imply:

$$\Psi_{xy} = \Psi_{yx} \text{ or } \frac{\ddot{x}}{\ddot{y}} = -\frac{\dot{y}}{\dot{x}} \tag{31a}$$

and

$$\dot{x}\frac{d\dot{x}}{dt} + \dot{y}\frac{d\dot{y}}{dt} = 0 \tag{31b}$$

When this is integrated, the results reveal the kinetic energy portion of the energy integral and a constant of integration that is a function of both potential energy and the gravity potential. Thus, this definition possess both mathematical properties and also satisfies energy considerations. Results satisfy the energy integral requirement and compatibility suggesting that the expression is admissable.

The potential is a function of both spatial variables and time. The second derivative or acceleration in the x direction can be defined as:

$$\ddot{x} = \Psi_{xt} + \dot{x}\,\Psi_{xx} + \dot{y}\,\Psi_{xy} = \Psi_{xt} + \Psi_x\,\Psi_{xx} - \Psi_y\,\Psi_{yx} \qquad (32)$$

with a similar expression for acceleration in the y component.

Substituting these terms into equations (26a) and (26b), with no force components, these equations are further differentiated and when combined, the resulting equation has the form:

$$\nabla^2\Psi = \Psi_{xx} + \Psi_{yy} = -V_{xy} \qquad (33)$$

This resulting equation is elliptical in the canonical partial differential sense and suggests this transformation is a psuedo-analytical function. Due to superposition, the potential can consist of an analytical function and an inhomogeneous term accounting for the gravity potential. This additional term can also be a pseudo-analytical function. A general solution to this equation has the form:

$$\Psi(x, y) = -\iint_D G(\xi, \eta; x, y)V_{\xi\eta}\,d\xi\,d\eta + \ldots \qquad (34)$$

where additional terms satisfy boundary conditions and $G(\xi, \eta; x, y)$ is the Greens function:

$$G(\xi, \eta; x, y) = -\frac{(1-\mu)}{2\pi}\log\left[(x-x_1-\xi)^2 + (y-\eta)^2\right] - \frac{\mu}{2\pi}\log\left[(x-x_2-\xi)^2 + (y-\eta)^2\right] \qquad (35)$$

These two terms represent point source distributions. The Greens function retains the mathematical behavior near the origins of the primaries. Integration should be performed over the domain bound by the zero-velocity curves. No contributions are added to this expression from the region beyond the zero-velocity curve because the spacecraft can not cross into this forbidden zone on the basis of energy considerations. Thus there is consistency between the mathematics and physics of the problem.

C-2. No Thrust in Three-Dimensions

The potential for this problem is defined such that: $\dot{x} = \Psi_x$ $\dot{y} = -\Psi_y$ and $\dot{z} = \Psi_z$ Using similar substitution into eqs (34a)-(34c) and cross-differentiation results in several partial differential equations:

$$\Psi_{xx} + \Psi_{yy} = -V_{xy} \qquad (36a)$$

$$\Psi_{xz} = -V_{yz} \qquad (36b)$$

$$\Psi_{yz} = 0\,. \qquad (36c)$$

Note that (36a) is the same as previously derived. The latter two equations are additional expressions that show the gravity potential drives the motion.

C-3. Thrust in Two-Dimensions

With such simplifications, the problem is reduced to altering the partial differential equation form by specifying thrust. This eliminates coupling appearing in the momentum equation in a given direction or removes coupling in another momentum equation.

Results are shown in Table I for several forms of thrust components. Basically, the elliptical canonical nature of these expressions is preserved. For the third case, the results is equivalent to motion in a simplistic linear potential field and there is no clearcut way of accurately predicting the spacecraft's motion. In the last case, thrust is selected to nullify force from the gravity potential reflecting earlier comments regarding large sustained thrust-to-weight ratios. Consequently in this situation, the potential is truly analytical.

Table I

$\dot{x}$	$\dot{y}$	F_x	F_y	Functional Form
Ψ_x	$-\Psi_y$	$+2\dot{x}$	$-2\dot{y}$	$\Psi_{xx} + 2\Psi_{xy} + \Psi_{yy} = -V_{xy}$
Ψ_x	$-\Psi_y$	$-2\dot{x}$	$+2\dot{y}$	$\Psi_{xx} - 2\Psi_{xy} + \Psi_{yy} = -V_{xy}$
Ψ_x	$-\Psi_y$	$+2\dot{y}$	$-2\dot{x}$	$V_{xy} = 0.$
Ψ_x	$-\Psi_y$	$V_y - x$	$V_y - y$	$\Psi_{xx} + \Psi_{yy} = 0.$

Depending upon the judicious selection of thrust, the governing equations are reduced to an equation having the form:

$$\nabla^2\Psi + \gamma\Psi_{xy} + \xi\Psi = -V_{xy} \tag{37}$$

where the constants depend upon the transformation function and thrust terms.

C-4. Analytical/Pseudo-Analytical Functions

Another means of solving the equation (37) would be to introduce a direct relationship between the velocity potential and gravity potential. This expression can be expanded to include a potential representing the thrust components. A direct relationship can be defined between the velocity and gravity potentials in a Beltrami equation:

$$\begin{aligned}\Psi_x &= \alpha V_x + \beta V_y \\ \Psi_y &= \delta V_x + \gamma V_y .\end{aligned} \tag{38}$$

Note the similarity with the Cauchy-Reimann equations governing complex variables. The problem is to determine the value of the constants to define the desired potential.

Inversely, when certain derivatives are taken, the resulting equation reduces to the inhomogeneous equation. However, when these derivatives are taken in reverse order, the resulting expres-

sion is a hyperbolic canonical partial differential equation that is a two-dimensional wave equation.

With these thoughts, define the psuedo-analytical function as:

$$\Psi_x = \phi_y - \frac{1}{2} V_y \qquad (39)$$

$$\Psi_y = -\phi_x - \frac{1}{2} V_x .$$

If different cross-derivatives are taken, the results yield partial differential equations that depend upon the gravity potential:

$$\Psi_{xx} + \Psi_{yy} = -V_{xy} \text{ and}$$

$$\phi_{xx} + \phi_{yy} = -\frac{1}{2}(V_{xx} - V_{yy}) \qquad (40)$$

To a degree this explains why these equations tend to demonstrate an elliptical and hyperbolic nature. For example, a spacecraft's trajectory near the zero-velocity curve domain tends to resemble mixed characteristics in the sense of a Tricomi partial differential equation.

Since this activity focuses upon finding a means for changing the nature of the spacecraft's trajectory, it is not clear how changes in the canonical form of the partial differential equation produces change in the spacecraft's trajectory. The above is provided only to demonstrate that the governing equations can be altered to result in real as well as imaginary characteristics which influence the type of spacecraft orbit.

A more lucid approach is available. Here the governing equations are reduced by phase-space notation into an inhomogeneous vector-matrix equation. The gravity potential represents the inhomogeneous expression which will be referred to in a similar sense as a control vector.

Using the following definitions:

$$x_1 = x \qquad y_1 = y$$

$$x_2 = \dot{x}_1 = \dot{x} \qquad y_2 = \dot{y}_1 = \dot{y} \qquad (41)$$

This transforms equation(26a) and (26b) into:

$$\frac{d}{dt}\begin{vmatrix} x_1 \\ x_2 \\ y_1 \\ y_2 \end{vmatrix} = \begin{vmatrix} 0 & 1 & 0 & 0 \\ 1 & 0 & 0 & 2 \\ 0 & 0 & 0 & 1 \\ 0 & -2 & 1 & 0 \end{vmatrix} \cdot \begin{vmatrix} x_1 \\ x_2 \\ y_1 \\ y_2 \end{vmatrix} - \begin{vmatrix} 0 \\ V_x \\ 0 \\ V_y \end{vmatrix} - \begin{vmatrix} 0 \\ F_x \\ 0 \\ F_y \end{vmatrix} \qquad (42)$$

or the vector-matrix equation:

$$\dot{\bar{x}} = \tilde{\tilde{A}}\bar{x} + \bar{u} \qquad (43)$$

The dot denotes time differentiation and the matrix has constant coefficients. A bar denotes a vector and a double bar signifies a matrix.

This vector-matrix equation is subject to boundary conditions as a function of the control vector. Due to the elliptical nature of some orbits, one should expect periodic solutions. The solution

of this equation has the form:

$$\bar{x}(t) = \bar{X}_o e^{\tilde{\tilde{A}}t} + \int_o^t e^{\tilde{\tilde{A}}(t-\xi)} \bar{u}(\xi)\, d\xi \qquad (44)$$

where the vector, $\bar{X}_o$, represents initial conditions. To evaluate the degenerate kernel in the integral, let:

$$e^{\tilde{\tilde{A}}(t-\xi)} = \alpha_o \tilde{\tilde{I}} + \alpha_1 \tilde{\tilde{A}} + \alpha_2 \tilde{\tilde{A}}^2 + \alpha_3 \tilde{\tilde{A}}^3 \qquad (45)$$

where the constants are determined by the eigenvalues of the constant matrix. For this particular matrix, the eigenvalues are repeated according to the following characteristic expression:

$$\lambda^4 + 2\lambda^2 + 1 = 0 \quad \textbf{Then:} \quad \lambda = \pm i, \pm i \qquad (46)$$

Since the eigenvalues repeat, the problem is to solve for the coefficients in:

$$(t-\xi) e^{\tilde{\tilde{A}}(t-\xi)} = \alpha_o \tilde{\tilde{I}} + \alpha_1 \tilde{\tilde{A}} \qquad (47)$$

where $\tilde{\tilde{I}}$ is the identity matrix.

After finding the coefficients and using the Cayley-Hamilton theorem, the final matrix becomes:

$$e^{\tilde{\tilde{A}}t} = \begin{vmatrix} \cos t & \sin t & 0 & 0 \\ \sin t & \cos t & 0 & 2\sin t \\ 0 & 0 & \cos t & \sin t \\ 0 & -2\sin t & \sin t & \cos t \end{vmatrix} \qquad (48)$$

Subsequently, the resulting matrix has the desired features of periodicity due to the embedded circular functions within the kernel displaying an elliptical nature. However, to examine changes to the 'type' of trajectory with thrust, eigenvalue decomposition is necessary. If the vector defining thrust is provided as a function of the initial state vector (i.e.: thrust as a function of either position or velocity), the matrix is altered by including additional coefficients to those within the A matrix. Here, the thrust acceleration term can have the form:

$$\begin{vmatrix} 0 \\ F_x \\ 0 \\ F_y \end{vmatrix} = \begin{vmatrix} 0 & 0 & 0 & 0 \\ \beta_0 & \beta_1 & \beta_2 & \beta_3 \\ 0 & 0 & 0 & 0 \\ \delta_0 & \delta_1 & \delta_2 & \delta_3 \end{vmatrix} \cdot \begin{vmatrix} x_1 \\ x_2 \\ y_1 \\ y_2 \end{vmatrix} \qquad (49)$$

The resulting characteristic equation has the form:

$$\lambda^4 + \gamma_0 \lambda^3 + (2+\gamma_1)\lambda^2 + \gamma_2 \lambda + \gamma_3 = 0. \qquad (50)$$

This provides several interesting insights. For real solutions, coefficients of the odd powers of the eigenvalue should not vanish. This eliminates eigenvalue multiplicity. If these particular terms are negative, eigenvalues are no longer imaginary but

real. Solution for these real eigenvalues results in hyperbolic sine and hyperbolic cosine terms as a function of time. Similar changes could provide eigenvalues producing parabolic solutions. In this fashion, changing thrust can produce trajectories which can linearly vary as a function of time, or vary in a hyperbolic fashion. Again, as mentioned earlier in the original analysis, the form of the equation can easily be altered without a strong dependency upon an initial velocity constraint.

III. CONCLUSIONS

This generalized approach demonstrates that Tsien's method leads to a class of solutions where thrust and other acceleration effects change the trajectory classification. In addition to explaining deviate behavior when viewed from the classical sense, constraints placed upon a trajectory based upon energy considerations may no longer be valid under certain thrust applications. The zero-order solution, without consideration of thrust, for classical Keplerian dynamics should be viewed as a small subset of a much larger non-Keplerian domain.

REFERENCES

1. P. A. Murad: **"Tsien's Method for Generating Non-Keplerian Trajectories"**, AIAA Paper 91-0678, presented at the AIAA 29th Aerospace Sciences Meeting, Reno, Nevada, 7-10 January 1991

2. R. R. Bate, et al: **Fundamentals of Astrodynamics**, 1970, Dover Press.

3. R. M. L. Baker, jr.: **Astronautics- Applications and Advanced Topics**, 1967, Academic Press, New York and London.

4. R. H. Battin: **An Introduction to the Mathematics and Methods of Astrodynamics**, AIAA Education Series, 1987.

5. This effort is a result of a private conversation with Victor R. Bond from McDonnel Douglas Space Systems Company-Houston Division, Texas. The author wishes to acknowledge and deeply appreciates the insights gained during this chance meeting.

6. Major I. Postovit: **"Will There be a 'Shuttle-C'?"**, Prospects for New U.S. Heavy Launch Vehicle Surveyed, 91SV0011R Moscow Aviatsiya I Kosmonavtika, No. 12, Dec 90 pp 42-43, JPRS-UAC-91-005, 15 Aug 1991.

7. A. A. Ivanov, V. D. Kolganov, V. A. Pavshuk, V. F. Semenov, I. V. Kurchatov Institute of Atomic Energy, Moscow: **Conception of the Nuclear Electromotive Power Plant of the Manned Mars System**, presented at the VI symposium on Cosmic/Space Nuclear Energy Systems, Albuquerque, USA, 8-12 January 1989.

8. M. R. LaPointe: **"Antiproton Powered Propulsion with Magnetically Confined Plasma Engines"**, AIAA Journal of Propulsion & Power, Vol

7, Number 5, pp 749-759, Sept-Oct 1991.

9. C. Powell: **"Propulsion by Tachyon Beams"**, AIAA Paper 89-2335, presented at the AIAA/ ASME/SAE/ASEE 25th Joint Propulsion Conference, Monterey, California, 10-12 July 1989.

10. R. Forward: Space Warps: **"A Review of one Form of Propulsionless Transport"**, AIAA Paper 89-2332, presented at the AIAA/ASME/SAE/ASEE 25th Joint Propulsion Conference, Monterey, California, 10-12 July 1989.

11. C. Tarpley, M. J. Lewis, A. P. Kothari: **"Radiation Safety Issues in Single-Stage-To-Orbit Spacecraft Powered by Antimatter Rocket Engines"**, AIAA Journal of Propulsion & Power, Vol 8, Number 1, pp 127-135, Jan-Feb 1991.

12. H. S. Tsien: **"Optimum Thrust Programming for a Sounding Rocket"**, J. Am. Rocket Soc. 21, No. 5(1951) 99.

13. H. S. Tsien: **"Take-off From a Satellite Orbit"**, Jet Propulsion 23, 233, 1953.

14. H. S. Tsien: **"Escape From a Circular Orbit Using Tangential Thrust"**, Jet Propulsion, Vol 28, March, 1958, pp. 167-169.

15. B. E. Baxter: **"Keplerian Representation of a Non-Keplerian Orbit"**, J. Guidance and Control, Vol. 3, No. 2, March-April 1980.

16. R. H. Battin and T. J. Fill: **"Extension of Gauss' Method for the Solution of Kepler's Equation"**, Journal of Guidance and Control, Vol. 2, No. 3, May-June 1979.

17. P. A. Murad: **"A Mathematical Treatise on the Restricted Three-Body Problem of Celestial Mechanics"**, AIAA Paper 75-8, presented at the AIAA 13th Aerospace Sciences Meeting, Pasadena, California, 20-22 January 1975.

Practical Aspects of Transfer from GTO to Lunar Orbit

by
Chauncey Uphoff
Ball Space Systems Division
Boulder, Colorado

Abstract:

This paper is a presentation of some practical aspects of orbital transfer from Geosynchronous Transfer Orbit (GTO) to close, near-circular orbits of the Moon. The intent is to identify the important parameters affecting the problem and to bound (approximately) the range of required ΔV for a spacecraft that has been placed in GTO. The basic geometric relationships are described and the dynamics are simulated by use of the Zero-Sphere-of Influence Patched Conic method. It is found that the inclination of the transfer orbit to the Earth-Moon plane is relatively unimportant while the position of the line of apsides with respect to the Moon's orbit is the main geometric parameter of interest. It is shown that this parameter can be controlled by selecting the time of day for launch and that two launch windows of approximately 45 minutes duration are available each day of the year if use is made of the recommended phasing orbit transfer. The phasing orbit transfer not only provides twice-daily launch windows, but also provides a mechanism for efficacious correction of GTO injection errors. ΔV penalties for out-of-plane transfer and for late launch are evaluated and the method is recommended for use as an affordable means of achieving lunar orbit.

Introduction:

It is not generally recognized that daily launch windows are available for launch to GTO that are compatible with reasonably efficient transfer from GTO to lunar orbit. This study described in this paper (Reference 1) was undertaken for a private company that has compelling reasons for minimizing the funding requirements for the launch vehicle. The study revealed that transfer from GTO to lunar orbit is not only viable but that it may be the most affordable means of such transfer because of the relatively high traffic to GTO. The recent renewal of interest in lunar exploration suggests the need for a wider distribution of the study results.

It is pointed out that the correct relationship between the transfer orbit line-of-apsides and the Earth-Moon plane can be established by waiting in GTO until the Earth's oblateness rotates the orbit into position. For some initial orientations, this wait is not practical as the rotation proceeds at only about 0.8 degrees per day. If , however, the daily launch windows are chosen as suggested in this paper, it is possible to define realistic GTO waiting periods (10 to 20 days) that permit near minimal energy transfer from GTO to lunar orbit that extend the twice-daily launch windows.

One of the concerns for the viability of this mode of transfer is the possibility of radiation damage to the spacecraft during repeated passages through the Earth's radiation belts as the orbit rotates into position for final insertion into the lunar transfer orbit. This effect may be one of the major tradeoffs in mission design for some missions and it is suggested that it is important to weigh the requirements for radiation shielding against those for propulsive adjustment of the perigee position to account for launch time variations.

It is recommended that the propulsion system be a restartable bipropellant hydrazine/NTO system (or the equivalent) so that the transfer impulses can be applied at various points on the GTO and phasing orbits . Lunar orbit insertion is accomplished using about 850 m/s of ΔV to yield a near circular orbit 100 km above the lunar surface with any inclination in the range $30° < i < 150°$ to the lunar equator.

It is suggested that orbit sustenance requirements will be at least 100 m/s per year due to the uncertainty in our knowledge of the lunar gravity field for close, high inclination orbiters. The judicious use of this impulse to adjust the eccentricity and argument of perilune may yield a "frozen" polar lunar orbit that will not only provide stability but will aid in discrimination between the various models of the lunar gravity.

Geometry of the Earth-Moon System:

Figure 1 is a diagram of the geometry of the Earth-Moon system showing the pertinent relationships between the various orbits required for transfer from GTO to lunar orbit. The figure is an edge-on view of the Earth-Moon system and shows the (dark) GTO, the lighter shaded geosynchronous orbit (GSO), the lightest Earth-Moon plane, and the unshaded phasing and lunar transfer orbits. The GTO is assumed to be inclined to the Equator (shown by the GSO) by about 7° which is compatible with a typical launch on the Ariane launch vehicle. It is assumed that the perigee of the GTO is within about 5° of the Earth-Moon plane so that, with a reasonable waiting period (10 to 20 days), the orbit can be allowed to precess into a favorable alignment for initiation of the phasing orbit and then the lunar transfer orbit. The figure shows the line of apsides of the phasing and translunar orbits along the line of intersection of the equator and Earth-Moon plane. It is not necessary to have this alignment but it is most probable because the perigee of the GTO will be near the equator. In case it is required to wait while the GTO precesses until its line of apsides is near the Earth-Moon plane, the orientation could be quite different from that shown in the figure. What is important is that the transfer from GTO to phasing orbit be done when their common perigee is near the Earth-Moon plane.

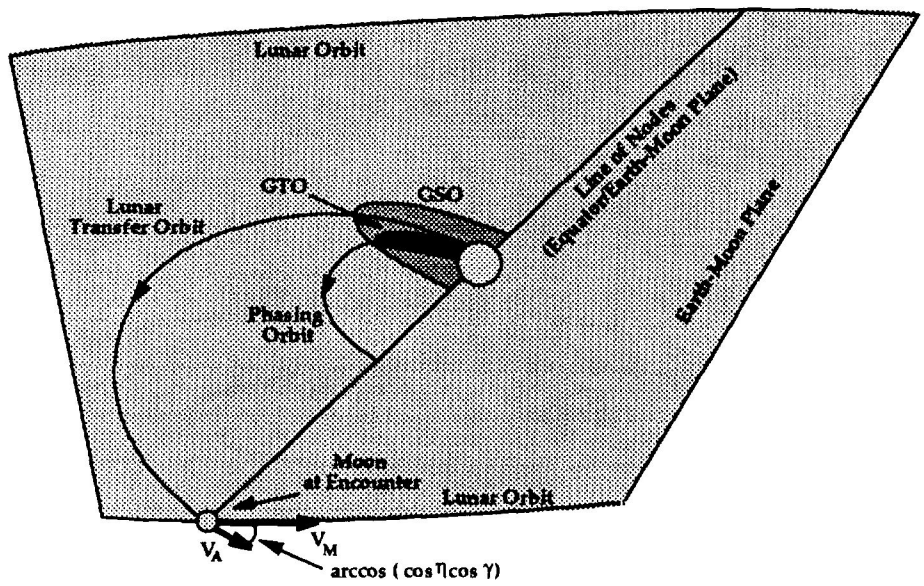

Fig. 1 Geometry of GTO to Lunar Orbit Transfer

The Moon's orbit plane is inclined about 5.14° to the ecliptic and, because of the solar gravitational perturbations, its node (on the ecliptic) regresses about 20° per year. This regression causes a change in the inclination, η', of the Earth-Moon plane to the Earth's equator. This inclination varies between about 18.5° and 28.6° with a period of about 18 years. In the early 1990's, the inclination η' is about midway between these extremes at about 24°. Thus, a GTO orbit with an inclination of 7° to Earth's equator will have an inclination, η, with respect to the Earth-Moon plane of no less than about 17° and no more than about 31°. It is recommended that this inclination be a free variable in preliminary analyses because its effect on the total ΔV required to achieve lunar orbit is less than 75 m/s. If the transfer orbits and vehicle sizing exercises use the larger value of 31°, then launch may be accomplished on any day of the year with varying degrees of payload margin.

The Phasing Orbit:

Use of an intermediate phasing orbit is recommended so as to provide the capability for launching any day of the month and to eliminate the need for a plane change maneuver. It also provides the capability to make midcourse corrections at near-optimal positions. For the "nominal" case, it is assumed that transfer from GTO to the phasing orbit is made at perigee (of both orbits) and at a time when perigee is in the Earth-Moon plane. The period of the phasing orbit is chosen so that, after an integral number of revolutions in that orbit, a second impulse is applied at perigee to place the spacecraft on the lunar transfer orbit (LTO) at a time which will insure intercept with the Moon when the spacecraft reaches the Moon's orbit. It should be noted that the impulse to go from GTO to the

phasing orbit is not "wasted", it is an impulse that would have to be added in any case to effect the complete transfer from GTO to the LTO. Then, after the proper timing has been established by selection of the period of the phasing orbit, the remainder or the GTO to LTO impulse is applied at perigee of the phasing orbit and the lunar encounter is assured.

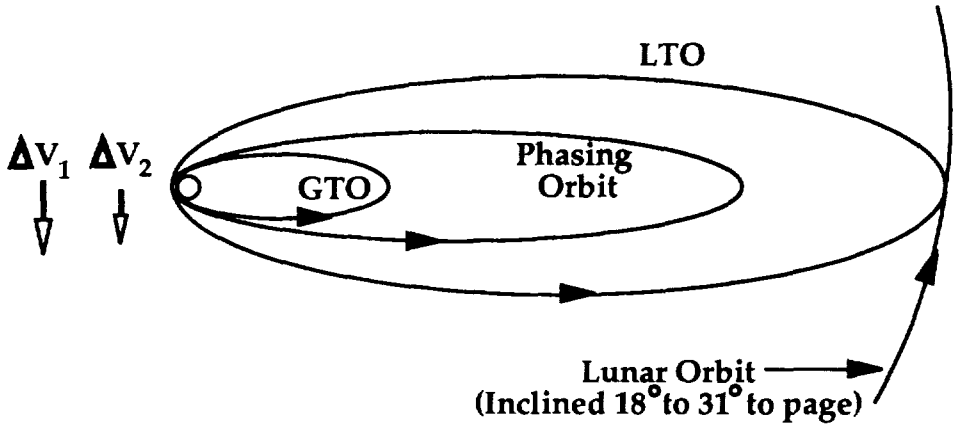

Fig. 2 Two-Impulse Lunar Transfer

Fig. 2 is a diagram of the GTO, the phasing orbit and the LTO. The impulse ΔV_1 takes the spacecraft from GTO to the phasing orbit and ΔV_2 provides the transfer from the phasing orbit to LTO. Later studies will probably reveal an optimal split between these two impulses but, for these studies, it is sufficient to require only that their sum equal the ΔV required to go from GTO to LTO. Assuming that GTO is a typical Ariane-launched orbit, (200 km x 35975 km with an inclination of 7° and an argument of perigee of 178° wrt the equator) and that the LTO has a semi-major axis of 198,000 km (C_3 = -2.013 km^2/s^2), we obtain for the total of the two impulses the difference between the perigee speeds of the initial and final orbits, that is,

$$\Delta V_1 + \Delta V_2 = V_{p_{LTO}} - V_{p_{GTO}}$$

$$= \sqrt{\mu}\left\{\sqrt{\frac{2}{r_p} - \frac{1}{a_{LTO}}} - \sqrt{\frac{2}{r_p} - \frac{1}{a_{GTO}}}\right\},$$

where r_p represents the common perigee radius of the two orbits, a_{GTO} and a_{LTO} represent their semi-major axes, and μ is the gravity constant (GM) of the Earth (=398600.5 km^3/s^2). Using the typical values quoted above and taking the equatorial radius of the Earth as 6378.14 km, we obtain,

$$\Delta V_1 + \Delta V_2 = 0.675 \text{ km/s},$$

to be applied so as to ensure lunar encounter near apogee of the LTO.

The Zero-Patched Conic Method:

One of the most powerful and simple methods for estimating the energy during Moon passage is the zero sphere of influence or point to point patched conic method. It can be shown that this method conserves the Jacobian integral in the restricted three-body problem and is capable of predicting the Moon-relative energy at perilune to within terms of the order of the Moon/Earth mass ratio and the ratio of the passage distance to the Moon's distance from the Earth. For preliminary analysis of an orbiter mission, it yields the excess speed of the lunar encounter hyperbola to within a few percent and permits estimation of the orbit insertion requirements to the same level of accuracy.

The method is basically the same as that used by Professor Rutherford in his famous analysis of the nuclear scattering problem except, in the orbital case, there is no appreciable recoil and, therefore, no need to transform to "laboratory" coordinates. The essence of the method is to determine a Keplerian ellipse that goes from the launch point to the center of the Moon in some desired transfer time (Lambert's problem). The Keplerian velocity at encounter is transformed to a Moon-centered frame and that transformed velocity is taken to be the hyperbolic excess velocity of the Moon-passage trajectory. This method cannot yield any information about the lunar passage distance and the transfer times will be in error by several hours but the Moon-relative energy is surprisingly accurate. This technique is used for most preliminary lunar and interplanetary transfer studies.

Let $\mathbf{V}_M$ represent the velocity vector of the Moon at the time of encounter (when the spacecraft is assumed to have the same position as the center of the Moon) and let $\mathbf{V}_A$ represent the Earth-relative velocity vector on the Keplerian transfer orbit at encounter. The Moon-relative excess velocity, $\mathbf{V}_\infty$, is simply

$$\mathbf{V}_\infty = \mathbf{V}_A - \mathbf{V}_M,$$

where the bold quantities represent vectors. In the nomenclature of spherical astronomy, if η represents the inclination of the Keplerian transfer orbit to the Earth-Moon plane, and γ is the elevation path angle of the Keplerian velocity vector at encounter (see Fig. 1), then

$$V_\infty^2 = |\mathbf{V}_\infty|^2 = V_M^2 + V_A^2 - 2\, V_M\, V_A \cos\eta \cos\gamma.$$

The excess speed is related to the selenocentric energy (the vis-viva energy of the spacecraft with respect to the Moon) as

$$E_M = V_\infty^2/2 = v^2/2 - \mu_M/r\ ,$$

where μ_M is the gravitational constant (GM) of the Moon (= 4903.2 $km^3/s^{2)}$ and v and r represent the speed and radial distance of the spacecraft with respect to the Moon during the encounter.

Now, with an accurate estimate of the Moon-relative energy, it is a simple matter to determine the orbit insertion requirements. Assume that the lunar transfer orbit has been targeted for a closest approach distance, r_p, of 1838 km (100 km above the lunar surface). This targeting is achieved by selection of launch time and does not appreciably affect the value of V_∞ given above. The Moon-relative speed at closest approach, then, is

$$v_p = \{V_\infty^2 + 2\mu_M/r_p\}^{1/2} ,$$

and the (circular) orbit insertion impulse required is

$$\Delta V_C = v_p - v_C = \{V_\infty^2 + 2\mu_M/r_p\}^{1/2} - \{\mu_M/r_p\}^{1/2} .$$

For a typical value of V_∞ of 0.85 km/s, we obtain

$$\Delta V_C = \{(0.85)^2 + 2\cdot(4903)/1838\}^{1/2} - \{4903/1838\}^{1/2} = 0.828 \text{ km/s}.$$

Fig. 3 shows the orbit insertion ΔV as a function of V_∞ throughout the range of values to be expected for a GTO to lunar orbit mission.

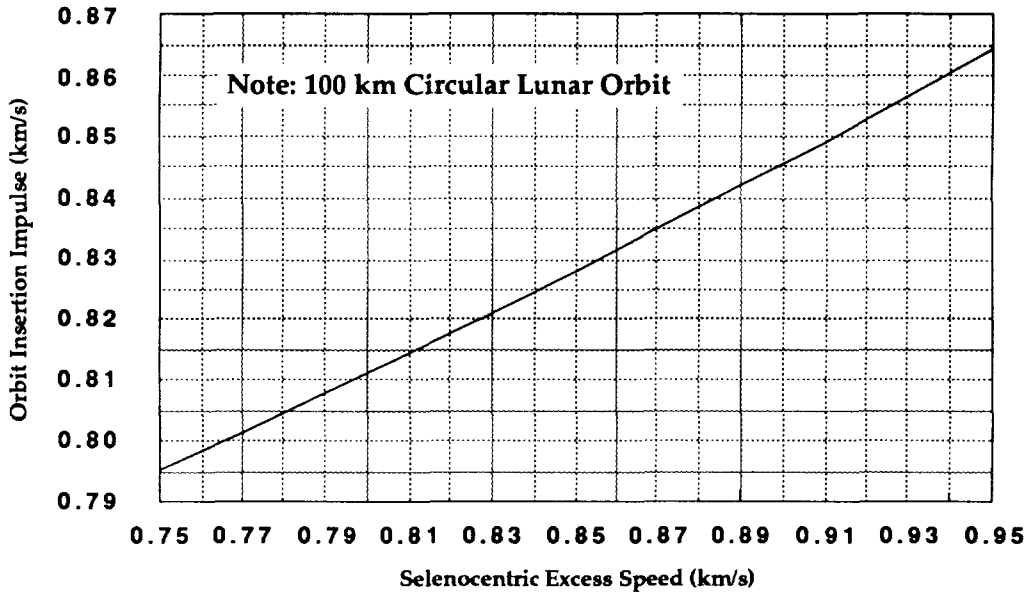

Fig. 3 Circular Orbit Insertion ΔV vs Hyperbolic Excess Speed

Sensitivity of Requirements to Launch Window:

It is important in studies of this type to identify the sensitivity of the performance to various parameters that may have to change from the nominal situation during an actual mission. Perhaps the most important of these is the time of launch. It is recommended that the launch vehicle contractor be asked to provide a launch to GTO at a time of day that will place the perigee of the orbit within 5° of the Earth-Moon plane anytime within 15 days after launch. If there were no other constraints, this could be accomplished twice per day by launching just before the GTO injection point crosses the Earth-Moon plane. But for a shared launch, there will be constraints on launch windows as a result of requirements placed by the primary payload such as solar aspect angles at injection or apogee passage. Primary payload constraints may eliminate one or both of the lunar transfer options during certain times of the year and should be the subject of more careful consideration than given here. Because of this kind of interaction between primary and secondary payload constraints, it is of interest to evaluate the penalties associated with launch at non-optimal times and to consider practical (near-optimal) strategies for correcting the effects of variations in the initial argument of perigee with respect to the Earth-Moon plane.

Fig. 4 shows the positions of the relevant planes as they will be in Jan of 1993. The best time to launch is just before the GTO injection point (which can be assumed to rotate with the Earth) reaches the Earth-Moon plane. This can be accomplished twice per day (see Reference 2), once near the ascending node of the Earth-Moon plane on the equator or just prior to crossing the descending node about 12 hours later than the situation shown in Fig. 4. During the 1990's, the ascending node of the Earth-Moon plane never gets far from the vernal equinox as it oscillates from about -13° to +13° in Right Ascension. In the early 1990's the ascending node of the Earth-Moon plane on the equator regresses from about -7° relative to the vernal equinox (in Jan 1990) to its minimum at about -13° (in Jan 1993). The node then advances from -13° to -7° during the next three years and will not cross into positive longitudes until near the turn of the century. Thus the optimum injection point in Jan 1993 would have a celestial longitude of -15° (that is 15 degrees West of the vernal equinox) which would allow for about 2° of perigee advance or about 2.5 days of waiting time until the oblateness rotates the perigee into the Earth-Moon plane at which time the spacecraft could be injected into the phasing orbit.

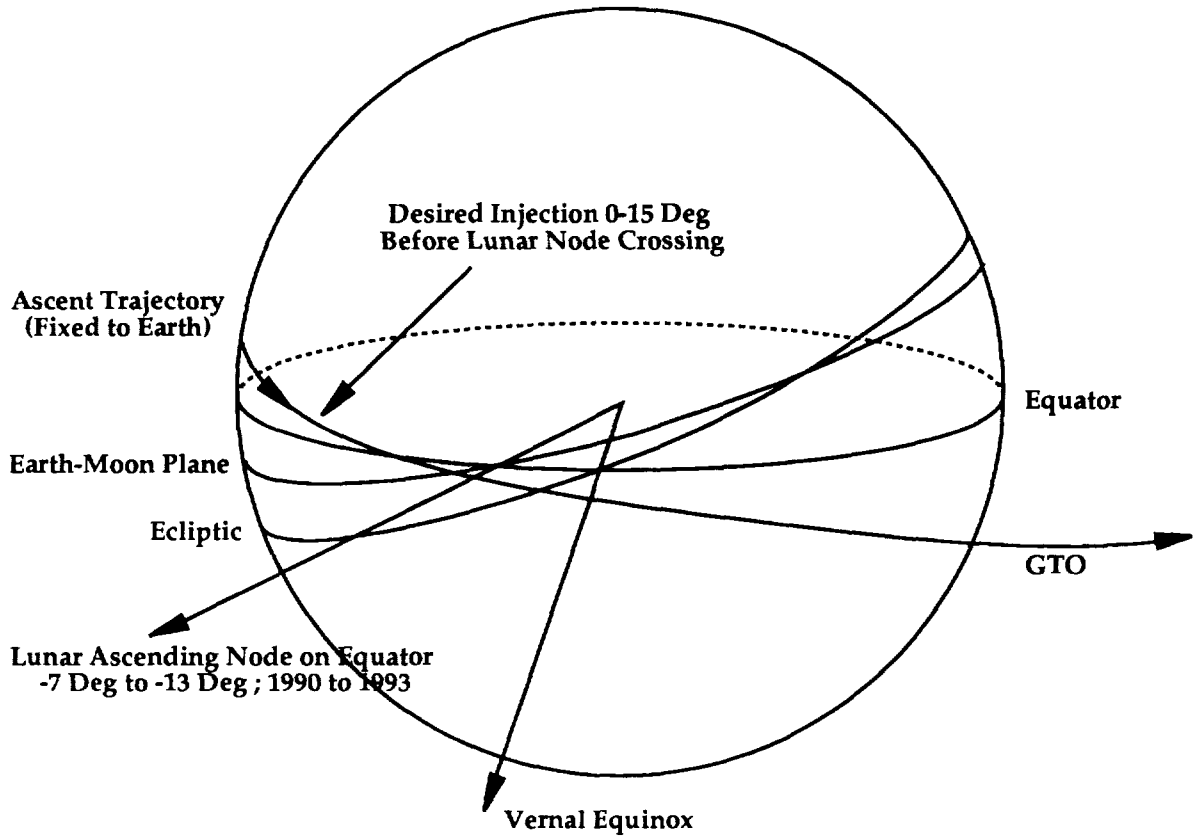

Fig. 4 Geometry of the Earth-Moon System in Jan 1993

But launch windows are not instantaneous and should be about 45 minutes wide to account for weather and other types of delays and still provide a reasonable probability of launch. Notice that the text of Fig. 4 calls for a 15° window. This corresponds to a one hour launch window ending with an injection exactly at the Earth-Moon plane. However, in the example above, the launch window should open about 45 minutes before the example time or about 11.25 degrees of Earth rotation earlier than the optimum which is to say that the launch window should open at a time which yields a GTO injection point whose celestial longitude is -26.25°. Then, in case the vehicle is launched at the beginning of the window, there would be a waiting time of about 16 days (approximately 13.25° / 0.816° per day) while the oblateness rotates the perigee into the Earth-Moon plane (see discussion of correction method 1 below). The other launch window (near the descending node of the Earth-Moon plane on the equator) would open at a time which would yield an injection celestial longitude of about 180° - 13.25° = 166.75° East of the vernal equinox. Either option would yield a 45 minute launch window ending with a trajectory whose perigee point is about 2° out of the Earth-Moon plane and approaching it. Thus, even for a launch at the end of either window, there would be about 2.5 days of waiting while the perigee advanced to the Earth-Moon plane. This would give ample time for orbit trim, orbit and attitude

determination, and spacecraft checkout and maneuvers prior to insertion into the phasing orbit. The example above is for illustrative purposes. It is recommended that the trajectory requirements be stated as in a previous section, i.e. that the GTO perigee shall be within 5° of the Earth-Moon plane at some time within 15 days of GTO injection. The exact values of these requirements may change but the method of specification leaves nothing to the imagination.

Correction Strategies:

The first method using the simplest strategy, as suggested earlier, is to wait until the Earth's oblateness rotates the perigee into the Earth-Moon plane. Such a strategy would involve no direct performance penalty except perhaps a few meters per second for orbit maintenance. But this strategy may require six or seven month waiting periods in the worst cases. As such a wait would almost certainly be unacceptable because of the long time spent in the Earth's radiation belts, it seems wise to investigate alternate techniques. The rates of the orbital ascending node and argument of perigee with respect to the Earth's equator for an orbiter under the influence of the Earth's oblateness parameter, J_2, are given by (see e.g. Ref. 3)

$$\frac{d\Omega}{dt} = -\frac{3}{2} J_2 n \left(\frac{R_e^2}{a^2 (1 - e^2)^2} \right) \cos i \ , \quad \text{and} \quad \frac{d\omega}{dt} = -\frac{3}{2} J_2 n \left(\frac{R_e^2}{a^2 (1 - e^2)^2} \right) \left[\frac{1}{2} - \frac{5}{2} \cos^2 i \right],$$

where Ω and ω are the longitude of the ascending node and argument of perigee, n is the orbital mean motion ($n = \{\mu/a^3\}^{1/2}$), a and e are the orbital semi-major axis and eccentricity, i is the equatorial inclination, R_e is the Earth's equatorial radius, and J_2 is the Earth's dynamical oblateness parameter ($J_2 = 1.082 \times 10^{-3}$). For a GTO with a 7° inclination (see Ref. 4), these rates are

$$\frac{d\Omega}{dt} = -0.413 \text{ deg/day} \ , \text{ and } \ \frac{d\omega}{dt} = +0.816 \text{ deg/day} .$$

Because the perigee advances (moves in the direction of spacecraft motion) it is better to launch early than late with respect to the Earth-Moon plane crossing.

A second method for adjusting the argument of perigee with respect to the Earth-Moon plane is to seek a large phasing orbit that is strongly perturbed by the gravitational perturbations of the Sun and Moon in such a way as to move the line of apsides into the Moon's orbit plane. This may be quite a complex solution because if the perturbations are strong enough to rotate the orbit quickly, they will also change the shape and probably the energy of the orbit. Such a solution to extend the launch window could alleviate any radiation problems associated with remaining in GTO for long periods of time. A large phasing orbit could be selected so that the spacecraft spends most of its time outside the severe

radiation, and an optimal multi-impulse transfer be selected to complete the transfer to the TLO. It is suggested that this possibility be investigated in more detailed studies as a possible means of improving overall performance in case margins are considered inadequate or if the radiation dose is considered excessive as the mission plan and spacecraft system become more mature.

The third technique considered is the brute force method in which the spacecraft propulsion is used to correct for the effects of an early or late launch on the argument of perigee.

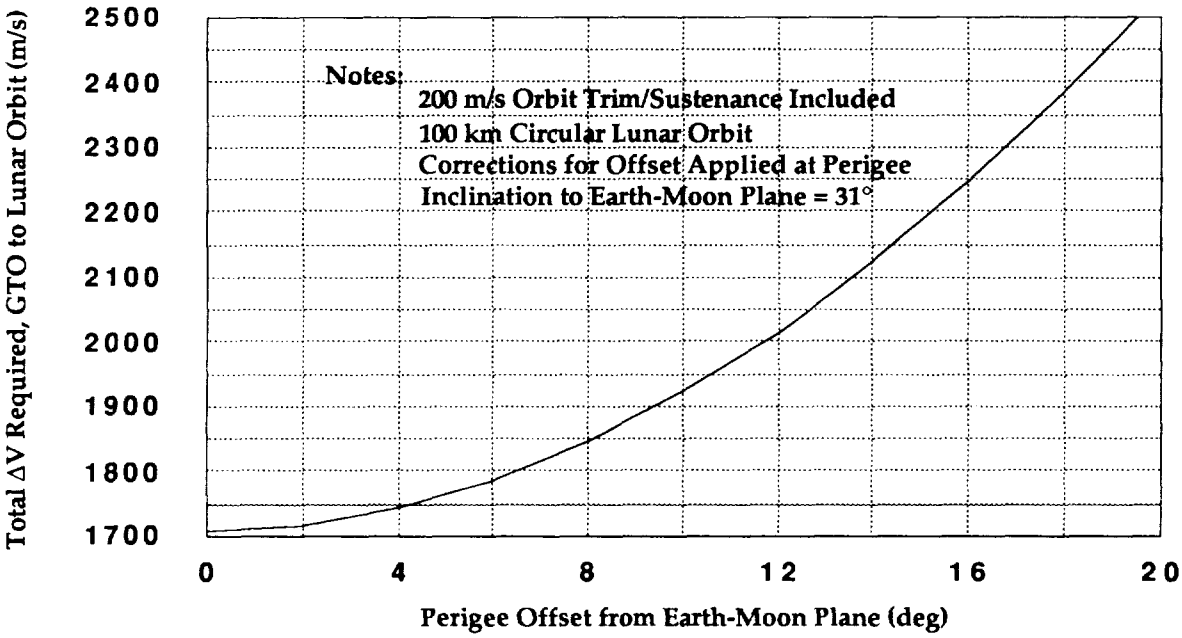

Fig. 5 Total ΔV versus Angular Perigee Offset

Fig. 5 shows the total ΔV required to transfer from GTO (200 x 35975 km) to a 100 km circular lunar orbit as a function of the perigee offset from the Earth-Moon plane. The perigee offset is the angle from the Earth-Moon plane (measured along the orbit) to perigee of the phasing orbit at the time of injection into the phasing orbit. It is assumed that perturbations acting on the phasing orbit itself are negligible and, therefore, the perigee of the phasing orbit and the LTO are at the same point in space. In the calculations, it is assumed that the inclination of the phasing and lunar transfer orbits is 31° (the greatest possible) and that 200 m/s ΔV budget has been allocated for transfer orbit corrections and lunar orbit sustenance maneuvers. The calculations for Fig. 5 also include the assumption that the Moon's orbit is circular at 384,000 km from the Earth. This corresponds to the mean distance of the Moon from the Earth which varies by ± 5% during any month. The strategy used to compensate for perigee offset is to increase the size of the LTO by a small additional impulse applied at perigee. The additional impulse is just that required to increase the radial distance from the Earth at the largest node on the

Earth-Moon plane. This increase exactly compensates for the decrease in radial distance caused by the angular offset of the perigee at injection. Although this is not necessarily the optimal strategy, it is a practical one and the figure shows that offsets of 4 to 6 degrees are probably tolerable as they can be accounted for by the use of less than 100 m/s. Of course, such a strategy would increase the moon-relative excess speed and some (small) additional ΔV would be required for lunar orbit insertion. The point here is that there are many transfer strategies available that will permit an adequate launch window for achieving the objectives of both the primary and secondary payloads on the launch vehicle.

Preliminary Mass Calculations:

It is instructive to estimate the amount of payload mass that can be delivered to lunar orbit for various levels of required ΔV as estimated above. Fig. 6 shows the net payload delivered to end of mission assuming a single on-board propulsion system with a specific impulse of 310 seconds and for stage propellant mass fractions from 0.65 to 0.85. (This is the ratio of the mass of propellant to the total wet mass of the stage not including payload). The performance is given as payload mass as a percent of the spacecraft liftoff mass. This is the mass of the spacecraft after separation from the launch vehicle and jettison of any adaptors or extra mass that will not be accelerated by the spacecraft propulsion system. The analyst should be forewarned that stage propellant mass fractions of 0.85 are not generally achievable with very small spacecraft (< 100 kg). The minimum mass of existing valves, tanks, and other necessary propulsion system hardware dictate a stage propellant mass fraction of the order of 0.65 to 0.70 for spacecraft in the 50 to 100 kg range. As improvements in small spacecraft propulsion systems become available to the general user, these values will improve but, for current studies, it is suggested that the performance be calculated using the masses of the propulsion system component parts that are actually available for use.

Preliminary studies of optimal staging indicate that very little is to be gained by going to a two-stage propulsion system in the cases of the larger propellant mass fractions. The flexibility afforded by a restartable, single-stage system will probably turn out to be the deciding factor in selection of the propulsion system. For smaller spacecraft systems, it may prove wise to use a small solid for one of the larger maneuvers. Based on these preliminary deliberations, it appears that an on-orbit payload mass of from 50% to 20% of the mass in GTO can be expected, depending upon the exact time of launch, vehicle size, and final strategies selected.

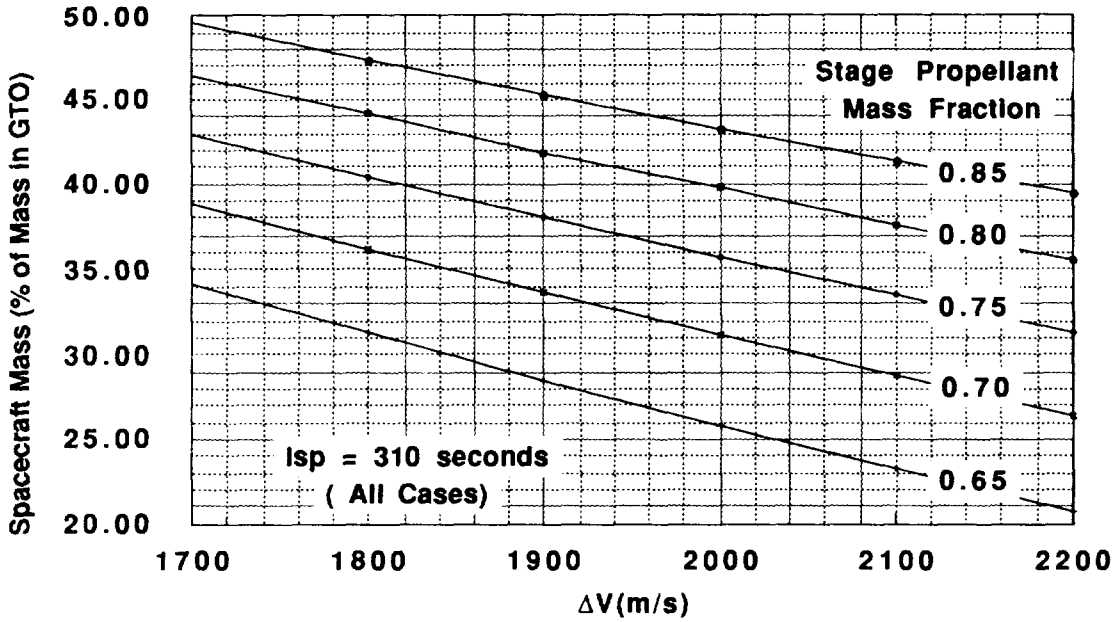

Fig. 6 Payload Fraction vs. Total Impulse

Acknowledgments:

Among the many people to whom the author is indebted for inputs to this work are, in particular, J. R. French, D. Gump, K. Lindas, and J. R. Stuart. Any opinions expressed are strictly those of the author and in no way represent the institutional policy of any organization with which the author is associated. This work was supported by LunaCorp, Inc. and by internal funding from Ball Space Systems Division.

References:

1. Uphoff, C., " Practical Aspects of Transfer from GTO to Lunar Orbit", A Working Paper Prepared for LunaCorp. Study Report. Feb 1990.

2. Uphoff, C., " The Art and Science of Lunar Gravity Assist", Paper No. AAS 89-170, Presented to the AAS/GSFC International Symposium on Orbital Mechanics and Mission Design. Greenbelt, Maryland. April 1989.

3. Brouwer,D., and Clemence,G., "Methods of Celestial Mechanics", Academic Press, 1961.

4. ArianeSpace, "Ariane User's Manual", Issue No. 1, Rev. 4, Sept 1988.

An Approach For Finding Long Period Elliptical Orbits For Precursor SEI Missions

by

Michael F. Fraietta
Victor R. Bond

McDonnell Douglas Space Systems Company
Houston Division

ABSTRACT

Precursors for Solar System Exploration Initiative (SEI) missions may require long period elliptical orbits about a planet. These orbits will typically have periods on the order of tens to hundreds of days. Some potential uses for these orbits may include the following: studying the effects of galactic cosmic radiation, parking orbits for engineering and operational test of systems, and ferrying orbits between libration points and low altitude orbits.

This report presents an approach that can be used to find these orbits. The approach consists of three major steps. First it uses a restricted three-body targeting algorithm to determine the initial conditions which satisfy certain desired final conditions in a system of two massive primaries. Then the initial conditions are transformed to an inertial coordinate system for use by a special perturbation method. Finally, using the special perturbation method, other perturbations (e.g., sun third body and solar radiation pressure) can be easily incorporated to determine their effects on the nominal trajectory.

An algorithm potentially suitable for on-board guidance will also be discussed. This algorithm uses an analytic method relying on Chebyshev polynomials to compute the desired position and velocity of the satellite as a function of time. Together with navigation updates, this algorithm can be implemented to predict the size and timing for ΔV corrections.

1.0 Introduction

During the summer of 1991 the authors were approached (by NASA-JSC) to assist in a trajectory design problem for the "Life Sat" mission. The objective of Life Sat is to determine the biological impact of deep space radiation on the cells of living animals. Data gathered from this mission will be used to estimate the effects of deep space radiation on human beings. Such effects must be well understood prior to sending humans on the necessarily long transfer trajectories to explore Mars.

A major problem in the experiment is that the data can be corrupted by another type of radiation, found in the Van Allen radiation belt region, relatively near the Earth. The trajectory should therefore be designed such that the spacecraft is near the Earth for relatively small amounts of time compared to the time spent in deep space. The ideal trajectory design requirements that would maximize scientific return are:

1.The spacecraft must remain outside the Van Allen region for 60 days.
2.The spacecraft should enter the Van Allen region only twice - once for departure and once for the return
3.The cost of the mission (i.e. ΔV) must be minimized.

This report describes an approach for finding a deep space geocentric orbit which will satisfy the above stated requirements. A key element to this approach is the use of the Double Lunar Swing-by technique first proposed by Farquhar and Dunham (1981). Using this technique the gravitational force of the moon is a significant perturbation to the solution. However, it was found that the moon is of some benefit to mission performance since it can be used to increase the energy of the outbound leg while decreasing the energy on the inbound leg.

A second goal is to present a guidance algorithm, possibly suitable for on-board computations, which keeps the vehicle on the prescribed trajectory even in the presence of other perturbations (e.g. solar third body effects). This algorithm uses a Chebyshev polynomial approach to analytically estimate the desired state as a function of time. This state is then compared to the navigation state and ΔV corrections are applied to maintain the desired trajectory.

2.0 Restricted Three Body Analysis

This section is provided in two parts. First, a description of a restricted three body targeting algorithm which solves the problem of: Given two position vectors and the flight time between these positions find the initial velocity. This is a two point boundary value problem which in the two-body theory is called Lambert's problem. However, since the strong perturbation of the moon must be accounted for, we started with the equations of motion in the restricted three body problem and then solved for the trajectory between the two specified position vectors. The solution is more difficult than in the two-body case since numerical integration is required. The technique for finding a solution is well known (D'Amario and Edelbaum, 1973; Bond and Fraietta, 1991) and will be used in this report. The second part describes how the restricted three body targeting algorithm is used to determine a double lunar swing-by solution suitable for the Life Sat mission.

2.1 Targeting Algorithm

The differential equations of the restricted three body theory are given in a coordinate system whose origin is at the center of mass of the primaries, m_1 and m_2, and is rotating with the line (i.e., the x-axis) connecting the primaries. The z-axis is normal to the plane of motion of m_1 and m_2, and the y-axis lies in the plane of motion. The x-axis rotates about

the z-axis at a angular speed which is the mean motion of the primaries. This system appears in Figure 1.

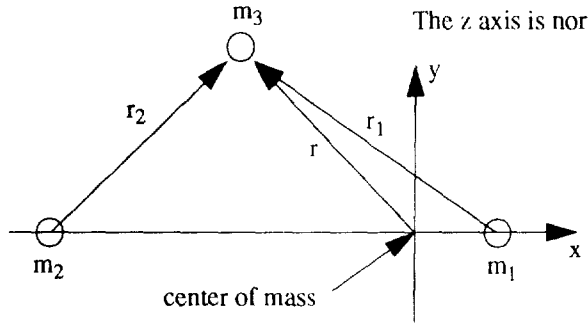

Figure 1 - Rotating (x,y) system

An inertial (X, Y, Z) system remains fixed with respect to the rotating system and is depicted in Figure 2.

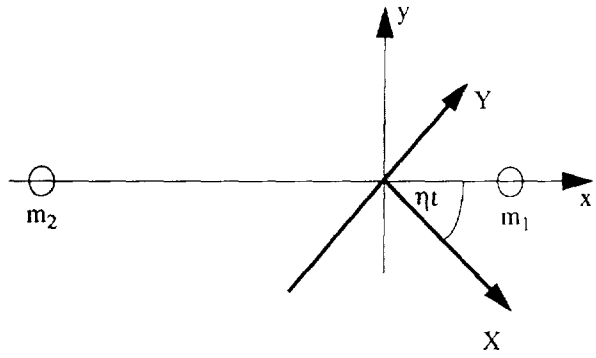

The z and Z axes are normal to the x,y plane
η = mean motion of m_1 and m_2

Figure 2 - Rotating (x,y) system in relation to an inertial (X, Y) system

The nonlinear differential equations describing the motion of m_3 (assumed to be massless) in the restricted three body system are given by (Szebehely, 1967)

$$\ddot{x} - 2\dot{y} = \Omega_x = \frac{\partial \Omega}{\partial x}$$

$$\ddot{y} + 2\dot{x} = \Omega_y = \frac{\partial \Omega}{\partial y}$$

$$\ddot{z} = \Omega_z = \frac{\partial \Omega}{\partial z}$$

Where the force function $\Omega(x, y, z)$ is

$$\Omega = \frac{1}{2}(1-\mu)\mu + \frac{1}{2}(x^2+y^2) + \frac{1-\mu}{r_1} + \frac{\mu}{r_2}$$

and

$$\mu = \frac{m_2}{m_1 + m_2}$$

$$r_1^2 = (x - \mu)^2 + y^2 + z^2$$

$$r_2^2 = (x + 1 - \mu)^2 + y^2 + z^2$$

An approximate targeting solution, specified by the initial conditions $(\underline{r}_o, \underline{v}_o)$ at t_0, is used as a first guess for solving the restricted three body system of differential equations. The initial velocity is then corrected according to the equation

$$\underline{v}_o^p = \underline{v}_o + \phi_{12}^{-1}(t_f, t_o)\,[\underline{r}_f - \underline{r}(t_f, t_o, \underline{v}_o)]$$

where $\underline{r}_f$, the final or target position is specified. The solution is then recomputed with $\underline{v}_o^p$ instead of $\underline{v}_o$. The matrix ϕ_{12} is a sub-matrix of the transition matrix

$$\Phi(t_o, t_f) = \begin{bmatrix} \phi_{11} & \phi_{12} \\ \phi_{21} & \phi_{22} \end{bmatrix}$$

which is associated with the differential equations of motion of the restricted three body problem. The matrix ϕ_{12} is found via numerical integration of the differential equations

$$\frac{d\phi_{12}}{dt} = \phi_{22}$$

$$\frac{d\phi_{22}}{dt} = M\phi_{12} + 2J\phi_{22}$$

where M is the matrix of second partials

$$M = \begin{bmatrix} \Omega_{xx} & \Omega_{xy} & \Omega_{xz} \\ \Omega_{xy} & \Omega_{yy} & \Omega_{yz} \\ \Omega_{xz} & \Omega_{yz} & \Omega_{zz} \end{bmatrix}$$

and J is

$$J = \begin{bmatrix} 0 & 1 & 0 \\ -1 & 0 & 0 \\ 0 & 0 & 0 \end{bmatrix}$$

The initial conditions for the transition sub matrices are

$$\phi_{12}(t_o, t_o) = 0 \quad \text{(null matrix)}$$
$$\phi_{22}(t_o, t_o) = I \quad \text{(identity matrix)}$$

This procedure continues iteratively until the computed final position vector $(\underline{r}(t_f, t_o, \underline{v}_o))$ becomes arbitrarily close to the specified final position vector $(\underline{r}_f)$, that is

$$|\underline{r}_f - \underline{r}(t_f, t_o, \underline{v}_o)| \to 0$$

2.2 The Double Lunar Swing-by

A typical trajectory for a double lunar swing-by requires the vehicle to fly by the moon's eastern limb on the outbound leg. The lunar encounter changes the velocity of the vehicle such that a second lunar encounter is achieved after a specified time interval. The second lunar fly by on the inbound leg, occurs on the western limb which acts to decrease the vehicle velocity prior to encountering the earth.

In their paper Farquhar and Dunham (1981) used a closest approach to the moon of approximately 16,000 kilometers. Adopting this value the restricted three body targeting algorithm is employed to find a solution targeting from the east limb of the moon to the symmetrical location on the west limb given a 60 day flight time. The vehicle motion is restricted to the Earth-Moon plane. After convergence the state required at the east limb of the moon that would attain the target conditions on the west limb 60 days later is known.

The next step is to determine the initial conditions required to depart a 400 kilometer altitude circular orbit at the earth (orbit lies in earth-moon plane) such that the state vector at the moon would exactly match the solution found above for the east limb. It is desirable that no additional ΔV corrections be necessary beyond that required for the Trans-Lunar Injection burn. This is essentially a patched solution in the restricted three body system. Again, the restricted three body targeting algorithm was used to determine the solution. However, this problem requires iteration to obtain the solution using two parameters namely, the longitude of the departure orbit and the time of flight to the patch point.

As a result of the symmetry found in the restricted three body system it was not necessary to patch the inbound trajectory from the moon to the earth since it is the mirror of the earth to moon trajectory. The complete double lunar swing-by trajectory in the rotating system is displayed in Figure 3.

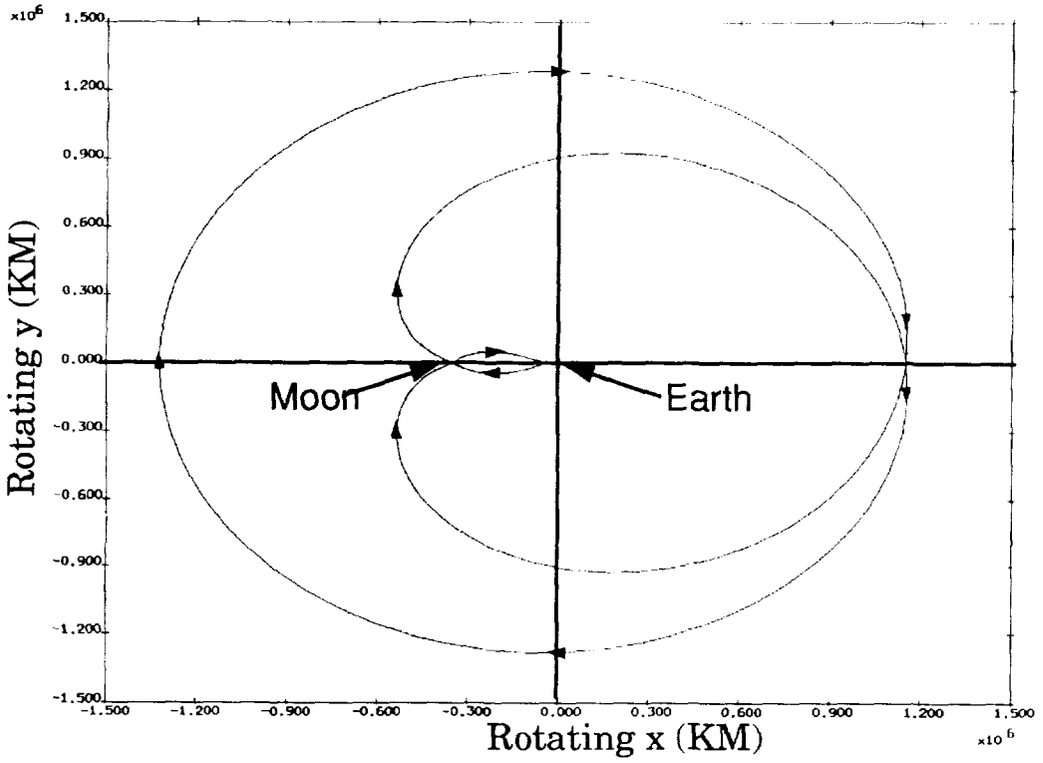

Figure 3 - Double Lunar Swing-by Trajectory

The Earth departure conditions specified by the targeting algorithm are depicted in Figure 4. As shown by the figure the Trans-Lunar Injection (TLI) burn required a ΔV of 3.119 kilometers per second at a longitude of 100.11 degrees with a transfer time of about 2.66 days to the patch point. Using these initial conditions, with no other additional ΔV, the vehicle will arrive at the moon with the required position and velocity for the 60 day moon

to moon transfer. It should be noted that the TLI ΔV is very near the Hohmann (minimum energy) value.

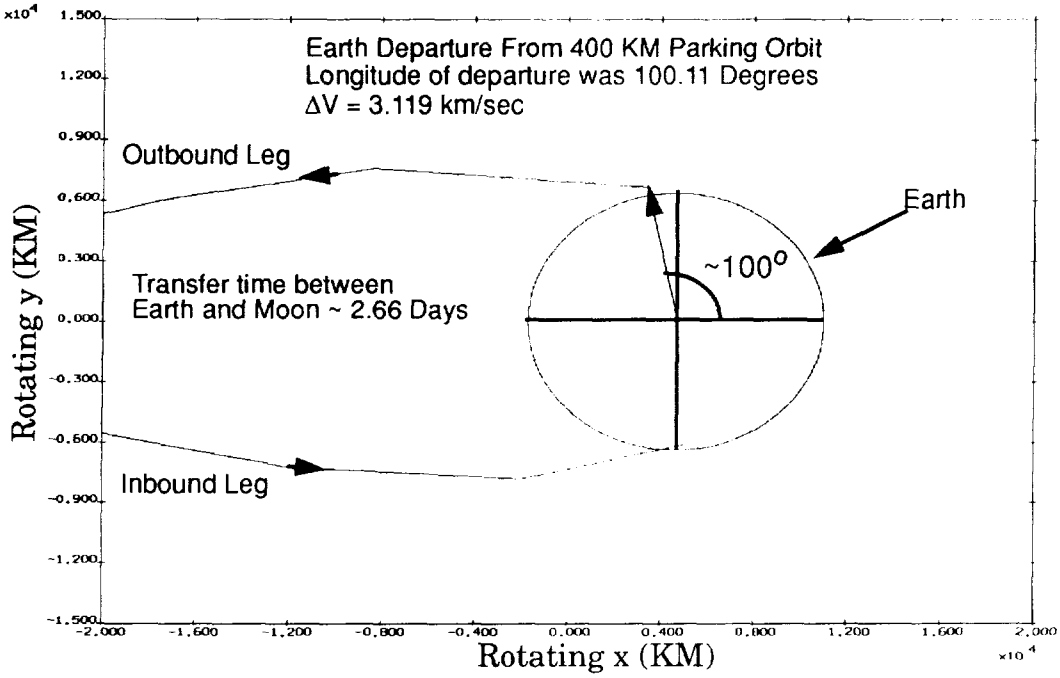

Figure 4 - Earth Departure and Arrival

The vehicle trajectory in the vicinity of the moon is displayed in Figure 5. As shown both lunar encounters have a closest approach to the moon at a relatively safe distance of 16,000 kilometers. The lunar encounter during both flyby's assists the vehicle performance. On the outbound leg the vehicle experiences a net gain in velocity, provided by the

lunar gravity, which propels it onto a very large elliptical orbit. On the inbound leg the vehicle experiences a net loss in velocity which is desirable prior to earth encounter.

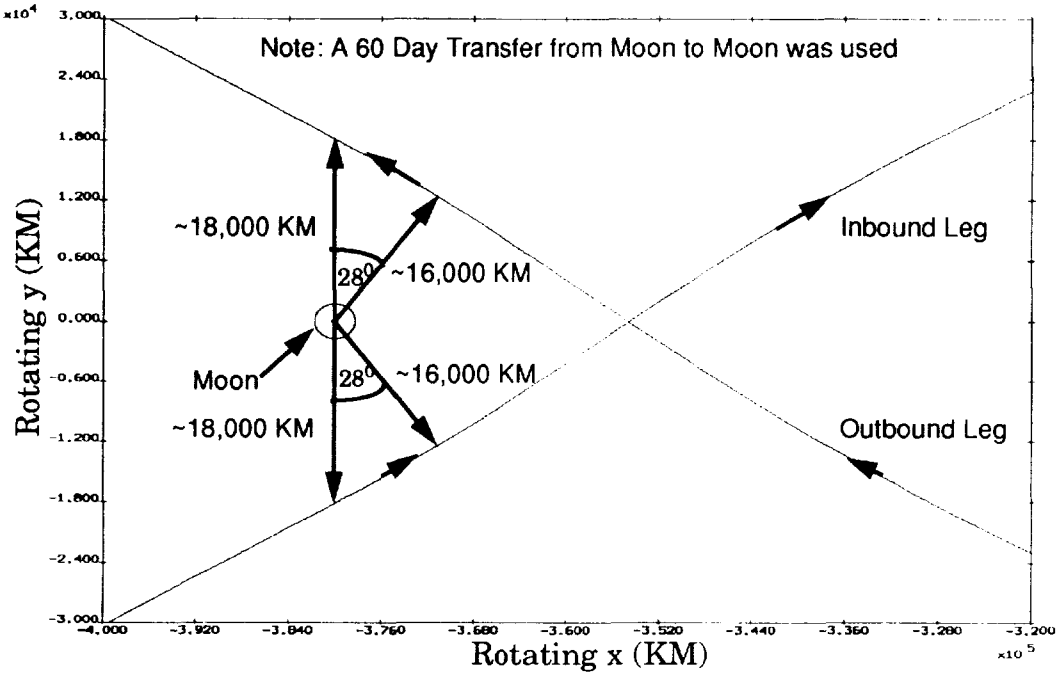

Figure 5 - Outbound/Inbound Lunar Fly by

Preliminary analysis has shown that relatively small amounts of ΔV (about 5 meters per second), applied during the lunar encounter on the inbound leg, would suffice for re-targeting for a specified entry interface (i.e. altitude and longitude). Entry velocities would be similar to those encountered during the Apollo missions (i.e. ~36,000 fps).

3.0 Perturbed Two-Body Analysis

From this point on the problem will be considered as a perturbed two-body problem. Solutions will be found by the special perturbation program, known as BG14, described in Bond and Fraietta (1991). There are several reasons for this change in point of view. For example, navigation, guidance and communication studies are more amenable to standard inertial coordinate systems. Also, even though the most significant perturbation, the moon, is included in the restricted three-body analysis, other significant perturbations such as the solar gravitational perturbations, high order gravitational fields of the Earth and moon, solar radiation pressure are not.

3.1 Transformation to Inertial Coordinates

Once the solution in the restricted three body system is determined the next step is to compute the initial state vector in the inertial coordinate system suitable for use in perturbed two-body analysis. The transformation from the rotating system to the inertial system is a two step process: (1) translate the position vector from the center of mass to the center of

the earth and (2) rotate the state vector into the Earth-Moon plane for a particular date. This translation and rotation is given by

$$\begin{bmatrix} X \\ Y \\ Z \end{bmatrix} = M \begin{bmatrix} x - \mu \\ y \\ z \end{bmatrix}$$

The matrix M provides the rotation into the Earth-Moon plane. For our analysis we used the J2000 inertial system.

3.2 Lunar Perturbation Only

Prior to investigating the effects of other perturbations, the method was first verified by duplicating the results found in the restricted three body system in the perturbed two-body system. To this end a circular lunar orbit, consistent with the computed initial conditions, was implemented in BG14 as a perturbation. The initial conditions were then integrated for the desired flight time (about 65.32 days) in the presence of the lunar third body perturbation. The trajectory, as viewed in the X-Y inertial plane, is displayed in Figure 6.

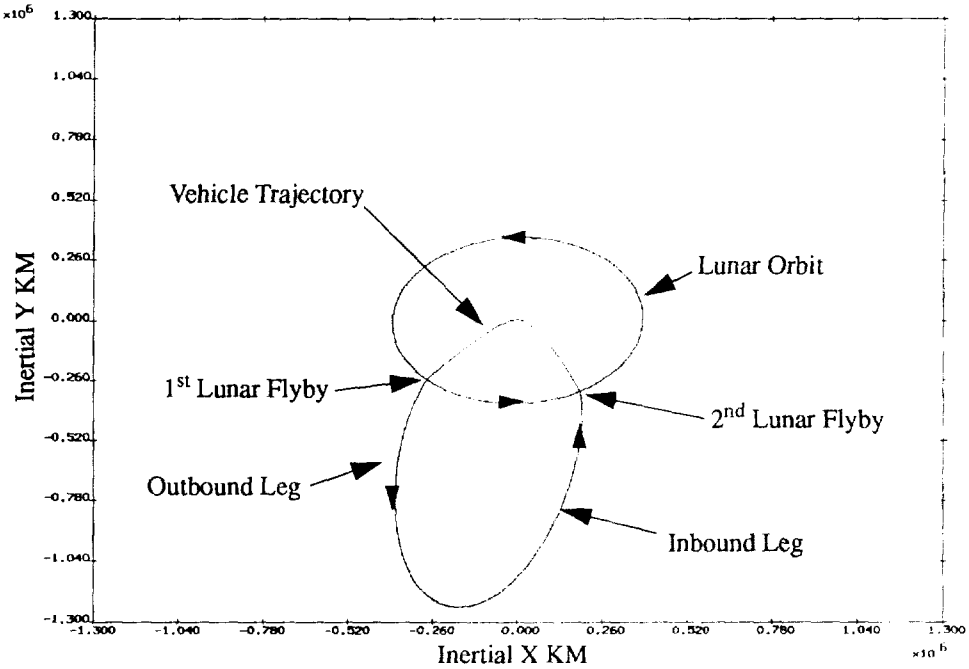

Figure 6 - Double Lunar Swing-by In Inertial Coordinates

As shown by the figure the trajectory experiences a significant bending on both the outbound and inbound legs as a result of the lunar swing-by.

3.3 Lunar and Solar Perturbations

Analysis performed during the preparation of this report has shown that the effects of the solar third body perturbations can not be ignored (especially for elliptical orbits with large semi-major axes.) It will therefore be necessary for the vehicle to periodically apply ΔV corrections to maintain the nominal trajectory. In an effort towards solving this problem a simple guidance control law using Chebyshev polynomials has been developed. This control law is then applied to the problem described in Section 3.2 with the addition of the third body perturbation due to the sun.

3.3.1 Chebyshev Guidance Algorithm

A guidance algorithm using Chebyshev polynomials, which can be expressed as

$$T_{n+1}(x) = 2xT_{n-1}(x) - T_{n-1}(x) \qquad n \geq 1$$

with starting values

$$T_0(x) = 1$$
$$T_1(x) = x$$

has been developed. Using the recursive nature of Chebyshev polynomials, this algorithm analytically provides the required state vector in the restricted three body coordinate system as a function of time using coefficients generated for a particular trajectory. Since for the restricted three body system the motion was restricted to the Earth-Moon plane, only the x-y components of the state vector are required. The restricted three body state vector is then transformation to the J2000 inertial system (in an identical manner to that described in Section 2.3). Once in the inertial system the actual state of the vehicle, as provided by navigation, can be compared to the desired state as provided by the Chebyshev polynomial solution. ΔV corrections are then applied at appropriate intervals to maintain the vehicle on the nominal path.

Using the entire earth to earth trajectory to compute the coefficients for the Chebyshev polynomials, it was found that the accuracy of the approximate state compared to the numerically computed state is a strong function of the number of Chebyshev coefficients used in the approximation. Figure 7 shows the maximum RSS position error between the

Chebyshev approximation and the numerically integrated state as a function of the number of Chebyshev coefficients.

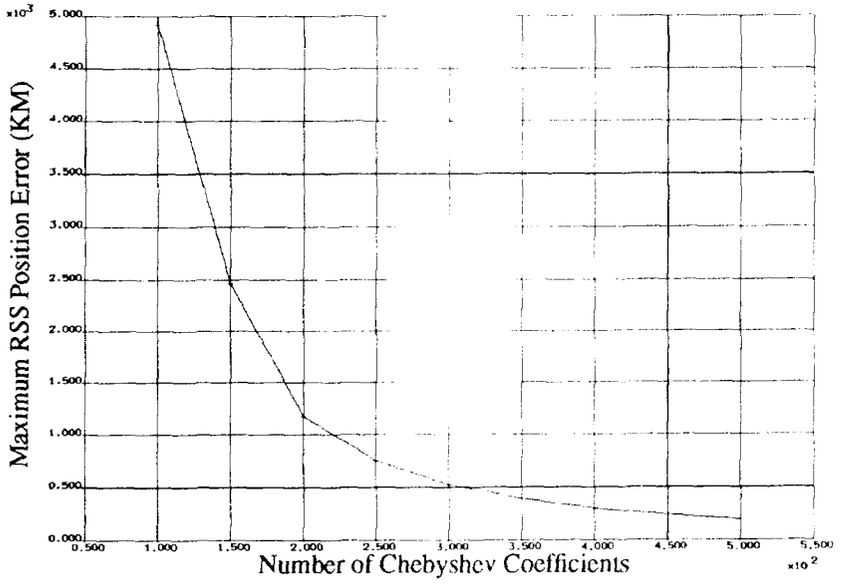

Figure 7 - Maximum RSS Position Error as a function of the Number of Chebyshev Coefficients Used

Note that the RSS position errors are dramatically reduced as the number of coefficients used increases. For example, as shown by the figure, the RSS position errors are reduced by about a factor of 5 by doubling the number of coefficients. Although not shown the velocity error behaves in a similar fashion.

3.3.2 Guidance Algorithm Results with Solar Perturbations

The Chebyshev guidance algorithm presented in Section 3.3.1 was implemented in BG14 along with a function to compute the solar third body perturbation. BG14 was then executed (with the same initial conditions and flight times as described in section 3.2) using

both lunar and solar third body perturbations with periodic ΔV corrections being applied by the guidance algorithm. The required ΔV is displayed in Figure 8.

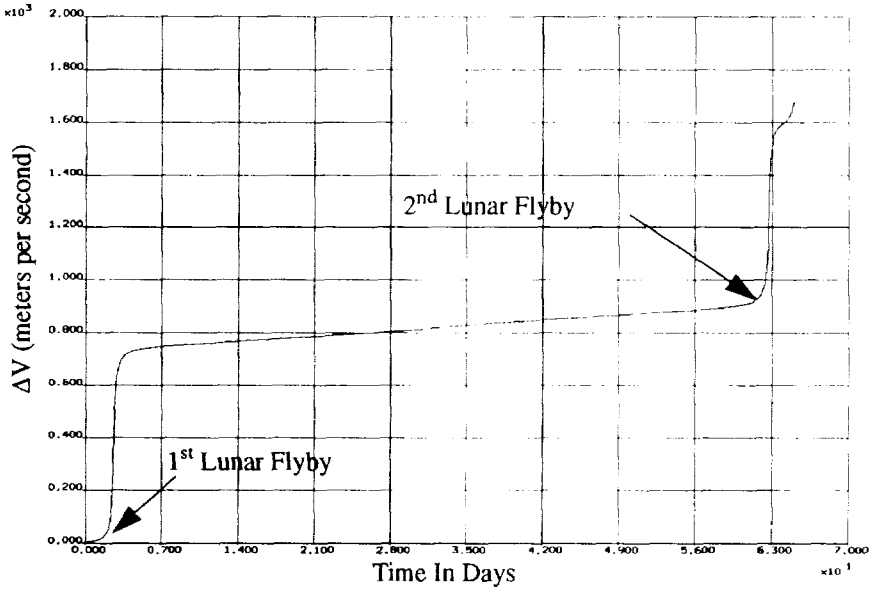

Figure 8 - ΔV vs Time With Sun Perturbations

As shown by the figure the ΔV required to maintain the nominal trajectory during the lunar flyby's approaches several hundred meters per second. These large values do not seem reasonable and are attributed to the fact that the Chebyshev approximation is not doing an adequate job in this region. However, once past the lunar encounter the total ΔV cost (a linear function in time) is only about 182 meters per second during the 60 day moon to moon transfer. It should be noted that it is on this part of the trajectory where the solar perturbation effects are largest.

Although time did not permit it for this study, it is felt that instead of fitting the entire earth to earth transfer with one Chebyshev fit it might be better to break up the trajectory into three different legs (i.e. earth to moon, moon to moon and moon to earth). A Chebyshev fit could then be provided for each leg. It is hoped that this technique would provide the accuracy required for the lunar encounter, thereby reducing the excessively large ΔV's shown in Figure 8.

4.0 Summary

An approach for finding long period elliptical orbits has been presented. The approach uses a targeting algorithm to solve the two point boundary value problem in the restricted three body system. The restricted three body solution found by the targeting algorithm was then transformed to the J2000 inertial system for use in a special perturbation method. This method allows modelling of other perturbations (due to for example the solar third body and solar radiation pressure) which are not easily modelled in the restricted three body system.

The approach was then used, in conjunction with the Double Lunar Swing-by technique, to obtain a candidate trajectory for the Life Sat mission. The candidate trajectory satisfies ideal trajectory design requirements which would maximize scientific return.

Finally, an estimate of the ΔV required to keep a vehicle on the desired trajectory in the presence of the solar third body perturbation was provided using a Chebyshev guidance algorithm. The algorithm was found to work well on the long elliptical trajectory once past lunar encounter. A suggestion for improving the performance of the guidance algorithm during lunar encounter was offered.

5.0 References

Bond, V. and Fraietta, M.: *Targeting in the Restricted Three-Body Problem*. NASA JSC-32158, October 1991.

Bond, V. and Fraietta, M.: *Elimination of Secular Terms from the Differential Equations for the Elements of Perturbed Two-Body Motion*. Flight Mechanics/Estimation Theory Symposium 1991, NASA Conference Publication 3123.

D'Amario, L. and Edelbaum, T. N.: *Minimum Impulse Three-Body Trajectories*. AIAA Paper No. 73-145, January 1973.

Farquhar, R.W. and Dunham, D.W.: *A New Trajectory Concept for Exploring the Earth's Geomagnetic Tail*. J. Guidance and Control, Vol. 4, No. 2, March-April 1981.

Szebehely, V.: Theory of Orbits. Academic Press, 1967.

ORBIT DETERMINATION ERROR ANALYSIS AND COMPARISON OF STATION-KEEPING COSTS FOR LISSAJOUS AND HALO-TYPE LIBRATION POINT ORBITS AND SENSITIVITY ANALYSIS USING EXPERIMENTAL DESIGN TECHNIQUES

Lieutenant Colonel Steven C. Gordon†

ABSTRACT

Spacecraft in orbit near libration point L1 in the Sun-Earth system are excellent platforms for research concerning solar effects on the terrestrial environment. One spacecraft mission launched in 1978 used an L1 orbit for nearly 4 years, and future L1 orbital missions are also being planned. Orbit determination and station-keeping are, however, required for these orbits. In particular, orbit determination error analysis may be used to compute the state uncertainty after a predetermined tracking period; the predicted state uncertainty levels then will impact the control costs computed in station-keeping simulations. Error sources, such as solar radiation pressure and planetary mass uncertainties, are also incorporated. For future missions, there may be some flexibility in the type and size of the spacecraft's nominal trajectory, but different orbits may produce varying error analysis and station-keeping results. The nominal path, for instance, can be (nearly) periodic or distinctly quasi-periodic. A periodic "halo" orbit may be constructed to be significantly larger than a quasi-periodic "Lissajous" path; both may meet mission requirements, but perhaps the required control costs for these orbits are provably different. Also for this spacecraft tracking and control simulation problem, experimental design methods can be used to determine the most significant uncertainties. That is, these methods can determine the error sources in the tracking and control problem that most impact the control cost (output); it also produces an equation that gives the approximate functional relationship between the error inputs and the output.

INTRODUCTION

In one formulation of the problem of three bodies, when the mass of one of the bodies is sufficiently small (infinitesimal) so that it does not affect the motion of the other two bodies (primaries), the "restricted three-body problem" results. Five libration (Lagrange) points can be found as particular solutions of the equations of motion governing the path of the infinitesimal mass moving within the gravitational fields of the primaries. These equilibrium points are defined relative to a coordinate system rotating with the primaries. One Lagrange point, L1, is located between the primaries and is the libration point of interest here.

Three-dimensional, periodic and quasi-periodic orbits are currently being studied for upcoming missions. Periodic "halo" orbits in the vicinity of libration points have been studied since the late 1960s. Robert Farquhar coined the term "halo" to describe a three-dimensional, periodic orbit near a libration point on the far side of the Moon in the Earth-Moon system.[1] These orbits were designed to be large enough so that the spacecraft would be constantly in view of the Earth and thus would appear as a halo around the Moon. Alternatively, the variations in size and shape that a quasi-periodic orbit can exhibit may add

†Head, Department of Math Sciences, U.S. Air Force Academy Co 80840, (719) 472-4470. This research is supported by Frank J. Seiler Research Laboratory.

valuable flexibility for mission planning. This type of bounded, three-dimensional libration point trajectory is called a "Lissajous" orbit since specific planar projections of these quasi-periodic trajectories may look like a special type of Lissajous curve.

Howell and Pernicka[2] have developed a numerical technique for determination of three-dimensional, bounded libration point trajectories of arbitrary size and duration. Their numerical algorithm uses an analytic solution as a first approximation and then constructs a trajectory continuous in position and velocity. Their method is used in this study to define nominal paths in the Sun-Earth+Moon problem. The notation "Earth+Moon" means that the Earth plus the Moon are treated as one body with mass center at the Earth-Moon barycenter. The numerical data is then curve fit using a cubic spline routine, although the use of other curve fit methods[3] is possible. The assumed dynamic model is the elliptic restricted three-body problem (ER3BP), where the primaries move on known elliptic paths. The force model used here includes solar radiation pressure[4], the gravitational attractions of the Sun and the Earth+Moon barycenter, and the centrifugal force associated with rotation of the system.

The forces affecting the spacecraft orbit have differing levels of uncertainty, and, unfortunately, the spacecraft will drift from the nominal path. Both range and range-rate tracking also include inaccuracy in measurement. The accumulated error in the spacecraft's position and velocity relative to the nominal path after a predetermined period of tracking can be computed. This error, or uncertainty, in the spacecraft state is measured through simulations, commonly referred to as orbit determination error analysis, and is presented as a vector of standard deviations of the states. In this work, the state vector includes three position and three velocity states. The state uncertainty computed in the error analysis can then be input to a station-keeping algorithm that computes control manuevers to return the spacecraft to the vicinity of the nominal path. The algorithms incorporate certain minimal constraints for time between manuevers, control magnitude, and distance from the nominal path before a control manuever is input. For these algorithms, variations in orbital shapes and sizes may have some effect on the station-keeping costs.

BACKGROUND

Coordinate Systems

The coordinate systems used in this analysis have a common origin at the primaries' center of mass. Primaries with masses m_1 and m_2 such that $m_1 \geq m_2$ are assumed here. The infinitesimal mass is denoted as m_3. These masses (m_1,m_2,m_3) correspond to particles situated at points P_1, P_2, and P_3, respectively. The barycenter is denoted as "B," and the resulting arrangement is shown in Fig. 1. The rotating coordinate system is defined as $X_RY_RZ_R$, and the inertial system is identified as $X_IY_IZ_I$.

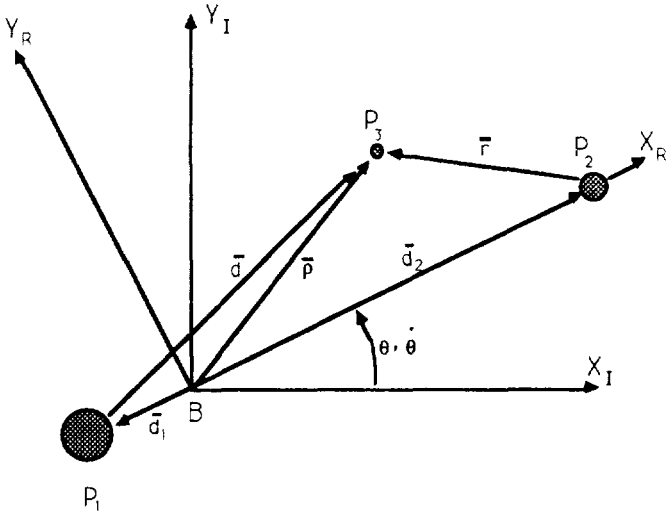

Fig. 1 Coordinate Systems Used

Note that both coordinate systems are right-handed, and the X and Y axes for both systems are in the plane of motion of the primaries. The rotating X_R axis is defined along the line that joins the primaries and is directed from the larger toward the smaller primary.

Equations of Motion

The equations of motion for m_3 (the spacecraft) relative to B as observed in the inertial reference frame are now formulated. The sum of the forces on m_3 resulting from both the gravity fields of masses m_1 (the Sun) and m_2 (the Earth-Moon barycenter) and from the solar radiation pressure can be used to produce the following second-order vector differential equation:

$$\bar{\rho}'' = -G\left(\frac{m_1}{d^3}\right)\bar{d} - G\left(\frac{m_2}{r^3}\right)\bar{r} + \left(\frac{kS}{d^3}\right)\bar{d}. \tag{1}$$

The overbar denotes a vector, and primes indicate differentiation with respect to dimensional time. All quantities are dimensional, as appropriate, and the quantity "G" is the universal gravitiational constant. The scalars "d" and "r" in Eq. (1) denote the magnitudes of vectors $\bar{d}$ and $\bar{r}$, respectively, depicted in Fig. 1. The dimensionless scalar "k" is the solar reflectivity constant, and "S" is the solar radiation pressure constant[5]. The position vector $\bar{\rho}$ is written in rotating components as

$$\bar{\rho} = x\,\hat{X}_R + y\,\hat{Y}_R + z\,\hat{Z}_R \tag{2}$$

where $\hat{X}_R, \hat{Y}_R, \hat{Z}_R$ are unit vectors. The kinematic expression for $\bar{\rho}''$ is:

$$\bar{\rho}'' = (x''-\theta''y-2\theta'y'-\theta'^2x)\,\hat{X}_R + (y''+\theta''x+2\theta'x'-\theta'^2y)\,\hat{Y}_R + z''\,\hat{Z}_R. \tag{3}$$

Three scaled equations of motion for P_3 can be derived using the following definitions: the sum of the primary masses is one mass unit, the mean distance between the primaries is one distance unit, and the universal gravitational constant is equal to one unit by proper choice of characteristic time. The equations of motion can then be simplified and scaled by also introducing the nondimensional mass ratio μ, "psuedo-potential" U, and the scaled solar radiation constant s:

$$\mu = \frac{m_2}{m_1 + m_2} \tag{4}$$

$$U = \frac{(1-\mu)}{d} + \frac{\mu}{r} + \frac{1}{2}\dot{\theta}^2(x^2 + y^2) - \frac{k\,s}{d} \tag{5}$$

where the dot denotes the derivative with respect to characteristic time. Then the vector magnitudes, "d" and "r," are written in terms of scaled quantities as:

$$d = [(x + \mu R)^2 + y^2 + z^2]^{1/2}, \tag{6}$$

$$r = [(x - R + \mu R)^2 + y^2 + z^2]^{1/2}. \tag{7}$$

The three second-order differential equations that result can be written in terms of characteristic (scaled) quantities as

$$\ddot{x} - 2\dot{\theta}\dot{y} = \frac{\partial U}{\partial x} + \ddot{\theta}y = U_x + \ddot{\theta}y, \tag{8}$$

$$\ddot{y} + 2\dot{\theta}\dot{x} = \frac{\partial U}{\partial y} - \ddot{\theta}x = U_y - \ddot{\theta}x, \tag{9}$$

$$\ddot{z} = \frac{\partial U}{\partial z} = U_z. \tag{10}$$

These three equations can then be used to propagate the spacecraft state forward in both the error analysis and station-keeping simulations.

Reference Paths Generated for This Work

In the ER3BP, precisely periodic halo orbits exist, but nearly periodic orbits are more practical and likely to be used in mission planning. Therefore, the goal here will be to compare results for quasi-periodic Lissajous and nearly periodic "halo-type" orbits. Fig. 2 depicts one orthographic view of the Lissajous and halo-type orbits used here. The halo-type orbit is significantly (approximately four times) larger in both the X and Y excursions from L_1.

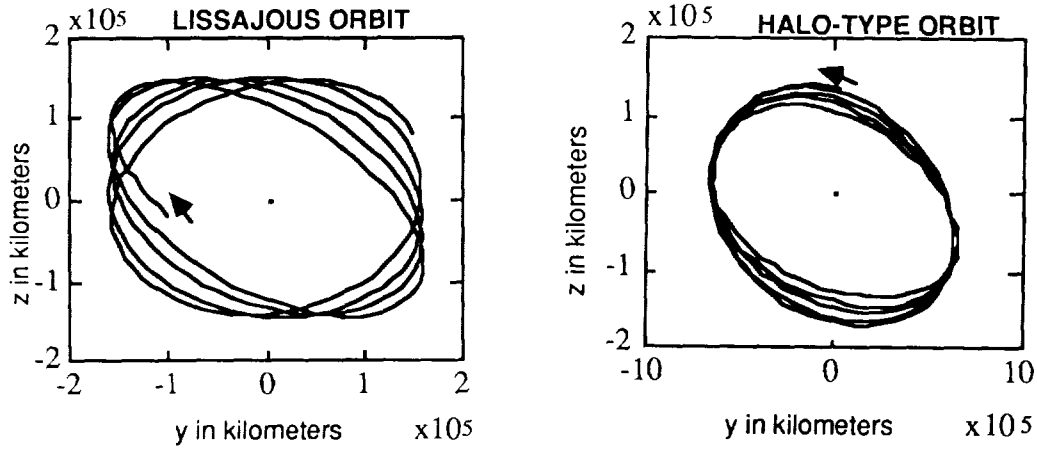

Fig. 2 Orthographic Depictions of the Reference Trajectories

Curve Fitting the Nominal Path

A numerical integration method developed by Howell and Pernicka[2] is used to generate a set of reference points at specified times for both position (three states) and velocity (three states), relative to the libration point of interest. The method computes numerical data in a reference frame that is centered at the libration point (in this case L_1) and rotates with the primaries. However, the state estimation techniques and station-keeping algorithms used in this work require access to a continuous nominal path of acceptable accuracy. In one study, Pernicka[6] found that station-keeping costs for a libration point orbit were sensitive to the accuracy of the curve fit. A cubic spline interpolation routine was selected to model the reference trajectory here; the results of using other methods are summarized in the station-keeping section of this effort.

Examples of Experimental Design (DOE) Methods

DOE methods are used to purposefully change the most important inputs to a process in order to analyze the output. The inputs are coded and alternately set at predetermined values for each experimental run so that the design is orthogonal; the relative contribution of each input can thus be judged independently. The output of interest may be the mean response and its variation, with the ultimate goal being to hit an output target value and minimize the output variability. However, the results from the set of experimental runs also determine the estimated function that relates the inputs to the output(s). Experimental design methods are also used to reduce the required number of runs or screen out relatively unimportant input variables. When only three inputs at two different input levels are considered, a two-level, "full-factorial" design consisting of every possible combination of input factors would require $2^3 = 8$ total runs. This design allows the experimenter to obtain the full model with all possible interactions. However, if 7 inputs in a 2-level design were used, $2^7 = 128$ individual runs would be necessary. These 128 runs may be expensive in

terms of both time and money. As a result, fewer runs may certainly be desired. A full-factorial two-level design will include all input variables and their interactions in the output equation model, but this may not be required. If some interactions are known to be relatively unimportant, a fractional-factorial[7] design consisting of a fraction of the number of runs required in a full-factorial can be constructed. For instance, for 3 inputs, a full-factorial would necessitate $2^3 = 8$ runs, while one type of fractional-factorial would require as few as 4 runs to determine the significance of main effects (modeling no interactions).

In a recent work by Garrett[8], several simple, yet educational, examples of the use of DOE are described. A similar example is included here: it is assumed that the area of a rectangle can be measured precisely, but the functional relationship between area and the length and width is not known. This example is truly hypothetical, but it can be used to illustrate simple DOE computations. The "design space" (where the computed model can be considered a good approximation to the true system) is defined by $1 \le$ width ≤ 2 meters and $1 \le$ length ≤ 3 meters. Here, "w" is used for width and "ℓ" for length. Runs are accomplished at the extreme values of the input variables, with $w = 1$ or 2 meters and $\ell = 1$ or 3 meters; however, first these measurements are generally coded. The data is coded by using the averages of both measurements and their ranges (highest value minus lowest). With $R(\ell)$ = range of ℓ, $R(w)$ = range of w, $\bar{w}$ = average of the w extremes, and $\bar{\ell}$ = average of the ℓ extremes, the coded settings are w_c and ℓ_c:

$$w_c = 2\left(\frac{w-\bar{w}}{R(w)}\right), \qquad \ell_c = 2\left(\frac{\ell-\bar{\ell}}{R(\ell)}\right). \tag{11}$$

When coded, the extreme values become +1 and -1 for each input, and these values are more simply denoted as "+" and "-", respectively. A balanced design with 4 runs then yields a design matrix of

RUN	w_c	ℓ_c	$(w_c)(\ell_c)$
1	-	-	+
2	-	+	-
3	+	-	-
4	+	+	+

The experiment is conducted using these high and low settings, and the measured areas of the rectangle (outputs) are 1, 3, 2, and 6 square meters for runs 1 through 4, respectively. Schmidt and Launsby[7] discuss interesting hand computational methods to determine the output equation; however, simple least squares methods also provide identical results. The prediction equation for the output is assumed to be

$$\hat{a} = b_o + b_1 w_c + b_2 \ell_c + b_3(w_c)(\ell_c) \tag{12}$$

where $\hat{a}$ = estimated area and the coefficients are computed using a least squares method with

$$C = \begin{bmatrix} 1 & -1 & -1 & 1 \\ 1 & -1 & 1 & -1 \\ 1 & 1 & -1 & -1 \\ 1 & 1 & 1 & 1 \end{bmatrix} \quad \text{and} \quad \bar{a} = \begin{bmatrix} 1 \\ 3 \\ 2 \\ 6 \end{bmatrix} \quad \text{in}$$

$$\bar{b} = (C^T C)^{-1} C^T \bar{a} = [b_o \; b_1 \; b_2 \; b_3]^T. \tag{13}$$

This method yields

$$\hat{a} = 3 + w_c + 1.5\,\ell_c + .5\,(w_c)(\ell_c). \tag{14}$$

A similar method could be used to derive a prediction equation for the variance (or the natural logarithm of the standard deviation) of the output[7]. The

resulting model in Eq. (14) is normally checked by completing test (confirmation) runs at extreme values and at the midpoint of the design space. For this example, that could mean using values of +1 for both w_c and ℓ_c for an extreme run or 0 for both inputs for the midpoint run. Suppose a confirmation run was conducted at the extreme values and the resulting output was a = 6 meters. Using Eq. (14), the predicted output is

$$\hat{a} = 3 + 1 + 1.5(1) + .5(1)(1) = 6 \text{ meters.}$$

For a confirmation run at the midpoints, the measured answer is a = 3 meters. Using Eq. (14), the predicted output equation is

$$\hat{a} = 3 + 0 + 1.5(0) + .5(0)(0) = 3 \text{ meters.}$$

Hence, the confirmation runs verify the model; a significant disagreement would require further investigation. (In fact, this is the exact functional model--it's just coded.) When noise in the system exists, statistical tests are used to test confirmation. The coded Eq. (14) can now be converted to use uncoded inputs by using Eq. (11):

$$\hat{a} = 3 + (2)(w - 1.5) + (1.5)(2)\left(\frac{\ell-2}{2}\right) + (.5)(2)(w-1.5)(2)\left(\frac{\ell-2}{2}\right) = (w)(\ell).$$

This example was simplified because we obviously knew the actual output equation. In manufacturing or engineering problems, the relationship between inputs and outputs is only generally known, and DOE can be used to gain problem insight. In the next section, the orbit determination error analysis methods used in this effort are summarized. The following section describes the station-keeping methods derived for this work and summarizes the control-cost comparisons of halo and Lissajous orbits. Finally, modeling the inputs of the station-keeping routine in an experimental design is presented.

ORBIT DETERMINATION ERROR ANALYSIS

Complete, exact knowledge of the state of a spacecraft in orbit is generally not possible. Available measurements are usually some function of the state variables and are not precise. For instance, a spacecraft in a libration point trajectory in the Sun-Earth system may be tracked using range and range-rate measurements containing random errors. The spacecraft may be affected by forces inadequately represented in the dynamic model, and model parameters may be uncertain. By definition, the linearized system of equations used to model the nonlinear system is a further approximation. These sources of error make knowledge of the spacecraft state uncertain. Computation of the most likely current state of the spacecraft in the presence of measurement and model uncertainty is the focus of orbit determination.

Error analysis involves an investigation of the impact of various error sources on orbit determination. The outputs of this error analysis are the standard deviations of the states. These outputs could then be used to predict how an improvement in measurement accuracy, for instance, would lessen state uncertainty. One benefit of more accurate knowledge of the state might be a reduction in station-keeping costs. A mathematical procedure can be developed to combine all information about the spacecraft state, filtering this observed data based on the varying degrees of uncertainty, to obtain a "best estimate" of the state and an estimate of the resulting state variable uncertainties.

The measurement and dynamic models are first summarized, three error analysis methods are briefly discussed, and then results are summarized. The three error analysis methods used here are the Kalman filter, batch weighted least squares , and consider covariance analysis[5,11]. Each technique computes a covariance matrix

at a specified epoch, and the positive square roots of the diagonal entries are indicators of state uncertainty levels.

Measurement and Dynamic Models

The measurement and dynamic models used in the filter derivations are

$$\text{Measurements:} \quad \tilde{Z}_k = M_k \tilde{X}_k + \bar{V}_k, \tag{15}$$

$$\text{Dynamic Model:} \quad \tilde{X}_{k+1} = \Phi(t_{k+1}, t_k)\tilde{X}_k = \Phi(k+1,k)\tilde{X}_k, \tag{16}$$

where $\tilde{Z}_k$ is the measurement residual vector at time step k; $\tilde{X}_k$ is the residual state vector at time step k; M_k is the measurement matrix that is linearized about the nominal path; $\Phi(k+1,k)$ is the state transition matrix at time step k+1 relative to time step k; and $\bar{V}_k$ is the measurement noise vector with assumed statistics $E(\bar{V}_k)=\bar{0}$ and $E(\bar{V}_k\bar{V}_k^T)=V_k$, where "E" is the expectation operator, $\bar{0}$ is the zero vector, and V_k is the measurement noise covariance matrix. Range and range-rate measurements are assumed; the matrix, M, is then a time-varying matrix of dimension 2x6, evaluated along the nominal path.

Error Analysis Methods Used

Early work in this area was designed to compare the error levels obtained here to those found in other works and to determine error levels for use in follow-on station-keeping simulations. Three methods of orbit determination error analysis (using covariance analysis) were formulated: Kalman filter, batch weighted least squares, and consider covariance analysis. The results of Kalman and batch weighted least squares filters were virtually identical, as expected, but nonetheless helped to confirm the analysis. Both methods were formulated to compute state uncertainty after a predetermined number of tracking updates, simulating range and range-rate measurements with associated error statistics. Consider covariance analysis also uses a batch weighted least squares formulation but includes parameter uncertainty. Model parameters that were initially considered uncertain in this work were the planetary masses (through the dimensionless mass parameter μ), the locations of the tracking stations, and the solar reflectivity constant. In general, at the epoch of interest, the state uncertainty is considered the consequence of the accumulated uncertainties in the model, the parameters of interest, and the measurements[5,9-11].

Orbit Determination Error Analysis Results

A survey of input error levels used in similar error analysis studies serves as a valuable introduction. The values of these uncertainties may be used to compute diagonal entries of input covariance matrices for an error analysis, or, alternatively, may be used as error sources in a station-keeping simulation. Table 1 lists the input error levels assumed in several error analysis studies. The errors are denoted by the symbols generally used in the derivation sections of this work. The solar reflectivity constant is k; the tracking site location uncertainty is S and is input as an equal uncertainty level for each of the site coordinates x_s, y_s, z_s; range tracking is R; range-rate tracking is RR; and the uncertain mass parameters are μ_e for Earth, μ_s for the Sun, and μ_m for the Moon. The last column contains the uncertainty in dimensionless mass parameter μ that would be "equivalent" to the errors listed for the individual mass parameters. (Recall that $\mu = (\mu_e + \mu_m)/(\mu_s + \mu_e + \mu_m)$ for the three-body system of interest in this work.) The approximate value of $\sigma(\mu)$ (standard deviation of μ) is calculated

from extensive (10,000) Monte Carlo trials for each of these studies. An entry in Table 1 of "--" means the particular study did not indicate if an uncertainty of this type was used.

Table 1
SURVEY OF ERROR ANALYSIS INPUT ERRORS

STUDY	ONE STANDARD DEVIATION ERRORS							
	k	S (km)	R (km)	RR (m/sec)	μ_e	μ_s (← km^3/sec^2 →)	μ_m	$\sigma(\mu)$ (x μ)
Mistretta[13]	15%	--	.010	.007	1.000	3.08×10^6	.0726	2.335×10^{-5}
Joyce[14]	10%	.002	.015	.002	.3986	1.327×10^4	.0490	1.411×10^{-7}
Efron[15,17]	10%	.002	.015	.002	.3986	1.327×10^4	.0490	1.411×10^{-7}
Rodriguez-Canabal[16]	--	.010	.015	.003	--	--	--	--
Longuski[17]	13%	.0003	.010	.001	.4903	4030.7	.0100	1.231×10^{-7}
This Work	13%	.010	.015	.003	.3986	1.327×10^4	.0490	1.411×10^{-7}

The error analysis conducted here assumes a 20-day tracking arc with 3 passes per day from 3 tracking sites. These assumptions closely match those of Joyce[14]. Using this tracking schedule and the R and RR measurement errors listed for this work in Table 1, the Kalman filter produces error levels presented in Table 2.

Table 2
RESULTS USING A KALMAN FILTER FOR ERROR ANALYSIS

ONE STANDARD DEVIATION LEVELS OF STATE ERRORS					
x (km)	y (km)	z (km)	$\dot{x}$ (mm/sec)	$\dot{y}$ (mm/sec)	$\dot{z}$ (mm/sec)
.550	1.600	4.450	.430	.775	2.250

The error levels listed in Table 2 are a result of a covariance analysis for the halo-type nominal path. The magnitudes of the error levels listed in Table 2 are, in fact, quite small; when additional error sources, such as mass parameter and station location uncertainties, are included in a consider covariance analysis, the resulting state error levels increase. The results in Table 3 are from a consider covariance analysis incorporating R and RR tracking, station location, and mass parameter uncertainties at the levels listed in Table 1 for this work.

Table 3
ERROR LEVELS PRODUCED FROM CONSIDER COVARIANCE ANALYSIS

	One Standard Deviation Levels	
Coordinate	Halo-Type Orbit	Lissajous Orbit
x (km)	1.46	1.25
y (km)	2.64	3.35
z (km)	4.81	3.19
$\dot{x}$ (mm/sec)	1.40	1.25
$\dot{y}$ (mm/sec)	1.85	1.41
$\dot{z}$ (mm/sec)	2.49	2.51

It certainly may be of great interest to compare the error levels found in this effort with the results of other investigations involving spacecraft in halo (or halo-type) orbits near the interior Sun-Earth libration point. Table 4 lists the results of four studies that do not include solar reflectivity as an error source and have small differences in the nominal paths and force models.

Table 4
COMPARISON OF ERROR ANALYSIS RESULTS FROM SEVERAL SOURCES

	One Standard Deviation Error Levels			
Coordinate	Rodriquez-Canabal[16]	Simó[18]	Simó[19]	This Work
x (km)	2.7	1.5	1.73	1.46
y (km)	3.9	2.5	2.24	2.64
z (km)	3.4	15.0	5.48	4.81
$\dot{x}$ (mm/sec)	2.4	1.0	1.41	1.40
$\dot{y}$ (mm/sec)	3.5	1.0	1.41	1.85
$\dot{z}$ (mm/sec)	1.3	3.0	2.45	2.49

The differences in error levels listed in Tables 3 and 4 may not be statistically significant; that is, station-keeping costs, determined through simulations using these error levels, may or may not differ statistically[5,12]. The results using one derived control scheme and the data in Table 3 are summarized in the next section.

STATION-KEEPING SIMULATIONS

For a collinear libration point orbit, a small deviation from the(unstable) nominal trajectory can lead to rather large drift from the path in a short time. In effect, a station-keeping algorithm must combat both the current drift from the path in addition to the exponential increase in the drift that is expected if no correction is implemented. Any delay in the control actuation may allow the drift to increase and thus compound the station-keeping problem. The goal of the station-keeping routine is then to keep the spacecraft "close enough" to the reference trajectory. The allowable deviations may depend on the simulation experience with a given control algorithm and on mission constraints, including the propellant cost that can be tolerated and the minimal time between control

inputs. When the spacecraft is "near" the nominal trajectory, it is reasonable to model the deviations from the reference path using a linear analysis.

Derivation of Method

For the linear control scheme developed here, the state transition matrix is partioned into four 3x3 submatrices as

$$\Phi(t_k, t_\emptyset) = \begin{bmatrix} A_{k\emptyset} & B_{k\emptyset} \\ C_{k\emptyset} & D_{k\emptyset} \end{bmatrix} = \begin{bmatrix} A_k & B_k \\ C_k & D_k \end{bmatrix} \tag{17}$$

A $\overline{\Delta v}$ input (a 3x1 vector), with magnitude denoted as Δv, is assumed to be added at a time $t_\emptyset$. The $\overline{\Delta v}$ (delta-velocity) is added to the initial velocity states in the numerical integration routine in order to change the deviation of the spacecraft from the nominal path at some future time. In this derivation, $\bar{p}_k$ is the position deviation (a 3x1 vector) and $\bar{v}_k$ is the velocity deviation (a 3x1 vector) of the spacecraft from the nominal path at time t_k, with k = 1, 2, 3 and 4. If $\bar{v}_\emptyset$ is the residual velocity (a 3x1 vector) and $\bar{p}_\emptyset$ is the residual position (a 3x1 vector) relative to the nominal path at time $t_\emptyset$, then a $\overline{\Delta v}$ input at $t_\emptyset$ could be used to predict $\bar{p}_k$ for k = 1, 2, 3 and 4. For instance, when the initial position $\tilde{X}_\emptyset$ includes an initial velocity perturbation $\bar{v}_\emptyset$, a delta velocity $\overline{\Delta v}$, and an initial position perturbation $\bar{p}_\emptyset$, the state propagation equation results in

$$\tilde{X}_k = \begin{bmatrix} \bar{p}_k \\ \bar{v}_k \end{bmatrix} = \Phi(t_k, t_\emptyset)\, \tilde{X}_\emptyset = \Phi(t_k, t_\emptyset) \begin{bmatrix} \bar{p}_\emptyset \\ \bar{v}_\emptyset + \overline{\Delta v} \end{bmatrix}. \tag{18}$$

The cost function used to derive this control scheme is

$$J(\overline{\Delta v}) = \overline{\Delta v}^T Q\, \overline{\Delta v} + \bar{p}_1^T R\, \bar{p}_1 + \bar{v}_1^T R_v\, \bar{v}_1 + \bar{p}_2^T S\, \bar{p}_2 + \bar{v}_2^T S_v\, \bar{v}_2 + \bar{p}_3^T T\, \bar{p}_3 + \bar{v}_3^T T_v\, \bar{v}_3 + \bar{p}_4^T U\, \bar{p}_4 + \bar{v}_4^T U_v\, \bar{v}_4, \tag{19}$$

where Q is a positive definite weighting matrix and R, R_v, S, S_v, T, T_v, U, and U_v are positive semidefinite weighting matrices. The cost function can be written in terms of $\overline{\Delta v}$ by using substitutions for $\bar{p}_k$ and $\bar{v}_k$, with k = 1, 2, 3, and 4, derived from Eqs. (17) and (18). The minimum is then $\overline{\Delta v}^* =$

$$-[Q + B_1^T R B_1 + B_2^T S B_2 + B_3^T T B_3 + B_4^T U B_4 + D_1^T R_v D_1 + D_2^T S_v D_2 + D_3^T T_v D_3 + D_4^T U_v D_4]^{-1}$$
$$\times[(B_1^T R B_1 + B_2^T S B_2 + B_3^T T B_3 + B_4^T T B_4 + D_1^T R_v D_1 + D_2^T S_v D_2 + D_3^T T_v D_3 + D_4^T U_v D_4)\bar{v}_\emptyset +$$
$$(B_1^T R A_1 + B_2^T S A_2 + B_3^T T A_3 + B_4^T U A_4 + D_1^T R_v C_1 + D_2^T S_v C_2 + D_3^T T_v C_3 + D_4^T U_v C_4)\bar{p}_\emptyset].$$

A simpler version of this controller can be used by setting, for instance, the weighting matrices U and U_v equal to the 3x3 zero matrix. This modified controller is the one used in the following section.

Comparison of Halo-Type and Lissajous Orbits

The cost of maintaining the spacecraft in orbit for 2 years is selected as the comparison value. For each simulation run, tracking updates, with assumed error levels listed in Table 3, are input every 20 days. Solar radiation pressure uncertainty is also input as an error source with magnitude listed in Table 1. The errors are modeled as zero-mean Gaussian random variables. Each simulation of the station-keeping algorithm will be a random trial with the random variable of

interest being the total magnitude of the station-keeping costs (ΔV_T) for the 2-year simulation. A sequence of 30 Monte Carlo station-keeping simulations produces a random sample of 30 random variables. Sample statistics, such as means and standard deviations, can then be calculated, and statistical tests can be conducted to compare the mean control costs for halo-type and Lissajous orbits[5,12]. Table 5 contains the results of one set of simulations using 30 Monte Carlo trials for each type of orbit.

Table 5
COMPARISON OF STATION-KEEPING COSTS

Lissajous Orbit			Halo-Type Orbit		
Avg ΔV_T (m/s)	Std Dev (m/s)	Range (m/s)	Avg ΔV_T (m/s)	Std Dev (m/s)	Range (m/s)
.8450	.1603	.57 - 1.15	.8124	.1233	.62 - 1.08

Statistical hypothesis tests conclude that the 2-year mean control cost, using the two nominal paths and this particular controller, are equal. The conclusion of equal station-keeping costs for all nominal paths near this libration point and any control scheme cannot be drawn from this work.

Comparison of Station-Keeping Costs for Different Curve Fitting Options

Various curve fitting methods have been developed to model the nominal paths. While cubic splines are used here, least squares curve fits for a trigonometric series and linear interpolation routines have also been tested. The data in Table 6 summarizes efforts to date. The curve fits are indexed by the number of terms included in the Fourier series. The cubic spline and linear interpolation schemes are indexed by the time between points.

Table 6
COMPARISON OF CONTROL COSTS BY CURVE FITTING TECHNIQUES

Cubic Spline	Average 2-Year Cost (meters/sec)
Days between points = 3, 6, 9	1.234, 1.801, 10.324
Fourier Series	
Terms Used = 28, 91, 121, 161	9.577, 8.147, 1.419, 1.414
Linear Interpolation	
Days between points = .5, 1, 2, 6	1.290, 1.307, 1.333, 38.604

EXPERIMENTAL DESIGN RESULTS

The process of interest here is station-keeping for a 2-year halo-type Lagrange point orbit in the Sun-Earth+Moon elliptic restricted three-body problem. The input variables include tracking errors (track), solar radiation pressure (SRP) and mass ratio (mass) uncertainties, orbit injection errors (inject), and thruster (thrust) errors. The outputs of interest are the 2-year control cost (ΔV_t) and its variance. Other inputs could be considered, and additional outputs, such as the number of ΔV inputs required or the average separation time between control inputs, could also be evaluated in future efforts. The relationship of the inputs, the process, and the outputs is depicted in Fig. 3.

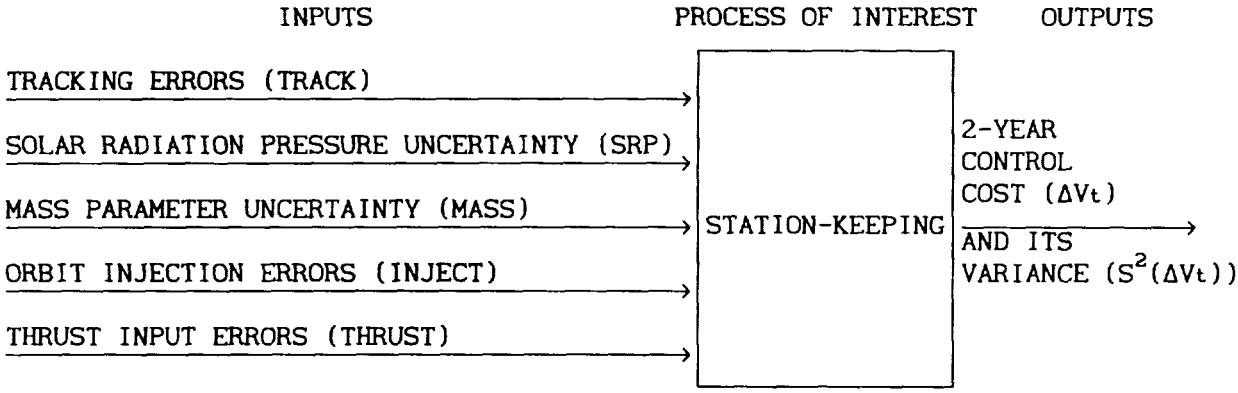

Fig. 3 Process of Interest

For this analysis, a fractional factorial two-way design was selected in order to limit the total number of runs. A fractional factorial 2^{5-1} design[7] allows use of only 16 runs to pick out contributions of the 5 main inputs and 10 two-way interactions. The design matrix, with only the main effects listed, is depicted in Fig. 4.

RUN	INPUT VARIABLES				
	a	b	c	d	e=abcd
	TRACK	THRUST	SOLAR	MASS	INJECT
1	-	-	-	-	+
2	-	-	-	+	-
3	-	-	+	-	-
4	-	-	+	+	+
5	-	+	-	-	-
6	-	+	-	+	+
7	-	+	+	-	+
8	-	+	+	+	-
9	+	-	-	-	-
10	+	-	-	+	+
11	+	-	+	-	+
12	+	-	+	+	-
13	+	+	-	-	+
14	+	+	-	+	-
15	+	+	+	-	-
16	+	+	+	+	+

Fig. 4 Design Matrix

A full factorial would enable analysis of 5 main effects, 10 two-way interactions, 10 three-way interactions, 5 four-way interactions, and 1 five-way interactions. Generally, interactions above two-way are not significant contributors to a model[7]. The modeled interactions not depicted in Fig. 4 are ab, ac, ad, ae, bc, bd, be, cd, ce, and de. Note also that the main effect "inject" is aliased[7] with the abcd four-way interaction. The full factorial two-level design would allow analysis of all possible interactions that could affect the output. It would not allow curvature analysis (quadratic effects), but these could be analyzed using a sequential central composite design approach[7]. Investigation of quadratic effects would be necessary only if confirmation runs indicate poor agreement at the midpoint of the design space. The design space is determined by the extreme values selected for each input. That is, the low and high settings for each input determine the region over which the approximate

output equations are defined. A large range for an input will also have a great bearing over whether it will be found significant. For this design, the low and high settings for each input are depicted in Table 7.

Table 7
LISTING OF DESIGN INPUTS AND SETTINGS

Input	Settings	
	Low (-)	High (+)
Track		
x	1 KM	3 KM
y	2 KM	10 KM
z	4 KM	15 KM
x dot	.0010 m/sec	.008 m/sec
y dot	.0015 m/sec	.010 m/sec
z dot	.0020 m/sec	.015 m/sec
Solar	2.5%	15%
Mass	1.231×10^{-7}	5.000×10^{-6}
Inject		
Each position coordinate	1.5 KM	50 KM
Each velocity coordinate	.001 m/sec	.05 m/sec
Thrust (each direction)	2.5%	10%

These input settings are representative of those used in other orbit determination error analysis and station-keeping studies. (See Tables 1 and 4.) The resulting output equations for the predicted ΔV (here denoted as $\Delta\hat{V}$) and natural logarithm of the output variance (denoted as $\ln(\hat{S})$) are

$$\begin{aligned}\Delta\hat{V} = {} & 2.9348 + 1.3627\,\text{Track} + .2953\,\text{Thrust} + .0263\,\text{Solar} + .0028\,\text{Mass} \\ & - .0904\,\text{Track-Thrust} - .0605\,\text{Track-Solar} - .0215\,\text{Thrust-Solar} \\ & - .0103\,\text{Track-Mass} - .0065\,\text{Thrust-Mass} + .0395\,\text{Solar-Mass} + \\ & - .0090\,\text{Solar-Inject} + .0551\,\text{Thrust-Inject} + .0094\,\text{Mass-Inject} \\ & - .0299\,\text{Track-Inject} + .05\,\text{Inject},\end{aligned} \tag{20}$$

$$\begin{aligned}\ln(\hat{S}) = {} & 0.2027 + 0.5948\,\text{Track} + .2334\,\text{Thrust} + .1221\,\text{Solar} + .0567\,\text{Mass} \\ & - .1614\,\text{Track-Thrust} - .0959\,\text{Track-Solar} + .0093\,\text{Thrust-Solar} \\ & + .0517\,\text{Track-Mass} + .0074\,\text{Thrust-Mass} - .0297\,\text{Solar-Mass} \\ & - .0339\,\text{Solar-Inject} - .0394\,\text{Thrust-Inject} \\ & + .0238\,\text{Mass-Inject} - .0127\,\text{Track-Inject} + .0292\,\text{Inject}.\end{aligned} \tag{21}$$

Additional experimental runs showed that the output model confirmed at the design midpoint and at both extremes. Often, this sort of model is used to determine optimal input settings: in order to minimize both ΔV and $\ln(S)$ in Eqs. (20) and (21), all inputs should be set at the minimum settings. However, a more realistic

use of these equations is for sensitivity analysis: the size of the coefficient of each input is a measure of that variable's influence on the output. These results show that tracking and thrust input errors are responsible for a large portion of the control cost. By reducing these two errors to their minimum, nominal savings on the order of 50% are predicted.

CONCLUSION

With the continuing importance of solar research, the use of libration point orbits between the Sun and the Earth is both an interesting and valuable area of effort. The need for orbit determination error analysis in conjunction with pre-mission station-keeping simulations was the original driving force behind this work. The results of three error analysis methods were compared with other similar libration point studies. The outputs of the error analysis were the six states' standard deviations. These error levels could then, in turn, be used as error sources in Monte Carlo simulations of derived station-keeping routines. With nominal paths that could be constructed as nearly periodic halo-type, or distinctly quasi-periodic and smaller Lissajous trajectories, the error analysis and station-keeping results may differ by the type of orbit selected. Statistical tests for the equality of the average 2-year control costs using halo-type and Lissajous paths strongly suggest that there is no difference in mean station-keeping costs. It should, however, be noted that the results are presented for only one particular control algorithm and for two specific nominal trajectories. Experimental design methods are then used to determine the approximate functional relationship between the input uncertainties and the output 2-year control cost. This type of functional relationship seems more useful than a series of tabular entries of control costs, each corresponding to a different set of input error levels.

REFERENCES

1. R.W. Farquhar, "A Halo-Orbit Lunar Station," *Astronautics and Aeronautics*, June 1972, pp. 59-63

2. K.C. Howell and H.J. Pernicka, "Numerical Determination of Lissajous Trajectories in the Restricted Three-Body Problem," *Celestial Mechanics*, Vol. 41, 1988, pp. 107-124

3. S.C. Gordon, "Representing the Nominal Path for an Interior Libration Point Orbit in the Sun-Earth+Moon Elliptic Restricted Three-Body Problem," USAFA-TR-91-11, United States Air Force Academy, Colorado, Sept. 7, 1991

4. J.L. Bell, "The Impact of Solar Radiation Pressure on Sun-Earth L_1 Libration Point Orbits," M.S. Thesis, School of Aeronautics and Astronautics, Purdue University, West Lafayette, Indiana, Aug. 1991

5. S.C. Gordon, "Orbit Determination Error Analysis and Station-Keeping for Libration Point Trajectories," PhD Dissertation, School of Aeronautics and Astronautics, Purdue University, West Lafayette, Indiana, Dec. 1991

6. H.J. Pernicka, "The Numerical Determination of Nominal Libration Point Trajectories and Developement of a Station-Keeping Strategy," PhD Dissertation, School of Aeronautics and Astronautics, Purdue University, West Lafayette, Indiana, May 1990

7. S.R. Schmidt and R.G. Launsby, Understanding Industrial Designed Experiments, CQG Printing, Longmont, Colorado, 2nd Ed, 1992

8. D.W. Garrett, "Experimental Design: Explanation by Example," DFMS TR 91-2, United States Air Force Academy, Colorado, Feb. 1991

9. B.D. Tapley and V. Szebehely, Editors, *Recent Advances in Dynamical Astronomy*, B.D. Tapley, "Statistical Orbit Determination Theory," D. Reidel, Dordrecht-Holland, 1988, pp. 396-425

10. B.D. Tapley, G. H. Born, and B. E. Schutz, *Satellite Orbit Determination,* University of Texas at Austin, June 1985

11. S.C. Gordon, "Orbit Determination Error Analysis for an Interior Libration Point Orbit in the Sun-Earth+Moon Elliptic Restricted Three-Body Problem," USAFA-TR-91-12, United States Air Force Academy, Colorado, Sept. 7, 1991

12. S.C. Gordon, "Comparison of Station-Keeping Algorithms for an Interior Libration Point Orbit in the Sun-Earth+Moon Elliptic Restricted Three-Body Problem," USAFA-TR-91-12, United States Air Force Academy, Colorado, Oct. 10, 1991

13. G.D. Mistretta, "Preliminary Considerations for an ISEE-C Least Squares Orbit Determination Strategy," Goddard Space Flight Center, Report X-580-76-251, Nov. 1976

14. J.B. Joyce, S.J. Leszkiewicz, and A.F. Schanzle, "Trajectory Determination Support and Analysis for ISEE-3 from Halo Orbit to Escape from Earth/Moon System," AAS Paper 79-128

15. L. Efron, D.K. Yeomans, and A.F. Schanzle, "ISEE/ICE Navigation Analysis," *The Journal of the Astronautical Sciences*, Vol. 33, Number 3, July-Sept. 1985, pp. 301-323

16. J. Rodriguez-Canabal, "SOHO Mission Analysis," ESOC Mission Analysis Office, June 1984

17. Personal Communications with J.M. Longuski (School of Aeronautics and Astronautics, Purdue University, West Lafayette, Indiana) and with L. Efron, J. Campell, and M. Standish (Jet Propulsion Laboratory, California Institute of Technology, Pasadena, California), Aug. 29, 1991

18. C. Simó, G. Gómez, J. Llibre, and R. Martínez, "Station Keeping of a Quasiperiodic Halo Orbit Using Invariant Manifolds," Proceedings of the Second International Symposium on Spacecraft Flight Dynamics, Darmstadt, Federal Republic of Germany, 20-23 Oct. 1986

19. G. Simó, G. Gómez, J. Llibre, R. Martínez, and J. Rodriguez, "On the Optimal Station Keeping Control of Halo Orbits," *Acta Astronautica*, Vol. 15, No. 6/7, 1987, pp. 391-397

FLIGHT MECHANICS/ESTIMATION THEORY SYMPOSIUM

MAY 5-7, 1992

SESSION 5

Analysis of the Command and Control Segment (CCS) Attitude Estimation Algorithm

7 May 1992

Prepared for the Consolidated Space Test Center / VOF
by
Lockheed Technical Operations Company

Catherine Stockwell

Technical Contributions
Gary Downs
Kjell Stakkestad
Larry Armstrong

ABSTRACT

This paper categorizes the qualitative behavior of the Command and Control Segment (CCS) differential correction algorithm as applied to attitude estimation using simultaneous spin axis sun angle and Earth cord length measurements. The categories of interest are the domains of convergence, divergence, and their boundaries.

Three series of plots are discussed that show the dependence of the estimation algorithm on the vehicle radius, the sun/Earth angle, and the spacecraft attitude. Common qualitative dynamics to all three series are tabulated and discussed.

Out-of-limits conditions for the estimation algorithm are identified and discussed.

INTRODUCTION

This paper outlines the approach taken to determine the qualitative behavior of the attitude estimation algorithm used by the Command and Control Segment (CCS) system at the Air Force Consolidated Space Test Center (CSTC). For the purposes of this paper, determining the qualitative behavior means defining the regions of convergence and divergence in terms of the Earth, sun, and spacecraft attitude parameters.

This study is an outgrowth of the Information Processing and Analysis System (IPAS) project undertaken by Test Support Complex-1 (TSC-1) at CSTC. The purpose of this project was to evaluate the feasibility of incorporating commercially available hardware and software into an operational mission control center (MCC) design. The result of IPAS was a prototype for a telemetry monitoring system employing a real-time expert system that performs out-of-limits checking and recommends appropriate actions for telemetry anomaly resolution.

This paper supports a follow-on project that determines requirements for an autonomous real-time orbit and attitude estimation expert system prototype that would supplement the telemetry monitoring system. Creating a knowledge base for the estimation expert system requires defining out-of-limits criteria for the estimation algorithms used. This is the motivation for researching the qualitative behavior.

As a first step to understanding the equations that govern the out-of-limits criteria, an attitude estimation package that graphically shows the affects of geometry on attitude estimation was prototyped using Mathematica software on a Sun SPARCstation 1. This analysis tool could also be used for mission planning as well as training.

Work in progress is to mathematically support the visual conclusions drawn from the plots about the relationships between the Earth, sun, and attitude geometry to convergence or divergence of the estimation algorithm. These results will in turn be used as input to the estimation expert system knowledge base.

QUALITATIVE DYNAMICS

The Algorithm. The estimation algorithm chosen to be studied is as follows:

$$\Delta \mathbf{x}_k = [\Sigma_i [P_i^t [x_k] P_i [x_k]]^{-1} \Sigma_i [P_i^t [x_k] \Delta \mathbf{y}_i [x_k]]$$

with $\Delta \mathbf{x}$ the state vector correction, $\Delta \mathbf{y}$ the residuals vector, and P is the matrix of measurement partials with respect to the state variables. The sum is with respect to the ith time point in the measurement set. For simplicity, this paper considers the case of just one measurement in time consisting of an Earth cord length and a sun angle. For this case, the algorithm reduces to:

$$\Delta x_k = P^{-1}[x_k]\Delta y[x_k]$$

The following standard notation is used:

A is the spacecraft attitude

$x = \{\alpha, \delta\}$ is A in spherical coordinates

$y = \{\Omega, \beta\}$ is the measurement vector

Ω is the earth cord length

η is the nadir angle

β is the sun angle

γ is the sensor cant angle

ρ is the apparent earth radius

E is the earth vector

S is the sun vector

To reduce the number of parameters needed to specify the Earth, sun, and attitude geometry, construct the {e1, e2, e3} vehicle centered coordinate system as follows:

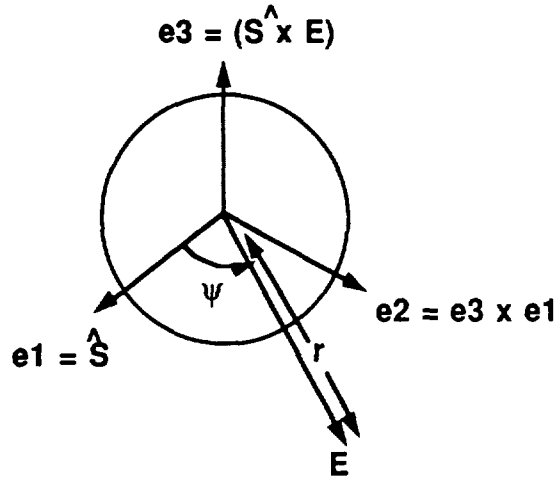

In this system, specifying the sun and Earth position requires only two parameters (the sun Earth angle ψ and the vehicle radius r) as compared to five (sun and Earth right ascensions and declinations as well as vehicle radius) in the standard vehicle centered coordinate system.

In the {e1, e2, e3} coordinate system the following relationships hold:

$$\cos[\Omega/2] = \frac{\cos[\rho] - \cos[\eta]\cos[\gamma]}{\sin[\eta]\sin[\gamma]}$$

$$\cos[\eta] = \cos[\alpha - \psi]\cos[\delta]$$

$$\cos[\beta] = \cos[\alpha]\cos[\delta]$$

$$P = \begin{pmatrix} \frac{-2(\cos[\rho]\cos[\eta] - \cos[\gamma])}{\sin^3[\eta]\sin[\gamma]\sin[\Omega/2]} & 0 \\ 0 & \frac{-1}{\sin[\beta]} \end{pmatrix} \begin{pmatrix} -\sin[\alpha - \psi] & -\cos[\alpha - \psi] \\ -\sin[\alpha] & -\cos[\alpha] \end{pmatrix} \begin{pmatrix} \cos[\delta] & 0 \\ 0 & \sin[\delta] \end{pmatrix}$$

Out-Of-Limits Criteria. The estimation out-of-limits criteria are based on the existence, uniqueness, and convergence behavior of the algorithm. The existence and uniqueness are well defined in terms of the geometry, leaving the convergence behavior for study. The following paragraphs briefly summarize each.

Existence. The algorithm will exist whenever P is invertible. It is easily seen that P is not invertible for the following geometries:

Attitude, sun, and Earth vectors are coplanar. When this happens, δ is zero and the last matrix in the above equation becomes singular.

Attitude has a $\pm$ 90 degree declination. For this geometry, the right ascension is undefined and therefor not recoverable. Again, this makes the last matrix singular.

The Sun and Earth are coplanar. This makes the rows of the second matrix dependent and thus singular.

The nadir angle is such that it maximizes the Earth cord length measurement. This causes the first matrix to be singular.

Uniqueness. The algorithm solutions are not unique. Since one Earth cord length corresponds to two possible nadir angles, simultaneous Earth cord length and sun angle measurements define four cones of possible attitude solutions. These cones will intersect in two and possibly four points. Therefor there are two and possibly four choices for the attitude vector that will give zero residuals, resulting in convergence.

Convergence. The estimation algorithm studied here is an iterative algorithm and is therefor susceptible to complicated dynamics. An estimation expert system needs to be able to recognize when divergence will occur due not only to the type of geometry that would make the algorithm not exist, but also due to the choice of algorithm itself. When this occurs, the expert system should know to automatically switch to a better algorithm.

In order to develop the appropriate knowledge base, convergence criteria in terms of the geometry need to be established. For this paper, convergence is defined to be when the arc length of the correction is less than a prescribed tolerance value. Divergence is defined to be when the algorithm doesn't exist or when convergence hasn't occurred within a prescribed number of iterations. The k+1 iteration arc length correction θ is defined as:

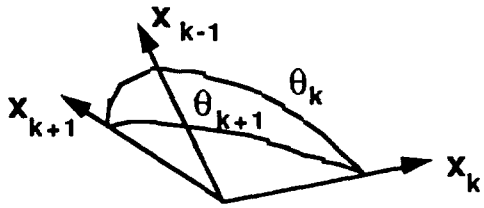

$$\theta_{k+1} = \arccos[\cos[\delta_{k+1}]\cos[\delta_k] + \sin[\delta_{k+1}]\sin[\delta_k]\cos[\alpha_{k+1} - \alpha_k]]$$

The work in progress is to rewrite this expression solely in terms of constants and the k-th itera θ.

The Analysis Tool. In order to gain insight into this rewrite problem, an analysis tool was prototyped using Mathematica software on a Sun SPARCstation 1 that graphically shows the affects of geometry on estimation. User inputs to this tool are the Earth cord length and sun angle measurement, the vehicle and sun position, the Earth horizon sensor cant angle and the choice of positive or negative declination hemisphere.

The output of the tool is a plot showing a colored disk. This disk represents attitude right ascension and declination pairs $\{\alpha, \delta\}$ for the chosen hemisphere as shown below.

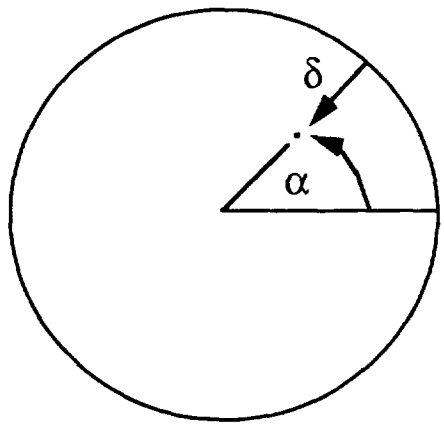

Each {α, δ} pair is input to the estimation algorithm and then colored according to what it converged to. The coloring algorithm was Hue[αc/360] and Brightness[1-δc/380], where {αc, δc} are the converged values. If the algorithm didn't converge, then {αc, δc} were set to {360, 100}, corresponding to the darkest regions in the plot. With this tool, regions that converge to the same value can be easily spotted and the size of the convergent region can be visually estimated.

Due to memory and time constraints, the plot resolution is limited to two degrees.

Results. In order to understand how each geometric parameter affects estimation, three series of plots were made. Each series tries to hold all parameters fixed except for one. All plots chose the negative declination hemisphere (the brighter colors were chosen since they show more contrast when rendered in black and white). In Figures 1-3, the values for n defined below increase from left to right.

Vehicle radius series. The plots in Figure 1 were made with these inputs:

ψ = 90;

r = 8000 + n 500 km: n=0,4;

A = {45, 45};

Sun Earth angle series. The plots in Figure 2 were made with these inputs:

ψ = n 20: n = 4,8;

r = 8000 km;

A = {45, 45};

Attitude series. The plots in Figure 3 were made with these inputs:

ψ = 90;

r = 8000 km;

A = {5 + 10 n, -5 n^2 + 40 n + 5}: n = 5,9;

CONCLUSIONS

Plot Features. There appear to be several features common to all the plots.

Figure 1. The vehicle radius series.

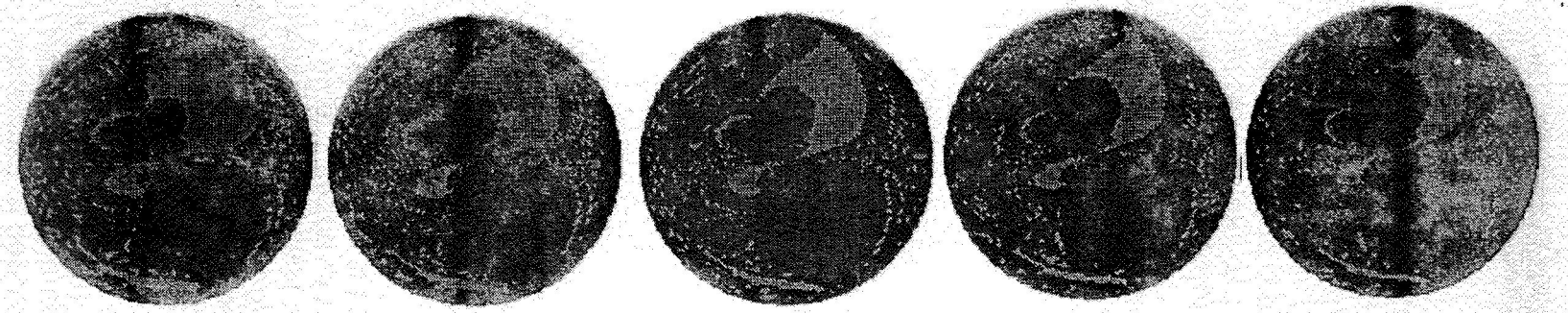

Figure 2. The sun/Earth angle series.

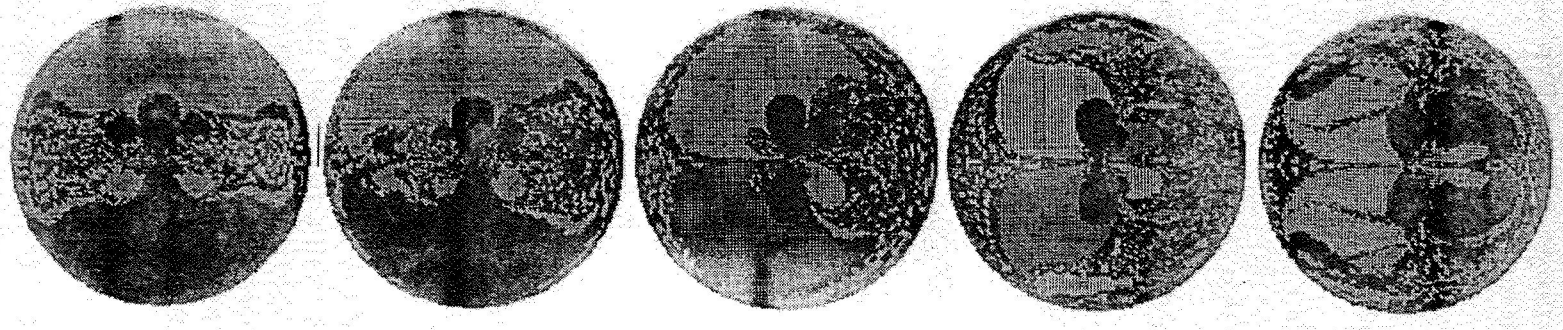

Figure 3. The attitude series.

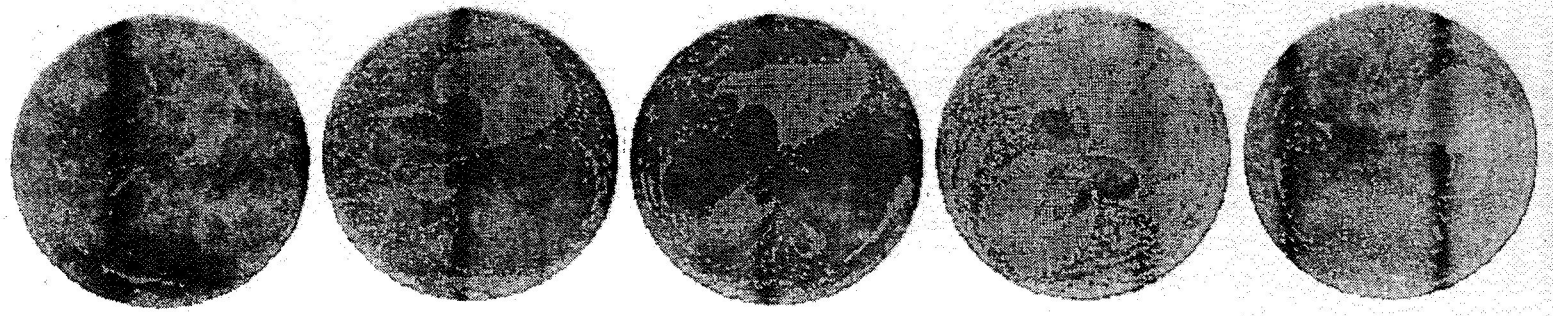

The divergent figure eight. Each plot has a divergent region at the declination poles that is shaped like a figure eight. The size of this region appears to only depend on the vehicle radius and increases as the radius increases. The direction of the long axis lines up with the Earth vector, suggesting that this affect is independent of the sun geometry.

The convergent region. Each possible attitude solution has a convergent region around it. The size and shape of this region appears to be affected by all the geometric parameters, since it varies throughout all the series.

The "image" convergent region. There appears to always be a convergent region 180 degrees away in right ascension from the possible attitude solutions. This region is typically smaller than the region containing the attitude solution.

The Earth perpendicular divergent region. The line perpendicular to the Earth vector has very unstable behavior. Attitudes arbitrarily close to each other converge to different solutions. Figure 4 shows an example of this. Here declination is plotted against the converged right ascension for the input attitudes $\{0, \delta\}$. The geometry is from n=1 in the vehicle radius series.

Figure 4. Declination vs converged right ascension.

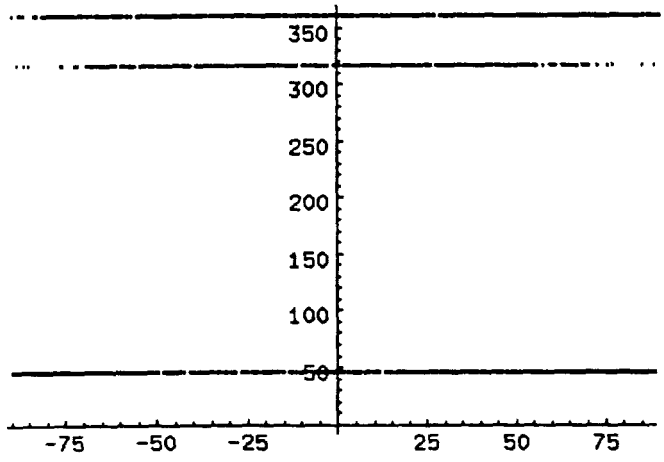

Topology. The dynamics of the topology for each series is difficult to determine from only a two degree resolution. However, there always appears to be alternating layers of convergent and divergent regions, with only the relative size and shapes varying. This suggests that even though the geometry might be in a region far away from the region where the algorithm doesn't exist, the algorithm might still diverge due to the iterative dynamics.

AREAS OF FUTURE RESEARCH

The Analysis Tool. In order to apply this visualization approach to other estimation problems, the analysis tool needs to be extended to estimation problems with more than two variables. For instance, orbit position and velocity

estimation would require plotting a six dimensional variable against another six dimensional variable. To get around this plotting difficulty, the dimension of the estimation problem must somehow be reduced. Translating the analysis tool into 'C' code is also planned to make the prototype more operational (ie faster).

More than one measurement. Future work includes extending the results here to the case of more than one measurement in time, or batch estimation. This is the more common case for the algorithm studied here.

Convergence criteria. Work is currently in progress to develop closed form convergence criteria in terms of the geometric parameters. These criteria will then be converted to out-of-limits conditions for the estimation algorithm for input to an estimation expert system knowledge base. Rules will also be developed to determine what algorithm to substitute when out-of-limits conditions occur.

Algorithms. A robust estimation expert system will have several algorithms to choose from, so similar analysis of other estimation algorithms is planned.

SUMMARY

An analysis tool that graphically shows the affects of geometry on attitude estimation has been made. This tool can be used during the readiness phase for a satellite mission to validate or define operational requirements. This tool can also be incorporated into a training program for those needing a high level view of attitude estimation.

Visual inspection of plot output from the analysis tool has lead to an increased understanding of the qualitative behavior of the estimation algorithm. This understanding is currently being quantified mathematically for input to an estimation expert system knowledge base.

BIBLIOGRAPHY

CG-SCF-230B, 1 December 1986. *Computer Program Development Specification for Mission Orbit Planning, (Math Appendix),* IBM.

Wertz, J.R., *SPACECRAFT ATTITUDE DETERMINATION AND CONTROL*, D. Reidel Publishing, 1985.

Optimizing the Fine Lock Performance of the Hubble Space Telescope Fine Guidance Sensors

David J. Eaton
Richard Whittlesey
Linda Abramowicz-Reed
Robert Zarba

Hughes Danbury Optical Systems, Inc.
100 Wooster Heights Road
Danbury, Connecticut 06810

ABSTRACT

This paper summarizes the on-orbit performance to date of the three Hubble Space Telescope Fine Guidance Sensors (FGS's) in Fine Lock mode, with respect to acquisition success rate, ability to maintain lock, and star brightness range. The process of optimizing Fine Lock performance, including the reasoning underlying the adjustment of uplink parameters, and the effects of optimization are described.

The Fine Lock optimization process has combined theoretical and experimental approaches. Computer models of the FGS have improved understanding of the effects of uplink parameters and fine error averaging on the ability of the FGS to acquire stars and maintain lock. Empirical data have determined the variation of the interferometric error characteristics (so-called "s-curves") between FGS's and over each FGS field of view, identified binary stars, and quantified the systematic error in Coarse Track (the mode preceding Fine Lock). On the basis of these empirical data, the values of the uplink parameters can be selected more precisely.

Since launch, optimization efforts have improved FGS Fine Lock performance, particularly acquisition, which now enjoys a nearly 100 percent success rate. More recent work has been directed towards improving FGS tolerance of two conditions that exceed its original design requirements. First, large amplitude spacecraft jitter is induced by solar panel vibrations following day/night transitions. This jitter is generally much greater than the FGS's were designed to track, and while the tracking ability of the FGS's has been shown to exceed design requirements, losses of Fine Lock after day/night transitions are frequent. Computer simulations have demonstrated a potential improvement in Fine Lock tracking of vehicle jitter near terminator crossings.

Second, telescope spherical aberration degrades the interferometric error signal in Fine Lock, but use of the FGS two-thirds aperture stop restores the transfer function with a corresponding loss of throughput. This loss requires the minimum brightness of acquired stars to be about one magnitude brighter than originally planned.

1. INTRODUCTION

The Hubble Space Telescope (HST) Fine Guidance Sensors (FGS's) serve the dual functions of providing an absolute pointing reference to the telescope pointing control system (PCS), and, as a goal, serving as an astrometry instrument. The FGS's have been used extensively since the telescope was launched in April, 1990.

The FGS's are capable of tracking stars in two modes: Coarse Track, and Fine Lock. This paper reviews FGS performance in Fine Lock, the more accurate of the tracking modes, and discusses the methods by which Fine Lock performance has been and is continuing to be improved.

Section 2 provides an overview of FGS design and function, while Section 3 summarizes on-orbit Fine Lock performance to date. A discussion of the Fine Lock optimization processes is given in Section 4. Finally, Section 5 presents a brief summary.

2. FGS DESCRIPTION

The descriptions of the HST Fine Guidance Sensors in References 1 and 2 are summarized here.

2.1 Optical/Mechanical Description

In the HST, there are four Radial Bay Modules, three of which containing an FGS. An optical schematic is given in Figure 1. Light from the outer portion of the HST field of view, 10 to 14 arcminutes from the optical axis, strikes the FGS pickoff mirror and is collimated and directed through apertures in a pair of star selector servos. The beam then passes through beamsplitters and Koester prisms before reaching four photomultiplier tubes (PMT's). The angular positions of the servos determine which 5 by 5 arcsecond portion of the FGS field of view enters the fieldstops of the PMT's.

2.2 FGS Control and Modes of Operation

The Fine Guidance Electronics (FGE), an electronics box that includes two microprocessors, controls the FGS. The FGE receives commands, accepts pulse trains from the four PMT's, and receives data from the servo encoders. FGE algorithms define a set of complex operating modes. Among the FGE commands are those that set the values of 38 uplink parameters, which are used to adapt the system to specific mission requirements or special operating conditions. The FGE also outputs data, such as PMT counts, servo encoders, and status bits.

The FGS modes relating to acquisition, pointing and tracking are Search, Coarse Track, and Fine Lock. In Search, the servos define a spiral scan of a region of the FGS field of view, until the target star image enters the PMT fieldstops. When the summed output (counts) of the four PMT's exceeds a commanded threshold, the FGS autonomously terminates Search Mode and enters Coarse Track. In Coarse Track, the FGE commands the servos to move the images of the target star in circular paths (called nutation circles) about the PMT fieldstops. The Coarse Track algorithm monitors the total output of the four PMT's and adjusts the centers of the nutation circles until the circles are centered on the fieldstops.

About 70 percent of all observations are done with the guidance FGS's in Coarse Track mode. The remaining observations require the low jitter provided by Fine Lock. Also, to achieve the positional accuracy required by astrometry observations, Fine Lock is necessary.

While Search and Coarse Track modes use the sum of the outputs from all four PMT's as feedback, Fine Lock uses the PMT's as part of a unique Koester prism interferometer (Figure 2). Fine Lock creates a two-axis position control loop that drives the interferometer to null.

To acquire a star in Fine Lock, the FGS line of sight, as determined by the servo positions, is offset from the center of the Coarse Track nutation circle, the center being the best estimate of the star position in Coarse Track. The servos are then stepped along a straight path toward the star (Figure 3). When the servo positions are within about 0.040 arcseconds of interferometer null along an axis, the error signal increases above a preset threshold, and the FGE reduces the speed of the "walk" toward the star. For each axis, if the error signal exceeds the threshold for 3 consecutive samples, that axis is "locked"; that is, closed-loop operation of the servos is initiated, with the interferometric error signal as position feedback. When both axes are locked, the Fine Lock acquisition is complete, and the servo loop acts to maintain the pointing error at null.

3. FGS ON-ORBIT PERFORMANCE

References 2 and 3 reported on-orbit FGS performance, and compared that performance to the original design requirements. FGS performance that is related to Fine Lock acquisition, pointing and tracking is summarized below.

3.1 Fine Lock Acquisitions

The original FGS design requirements included a star brightness range of 9 to 14.5 Mv for guidance and 10 to 17 Mv for astrometry. However, as a result of spherical aberration in the telescope, it is necessary to operate the FGS's with the two-thirds aperture stop in place. While this aperture stop improves the Fine Lock error signal, there is a reduction in the number of photons reaching the PMT's for a given star, and, consequently, the limiting star magnitude is one Mv brighter than originally expected.

Operating within the above brightness constraint, the FGS's have accomplished a high success rate in Fine Lock acquisitions, at least 93 percent in both guidance and astrometry.

3.2 Moving Target Tracking

Due to solar panel vibrations following day/night transitions, the spacecraft jitter velocities and accelerations greatly exceed the original FGS specifications. In Fine Lock, the FGS'S maintain lock through about 70 percent of the transitions.

3.3 Dynamic Pointing Error

Dynamic pointing error refers to pointing errors that vary over an observation interval and degrade the point spread function of the target image. Dynamic pointing error of the HST has been shown to meet the original requirement of 7 milliarc-seconds, rms, during quiescent periods, with the guidance FGS's in Fine Lock. This result indicates indirectly that the FGS's contribution to dynamic pointing error meets requirements.

Temperature-induced deformations of internal FGS components affect the dynamic pointing error over long-term observations. Temperature measurements of those FGS components that affect pointing stability have indicated that long-duration dynamic pointing error would also meet requirements, were it not for disruptions from vehicle jitter near terminator crossings.

4. FGS FINE LOCK ON-ORBIT OPTIMIZATION

4.1 Optimization Methods

The Fine Lock optimization process has combined theoretical and experimental approaches. Computer analyses and simulations have improved understanding of the effects of uplink parameters and other commands and have been used to evaluate proposed changes. In addition, certain measurements have characterized the on-orbit environment and have been essential to improving FGS performance.

4.1.1 Computer Analyses and Simulations

Several computer-based FGS analyses and simulations have been used before and after launch of the HST.

An analysis of the probability of successful acquisition in Fine Lock, as a function of the relevant uplink

parameters (such as acquisition threshold, s-curve scale factor, walk duration and step size), s-curve degradation, star brightness, PMT responsivity and noise, background illumination, the length of the PMT averaging interval, and spacecraft drift rate, was exercised extensively before and during the ground testing of the FGS's. This analysis helped establish baseline parameter settings, which have been changed only slightly to adapt the FGS's to on-orbit conditions, and verified changes that were made to FGE firmware before launch.

Monte Carlo FGS simulations were used to evaluate probabilities of Fine Lock acquisition and Fine Lock maintenance. The acquisition simulation verified the analysis described in the preceding paragraph. The loss-of-lock simulation was used to set uplink parameters and verify changes to the FGE firmware. It also showed that loss of lock would not occur unless precipitated by a large disturbance, cosmic rays in particular. On-orbit, cosmic rays have not been a problem, but losses of lock are caused by the South Atlantic Anomaly and vehicle jitter following day/night transitions.

A detailed FGS simulation/emulation was developed and used extensively throughout the development, ground testing and on-orbit optimization of the FGS's. This software combines simulations of FGS optics, servo mechanics and electronics, and the HST Pointing Control System with a complete emulation of the FGE firmware. The simulation/emulation is used for problems that require a highly accurate FGS model, but, due to its computational speed, is not suitable for long runs or large numbers of runs, as in Monte Carlo simulations.

Finally, a simple, fast-running Fine Lock simulation, described in more detail in Section 4.3.2, was developed to investigate optimization of FGS tracking performance. Frequency-domain analyses, based on the model used in this simulation, were also developed.

4.1.2 Measured Data

Collecting and cataloging on-orbit data have been essential to the process of optimizing Fine Lock. These data have included s-curves as functions of FGS number and field position, Coarse Track bias errors, vehicle jitter resulting from terminator crossings (day/night transitions), the identification of binary stars, the effects of the South Atlantic Anomaly, sky background illumination, and PMT output and noise vs. star brightness.

4.2 Fine Lock Acquisition Optimization

The most common Fine Lock acquisition failures fall into two general categories. First, the acquisition threshold may fail to be exceeded three samples in succession, and, as a consequence, closed-loop operation may not be initiated in one or both axes. Second, the threshold may be exceeded by noise ("false lock") before the lobes of the s-curve are reached, and the star will drift out of the PMT fieldstops and be lost. When acquisition uplink parameters are adjusted, the probability of one type of failure will increase, while the other decreases. A compromise is therefore required.

4.2.1 Uplink Parameter Adjustment

A block diagram of Fine Lock acquisition (Figure 4) shows the most important acquisition uplink parameters. The Fine Error Signal (FES) is calculated at the end of a PMT averaging period as follows:

$$FESX = K0X + K1X*QX \quad (1)$$
$$FESY = K0Y + K1Y*QY, \quad (2)$$

where K0X, etc., are uplink parameters and QX and QY are calculated from the PMT counts, AX, BX, AY, and BY from the equations

$$QX = (AX - BX - DIFFX)/(SUMX) \quad (3)$$
$$QY = (AY - BY - DIFFY)/(SUMY). \quad (4)$$

The quantities DIFFX, DIFFY, SUMX and SUMY are the initial sums and differences of the PMT counts measured over an interval at the beginning of Fine Lock mode, before the "walk", and held constant until Fine Lock is terminated.

A plot of QX or QY against true FGS pointing error has the shape of the "s-curve" shown in Figure 2b. (The DIFF terms in equations 3 and 4 are assumed to be zero in Figure 2b.) With reference to Figure 2a, a true pointing error of zero (interferometer null) corresponds to an incoming wavefront being parallel to the face of the Koester prism. At null, each PMT receives equal illumination, and the output of PMT A equals the output of PMT B; therefore QX or QY is zero. For a small wavefront tilt (true pointing error slightly nonzero), constructive and destructive interference is set up in the Koester prism, such that the illumination entering one PMT is increased and illumination entering the other PMT is decreased. Thus the difference (A - B) and consequently QX or QY are nonzero. For larger pointing errors, interference no longer occurs and the PMT outputs are about equal. QX and QY are nominally zero for pointing errors greater than about 0.04 arcsecond.

In a nominal configuration, the PMT counts are averaged over 0.025 second and the servo commands are updated at the same rate. If PMT averaging is commanded, this period is increased by a factor that is a power of two. For example, with "two-sample averaging", the PMT averaging and servo update interval is doubled to 0.05 second. PMT averaging is used to reduce PMT photon noise with dim stars during astrometry acquisitions.

The most important acquisition parameters are K1X, K1Y and KZ. The first two scale the s-curve to compensate for variations in the s-curve shape and are selected to calibrate the FES; that is, the slope of the scaled s-curve is adjusted to unity. KZ sets the acquisition threshold. Pre-launch analyses, Monte Carlo simulations and tests established the best value of KZ to be 60 percent of the scaled s-curve peak. However, on-orbit, it was soon found that 50 percent resulted in a significantly improved acquisition success rate. Since sky background illumination and the resulting PMT noise were smaller than assumed prior to launch, the threshold could be lowered without a risk of "false lock".

In general, KZ has been held constant, and K1X and K1Y have been adjusted to correct the s-curves, as much as possible, to a "standard" shape. Different FGS's are assigned different values, but the adjustment for star brightness is small. Since the s-curves vary over the FOV of an FGS, K1X and K1Y should ideally vary over the FOV as well. However, for practical reasons, this is not done; rather, the values of K1X and K1Y are determined for the s-curve having the smallest modulation.

Parameters K0X and K0Y can correct bias in the s-curves; however, this correction has not been made (K0X = K0Y = 0), since the bias is generally not known a priori. The limiters K3X and K3Y have been set slightly above the highest s-curve peak to clip noise. These parameters do not affect Fine Lock acquisitions, as long as the products, K1X*K3X and K1Y*K3Y are greater than KZ.

The geometry of the Fine Lock walk is determined by parameters KD (step size), K10 (servo rate command gain), K05 (total number of steps) and KB (offset of start point from the center of the Coarse Track circle). Together, KD and K10 determine the actual step size, which is usually different from the value of KD itself. Selection of KD and K10 is another compromise. A large step size (rapid walkdown) is desirable, as it reduces susceptibility to noise; however, if the step is too large, too few samples of the FES will be taken in the lobes of the s-curves, and the peaks may be missed. The current values of K10 and KD are selected to give an actual step size of about 0.006 arcseconds, per axis. This step size is less than the pre-launch value of 0.009 arcsecond and reflects the fact that PMT noise on-orbit is lower than expected, as noted above. The walkdown rate relative to the star also depends on spacecraft drift; however, drift rate is not known beforehand, and is therefore not

compensated.

The starting and ending points of the Fine Lock walk are determined by KB, K05, and the actual step size established by K10 and KD. Knowledge of the Coarse Track bias error, the difference between the steady-state center of the Coarse Track nutation circle and the Fine Lock null, is necessary to set KB and K05. During early attempts to acquire stars in Fine Lock, shortly after HST launch, it was observed that FGS number 1 would frequently fail to acquire. Data analysis revealed a large Coarse Track bias in the x axis, and it was necessary to increase KB from about 0.6 arcsecond to about 1 arcsecond to compensate. It was also necessary to increase K05 to prevent the walk from terminating before the null was reached.

It is also possible to reverse the direction of the walk, i. e., start the walk in the third rather than first quadrant, by changing the signs of KB and KD. This capability may help acquisitions with certain types of asymmetric s-curves, but it has not yet been utilized.

4.2.2 The Effect of the South Atlantic Anomaly on Acquisitions

The charged particles present in South Atlantic Anomaly (SAA) increase PMT counts. Consequently, the PMT noise level and the probability of false lock increase. While partial compensation may be achieved by increasing KZ, in practice acquisitions in the SAA are avoided when observations are planned.

4.3 Optimization of the FGS's Ability to Maintain Fine Lock

After Fine Lock Acquisition is complete, the FGS, under FGE control, functions as a position control system (the "Fine Lock Loop"), with feedback from the Koester prism interferometer. This control system has a closed-loop bandwidth of about 9 Hz (-3 db), when the interferometer error is in the linear region of the s-curve, the relevant uplink parameters are set at nominal values, and PMT averaging is not in effect. Since the error characteristic is nonlinear, a large disturbance to the position loop can potentially create errors beyond a lobe of the s-curve, and Fine Lock can be lost. In practice, the only disturbances that cause loss of Fine Lock are 1) vehicle jitter caused by terminator crossings (solar panel vibrations), 2) the South Atlantic Anomaly, and 3) vehicle slews, with rate feedforward provided to the FGS's by the PCS. The success of vehicle slews depends on the quality of the feedforward commands and is not discussed further in this paper.

4.3.1 Tracking Vehicle Jitter Caused by Terminator Crossings

A simplified block diagram of one axis of the Fine Lock Loop is shown in Figure 5. The dynamic characteristics of the system, including bandwidth, are controlled by several uplink parameters: K1X, K1Y, K3X, K3Y, K13 (proportional gain), K14 (integral gain), K15 (differential gain) and K31 (integral limit). Note that the FES is calculated in the same way as it is during acquisitions (Equations 1-4). Potentially, tracking through terminator disturbances can be improved by adjusting these parameters.

In general, parameter adjustments that increase the bandwidth of the Fine Lock Loop should improve tracking of spacecraft jitter; however, FGS noise equivalent angle (NEA), servo motion in response to PMT photon noise, also increases with bandwidth. Thus, as in Fine Lock acquisition optimization, adjusting Fine Lock loop parameters involves a compromise.

Since FGS dynamic pointing error, to which NEA is a contributor, has been low, it should be possible to significantly increase the bandwidth of the system and still have acceptable NEA. Furthermore, depending on the frequency content of the solar panel jitter, some parameter adjustments are more effective than others in improving tracking with an equal increase in NEA.

4.3.2 Predictions From Simulations

To determine the effects of uplink parameters on tracking, a simple computer simulation of one axis of the Fine Lock loop was programmed. This simulation basically follows the block diagram in Figure 5. The following assumptions and approximations were made:

1. PMT integration was approximated by averaging the pointing errors at the start and end of an integration period;

2. The Pointing Control System (PCS) was not included in the simulation;

3. The s-curve was approximated by a single cycle of a sine wave;

4. The star selector servo was modelled as an ideal rate servo (integrator); and

5. Quantization effects in the FGE were not included.

Initial simulations were run with a spacecraft jitter of 0.1 arcsecond amplitude (zero to peak) and 0.6 Hz frequency. Jitter of this amplitude is sometimes observed near a terminator crossing. Furthermore, a solar panel vibration mode of about 0.6 Hz is frequently in evidence in the jitter.

The simulations showed that increasing the bandwidth of the Fine Lock loop, by increasing the gains K13 (proportional) and/or K14 (integral) reduced the amplitude of the steady-state FGS tracking error. (See example in Figure 6.) Furthermore, certain parameter adjustments, particularly increased integral gain (K14), yielded lower tracking error for the same increase in NEA. Table 1 compares the effects of K13 and K14 on tracking error and NEA. The reason K14 was effective was that it boosted the open-loop gain at low frequencies (relative to the system bandwidth of 9 Hz, without increasing the crossover frequency as much as other parameter adjustments did. This gain increase reduced the tracking error for low frequencies, including 0.6 Hz.

Fine Lock tracking performance with two-sample (0.05 second) PMT averaging, null by-pass on, was also simulated. (When null by-pass is on, the servos move according to their last rate command update during the PMT averaging period.) PMT averaging has the effect of "time scaling" the Fine Lock loop in proportion to the duration of the averaging period. Thus, the 8-10 Hz Fine Lock loop, without PMT averaging, becomes a 4-5 Hz loop with two-sample averaging, and tracking performance is progressively degraded as the averaging period is increased. As shown in Table 2, it was necessary to reduce the jitter amplitude to allow the FGS to stay in lock at all. Note that K14 was not as effective in reducing the tracking error as in Table 1, since 0.6 Hz is not as low a frequency relative to the bandwidth.

The values of differential gain, K15, that can be commanded were found to be too small to significantly affect tracking performance.

4.3.3 Experimental Results

The FGS's were operated with the integral gain, K14, increased to eight times its nominal value, on several occasions in late 1991 and early 1992. Since these experiments were not controlled, no definite conclusions can be drawn. However, a high percentage of the terminator crossings resulted in loss of Fine Lock, so there was no apparent improvement from increasing K14. Data from these tests is being analyzed to determine why no improvement was obtained.

Two losses of lock with increased K14 have been analyzed to date. In the first example, the vehicle jitter,

obtained from gyro data sampled at 40 Hz, was seen to be dominated by a frequency near 1.4 Hz, rather than 0.6 Hz (Figure 7). Thus, the conclusions of the preceding section, which were based on 0.6 Hz jitter, do not apply to this case. In the second example (Figure 8), 0.6 Hz was the dominant frequency, but the amplitude was very large, up to 0.25 arcsecond. Note that the FGS was apparently able to track 0.6 Hz jitter with an amplitude over 0.20 arcsecond, but not 0.25 arcsecond. Therefore, it should have been able to track more "typical" jitter, having an amplitude of 0.10 arcsecond. Since there was no experimental control, we cannot conclude that increasing K14 was ineffective in this case.

Further analysis of jitter data is necessary to determine what terminator jitter looks like. Once this is done, the problem of determining the best settings of the Fine Lock Loop parameters can be re-visited.

4.3.4 Effects of the South Atlantic Anomaly (SAA) on Loss of Fine Lock

When the HST is in the SAA, charged particles increase the outputs of the FGS PMT's. The increases may be equal in all PMT's, or unequal, depending on how well each PMT is shielded from the particles. With reference to Equations (1-4), if a Fine Lock acquisition occurs in the SAA, the "SUM" quantities will be larger than normal, and the gain and bandwidth of the Fine Lock Loop will be reduced. Furthermore, one or both of the "DIFF" quantities may be large, leading to a large bias in the FES when the HST leaves the SAA. The bandwidth reduction and the bias increase the chances of a loss of lock caused by disturbances, such as spacecraft jitter.

If a Fine Lock Acquisition occurs outside of the SAA, the "SUM" and "DIFF" terms are nominal. However, if the HST subsequently enters the SAA, the photon noise level increases. There may also be a bias in the FES if the PMT's are not affected equally. Again, the chances for a loss of lock are increased.

Observations are scheduled to avoid operation in the SAA.

5. SUMMARY

The HST Fine Guidance Sensors have been performing well on-orbit and have met or performed better than original requirements relating to Fine Lock acquisitions, moving target tracking, and dynamic pointing error. A combined theoretical and experimental approach has been used to optimize Fine Lock performance. Prior to launch, analyses and simulations of Fine Lock, as well as ground tests, established the best estimates for Fine Lock uplink parameters. Since launch, further analyses, simulations and measured data have been used to refine these estimates. Table 3 lists the Fine Lock uplink parameters, with their before-launch and current values.

Particular attention has been given to the effects of telescope spherical aberration and the effects of spacecraft jitter from terminator crossings. Measurements of the Fine Lock error characteristics (s-curves) have been used to set error gains and acquisition thresholds. The on-board two-thirds aperture filter has reduced the effects of spherical aberration on the s-curves; however, the loss of throughput to the PMT's requires that the minimum brightness of acquired stars be about one magnitude brighter than originally planned. As shown in Table 3, the values of interferometer parameters (K1X, K1Y, K3X, and K3Y) are set on the basis of measured s-curves, which vary between FGS's and over the field of view of an FGS.

While FGS tracking capability has been better than originally required, computer simulations have demonstrated a potential improvement in Fine Lock tracking of vehicle jitter near terminator crossings, by adjustment of the control loop gains (K13, K14 and K15). Jitter data is presently being reviewed to establish the amplitude and frequency content of the jitter, so that the best parameter values may be selected.

6. ACKNOWLEDGEMENTS

The work reported here was sponsored by NASA Marshall Space Flight Center, Huntsville, Alabama, under contract no. NAS-8-32700, and by NASA Goddard Space Flight Center, Greenbelt, Maryland, under contract no. NAS-8-38494.

A very large number of individuals from Hughes Danbury Optical Systems, NASA, Lockheed Missiles and Space Company, and other organizations contributed to the design, fabrication, calibration, testing and operation of the HST Fine Guidance Sensors. The authors wish to acknowledge the extensive work of these contributors and would like to thank the organizations involved for the privilege of presenting this paper. In particular, we would like to thank Greg Andersen and Theresa Gaston of Jackson and Tull, Inc., and Darrell Story of the University of Texas, for their technical contributions. We would also like to thank Geralyn Fischer for her assistance in preparing the manuscript.

7. REFERENCES

1. G. S. Nurre, S. J. Anhouse, and S. N. Gullapalli, Hubble Space Telescope Fine Guidance Sensor Control System, SPIE Technical Symposium, Orlando, Florida, March, 1989.

2. D. Eaton, et al., On-Orbit Performance of the Hubble Space Telescope Fine Guidance Sensors, Space Optics for Astrophysics, Williamsburg, Virginia, November 18-19, 1991.

3. D. Eaton, et al., Acquisition, Pointing, and Tracking Performance of the Hubble Space Telescope Fine Guidance Sensors, SPIE Aerospace Sensing Symposium, Orlando, Florida, April 20-24, 1992.

Table 1. Simulated FGS Fine Lock tracking performance, no PMT averaging; shows tracking error as a function of parameters K_{13} and K_{14}

UPLINK PARAMETERS		AMPLITUDE OF STEADY-STATE POINTING ERROR (M.A.S.)	NEA** INCREASE WITH RESPECT TO NOMINAL (PERCENT)
K_{13}	K_{14}		
NOMINAL	NOMINAL	LOCK LOST*	0
NOMINAL	2 X NOMINAL	16.5*	7
NOMINAL	5 X NOMINAL	7*	30
NOMINAL	8 X NOMINAL (MAX. COMMANDABLE)	4	57
.8 X NOMINAL	8 X NOMINAL	4	52
1.5 X NOMINAL	1.5 X NOMINAL	12	42
2 X NOMINAL	2 X NOMINAL	8	98

*PLOTTED IN FIGURE 6.
**NOISE EQUIVALENT ANGLE.

INPUT JITTER: 100 M.A.S. AMPLITUDE, 0.6 HZ

Table 2. Simulated FGS Fine Lock tracking performance, two-sample PMT averaging; shows tracking error as a function of parameters K_{13} and K_{14}

UPLINK PARAMETERS		AMPLITUDE OF STEADY-STATE POINTING ERROR (M.A.S.)	NEA** INCREASE WITH RESPECT TO NOMINAL (PERCENT)
K_{13}	K_{14}		
NOMINAL*	NOMINAL*	LOCK LOST	0
NOMINAL	2 X NOMINAL	LOCK LOST	7
NOMINAL	5 X NOMINAL	14	30
NOMINAL	10 X NOMINAL	7	79
NOMINAL	15 X NOMINAL	4.5	160
1.5 X NOMINAL	1.5 X NOMINAL	14	42
2 X NOMINAL	2 X NOMINAL	9	98

*NOMINAL SETTINGS ARE ONE-HALF THE NO-AVERAGING VALUES.
**NOISE EQUIVALENT ANGLE.

INPUT JITTER: 50 M.A.S. AMPLITUDE, 0.6 HZ

Table 3. Summary of Fine Lock uplink parameters and their values

PARAMETER	NAME	VALUE PRIOR TO HST LAUNCH (LSB'S)	CURRENT VALUES (LSB'S)
K_{ax}, K_{ay}	Interferometer bias	0	0
K_{1x}, K_{1y}	Interferometer scale factor	Based on measured s-curves	Based on measured s-curves
K_{3x}, K_{3y}	Interferometer limit		
K_8	Radial offset for start of Fine Lock walk	566	Based on measured Coarse Track bias
K_D	Step size during walk	226**	162**
K_{10}	Gain during walk	384	384
K_2	Acquisition threshold	100	88
K_{13}	Proportional gain	432	432*
K_{14}	Integral gain	173	173*
K_{15}	Differential gain	0	0*
K_{31}	Integral limit	411	411

*Being investigated for tracking improvement.
**No PMT averaging.

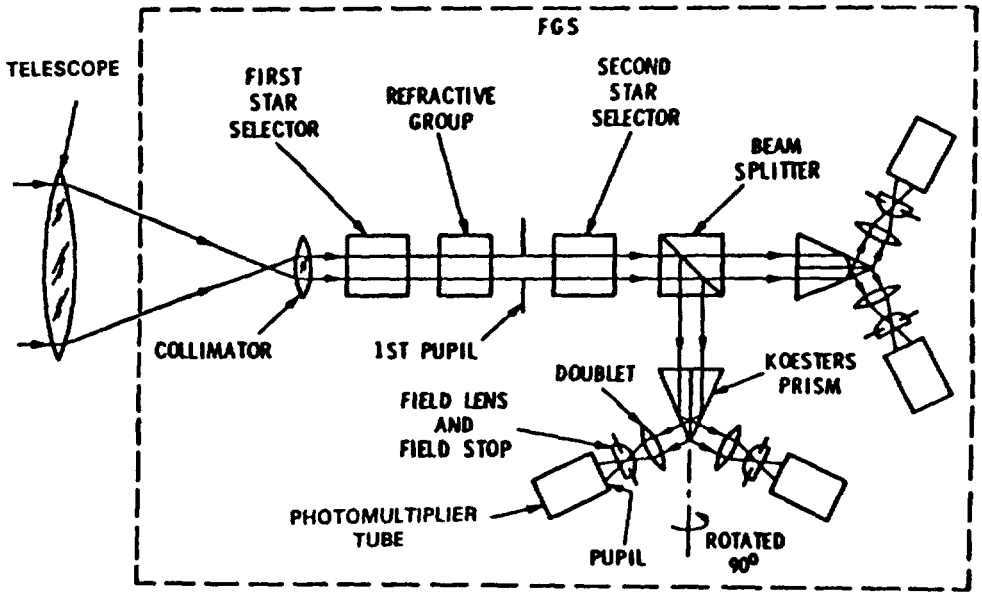

Figure 1. Simplified FGS schematic, showing star selector servos, Koester's prisms and photomultiplier tubes

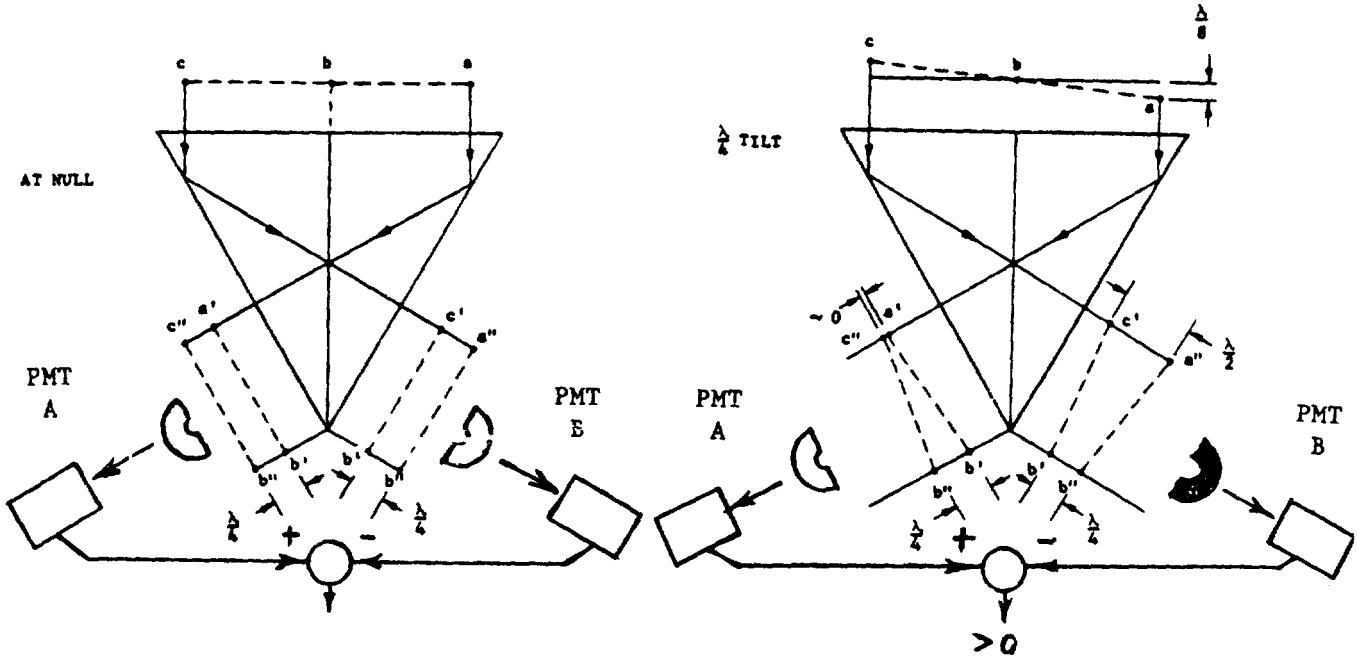

Figure 2a. Koester prism interferometer. Interferometer null is obtained when the incoming wavefront is parallel to the face of the prism and the PMTs are equally illuminated

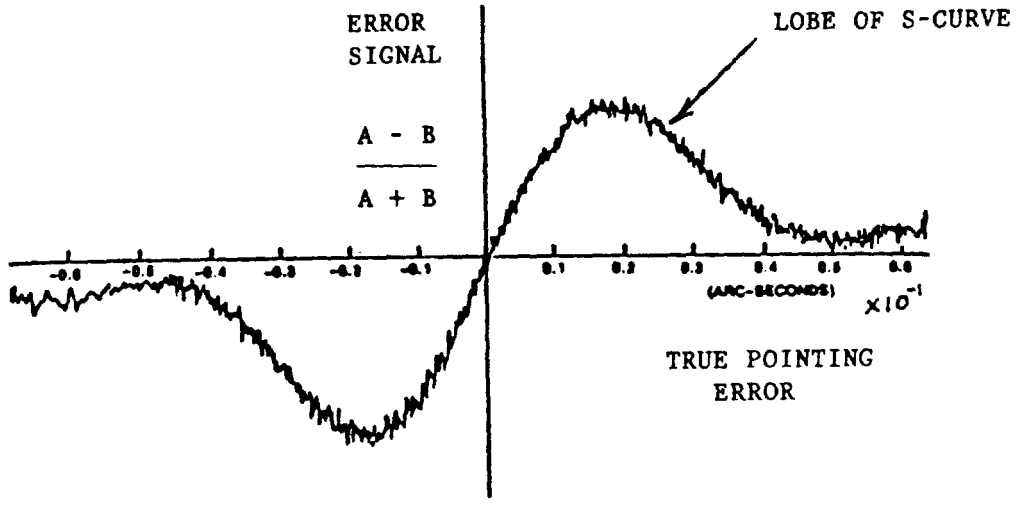

Figure 2b. Measured FGS interferometer characteristic. The "s-curve" is a plot of measured pointing error vs. true pointing error

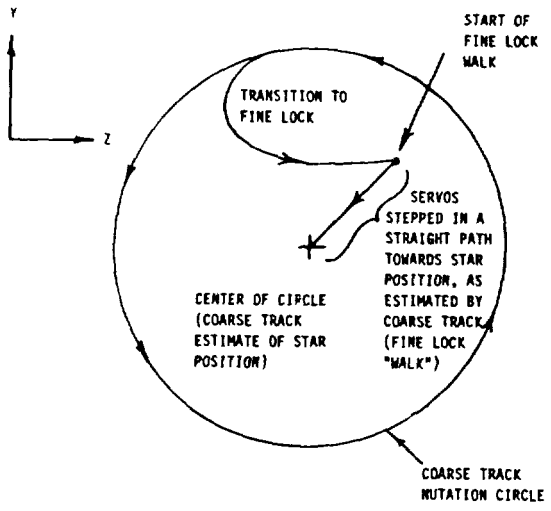

Figure 3. Transition from Coarse Track to Fine Lock
Plot of FGS line of sight as determined by star selector servos

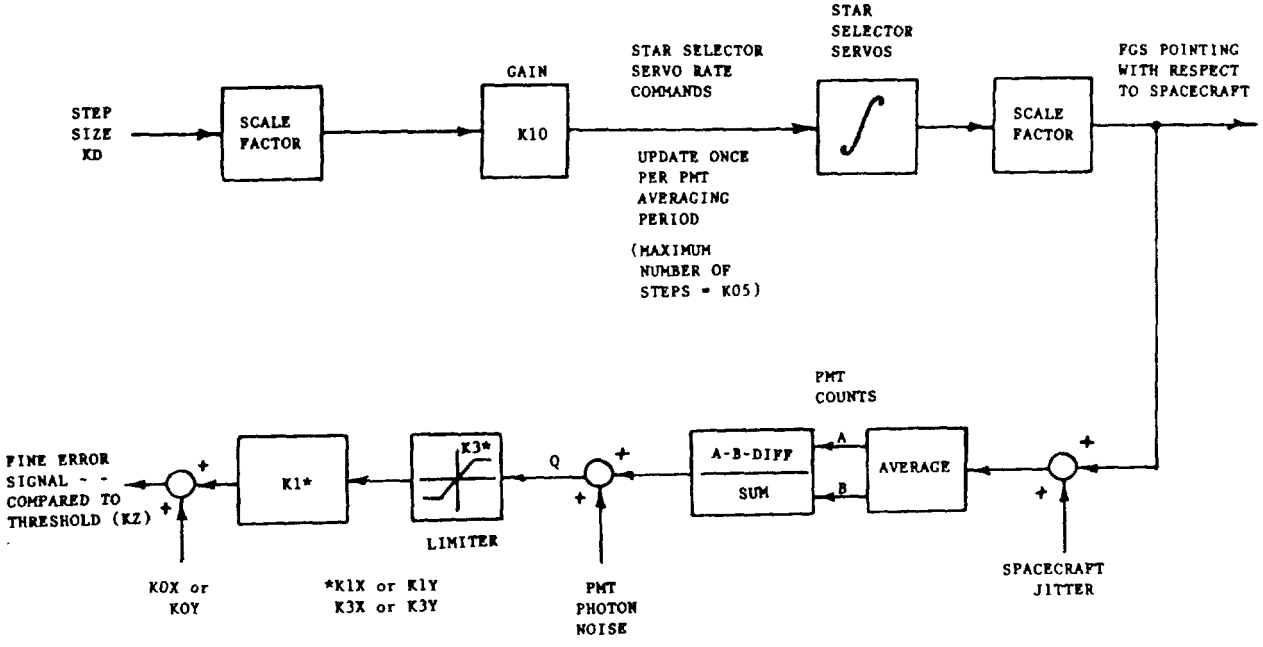

Figure 4. Simplified Fine Lock acquisition block diagram
(one axis)

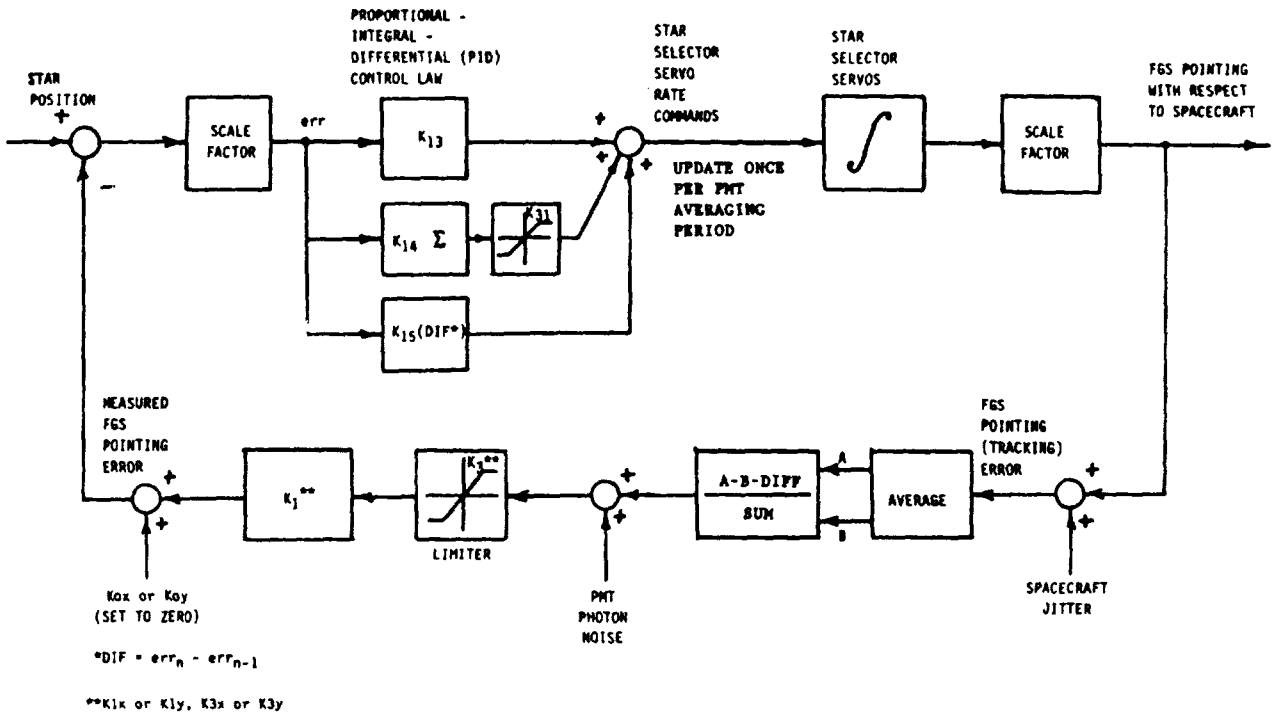

Figure 5. Simplified block diagram of one axis of the Fine Lock position loop

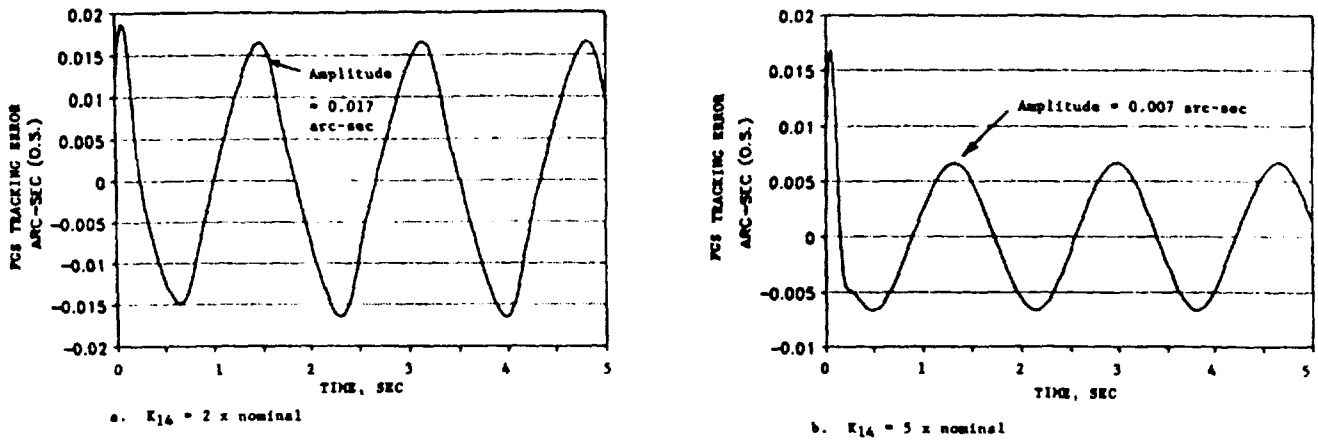

Figure 6. Simulations showing the sensitivity of FGS tracking error to increased bandwidth of the Fine Lock loop (via parameter K_{14}) Spacecraft jitter: 0.1 arc-second (object space) amplitude (zero-peak), 0.6 hz

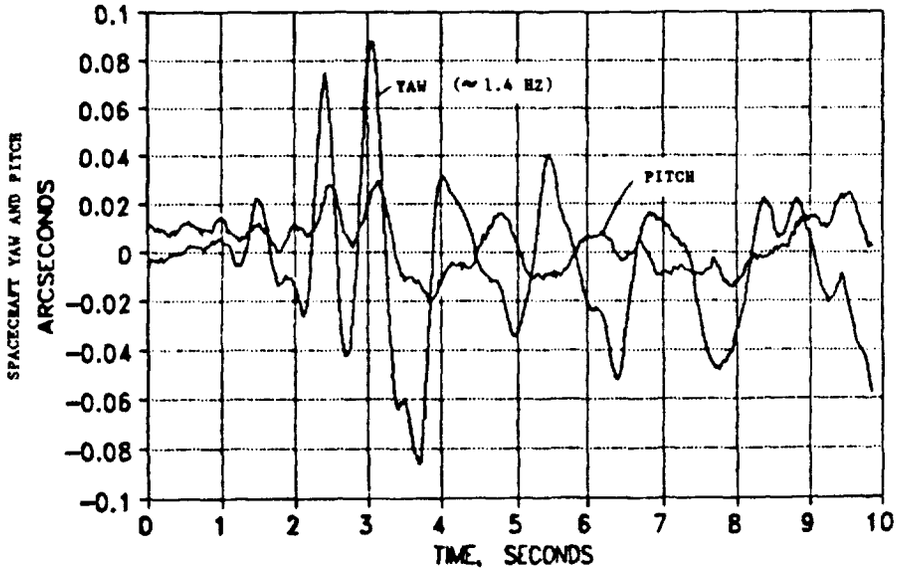

Figure 7. First example of spacecraft jitter from solar panel vibrations near the terminator

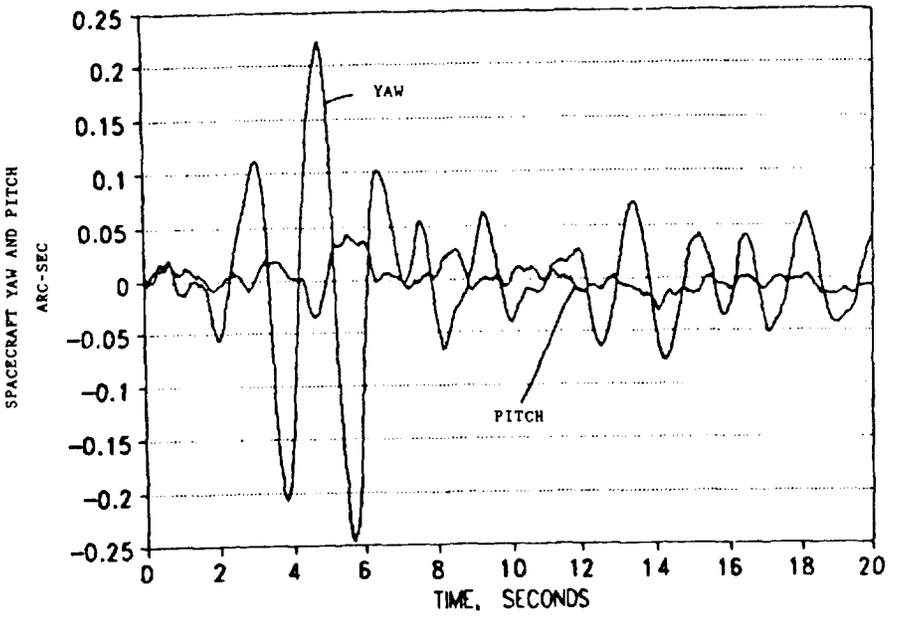

Figure 8. Second example of spacecraft jitter from solar panel vibrations near the terminator

N93-24724

Title: The Hubble Space Telescope Fine Guidance System Operating in the Coarse Track Pointing Control Mode

Author: Richard Whittlesey

Affiliation: Hughes Danbury Optical Systems, Inc.
100 Wooster Heights Road
Danbury, Connecticut 06810
(203) 797-5738

The Hubble Space Telescope (HST) Fine Guidance System has set new standards in pointing control capability for earth orbiting spacecraft. Two precision pointing control modes are implemented in the Fine Guidance System; one being a Coarse Track Mode which employs a pseudo-quadrature detector approach and the second being a Fine Mode which uses a two axis interferometer implementation. The Coarse Track Mode was designed to maintain FGS pointing error to within 20 milli-arc seconds(rms) when guiding on a 14.5 Mv star. The Fine Mode was designed to maintain FGS pointing error to less than 3 milli-arc seconds (rms). This paper addresses the HST FGS operating in the Coarse Track Mode.

An overview of the implementation, the operation, and both the predicted and observed on orbit performance is presented. The discussion includes a review of the Fine Guidance System hardware which uses two beam steering Star Selector servos, four photon counting photomultiplier tube detectors, as well as a 24 bit microprocessor, which executes the control system firmware.

Unanticipated spacecraft operational characteristics are discussed as they impact pointing performance. These include the influence of spherically aberrated star images as well as the mechanical shocks induced in the spacecraft during and following orbital day/night terminator crossings. Computer modelling of the Coarse Track Mode verifies the observed on orbit performance trends in the presence of these optical and mechanical disturbances. It is concluded that the coarse track pointing control function is performing as designed and is providing a robust pointing control capability for the Hubble Space Telescope.

Introduction

The Hubble Space Telescope (HST) fine guidance control is performed by the Fine Guidance Sensors (FGSs) under the control of computer firmware which is implemented in the Fine Guidance Electronics (FGEs). For any given telescope observation, two of the three fine guidance systems provide pointing control such that the target being studied is maintained in the desired Science Instrument (SI) aperture. Figure 1 illustrates the HST Field of View (FOV) including the FGSs and the SI locations in that field. Selection of guide stars in any two FGSs can support three axis pointing control.

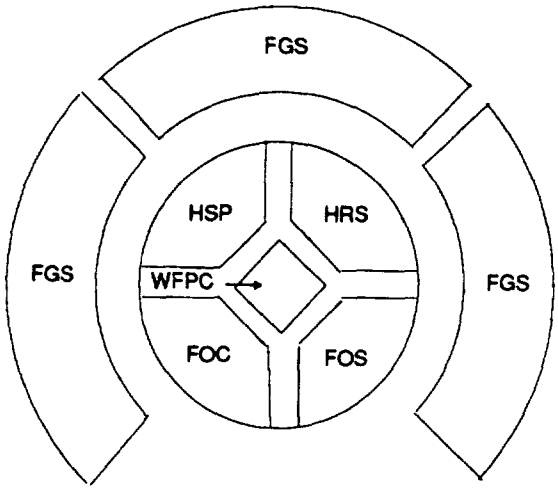

FGS - Fine Guidance Sensor

WFPC - Wide Field/Planetary Camera

HRS - High Resolution Spectrograph

FOS - Faint Object Spectrograph

FOC - Faint Object Camera

HSP - HIgh-Speed Photometer

Figure 1. Hubble Space Telescope Field of View

Guidance control is achieved by locking onto a dominant guide star with one FGS and then locking on the non-dominant guide star with a second FGS. The dominant guide star is used to control pitch and yaw while the non-dominant guide star is used to control roll in the telescope. The HST Pointing and Control System (PCS) orients the guide stars in the FGS FOV such that the line of sight of the telescope is coincident with the desired SI aperture. The FGSs then provide continuous guide star lock and periodic feedback to the PCS to maintain the telescope line of sight. This paper addresses one of the two FGS fine pointing control modes, the Coarse Track Mode. The Coarse Track Mode is designed to provide a pointing accuracy of 20 milli-arc seconds (rms) when viewing a 14.5 Mv star. This control mode was originally expected to be used for guidance in about 50 % of the HST science observations. In fact, it is now used for about 70 % of all HST science observations because of it's inherent ability to maintain lock under adverse dynamic disturbance conditions which occur during day-to-night and night-to-day orbital transitions.

Coarse Track Control Implementation

Figure 2 shows the major functional components used to implement the Coarse Track Control Mode. The optical path includes a flat pick-off mirror located in the HST radial field which diverts a portion of the telescope FOV into the FGS Radial Bay Module optical path. An aspheric collimating mirror provides magnification and collimation of the beam. The beam is then relayed to the "A" Star Selector assembly which includes two flat deviation mirrors and a integral five element refractive corrector group. Next it passes through the four "B" Star Selector flat deviation mirrors and is directed to a Polarized Beam Splitter which produces X and Y orthogonal outputs. The orthogonal beams then pass through individual Koesters prisms and the resulting beams are re-imaged. Photon flux is measured using four photomultiplier tubes (PMTs); two in each axis. The PMTs and associated signal processing hardware convert the impinging photon flux into digital counts. The flux measurements in each of the four PMTs are then used to perform a pseudo-quadrature line of sight pointing error estimate and a feedback signal is generated to null out pointing errors.

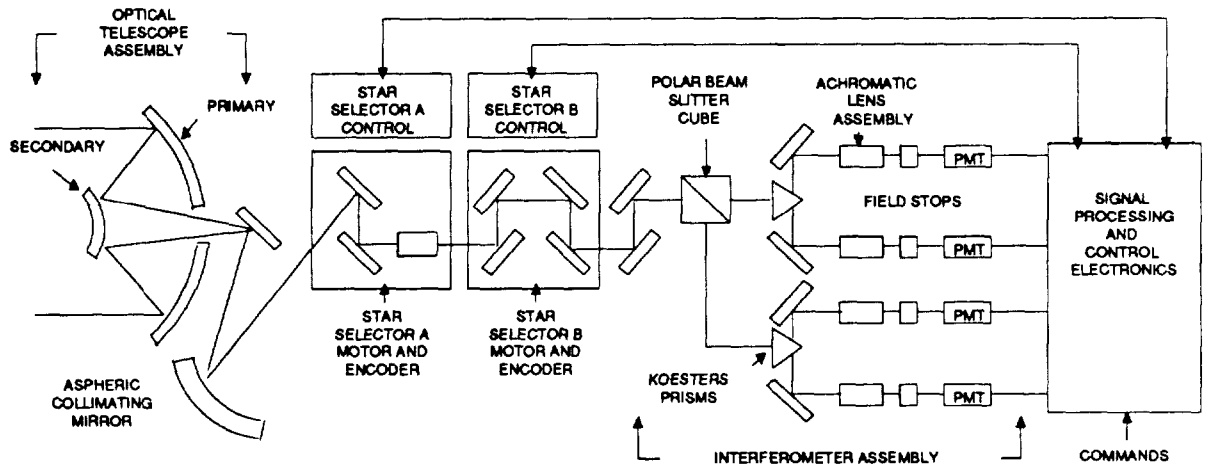

Figure 2. Functional Optical Path Diagram for Coarse Track

The Star Selector servos can be controlled in such a manner that the flux from any star in the FGS FOV can be directed to the fixed position PMTs. The control algorithms are executed in a 24 bit micro-computer located in the FGE. The FGE controls the initial guide-star acquisition following the coarse positioning of the telescope by the PCS hardware. The acquisition is accomplished during a Spiral Search Mode which creates an spiral search pattern in the proximity of the guide star. The FGE, by automatically monitoring the PMT counts and comparing them to the expected counts based on a priori knowledge of the guide star magnitude, accomplishes guide star detection. At this point a control mode transition occurs which establishes the Coarse Track Mode.

Figure 3 shows the fundamental relationships between the Star Selector servo rotational positions and the resulting pointing within the FOV.

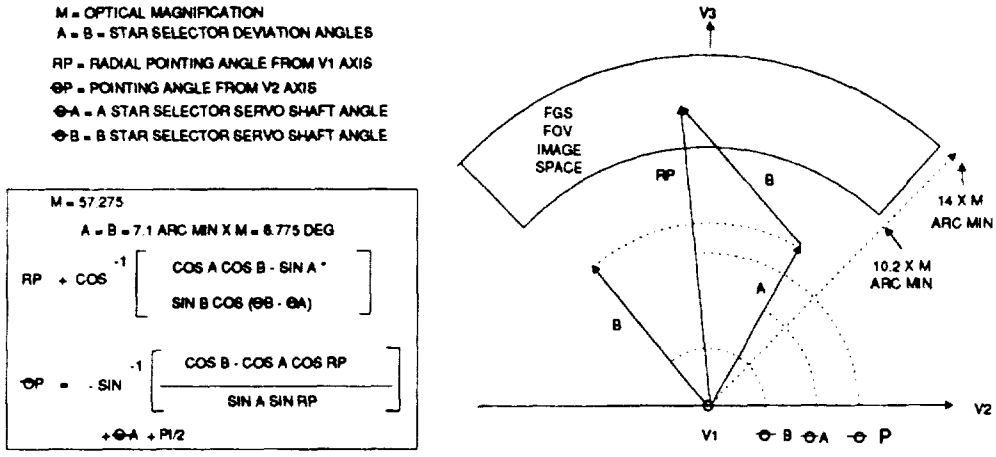

Figure 3 Star Selector Servo Pointing Relationships

Figure 4 illustrates the Search Mode to Coarse Track Mode transition as well as the coarse track guide star lock scenario in terms of the servo generated beam steering trajectories. The coarse track portion of the trajectory is controlled by the FGE and is basically an incremental nutation about the estimated line of sight of the guide star.

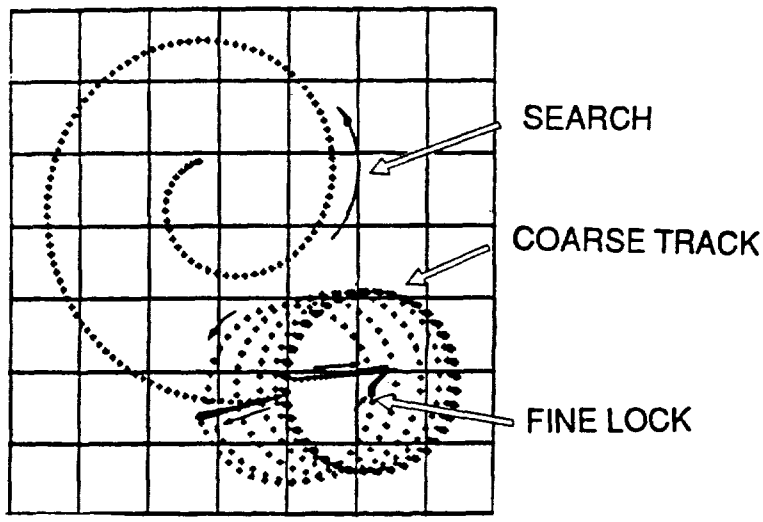

Figure 4 Search Mode and Coarse Track Guide Star Acquisition

Coarse Track Control Algorithms

The Coarse Track control algorithm operates in a manner similar to a quadrature detector in that it measures photon energy in four

quadrants as the star image is nutated in a circular pattern in and out of the square field stops of the FGS PMT sensors. Figure 5 shows the nutation pattern which consists of 40 discrete points on the nutation circle. The pattern is created once per second by commanding the two FGS Star Selector Servos to slew the image from point to point. Photon energy is integrated during each 25 milli-second servo slew, resulting in a PMT count "I" which is the sum of the four individual PMT values. These PMT measurements are used in the error signal control equations to adjust the FGS pointing angle toward the line of sight of the star.

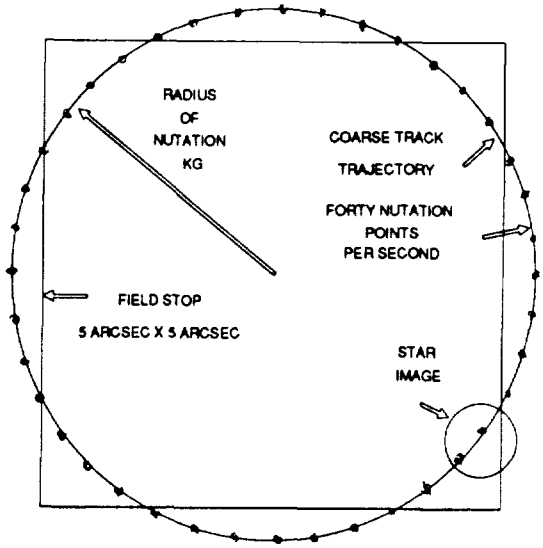

Figure 5 Coarse Track Nutation Trajectory at Null

The basis for generating the Coarse Track error is the prediction of the displacement of the nutation center from ideal and the subsequent adaptation of the center position to attempt to null the pointing error. Equation 1 is the static error equation for the X direction (Y is similar) which goes to zero when each of the four quadrants have identical intensities.

$$EX = I(X)/SUMA \qquad \text{EQ 1}$$

Where: $I(X) = -[I(1) + \ldots I(10)] + [I(11) + \ldots I(20)] + [I(21) + \ldots I(30)] - [I(31) + \ldots I(40)]$

$$SUMA = [I(1) + I(2) + \ldots I(40)]$$

Equation 2 illustrates the dynamic update to the iterative error equation which is done at each nutation point.

$$E5 = [I(X) + I(5) - I(5)']/[SUMA + I(5)' - I(5)] \qquad \text{EQ 2}$$

Where: I(X) is the computed I(X) value for nutation point 4
SUMA is the resultant SUMA at nutation point four
I(5) is the I(5) from the previous nutation cycle
I(5)' is the current I value measurement

The numerator is updated based on the difference between the previous I(5) and the current I(5) intensity. The SUMA value is adjusted to maintain a normalized error value. In a noise free system, the control algorithm will drive the X and Y errors to zero resulting in perfect alignment of the center of nutation with the guide star line of sight.

The actual performance of the Coarse Track control mode is influenced and limited by both Poisson noise in the intensity measurements and the dynamics of the overall telescope assuming other error sources are small. Photon noise impacts the rms pointing error in proportion to the square root of the intensity I where I represents the average photon count for a specific star magnitude Mv. The error equation will always have a residual value and its rms amplitude will be a function of the intensity of the star image. The optimum operation of the algorithm occurs when the image spot size is small enough to permit 100% of the photons to fall at times completely inside or completely outside of the image detector field stops. This maximizes the signal-to-noise ratio as well as the quadrature signal discrimination. This optimum condition is currently not met in the HST due to spherical aberration of the star image (see figure 6) which in effect spreads the image intensity over a large spatial domain. This effectively diminishes both the signal to noise ratio and the quadrature signal discrimination performance.

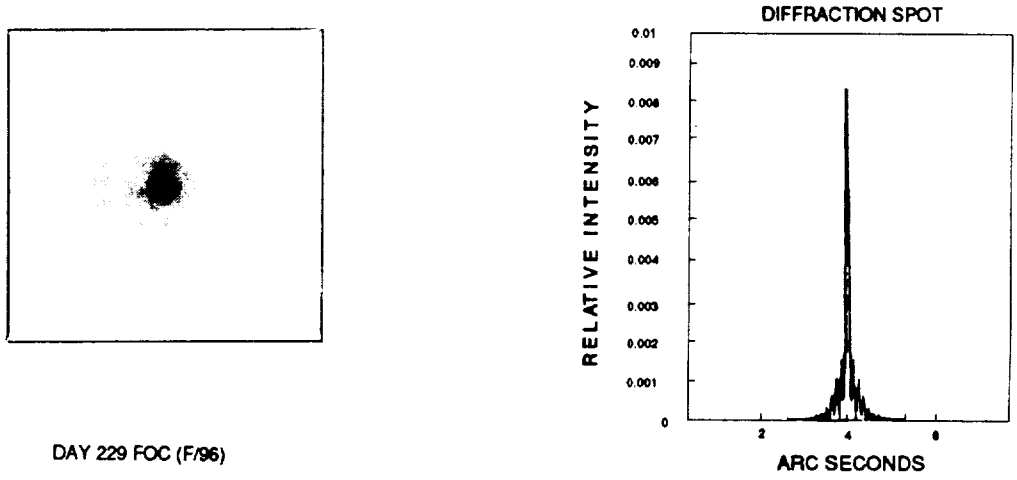

Figure 6 The Spherically Aberrated Image and Energy Distribution

The coarse track algorithms also control dynamic servo system response performance. The predicted on orbit dynamic disturbances were expected to be minimal based on an evaluation of disturbance levels of the various moving parts on the telescope. In reality, significant thermally-induced mechanical vibrations or "shocks" occur in the orbiting telescope. These mechanical shocks impact coarse track performance in that the basic control recovery

can take up to ten to fifteen seconds or longer if the disturbance causes a temporary but significant change in the line of sight of the telescope.

The Star Selector servo control implementation was designed to permit a limited amount of adjustment in the servo control loop performance characteristics. Two up-link parameters, KG (radius of nutation) and KJ(closed loop gain) are programmable. Figure 7 illustrates the on-axis transfer function for various values of KG. Large KG values maintain a saturated error signal closer to the null region and offer higher gain in the null transition region. Large disturbances are corrected faster by the selecting a higher KG value. KJ controls the closed loop servo gain and transient response. Figure 8 shows the closed loop transient response as a function of KJ with KG set to the default value of 2.68 arc seconds (object space). Increasing KJ much above 0.05 arc seconds results in close loop instabilities which must be avoided when attempting performance optimization. The nominal (default) settings of KG = 2.68 arc seconds and KJ = 0.026 arc seconds were selected for orbital use prior the HST launch. The KG value was selected to provide a radius of nutation which results in the star image being inside the field stops 50 % of the time and outside 50% of the time. This provides good signal discrimination in each quadrant. KJ was selected to provide a damped response to avoid extending the transient settling time caused by ringing when higher values are selected. The observed orbital coarse track servo performance is moderately degraded when compared to the predicted performance. The coarse track control sensitivity is within about 0.5 to 0.8 Mv of the diffraction limited performance. A computer model has been developed to verify that this decreased sensitivity is attributed to the aberrated star image.

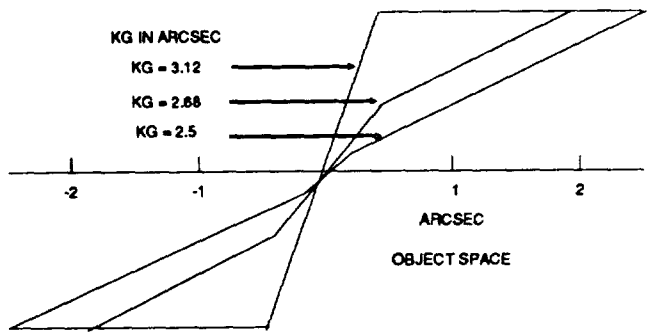

Figure 7 On Axis Open Loop Transfer Function

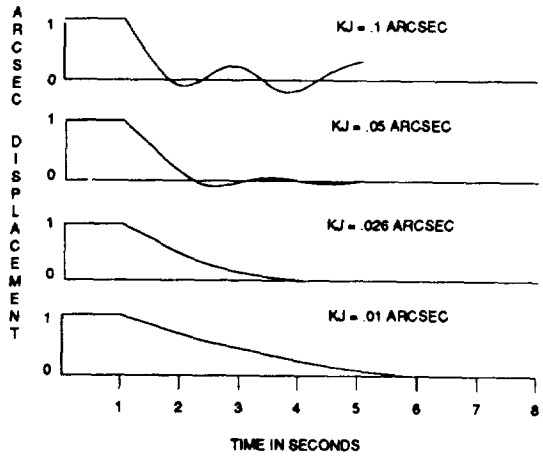

Figure 8 Close Loop Transient Response

Computer Modelling

Figure 9 shows a top level flow diagram for the coarse track control computer simulation model. User inputs include star magnitude, KG(radius of nutation), KJ (closed loop gain), nutation center offset, image spot size, and signal amplitude distribution. A 100 point star image is used to simulate the image energy distribution. The program outputs include the nutation point (1-40) being operated on, the PMT counts at each point, X and Y coordinate error values, X and Y center values, X and Y rms squared error values, and graphical plots of selected parameters versus time. Using this model, simulations have been performed for both predicted coarse track performance and the on-orbit performance with a diffuse image.

PROGRAM INPUTS INCLUDE:

STAR MAGNITUDE
KG - RADIUS OF NUTATION
KJ - GAIN
CENTER OFFSET
SPOT SIZE
SPOT ENERGY DISTRIBUTION

PROGRAM OUTPUTS INCLUDE:

NUTATION POINT (1- 40)
PMT COUNTS
DELTA X
DELTA Y
CENTER X
CENTER Y
X RMS SQUARED ERROR
Y RMS SQUARED ERROR
NORMALIZED ERROR DENOMINATOR
NORMALIZED X ERROR
NORMALIZED Y ERROR

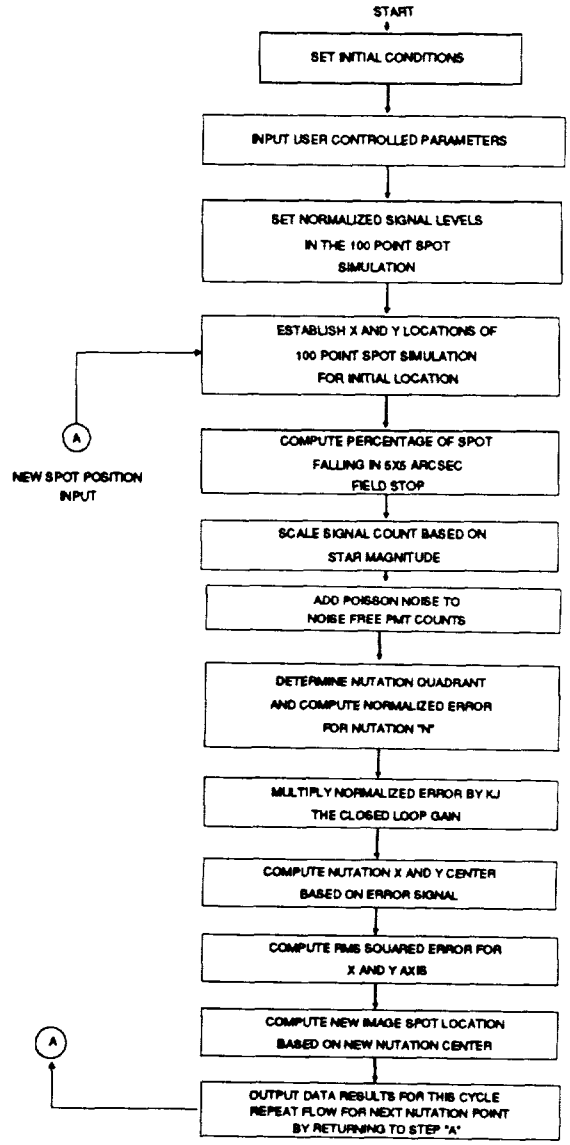

Figure 9 Coarse Track Computer Simulation Model

Figure 10 shows the impact of the diffuse star image on the open loop transfer function. Error signal gain is reduced for all values of KG when compared with figure 7 . Figure 11 illustrates the impact of the diffuse star image on the closed loop rms pointing error. With a diffraction limited spot, there are sharp cut off points defined by the 5X5 arc second field stops i.e. at KG setting of less than 2.5, the image center can move within the field stop and at times provide no error feedback; likewise when the radius of nutation is greater than 3.54 arc seconds the image can be outside of the field stop resulting in loss of feedback. For a diffuse image with the energy spread over a larger area, the modelling shows a general flattening of response of the pointing control error for all KG radius values. The rms error increases under these conditions. The relatively flat response suggests that performance cannot be significantly improved by adjusting KG, the coarse track radius of nutation. This has been demonstrated by on orbit testing (Bely and Liu).

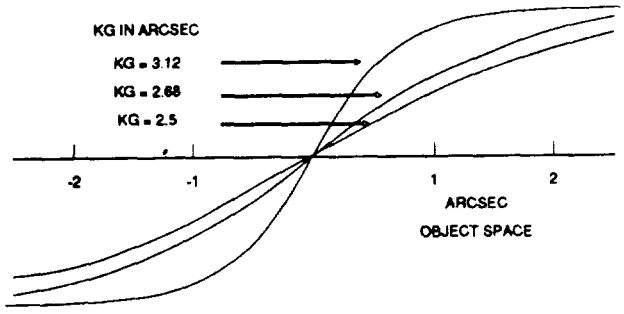

Figure 10. The Open Loop Transfer Function with a Diffuse Star Image

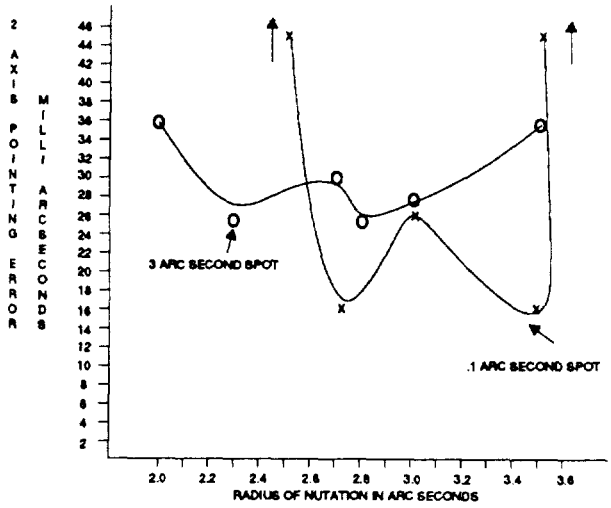

Figure 11. The Impact of a Diffuse Star Image on RMS Pointing Error

In order to gain further insight into the coarse track control characteristics, several simulations were run using the computer model. Parameters including star magnitude(Mv), image spot size, as well as KJ and KG were varied and the resultant servo response was plotted versus time. Figure 12 demonstrates the response for a high intensity star magnitude (11Mv) with the KG and KJ set to default. The diffuse image (3.0 arc seconds) and the diffraction limited image (0.1 arc second) conditions are shown to have similar rms errors and good overall settling trends. This is due to the fact that the Poisson noise is a small percentage (about 2%) of the signal in both cases, resulting in low rms errors.

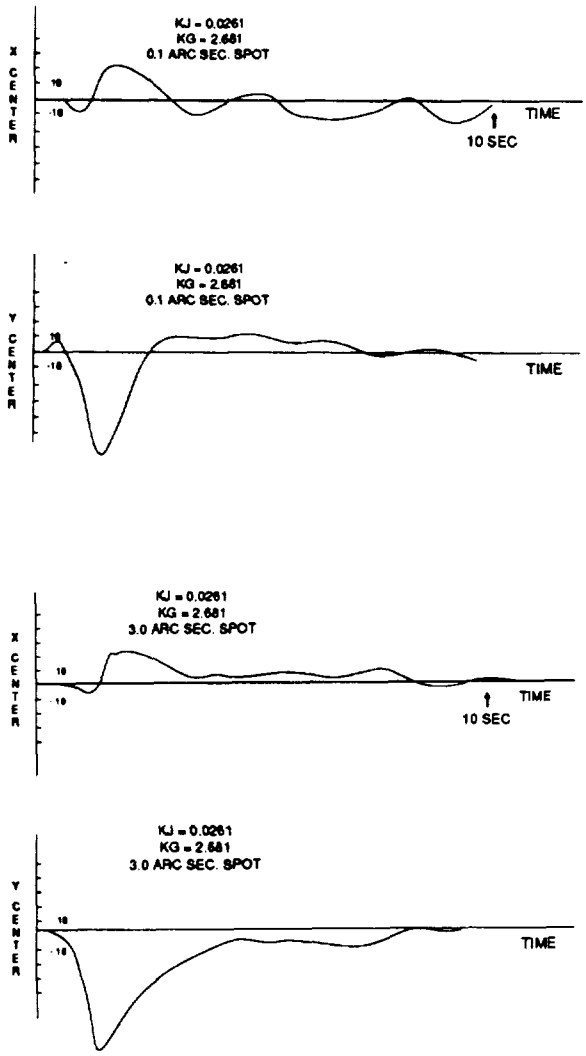

Figure 12 Coarse Track Settling for a Diffraction Limited and a Diffuse Star Image (11Mv)

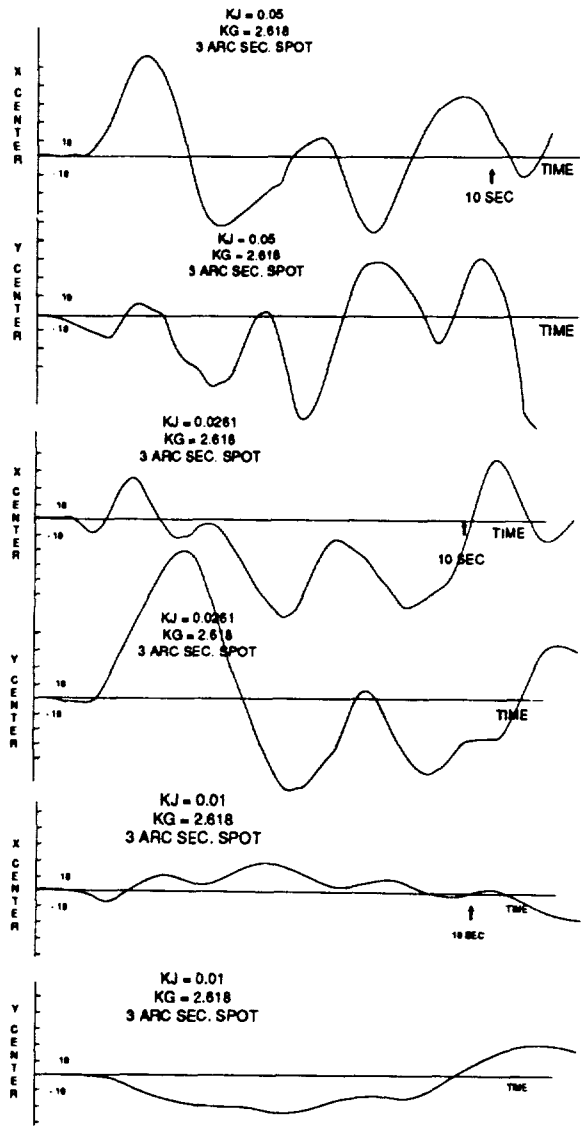

Figure 13 Coarse Track Settling for a Diffuse Star Image (14.5 Mv) for various KJ values

Figure 13 provides typical coarse track performance for a 14.5 Mv (fine guidance design limiting magnitude) star with a spot size of 3.0 arc seconds and various closed loop gains (KJ = 0.05, 0.0261, and 0.01 arc seconds). Since the signal to noise level ratio is quite poor with the diffuse image, any attempt to improve loop response by increasing KJ results in servo loop hunting. The loop is unlikely to settle over time since the noise constantly injects erroneous inputs at each of the 40 coarse track algorithm sample points. The higher closed loop gain emphasizes these random noise excursions. It will be noted that reducing KJ to 0.01 attenuates the effects of noise, but when the servo operates at this value dynamic response is severely impacted. Spacecraft disturbances cannot be followed with any fidelity in this case.

Figure 14 indicates the impact of changing KG, the radius of nutation. The star magnitude is once again set to 14.5 Mv and KJ is set to the default. Small values of KG (2 arc seconds) and large values of KG (3.5 arc seconds) result in responses which do not converge in an orderly manner. Rms errors can be large and biases can persist which will look like shifts in the average center position over time. For KG values of 2.3 arc seconds and 2.8 arc seconds, a slight improvement in rms pointing error (about 4 milli-arc seconds) occurs when compared with the case where the default parameters are used (see figure 13). Changing KG will not produce a significant performance improvement under the conditions of a spherically aberrated image. In this respect, the only approach to making inroads into improving rms pointing is to make use of high intensity guide stars whenever possible.

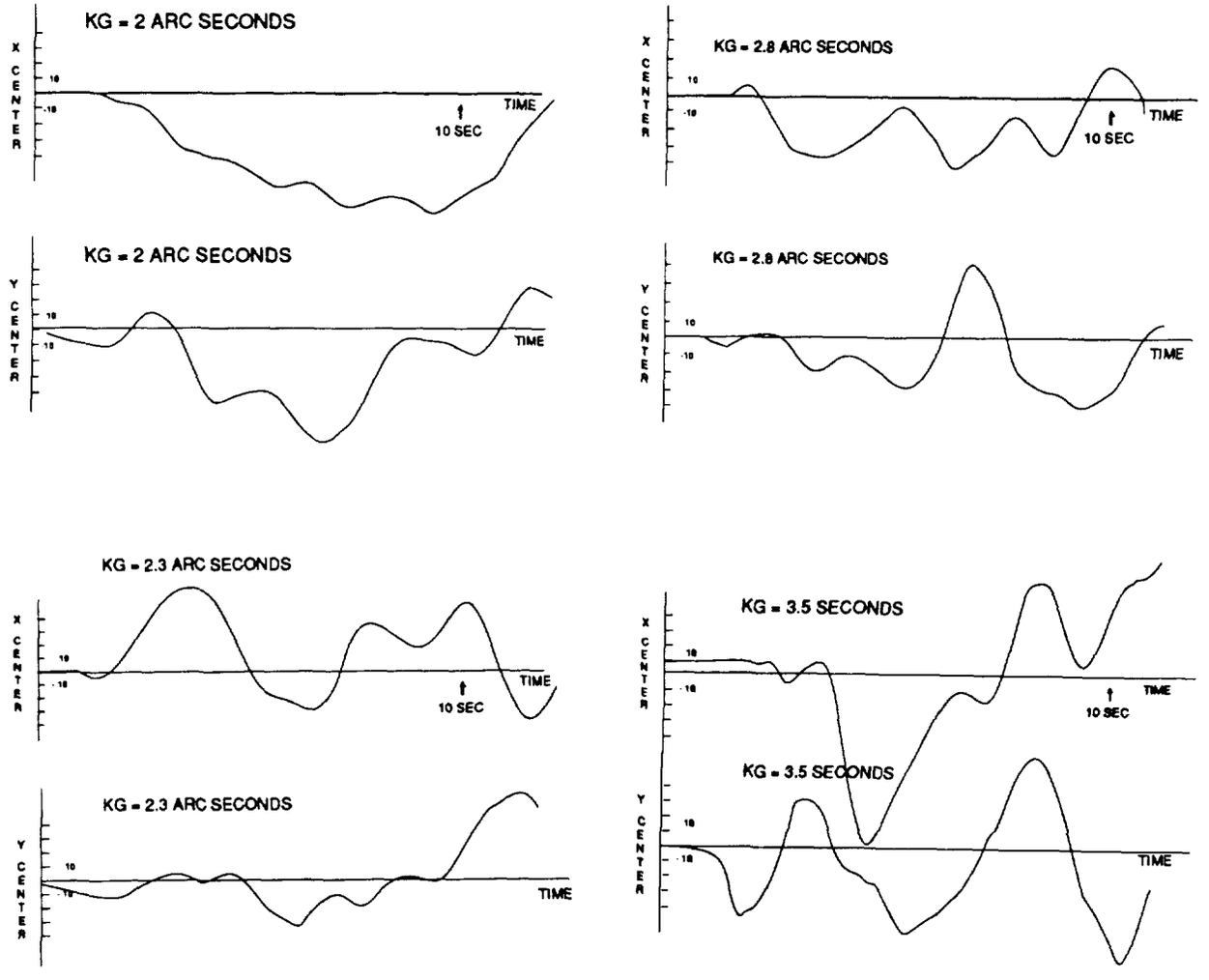

Figure 14. Coarse Track Response for Various Values of KG

Other modelling results indicate the following trends:

Figure 15 illustrates the general relationship of the quadrature modulation versus image size. It will be noted that significant modulation amplitude reduction occurs as the image size increases. The overall peak signal amplitude is also reduced if a symmetrical modulation (50% in and 50% out) is to be achieved. This condition results in decreased signal to noise as well as poorer quadrature discrimination.

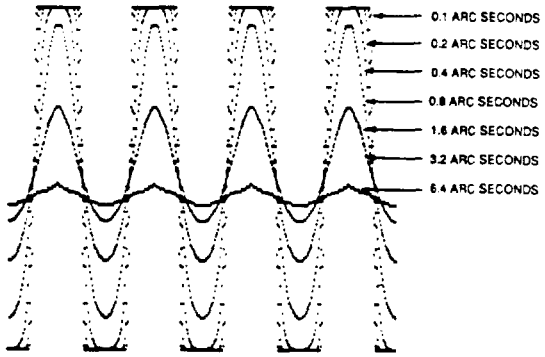

Figure 15. Quadrature Modulation Versus Image Size

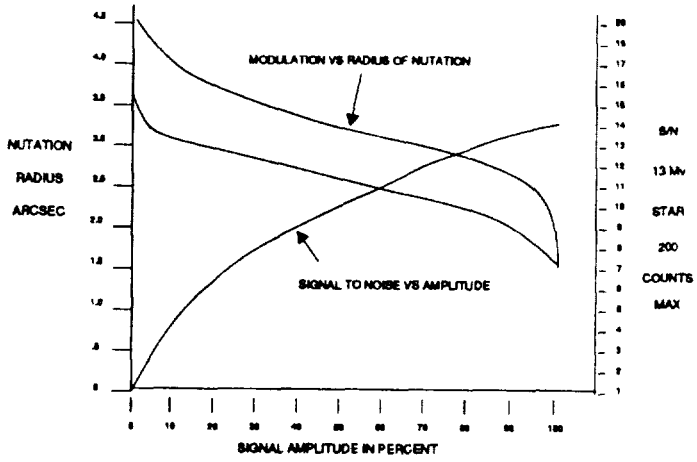

Figure 16. Relationships Between Signal Modulation, S/N Ratio and Radius of Nutation

Figure 16 illustrates the general relationships between signal modulation, signal amplitude and radius of nutation KG. Ideally, selection of the maximum modulation would provide the best control. With a diffuse image, a compromise must be made. Selection of the maximum signal amplitude, in an effort to achieve maximum signal to noise ratio, results in a very limited signal modulation level. At best, selection of a KG radius of nutation in the 2.5 to 3.0 arc second range results in reasonably good signal amplitude and modulation. The default KG value of 2.68 arc seconds is not an unreasonable choice even for the case where the star image is diffuse.

Figure 17 provides predicted (RMS) coarse track performance with and without spherical aberration of the star image. Attempts to improve control performance by increasing KJ, the closed loop gain, in the presence of a diffuse image in general has a deleterious impact. While response time is improved somewhat, the impact of Poisson noise is increased particularly for dim guide stars. RMS jitter is increased.

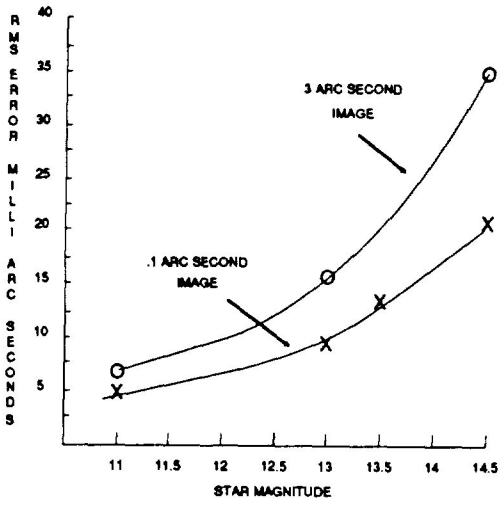

Figure 17. Coarse Track RMS Pointing Jitter Versus Image Size

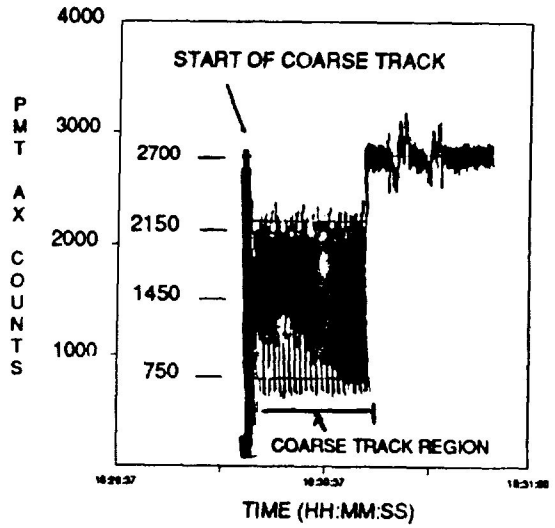

Figure 18. On-Orbit PMT Counts Versus Time

On-Orbit Performance

Typical on-orbit observed pointing jitter is on the order of 10 to 20 milli-arc seconds (rms) for 11 Mv stars, 20 to 45 milli-arc seconds for 13.8 Mv stars and 30 to 60 milli-arc seconds for 14.5 Mv stars. Figure 18 illustrates the observed decrease in sensitivity in both PMT count amplitude and depth of modulation in the coarse track control mode. Peak PMT signal amplitudes reach only 60 to 70 % of the expected amplitudes. Good correlation between the simulations and the observed performance implies that the HST Fine Guidance Sensors are performing nominally in the presence of a spherically aberrated image.

The influence of higher than expected vehicle vibrations caused by thermally induced shocks from the spacecraft solar array panels result in hunting in the control loop as it attempts to maintain the pointing line of sight. The coarse track control has been shown to be quite robust in the sense that it can maintain lock on the guide stars even during the significant disturbances which occur during day/night thermal transitions. This has permitted longer science

observations that would likely have been impossible if only the FGS Fine Lock capability had been implemented. It is expected that, with the replacement of the solar panels on the future repair mission to HST, overall HST orbit-to-orbit pointing stability will be significantly improved. This should also improve the Fine Lock control performance which is designed to provide pointing control in the 3 milli- arc second range when the vehicle disturbances are low.

Conclusions

In spite of un-anticipated HST anomalies including spherical aberration in the primary mirror and significant mechanical "shocks" from the Solar Panels, the Fine Guidance Systems are performing reliable pointing control in Coarse Track Mode. A large percentage of the planned HST science observations are being accomplished using this robust pointing control mode. The fine guidance system implementation using quadrature centroiding principles coupled with the beam steering servos and the associated control algorithms demonstrates a sound design concept for highly accurate pointing control of earth orbiting spacecraft.

Acknowledgements

The work reported herein was sponsored by NASA GSFC under contract number NAS-38494. The author wishes to thank Linda Abramowicz-Reed, Pierre Bely, Henry Blazek and David Eaton for the informative technical discussions which provided much insight into the operation of the Hubble Space Telescope Fine Guidance system.

Reference: Bely,P. and Liu, 1991, Space Telescope Science Institute Memorandum

-15

SCATHA
Mission Termination Report

154751
N93-24725
p-17

1 August 1991

Prepared for the Consolidated Space Test Center / VOF
by
Lockheed Technical Operations Company

Kjell Stakkestad
Richard Fennessey

Technical Contributions
Chris Bryan
Nick Padayao
Eric Fons

1. ABSTRACT

The SCATHA (Spacecraft Charging at High Altitudes) satellite was operated from the Consolidated Space Test Center in Sunnyvale, California from February 1979 to May 1991. It was a spin stabilized vehicle in a highly eccentric orbit that collected data on spacecraft charging. The purpose of such data gathering was to predict and/or model the effects of the Earth's magnetic field on synchronous and near synchronous satellites.

During the majority of its lifetime, attitude precession maneuvers were done every 10-15 days to maintain solar panel orientation. Maneuver planning was difficult due to the structural characteristics of SCATHA. It is cylindrically shaped and has seven booms ranging in length from 2 to 50 meters. These precession maneuvers induced predictable nutation that damped out after a few days. Eventually fuel began running low due to these frequent maneuvers. Experiments that had required the spin axis be in the orbit plane had already been turned off or had collected all their data. To increase the vehicle lifetime, the spin axis was moved to ecliptic normal. While this stopped the need for frequent attitude maneuvering (only two per year required now), this movement of the spin axis caused nutation that would not damp out for the remainder of the mission.

This phase of the mission, with the ecliptic normal orientation, lasted for approximately three years. Although nutation never damped, data gathering was uninterrupted. In late 1990, when SCATHA's transmitter became seriously degraded, the Air Force decided to turn SCATHA off. This would only be done after the satellite was made "safe". The most difficult part of making the vehicle safe was quickly purging the fuel. Several plans were considered. The selected plan was to perform a series of 20 degree attitude precession maneuvers (3 days apart to allow for the worst nutation to damp) until the fuel was depleted. Although this sounded simple, the actual execution proved difficult. This was due to a nearly complete lack of available telemetry data, large undamped motion of the long booms, inadequacies in attitude determination software, and an error in the fuel level calculation software.

This paper discusses the various proposed termination plans and execution of the selected one. Attitude determination methodologies, nutation from maneuvers, and effects of the flexible booms on the termination mission are presented and analyzed from a satellite analyst point of view.

2. BACKGROUND

2.1 Mission and Orbit

The SCATHA mission was to investigate the cause or causes of numerous spacecraft anomalies due to spacecraft charging phenomena which plagued high altitude, near synchronous vehicles throughout the 1960's and 70's. On January 30, 1979, a McDonnell Douglas Delta rocket launched SCATHA into a 176 by 43,278 km transfer orbit. On February 2 it was injected into a 27,578 by 43,288 km, 7.9 degree inclination final orbit. For most of the mission, the spin stabilized satellite was operated at near 1 rpm.

SCATHA was managed and funded by the United States Air Force (USAF) Space Test Program (STP). It was one element of a cooperative NASA/USAF program to investigate various aspects of the electrical charging and discharging of geosynchronous spacecraft surfaces. Mission operations were under the administration of the U.S. Air Force office "Vehicle Operations - Complex F" (VOF). As one of several VO offices within the Consolidated Space Test Center (CSTC), VOF has historically been responsible for research and development programs. Mission planning and real-time operations were performed by the Lockheed Technical Operations Company (LTOC) Mission Control Team (MCT). Together the two organizations functioned as a mission control complex referred to as Test Support Complex-1 (TSC-1).

2.2 Vehicle Description

The primary systems relevant to fuel depletion and maneuver activity are the vehicle structure and attitude control systems.

Structure. The SCATHA vehicle has a cylindrical body with diameter and height of approximately 1 3/4 meters that supports all the subsystems and the experiments. In the on-orbit configuration it has experiments located on five extended booms (ref figure 2-1). In addition there are two 50 meter booms which comprise NASA's Electric Field Detector 100 meter antenna.

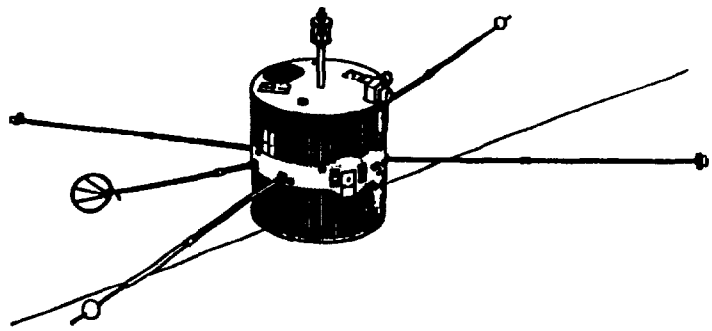

Figure 2-1. SCATHA On-orbit Configuration

Attitude Control and Determination Subsystem (AC&D). The AC&D subsystem provides attitude sensing and thrust impulse for control of the spin rate, spin axis attitude, and orbital velocity adjustments. All attitude control commands are executed in real-time. There are no provisions for on-board storage of time-tagged commands.

The AC&D system, in conjunction with ground based mission unique software, provides for attitude determination using data from two groups of space vehicle (SV) attitude sensor units. The first group consists of four digital sun sensors. Each DSAS (Digital Sun Aspect Sensor) measures the angle between the sun vector and the vehicle spin axis once per revolution. The second group of sensors consists of two Steerable Horizon Crossing Indicators (SHCIs). These detect a thermal discontinuity as the line of sight crosses the earth horizon. The line-of-sight of each unit is adjustable and capable of expanding its field-of-view (FOV) to

4π steradians. The sensor output gives the instantaneous line of sight position and horizon crossing times. Figure 2-2 shows the sun and horizon sensor configuration.

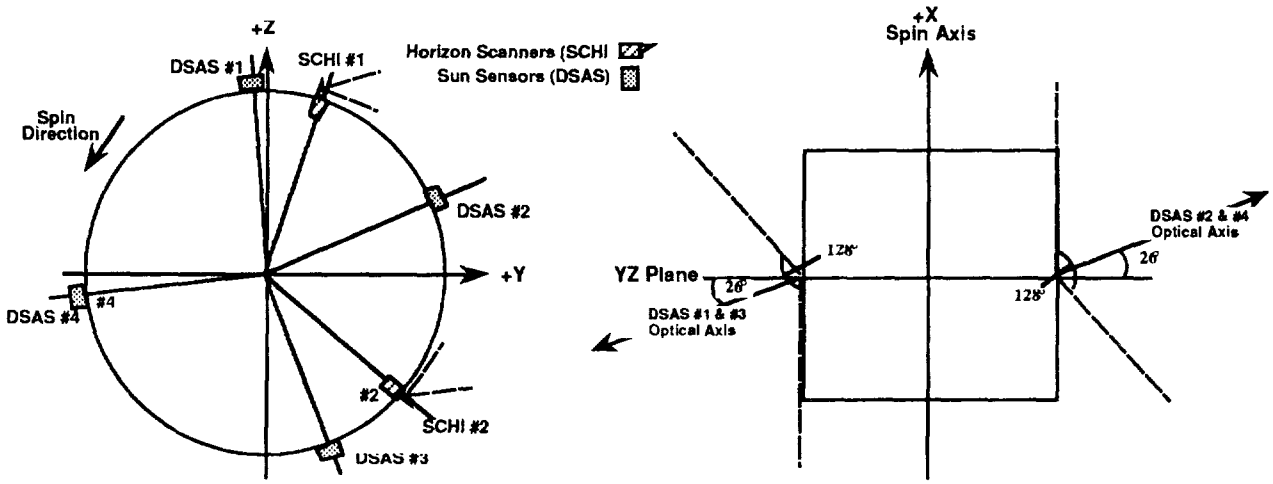

Figure 2-2. Sun and Earth Horizon Sensor Configurations

Two nutation dampers are installed to provide damping of residual nutation. The hollow rings are filled with Dow Corning dimethyl silicone fluid. They are mounted 180 degrees apart with the ring planes parallel to the vehicle spin axis and perpendicular to the axis of maximum transient moment of inertia when all experiments are fully deployed. The damping time constant for the 1.0 ± 0.1 rpm spin rate (all booms deployed) is 8 hours over the operating range.

2.3 Spacecraft Attitude Determination Methods

The DSAS and SHCI telemetered values are used together in determining the SV attitude by the ground based mission unique software. The software takes in the telemetry from the DSAS and SHCIs and combines it with calculated vehicle and solar ephemerides to obtain three derived measurement angles: Sun-vehicle-earth angle (SVE), Earth aspect angle (EA - from SHCI data), and solar aspect angle (SA - from DSAS data). The SVE angle is defined as the included angle between the nadir vector and the vector from the sun to the space vehicle (SV). The EA is defined as the included angle between the nadir vector and the positive spin axis. The SA is the angle between the positive spin axis and the sun vector.

Attitude determination software uses sets of these three derived angles in a least squares batch processor which provides a minimum variance estimate of the average inertial attitude state at a user-defined epoch. This state is output in the form of two angles: spin axis right ascension (SARA) and spin axis declination (SADEC). The specification for ground software attitude determination error is ± 1.4 degrees (3 sigma).

2.4 Orbit and Attitude Maneuvering System

The spacecraft is capable of performing three types of maneuvers: delta velocity, spin (up or down), and attitude precession (re-orientation of the vehicle's spin axis). During SCATHA's lifetime the vast majority of the maneuvers were attitude precession maneuvers to keep enough sun on the arrays to power the vehicle. SCATHA had two hydrazine fueled rocket engine modules, each with three .2 lb thrusters and a 5 lb thruster. Details on the ground based maneuver planning software are available in references 1 and 2.

3. MANEUVER OPERATION PHASES

The SCATHA mission can be broken into three different phases: Nominal, Re-orientation/Extended Life, and Termination.

3.1 Nominal Phase Maneuvers

For the first eight years of the mission (after the approximate 1 month orbit and spin axis initialization phase), the nominal attitude of SCATHA placed the vehicle spin axis oriented within the orbit plane. Due to power constraints, the vehicle sun angle (angle between spin axis and sun vector) had to be kept within +10 and -5 degrees of normal to the sun line. To stay within these bounds, attitude maneuvers with sizes between 10 and 15 degrees had to be performed every 10-15 days to counteract the apparent motion of the Sun due to the Earth's orbital motion throughout the year (approx 1 deg/day).

During this time (25 Feb 79 - 01 Jan 87), all maneuvers performed were attitude precession maneuvers. After this eight year nominal phase, software indicated approximately 2.68 lbs of fuel remained on board (originally there was 21.3 lbs). A summary of this phase can be found in figure 3-1.

Parameters	Nominal Phase Feb 79 - Jan 87	Re-orientation Phase Jan 87 - Jan 91	Termination Phase Jan 91 - May 91
Precession/Spin Maneuvers	233	11	48
Fuel Used (lbs)	10.82	.339	3.3953
Average Time Between Maneuvers	12.30 Days	200.3 Days	3.0 Days
Fuel Usage per Maneuver (lbs)	.046	.0375	.0707

Figure 3-1. Summary of SCATHA Precession/Spin Maneuvers

The performance of the attitude maneuver generation software during this phase was exceptional. The total angular error between the predicted spin axis and the determined spin axis was never greater than 1.0 degrees and 99 % of the time it was less than .5 degrees. Due to the effect of the motion of the long booms (caused by the maneuver) on the satellite, the MCT had to wait 3 days after each maneuver in order to gather useable telemetry for an accurate post maneuver attitude determination. Telemetered sun angle values showed that successive values differed by as much as 4 to 6 degrees per revolution. This difference, referred to (by the MCT) as "out-of-plane nutation", always damped to less than 2.0 degrees within 3-5 days. Undamped nutation was never a problem during this phase of the mission.

3.2 Extended Reorientation / Extended Life Maneuvers

In January of 1983, a study was performed by the MCT and the Aerospace Corporation to determine the projected date of hydrazine depletion and to recommend a course of action which might extend the fuel supply and therefore extend mission life. It was estimated that "blowdown pressure" (i.e. the point at which the pressure of N_2 would no longer be enough to move the hydrazine to the engines (approx 122 psia)) would

be reached by August of 1988 if no change to vehicle operations were implemented. As a result of these studies and talks with the remaining experimenters, it was determined that the vehicle's fuel supply could be greatly extended if the vehicle were oriented so that its spin axis was normal to the ecliptic plane (see Figure 3-2). In this orientation there would be far fewer attitude maneuvers required to stay within 10-20 of normal to the sun line.

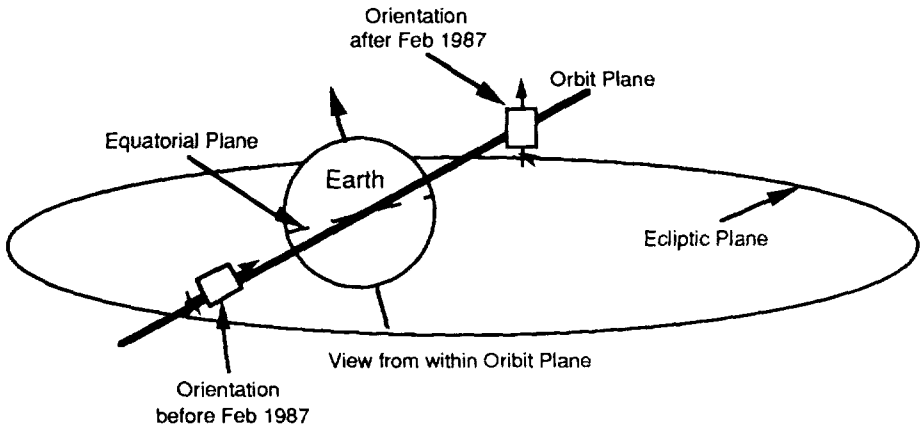

Figure 3-2. Spin Axis Orientation Relative to Orbit Plane

The requirements for a maneuver of this magnitude were extensive, especially considering the effects of such maneuvering on the long booms. It was hoped that the booms could be pulled in prior to the maneuver, thus minimizing possible damage to the booms as well as reducing the number of maneuvers. However, analysis done by the spacecraft dynamics department at Goddard Space Flight Center (GSFC) showed that dangerous resonance points would be reached at various lengths as the booms were retracted. So any plan for maneuvering would have to be performed with the booms fully deployed. After much deliberation, it was finally decided to break up the maneuver into 5 smaller maneuvers with ample time between each to allow "out of plane" nutation to damp out (nutation had to be < 6 degrees in order for the next maneuver to proceed). The attitude maneuvers were completed on 4 Feb 87, 20 days after the 1st burn. Out-of-plane nutation during these maneuvers, while higher than had been seen prior to the re-orientation maneuvers (reached 15 degrees at one point), damped out to well under the 6 degree limit within one week following the last maneuver.

Once these maneuvers were complete it was decided to do something about the vehicle's spin rate which had dropped to 0.928 RPM (very close to the lower limit for experiments). A series of small spin up maneuvers (each three days apart) was planned to raise the spin rate to its original value. After the first four maneuvers were completed, raising the spin rate to 1.021 RPM, the out of plane nutation limit of 6.0 degrees was exceeded (it was greater than 8.5 degrees). More alarming, was the spin rate variation (time from a DSAS sun cross reading to its next sun cross reading) -- it had become quite large. Measuring it in terms of an angle, called "in-plane" nutation by the MCT, it reached in excess of 14 degrees. During the following five weeks, neither the in-plane nor out-of-plane nutation consistently dropped below the 6 degree limit. Clearly, the nutation dampers, designed expressly for handling out-of-plane nutation, were unable to handle the apparent coupling of these two motions. As a result of the increased and undamped nutation, the remaining planned spin-up maneuvers were postponed indefinitely.

At the end of these maneuvers, the vehicle sun angle was 95 degrees (non-normality to sun line of 5 degrees) and the out of ecliptic plane angle was 85 degrees. This attitude, assuming no precession, should have resulted in an annual sun angle cycle of 95 to 90 to 85 to 90 to 95 degrees, etc. There was, however, a slight precession of the spin axis about the Earth's polar axis, which changed the amplitude and timing of the annual Sun cycle. As it turned out, the SARA and SADEC rates were fairly close to constant. Plots of these values were performed weekly. Figures 3-3 (a) and (b) are examples of these. First order least squares fits

were performed on the data. In general the SARA drift rate was approximately -0.2 deg/day (+/- 0.02) and the SADEC drift rate was nearly 0 deg/day.

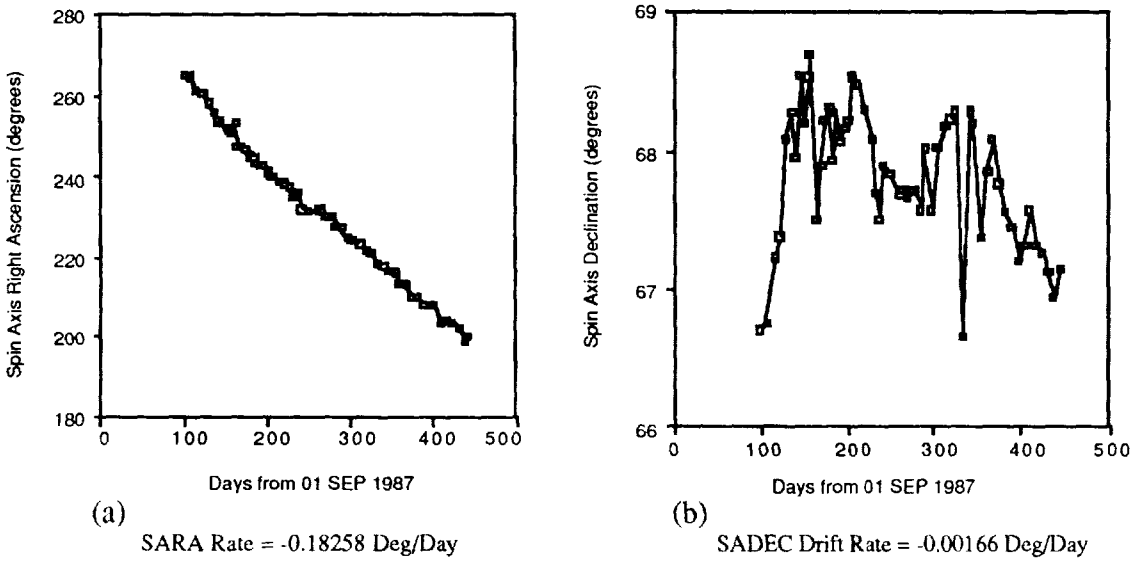

Figure 3-3. SARA and SADEC for Rate Calculation.

This motion is recognized as nearly pure precession of the spin axis about the Earth's polar axis and has a period of approximately 360/.2 = 1800 days (4.93 years). The MCT then wrote a program to predict sun angle using these rates and a Sun ephemeris generator. A resulting plot can be seen in figure 3-4 . This prediction was very accurate on the average (nutation, of course causes small deviations from the precession path). Plots of the Sun angles from actual determined attitudes were always within a degree of the predicts.

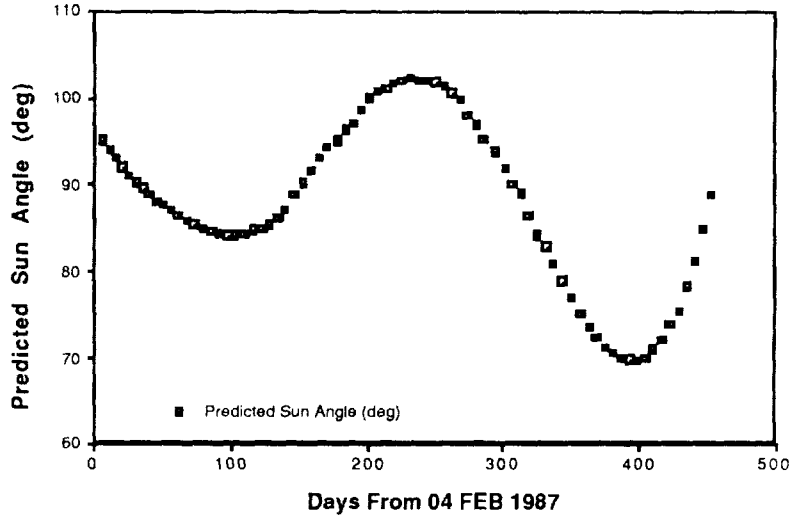

Figure 3-4. Spin Axis Sun Angle Relative to Earth-Sun Orbit Plane

During this re-orientation phase of the mission (1 Jan 87 to 1 Jan 91) only seven precession maneuvers were performed to maintain the sun angle within limits. A summary of the maneuvers in this phase can be found in Figure 3-5. At this rate of fuel consumption, the entire amount of remaining fuel would not be exhausted (ignoring blow down pressure) until the year 2025.

Initial Fuel	2.68 lbs
Final Fuel	2.34 lbs
Fuel Used by Original 5 Maneuvers	0.064 lbs
Fuel Used by 4 Spin Maneuvers	0.012 lbs
Fuel Used by 7 Normal Precession Maneuvers	0.26 lbs
Total Fuel Used	0.339 lbs
Average Time Between Maneuvers (1 Mar 87 to 1 Jan 91)	200.3 days
Average Fuel Used per Maneuver (1 Mar 87 to 1 Jan 91)	0.0375 lbs

Figure 3-5. SCATHA Re-orientation Phase Maneuver Summary

Maneuver performance for the seven normal precession maneuvers was good (see figure 3-6), although attitude determination was much more difficult during this phase due to the large amount of nutation experienced. There was more error than usual in the determined attitudes (both before and after the maneuver) as well as increased error in maneuver efficiency due to the high nutation. Still, the final attitudes were within operational accuracies (less than 1.5 deg).

Maneuver Date	Maneuver Size (Degrees)	Estimation Error (Degrees)	Max Observed In and Out of Plane Nutation(Deg) Out	In
09 Dec 87	16.20	<< 1	12.0	14.0
19 Nov 88	14.998	1.4	7.0	12.0
03 Jan 89	15.014	1.1	8.5	8.5
13 Jul 89	6.006	<< 1	4.0	5.5
08 Aug 89	6.001	1.45	5.0	6.0
17 Aug 89	4.060	< 1	4.0	6.5
09 Jul 90	12.113	No Telemetry	No Telemetry	

Figure 3-6. Maneuver Errors and Maximum Nutation for SCATHA During the Re-orientation Phase

Since the nutation did not appear to be damping, regular nutation analyses were performed. Data was collected from each contact (approximately 3 times a day) in order to calculate both in-plane and out-of-plane nutation values. Figure 3-7 shows the maximum daily calculated nutation values for a span from 1 Jan 88 to 20 May 91. Since these were derived from data collected during vehicle contacts only, the maximum values are only estimates of the true maximums during the span.

Deriving nutation maximum values using only data from contacts presented the problem of missing data (up to 19 hours of each day). The MCT explored other ways of examining the nutation data. Continuous data gathered by the vehicle tape recorders was downlinked to tracking sites and subsequently shipped to experimenters. Upon contacting some experimenters, a full week of continuous data was provided to the MCT for analysis. Figure 3-8 below shows one complete day of this data. This data was very representative of the week and shows that there is a fairly rapid short-term periodic variation in sun angle as well as a longer overriding variation. Overall, short term sun angle variations appear to occur at very regular time intervals (periods on the order of 1200 seconds) while the longer term variations are not so regular (periods of between 25000 and 30000 seconds).

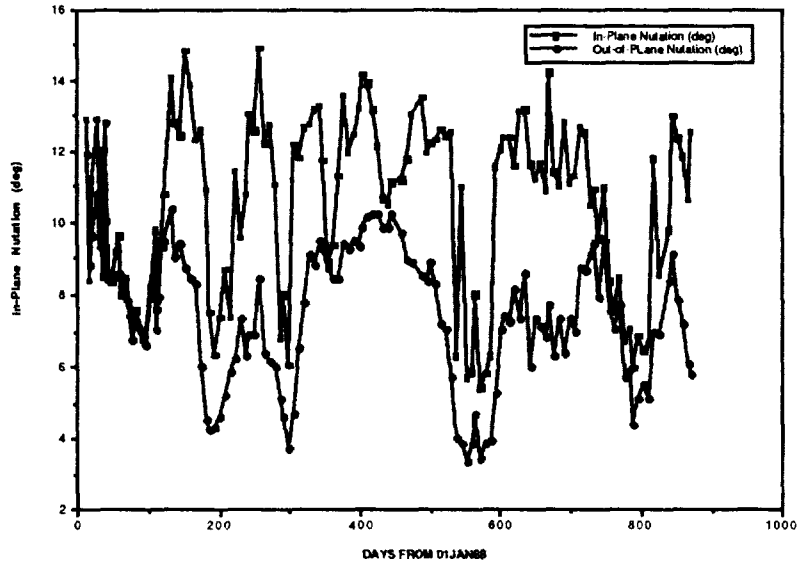

Figure 3-7. In-plane and Out-of-Plane Nutation

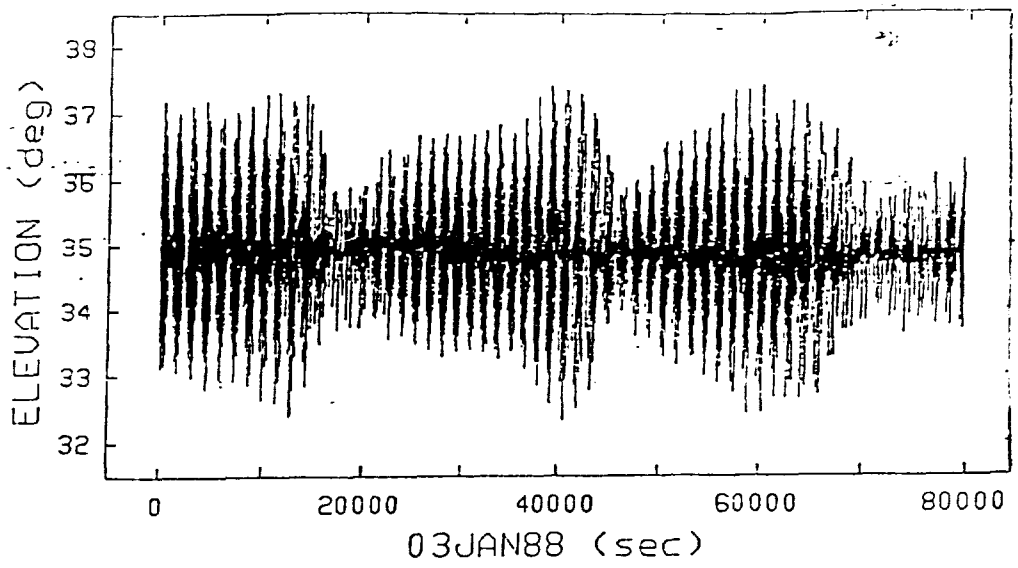

Figure 3-8. Full Day of Out-of-plane Nutation Data .

Although plots of data from the other three sun sensors (for the same time span) appear to be similar, much more data needs to be collected and processed to be able to determine a true pattern and to derive a method to predict nutation. With a large data base of this type of information, it was hoped to be able to at least find a pattern in the data that will suggest methods of predicting the nutation. Being able to predict "quiet" times would have helped dramatically in chosing future maneuver times. Unfortunately facilities to quickly process this data were not available at this time and now much of the experimenter data is no longer available so plans for future analysis are up in the air.

Figure 3-9 shows another way of looking at the details of out of plane nutation. This plot combines data from all four sun sensors, rather than waiting an entire spin period (about 1 minute) for a sun angle reading. This allows for a plot of sun angle every one-quarter spin period and may provide indication of any very short-term variation patterns in sun angle.

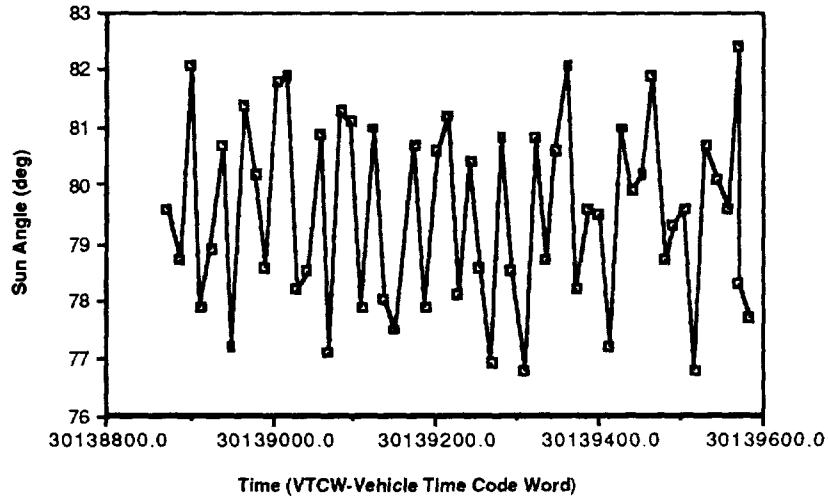

Figure 3-9. High Resolution Sun Angle Data.

4. MISSION TERMINATION

4.1 Pre-termination Activities

On May 20, 1990 SCATHA's transmitter #1, while in real-time support, displayed a sudden cut off to zero power output. All attempts to "revive" it failed. The only possible alternative was to go to transmitter #2 (the backup). Unfortunately, three years earlier, transmitter #2 had exhibited a similar drop in power, although only from the nominal 14.8 watts to 8.5 watts.

Real-time data retrieval became minimal and distorted. Playback data was all but impossible to retrieve. The ability of the MCT to collect attitude data was almost completely gone. Signal strength was very low, causing frequent loss of sync and data dropouts. These dropouts were especially detrimental to the collection of earth chords, one of the two types of attitude data. In order to get a valid earth chord angle, both a leading and trailing edge for that passage must be collected. Unfortunately, the dropouts were so common that valid earth chord data was extremely rare. The ground based software was completely unable to cope with such poor earth chord data. Many attempts were made to process the data but all failed. Attitude determination with sun sensor data only was tried but it gave unreliable results since data was too sparse. The last valid attitude determination by the original ground based software was done on May 19, 1990. For the next nine months, predictions of sun angles, earth chords, and attitudes were done using known SARA and SADEC rates and this last derived attitude.

By December, the retrieval of this low quality data became a major issue. The only useable telemetry that could be retrieved was collected during perigee supports which were available only 15 minutes a day. Even then only about 50% of the downlink data was usable. Even out-of-plane nutation calculations could rarely be done since it was so difficult to get consecutive sun crossings.

4.2 Termination Plan

The Systems Program Office (SPO) directed TSC-1 that SCATHA no longer needed to remain active after 31 Dec 1990. The MCT was directed to put SCATHA into a safe orientation and deplete all remaining fuel.

Many studies were done and options considered for using up all the remaining fuel as quickly and safely as possible. The quickest way to do this was to first retract the large booms and then perform a large velocity change maneuver (or series of maneuvers) to lower perigee as much as possible. This method had th added benefit of giving even better link margins at perigee and hence having more opportunities to gather goo data. However, this method was rejected for a number of reasons. First, in order to do an efficient burn to lower perigee, a huge precession maneuver (>50 deg) had to be done to align the spin axis with the negative velocity vector. This would use quite a bit of the remaining fuel and the subsequent delta velocity maneuver could only lower perigee by a couple hundred nautical miles. Second, and most importantly, the GSFC study (ref section 3.2, para 3) showed that bringing in the booms was extremely dangerous to vehicle stability. Of course, if the velocity change maneuver were done with the long booms out, they would bend and wrap around the vehicle if not break off entirely. Either way, the vehicle could not be considered to be in a safe configuration. So all future options would only be considered if the long booms remained fully deployed.

A second option considered was to spin the vehicle up (slowly) with hopes of placing it in a more stable configuration. However, the MCT experience with spin up maneuvers in the ecliptic normal configuration had not been very successful. The spin axis motion had not been the same since those four spin up maneuvers in February of 1987. The MCT considered the idea of bringing the spin axis back down into the orbit plane and then spinning it up, but spin maneuvers of any kind were viewed by the Air Force as too unsafe.

Finally, the decision was made to execute a series of 20 degree attitude precession maneuvers until the remaining fuel was gone. From past experience the worst (short term) out-of-plane nutation had taken three days to a week to damp out to smaller acceptable levels. As 1 January 1991 approached, there was a strong desire by the Air Force to "terminate" the satellite as soon as possible. Thus, only a 2 to 3 day separation between maneuvers was considered an acceptable risk. The Orbit Analysts in TSC-1 then performed a study to deplete the fuel in the requested manner. For purposes of study, the maneuvers were chosen so that only SADEC changed (i.e. add 20 degrees to SADEC, then subtract 20 degrees, then add, etc.). This study showed that it would take about 31 maneuvers to deplete all the remaining fuel. It was hoped that blow down pressure would be reached well before then, but the ground based software indicated that a tank pressure of 133 psia would be reached as the fuel hit 0 lbs. This was not the only odd output from the software. Maneuvers were allowed to be planned even after reaching 0 lbs of fuel remaining. The software even printed out a negative amount of fuel remaining. Although we found these things alarming (and they haunted us later on), the ultimate objective forced the MCT to continue with the plan and assume the ground software would accurately generate maneuvers with low or negative fuel indicated.

The Orbit Analysts performed one more study before taking the results to the Air Force. This study was to determine the best attitude in which to leave the satellite. From past experience, the MCT has been asked to turn off satellites with no regard to the spacecraft orientation. On a couple of occasions, vehicles were attempted to be turned on 1 to 2 years later. On all occasions it was impossible to turn on the vehicles due to their orientations. So, this time it was decided to try and leave SCATHA in an attitude that would leave it secure, but allow it to be possibly turned on in the future if needed. The attitude chosen was one that put the spin axis parallel to the Earth's polar axis. The natural precession of the satellite's spin axis about the vector parallel to the Earth's polar axis causes the sun angle to sinusoidally walk further from normality to the sun-line (ref section 3.2 and figure 3-4). With this choice of final attitude, the spin axis would not precess and the sun angle would constantly (and sinusoidally) walk between -23.5 degrees non-normality to sun line and +23.5 degrees non-normality to the sun line. These sun angles would provide SCATHA enough power to turn on in the future if needed . Fuel depletion and achievement of the final attitude for this plan would not occur until April 6th, if maneuvers were performed every three days. However, there appeared to be no viable, safe, alternative plan.

Unfortunately, the plan did have some problems. The maneuver sequence would be planned with attitudes that were propagated from the last determination in May 1990, which was when the last viable attitude data was collected. Attitude prediction accuracy studies had not been done for so long a span. However, sun angle predictions from the last good attitude and the sun angle observed were within a couple of degrees of each other. While this certainly didn't imply that the predicted attitude was within two degrees of actual attitude (since an infinite number of attitudes have the same sun angle), it was probable that the attitude estimate was useable. Further confirmation of this fact came from new prediction accuracy studies. Estimates were made by predicting old attitude states six months or more ahead (no maneuvers included) and comparing them with actual determined attitudes at that time. For nearly all of the spans covered, the error of prediction was less than 1.0 degree when predicting for 200 days. Figure 4-1 shows a representative sample of predicted and determined attitudes.

Attitude Epoch	Determined (Deg)		*Predicted (Deg)		Total Angular
	SARA	SADEC	SARA	SADEC	Error (Deg)
08 Jan 88 0000Z	257.865	68.094			
08 Jul 88 0000Z	223.775	68.173	224.635	67.794	0.4976
11 Aug 88 0000Z	216.683	68.195	218.428	67.738	0.7980

* Rates Used: SARA rate = -.18258 deg/day; SADEC rate = -.0016502 deg/day

Figure 4-1. Predicted and Determined SARA and SADEC

While these predicts worked well for times when there were no attitude maneuvers, they could not be solely relied on for times when attitude maneuvers were being performed. Each maneuver introduces a small uncertainty in the predicted attitude after the maneuver due mostly to spacecraft nutation but also to imperfect knowledge of thruster efficiencies and non-perfect attitude rates. It was readily apparent when the maneuvers started that some method of estimating the vehicle attitude would be needed.

As it turned out, the Orbit Analysts had already been working on a simpler version of generic attitude determination software. This method is based on the Earth Midscan Rotation Angle / Sun Angle method found in Wertz "Spacecraft Attitude Determination and Control". It requires only one sun sensor (DSAS) measurement and one steerable horizon crossing indicator (SHCI) leading edge-trailing edge pair collected within the same spin period. Using this data, as well as vehicle and sun position, the method produces four possible choices for the attitude (the intersection of two cones). Two of these values can be immediately eliminated since they are physically impossible. The user can then eliminate the remaining bad attitude by comparison with an apriori approximation of the true attitude. While this method is fairly easy to perform (once you've gathered all the data), it's accuracy is very much affected by variations in spin period and measured sun angle. Unfortunately, variation in spin period and out of plane nutation were common during this time and so determined attitudes even from data in the same pass were often not consistent. Sometimes averaging a few of the determined attitudes assisted in getting a better attitude state.

4.3 Summary of Termination Phase Maneuvers

The final phase of SCATHA's mission life covered the span from 01 Jan 91 through 24 May 91. During this time, 48 precession maneuvers were performed 45 of which were 20 degrees in size while the others were less. Figure 4-2 provides a summary of fuel usage for the final maneuvers. As the chart shows, things did not go as anticipated. The predicted end date of April 6th passed without depleting the fuel. The software continued to operate accurately even though it was using "negative fuel". Also, the sequence of maneuvers was disrupted at times and new requirements were given to the MCT as the maneuvers progressed. The remainder of section 4 is devoted to explaining how events differed from the original schedule along with an analysis and explanation of the gathered data.

Number of Maneuvers	48
Initial Fuel	2.3425 lbs
Final Fuel (Apparent)	-1.0523 lbs
Total Fuel Used	3.3953 lbs
Average Time Between Maneuvers	3.0 days
Average Fuel Used per Maneuver	0.0707

Figure 4-2. Summary of Termination Phase Maneuvers

4.4 Maneuver Schedule and Analysis

The first maneuver was executed as planned on 4 Jan 1991. The next maneuver was to be performed three days later, but was postponed. Due to reduced tracking supports covering only the perigee half of the orbit, the Orbit Analysts had a very difficult time determining the vehicle's orbit. Predictions with a newly determined orbit the day prior to the next maneuver were very poor so the maneuver was postponed until January 9th when the orbit was better defined. The next five maneuvers went as planned through January 21 (9th, 12th, 15th, 18th, and 21st). At that point, the lack of tracking data caused an inability to obtain lockup on the vehicle for a sizeable portion of the pass. Clearly, the lack of good tracking data and inaccuracies in maneuver modeling were making maneuver planning and operations difficult. Also, at this time, there was still no ability to determine the post maneuver attitudes. For the next two weeks the Orbit Analysts worked at determining the actual orbit based on increased tracking data. At the end of the two weeks, it was decided that the increased number of passes needed for orbit determination accuracy couldn't be justified for a vehicle that was being phased out. Vectors (2 Line Mean Element Sets) for SCATHA were sent from the NORAD (North American Air Defense Command) Space Surveillance Center on a daily basis. This solved the problem for the remainder of the mission.

Maneuvers resumed on February 2nd. However, there was a new twist to the maneuvers. One of the experimenters requested that when doing the maneuvers, the MCT try to keep the sun angle at a 100 degrees ± 2.0 degrees. Until this point, the only restriction on maneuvers was that they be 20 degrees in size and within 15 degrees of the sun line. However, this request was met as well as all other requirements. The 20 degree maneuvers continued approximately every three days until April 16 when the software indicated that the fuel had dipped below 0.1 lbs. At this point the spin axis was very near parallel to the Earth's polar axis. Smaller maneuvers were decided to be used to deplete the remaining fuel but not stray far from the desired final attitude. After two 6 degree maneuvers on the 16th and 18th of April, it was realized that we were still 5 psia above blowdown pressure. Also, the Orbit Analyst attitude determination program was now complete, and it became apparent that the maneuvers were reaching very near the full arc length (although not necessarily to the right target).

At this point there was confirmation that the maneuver software or database definitely had a problem. However, at that time it wasn't known what was wrong. Investigations into the problem began and the twenty degree maneuvers continued again since there was clearly more fuel on-board than the ground software indicated and the Air Force was pushing to quickly turn-off the satellite.The 20 degree maneuvers continued every Tuesday, Thursday, and Saturday until the final maneuver on May 24. At this point, the maneuvers were still executing efficiently (not expected at such impossible propellant levels), but the MCT was asked to discontinue maneuvers anyway. The final maneuver was only 9.1 degrees in arc length, putting the spin axis as near as could be estimated to parallel to the Earth's polar axis.

4.5 Fuel Consumption / Depletion Analysis

It had been hoped to carefully analyze the propulsion system performance as the fuel was depleted. Careful analysis of the changing thruster efficiencies and an accurate measure of actual blowdown pressure could have been invaluable for future missions. However, at this time the CSTC was in the final stages of the process of converting from an old computer system to a new brand new one. The telemetry processing and attitude determination software for SCATHA was hosted on the old system. Also, SCATHA was one of the

few programs with software on this system and its mission was considered to be finished by the Air Force. So, termination of the mission as soon as possible was a very high priority. It was assumed that there was very little fuel remaining in the tanks and so the vehicle was considered "safe" enough to turn off.

Although analysis of the propulsion system could not be performed at this time, regular monitoring of propulsion system parameters was done during the final phase. Predicted and actual telemetry values were very close. Figure 4-3 shows tank pressure for the final months before turnoff. Occasional discontinuities in calculated pressure values are due to software database updates with an actual telemetered value. The Orbit Analysts made changes at these points in order to more accurately reflect the on-board pressure and temperature. With these periodic updates, the ground based software performed accurate modeling of the actual telemetered values.

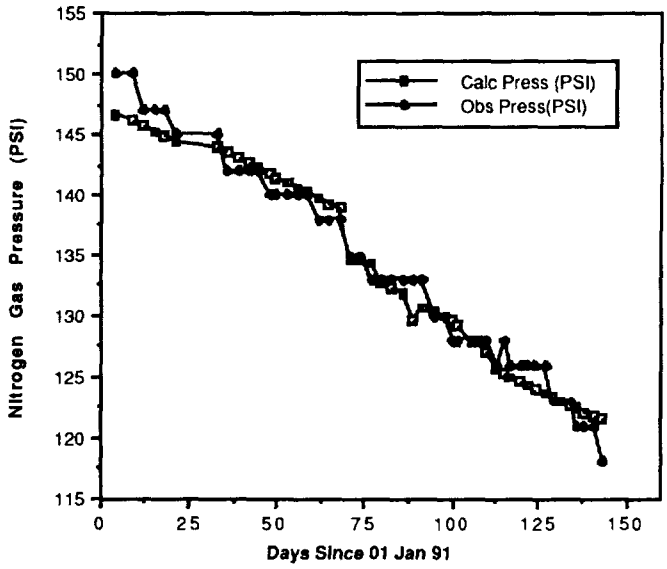

Figure 4-3. Observed and Calculated Nitrogen Tank Pressure vs Time

Unfortunately the problem of negative fuel went unsolved until after SCATHA had been terminated. As it turns out, the error lies in two places: the software and the database. The program that generated the maneuver calls a subroutine to actually calculate the maneuver and the amount of fuel necessary. The amount of fuel necessary for the maneuver was passed to the main program but the newly calculated pre-maneuver fuel mass was not. The main program then updates the latest stored value of fuel remaining by subtracting the amount of fuel needed for the maneuver. This would not be a problem unless the stored initial propellant mass was incorrect. Unfortunately, this value was incorrectly updated during the first week or so of the mission (back in 1979). The value input was approximately three lbs too low. The error was further compounded when new tank temperature and pressures from observed telemetry were manually input. While the calculated starting mass was accurate, the initial stored mass was incorrect. Since the stored initial mass is never really used for anything but display, it was never noticed as being a problem especially since all maneuvers appeared to reach the target attitude (within attitude determination accuracies). Maneuvers were done with the mass calculated from input data, not from the displayed mass.

With the error discovered, it is then appropriate to figure out how much fuel was really left in the tanks. Quick calculation shows there was nearly 2.5 lbs of fuel remaining on board SCATHA. It can be seen that thirty-three 20 degree maneuvers would have been necessary to use all the fuel remaining (blowdown pressure and thruster efficiencies permitting). If maneuvers were continued at the same rate, three times per

week, the fuel would would have been depleted by August 10, 1991. This probably would be completed at least 2-3 weeks before due to blowdown pressure being reached.

4.6 Termination Phase Nutation Analysis

It was very difficult to get a true measure of the out-of-plane nutation and nearly impossible to get any measure of in-plane nutation during this phase. As mentioned in section 4.1, consistent telemetry data collection was difficult due to degraded transmitter performance. It was a tedious process to manually go through the telemetry, find consecutive sun angle readings, and calculate out-of-plane nutation. However, data was calculated for all available telemetry and the maximum values (among all four sun sensors) per pass were plotted in the graph show in figure 4-4.

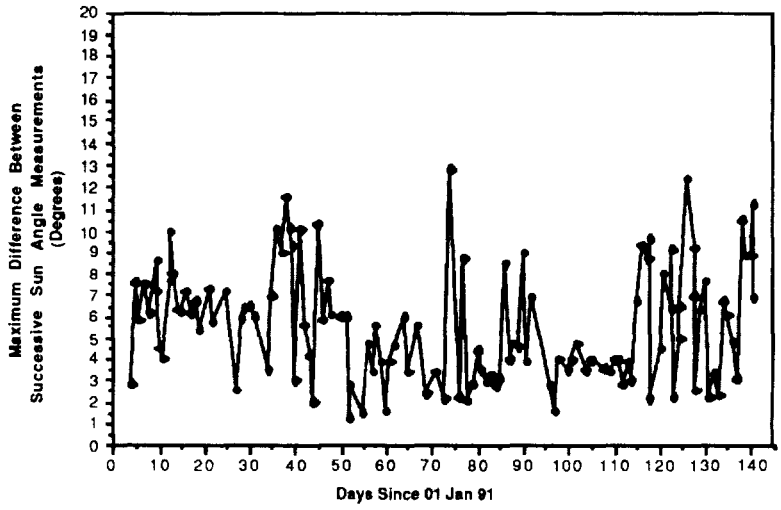

Figure 4-4. Maximum Sun Angle Difference

It is important to note that quality data was gathered for only 2 1/2 hours a day at most. Even if 2 1/2 hours of good data was gathered every day (1 hour was close to reality) for the entire termination phase (144 days), then only 10% of all possible SCATHA data was available for examination. Thus the graph in figure 4-4 shows the smallest that the maximum nutation could be during each day of the final termination phase. Clearly, there was a large amount of nutation throughout the entire phase.

In-plane nutation turned out to be extremely difficult to calculate accurately since the instantaneous spin rate was not output in telemetry and output sun crossing times were rounded to the nearest second. For this reason the in-plane nutation was not computed and plotted for this phase. At times, however, that successive spin rate calculations using successive sun crossing times (for a particular DSAS) were as much as 2 seconds off. This indicates a possible 12 degree in-plane nutation error.

4.7 Determined Attitudes and Maneuver Performance

Due to the nutation and lack of consistent telemetry information, attitude determination during this phase was difficult and at times required many attempts. The following chart (figure 4-5) gives a comparison of the determined sun angle (from the determined attitude) and the observed sun angle during the last half of the termination phase. The data in figure 4-5 does not prove that the determined attitude was actually quite close to the observed, since there are an infinite number of attitudes with the same sun angle. Still, it seems appropriate to assume that the predicted attitude is well within 5 degrees of the actual attitude, since the above data is consistently within 3 degrees at a wide variety of attitudes.

Pre-Maneuver Date (1991)	Determined Sun Angle(Deg)	Observed Sun Angle (Deg)
16 Apr	101.98	103
20 Apr	105.37	103
23 Apr	103.76	102
25 Apr	97.76	95
27 Apr	114.73	113
30 Apr	95.86	95
2 May	114.11	113
4 May	98.79	99
7 May	116.28	113
14 May	93.15	95
16 May	112.82	111
18 May	105.97	107
21 May	119.49	117
23 May	105.62	103

Figure 4-5. Determined and Observed Sun Angle

Maneuver performance is very difficult to analyze for the termination phase of the mission. From 1 Jan 91 to 16 Apr 91 there was no method of attitude determination following the maneuvers. During this time, there were three basic criteria for determining whether to continue with maneuvers:

(1) Nutation must be consistently less than 10 degrees on the pass prior to the maneuver.
(2) The Sun angle must be within 3 degrees of the predicted Sun angle.
(3) The orbit must be good enough to acquire the vehicle.

For this time span, the maneuvers had to be stopped twice. Both times were due to poor orbit predictions. The other two criteria were violated only once, the exception being the 21 degree maneuver at the end of the span. Since the Sun angle was consistently within 3 degrees of the observed through a wide variety of attitudes, it seemed very probable that the attitude was within 3-5 degrees of the actual attitude. The difference between the determined and predicted Sun angles during the termination phase are shown in figure 4-6.

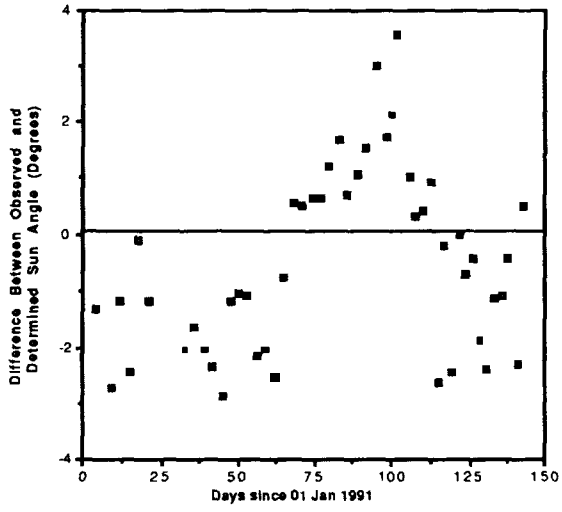

Figure 4-6. Difference Between Observed and Predicted Sun Angle

By April 20th, the in-house attitude software was completed and checked out. A rough attitude determination, using this software, was now possible before most of the remaining attitude maneuvers. For the maneuvers from April 20th to May 23rd, the difference in observed and predicted Sun angles (see figure 4-6) as well as the total angular error between attitude fits could be determined. The total angular errors are shown in Figure 4-7

Maneuver Date (1991)	Angular Error Between Predicted and Determined (Deg)
18 Apr	21.067
20 Apr	3.900
23 Apr	19.223
25 Apr	4.949
27 Apr	0.611
30 Apr	5.174
2 May	2.385
4 May	7.101
11 May	5.034
14 May	10.766
16 May	2.490
18 May	4.979
21 May	7.650

Figure 4-7. Angular Error Between Predicted and Determined Post-maneuver Attitudes

The results are mixed. While the differences between predicted and observed sun angles are consistently within 3 degrees of the actual (exception in the case of the largest maneuver), the angular error between determined (post-maneuver) and predicted attitude was quite variable. The largest errors are most likely due tc selecting the image solution rather than the correct solution. The large nutation also contributes to attitude determination error. Most of the errors can be explained this way. These solutions seemed reasonable considering there was so little consistent data and so much nutation.

5. SUMMARY

SCATHA presented the MCT with several challenges over it's 12 year life with the termination phase being the most demanding. A summary of the MCT's activity and findings follow:

1) The fuel depletion sequence was only partially successful. Most of the fuel was depleted but an estimated 2.5 lbs still remains on-board.

2) The maneuver planning and execution were severely restrained by SCATHA's flexible booms that spanned 100 meters.

3) Undamped nutation became a problem only after the spin-up maneuvers in the new ecliptic normal attitude. The undamped nutation required attitude maneuvers be spaced at least 3 days apart, dramatically hindered accurate attitude determination, and made precession maneuvers potentially very inaccurate.

4) A long standing error in the software and database was discovered. The error remained hidden due in large part to the high degree of accuracy and efficiency of all maneuvers performed. Correction of this error provided the basis for estimating the on-board fuel left on SCATHA after mission termination.

5) Attitude determination software, created in the final days of the mission, worked well at providing a rough attitude despite the nutation.

6) The series of 48 attitude maneuvers during the termination phase appeared nominal even though telemetry was scarce and attitude determination rough.

7) The final attitude should leave SCATHA in an attitude that will provide enough power so there is a good chance of turning on the vehicle in the future.

Bibliography

TM-(L)-5692/10/02 Conner, G. R., Davidson, D. A., Kyalla, J. P., 15 July 1977. *STP P78-2 ATTITUDE DETERMINATION AT THE STC (NADSTC) COMPUTER PROGRAM DEVELOPMENT SPECIFICATION, (Part I),* System Development Corporation.

TM-(L)-5692/10/02 Kyalla, J. P., Auer, P. J., 1 September 1977. *STP P78-2 ATTITUDE DETERMINATION AT THE STC (NADSTC) COMPUTER PROGRAM DEVELOPMENT SPECIFICATION, (Part II),* System Development Corporation.

TM-(L)-5551/270/01, 17 September 1979. *STP P78-2 ATTITUDE DETERMINATION AT THE STC (NADSTC) THE STC (NADSTC) USERS MANUAL*, System Development Corporation.

90-06 Directorate of Test Operations, 15 March 1990, Onizuka Air Force Base, California,*TEST OPERATIONS ORDER (DSM),* Consolidated Space Test Center.

June 1991,*THE SCATHA MISSION, THE ENGINEERING ANALYSIS BEHIND REALTIME OPERATIONS* , Lockheed Technical Operations Company.

Wertz, J.R., *SPACECRAFT ATTITUDE DETERMINATION AND CONTROL*, D. Reidel Publishing, 1985.

ACCURATE ATTITUDE DETERMINATION OF THE LACE SATELLITE

by

M.F. Miglin‡, R.E. Campion*, P.J. Lemos*, and T. Tran*

ABSTRACT

The Low-power Atmospheric Compensation Experiment (LACE) satellite, launched in February 1990 by the Naval Research Laboratory, uses a magnetic damper on a gravity gradient boom and a momentum wheel with its axis perpendicular to the plane of the orbit to stabilize and maintain its attitude. Satellite attitude is determined using three types of sensors: a conical Earth scanner, a set of sun sensors, and a magnetometer. The Ultraviolet Plume Instrument (UVPI), on board LACE, consists of two intensified CCD cameras and a gimballed pointing mirror. The primary purpose of the UVPI is to image rocket plumes from space in the ultraviolet and visible wavelengths. Secondary objectives include imaging stars, atmospheric phenomena, and ground targets. The problem facing the UVPI experimenters is that the sensitivity of the LACE satellite attitude sensors is not always adequate to correctly point the UVPI cameras. Our solution is to point the UVPI cameras at known targets and use the information thus gained to improve attitude measurements. This paper describes the three methods developed to determine improved attitude values using the UVPI for both real-time operations and post observation analysis.

INTRODUCTION

LACE Satellite Description

The LACE satellite was designed and built by the Naval Research Laboratory (NRL) in Washington, DC. The satellite was launched on February 14, 1990 into a nearly circular orbit with an altitude of 541 km and a 43° inclination. It has no orbit adjustment capability. The spacecraft weighs 1440 kg. Its body is basically box shaped, 1.2 m by 1.2 m, and 2.4 m high. Gravity gradient stabilization is provided by a 45.7 m retractable boom, emerging from the top of the spacecraft, with a 91 kg tip mass including a magnetic damper. Foldout panels on the top and bottom support the solar arrays and sensor arrays respectively. Figure 1 is a drawing of the LACE satellite. The satellite's primary purpose is to provide an orbiting instrumented target board capable of measuring the effects of active compensation of a ground based laser beam propagated through the atmosphere. The LACE spacecraft was designed to support the experiment for 30 months. NRL operates a fixed and two transportable ground stations to communicate with, and control the satellite. Built by NRL, each transportable ground station is housed in two eighteen foot truck trailers. One trailer houses the telemetry, command and radio equipment, and the other provides an uninterruptable power supply and work area. The third ground station is permanently located in Maryland. These stations provide all the command and communication links for the LACE spacecraft.

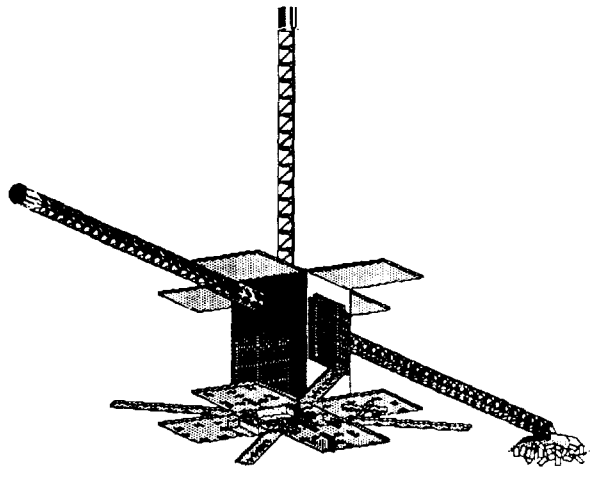

Figure 1
LACE Spacecraft

‡ Barrios Technology Inc. ; * Bendix Field Engineering Corp.

History and Statement of the Problem

When the LACE spacecraft design was complete and major subsystems, such as structure, power, and attitude control, were being fabricated and tested, an additional experiment was proposed for integration into the spacecraft. This new experiment was the Ultraviolet Plume Instrument, or the UVPI. The purpose of the UVPI is to point to, acquire, and actively track the plume of a rocket launched from the Earth's surface, and collect images of the plume in the ultraviolet wavelengths. The UVPI was accepted for integration into the LACE spacecraft with the ground rule that it have minimum impact on the already existing LACE design. This meant minimum volume, weight, power, telemetry, and command usage. It also meant no change to the spacecraft's proposed orbit, nor to the attitude control, radio frequency, or navigation subsystems, and no operational impact on the primary mission of the satellite. To fulfill its goal, the UVPI was designed with an independently pointable camera with a field of view of about 2°. The LACE spacecraft was designed to maintain one side pointing to nadir to within ±3° and with an attitude knowledge of about ±1°. Initial UVPI pointing error analysis showed that the spacecraft attitude was the dominant source of pointing error, followed by spacecraft and target position uncertainty. The fundamental problem, then, was to be able to accurately point the UVPI when it is aboard a space platform with inadequately certain attitude. The solution that was developed during the operational planning was to use the UVPI imaging and precision pointing capability to augment the spacecraft's attitude sensor system. Using stellar and Earth fixed targets, the spacecraft attitude, both realtime and reconstructed, could be significantly improved. Three techniques to improve attitude knowledge were developed. These techniques became known as Yaw Scan, Beacon Tracking, and Star Pattern. The purpose of this paper is to describe these attitude determination techniques and show the results obtained when they were applied.

Description of the UVPI

The UVPI is mounted within the satellite and views through an aperture in the Earth oriented panel. By use of a gimballed mirror, the UVPI has a field of regard of a 50° half-angle cone about the satellite's nadir. When the UVPI is not in use, a door covers the aperture. Attached to the inside of this door is a flat mirror which, when the door is opened part way, allows the UVPI cameras to view celestial objects near the negative orbit normal or the Earth's limb. On-orbit photometric calibration is accomplished by observing stars with a known spectral signature. The UVPI has two cameras which share a common telescope and pointing system. The tracker camera has a field of view of 2.0° by 2.6°. It is sensitive in the UV and part of the blue portion of the visible spectrum, from 250 to 450 nm. The primary purpose of the tracker camera is to provide images to a closed loop tracking system. The plume camera has a field of view of 0.18° by 0.14°. It has four selectable filters and is sensitive in the UV from 195 nm to 350 nm. Open loop pointing is performed by providing, for each axis of the gimballed mirror, a polynomial function that is evaluated by an onboard computer which drives the gimbals. These polynomials are generated on the ground and transmitted the instrument as command data. When the UVPI tracker electronics detects a target in the tracker camera field of view, the centroid of the target image is computed. In addition, if the UVPI is commanded to do so, the gimballed mirror moves so as to bring the target image to the center of the plume camera field of view. This is referred to as closed loop tracking. If, during closed loop tracking, the target is lost, the UVPI will continue pointing by extrapolating the most recent gimbal readings, or revert to the polynomial pointing functions. If a target reappears, the UVPI will reacquire and track the target. Should the tracker electronics fail to identify a target, a method of manually assisted tracking is available. An operator viewing the telemetry images at a ground station can apply a vernier adjustment, using a joystick, to the gimbal position or velocity. In this way, targets of interest which are low contrast or are obscured by clutter, such as clouds, can be brought into the plume camera's field of view. This method of joystick tracking was implemented while the spacecraft was in orbit.

All the necessary commands and pointing functions can be stored onboard the spacecraft to perform one or several complete observations over remote parts of the Earth. The resulting image data is recorded by a 3 1/2 minute tape recorder. As of this date, four rockets launched from the Earth's surface have been tracked and imaged by the UVPI.

LACE Attitude Determination and Control

The attitude control system used for LACE was designed to meet the requirements of the primary experiment. This experiment required one side of the spacecraft to point toward nadir with a ±3° accuracy. In addition, it was required that a leading, retractable boom remain within ±2° of the orbit plane (see figure 1 for a drawing of the spacecraft). To meet these needs, a gravity gradient system was used. This system consists of a boom with a 92 kg tip mass, rising from the top of the spacecraft. A magnetic damper makes up part of the tip mass. A momentum wheel with its axis perpendicular to the orbit plane is used for yaw stiffening.

Three types of sensors are employed to make attitude measurements. These are: A five eye sun sensor system which provides the direction to the sun from the spacecraft, a conical Earth scanner which identifies the nadir direction by sensing the Earth's limb, and a magnetometer which measures the spacecraft's orientation with respect to the Earth's magnetic field. These sensors were selected to meet the requirement that the spacecraft's attitude be determined to ±1° after post observation processing. In practice, the conical Earth scanner alone provided spacecraft roll and pitch measurements accurate to about ±0.5°. The yaw, however, remained uncertain to about ±1°. In addition, the sun sensors provided no data during nighttime operations when most of the UVPI rocket target and stellar target

observations were made. Figure 2 is a plot of typical spacecraft attitude for two complete spacecraft orbits. Although roll and pitch have a relatively smooth and predictable behavior, instrument calibration and alignment contribute to measurement uncertainty. The yaw component shows large (~1°) discontinuities when the spacecraft transitions from light to dark. The sinusoidal oscillation pattern of the spacecraft attitude is a typical feature of gravity gradient stabilized systems. The dominant period of these oscillations is equal to the spacecraft orbital period.

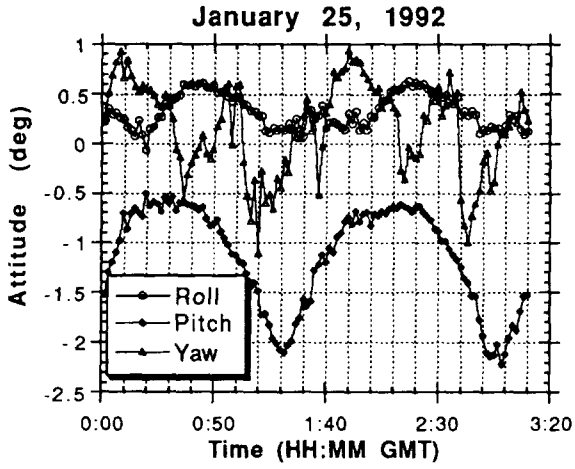

Figure 2.
Typical Spacecraft Attitude Values

The attitude sensors can be sampled at various rates and the data transmitted to the ground station in real time, or stored onboard for later transmission. Typically, real-time data is sampled about once per second and the non-realtime data is sampled and stored at a rate of once per 100 seconds. The QUaternion ESTimator (QUEST) program is used to process the measurements (both realtime and non-realtime) into attitude estimates. In addition the Real Time Attitude Computation (RTAC) program is also used to estimate the attitude using realtime measurements.

TECHNIQUES AND APPLICATIONS

Yaw Scan of Star

Description of Method

Since the uncertainty of the spacecraft's yaw was about ±1°, about the distance form the center to the edge of tracker camera field of view, a method of searching for targets was developed. To aid in locating stellar targets, a search pattern was superimposed onto the open-loop pointing function. This search pattern was a sinusoidal scan in the spacecraft's yaw direction. It typically had an amplitude of about 1° and a period of about 16 seconds. An operator, viewing the downlinked images in real time, observes the target entering the field of view. Noting the exact time when the target crossed the center line of the tracker camera, the operator, using ground based computer programs, can compute the spacecraft's yaw value and re-compute the UVPI pointing polynomials, transmit them, and center the target in the tracker camera. This method worked particularly well for stellar objects. The UVPI can only view stellar objects near the negative orbit normal direction. With this geometry, the errors in spacecraft roll and pitch have little effect on the image. The error in yaw, however, is nearly coincident to the error in pointing. To help the operator identify targets, stars were selected which were relatively bright in the blue and UV, and which were isolated by a few degrees from other bright objects. In addition, an estimate of the star's intensity, as seen in the downlinked image, was made so the operator was confident that the correct star was in view.

Application

Once a value for yaw was determined using the star scanning technique, it could be used as input to any UVPI pointing function in the next few minutes. Since the spacecraft oscillates in the yaw direction with an amplitude of about 0.4° and a period of about 95 minutes, the maximum rate of change of the yaw value would be about 0.03°/min. Over the next 10 minutes the change in yaw would be less than 0.3°; comparable to the uncertainty in the roll and pitch values. The roll and pitch values used to compute the UVPI pointing functions were determined from the spacecraft attitude sensors.

Results

Table 1 lists the results of determining the yaw on 23 occasions using the yaw scanning technique. The data spans a little more than one year of instrument operation. The table shows the yaw value which was determined by the image scan method and by the spacecraft attitude sensing system. What is evident from these data is that the peak-to-peak oscillation of the yaw is much less than what is indicated by the attitude sensors alone. In fact, the total variation in yaw based on the scanning technique, from 0.2° to 1.0°, is less than the uncertainty of ±1° ascribed to the attitude sensor measurements. Recent stellar observations which used a fixed yaw value of 0.3° resulted in good initial pointing and did not require any pointing adjustment based on the location of the target star in the image field of view.

Beacon Tracking

Description of Method

The roll and pitch attitude measurements, provided primarily by the conical Earth scanner, were thought to be precise (i.e., repeatable) to within about 0.25°. Figure 2 shows very consistent roll and pitch measurements. The uncertainty of 0.5° assigned to roll and pitch were due mainly to biases or offsets in the Earth scanner and alignment of the UVPI to the attitude reference frame. By determining accurate attitude values using the UVPI alone, independent of the spacecraft attitude measuring system, any mutual offset or misalignment could be measured. This measured offset could then be applied to improve spacecraft attitude measurements.

Table I
Comparison of the Yaw as Determined by the UVPI Star Scan and by the Spacecraft Attitude Sensors

Date	Scanned with UVPI	Measured by Spacecraft	Diff.
DD-MM-YY	(deg)	(deg)	(deg)
11-11-90	0.88	0.16	-0.72
12-11-90	1.00	1.08	0.08
16-12-90	0.24	-0.40	-0.63
18-12-90	0.41	-0.35	-0.76
19-12-90	0.47	1.02	0.55
20-12-90	0.41	-0.08	-0.49
13-2-91	0.26	-0.60	-0.86
14-2-91	0.36	-0.67	-1.03
15-2-91	0.76	1.07	0.31
14-4-91	0.64	-0.71	-1.35
22-4-91	0.64	0.72	0.08
23-4-91	0.47	0.98	0.51
24-4-91	0.65	0.74	0.09
25-4-91	0.57	0.78	0.21
13-6-91	0.43	0.84	0.41
14-6-91	0.81	0.79	-0.02
8-8-91	0.29	0.87	0.58
9-8-91	0.31	1.11	0.80
14-9-91	0.28	-0.40	-0.68
16-11-91	0.21	-0.85	-1.07
18-11-91	0.22	-0.84	-1.06
19-11-91	0.22	-0.78	-1.01
9-1-92	0.60	-0.92	-1.52
Average	0.48	0.15	-0.33
Std.	0.23	0.78	0.70
Max.	1.00	1.11	0.80
Min.	0.21	-0.92	-1.52

The approach used, was to have the UVPI track a fixed, known location on the surface of the Earth. The UVPI's gimballed pointing mirror provided a sequence of unit vectors pointing to the target in the body frame of the spacecraft. For each measurement there was a corresponding computed unit vector pointing from the spacecraft to the target in the local reference, or attitude frame. The difference between these two unit vectors was viewed as the attitude. A more detailed description of this method is provided in Appendix A. Since the spacecraft's attitude in each axis was always less than about ±3°, and oscillates at orbital periods (about 95 minutes), it could be assumed that the spacecraft attitude did not change over the solution period, which was typically 5 seconds.

A portable ground beacon was used as the target for the UVPI. The beacon consists of four 6 kW metal halide bulbs, each with its own power supply. About 10% of the bulbs output is in the bandwidth of the UVPI tracker camera which, at night, provides a target bright enough for the UVPI to track. This beacon was used for various instrument calibration and tracking tests, and has been located at: Southern Maryland; Wallops Is., Virginia; Titusville, Florida; Vandenberg AFB, California; Table Mt., California; and Hawaii.

Results

Table 2 shows the results of the attitude determination using seven different UVPI ground beacon observations. The table also shows the attitude measured by the spacecraft attitude sensing system at the same time, and the difference between the two values. A bias of 0.7° is clearly evident in the roll measurements. A standard deviation of the differences in roll values of only 0.1° indicates that the roll measurements made by the spacecraft attitude sensing system are quite accurate once the bias is accounted for. The pitch parameter shows no systematic offset. It is known that the spacecraft has a natural pitch bias due to an offset of the spacecraft center of mass. The calculated yaw values show an average of 0.4° with a standard deviation of 0.2°. This is consistent with the previous results where the yaw was calculated using the star scanning technique. The difference between the calculated yaw and the yaw measured by the spacecraft attitude sensors is too uncertain to estimate any possible offset.

The seven observations used for this analysis tracked the ground beacon target from 20 seconds to over 2 minutes. Attitude values were calculated using 5 second data segments. This resulted in a sequence of solutions spanning the observation interval. Figure 3 is a plot of the sequence of attitude solutions for one of these observations. This plot, typical of the seven cases, shows a larger variation in each attitude component than could be expected from the natural oscillations of the spacecraft. From the observed amplitudes of oscillation in each axis, 0.25°, 0.9°, and 0.3° for roll, pitch, and yaw, the maximum rates of change are $2\pi A/P$, where A is the amplitude and P is the period of about 95 minutes. This gives maximum rates of change of 0.02°/min, 0.06°/min, and 0.02°/ min for roll, pitch, and yaw which are clearly smaller than the calculated values shown in Figure 3.

Table II
Comparison of Attitude Calculated Using UVPI Tracking Beacon and Measured by Spacecraft Attitude Sensing System

Date DD-MMM-YY	Calculated Using UVPI Beacon Track Roll (deg)	Pitch (deg)	Yaw (deg)	Measured Using S/C Attitude Sensors Roll (deg)	Pitch (deg)	Yaw (deg)	Difference (Measured - Calculated) Roll (deg)	Pitch (deg)	Yaw (deg)
	-0.25	0.10	0.29	0.41	-0.25	-0.32	0.66	-0.35	-0.61
22-Apr-91	-0.18	-0.44	0.25	0.49	-0.75	0.72	0.67	-0.31	0.47
24-Apr-91	-0.27	-0.68	0.64	0.47	-0.76	0.74	0.74	-0.09	0.10
25-Apr-91	-0.04	-0.66	0.43	0.44	-0.77	0.78	0.48	-0.11	0.35
13-Jun-91	-0.37	-0.36	-0.02	0.45	-0.26	0.84	0.82	0.10	0.86
14-Jun-91	-0.19	-0.59	0.50	0.40	-0.52	0.79	0.60	0.07	0.28
11-Nov-90	-0.28	-1.09	0.29	0.55	-0.58	0.97	0.83	0.51	0.67
					Average		0.69	-0.02	0.30
					Std. Dev		0.12	0.29	0.47

To determine if the large variations in the calculated attitude parameters could be attributed to errors in other model parameters, a sensitivity analysis was performed. Using simulated data, errors were introduced one at a time in selected model parameters. These parameters and errors were: 0.5 km in the North and East components of the location of the ground beacon, 1.5 km in the along track direction of the spacecraft, and 0.01° in the azimuth and elevation angle of the UVPI gimballed mirror. The ground beacon was located at various sites in the continental US. Its location was determined, for each of these locations, either by estimates from the proximity to known geodetic locations such as fixed tracking antennas, or from a Global Positioning System receiver. The spacecraft position is obtained from the Naval Center for Space Surveillance (NAVSPASUR) in Dalhgren Virginia, and is accurate to within 1.5 km during the time period of ground beacon tracking. These orbit elements are provided especially for UVPI operations and use special propagation models to attain high accuracy. The pointing error due to the UVPI gimballed mirror was assumed to be two times the readout of the least significant bit in the telemetry. Gimbal measurement noise, estimated from gimbal readings and target image centroiding, is estimated to be about 0.002°. Figures 5, 6, and 7 are the results of this analysis for roll, pitch, and yaw respectively. Comparing these results to the calculated results in Figure 3 shows that none of the examined error sources are sufficient to account for the wide variation in the calculated attitude.

Verification

Two methods of verification were used. First, images of the ground beacon, where the UVPI was pointing but not tracking, were adjusted by 0.7° in the roll direction during post observation processing. Figure 7 shows several observation results, plotting the original location along with the location after an adjustment for roll bias. In each case the adjustment resulted in the ground beacon target being moved closer to the center of the UVPI field of view (FOV). The second method used was to apply the 0.7° roll bias to the UVPI pointing functions when attempting to acquire the ground beacon target. Previously, the approach had been to perform a circular scan of about 0.5° about the nominal pointing function to ensure that, at some point during the scan, the target would enter the FOV and could be identified and acquired. Recent operations have applied the roll bias identified in this analysis and did not apply a scan pattern. In all cases where this was done, the target beacon fell well within the camera's FOV.

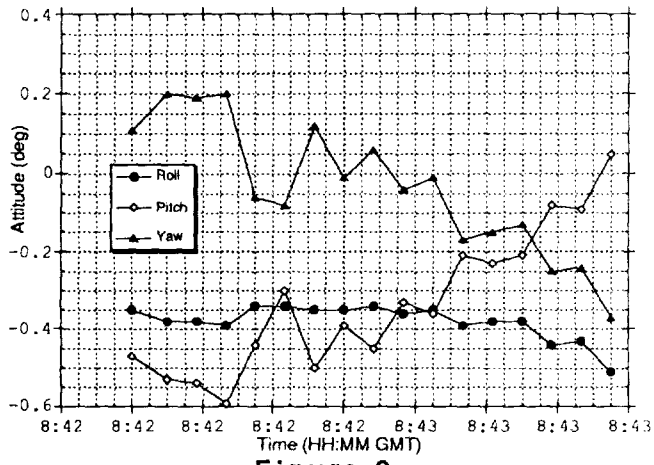

Figure 3
Calculated Attitude Values using Beacon Tracking. June 13, 1991

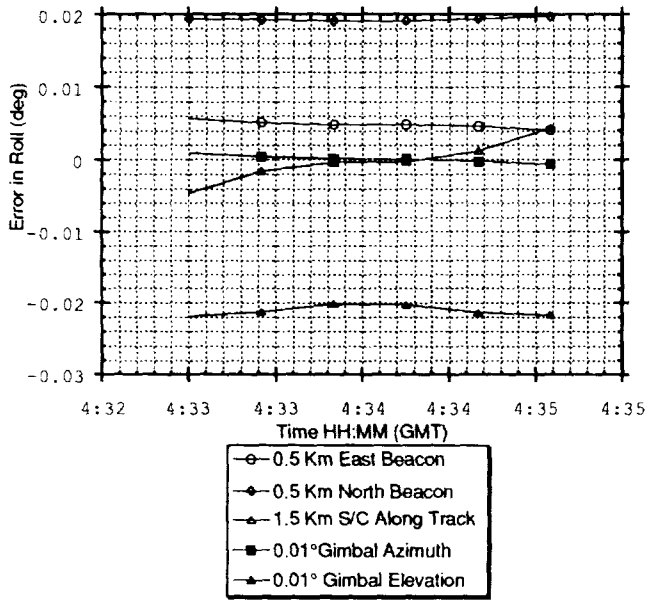

Figure 4
Sensitivity of the Calculated Roll to Model Parameters and Legend for Figures 4, 5, and 6

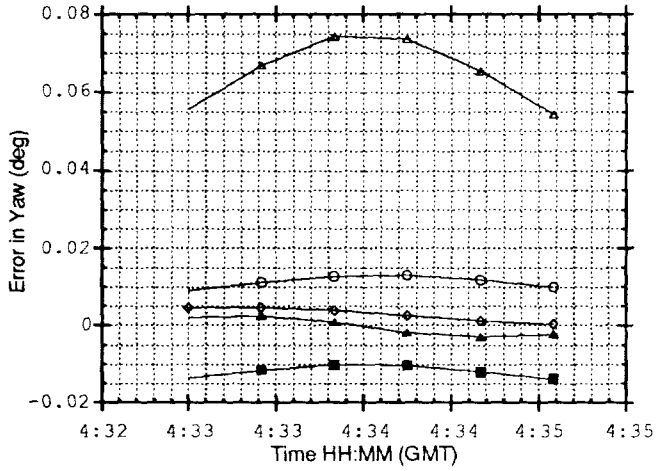

Figure 6
Sensitivity of the Calculated Yaw to Model Parameters

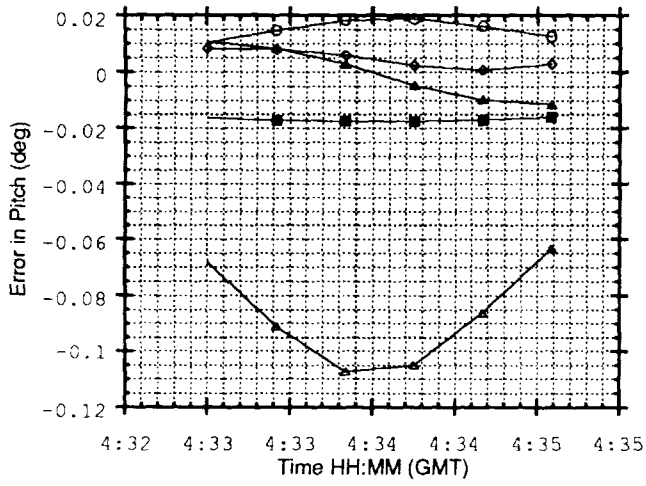

Figure 5
Sensitivity of the Calculated Pitch to Model Parameters

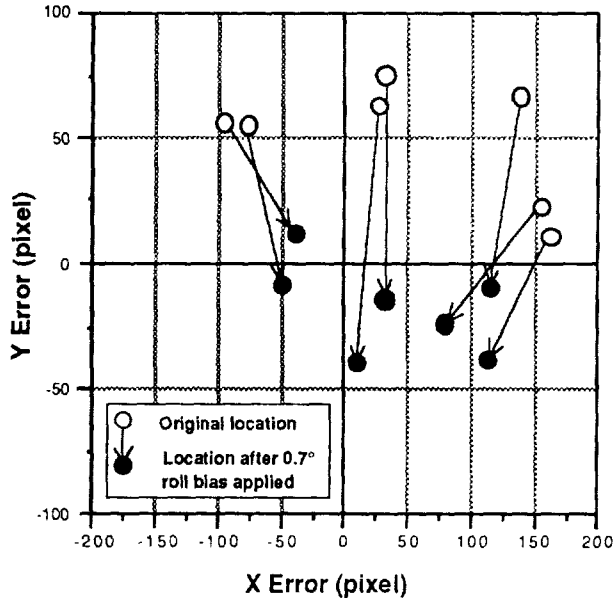

Figure 7
Applied 0.7° Roll Bias Post-pass to Three Ground Beacon Observations

Star Pattern

Technique

One mission of the UVPI is to gather rocket plume images. Since the instrument's data collection mission was expected to last for at least one year, with plume observations made throughout this period, it was felt necessary to regularly verify the UVPI radiometric response. The method used to do so is to image one or more stars whose spectra and magnitudes are known. Based on the photon counts from these known stars, UVPI calibration parameters are calculated. A typical calibration observation consists of pointing the instrument in the appropriate direction, and tracking a star for some time. Pointing direction is determined by calculating needed gimbal functions and door mirror angles using projected satellite location and attitude. Because of LACE attitude uncertainty and the requirement that the star or stars imaged be positively identified, stars and star patterns imaged by UVPI are compared with a star map after the observation. After stars in a pattern are matched to an image, as required for a positive identification, error in the LACE attitude sensors can be easily determined using the following technique.

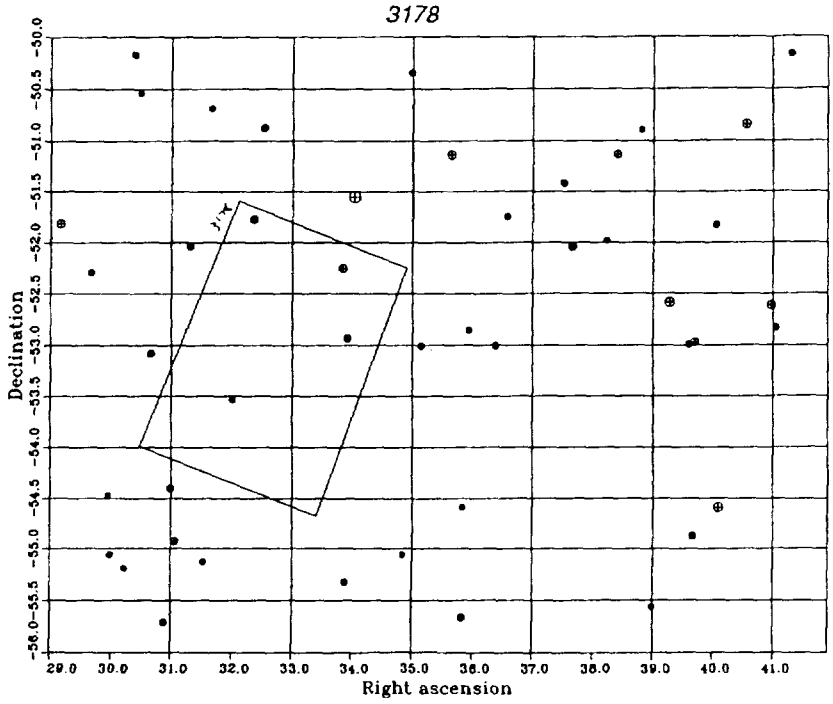

Figure 8
Star Map with Calculated UVPI tracker Camera FOV Superimposed
September 23, 1991

After a star observation is performed, a computer program, called the Line of Sight (LOS) program, is used to calculate the Right Ascension and Declination of the four corners of the FOV box. Inputs to this program are: LACE position, LACE attitude (LACE attitude sensor data smoothed to fit a 2nd order curve), UVPI gimbal angles, and UVPI door angle (since the observed star images are reflected on the door mirror). A plot is then produced which shows a star map in the vicinity of the calculated FOV of a particular frame and includes the calculated FOV box. Figure 8 shows an example of this type of plot. The corresponding frame showing the star pattern actually imaged by the camera is then transferred to hard copy for comparison to the star map. By scaling the hard copy of the image properly, the star pattern in the image can be matched to a star pattern on the star map. Once a match is found, it provides the actual location of the FOV, which is manually traced onto the FOV/star map plot. The relative offset of the two FOV rectangles is the result of program input uncertainties, of which the predominant ones are inaccuracies in the LACE attitude inputs. Rotation between the two boxes is attributed to pitch error. Pitch error is difficult to measure accurately so frames showing large pitch errors have not been included in this analysis. Small apparent pitch errors are approximated to zero. Linear offset between the actual and calculated FOV's is attributed to error in roll and yaw. Roll error is manifested as offset in a direction parallel to the short sides of the FOV rectangle. Yaw error is manifested as offset in a direction parallel to the long sides of the FOV rectangle. Error is defined as actual attitude minus calculated attitude. The simplification of decoupling roll and yaw is valid and yields sufficiently accurate results for the small angles usually encountered. It should be noted that, for this technique, any error in the roll includes error caused by inaccurate door angle measurements.

Application

Figure 8 shows a plot of a typical star map with the calculated FOV of UVPI for a particular frame included. Figure 9 shows the corresponding image that was recorded in the UVPI camera. When the two are superimposed and the pattern in the image is matched to stars in the star map, the actual FOV can be traced onto the star map. Figure 10 shows both the actual and calculated FOV traced onto a star map. The error in attitude is quantified using the angular dimensions of the UVPI FOV as a scale. As mentioned earlier the UVPI FOV is 2.0° by 2.6°. In Figure 10 it is seen that pitch error is minimal, yaw error is also small, and roll error is approximately -0.6°.

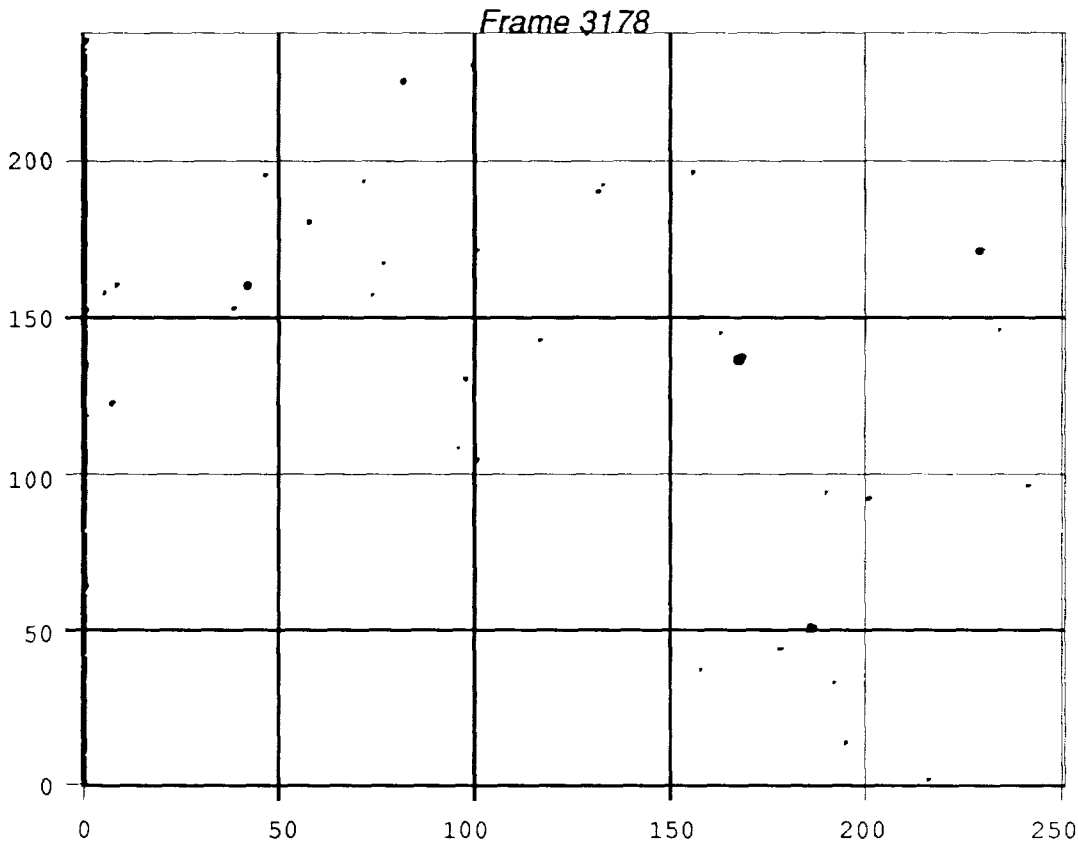

Figure 9
UVPI Tracker Camera Image, September 23, 1991

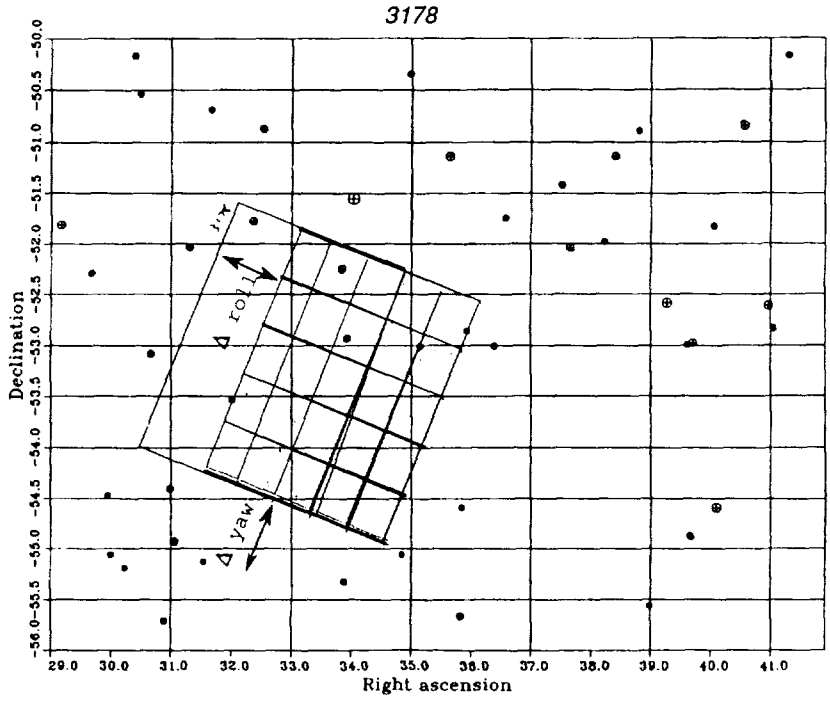

Figure 10
Star Map with Calculated and Actual FOV, September 23, 1991

Results

Table III lists the mean and standard deviation of the corrected roll, pitch, and yaw calculated from over 50 individual frames spanning a little over one year of UVPI operations. Notice that the mean of yaw is near zero. This indicates that there is no detectable rotational offset in yaw between the UVPI and the LACE coordinate systems. The large standard deviation in the yaw shows that data from the sensors is especially inaccurate for yaw measurements. The 0.7° mean for the roll represents a rotational offset between the UVPI and LACE coordinate systems. The large standard deviation in roll error is attributed to random door angle error. The 0.7° offset is corroborated by findings from beacon observations, shown in Table II. The relatively small standard deviation in roll error shown in Table II results from the fact that beacon observations do not use the door mirror. Hence this source of error is eliminated from beacon observation derived measurements. Appendix B contains the data used to calculate values shown in Table III.

Table III
Attitude Error Data from Star Pattern Technique

	Attitude Error	
	Roll	Yaw
Mean	0.74	0.07
Standard Deviation	0.78	0.80

Table III shows that while statistical analysis of attitude error data from many passes can reveal systematic attitude errors, even error from a single frame during an observation can help in improving attitude data. If it is assumed that attitude error stays constant during the time period of a typical observation (5 to 10 minutes) then it follows that the attitude error measured for a single frame can be applied to every frame in that pass. This procedure represents the second step in attitude data processing (the first is 2nd order smoothing) and is called enhancement. When this enhanced attitude data is used as an input to the LOS program, each and every FOV rectangle should be very close to where the UVPI was actually looking. This idea has been tested and was found to be valid for most cases. This enhanced attitude data represents the best attitude of UVPI for the particular time period. Figures 11 and 12 show the yaw and roll error versus frame number (i.e., time). It is seen that unsmoothed roll and yaw show significant error and scatter while enhanced roll and yaw show average error near zero and very little scatter. It is noted that smoothing alone reduces scatter significantly. Applying the observed error back to the data simply moves the average error closer to zero. The data shown in the following graphs was generated using the error calculated from Figure 10. Again, it is noted that for this technique, roll error includes LACE attitude sensor error and door mirror angle error. It is known that as long as the door mirror is not moved, the door mirror angle error also remains constant. This is the case for most star tracking sequences. Figures 11 and 12 demonstrate that these assumptions are valid. Note that the time period shown in Figures 11 and 12 begins some time after the frame depicted in Figure 10. Therefore, what appears to be an inconsistency in the calculation of roll and yaw error between Figure 10 and Figures 11 and 12, is in fact due to sensor measurement noise at two different times. Enhancement of attitude data as described above has become a standard procedure in UVPI data processing and has shown to result in average attitude errors of approximately .1°.

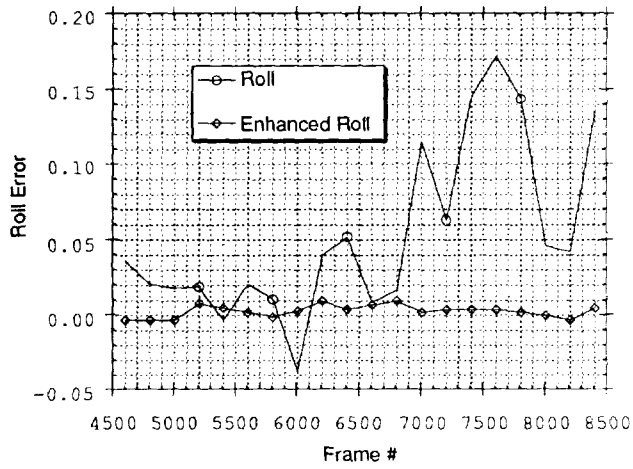

Figure 11
Roll Error Before and After Enhancement

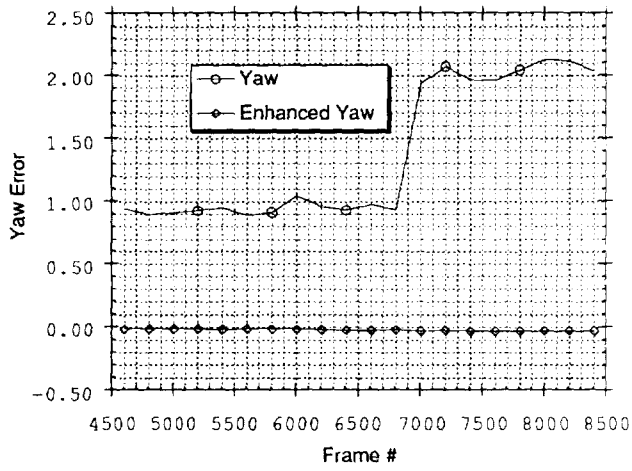

Figure 12
Yaw Error Before and After Enhancement

Other Applications

Another application of this technique has automated some of the processing. Once a star pattern has been identified, a computer program is used to directly calculate the attitude of the spacecraft. This is an improvement over the preceding technique in that roll, pitch, and yaw are calculated as a triplet. While valid, this technique is a recent development

and has little supporting data. The basic technique is shown in Appendix A.

SUMMARY

The precision pointing and imaging capability of the UVPI has been used to improve the LACE spacecraft attitude sensing and determination. Utilizing these capabilities, the instrument was used to determine attitude in real time, estimate offsets, and to more accurately characterize the spacecraft's attitude sensing system. This was accomplished by viewing stars which were near the normal to the orbit plane, and by tracking a ground target with a known location. Based on these results three conclusions were reached: (1) There was an offset between the attitude reference frame and the imaging instrument of 0.7° in the roll direction, (2) The roll and pitch provided by the spacecraft attitude sensors were better than expected, and (3) The total variation in the yaw was much less (±0.4° vs. ±1.0°) than the spacecraft sensors indicated. These results were then implemented into instrument operations resulting in improved camera pointing accuracy.

The experience with the LACE spacecraft and the UVPI has demonstrated that a precision pointing instrument can be operated from a spacecraft with simple and inexpensive attitude control and sensing systems. The imaging instrument itself can be used to improve the spacecraft attitude determination.

References:

Smathers, H. W., G. R. Carruthers, W. Ramsey, G. Steiner, W. Louissant, Calibration and performance of the Ultraviolet Plume Instrument (UVPI), *Proc. SPIE Ultraviolet Technology III, 1158*, 212, 1989.

Spacecraft Attitude Determination and Control, edited by James R. Wertz, Kluwer Academic Publishers, Dordrecht, The Netherlands, 1978.

Escobal P. R., Methods of Orbit Determination, Robert E. Krieger Publishing Company, Malabar, Florida, 1965, pp 32- 66 of 1983 reprint with corrections

Explanatory Supplement to the Astronomical Ephemeris and the American Ephemeris and Nautical Almanac (prepared jointly by the Nautical Almanac offices of the United Kingdom and the United States of America) London, Her Majesty's Stationery Office, 1961

Warren W. H. and Kang Y.W. 1987, *Skymap Catalog of 248516 Stars Version 3.3* , NSSDC/WDC-A-R&S 87-15

Acknowledgements:

Bruce Gilson and Mike Horan of BFEC for developing and running software used to produce data for the Star Pattern Technique.

Dean Bakeris of BFEC and John Ivory of RSI for help in understanding LACE attitude sensor data.

Paul Flynn of BFEC, Don Horan of NRL, Lowell Plackett of BFEC, and Tony Smathers of NRL

Work for this paper was done for the Naval Research Laboratory under contracts N0014-89-C-2011 and N0014-91-C-2316.

Appendix A

Attitude Determination Technique
for Ground Beacon Tracking or Star Pattern Observation

Let L be an orthogonal coordinate system having L1, L2, L3 as its axes where L3 is along the spacecraft radial, L2 is pointing opposite to the orbit normal, and L1 completes the right-handed rectangular coordinate system.

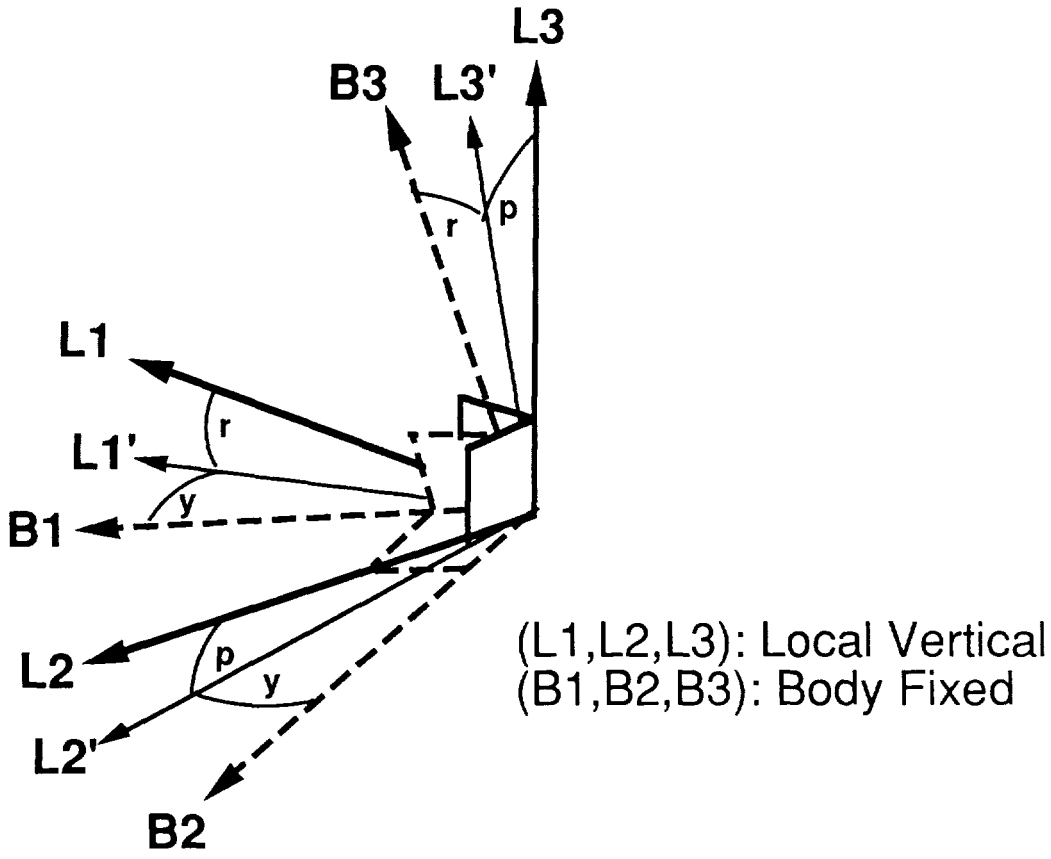

Figure A1
Coordinate System

Let B be an orthogonal coordinate system attached to the body of the spacecraft whose axes are B1, B2, and B3 such that if the attitude of the spacecraft is zero (i.e., roll = pitch = yaw = 0°), then the coordinate systems L and B are identical. Figure A1 illustrates the two coordinate systems.

To establish a relationship between the two coordinate systems, we rotate the L system first about the L1 axis in the clockwise direction an angle equal to +p, forming the (L1, L2', L3') system. Next rotate counter clockwise about the L2' axis an angle equal to +r, forming the (L1',L2',B3) system. Finally, rotate counter clockwise about the B3 axis an angle equal to +y, forming the (B1,B2,B3) system.

The rotational matrices that correspond to the three rotations described above can be expressed as:

$$[P] = \begin{bmatrix} 1 & 0 & 0 \\ 0 & +\cos(p) & -\sin(p) \\ 0 & +\sin(p) & +\cos(p) \end{bmatrix}$$

$$[R]=\begin{bmatrix}+\cos(r) & 0 & -\sin(r)\\ 0 & 1 & 0\\ +\sin(r) & 0 & +\cos(r)\end{bmatrix}$$

$$[Y]=\begin{bmatrix}+\cos(y) & +\sin(y) & 0\\ -\sin(y) & +\cos(y) & 0\\ 0 & 0 & 1\end{bmatrix}$$

The three rotations can be combined into a single rotational matrix [A], the attitude matrix, by multiplying the rotational matrices [Y], [R], and [P] in that order to give:

$$[A]=\begin{bmatrix}\cos(y)\cos(r) & -\cos(y)\sin(p)\sin(r)+\sin(y)\cos(p) & -\cos(y)\cos(p)\sin(r)-\sin(y)\sin(p)\\ -\sin(y)\cos(r) & \sin(y)\sin(p)\sin(r)+\cos(y)\cos(p) & \sin(y)\cos(p)\sin(r)-\cos(y)\sin(p)\\ \sin(r) & \sin(p)\cos(r) & \cos(p)\cos(r)\end{bmatrix}$$

the attitude matrix [A], an orthonormal matrix such that $[A]^{-1} = [A]^{T}$, transforms vectors expressed in the L coordinate system to the B coordinate system.

Let $\vec{l} = (l_1, l_2, l_3)^{T}$ be the LOS unit vector from the spacecraft to the target (a ground beacon or a star) in the L coordinate system. Then $\vec{l}$ is a function only of the spacecraft ephemeris and target position. Next let $\vec{b} = (b_1, b_2, b_3)^{T}$ be the LOS unit vector from the spacecraft to the target expressed in the B coordinate system. The vector $\vec{b}$ is a function of the characteristics of the body-fixed pointing system which, for UVPI, included the location of the target (in terms of the x- and y-pixels location on the focal plane) relative to the center of the FOV of the camera and the azimuth and elevation of the gimbal mirror (and of the UVPI door angle if the target is a star). The vectors $\vec{l}$ and $\vec{b}$ are then related by:

$$[A]\cdot\vec{l} = \vec{b} \qquad \text{Eq. (1)}$$

Since the attitude of the spacecraft is within ± 3°, the small angle approximations can be made. The matrix [A] can be linearized, keeping only the zeroth and first order terms, to give:

$$[A] \approx [A]_0 = \begin{bmatrix}1 & +y & -r\\ -y & 1 & -p\\ +r & +p & 1\end{bmatrix} \qquad \text{Eq. (2)}$$

where r, p, and y are roll, pitch, and yaw angles expressed in radians, necessarily.

Now, treating vectors $\vec{l}$ and $\vec{b}$ as known quantities, and r, p, and y as unknowns, Eq. (1) can be rewritten as:

$$\begin{bmatrix} -l_3 & 0 & +l_2 \\ 0 & -l_3 & -l_1 \\ l_1 & l_2 & 0 \end{bmatrix} \bullet \begin{bmatrix} r \\ p \\ y \end{bmatrix} = \begin{bmatrix} b_1 \\ b_2 \\ b_3 \end{bmatrix} - \begin{bmatrix} l_1 \\ l_2 \\ l_3 \end{bmatrix}$$

or $$[m] \cdot \vec{x} = \vec{c} \qquad \text{Eq. (3)}$$

where

$$[m] = \begin{bmatrix} -l_3 & 0 & +l_2 \\ 0 & -l_3 & -l_1 \\ l_1 & l_2 & 0 \end{bmatrix} \quad , \quad \vec{x} = \begin{bmatrix} r \\ p \\ y \end{bmatrix} \quad , \quad and \quad \vec{c} = \begin{bmatrix} b_1 \\ b_2 \\ b_3 \end{bmatrix} - \begin{bmatrix} l_1 \\ l_2 \\ l_3 \end{bmatrix}$$

Note that [m] is of rank 2 and det[m] = 0 in which case r, p, and y cannot be solved uniquely using just a single equation. However, using a series of LOS unit vectors during a short observation interval for the case of the beacon or using the star patterns in the case of star observation, the attitude can be solved uniquely. In practice, the LOS vectors are obtained by tracking the beacon source or observing the night sky to collect star patterns.

Let's assume that there are n LOS unit vectors that can be obtained during an observation, Eq. (3) can be written for each LOS unit vector.

We thus have :

$$\begin{aligned} [m]_1 \cdot \vec{x} &= \vec{c}_1 \\ [m]_2 \cdot \vec{x} &= \vec{c}_2 \\ [m]_3 \cdot \vec{x} &= \vec{c}_3 \\ &\vdots \\ [m]_n \cdot \vec{x} &= \vec{c}_n \end{aligned} \qquad \text{Eq. (4)}$$

Eq. (4) is a system of 3n equations in three unknowns, namely the vector $\vec{x}$. Eq. (4) can be written in a more compact form as:

$$[M] \cdot \vec{x} = \vec{C} \qquad \text{Eq. (5)}$$

where [*M*] is a 3n x 3 augmented matrix and C is a 3n dimensioned vector.

The over-determined system in Eq. (5) can be solved either by the standard least-square method by forming the residual function $\vec{R} = [M] \cdot \vec{x} - \vec{C}$ and minimizing $|\vec{R}|^2$, or by forming the transpose of [*M*] and solving for $\vec{x}$ directly. The former technique is more general in that it can be applied even when the linearization of the matrix [*A*] is not invoked. The latter technique is more efficient with the linearized version. In this case, one would form $[M]^T[M] \cdot \vec{x} = [M]^T \cdot \vec{C}$ and $\vec{x} = \left\{[M]^T[M]\right\}^{-1}[M]^T \cdot \vec{C}$ where the inverse, $\left\{[M]^T[M]\right\}^{-1}$, can easily be determined since it is a 3 x 3 matrix.

Appendix B

Rev #	Frame #	Total Correction roll	pitch	yaw
597	6706	0.65	0.00	-0.97
	10054	0.70	0.00	-1.05
	10510	0.73	0.00	-0.94
1281	3790	0.41	0.00	0.49
1584	3766	0.33	0.00	-0.40
	7738	0.44	0.00	-0.31
1897	4198	0.40	0.00	-0.65
2439	10903	-0.00	0.00	-0.75
2622	9928	1.48	0.00	-0.19
	9994	1.59	0.00	-0.49
2636	3576	0.69	0.00	-0.48
	11947	0.68	0.00	-0.67
2837	3790	0.36	0.00	0.99
3078	7894	0.60	0.00	-0.60
3182	17094	1.33	0.00	-0.05
	4378	1.23	0.00	-0.23
3686	4228	0.75	0.00	0.90
3820	5632	0.35	0.00	1.48
	5650	0.35	0.00	1.48
3835	6196	0.59	0.00	1.23
3866	4564	-0.25	0.00	0.39
4090	11740	-0.52	0.00	0.12
4423	4120	0.80	0.00	0.22
	9339	0.10	0.00	0.40
	13332	1.00	0.00	0.25
4592	9880	-0.76	0.00	-0.57
4621	9583	1.07	0.00	0.78
4669	10426	1.45	0.00	0.17
4983	17896	1.04	0.00	-0.36
5279	7174	-0.38	0.00	0.77
	18244	0.35	0.00	0.86
	18316	0.53	0.00	0.93
5321	3712	1.05	0.00	-0.05
	4588	1.14	0.00	-0.25
	13771	0.72	0.00	-1.64
	13783	0.89	0.00	-1.57
5336	4132	-0.08	0.00	0.88
	4282	-0.08	0.00	0.88
5351	7360	2.01	0.00	0.92
5396	7150	0.85	0.00	0.64
	11601	0.83	0.00	0.35
	22516	0.80	0.00	0.36
5487	6338	0.90	0.00	0.81
	17389	0.17	0.00	2.04
5537	4414	1.54	0.00	-0.45
	4504	1.52	0.00	-0.55
	4942	1.52	0.00	-0.45
5567	6394	2.20	0.00	-0.14
	6412	4.25	0.00	-0.67
5582	4342	-0.30	0.00	-1.43
6411	18121	0.01	0.00	0.19
	25127	0.33	0.00	-0.23
	25288	0.66	0.00	-0.39
6456	3910	1.05	0.00	0.76
6456	4360	0.40	0.00	0.83
Mean		0.74	0.00	0.07
Std. Dev		0.78	0.00	0.80

ATTITUDE CONTROL OF THE LACE SATELLITE: A GRAVITY GRADIENT STABILIZED SPACECRAFT

J. E. Ivory*
Research Support Instruments, Alexandria, VA 22314
and
R. E. Campion† and D. F. Bakeris†
Bendix Field Engineering Corporation, Alexandria, VA 22314

ABSTRACT

The Low-power Atmospheric Compensation Experiment (LACE) satellite was launched in February 1990 by the Naval Research Laboratory. The spacecraft's pitch and roll are maintained with a gravity gradient boom and a magnetic damper. There are two other booms with much smaller tip masses, one in the velocity direction (lead boom) of variable length and the other in the opposite direction (balance boom) also of variable length. In addition, the system uses a momentum wheel with its axis perpendicular to the plane of the orbit to control yaw and keep these booms in the orbital plane.

The primary LACE experiment requires that the lead boom be moved to lengths varying from 4.6 m to 45.7 m. This and other onboard experiments require that the spacecraft attitude remain within tight constraints while operating. The problem confronting the satellite operators was to move the lead boom without inducing a net spacecraft attitude disturbance. A description of a method used to change the length of the lead boom while minimizing the disturbance to the attitude of the spacecraft is given. Deadbeating to dampen pitch oscillations has also been accomplished by maneuvering either the lead or balance boom and will be discussed.

---

* Project Scientist, LACE Project
† Project Engineer, LACE Project
† Project Engineer, LACE Project

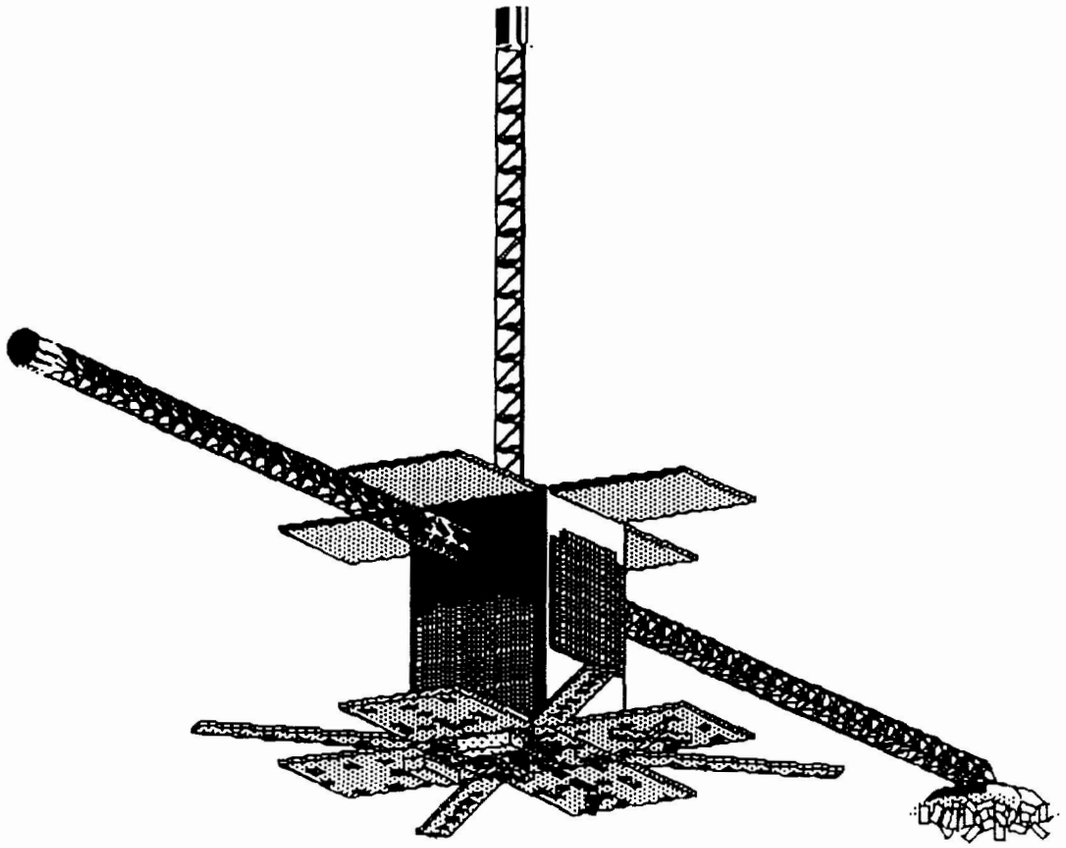

Figure 1. Drawing of the LACE satellite.

LACE SATELLITE DESCRIPTION

The Low-power Atmospheric Compensation Experiment (LACE) satellite was designed and built by the Naval Research Laboratory (NRL) in Washington, DC. The satellite was launched on 14 February 1990 into a circular orbit with an altitude of 541 km and a 43° inclination. The spacecraft weighs 1440 kg and the body of the spacecraft is basically box shaped, 1.2 m by 1.2 m and 2.4 m high. Figure 1 is a drawing of the LACE satellite. The LACE satellite has no orbit adjustment capability. Attitude is controlled with gravity gradient stabilization provided by a retractable boom emerging from the top of the spacecraft with a 91 kg tip mass containing a magnetic damper. There are two additional retractable booms with tip masses each of 12.7 kg; one in the velocity direction of variable length up to 45.7 m (lead boom), and the other in the anti-velocity direction, also variable to 45.7 m (balance boom). The system uses a momentum wheel with its axis perpendicular to the plane of the orbit to keep these booms in the orbital plane. Spacecraft attitude is determined using the output from

change in the frequency, amplitude, or phase of any of the attitude components. A very large change was performed to demonstrate the effectiveness of this method. Figure 4 shows the pitch as a function of time for a change in lead boom from 4.6 to 43.3 m and balance boom from 45.7 to 16.5 m. The pitch bias changed by 1° with no significant change in pitch amplitude. In addition, the pitch frequency is not altered during these moves. For completeness, the plots for roll and yaw for the same event are shown in Figure 5 and Figure 6. It was also noted that the step size of 1.5 meters was conservative and one experiment indicated that larger steps could have been used without disturbing the amplitudes of the attitude components.

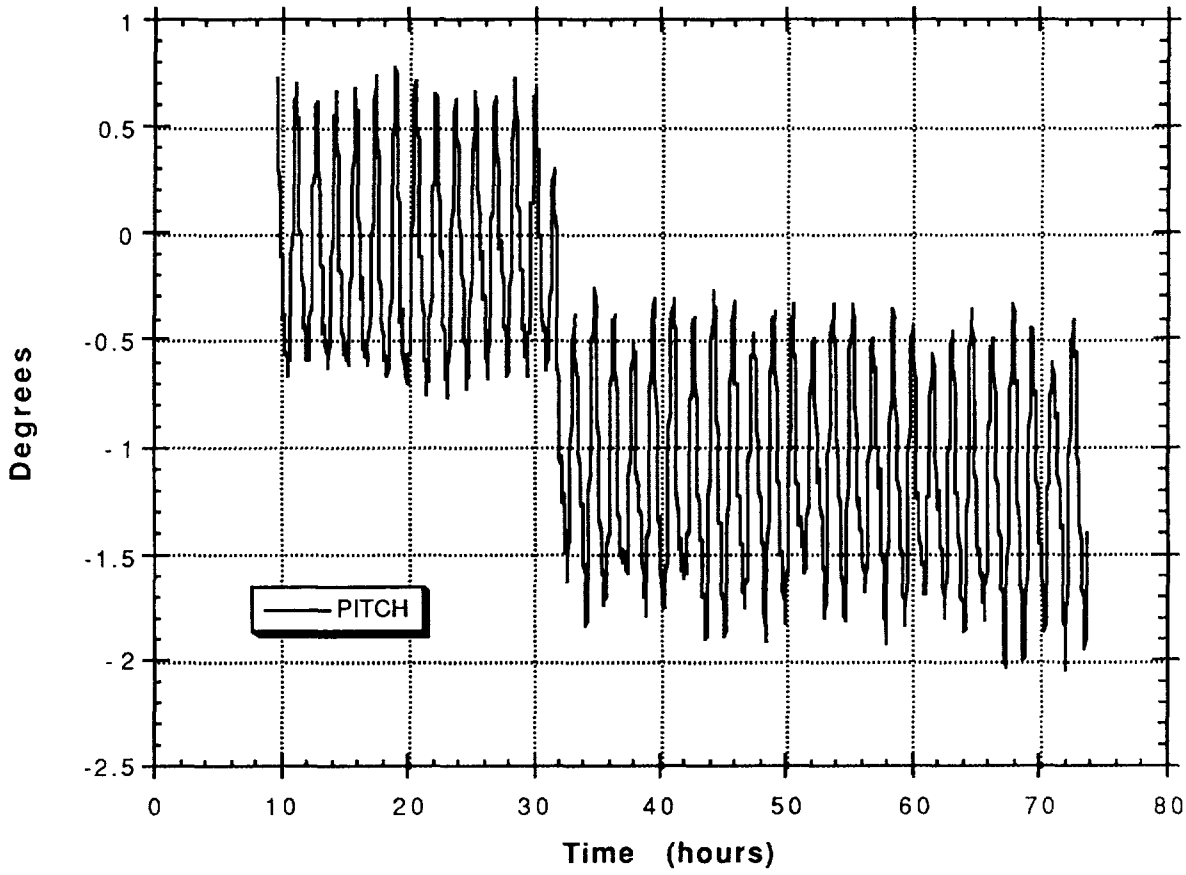

Figure 4. Pitch variations during boom movements.

three sets of sensors: a conical Earth scanner, a set of three magnetometers, and five sun sensors.

NRL operates three ground stations to communicate with and control the LACE spacecraft and its experiments. The LACE spacecraft was designed to support its experiments for 30 months.

ONBOARD EXPERIMENTS

The satellite's primary purpose is to provide an orbiting instrumented target board capable of measuring the effects of active compensation of a ground based laser beam propagated through the atmosphere. This target board consists of an array of sensors on the bottom of the spacecraft. A panel of corner cube reflectors on the end of the lead boom provides a preliminary laser target. The position of the lead boom is fixed for the duration of the pass by the particular requirements of the experiment, but the length varies from one experiment to another.

A second experiment aboard the LACE satellite is the Ultraviolet Plume Instrument (UVPI). This is an ultraviolet imaging system with a maximum field of view of 2.0° x 2.6°. This camera views through the Earth facing side of the LACE spacecraft and is pointed using a precision gimbaled mirror pointing system. Knowledge of the spacecraft attitude to better than ±1° is needed in each axis for UVPI observations. Moving booms for the primary experiment could disturb the spacecraft attitude by inducing unacceptably large oscillations in the pitch direction. Although the large pitch oscillations would damp out in several days, these movements would make attitude predictions for the secondary UVPI experiment pointing functions very difficult since the attitude motion would consist of both transient and steady state oscillations. A method of moving the lead and trailing booms was developed which would not cause a net disturbance to the spacecraft attitude.

MOTION OF LACE

The angular momentum of the spacecraft is dominated by the once per orbit rotation about the pitch axis as the spacecraft keeps one side facing Earth. Added to this once per orbit rotation are perturbations caused by the magnetic damper, by the orbit eccentricity of 0.02, and by aerodynamic forces. These perturbations result in a driven oscillation of the spacecraft's roll, pitch, and yaw about their equilibrium values. The natural oscillation rates of this system are

dependent on the moment of inertia (MOI) about each axis. The calculated MOIs of the spacecraft give a natural period of oscillation about the roll, pitch, and yaw axes of 56 minutes, 71 minutes, and 60 minutes respectively. In the steady state condition the natural oscillations are completely damped, but the driven oscillations about the equilibrium attitude remain. This results in oscillations in roll, pitch, and yaw with dominate periods which are orbital (approximately 95 minutes) and half orbital. As with any gravity gradient spacecraft with a momentum wheel in the orbit plane, the roll and yaw are coupled to each other and the pitch is independent of the two. Figure 2 shows typical roll, pitch, and yaw values over two orbits. Note that only the forced oscillations are present. The widely varying yaw values around 2.6, 4.3, and 5.9 hours are associated with the periods when the spacecraft is in darkness. Only the magnetometers, with accuracies of $\pm 1°$, are used for yaw angle determination during this time when the sun sensors are not available.

DAMPING OF LACE

The spacecraft is equipped with an attitude damper consisting of a collection of magnets imbedded in a sphere of oil, located at the tip of the gravity gradient boom. As the spacecraft oscillates, the magnets attempt to align themselves to the Earth's magnetic field. This forced motion in a viscous fluid removes unwanted energy from the the attitude system. Although very effective in removing unwanted natural oscillations in the attitude system, the magnetic damper requires considerable time to remove even a moderate disturbance. Figure 3 shows the natural decay of the spacecraft's pitch motion after an induced disturbance. The time required to damp the oscillations to one half their initial amplitude is about 88.8 hours. This is an unacceptably long time for pitch disturbances caused by moving the boom to return to the steady state oscillations in the pitch axis.

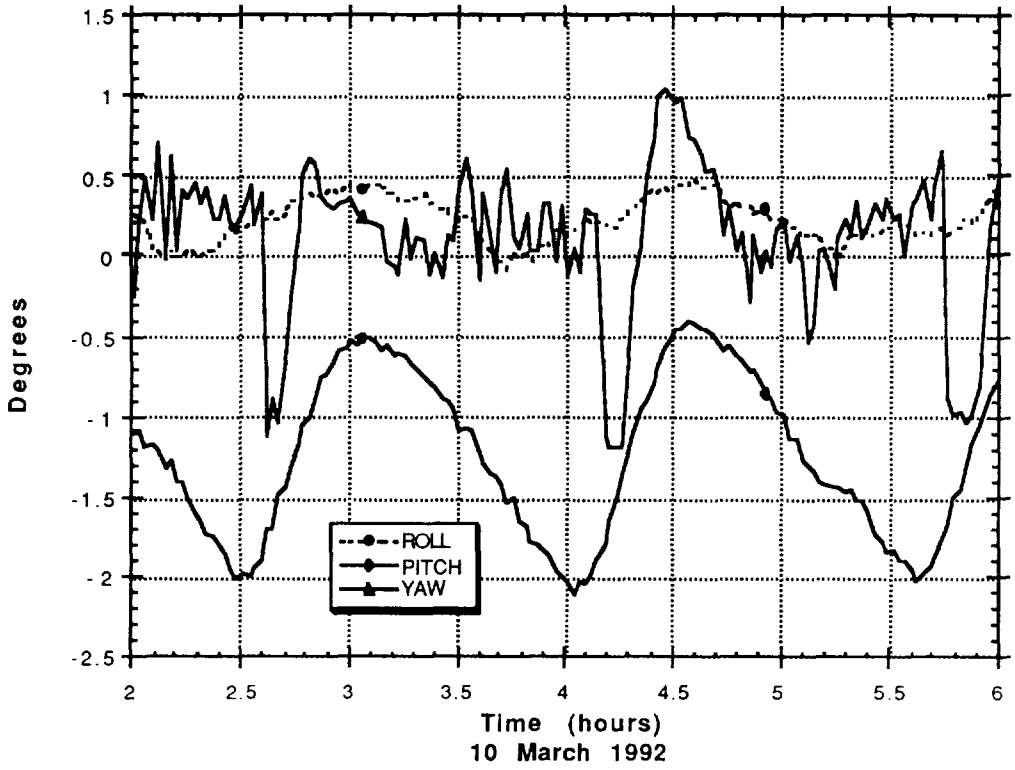

Figure 2. Typical LACE attitude values.

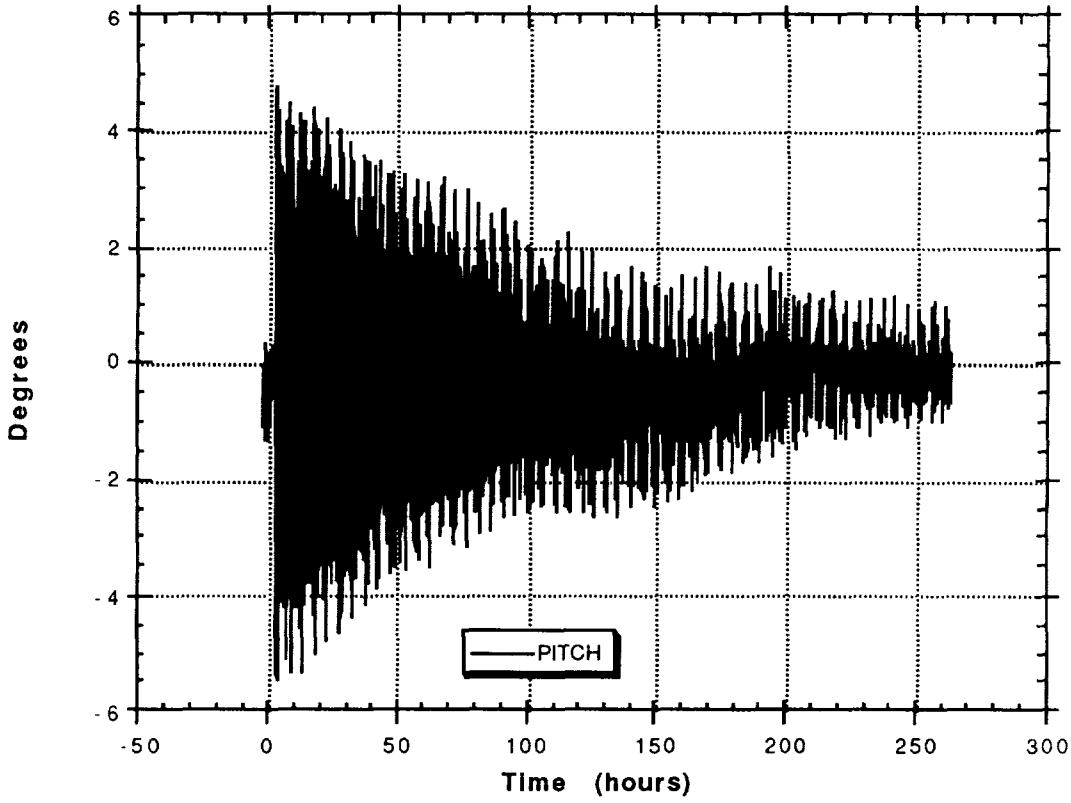

Figure 3. Effect of magnetic damper on LACE pitch value.

DISCUSSION OF ATTITUDE CONTROL DURING BOOM MOVEMENTS

During pre-launch operations planning, a computer program was used to simulate the spacecraft's dynamics. This program simulated naturally occurring forces on the spacecraft such as gravity, aerodynamics, the magnetic damper, and solar pressure. In particular, this program also simulated the effects of the movements in all three spacecraft booms.

It was noted that changing the boom lengths in one step caused changes in pitch amplitude even though the MOI about the pitch axis was the same before and after the move. The difference in MOI due to the uncertainty in the final boom positions and the variation in the MOI during the movement is less than 0.1% of the total and is, therefore, negligible.

The subsequently disturbed pitch motion varied with the magnitude of the change in boom length and the time in the phase cycle of the movement. Therefore, moving booms in one large step was not an acceptable solution to the attitude control requirement. It was also noted that a change in pitch bias (the equilibrium position about which the pitch oscillations occur) is associated with the change in boom positions and is a factor in the change in pitch amplitude. That is, if initially there is no pitch oscillation and the booms are moved in one step with constant MOI, the resulting pitch amplitude will equal the incurred pitch bias change. Simulations showed that changing the boom lengths slowly (making the moves over a time comparable to the pitch period) did not cause changes in the amplitudes of any of the attitude components. Since the speed of movement of the booms is fixed at about 9.1 cm/sec, the slow movement can be approximated by making the moves in small steps. In performing these changes in boom positions, the pitch bias changes and the change can be calculated and included in attitude predictions. Roll and yaw remain unchanged during these moves. A simple calculation of the change in position of the center of mass of the spacecraft yields very good information about the change in the pitch bias.

SPACECRAFT DATA WITH BOOM MOVEMENTS

In normal operation on the LACE satellite the changes required in the position of the lead boom were usually less than 5 meters with an average of 2.5 meters. These movements have been made about 65 times and as often as once per day. The lead boom is usually positioned between 27 to 38 meters, but four special experiments required the lead boom to be at 4.6 meters. Performing these changes using steps of 1.5 meters spread over 95 minutes results in no

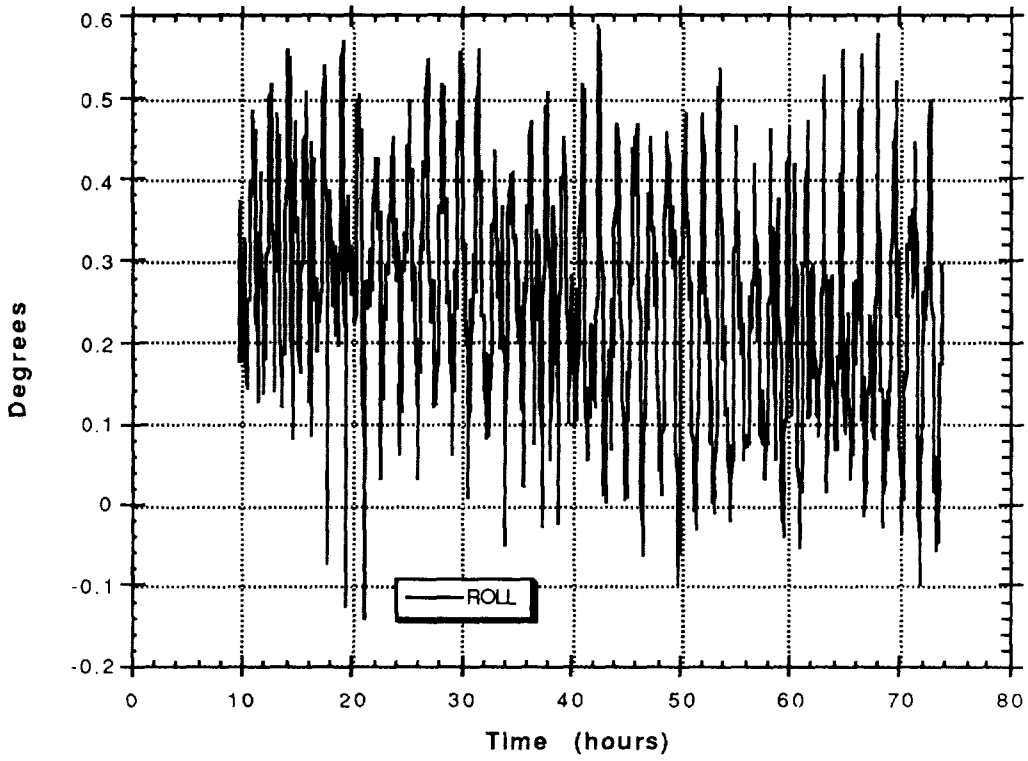

Figure 5. Roll variations during boom movements.

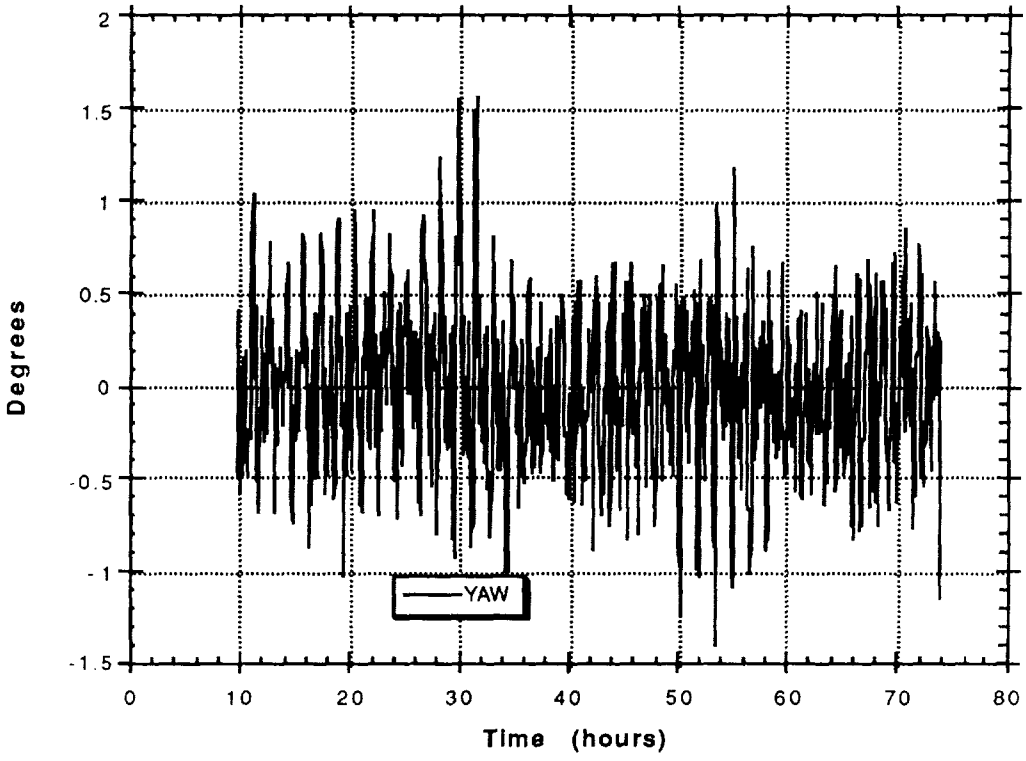

Figure 6. Yaw variations during boom movements.

DISCUSSION OF ATTITUDE CONTROL USING DEADBEATING

Although attitude control using step movements was done by computer simulations prior to launch, it was desired to have a backup solution to the problem. Deadbeating was explored for this purpose. Deadbeating is a method of decreasing the amplitude of pitch motion by moving one boom out at maximum pitch angular velocity and then moving the same boom in to its original position at minimum pitch angular velocity. The orbital angular velocity must be included in the determination of the pitch angular velocity since it is the dominant term in the pitch angular velocity. Because of this, deadbeating has its greatest effect on the pitch motion. The order of these boom moves for deadbeating can be reversed. The magnitude of the boom movement depends on the MOI about the pitch axis and the amplitude of pitch oscillation to be damped. Deadbeating is described in Wertz[1] for a dumbbell and the equation given there can be modified to apply to the LACE configuration by replacing the angular pitch frequency of the dumbbell by that of LACE. Deadbeating maneuvers can be done with any one of the three booms.

SPACECRAFT DATA WITH DEADBEATING

Since boom movements with the small step method caused no disturbance in attitude, the backup deadbeating method used in prelaunch simulations was not required. However, in order to further study the dynamics of large space structures, deadbeating maneuvers were preformed. Testing with simulators, the phasing of the boom movements could be done precisely. This was not possible on the spacecraft since the decision on the timing of the movements had to to predicted in advance of the movements. Several attempts were needed to achieve the proper phasing. Best results were obtained when one movement of the booms was executed, results of the move examined and, based on these results, the timing of the second move was calculated for completion of the deadbeating operation.

Figure 7 shows the change in pitch as a result of this type of deadbeating. Since the configuration of the boom is the same before and after the deadbeating, there is no change in pitch bias. Figures 8, 9 and 10 are blowups of Figure 7 to show the boom movements. Figures 11 and 12 show roll and yaw. Yaw shows little or no effect while there is some change in roll associated with the boom movements. In order to increase the pitch amplitude prior to deadbeating, the principles of deadbeating were used but the phasing of the

boom movements were selected to increase the amplitude. This was another application of the deadbeating idea.

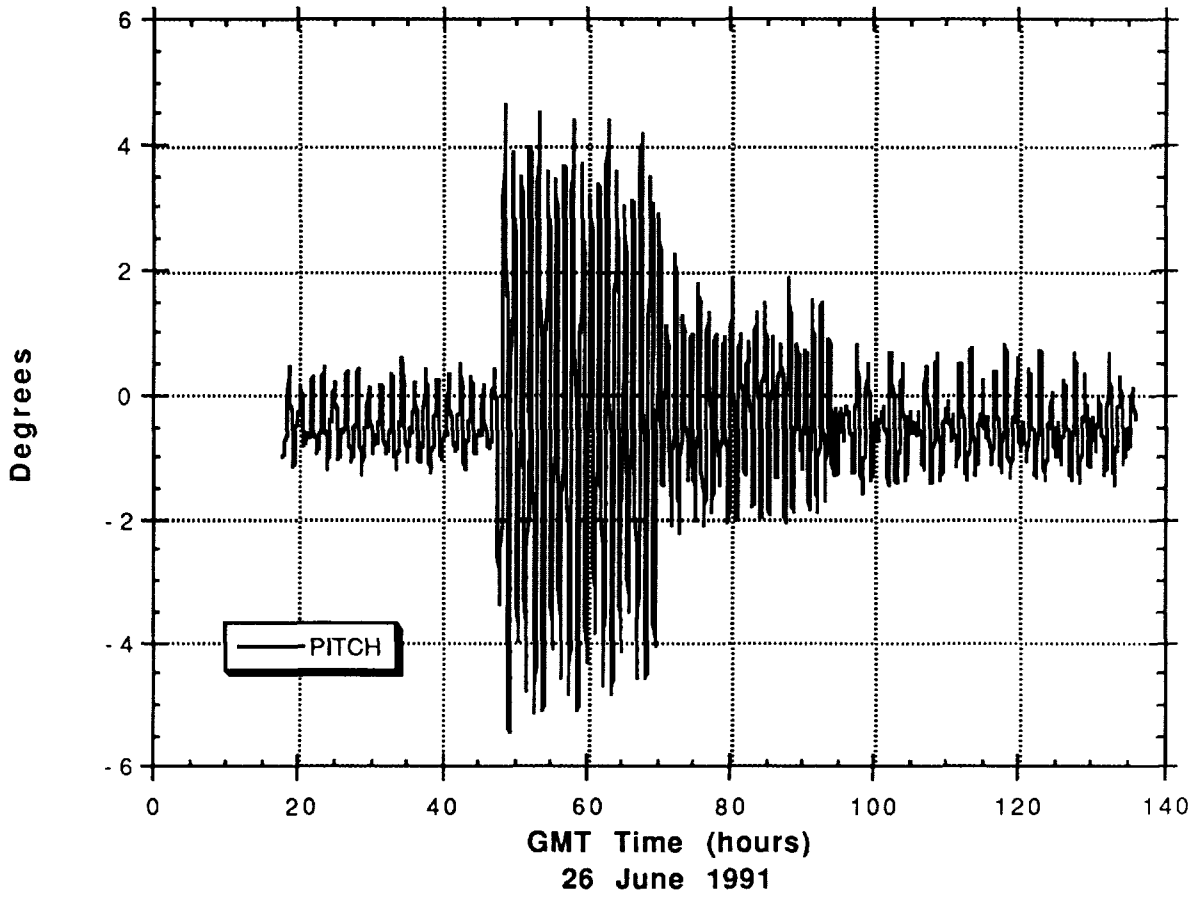

Figure 7. Pitch variations during deadbeating experiment.

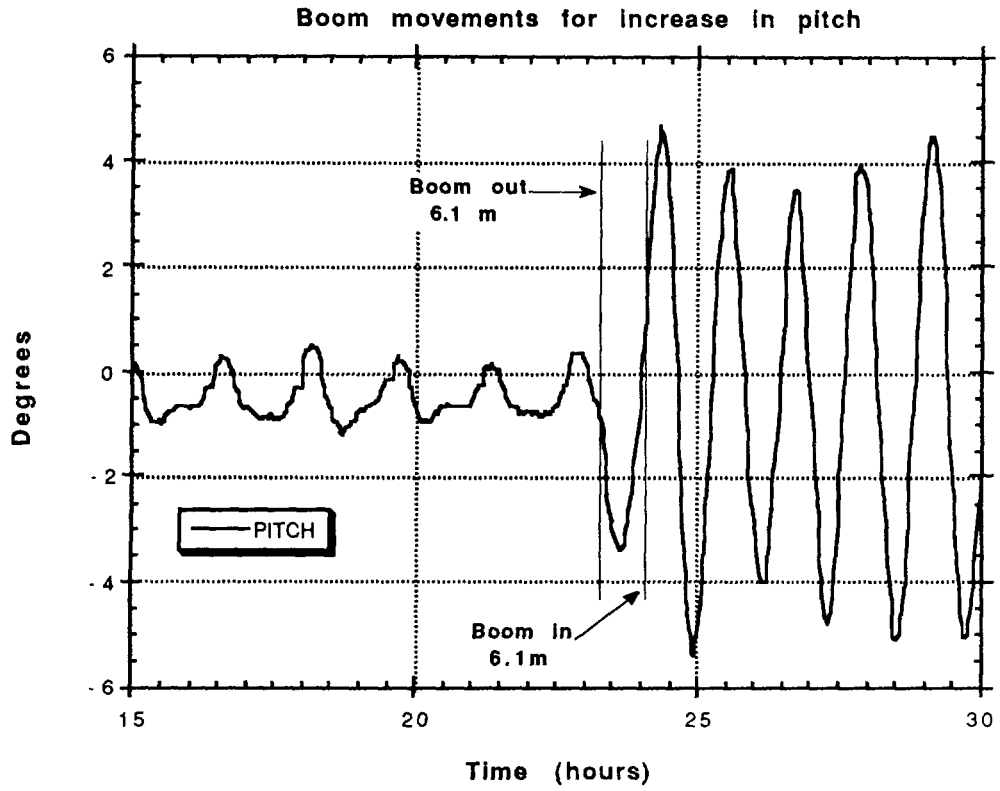

Figure 8. Expansion of figure 7 showing initial disturbance.

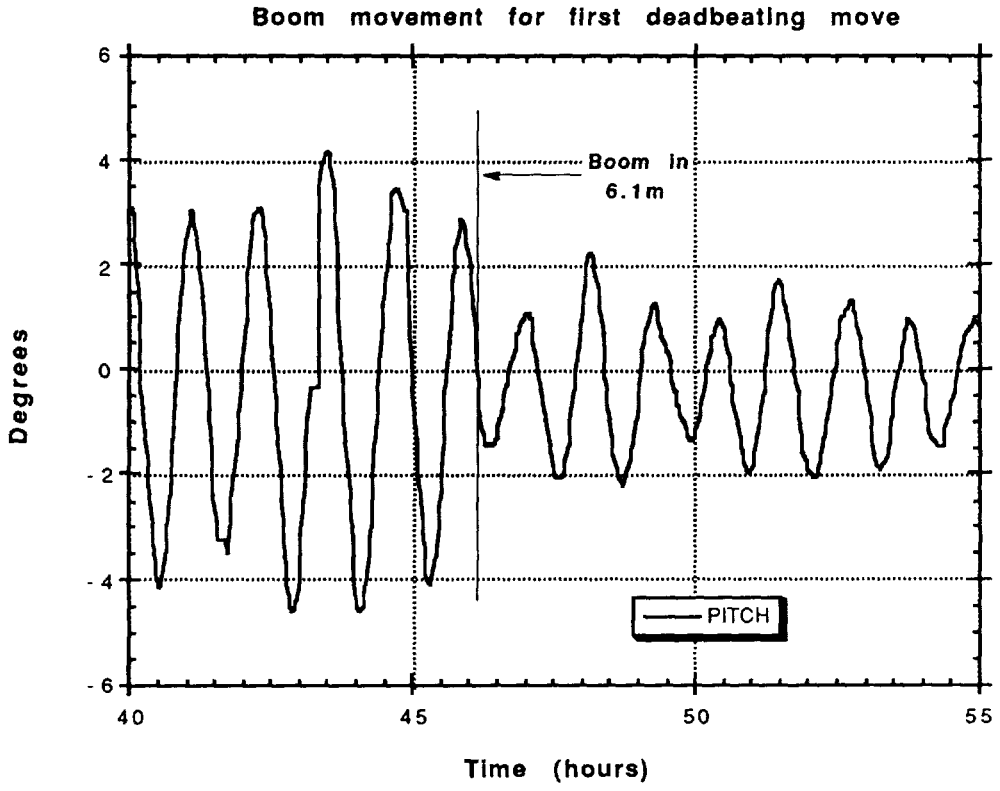

Figure 9. Expansion of figure 7 showing first step of deadbeating.

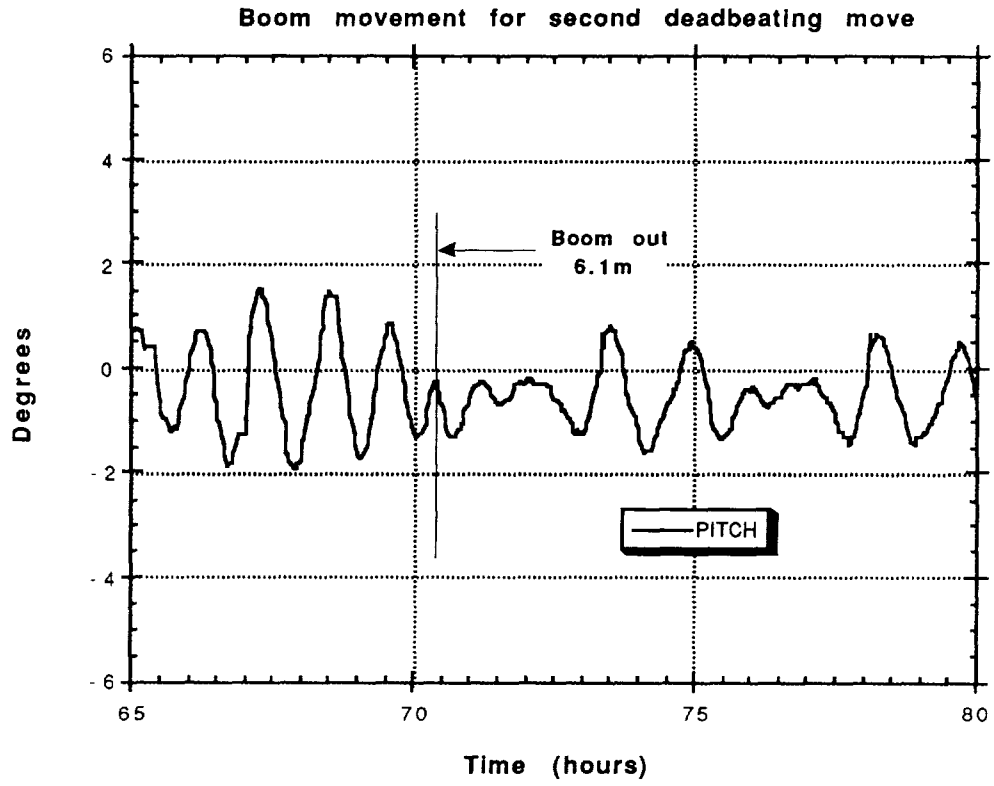

Figure 10. Expansion of figure 7 showing second step of deadbeating.

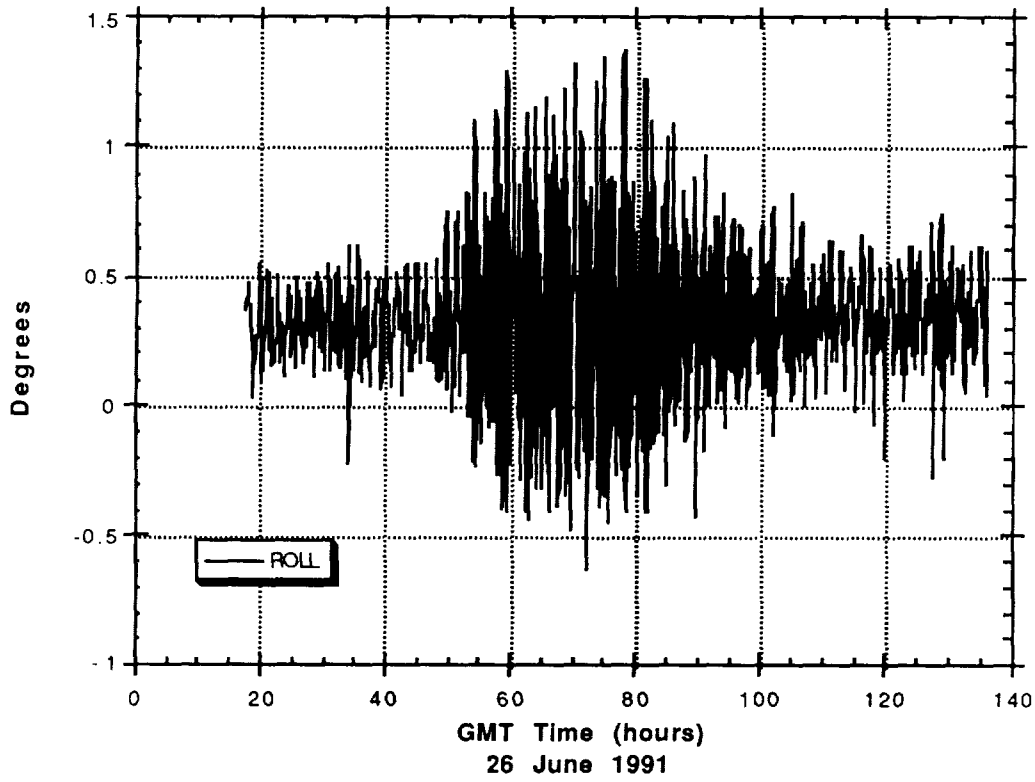

Figure 11. Roll variations during deadbeating experiment.

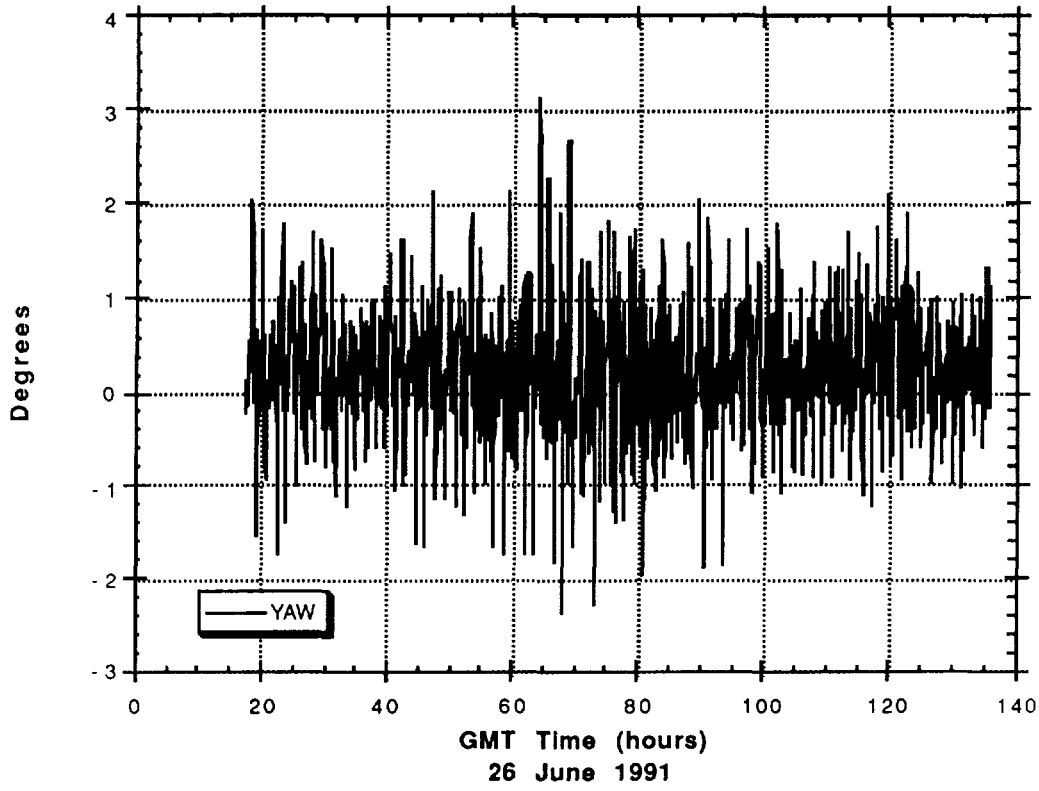

Figure 12. Yaw variations during deadbeating experiment.

CONCLUSIONS

Positioning of the lead boom as required by laser experiments has been satisfied without changing the restrictions demanded by the imaging experiments on the spacecraft. Movement of the booms was repeated many times as required by the experiments without affecting the overall attitude of the spacecraft. The change in pitch bias was expected and predictable.

Deadbeating the pitch oscillations was demonstrated using the lead or balance boom.

ACKNOWLEDGEMENTS

We are indebted to Dr. D. M. Horan of NRL for his support and suggestions in many areas of this program; to the flight operations group at BFEC who were responsible for moving the booms and for supplying the attitude information from the spacecraft.

Work for this paper was done for the Naval Research Laboratory under contracts N0014-89-C-2011 and N0014-91-C-2316.

REFERENCE

Spacecraft Attitude Determination and Control, edited by James R. Wertz, Kluwer Academic Publishers, Dordrecht, The Netherlands, 1978.

MINIATURE OPTICAL WIDE-ANGLE-LENS STARTRACKER (MINI-OWLS)

Major Rick Miller, Wright Laboratory,
WL/MNSI, Eglin AFB, Florida

Joe E. Coulter and Seymour Levine
Northrop Corporation, Electronics Systems Division,
Hawthorne, California

ABSTRACT

This paper provides a brief overview of the design considerations and the current status of the Miniature Optical Wide-Angle Lens Startracker program. Mini-OWLS offers a revolutionary alternative to the conventional startracker. It is a small, lightweight, low-cost, high performance startracker that can be used in a variety of applications including calibration and alignment of Inertial Measurement Units (IMUs).

Mini-OWLS makes use of a strapdown design incorporating Holographic Optical Elements (HOEs) in place of conventional optics. HOEs can be multiplexed so that the same aperture can be used for multiple separate optical paths looking in several directions simultaneously without startracker rotation. Additionally, separate Schmidt corrector plates are not required to compensate for spherical aberration. The optical assembly, or what would normally be considered as the telescope, is less than 20 cm^3 in volume, weighs less than 55 grams, and contains the equivalent of three individual telescopes. Each one has a 4 deg Field of View (FOV) with a field of regard of 48 square degrees. Mini-OWLS has a bandwidth of approximately 300 nm in or near the visible wavelength. The projected resolution of the startracker is 5 to 10 arc-seconds, depending on the centroiding algorithm used.

The Mini-OWLS program was initiated last year and represents a miniaturized version of a similar design for aeronautical applications. The contract is managed by Wright Laboratory, Air Force Systems Command, Wright-Patterson AFB, Ohio, with funding from the Strategic Defense Initiative Organization through Eglin AFB. The initial phase of the program is to build and test a development unit. The second phase is to integrate the startracker with the Charles Stark Draper Laboratory Micromechanical Inertial Guidance System (MIGS) and the Signal Processing Packaging Design (SPPD) being developed by Texas Instruments. The preliminary design review was conducted in November 1991. Three-axes prototype telescope assemblies have been built and design evaluation tests initiated.

INTRODUCTION

Stellar trackers can provide the fiducial reference for attitude control systems for air vehicles, satellites, and space-based interceptors. The independence of stellar fixes from radio aids has provided a reliable source of navigation information in both peace and war. When the stellar tracker is used to augment an IMU, a synergistic blending of data occurs where the high-frequency attitude data is derived from the IMU, and the low-frequency information is derived from stellar fixes. This process of complementary filtering of data provides excellent attitude information that is accurate over a wide range of frequencies. Furthermore, since the low frequency is derived from the stellar tracker, the requirement for precision and costly gyroscopes for attitude control has been reduced.

Figure 1 shows the probability of seeing the sky from sea level. Above 13.7 km (45,000 ft) in altitude, the probability of having an unobstructed view of the stars is essentially 100 percent. Although at an altitude of 13.7 km your view of the sky is unobstructed by cloud coverage, the sky background light will prevent you from observing the stars in the daylight. Yet at night, the view of the stars, from that altitude, is spectacular. Above 13.7 km, the daytime sky background, not in the direct vicinity of the sun, grows progressively darker with increases in altitude until it essentially turns black and is indistinguishable from the nighttime sky. Figure 2 shows the star magnitude capability versus altitude for two different-aperture telescopes in daylight. Basically, it shows that observing stars in daylight at sea level with a 232 cm^2 (36 in^2) aperture, 3 deg FOV telescope has essentially the same stellar magnitude capability as a 4.65 cm^2 (0.72 in^2) aperture operating at 97 km (60 mi) above the earth. It also shows that at altitudes above 97 km, there is no improvement in star magnitude capability, for a given telescope, since the sky background noise has reached a minimum and the stellar irradiance experiences no loss due to atmospheric transmission. Table 1 is a simplistic Signal-to-Noise Ratio (SNR) equation definition for stellar trackers. The small-aperture telescope is in good correlation with our experience on a clear, moonless, desert night. Under these conditions an observer can easily see the Little Dipper constellation, which has 4.7 magnitude stars. In fact, under good stellar observation conditions, the human eye can detect magnitude 6 stars at sea level. The eye has a pupil diameter of between 6 and 9 mm, corresponds to an aperture of about 0.6 cm^2, and is

much smaller than the 4.6 cm^2 telescope in the star magnitude capability curve of Figure 2.

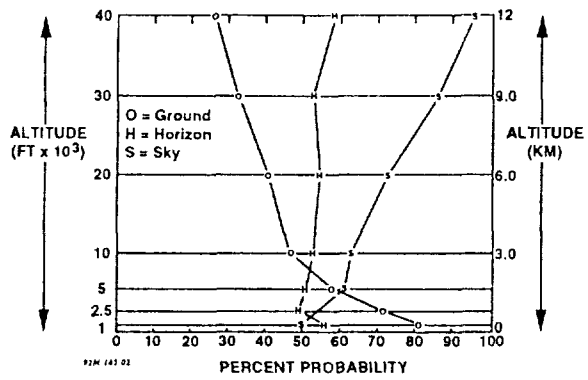

Figure 1. Probability of Clear Lines of Sight Over the Northern Hemisphere for All Seasons Combined (72,000 Observations)

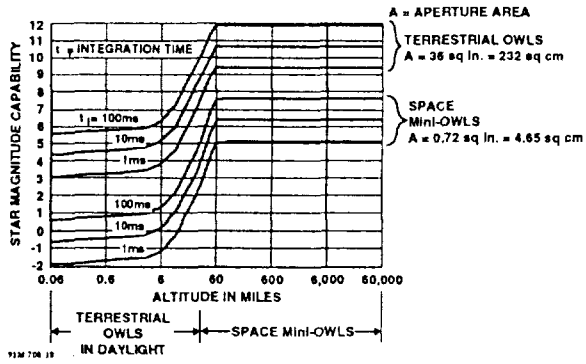

Figure 2. Star Tracker Sensed Magnitude Versus Altitude for a Silicon Detector and a 3 Deg FOV

Thus, based on our experience, empirical measurements, and analysis, the SDI Organization in Washington, D.C., Wright Laboratories in Dayton, Ohio, and Eglin AFB, Florida, and Northrop have embarked on the design of a Miniature Optical Wide-Angle Startracker. This telescope is specifically designed to correct the attitude of spaceships, satellites, and space-based interceptors. In this capacity it provides the fiducial reference for the vehicle's attitude control system.

STELLAR TRACKER CONCEPTS

The stellar tracker, unlike an observation telescope, is specifically designed to correct the attitude control system of a vehicle and is therefore primarily concerned with the line of sight (LOS) to the stars. Thus the spectral content and stellar magnitude are of minor significance if they provide sufficient stellar irradiance to satisfy the functional

Table 1. Signal-To-Noise Ratio Equations For a Stellar Tracker

Signal-To-Noise Ratio (SNR)

$$Q_{SP} = q \cdot \Phi_S \cdot \Delta\lambda \cdot A_T \cdot A_a \cdot T_T \cdot \eta \cdot I_t \cdot N_I / N_S$$

Where:

- Q_{SP} = Star signal charges per pixel
- q = Electronic charge
- Φ_S = Stellar spectral radiance
- $\Delta\lambda$ = Wavelength bandwidth of telescope system
- A_T = Atmosphere transmission
- A_a = Aperture area
- T_T = Telescope transmission
- η = Quantum efficiency
- I_t = Integration time of a frame (stellar snapshot)
- N_I = Number of frame snapshots utilized
- N_S = Number of pixels containing the star image (star blur factor)

$$Q_{BP} = \frac{q \cdot \Phi_B \cdot \Delta\lambda \cdot A_a \cdot T_T \cdot FOV \cdot \eta \cdot I_t \cdot N_I}{N \cdot O_F}$$

Where:

- Q_{BP} = Background photo charges per pixel
- Φ_B = Sky background spectral radiance
- FOV = Field of view
- N = Total number of pixels in sensor array
- O_F = Sky background attenuation of optical filter

$$Q_{DP} = q \cdot n^2/\tau \cdot V_B \cdot I_t \cdot N_I$$

Where:

- Q_{DP} = Detector dark durrent charges per pixel
- n = Detector intrinsic carrier concentration
- τ = Detector dark current charge generation time
- V_B = Detector charge generation bucket volume

$$Q_{NP} = \sqrt{(Q_{SP} + Q_{BP} + Q_{DP})\, Q_{ES}}$$

Where:

- Q_{NP} = Noise charges per pixel
- Q_{SP} = Star photo charges per pixel
- Q_{BP} = Background photo charges per pixel
- Q_{DP} = Dark detector charges per pixel
- Q_{ES} = Electronic system bandwidth noise coefficient

$$SNR = \frac{Q_{SP}}{\sqrt{(Q_{SP} + Q_{BP} + Q_{DP})\, Q_{ES}}}$$

For Sea-Level Daytime Tracking in a Non-Nuclear-Event Environment, the SNR equation simplifies to:

$$Q_{BP} >> Q_{SP} + Q_{DP}$$

$$SNR \approx \frac{Q_{SP}}{\sqrt{Q_{BP} \cdot Q_{ES}}}$$

$$SNR \approx \frac{\Phi_S \cdot A_T}{N_S} \cdot \sqrt{\frac{q \cdot \Delta\lambda \cdot A_a \cdot T_T \cdot \eta \cdot I_t \cdot N_I \cdot N \cdot O_F}{\Phi B \cdot FOV \cdot Q_{ES}}}$$

92M-165-07

SNR requirements of the tracker. This occurs when there is sufficient stellar photon flux to offset the corrupting noise sources. Figure 3 shows the conceptual design of the Mini-OWLS. It is made up of three 4-deg-FOV star trackers spaced 120 deg apart in azimuth and 30 deg off the zenith, all embedded in a single housing. The star tracker's function is to measure the attitude drift about three orthogonal vehicle axes. A single stellar fix only provides an attitude update about the two vehicle's axes normal to the star's LOS. Thus, in order to provide a complete three-axes attitude update, an additional fix from a different LOS is required. The ideal geometric separation is to have the two LOSs cross each other and thus have an angular separation of 90 deg. This 90-deg separation in the LOSs could be accomplished by mounting a single axis telescope in gimbals and then rotating the gimbals to observe a different LOS. Another method of obtaining different LOSs is to have a strapdown telescope and then rotate the vehicle to observe a different LOS. Both of the above methods of obtaining different LOSs either add costly moving parts to the system or impose constraints on the vehicle. The low-cost Mini-OWLS, with its three implicit strapdown telescopes, requires no gimbals or vehicle rotations to observe multiple LOSs.

When the optimum 90-deg separation isn't achieved, there is a Geometric Dilution of Precision (GDOP). Although the Mini-OWLS has a 51.3-deg separation in telescope axes, its GDOP, as shown in Figure 4, is negligible. This figure also shows that a single 20-deg very wide FOV telescope, or dual telescopes with an angular separation of 20 deg, experiences significant GDOP problems. Furthermore, having three telescopes, each of which provides two axes of attitude updates, enables the system to provide a redundant attitude compensation for all three vehicle axes.

In addition, the redundant telescope design provides a measure of self compensation for thermal mechanical expansion of the stellar tracker. Figure 5 shows a two-axis tracker with stars in each FOV. When the attitude of the vehicle changes about an axis orthogonal to the plane of the telescopes, both telescopes observe identical variations in attitude and direction. Conversely, when the telescope

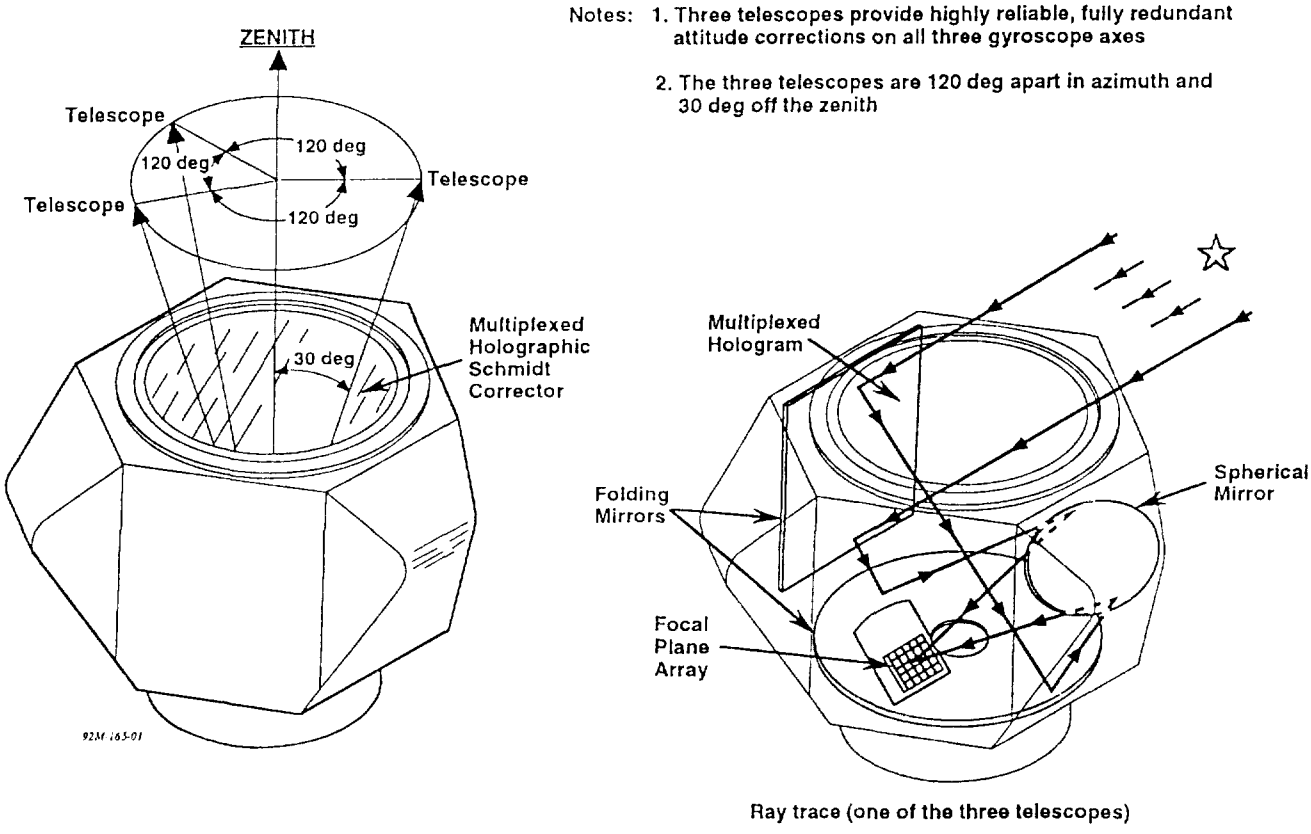

Figure 3. Mini-OWLS Multiplexes Three Wide-Field Schmidt Telescopes in a Single Housing

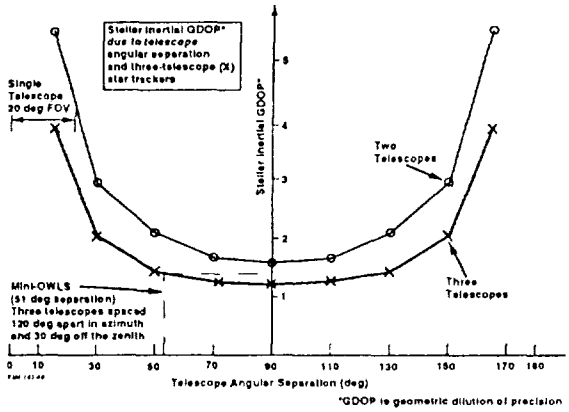

Figure 4. Astro-Inertial GDOP Due to Telescope Angular Separation

structure expands homogeneously, then the attitude variations of the telescopes change equally in magnitude but in opposite directions. Thus the average attitude associated with the expansion of the telescopes is zero.

This self-compensation feature is optimized in the Mini-OWLS design since three telescopes represent the minimum number of stellar trackers required to achieve self compensation.

TELESCOPE CONSTRUCTION

Figure 6 shows the spherical aberration of an uncompensated spherical mirror. Its focus occurs at half the mirror's radius for the plane-wave rays close to the principal axis ray. As the height, h, of the plane wave increases from the principal ray axis, the focus decreases slightly from its half-radius focal length, resulting in a blurred focus. This spherical aberration can be minimized by the insertion of an aspheric Schmidt corrector plate positioned at the mirror radius. The aspheric corrector plate attempts to deviate the plane-wave rays such that all plane rays focus at a single point or focal length independent of the height of the plane wave above the principal ray axis.

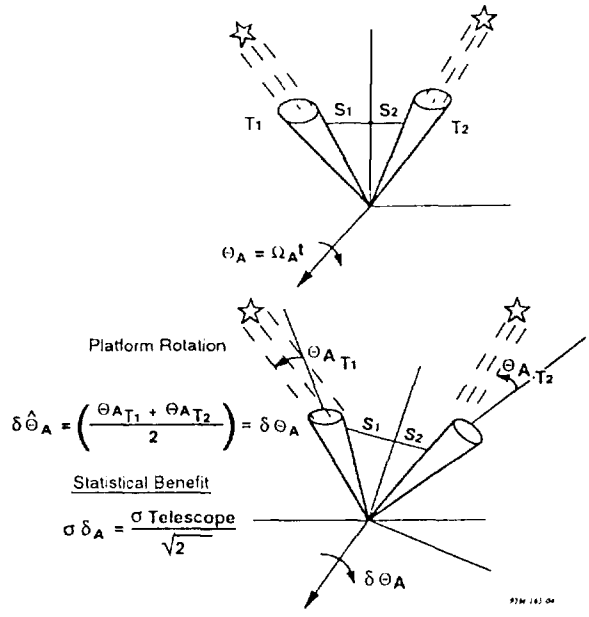

Figure 5a. Mini-OWLS Provides the Benefit of Redundant Observations

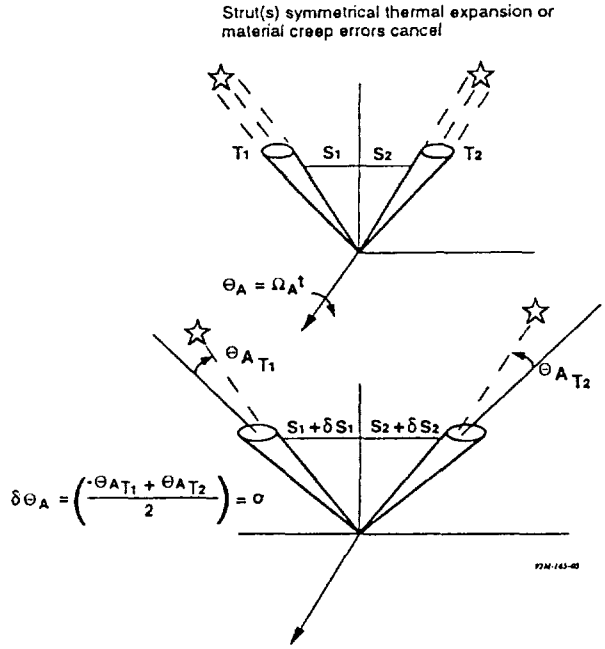

Figure 5b. Mini-OWLS Minimizes Telescope Strut Expansion Errors

Figure 5. Mini-OWLS Provides the Benefit of Redundancy and Self Compensation for Thermal Expansion and Material Creep

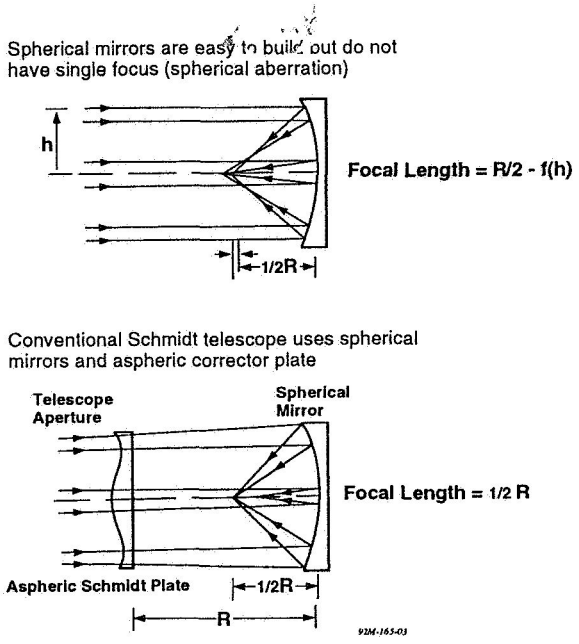

Figure 6. Spherical Aberration

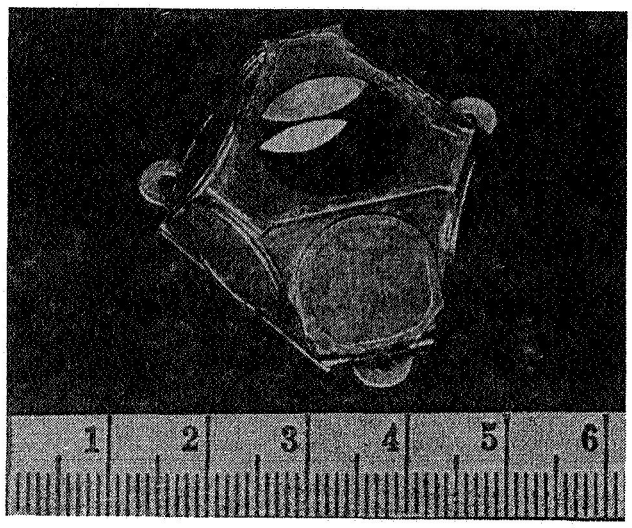

Figure 7. Mini Optical Wide-Angle Lens Startracker (Size in Centimeters)

The aspheric Schmidt corrector plate is costly to make and could be replaced by a single Holographic Optical Element (HOE). Furthermore, three holographic Schmidt corrector plates can be multiplexed in a single aperture. A picture of the Mini-OWLS is shown in Figure 7.

The Mini-OWLS is composed of three wide-FOV Schmidt camera telescopes. The corrector plate for all three telescopes is a multiplexed HOE in lieu of the costly aspheric corrector plates in conventional Schmidt cameras. This unique HOE construction eliminates all costly optical elements since the plane and spherical mirror surfaces are simple to construct. Because all of the optical elements are essentially surface phenomena (i.e., mirrors and HOEs), the telescope can be made extremely lightweight. The telescope construction is based on proven industrial techniques with the single three-axes multiplexed HOE Schmidt corrector plate fastened to the telescope along with the FPAs. The telescope's major precision assemblies are in the mirror housing. The single multiplexed HOE provides the corrector plates for the spherical aberration, while the FPAs provide the electrical readouts of the stellar irradiances.

SUN THERMAL ANALYSIS

Solar heating effects on a silicon FPA in the Mini-Owls star sensor at its operating bandwidth are not important. Under space illumination conditions with the sun focused on four pixels, assuming a constant-temperature mounting surface at any temperature, only a 4.5 °C temperature change will occur.

STRAY LIGHT MEASUREMENTS

Stray light measurements were made using the Mini-OWLS prototype telescope. Figure 8 depicts the experiment setup. With the simulated sun set 30 deg off one telescope axis, the stray light detected in the other two axes as a fraction of the incident beam was negligible. With the simulated sun directly on-axis, the optical crosstalk detected at the FPA for a second telescope was higher, as expected, and is readily reducible to an acceptable level by optimizing the optical surfaces to reduce the scattered light.

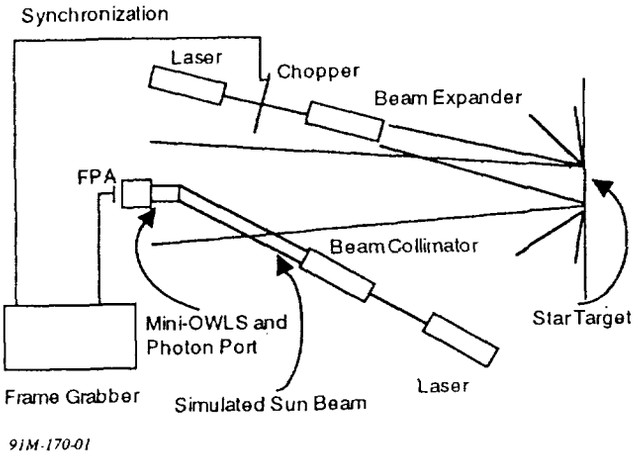

Figure 8. Solar Stray Light Experiment

CONCLUSION

The Mini-OWLS represents a radical departure in star tracker design. It is an optimum configuration that is specifically designed to provide a three-axes fiducial attitude reference system that augments the high-frequency attitude control system for a host of vehicles. The design minimizes weight and telescope expansion errors. It maximizes mission success by providing high accuracy and reliability along with built-in redundancy and self test.

FLIGHT MECHANICS/ESTIMATION THEORY SYMPOSIUM

MAY 5-7, 1992

SESSION 6

SCALAR GAIN INTERPRETATION OF LARGE ORDER FILTERS

Paul A.C. Mason
Research Assistant
N.A.S.A. Graduate Fellow

D. Joseph Mook
Associate Professor
Member AIAA

Department of Mechanical and Aerospace Engineering
State University of New York at Buffalo, NY 14260

Abstract

A technique is developed which demonstrates how to interpret a large fully-populated filter gain matrix as a set of scalar gains. The inverse problem is also solved, namely, how to develop a large-order filter gain matrix from a specified set of scalar gains. Examples are given to illustrate the method.*

Introduction

The intent of the present work is twofold. First, the Scalar Gain Interpretation (SGI) of the gain matrix for discrete filters is developed. The scalar interpretation provides the filter designer with an easily understood description of large-order Multi-Input Multi-Output (MIMO) filters. This interpretation can be used to aid filter designers in analyzing the effects of changes in the gain matrix or other filter parameters. Second, a technique for determining a, fully-populated gain matrix which satisfies specified scalar equivalent gains is demonstrated. Thus, in the common instance that a filter designer does not know certain filter parameters, making the choice of the gain somewhat arbitrary, the gain may be selected based on the scalar equivalents directly rather than by assuming values for the unknown covariances.

The motivation for filtering is to obtain the best estimates of the true states of a dynamic system, given a (generally imperfect) model and a (generally imperfect) set of measurements[5]. To illustrate the concepts of the paper and to motivate the discussion, consider the simple linear discrete Kalman filter, which may be represented as [3]:

$$x_k^- = \Phi_k x_{k-1}^+ \tag{1a}$$

$$P_k^- = \Phi_{k-1} P_{k-1}^- \Phi_{k-1}^T + Q_{k-1} \tag{1b}$$

$$K_k = P_k^- H_k^T \left[H_k P_k^- H_k^T + R_k \right]^{-1} \tag{1c}$$

$$x_k^+ = x_k^- + K_k (z_k - H_k x^-{}_k) \tag{1d}$$

$$P_k^+ = [I - K_k H_k] P_k^- \tag{1e}$$

*. This work was supported by the National Aeronautics and Space Administration (NASA)/Langley Research Center

where x is the $nx1$ state vector, Φ is the nxn state transition matrix, P_k is the nxn state error covariance matrix, Q_k is the nxn process noise, K_k is the nxm gain matrix, z_k is an $mx1$ measurement vector modeled by

$$z_k = H_k x_k + v_k \tag{2}$$

where H is the mxn measurement model, v is the measurement error vector, and R_k is the mxm measurement covariance matrix. The subscripts $k-1$, k refer to discrete times t_{k-1}, t_k. The superscript (-) refers to values based on measurements up to but not including z_k, and the superscript (+) refers to values obtained after including measurement z_k.

The operation of the filter proceeds as follows. Eqs. (1a) and (1b) are used to calculate the state estimate and its error covariance between measurements. When a new measurement set z_k is obtained, Eqs. (1d) and (1e) are used to update the values of the state estimate and its error covariance. The updated values depend on the value of the gain matrix calculated using Eq. (1c), and so the accuracy of the filter is directly tied to the determination of K_k. K_k depends on the two covariance matrices: R, representing the error covariance matrix of the measurements, and Q, representing the state error covariance introduced as a result of the approximation of the system dynamics via Eq. (1a).

Theoretically, the Kalman and related filters find the unbiased minimum variance (or maximum likelihood) estimate of the state vector. Unfortunately, this is only true if all the noise and system parameters are known exactly. In practice, neither the measurement noise covariance,R, nor the process noise covariance,Q, is perfectly known. In fact, modeling errors may be far more complex than what is theoretically modeled by the process noise. Moreover, the initial value for P_0 may not be known. Thus, the filter design problem normally requires these matrices to be assumed at least somewhat arbitrarily. For a large, fully populated, non-square gain matrix, it is very difficult to interpret the correlation between the assumed covariances and the filter performance. Often, the gain matrix itself is simply assumed directly. If the assumptions are poor, then the filter will be suboptimal, and in certain cases, the filter may itself become unstable [11].

The main motivation behind the scalar gain interpretation is to give the filter designer some insight into the process of designing a filter and an understanding of how the gain matrix affects the MIMO estimation. Although the theoretical development of classical filtering techniques is sound, the practical implementation of the theory is difficult due to the unknown numerical values of the process noise covariance matrix, and measurement noise covariance matrix. In the case of a scalar filter, the effect of the gain is readily apparent. In order to find an easily understood interpretation of the MIMO gain matrix, a parallel between the scalar filter and the MIMO filter gain is found. This parallel then allows the filter designer to visualize the MIMO filter as several scalar filters.

There are two major reasons why the filter designer's intuition has been removed from the design process. The first reason is due to breakthroughs in estimation theory. For example, many algorithms and theories have been developed to find the noise and filter parameters for the Kalman

filter and its gain. Mehra [1] used the innovation sequence property to identify the process noise covariance matrix and the measurement noise covariance matrix. In other methods adaptive Kalman filters have been devised to determine the unknown noise and system parameters [8]. Algorithms such as least squares [8] and the dead beat process noise estimator [7] have also been used to determine the noise and system parameters. However, these algorithms do not describe the effect that the newly found Kalman gain has on the estimation. Other adaptive filters attempt to find the Kalman gain directly [2,9,10]. The accuracy of these techniques varies greatly from case to case, but in any event the interpretation of the gain matrix is difficult at best.

The second reason is that high order systems diminish a designer's general understanding of the effect the Kalman gain has on the estimation. In the scalar case, the affect of the Kalman gain on the estimation is obvious. But as the order of the system increases, the interpretation of the Kalman gain matrix, which determines the optimal estimates, becomes vague.

Incorporating the robust methods mentioned above and the scalar gains interpretation, the MIMO filter designer can determine the best gain and still retain insight as to how the gain affects the estimation.

Scalar Interpretation

The Scalar Filter

To define the problem in this paper, consider a scalar system represented by Eqs.(1). Eq.(1a) provides the state estimate, from the filter model, at time t_k, based on the estimates obtained through time t_{k-1}. At t_k, measurement z_k becomes available. Eq.(1d) is used to update the state estimate based on the residual between z_k and the predicted value $H_k x_k^-$.

In the scalar case, if H=1 (i.e., the state is measured directly), the gain K_k has a value between 0 and 1. At K_k=1, the filter relies only on the measurement

$$x_k^+ = x_k^- - 1\,(z_k - x^-_k) = z_k$$

At K_k= 0 the filter relies only on the model estimate:

$$x_k^+ = x_k^- - 0\,(z_k - x^-_k) = x^-_k$$

When the value of K_k is between one and zero, the filter takes a weighted average of the model and the measurements. In the scalar case, Eq.(1d) can be solved for K_k to obtain

$$K_k = \frac{x_k^+ - x_k^-}{z_k - H_k x^-_k} \tag{3}$$

To "normalize" the gain to lie within 0 and 1 we define the "physical scalar gain" (PSG) as

$$PSG = \frac{H_k x^+ - H_k x^-}{z_k - H_k x^-} \tag{4}$$

This concept is illustrated in Figure 1.

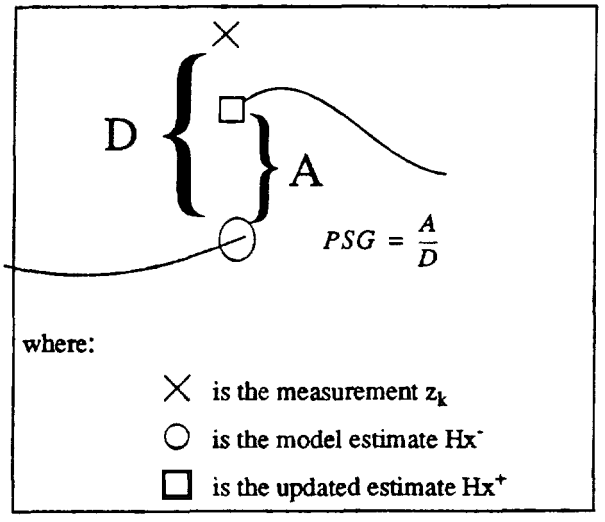

***Figure 1* Graphical interpretation of the scalar filter gain**

In Figure 1, D is the residual between the model output estimate and the measurement. It can be seen that the PSG represents the amount, A, of the residual used in the update, divided by the total residual, D, i.e.,

$$PSG = \frac{H_k x^+ - H_k x^-}{z_k - H_k x^-} = \frac{\text{total correction}}{\text{total residual}} = \frac{\text{update estimate - model estimate}}{\text{measurement - model estimate}} \tag{5}$$

Thus in the scalar case, the physical scalar gain and the Kalman gain are equivalent if the measurement is the state of the filter.

The effect of the filter parameters Q and R on the gain and state estimates can be seen by examining the scalar Kalman gain given by Eq.(1c)

$$K_k = \frac{P_k^- H_k^T}{\left[H_k P_k^- H_k^T + R_k\right]} \tag{6}$$

The Kalman gain can be written as a function of Q and R by substituting the error covariance P^-:

$$K_k = \frac{(\Phi_{k-1} P_{k-1}^+ \Phi_{k-1}^T + Q_{k-1}) H_k^T}{\left[H_k (\Phi_{k-1} P_{k-1}^+ \Phi_{k-1}^T + Q_{k-1}) H_k^T + R_k\right]} \tag{7}$$

For the scalar case where H=1 this simplifies to

$$K_k = \frac{\Phi_{k-1} P_{k-1}^{+} \Phi_{k-1}^{T} + Q_{k-1}}{\Phi_{k-1} P_{k-1}^{+} \Phi_{k-1}^{T} + Q_{k-1} + R_k} \tag{8}$$

From Eq.(8) it can be seen that if Q is large and R is small, then the denominator and the numerator will be approximately equal. This scenario describes the filtering of a good measurement with a poor model. In this situation the optimal filter relies primarily on the measurements. The other extreme occurs when Q is small and R is large (poor measurements and a good model). The gain for this case is close to zero.

The effect of Q and R on the Kalman gain matrix is very difficult to interpret in the MIMO filter case. With the scalar gain interpretation one can clearly see the effect of Q and R on the Kalman gain matrix, by examining the scalar equivalents.

The Scalar Equivalents for the MIMO filter

In the previous section, the theory of the Kalman filter and the concept of the physical scalar gain (PSG) have been given. In this section, the scalar gain interpretation for MIMO filters is derived. The concepts of the scalar gain interpretation are applicable to any order MIMO system, and to any filter gain. Consider the matrices of Eq.(1d):

$$K_k = \begin{bmatrix} k_{11} & \cdots & k_{m1} \\ k_{21} & \cdots & \vdots \\ \vdots & \cdots & \vdots \\ k_{n1} & \cdots & k_{nm} \end{bmatrix}_k \qquad H_k = \begin{bmatrix} h_{11} & \cdots & h_{1n} \\ \vdots & \cdots & \vdots \\ h_{m1} & \cdots & h_{mn} \end{bmatrix}_k$$

$$x_k^{-} = \begin{bmatrix} x_1^{-} \\ \vdots \\ x_n^{-} \end{bmatrix}_k \qquad z_k = \begin{bmatrix} y_1 \\ \vdots \\ y_m \end{bmatrix}_k$$

Expanding Eq.(1d)at time t_k, we may write

$$\begin{aligned} x_1^{+} &= x_1^{-} + k_{11}(z_1 - h_{1,1}x_1^{-} - \ldots - h_{1,n}x_n^{-}) + \\ &\ldots + k_{1,m}(z_m - h_{m,1}x_1^{-} - \ldots - h_{m,n}x_4^{-}) \\ &\vdots \quad \vdots \quad \vdots \\ &\vdots \quad \vdots \quad \vdots \\ x_n^{+} &= x_n^{-} + k_{n,1}(z_1 - h_{1,1}x_1^{-} - \ldots - h_{1,n}x_n^{-}) + \\ &\ldots + k_{n,m}(z_m - h_{m,1}x_1^{-} - \ldots - h_{m,n}x_n^{-}) \end{aligned} \tag{9}$$

where the subscripts now refer to position in the vector or matrix at time t_k. Eq.(9) can be written

in a simplified form by defining D_i as

$$D_i = (z_i - h_{i,1}\bar{x_1} - \ldots\ldots - h_{i,n}\bar{x_n}) \qquad i = 1, \ldots m \tag{10}$$

D_i represents the residual between the i^{th} measurement and the i^{th} element of the predicted model output $H\bar{x}$. Eq.(1d) can now be written as

$$x_j^+ = \bar{x_j} + K_{j,i}D_i \qquad j = 1 \ldots n \tag{11}$$

Thus, the elements of the j^{th} row vector of K_k describes how much of each residual is used in the estimation of the j^{th} state.

In order to find the PSG associated with each residual D_i, the state estimates must be converted to the output estimates by multiplying by output matrix H:

$$y_j = H_j\bar{x_i} + \sum_{i=1}^{m} (HK)_{j,i}D_i \tag{12}$$

In Eq.(12), y_j is the estimate of the j^{th} output at time t_k using all measurements including z_k, and H_j is the j^{th} row of the output matrix. Comparing Eq.(12) with Eq.(4), the physical scalar gain for a MIMO filter is described mathematically as:

$$PSG_i = \frac{(HK)_{i1}(z - H\bar{x})_1 + \ldots + (HK)_{im}(z - H\bar{x})_m}{(z - H\bar{x})_i} \tag{13}$$

In the typical case where the i^{th} estimated output is strongly dependent on the i^{th} measurement but not on the other measurements, Eq.(13) simplifies into:

$$PSG_i \approx \frac{(HK)_{ii}(z - H\bar{x})_i}{(z - H\bar{x})_i} = (HK)_{ii} \tag{14}$$

If this assumption is not valid then the concept of the physical scalar gain is still valid, but the PSG is not a constant since the random elements of the numerator in Eq.(13) are not canceled by the denominator as in Eq.(14). However, for stationary measurement noise statistics, the expected value of the PSG's are constant. The HK matrix still contains the scalar percentages of the residuals used in the estimation of each output estimate. Comparing Eq.(13) and Eq.(14), the PSG's approach constants if HK becomes diagonal dominant. The concept of the scalar gain interpretation and the diagonal assumption for the HK matrix is reinforced in the expectation analysis section.

The scalar gains can be used to monitor the effect of Q and R. If Q is large and R is small then the corresponding scalar equivalent gains should all be close to 1. In the inverse case if R is large and Q is small the scalar gains should be close to zero. In the common situation where Q and R are not well known, checking the scalar gains can aid in interpreting the effect of assumed values of Q and R.

To illustrate the equivalence between the physical scalar gains and the full gain matrix consider the following simple example, where n=4 and m=2.

Let

$$H = \begin{bmatrix} 1 & 0 & 0 & 0 \\ 0 & 1 & 0 & 0 \end{bmatrix} \qquad z = \begin{bmatrix} 0.5 \\ 0.3 \end{bmatrix}$$

$$k = \begin{bmatrix} 0.5 & 0 \\ 0 & 0.5 \\ 0.5 & 0 \\ 0 & 0.5 \end{bmatrix} \qquad x^- = \begin{bmatrix} 0.1 \\ 0.2 \\ 0.3 \\ 0.4 \end{bmatrix}$$

Substituting into Eqs.(1), we find

$$Hx^- = \begin{bmatrix} 0.1 \\ 0.2 \end{bmatrix} \qquad D = (z - Hx^-) = \begin{bmatrix} 0.4 \\ 0.1 \end{bmatrix}$$

$$KD = \begin{bmatrix} 0.2 \\ 0.05 \\ 0.2 \\ 0.05 \end{bmatrix}$$

$$x^+ = x^- + KD = \begin{bmatrix} 0.3 \\ 0.25 \\ 0.5 \\ 0.45 \end{bmatrix}$$

$$y = Hx^+ = \begin{bmatrix} 0.3 \\ 0.25 \end{bmatrix}$$

$$HK = \begin{bmatrix} 0.5 & 0. \\ 0. & 0.5 \end{bmatrix}$$

The physical scalar gains (PSG) are

$$\frac{Hx^+ - Hx^-}{z - Hx^-} = \frac{\begin{bmatrix} 0.3 \\ 0.25 \end{bmatrix} - \begin{bmatrix} 0.1 \\ 0.2 \end{bmatrix}}{\begin{bmatrix} 0.5 \\ 0.3 \end{bmatrix} - \begin{bmatrix} 0.1 \\ 0.2 \end{bmatrix}} = \begin{bmatrix} 0.5 \\ 0.5 \end{bmatrix}$$

The physical scalar gains are the same as the diagonal elements of the diagonally dominant HK matrix.

The Expectation Analysis

The PSG described in Eq.(14) can be written in the following simplified form:

$$(PSG)_j = \frac{\sum_{i=1}^{m} (HK)_{ji}[z_i - (Hx^-)_i]}{[z_j - (Hx^-)_j]} \tag{15}$$

Performing the expectation analysis of the PSG results in the predicted numerical value of the PSG at steady state. This value describes how much weight is placed on the measurement vs. the model of a particular measurement estimate. The expectation analysis of the PSG is similar to the analysis of the error covariance [3]. As in the case of the error covariances the PSG is squared and then the expectation is taken:

$$E[(PSG)_j^2] = E\left[\left(\frac{\sum_{i=1}^{m} (HK)_{ji}[z_i - (Hx^-)_i]}{[z_j - (Hx^-)_j]}\right)^2\right] \tag{16}$$

Since H and K matrices are time invariant (constants), they can be taken outside the expectation

$$E[(PSG)_j^2] = \frac{\sum_{i=1}^{m}\sum_{l=1}^{m} (HK)_{ji}(HK)_{jl} E\{[z_i - (Hx^-)_i][z_l - (Hx^-)_l]\}}{E\{[z_j - (Hx^-)_j][z_j - (Hx^-)_j]\}} \tag{17}$$

The expected value in the numerator and denominator is expanded by substituting for $z=Hx+v$.

$$E\{[Hx+v-Hx^-][Hx+v-Hx^-]^T\} = E\{[H(x-x^-)+v][H(x-x^-)+v]^T\} = RHS$$

The right-hand side can be expanded by multiplying out the internal terms to obtain

$$RHS = E\{H(x-x^-)(x-x^-)^T H^T + vv + H(x-x^-)v^T + v(x-x^-)^T H^T\} \tag{18}$$

Note that $(x-x^-) = e^-$, $E[vv^T] = R$ and $E[e^-(e^-)^T] = P_{xx}^-$. Eq.(18) now simplifies into

$$RHS = HP_{xx}^- H^T + R + HE\{v(e^-)^T\} + E\{(e^-)v^T\}H^T \tag{19}$$

Assuming that the noise vector, v, and the estimation error, e, are uncorrelated, the last two terms in Eq.(19) are zero. Eq.(19) can now be written as:

$$RHS = HP_{xx}^- H^T + R \tag{20}$$

Substituting this back into Eq.(17) yields

$$E[(PSG)_j^2] = \frac{\sum_{i=1}^{m}\sum_{l=1}^{m} (HK)_{ji}(HK)_{jl}(HP_{xx}^- H^T + R)}{[H_j(P_{xx}^-)_{jj}H_j^T + R_{jj}]} = \frac{(HK)_j[HP_{xx}^- H^T + R](HK)_j^T}{[H_j(P_{xx}^-)_{jj}H_j^T + R_{jj}]} \tag{21}$$

If HK, R and $HP_{xx}^- H^T$ are diagonal matrices, then Eq.(21) may be simplified to

$$E[(PSG)_j^2] = (HK)_{jj}^2 \tag{22}$$

This assumption is valid for systems where the covariance error matrix is diagonal; therefore, the errors associated with the states are not coupled. Taking the square root of both sides gives the

expression for the approximation of the expected magnitude of the PSG.

$$\sqrt{E\left[(PSG)_j^2\right]} = \sqrt{\frac{(HK)_j\left[HP_{xx}^{-}H^T + R\right](HK)_j^T}{\left[H_j(P_{xx}^{-})_{jj}H_j^T + R_{jj}\right]}} \tag{23}$$

The square root of the squared expected value PSG is a function of not only the j^{th} measurement but also of the other measurements and the residuals associated with them [Eq.(23)].

Finding a Fully Populated Gain Matrix

Determination of Q and R (or directly, K) is rarely simple for a large order filter. Since it is easier to determine and understand a scalar gain rather than a fully populated gain matrix, MIMO filters are often written as sets of decoupled scalar filters. The process of transforming a MIMO filter into several scalar ones is clumsy and may result in errors. This is the primary motivation for finding a method to determine an equivalent fully populated gain matrix from a set of scalar gains.

Let the specified scalar gains be placed in the diagonal G_d matrix (mxm). The fully populated K matrix is determined by equating the scalar gains to the HK matrix. If H is a square matrix, then premultiplying both sides by the inverse of H yields an equation for the gain matrix as a function of the scalar gains:

$$\begin{aligned} H^{-1}HK_d &= H^{-1}G_d \\ K_d &= H^{-1}G_d \end{aligned} \tag{24}$$

where K_d is the MIMO filter gain matrix designed from the scalar gains. Since H is generally not a square matrix one can not use this procedure to determine K_d. To circumvent this problem the Moore -Penrose Pseudoinverse [4,6] is utilized to determine the pseudoinverse of a non-square matrix H:

$$K_d = (H)^{*-1}G_d \tag{25}$$

where $(\ )^{*-1}$ represents the pseudoinverse.

This method of determining a fully populated gain matrix from a set of scalar gains, constrains the output of the filter. It does not constrain the states of the filter. Since the scalar gain interpretation is associated with the output of the filter and not the states, then the fully populated gain matrix found from these gains is forced to have the same output as dictated by the scalar gains. A design gain matrix that has the same scalar gains as another fully populated gain matrix will have the same output estimate but not necessarily the same states.

Simulation Results

A filter simulation is used to verify the theory of the scalar gain interpretation. There are two objectives of this section. The first objective is to demonstrate that the SGI does approximate the scalar gains of the filter. The second objective is to verify that a fully populated gain matrix can be determined from a set of specified scalar gains.

To accomplish the first objective an 8th-order time-varying Kalman filter is used. During the execution of this filter the average physical scalar gains are calculated. These averages are compared to the expected scalar gains to validate the scalar gain interpretation. To ensure a fair comparison, the constant gain filter is implemented with the steady-state gain matrix, K. The physical scalar gains of both filters are compared to prove the equivalence of the scalar gains interpretation. The parameters and model of the filter are described in a problem statement.

The second part of this section uses the scalar gains from part 1 to determine the fully populated design gain matrix, K_d A constant gain filter is implemented using K_d. The physical scalar gains are calculated during the execution of the filter. The physical scalar gains are compared to expected scalar gains to prove the equivalence of the design gain matrix to the set of scalar gains. Then, the output estimates of both filters are compared to prove that the K_d and the original steady-state gain matrix produces the same output estimates.

Consider the following example to illustrate the scalar gain interpretation. The measurements are created from the following state space equations.

$$\begin{aligned} \dot{x} &= Ax \\ measurements &= Cx + noise \end{aligned} \tag{26}$$

A is the model of the states and C is the output matrix of a 8 state system. The true model of the system is

A =

0.0	0.0	0.0	0.0	1.0	0.0	0.0	0.0
0.0	0.0	0.0	0.0	0.0	1.0	0.0	0.0
0.0	0.0	0.0	0.0	0.0	0.0	1.0	0.0
0.0	0.0	0.0	0.0	0.0	0.0	0.0	1.0
-10.0	5.0	0.0	0.0	0.0	0.0	0.0	0.0
5.0	-10.0	5.0	0.0	0.0	0.0	0.0	0.0
0.0	5.0	-10.0	5.0	0.0	0.0	0.0	0.0
0.0	0.0	5.0	-5.0	0.0	0.0	0.0	0.0

The state transition matrix is use to find the state trajectories of the true model. A perturbed model is used as the filter model. This perturbed model is created by changing the last four elements in the true A matrix to -3.5 and changing -10.0 , -5.0 to -9.5 , -4.5 respectively. After the states have been converted to output via the output matrix, 26% noise is added to the output to create the measurements. The measurement noise covariances is $R \approx 2.2 \cdot I_{4x4}$. These perturbations and simulated measurements noise are arbitrarily; the values given here are simply for demonstration purposes.

The simulation is implemented for 500 and 1000 measurement points. The Kalman gain reaches steady state at approximately the 200th time step. The steady state Kalman gain matrix is.

K =

0.5124	0.0068	0.0033	-0.0051
0.0115	0.6262	0.0057	-0.0002
0.0032	0.0039	0.5161	-0.0012
-0.0052	0.0001	-0.0013	0.5175
-0.0913	0.0622	0.0054	-0.0018
0.0740	-0.0829	0.0722	0.0058
0.0052	0.0615	-0.0847	0.0767
-0.0021	0.0023	0.0753	0.0407

The H*K matrix at steady state is

0.5124	0.0068	0.0033	-0.0051
0.0115	0.6262	0.0057	-0.0002
0.0032	0.0039	0.5161	-0.0012
-0.0052	0.0001	-0.0013	0.5175

The expected PSGs and the diagonal elements of the H*K matrix are almost identical, since the noise covariance, error covariance, and process noise are assumed to be diagonal. Since the H*K matrix and the expectation gain are diagonally dominant the scalar gains can be found by Eq.(23) or by taking the ii^{th} element of H*K. The expected scalar gains are

Table 1: The Scalar Gain

gain 1	gain 2	gain 3	gain 4
0.5122	0.6261	0.5161	0.5174

The average physical scalar gains (PSGs), of the time-varying filter simulation, are calculated using the matrix form of Eq.(4), which is equivalent to Eq.(13). The average physical scalar gains of the time-varying filter are

Table 2: The average PSG of the variable gain filter

ave PSG	gain 1	gain 2	gain 3	gain 4
500 pts	0.5851	0.6191	0.5743	0.5211
1000 pts	0.5591	0.6188	0.5156	0.5190

Notice the similarity between these gains and the expected gains.

Next a constant gain filter is executed with the steady-state gain matrix shown above. The average PSGs of the constant gains filter are

Table 3: The average PSG of the constant gain filter

ave PSG	gain 1	gain 2	gain 3	gain 4
500 pts	0.5842	0.6189	0.5747	0.5202
1000 pts	0.5586	0.6187	0.5158	0.5185

The PSGs of the constant gain filter and the time-varying filter approximate the expected scalar gains in Table 1. The average PSGs from the constant gain filter are closer to the predicted physical scalar gains, since the gain matrix of the time-varying filter does not reach steady state instantly. As the number of cycles increases this average approaches the predicted value. This trend can be seen in the comparison between the 500 and 1000 point average. The physical scalar gains of these filters are constantly fluctuating, but the average of these gains approach the expected PSGs as time goes to infinity. This fluctuation is due to the off-diagonal residuals of the H^*K matrix.

The second objective of this section is to prove that the design gain matrix can be found from the scalar gains. This gain matrix will produce the same estimated outputs. The set of scalar gains used in this part are taken from Table 1. The design gain, K_d is determined for a diagonal dominant H^*K matrix and the diagonal G_d. This is done to test the uniqueness of the method.

The K_d is found from the diagonally dominant H^*K matrix. A constant gain filter is executed with this K_d. matrix and the same initial conditions as in part 1. The average physical scalar gains of this filter are

Table 4: The average PSG of the design gain filter

ave PSG	gain 1	gain 2	gain 3	gain 4
500 pts	0.5948	0.6175	0.5109	0.5288
1000 pts	0.5510	0.5936	0.5176	0.5216

Like the constant gain and time varying gain filter, the PSGs of this filter are not constant.

Next, the K_d for a diagonal G_d is found. The gain matrix that is produced from this method only uses the i^{th} residual to determine the i^{th} estimate. The PSGs are not a function of the off-diagonal residual effects, therefore physical scalar gains of the diagonal gain filter are constant. The diagonal elements of the G_d matrix are taken from Table 1. The average PSGs are

Table 5: The average PSG of design-diagonal gain filter

ave PSG	gain 1	gain 2	gain 3	gain 4
500 pts	0.5122	0.6261	0.5161	0.5174
1000 pts	0.5122	0.6261	0.5161	0.5174

The physical scalar gains of the diagonal gain filter are constant; therefore, the average PSG is also constant.

Tables 2,3,5 illustrate how all three constant gain filters approach the predicted scalar gains. The comparison of 500 and 1000 points sets of average gains illustrate how the accuracy of approximation increases as time goes to infinity. Therefore it can be inferred that the SGI is a good approximation of the true physical gains of the filter.

Since the scalar gains are the same, the output estimates should be the same. Figures 2-4 contain the first output estimates of the three constant gains filters.

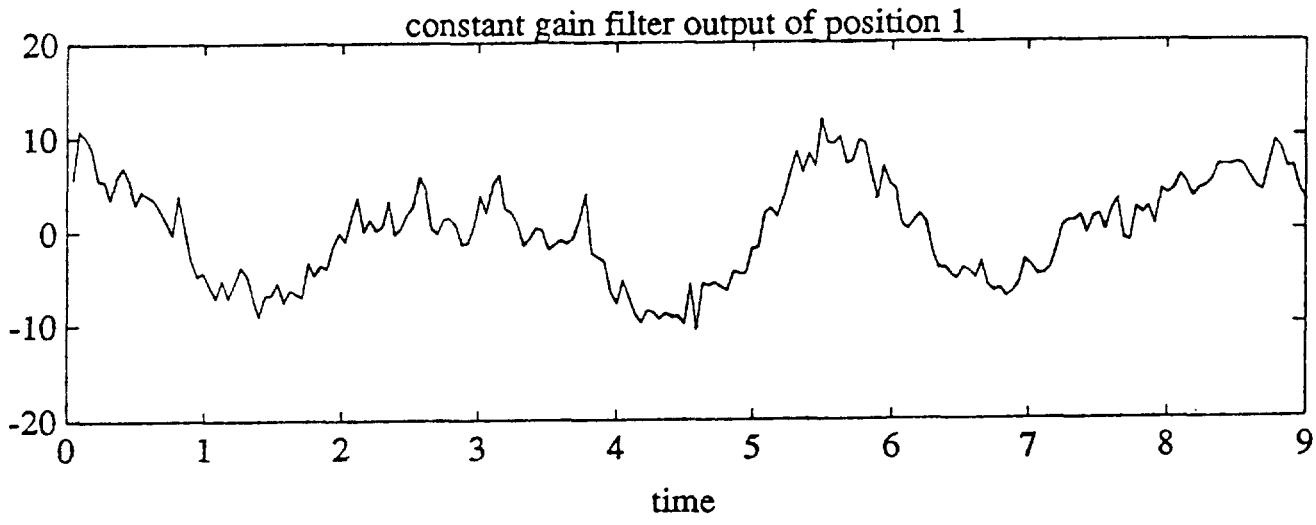

Figure 2 **The output estimates of the constant filter**

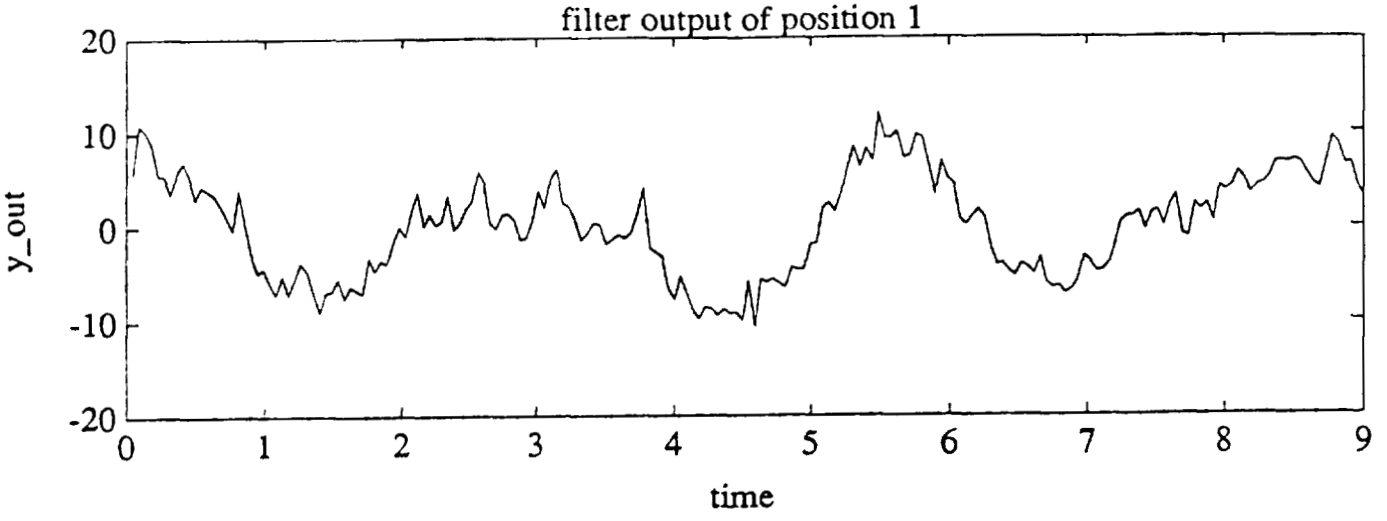

Figure 3 **The output estimates of the constant design gain filter**

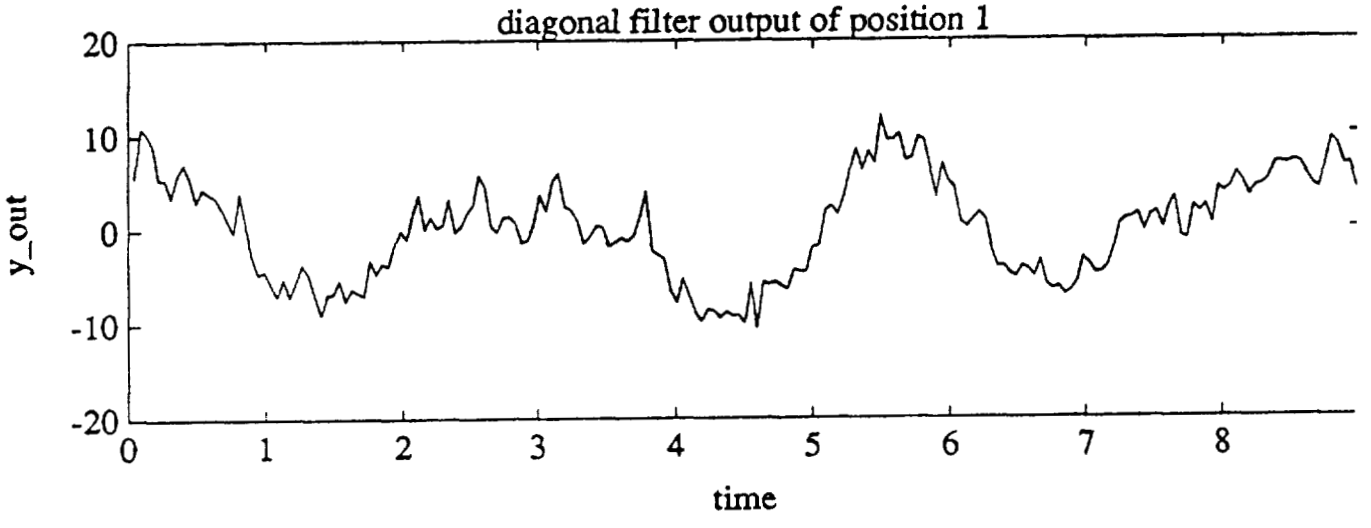

Figure 4 **The output estimates of the constant diagonal design gain filter**

Figures 2-4, which contain the first output estimate, are essentially identical. Therefore the three constant gain filters have an equivalent effect on the output estimates and it can be inferred that a gain matrix can be found from a set of scalar gains. This accomplishes the second objective.

Conclusion

This paper has demonstrated that a large fully populated gain matrix can be interpreted as a set of scalar gains; and, conversely, a fully populated gain matrix can be developed from a specified set of scalar equivalences. The simulation results verify that the scalar gain interpretation is a good approximation of the true filter scalar gains associated with the gain matrix. The accuracy of this approximation increases as the number of measurements samples approaches infinity. Also, the results showed that a fully populated gain matrix can be found from a set of scalar gains. The fully populated gain matrix found from this method is not unique. This was demonstrated by the comparison of the filtering results of the Kalman gains found by the diagonal G_d and the diagonal dominant H^*K matrix.

With the scalar gain interpretation, filter designers can easily interpret the effect of assumed values for the covariance matrices Q and R (or, the gain matrix itself). Alternatively, the scalar gains may be specified directly and the equivalent fully populated gain matrix may be found.

References

[1] Mehra, R. K.," On The Identification Of Variance And Adaptive Kalman Filtering", **IEEE Transactions Automatic Control,** vol. AC-15, pp. 175-184. 1970.

[2] Leondes, C. T., and Siu, T. K. "Identification Of Both The Unknown Plant And Noise Parameters Of The Kalman Filter", **Inter. J. Sys. Sci.**,vol II, no. 6, pp. 711-720., 1980.

[3] Gelb, A., **Applied Optimal Estimation**, MIT Press,1974.

[4] Golub, G.H., and Van Loan, C., **MATRIX Computations**, John Hopkins University Press, 1985.

[5] Chui, C. K., and Chen, G, **Kalman Filtering With Real-Time Applications**, Springer Series in Information Science 17, Springer-Verlag, 1987.

[6] Albert, A., **Regression And The Moore-Penrose Pseudoinverse**, Academics Press 1972.

[7] Gutman, P., and Velger, M., "Tracking Targets With Unknown Process Noise Using Adaptive Kalman Filtering", **Proceedings of the 27th IEEE Conference on Decision and Control**, vol 1., pp. 869-874, 1988.

[8] Moghaddamjoo, A., and Kirlin, R.L., "Robust Adaptive Kalman Filtering With Unknown Inputs", **IEEE Transactions on Acoustics, Speech, and Signal Processing**, v27, n8, pp. 1166-1175, Aug 1989.

[9] Sinha, N.K., and Alvan, T., " Adaptive State Estimation For Systems With Unknown Noise Covariance", **Int. J. System Sci.**, v 8, n4, pp. 377-384, 1977.

[10] Carew, B., and Belanger, P. R., "Identification Of Optimal Filter Steady State Gain For Systems With Unknown Noise Covariance," **IEEE Tran. A.C.**, vol. AC-18, pp. 582-589, 1973.

[11] Fitzgerald, R. J., "Divergence Of The Kalman Filter", **IEEE Tran. A.C.**, vol. AC-16, pp. 736, 1971.

QUATERNION NORMALIZATION IN SPACECRAFT ATTITUDE DETERMINATION

by

J. Deutschmann*, F.L. Markley+, and I.Y. Bar-Itzhack#

Attitude determination of spacecraft usually utilizes vector measurements such as Sun, center of Earth, star, and magnetic field direction to update the quaternion which determines the spacecraft orientation with respect to some reference coordinates in the three dimensional space. These measurements are usually processed by an extended Kalman filter (EKF) which yields an estimate of the attitude quaternion.

Two EKF versions for quaternion estimation were presented in the literature; namely, the multiplicative EKF (MEKF) and the additive EKF (AEKF). In the multiplicative EKF it is assumed that the error between the correct quaternion and its a-priori estimate is, by itself, a quaternion that represents the rotation necessary to bring the attitude which corresponds to the a-priori estimate of the quaternion into coincidence with the correct attitude. The EKF basically estimates this quotient quaternion and then the updated quaternion estimate is obtained by the product of the a-priori quaternion estimate and the estimate of the difference quaternion. In the additive EKF it is assumed that the error between the a-priori quaternion estimate and the correct one is an algebraic difference between two four-tuple elements and thus the EKF is set to estimate this difference. The updated quaternion is then computed by adding the estimate of the difference to the a-priori quaternion estimate.

If the quaternion estimate converges to the correct quaternion, then, naturally, the quaternion estimate has unity norm. This fact was utilized in the past to obtain superior filter performance by applying normalization to the filter measurement update of the quaternion. It was observed for the AEKF that when the attitude changed very slowly between measurements, normalization merely resulted in a faster convergence; however, when the attitude changed considerably between measurements, without filter tuning or normalization, the quaternion estimate diverged. However, when the quaternion estimate was normalized, the estimate converged faster and to a lower error than with tuning only.

In last year's symposium we presented three new AEKF normalization techniques and we compared them to the brute force method presented in the literature. The present paper presents the issue of normalization of the MEKF and examines several MEKF normalization techniques.

1. INTRODUCTION

The normalization of the attitude quaternion in the AEKF was presented in past work [1,2]. Several techniques were developed and briefly tested. Those techniques included the following: brute force normalization of the quaternion (BF), considering the normalized quaternion a 'pseudo-measurement' and udpating the quaternion in the usual manner (QPM), considering the magnitude of the norm a 'pseudo-measurement' and updating the quaternion in the usual manner (MPM), and finally developing the AEKF algorithm with a normalized attitude matrix, or the 'linearized orthogonalized matrix' normalization (LOM). Each method was shown to improve the attitude estimate and to speed convergence of the filter.

Several normalization techniques are also presented for the MEKF. We found that normalization in the MEKF is necessary to avoid divergence, even when the attitude does not change considerably between

* Aerospace Engineer, Attitude Analysis Section, Flight Dynamics Analysis Branch, NASA Goddard Space Flight Center, Greenbelt, MD 20771

+ Assistant Head, Guidance and Control Branch, NASA Goddard Space Flight Center, Greenbelt, MD 20771

Professor, Faculty of Aerospace Engineering, Technion - Israel Institute of Technology, member Technion Space Research Institute, Haifa, Israel 32000

measurements. In the MEKF there are three points in the update cycle at which normalization can be performed. We present the methods for each, along with QPM and MPM methods, developed for the MEKF.

Each of the AEKF and MEKF methods are tested with data from a spacecraft in which the attitude does not change considerably between measurements. Fine Sun sensor, Earth sensor, magnetometer, and gyro data are used from each spacecraft. Finally, the results of the MEKF normalization methods are compared to those of the AEKF. Tests using data from a spacecraft undergoing high turning rates are currently being conducted but were not ready for publication in this paper.

In the next section we summarize the use of the AEKF and MEKF for attitude determination. In section III we explain the role of quaternion normalization in the AEKF and MEKF. In the following sections we present each of the normalization methods for both filters. Test results using simulated Earth Radiation Budget Satellite (ERBS) and Upper Atmospheric Research Satellite (UARS) data are given in Section VI and the conclusions follow in Section VII.

II. THE EKF ALGORITHM

The EKF algorithm is based on the following assumed models

$$\text{System model:} \quad \dot{\underline{X}} = \underline{f}(\underline{X}(t),t) + \underline{w}(t) \tag{1}$$

$$\text{Measurement model:} \quad \underline{z}_k = \underline{h}_k(\underline{X}(t_k)) + \underline{v}_k \tag{2}$$

where: $\underline{X}(t)$ = state vector
$\underline{w}(t)$ = zero mean white process
$\underline{v}_k$ = zero mean white sequence

The measurement update and the propagation of the state estimate and of the error covariance are performed as

$$\hat{\underline{X}}_k(+) = \hat{\underline{X}}_k(-) + K_k[\underline{z}_k - \underline{h}_k(\hat{\underline{X}}_k(-))] \tag{3}$$

$$P_k(+) = [I - K_kH_k]P_k(-)[I - K_kP_k(-)]T + K_kR_kK_kT \tag{4}$$

$$\dot{\hat{\underline{X}}}(t) = \underline{f}(\hat{\underline{X}}(t),t) \tag{5}$$

$$\dot{P}(t) = F(\hat{\underline{X}}(t),t)P(t) + P(t)FT(\hat{\underline{X}}(t),t) + Q(t) \tag{6}$$

where: $F(\hat{\underline{X}}(t),t) = \left.\dfrac{f(\underline{X}(t,t)}{\underline{X}(t)}\right|_{\underline{X}(t)=\hat{\underline{X}}(t)}$

$$H(\underline{X}(-)) = \left.\frac{h(\underline{X}(t))}{\underline{X}(t)}\right|_{\underline{X}(t)=\hat{\underline{X}}(t)}$$

P_k = estimation error covariance matrix
R_k = covariance of the white sequence, $\underline{v}_k$
Q_k = spectral density matrix of the white process, $\underline{w}_k$
K_k = gain matrix

The state vector is given as

$$\underline{X}^T = \begin{bmatrix} \underline{g}^T, \underline{b}^T \end{bmatrix} \tag{7}$$

where: $\underline{g}$ = four quaternion components
$\underline{b}$ = three gyro bias components

Note that equation (3) is the combination of the following

$$\hat{\underline{x}}_k(+) = \hat{\underline{x}}_k(-) + \hat{\underline{x}}_k(t_k) \tag{8}$$

$$\hat{\underline{x}}_k(t_k) = K_k \underline{Y}_k \tag{9}$$

$$\underline{Y}_k = \underline{z}_k - \underline{h}_k(\hat{\underline{x}}_k(-)) \tag{10}$$

where: $\underline{Y}_k$ = effective measurement or residual
$\underline{z}_k$ = actual measurement
$\underline{h}_k(\hat{\underline{x}}_k(-))$ = the estimate of the actual measurement

The relationship between (3) and (8) has been presented in past work [3]. The first four components of $\hat{\underline{x}}_k$ are corrections to the $\underline{q}$ estimate by the EKF, denoted as $d\underline{q}$. These are added to $\hat{\underline{q}}_k(-)$, the best estimate of $\underline{q}$, to give $\hat{\underline{q}}_k(+)$. The remaining elements in $\hat{\underline{x}}_k$ are the corrections to the gyro bias which are also then added to the best estimate of the gyro bias.

In the MEKF the quaternion elements of $\underline{x}$ are treated differently. The definition of $\underline{x}$ is given as

$$\underline{x}^T(t_k) = \left[\, \underline{\alpha}^T, \; \delta\underline{b}^T \,\right] \tag{11}$$

where: $\underline{\alpha}^T = \left[\, \phi, \theta, \mu \,\right]$ = three small angles based on the assumption that the error quaternion is composed of three small angles (vector) and 1 (scalar)

$\delta\underline{b}$ = corrections to the gyro bias

The correction to the quaternion, given as $d\hat{\underline{q}}_k$, is then constructed according to

$$d\hat{\underline{q}}^T_k = [\tfrac{1}{2}\phi \mid \tfrac{1}{2}\theta \mid \tfrac{1}{2}\mu \mid 1\,] \tag{12}$$

and the quaternion is updated as

$$\hat{\underline{q}}_k(+) = \hat{\underline{q}}_k(-) d\hat{\underline{q}}_k^{-1} \tag{13}$$

Whereas the gyro bias is updated according to (8). The udpated gyro bias components and $\hat{\underline{q}}_k(+)$ are augmented into the state vector (7). For further discussion of the MEKF see [4].

The dynamics for both filters has been presented extensively in previous work and will not be included here. For reference see [1,2,3].

III. THE ROLE OF QUATERNION NORMALIZATION

The state measurement update equations are given in (8) for the AEKF and in (12) for the MEKF. Unless convergence has been attained, the updated quaternion $\hat{\underline{q}}(+)$, is not necessarily normal, even if $\hat{\underline{q}}(-)$ is. We know, however, that the quaternion which the algorithm is trying to estimate is necessarily normal. We can then enforce normalization on $\hat{\underline{q}}_k(+)$ with the hope that the enforcement of this quality of the correct quaternion will direct the estimated quaternion in the right track and will enhance its convergence. Indeed, it was found in the past [2,5] that normalization is helpful. In particular, it was found that when the attitude varies slowly between measurements, normalization, although not necessary, resulted in a faster convergence; however, when the attitude changed rapidly between measurements, either filter tuning or normalization were necessary to avoid divergence. The use of normalization is superior to tuning because, first, tuning involves a tedious trial and error process, second, tuning is not a robust solution, and third, with quaternion normalization the final attitude estimate is closer to the correct quaternion.

IV. AEKF NORMALIZATION TECHNIQUES

Following is a summary of the AEKF normalization methods. The details are given in [1].

4.1 Brute Force Normalization (BF)

After $\hat{\underline{X}}_k$ has been computed in (8) the quaternion part of the state is normalized as

$$\hat{\underline{q}}_k^* = \hat{\underline{q}}_k(+)/|\hat{\underline{q}}_k(+)| \qquad (14)$$

and is augmented into $\hat{\underline{X}}_k(+)$. This method was first presented in [5], where it was shown that the operation performed in (14) is equivalent (to first order) to

$$\hat{\underline{q}}_k^*(+) = [\hat{\underline{q}}_k(-) + d\hat{\underline{q}}_k(+)] - \hat{\underline{q}}_k(-)\hat{\underline{q}}_k^T d\hat{\underline{q}}_k(+) \qquad (15)$$

The final term, $-\hat{\underline{q}}_k(-)\hat{\underline{q}}_k^T d\hat{\underline{q}}_k(+)$, is a residual term, not found in (8) that must be compensated for in the filter computations. This term is retained after the normalization is performed and accounted for in the next stage of the filter operation. This mode of normalization does not affect the covariance computation of the EKF [5]. This computation constitutes an outside interference in the EKF algorithm and adds a certain complication to the algorithm.

4.2 Quaternion Pseudo-measurement (QPM)

In this algorithm the updated quaternion, $\hat{\underline{q}}_k$, is used to form a pseudo-measurement as follows

$$\underline{Y}_{n,k} = \hat{\underline{q}}_k(+)/|\hat{\underline{q}}_k(+)| \qquad (16)$$

The pseudo-measurement $\underline{Y}_{n,k}$ is, of course, a normalized quaternion. A measurement update is performed based on this measurement. The relationship between the measurement $\underline{Y}_{n,k}$ and the state vector is formulated as

$$\underline{Y}_{n,k} = H_{n,k}\underline{X}_k + \underline{n}_{n,k} \qquad (17)$$

where: $H_{n,k}$ = diag[1,1,1,1|0..0]
$\underline{n}_{n,k}$ = white measurement error

The covariance, $R_{n,k}$, of $\underline{n}_{n,k}$ is set to be the diagonal matrix

$$R_{n,k} = \text{diag}\,[r^2, r^2, r^2, r^2] \qquad (18)$$

where r is a small number. By adjusting the value of r we determine the degree of the imposed normalization on $\hat{\underline{q}}_k(+)$.The QPM is performed after the state update, so the apriori state estimate is $\hat{\underline{X}}_k(+)$. The output of this update is the full state vector, not just the estimate of $\underline{x}$ which is the difference between $\underline{X}_k$ and its estimate $\hat{\underline{X}}_k(+)$. The state update is performed as

$$\hat{\underline{X}}_k^*(+) = \hat{\underline{X}}_k(+) \bullet K_{n,k}[\underline{Y}_{n,k} - H_{n,k}\hat{\underline{X}}_k(+)] \qquad (19)$$

where $K_{n,k}$ is computed using the updated covariance which corresponds to $\hat{\underline{X}}_k(+)$ and $H_{n,k}$ and $R_{n,k}$ above. The covariance is then recomputed according to (4) and the new state and covariance are propagated as before.

It is important that r be well tuned. If r is too small the filter will attempt to replace the quaternion estimate by the normalized quaternion. However, a small r increases the variance of the quaternion estimation error, and a high credibility is assigned to the normalized quaternion even when it is not yet the correct quaternion. New measurements are not allowed to alter the quaternion estimate and the filter is stuck on a wrong estimate. This required tuning gives the algorithm a disadvantage. This disadvantage is overcome when the following normalization scheme is used.

4.3 Magnitude Pseudo-measurement (MPM)

In this scheme we use the square of the quaternion Euclidean norm, whose magnitude is assumed to be 1, as the measurement; that is

$$z_{n,k} = 1 + v_{n,k} \tag{20}$$

where $v_{n,k}$ is assumed to be a white measurement noise with variance r. This measurement quantity is a non-linear function of the quaternion components. The effective measurement, $y_{n,k}$, is computed as

$$y_{n,k} = z_{n,k} - [\hat{q}(+)_{1,k}^2 + \hat{q}(+)_{2,k}^2 + \hat{q}(+)_{3,k}^2 + \hat{q}(+)_{4,k}^2] \tag{21}$$

Following the derivations of [1] this is rewritten as

$$y_{n,k} = 1 - |\hat{g}_{j,k}|^2 \tag{22}$$

and $R_{n,k} = r$. This method does not have the tuning problems of the QPM. A small r does not imply that the measurement of $\underline{g}$ is precise, it implies that the measurement of $|\underline{g}|^2$ is precise. So the estimate of $\underline{g}$ does not stick to a wrong value, since the variance of $\underline{g}$ doesn't approach the value of r.

4.4 Linearized Orthogonalized Matrix (LOM)

When the quaternion is of unit length the attitude matrix, $A(\underline{g})$, is orthonormal. It was proven in [6] that

$$A^*(\hat{\underline{g}}) = \frac{1}{|\hat{\underline{g}}|^2} A(\hat{\underline{g}}) \tag{23}$$

is orthonormal and is the closest orthonormal matrix to $A(\underline{g})$. Using $A^*(\hat{\underline{g}})$ in the development of the AEKF, rather than $A(\underline{g})$, practically enforces normalization.

V. MEKF NORMALIZATION TECHNIQUES

The normalization methods developed for the MEKF are presented here. In contrast to the AEKF algorithm, normalization is essential in the MEKF to avoid divergence. The first three methods, discussed in the ensuing, force normalization during the udpate of the quaternion. The final two methods are pseudo-measurement techniques similar to those presented for the AEKF.

5.1 Forced Normalization

After $\hat{\underline{g}}_k(+)$ has been computed in (13), normalization is forced as

$$\hat{\underline{g}}_k^* = \hat{\underline{g}}_k(+)/|\underline{g}_k(+)| \tag{24}$$

No compensation is performed because no consequent divergence of the MEKF has been reported in the literature [7]. We refer to this method as 'normalized q'.

The next method of forced normalization is to normalize $d\underline{g}$ from (12). This is performed as

$$|d\underline{g}| = (dq_{1,k}^2 + dq_{2,k}^2 + dq_{3,k}^2 + 1)^{1/2} \tag{25}$$

$$\begin{aligned} d\underline{g}^*_{i,k}(+) &= dq_{i,k}(+)/|d\underline{g}| \\ dq_{4,k} &= 1/|d\underline{g}| \end{aligned} \tag{26}$$

The normalized $d\underline{g}^*_k$ is then used in (13) to compute $\hat{\underline{g}}_k$. This method is referred to as 'normalized dq'.

The final method forces normalization of the three small angles which form the attitude portion of the MEKF state, given in (11). Each of the angles is scaled to yield

$$\phi^* = 2\phi/[\phi^2 + \theta^2 + \mu^2 + 4]^{1/2} \tag{27a}$$

$$\theta^* = 2\theta/[\phi^2 + \theta^2 + \mu^2 + 4]^{1/2} \tag{27b}$$

$$\tau^* = 2\tau/[\phi^2 + \theta^2 + \mu^2 + 4]^{1/2} \qquad (27c)$$

The elements of $d\underline{q}$ are computed as

$$dq_{1,k}^* = \tfrac{1}{2}\phi^* \qquad (28a)$$
$$dq_{2,k}^* = \tfrac{1}{2}\theta^* \qquad (28b)$$
$$dq_{3,k}^* = \tfrac{1}{2}\mu^* \qquad (28c)$$
$$dq_{4,k}^* = 2/[\phi^2 + \theta^2 + \mu^2 + 4]^{1/2} \qquad (28d)$$

Performing the scaling given in (27) results in the $d\underline{q}^*$ given in (28) being normal. The normalized $d\underline{q}^*$ is then used in (13) to compute $\underline{q}_k(+)$. This method will be called 'normalized alpha', in reference to the vector, $\underline{\alpha}$, of small angles in (11).

These methods constitute an outside interference in the MEKF algorithm. The covariance matrix is not affected. The complication of compensation is not added since divergence was not detected.

5.2 Quaternion Pseudo-measurement (QPM)

In this method we normalize the small angles of (11) and use them as the 'pseudo-measurement'. The relationship between $d\underline{q}$ and the angles is given in (12) and is repeated here.

$$\hat{dq}_1 = \hat{\phi}/2 \quad \hat{dq}_2 = \hat{\theta}/2 \quad \hat{dq}_3 = \hat{\mu}/2 \quad \hat{dq}_4 = 1 \qquad (29)$$

Normalizing $\hat{d\underline{q}}$ gives

$$\hat{dq}_i^* = \frac{\hat{dq}_i}{(\hat{dq}_1^2 + \hat{dq}_2^2 + \hat{dq}_3^2 + 1)} \qquad (30)$$

Use (30) in (29) to obtain

$$\tfrac{1}{2}\hat{\phi}^* = \tfrac{1}{2}\hat{\phi}/[(\hat{\phi}/2)^2+(\hat{\theta}/2)^2+(\hat{\mu}/2)^2+1]^{1/2} \qquad (31a)$$
$$\tfrac{1}{2}\hat{\theta}^* = \tfrac{1}{2}\hat{\theta}/[(\hat{\phi}/2)^2+(\hat{\theta}/2)^2+(\hat{\mu}/2)^2+1]^{1/2} \qquad (31b)$$
$$\tfrac{1}{2}\hat{\mu}^* = \tfrac{1}{2}\hat{\mu}/[(\hat{\phi}/2)^2+(\hat{\theta}/2)^2+(\hat{\mu}/2)^2+1]^{1/2} \qquad (31c)$$

or

$$\hat{\phi}^* = p\hat{\phi}, \quad \hat{\theta}^* = p\hat{\theta}, \quad \hat{\mu}^* = p\hat{\mu} \qquad (32)$$

where $p = 2(\hat{\phi}^2 + \hat{\theta}^2 + \hat{\mu}^2 + 4)^{-1/2}$

Note that $\hat{dq}_4$ is not a part of the filter state. We assign it a value such that $\hat{d\underline{q}}$ will be normal after the QPM update. Following is a summary of the algorithm computations in the order in which they are performed by the filter.

First p from (32) is computed using the updated angles of (10). The pseudo-measurement $\underline{z}$ is then computed as

$$z_1 = p\hat{\phi} \qquad z_2 = p\hat{\theta} \qquad z_3 = p\hat{\mu} \qquad (33)$$

The vector $\underline{z}$ is related to the state vector as $\underline{z} = H_n\underline{x} + \underline{n}_n$, where $\underline{x}$ is given in (10). The measurement matrix, H_n, and the noise covariance matrix, R_n, are, therefore, defined as

$$H_n = [I_{3x3} \mid 0_{3x3}] \qquad (34)$$
$$R = [\text{diag } r]_{3x3} \qquad (35)$$

where r is a small number. A Kalman update is performed and the new covariance matrix is computed as follows

$$K_n = P(+)H_n^T[H_nP(+)H_n^T + R_n]^{-1} \qquad (36)$$

$$\hat{\underline{x}}^*(+) = \hat{\underline{x}}(+) + K_n[\underline{z} - H_n\hat{\underline{x}}(+)] \tag{37}$$

$$P^*(+) = (I - K_nH_n)P(+)(I - K_nH_n]^T + K_nR_nK_n^T \tag{38}$$

where $P(+)$ = updated covariance matrix (before normalization)
$\underline{x}(+)$ = results of measurement update given in (9),
with $x_1 = \hat{\phi}$, $x_2 = \theta$, $x_3 = \mu$

The elements of $d\hat{\underline{q}}^*$ are computed as

$$d\hat{q}^*_1 = \hat{\phi}^*/2 \quad d\hat{q}^*_2 = \hat{\theta}^*/2 \quad d\hat{q}^*_3 = \hat{\mu}^*/2 \tag{39}$$

where the angles, $\hat{\phi}^*$, $\hat{\theta}^*$, and $\hat{\mu}^*$ are the first three components of $\hat{\underline{x}}^*(+)$. The fourth element of $d\hat{\underline{q}}^*$ is computed as

$$d\hat{q}^*_4 = 2(\hat{\phi}^2 + \hat{\theta}^2 + \hat{\mu}^2 + 4)^{-1/2} \tag{40}$$

Finally, the quaternion is computed using (13).

$$\hat{\underline{q}}^*_k(+) = \hat{\underline{q}}_k(+)d\hat{\underline{q}}^{*-1} \tag{41}$$

This method exhibits the same tuning problems as the AEKF QPM. Here, too, it is important that the r be well tuned to avoid getting the quaternion estimate stuck on the wrong value. Again this presents somewhat of a disadvantage for this method.

5.3 Magnitude Pseudo-measurement

This method uses the magnitude of the normalized angles (10) as the measurement. Recall from (32)

$$p = 2(\hat{\phi}^2 + \hat{\theta}^2 + \hat{\mu}^2 + 4)^{-1/2} \tag{42}$$

We use p to normalize the angles

$$\hat{\phi}_n = p\hat{\phi}, \quad \hat{\theta}_n = p\hat{\theta}, \quad \hat{\mu}_n = p\hat{\mu} \tag{43}$$

Following (11), we rewrite (44) as

$$\hat{\underline{\alpha}}_n = p\hat{\underline{\alpha}} \tag{44}$$

The magnitude of $\hat{\underline{\alpha}}_n$ is related to the estimate of the individual angles as follows

$$|\hat{\underline{\alpha}}_n|^2 = p^2(\hat{\phi}^2 + \hat{\theta}^2 + \hat{\mu}^2) \tag{45}$$

The measurement z is defined as

$$z = |\hat{\underline{\alpha}}_n|^2 + n \tag{46}$$

The effective measurement to be processed by the MEKF is then given as

$$y = z - |\hat{\underline{\alpha}}|^2 \tag{47}$$

We need to express y as a linear combination of the difference between $\hat{\underline{\alpha}}_n$ and $\hat{\underline{\alpha}}$. Substituting (46) into (47) yields

$$y = |\hat{\underline{\alpha}}_n|^2 + n - |\hat{\underline{\alpha}}|^2 \tag{48}$$

Define $\delta\underline{\alpha}$ as

$$\underline{\alpha}_n = \underline{\alpha} + \delta\underline{\alpha} = \begin{bmatrix} \dot{\phi} + \delta\dot{\phi} \\ \dot{\theta} + \delta\dot{\theta} \\ \dot{\mu} + \delta\dot{\mu} \end{bmatrix} \tag{49}$$

Substituting (49) into (48) gives

$$y = (\dot{\phi} + \delta\dot{\phi})^2 + (\dot{\theta} + \delta\dot{\theta})^2 + (\dot{\mu} + \delta\dot{\mu})^2 - (\dot{\phi}^2+\dot{\theta}^2+\dot{\mu}^2) - n \tag{50}$$

Neglecting squares of $\delta\dot{\phi}$, $\delta\dot{\theta}$, $\delta\dot{\mu}$ yields

$$y = 2\dot{\phi}\delta\dot{\phi} + 2\dot{\theta}\delta\dot{\theta} + 2\dot{\mu}\delta\dot{\mu} + n \tag{51}$$

or

$$y = [2\dot{\phi}, 2\dot{\theta}, 2\dot{\mu}] \begin{bmatrix} \delta\dot{\phi} \\ \delta\dot{\theta} \\ \delta\dot{\mu} \end{bmatrix} \tag{52}$$

This defines the measurement matrix, H_n, as

$$H_n = [2\dot{\phi}, 2\dot{\theta}, 2\dot{\mu}, 0, 0, 0] \tag{53}$$

The MPM algorithm is then carried out as follows.

First p^2 is computed and used to obtain y.

$$y = (p^2 - 1) \tag{54}$$

Then H_n is computed and a small value is assigned to r, the uncertainty corresponding to n of (46). A Kalman update is performed and the covariance is updated.

$$K_n = P(+)H_n^T/[H_nP(+)H_n^T + r] \tag{55}$$

$$\underline{\hat{x}}^*(+) = \underline{\hat{x}}(+) + K_n[y - H_n\underline{\hat{x}}(+)] \tag{56}$$

$$P^*(+) = (I - K_nH_n)P(+)(I - K_nH_n)^T + K_nR_nK_n^T \tag{57}$$

where $P(+)$ = updated covariance matrix (before normalization)

$\underline{\hat{x}}(+)$ = results of measurement update given in (9), with $x_1 = \phi$, $x_2 = \theta$, $x_3 = \mu$

The normalized $d\underline{\hat{q}}^*$ is then constructed.

$$dq^*_1 = \tfrac{1}{2}\dot{\phi}^*, \quad dq^*_2 = \tfrac{1}{2}\dot{\theta}^*, \quad dq^*_3 = \tfrac{1}{2}\dot{\mu}^* \tag{58}$$

Again, since dq^*_4 is not a part of the state we assign it a value such that $d\underline{\hat{q}}^*$ will be normal after the MPM update.

$$dq^*_4 = 2(\dot{\phi}^{*2} + \dot{\theta}^{*2} + \dot{\mu}^{*2} + 4)^{-\frac{1}{2}} \tag{59}$$

The quaternion is then updated according to (13).

$$\underline{\hat{q}}^*_k(+) = \underline{\hat{q}}_k(+)d\underline{\hat{q}}^{*-1} \tag{60}$$

This method is not subject to the tuning problems of the QPM for the same reasons as those given above for the AEKF MPM.

VI. RESULTS

The algorithms presented in this paper were tested using clean, nominal simulated data from the Earth Radiation Budget Satellite (ERBS) and noisy simulated data from the Upper Atmospheric Research Satellite (UARS). Two UARS datasets were created. One contains simulated data from a nominal 1 revolution per orbit (RPO) attitude and the other contains a 0.5 deg/sec simulated yaw maneuver. The ERBS data is taken with the spacecraft in its nominal 1 RPO attitude. The initial attitude error was 5 degrees and the value of r for the QPM and MPM algorithms was 10^{-5} for both the AEKF and the MEKF. We studied the behavior of each algorithm early, which we refer to as the transient period, and after convergence was achieved, which we refer to as steady state. Note also that each of the figures included starts with the first update, not with the initial attitude error of 5 degrees.

We first compared the AEKF normalization algorithms. All of the methods, including not normalizing at all, converged quickly. Figure 1 shows the first 5 seconds using ERBS data. The BF converges the quickest and the LOM the slowest. The QPM and MPM are similar to not normalizing. Figure 2 shows the transient period using the 1 RPO UARS data. ALl the methods converge quickly; the QPM has a slightly lower initial RSS attitude error. In the steady state, all the methods, including not normalizing at all, achieved similar, low RSS attitude errors. Figure 3 shows results from the UARS yaw maneuver. The LOM has the lowest error.

For the MEKF, normalization was found to be essential. Figure 4 shows the MEKF transient results from the UARS 1 RPO data. All the methods converge quickly. The results of not normalizing don't converge as low as the normalization results, and beyond the 10 seconds shown begin to diverge. In steady state, all the normalization methods achieved low RSS attitude errors. Figure 5 shows results from the UARS yaw maneuver. The three BF methods are slightly better than the QPM and MPM methods. Figure 6 shows steady state results, using ERBS data, for the three BF methods. The 'normalized dq' and 'normalized alpha' results are slightly better than the 'normalized q' results.

Finally, the two filters were compared. Figure 7 shows the BF method for the AEKF versus the 'normalized dq' method for the MEKF, in the transient period, using ERBS data. The AEKF converges a little faster than the MEKF. Figure 8 shows the steady state results from the UARS yaw maneuver, comparing the AEKF LOM and BF to the MEKF 'normalized q'. The MEKF 'normalized q' method has a lower RSS attitude error. The results of these comparisons of the two filters, in both the transient and steady state periods, were found to be true for the other methods as well.

VII. CONCLUSIONS

We found that all of the normalization methods presented work well and yield comparable results. In the AEKF, normalization is not essential since the data chosen for the test does not have a rapidly varying attitude. In the MEKF, normalization is necessary to avoid divergence of the attitude estimate. When the spacecraft experiences low angular rates, all of the methods for each of the filters have similar behavior. The choice of which algorithm to select as superior depends on the complexity of each algorithm. The pseudo-measurement techniques, for both the AEKF and MEKF, blend the normalization into the Kalman filter algorithm, but they don't represent an actual physical measurement, and are therefore somewhat obscure in their derivation. In addition, the QPM method requires the added burden of tuning. The AEKF BF algorithm is complicated by the need to compensate. The LOM method blends naturally into the filter development, using a normalized attitude to derive the filter update equations. The LOM is the slowest to converge but achieves the lowest RSS attitude error. In the MEKF, the brute force technique of normalizing the quaternion is the easiest to implement and is the most straight forward, but the other two brute force techniques have slightly better performance. All of the algorithms will be further tested with data from UARS undergoing a high turning rate. This may help to determine which of the algorithms, for each of the filters, has the best performance and may further substantiate the claim that under high rates normalization helps speed convergence and eliminate the need for tuning.

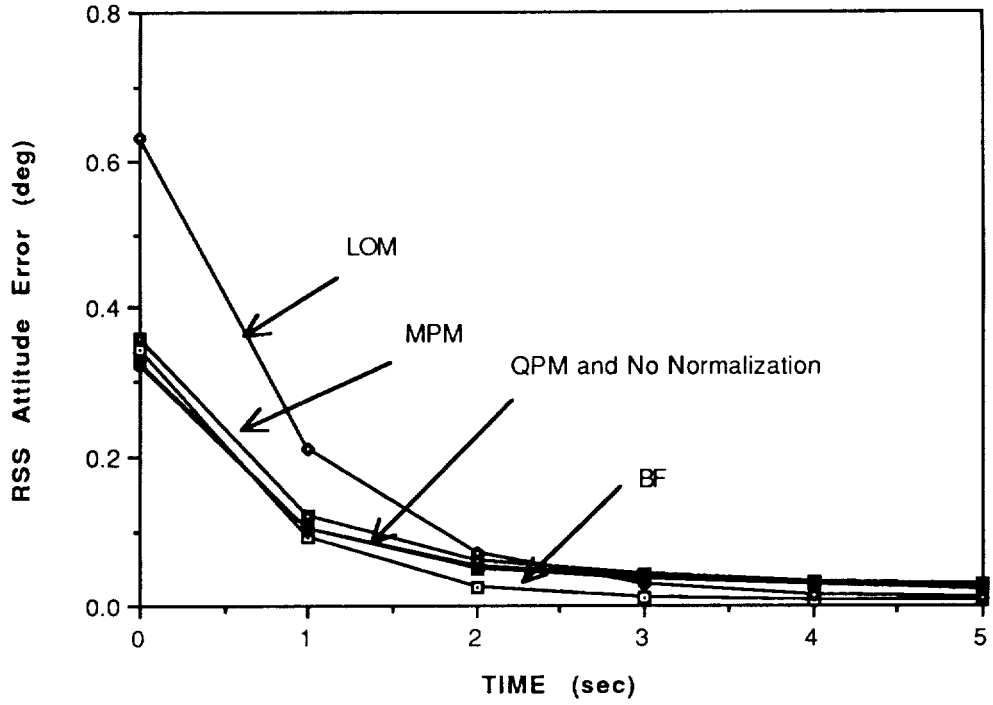

Fig. 1. ERBS AEKF: BF, QPM, MPM, LOM and No Normalization

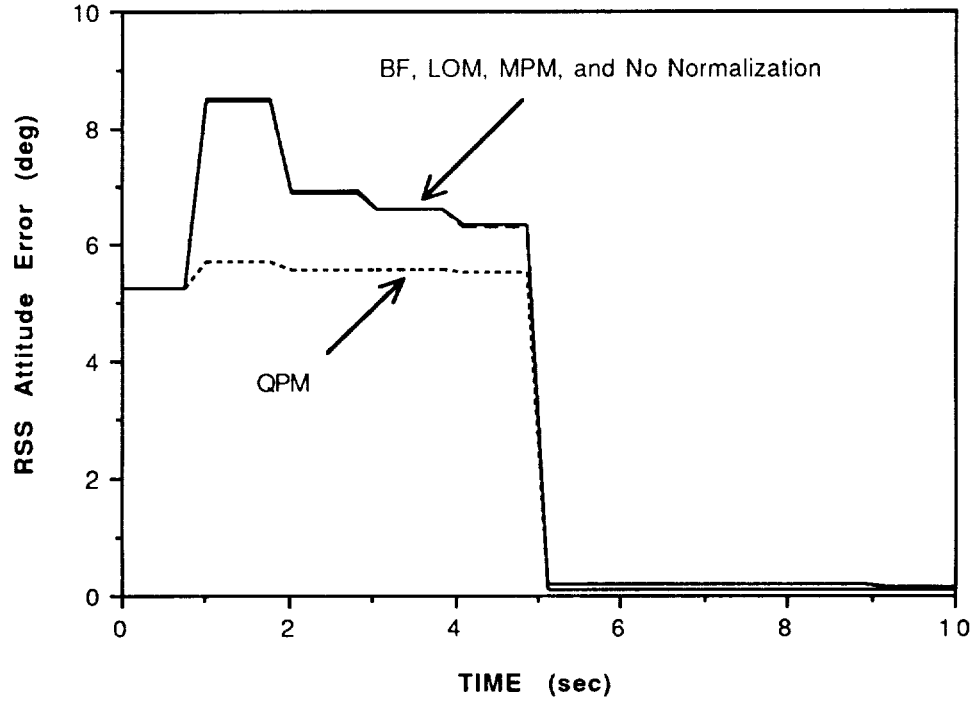

Fig. 2 UARS AEKF: Noisy Data, 1 RPO Attitude

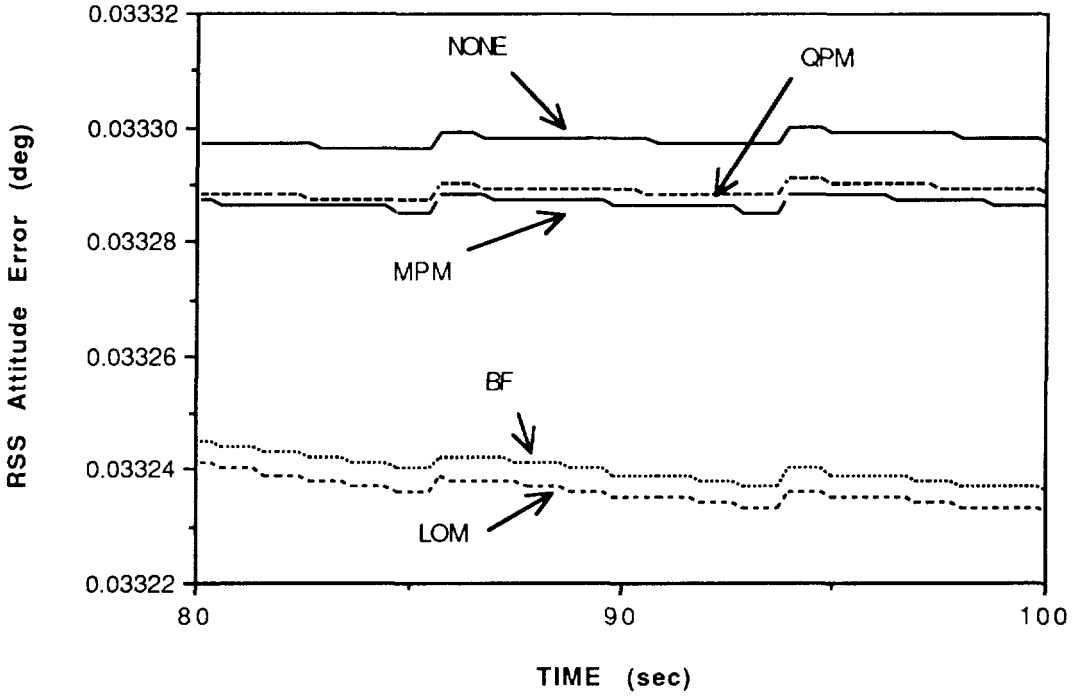

Fig. 3. UARS AEKF: Yaw Maneuver, Noisy Data

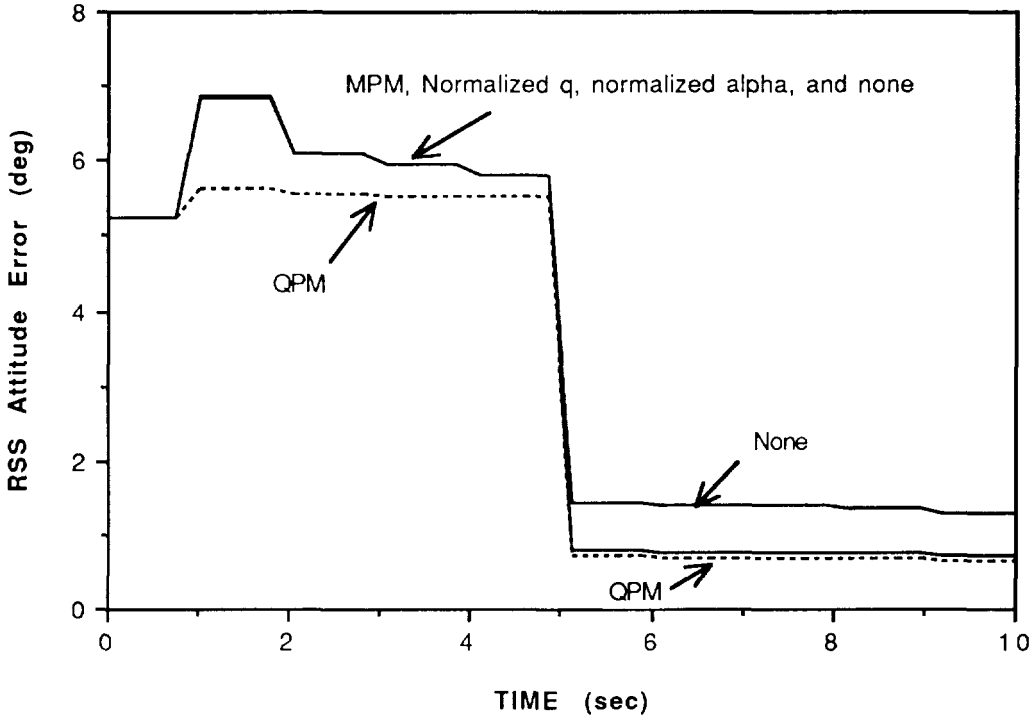

Fig. 4. UARS MEKF: Noisy Data, 1 RPO Attitude

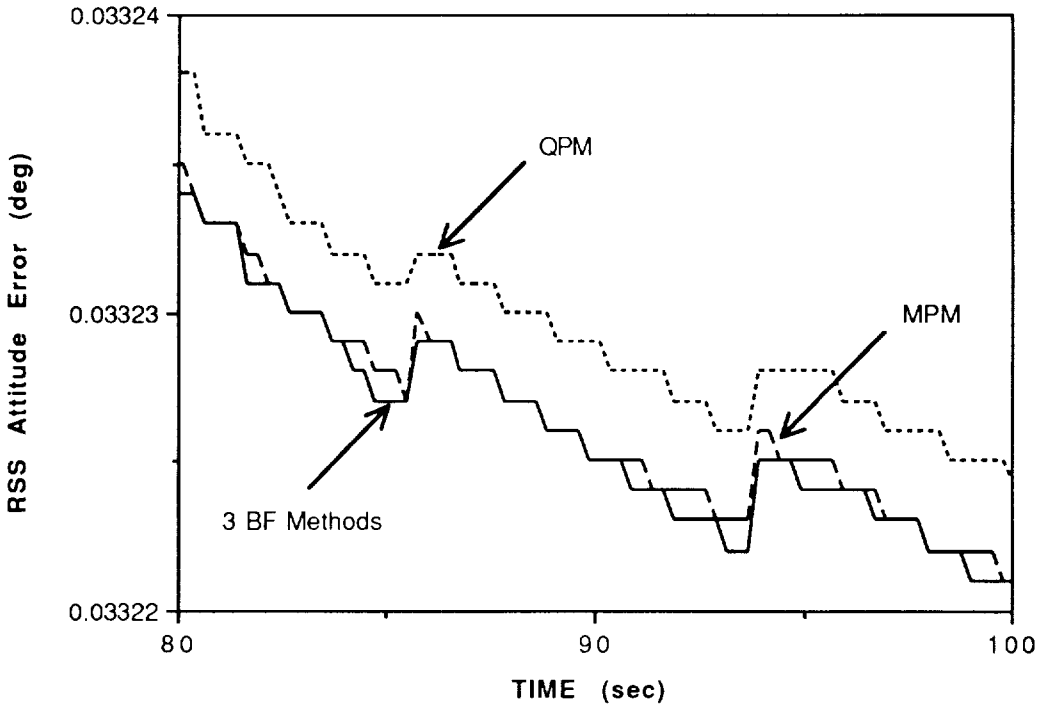

Fig. 5. UARS MEKF: Yaw Maneuver, Noisy Data

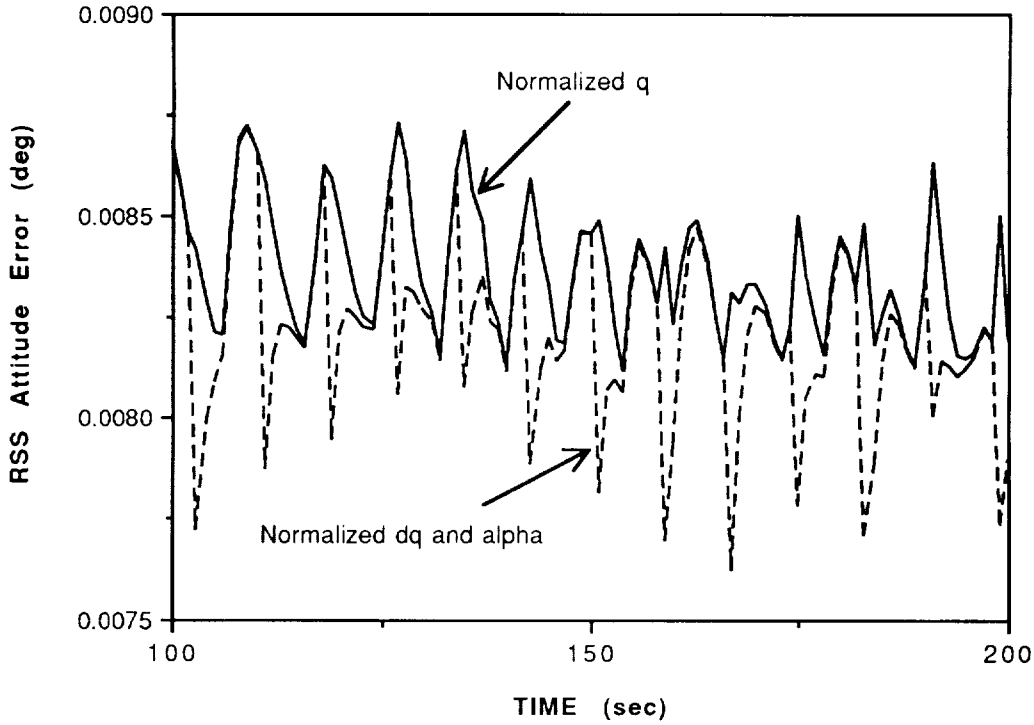

Fig. 6. ERBS MEKF: Normalized q, dq, and alpha

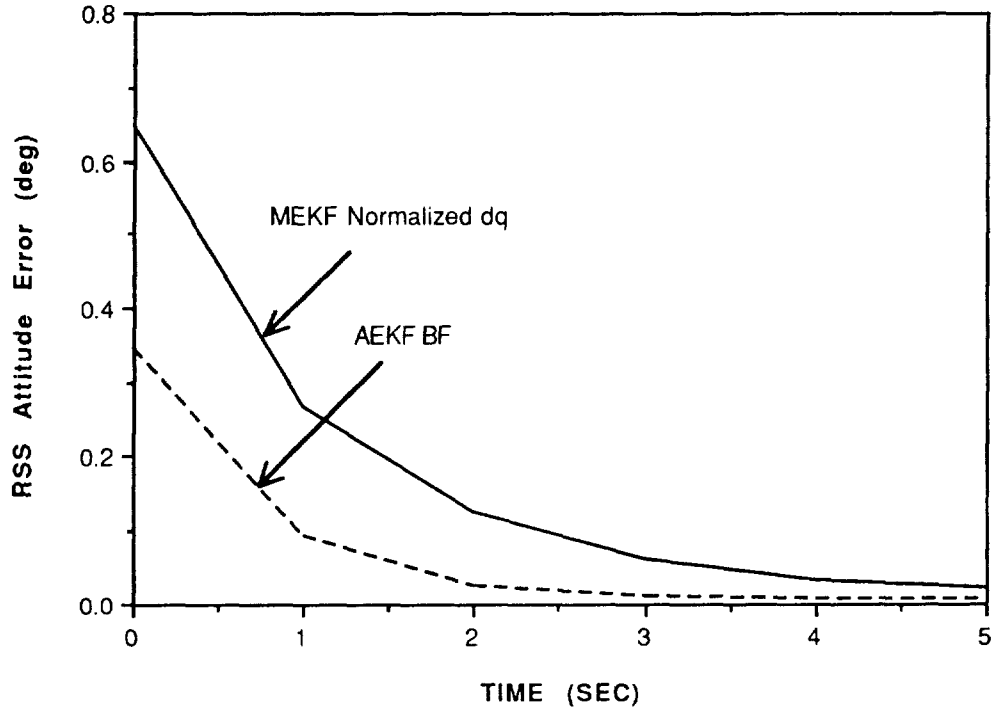

Fig. 7. ERBS BF Normalization: AEKF vs MEKF

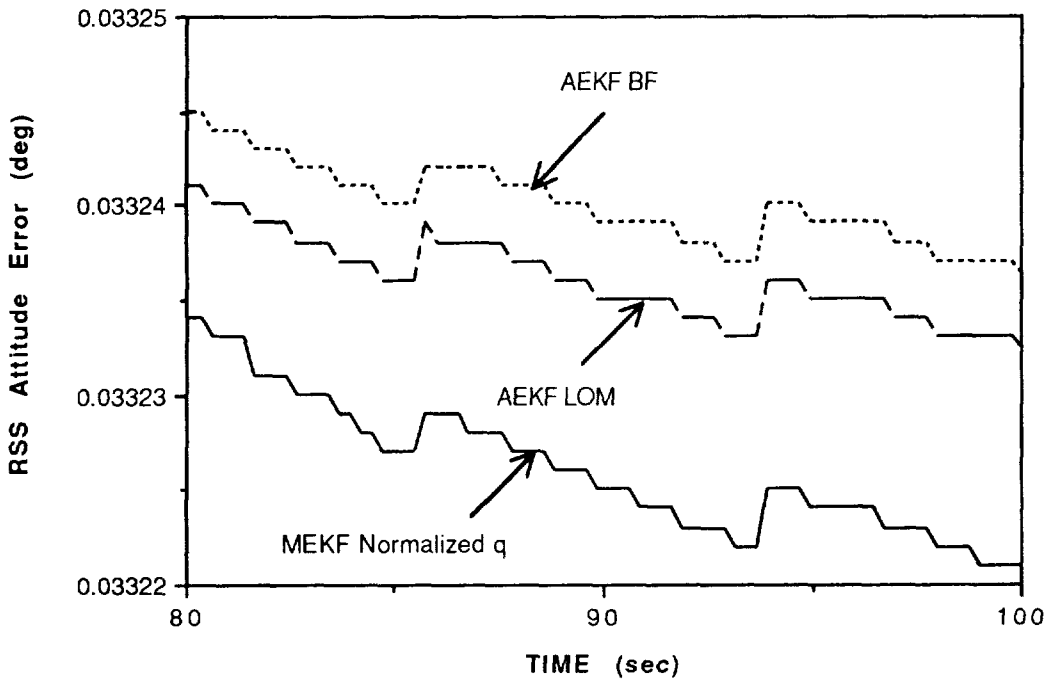

Fig. 8. UARS AEKF LOM,BF vs MEKF Normalized q: Yaw Maneuver, Noisy Data

IX. REFERENCES

1. Bar-Itzhack, I.Y. and Deutschmann, J., "Quaternion Normalization in Additive EKF for Spacecraft Attitude Determination", Flight Mechanics/Estimation Theory Symposium, NASA Goddard Space Flight Center, May 1991.

2. Bar-Itzhack, I.Y. and Deutschmann, J., "Extended Kalman Filter for Attitude Estimation of the Earth Radiation Budget Satellite", AAS Astrodynamics Conference, Portland, Oregon, Aug. 1990.

3. Deutschmann, J. and Bar-Itzhack, I.Y., " Extended Kalman Filter for Attitude Estimation of the Earth Radiation Budget Satellite", Flight Mechanics/Estimation Theory Symposium, NASA Goddard Space Flight Center, May 1989.

4. Bar-Itzhack, I.Y. and Harman, R.R., "True Covariance Simulation of the EUVE Update Filter", Flight Mechanics/Estimation Theory Symposium, NASA Goddard Space Flight Center, May 1989.

5. Bar-Itzhack, I.Y. and Oshman, Y., "Recursive Attitude Determination from Vector Observations: Quaternion Estimation", IEEE Transactions on Aerospace and Electronics Systems, Vol. AES-21, Jan. 1985, pp. 128-136.

6. Giardina, C.R., Bronson, R., and Wallen, I., "An Optimal Normalization Scheme", IEEE Transactions on Aerospace and Electronics Systems, Vol. AES-11, July 1975, pp. 443-446.

7. Murrell, J.W., "Precision Attitude Determination for Multimission Spacecraft", AIAA Guidance and Control Conference, Palo Alto, CA, August 1978.

ATTITUDE DETERMINATION USING VECTOR OBSERVATIONS: A FAST OPTIMAL MATRIX ALGORITHM

F. Landis Markley[1]

Abstract

The attitude matrix minimizing Wahba's loss function is computed directly by a method that is competitive with the fastest known algorithm for finding this optimal estimate. The method also provides an estimate of the attitude error covariance matrix. Analysis of the special case of two vector observations identifies those cases for which the TRIAD or algebraic method minimizes Wahba's loss function.

Introduction

In 1965, Wahba posed the problem of finding the proper orthogonal matrix A that minimizes the non-negative loss function [1]

$$L(A) \equiv \frac{1}{2}\sum_{i=1}^{n} a_i \left| \mathbf{b}_i - A\mathbf{r}_i \right|^2, \tag{1}$$

where the unit vectors $\mathbf{r}_i$ are representations in a reference frame of the directions to some observed objects, the $\mathbf{b}_i$ are the unit vector representations of the corresponding observations in the spacecraft body frame, the a_i are positive weights, and n is the number of observations. The motivation for this loss function is that if the vectors are error-free and the true attitude matrix A_{true} is assumed to be the same for all the measurements, then $\mathbf{b}_i$ is equal to $A_{true}\mathbf{r}_i$ for all i and the loss function is equal to zero for A equal to A_{true}.

Attitude determination algorithms based on minimizing this loss function have been used for many years [2-9]. The original solutions to Wahba's problem solved for the spacecraft attitude matrix directly [2-5], but most practical applications have been based on Davenport's q-method [6-8], which solves for the quaternion representing the attitude matrix. In this paper, we present a new method that solves for the attitude matrix directly, as well as the covariance matrix, and which is competitive with the well known QUEST algorithm [9] in speed. Analysis of the special case of two observations serves to relate this method to the TRIAD or algebraic method [8, 9].

Statement of the problem

Simple matrix manipulations transform the loss function into

$$L(A) = \lambda_0 - \mathrm{tr}(AB^T), \tag{2}$$

where

$$\lambda_0 \equiv \sum_{i=1}^{n} a_i , \tag{3}$$

$$B \equiv \sum_{i=1}^{n} a_i \mathbf{b}_i \mathbf{r}_i^T , \tag{4}$$

[1]Assistant Head, Guidance and Control Branch, Code 712, Goddard Space Flight Center, Greenbelt, MD 20771

tr denotes the trace, and the superscript T denotes the matrix transpose. Thus Wahba's problem is equivalent to the problem of finding the proper orthogonal matrix A that maximizes the trace of the matrix product AB^T. The weights are often chosen so that $\lambda_0 = 1$, but this is not always the most convenient choice, as will be discussed below.

This optimization problem has an interesting relation to a matrix norm. The Euclidean norm (also known as the Schur, Frobenius, or Hilbert-Schmidt norm) is defined for a general real matrix M by [10, 11]

$$\| M \|^2 \equiv \Sigma M_{ij}^2 = \mathrm{tr}(MM^T), \tag{5}$$

where the sum is over all the matrix elements. The assumed orthogonality of A and properties of the trace give

$$\| A - B \|^2 = \mathrm{tr}[(A - B)(A - B)^T] = \mathrm{tr}\, I - 2\mathrm{tr}(AB^T) + \| B \|^2, \tag{6}$$

where I is the 3×3 identity matrix. The orthogonal matrix A that maximizes $\mathrm{tr}(AB^T)$ minimizes this norm, so Wahba's problem is also equivalent to the problem of finding the proper orthogonal matrix A that is closest to B in the Euclidean norm [12].

The matrix B can be shown to have the decomposition [13]

$$B = U_+ \,\mathrm{diag}[S_1, S_2, S_3] V_+^T \tag{7}$$

where U_+ and V_+ are proper orthogonal matrices; diag[...] denotes a matrix with the indicated elements on the main diagonal and zeros elsewhere; and S_1, S_2, and $|S_3|$, the singular values of B, obey the inequalities

$$S_1 \geq S_2 \geq |S_3|. \tag{8}$$

The optimal attitude estimate is given in terms of these matrices by [13]

$$A_{opt} = U_+ V_+^T. \tag{9}$$

Equation (7) differs from the singular value decomposition (SVD) [10, 11] in that U_+ and V_+ are required to have positive determinant. In reference [13], S_3 was denoted by ds_3, where $d = \pm 1$ and $s_3 \geq 0$.

The SVD provides a robust method for computing the matrices U_+ and V_+, and thus the optimal attitude estimate, but it is not very efficient [13]. The purpose of this paper is to present a more efficient method to estimate the attitude.

Computation of the attitude matrix

Noting that the adjoint of the transpose of B and the product BB^TB can be written as

$$\mathrm{adj}\, B^T = U_+ \,\mathrm{diag}[S_2S_3, S_3S_1, S_1S_2]\, V_+^T, \tag{10}$$

and

$$BB^TB = U_+ \,\mathrm{diag}[S_1^3, S_2^3, S_3^3]\, V_+^T, \tag{11}$$

it is a matter of simple algebra to see that

$$A_{opt} = [(\kappa + \| B \|^2) B + \lambda \operatorname{adj} B^T - B B^T B]/\zeta, \tag{12}$$

where

$$\| B \|^2 = S_1^2 + S_2^2 + S_3^2, \tag{13}$$

and the other scalar coefficients are defined by

$$\kappa \equiv S_2 S_3 + S_3 S_1 + S_1 S_2, \tag{14}$$

$$\lambda \equiv S_1 + S_2 + S_3, \tag{15}$$

and

$$\zeta \equiv (S_2 + S_3)(S_3 + S_1)(S_1 + S_2). \tag{16}$$

The matrices in equation (12) can be computed without performing the singular value decomposition, but this equation is an improvement over equation (9) only because the scalar coefficients κ, λ, and ζ can also be computed without the SVD, as we will show below.

Iterative computation of the scalar coefficients

We first find expressions for the other scalar coefficients in terms of λ. A little algebra shows that

$$\kappa = \tfrac{1}{2} (\lambda^2 - \| B \|^2) \tag{17}$$

and

$$\zeta = \kappa \lambda - \det B. \tag{18}$$

Let $A(\lambda)$ denote the expression for the attitude matrix given by equations (12), (17), and (18) as a function of λ and B. This is equal to A_{opt} if λ is given by equation (15). Equations (7), (9), and (15) give

$$\lambda = \operatorname{tr}(A_{opt} B^T), \tag{19}$$

so λ can be computed as a solution of the equation

$$\lambda = \operatorname{tr}[A(\lambda) B^T] = \operatorname{tr}[(\kappa + \| B \|^2) B B^T + \lambda (\det B) I - (B B^T)^2]/\zeta. \tag{20}$$

Substitution of equations (17), (18), and the identity

$$\| B \|^4 - \operatorname{tr}[(B B^T)^2] = 2 \| \operatorname{adj} B \|^2 \tag{21}$$

lets us write this as

$$0 = Q(\lambda) \equiv \kappa^2 - 2 \lambda \det B - \| \operatorname{adj} B \|^2. \tag{22}$$

Since κ is a quadratic function of λ, $Q(\lambda)$ is a quartic polynomial. It can be shown to be the same quartic that is used in QUEST, up to an irrelevant factor of one-fourth. Substitution of equation (7) into equation (22) gives the four roots of the quartic in terms of S_1, S_2, and S_3. We must use equation (17) for κ rather than equation (14) in this substitution, which gives

$$4Q(\lambda) = (\lambda - S_1 - S_2 - S_3)(\lambda - S_1 + S_2 + S_3)(\lambda + S_1 - S_2 + S_3)(\lambda + S_1 + S_2 - S_3). \tag{23}$$

The roots of this equation are all real, and they are the four eigenvalues of the K matrix in the q-method, as is well known [7, 9]. Equations (8) and (15) show that we require the maximum root, and that this root is distinct unless $S_2 + S_3 = 0$. When $S_2 + S_3 = 0$, the attitude solution is not unique, as is discussed in reference [13]; in the method introduced in this paper, this results in $\zeta = 0$ and all the elements of A_{opt} having the indefinite form 0/0.

We now note from equations (2) and (19) that

$$L(A_{opt}) = \lambda_0 - \lambda \geq 0. \tag{24}$$

For small measurement errrors, the loss function should be close to zero, so the maximum root of equation (22) should be close to λ_0 [9]. Thus we can find λ by Newton's method, starting with this value. This defines a sequence of estimates of λ by

$$\lambda_i = \lambda_{i-1} - Q(\lambda_{i-1})/Q'(\lambda_{i-1}), \quad i = 1, 2, \ldots. \tag{25}$$

Substitution of equation (23) shows that this sequence would be monotonically decreasing with infinite-precision arithmetic, but a computation with finite-precision arithmetic eventually finds a $\lambda_i \geq \lambda_{i-1}$. At this point, the iterations are terminated and λ_{i-1} is taken to be the desired root to full computer precision. This iteration converges extremely rapidly in practice, except in the case that the maximum root of $Q(\lambda)$ is not unique. In that case the derivative in the denominator of equation (25) goes to zero as the root is approached, so the computation is terminated and a warning is issued that the attitude is indeterminate. Halley's method [14] would give convergence in fewer iterations than Newton's method, but would require more computations per iteration, so it was not investigated further.

It is important to carry out the computation of λ to full machine precision, since otherwise the computed attitude matrix will not be orthogonal. Straightforward matrix computation gives

$$A(\lambda)A^T(\lambda) = I - Q(\lambda)(\lambda^2 I - BB^T)/\zeta^2. \tag{26}$$

This shows the orthogonality of the computed attitude matrix if λ is a root of $Q(\lambda)$, and estimates the departure from orthogonality otherwise.

Analytic computation of the scalar coefficients

The scalar coefficients can also be computed as functions of the largest singular value S_1 of B by

$$\kappa = S_1(S_2 + S_3) + S_2S_3 = S_1(S_2 + S_3) + S_1^{-1}\det B, \tag{27}$$

$$\lambda = S_1 + (S_2 + S_3), \tag{28}$$

and

$$\zeta = (\kappa + S_1^2)(S_2 + S_3), \tag{29}$$

where

$$S_2 + S_3 = \{S_1^{-2}[\,\|\text{adj}\, B\|^2 - (S_1^{-1}\det B)^2] + 2S_1^{-1}\det B\}^{1/2}. \tag{30}$$

This form is chosen to avoid near-cancellations in near-singular cases. The largest singular

value is found as the positive square root of the largest root of the cubic characteristic equation of the matrix BB^T [7]:

$$0 = (S_1^2)^3 - \mathrm{tr}(BB^T)(S_1^2)^2 + \mathrm{tr}[\mathrm{adj}(BB^T)]S_1^2 - \det(BB^T)$$
$$= (S_1^2)^3 - \|B\|^2(S_1^2)^2 + \|\mathrm{adj}\, B\|^2 S_1^2 - (\det B)^2. \tag{31}$$

The largest root of this equation is given by [7, 15]

$$S_1^2 = \tfrac{1}{3}\{\|B\|^2 + 2\alpha^{1/2}\cos[\tfrac{1}{3}\cos^{-1}(\alpha^{-3/2}\beta)]\}, \tag{32}$$

where

$$\alpha \equiv \|B\|^4 - 3\|\mathrm{adj}\, B\|^2, \tag{33}$$

and

$$\beta \equiv \|B\|^6 - (9/2)\|B\|^2\|\mathrm{adj}\, B\|^2 + (27/2)(\det B)^2. \tag{34}$$

Equation (7) can be used to show that $\alpha \geq 0$, with equality if and only if $S_1 = S_2 = |S_3|$, in which case $\beta = 0$ also. Thus we have a complete analytic solution of Wahba's problem.

Computation of the covariance matrix

The quality of the attitude estimate is best expressed in terms of the covariance of the three-component column vector ϕ of attitude error angles in the spacecraft body frame. This parameterization gives the following relation between the estimated and true attitude matrices A and A_{true}:

$$A = \{\exp[(-\phi)\times]\}A_{true} = \{I - [\phi\times] + \tfrac{1}{2}[\phi\times]^2 + \ldots\}A_{true}, \tag{35}$$

where the matrix $[\mathbf{u}\times]$ is defined for a general three-component column vector $\mathbf{u}$ as

$$[\mathbf{u}\times] \equiv \begin{bmatrix} 0 & -u_3 & u_2 \\ u_3 & 0 & -u_1 \\ -u_2 & u_1 & 0 \end{bmatrix}. \tag{36}$$

This notation reflects the equality of the matrix product $[\mathbf{u}\times]\mathbf{v}$ and the cross product $\mathbf{u}\times\mathbf{v}$.

Shuster [16] has recast the Wahba problem as a maximum likelihood estimation problem [17], which leads to a very convenient method for computing the covariance matrix. Asymptotically, as the amount of data becomes infinite, the covariance matrix tends to the inverse of the Fisher information matrix F, which is the expected value of the Hessian of the negative-log-likelihood function J;

$$F_{jk} \equiv \mathrm{E}[\partial^2 J/\partial\phi_j\partial\phi_k]. \tag{37}$$

The distribution of the components of the i^{th} measurement error vector perpendicular to the true vector are assumed to be Gaussian and axially symmetric about the true vector with variance σ_i^2 per axis. Then the negative-log-likelihood function for this problem is [13, 16]

$$J = \tfrac{1}{2}\sum_{i=1}^{n}\sigma_i^{-2}|\mathbf{b}_i - A\mathbf{r}_i|^2 + \ldots, \tag{38}$$

where the omitted terms are independent of attitude. For any positive λ_0 and with

$$\sigma_{tot}^{\ 2} \equiv (\sum_{i=1}^{n} \sigma_i^{-2})^{-1}, \tag{39}$$

the weights

$$a_i = \lambda_0 \sigma_{tot}^{\ 2} / \sigma_i^{\ 2} \tag{40}$$

are positive and satisfy equation (3). With this choice

$$J = \lambda_0^{-1} \sigma_{tot}^{-2} L(A) + \ldots , \tag{41}$$

which means that the solution to Wahba's problem is a maximum-likelihood estimate, since it minimizes the negative-log-likelihood function. Substituting equation (35) into equation (2) and using the identity

$$[\mathbf{u}\times][\mathbf{v}\times] = -(\mathbf{v}^T\mathbf{u})I + \mathbf{v}\mathbf{u}^T \tag{42}$$

gives, to second order,

$$\begin{aligned} L(A) &= \lambda_0 - \mathrm{tr}(A_{true}\, B^T) + \mathrm{tr}\{[\phi\times]A_{true}\, B^T\} + \tfrac{1}{2}\,\mathrm{tr}\{[(\phi^T\phi)I - \phi\phi^T]A_{true}\, B^T\} \\ &= \lambda_0 - \mathrm{tr}(A_{true}\, B^T) + \mathrm{tr}\{[\phi\times]A_{true}\, B^T\} + \tfrac{1}{2}\,\phi^T[\mathrm{tr}(A_{true}\, B^T)I - A_{true}\, B^T]\phi. \end{aligned} \tag{43}$$

Inserting this into equation (41) and then equation (37) gives the Fisher information matrix

$$F = \lambda_0^{-1}\sigma_{tot}^{-2}\,[\mathrm{tr}(A_{true}\, B^T)I - \tfrac{1}{2}\,(A_{true}\, B^T + BA_{true}^{\ T})], \tag{44}$$

and, by matrix inversion, the covariance matrix

$$P = \lambda_0 \sigma_{tot}^{\ 2}[\mathrm{tr}(A_{true}\, B^T)I - \tfrac{1}{2}\,(A_{true}\, B^T + BA_{true}^{\ T})]^{-1}. \tag{45}$$

The true attitude matrix is not known in a real attitude estimation problem, of course, so A_{opt} must be used in place of A_{true} in computing the covariance. Making this replacement in equation (46) gives, with equation (19) and the symmetry of the matrix product $A_{opt}\, B^T$, which follows from equations (7) and (9),

$$P = \lambda_0 \sigma_{tot}^{\ 2}(\lambda I - A_{opt}\, B^T)^{-1} = \lambda_0 \sigma_{tot}^{\ 2}\,\mathrm{adj}(\lambda I - A_{opt}\, B^T)/\det(\lambda I - A_{opt}\, B^T). \tag{46}$$

Equation (46) is one of the forms for the covariance matrix given in Appendix B of [13], which is also the result obtained in [18], simplified to the case that only the attitude is estimated. The computation of the matrix inverse can be avoided as follows [19]. Equations (7), (9), and (15) show that

$$\lambda I - A_{opt}\, B^T = U_+\,\mathrm{diag}[S_2 + S_3,\, S_3 + S_1,\, S_1 + S_2]\, U_+^{\ T}. \tag{47}$$

The determinant of this matrix is given by equation (16) as

$$\det(\lambda I - A_{opt}\, B^T) = \zeta, \tag{48}$$

and its adjoint is

$$\mathrm{adj}(\lambda I - A_{opt}\, B^T) = \kappa I + BB^T, \tag{49}$$

yielding the desired manifestly symmetric result

$$P = \lambda_0 \sigma_{tot}^{\ 2}(\kappa I + BB^T)/\zeta. \tag{50}$$

We see that the covariance matrix is infinite when $\zeta = 0$, which agrees with the conditions for indeterminacy of the attitude solution discussed above. In the case of near-indeterminacy, the singular values are approximately $S_1 \approx \lambda$, $S_2 \approx S_3 \approx 0$ [13], which gives the covariance

$$P \approx \lambda_0 \sigma_{tot}^{\ 2} U_+ \, \mathrm{diag}[\lambda^2/\zeta, \lambda^{-1}, \lambda^{-1}] U_+^{\ T}. \tag{51}$$

A good criterion for terminating the iterative solution for λ by equation (25) is

$$Q'(\lambda) = 2\zeta < \tfrac{1}{2} \lambda_0^{\ 3} \sigma_{tot}^{\ 2}, \tag{52}$$

since equation (51) predicts attitude estimation error standard deviations larger than $2\lambda/\lambda_0$ radians when this inequality is satisfied. This error can only be small if $\lambda \ll \lambda_0$, in which case the attitude estimate is poor because the loss function is large.

Normalization of the weights

The results above are valid for any positive value of the parameter λ_0, but only two choices are useful:

$$\lambda_0 = 1 \quad \text{(normalized weights)} \tag{53}$$

or

$$\lambda_0 = \sigma_{tot}^{\ -2} \quad \text{(unnormalized weights).} \tag{54}$$

Past treatments of this problem have generally used normalized weights, which give a B matrix with elements of order unity. This is convenient in computations using fixed-point arithmetic, but floating-point arithmetic is an option on virtually all present-day computers. The normalized form may also be useful if the measurement weights are arbitrarily assigned.

The unnormalized form is more natural if the weights are computed in terms of measurement variances, as in equation (40), since the unnormalized weights are just equal to the inverse variances. The unnormalized form also simplifies the computation of the covariance, as shown by equation (50), but this form can potentially lead to numerical problems. The elements of B are of order $\sigma_{tot}^{\ -2}$ if the weights are not normalized, which means that $\| \mathrm{adj}\, B \|^2$ is of order $\sigma_{tot}^{\ -8}$. Since σ_{tot} can be of order 10^{-6} for highly accurate sensors, $\| \mathrm{adj}\, B \|^2$ can be of order 10^{48}, leading to exponent overflow in floating-point representations that do not provide an adequate exponent range. This is not a problem with double-precision arithmetic in conformity with ANSI/IEEE Standard 754-1985 for binary floating-point arithmetic [20], since this standard mandates eleven bits for the exponent, allowing representation of numbers as large as 10^{308}. The Standard Apple Numerical Environment [21] and VAX G_FLOATING [22] double-precision arithmetic employ eleven-bit exponents, but VAX D_FLOATING double-precision arithmetic allots only eight bits for the exponent. This is the same as in IEEE-standard single-precision arithmetic, and allows representation of numbers only as large as 10^{38}. Single-precision arithmetic would lead to exponent overflow problems for measurement variances $\sigma_{tot}^{\ 2}$ less than about 10^{-9}, but double-precision arithmetic is certainly preferred in such cases.

Algorithm test - accuracy

Two forms of the new algorithm, the form with the iterative solution for λ (FOAM — Fast Optimal Attitude Matrix), and the form with the analytic solution for S_1 (SOMA — Slower Optimal Matrix Algorithm), were compared with the SVD method [13] for minimizing Wahba's loss function. The three methods were implemented in double-precision FORTRAN and executed on a DEC VAX 8830 computer. FOAM and SOMA were implemented in G_FLOATING arithmetic with unnormalized weights. FOAM was also implemented with normalized weights in both G_FLOATING and D_FLOATING arithmetic, while the SVD method was implemented with unnormalized weights in D_FLOATING arithmetic.

Four sets of reference vectors were used for the tests:

$$\mathbf{r}_1 = [1, 0, 0]^T, \mathbf{r}_2 = [0, 1, 0]^T, \mathbf{r}_3 = [0, 0, 1]^T, \tag{55}$$

$$\mathbf{r}_1 = [0.6, 0.8, 0]^T, \mathbf{r}_2 = [0.8, -0.6, 0]^T, \tag{56}$$

$$\mathbf{r}_1 = [1, 0, 0]^T, \mathbf{r}_2 = [1, 0.01, 0]^T, \mathbf{r}_3 = [1, 0, 0.01]^T, \tag{57}$$

and

$$\mathbf{r}_1 = [1, 0, 0]^T, \mathbf{r}_2 = [0.96, 0.28, 0]^T, \mathbf{r}_3 = [0.96, 0, 0.28]^T. \tag{58}$$

Set (55) models three sensors with orthogonal boresights along the spacecraft body axes, while set (56) models two sensors with orthogonal boresights not along the body axes. Reference vector set (57) is intended to model three star measurements in a single star sensor with a small field-of-view. Set (58) models one sensor with its boresight along the body x- axis and two sensors with boresights 16.26 degrees off this axis. The observation vectors were computed as

$$\mathbf{b}_i = A_{true}\, \mathbf{r}_i + \mathbf{n}_i, \tag{59}$$

where

$$A_{true} = \begin{bmatrix} 0.352 & 0.864 & 0.360 \\ -0.864 & 0.152 & 0.480 \\ 0.360 & -0.480 & 0.800 \end{bmatrix}, \tag{60}$$

which has all non-zero matrix elements with exact decimal representations and is otherwise arbitrary, and $\mathbf{n}_i$ is a vector of measurement errors. The tests were run both with $\mathbf{n}_i = \mathbf{0}$ and with measurement errors simulated by zero-mean Gaussian white noise on the components of $\mathbf{n}_i$. All the methods normalize the input observation and reference vectors; some efficiencies in the normalization process were found and applied to the three algorithms.

The results of the accuracy tests are presented in Table 1. The reference vector sets are labeled REF. The standard deviations (in radians) in the table were used to compute the measurement weights and also the level of measurement errors in the tests where these were simulated. Only two measurements were used in the tests in which only two standard deviations are given. The quantities presented in the table are the estimation error in radians

(computed with simulated measurement errors),

$$EST = \sin^{-1}(2^{-3/2} \| A_{opt} A_{true}^T - A_{true} A_{opt}^T \|), \tag{61}$$

the maximum computation error for all FOAM and SOMA variants (computed with $\mathbf{n}_i = \mathbf{0}$),

$$COMP = \| A_{opt} - A_{true} \|, \tag{62}$$

and the maximum orthogonality error for FOAM and SOMA,

$$ORTH = \| A_{opt} A_{opt}^T - I \|. \tag{63}$$

The estimation error was the same for all methods, to the accuracy of the computation errors. As expected, the very robust SVD method gives the smallest maximum orthogonality error (2.16×10^{-16}) and computation errors (4.72×10^{-17} for cases 1 - 4, 1.63×10^{-10} for case 5, 3.74×10^{-15} for cases 6 - 11, and 2.10×10^{-9} for case 12). No significant differences were seen between FOAM and SOMA or between normalized and unnormalized weights. D_FLOATING arithmetic was about one decimal digit more precise than G_FLOATING arithmetic, as expected [22]; but this is not significant, since the computation errors are much less than the estimation errors in all cases with realistic noise. It is clear that cases with widely differing measurement accuracies furnish the greatest computational challenges.

Algorithm test - speed

The above methods were compared with Shuster's QUEST (QUaternion ESTimation) algorithm [9] for computational speed, since QUEST is the fastest previously known algorithm for solving Wahba's problem. In addition to the reference and observation vectors

Table 1

Accuracy Test Results. See text for explanation

CASE	REF	σ_1	σ_2	σ_3	EST	COMP	ORTH
1	(55)	10^{-6}	10^{-6}	10^{-6}	1.38×10^{-6}	4.61×10^{-16}	1.12×10^{-15}
2	(55)	10^{-6}	10^{-6}	—	2.02×10^{-6}	3.05×10^{-16}	6.11×10^{-16}
3	(55)	.01	.01	.01	1.39×10^{-2}	5.27×10^{-16}	1.01×10^{-15}
4	(55)	.01	.01	—	2.05×10^{-2}	3.05×10^{-16}	1.12×10^{-15}
5	(56)	10^{-6}	.01	—	1.12×10^{-2}	7.83×10^{-9}	2.73×10^{-8}
6	(57)	10^{-6}	10^{-6}	10^{-6}	2.51×10^{-5}	4.66×10^{-12}	8.94×10^{-12}
7	(57)	10^{-6}	10^{-6}	—	3.18×10^{-5}	7.84×10^{-12}	1.54×10^{-11}
8	(57)	.01	.01	.01	0.186	4.04×10^{-12}	7.50×10^{-12}
9	(57)	.01	.01	—	8.82×10^{-2}	5.70×10^{-12}	1.12×10^{-11}
10	(58)	10^{-6}	.01	.01	1.72×10^{-2}	1.49×10^{-7}	2.97×10^{-7}
11	(58)	10^{-6}	.01	—	3.33×10^{-2}	1.45×10^{-7}	2.87×10^{-7}
12	(58)	.01	10^{-6}	—	3.48×10^{-2}	3.01×10^{-7}	6.00×10^{-7}

and the measurement standard deviations, QUEST requires the input of five control parameters, which were taken as $QUIBBL = 0.1$, $FIBBL = 10^{-5}$, $QUACC = 10^{-8}$, $NEWT = 10$, and $IMETH = 1$. The measured CPU times were effectively the same for normalized and unnormalized weights. They consist of a part that is independent of the number of observations processed and a part proportional to the number of observations:

$$t_{\mathrm{QUEST}} = 0.24 + 0.09\,n \quad \text{msec.} \tag{64}$$

$$t_{\mathrm{FOAM}} = 0.27 + 0.07\,n \quad \text{msec,} \tag{65}$$

$$t_{\mathrm{SOMA}} = 0.36 + 0.07\,n \quad \text{msec,} \tag{66}$$

$$t_{\mathrm{SVD}} = (3 \pm 1) + 0.07\,n \quad \text{msec.} \tag{67}$$

The greater n-dependent time in QUEST as compared to the other algorithms is due to the method used to compute the covariance matrix in QUEST. The computation of λ generally requires one or two iterations in QUEST and two to six iterations in FOAM, due to the need to iterate to convergence in the latter method, which accounts for the greater n-independent time in FOAM. The transcendental function calls in SOMA account for its longer running time compared to FOAM, which is definitely preferable to SOMA since it is faster and no less accurate. The range of times for the SVD method is related to the rank and conditioning of the B matrix. This method is significantly slower than all the other methods tested, as has been noted previously; but the SVD method may still find applications in nearly singular estimation problems. The exact CPU times will vary from case to case, and the time required for either FOAM or QUEST appears to be quite modest in comparison with other computations performed in spacecraft attitude determination.

It should be pointed out that FOAM computes the attitude matrix directly, while QUEST computes an attitude quaternion. If an attitude matrix is required from QUEST, an additional step is required to compute it from the quaternion. This requires only multiplications and additions, though, and no transcendental function evaluations. If it is desired to compute a quaternion from FOAM, the standard method for extracting it from the attitude matrix can be used [23]. This requires the evaluation of one square root, but FOAM is faster than QUEST even with this addition. The principal advantage of FOAM over QUEST in practice is that it requires no control parameter input; its only inputs are the number of observations, the reference and observation vectors, and the measurement standard deviations.

Two-observation case

In the special case of two observations, the rank of B is at most two, so $\det B = 0$, which gives with equation (22)

$$\kappa = \| \operatorname{adj} B \|, \tag{68}$$

$$\lambda = (2\kappa + \| B \|^2)^{1/2}, \tag{69}$$

and

$$\zeta = \kappa\lambda. \tag{70}$$

Both κ and λ must be positive in order for λ to be the largest root of $Q(\lambda)$. The explicit form for B as a function of the reference and observation vectors then yields

$$\text{adj}\, B^T = a_1 a_2 (\mathbf{b}_1 \times \mathbf{b}_2)(\mathbf{r}_1 \times \mathbf{r}_2)^T, \tag{71}$$

$$\kappa = a_1 a_2 |\mathbf{b}_1 \times \mathbf{b}_2| \, |\mathbf{r}_1 \times \mathbf{r}_2|, \tag{72}$$

and

$$\lambda = \{a_1^2 + 2 a_1 a_2 [\, |\mathbf{b}_1 \times \mathbf{b}_2| \, |\mathbf{r}_1 \times \mathbf{r}_2| + (\mathbf{b}_1^T \mathbf{b}_2)(\mathbf{r}_1^T \mathbf{r}_2)] + a_2^2\}^{1/2}. \tag{73}$$

The attitude is indeterminate if either the two reference vectors or the two observation vectors are parallel or antiparallel. Thus we will assume that both θ_r, the angle between $\mathbf{r}_1$ and $\mathbf{r}_2$, and θ_b, the angle between $\mathbf{b}_1$ and $\mathbf{b}_2$, are strictly greater than zero and strictly less than pi. Now set $\lambda_0 = a_1 + a_2 = 1$ for the remainder of the discussion in this section, define

$$\varepsilon \equiv (\theta_b - \theta_r)/2, \tag{74}$$

and note that $|\varepsilon| < \pi/2$. This allows the expression for λ to be written more compactly as

$$\lambda = (1 - 4 a_1 a_2 \sin^2 \varepsilon)^{1/2}. \tag{75}$$

These expressions for λ in the two-observation case are equivalent to equation (72) in [9].

It is convenient to write the optimal attitude estimate in terms of the orthonormal triads:

$$\mathbf{r}_+ \equiv (\mathbf{r}_2 + \mathbf{r}_1)/[2\cos(\theta_r/2)], \tag{76a}$$

$$\mathbf{r}_- \equiv (\mathbf{r}_2 - \mathbf{r}_1)/[2\sin(\theta_r/2)], \tag{76b}$$

$$\mathbf{r}_+ \times \mathbf{r}_- = (\mathbf{r}_1 \times \mathbf{r}_2)/|\mathbf{r}_1 \times \mathbf{r}_2|, \tag{76c}$$

and

$$\mathbf{b}_+ \equiv (\mathbf{b}_2 + \mathbf{b}_1)/[2\cos(\theta_b/2)], \tag{77a}$$

$$\mathbf{b}_- \equiv (\mathbf{b}_2 - \mathbf{b}_1)/[2\sin(\theta_b/2)], \tag{77b}$$

$$\mathbf{b}_+ \times \mathbf{b}_- = (\mathbf{b}_1 \times \mathbf{b}_2)/|\mathbf{b}_1 \times \mathbf{b}_2|. \tag{77c}$$

Other orthogonal triads can be defined, but these preserve the maximum symmetry between the two measurements. The optimal attitude matrix expressed in terms of these triads is

$$A_{opt} = (1 - 4 a_1 a_2 \sin^2 \varepsilon)^{-1/2} [\cos\varepsilon\,(\mathbf{b}_+ \mathbf{r}_+^T + \mathbf{b}_- \mathbf{r}_-^T) + (a_1 - a_2)\sin\varepsilon\,(\mathbf{b}_+ \mathbf{r}_-^T - \mathbf{b}_- \mathbf{r}_+^T)] + (\mathbf{b}_+ \times \mathbf{b}_-)(\mathbf{r}_+ \times \mathbf{r}_-)^T. \tag{78}$$

It is interesting to note that a factor of $a_1 a_2$ in the denominator of equation (12) has cancelled an identical factor in the numerator. Thus the attitude estimate has a well-defined limit as either a_1 or a_2 tends to zero, even though Wahba's loss function does not have a unique minimum in either limit. Another interesting property of the two-observation case is that the optimal estimate is independent of the weights when $\varepsilon = 0$. Equations (24) and (75) with $\lambda_0 = 1$ show that the optimized loss function is zero if any of a_1, a_2, or ε is zero.

We now investigate the conditions under which this optimal attitude estimate can be obtained by a generalization of the simpler TRIAD or algebraic method [8, 9]. This is a well-known algorithm for computing an attitude matrix from two vector observations by forming orthonormal triads from the reference and observation vectors. One of vectors in the reference triad is the normalized cross product of the two reference vectors, and the other two are orthonormal linear combinations of the two reference vectors. The most general form for the reference triad that we will consider is:

$$\mathbf{r}_{\mathrm{I}} \equiv \cos\psi_r\, \mathbf{r}_+ - \sin\psi_r\, \mathbf{r}_- = [\sin(\psi_r + \theta_r/2)\mathbf{r}_1 - \sin(\psi_r - \theta_r/2)\mathbf{r}_2]/\sin\theta_r\,, \tag{79a}$$

$$\mathbf{r}_{\mathrm{II}} \equiv \cos\psi_r\, \mathbf{r}_- + \sin\psi_r\, \mathbf{r}_+ = [\cos(\psi_r - \theta_r/2)\mathbf{r}_2 - \cos(\psi_r + \theta_r/2)\mathbf{r}_1]/\sin\theta_r\,, \tag{79b}$$

$$\mathbf{r}_{\mathrm{I}} \times \mathbf{r}_{\mathrm{II}} = \mathbf{r}_+ \times \mathbf{r}_-\,, \tag{79c}$$

where ψ_r is some rotation angle in the plane spanned by $\mathbf{r}_1$ and $\mathbf{r}_2$. The observation triad is

$$\mathbf{b}_{\mathrm{I}} \equiv \cos\psi_b\, \mathbf{b}_+ - \sin\psi_b\, \mathbf{b}_- = [\sin(\psi_b + \theta_b/2)\mathbf{b}_1 - \sin(\psi_b - \theta_b/2)\mathbf{b}_2]/\sin\theta_b\,, \tag{80a}$$

$$\mathbf{b}_{\mathrm{II}} \equiv \cos\psi_b\, \mathbf{b}_- + \sin\psi_b\, \mathbf{b}_+ = [\cos(\psi_b - \theta_b/2)\mathbf{b}_2 - \cos(\psi_b + \theta_b/2)\mathbf{b}_1]/\sin\theta_b\,, \tag{80b}$$

$$\mathbf{b}_{\mathrm{I}} \times \mathbf{b}_{\mathrm{II}} = \mathbf{b}_+ \times \mathbf{b}_-\,, \tag{80c}$$

similarly. The angles ψ_r and ψ_b are chosen to give more or less weight to the two vector measurements. The choice $\psi_r = \psi_b = 0$, for example, gives equal weight to the two measurements. The choice $\psi_r = \theta_r/2$ and $\psi_b = \theta_b/2$ gives

$$\mathbf{r}_{\mathrm{I}} = \mathbf{r}_1, \tag{81a}$$

$$\mathbf{r}_{\mathrm{II}} = (\mathbf{r}_2 - \cos\theta_r\, \mathbf{r}_1)/\sin\theta_r\,, \tag{81b}$$

and similar relations for $\mathbf{b}_{\mathrm{I}}$ and $\mathbf{b}_{\mathrm{II}}$, with maximum weight on the first measurement. The choice $\psi_r = -\theta_r/2$ and $\psi_b = -\theta_b/2$, on the other hand, gives

$$\mathbf{r}_{\mathrm{I}} = \mathbf{r}_2, \tag{82a}$$

$$\mathbf{r}_{\mathrm{II}} = -(\mathbf{r}_1 - \cos\theta_r\, \mathbf{r}_2)/\sin\theta_r\,, \tag{82b}$$

and similarly for $\mathbf{b}_{\mathrm{I}}$ and $\mathbf{b}_{\mathrm{II}}$, with maximum weight on the second measurement. The key point is that ψ_r is some function of θ_r and the measurement weights, and ψ_b is *the same* function of θ_b and the weights. Note that this does not imply that $\psi_r = \psi_b$ except in the case that $\varepsilon = 0$. Often, the TRIAD method is understood to mean only the special cases of equations (81) or (82), rather than the generalized method specified by equations (79) and (80).

The TRIAD attitude estimate is given by

$$\begin{aligned} A_{\mathrm{TRIAD}} &= [\mathbf{b}_{\mathrm{I}} \vdots \mathbf{b}_{\mathrm{II}} \vdots \mathbf{b}_{\mathrm{I}} \times \mathbf{b}_{\mathrm{II}}]\,[\mathbf{r}_{\mathrm{I}} \vdots \mathbf{r}_{\mathrm{II}} \vdots \mathbf{r}_{\mathrm{I}} \times \mathbf{r}_{\mathrm{II}}]^T = \mathbf{b}_{\mathrm{I}}\mathbf{r}_{\mathrm{I}}^T + \mathbf{b}_{\mathrm{II}}\mathbf{r}_{\mathrm{II}}^T + (\mathbf{b}_{\mathrm{I}} \times \mathbf{b}_{\mathrm{II}})(\mathbf{r}_{\mathrm{I}} \times \mathbf{r}_{\mathrm{II}})^T \\ &= \cos(\psi_b - \psi_r)(\mathbf{b}_+\mathbf{r}_+^T + \mathbf{b}_-\mathbf{r}_-^T) + \sin(\psi_b - \psi_r)(\mathbf{b}_+\mathbf{r}_-^T - \mathbf{b}_-\mathbf{r}_+^T) \\ &\qquad + (\mathbf{b}_+ \times \mathbf{b}_-)(\mathbf{r}_+ \times \mathbf{r}_-)^T. \end{aligned} \tag{83}$$

We now attempt to find angles ψ_r and ψ_b such that the TRIAD solution gives the optimal

attitude estimate of equation (78). We immediately find such angles in four special cases:

1) If $\varepsilon = 0$, then $\psi_r = \psi_b$ automatically, all TRIAD solutions are the same, and they all agree with the optimal estimate, which is independent of the weights in the loss function.

2) If $a_1 = a_2 = 1/2$, the TRIAD solution with $\psi_r = \psi_b = 0$ and with vector triads given by equations (76) and (77) gives the optimal estimate.

3) If $a_1 = 1, a_2 = 0$, the TRIAD solution with $\psi_r = \theta_r/2$, $\psi_b = \theta_b/2$ and with triads as in equations (81) gives the optimal estimate.

4) If $a_1 = 0, a_2 = 1$, the TRIAD solution with $\psi_r = -\theta_r/2$, $\psi_b = -\theta_b/2$ and with triads as in equations (82) gives the optimal estimate.

We will now show that the TRIAD solution does not minimize Wahba's loss function except in these four special cases. Comparing equations (78) and (83) gives the following necessary condition for agreement of the TRIAD and optimal attitude estimates:

$$\tan(\psi_b - \psi_r) = (a_1 - a_2)\tan\varepsilon. \tag{84}$$

Set $\theta_r = \theta_0$, some arbitrarily chosen angle, and denote the corresponding value of ψ_r by ψ_0, which is also a function of the observation weights. Then

$$\tan(\psi_b - \psi_0) = (a_1 - a_2)\tan[(\theta_b - \theta_0)/2] \equiv (a_1 - a_2)\tau_b. \tag{85}$$

This equation must hold for any θ_r, with ψ_0 and θ_0 regarded as fixed parameters, since ψ_b is required to be a function of θ_b and the weights only, and not of θ_r. Now setting $\theta_b = \theta_0$ in equation (84) gives $\psi_b = \psi_0$ and

$$\tan(\psi_r - \psi_0) = (a_1 - a_2)\tan[(\theta_r - \theta_0)/2] \equiv (a_1 - a_2)\tau_r, \tag{86}$$

which must hold for any θ_b. In fact, equation (86) could have been written directly in analogy with equation (85), since ψ_r is required to be the same function of θ_r and the measurement weights as ψ_b is of θ_b and the weights. Now combining equations (85) and (86) with some elementary trigonometry gives

$$\begin{aligned}\tan(\psi_b - \psi_r) &= \tan[(\psi_b - \psi_0) - (\psi_r - \psi_0)] = (a_1 - a_2)(\tau_b - \tau_r)/[1 + (a_1 - a_2)^2\tau_b\tau_r] \\ &= (a_1 - a_2)\tan\varepsilon\,(1 + \tau_b\tau_r)/[1 + (1 - 4a_1a_2)\tau_b\tau_r].\end{aligned} \tag{87}$$

Equating the right sides of equations (84) and (87) gives, after some cancellations, the necessary condition

$$4a_1a_2\tau_b\tau_r(a_1 - a_2)\tan\varepsilon = 0, \tag{88}$$

which is satisfied in the four special cases discussed above. It is also satisfied if either τ_b or τ_r is zero, but these conditions cannot be satisfied in general since θ_0 is an arbitrarily chosen angle. Thus the TRIAD method cannot find the optimal attitude minimizing Wahba's loss function in the general case, but only in the special cases $\varepsilon = 0$, $a_1 = 0$, $a_2 = 0$, and $a_1 = a_2$.

Conclusions

A new algorithm for minimizing Wahba's loss function has been found, which solves for the optimal attitude matrix directly, without the intermediate computation of a quaternion or other parameterization of the attitude. The attitude quaternion can be computed from the attitude matrix, if desired; and the new method with iterative solution of the scalar coefficients in the attitude matrix is at least as fast as existing methods even with this additional computation. The scalar coefficients used in computing the optimal attitude matrix are also used to compute the covariance of the attitude error angles. Since the attitude matrix is inherently nonsingular, there are no problems with special cases like 180 degree rotations, and no special procedures are needed to deal with such cases. The principal practical advantage of the new method over existing fast optimal attitude estimators is that it requires no control parameter input; its only inputs are the number of observations, the reference and observation vectors, and the measurement standard deviations.

A closed-form solution for the optimal attitude matrix is presented for the special case of two observations. This solution is compared with the estimate produced by the well-known non-optimal method based on orthonormal triads formed from the observation and reference vectors. When the angle between the two reference vectors is equal to the angle between the two observation vectors, all triad choices give the optimal estimate, which is independent of the weights in the loss function. Except for this case, the optimal and triad-based attitude estimates agree only when the two vector measurements are given equal weights in the loss function or when the weight given to one vector measurement is negligible compared to the weight given to the other.

Acknowledgements

I want to thank G. A. Natanson and especially Malcolm D. Shuster for helpful comments on earlier versions of this paper.

References

[1] WAHBA, GRACE "A Least Squares Estimate of Spacecraft Attitude," *SIAM Review*, Vol. 7, No. 3, July 1965, p. 409.

[2] FARRELL, J. L. and STUELPNAGEL, J. C. "A Least Squares Estimate of Spacecraft Attitude," *SIAM Review*, Vol. 8, No. 3, July 1966, pp. 384-386.

[3] WESSNER, R. H. ibid.

[4] VELMAN, J. R. ibid.

[5] BROCK, J. E. ibid.

[6] DAVENPORT, PAUL B. "A Vector Approach to the Algebra of Rotations with Applications," NASA X-546-65-437, November 1965.

[7] KEAT, J. "Analysis of Least Squares Attitude Determination Routine DOAOP," Computer Sciences Corporation, CSC/TM-77/6034, February 1977.

[8] LERNER, GERALD M. "Three-Axis Attitude Determination," in *Spacecraft Attitude Determination and Control*, James R. Wertz, ed., D. Reidel, Dordrecht, Holland, 1978.

[9] SHUSTER, M. D. and OH, S. D. "Three-Axis Attitude Determination from Vector Observations," *Journal of Guidance and Control*, Vol. 4, No. 1, January-February 1981, pp. 70-77.

[10] GOLUB, GENE H. and VAN LOAN, CHARLES F. *Matrix Computations*, the Johns Hopkins University Press, Baltimore, MD, 1983

[11] HORN, ROGER A. and JOHNSON, CHARLES R. *Matrix Analysis*, Cambridge University Press, Cambridge, UK, 1985

[12] DAVENPORT, PAUL B. "Attitude Determination and Sensor Alignment via Weighted Least Squares Affine Transformations," AAS Paper No. 71-396, AAS/AIAA Astrodynamics Specialists Conference, Ft. Lauderdale, FL, August 1971.

[13] MARKLEY, F. LANDIS "Attitude Determination Using Vector Observations and the Singular Value Decomposition," *Journal of the Astronautical Sciences* , Vol. 36, No. 3, July-September 1988, pp. 245-258

[14] DANBY, J. M. A. *Fundamentals of Celestial Mechanics*, 2nd edition, Willman-Bell, Inc., Richmond, VA, 1988

[15] BEYER, WILLIAM H. *CRC Standard Mathematical Tables, 2nd Edition*, CRC Press, Inc., Boca Raton, FL, 1987

[16] SHUSTER, MALCOLM D. "Maximum Likelihood Estimation of Spacecraft Attitude," *Journal of the Astronautical Sciences*, Vol. 37, No. 1, January-March 1989, pp. 79-88

[17] SORENSON, HAROLD W. *Parameter Estimation: Principles and Problems*, Marcel Dekker, New York, NY, 1980

[18] MARKLEY, F. LANDIS "Attitude Determination and Parameter Estimation Using Vector Observations: Theory," *Journal of the Astronautical Sciences* , Vol. 37, No. 1, January-March 1989, pp.41-58

[19] MARKLEY, F. LANDIS "Attitude Determination and Parameter Estimation Using Vector Observations: Application," *Journal of the Astronautical Sciences* , Vol. 39, No. 3, July-September 1991, pp. 367-381

[20] *IEEE Standard for Binary Floating-Point Arithmetic*, ANSI/IEEE Standard 754-1985, The Institute of Electrical and Electronics Engineers, Inc., New York, NY, 1985

[21] *Apple Numerics Manual, 2nd Edition*, Addison-Wesley, Reading, MA, 1988

[22] *VAX-11 FORTRAN Language Reference Manual*, Digital Equipment Corporation, Maynard, MA, 1982

[23] SHEPPERD, STANLEY W. "Quaternion from Rotation Matrix," *Journal of Guidance and Control*, Vol. 1, No. 3, May-June 1978, pp. 223-224

UPPER ATMOSPHERIC RESEARCH SATELLITE (UARS) ONBOARD ATTITUDE DETERMINATION USING A KALMAN FILTER

by

Joseph Garrick
Code 554/Flight Dynamics Analysis Branch
NASA - Goddard Space Flight Center
Greenbelt, Maryland

ABSTRACT

The Upper Atmospheric Research Satellite (UARS) requires a highly accurate knowledge of it's attitude to accomplish it's mission. Propagation of the attitude state using gyro measurements is not sufficient to meet the accuracy requirements, and must be supplemented by a observer/compensation process to correct for dynamics and observation anomalies. The process of amending the attitude state utilizes a well known method, the discrete Kalman Filter.

This study will be a sensitivity analysis of the discrete Kalman Filter as implemented in the UARS Onboard Computer (OBC). The stability of the Kalman Filter used in the normal on-orbit control mode within the OBC, will be investigated for the effects of corrupted observations and nonlinear errors. Also a statistical analysis on the residuals of the Kalman Filter will be performed. These analysis will be based on simulations using the UARS Dynamics Simulator (UARSDSIM) and compared against attitude requirements as defined by General Electric (GE). An independent verification of expected accuracies will performed using the Attitude Determination Error Analysis System (ADEAS).

1.0 Introduction

The Upper Atmosphere Research Satellite (UARS) is a three axis stabilized spacecraft, designed to make a global, continuous and comprehensive look at the Earth's upper atmosphere. The spacecraft was launched on September 12, 1991 onboard Space Transportation System 48 (STS-48) and placed in a circular, low earth orbit before ascending to it's final mission orbit with mean altitude of 585 km. and inclination of 57 degrees. The mission lifetime will cover two northern hemisphere winters and have a nominal life expectancy of 18 months, with possible extensions up to 15 years.

The UARS observatory consists of ten science instruments, an instrument module (IM) including mission-unique hardware, and the Multimission Modular Spacecraft (MMS). The MMS will provide precision pointing for the science instruments on an Earth-oriented platform, with periodic routine maneuvers to maintain a favorable sun orientation. The MMS is an on-orbit serviceable spacecraft bus that has a modular design to allow for use on most science related satellites. The observatory uses the MMS to provide attitude control, communications and data handling, electrical power storage and regulation, and propulsion.

Of interest to this study is the MMS Modular Attitude Control Subsystem (MACS) which provides the Attitude Determination and Control (AD&C) subsystem software that is implemented in the Onboard Computer (OBC), which is part of the Command and Data Handling (C&DH) subsystem. The OBC provides the estimation model for meeting the attitude determination accuracy during the precision mode of the normal on-orbit mission mode of 60 arcsec. (3 sigma). An important part of the attitude determination scheme implemented in the OBC is to compensate the propagated state using gyro data with periodic measurement data from the Fixed Head Star Trackers (FHSTs) to obtain a better estimate of the current attitude error and gyro drift bias. This compensator is known as the discrete Kalman Filter. This study will address the attitude determination capabilities of the discrete Kalman Filter during the precision pointing mode of the normal on-orbit mission as implemented in the OBC of the UARS spacecraft.

2.0 Attitude Modeling

This study will be a sensitivity analysis of the discrete Kalman Filter as implemented in the UARS spacecraft. The stability of the Kalman Filter will be investigated for the effects of corrupted observations and nonlinear errors. Also a statistical analysis on the residuals of the Kalman Filter will be performed. These analysis will be based on simulations using the UARS Dynamics Simulator (UARSDS), a software implementation of the spacecraft's hardware and control systems. An independent verification of expected accuracies will also be performed using the Attitude Determination Error Analysis System (ADEAS).

2.1 Attitude Determination Error Analysis System (ADEAS)

One of the attitude tools used in this study was the Attitude Determination Error Analysis System (ADEAS), which allowed for a quick verification of expected accuracies. ADEAS can model estimation by using either a batch filter or a Kalman Filter. The estimation choices found in ADEAS makes this tool ideal for comparison against simulation results using the UARSDS and the definitive attitude ground solutions using a batch filter. The means by which ADEAS computes the attitude accuracies is the solve-for and consider parameters supplied by the user. The solve-for parameter are those found in the UARS state vector. In the UARS case these are the attitude errors and the gyro drift errors. The consider parameters are those not found in the state vector of the OBC and not taken into account by the filter, such as misalignments.

2.2 UARS Dynamics Simulator (UARSDS)

The UARS Dynamics Simulator (UARSDS) is an analytical tool developed to give the analysts an insight into the performance of the attitude determination and control system used onboard the spacecraft. By means of interactive screen displays the user can configure the UARS spacecraft to include misalignments, noises, biases and scale factors to all of the modeled hardware. The dynamics can be configured to include initial attitude and rate errors, as well as the ability to include or exclude the effects due to external perturbations, such as environmental torques and cryogenic venting. Also, the user can specify the desired orbital characteristics for a given epoch to allow the choice of seasonal variations of sun and moon viewing data, as well as continually changing star and target position vectors. A simulation using the UARSDS is controlled using the same set of ground commands used by the actual spacecraft, thus allowing the simulator to create a realistic scenario actually employed during the spacecraft's mission.

2.3 UARS Attitude Determination

The UARS onboard attitude determination function is contained in two parts within the OBC. The first part contains the routines which propagate the state vector using gyro data and compensates the state vector during the normal on-orbit modes every 32.768 seconds (64 OBC cycles) using the results from the second part, the attitude estimation function. The attitude estimation function contains the discrete extended Kalman Filter and is processed every 64 OBC cycles to produce update parameters. The following sections give a more detailed mathematical view of the attitude determination process.

2.3.1 Kinematic Equations (Time Propagation)

This process updates the spacecraft Euler parameters using the angular increments furnished by the gyro data processor. When the update filter (the Kalman Filter) processing is enabled, the Euler parameters are also compensated using update parameters from the attitude estimation function. Also the gyro biases, which are used in the gyro data processor, are corrected. The equations for propagating and compensating the OBC state vector are as follows:

1. Compute the Euler parameter updates

$$\delta Q = \tfrac{1}{2}\,\Omega(\theta)\,Q \qquad (2\text{-}1)$$

$$\text{where } \Omega(\theta) = \begin{bmatrix} 0 & \theta_z & -\theta_y & \theta_x \\ -\theta_z & 0 & \theta_x & \theta_y \\ \theta_y & -\theta_x & 0 & \theta_z \\ -\theta_x & -\theta_y & -\theta_z & 0 \end{bmatrix}$$

$\theta_{x,y,z}$ are gyro compensated data

$Q = [q_1, q_2, q_3, q_4]^T$

2. Update the Euler parameters

$$Q_{t+1} = Q_t + \delta Q \qquad (2\text{-}2)$$

3. Normalize the update Euler parameters

$$Q_{t+1} = Q_{t+1} * Q\text{-}1 \qquad (2\text{-}3)$$

where $Q^{-1} = 1 + \tfrac{1}{2}\,(1 - | Q_{t+1} |^2)$

4. If update filter processing is enabled update the attitude and gyro biases.

   a. Compute the Euler parameter updates

$$\delta Q' = \tfrac{1}{2}\,\Omega(\delta\theta)\,Q_{t+1} \qquad (2\text{-}4)$$

   where $\delta\theta = S_i \qquad i = 1,2,3$

   $S = [s_1, s_2, s_3, s_4, s_5, s_6]$ and is the update parameters from the attitude estimation function

   b. update the Euler parameters

$$Q_{t+1} = Q_{t+1} + \delta Q' \qquad (2\text{-}5)$$

   c. update the gyro biases

$$b_i = b_i + (S_{i+3} * t_c) \quad i = 1,2,3 \qquad (2\text{-}6)$$

   where b_i are gyro biases

   t_c is the OBC cycle time (0.512 sec.)

2.3.2 Discrete Kalman Filter

The discrete Kalman Filter has three processing steps. The first is the computation of the state transition matrix, the state noise covariance matrix, and the state covariance matrix. The state transition matrix and the state noise covariance matrices are computed once and recomputed only if the measurement update interval changes. The second step is the measurement model. The measurement model uses two Fixed Head Star Trackers (FHST) as the source of measurement data for nominal processing. In the event one of the FHSTs degrade in performance, then a Fine Sun Sensor (FSS) replaces the failed FHST as the source of data. FHST data is compared against a list of OBC guide stars to find a match based on magnitude and position thresholds, to produce an estimate of position error. The FSS makes use of an onboard ephemeris generator for the 'true' Sun position in it's computation of a position error. The output of the measurement model is the Kalman gains used to compensate the state vector, which contains a representation of the attitude error and the gyro biases. Finally, the third step uses the Kalman gain and measurement matrices from the second step to propagate the state covariance matrix, to be used during the next measurement update.

2.3.2.1 Dynamics Model

The state transition and state noise covariance matrices are obtained from the dynamics model. The derivation of the dynamics model and thus the matrices are presented in the following paragraphs. First, the gyro rates are described as

$$\dot{\theta} = \dot{w} - b_o - b + n_v \qquad (2\text{-}7)$$

$$\dot{b} = n_u \qquad (2\text{-}8)$$

where $\dot{\theta} = [\dot{\theta}_x, \dot{\theta}_y, \dot{\theta}_z]$ is gyro rate measurements

$\dot{w} = [w_x, w_y, w_z]$ is true spacecraft body rates

$b_o = [b_{ox}, b_{oy}, b_{oz}]$ is gyro bias

$b = [b_x, b_y, b_z]$ is gyro drift bias

$n_v = [n_{vx}, n_{vy}, n_{vz}]$ is float torque noise (Gaussian white noise)

$n_u = [n_{ux}, n_{uy}, n_{uz}]$ is float torque derivative noise (Gaussian white noise)

The attitude rate error is defined as follows:

$$\alpha = \dot{\theta} - \dot{w} = -b_o - b + n_v \qquad (2\text{-}9)$$

The gyro bias is assumed to be known and therefore it can be removed from equation 2-9, leaving the following:

$$\alpha = -b + n_v \qquad (2\text{-}10)$$

The two equations, 2-8 and 2-10, then give the dynamics model. It can be written in the form

$$\dot{X}(t) = [A]\, X(t) + W(t) \qquad (2\text{-}11)$$

where $X(t) = [\alpha_i, b_i]^T$ is the state vector

$$W(t) = [nv_i, nu_i]^T \qquad i = 1,2,3$$

$$[A] = \begin{bmatrix} 0_{3\times3} & : & -I_{3\times3} \\ \cdots & \cdots & \cdots \\ 0_{3\times3} & : & 0_{3\times3} \end{bmatrix}$$

The discrete state transition matrix is derived from [A] and is given by

$$\Phi_T = e^{[A]T} \qquad (2\text{-}12)$$

Where T is the measurement update interval. This expression can be approximated by a Taylor's expansion as

$$\Phi_T = I + [A]T + 1/2([A]T)^2 + 1/6([A]T)^3$$

$$\Phi_T = \Phi(t_k, t_{k-1})$$

$$T = t_k - t_{k-1}$$

Knowing the state transition matrix we can now solve for the noise covariance matrix, $[W_T]$.

$$W_T = \int_{t_{k-1}}^{t_k} \Phi(t_k, \tau)\, Q(\tau)\, \Phi T(tk, \tau)\, d\tau \qquad (2\text{-}13)$$

Where Q(t) = E[W(t) WT(t)] and is known as the spectral density matrix. The evaluation of Q(t) is

$$Q(t) = \begin{bmatrix} n_v n_v^T & : & 0_{3\times3} \\ \cdots & \cdots & \cdots \\ 0_{3\times3} & : & n_u n_u^T \end{bmatrix}$$

The resulting matrix is a main diagonal matrix since the following characteristics hold

$$E[n_{vi}\, n_{vj}] = 0 \quad \text{for } i \neq j$$

$$E[n_{ui}\, n_{uj}] = 0 \quad \text{for } i \neq j$$

$$E[n_{vi}\, n_{uj}] = 0 \quad \text{for any } i \text{ and } j$$

Now we have everything to propagate the state covariance matrix. The equation for the propagation of the state covariance matrix in the time update step is

$$P_i^- = \Phi_T\, P^+_{i-1}\, \Phi^T_T + W_T \qquad (2\text{-}14)$$

where P_i^- is the a priori propagated state covariance matrix for this update interval

P^+_{i-1} is the a postiori updated state covariance matrix from previous interval

At initialization the state covariance matrix is a main diagonal matrix given initial values as specified by the ground for the attitude error variances, upper left submatrix, and the gyro bias variances, lower right submatrix. The other submatrices are given the initial value of zero.

2.3.2.2 Measurement Model

This process determines whether the update filter state covariance matrix require updates and, if so, which sensor data are used to perform the update. The ground has the ability to select different sensor configurations. In nominal conditions the two FHSTs are used as the source of measurement data. In the event of a degraded FHST then an FSS can be selected by the ground to replace the failed sensor. Data is used from only one of the sensor pair at each update interval, and is the sensor that has gone the longest time period without providing update data. This is nominally an alternating scheme between the sensor pair with targets visible in each field of view (FOV). The measurements from the sensor is compared against known 'true' data provided by the OBC system tables, for guide stars, or an ephemeris generation routine, for sun data. Once valid data is found, position errors are generated, which are used to generate the update state vector used in the kinematic equations and to generate measurement matrices used in the Kalman Filter update routines.

The algorithms for the measurement model are as follows:

1. Compute the residuals

$$Z(i) = OS(i) - CS(i) \quad i = x,y \quad (2\text{-}15)$$

where OS is the observed target vector in the sensor coordinate frame created from sensor measurement data

CS is the computed target vector in the sensor coordinate frame created from OBC 'true' data

2. Form the measurement matrix

The measurement model is given by the equation

$$Z_k = H_k X_k + R_k$$

where Z_k is a measurement at time k
H_k is transformation matrix
R_k is Gaussian white noise

$$H_k = \begin{bmatrix} (X \times S_k)^T : & 0_{1x3} \\ \cdots\cdots\cdots\cdots & \\ (Y \times S_k)^T : & 0_{1x3} \end{bmatrix}$$

where S_k is observed target vector in the spacecraft body frame

X,Y are the reference vectors and are defined as follows:

FHST: X and Y are just the x-axis and the y-axis unit vectors of the FHST in the spacecraft body frame

FSS: X and Y are defined as

$$X_i = (X_{Fi} - XE*Z_{Fi})/S_k(z) \quad i = x,y,z$$

$$Y_i = (Y_{Fi} - YE*Z_{Fi})/S_k(z) \quad i = x,y,z$$

where X_f is the FSS x-axis in the spacecraft frame

Y_f is the FSS y-axis in the spacecraft frame

Z_f is the FSS z-axis in the spacecraft frame

XE,YE are the FSS 'true' x and y axis vectors computed from sun vector in FSS coordinates

3. Form the measurement error variance matrix

$$R = \begin{bmatrix} R_1 & 0 \\ 0 & R_2 \end{bmatrix} \quad (2\text{-}16)$$

$$R_k = E[V_k V_k T]$$

where V_k is the sensor noise (Gaussian)

2.3.2.3 Update Algorithms (Measurement Update)

The final step in the Kalman Filter is to update the state covariance matrix and compute the state vector update parameters used in the kinematic equations. The algorithms in matrix form for the update are

1. Gain matrix computation (2-17)

$$K_k = P_k^- H_k^T (H_k P_k^- H_k^T + R_k)^{-1}$$

2. Gyro Bias and Euler parameter correction (2-18)

$$X_k^+ = X_k^- + K_k(Z_k - H_k X_k^-)$$

3. State covariance matrix update (2-19)

$$P_k^+ = P_k^- - K_k H_k P_k^-$$

In the UARS OBC the algorithms are processed in a sequential manner, thus changing it to a scalar implementation and requiring a two pass system to process both measurement vectors. Equation 2-18 is actually implemented in the kinematic equations, with the state update vector computed in the measurement model. It is easier to follow the scalar two pass implementation by first noting the following

$$P_k = \begin{bmatrix} P_{11} : P_{12} \\ \cdots\cdots\cdots \\ P_{21} : P_{22} \end{bmatrix}$$

$$K_k = [K_1 \ldots\ldots K_6]$$

Pass One:

$$H = [(X \times S_k)^T : 0_{1x3}]$$

$$K_k = P_{12} H^T / (H P_{11} H^T + R_1)$$

$$S = Z_1 K_k$$

$$P_k = P_k^- - K_k H P_k^-$$

Pass Two:

$$H = [(Y \times S_k)^T : 0_{1x3}]$$

$$K_k = P_{12} H^T / (H P_{11} H^T + R_2)$$

$$S = S + (Z_2 - H S) K_k$$

$$P_k^+ = P_k - K_k H P_k$$

2.4 Sensor Models and Coordinate Systems

The next few sections will give a brief description of the sensor models and their coordinate systems as modeled by the UARS Dynamics Simulator.

Detailed descriptions of the models can be found in reference 1.

2.4.1 Fixed Head Star Tracker (FHST)

The FHST is an attitude sensor that searches for, detects, and tracks stars; provides accurate position and intensity information for stars in its field of view (FOV); and generates status flags and parameters characterizing the sensor operation. The position of the star is output as a horizontal (H) and vertical (V) coordinate pair, with the H and V axis describing the projection onto a plane perpendicular to the camera boresight.

The nominal coordinate system of the FHST is defined by a series of rotations from the spacecraft body coordinate system (BCS) to the FHST coordinate system (FCS). The transformation is a 3-2-3 Euler sequence:

$$M_{FB} = M_3(\theta_1)\, M_2(\theta_2)\, M_3(\theta_3)$$

where for FHST 1;

$$\theta_1 = 51.9 \text{ deg.}, \ \theta_2 = 105.6 \text{ deg.}, \ \theta_3 = 0 \text{ deg.}$$

and for FHST 2;

$$\theta_1 = 128.1 \text{ deg.}, \ \theta_2 = 105.6 \text{ deg.}, \ \theta_3 = 0 \text{ deg.}$$

The subscript FB denotes a transformation from BCS to FCS.

2.4.2 Fine Sun Sensor (FSS)

The FSS is an attitude sensor that provides two-axis Sun direction information with respect to the sensor axis. Output consists of angles between the boresight and the sun vector, which are projected into a plane described by a vertical axis (beta) and the horizontal axis (alpha).

The nominal FSS coordinate system is defined by a 3-2-3 Euler rotation:

$$M_{SB} = M_3(\theta_1)\, M_2(\theta_2)\, M_3(\theta_3)$$

where the rotations are

$$\theta_1 = 33.1 \text{ deg.}, \ \theta_2 = -100.5 \text{ deg.}, \ \theta_3 = 0 \text{ deg.}$$

The subscript SB denotes a transformation from BCS to sun sensor coordinate system (SCS).

2.4.3 Inertial Reference Unit (IRU)

The IRU is an attitude rate sensor consisting of a gyro package that measures inertial vehicle rates about the sensor axis. The output of the IRU consists of analog rates, accumulated angles, range status and temperature.

The nominal IRU coordinate system is defined as being coincident with the spacecraft body axis coordinate system. Equation 2-7 describes each gyro output, where w in the equation is the measured body rate for that gyro.

3.0 Onboard Attitude Accuracy

As stated earlier, UARS requires a highly accurate knowledge of it's attitude to allow the instruments on board to perform precise measurements of the earth's atmosphere. The attitude determination requirement placed on the OBC during the normal mission phase is 60 arcsec. (3 sigma) per axis using two FHSTs and 70 arcsec. (3 sigma) using one FHST. The requirements for attitude determination were generated by G.E. using prelaunch sensor alignments, which accounts for the overwhelming majority of the attitude determination uncertainties. The prelaunch alignment uncertainties for the FHST and FSS sensors are

Sensor	Prelaunch Alignment Uncertainty (arcsec, 3 sigma)		
	Roll	Pitch	Yaw
FHST 1	55.3	55.3	55.2
FHST 2	55.3	55.3	55.2
FSS	200.0	200.0	200.0

A study was done by Flight Dynamics to determine the expected on-orbit attitude uncertainties after sensor calibration. The first step in this process was to determine the expected on-orbit sensor alignment accuracies after calibration. The procedure for this analysis is given in reference 2, with the results of this analysis given as

Sensor	Postlaunch Alignment Uncertainty (arcsec, 3 sigma)		
	Roll	Pitch	Yaw
FHST 1	39	47	49
FHST 2	40	48	48
FSS	63	65	44

Using these calculated on-orbit sensor alignment uncertainties, the on-orbit attitude uncertainties were determined using ADEAS. Because UARS is a momentum biased system with a one rotation per orbit about the pitch axis, a few different scenarios arises with target availability for the sensors. With the two FHST configuration, most of the time there is an abundance of target opportunities per orbit. However, during certain times of the year the availability of guides stars drops to around only five per orbit. With one FHST and one FSS to replace the failed FHST, not only is guide stars of concern, but also the amount of time the Sun is in the FSS FOV. Nominally the Sun is in the FOV for about twenty minutes out of the orbit, but there will be times when the FSS will not see the sun for the entire orbit. The attitude accuracies were determined for these scenarios using ADEAS with expected alignment uncertainties, and measurement and dynamics noise values. The results are given as

C-7

Sensor	Post-calibration Attitude Uncertainty (arcsec., 3 sigma) Roll	Pitch	Yaw	RSS
Two FHSTs (star rich)	41	55	32	76
Two FHSTs (star poor)	43	62	32	82
FHST/FSS (star rich)	53	60	41	90
FHST/FSS (star poor)	55	63	44	95
One FHST (star rich)	56	63	43	95
One FHST (star poor)	58	70	44	100

Based upon this prelaunch analysis, the attitude determination function should be able to meet the requirements set up by the project office after calibration of the sensor alignments. It's interesting to note that FSS data does not seem to affect the attitude accuracy significantly when comparing the FHST/FSS and the one FHST configurations for both star rich and star poor orbits.

Comparisons of typical OBC and ground attitude solutions over an orbit for the two FHST configuration after calibration are given below

	3 Sigma (arcsec.) Roll	Pitch	Yaw	RSS
UARS OBC star rich	5.1	28.2	7.2	29.5
UARS OBC star poor	12.6	31.9	13.2	36.8

The attitude solution shows a dramatic improvement over what was expected. To compare actual results and ADEAS results with the dynamics simulator andestablish some bounds for expected performance of the OBC, two simulations were made, one with perfect knowledge of alignments and noises by the OBC, and another using anticipated post-calibration alignments with perfect knowledge of noise for a star rich orbit. The results are

	3 Sigma (arcsec.) Roll	Pitch	Yaw	RSS
Dyn. Sim (perfect)	1.0	21.2	1.2	21.3
Dyn. Sim (expected)	25.0	33.8	24.4	48.6

In comparing the dynamics simulators runs with the actual results of a star rich orbit, similar results are given verifying the dynamics simulator as a reasonably accurate tool for this analysis. The results also made clear that the post-calibration alignment uncertainties were better than expected. Similar runs were made for the FHST/FSS sensor configuration as for the two FHST configuration, with the following results.

	3 Sigma (arcsec.) Roll	Pitch	Yaw	RSS
FHST/FSS (perfect)	4.9	31.4	3.3	31.9
FHST/FSS (expected)	31.2	61.0	23.7	72.5

The dynamics simulator case with the expected post-calibration alignments are comparable with the ADEAS results. Then depending on the actual alignment uncertainties the results should fall somewhere in between these two bounds. This also is a good illustration of how the alignment uncertainties dominate the attitude determination accuracy. One final simulation was made using only one FHST in a star rich orbit with perfect alignment and expected noise.

	3 Sigma (arcsec.) Roll	Pitch	Yaw	RSS
One FHST (perfect)	11.9	41.1	2.4	42.9

Notice how little improvement is made by adding the FSS along with a FHST. This is due to the availability of an abundance of star measurements, while the FSS approximately has the Sun in the FOV for at most twenty minutes of each orbit.

4.0 Sensitivity Analysis

This sensitivity analysis is designed to determine the responses of the attitude determination function (which includes the Kalman Filter) due to noise and modeling errors, via analysis of simulations using the dynamics simulator by varying parameters. To keep this paper within a respectable length, only the sensor configurations for a star rich orbit will be considered. The study will look at the attitude determination accuracy, steady state values and measurement residual statistics as a result of varying alignment and modeling errors. The results are given in tabular and graphical form, whichever is most informative. The graphical representations will include a polynomial fit to show any trends for possible predictions.

4.1 Misalignment of Sensors

The affect of misaligning the sensors is to create an offset from the normal pointing, around which the sensors will try to null out measurement errors. This change in attitude pointing will necessitate a compensation of the measured body rates in the OBC for any movement of the boresights within or out of the plane that is described by the two sensor boresights. The misalignments were applied to both of the FHST sensors, such as not to separate the boresights in or out of the plane. Figure 1 shows what the OBC determines its attitude to be as a result of increasing misalignments about each of the FHSTs axis. Figure 2 gives the actual attitude determination error from the known truth.

Comparison of the two plots shows that the misalignments are not observable in the attitude, as expected. Notice also, that the attitude is insensitive to small rotations about the boresight, because of this rotation is about the body pitch axis and is interpreted as an insignificant pitch rate bias. The residuals did not show any increase in variance (lack of observability of boresight reorientation and rotations about the boresight), but the gyro biases increased due to the reorientation of the spacecraft's attitude pointing.

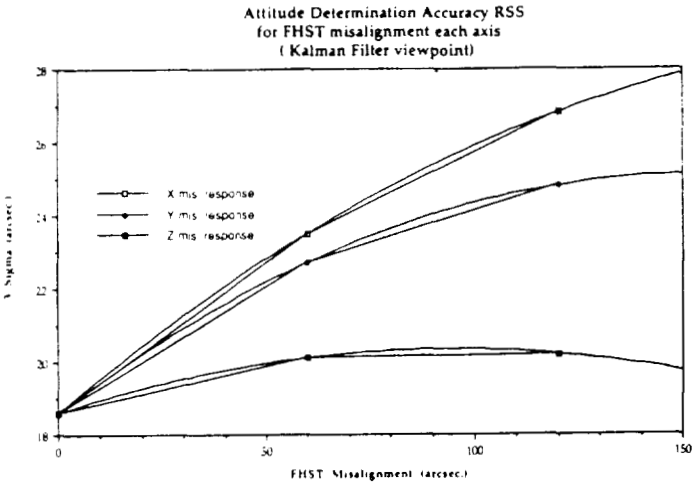

Figure 1

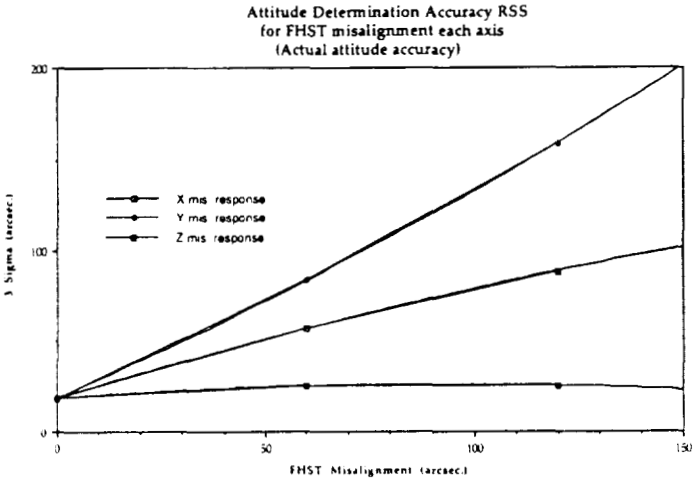

Figure 2

The gyro bias needed to compensate for each of the misalignments are given for each axis in Figures 3, 4 and 5.

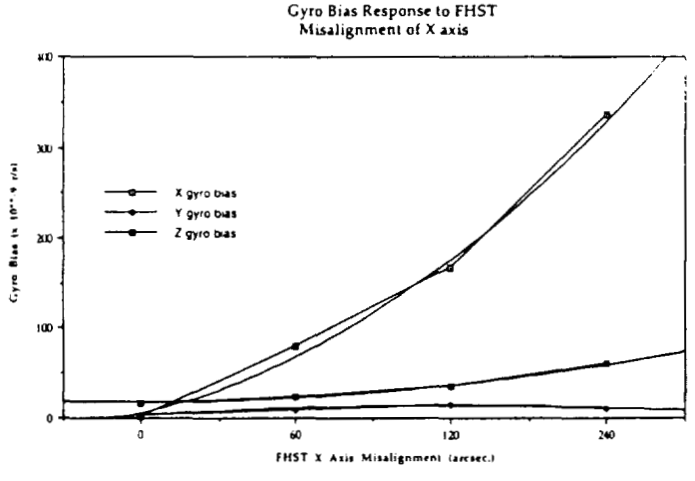

Figure 3

The y-axis (pitch axis) shows no change in gyro bias for any of the rotations. This is because the bias is very small as compared to the pitch rate, and therefore indistinguishable. Attitude determination accuracy was more sensitive to misalignments about the FHST x-axis, which is also reflected in the gyro bias results. Of interest would be how much misalignment would be tolerated *before a particular axis exceeds the 60 arcsecond* (3 sigma) requirement. The prediction is obtained from the polynomial fit to the data and are estimated to in the following table. The dominate axis is the one most sensitive to the disturbance and first exceeds the requirement.

	FHST Alignment Tolerance (arcsec., 3 sigma)		
	X-axis	Y-axis	Z-axis
Misalignment (arcsec.)	54	39	None
Dominate Axis	Z	X	--

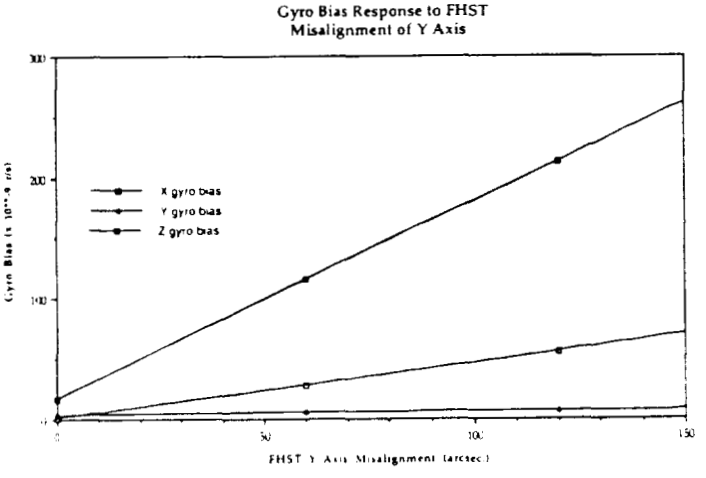

Figure 4

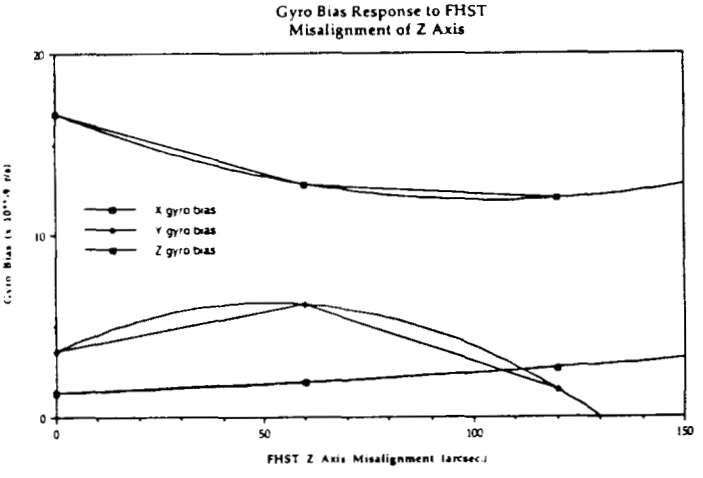

Figure 5

The comparison of the attitude determination accuracy for the misalignment of the FSS are given in figures 6 and 7. In these simulations only the FSS was misaligned about each of its axis.

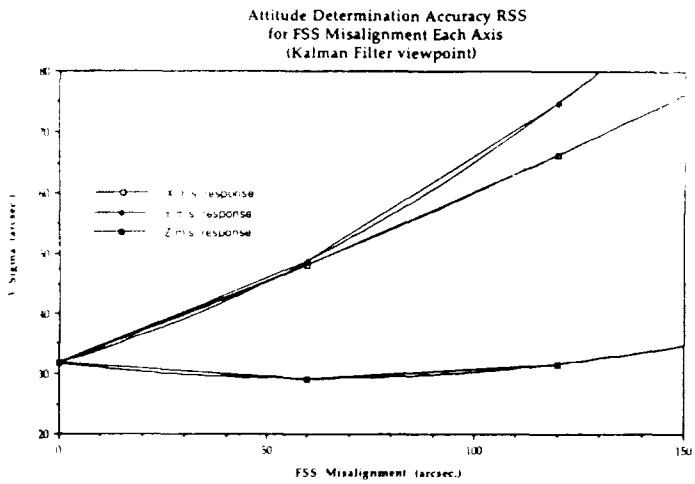

Figure 6

Again, it is seen that the OBC has no accurate knowledge in the attitude for movement of the boresights relative to each other (nor would there be any notice in the residuals or gyro bias for any common movement to each other).

However, the Kalman Filter this time reflects some change in attitude.

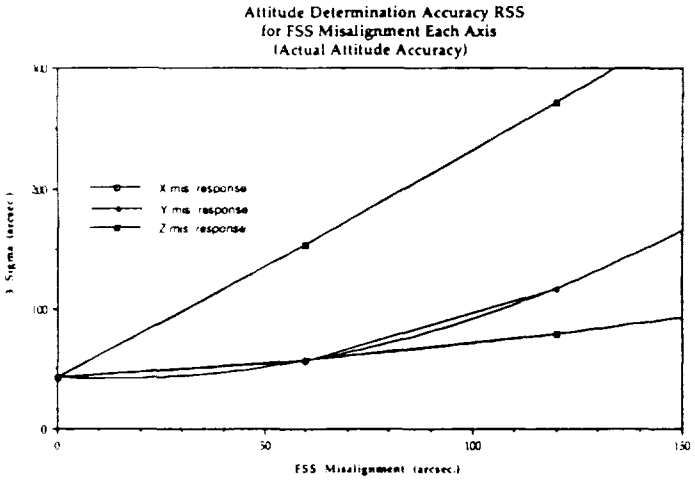

Figure 7

This is because there is some separation between the two boresights, which in turn produces residuals each time sensors are toggled for data. The variance of the residuals are given by

FSS Misalignment Residual Variances (arcsec**2)

Rotation	X-axis		Y-axis		Z-axis	
(arcsec.)	z1	z2	z1	z2	z1	z2
0	1069	2845	1069	2845	1069	2845
60	1273	3370	1644	3115	1105	2773
120	1524	4180	3307	3477	1225	2789

This bouncing affect is of course more pronounced as the misalignments increase. The increase in residual variance in turn is observed in the measurement model, which acts to null out the measurement error around the new pointing. It can be seen that the attitude accuracy is sensitive in this case to a misalignment about all axis, including the boresight (because this rotation is mostly about the body roll axis, the x-axis). The z-axis showed no residual response to misalignment. The boresight didn't move with respect to the FHST, and therefore there was no bouncing in switching between sensors. Also the FHST dominated around the orbit with its perfect measurements, compared with only twenty minutes shared between the FHST and FSS when the sun was in the FOV. Figures 8, 9 and 10 show the gyro bias response to the new attitude pointings. It is also seen here that the gyro biases are sensitive to a rotation about the boresight. As with the two FHST case, an estimate of the alignment tolerance before the accuracy exceeds the 70 arcsecond (3 sigma) requirement is

	FSS Alignment Tolerance (arcsec.)		
	X-axis	Y-axis	Z-axis
Misalignment	16	78	98
Dominate Axis	Y	Y	Y

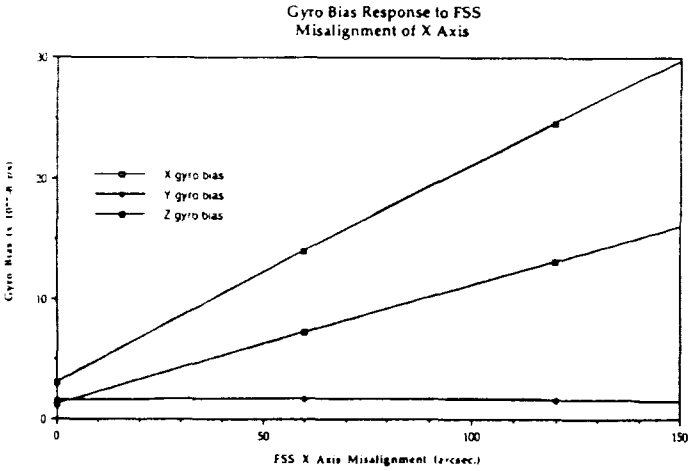

Figure 8

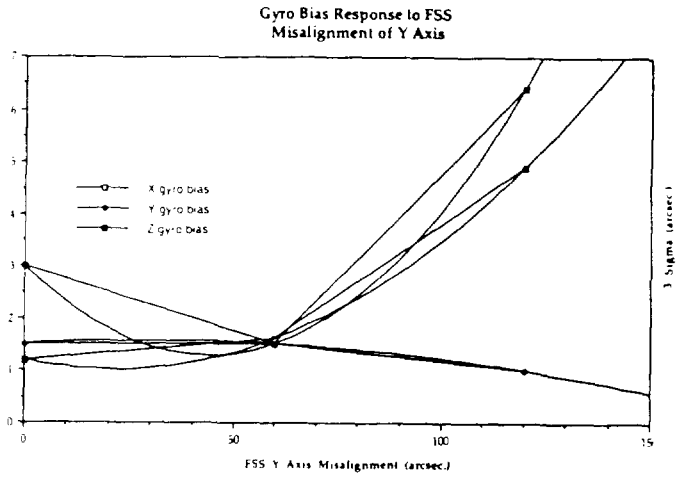

Figure 9

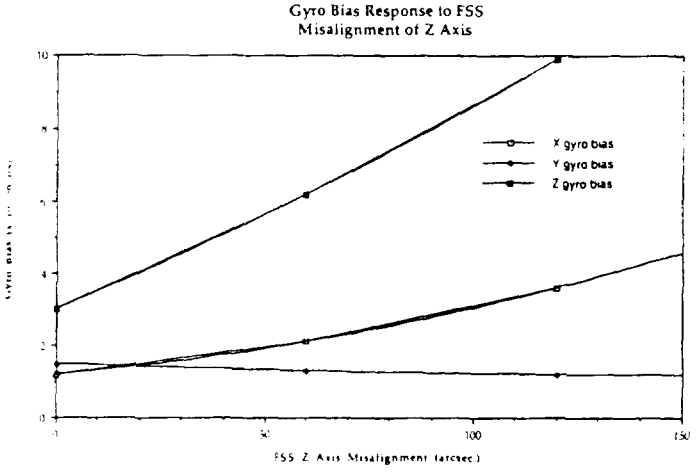

Figure 10

As expected the misalignment of the gyro's has no affect on the measurement residuals and attitude determination accuracy. The OBC compensates for gyro misalignments by solving for gyro biases that maintain the correct pointing. The same holds true for an incorrect modeling in the scale factor that converts the digital information into engineering units. A difference in the scale factor is like introducing a bias to the rate information, and is handled by solving for a OBC gyro bias to compensate.

4.2 Measurement Noise

The attitude determination accuracy response to measurement noise on the FHST and FSS was determined by setting the OBC to have perfect knowledge about alignments and dynamics noise. Thus all changes in response can be attributed to only measurement noise variation. The measurement noise is taken to be Gaussian white noise, with zero mean and increasing variance. The noise is applied to the output measurements. Figure 11 shows the attitude determination accuracy response to noise applied to each of the FHST axis independently.

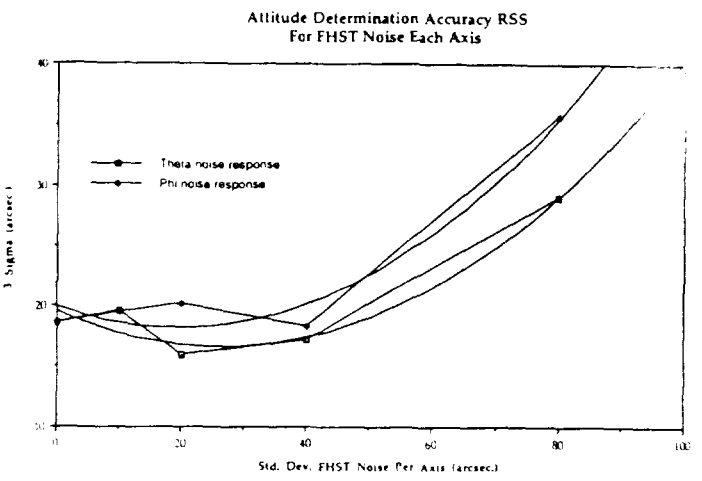

Figure 11

The graph of the two axis show a minimum around 20 to 30 arcseconds. This is where the measurement noise is correctly accounted for by the OBC model, which has lower and upper measurement noise range of 14 and 28 arcseconds, respectively. So this graph shows the affect of the difference of the actual sensor noise from the modeled or expected. As before a prediction is made of when the response will exceed the 60 arcsecond (3 sigma) requirement.

	FHST Measurement Noise Tolerance (arcsec.)	
	Theta	Phi
Noise (sigma)	126	124
Dominate Axis	Y	Y

The attitude determination accuracy in response to measurement noise on each of the FSS axis is shown in Figure 12.

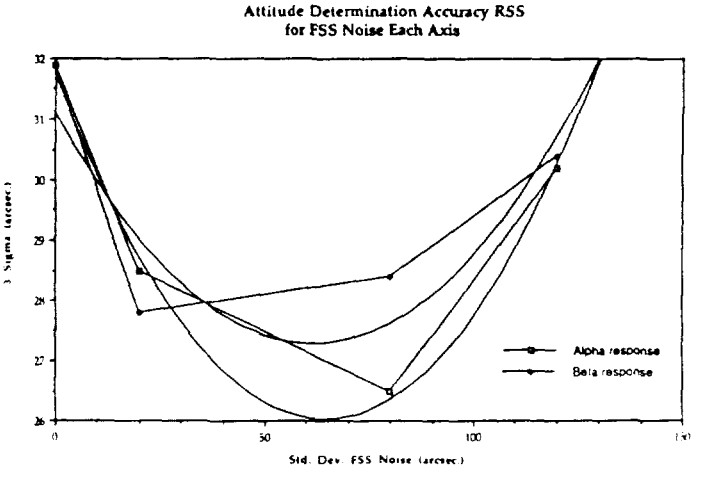

Figure 12

In this case the few data points produces a poor polynomial fit to the data. But like the FHST case, this graph shows the affect of a difference in actual measurement noise and that which is modeled in the OBC. Here, the minimum seems to exist over a larger range of noise. An approximation to this range from this graph seems to be 20 to 80 arcseconds. The OBC model in fact computes the lower and upper measurement noise as a function of the alpha and beta measurements, which produces a range of 24 to 96 arcseconds. An estimate is given for the noise tolerance on the FSS before the attitude determination exceeds the 70 arcseconds (3 sigma), with the note that a larger uncertainty is present do to the poor fit of the data.

	FSS Measurement Noise Tolerance (arcsec., 3 sigma)	
	Theta	Phi
Noise (sigma)	242	267
Dominate Axis	Y	Y

As expected, the increase in measurement noise, increased the residual variance for both the FHST and FSS. An example is given for the worse case, the FSS, in Figure 13.

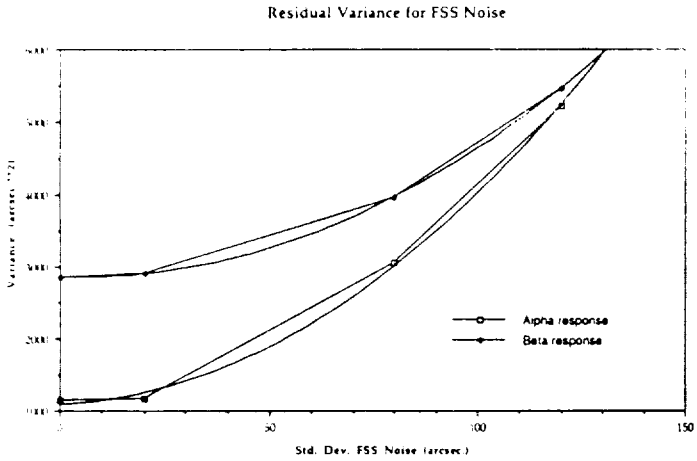

Figure 13

4.3 Dynamic Noise

Equation 2-11 shows that the attitude is affected by both float torque noise (Gaussian white) and float torque derivative noise (also called random walk). The float torque noise produced no significant response to the attitude determination accuracy. The random walk noise, however, showed a large effect in the accuracy. This is because the random walk is integrated over time to produce a gyro drift bias, which at the next measurement time is not estimated accurately by the dynamics model in the Kalman Filter. The float torque noise is a discrete Gaussian random variable that has no correlation with previous or future samples of the noise, and no accumulative affect between measurement updates. Figure 14 show the affect of a random walk noise that is different from the modeled.

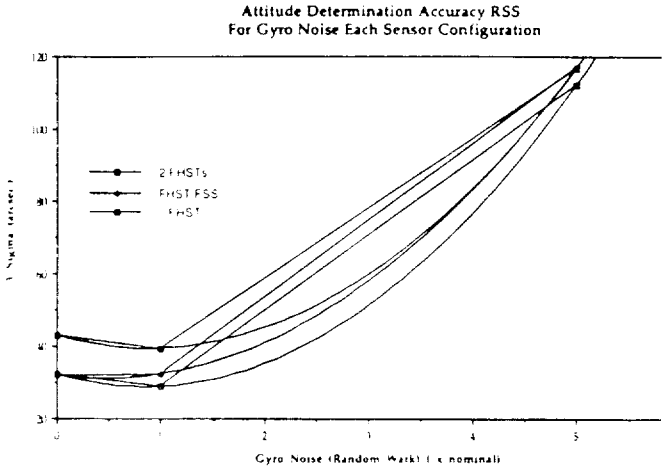

Figure 14

The minimum occurs, as it should, at the gain of one, where the model and actual agree. The random walk noise at this point is approximately 2.0e-10 r/(s**1.5) (or approximately 4.0e-5 arcsec/(s**1.5). The response diverges rapidly as the difference from the modeled increases. The graph also demonstrates that the response is the same for each of the sensor configurations. This is not unexpected, since the noise is applied to the gyro rate measurements and compensated for by estimating a correctional gyro bias in the filter. The estimated tolerance for dynamic noise is

	Dynamic Noise Tolerance (gain x nominal)		
	2 FHST	FHST/FSS	1 FHST
Noise (gain)	5.1	4.7	2.7
Dominate Axis	X or Y	Y	Y

5.0 Conclusions

It's been demonstrated with this analysis how the attitude uncertainties is being, and can be met for the three sensor configurations. The FHST alignment uncertainty is currently well within specifications according to the ground attitude solutions, with the jury still out on how well the FSS will perform. With the aid of analysis tools like ADEAS and the dynamics simulator, it can be predicted what to expect for each of these scenarios. The question that needs to be asked now is how important is the need to calibrate the sensors for misalignments and under what circumstances will misalignments not be observable by the Kalman Filter. Also, when will retuning of the Kalman Filter model be necessary and what are the consequences of changing measurement and dynamic noise models.

Looking at the misalignments, the FHST/FSS cases demonstrated the response to separation of the boresights relative to one another. The FSS showed a dramatic sensitivity to rotations about the sensor x-axis, whereas very little influence on attitude determination about the other two axis.

This is surely because the FHST, which was not perturbed, provided accurate measurement data for the body pitch and yaw axis. The rotation about the FSS x-axis, is mostly about the body x and y-axis. It seems that the x-body motion was observable and the gyro bias was computed to compensate for this component of the rotation and the change in attitude pointing about this axis. However, the pitch (body y-axis) motion for any of the three axis rotations,seemed to be absorbed into the large pitch rate without affecting the attitude estimation or gyro bias about this axis. In the two FHST case, where the misalignments of the sensors were the same relative to another, the results show a lack of observability by the Kalman Filter for any of the rotations in the attitude state. The ability to calibrate the alignments of the FHSTs in this case is dependent on the availability of accurate measurements from a third source. Both scenarios shows that the Kalman Filter is at least partially blind to misalignments of the sensors. The process of eliminating these uncertainties, as much as possible, greatly improves the attitude determination error.

The coarser measurement source, the FSS, is able to tolerate more measurement noise than the FHST before the attitude determination shows any divergence and the requirement is exceeded. The OBC measurement model allows the FSS measurements to accommodate a larger tolerance to noise in the data than the FHST, before it begins to affect the attitude state. The consequence though of allowing larger measurement noise is a larger transient to steady state and indeed a different value of steady state do to the increased tolerance to a noisy signal, and therefore larger uncertainty to the true attitude knowledge. The same concern is present in the dynamics with the introduction of a random walk noise. The results of the analysis show the same effect of not properly modeling the drifting gyro measurements. And like the measurement noise, the dynamic noise at some point will cause enough uncertainty in the rate data to warrant an alternative source of rate measurements and/or adjusting filter parameters, with the same consequences.

The choice of preferred sensor configuration is dictated not only by the modeling parameters and filter transient and steady state behavior, but also the availability of stars in the orbit. It was shown in this study that all three configurations would be able to meet requirements with a star rich orbit, and that sun measurements added little to the attitude determination capability. Thus, it might be just as good to use the remaining FHST if one should fail or degrade. It may be desirable if the FSS exhibits large alignment uncertainties or a large noise variance in the signal. When a star poor orbit is encountered, the FSS measurements are sure to be a welcome source for added information to supplement the few FHST measurements, even if it is at most only twenty minutes out of the orbit.

References

1. T. Sheu Upper Atmosphere research Satellite (UARS) Dynamics Simulator Engineering Model Specifications, Volume 1 and 2, April 1989

2. J. Golder, M. Nicholson, Upper Atmosphere Research Satellite (UARS) Ground Definitive Attitude Determination Error Analysis, January, 1991

3. G.E., Astro Space Division, UARS Critical Design Review Documentation, May 1986

4. G.E., Astro Space Division, Computer Program Design Specification for the Upper Atmosphere Research Satellite (UARS) Flight Software (As-built), April 1990

5. J. Wertz, Spacecraft Attitude Determination and Control, D. Reidel Publishing Company, 1985

Goddard Space Flight Center (GSFC) Flight Dynamics Facility (FDF) Calibration Of The Upper Atmosphere Research Satellite (UARS) Sensors*

J. Hashmall
COMPUTER SCIENCES CORPORATION (CSC)

J. Garrick
GODDARD SPACE FLIGHT CENTER (GSFC)

ABSTRACT

Flight Dynamics Facility (FDF) responsibilities for calibration of Upper Atmosphere Research Satellite (UARS) sensors included alignment calibration of the fixed-head star trackers (FHSTs) and the fine Sun sensor (FSS), determination of misalignments and scale factors for the inertial reference units (IRUs), determination of biases for the three-axis magnetometers (TAMs) and Earth sensor assemblies (ESAs), determination of gimbal misalignments of the Solar/Stellar Pointing Platform (SSPP), and field-of-view calibration for the FSSs mounted both on the Modular Attitude Control System (MACS) and on the SSPP. The calibrations, which used a combination of new and established algorithms, gave excellent results.

Alignment calibration results markedly improved the accuracy of both ground and onboard Computer (OBC) attitude determination. IRU calibration results allowed UARS to identify stars in the period immediately after yaw maneuvers, removing the delay required for the OBC to reacquire its fine pointing attitude mode. SSPP calibration considerably improved the pointing accuracy of the attached science instrument package.

This paper presents a summary of the methods used and the results of all FDF UARS sensor calibration.

* This work was supported by the National Aeronautics and Space Administration (NASA)/Goddard Space Flight Center (GSFC), Greenbelt, Maryland, Contract NAS 5-31500.

1. INTRODUCTION

The Upper Atmosphere Research Satellite (UARS) was launched on September 12, 1992, aboard the Space Shuttle Discovery on a mission to investigate the chemistry of the Earth's upper atmosphere. It was equipped with a variety of sensors, most of which would be aimed at the edge of the atmosphere, at precise heights above the surface. To achieve the required science instrument pointing precision, the UARS attitude knowledge was required to have a small uncertainty—less than 60 arcseconds (3σ).

UARS uses two fixed-head star trackers (FHSTs) as primary attitude sensors. It propagates attitudes using two inertial reference units (IRUs) (primary and backup channels on each axis). It also has one fine Sun sensor (FSS) with a 64-degree square field of view (FOV) as a backup fine attitude sensor, and a second FSS with a 4-degree square FOV, mounted on the Solar/Stellar Pointing Platform (SSPP) as a reference sensor for the science instruments mounted on that platform. For coarse attitude sensors it has two three-axis magnetometers (TAMs), two coarse Sun sensors (CSSs), and two Earth sensor assemblies (ESAs). These last are used primarily for acquiring Earth pointing attitude prior to fine pointing.

UARS travels in a near circular orbit with an inclination of about 57 degrees. Its attitude rotates at 1 revolution per orbit (RPO) about an axis approximately parallel to the orbit normal. Consequently, the UARS body maintains an attitude that is nearly fixed with respect to the Earth.

The UARS orbital plane precesses about 4 degrees a day, which has two effects of consequence for calibration. As the solar β angle (the angle between the Sun vector and the orbit normal) changes, the apparent path of the Sun through the FSS FOV changes, moving from below one edge (outside the FOV) to near the other. In addition, as the orbit plane precesses, the Sun moves from one side of the spacecraft to the other. At about 6-week intervals, UARS is commanded to yaw 180 degrees in order to maintain the Sun on one side of the spacecraft.

The Goddard Space Flight Center (GSFC) Flight Dynamics Facility (FDF) helped satisfy the UARS attitude knowledge accuracy requirement by performing on-orbit calibration of the attitude sensors, and also supported the UARS mission with two other calibrations. The major on-orbit calibrations that were performed included

- Determination of the misalignments of the FHSTs and FSS and determination of the coefficients in the FSS FOV transfer function, which converts detected sensor counts to Sun position angles. Determination of the misalignments and FOV coefficients was intended to improve the spacecraft attitude accuracy.
- Determination of the IRU misalignments, scale factors, and biases. Determination of these values was intended to improve the propagation of UARS attitude through maneuvers, allowing the onboard computer (OBC) to converge on an attitude rapidly after maneuvers.
- Determination of the SSPP gimbal misalignments and FOV coefficients for the FSS mounted on the SSPP. Determination of these quantities was intended to improve the pointing accuracy of the science instruments mounted on the SSPP and coaligned with the platform FSS.

In addition, biases for the ESA and TAMs were determined, but the values determined in these calibrations were small enough that the impact of their use was considered unimportant to the mission and the values have not yet been transmitted to the spacecraft.

2. ALIGNMENT CALIBRATION

Alignment calibration is intended to determine the true pointing directions of the attitude sensors. Sensor alignments are determined before launch, but removal of gravitational load and vibrations during launch shift the alignments, making it necessary to redetermine sensor alignments on orbit.

The alignment calibrations were performed using Shuster's algorithm with a postprocessing step added to minimize variation of the mean OBC attitude. The methods used do not require accurate attitude knowledge to yield accurate alignments.

Shuster's algorithm minimizes a loss function that contains two types of terms. The first type represents differences in the angles between simultaneously measured observation vectors and the angles between corresponding reference vectors. The second type represents differences between modeled alignments and those measured before launch. This second term allows determination of the three degrees of freedom that cannot be resolved using sensor data alone. The method resolves these indeterminate degrees of freedom by minimizing these terms.

After launch, the UARS scientific instruments were calibrated by the UARS scientists using the OBC attitude as a reference. The scientists requested that when the FDF calibration values were uplinked, the OBC attitude should change as little as possible so that the science instrument calibration would remain valid. To accommodate the scientists, an algorithm was developed to maintain a reference frame that would not change as the alignments were changed.

The UARS OBC attitude is determined using a Kalman filter with FHST data as attitude input. Data are used alternately from the two FHSTs, with the FHST selected changing frequently compared to the time constant of the Kalman filter. On the average, the attitude reference is the mean of the two FHST boresights. At any time, however, the OBC attitude will deviate from this toward the direction of misalignment of the particular FHST currently used as a reference. During periods when few stars appear in the FHSTs, the deviation will be especially evident because it is more likely that there will be no observations in one of the trackers for a considerable period of time.

To minimize the deviations from the true attitude while keeping the mean attitude independent of calibration, the following three orthonormal vectors were established as the basis of a mean boresight reference frame defined by the nominal FHST boresights:

$$\hat{X} = \frac{\vec{B}_1 + \vec{B}_2}{|\vec{B}_1 + \vec{B}_2|} \qquad \hat{Y} = \frac{\vec{B}_1 \times \vec{B}_2}{|\vec{B}_1 \times \vec{B}_2|} \qquad \hat{Z} = \hat{X} \times \hat{Y} \tag{2}$$

where $\vec{B}_1$ and $\vec{B}_2$ represent the FHST boresight vectors in the nominal body frame.

A matrix **M** is constructed with the rows composed of the three vectors:

$$M = \begin{bmatrix} \vec{X}^T \\ \vec{Y}^T \\ \vec{Z}^T \end{bmatrix} \tag{3}$$

M transforms vectors in the nominal body frame to corresponding vectors in the mean boresight frame.

Any subsequent FHST alignment calibration generates misalignment matrixes and corresponding misaligned boresight vectors $\vec{B}'_1$ and $\vec{B}'_2$. A new matrix **M'** can be constructed from these vectors using equations 1 and 2. The matrix which transforms **M'** into **M** was determined and used to correct the misalignments of all sensors so that their mean FHST frame remained invariant.

Three periods of data were used for alignment calibration of the FHSTs and FSS. Each period started when the Sun entered the FSS FOV in one orbit and ended when the Sun left the FSS FOV in the next orbit. Initially,

data were used from shortly after deployment, when the solar β angle resulted in the path of the Sun through the FSS FOV being near its edge.

Before alignment calibration results were accepted, data became available from a period about 3 weeks after deployment, at which time the Sun passed near the center of the FSS FOV. Use of data from this period was expected to improve the FSS alignment accuracy because the FSS FOV transfer function is significantly less accurate at the edges of the FOV than at its center. For this reason, about three orbits (320 minutes) of data from this period were processed for calibration. As anticipated, this second calibration yielded FHST misalignments that were almost identical to the first, but yielded somewhat improved FSS misalignments. The new misalignment matrixes were chosen as the calibration baseline and transmitted to the OBC.

FHST alignments were determined first, followed by determination of FSS alignments using artificially high weights to the FHST observations so that their misalignments would not be altered by the addition of FSS data. The resulting misalignments were transformed to maintain an invariant mean boresight.

The determined angular deviations of the sensor boresights are summarized in Table 1.

Table 1. Determined Misalignment Magnitude of Sensor "Boresights"

SENSOR	MISALIGNMENT (ARC-SECONDS)
FHST1	62
FHST2	62
FSS	417

The large value of the FSS boresight shift was realistic. This sensor's alignment had been measured before launch, but the sensor had subsequently been removed from the spacecraft and remounted without redetermining the alignment.

The principal validation of the misalignment calibration was achieved by computing fine attitude solutions using sensor data with and without application of the determined misalignments. The attitude solutions were taken for periods of about one orbit with times different from the times of the data used for calibration. In FSS validation, the weight of the FSS observations was set to a small value so the attitudes determined were exclusively FHST based.

Residuals between observed and reference sensor observation vectors from the two solutions were compared. For all three sensors the results were as expected: the mean of the observation residuals moved toward zero and the dispersion about the mean decreased.

These validation results are summarized in Table 2.

An attempt was also made to verify that attitudes determined after calibration and rotated to maintain an invariant mean boresight frame would not change, on the average, from the attitudes computed with uncalibrated sensors. To achieve this goal, attitudes were calculated for a one-orbit period using the same sensor data but using the pre- and postcalibration alignments. These attitudes were compared at epoch and at 5-second intervals throughout the orbit. Table 3 presents the RMS attitude change at 5-second intervals, the attitude change at epoch, and the maximum attitude change found.

Table 2. Sensor Residuals Before and After Calibration

CASE	RMS RESIDUAL (ARC-SECONDS)		
SENSOR	FHST1	FHST2	FSS
PRELAUNCH ALIGNMENTS	26.8	25.27	250
FDF ALIGNMENTS	6.17	6.35	32.8

Table 3. Attitude Change Due To Calibration (arc-seconds)

	YAW	ROLL	PITCH
RMS CHANGE	14	13	6
CHANGE AT EPOCH	11	5	3
MAXIMUM CHANGE	25	20	13

When the misalignments were uplinked to the OBC the results were dramatic. Neither the flight operations team (FOT) nor the project scientists detected any attitude shift, but the OBC attitude sensor residuals decreased by an order of magnitude. The attitude pointing knowledge improved from barely meeting requirements to exceeding them by about a factor of 3.

3. IRU CALIBRATION

Calibration of the UARS IRUs was intended to allow precise propagation of attitudes during intervals when no attitude sensor measurements are available and therefore minimize differences between calculated OBC attitudes and true values. Calibration consists of determining a bias vector $\vec{b}$ and a matrix G. The corrected rate vector, $\vec{\omega}_{c'}$, is related to the observed rate vector, $\vec{\omega}_{o'}$, by

$$\vec{\omega}_c = G\ (\vec{\omega}_o - \vec{b}) \tag{4}$$

Because the IRUs three axes behave as separate rate sensors, their misalignments are independent. It follows that the G matrix need not be orthogonal. It is also customary to multiply each column of the G matrix by an independent scale factor, so the G matrix need not be normal.

During periods with spacecraft motions at constant angular velocities, errors in the alignment cannot be separated from biases. The misalignment projects components of each axis' constant angular velocity onto other axes, resulting in a constant contribution to the other axes' biases. Both the OBC and ground attitude determination systems solve for IRU biases along with attitudes, so as long as the spacecraft has negligible angular acceleration, IRU misalignments result in very small attitude errors.

In order to separate biases from misalignments and scale factors, data for calibration must include maneuvers during which the rates about the axes change. Ideally, at least three maneuvers would be used, each containing an acceleration about one of the axes and an eventual return to the original velocity. Maneuvers in which the spacecraft slews by 90 degrees around a single body axis should yield the best results.

Because of UARS mission constraints, no pitch maneuvers were performed. Data for calibration were taken during a normal mission yaw maneuver (180 degrees) and a special roll maneuver in which the spacecraft was rolled by 10 degrees, and after a period at this attitude, rolled back to its nominal attitude. During both maneuvers the pitch rate was maintained at its nominal 1 RPO value. IRU calibration was performed using intervals of data, each starting just before a maneuver and ending just after. The roll forward and roll back were treated as separate maneuvers. In addition, intervals of data containing no maneuvers were used. In all, more than 600 minutes of IRU data were used for calibration.

The calibration algorithm requires an accurate attitude at the start and end of each calibration interval. These attitudes were determined using FHST data in the periods before and after each maneuver while the spacecraft angular velocities were constant. The epochs of each attitude solution were set at an end of one of the calibration intervals.

If IRU data are used to propagate the spacecraft attitude from an epoch at the start of each interval to one at the end, the difference between the propagated attitude at the second epoch and the attitude determined at the

same epoch from sensor data will depend chiefly on the errors in IRU misalignments, scale factors, and biases. The calibration software determines the least-squares minimum deviation of these attitudes over a number of such intervals. Note that for the least-squares process each interval corresponds to only three observations – one for each axis – so that for the small number of maneuvers used, the solution is not much more than minimally determined.

The results of the IRU calibration are shown in Table 4. In this table, the change in direction of each IRU axis and the scale factor corresponding to the axis are given.

Calibration results were validated by determining the accuracy of propagation for the second normal mission yaw maneuver – a maneuver that was not used in the calibration itself. Data from before and after but not during this maneuver were processed to produce accurate attitudes with epochs immediately before and after the maneuver. The attitudes were then propagated through the maneuver using pre- and postcalibration IRU parameters. The attitude differences between the attitude solutions and the propagated attitudes are shown in Table 5.

The mission consequences of IRU calibration were significant. At the end of the first scheduled yaw maneuver, the spacecraft attitude (propagated onboard from premaneuver solutions) was sufficiently far from the actual attitude (> 0.2 degree) that the OBC could not identify stars. The spacecraft dropped out of fine pointing mode and had to use the ESAs to establish sufficient attitude accuracy to resume normal operations. The IRU calibration parameters were uplinked before the second scheduled yaw maneuver, and fine pointing was never lost throughout the maneuver.

Table 4. Changes of IRU Parameters Due To Calibration

AXIS	POSTCALIBRATION SCALE FACTORS (UNITLESS)	ALIGNMENT CHANGE (ARC-SECONDS)
X	0.999818	79.7
Y	0.999144	88.5
Z	0.999057	310.8

Table 5. Propagation Errors (degrees)

AXIS	BEFORE CALIBRATION	AFTER CALIBRATION
YAW	0.087	0.010
ROLL	0.132	0.044
PITCH	0.081	0.045
TOTAL (RSS)	0.178	0.065

4. SSPP CALIBRATION

Several of the scientific instruments on UARS are mounted on the SSPP. This platform is attached to the spacecraft through two nominally orthogonal gimbals, which are normally rotated to follow the Sun. The platform may also be driven to track a star. An FSS (called the platform Sun sensor – PSS) is mounted on the SSPP, and the scientific instruments are aligned relative to it.

The alignment of the platform was parameterized and solved as two misalignment matrixes and an intergimbal misalignment angle. The matrixes, $M_{\beta S}$ and $M_{M\alpha}$, represent misalignments from the PSS boresight to the β (or outer) gimbal and from the α (or inner) gimbal to the body frame. The intergimbal angle,

γ, is the rotation of the β gimbal axis from the α gimbal axis about an axis perpendicular to both. Since the α and β gimbals are nominally aligned (at index) to rotate about the Y- and X-axes respectively, the intergimbal rotation is about the Z-axis.

An observed Sun vector, $\hat{S}_{obs}$, may be transformed into GCI, by

$$\hat{S}_{gci} = AM_{M\alpha}M_2(\alpha)M_3(\gamma)M_1(\beta)M_{\beta S}\hat{S}_{obs} \tag{5}$$

where A is the attitude matrix and $M_2(\alpha)$, $M_1(\beta)$, and $M_3(\gamma)$ are rotation angles about single euler axes by the angles α, β, and γ. $M_{\beta S}$ and $M_{M\alpha}$ are represented as functions of two misalignment vectors, $\vec{\delta}$ and $\vec{\varepsilon}$ by:

$$M_{\beta S} \text{ or } M_{M\alpha} = I\cos(\theta) + (1 - \cos(\theta))\ \hat{\theta}\hat{\theta}^T - \sin(\theta)[\theta] \tag{6}$$

where I is an identity matrix and

$$\vec{\theta} = \vec{\varepsilon} \text{ or } \vec{\delta}$$

$$\theta = |\vec{\theta}|$$

$$\hat{\theta} = \frac{\vec{\theta}}{|\vec{\theta}|}$$

$$[\theta] = \begin{bmatrix} 0 & -\theta_z & \theta_y \\ \theta_z & 0 & -\theta_x \\ -\theta_y & \theta_x & 0 \end{bmatrix}$$

The gimbal rotation angles α and β, and information that can be converted into a Sun vector in the sensor frame are available from telemetry, the attitude can be computed from other sensor data (FHSTs), and the true Sun position can be obtained from known ephemerides, so the difference between observed and reference Sun vectors depends only on the unknown misalignment parameters $\vec{\delta}$, $\vec{\varepsilon}$, and γ. The calibration software minimizes the least-squares residuals with respect to a state vector containing the elements of the two misalignment vectors and the intergimbal misalignment angle.

Data for calibration were taken over a period of 15 days, using one orbit per day. The spacecraft solar β angle changed through most of its possible range during this period, so the data spanned almost the full range of gimbal angles.

Prelaunch analysis had shown that a large amount of data would be needed for resolving the partial correlations among the SSPP alignment parameters. Even with the large amount of data used, the parameter corresponding to a rotational misalignment around the β gimbal Z-axis could not be properly determined. This parameter correlates with a rotation about the PSS boresight. Since the PSS tracks the Sun, its boresight is always near the center of the FOV and rotations about it are not easily distinguished.

This problem was resolved by using additional data from a science instrument calibration maneuver (for SOLSTICE and SUSIM). During this maneuver, the PSS was slewed to follow a path where the Sun was tracked at a 1-degree offset from the center of the FOV. Several slews were performed so that the Sun position was maintained 1 degree on either side of both axes.

The seven alignment parameters and their uncertainties are presented in Table 6. This table also contains the RMS difference between Sun vectors, computed using these misalignments, and reference Sun vectors. The largest uncertainty is about the Z-axis of the β gimbal, but this uncertainty is greatly reduced from the value of 1.656 degrees obtained using all data except that from the maneuver.

Table 6. Comparison of SSPP Alignments

VARIABLE	VALUE ± UNCERTAINTY (DEG)
Rotation around α gimbal X-axis	-0.036 ± 0.001
Rotation around α gimbal Y-axis	-0.125 ± 0.005
Rotation around α gimbal Z-axis	0.072 ± 0.001
Rotation around β gimbal X-axis	-0.026 ± 0.001
Rotation around β gimbal Y-axis	0.030 ± 0.005
Rotation around β gimbal Z-axis	-0.035 ± 0.012
Intergimbal angle	0.001 ± 0.003
RMS Attitude Residuals (deg)	0.0048

The RMS error is an order of magnitude reduced from the value of 0.0535 degree obtained using prelaunch alignments.

Determination of the gimbal alignments greatly improved the pointing accuracy of the SSPP instruments. The improvement as a function of the two gimbal angles is shown in Figure 1.

5. FOV CALIBRATION

FOV calibration consists of determining the coefficients of the transfer function that converts the digitized FSS signal into angles. This function, supplied by the FSS manufacturer, is of the form

$$\phi = a_0 + \tan^{-1}\left(a_1 + a_2\, N + a_3 \sin\left(a_4\, N + a_5\right) + a_6 \sin\left(a_7\, N + a_8\right)\right) \qquad (7)$$

where ϕ is one of the desired angles (α or β), N is the digitized signal, and a_i is the set of coefficients. The axes are treated as entirely independent, and separate sets of coefficients are solved for each.

Calibration was performed both for the FSS mounted on the MACS and the PSS. These calibrations were performed only after the alignments had been determined. For the FSS, data from a period of about 2 weeks were needed to ensure that Sun observations from the entire FOV were used. For the PSS, since the PSS normally tracks the Sun, the only data that could be used were those from the SOLSTICE/SUSIM calibration maneuver described above.

The FSS FOV calibration resulted in coefficients that were only slightly changed from their ground-measured value. The sensor residuals determined using these coefficients were very slightly lower than those before calibration, and were not loaded into the OBC.

The PSS calibrations showed a somewhat larger change, and sensor residuals decreased from 12.2 to 8.8 arc-seconds for Sun measurements at the center of the FOV and from 15.0 to 12.2 arc-seconds for all measurements during the offset maneuver. These improvements were considered too small to merit uplink of the new coefficients.

6. CONCLUSIONS

Overall, the calibration of the UARS attitude sensors produced a marked increase in the accuracy of both ground- and OBC-determined attitudes. The pointing accuracy of the UARS science instruments was increased correspondingly, enhancing the attainable precision of scientific studies of upper atmosphere chemistry.

Over the life of the mission, the FDF will regularly monitor sensor calibration and is prepared to recalibrate any sensors that drift as the spacecraft ages.

UARS SSPP ALIGNMENT

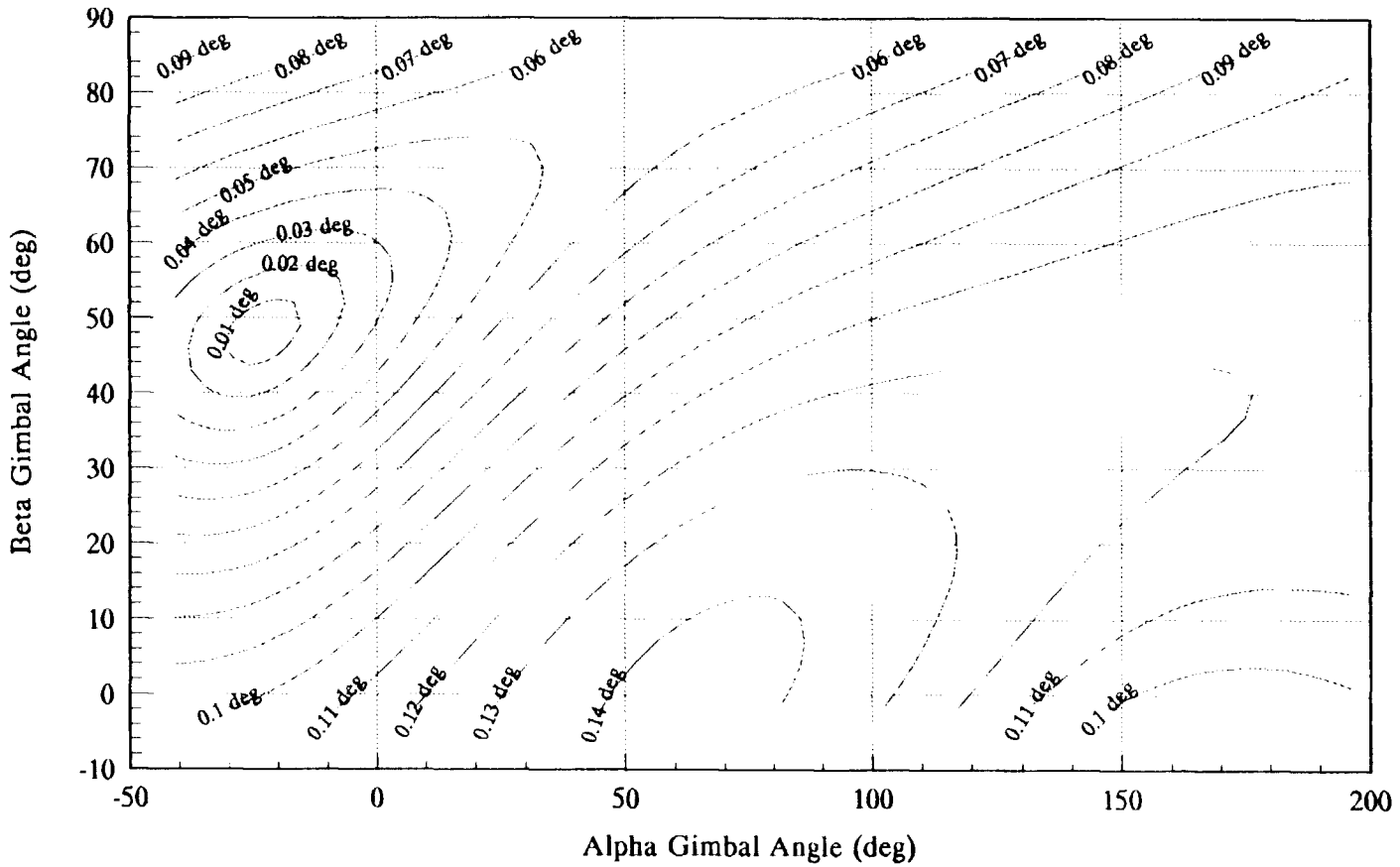

Contour Plot of SSPP pointing error (deg) as a function of Gimbal Angle

Figure 1. SSPP Gimbal Alignment Corrections

Solar Array Thermal Snap and the Characteristics of Its Effect on UARS

M. Lambertson and D. Rohrbaugh
COMPUTER SCIENCES CORPORATION (CSC)

J. Garrick
GODDARD SPACE FLIGHT CENTER (GSFC)

ABSTRACT

The single solar array on the Upper Atmosphere Research Satellite (UARS) is subjected to a thermal distortion when the spacecraft enters and exits the Earth's shadow. The distortion results in a torque that alters the spacecraft attitude. Due to the sudden nature of the attitude discontinuity, the effect has been termed "thermal snap." Thermal snap has also been experienced by Landsats 4 and 5.

Analyses by the spacecraft builder addressed the impact of the resultant torque on the onboard control system. This paper discusses the results of comparisons between the predicted effects of thermal snap on UARS and actual attitude solutions from UARS telemetry data. In addition, this paper describes the characteristics of the thermal snap on UARS in terms of maximum displacement, solar beta angle, and solar array drive angle. Comparisons are made between the actual times of thermal snaps and the predicted spacecraft sunrise and sunset times. The effects of the UARS thermal snap are summarized and a general comment is made relating possible effects of thermal snap on other satellites. Also, an analysis of UARS attitude solutions that span periods of thermal snap was performed to determine whether the gyro sampling time of 1/8 second is sufficient to properly model the resulting spacecraft attitude without compromising the accuracy requirements. The results of this analysis are discussed in this paper.

* This work was supported by the National Aeronautics and Space Administration (NASA)/Goddard Space Flight Center (GSFC), Greenbelt, Maryland, Contract NAS 5-31500.

1. INTRODUCTION

1.1 History and Motivation

It has been observed for some time that certain spacecraft entering or leaving the Earth's shadow experience attitude perturbations believed to result from a variety of thermal effects. Particularly large perturbations have been observed in spacecraft having flexible solar arrays. Flight data from Landsats 4 and 5, for example, showed large disturbances about the roll and yaw axes whenever the spacecraft entered or exited sunlight. Richmond [Reference 1] has postulated that these disturbances were caused by torques created by the flexing of the solar arrays. This effect has been termed "thermal snap" due to the sudden nature of the attitude disturbance. The possibility of such attitude disturbances during the UARS mission was a concern because the design of the solar array is similar to that of Landsat-4. Prelaunch analysis reports examined the control and stability implications of thermal snap. Jasper and Neste [Reference 2] and Freesland [Reference 3] developed models that reproduced Landsat-4 data to make predictions of UARS perturbations.

As predicted, attitude disturbances near spacecraft sunrise and sunset have been observed in UARS flight data. This paper examines the characteristics of these disturbances, discusses them in light of the predictions, and discusses the implications for UARS and other satellites.

2. DEFINITION OF SOLAR ARRAY THERMAL SNAP

2.1 Geometry

UARS is in a low Earth orbit with an inclination of approximately 57 degrees. The solar beta angle is the complement of the angle between the UARS orbit normal and the Earth-to-Sun vectors. Because of the precession of the UARS orbit and the relative motion of the Sun, the beta angle is constantly changing. The maximum beta angle is approximately 80 degrees.

The normal mission mode attitude reference frame for UARS is the orbital coordinate system (OCS). In the OCS, the spacecraft yaw axis is parallel to the Earth-to-spacecraft vector, and the pitch axis is parallel to the orbit normal vector. Therefore, UARS constantly pitches at the orbital rate.

UARS has a single solar array that is made up of six panels and is offset from the pitch axis by 17 degrees (Figure 1). The orientation of the solar array in the UARS body frame varies with spacecraft local time. At noon, the array is positioned at 270 degrees; at midnight it is at 90 degrees. The solar array drive angle at sunset and sunrise is near 180 or 0 degrees at low beta angles (depending on flying direction, which is explained below) and approaches 90 degrees for high beta angles. This is because the local times for sunset and sunrise become closer to midnight as the beta angle increases. The solar array is nominally driven around the pitch axis at the orbital rate in order to maximize the intensity of the Sun on the solar cells for power considerations. The intensity of the Sun on the array is primarily a function of the solar beta angle. Due to the offset from the pitch axis, the solar intensity on the array is maximum at the beta angle of 17 degrees.

Sunsets and sunrises as observed by UARS appear differently depending on the solar beta angle. At a low solar beta angle, the Sun appears to move perpendicularly to the limb of the Earth. At a high solar beta angle, the Sun appears to move along the limb. Therefore, the UARS solar array sees day/night transitions that decrease in speed and intensity as the beta angle increases.

The changing beta angle also forces UARS to perform an attitude maneuver on approximately a monthly basis. The Sun must be kept in the hemisphere bounded by the X-Z plane and containing the solar array for instrument and power considerations. As the beta angle passes through 0 degrees, UARS performs a yaw

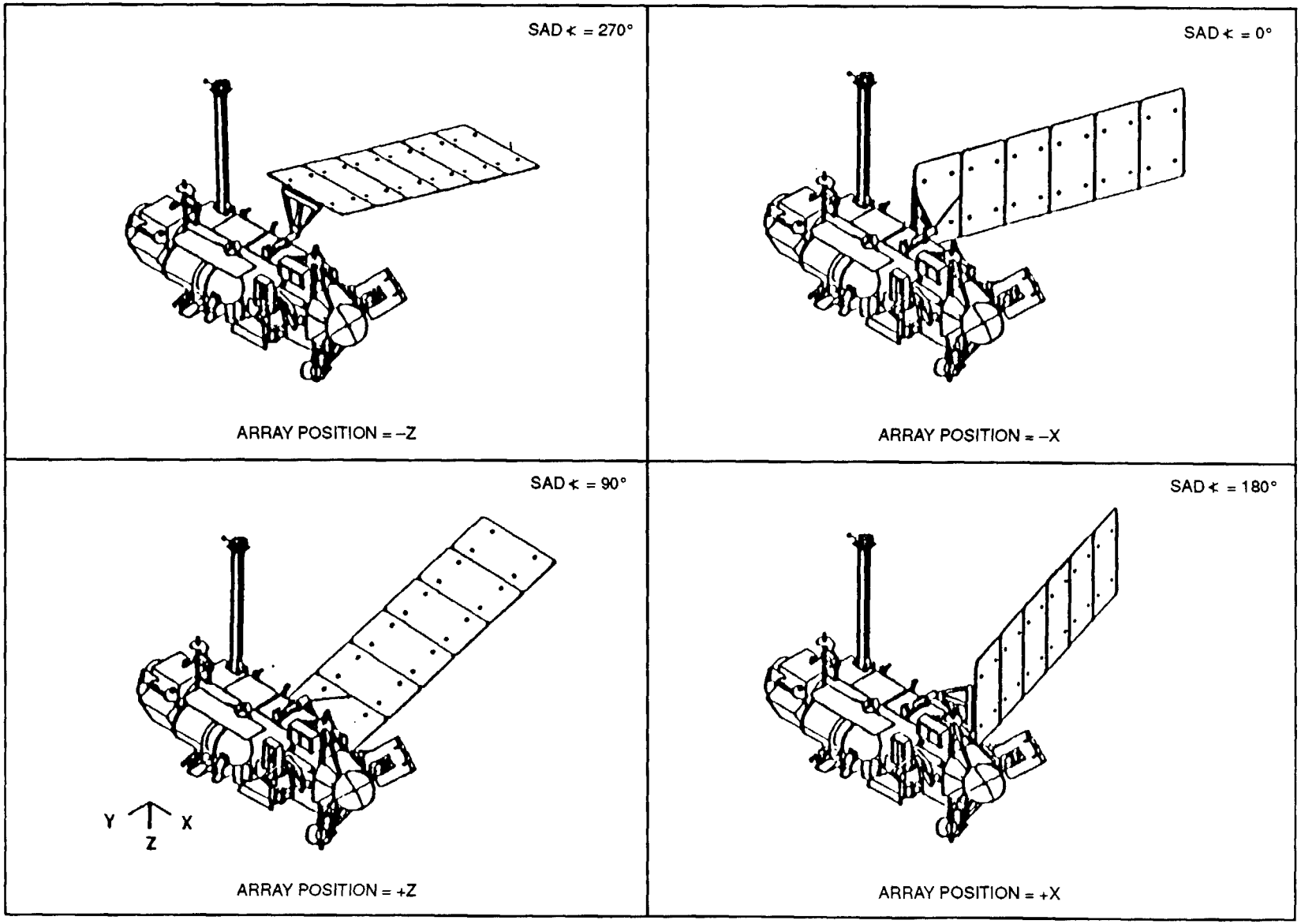

Figure 1. The UARS Observatory Solar Array Drive Positions

maneuver of 180 degrees about its Z-axis. UARS is said to be flying forward when its positive X-axis is aligned with its velocity vector; UARS is said to be flying backward when its negative X-axis is aligned with its velocity vector. The data used by the UARS attitude task in this study were obtained while the spacecraft was flying backward from December 5 to 20, 1991. However, a survey of the data for the spacecraft in the forward-flying mode indicates that the behavior is symmetric, as would be expected.

2.2 Mechanics of Thermal Snap

The single solar array on UARS is about 30 feet long and is made up of six panels of equal size. Each panel is constructed mainly of aluminum facesheet and aluminum honeycomb. Jasper and Neste and Zimbelman, et al. [Reference 4], have described the bending of the solar array in terms of time derivatives of the thermal gradient across the panels. When the spacecraft enters sunlight, the hot side of the panel heats up faster than the cold side, causing the panel to bend away from the sun. When the spacecraft exits sunlight, the hot side cools down more rapidly than the cold side and the array bends back again. This bending creates torques about the spacecraft axes. Conserving angular momentum, the spacecraft responds with a rapid change of attitude (Figure 2). The duration of sunrise and sunset and solar intensity, as seen by the spacecraft, depends on the solar beta angle, as discussed in the previous section. This in turn will affect the magnitude and timing of the thermal snap because the temperature gradients will differ. Plots of temperature gradients versus time presented by Jasper and Neste indicate that the disturbance should occur at the penumbral entrance for both sunset and sunrise (where the temperature gradient across the array changes most rapidly).

3. ANALYSIS RESULTS AND DISCUSSION

3.1 Discussion of Predicted Effects of Thermal Snap on UARS

Freesland has presented several estimates of the magnitude of UARS attitude disturbances. Early predictions concentrated on the effects at a solar beta angle of 18 degrees because the total torque on the spacecraft should be maximum there. It was also felt that the effects at sunrise and sunset would be very similar, so while the numbers cited here are for sunrise, it is not clear that the thermal modeling was sophisticated enough to draw any distinction that may exist between sunrise and sunset. Two sets of numbers from Reference 3 are given in Table 1 as Cases 1 and 2. The primary distinction between them is in the mass properties used. Note that Case 2 shows increased disturbances for the reduced mass properties.

A more recent estimate is included as Case 3 [Reference 5]. Case 3 is compared in Reference 5 to flight data in which the spacecraft is entering sunset at a beta angle of 35 degrees. It is assumed here that the estimate was produced under these conditions.

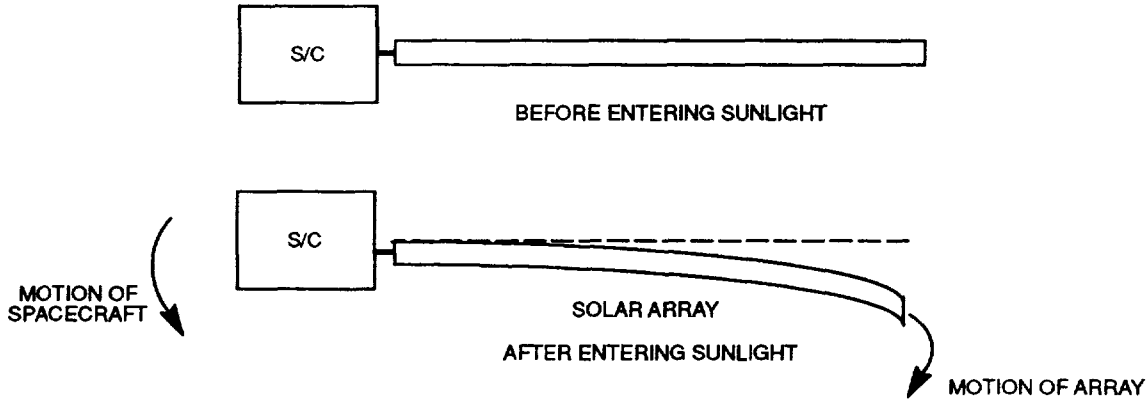

Figure 2. Bending of Solar Array

Table 1. Predictions of Attitude Disturbances (arcseconds)

Case	Disturbance		Mass Properties (FT-LB-sec^2)						
	Yaw	Roll	Ixx	Iyy	Izz	Ixy	Ixz	Iyz	
1	144	197	13200	34500	38200	–3610	–920	1360	Baseline
2	155	221	11808	31910	35449	–3344	–847	1443	
3	150	250	13400	35209	39974	–4366	–1089	1751	Beginning of Mission
			12632	31519	35623	–3236	–909	1696	End of Mission

Finally, predicted end-of-mission mass properties are included for reference. Note that the principal moments of inertia for the end-of-mission mass properties lie between those for Cases 1 and 2.

3.2 Magnitude of Attitude Disturbances

The simple model described in Figure 2 can be taken to another level of sophistication using vector analysis. Figure 3 shows the torque that should result from UARS flying backward into the sunset. The spacecraft attitude data agree with the predictions of such diagrams on the direction of the disturbances for any configuration (flying forward or backward at sunset or sunrise). It remains then to examine the magnitudes of the disturbances.

Figures 4 and 5 show the magnitude of the attitude disturbance at various solar beta angles for both sunrise and sunset. The magnitude shown in the plots was derived by examining characteristic signatures of the disturbance in OBC attitude solutions for the time at which the initial disturbance is maximum (Figure 6). Three sunrise and sunset events were examined for each of seven different beta angles ranging from 0 to 65 degrees. The baseline attitude, determined as indicated in Figure 7, was then subtracted from the peak attitude. At each sunrise and sunset the three events were averaged. Generally, the solar array disturbance affects the attitude about all three spacecraft axes. The effect on the pitch axis is often less dramatic; therefore, only the roll and yaw axes disturbances will be discussed here.

The peak disturbances are defined when the reaction wheels begin to return the spacecraft to the nominal attitude. They are therefore dependent upon the beta angle in the sense of the total torque input to the spacecraft; upon the solar array drive angle insofar as how the total torque is distributed among the axes; and upon the control system reaction to the position and rate errors computed onboard.

The values listed as Case 1 Table 1 compare well with the disturbances at sunset for an 18-degree beta angle (yaw = 113 arcseconds; roll = 198 arcseconds) although the yaw axis is somewhat overestimated. The mass properties were probably close to the values cited for this case (by inference of interpolation of the beginning-of-mission and end-of-mission mass properties). Case 2 exceeds the values seen in this study, probably because the mass properties resemble the end-of-mission mass properties. It may be a good indication of what to expect at the end of the mission. For comparison to Case 3, flight data for that specific event (occurring on October 5, 1991, around 00h:22m GMT) were examined, indicating 100 arcseconds for yaw and 195 arcseconds for roll. Case 3 is then an overestimate, but it may be that the assumptions in the previous section were incorrect. Generally, it seems that the model used by Freesland, Jasper, and Neste is capable of making reasonable predictions. Some overestimate may be desirable from a conservative standpoint regarding instrument stabilities.

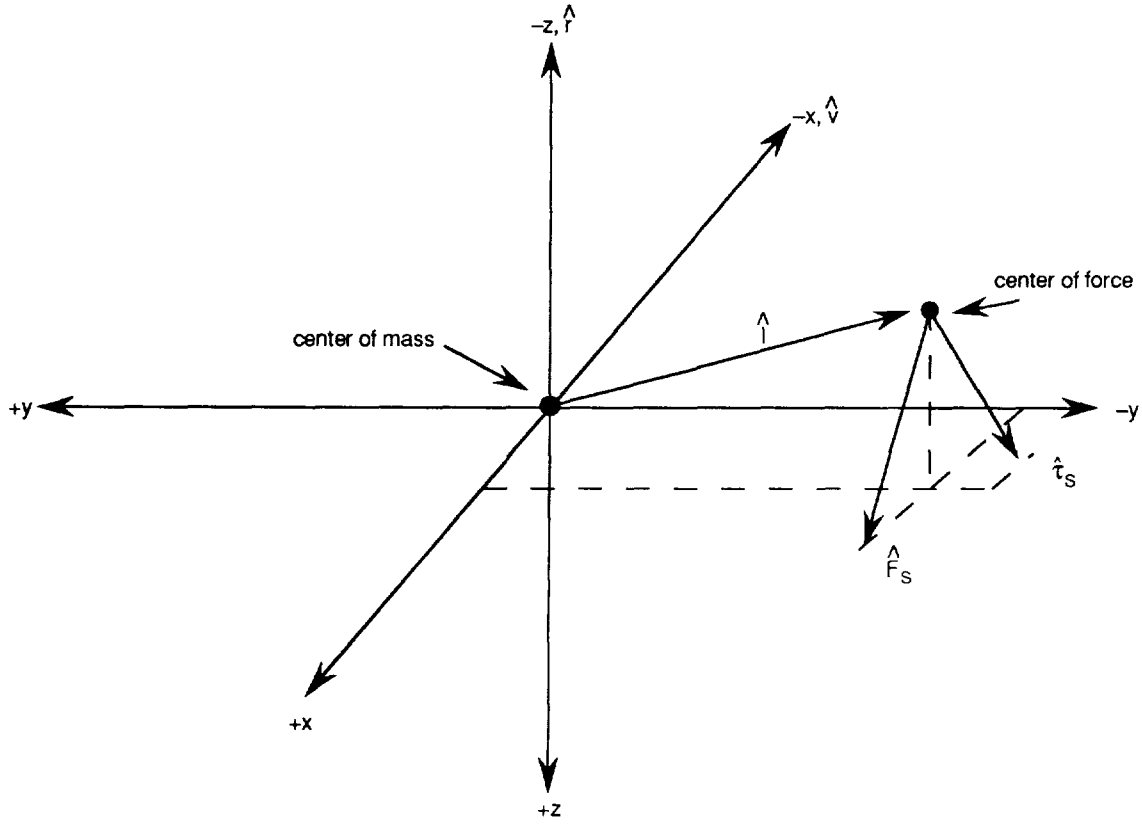

Figure 3. Torque at Sunset

NOTE: When UARS is flying backward into the sunset at a beta angle of 18°, the solar array drive angle is around 150°. The solar array straightens, creating the force with the resulting torque. This torque has components in the –x, –y, and +z spacecraft axes. The spacecraft responds with positive roll and pitch and negative yaw in order to conserve momentum. A similar analysis for any other configuration yields qualitative agreement with the data.

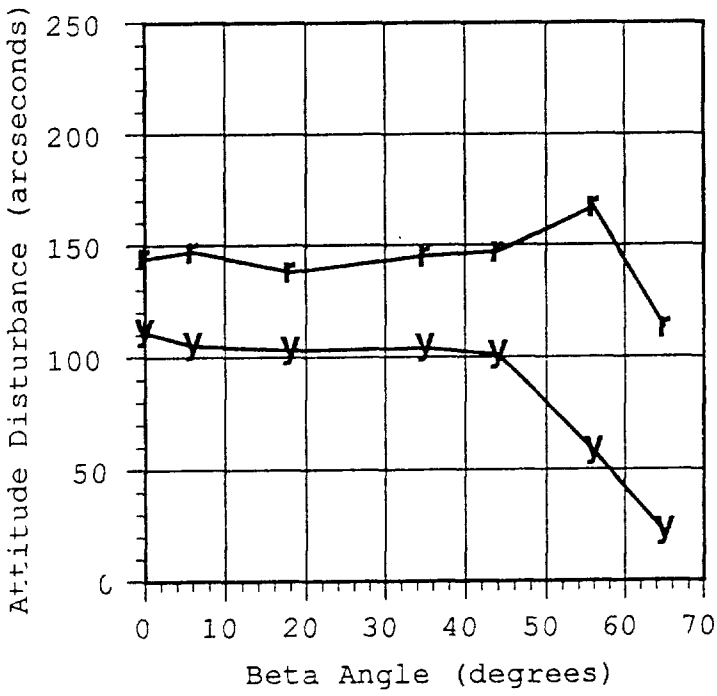

Figure 4. Actual Disturbance at Sunrise; r–roll, y–yaw

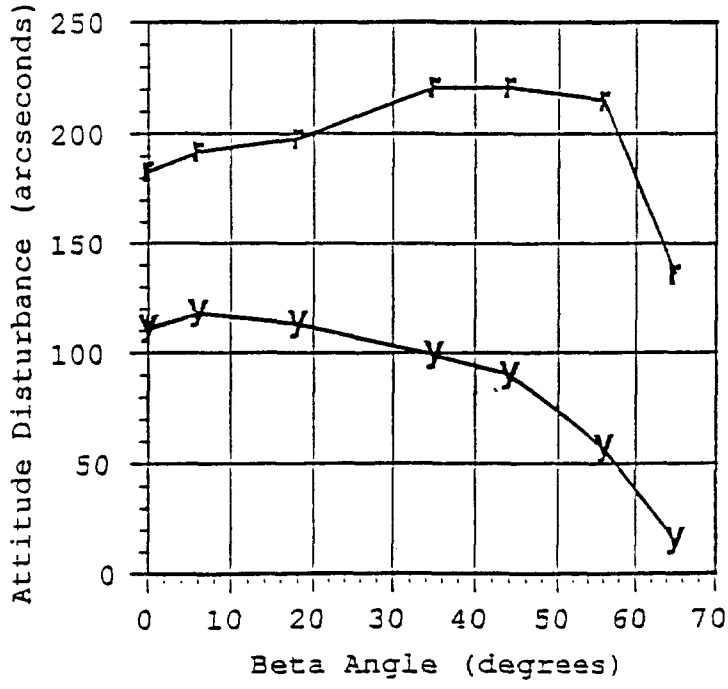

Figure 5. Actual Disturbance at Sunset; r–roll, y–yaw

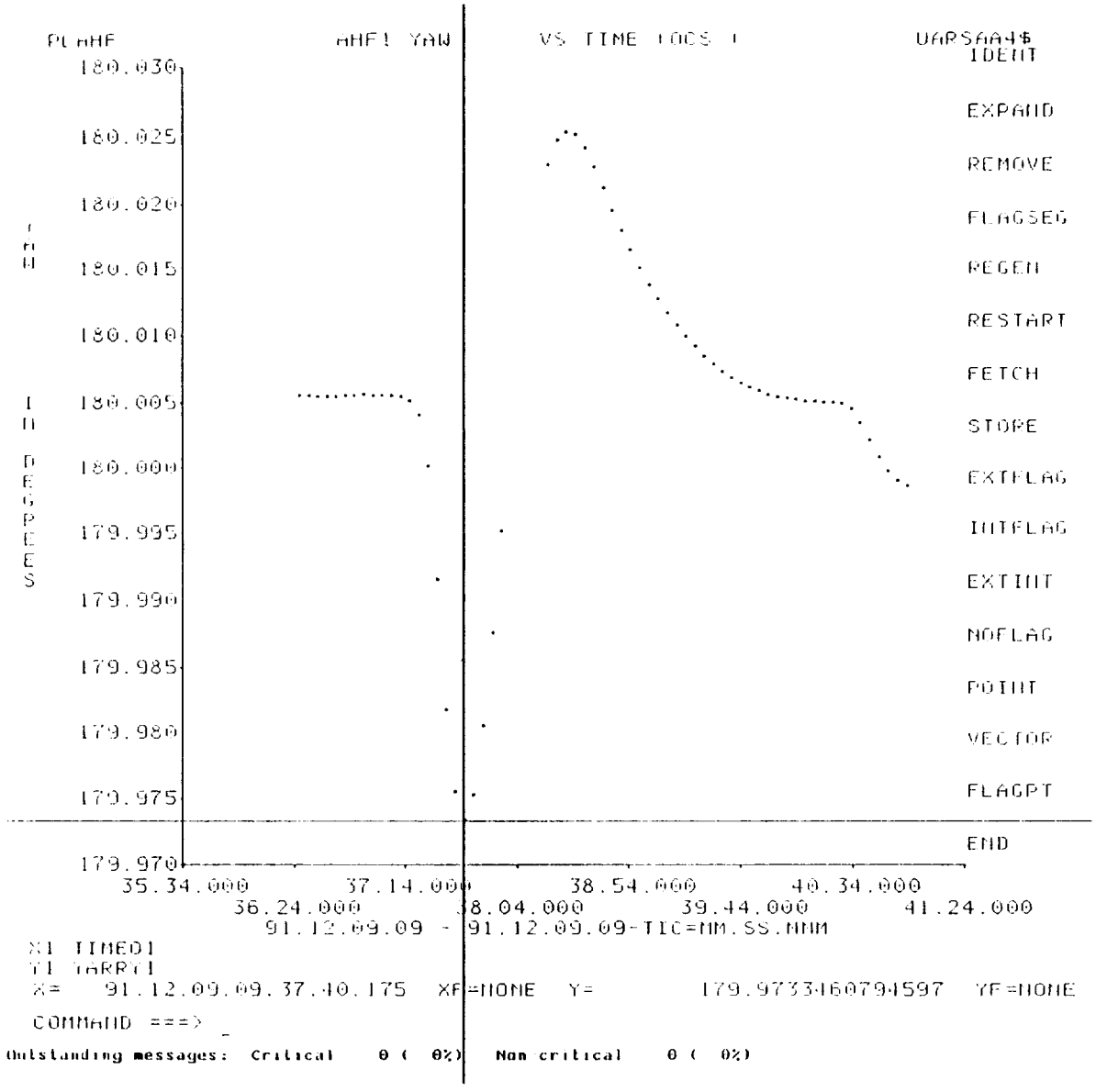

Figure 6. Determination of Maximum Attitude Disturbance

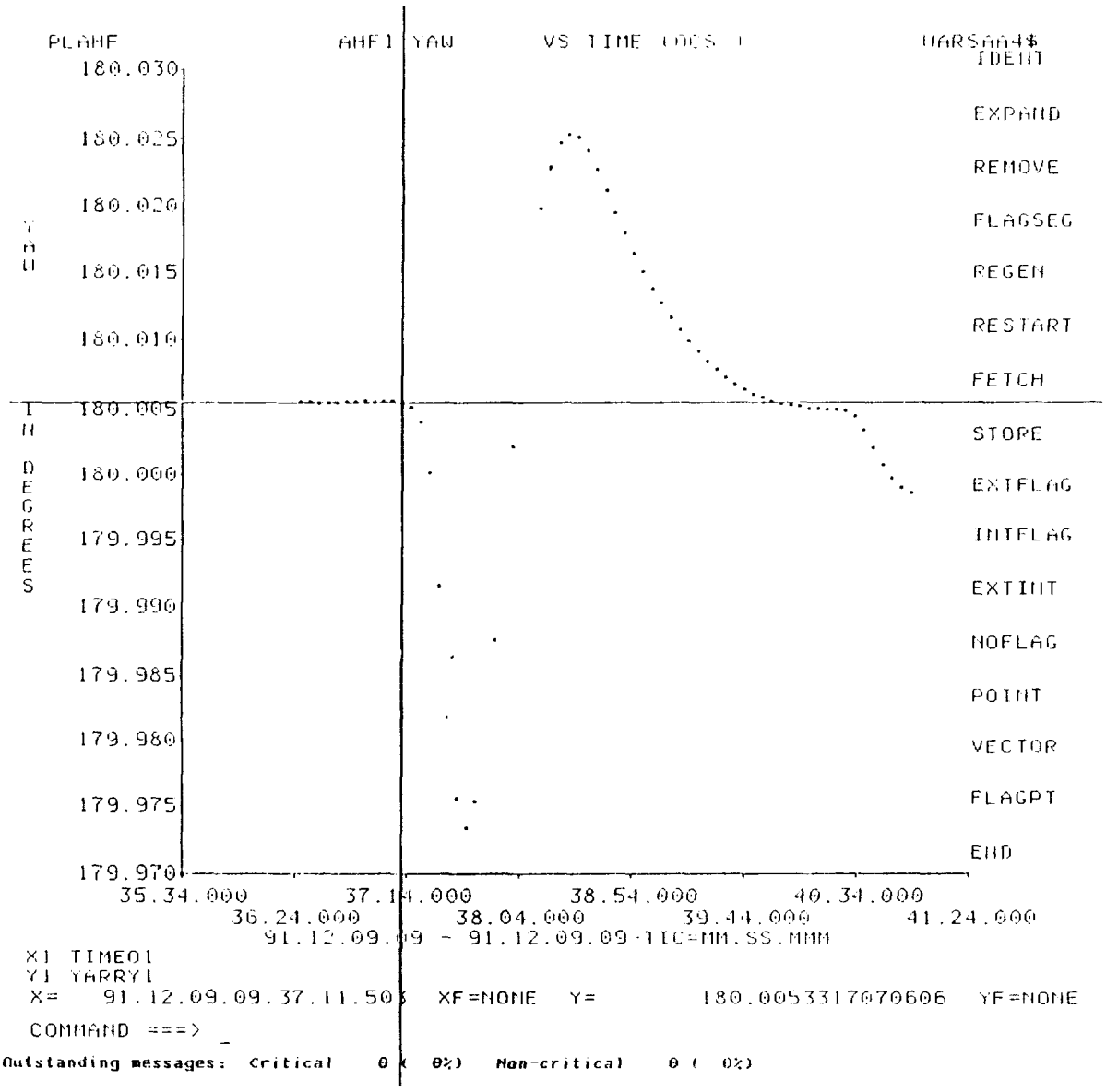

Figure 7. Determination of Baseline Attitude

There are two features in these plots that have not yet been fully explained. First, while the yaw axis shows maximum disturbance at low beta angles (where the total torque should be maximum) as might be expected, the roll axis is disturbed mostly at high beta angles, where the total torque should be falling off. One possible explanation is that, because the solar array drive angle is approaching 90 degrees for high beta angles, more of the total torque should be input to the roll axis, which has a relatively low moment of inertia. Secondly, the roll disturbances for sunset are significantly larger than those for sunrise, while the yaw disturbances are relatively the same. These characteristics of the roll disturbances are likely to be understood only with detailed examination of the control system reaction and possibly with better thermal modeling. It is also possible that there are more dynamics that need to be accounted for, such as motion of the Zenith Energetic Particle experiment boom (in Figure 1, the boom that lies along the Z-axis).

3.3 Timing of Attitude Disturbances

An analysis was undertaken to determine a model for estimating the timing of UARS attitude disturbances due to torques produced by the solar array at sunrise and sunset [Reference 6]. The UARS Flight Dynamics Facility (FDF) attitude task generates a variety of planning aids for the UARS project. Among these aids are predictions of sunrise and sunset times for the spacecraft. More specifically, these are referred to as "zero kilometer" sunset and sunrise events, meaning that the center of the Sun is at the limb of the Earth. When UARS observes a zero-kilometer event, it is at the halfway mark on its path through the penumbra. The peak attitude disturbances as determined above were correlated with the sunrise and sunset times as predicted in the planning aids.

The predicted sunrise and sunset times were then subtracted from the time of maximum initial attitude disturbance for each event. Averages and standard deviations were computed for each event. Because the disturbances in the roll and yaw axes occur at very nearly the same time, only the roll axis plots are included; however, they are valid for the yaw axis as well. The results are tabulated in Table 2 and plotted in Figure 8.

The sunset events show a tendency to move into the day as the beta angle increases. At a beta angle of 0 degrees, the attitude disturbance occurs around 7 seconds after the zero-sunset prediction. At a beta angle of 65 degrees, the snap occurs at 47 seconds prior to the zero-sunset prediction. The sunrise events show a similar tendency to move into the day. At a beta angle of 0, the disturbance occurs about 26 seconds after the zero-sunrise prediction. At a beta of 65 degrees, the disturbance occurs 71 seconds after the prediction.

As noted in Section 2.2, the plots of gradients indicate that the solar snap should occur at the entrance to the penumbra for both sunset and sunrise events. At sunset and sunrise, the spacecraft enters the penumbra increasingly earlier than the zero-kilometer event as the beta angle increases. The data for the sunset events appear to agree with this model; the solar snap occurs increasingly earlier than sunset as the beta angle increases. However, the sunrise events show the opposite behavior: they occur later and later than sunrise as the beta angle increases. It should be remembered that the differences presented here are based on the times of the peak disturbance, which are ultimately determined by the control system. It would be perhaps more correct to examine the predictions in terms of the timing of the "shoulder time" (i.e., the times at which the attitude begins to be disturbed as shown in Figure 7) or in terms of the peak torque due to solar snap. But a casual survey of shoulder times indicates the same trend. A torque analysis had not been completed at the time of this writing. This discrepancy indicates the need for a detailed understanding of the thermal behavior of the array.

3.4 Predicted/Actual Effects on Propagation

The UARS FDF attitude task routinely computes attitude solutions using Fixed-Head Star Tracker (FHST) and digital gyro telemetry in a batch least squares algorithm for confirmation of the attitude computed onboard UARS.

Table 2. Timing of Roll Attitude Disturbance With Respect to Zero-Kilometer Sunset/Sunrise Predictions

SUNSET		
Solar Beta Angle (degrees)	Timing Difference (seconds)*	Standard Deviation (seconds)
0	9	1
6	9	1
18	9	1
35	6	1
44	4	1
56	-7	1
65	-41	4
SUNRISE		
inertia values ($ft.lb.sec^2$)	Timing Difference (seconds)*	Standard Deviation (seconds)
0	26	1
6	26	1
18	26	1
35	29	2
44	31	2
56	40	1
65	71	4

*Maximum attitude disturbance minus predicted zero-km Sunrise/Sunset.

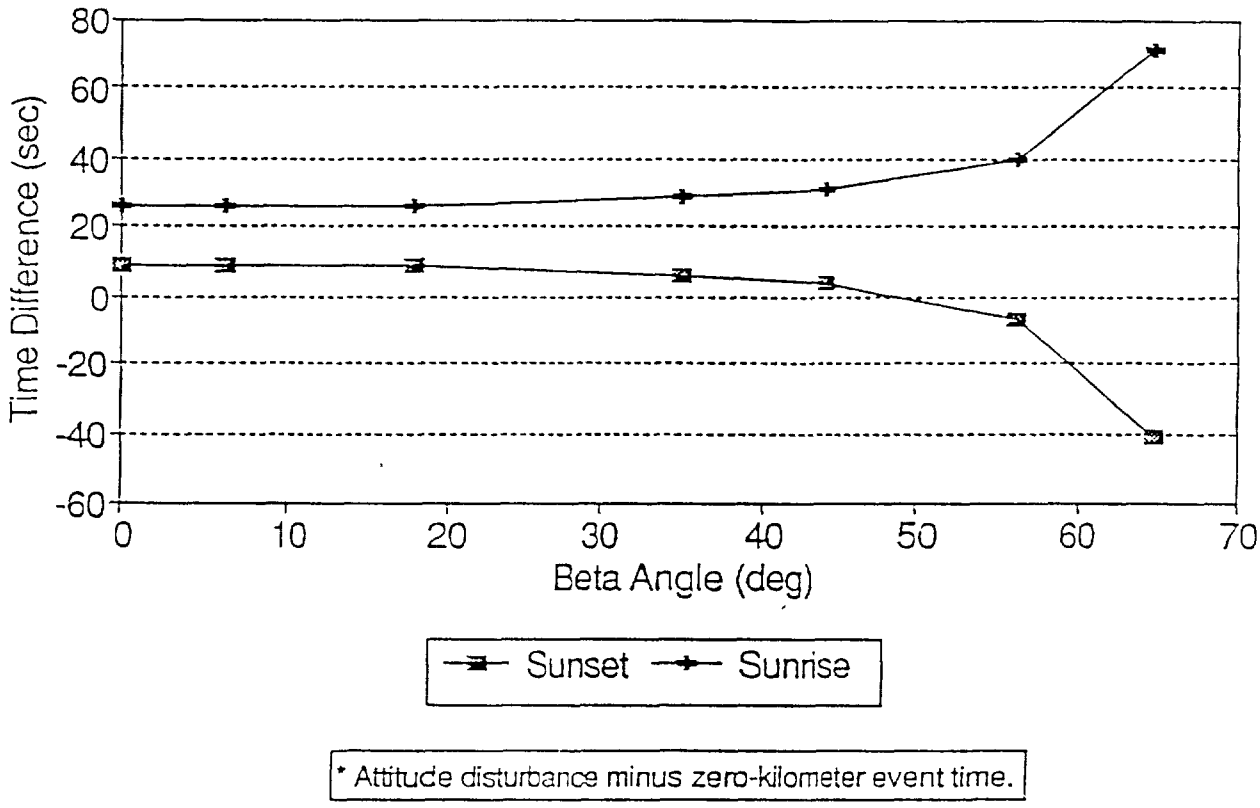

Figure 8. Times of Attitude Disturbance for Sunrise and Sunset versus Solar Beta Angle

To obtain an analytical expression for the attitude propagation matrix, one assumes that the angular velocity is constant over the sampling interval. In reality, there are accelerations in the angular velocities due to a variety of factors. Since the gyro sampling rate is very small, 1/8 second, most of these accelerations do not present a problem. In the case of thermal snap, however, the disturbance is relatively large and occurs over a short period of time (i.e., less than one minute). One concern was that the ground-computed attitudes would not properly model the thermal snap. Errors could even accumulate when spacecraft nights are short.

An analysis was performed to determine whether the attitude ground support system (AGSS) is able to meet the 60-arcsecond-per-axis attitude determination requirement. Attitude solutions for periods just prior to and during sunset were generated using the AGSS. The results were compared with the OBC attitude solutions over the same time period. The magnitude of the residuals from the attitude solutions prior to sunset are of the same magnitude as those during sunset. Table 3 gives the root mean square (RMS) values for the comparison. This indicates that the UARS AGSS is able to propagate attitude solutions during periods of thermal snap without compromising the attitude determination requirements.

Table 3. Comparison of OBC and Ground Attitudes

	RMS VALUES (ARCSEC)		
	Yaw	Roll	Pitch
Before Snap	5	9	27
During Snap	12	12	18

4. CONCLUSIONS

From this analysis and the prelaunch studies, it can be concluded that the attitude disturbances experienced by UARS are caused primarily by bending of the solar arrays as the spacecraft enters and exits sunlight.

The disturbances were predicted to occur for UARS based on its design similarity to the Landsats (i.e., an asymmetric solar array configuration). The disturbances are not reported to the same extent for satellites with smaller solar arrays or more symmetric configurations.

The direction of the attitude discontinuities for UARS confirms that the torque being applied as the spacecraft enters and exits sunlight coincides with the predictions from the model described in Section 2.2. In addition, the magnitude of the thermal snap modeled by the spacecraft builder in References 2 and 5 is a fairly good predictor of what the actual magnitudes are, as described in Sections 3.1 and 3.2.

On the other hand, there remain some questions concerning the magnitude and timing of the disturbances. Specifically, why are sunset roll disturbances so much larger than those at sunrise? Why do the roll disturbances become larger at high beta angles? And why does the timing of the sunrise disturbances appear to be opposite of that predicted? A key to answering these questions may be provided by the TOPEX satellite, which will be flown with temperature sensors on either side of the array, allowing observational checks for the thermal modeling. Jasper and Neste have also proposed using strain gauges for direct measurements of solar array bending.

Whatever the details are of the process taking place, the Landsat-design spacecraft have demonstrated that there is a potential for large attitude disturbances at sunset and sunrise. It is important that this process be better understood. It should be considered in stability analysis for any satellite, even ones with small symmetric arrays.

Because the UARS moments of inertia will continue to decrease (due to cryogen boiloff and propellant use), efforts should be made to determine any trends in the disturbances.

5. ACKNOWLEDGMENTS

The authors are grateful to Don Chu and members of the UARS FDF attitude task for their support and comments: Kenneth Krack, Deborah Foch, Carol Woolsey, Stanley Underwood, Craig Woodruff, and Andrew Garber. One of the authors (M. Lambertson) also is thankful to Daniel Wise of the UARS Flight Operations Team (General Electric) for his insights concerning solar array behavior.

REFERENCES

1. W. Richmond, "Landsat Thermal Snap At Sunrise/Sunset," PIR U-1WOO-UARS-030, General Electric Space Division, January 8, 1985

2. P. E. Jasper and S. Neste, "UARS Solar Array Snap," PIR U-1K21-UARS-481, General Electric Space Division, July 9, 1986

3. D. Freesland, "ACS Transient Response to Solar Array Thermal Bending," PIR U-1K21-UARS-482, General Electric Space Division, June 20, 1986

4. D. F. Zimbleman, et al., "A Technique for Optimal Temperature Estimation for Modeling Sunrise/ Sunset Thermal Snap Disturbance Torque," National Aeronautics and Space Administration Conference Publication 31062, May 1990

5. D. Freesland, "Upper Atmosphere Research Satellite Attitude Determination and Control," American Astronautical Society Conference Paper 92-072, February 1992

6. M. Lambertson, UARS-471-92004, "Timing of Sunrise/Sunset Attitude Disturbances," SEAS QUICKNOTE, Computer Sciences Corporation, January 13, 1992

Upper Atmosphere Research Satellite (UARS) Attitude Accuracy Using Coarse Attitude Sensors

K. Krack, D. Foch, M. Lambertson, C. Woolsey,
S. Underwood, and C. Woodruff

COMPUTER SCIENCES CORPORATION (CSC)

J. Garrick
GODDARD SPACE FLIGHT CENTER (GSFC)

ABSTRACT

The Upper Atmosphere Research Satellite (UARS) uses fixed-head star trackers (FHSTs) and inertial reference units (IRUs) to determine and control its attitude. This combination of fine sensors results in attitude knowledge accuracies to better than 10 arc-seconds (1σ). UARS also has a variety of coarse attitude sensors onboard: the three-axis magnetometer (TAM), the coarse Sun sensor (CSS), the fine Sun sensor (FSS), and the Earth sensor assembly (ESA). By comparing attitude solutions using coarse sensors with FHST-determined attitude solutions, estimates can be made of the accuracy of the coarse sensors. This paper presents the results of an analysis that compares attitude solutions using various combinations of UARS coarse attitude sensor data with FHST attitude solutions.

REPORT DOCUMENTATION PAGE

Form Approved
OMB No. 0704-0188

1. AGENCY USE ONLY *(Leave blank)*	2. REPORT DATE	3. REPORT TYPE AND DATES COVERED
	February 1993	Conference Publication

4. TITLE AND SUBTITLE

Flight Mechanics/Estimation Theory Symposium--1992

5. FUNDING NUMBERS

550

6. AUTHOR(S)

Thomas H. Stengle, Editor

7. PERFORMING ORGANIZATION NAME(S) AND ADDRESS(ES)

Flight Dynamics Division
Goddard Space Flight Center
Greenbelt, Maryland 20771

8. PERFORMING ORGANIZATION REPORT NUMBER

93B00012

9. SPONSORING/MONITORING AGENCY NAME(S) AND ADDRESS(ES)

National Aeronautics and Space Administration
Washington, D.C. 20546-0001

10. SPONSORING/MONITORING AGENCY REPORT NUMBER

NASA CP-3186

11. SUPPLEMENTARY NOTES

T. Stengle is Head, Attitude Analysis Section, Flight Dynamics Analysis Branch at the Goddard Space Flight Center, Greenbelt, Maryland.

12a. DISTRIBUTION/AVAILABILITY STATEMENT

Unclassified - Unlimited
Subject Category 13

12b. DISTRIBUTION CODE

13. ABSTRACT *(Maximum 200 words)*

This conference publication includes 40 papers and abstracts presented at the Flight Mechanics/Estimation Theory Symposium on May 5-7, 1992. Sponsored by the Flight Dynamics Division of Goddard Space Flight Center, this symposium featured technical papers on a wide range of issues related to orbit-attitude prediction, determination and control; attitude sensor calibration; attitude determination error analysis; attitude dynamics; and orbit decay and maneuver strategy. Government, industry, and the academic community participated in the preparation and presentation of these papers.

14. SUBJECT TERMS

Flight Mechanics, Estimation Theory, Attitude Determination, Mission Analysis, Spacecraft Dynamics, Orbit Determination

15. NUMBER OF PAGES

600

16. PRICE CODE

A25

17. SECURITY CLASSIFICATION OF REPORT	18. SECURITY CLASSIFICATION OF THIS PAGE	19. SECURITY CLASSIFICATION OF ABSTRACT	20. LIMITATION OF ABSTRACT
Unclassified	Unclassified	Unclassified	Unlimited

NSN 7540-01-280-5500

Standard Form 298 (Rev. 2-89)
Prescribed by ANSI Std. 239-18, 298-102

NASA-Langley, 1993

PRECEDING PAGE BLANK NOT FILMED